ADVANCES IN BIOMEDICAL AND MOLECULAR NEUROSCIENCE

EDITED BY: Robert J. Harvey, Jochen C. Meier and Christopher Alan Reid
PUBLISHED IN: Frontiers in Molecular Neuroscience,
Frontiers in Cellular Neuroscience,
Frontiers in Behavioral Neuroscience and
Frontiers in Aging Neuroscience

frontiers Research Topics

Frontiers eBook Copyright Statement

The copyright in the text of individual articles in this eBook is the property of their respective authors or their respective institutions or funders. The copyright in graphics and images within each article may be subject to copyright of other parties. In both cases this is subject to a license granted to Frontiers.

The compilation of articles constituting this eBook is the property of Frontiers.

Each article within this eBook, and the eBook itself, are published under the most recent version of the Creative Commons CC-BY licence. The version current at the date of publication of this eBook is CC-BY 4.0. If the CC-BY licence is updated, the licence granted by Frontiers is automatically updated to the new version.

When exercising any right under the CC-BY licence, Frontiers must be attributed as the original publisher of the article or eBook, as applicable.

Authors have the responsibility of ensuring that any graphics or other materials which are the property of others may be included in the CC-BY licence, but this should be checked before relying on the CC-BY licence to reproduce those materials. Any copyright notices relating to those materials must be complied with.

Copyright and source acknowledgement notices may not be removed and must be displayed in any copy, derivative work or partial copy which includes the elements in question.

All copyright, and all rights therein, are protected by national and international copyright laws. The above represents a summary only. For further information please read Frontiers' Conditions for Website Use and Copyright Statement, and the applicable CC-BY licence.

ISSN 1664-8714
ISBN 978-2-88974-838-9
DOI 10.3389/978-2-88974-838-9

About Frontiers

Frontiers is more than just an open-access publisher of scholarly articles: it is a pioneering approach to the world of academia, radically improving the way scholarly research is managed. The grand vision of Frontiers is a world where all people have an equal opportunity to seek, share and generate knowledge. Frontiers provides immediate and permanent online open access to all its publications, but this alone is not enough to realize our grand goals.

Frontiers Journal Series

The Frontiers Journal Series is a multi-tier and interdisciplinary set of open-access, online journals, promising a paradigm shift from the current review, selection and dissemination processes in academic publishing. All Frontiers journals are driven by researchers for researchers; therefore, they constitute a service to the scholarly community. At the same time, the Frontiers Journal Series operates on a revolutionary invention, the tiered publishing system, initially addressing specific communities of scholars, and gradually climbing up to broader public understanding, thus serving the interests of the lay society, too.

Dedication to Quality

Each Frontiers article is a landmark of the highest quality, thanks to genuinely collaborative interactions between authors and review editors, who include some of the world's best academicians. Research must be certified by peers before entering a stream of knowledge that may eventually reach the public - and shape society; therefore, Frontiers only applies the most rigorous and unbiased reviews.
Frontiers revolutionizes research publishing by freely delivering the most outstanding research, evaluated with no bias from both the academic and social point of view. By applying the most advanced information technologies, Frontiers is catapulting scholarly publishing into a new generation.

What are Frontiers Research Topics?

Frontiers Research Topics are very popular trademarks of the Frontiers Journals Series: they are collections of at least ten articles, all centered on a particular subject. With their unique mix of varied contributions from Original Research to Review Articles, Frontiers Research Topics unify the most influential researchers, the latest key findings and historical advances in a hot research area! Find out more on how to host your own Frontiers Research Topic or contribute to one as an author by contacting the Frontiers Editorial Office: frontiersin.org/about/contact

ADVANCES IN BIOMEDICAL AND MOLECULAR NEUROSCIENCE

Topic Editors:
Robert J. Harvey, University of the Sunshine Coast, Australia
Jochen C. Meier, Technische Universitat Braunschweig, Germany
Christopher Alan Reid, University of Melbourne, Australia

Citation: Harvey, R. J., Meier, J. C., Reid, C. A., eds. (2022). Advances in Biomedical and Molecular Neuroscience. Lausanne: Frontiers Media SA.
doi: 10.3389/978-2-88974-838-9

Table of Contents

06 ***Mutation p.R356Q in the Collybistin Phosphoinositide Binding Site Is Associated With Mild Intellectual Disability***
Tzu-Ting Chiou, Philip Long, Alexandra Schumann-Gillett, Venkateswarlu Kanamarlapudi, Stefan A. Haas, Kirsten Harvey, Megan L. O'Mara, Angel L. De Blas, Vera M. Kalscheuer and Robert J. Harvey

19 ***Could an Impairment in Local Translation of mRNAs in Glia be Contributing to Pathogenesis in ALS?***
Samantha K. Barton, Jenna M. Gregory, Siddharthan Chandran and Bradley J. Turner

27 ***Can We Use 2,3,5-Triphenyltetrazolium Chloride-Stained Brain Slices for Other Purposes? The Application of Western Blotting***
Sonia Sanchez-Bezanilla, Michael Nilsson, Frederick R. Walker and Lin Kooi Ong

39 ***Emerging Evidence of Macrophage Contribution to Hyperinnervation and Nociceptor Sensitization in Vulvodynia***
Christine Mary Barry, Dusan Matusica and Rainer Viktor Haberberger

46 ***Secreted Amyloid Precursor Protein-Alpha Promotes Arc Protein Synthesis in Hippocampal Neurons***
Rhys W. Livingstone, Megan K. Elder, Maya C. Barrett, Courteney M. Westlake, Katie Peppercorn, Warren P. Tate, Wickliffe C. Abraham and Joanna M. Williams

63 ***TrkB Agonist LM22A-4 Increases Oligodendroglial Populations During Myelin Repair in the Corpus Callosum***
Huynh T. H. Nguyen, Rhiannon J. Wood, Alexa R. Prawdiuk, Sebastian G. B. Furness, Junhua Xiao, Simon S. Murray and Jessica L. Fletcher

75 ***New Insights Into Cholinergic Neuron Diversity***
Noorya Yasmin Ahmed, Rhys Knowles and Nathalie Dehorter

87 ***Using a Multiplex Nucleic Acid* in situ *Hybridization Technique to Determine HCN4 mRNA Expression in the Adult Rodent Brain***
Julia Oyrer, Lauren E. Bleakley, Kay L. Richards, Snezana Maljevic, A. Marie Phillips, Steven Petrou, Cameron J. Nowell and Christopher A. Reid

100 ***Dimethylethanolamine Decreases Epileptiform Activity in Acute Human Hippocampal Slices* in vitro**
Larissa Kraus, Florian Hetsch, Ulf C. Schneider, Helena Radbruch, Martin Holtkamp, Jochen C. Meier and Pawel Fidzinski

111 ***Pavlovian Olfactory Fear Conditioning: Its Neural Circuity and Importance for Understanding Clinical Fear-Based Disorders***
Marziah Hakim, Andrew R. Battle, Arnauld Belmer, Selena E. Bartlett, Luke R. Johnson and Fatemeh Chehrehasa

121 ***Developmental Expression of Mutant PFN1 in Motor Neurons Impacts Neuronal Growth and Motor Performance of Young and Adult Mice***
Merryn Brettle, Holly Stefen, Aleksandra Djordjevic, Sandra Y. Y. Fok, Josephine W. Chan, Annika van Hummel, Julia van der Hoven, Magdalena Przybyla, Alexander Volkerling, Yazi D. Ke, Fabien Delerue, Lars M. Ittner and Thomas Fath

133 ***The Tripeptide RER Mimics Secreted Amyloid Precursor Protein-Alpha in Upregulating LTP***
Jodi A. Morrissey, Erin Bigus, Julie C. Necarsulmer, Vinay Srinivasan, Katie Peppercorn, Daniel J. O'Leary, Bruce G. Mockett, Warren P. Tate, Stephanie M. Hughes, Karen D. Parfitt and Wickliffe C. Abraham

145 ***The Role of Microglia and Astrocytes in Huntington's Disease***
Thulani H. Palpagama, Henry J. Waldvogel, Richard L. M. Faull and Andrea Kwakowsky

160 ***Imaging and Quantification of Myelin Integrity After Injury With Spectral Confocal Reflectance Microscopy***
David G. Gonsalvez, SangWon Yoo, Jessica L. Fletcher, Rhiannon J. Wood, Georgina A. Craig, Simon S. Murray and Junhua Xiao

173 ***Application of Urine-Derived Stem Cells to Cellular Modeling in Neuromuscular and Neurodegenerative Diseases***
Mitsuto Sato, Hotake Takizawa, Akinori Nakamura, Bradley J. Turner, Fazel Shabanpoor and Yoshitsugu Aoki

182 ***Separating Probability and Reversal Learning in a Novel Probabilistic Reversal Learning Task for Mice***
Jeremy A. Metha, Maddison L. Brian, Sara Oberrauch, Samuel A. Barnes, Travis J. Featherby, Peter Bossaerts, Carsten Murawski, Daniel Hoyer and Laura H. Jacobson

191 ***Dopamine and Noradrenaline in the Brain; Overlapping or Dissociate Functions?***
Yadollah Ranjbar-Slamloo and Zeinab Fazlali

199 ***Analyzing Event-Related Transients: Confidence Intervals, Permutation Tests, and Consecutive Thresholds***
Philip Jean-Richard-dit-Bressel, Colin W. G. Clifford and Gavan P. McNally

209 ***Expanding Clinical Presentations Due to Variations in THOC2 mRNA Nuclear Export Factor***
Raman Kumar, Elizabeth Palmer, Alison E. Gardner, Renee Carroll, Siddharth Banka, Ola Abdelhadi, Dian Donnai, Ype Elgersma, Cynthia J. Curry, Alice Gardham, Mohnish Suri, Rishikesh Malla, Lauren Ilana Brady, Mark Tarnopolsky, Dimitar N. Azmanov, Vanessa Atkinson, Michael Black, Gareth Baynam, Lauren Dreyer, Robin Z. Hayeems, Christian R. Marshall, Gregory Costain, Marja W. Wessels, Julia Baptista, James Drummond, Melanie Leffler, Michael Field and Jozef Gecz

224 ***Building a Human Brain for Research***
Maina Bitar and Guy Barry

229 ***Probing Cortical Activity During Head-Fixed Behavior***
Ann-Sofie Bjerre and Lucy M. Palmer

238 ***Impaired Fluid Intake, but Not Sodium Appetite, in Aged Rats Is Mediated by the Cyclooxygenase-Prostaglandin E_2 Pathway***
Denovan P. Begg, Andrew J. Sinclair and Richard S. Weisinger

244 ***Transgenic Cross-Referencing of Inhibitory and Excitatory Interneuron Populations to Dissect Neuronal Heterogeneity in the Dorsal Horn***
Tyler J. Browne, Mark A. Gradwell, Jacqueline A. Iredale, Jessica F. Maden, Robert J. Callister, David I. Hughes, Christopher V. Dayas and Brett A. Graham

264 ***Functional and Molecular Analysis of Proprioceptive Sensory Neuron Excitability in Mice***
Jessica F. Madden, Olivia C. Davis, Kieran A. Boyle, Jacqueline A. Iredale, Tyler J. Browne, Robert J. Callister, Douglas W. Smith, Phillip Jobling, David I. Hughes and Brett A. Graham

frontiers in Molecular Neuroscience

ORIGINAL RESEARCH
published: 12 March 2019
doi: 10.3389/fnmol.2019.00060

Mutation p.R356Q in the Collybistin Phosphoinositide Binding Site Is Associated With Mild Intellectual Disability

*Tzu-Ting Chiou[1], Philip Long[2], Alexandra Schumann-Gillett[3], Venkateswarlu Kanamarlapudi[4], Stefan A. Haas[5], Kirsten Harvey[2], Megan L. O'Mara[3], Angel L. De Blas[1], Vera M. Kalscheuer[6] and Robert J. Harvey[7,8]**

[1]Department of Physiology and Neurobiology, University of Connecticut, Storrs, CT, United States, [2]Department of Pharmacology, UCL School of Pharmacy, London, United Kingdom, [3]Research School of Chemistry, The Australian National University, Canberra, ACT, Australia, [4]Institute of Life Science, School of Medicine, Swansea University, Singleton Park, Swansea, United Kingdom, [5]Department of Computational Molecular Biology, Max Planck Institute for Molecular Genetics, Berlin, Germany, [6]Group Development and Disease, Max Planck Institute for Molecular Genetics, Berlin, Germany, [7]School of Health and Sport Sciences, University of the Sunshine Coast, Sippy Downs, QLD, Australia, [8]Sunshine Coast Health Institute, Birtinya, QLD, Australia

The recruitment of inhibitory $GABA_A$ receptors to neuronal synapses requires a complex interplay between receptors, neuroligins, the scaffolding protein gephyrin and the GDP-GTP exchange factor collybistin (CB). Collybistin is regulated by protein-protein interactions at the N-terminal SH3 domain, which can bind neuroligins 2/4 and the $GABA_AR$ α2 subunit. Collybistin also harbors a RhoGEF domain which mediates interactions with gephyrin and catalyzes GDP-GTP exchange on Cdc42. Lastly, collybistin has a pleckstrin homology (PH) domain, which binds phosphoinositides, such as phosphatidylinositol 3-phosphate (PI3P/PtdIns3P) and phosphatidylinositol 4-monophosphate (PI4P/PtdIns4P). PI3P located in early/sorting endosomes has recently been shown to regulate the postsynaptic clustering of gephyrin and $GABA_A$ receptors and consequently the strength of inhibitory synapses in cultured hippocampal neurons. This process is disrupted by mutations in the collybistin gene (*ARHGEF9*), which cause X-linked intellectual disability (XLID) by a variety of mechanisms converging on disrupted gephyrin and $GABA_A$ receptor clustering at central synapses. Here we report a novel missense mutation (chrX:62875607C>T, p.R356Q) in *ARHGEF9* that affects one of the two paired arginine residues in the PH domain that were predicted to be vital for binding phosphoinositides. Functional assays revealed that recombinant collybistin $CB3_{SH3\text{-}}{}^{R356Q}$ was deficient in PI3P binding and was not able to translocate EGFP-gephyrin to submembrane microaggregates in an *in vitro* clustering assay. Expression of the PI3P-binding mutants $CB3_{SH3\text{-}}{}^{R356Q}$ and $CB3_{SH3\text{-}}{}^{R356N/R357N}$ in cultured hippocampal neurones revealed that the mutant proteins did not accumulate at inhibitory synapses, but instead resulted in a clear decrease in the overall number of synaptic gephyrin clusters compared to controls. Molecular dynamics simulations suggest that the p.R356Q substitution influences PI3P binding by altering the range of structural

OPEN ACCESS

Edited by:
Verena Tretter,
Medical University of Vienna, Austria

Reviewed by:
Hans Michael Maric,
Universität Würzburg, Germany
Yuchio Yanagawa,
Gunma University, Japan

***Correspondence:**
Robert J. Harvey
r.j.harvey@usc.edu.au

Received: *02 October 2018*
Accepted: *19 February 2019*
Published: *12 March 2019*

Citation:
Chiou T-T, Long P, Schumann-Gillett A, Kanamarlapudi V, Haas SA, Harvey K, O'Mara ML, De Blas AL, Kalscheuer VM and Harvey RJ (2019) Mutation p.R356Q in the Collybistin Phosphoinositide Binding Site Is Associated With Mild Intellectual Disability. Front. Mol. Neurosci. 12:60. doi: 10.3389/fnmol.2019.00060

conformations adopted by collybistin. Taken together, these results suggest that the p.R356Q mutation in *ARHGEF9* is the underlying cause of XLID in the probands, disrupting gephyrin clustering at inhibitory GABAergic synapses *via* loss of collybistin PH domain phosphoinositide binding.

Keywords: *ARHGEF9*, Collybistin, Gephyrin, PH domain, PI3P, XLID

INTRODUCTION

The Dbl-family guanine nucleotide exchange factor collybistin was initially identified as an interactor of the inhibitory postsynaptic clustering protein gephyrin (Kins et al., 2000). Collybistin exists in several splice isoforms differing in the N- or C-termini (CB1-CB3), and the presence or absence of an exon encoding a regulatory SH3 domain (e.g., $CB3_{SH3+}$, $CB2_{SH3-}$; Kins et al., 2000; Harvey et al., 2004). Collybistin variants lacking the SH3 domain (e.g., $CB2_{SH3-}$/$CB3_{SH3-}$) are capable of forming submembrane gephyrin microclusters in cellular models (Kins et al., 2000; Harvey et al., 2004). By contrast, collybistin variants containing SH3 domain (e.g., $CB2_{SH3+}$/$CB3_{SH3+}$) do not trigger clustering, but co-localize with gephyrin in large intracellular aggregates (Kins et al., 2000; Harvey et al., 2004). Later studies revealed that SH3 domain containing variants adopt a closed and autoinhibited conformation that largely prevents membrane binding (Soykan et al., 2014). Since collybistin variants containing SH3 domains predominate in the brain and spinal cord (Harvey et al., 2004; Soykan et al., 2014) this triggered a search for neuronal regulatory proteins that could bind to the SH3 domain and trigger collybistin activity. This resulted in the identification of neuroligin-2 (NL2), neuroligin-4 (NL4) and the $GABA_A$ receptor α2 subunit as collybistin SH3 domain interactors (Poulopoulos et al., 2009; Saiepour et al., 2010; Hoon et al., 2011). The intracellular domains of these proteins contain collybistin-binding motifs that interact with the SH3 domain, triggering collybistin-mediated gephyrin clustering by conformational "opening" of SH3 domain containing collybistin variants. Consistent with these findings, knockout mice lacking collybistin, or collybistin activators, show a brain region specific loss of gephyrin clusters at inhibitory synapses and defects in inhibitory synaptic transmission (Papadopoulos et al., 2007, 2008; Jedlicka et al., 2009, 2011; Poulopoulos et al., 2009; Hoon et al., 2011; Panzanelli et al., 2011). Disruption of collybistin-$GABA_A$ receptor α2 subunit interactions in mice also leads to loss of a subset of inhibitory synapses, spontaneous seizures and early mortality, with surviving animals showing anxiety-like behavior (Hines et al., 2018).

All known collybistin isoforms also contain tandem RhoGEF and pleckstrin-homology (PH) domains. The RhoGEF domain catalyzes GDP-GTP exchange on the small GTPase Cdc42 and also mediates interactions with gephyrin (Xiang et al., 2006). However, the role of RhoGEF activity on Cdc42 in gephyrin clustering is unclear. Gephyrin binding inhibits collybistin activity on Cdc42 (Xiang et al., 2006) implying that gephyrin binding inhibits collybistin GDP-GTP exchange. Moreover, artificial collybistin mutants lacking RhoGEF activity on Cdc42 (T91A, K192A and N232A-N233A) are still capable of inducing the formation of submembrane gephyrin clusters in transfected cells and in cultured hippocampal neurons (Reddy-Alla et al., 2010). Lastly, gephyrin and $GABA_AR$ clustering is not affected by hippocampal deletion of Cdc42 in mice (Reddy-Alla et al., 2010). By contrast, the PH domain plays a more vital role in clustering, since deletion of the collybistin PH domain, or mutation of two key arginine residues (R356/R357) abolishes collybistin-mediated gephyrin clustering in functional assays (Harvey et al., 2004; Kalscheuer et al., 2009; Reddy-Alla et al., 2010). This is because the PH domain and in particular R356/R357 are key determinants of binding of phosphoinositides, including phosphatidylinositol 3-phosphate (PI3P/PtdIns3P; Kalscheuer et al., 2009; Reddy-Alla et al., 2010) and phosphatidylinositol 4-monophosphate (PI4P/PtdIns4P; Ludolphs et al., 2016). Consistent with this view, PI3P located in early/sorting endosomes has recently been shown to regulate the postsynaptic clustering of gephyrin and $GABA_A$ receptors and consequently the strength of inhibitory synapses in cultured hippocampal neurons (Papadopoulos et al., 2017).

The critical role of collybistin in inhibitory synaptic structure and function was confirmed by the discovery of missense and nonsense mutations, deletions and complex re-arrangements affecting the collybistin gene (*ARHGEF9*) in patients with X-linked intellectual disability (XLID; Harvey et al., 2004; Marco et al., 2008; Kalscheuer et al., 2009; Lesca et al., 2011; Shimojima et al., 2011; Lemke et al., 2012; de Ligt et al., 2012; Long et al., 2016; Alber et al., 2017; Klein et al., 2017; Wang et al., 2018). However, the associated clinical phenotypes vary significantly, perhaps depending on whether mutant proteins can act in a dominant-negative manner, or other factors, such as skewed X-inactivation in females or the involvement of other nearby genes in chromosomal deletions or rearrangements (Long et al., 2016; Alber et al., 2017; Aarabi et al., 2018). For example, a p.G55A mutation in the SH3 domain acted in a dominant-negative manner, disrupting gephyrin clustering in transfected cells and neurons by affecting $GABA_AR$ α2 subunit and NL2/NL4 interactions (Harvey et al., 2004; Poulopoulos et al., 2009; Saiepour et al., 2010; Hoon et al., 2011). This mutation was associated with hyperekplexia, early infantile epileptic encephalopathy and severe psychomotor retardation (Harvey et al., 2004). By contrast, a balanced chromosomal translocation resulting in collybistin isoforms that lacked a complete PH domain resulted in disrupted synaptic localization of endogenous gephyrin and $GABA_A$ receptors (Kalscheuer et al., 2009). This mutation was associated with a disturbed sleep-wake cycle, increased anxiety and aggressive behavior. However, more recently a series of missense mutations in *ARHGEF9* have been shown to impact collybistin phosphoinositide binding (Papadopoulos et al., 2015; Long et al., 2016). These include

p.R290H and p.R338W missense mutations in the RhoGEF domain, which were linked to XLID/epilepsy and non-syndromic (NS)-XLID with variable macrocephaly and macro-orchidism, respectively. Substitution p.R290H was predicted to alter the strength of intramolecular interactions between the RhoGEF and PH domains, while p.R338W was predicted to result in clashes with adjacent amino acids (K363 and N335) and disruption of electrostatic potential and local folding of the PH domain. Thus, both mutations *indirectly* result in a loss of PI3P binding affinity and collybistin-mediated gephyrin clustering (Papadopoulos et al., 2015; Long et al., 2016). In this study, we report the identification of a novel pathogenic missense variant in *ARHGEF9* using next-generation sequencing and variant filtering in a family with mild NS-XLID, which was recently included in a case series (Alber et al., 2017). The identified mutation (p.R356Q) *directly* affects one of the two paired arginine residues in the PH domain that are vital for binding phosphoinositides. Using a combination of PI3P binding assays, gephyrin clustering assays, and molecular dynamics simulations, we present compelling evidence that this mutation not only disrupts phosphoinositide binding, but also results in defective gephyrin clustering in both cellular and neuronal models.

MATERIALS AND METHODS

Exon Capture and DNA Sequencing

X-chromosome exome resequencing and bioinformatics analysis was performed as recently described (Hu et al., 2014, 2016). However, for mapping of the 101bp reads BWA (version 0.5.9-r16, maximal mismatches: *-n* 5) was applied, partial mapping was still performed by using SplazerS (Emde et al., 2012). Genomic DNA from the affected male II:8 was used for constructing the sequencing library using the Illumina Genomic DNA Single End Sample Prep kit (Illumina, San Diego, CA, USA). Enrichment of the X-chromosome exome was then performed using the Agilent SureSelect Human X Chromosome Kit (Agilent, Santa Clara, CA, USA). PCR primers for mutation confirmation and segregation analysis were *ARHGEF9*-D228F 5'-TTTTTCCTCCAGCTTCTTGG-3' and *ARHGEF9*-D228R 5'-AACCAACCCCCATTGGTACT-3'. This study was carried out in accordance with the recommendations of the University of Welfare and Rehabilitation Sciences in Iran with written informed consent from all subjects. All subjects gave written informed consent in accordance with the Declaration of Helsinki. The protocol was approved by the University of Welfare and Rehabilitation Sciences in Iran.

Site-Directed Mutagenesis and Expression Constructs

Full-length human collybistin (CB) cDNAs were cloned into the vector pRK5 as previously described (Kalscheuer et al., 2009). Mutations were introduced into pRK5myc-CB3$_{SH3-}$ construct using the QuikChange site-directed mutagenesis kit (Agilent, Santa Clara, CA, USA) and confirmed by Sanger DNA sequencing of the entire coding region.

PI3P Pull-Down Assays

Affinity purification assays using PI3P agarose beads were carried out as described previously (Kanamarlapudi, 2014). Human embryonic kidney 293 (HEK293) cells were grown in DMEM supplemented with 10% (v/v) fetal bovine serum at 37°C, 5% CO_2 and transfected with 4 μg pRK5myc-CB3$_{SH3-}$ (wild-type), pRK5myc-CB3$_{SH3-}^{R356Q}$, pRK5myc-CB3$_{SH3-}^{R290H}$ (XLID mutants) or pRK5myc-CB3$_{SH3-}^{R356N/R357N}$ (artificial phosphoinositide binding site mutant, Reddy-Alla et al., 2010) using JetPrime transection reagent (Polyplus; 2 μl/μg DNA). After 48 h, transfected cells were solubilized in a buffer containing 0.5% (v/v) Nonidet P-40, 150 mM NaCl, 50 mM Tris pH 7.4 and protease inhibitor cocktail (Sigma). Insoluble material was removed by centrifugation at 16,100× *g* for 20 min. Phosphatidylinositol-3-phosphate (PI3P/PtdIns3P) agarose beads (40 μl; Eschelon Biosciences) were incubated with cell lysates for 2 h at 4°C, followed by washing four times in buffer. Proteins were eluted from beads by heating at 98°C for 3 min in 2× sample loading buffer and then subjected to SDS-PAGE. Proteins binding to beads were detected by Western blotting using mouse anti-c-myc antibody (Sigma, 1:1000) and HRP-conjugated goat anti-mouse (Santa Cruz, 1:2000). Immunoreactivity was visualized using West Pico Chemiluminescent Substrate (Pierce). Quantification of PI3P pulldown assay results for myc-CB3$_{SH3-}$, myc-CB3$_{SH3-}^{R356Q}$, myc-CB3$_{SH3-}^{R290H}$ and myc-CB3$_{SH3-}^{R356N/R357N}$ was performed in triplicate and differences in PI3P binding were assessed using an unpaired, two-tailed Student's *t*-test.

In vitro Gephyrin Clustering Assays

These were performed essentially as previously described (Long et al., 2016). HEK293 cells were co-transfected with the pRK5myc-hCB3$_{SH3-}^{R356Q}$ construct at a 1:1 ratio with pEGFP-gephyrin using electroporation (Gene Pulser II, Bio-Rad). Cells were fixed after 24 h for 2 min in 4% (w/v) PFA in PBS. Immunostaining to detect collybistin was performed using a mouse anti-c-myc antibody (1:200, Sigma) and detected using an AlexaFluor 546 goat anti-mouse secondary antibody (1:600; Invitrogen). Counterstaining for cell nuclei was performed with DAPI (1:500; Life Technologies). Confocal microscopy was performed using a Zeiss LSM 710 META. All images were taken with a ×63 objective.

Neuronal Cell Culture, Transfections and Immunofluorescence

The sheep anti-GAD (lot 1440-4) antibody was a gift from Dr. Irwin J. Kopin (NINDS, Bethesda, MD, USA). This antibody, raised against purified rat GAD, recognizes a 65-kDa protein in rat brain immunoblots. The antibody precipitated GAD from rat brain and detected purified GAD in crossed immunoelectrophoresis (Oertel et al., 1981). The Rb antibody to gephyrin (catalog # 261003) was from Synaptic Systems (Gottingen, Germany). The mouse mAb to cMyc was from Millipore (Temecula, CA; clone 4A6, catalog no.05–724). Fluorophore-labeled species-specific anti-IgG cross-adsorbed secondary antibodies were made in donkey. The fluorescein isothiocyanate (FITC), or aminomethylcoumarin

were from Jackson ImmunoResearch Laboratories, West Grove, PA and the AlexaFluor 594 was from Invitrogen. Hippocampal (HP) neuronal cultures were prepared according to Goslin et al. (1998) as described elsewhere (Christie et al., 2002a,b; Christie and De Blas, 2003). Briefly, dissociated neurons from embryonic day 18 (E18) rat hippocampi were plated (10,000–20,000 cells per 18 mm diameter coverslip) and maintained in rat glial cell conditioned medium. HP neurons (10 DIV) cultures were transfected with 1 μg of plasmid using the CalPhos Mammalian Transfection Kit (BD Biosciences, San Jose, CA, USA), according to the instructions provided by the manufacturer. Cultures were fixed 72 h later, permeabilized and subjected to immunofluorescence as described elsewhere (Christie et al., 2002a,b; Li et al., 2010, 2012; Chiou et al., 2011; Fekete et al., 2015). Fluorescence images of cultured hippocampal neurons were collected using a Nikon Plan Apo 60×/1.40 objective on a Nikon Eclipse T300 microscope with a Photometrics CoolSNAP HQ2 CCD camera driven by IPLab 4.0 (Scanalytics, Rockville, MD) acquisition software. Images were processed with Photoshop 7.0 (Adobe, San Jose, CA), adjusting brightness and contrast, as described elsewhere (Christie et al., 2002b; Li et al., 2005).

Molecular Dynamics Simulations

Molecular dynamics (MD) simulations were performed using the GROMACS engine, version 2016.1 in conjunction with the GROMOS54A7 force field (Schmid et al., 2011; Abraham et al., 2015). The coordinates and parameters for PI3P were developed using the Automated Topology Builder (ATB) and Repository (Malde et al., 2011; Koziara et al., 2014) and are available for download from the ATB (molecule ID: 294885). The coordinates for the open conformation, wild-type collybistin ($CB1_{SH3-}$) were taken from the protein data bank (PDB ID: 4MT7). The p.R356Q substitution was introduced computationally to produce a structural model of the collybistin mutant p.R356Q (collybistin^{R356Q}). The PI3P head group was docked to both wild-type and mutant collybistin using Autodock vina (Trott and Olson, 2010) in the vicinity of R356, to provide a range of putative interaction conformations. The lowest energy docked conformation was used as a template to rebuild the intact PI3P molecule prior to MD simulations. Two separate systems were used to initiate MD simulation: PI3P complexed with wild-type collybistin and PI3P complexed with collybistin^{R356Q}. Each system was explicitly solvated with SPC water molecules and Na^+ counter-ions were added to ensure the overall charge neutrality of the system. A detailed description of the system set-up is provided as **Supplementary Information**. After energy minimization and equilibration, each system was simulated in triplicate for 200 ns. Following MD simulation, the triplicate simulations from the PI3P/collybistin system were combined to give a 600 ns trajectory containing 1,200 frames. Cluster analysis was performed on the backbone structure of the collybistin protein using the clustering algorithm described by Daura et al. (1999). Protein conformations were grouped using a 2.5 Å distance cut-off. Here, two conformations were considered to fall within the same cluster if the backbone RMSD between the conformations was less than the specified cut-off of 2.5 Å. This procedure was repeated for the PI3P/collybistin^{R356Q} system. The central (median) conformation from the top two most populated conformational clusters for the PI3P/collybistin system and the PI3P/collybistin^{R356Q} system were taken as representative conformations of PI3P-bound collybistin and collybistin^{R356Q}. Protein residues within 3 Å of PI3P were considered binding residues and were determined using the Visual Molecular Dynamics (VMD) software (Humphrey et al., 1996).

RESULTS

Identification of a p.R356Q Mutation in *ARHGEF9*

The three affected males from this family presented with mild NS XLID (**Figure 1A**) without seizures, neurologic, ocular or other phenotypes. X-chromosome exome resequencing of individual II:8 followed by bioinformatics analysis and filtering against public datasets revealed four novel missense changes: *ARHGEF9*, chrX:62875607C>T, p.R356Q (**Figures 1B–D**), consensus score 5.13, predicted as probably damaging (PolyPhen-2; Adzhubei et al., 2013) and damaging (SIFT; Kumar et al., 2009) with a CADD score (Kircher et al., 2014) of 26; *CCDC22*, chrX: 49105321A>G, p.A492G with a conservation score of 5.56 and predicted as benign (Polyphen-2) and tolerated (SIFT) and CADD of 18; *FAM3A*, chrX:153736880T>C, p.E37G with a conservation score 2.67 and predicted as benign and tolerated and CADD of 15; *GLUD2*, chrX:120181572T>C, p.S12P with a low conservation score (0.06) and predicted as benign and damaging with a CADD score of 11. This strongly suggested that one of the novel missense variants identified in the established XLID genes *ARHGEF9* (Harvey et al., 2004; Marco et al., 2008; Kalscheuer et al., 2009; Lesca et al., 2011; Shimojima et al., 2011; Lemke et al., 2012; de Ligt et al., 2012; Long et al., 2016; Alber et al., 2017; Klein et al., 2017; Wang et al., 2018) and *CCDC22* (Voineagu et al., 2012; Kolanczyk et al., 2015) or a combination of both could be responsible for XLID in this family. Subsequent segregation analysis using Sanger DNA sequencing indicated that both variants were present in the three affected males (**Figures 1A–D**), and in heterozygous form in their mother, whereas the unaffected brother did not have these variants. Thus, both variants co-segregated with the XLID phenotype in all individuals tested. We subsequently performed functional assays on the *ARHGEF9* missense mutation, which had the highest CADD score.

XLID Mutation p.R356Q Disrupts PH Domain—PI3P Interactions and Collybistin-Mediated Gephyrin Clustering in Cellular Assays

Collybistin has a multi-domain structure consisting of a regulatory SH3 domain, a catalytic RhoGEF domain and a PH domain (**Figure 1E**). Substitution p.R356Q is the first reported *ARHGEF9* missense mutation affecting a highly-conserved phosphoinositide-binding residue in the PH domain (**Figure 1F**). In order to determine whether the p.R356Q mutation affected collybistin binding to PI3P, we performed

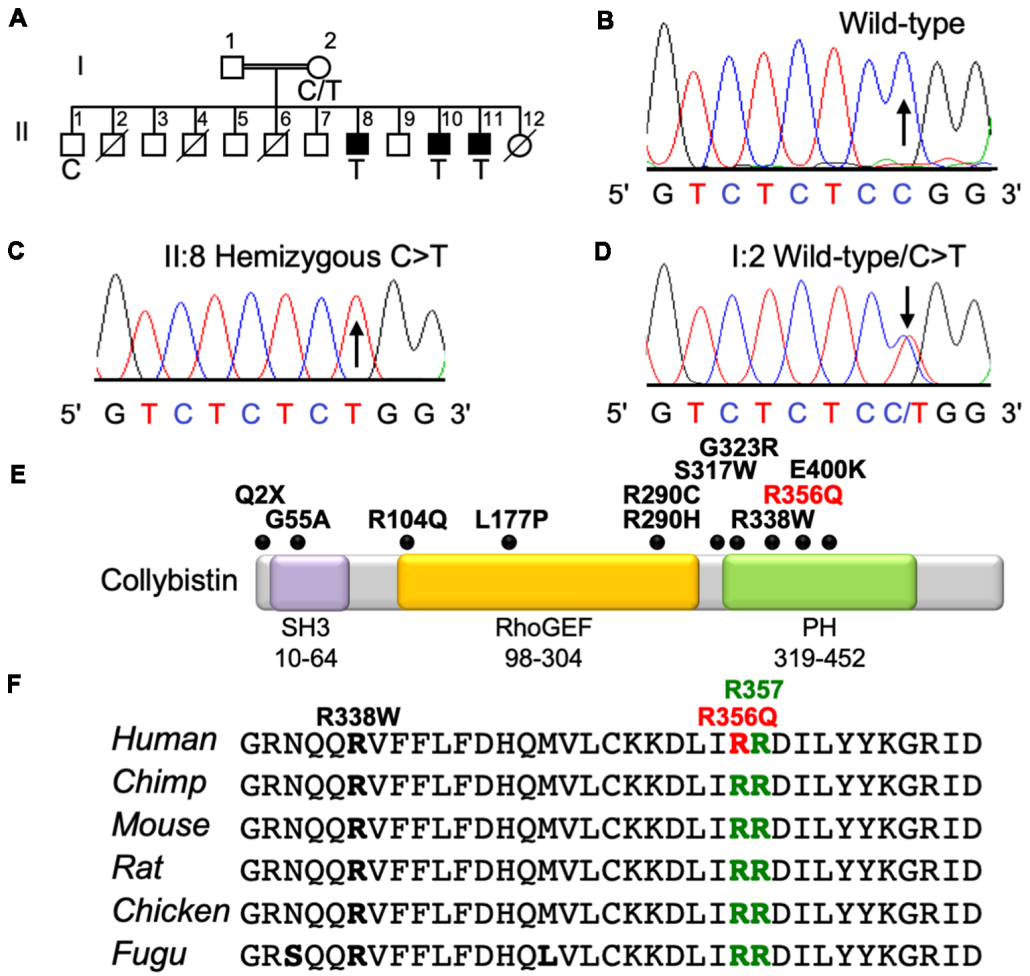

FIGURE 1 | Identification of a p.R356Q mutation in *ARHGEF9* in family D228. **(A)** Pedigree of the D228 family. Open symbols represent normal individuals, filled squares represent affected males. Individuals who are deceased have a slash through the symbol. Individuals tested for the nucleotide substitution in each family are indicated with either a T (mutant allele) or a C (normal allele). **(B–D)** DNA sequence electropherograms for the chrX:62875607C>T, p.R356Q variant reported in this study, showing wild-type, hemizygous and heterozygous states. **(E)** Schematic of the human collybistin protein with a regulatory SH3 domain, a catalytic RhoGEF domain and a pleckstrin homology (PH) domain. The relative locations of known missense and nonsense variants in *ARHGEF9* are shown. **(F)** Sequence alignments of collybistin proteins from various species showing the high conservation of R356 in the PH domain. R356 is one of two predicted PI3P binding residues (R356 and R357, green highlighting).

pulldown assays (**Figures 2A,B**) using PI3P immobilized on agarose beads incubated with lysates of HEK293 cells transfected with either tagged wild-type collybistin (myc-$CB3_{SH3-}$), the new mutant myc-$CB3_{SH3-}^{R356Q}$, a known human XLID mutant known to be deficient in PI3P binding (myc-$CB3_{SH3-}^{R290H}$; Papadopoulos et al., 2015) or an artificial phosphoinositide binding site mutant myc-$CB3_{SH3-}^{R356N/R357N}$ (Reddy-Alla et al., 2010). A significant reduction of PI3P binding was observed for myc-$CB3_{SH3-}^{R356Q}$ (7.62 ± 0.97), myc-$CB3_{SH3-}^{R290H}$ (8.73 ± 0.79) and myc-$hCB3_{SH3-}^{R356N/R357N}$ (3.41 ± 0.85) compared to wild-type collybistin (**Figures 2B,C**; pull-down fraction ± SEM, $n = 3$, $p < 0.0001$, unpaired student's t-test). Given the key role of collybistin in gephyrin clustering at inhibitory synapses, we also investigated whether the p.R356Q substitution influenced collybistin-mediated translocation of EGFP-gephyrin to submembrane microaggregates in a cellular clustering assay (Harvey et al., 2004; Kalscheuer et al., 2009; Long et al., 2016). Collybistin variants containing the regulatory SH3 domain (e.g., myc-$CB3_{SH3+}$) typically co-localize with EGFP-gephyrin in large intracellular aggregates (Kins et al., 2000; Harvey et al., 2004; Kalscheuer et al., 2009; Long et al., 2016) and require neuroligin 2/4, $GABA_AR$ α2 or the GTPase TC10 for activation (Poulopoulos et al., 2009; Saiepour et al., 2010; Mayer et al., 2013). By contrast, variants lacking the N-terminal SH3 domain (e.g., myc-$CB3_{SH3-}$) result in the formation of submembrane EGFP-gephyrin clusters (Kins et al., 2000; Harvey et al., 2004; Kalscheuer et al., 2009; Long et al., 2016; **Figures 2D–G**). On co-expression with EGFP-gephyrin, myc-$CB3_{SH3-}^{R356Q}$ was not capable of forming submembrane microaggregates, but co-localized

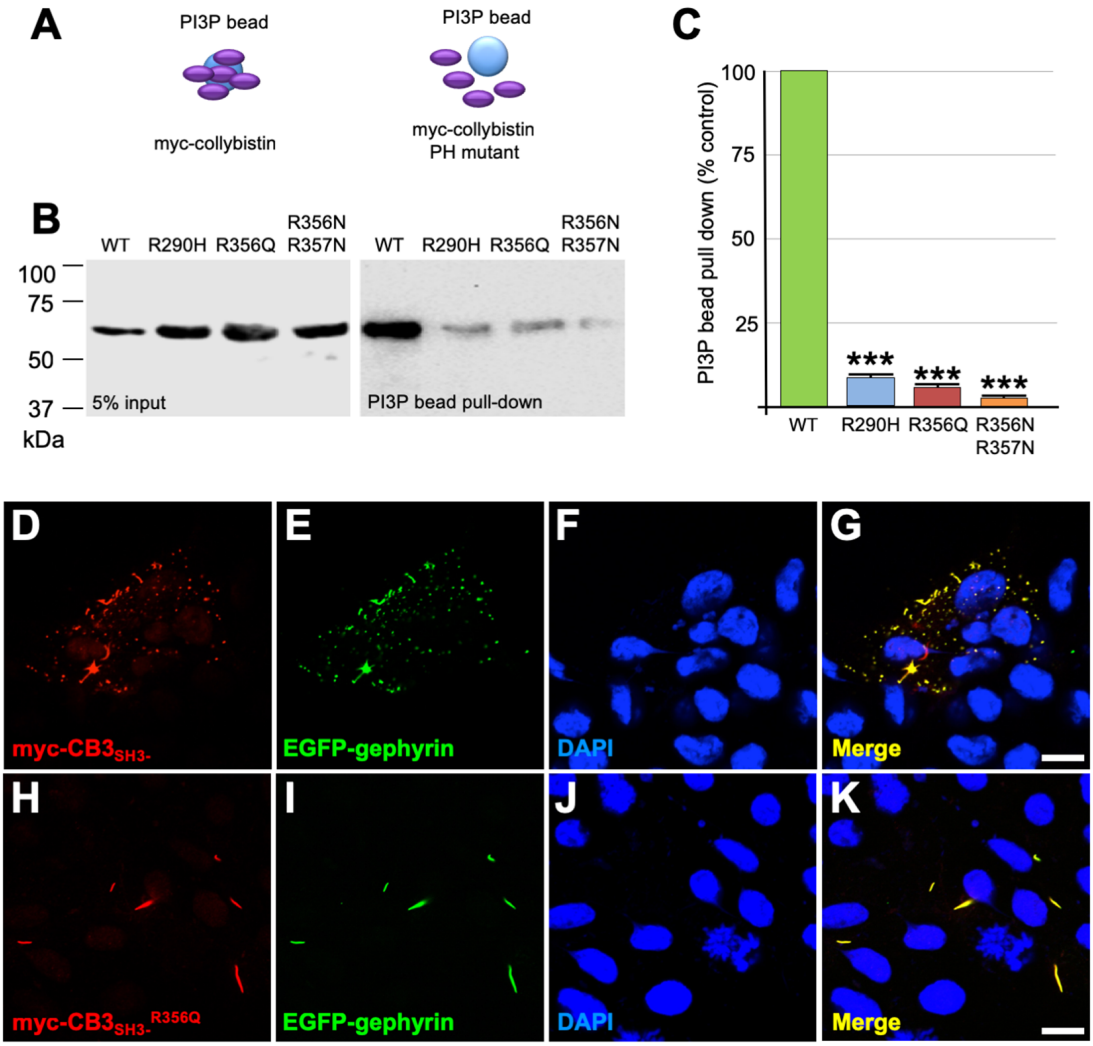

FIGURE 2 | R356Q reduces collybistin PI3P binding and gephyrin cluster formation in cellular assays. **(A,B)** Human embryonic kidney 293 (HEK293) cells were transfected with plasmids encoding myc-CB3$_{SH3-}$ (wild-type, WT), myc-CB3$_{SH3-}^{R356Q}$ (R356Q), myc-CB3$_{SH3-}^{R290H}$ (R290H) or myc-CB3$_{SH3-}^{R356Q}$ (R356N/R357N) and cell lysates were incubated with PI3P-conjugated agarose beads. After washing, bound material was subjected to SDS-PAGE and analyzed by immunoblotting with an anti-myc antibody (Sigma). No significant differences were observed in total level of myc-CB3$_{SH3-}^{R356Q}$, myc-CB3$_{SH3-}^{R290H}$ or myc-CB3$_{SH3-}^{R356N/R357N}$ expression in comparison with myc-CB3$_{SH3-}$ (left panel, 5% input protein). However, myc-CB3$_{SH3-}^{R356Q}$ myc-CB3$_{SH3-}^{R290H}$ and myc-CB3$_{SH3-}^{R356N/R357N}$ binding to PI3P was significantly reduced (right panel, PI3P bead pull-down). **(C)** Quantification of PI3P pull-down assays normalized to wild-type myc-CB3$_{SH3-}$: myc-CB3$_{SH3-}^{R290H}$: 8.73 ± 0.79, 1.37; myc-CB3$_{SH3-}^{R356Q}$: 7.62 ± 0.97, 1.68; myc-hCB3$_{SH3-}^{R356N/R357N}$: 3.41 ± 0.85, 1.47; pull-down fraction ± SEM, SD; $n = 3$, *** $p < 0.0001$, unpaired student's *t*-test. **(D–K)** HEK293 cells were co-transfected with EGFP-gephyrin and either wild-type myc-CB3$_{SH3-}$ or mutant myc-CB3$_{SH3-}^{R356Q}$, immunostained using anti-myc and AlexaFluor 546 antibodies and co-stained with a nuclear marker (DAPI). Note that while wild-type myc-CB3$_{SH3-}$ (red) co-localizes with gephyrin (green) in submembrane microaggregates **(D–G)**, mutant myc-CB3$_{SH3-}^{R356Q}$ (red) co-localizes with EGFP-gephyrin (green) in elongated cytoplasmic aggregates **(H–K)**, consistent with a lack of CB-mediated gephyrin clustering activity for the p.R356Q mutant. Scale bar = 10 μm.

with EGFP-gephyrin in elongated cytoplasmic aggregates (**Figures 2H–K**). This distribution is similar to that previously observed for collybistin variants lacking the PH domain (Harvey et al., 2004) or containing missense mutations that disrupt PI3P binding, such as p.R290H, p.R338W and p.R356N/R357N (Reddy-Alla et al., 2010; Papadopoulos et al., 2015; Long et al., 2016). These results demonstrate that the p.R356Q substitution disrupts both collybistin PI3P binding and collybistin-mediated accumulation of EGFP-gephyrin in submembrane microclusters.

Collybistin Phosphoinositide Binding Mutants p.R356Q and p.R356N/R357N Alter Gephyrin Cluster Number and Size in Cultured Hippocampal Neurones

To assess the impact of the p.R356Q mutation on collybistin-mediated neuronal gephyrin clustering, we overexpressed either wild-type myc-CB3$_{SH3-}$, myc-CB3$_{SH3-}^{R356Q}$ or the artificial PI3P binding mutant myc-CB3$_{SH3-}^{R356N/R357N}$ in primary cultures of rat hippocampal neurons. Previous studies in this neuronal

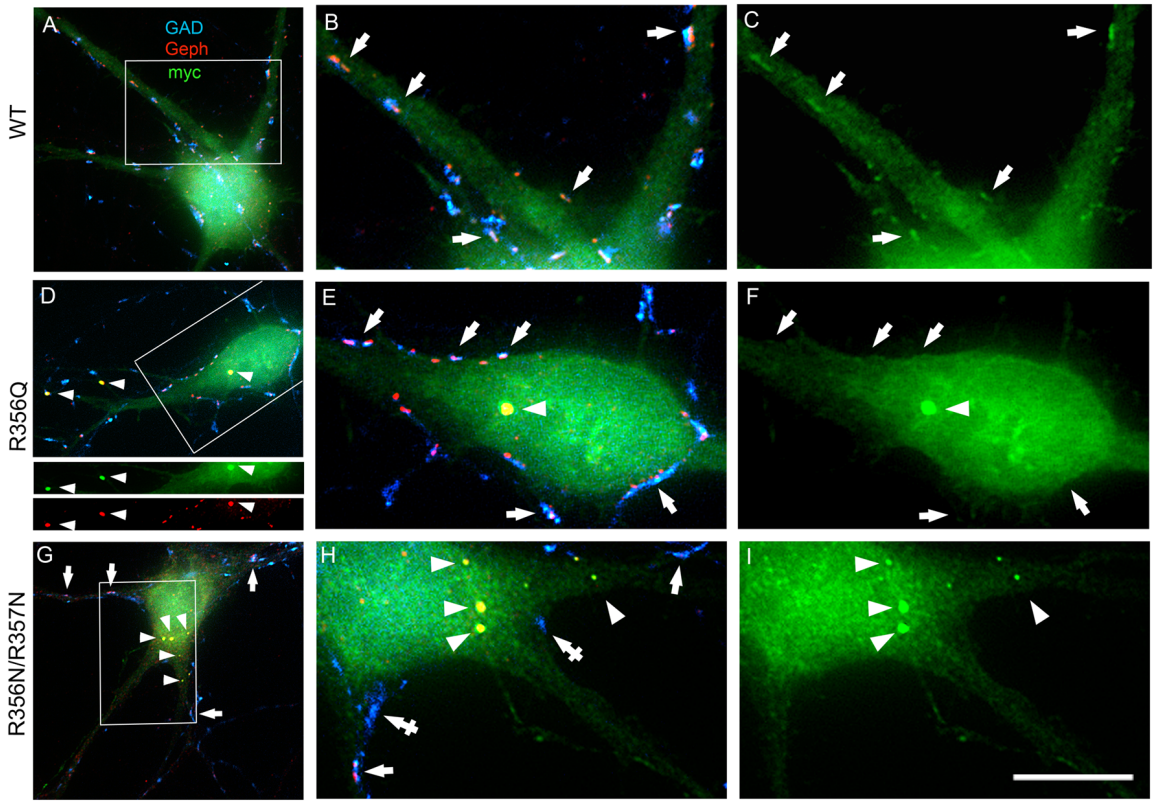

FIGURE 3 | Collybistin phosphoinositide binding mutants R356Q and R356N/R357N alter gephyrin cluster number and size in cultured hippocampal neurones. Triple-label immunofluorescence of transfected hippocampal neurons with mouse anti-myc (green), rabbit anti-gephyrin (red) and sheep anti-GAD (blue). **(A–C)** Transfection with myc-$CB3_{SH3-}$ (wild-type, WT). **(D–F)** Transfection with myc-$CB3_{SH3-}^{R356Q}$ (R356Q). **(G–I)** Transfection with myc-$CB3_{SH3-}^{R356N/R357N}$ (R356N/R357N). The two panels on the right side of each row correspond to the boxed areas in **(A,D,G)**, respectively. Arrows point to GABAergic synapses. Arrowheads point to aggregates of gephyrin that form in transfections with collybistin R356Q or R356N/R357N. Note that there is colocalization of mutant collybistin and gephyrin in these aggregates. Wild-type collybistin does not induce the formation of aggregates but accumulates at GABAergic synapses and colocalizes with gephyrin (arrows, panel **C**). The R356Q and the R356N/R357N mutants do not accumulate at synapses (arrows, panels **F,I**). The R356N/R357N mutant (panels **H,I**) shows a clear decrease in the overall number of gephyrin clusters, including synaptic gephyrin clusters. In neurons overexpressing the R356N/R357N mutant, GAD positive puncta often make contacts without apposed gephyrin clusters (crossed arrows). Scale bar = 26 μm for **(A,D,G)** and 10 μm for **(B,C,E,F,H,I)**.

expression system have shown that wild-type recombinant collybistin isoforms (e.g., $CB2_{SH3+}$, $CB2_{SH3-}$, $CB3_{SH3+}$, and $CB3_{SH3-}$) target to and concentrate at GABAergic postsynapses (Chiou et al., 2011). Notably, isoforms lacking the SH3 domain (e.g., $CB2_{SH3-}$ and $CB3_{SH3-}$) induce the formation of synaptic gephyrin superclusters (Chiou et al., 2011; Fekete et al., 2017) that are accompanied by a significant increase in the amplitude of miniature inhibitory postsynaptic currents (mIPSCs). In this study, we utilized triple-label immunofluorescence with mouse anti-myc, rabbit anti-gephyrin and sheep anti-GAD to reveal exogenous wild-type and mutant collybistin, native gephyrin and GAD, respectively (**Figures 3A–C**). As expected, overexpressed wild-type collybistin (myc-$CB3_{SH3-}$; **Figures 3A–C**) accumulated at GABAergic synapses, colocalizing with gephyrin and GAD65 (**Figures 3B,C**, arrows). By contrast, overexpression of myc-$CB3_{SH3-}^{R356Q}$ and myc-$CB3_{SH3-}^{R356N/R357N}$ (**Figures 3D–I**) resulted in the formation of non-synaptic aggregates (**Figures 3D–I**, arrowheads) characterized by a circular shape and bright fluorescence. Mutant myc-$CB3_{SH3-}^{R356Q}$ and myc-$CB3_{SH3-}^{R356N/R357N}$ in these aggregates co-localized with gephyrin (see, e.g., **Figure 3D**, lower panels) but did not associate with GAD-positive terminals (**Figures 3D–I**). Hence, myc-$CB3_{SH3-}^{R356Q}$ and myc-$CB3_{SH3-}^{R356N/R357N}$ do not accumulate at inhibitory synapses (arrows in **Figures 3F,I**). We also noted that in neurons overexpressing the myc-$CB3_{SH3-}^{R356N/R357N}$ mutant, GAD-positive puncta often make contacts without apposed gephyrin clusters (**Figure 3H**, crossed arrows)—an effect that was not seen for myc-$CB3_{SH3-}$ or myc-$CB3_{SH3-}^{R356Q}$.

We also assessed the effect of wild-type and mutant collybistin isoforms on synaptic gephyrin cluster density (**Figure 4A**) and size (**Figure 4B**), excluding the large non-synaptic gephyrin/mutant aggregates (for myc-$CB3_{SH3-}^{R356Q}$ and myc-$CB3_{SH3-}^{R356N/R357N}$) from this analysis. No significant differences in cluster density were observed comparing non-transfected neurones with those expressing wild-type myc-$CB3_{SH3-}$ (non-transfected = 9.33 ± 0.33 vs. myc-$CB3_{SH3-}$ = 8.73 ± 0.88; mean clusters/100 μm^2 ± SEM). However, gephyrin cluster density was significantly decreased for myc-$CB3_{SH3-}^{R356Q}$

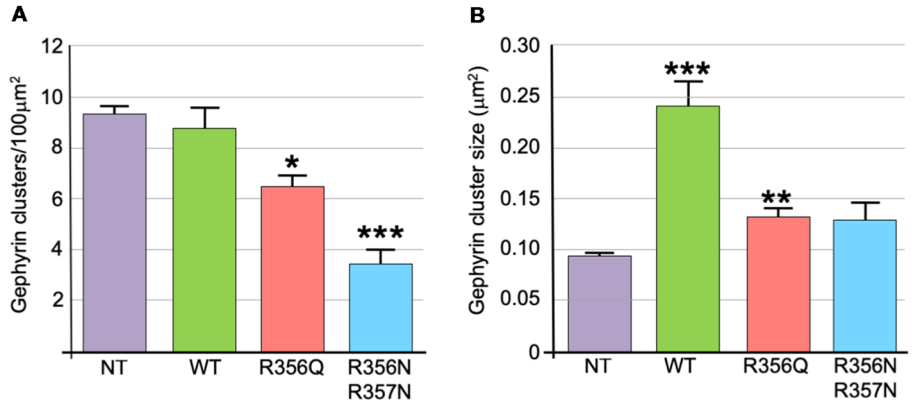

FIGURE 4 | Quantification of gephyrin cluster number and cluster size for wild-type collybistin and mutants R356Q and R356N/R357N in cultured hippocampal neurones. **(A)** To quantify the effect of these mutants, we measured gephyrin cluster density/100 μm^2 in non-transfected neurones (NT = 9.33 ± 0.33, 1.04) and neurones transfected with wild-type collybistin (WT = 8.73 ± 0.88, 2.77) and collybistin phosphoinositide binding mutants (R356Q = 6.42 ± 0.52, 1.65; R356N/R357N = 3.37 ± 0.63, 1.99; mean ± SEM, SD). The gephyrin cluster density was decreased for R356Q but not as much as for R356N/R357N, $*p < 0.05$; $***p < 0.001$ for each mutant respectively compared with either NT or WT, $n = 10$ neurons each. The total number of clusters counted for density were 283, 273, 189 and 99 for NT, WT, R356Q and R356N/R357N, respectively. For quantification of cluster density, two independent transfections were made for each construct, and all constructs were used in each experiment. A total of 60 dendritic fields (50 μm^2 each) per construct from 10 randomly selected neurons (10 neurons/construct, 3 dendrites/neuron, 2 dendritic fields/dendrite) were analyzed. **(B)** Gephyrin cluster size was NT = 0.095 ± 0.003, 0.011; WT = 0.240 ± 0.024, 0.076; R356Q = 0.132 ± 0.008, 0.026; R356N/R357N = 0.129 ± 0.016, 0.051. Values are mean ± SEM, SD / μm^2, $n = 10$ neurons each. For quantification of cluster size, two independent transfections were made for each construct, and all constructs were used in each experiment. $***p < 0.001$ for WT with each of the other plasmids; $**p < 0.01$ for R356Q compared with NT indicates a slight increase in cluster size in this mutant. The total number of clusters counted for size were 680, 584, 492 and 180 for NT, WT, R356Q and R356N/R357N, respectively. No significant difference was observed for R356N/R357N compared with NT or R356Q. The data were analyzed by one-way analysis of variance with a Tukey-Kramer multiple comparisons test.

(6.42 ± 0.52 clusters/100 μm^2) with a further decrease for myc-$CB3_{SH3-}^{R356N/R357N}$ (3.37 ± 0.63 clusters/100 μm^2). As expected from previous studies (Chiou et al., 2011), synaptic gephyrin cluster size was significantly increased on overexpression of myc-$CB3_{SH3-}$ (non-transfected = 0.095 ± 0.003 vs. wild-type myc-$CB3_{SH3-}$ = 0.240 ± 0.024; mean clusters μm^2 ± SEM). However, only a slight increase in cluster size was observed for myc-$CB3_{SH3-}^{R356Q}$ (0.132 ± 0.008) with no significant difference observed for myc-$CB3_{SH3-}^{R356N/R357N}$ (0.129 ± 0.016) compared non-transfected neurones.

Molecular Dynamics Simulations Reveal That Wild-Type Collybistin and Collybistin^{R356Q} Display Distinct Conformations That May Underlie Observed Differences in PI3P Binding

MD simulations revealed that both wild-type and mutant collybistin^{R356Q} adopted a range of conformations that could be grouped into two distinct conformational clusters. These differed from the reported crystallographic conformation of wild-type collybistin and the mutant collybistin^{R356Q} model with docked PI3P (**Figures 5A,B**), which were used as starting structures to initiate the simulations. Cluster analysis of wild-type collybistin showed that it adopted a more elongated conformation for approximately 68% (814 out of 1200 structures) and an "open clam" conformation for approximately 32% (380 out of 1200 structures) of the combined trajectory. The central conformations of each are shown in **Figures 5C,E**, respectively. Cluster analysis of collybistin^{R356Q} also revealed two distinct conformations during the combined trajectories, that differed from the conformations adopted by wild-type collybistin. Collybistin^{R356Q} predominantly displayed a "side saddle" conformation for 64% (**Figure 5D**, 769 out of 1,200 structures) and a "shut clam" conformation for 31% (**Figure 5F**, 373 out of 1,200 structures) of the combined simulation trajectory. During MD simulations, both the position and orientation of the PI3P molecule changed significantly from its initial docked location in both wild-type collybistin and collybistin^{R356Q} simulations (**Figures 5A,B**, respectively), binding to a unique site in the PH domain in each conformational cluster, as shown in **Figure 5**. **Table 1** and **Figure 6** show that there was little overlap in the residues that bind PI3P in each of the predominant conformational clusters. There was more overlap in the PI3P-binding residues in the starting conformation of collybistin^{R356Q} and its two predominant conformational clusters than in the representative conformations than for wild-type collybistin. Intriguingly, in the second most populated conformational cluster of wild-type collybistin, PI3P moves far from the initial docked location to bind in the deep binding cleft of the "open clam" conformation shown in **Figures 5E**, **6E**.

DISCUSSION

This study reports the identification and functional characterization of a novel PH domain mutation (p.R356Q) in the RhoGEF collybistin that is likely to represent the cause of

TABLE 1 | The PI3P-binding residues in molecular dynamics simulations of wild-type collybistin and collybistin^{R356Q}.

	Putative PI3P-binding residues	
	Wild-type collybistin	**collybistin^{R356Q}**
Crystal structure	K408	Q337
		R357
Most prevalent conformation (~60%)	A326	Q337
	N335	R338
	Q336	K351
	Q337	K352
	F406	D353
	K408	I354
		R357
Second most prevalent conformation (~30%)	Y332	Q218
	N335	Q222
	F384	K351
	M388	D353
	K389	I354
		I355
		R357

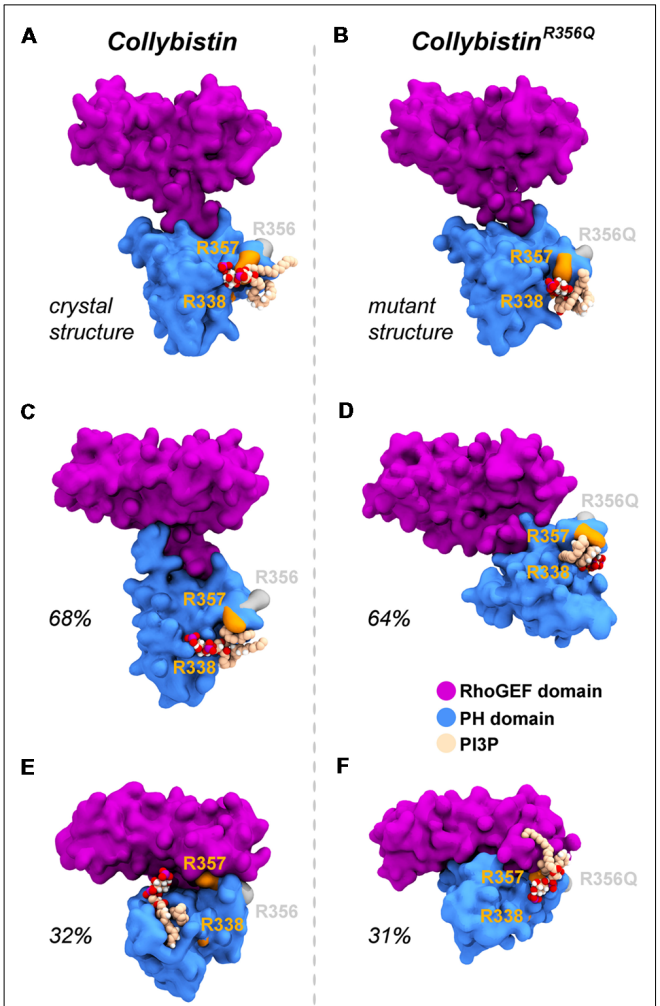

FIGURE 5 | Wild-type collybistin and collybistin^{R356Q} adopt two distinct conformations in solution with unique PI3P binding sites. PI3P (shown in space-fill representation, colored by atom where carbon = tan, oxygen = red, nitrogen = blue, hydrogen = white and phosphorous = purple) is docked to wild-type collybistin **(A)** and collybistin^{R356Q} **(B)** structures (collybistin is shown as a purple and blue surface). Representative collybistin conformations and PI3P binding poses from the most frequently adopted conformations during molecular dynamics simulations are shown in panels **(C–F)**. A 2.5 Å cut-off distance was used to perform the cluster analysis and the proportion of the simulation that each conformation represents is labeled. Key arginine residues R338, R357 and R356 are colored orange (R338 and R357) and gray (R356).

XLID in this family. Using X-exome sequencing, bioinformatics analysis and inheritance testing, we found a novel SNV (chrX:62875607C>T, p.R356Q) in *ARHGEF9* that segregated with the disease phenotype. This substitution of a highly conserved functionally important residue in the PH domain had a consensus score of 5.13, and was predicted as probably damaging and damaging by PolyPhen-2 and SIFT, with a CADD score of 26. Although we did not exclude a further potential variant in *CCDC22*, a gene that has previously been linked to ID, this substitution was predicted as benign and tolerated by Polyphen-2 and SIFT and had a lower CADD score of 18. It is also noteworthy that missense mutations in *CCDC22* are associated with Ritscher-Schinzel syndrome-2 (Kolanczyk et al., 2015) an X-linked recessive syndromic form of ID associated with posterior fossa defects, cardiac malformations, and minor abnormalities of the face and distal extremities. These additional phenotypic features have not been observed in the family under study to date.

Using multiple biochemical and cellular functional assays, we were able to establish the likely pathomechanism for collybistin p.R356Q—a reduction in PI3P binding in pulldown assays, leading to a loss of gephyrin clustering activity in an *in vitro* EGFP-gephyrin clustering assay (Harvey et al., 2004). It is noteworthy that collybistin constructs tested in this study represent $CB3_{SH3-}$, i.e., lack the N-terminal SH3 domain, because isoforms containing the SH3 domain do not show EGFP-clustering activity in HEK293 cells without the addition of additional regulatory proteins such as neuroligin 2 or the $GABA_AR$ α2 subunit (Harvey et al., 2004; Poulopoulos et al., 2009; Saiepour et al., 2010). In the absence of these interactors, collybistin isoforms harboring the N-terminal SH3 domain (e.g., $CB3_{SH3+}$) adopts a closed and autoinhibited conformation that prevents the PH domain from binding to phosphoinositides (Ludolphs et al., 2016). Hence, we used $CB3_{SH3-}$ rather than $CB3_{SH3+}$ in our PI3P pull-down and cellular clustering assays. In cultured hippocampal neurones, all tested collybistin isoforms ($CB2_{SH3+}$, $CB2_{SH3-}$, $CB3_{SH3+}$ and $CB3_{SH3-}$) target to and concentrate at GABAergic postsynapses (Chiou et al., 2011; Fekete et al., 2017) with the major difference being that transfection of de-regulated isoforms that lack the SH3 domain (e.g., $CB3_{SH3-}$) results in large postsynaptic gephyrin and $GABA_A$ receptor superclusters, while isoforms containing the SH3 domain induce the formation of supernumerary non-synaptic clusters (Chiou et al., 2011; Fekete et al., 2017). In this system, overexpression of the myc-$CB3_{SH3-}^{R356Q}$ mutant resulted in a decrease in the overall number of synaptic gephyrin clusters compared to controls. Notably, p.R356Q

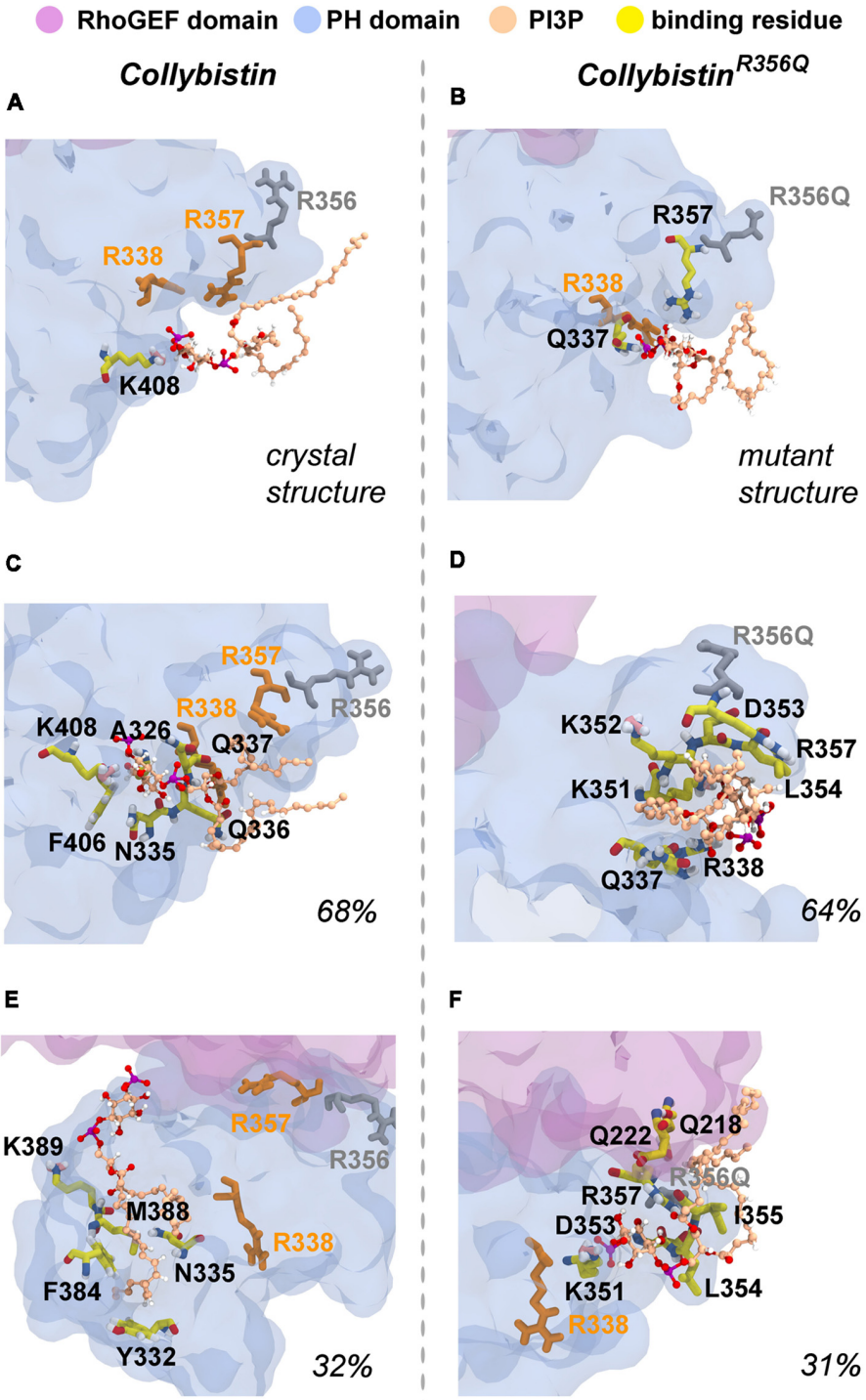

FIGURE 6 | Predicted PI3P-binding residues in wild-type collybistin and collybistin^{R356Q}. Predicted PI3P binding residues in the protein conformation obtained from PI3P docking to **(A)** the wild-type collybistin crystal structure (PDB ID: 4MT7) and **(B)** the computational model of the collybistin^{R365Q} mutation. PI3P binding residues from MD simulations of the most populated conformational cluster of **(C)** wild-type collybistin and **(D)** collybistin^{R365Q}. PI3P binding residues from MD simulations of the second most populated conformational cluster of **(E)** wild-type collybistin and **(F)** collybistin^{R365Q}. The PH and RhoGEF domains are shown in transparent gray-blue and mauve, respectively. R357 and R338 are shown in gold licorice. R556 and R356Q are shown as gray licorice. The PI3P lipid is shown as a ball-and-stick model, colored by atom (carbon = tan, oxygen = red, nitrogen = blue, hydrogen = white and phosphorous = purple). The PI3P-binding residues, taken as those within 3 Å of the PI3P molecule, are shown in stick representation, colored by atom (carbon = yellow, oxygen = red, nitrogen = blue, hydrogen = white, pink = resonance structure). Key arginine residues that impact phosphoinositide binding, including R338 (Long et al., 2016), R356 and R357 (Reddy-Alla et al., 2010) are shown as sticks and are colored orange (R338 and R357) and gray (R356). All residues shown are labeled, with binding residues labeled with black lettering.

also abrogated the ability of myc-$CB3_{SH3-}$ to form gephyrin superclusters (Chiou et al., 2011; Fekete et al., 2017). Taken together, our analysis strongly suggests that the collybistin p.R356Q variant is responsible for the mild intellectual disability observed in this family—due to disruption of collybistin PI3P binding, leading to a decrease in synaptic gephyrin and $GABA_A$ receptor clustering.

A number of mutations in *ARHGEF9* have been identified in patients encompassing missense and nonsense mutations, deletions and complex rearrangements (Long et al., 2016; Alber et al., 2017). As noted by recent reviews aimed at correlating genotypes and patient phenotypes (Alber et al., 2017; Wang et al., 2018), the associated patient phenotypes vary quite substantially. Individuals with mutations in *ARHGEF9* present in early childhood, with delayed motor development sometimes in combination with seizures. Intellectual disability generally ranges from moderate to severe, although males with severe intellectual disability often have intractable epilepsy and facial dysmorphism, including enlarged, fleshy earlobes, a sunken appearance of the middle face in combination with a protruding of the jaw (Alber et al., 2017). Curiously, several patients with mutations affecting the PH domain (p.R338W, Long et al., 2016; p.E400K, de Ligt et al., 2012; p.R356Q, this study) appear to have mild or moderate XLID and do not develop seizures. A further PH domain mutation close to the RhoGEF-PH linker, p.G323R, also resulted in a low frequency of delayed onset febrile and afebrile seizures (Klein et al., 2017).

So why do PH domain mutations appear to have less impact? There are several possibilities as to why this might be the case. Certainly, mutations that affect the N-terminal SH3 domain have the potential to be extremely deleterious, either unlocking collybistin into a conformationally "open" state (Soykan et al., 2014; Ludolphs et al., 2016), or disrupting key synaptic interactors. For example, the collybistin mutation p.G55A associated with early infantile epileptic encephalopathy and severe psychomotor retardation has a clear dominant-negative effect, causing gephyrin aggregation in neurons and subsequent loss of synaptic gephyrin and $GABA_A$ receptor clusters (Harvey et al., 2004). The p.G55A mutation also disrupts collybistin interactions with key synaptic molecules that interface with the SH3 domain, including neuroligin 2 (Poulopoulos et al., 2009) and $GABA_A$ receptor α2 subunit (Saiepour et al., 2010). By contrast, mutations found in the RhoGEF domain could potentially affect GDP-GTP exchange on the small GTPase Cdc42 (Reddy-Alla et al., 2010), gephyrin binding (Xiang et al., 2006) or alter the strength of intramolecular interactions RhoGEF and PH domains, as in the case of the p.R290H mutation (Papadopoulos et al., 2015) that indirectly affected PI3P binding. To date, two of the reported PH domain mutations (p.R338W, Long et al., 2016; p.R356Q, this study) appear to operate by reducing the affinity of collybistin for phosphoinositides such as PI3P, although interactions with the small Rho-like GTPase TC10—which also binds to the collybistin PH domain (Mayer et al., 2013)—have not yet been assessed. Our MD simulations show that wild-type collybistin adopted at least two distinct conformations in solution (**Figures 5C,D**). These are distinct from the two conformations adopted by mutant collybistin^{R356Q} (**Figures 5E,F**). Furthermore, PI3P did not remain bound at the docking location during the simulations, but instead bound in unique locations on the PH domain that depended on the protein conformation (**Figure 6**). Our MD results suggest that the range of conformations adopted by wild-type collybistin are likely to be impacted by the p.R356Q variant, and hence affect PI3P binding. Indeed, there was little overlap in the PI3P-binding residues for wild-type collybistin, as shown in **Table 1** and **Figure 6**. However, residue Q337 bound PI3P in both of the most prevalent conformations of collybistin and is likely to be an important PI3P-binding residue.

Although the p.R356Q and p.R338W substitutions completely inhibit collybistin-mediated gephyrin clustering in cellular models (**Figure 2**; Long et al., 2016), the effects observed for p.R356Q in primary neurones were more modest. Although overexpression of myc-$CB3_{SH3-}^{R356Q}$ resulted in the formation of non-synaptic collybistin-gephyrin aggregates, $CB3_{SH3-}^{R356Q}$ was not able to localize to synaptic sites and is therefore unlikely to have dominant-negative effects. Rather, $CB3_{SH3-}^{R356Q}$ modestly reduced synaptic gephyrin cluster density, without affecting cluster size (**Figure 3**). Under these circumstances, we would predict that missense mutations in the collybistin PH domain that disrupt PI3P binding will show milder disease course than dominant-negative collybistin mutations in the SH3 or RhoGEF domains that substantially reduce gephyrin cluster number and size, so disrupting associated inhibitory GABAergic transmission.

AUTHOR CONTRIBUTIONS

RH, VK, MO, ADB and VMK designed the experiments. T-TC, PL, AS-G, VK and KH performed the experiments. RH, VK, MO, SH, ADB and VMK analyzed the data. RH, VK, AS-G, MO, ADB and VMK wrote the article. All authors were involved in revising the article for important intellectual content, and gave final approval of the version to be published.

FUNDING

This work was supported by the Medical Research Council (J004049 to RH and KH and G0401232 to VK), the National Health and Medical Research Council (NHMRC; 1117394 to RH) and the National Institute of Neurological Disorders and Stroke, National Institutes of Health (Grant number: R01NS038752 to ADB) and with the assistance of resources and services from the National Computational Infrastructure (NCI), which is supported by the Australian Government. AS-G is supported by a Westpac Bicentennial Foundation Future Leaders Scholarship. The funders had no role in study design, data collection and analysis, decision to publish, or preparation of the manuscript.

SUPPLEMENTARY MATERIAL

The Supplementary Material for this article can be found online at: https://www.frontiersin.org/articles/10.3389/fnmol.2019.00060/full#supplementary-material

REFERENCES

Aarabi, M., Kessler, E., Madan-Khetarpal, S., Surti, U., Bellissimo, D., Rajkovic, A., et al. (2018). Autism spectrum disorder in females with *ARHGEF9* alterations and a random pattern of X chromosome inactivation. *Eur. J. Med. Genet.* doi: 10.1016/j.ejmg.2018.07.021 [Epub ahead of print].

Abraham, M. J., Murtola, T., Schulz, R., Páll, S., Smith, J. C., Hess, B., et al. (2015). Gromacs: high performance molecular simulations through multi-level parallelism from laptops to supercomputers. *SoftwareX* 1–2, 19–25. doi: 10.1016/j.softx.2015.06.001

Adzhubei, I., Jordan, D. M., and Sunyaev, S. R. (2013). Predicting functional effect of human missense mutations using PolyPhen-2. *Curr. Protoc. Hum. Genet.* 7:7.20. doi: 10.1002/0471142905.hg0720s76

Alber, M., Kalscheuer, V. M., Marco, E., Sherr, E., Lesca, G., Till, M., et al. (2017). *ARHGEF9* disease: phenotype clarification and genotype-phenotype correlation. *Neurol. Genet.* 3:e148. doi: 10.1212/nxg.0000000000000148

Chiou, T. T., Bonhomme, B., Jin, H., Miralles, C. P., Xiao, H., Fu, Z., et al. (2011). Differential regulation of the postsynaptic clustering of γ-aminobutyric acid type A ($GABA_A$) receptors by collybistin isoforms. *J. Biol. Chem.* 286, 22456–22468. doi: 10.1074/jbc.M111.236190

Christie, S. B., and De Blas, A. L. (2003). GABAergic and glutamatergic axons innervate the axon initial segment and organize $GABA_A$ receptor clusters of cultured hippocampal pyramidal cells. *J. Comp. Neurol.* 456, 361–374. doi: 10.1002/cne.10535

Christie, S. B., Li, R. W., Miralles, C. P., Riquelme, R., Yang, B. Y., Charych, E., et al. (2002a). Synaptic and extrasynaptic $GABA_A$ receptor and gephyrin clusters. *Prog. Brain Res.* 136, 157–180. doi: 10.1016/S0079-6123(02)36015-1

Christie, S. B., Miralles, C. P., and De Blas, A. L. (2002b). GABAergic innervation organizes synaptic and extrasynaptic $GABA_A$ receptor clustering in cultured hippocampal neurons. *J. Neurosci.* 22, 684–697. doi: 10.1523/JNEUROSCI.22-03-00684.2002

Daura, X., Gademann, K., Jaun, B., Seebach, D., van Gunsteren, W. F., and Mark, A. E. (1999). Peptide folding: when simulation meets experiment. *Angew. Chem. Int. Ed.* 38, 236–240. doi: 10.1002/(sici)1521-3773(19990115)38:1/2<236::aid-anie236>3.0.co;2-m

de Ligt, J., Willemsen, M. H., van Bon, B. W., Kleefstra, T., Yntema, H. G., Kroes, T., et al. (2012). Diagnostic exome sequencing in persons with severe intellectual disability. *N. Engl. J. Med.* 367, 1921–1929. doi: 10.1056/NEJMoa1206524

Emde, A. K., Schulz, M. H., Weese, D., Sun, R., Vingron, M., Kalscheuer, V. M., et al. (2012). Detecting genomic indel variants with exact breakpoints in single- and paired-end sequencing data using SplazerS. *Bioinformatics* 28, 619–627. doi: 10.1093/bioinformatics/bts019

Fekete, C. D., Chiou, T. T., Miralles, C. P., Harris, R. S., Fiondella, C. G., Loturco, J. J., et al. (2015). *In vivo* clonal overexpression of neuroligin 3 and neuroligin 2 in neurons of the rat cerebral cortex: differential effects on GABAergic synapses and neuronal migration. *J. Comp. Neurol.* 523, 1359–1378. doi: 10.1002/cne.23740

Fekete, C., Goz, R. U., Dinallo, S., Miralles, C. P., Chiou, T. T., Bear, J. Jr., et al. (2017). *In vivo* transgenic expression of collybistin in neurons of the rat cerebral cortex. *J. Comp. Neurol.* 525, 1291–1311. doi: 10.1002/cne.24137

Goslin, K., Asmussen, H., and Banker, G. (1998). "Rat hippocampal neurons in low density culture," in *Culturing Nerve Cells*, 2nd Edn. eds G. Banker and K. Goslin (Cambridge, MA: MIT Press), 339–370.

Harvey, K., Duguid, I. C., Alldred, M. J., Beatty, S. E., Ward, H., Keep, N. H., et al. (2004). The GDP-GTP exchange factor collybistin: an essential determinant of neuronal gephyrin clustering. *J. Neurosci.* 24, 5816–5826. doi: 10.1523/JNEUROSCI.1184-04.2004

Hines, R. M., Maric, H. M., Hines, D. J., Modgil, A., Panzanelli, P., Nakamura, Y., et al. (2018). Developmental seizures and mortality result from reducing $GABA_A$ receptor α2-subunit interaction with collybistin. *Nat. Commun.* 9:3130. doi: 10.1038/s41467-018-05481-1

Hoon, M., Soykan, T., Falkenburger, B., Hammer, M., Patrizi, A., Schmidt, K. F., et al. (2011). Neuroligin-4 is localized to glycinergic postsynapses and regulates inhibition in the retina. *Proc. Natl. Acad. Sci. U S A* 108, 3053–3058. doi: 10.1073/pnas.1006946108

Hu, H., Haas, S. A., Chelly, J., Van Esch, H., Raynaud, M., de Brouwer, A. P., et al. (2016). X-exome sequencing of 405 unresolved families identifies seven novel intellectual disability genes. *Mol. Psychiatry* 21, 133–148. doi: 10.1038/mp.2014.193

Hu, H., Wienker, T. F., Musante, L., Kalscheuer, V. M., Kahrizi, K., Najmabadi, H., et al. (2014). Integrated sequence analysis pipeline provides one-stop solution for identifying disease-causing mutations. *Hum. Mutat.* 35, 1427–1435. doi: 10.1002/humu.22695

Humphrey, W., Dalke, A., and Schulten, K. (1996). VMD: visual molecular dynamics. *J. Mol. Graph.* 14, 33–38. doi: 10.1016/0263-7855(96)00018-5

Jedlicka, P., Hoon, M., Papadopoulos, T., Vlachos, A., Winkels, R., Poulopoulos, A., et al. (2011). Increased dentate gyrus excitability in neuroligin-2-deficient mice *in vivo*. *Cereb. Cortex* 21, 357–367. doi: 10.1093/cercor/bhq100

Jedlicka, P., Papadopoulos, T., Deller, T., Betz, H., and Schwarzacher, S. W. (2009). Increased network excitability and impaired induction of long-term potentiation in the dentate gyrus of collybistin-deficient mice *in vivo*. *Mol. Cell. Neurosci.* 41, 94–100. doi: 10.1016/j.mcn.2009.02.005

Kalscheuer, V. M., Musante, L., Fang, C., Hoffmann, K., Fuchs, C., Carta, E., et al. (2009). A balanced chromosomal translocation disrupting *ARHGEF9* is associated with epilepsy, anxiety, aggression and mental retardation. *Hum. Mutat.* 30, 61–68. doi: 10.1002/humu.20814

Kanamarlapudi, V. (2014). Exchange factor EFA6R requires C-terminal targeting to the plasma membrane to promote cytoskeletal rearrangement through the activation of ADP-ribosylation factor 6 (ARF6). *J. Biol. Chem.* 289, 33378–33390. doi: 10.1074/jbc.m113.534156

Kins, S., Betz, H., and Kirsch, J. (2000). Collybistin, a newly identified brain-specific GEF, induces submembrane clustering of gephyrin. *Nat. Neurosci.* 3, 22–29. doi: 10.1038/71096

Kircher, M., Witten, D. M., Jain, P., O'Roak, B. J., Cooper, G. M., and Shendure, J. (2014). A general framework for estimating the relative pathogenicity of human genetic variants. *Nat. Genet.* 46, 310–315. doi: 10.1038/ng.2892

Klein, K. M., Pendziwiat, M., Eilam, A., Gilad, R., Blatt, I., Rosenow, F., et al. (2017). The phenotypic spectrum of *ARHGEF9* includes intellectual disability, focal epilepsy and febrile seizures. *J. Neurol.* 264, 1421–1425. doi: 10.1007/s00415-017-8539-3

Kolanczyk, M., Krawitz, P., Hecht, J., Hupalowska, A., Miaczynska, M., Marschner, K., et al. (2015). Missense variant in *CCDC22* causes X-linked recessive intellectual disability with features of Ritscher-Schinzel/3C syndrome. *Eur. J. Hum. Genet.* 23, 633–638. doi: 10.1038/ejhg.2014.109

Koziara, K. B., Stroet, M., Malde, A. K., and Mark, A. E. (2014). Testing and validation of the automated topology builder (ATB) version 2.0: prediction of hydration free enthalpies. *J. Comput. Aided Mol. Des.* 28, 221–233. doi: 10.1007/s10822-014-9713-7

Kumar, P., Henikoff, S., and Ng, P. C. (2009). Predicting the effects of coding non-synonymous variants on protein function using the SIFT algorithm. *Nat. Protoc.* 4, 1073–1081. doi: 10.1038/nprot.2009.86

Lemke, J. R., Riesch, E., Scheurenbrand, T., Schubach, M., Wilhelm, C., Steiner, I., et al. (2012). Targeted next generation sequencing as a diagnostic tool in epileptic disorders. *Epilepsia* 53, 1387–1398. doi: 10.1111/j.1528-1167.2012.03516.x

Lesca, G., Till, M., Labalme, A., Vallee, D., Hugonenq, C., Philip, N., et al. (2011). *De novo* Xq11.11 microdeletion including *ARHGEF9* in a boy with mental retardation, epilepsy, macrosomia and dysmorphic features. *Am. J. Med. Genet. A* 155A, 1706–1711. doi: 10.1002/ajmg.a.34004

Li, R. W., Serwanski, D. R., Miralles, C. P., Li, X., Charych, E., Riquelme, R., et al. (2005). GRIP1 in GABAergic synapses. *J. Comp. Neurol.* 488, 11–27. doi: 10.1002/cne.20566

Li, Y., Serwanski, D. R., Miralles, C. P., Fiondella, C. G., Loturco, J. J., Rubio, M. E., et al. (2010). Synaptic and nonsynaptic localization of protocadherin-γC5 in the rat brain. *J. Comp. Neurol.* 518, 3439–3463. doi: 10.1002/cne.22390

Li, Y., Xiao, H., Chiou, T. T., Jin, H., Bonhomme, B., Miralles, C. P., et al. (2012). Molecular and functional interaction between protocadherin-γC5 and $GABA_A$ receptors. *J. Neurosci.* 32, 11780–11797. doi: 10.1523/jneurosci.0969-12.2012

Long, P., May, M. M., James, V. M., Grannò, S., Johnson, J. P., Tarpey, P., et al. (2016). Missense mutation R338W in *ARHGEF9* in a family with X-linked intellectual disability with variable macrocephaly and macro-orchidism. *Front. Mol. Neurosci.* 8:83. doi: 10.3389/fnmol.2015.00083

Ludolphs, M., Schneeberger, D., Soykan, T., Schäfer, J., Papadopoulos, T., Brose, N., et al. (2016). Specificity of collybistin-phosphoinositide interactions:

impact of the individual protein domains. *J. Biol. Chem.* 291, 244–254. doi: 10.1074/jbc.m115.673400

Malde, A. K., Zuo, L., Breeze, M., Stroet, M., Poger, D., Nair, P. C., et al. (2011). An automated force field topology builder (ATB) and repository: version 1.0. *J. Chem. Theory Comput.* 7, 4026–4037. doi: 10.1021/ct200196m

Marco, E. J., Abidi, F. E., Bristow, J., Dean, W. B., Cotter, P., Jeremy, R. J., et al. (2008). *ARHGEF9* disruption in a female patient is associated with X-linked mental retardation and sensory hyperarousal. *J. Med. Genet.* 45, 100–105. doi: 10.1136/jmg.2007.052324

Mayer, S., Kumar, R., Jaiswal, M., Soykan, T., Ahmadian, M. R., Brose, N., et al. (2013). Collybistin activation by GTP-TC10 enhances postsynaptic gephyrin clustering and hippocampal GABAergic neurotransmission. *Proc. Natl. Acad. Sci. U S A* 110, 20795–20800. doi: 10.1073/pnas.1309078110

Oertel, W. H., Schmechel, D. E., Tappaz, M. L., and Kopin, I. J. (1981). Production of a specific antiserum to rat brain glutamic acid decarboxylase by injection of an antigen-antibody complex. *Neuroscience* 6, 2689–2700. doi: 10.1016/0306-4522(81)90113-5

Panzanelli, P., Gunn, B. G., Schlatter, M. C., Benke, D., Tyagarajan, S. K., Scheiffele, P., et al. (2011). Distinct mechanisms regulate $GABA_A$ receptor and gephyrin clustering at perisomatic and axo-axonic synapses on CA1 pyramidal cells. *J. Physiol.* 589, 4959–4980. doi: 10.1113/jphysiol.2011.216028

Papadopoulos, T., Eulenburg, V., Reddy-Alla, S., Mansuy, I. M., Li, Y., and Betz, H. (2008). Collybistin is required for both the formation and maintenance of GABAergic postsynapses in the hippocampus. *Mol. Cell. Neurosci.* 39, 161–169. doi: 10.1016/j.mcn.2008.06.006

Papadopoulos, T., Korte, M., Eulenburg, V., Kubota, H., Retiounskaia, M., Harvey, R. J., et al. (2007). Impaired GABAergic transmission and altered hippocampal synaptic plasticity in collybistin-deficient mice. *EMBO J.* 26, 3888–3899. doi: 10.1038/sj.emboj.7601819

Papadopoulos, T., Rhee, H. J., Subramanian, D., Paraskevopoulou, F., Mueller, R., Schultz, C., et al. (2017). Endosomal phosphatidylinositol 3-phosphate promotes gephyrin clustering and GABAergic neurotransmission at inhibitory postsynapses. *J. Biol. Chem.* 292, 1160–1177. doi: 10.1074/jbc.m116.771592

Papadopoulos, T., Schemm, R., Grubmüller, H., and Brose, N. (2015). Lipid binding defects and perturbed synaptogenic activity of a collybistin R290H mutant that causes epilepsy and intellectual disability. *J. Biol. Chem.* 290, 8256–8270. doi: 10.1074/jbc.m114.633024

Poulopoulos, A., Aramuni, G., Meyer, G., Soykan, T., Hoon, M., Papadopoulos, T., et al. (2009). Neuroligin 2 drives postsynaptic assembly at perisomatic inhibitory synapses through gephyrin and collybistin. *Neuron* 63, 628–642. doi: 10.1016/j.neuron.2009.08.023

Reddy-Alla, S., Schmitt, B., Birkenfeld, J., Eulenburg, V., Dutertre, S., Böhringer, C., et al. (2010). PH-domain-driven targeting of collybistin but not Cdc42 activation is required for synaptic gephyrin clustering. *Eur. J. Neurosci.* 31, 1173–1184. doi: 10.1111/j.1460-9568.2010.07149.x

Saiepour, L., Fuchs, C., Patrizi, A., Sassoè-Pognetto, M., Harvey, R. J., and Harvey, K. (2010). Complex role of collybistin and gephyrin in $GABA_A$ receptor clustering. *J. Biol. Chem.* 285, 29623–29631. doi: 10.1074/jbc.M110.121368

Schmid, N., Eichenberger, A. P., Choutko, A., Riniker, S., Winger, M., Mark, A. E., et al. (2011). Definition and testing of the GROMOS force-field versions 54A7 and 54B7. *Eur. Biophys. J.* 40, 843–856. doi: 10.1007/s00249-011-0700-9

Shimojima, K., Sugawara, M., Shichiji, M., Mukaida, S., Takayama, R., Imai, K., et al. (2011). Loss-of-function mutation of collybistin is responsible for X-linked mental retardation associated with epilepsy. *J. Hum. Genet.* 56, 561–565. doi: 10.1038/jhg.2011.58

Soykan, T., Schneeberger, D., Tria, G., Buechner, C., Bader, N., Svergun, D., et al. (2014). A conformational switch in collybistin determines the differentiation of inhibitory postsynapses. *EMBO J.* 33, 2113–2133. doi: 10.15252/embj.201488143

Trott, O., and Olson, A. J. (2010). AutoDock Vina: improving the speed and accuracy of docking with a new scoring function, efficient optimization, and multithreading. *J. Comput. Chem.* 31, 455–461. doi: 10.1002/jcc.21334

Voineagu, I., Huang, L., Winden, K., Lazaro, M., Haan, E., Nelson, J., et al. (2012). *CCDC22*: a novel candidate gene for syndromic X-linked intellectual disability. *Mol. Psychiatry* 17, 4–7. doi: 10.1038/mp.2011.95

Wang, J. Y., Zhou, P., Wang, J., Tang, B., Su, T., Liu, X. R., et al. (2018). *ARHGEF9* mutations in epileptic encephalopathy/intellectual disability: toward understanding the mechanism underlying phenotypic variation. *Neurogenetics* 19, 9–16. doi: 10.1007/s10048-017-0528-2

Xiang, S., Kim, E. Y., Connelly, J. J., Nassar, N., Kirsch, J., Winking, J., et al. (2006). The crystal structure of Cdc42 in complex with collybistin II, a gephyrin-interacting guanine nucleotide exchange factor. *J. Mol. Biol.* 359, 35–46. doi: 10.1016/j.jmb.2006.03.019

Conflict of Interest Statement: The authors declare that the research was conducted in the absence of any commercial or financial relationships that could be construed as a potential conflict of interest.

Copyright © 2019 Chiou, Long, Schumann-Gillett, Kanamarlapudi, Haas, Harvey, O'Mara, De Blas, Kalscheuer and Harvey. This is an open-access article distributed under the terms of the Creative Commons Attribution License (CC BY). The use, distribution or reproduction in other forums is permitted, provided the original author(s) and the copyright owner(s) are credited and that the original publication in this journal is cited, in accordance with accepted academic practice. No use, distribution or reproduction is permitted which does not comply with these terms.

frontiers in Molecular Neuroscience

MINI REVIEW
published: 21 May 2019
doi: 10.3389/fnmol.2019.00124

Could an Impairment in Local Translation of mRNAs in Glia be Contributing to Pathogenesis in ALS?

Samantha K. Barton[1,2,3]*, *Jenna M. Gregory*[2,3,4], *Siddharthan Chandran*[2,3,4]† *and Bradley J. Turner*[1]†

[1]Florey Institute of Neuroscience and Mental Health, The University of Melbourne, Parkville, VIC, Australia, [2]Euan MacDonald Centre for MND Research, University of Edinburgh, Edinburgh, United Kingdom, [3]Centre for Clinical Brain Sciences, University of Edinburgh, Edinburgh, United Kingdom, [4]UK Dementia Research Institute at University of Edinburgh, Edinburgh, United Kingdom

One of the key pathways implicated in amyotrophic lateral sclerosis (ALS) pathogenesis is abnormal RNA processing. Studies to date have focussed on defects in RNA stability, splicing, and translation, but this review article will focus on the largely overlooked RNA processing mechanism of RNA trafficking, with particular emphasis on the importance of glia. In the central nervous system (CNS), oligodendrocytes can extend processes to myelinate and metabolically support up to 50 axons and astrocytes can extend processes to cover up to 100,000 synapses, all with differing local functional requirements. Furthermore, many of the proteins required in these processes are large, aggregation-prone proteins which would be difficult to transport in their fully translated, terminally-folded state. This, therefore, highlights a critical requirement in these cells for local control of protein translation, which is achieved through specific trafficking of mRNAs to each process and local translation therein. Given that a large number of RNA-binding proteins have been implicated in ALS, and RNA-binding proteins are essential for trafficking mRNAs from the nucleus to glial processes for local translation, RNA misprocessing in glial cells is a likely source of cellular dysfunction in ALS. To date, neurons have been the focus of ALS research, but an intrinsic deficit in glia, namely astrocytes and oligodendrocytes, could have an additive effect on declining neuronal function in ALS. This review article aims to highlight the key evidence that supports the contention that RNA trafficking deficits in astrocytes and oligodendrocytes may contribute to in ALS.

Keywords: RNA trafficking, local translation, ALS, oligodendrocytes, astrocytes

OPEN ACCESS

Edited by:
Jochen C. Meier, Technische Universitat Braunschweig, Germany

Reviewed by:
Jean-Marc Gallo, King's College London, United Kingdom
David W. Walker, RMIT University, Australia

***Correspondence:**
Samantha K. Barton
samantha.barton@florey.edu.au

†*These authors have contributed equally to this work*

Received: *18 February 2019*
Accepted: *26 April 2019*
Published: *21 May 2019*

Citation:
Barton SK, Gregory JM, Chandran S and Turner BJ (2019) Could an Impairment in Local Translation of mRNAs in Glia be Contributing to Pathogenesis in ALS? Front. Mol. Neurosci. 12:124. doi: 10.3389/fnmol.2019.00124

INTRODUCTION

Amyotrophic lateral sclerosis (ALS) and frontotemporal dementia (FTD) are characterized pathologically by the accumulation of cytoplasmic inclusions in affected neurons and glial cells that, in 97%–98% of cases, stain positive for TAR-DNA binding protein 43 (TDP-43; Neumann et al., 2006). TDP-43, like many of the proteins that have been associated with ALS pathogenesis, is a DNA and RNA-binding protein, implicating impaired RNA processing as a possible mechanism of disease.

Regulatory proteins bind to mRNA transcripts to aid in localization, translation and stability, whilst also playing important roles in transcription, alternative splicing and nuclear export.

The binding of regulatory proteins to mRNAs, as well as the accrual of various translation factors, forms an RNA granule. Dysregulation of RNA granule formation has been implicated in neurodegenerative disease (Buchan, 2014), including ALS and FTD (Fan and Leung, 2016). Their involvement ranges from an impaired ability of the RNA granule to sufficiently aid in localization, translation and stability of the mRNAs, to the formation of stress granules, all of which have been implicated in ALS and can initiate a cascade of downstream events predicted to play a role in neuronal decline (Fan and Leung, 2016). This review article will focus specifically on impaired mRNA localization, which is due to compromised nucleocytoplasmic export and impaired trafficking to glial processes.

Subcellular transportation of mRNAs provides cells with the ability to translate proteins in response to localized signals. Local translation has been extensively documented in neuronal cell types and is noted to be essential for their normal function as it allows a high level of cellular autonomy from the cell soma to the dendrites, particularly during axonal pathfinding (Yoon et al., 2009). It is also established that glia within the central nervous system (CNS) undergo local translation. The cellular complexity of glia coupled with their elaborate roles in the CNS (ranging from input into vascular control to providing physical, trophic and metabolic support to neurons to the stabilization of synapses) renders the requirement for local translation essential to allow the translation of proteins unique to the specific function of each glial process. Further, the dynamic nature of processes like myelination and synaptic activity means that cells can respond more readily. These concepts have not been extensively explored in disease models. The aggregation of RNA-binding proteins, and associated proteins involved in RNA trafficking, in pathological inclusions in ALS is well established and so this review article aims to detail what impact these aggregations could have on local translation of key mRNAs in glia. We propose that the proteinopathy present in the majority of ALS patients could be impacting on local translation of mRNAs, thereby hindering the normal function of glia in patients with ALS and FTD, potentially contributing to neuronal decline and disease progression.

GLIAL INVOLVEMENT IN ALS

Humans have the highest proportion of glial cells, with their primary role being to support neuronal function, whether that be *via* structural support, metabolic and trophic support or through protection from surrounding threats to neuronal health. Broadly, glial cells encompass oligodendrocytes, astrocytes and specialized immune cells called microglia. For the purpose of this review article, we will focus on non-immune glial cells; their key roles (all of which depend on effective mRNA trafficking and local translation) are highlighted in **Figure 1**.

Given the importance of glia as neuronal support cells, intrinsic glial dysfunction has been implicated in neurodegenerative diseases including ALS (Yamanaka et al., 2008; Kang et al., 2013; Serio et al., 2013; Ferraiuolo et al., 2016; Madill et al., 2017). In the TDP-43^{Q331K} mouse model, it was shown that selective removal of the mutation from motor neurons alone did not prevent motor neuron or neuromuscular junction loss and did not reduce the activation of microglia or astrocytes (Ditsworth et al., 2017). More specifically, it has been shown that co-culturing induced pluripotent stem cell (iPSC)-derived oligodendrocytes from sporadic ALS patients, as well as those harboring mutations in *C9orf72* and *TDP-43*, with HB9-GFP motor neurons led to significant motor neuron loss compared to co-cultures with iPSC-derived oligodendrocytes from healthy control patients (Ferraiuolo et al., 2016). Similarly, a detrimental effect of co-cultured astrocytes (derived from neural precursor cells isolated from post-mortem tissue of sporadic ALS patients) on mouse embryonic stem cell-derived motor neurons survival was also observed (Haidet-Phillips et al., 2011). Thus, glia are critically involved in ALS pathogenesis.

The majority of research into glial influence in ALS and FTD to date has been on what impact glial dysfunction has on neuronal health. This is obviously relevant given that the symptoms experienced by ALS patients are related to the loss of upper and lower motor neurons. However, it is important to also address the intrinsic glial deficit. What tends to be underappreciated is that glia have the metabolically demanding role of not only sustaining their own functions but are also required to support the surrounding environment. Astrocytes and oligodendrocytes, in particular, are required to metabolically support neuronal function by directly shuttling lactate to neurons as their primary fuel source (Dienel and Cruz, 2004; Fünfschilling et al., 2012; Saab et al., 2013, 2016). Thus, any process that amplifies metabolic demand, or interferes with normal metabolic processes, would have a detrimental effect directly on cellular function and indirectly on surrounding neurons. So, we suggest that impaired RNA processing in glia could be contributing to ALS and FTD pathogenesis.

ALS-LINKED RNA-BINDING PROTEINS

Many known genetic mutations linked with ALS and FTD are in genes involved in maintaining RNA homeostasis. Examples include *TARDBP* (encoding TDP-43), FUS RNA-binding protein (*FUS*), *C9orf72* and, to a lesser extent, heterogeneous nuclear ribonucleoproteins A1 (*hnRNP A1*) and A2/B1 (*hnRNP A2/B1*), EWS RNA-binding protein 1 (*EWSR1*), angiogenin (*ANG*), senataxin (*SETX*), matrin 3 (*MATR3*) ataxin-2 (*ATXN2*) and TATA-box binding protein associated factor 15 (*TAF15*; Ling et al., 2013; Kapeli et al., 2017). Many of these proteins have both loss-of-function and gain-of-function toxic effects on cells. For example, iPSC-derived motor neurons from patients harboring a mutation in the *hnRNP A2/B1* gene not only lost the function of this protein but also gained toxicity linked to failure in RNA processing (Martinez et al., 2016). The hypothesis that RNA-binding proteins aggregating in the cytoplasm of neurons being a pathogenic mechanism in ALS is not a new concept and has been suggested, and reviewed (Yasuda and Mili, 2016), previously. Briefly, it is suggested that the aggregation of RNA-binding proteins limits RNA transport along neuronal microtubules thus preventing local translation at the dendrites and even leading to ectopic translation in the cell body. RNA

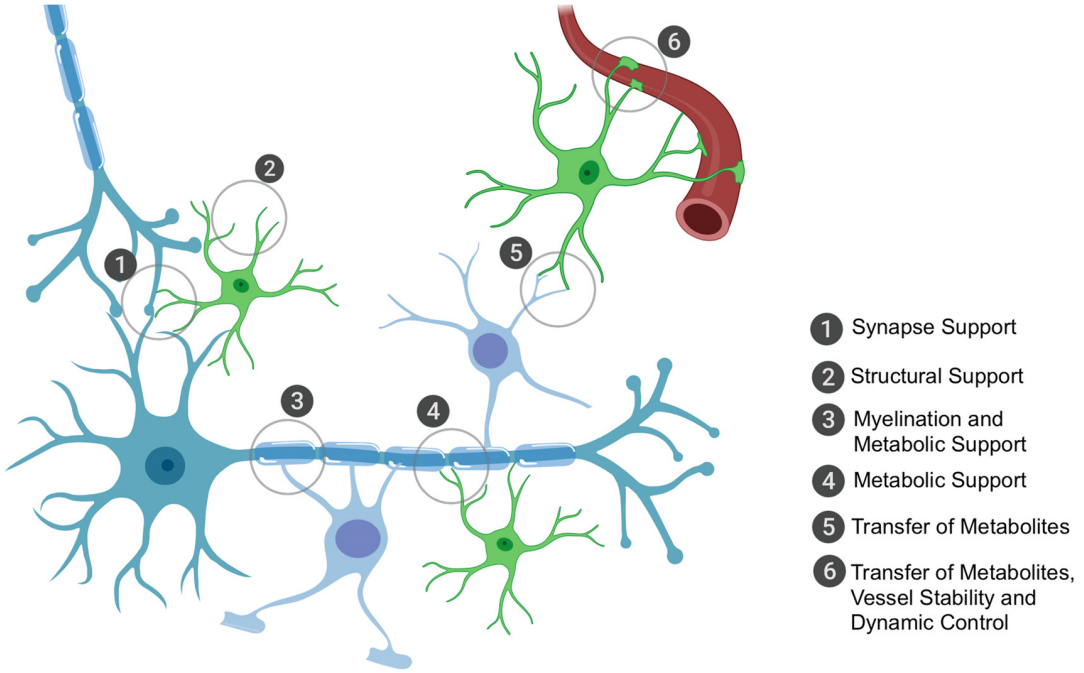

FIGURE 1 | The key roles of oligodendrocytes and astrocytes in the brain that rely on local translation of mRNAs. Astrocytes and oligodendrocytes have the ultimate role of supporting neuronal function. Astrocytes have a plethora of functions that range from structurally supporting synapse formation (1) to providing general structural support in the central nervous system (CNS) (2), especially in development during axon formation and pathfinding. Oligodendrocytes have the metabolically demanding function of myelinating axons for accelerated conductance (3) and it is through these myelin sheaths that oligodendrocytes can shuttle metabolic and trophic factors to neurons (3). Astrocytes are also critical in providing metabolic and trophic support to neurons (4) and can also shuttle metabolites to oligodendrocytes for their own use or to shuttle onwards to neurons (5). Astrocytes are also important for blood vessel stability and assist in tight junction formation; they also can receive glucose from the bloodstream (6) and can shuttle this to oligodendrocytes or themselves convert it to lactate (the end-product of glycolysis of glucose and the energy substrate for neurons) and shuttle this to oligodendrocytes as well or directly to neurons. Importantly, the key sites of support to neurons occur at the distal processes, thus local translation of mRNAs is critically important to ensure these processes are dynamic and in rapid response to the surrounding environment's requirements.

trafficking in glia in ALS remains relatively unexplored but we predict similar processes could apply and contribute to cellular pathogenesis. The current understanding of these processes is detailed below.

Many of the ALS-associated pathogenic proteins are known to be essential for nucleo-cytoplasmic mRNA trafficking and, importantly, many will interact with one another for efficient RNA metabolism. These interactions are highlighted in **Figure 2**; they have been reviewed elsewhere (Dormann and Haass, 2013; Vanderweyde et al., 2013; Balendra and Isaacs, 2018) so we will detail only those of relevance to glial mRNA trafficking.

TDP-43 has multiple roles in RNA processing and is known to bind to more than 6,000 RNA targets, equating to approximately 30% of the human transcriptome (Ling et al., 2013); it is topologically and functionally dysregulated in 97% of ALS patients (Neumann et al., 2006, 2007; Seilhean et al., 2009; Murray et al., 2011; Armstrong, 2017). FUS binds to over 5,000 RNA targets in the brain (Ling et al., 2013) but is topologically and functionally dysregulated in <1% of ALS patients and 9% of FTD patients (Blokhuis et al., 2013; Ling et al., 2013). Both TDP-43 and FUS have been associated with hnRNP A1 (Kamelgarn et al., 2016) with TDP-43 specifically linked with aberrant splicing of *hnRNP A1* (Deshaies et al., 2018) and altered expression and aberrant splicing of *hnRNP A2/B1* (Highley et al., 2014). Coady and Manley (2015) used the human glioblastoma cell line, U87, to show that mutations in *FUS* can lead to reduced MeCP2 levels (a transcription factor regulator); reduced MeCP2 protein levels in glia has previously been shown to be toxic to neurons leading to altered dendritic morphology and, ultimately, neuronal death (Ballas et al., 2009).

The most common genetic mutation underlying ALS and FTD is the *C9orf72* hexanucleotide repeat expansion (HRE), which pathologically presents as G_4C_2 repeat RNA foci and sense and anti-sense repeat-associated non-ATG (RAN) translation of di-peptide repeat proteins (DPRs) as well as TDP-43 aggregation. G_4C_2 repeat RNA foci co-localize with various RNA-binding proteins in neurons, including hnRNP A1 and hnRNP H/F, shown in post-mortem tissue (Cooper-Knock et al., 2014) and in cell lines, primary neurons and zebrafish embryos (Lee et al., 2013; Conlon et al., 2016). Of relevance, this has also been validated in human astrocytes derived from the autopsied motor cortex (Conlon et al., 2016). In addition to being an RNA-binding protein, hnRNP H is a key splicing regulator; notably, hnRNP H splices transcripts encoding other splicing proteins, which includes TDP-43 and FUS (Uren et al., 2016). Other RNA and nucleic acid-binding proteins known to bind to the G_4C_2

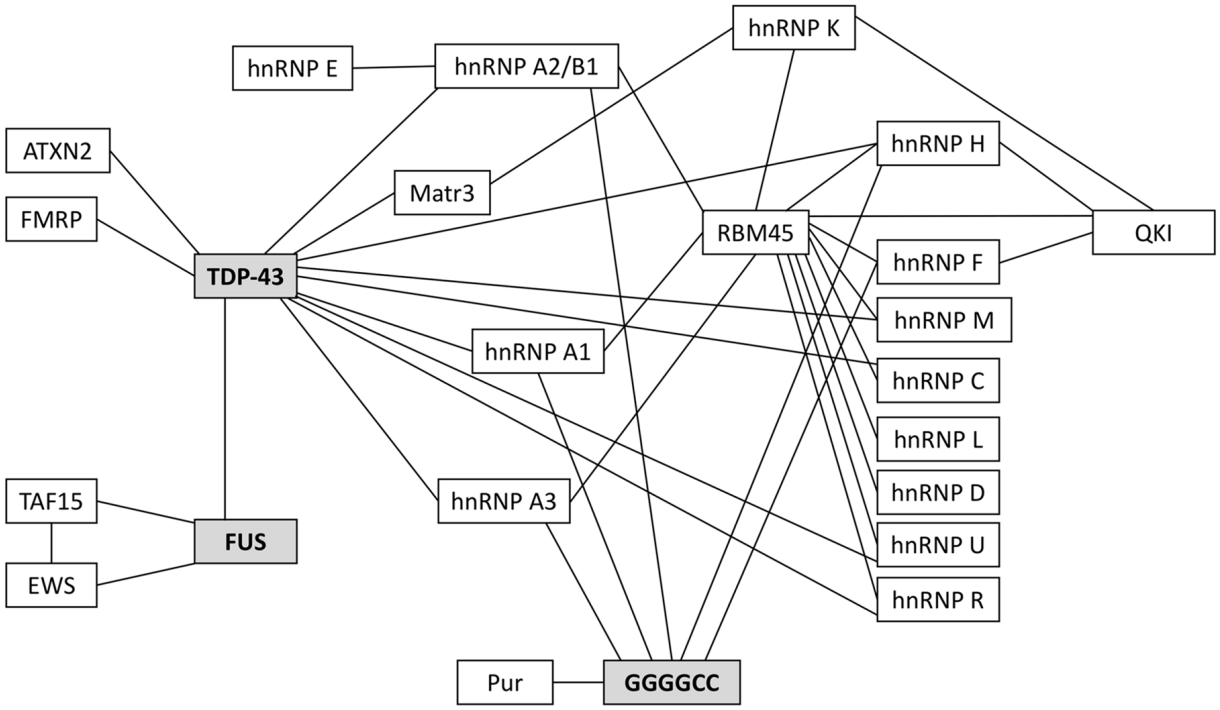

FIGURE 2 | Protein binding partners that have been implicated in ALS. 97–98% of ALS patients have pathogenic protein inclusions that stain positive for the RNA/DNA binding protein TDP-43. Most of the remaining 2%–3% of patients will have inclusions that stain positive for FUS. Currently, the most prevalent genetic mutation associated with familial and sporadic ALS is the *C9orf72* hexanucleotide repeat expansion (HRE); these patients characteristically have TDP-43-positive inclusions and/or TDP-43-negative, ubiquitin-positive inclusions and/or pathogenic RNA foci (composed of GGGGCC repeats), all of which are known to sequester RNAs and proteins. Many of the RNA-binding proteins in this schematic are critical for RNA trafficking and local translation of key mRNAs in astrocytes and oligodendrocytes.

repeats are hnRNP A3, which is important for nuclear export of mRNAs (Mori et al., 2013). DPRs have been more challenging to characterize given the limited access to efficient antibodies. *In vitro* work has demonstrated that DPRs are highly prone to aggregation and can sequester proteins, including RNA-binding proteins, which could contribute to abnormal RNA trafficking in neurons and glia (Gendron et al., 2013; Porta et al., 2015). DPRs can dock at the nuclear pore and disrupt the architecture of the nuclear envelope leading to limited nuclear import and export of macromolecules and mRNAs (Jovičić et al., 2015; Zhang et al., 2016; Shi et al., 2017). Both poly(GR) and poly(PR), two of the five DPRs, have been shown to interact with TDP-43-positive RNA as well as stress granules and are predicted to be involved in the fibrillization of TDP-43 and other RNA-binding proteins such as hnRNP A2/B1 (Molliex et al., 2015; Freibaum and Taylor, 2017). Importantly, Edbauer and colleagues demonstrated that poly(GA) can cause mislocalization of TDP-43 in neurons (Khosravi et al., 2017).

RNA TRAFFICKING IN ASTROCYTES

Astrocytes are the most abundant cell type in the human brain, with functions including: (i) neuronal support, including metabolic, trophic and structural support; (ii) neuronal synapse and axon formation; and (iii) regulation of cerebral blood flow (Blackburn et al., 2009). Their role in neurodegeneration remains contentious with astrocytes believed to have both protective and harmful effects (Phatnani and Maniatis, 2015), much like microglia (Geloso et al., 2017). Astrocytes have a complex morphology; in cerebral gray matter their processes can span 50 μm and up to 300 μm in the white matter, rendering local translation necessary for normal cellular function. There is also a high metabolic demand on astrocytes, both for their own function as well as metabolically supporting neurons; one astrocyte can be responsible for being in contact with up to 100,000 synapses (Sakers et al., 2017) covering a surface area of between 60,000 and 80,000 μm^2. The dynamic nature of astrocytic function means these cells have optimized their protein availability relying heavily on local translation (Boulay et al., 2017).

Glial fibrillary acidic protein (*GFAP*) mRNA is known to be translated locally at astrocytic processes and is an abundantly expressed protein in all astrocytes, despite the known heterogeneity among the astrocyte population. To further validate this, it has been shown to equate to 15% of an astrocyte's volume and the protein expression is isolated predominantly to its processes (Bushong et al., 2002). GFAP-null mice ranged

in phenotype, but half of the cohort were seen to have extensive deficits including abnormal myelination, reduced white matter vascularization and decreased integrity of the blood brain barrier (Liedtke et al., 1996). The RNA-binding protein responsible for shuttling *GFAP* to the peripheral astrocyte processes (PAP) is Quaking (QKI; Sakers et al., 2017). QKI is abundantly expressed in oligodendrocytes and astrocytes and has been implicated in schizophrenia (Aberg et al., 2006) and brain cancers (Molenaar et al., 2012) but is yet to be associated with ALS pathology. However, given it is known to bind to 2,500 mRNAs, as well as its close relationship to other affected RNA-binding proteins (it contains a hnRNP K homology domain, an hnRNP that has been implicated in ALS; Hafner et al., 2010), it deserves further investigation. Another key astrocytic mRNA known to be locally translated is excitatory amino acid transporter-2 (*EAAT2*) and whilst its trafficking has not been explored, *EAAT2* transcripts with both intron-retention and exon-skipping have been found in 65% of sporadic ALS patients in neuropathologically affected areas as well as in the cerebrospinal fluid (CSF; Lin et al., 1998). Other mRNAs known to be translated locally include *Aqp4* (encoding the main water channel protein in the CNS responsible for maintaining water homeostasis), *Aldh1a1* (encoding an enzyme that depicts mature astrocytes; Boulay et al., 2017), *Slc1a2*, *Slc1a3* and *GluI* (encoding enzymes important for glutamate metabolism), *Fads1*, *Fads2*, *Scd1*, *Scd2, Elovl5* and *Hadha* (encoding enzymes critical for fatty acid synthesis), *Kif1c* and *Myo1D* (encoding proteins that maintain the cytoskeleton), *Mertk, Sparc* and *Thbs4* (encoding proteins key for synapse regulation), *ApoE* (encoding a class of proteins required for fat metabolism) and *CLU* (encoding the chaperone protein clusterin that has been implicated in ALS; Sakers et al., 2017).

Thus, if these mRNAs failed to adequately translate, this would have a detrimental impact on neuronal function given that they are critically involved in supportive pathways like metabolism and synapse regulation. Further, not only could mRNAs become sequestered *via* their RNA-binding proteins, but key astrocytic proteins are also sequestered, impeding function. TDP-43 is a binding partner for EAAT2, the glutamate transporter introduced above, and it has been shown that TDP-43 aggregation correlates with decreased EAAT1/2 glutamate transporter levels in the spinal cords of both an ALS mouse model (Tong et al., 2013) and human patients (Rothstein et al., 1995). FMRP is a known binding partner of TDP-43; in patients with Fragile × syndrome (whereby they have a repeat-expansion in the *FMR1* gene and acquire FMRP inclusions), profiling these inclusions demonstrated that many astrocytic proteins have been associated with these FMR inclusions, including vimentin, GFAP, and hnRNP A2/B1 [and, interestingly, myelin basic protein (MBP; Iwahashi et al., 2005)] Given FMRP is a known binding partner of TDP-43, these protein associations are relevant to ALS.

Thus, the sequestration of key RNA-binding proteins in astrocytes is likely to have a detrimental effect by impeding the trafficking of mRNAs critical for cellular function to their site of local translation.

RNA TRAFFICKING IN OLIGODENDROCYTES

Oligodendrocytes have been underappreciated for their role in the CNS with the focus to date limited to their role in myelination. Recent research has uncovered their ability to metabolically support neurons through the shuttling of lactate (Fünfschilling et al., 2012; Saab et al., 2013, 2016), much like astrocytes, highlighting a critical role for oligodendrocytes in neuronal health, function and survival. Each oligodendrocyte has the capacity to produce up to 50 myelin sheaths, each of which can be up to 60 μm in length (Hughes et al., 2018), so their support and metabolic supply (and demand) is extensive.

It has long been established that many mRNAs in oligodendrocytes are translated locally at the myelin sheath (Campagnoni et al., 1980; Colman et al., 1982) including *MBP* (Kristensson et al., 1986; White et al., 2008), myelin-associated oligodendrocytic basic protein (*MOPB*; Holz et al., 1996), carbonic anhydrase II (*CAII*; Ghandour and Skoff, 1991), *tau* (LoPresti et al., 1995) and amyloid precursor protein (*APP*; Garcia-Ladona et al., 1997). This extends to the involvement of many RNA-binding proteins including hnRNP A2/B1, hnRNP A1, hnRNP E1, hnRNP H/F and hnRNP K, to name a few (White et al., 2008; Laursen et al., 2011; Torvund-Jensen et al., 2014).

hnRNP A1 and hnRNP A2/B1 are involved in *MBP* mRNA trafficking and both are also known binding partners of G_4C_2 repeats and TDP-43 (Highley et al., 2014). Of relevance, hnRNP A1 is also critically involved in the exon skipping of survival motor neuron 2 (*SMN2*; Kashima et al., 2007), involved in spinal muscular atrophy (SMA), another form of motor neuron disease and hnRNP A2/B1 has been implicated in Alzheimer's disease (Mizukami et al., 2005). hnRNP A2/B1 and hnRNP A1, as well as TDP-43, have intrinsically disordered, aggregation-prone domains at their C-terminal end (Kim et al., 2013) supporting the contention that these proteins are prone to fibrillization and misfolding. Further, TDP-43 depletion leads to upregulation of specific isoforms of hnRNP A1, one of which has been reported to be highly prone to aggregation (Deshaies et al., 2018). Another RNA-binding protein involved in *MBP* trafficking is QKI; QKI mutant mice actually have impaired nuclear export of *MBP* mRNA resulting in impaired myelination in these mice (Larocque et al., 2002). QKI was characterized to interact with hnRNP F and H during alternative splicing in myelinating glia (Mandler et al., 2014). Further, post-mortem samples from ALS patients harboring *C9orf72* mutations demonstrated that RNA foci sequester hnRNP H/F (Cooper-Knock et al., 2014); hnRNP H/F is necessary for PLP/DM20 alternative splicing (Wang et al., 2007, 2008), a process critical for normal myelination. Of relevance, in human post-mortem tissue, it has been shown that ALS patients have a significant reduction in MBP in both the motor cortex and ventral spinal cord (Kang et al., 2013); however, it remains unclear as to whether the reduced myelin is a downstream effect of axonal loss or whether it is an intrinsic deficit in oligodendrocytes.

Oligodendrocytes have a very low annual turnover of just 1 in 300 oligodendrocytes in humans, making them a very stable cell type in the CNS (Yeung et al., 2014). The production of myelin,

on the other hand, is a more dynamic process (Yeung et al., 2014) with one cell possessing the ability to produce three times its own weight in myelin per day, eventually supporting 100 times its own cell weight in myelin (McLaurin and Yong, 1995; Connor and Menzies, 1996; Ludwin, 1997). Thus, given that an oligodendrocyte also has to metabolically support neurons in addition to their own metabolically demanding myelination requirements, this makes them vulnerable to processes that may interfere with myelin modulation. Given that many of the RNA-binding proteins that are critical for myelin-related mRNA trafficking in oligodendrocytes have been implicated in ALS pathology, this poses a risk to cellular function and their ability to support neurons.

CONCLUSION

It is well established that the hallmark pathological signature of ALS is misfolding and accumulation of aggregation-prone proteins, the most common of these proteinopathies being TDP-43. To date, very little attention has been given to the role of glia, specifically astrocytes and oligodendrocytes, in the pathogenesis of ALS as a result of intrinsic cellular deficits arising from protein aggregation. It is known in neurons that pathological protein aggregation, as well as the formation of RNA foci in *C9orf72* cases, can have a toxic gain-of-function effect by sequestering other mRNAs and proteins, compromising normal cellular function. We suggest this process is also occurring in glia and is complicated by the fact that many critical mRNAs required for normal astrocytic and oligodendroglial function are locally translated. Given the association of many RNA-binding proteins with the typical protein aggregations found in ALS cases, and the known associations of these RNA-binding proteins with key mRNAs in astrocytes and oligodendrocytes, we suggest that this is a potential pathogenic pathway of disease contributing to cellular dysfunction in patients with ALS.

AUTHOR CONTRIBUTIONS

SB, JG, SC and BT contributed to the preparation, writing and editing of this review article.

FUNDING

SB (APP1110040) and BT (APP1137024) received support from National Health and Medical Research Council and Australian Research Council fellowships.

REFERENCES

Aberg, K., Saetre, P., Jareborg, N., and Jazin, E. (2006). Human QKI, a potential regulator of mRNA expression of human oligodendrocyte-related genes involved in schizophrenia. *Proc. Natl. Acad. Sci. U S A* 103, 7482–7487. doi: 10.1073/pnas.0601213103

Armstrong, R. A. (2017). White matter pathology in sporadic frontotemporal lobar degeneration with TDP-43 proteinopathy. *Clin. Neuropathol.* 36, 66–72. doi: 10.5414/np300991

Balendra, R., and Isaacs, A. M. (2018). *C9orf72*-mediated ALS and FTD: multiple pathways to disease. *Nat. Rev. Neurol.* 14, 544–558. doi: 10.1038/s41582-018-0047-2

Ballas, N., Lioy, D. T., Grunseich, C., and Mandel, G. (2009). Non-cell autonomous influence of MeCP2-deficient glia on neuronal dendritic morphology. *Nat. Neurosci.* 12, 311–317. doi: 10.1038/nn.2275

Blackburn, D., Sargsyan, S., Monk, P. N., and Shaw, P. J. (2009). Astrocyte function and role in motor neuron disease: a future therapeutic target? *Glia* 57, 1251–1264. doi: 10.1002/glia.20848

Blokhuis, A. M., Groen, E. J. N., Koppers, M., van den Berg, L. H., and Pasterkamp, R. J. (2013). Protein aggregation in amyotrophic lateral sclerosis. *Acta Neuropathol.* 125, 777–794. doi: 10.1007/s00401-013-1125-6

Boulay, A.-C., Saubaméa, B., Adam, N., Chasseigneaux, S., Mazaré, N., Gilbert, A., et al. (2017). Translation in astrocyte distal processes sets molecular heterogeneity at the gliovascular interface. *Cell Discov.* 3:17005. doi: 10.1038/celldisc.2017.5

Buchan, J. R. (2014). mRNP gradules: assembly, function and connections with disease. *RNA Biol.* 11, 1019–1030. doi: 10.4161/15476286.2014.972208

Bushong, E. A., Martone, M. E., Jones, Y. Z., and Ellisman, M. H. (2002). Protoplasmic astrocytes in CA1 stratum radiatum occupy separate anatomical domains. *J. Neurosci.* 22, 183–192. doi: 10.1523/jneurosci.22-01-00183.2002

Campagnoni, A. T., Carey, G. D., and Yu, Y. T. (1980). *In vitro* synthesis of the myelin basic proteins: subcellular site of synthesis. *J. Neurochem.* 34, 677–686. doi: 10.1111/j.1471-4159.1980.tb11197.x

Coady, T. H., and Manley, J. L. (2015). ALS mutations in TLS/FUS disrupt target gene expression. *Genes Dev.* 29, 1696–1706. doi: 10.1101/gad.267286.115

Colman, D. R., Kreibich, G., Frey, A. B., and Sabatini, D. D. (1982). Synthesis and incorporation of myelin polypeptides into cns myelin. *J. Cell Biol.* 95, 598–608. doi: 10.1083/jcb.95.2.598

Conlon, E. G., Lu, L., Sharma, A., Yamazaki, T., Tang, T., Shneider, N. A., et al. (2016). The *C9ORF72* GGGGCC expansion forms RNA G-quadruplex inclusions and sequesters hnRNP H to disrupt splicing in ALS brains. *Elife* 5:e17820. doi: 10.7554/elife.17820

Connor, J. R., and Menzies, S. L. (1996). Relationship of iron to oligodendrocytes and myelination. *Glia* 17, 83–93. doi: 10.1002/(SICI)1098-1136(199606)17:2<83::AID-GLIA1>3.0.CO;2-7

Cooper-Knock, J., Walsh, M. J., Higginbottom, A., Highley, J. R., Dickman, M. J., Edbauer, D., et al. (2014). Sequestration of multiple RNA recognition motif-containing proteins by *C9ORF72* repeat expansions. *Brain* 137, 2040–2051. doi: 10.1093/brain/awu120

Deshaies, J. E., Shkreta, L., Moszczynski, A. J., Sidibé, H., Semmler, S., Fouillen, A., et al. (2018). TDP-43 regulates the alternative splicing of hnRNP A1 to yield an aggregation-prone variant in amyotrophic lateral sclerosis. *Brain* 141, 1320–1333. doi: 10.1093/brain/awy062

Dienel, G. A., and Cruz, N. F. (2004). Nutrition during brain activation: does cell-to-cell lactate shuttling contribute significantly to sweet and sour food for thought? *Neurochem. Int.* 45, 321–351. doi: 10.1016/j.neuint.2003.10.011

Ditsworth, D., Maldonado, M., McAlonis-Downes, M., Sun, S., Seelman, A., Drenner, K., et al. (2017). Mutant TDP-43 within motor neurons drives disease onset but not progression in amyotrophic lateral sclerosis. *Acta Neuropathol.* 133, 907–922. doi: 10.1007/s00401-017-1698-6

Dormann, D., and Haass, C. (2013). Fused in sarcoma (FUS): an oncogene goes awry in neurodegeneration. *Mol. Cell. Neurosci.* 56, 475–486. doi: 10.1016/j.mcn.2013.03.006

Fan, A. C., and Leung, A. K. (2016). RNA granules and diseases: a case study of stress granules in ALS and FTLD. *Adv. Exp. Med. Biol.* 907, 263–296. doi: 10.1007/978-3-319-29073-7_11

Ferraiuolo, L., Meyer, K., Sherwood, T. W., Vick, J., Likhite, S., Frakes, A., et al. (2016). Oligodendrocytes contribute to motor neuron death in ALS *via* SOD1-dependent mechanism. *Proc. Natl. Acad. Sci. U S A* 113, E6496–6505. doi: 10.1073/pnas.1607496113

Freibaum, B. D., and Taylor, J. P. (2017). The role of dipeptide repeats in *C9ORF72*-related ALS-FTD. *Front. Mol. Neurosci.* 10:35. doi: 10.3389/fnmol.2017.00035

Fünfschilling, U., Supplie, L. M., Mahad, D., Boretius, S., Saab, A. S., Edgar, J., et al. (2012). Glycolytic oligodendrocytes maintain myelin and long-term axonal integrity. *Nature* 485, 517–521. doi: 10.1038/nature11007

Garcia-Ladona, F. J., Huss, Y., Frey, P., and Ghandour, M. S. (1997). Oligodendrocytes express different isoforms of β-amyloid precursor protein in chemically defined cell culture conditions: *in situ* hybridization and immunocytochemical detection. *J. Neurosci. Res.* 50, 50–61. doi: 10.1002/(sici)1097-4547(19971001)50:1<50::aid-jnr6>3.0.co;2-k

Geloso, M. C., Corvino, V., Marchese, E., Serrano, A., Michetti, F., and D'Ambrosi, N. (2017). The dual role of microglia in ALS: mechanisms and therapeutic approaches. *Front. Aging Neurosci.* 9:242. doi: 10.3389/fnagi.2017.00242

Gendron, T. F., Bieniek, K. F., Zhang, Y. J., Jansen-West, K., Ash, P. E., Caulfield, T., et al. (2013). Antisense transcripts of the expanded *C9ORF72* hexanucleotide repeat form nuclear RNA foci and undergo repeat-associated non-ATG translation in c9FTD/ALS. *Acta Neuropathol.* 126, 829–844. doi: 10.1007/s00401-013-1192-8

Ghandour, M. S., and Skoff, R. P. (1991). Double-labeling *in situ* hybridization analysis of mRNAs for carbonic anhydrase II and myelin basic protein: expression in developing cultured glial cells. *Glia* 4, 1–10. doi: 10.1002/glia.440040102

Hafner, M., Landthaler, M., Burger, L., Khorshid, M., Hausser, J., Berninger, P., et al. (2010). Transcriptome-wide identification of RNA-binding protein and microRNA target sites by PAR-CLIP. *Cell* 141, 129–141. doi: 10.1016/j.cell.2010.03.009

Haidet-Phillips, A. M., Hester, M. E., Miranda, C. J., Meyer, K., Braun, L., Frakes, A., et al. (2011). Astrocytes from familial and sporadic ALS patients are toxic to motor neurons. *Nat. Biotechnol.* 29, 824–828. doi: 10.1038/nbt.1957

Highley, J. R., Kirby, J., Jansweijert, J. A., Webb, P. S., Hewamadduma, C. A., Heath, P. R., et al. (2014). Loss of Nuclear TDP-43 in amyotrophic lateral sclerosis (ALS) causes altered expression of splicing machinery and widespread dysregulation of RNA splicing in motor neurones. *Neuropatho. Appl. Neurobiol.* 40, 670–685. doi: 10.1111/nan.12148

Holz, A., Schaeren-Wiemers, N., Schaefer, C., Pott, U., Collelo, R. J., and Schwab, M. E. (1996). Molecular and developmental characterisation of novel cDNAs of the myelin-associated oligodendrocytic basic protein. *J. Neurosci.* 16, 467–477. doi: 10.1523/jneurosci.16-02-00467.1996

Hughes, E. G., Orthmann-Murphy, J. L., Langseth, A. J., and Bergles, D. E. (2018). Myelin remodeling through experience-dependent oligodendrogenesis in the adult somatosensory cortex. *Nat. Neurosci.* 21, 696–706. doi: 10.1038/s41593-018-0121-5

Iwahashi, C. K., Yasui, D. H., Greco, C. M., Tassone, F., Nannen, K., Babineau, B., et al. (2005). Protein composition of the intranuclear inclusions of FXTAS. *Brain* 129, 256–271. doi: 10.1093/brain/awh650

Jovičić, A., Mertens, J., Boeynaems, S., Bogaert, E., Chai, N., Yamada, S. B., et al. (2015). Modifiers of *C9orf72* dipeptide repeat toxicity connect nucleocytoplasmic transport defects to FTD/ALS. *Nat. Neurosci.* 18, 1226–1229. doi: 10.1038/nn.4085

Kamelgarn, M., Chen, J., Kuang, L., Arenas, A., Zhai, J., Zhu, H., et al. (2016). Proteomic analysis of FUS interacting proteins provides insights into FUS function and its role in ALS. *Biochim. Biophys. Acta* 1862, 2004–2014. doi: 10.1016/j.bbadis.2016.07.015

Kang, S. H., Li, Y., Fukaya, M., Lorenzini, I., Cleveland, D. W., Ostrow, L. W., et al. (2013). Degeneration and impaired regeneration of gray matter oligodendrocytes in amyotrophic lateral sclerosis. *Nat. Neurosci.* 16, 571–579. doi: 10.1038/nn.3357

Kapeli, K., Martinez, F. J., and Yeo, G. W. (2017). Genetic mutations in RNA-binding proteins and their roles in ALS. *Hum. Genet.* 136, 1193–1214. doi: 10.1007/s00439-017-1830-7

Kashima, T., Rao, N., David, C. J., and Manley, J. L. (2007). hnRNP A1 functions with specificity in repression of SMN2 exon 7 splicing. *Hum. Mol. Genet.* 16, 3149–3159. doi: 10.1093/hmg/ddm276

Khosravi, B., Hartmann, H., May, S., Möhl, C., Ederle, H., Michaelsen, M., et al. (2017). Cytoplasmic poly-GA aggregates impair nuclear import of TDP-43 in *C9orf72* ALS/FTLD. *Hum. Mol. Genet.* 26, 790–800. doi: 10.1093/hmg/ddw432

Kim, H. J., Kim, N. C., Wang, Y. D., Scarborough, E. A., Moore, J., Diaz, Z., et al. (2013). Prion-like domain mutations in hnrnps cause multisystem proteinopathy and ALS. *Nature* 495, 467–473. doi: 10.1038/nature11922

Kristensson, K., Holmes, K. V., Duchala, C. S., Zeller, N. K., Lazzarini, R. A., and Dubois-Dalcq, M. (1986). Increased levels of myelin basic protein gene transcripts in virus-induced demyelination. *Nature* 322, 544–547. doi: 10.1038/322544a0

Larocque, D., Pilotte, J., Chen, T., Cloutier, F., Massie, B., Pedraza, L., et al. (2002). Nuclear retention of MBP mRNAs in the quaking viable mice. *Neuron* 36, 815–829. doi: 10.1016/s0896-6273(02)01055-3

Laursen, L. S., Chan, C. W., and Ffrench-Constant, C. (2011). Translation of myelin basic protein mRNA in oligodendrocytes is regulated by integrin activation and hnRNP-K. *J. Cell Biol.* 192, 797–811. doi: 10.1083/jcb.201007014

Lee, Y. B., Chen, H. J., Peres, J. N., Gomez-Deza, J., Attig, J., Štalekar, M., et al. (2013). Hexanucleotide repeats in ALS/FTD form length-dependent RNA foci, sequester RNA binding proteins and are neurotoxic. *Cell Rep.* 5, 1178–1186. doi: 10.1016/j.celrep.2013.10.049

Liedtke, W., Edelmann, W., Bieri, P. L., Chiu, F. C., Cowan, N. J., Kucherlapati, R., et al. (1996). GFAP is necessary for the integrity of CNS white matter architecture and long-term maintenance of myelination. *Neuron* 17, 607–615. doi: 10.1016/s0896-6273(00)80194-4

Lin, C. G., Bristol, L. A., Jin, L., Dykes-Hoberg, M., Crawford, T., Clawson, L., et al. (1998). Aberrant RNA processing in a neurodegenerative disease: the cause for absent EAAT2, a glutamate transporter, in amyotrophic lateral sclerosis. *Neuron* 20, 589–602. doi: 10.1016/s0896-6273(00)80997-6

Ling, S. C., Polymenidou, M., and Cleveland, D. W. (2013). Converging mechanisms in ALS and FTD: disrupted RNA and protein homeostasis. *Neuron* 79, 416–438. doi: 10.1016/j.neuron.2013.07.033

LoPresti, P., Szuchet, S., Papasozomenos, S. C., Zinkowski, R. P., and Binder, L. I. (1995). Functional implications for the microtubule-associated protein tau: localization in oligodendrocytes. *Proc. Natl. Acad. Sci. U S A* 92, 10369–10373. doi: 10.1073/pnas.92.22.10369

Ludwin, S. K. (1997). The pathobiology of the oligodendrocyte. *J. Neuropathol. Exp. Neurol.* 56, 111–124. doi: 10.1097/00005072-199702000-00001

Madill, M., McDonagh, K., Ma, J., Vajda, A., McLoughlin, P., O'Brien, T., et al. (2017). Amyotrophic lateral sclerosis patient iPSC-derived astrocytes impair autophagy *via* non-cell autonomous mechanisms. *Mol. Brain* 10:22. doi: 10.1186/s13041-017-0300-4

Mandler, M. D., Ku, L., and Feng, Y. (2014). A cytoplasmic quaking I isoform regulates the hnRNP F/H-dependent alternative splicing pathway in myelinating glia. *Nucleic Acids Res.* 42, 7319–7329. doi: 10.1093/nar/gku353

Martinez, F. J., Pratt, G. A., Van Nostrand, E. L., Batra, R., Huelga, S. C., Kapeli, K., et al. (2016). Protein-RNA networks regulated by normal and ALS-associated mutant HNRNPA2B1 in the nervous system. *Neuron* 92, 780–795. doi: 10.1016/j.neuron.2016.09.050

McLaurin, J. A., and Yong, V. W. (1995). Oligodendrocytes and myelin. *Neurol. Clin.* 13, 23–49. doi: 10.1016/s0733-8619(18)30060-4

Mizukami, K., Ishikawa, M., Iwakiri, M., Ikonomovic, M. D., Dekosky, S. T., Kamma, H., et al. (2005). Immunohistochemical study of the hnRNP A2 and B1 in the hippocampal formations of brains with Alzheimer's disease. *Neurosci. Lett.* 386, 111–115. doi: 10.1016/j.neulet.2005.05.070

Molenaar, J. J., Domingo-Fernandez, R., Ebus, M. E., Lindner, S., Koster, J., Drabek, K., et al. (2012). LIN28B induces neuroblastoma and enhances MYCN levels *via* let-7 suppression. *Nat. Genet.* 44, 1199–1206. doi: 10.1038/ng.2436

Molliex, A., Temirov, J., Lee, J., Coughlin, M., Kanagaraj, A. P., Kim, H. J., et al. (2015). Phase separation by low complexity domains promotes stress granule assembly and drives pathological fibrillization. *Cell* 163, 123–133. doi: 10.1016/j.cell.2015.09.015

Mori, K., Lammich, S., Mackenzie, I. R., Forné, I., Zilow, S., Kretzschmar, H. A., et al. (2013). hnRNP A3 binds to GGGGCC repeats and is a constituent of p62-positive/TDP43-negative inclusions in the hippocampus of patients with *C9orf72* mutations. *Acta Neuropathol.* 125, 413–423. doi: 10.1007/s00401-013-1088-7

Murray, M. E., DeJesus-Hernandez, M., Rutherford, N. J., Baker, M., Duara, R., Graff-Radford, N. R., et al. (2011). Clinical and neuropathologic heterogeneity of c9FTD/ALS associated with hexanucleotide repeat expansion in *C9ORF72*. *Acta Neuropathol.* 122, 673–690. doi: 10.1007/s00401-011-0907-y

Neumann, M., Kwong, L. K., Truax, A. C., Vanmassenhove, B., Kretzschmar, H. A., Van Deerlin, V. M., et al. (2007). TDP-43-positive white matter pathology in frontotemporal lobar degeneration with ubiquitin-positive inclusions. *J. Neuropathol. Exp. Neurol.* 66, 177–183. doi: 10.1097/01.jnen.0000248554.45456.58

Neumann, M., Sampathu, D., Kwong, L. K., Truax, A. C., Micsenyi, M., Chou, T., et al. (2006). Ubiquitinated TDP-43 in frontotemporal lobar degeneration and amyotrophic lateral sclerosis. *Science* 10, 130–133. doi: 10.1126/science.1134108

Phatnani, H., and Maniatis, T. (2015). Astrocytes in neurodegenerative disease. *Cold Spring Harb. Perspect. Biol.* 7:a020628. doi: 10.1101/cshperspect.a020628

Porta, S., Kwong, L. K., Trojanowski, J. Q., and Lee, V. M. (2015). Drosha inclusions are new components of dipeptide-repeat protein aggregates in FTLD-TDP and ALS *C9orf72* expansion cases. *J. Neuropathol. Exp. Neurol.* 74, 380–387. doi: 10.1097/nen.0000000000000182

Rothstein, J. D., Van Kammen, M., Levey, A. I., Martin, L. J., and Kuncl, R. W. (1995). Selective loss of glial glutamate transporter GLT-1 in amyotrophic lateral sclerosis. *Ann. Neurol.* 38, 73–84. doi: 10.1002/ana.410380114

Saab, A. S., Tzvetanova, I. D., and Nave, K. A. (2013). The role of myelin and oligodendrocytes in axonal energy metabolism. *Curr. Opin. Neurobiol.* 23, 1065–1072. doi: 10.1016/j.conb.2013.09.008

Saab, A. S., Tzvetavona, I. D., Trevisiol, A., Baltan, S., Dibaj, P., Kusch, K., et al. (2016). Oligodendroglial NMDA receptors regulate glucose import and axonal energy metabolism. *Neuron* 91, 119–132. doi: 10.1016/j.neuron.2016.05.016

Sakers, K., Lake, A. M., Khazanchi, R., Ouwenga, R., Vasek, M. J., Dani, A., et al. (2017). Astrocytes locally translate transcripts in their peripheral processes. *Proc. Natl. Acad. Sci. U S A* 114, E3830–E3838. doi: 10.1073/pnas.1617782114

Seilhean, D., Cazeneuve, C., Thuriès, V., Russaouen, O., Millecamps, S., Salachas, F., et al. (2009). Accumulation of TDP-43 and α-actin in an amyotrophic lateral sclerosis patient with the K17I ANG mutation. *Acta Neuropathol.* 118, 561–573. doi: 10.1007/s00401-009-0545-9

Serio, A., Bilican, B., Barmada, S. J., Ando, D. M., Zhao, C., Siller, R., et al. (2013). Astrocyte pathology and the absence of non-cell autonomy in an induced pluripotent stem cell model of TDP-43 proteinopathy. *Proc. Natl. Acad. Sci. U S A* 110, 4697–4702. doi: 10.1073/pnas.1300398110

Shi, K. Y., Mori, E., Nizami, Z. F., Lin, Y., Kato, M., Xiang, S., et al. (2017). Toxic PR(n) poly-dipeptides encoded by the *C9orf72* repeat expansion block nuclear import and export. *Proc. Natl. Acad. Sci. U S A* 114, E1111–E1117. doi: 10.1073/pnas.1620293114

Tong, J., Huang, C., Bi, F., Wu, Q., Huang, B., Liu, X., et al. (2013). Expression of ALS-linked TDP-43 mutant in astrocytes causes non-cell-autonomous motor neuron death in rats. *EMBO J.* 32, 1917–1926. doi: 10.1038/emboj.2013.122

Torvund-Jensen, J., Steengaard, J., Reimer, L., Fihl, L. B., and Laursen, L. S. (2014). Transport and translation of MBP mRNA is regulated differently by distinct hnRNP Proteins. *J. Cell Sci.* 127, 1550–1564. doi: 10.1242/jcs.140855

Uren, P. J., Bahrami-Samani, E., de Araujo, P. R., Vogel, C., Qiao, M., Burns, S. C., et al. (2016). High-throughput analyses of hnRNP H1 dissects its multi-functional aspect. *RNA Biol.* 13, 400–411. doi: 10.1080/15476286.2015.1138030

Vanderweyde, T., Youmans, K., Liu-Yesucevitz, L., and Wolozin, B. (2013). Role of stress granules and RNA-binding proteins in neurodegeneration: a mini-review. *Gerontology* 59, 524–533. doi: 10.1159/000354170

Wang, E., Dimova, N., and Cambi, F. (2007). PLP/DM20 ratio is regulated by hnRNPH and F and a novel G-rich enhancer in oligodendrocytes. *Nucleic Acids Res.* 35, 4164–4178. doi: 10.1093/nar/gkm387

Wang, E., Dimova, N., Sperle, K., Huang, Z., Lock, L., McCulloch, M. C., et al. (2008). Deletion of a splicing enhancer disrupts PLP1/DM20 ratio and myelin stability. *Exp. Neurol.* 214, 322–330. doi: 10.1016/j.expneurol.2008.09.001

White, R., Gonsior, C., Krämer-Albers, E., Stöhr, N., Hüttelmaier, S., and Trotter, J. (2008). Activation of oligodendroglial fyn kinase enhances translation of mRNAs transported in hnRNP A2-dependent RNA granules. *J. Cell Biol.* 181, 579–586. doi: 10.1083/jcb.200706164

Yamanaka, K., Chun, S. J., Boillee, S., Fujimori-Tonou, N., Yamashita, H., Gutmann, D. H., et al. (2008). Astrocytes as determinants of disease progression in inherited ALS. *Nat. Neurosci.* 11, 251–253. doi: 10.1038/nn2047

Yasuda, K., and Mili, S. (2016). Dysregulated axonal RNA translation in amyotrophic lateral sclerosis. *Wiley Interdiscip. Rev. RNA* 7, 589–603. doi: 10.1002/wrna.1352

Yeung, M. S., Zdunek, S., Bergmann, O., Bernard, S., Salehpour, M., Alkass, K., et al. (2014). Dynamics of oligodendrocyte generation and myelination in the human brain. *Cell* 159, 766–774. doi: 10.1016/j.cell.2014.10.011

Yoon, B. C., Zivraj, K. H., and Holt, C. E. (2009). Local translation and mRNA trafficking in axon pathfinding. *Results Probl. Cell Differ.* 48, 269–288. doi: 10.1007/400_2009_5

Zhang, Y. J., Gendron, T. F., Grima, J. C., Sasaguri, H., Jansen-West, K., Xu, Y. F., et al. (2016). *C9ORF72* poly(GA) aggregates sequester and impair HR23 and nucleocytoplasmic transport proteins. *Nat. Neurosci.* 19, 668–677. doi: 10.1038/nn.4272

Conflict of Interest Statement: The authors declare that the research was conducted in the absence of any commercial or financial relationships that could be construed as a potential conflict of interest.

Copyright © 2019 Barton, Gregory, Chandran and Turner. This is an open-access article distributed under the terms of the Creative Commons Attribution License (CC BY). The use, distribution or reproduction in other forums is permitted, provided the original author(s) and the copyright owner(s) are credited and that the original publication in this journal is cited, in accordance with accepted academic practice. No use, distribution or reproduction is permitted which does not comply with these terms.

frontiers in Molecular Neuroscience

ORIGINAL RESEARCH
published: 30 July 2019
doi: 10.3389/fnmol.2019.00181

Can We Use 2,3,5-Triphenyltetrazolium Chloride-Stained Brain Slices for Other Purposes? The Application of Western Blotting

Sonia Sanchez-Bezanilla[1,2], Michael Nilsson[1,2,3,4,5], Frederick R. Walker[1,2,3,4] and Lin Kooi Ong[1,2,3,6]**

[1] School of Biomedical Sciences and Pharmacy and Priority Research Centre for Stroke and Brain Injury, The University of Newcastle, Callaghan, NSW, Australia, [2] Hunter Medical Research Institute, New Lambton Heights, NSW, Australia, [3] NHMRC Centre of Research Excellence in Stroke Rehabilitation and Brain Recovery, Heidelberg, VIC, Australia, [4] Centre for Rehab Innovations, The University of Newcastle, Callaghan, NSW, Australia, [5] Lee Kong Chian School of Medicine, Nanyang Technological University, Singapore, Singapore, [6] School of Pharmacy, Monash University Malaysia, Bandar Sunway, Malaysia

2,3,5-Triphenyltetrazolium chloride (TTC) staining is a commonly used method to determine the volume of the cerebral infarction in experimental stroke models. The TTC staining protocol is considered to interfere with downstream analyses, and it is unclear whether TTC-stained brain samples can be used for biochemistry analyses. However, there is evidence indicating that, with proper optimization and handling, TTC-stained brains may remain viable for protein analyses. In the present study, we aimed to rigorously assess whether TTC can reliably be used for western blotting of various markers. In this study, brain samples obtained from C57BL/6 male mice were treated with TTC (TTC+) or left untreated (TTC−) at 1 week after photothrombotic occlusion or sham surgery. Brain regions were dissected into infarct, thalamus, and hippocampus, and proteins were extracted by using radioimmunoprecipitation assay buffer. Protein levels of apoptosis, autophagy, neuronal, glial, vascular, and neurodegenerative-related markers were analyzed by western blotting. Our results showed that TTC+ brains display similar relative changes in most of the markers compared with TTC− brains. In addition, we validated that these analyses can be performed in the infarct as well as other brain regions such as the thalamus and hippocampus. Our findings demonstrate that TTC+ brains are reliable for protein analyses using western blotting. Widespread adoption of this approach will be key to lowering the number of animals used while maximizing data.

Keywords: stroke, 2,3,5-triphenyltetrazolium chloride, western blotting, infarct, thalamus, hippocampus

OPEN ACCESS

Edited by:
Robert J. Harvey, University of the Sunshine Coast, Australia

Reviewed by:
Fabrizio Michetti, Catholic University of the Sacred Heart, Italy
Shyam Gajavelli, University of Miami, United States

****Correspondence:***
Sonia Sanchez-Bezanilla
sonia.sanchezbezanilla@uon.edu.au
Lin Kooi Ong
ong.linkooi@monash.edu

Received: *19 May 2019*
Accepted: *10 July 2019*
Published: *30 July 2019*

Citation:
Sanchez-Bezanilla S, Nilsson M, Walker FR and Ong LK (2019) Can We Use 2,3,5-Triphenyltetrazolium Chloride-Stained Brain Slices for Other Purposes? The Application of Western Blotting. Front. Mol. Neurosci. 12:181. doi: 10.3389/fnmol.2019.00181

INTRODUCTION

2,3,5-Triphenyltetrazolium chloride (TTC) is a marker of metabolic function and represents a reliable indicator of ischemic areas in experimental stroke models. TTC is a colorless water-soluble dye that is reduced by the mitochondrial enzyme succinate dehydrogenase of living cells into a water-insoluble, light sensitive compound (formazan) that turns healthy/normal tissue deep red.

In contrast, damaged/dead tissue remains white showing the absence of living cells, and thereby indicating the infarct region (Bederson et al., 1986; Li et al., 1997). TTC staining is a widely used technique in stroke and brain injury research because it is simple, cost effective, and offers a rapid visualization of infarct and penumbral areas (Benedek et al., 2006).

Currently, TTC is used as an immersion staining of fresh brain slices (Bederson et al., 1986) or by intracardiac injection (Sun et al., 2012). However, in the vast majority of studies, these TTC-stained brains are immediately discarded after infarct assessment as it is unclear whether the tissue is suitable for subsequent cellular and molecular analyses. Western blotting is a common method used to detect and analyze protein levels. This technique involves the separation of denatured proteins based on their molecular weight and visualization using antibodies specific to the target protein (Burnette, 1981; Liu et al., 2014). The simplicity and relevance of the method has led to its expansive application as a ubiquitous research tool in medical biochemistry.

TTC staining has been shown to be compatible for the analysis of some specific proteins. However, previous studies presented some limitations. A previous study by Sun et al. (2012) showed that *in vivo* TTC-labeling was compatible with immunofluorescence, mRNA, and protein analysis. However, this study only focused on apoptotic markers in penumbral tissue, and therefore it cannot be concluded that this technique can be used to study other markers and other brain regions. In addition, TTC was administered transcardially, which is highly toxic to the animals, instead of immersing the brain sections in a TTC-staining solution. Another study by Kramer et al. (2010) demonstrated that TTC processing *ex vivo* after middle cerebral artery occlusion in rats can be used for quantitative gene and protein expression analyses using RT-PCR and western blot. However, this study only analyzed the protein expression profile of the metalloprotease-disintegrin ADAM12 and the housekeeping protein β-actin. Additional work in this field has also demonstrated that TTC-stained brain sections can also be used for immunohistochemical quantification of Collagen IV and immunofluorescence analyses (Li L. et al., 2018; Li Z. et al., 2018).

Taken into account previous data, the main objective of the present study was to investigate whether TTC-treated tissues can be processed for downstream biochemical analyses, specifically by western blotting. We aimed to rigorously compare the protein expression profile of wide range of commonly used markers between TTC-treated (TTC+) and untreated (TTC−) brains across a number of different brain regions. We hypothesized that TTC treatment would not interfere with protein quantification in the regions studied.

MATERIALS AND METHODS

The data that support the findings for this study are available from the corresponding author on reasonable request.

Experimental Design

Animal research was undertaken in accordance with the ARRIVE guidelines (Animal Research: Reporting of *in vivo* Experiments). Experiments were approved by the University of Newcastle Animal Care and Ethics Committee (A-2013-340) and conducted in accordance with the New South Wales Animals Research Act and the Australian Code of Practice for the use of animals for scientific purposes. A total of 24 mice were randomly allocated to one of four groups: TTC− sham, TTC− stroke, TTC+ sham, and TTC+ stroke. At day 0, mice were subjected to photothrombotic occlusion or sham surgery. At day 7 post-stroke, mice were euthanized. Brains were collected and sliced using a matrix device into 2 mm coronal sections. One cohort (sham $n = 6$; stroke $n = 6$) was stained by TTC and the other cohort (sham $n = 6$; stroke $n = 6$) was not stained.

Sample Size Calculation

Sample size was estimated using G*Power 3.1 software. To determine the sample size required for this study, we used western blot data from our recent study (NeuN; sham = 1.00 ± 0.04 versus stroke = 0.65 ± 0.06; $n = 7$ per group). Allowing a type 1 error of 5%, $\alpha = 0.05$ with the power of 80%, $\beta = 0.2$ we calculated a sample size of six mice per group (Sanchez-Bezanilla et al., 2019).

Animals

C57BL/6 male mice (10 weeks old) were obtained from the Animal Services Unit at the University of Newcastle. Mice were maintained in a temperature (21°C ± 1) and humidity (∼55%) controlled environment with food and water available *ad libitum*. Lighting was on a 12:12 h reverse light–dark cycle (lights on 19:00 h) with all procedures conducted in the dark phase. In all experiments, mice were acclimatized to the environment for a minimum of 7 days prior to the start of the experiment. Mice were housed between 2 and 4 per cage.

Photothrombotic Occlusion

Photothrombotic occlusion was performed as previously described (Ong et al., 2017c; Sanchez-Bezanilla et al., 2019). Briefly, mice were anesthetized by 2% isoflurane (Isothesia #029404, Henry Schein) during surgical procedures on a temperature controlled (37°C ± 1) stereotaxic frame. The skull was exposed by incision of the skin along the midline of the scalp. Rose Bengal (200 μl, 10 mg/ml solution in sterile saline, Sigma–Aldrich #330000, United States) was injected intraperitoneally. After 8 min, the skull was illuminated for 15 min by a 4.5 mm diameter cold light source (Zeiss KL2500LCD, Germany) positioned at 2.2 mm left lateral of bregma 0.0 mm, targeting the left motor and somatosensory cortices. For the sham group, the same surgical procedure was conducted except Rose Bengal was replaced with 200 μl of sterile saline (0.9% NaCl, Pfizer #SYM273384, Australia).

Brain Regions Preparation and Collection

At day 7, mice were deeply anesthetized via intraperitoneal injection of 200 μl of sodium pentobarbital (Lethabarb #3729556, Virbac, Australia). Mice were transcardially perfused with ice cold 0.9% NaCl (UNIVAR #AJA465-2.5KG) with 0.1%

diethylpyrocarbonate (Sigma–Aldrich #D5758, Australia) for 3 min. Brains were dissected and sliced using a matrix device (Zivic Instruments #5325, United States) into 2 mm coronal sections from the olfactory bulb to the cerebellum. For TTC+ brains (sham n = 6, stroke n = 6), sections were taken and incubated in 2% TTC (Sigma–Aldrich #T8877) in saline at 37°C for 10 min. TTC+ brain sections were captured with a digital camera (Sony HDR-PJ790) for infarct volume analyses. Infarct (identified as non-TTC-stained region in stroke mice and equivalent region in sham mice), thalamus (Bregma −1.0 to −2.2), and hippocampus (Bregma −1.5 to −2.5) areas were identified and dissected from the coronal sections and then frozen at −80°C. For TTC− brains (sham n = 6, stroke n = 6), same brain regions were dissected (infarct identified as part of the cortex that appeared to be occluded) and immediately frozen at −80°C (**Figure 1A**).

Infarct Volume Quantification

Contralateral and ipsilateral hemisphere and infarct areas were traced using ImageJ software. Infarct volume was corrected for edema using the formula: corrected infarct volume (mm^3) = infarct volume × (contralateral volume/ipsilateral volume). Edema was calculated by infarct volume minus corrected infarct volume (Murtha et al., 2016; **Figure 1B**).

Protein Extraction and Western Blotting

Western blot was performed as previously described with minor modification (Ong et al., 2017b, 2018). Infarct, thalamus, and hippocampus samples were sonicated using a UP50H microsonicator (Hielscher Ultrasonics GmbH, Germany) for 3 × 30 s pulses at 4°C in radioimmunoprecipitation assay (RIPA) buffer [25 mM Tris buffer pH 7.4, 150 mM NaCl, 0.5% sodium deoxycholate, 0.1% SDS, 1% Triton X-100, 1 protease inhibitor cocktail tablet (every 50 ml), 1× phosphatase inhibitor cocktail tablet (every 50 ml)]. Samples were centrifuged at 14,000 ×g for 20 min at 4°C. The supernatant fractions were collected. Protein concentrations were determined using a Pierce BCA protein assay kit (Thermo Fisher Scientific #23225, United States) according to the manufacturer's instructions. Each sample's final concentration was adjusted to 1.5 mg/ml and aliquoted. Samples were mixed with sample buffer (2% SDS, 10% glycerol, 1% dithiothreitol). Equal amounts of tissue protein samples were electrophoresed into Bio-Rad Criterion TGC stain-free 4–20% gels (Bio-Rad #5678095, Australia). To ensure that an equal amount of protein was loaded, one gel per region was scanned using ChemiDoc XRS+ system (Bio-Rad) before the transfer (**Supplementary Figure S1**). Gels were transferred to polyvinylidene difluoride membranes (Bio-Rad #1620177, Australia). PVDF membranes were washed three times in Tris-buffered saline with Tween (TBST) (150 mM NaCl, 10 mM Tris, 0.075% Tween-20, pH 7.5) and incubated in 5% skim milk powder in TBST for 1 h at room temperature. Membranes were incubated with primary antibodies (amyloid-β, α-synuclein, NeuN, glial fibrillary acidic protein (GFAP), ADLH1L1, PSD95, Tau5, P-Tau, P-Tau Ser396, synaptophysin, LC3, caspase-3, CD11b, VEGFA, Collagen IV, and CD31) overnight at 4°C and secondary antibody for 1 h at room temperature (see **Table 1** for antibodies details and concentration). In between each incubation step, membranes were washed three times in TBST. Membranes were visualized on an Amersham Imager 600 using Luminata Classico (Millipore #WBLUC0500, Australia) or Luminata Forte (Millipore #WBLUF0500, Australia) western blotting detection reagents. The density of the bands was measured using Amersham Imager 600 analysis software. The housekeeping protein β-actin was used as a loading control to normalize the levels of target protein. For representative images, two out of six bands per group were cropped from the raw blots and aligned together. The bands were then minimally

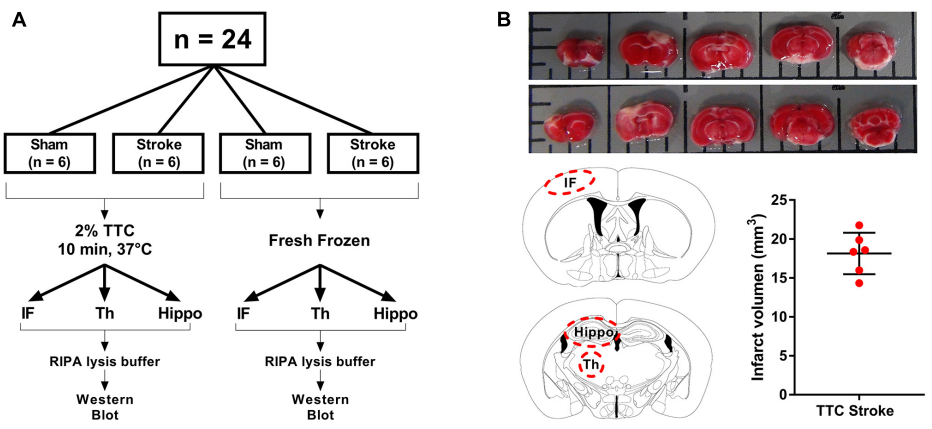

FIGURE 1 | Schematic illustration of the experimental design. **(A)** Mice were randomly allocated to sham or stroke group. At day 7 post-stroke mice were euthanized and brains were sliced into 2 mm thin sections using a matrix device. Brain samples were divided into two different groups. The brain slides from the first group (TTC+) were stained with 2% TTC at 37°C for 10 min, then further dissected into infarct (IF), thalamus (Th), and hippocampus (Hippo) and frozen at −80°C. The slices from the second group (TTC−) were dissected and immediately frozen at −80°C. **(B)** Top panel: images of TTC+ mouse brain slices after photothrombotic stroke. After the brain have been sliced, we placed the 2 mm section on a grid mat. Once we have taken a picture of one side (rostral, row 1) of the brain, we flipped the sections and take a picture of the other side (caudal, row 2). Bottom panel: schematic illustration showing the location of the examined regions (IF, Th, and Hippo) (left). Quantification of the IF volume in TTC+ stroke mice (right).

TABLE 1 | List of antibodies used for western blotting.

	Target	Description	Sources of antibodies	Dilution
Apoptosis and autophagy	Caspase-3	Caspase-3 is an intracellular proteases that mediates cell death and plays a critical role in apoptosis. Activation of caspase-3 requires proteolytic processing (Fernandes-Alnemri et al., 1994).	Sigma–Aldrich, anti-Caspase 3, #C8487-200UL	1:1000
	LC3	Light chain 3 (LC3) is an autophagy marker. Cleavage of LC3 yields the cytosolic LC3-I form. During autophagy, LC3-I is converted to LC3-II permitting LC3 to become associated with autophagic vesicles (Kabeya et al., 2000).	Sigma–Aldrich, anti-LC3, #L8918-200UL	1:1000
Neuronal	NeuN	Neuronal nuclei (NeuN) is a nuclear protein expressed in most post-mitotic neurons of the central and peripheral nervous systems (Mullen et al., 1992). Marker for mature neurons.	Cell Signaling, anti-NeuN (D3S31), #12943	1:2000
	Synaptophysin	Synaptophysin is an integral membrane protein of small synaptic vesicles in the brain (Wiedenmann et al., 1986).	Millipore, anti-Synaptophysin, #MAB329	1:10,000
	PSD95	Postsynaptic density protein 95 (PSD95) is a scaffolding protein involved in the assembly and function of the postsynaptic density complex (Chetkovich et al., 2002).	Cell Signaling, anti-Postsynaptic density protein 95, #2507	1:1000
Glial	GFAP	Glial fibrillary acidic protein (GFAP) forms intermediate filaments in astroglial cells and modulate their motility and shape. GFAP filaments are characteristic of differentiated and mature brain astrocytes (Eng et al., 2000).	Cell Signaling, anti-Glial Fibrillary Acidic Protein (GA5), #3670	1:5000
	ALDH1L1	10-Formyltetrahydrofolate dehydrogenase (ALDH1L1) is a multidomain protein that serves as a CNS astrocyte marker (Cahoy et al., 2008).	Millipore, anti-ALDH1L1 (N103/39), #MABN495	1:2000
	CD11b	Cluster of differentiation molecule 11b (CD11b) is a transmembrane protein expressed by neutrophils, monocytes, macrophages, and microglia (Solovjov et al., 2005).	Abcam, anti-CD11b, #ab75476	1:2000
Vascular	VEGFA	Growth factor active in angiogenesis, vasculogenesis, and endothelial cell growth. Induces endothelial cell proliferation, promotes cell migration, inhibits apoptosis, and induces permeabilization of blood vessels (Leung et al., 1989).	Abcam, anti-VEGFA #ab46154	1:1000
	CD31 (PECAM-1)	CD31 (Platelet Endothelial Cell Adhesion Molecule-1, PECAM-1) is a cell adhesion molecules expressed by circulating platelets, monocytes, neutrophils, some T cells, and makes up a large portion of endothelial cell intercellular junctions. Modulates cell adhesion, endothelial cell migration, and angiogenesis (Newman, 1997).	Cell Signaling, anti-CD31 (PECAM-1) (D8V9E) #77699 Sigma–Aldrich, anti-PECAM-1 #SAB4502167	1:1000 1:1000
	Collagen IV	Type IV collagen is the major structural component of basement membranes. Type IV collagen is a network-forming collagen that provides a molecular scaffold and interacts with cells, growth factors, and other basement membrane components such as laminin, nidogen, and perlecan (Kuhn, 1995).	Abcam, anti-Collagen IV #ab6586	1:1000
Neurodegeneration	Amyloid-β	Amyloid-β (Aβ) peptide produced through sequential proteolytic processing of amyloid precursor protein, and it is prone to aggregate in pathological conditions (Haass and Selkoe, 2007; Walsh and Selkoe, 2007).	Biolegend, anti-Amyloid-β (6E10), # SIG-39320	1:1000
	α-Synuclein	α-Synuclein (α-Syn) is expressed in brain, primarily in presynaptic nerve terminals. Although the exact function has not been determined, it has been linked to the prominent neurodegenerative disorders (Maroteaux et al., 1988; van der Putten et al., 2000).	BD Bioscience, anti-α-Synuclein, #610787	1:1000

(Continued)

TABLE 1 | Continued

	Target	Description	Sources of antibodies	Dilution
	Tau5	Tau5 detects total levels of Tau. Tau are a microtubule-associated proteins that bind to the tubulin subunits of microtubule structures, and promote and stabilize microtubule assembly (Avila et al., 2004; Johnson and Stoothoff, 2004).	Millipore, anti-Tau5, #MAB361	1:2000
	P-Tau (Ser400/ Thr403/Ser404)	Phospho-Tau (P-Tau) recognizes endogenous levels of tau protein when phosphorylated at Ser400 or Thr403 or Ser404. Studies have shown that tau phosphorylation at Ser404 destabilizes microtubules and that tau is hyperphosphorylated at Ser404 in Alzheimer's disease (Evans et al., 2000). Phosphorylation decreases the ability of tau to bind to microtubules, destabilizing the structure and driving it toward disassembly. Neurofibrillary tangles are a major hallmark of Alzheimer's disease; these tangles are composed of hyperphosphorylated tau (Johnson and Stoothoff, 2004).	Cell Signaling, anti-Phospo-Tau (Ser400/Thr403/Ser404), #11837	1:1000
	P-Tau (Ser396)	Phospho-Tau (Ser396) (P-Tau Ser396) detects endogenous levels of Tau only when phosphorylated at serine 396. Phosphorylation at Ser396 has shown to destabilize microtubules and contribute to different neurological disorders (Bramblett et al., 1993; Evans et al., 2000).	Cell Signaling, anti-Phospo-Tau (Ser396), #9632	1:1000
Housekeeping	β-Actin	β-Actin is a cytoskeletal housekeeping protein.	Sigma–Aldrich, monoclonal anti-β-actin-HRP antibody, A3854	1:50,000
Secondary	Rabbit IgG	Secondary antibody.	Bio-Rad, Anti-Rabbit-HRP antibody, #170-6515	1:7500
	Mouse IgG	Secondary antibody.	Bio-Rad, Anti-Mouse-HRP antibody, #170-6516	1:10,000

processed in term of brightness and contrast, and presented as the representative blots in the figures.

Statistics

All data were expressed as a fold increase of the mean ± SEM for each group relative to the mean of the TTC− sham group. These data were analyzed by using GraphPad Prism v7.02. Data from western blotting were analyzed using two-way analysis of variance (ANOVA) followed by Sidak's *post hoc* comparison. The significant differences shown on the graphs with asterisks (*) refer to the *post hoc* tests. All differences were considered to be significant at $p < 0.05$.

RESULTS

Apoptotic and Autophagy Markers

Protein levels of pro-caspase-3 and cleaved caspase-3 were significantly reduced in stroke mice compared to sham in the infarct area of both the TTC− (pro-caspase-3 $p = 0.0419$; cleaved caspase-3 $p = 0.0001$) and the TTC+ (pro-caspase-3 $p < 0.0001$; cleaved caspase-3 $p = 0.0432$) group. We found no significant differences in neither the thalamus nor hippocampus (**Figure 2A**). Quantification of LC3 showed a significant decrease in stroke mice compared to sham in the infarct of the TTC− (LC3I $p < 0.0001$; LC3II $p < 0.0001$) and TTC+ (LC3I $p < 0.0001$; LC3II $p < 0.0001$) group. Changes in the protein expression levels in the thalamus and hippocampus were not statistically significant between sham and stroke group (**Figure 2B**).

Neuronal Markers

Protein levels of NeuN were significantly reduced in stroke mice in the infarct and thalamus areas of both TTC− (NeuN infarct $p < 0.0001$, NeuN thalamus $p = 0.0021$) and TTC+ (NeuN infarct $p < 0.0001$; NeuN thalamus $p = 0.0086$) group. However, no significant differences were found in the hippocampus (**Figure 3A**). Protein levels of synaptophysin were significantly reduced in the infarct ($p = 0.0040$), thalamus ($p = 0.0019$), and hippocampus ($p = 0.0042$) of TTC− stroke. In the TTC+ group, synaptophysin was significantly reduced just in the hippocampus ($p < 0.0001$) (**Figure 3B**). We observed a significant decrease in PSD95 in the infarct area of TTC− ($p < 0.0001$) and TTC+ ($p < 0.0001$) brains. However, no significant changes were observed in the other regions (**Figure 3C**).

Glial Markers

Glial fibrillary acidic protein was significantly increased in all investigated regions in the TTC− stroke mice compared to sham (infarct $p = 0.0015$; thalamus $p < 0.0001$; hippocampus $p < 0.0001$). In the TTC+ stroke mice, GFAP was increased in the thalamus ($p = 0.0100$) and hippocampus ($p < 0.0001$)

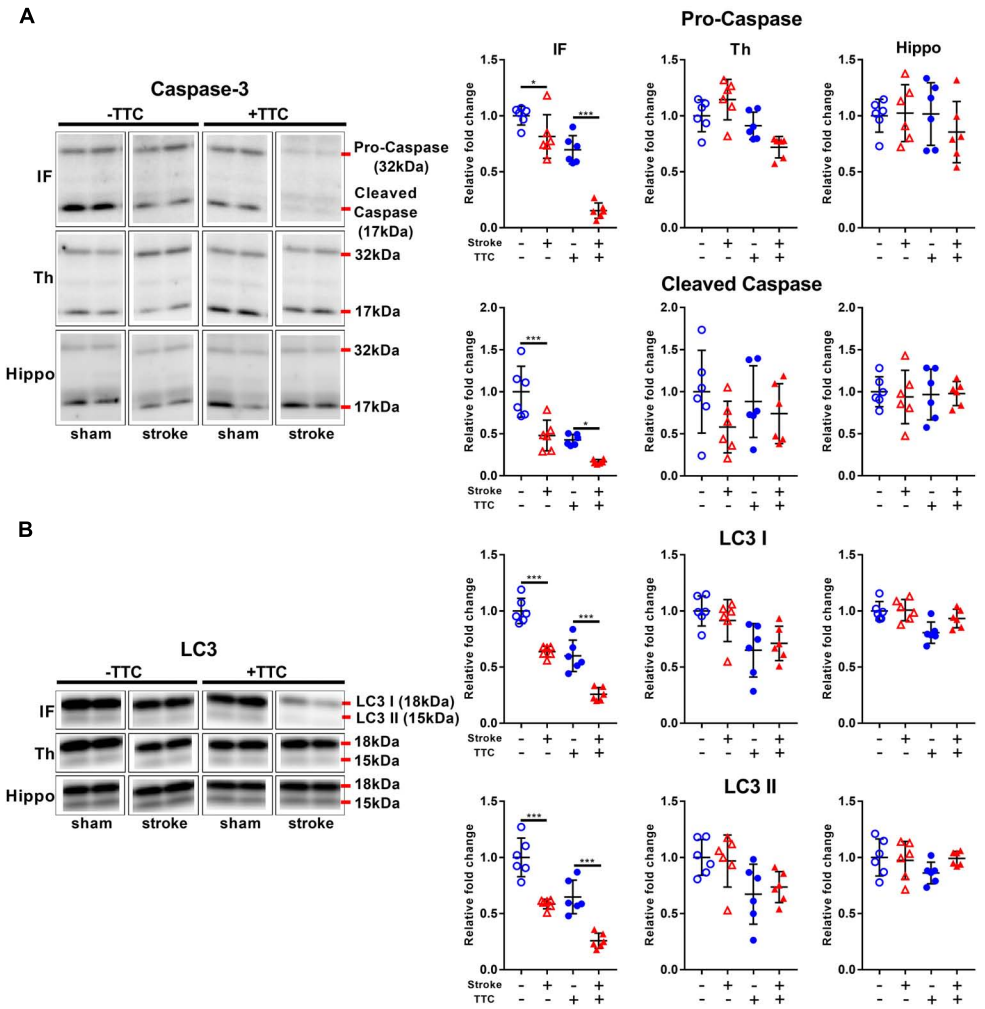

FIGURE 2 | Apoptotic and autophagy markers. Representative western blot and quantification of caspase-3 (pro-caspase and cleaved caspase) **(A)** and LC3 (LC3I and LC3II) **(B)** within the infarct (IF), thalamus (Th), and hippocampus (Hippo). Mean ± SEM (two-way ANOVA and Sidak's multiple comparisons). ○TTC– sham; △TTC– stroke; ●TTC+ sham; ▲TTC+ stroke. *$p < 0.05$, ***$p < 0.001$.

(**Figure 4A**). In contrast, ALDH1L1 was significantly downregulated in the infarct area of both TTC− ($p < 0.0001$) and TTC+ ($p < 0.0001$) stroke mice (**Figure 4B**). No significant differences were found in other areas. CD11b showed increased protein levels in the infarct area of TTC− ($p = 0.0029$) and TTC+ ($p < 0.0001$) stroke mice (**Figure 4C**). CD11b was also increased in the thalamus of TTC− stroke mice ($p < 0.0001$). There were no significant differences in the hippocampus.

Vascular Markers

We analyzed the expression of Collagen IV, CD31, and VEGFA. VEGFA showed a significant decrease in the infarct area of TTC+ stroked mice. There were no differences in the thalamus or hippocampus (**Supplementary Figure S2**). However, we could not detect any bands for Collagen IV or CD31. This could be due to the protein extraction protocol was not suitable for these target proteins or the recommended conditions of the antibodies used were not optimized. It will be of considerable interest in future studies, using appropriate lysis buffer and protein extraction procedure as well as validated primary antibodies, to examine vascular markers in TTC-treated tissues.

Neurodegeneration-Related Markers

We analyzed the expression levels of three commonly investigated neurotoxic protein markers. First, we analyzed amyloid-β (Aβ) oligomerization after stroke. Specifically, we quantitated the pentamer (25 kDa), intermediate size oligomers (30 kDa), decamer (50 kDa), and dodecamer (55 kDa). We observed showed a significant increase of all Aβ oligomers studied in the infarct area of both TTC− (pentamer $p < 0.0001$; intermediate size oligomer $p < 0.0001$; decamer $p = 0.0175$; dodecamer $p = 0.0336$) and TTC+ (pentamer $p < 0.0001$; intermediate size oligomer $p = 0.0047$; decamer $p < 0.0001$; dodecamer $p < 0.0001$) stroke mice. In the thalamus, we observed a significant increase in the pentamer ($p = 0.0366$), intermediate size oligomers ($p = 0.0021$), and

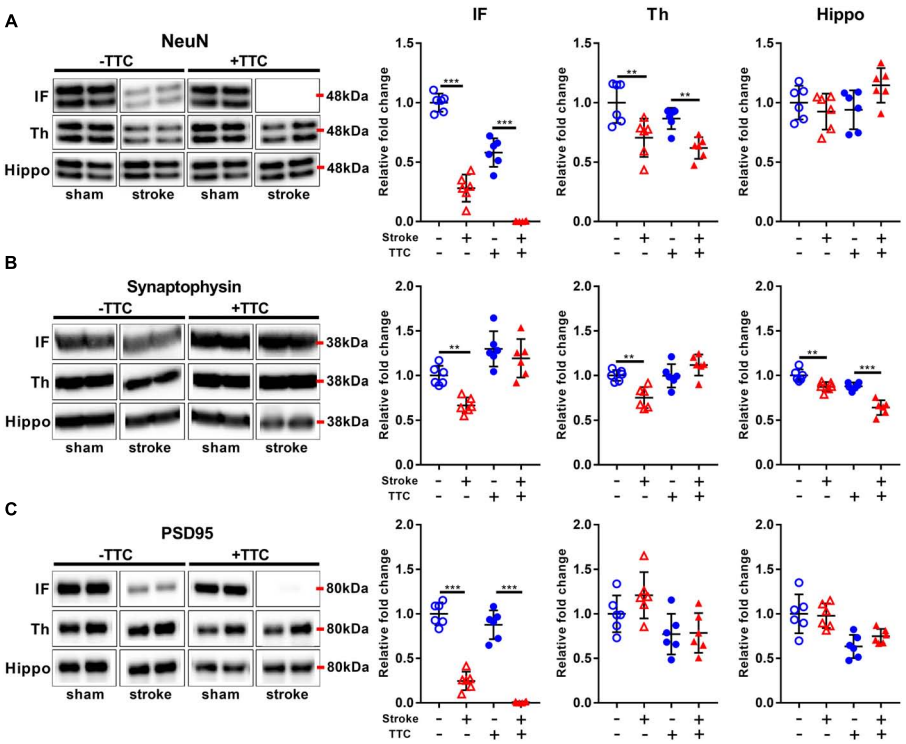

FIGURE 3 | Neuronal markers. Representative western blot and quantification of NeuN **(A)** Synaptophysin **(B)**, and PSD95 **(C)** within the infarct (IF), thalamus (Th), and hippocampus (Hippo). Mean ± SEM (two-way ANOVA and Sidak's multiple comparisons). ○TTC– sham; △TTC– stroke; ●TTC+ sham; ▲TTC+ stroke. $^{**}p < 0.01$, $^{***}p < 0.001$.

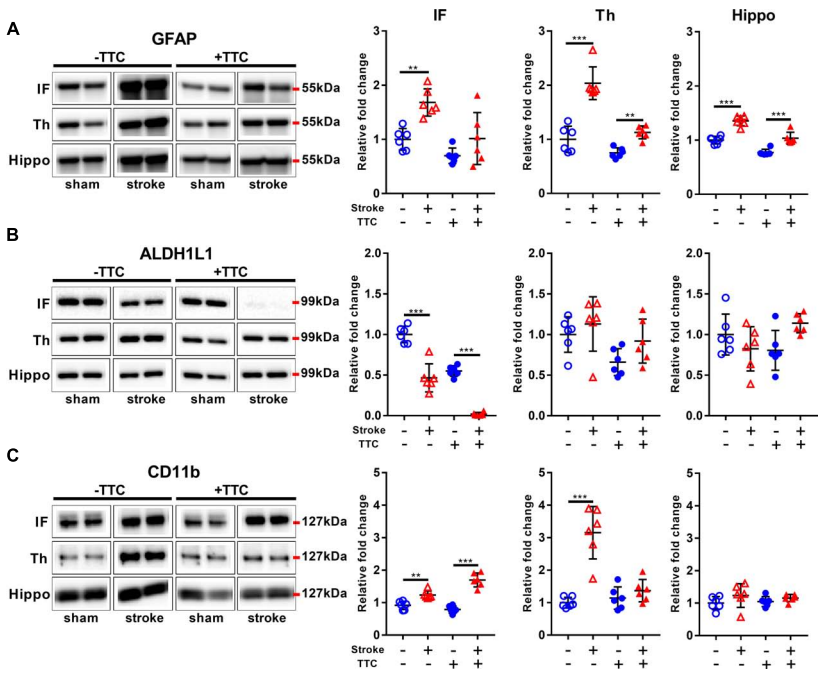

FIGURE 4 | Glial markers. Representative western blot and quantification of GFAP **(A)**, ALDH1L1 **(B)**, and CD11b **(C)** within the infarct (IF), thalamus (Th), and hippocampus (Hippo). Mean ± SEM (two-way ANOVA and Sidak's multiple comparisons). ○TTC– sham; △TTC– stroke; ●TTC+ sham; ▲TTC+ stroke. $^{**}p < 0.01$, $^{***}p < 0.001$.

decamer (p = 0.0022) in the TTC− stroke group. Protein levels in the TTC+ stroke group showed a trend toward an increase however was not statistically different to sham animals. Additionally, in the hippocampus we observed a significant increase in the pentamer in both TTC− (p = 0.0007) and TTC+ (p = 0.0009) group (**Figure 5**).

Secondly, we evaluated the monomer (14 kDa), dimer (28 kDa), and trimer (42 kDa) levels of α-Syn. In the infarct, we found a significant decrease of monomer levels, and a corresponding significant increase in α-Syn dimer and trimer levels in both TTC− (monomer $p < 0.0001$; dimer $p < 0.0001$; trimer $p < 0.0001$) and TTC+ (monomer $p < 0.0001$; dimer $p < 0.0001$; trimer $p < 0.0001$) group. In the thalamus, a significant reduction of monomer levels, and a corresponding significant increase in α-Syn trimer levels were observed in the TTC− group only (monomer p = 0.0026; dimer p = 0.0033; trimer p = 0.0011). The TTC+ group showed no significant differences in this region. In the hippocampus, we found no statistically significant changes in the monomer or trimer, but we observed a significant increase in the dimer levels in both groups (dimer TTC− $p < 0.0001$; dimer TTC+ p = 0.0378) (**Figure 6**).

Lastly, we evaluated protein levels of total Tau and two site-specific phosphorylated forms, which have been associated with the formation of neurofibrillary tangles in neurodegenerative diseases. The levels of total Tau, as evaluated by Tau5, were decreased in the infarct area of TTC− ($p < 0.0001$) and TTC+ ($p < 0.0001$) group. Thalamus and hippocampus showed no changes. We then assessed the levels of Phospho-Tau (Ser400/Thr403/Ser404) and Phospho-Tau Ser396 relative to the total Tau. Reduced P-Tau and P-Tau (Ser396) levels were observed in the infarct after stroke in both group (P-Tau TTC− $p < 0.0001$; P-Tau Ser396 TTC− p = 0.0203; P-Tau TTC+ $p < 0.0001$; P-Tau Ser396 TTC+ $p < 0.0001$). No significant differences were found in the thalamus and hippocampus (**Figure 7**).

DISCUSSION

In this study, we investigated whether TTC+ tissues can be processed for downstream biochemical analyses, specifically by western blotting. Our results suggest that brain samples that are processed by TTC staining can be routinely used for protein analyses. Overall, the hippocampus shows same relative changes between TTC− and TTC+ group for all the markers studied, whereas thalamus and infarct differ in a couple of makers (summary of the results **Supplementary Figure S3**). This study demonstrates and further supports the usage of TTC staining for downstream protein analysis.

Previous studies have demonstrated that TTC+ stroke brains can be used for histology, gene, and protein expression analyses (Kramer et al., 2010; Sun et al., 2012; Li L. et al., 2018; Li Z. et al., 2018). Taking all these studies together suggest that TTC-stained tissue can be used for biochemical analyses without restrictions. However, there are a few limitations regarding

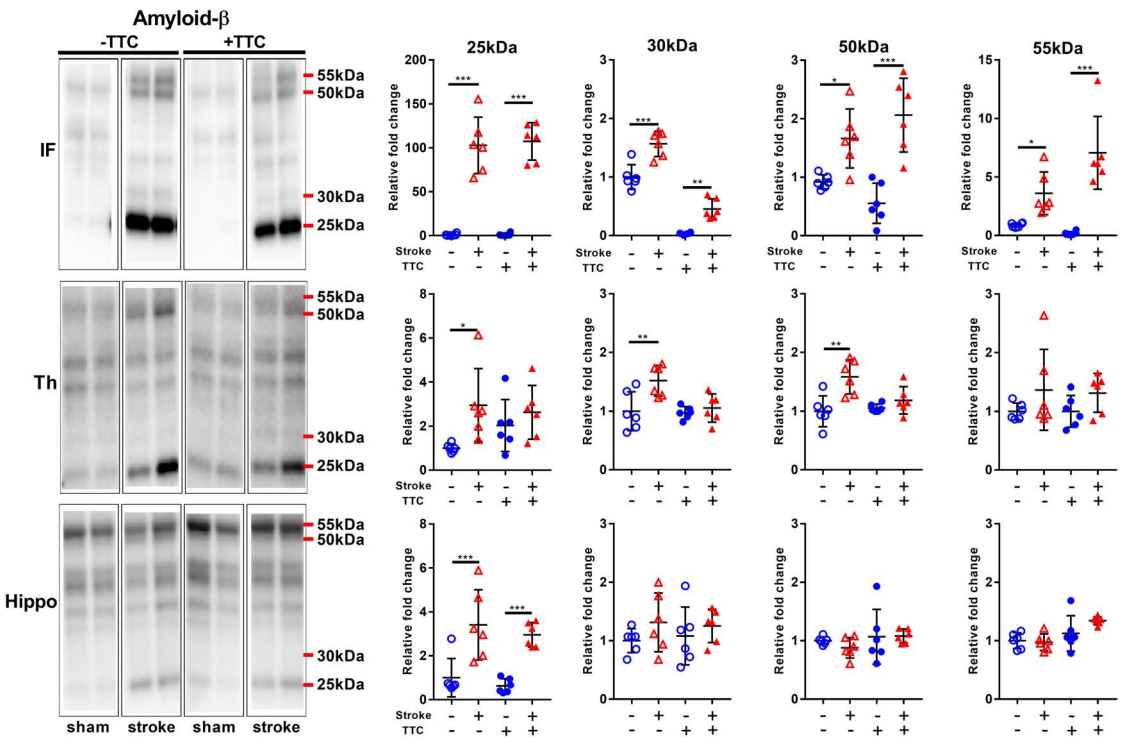

FIGURE 5 | Representative western blot and quantification of amyloid-β expression profile within the infarct (IF), thalamus (Th), and hippocampus (Hippo). Our analyses focused on different molecular weight oligomers (25, 30, 50, and 55 kDa). Mean ± SEM (two-way ANOVA and Sidak's multiple comparisons). ○TTC– sham; △TTC– stroke; ●TTC+ sham; ▲TTC+ stroke. *$p < 0.05$, **$p < 0.01$, ***$p < 0.001$.

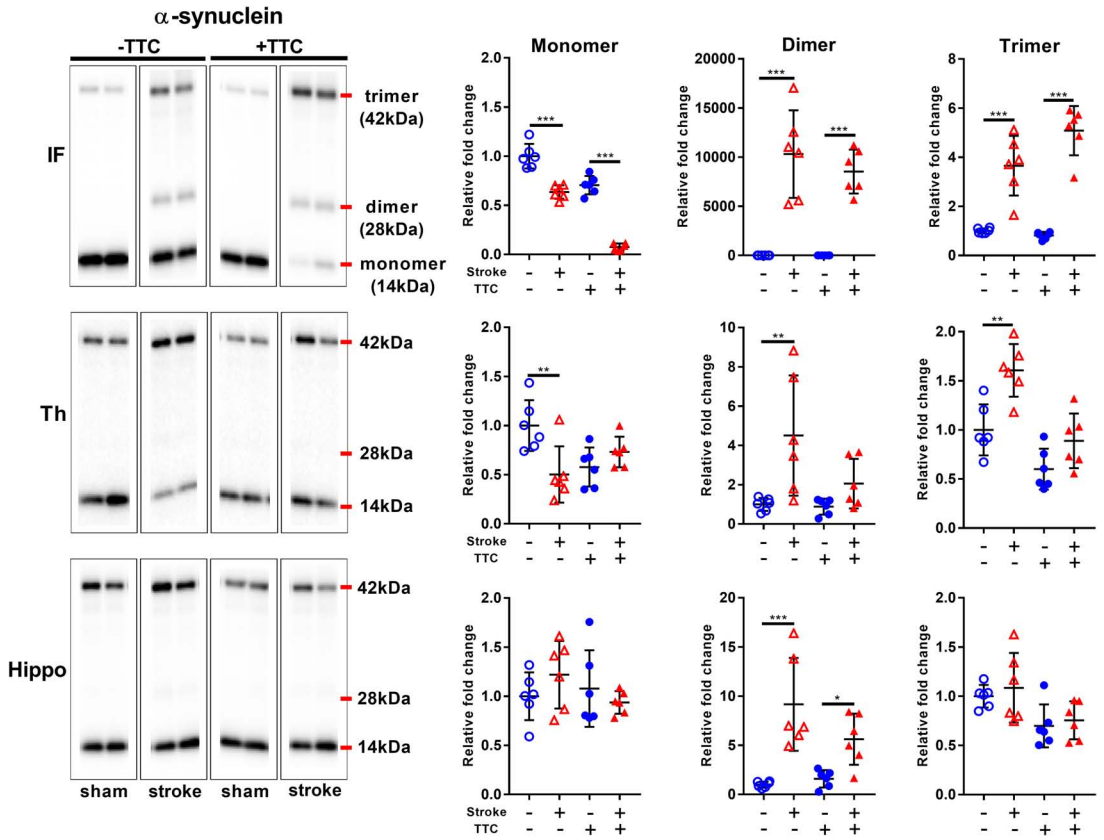

FIGURE 6 | Representative western blot and quantification of α-synuclein expression profile within the infarct (IF), thalamus (Th), and hippocampus (Hippo). Our analysis focused on the monomer (14 kDa), dimer (28 kDa), and trimer (42 kDa). Mean ± SEM (two-way ANOVA and Sidak's multiple comparisons). ○TTC– sham; △TTC– stroke; ●TTC+ sham; ▲TTC+ Stroke. *$p < 0.05$, **$p < 0.01$, ***$p < 0.001$.

the protein expression analyses that we wanted to address in our study. Firstly, previous studies have just focused on a limited number of markers, mainly apoptotic markers and housekeeping proteins (Kramer et al., 2010; Sun et al., 2012; Mohammad-Gharibani et al., 2014; Gharibani et al., 2015; She et al., 2018) and therefore it cannot be definitely asserted that other proteins can also be studied after TTC treatment. Secondly, other studies did not study the effects of TTC on protein modification such as phosphorylation and aggregation. Finally, the penumbra and surrounding areas have been the primary focus; however, there may be different reactions to TTC in other brain regions. Therefore, here we analyzed a total of 16 markers, which include apoptotic, autophagy, neuronal, glial, vascular, and neurodegeneration-related markers. In addition, we analyzed the changes in the primary infarct area and in regions that have been previously linked with secondary neurodegeneration processes (thalamus and hippocampus) (Xie et al., 2011; Ong et al., 2017a; Baumgartner et al., 2018; Sanchez-Bezanilla et al., 2019).

We observed that in the infarct region all the markers with the exception of synaptophysin, VEGFA, and GFAP presented the same relative changes in the TTC− and TTC+ group. In the thalamus, TTC-stained and non-stained tissue showed similar relative changes in 9 out of 13 markers studied. Aβ, α-Syn, CD11b, and synaptophysin were the only markers that exhibited different results when comparing TTC+ and TTC− in the thalamus. In the hippocampus, all the markers showed the same changes in both group. The discrepancies observed in the infarct region can be explained by the procedure used to define the area considered infarct. While in the TTC+ group the infarct area is clearly delineated as the colorless area, in the TTC− group is not easy to visually determine the infarct area. Therefore, surrounding tissue could have been potentially collected as part of the infarct in the TTC− group. Further, the differences observed in some of the markers studied could be related to the TTC staining protocol. Firstly, proteolysis may occur for some proteins when the brain sections are incubated at 37°C for 10 min. Secondly, the formazan pigment (deep red color) may interfere with the protein estimation using the BCA colorimetric protein assay. Interestingly, we observed that Tau5, P-Tau (Ser400/Thr403/Ser404), and P-Tau (S396) showed the same relative changes in all the areas, suggesting that TTC staining does not present a major interference with protein phosphorylation. We also observed that TTC does not interfere with protein aggregation processes in the infarct and

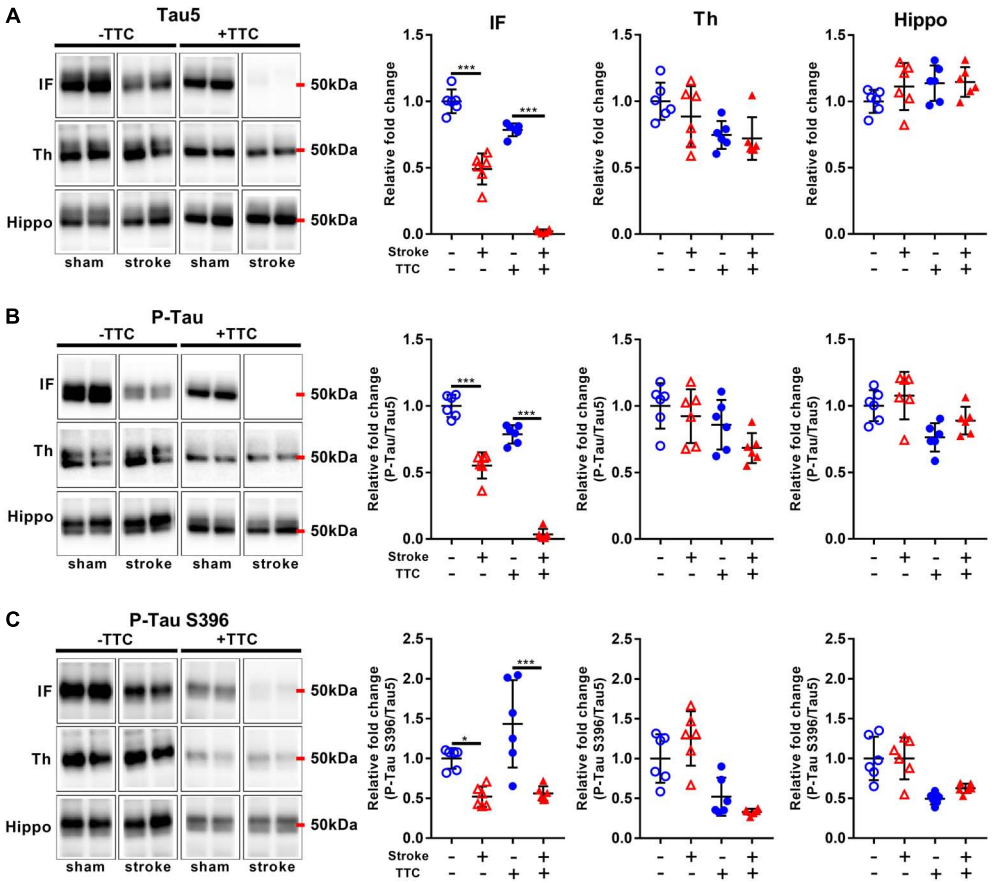

FIGURE 7 | Representative western blot and quantification of Tau5 **(A)**, P-Tau **(B)**, and P-Tau S396 **(C)** within the infarct (IF), thalamus (Th), and hippocampus (Hippo). Mean ± SEM (two-way ANOVA and Sidak's multiple comparisons). ○TTC– sham; △TTC– stroke; ●TTC+ sham; ▲TTC+ stroke. *$p < 0.05$, ***$p < 0.001$.

hippocampus as both Aβ and α-Syn presented the same relative changes. From these results, we can conclude that brain sections that are processed by TTC staining are viable for western blotting. While the usage of western blotting following TTC staining can produce high-throughput qualitative and semi-quantitative data for a variety of protein markers, the end-user should optimize the protocols and conditions accordingly.

In this study, we provide a useful procedure to repurpose brain sections after they have been treated with TTC staining, which brings multiple advantages. Firstly, TTC staining is a simple, rapid, and inexpensive method that allows to delineate the size of the cerebral infarct area and distinguish from the penumbra and intact tissue. Therefore, we can precisely select the area of the brain that it is more suited for protein expression analyses. Furthermore, we can select brains with the same infarct size and reduce the experimental variability. This procedure can also be used to investigate protein modification such as protein phosphorylation and aggregation. Another important benefit of this approach is that it permits a reduction in the number of animals required for investigation as the same brains can be used for infarct quantification and protein quantification. Specifically, we demonstrated that we could use western blotting for the simultaneous assessment of a large number of different markers as well as protein phosphorylation and aggregation after brains have been treated with TTC. In conclusion, our study demonstrates that TTC brains should not be discarded as they can be used for further protein analyses of a wide variety of commonly used markers.

DATA AVAILABILITY

The datasets generated for this study are available on request to the corresponding author.

ETHICS STATEMENT

The animal study was reviewed and approved by the University of Newcastle Animal Care and Ethics Committee (A-2013-340).

AUTHOR CONTRIBUTIONS

SS-B and LKO designed the research, performed the experiments, and prepared the first draft of the manuscript.

FRW and MN supervised the study. SS-B and LKO analyzed the data and interpreted the results. All authors reviewed and contributed to the final version of the manuscript.

FUNDING

This study was supported by the Hunter Medical Research Institute (HMRI 896), Faculty of Health and Medicine Pilot Grant, the Priority Research Centre for Stroke and Brain Injury Research Support Grant, the Mary Costello Alzheimer's Pilot Grant, and The University of Newcastle, Australia. LKO and SS-B also acknowledge the support from the Research Advantage for ECR Higher Degree by Research (HDR) Scholarship and Greaves Family Postgraduate Scholarships in Medical Research (HMRI 1054).

ACKNOWLEDGMENTS

We would like to acknowledge the insights and comments provided by Rebecca Hood on early versions of the manuscript.

SUPPLEMENTARY MATERIAL

The Supplementary Material for this article can be found online at: https://www.frontiersin.org/articles/10.3389/fnmol.2019.00181/full#supplementary-material

REFERENCES

Avila, J., Lucas, J. J., Perez, M., and Hernandez, F. (2004). Role of tau protein in both physiological and pathological conditions. *Physiol. Rev.* 84, 361–384. doi: 10.1152/physrev.00024.2003

Baumgartner, P., El Amki, M., Bracko, O., Luft, A. R., and Wegener, S. (2018). Sensorimotor stroke alters hippocampo-thalamic network activity. *Sci. Rep.* 8:15770. doi: 10.1038/s41598-018-34002-9

Bederson, J. B., Pitts, L. H., Germano, S. M., Nishimura, M. C., Davis, R. L., and Bartkowski, H. M. (1986). Evaluation of 2,3,5-triphenyltetrazolium chloride as a stain for detection and quantification of experimental cerebral infarction in rats. *Stroke* 17, 1304–1308.

Benedek, A., Moricz, K., Juranyi, Z., Gigler, G., Levay, G., Harsing, L. G. Jr., et al. (2006). Use of TTC staining for the evaluation of tissue injury in the early phases of reperfusion after focal cerebral ischemia in rats. *Brain Res.* 1116, 159–165. doi: 10.1016/j.brainres.2006.07.123

Bramblett, G. T., Goedert, M., Jakes, R., Merrick, S. E., Trojanowski, J. Q., and Lee, V. M. (1993). Abnormal tau phosphorylation at Ser396 in Alzheimer's disease recapitulates development and contributes to reduced microtubule binding. *Neuron* 10, 1089–1099.

Burnette, W. N. (1981). "Western blotting": electrophoretic transfer of proteins from sodium dodecyl sulfate–polyacrylamide gels to unmodified nitrocellulose and radiographic detection with antibody and radioiodinated protein A. *Anal. Biochem.* 112, 195–203.

Cahoy, J. D., Emery, B., Kaushal, A., Foo, L. C., Zamanian, J. L., Christopherson, K. S., et al. (2008). A transcriptome database for astrocytes, neurons, and oligodendrocytes: a new resource for understanding brain development and function. *J. Neurosci.* 28, 264–278. doi: 10.1523/jneurosci.4178-07.2008

Chetkovich, D. M., Bunn, R. C., Kuo, S. H., Kawasaki, Y., Kohwi, M., and Bredt, D. S. (2002). Postsynaptic targeting of alternative postsynaptic density-95 isoforms by distinct mechanisms. *J. Neurosci.* 22, 6415–6425.

Eng, L. F., Ghirnikar, R. S., and Lee, Y. L. (2000). Glial fibrillary acidic protein: GFAP-thirty-one years (1969-2000). *Neurochem. Res.* 25, 1439–1451.

Evans, D. B., Rank, K. B., Bhattacharya, K., Thomsen, D. R., Gurney, M. E., and Sharma, S. K. (2000). Tau phosphorylation at serine 396 and serine 404 by human recombinant tau protein kinase II inhibits tau's ability to promote microtubule assembly. *J. Biol. Chem.* 275, 24977–24983. doi: 10.1074/jbc.M000808200

Fernandes-Alnemri, T., Litwack, G., and Alnemri, E. S. (1994). CPP32, a novel human apoptotic protein with homology to caenorhabditis elegans cell death protein Ced-3 and mammalian interleukin-1 beta-converting enzyme. *J. Biol. Chem.* 269, 30761–30764.

Gharibani, P., Modi, J., Menzie, J., Alexandrescu, A., Ma, Z., Tao, R., et al. (2015). Comparison between single and combined post-treatment with S-Methyl-N,N-diethylthiolcarbamate sulfoxide and taurine following transient focal cerebral ischemia in rat brain. *Neuroscience* 300, 460–473. doi: 10.1016/j.neuroscience.2015.05.042

Haass, C., and Selkoe, D. J. (2007). Soluble protein oligomers in neurodegeneration: lessons from the Alzheimer's amyloid beta-peptide. *Nat. Rev. Mol. Cell Biol.* 8, 101–112.

Johnson, G. V., and Stoothoff, W. H. (2004). Tau phosphorylation in neuronal cell function and dysfunction. *J. Cell Sci.* 117, 5721–5729. doi: 10.1242/jcs.01558

Kabeya, Y., Mizushima, N., Ueno, T., Yamamoto, A., Kirisako, T., Noda, T., et al. (2000). LC3, a mammalian homologue of yeast Apg8p, is localized in autophagosome membranes after processing. *EMBO J.* 19, 5720–5728. doi: 10.1093/emboj/19.21.5720

Kramer, M., Dang, J., Baertling, F., Denecke, B., Clarner, T., Kirsch, C., et al. (2010). TTC staining of damaged brain areas after MCA occlusion in the rat does not constrict quantitative gene and protein analyses. *J. Neurosci. Methods* 187, 84–89. doi: 10.1016/j.jneumeth.2009.12.020

Kuhn, K. (1995). Basement membrane (type IV) collagen. *Mat. Bio.* 14, 439–445.

Leung, D. W., Cachianes, G., Kuang, W. J., Goeddel, D. V., and Ferrara, N. (1989). Vascular endothelial growth factor is a secreted angiogenic mitogen. *Science* 246, 1306–1309. doi: 10.1126/science.2479986

Li, F., Irie, K., Anwer, M. S., and Fisher, M. (1997). Delayed triphenyltetrazolium chloride staining remains useful for evaluating cerebral infarct volume in a rat stroke model. *J. Cereb. Blood Flow Metab.* 17, 1132–1135. doi: 10.1097/00004647-199710000-00016

Li, L., Yu, Q., and Liang, W. (2018). Use of 2,3,5-triphenyltetrazolium chloride-stained brain tissues for immunofluorescence analyses after focal cerebral ischemia in rats. *Pathol. Res. Pract.* 214, 174–179. doi: 10.1016/j.prp.2017.11.016

Li, Z., Bishop, N., Chan, S. L., and Cipolla, M. J. (2018). Effect of TTC treatment on immunohistochemical quantification of collagen iv in rat brains after stroke. *Transl. Stroke Res.* 9, 499–505. doi: 10.1007/s12975-017-0604-9

Liu, Z. Q., Mahmood, T., and Yang, P. C. (2014). Western blot: technique, theory and trouble shooting. *North Am. J. Med Sci.* 6:160. doi: 10.4103/1947-2714.128482

Maroteaux, L., Campanelli, J. T., and Scheller, R. H. (1988). Synuclein: a neuron-specific protein localized to the nucleus and presynaptic nerve terminal. *J. Neurosci.* 8, 2804–2815.

Mohammad-Gharibani, P., Modi, J., Menzie, J., Genova, R., Ma, Z., Tao, R., et al. (2014). Mode of action of S-methyl-N, N-diethylthiocarbamate sulfoxide (DETC-MeSO) as a novel therapy for stroke in a rat model. *Mol. Neurobiol.* 50, 655–672. doi: 10.1007/s12035-014-8658-0

Mullen, R. J., Buck, C. R., and Smith, A. M. (1992). NeuN, a neuronal specific nuclear protein in vertebrates. *Development* 116, 201–211.

Murtha, L. A., Beard, D. J., Bourke, J. T., Pepperall, D., McLeod, D. D., and Spratt, N. J. (2016). Intracranial pressure elevation 24 h after ischemic stroke in aged rats is prevented by early, short hypothermia treatment. *Front. Aging Neurosci.* 8:124. doi: 10.3389/fnagi.2016.00124

Newman, P. J. (1997). The biology of PECAM-1. *J. Clin. Invest.* 99, 3–8. doi: 10.1172/jci119129

Ong, L. K., Chow, W. Z., TeBay, C., Kluge, M., Pietrogrande, G., Zalewska, K., et al. (2018). Growth hormone improves cognitive function after experimental stroke. *Stroke* 49, 1257–1266. doi: 10.1161/strokeaha.117.020557

Ong, L. K., Walker, F. R., and Nilsson, M. (2017a). Is stroke a neurodegenerative condition? a critical review of secondary neurodegeneration and amyloid-beta accumulation after stroke. *AIMS Med. Sci.* 4, 1–16. doi: 10.3934/medsci.2017.1.1

Ong, L. K., Zhao, Z., Kluge, M., TeBay, C., Zalewska, K., Dickson, P. W., et al. (2017b). Reconsidering the role of glial cells in chronic stress-induced dopaminergic neurons loss within the substantia nigra? Friend or foe? *Brain Behav. Immun.* 60, 117–125. doi: 10.1016/j.bbi.2016.10.001

Ong, L. K., Zhao, Z., Kluge, M., Walker, F. R., and Nilsson, M. (2017c). Chronic stress exposure following photothrombotic stroke is associated with increased levels of amyloid beta accumulation and altered oligomerisation at sites of thalamic secondary neurodegeneration in mice. *J. Cereb. Blood Flow Metab.* 37, 1338–1348. doi: 10.1177/0271678x16654920

Sanchez-Bezanilla, S., TeBay, C., Nilsson, M., Walker, F. R., and Ong, L. K. (2019). Visual discrimination impairment after experimental stroke is associated with disturbances in the polarization of the astrocytic aquaporin-4 and increased accumulation of neurotoxic proteins. *Exp. Neurol.* 318, 232–243. doi: 10.1016/j.expneurol.2019.05.001

She, D. T., Wong, L. J., Baik, S. H., and Arumugam, T. V. (2018). SIRT2 inhibition confers neuroprotection by downregulation of foxo3a and mapk signaling pathways in ischemic stroke. *Mol. Neurobiol.* 55, 9188–9203. doi: 10.1007/s12035-018-1058-0

Solovjov, D. A., Pluskota, E., and Plow, E. F. (2005). Distinct roles for the alpha and beta subunits in the functions of integrin alphaMbeta2. *J. Biol. Chem.* 280, 1336–1345. doi: 10.1074/jbc.M406968200

Sun, Y. Y., Yang, D., and Kuan, C. Y. (2012). Mannitol-facilitated perfusion staining with 2,3,5-triphenyltetrazolium chloride (TTC) for detection of experimental cerebral infarction and biochemical analysis. *J. Neurosci. Methods* 203, 122–129. doi: 10.1016/j.jneumeth.2011.09.029

van der Putten, H., Wiederhold, K. H., Probst, A., Barbieri, S., Mistl, C., Danner, S., et al. (2000). Neuropathology in mice expressing human alpha-synuclein. *J. Neurosci.* 20, 6021–6029.

Walsh, D. M., and Selkoe, D. J. (2007). A beta oligomers - a decade of discovery. *J. Neurochem.* 101, 1172–1184. doi: 10.1111/j.1471-4159.2006.04426.x

Wiedenmann, B., Franke, W. W., Kuhn, C., Moll, R., and Gould, V. E. (1986). Synaptophysin: a marker protein for neuroendocrine cells and neoplasms. *Proc. Natl. Acad. Sci. U. S. A.* 83, 3500–3504. doi: 10.1073/pnas.83.10.3500

Xie, M., Yi, C., Luo, X., Xu, S., Yu, Z., Tang, Y., et al. (2011). Glial gap junctional communication involvement in hippocampal damage after middle cerebral artery occlusion. *Ann. Neurol.* 70, 121–132. doi: 10.1002/ana.22386

Conflict of Interest Statement: The authors declare that the research was conducted in the absence of any commercial or financial relationships that could be construed as a potential conflict of interest.

Copyright © 2019 Sanchez-Bezanilla, Nilsson, Walker and Ong. This is an open-access article distributed under the terms of the Creative Commons Attribution License (CC BY). The use, distribution or reproduction in other forums is permitted, provided the original author(s) and the copyright owner(s) are credited and that the original publication in this journal is cited, in accordance with accepted academic practice. No use, distribution or reproduction is permitted which does not comply with these terms.

frontiers in Molecular Neuroscience

MINI REVIEW
published: 06 August 2019
doi: 10.3389/fnmol.2019.00186

Emerging Evidence of Macrophage Contribution to Hyperinnervation and Nociceptor Sensitization in Vulvodynia

Christine Mary Barry[1]*, *Dusan Matusica*[2] and *Rainer Viktor Haberberger*[2]

[1]Musculoskeletal Neurobiology Laboratory, Centre for Neuroscience, College of Medicine and Public Health, Flinders University, Adelaide, SA, Australia, [2]Pain and Pulmonary Neurobiology Laboratory, Centre for Neuroscience, Órama Institute, College of Medicine and Public Health, Flinders University, Adelaide, SA, Australia

Vulvodynia is an idiopathic chronic pain disorder and a leading cause of dyspareunia, or pain associated with sexual intercourse, for women. The key pathophysiological features of vulvodynia are vaginal hyperinnervation and nociceptor sensitization. These features have been described consistently by research groups over the past 30 years, but currently there is no first-line recommended treatment that targets this pathophysiology. Instead, psychological interventions, pelvic floor physiotherapy and surgery to remove painful tissue are recommended, as these are the few interventions that have shown some benefit in clinical trials. Recurrence of vulvodynia is frequent, even after vestibulectomy and questions regarding etiology remain. Vestibular biopsies from women with vulvodynia contain increased abundance of immune cells including macrophages as well as increased numbers of nerve fibers. Macrophages have multiple roles in the induction and resolution of inflammation and their function can be broadly described as pro-inflammatory or anti-inflammatory depending on their polarization state. This state is not fixed and can alter rapidly in response to the microenvironment. Essentially, M1, or classically activated macrophages, produce pro-inflammatory cytokines and promote nociceptor sensitization and mechanical allodynia, whereas M2, or alternatively activated macrophages produce anti-inflammatory cytokines and promote functions such as wound healing. Signaling between macrophages and neurons has been shown to promote axonal sprouting and nociceptor sensitization. This mini review considers emerging evidence that macrophages may play a role in nociceptor sensitization and hyperinnervation relevant to vulvodynia and considers the implications for development of new therapeutic strategies.

Keywords: vulvodynia, vestibulodynia, hyperinnervation, nociceptor sensitization, pain, macrophage polarization, nerve growth factor

OPEN ACCESS

Edited by:
Jochen C. Meier, Technische Universitat Braunschweig, Germany

Reviewed by:
Antje Kroner, Medical College of Wisconsin, United States
Temugin Berta, University of Cincinnati, United States

***Correspondence:**
Christine Mary Barry
christine.barry@flinders.edu.au

Received: *21 May 2019*
Accepted: *19 July 2019*
Published: *06 August 2019*

Citation:
Barry CM, Matusica D and Haberberger RV (2019) Emerging Evidence of Macrophage Contribution to Hyperinnervation and Nociceptor Sensitization in Vulvodynia. Front. Mol. Neurosci. 12:186. doi: 10.3389/fnmol.2019.00186

INTRODUCTION

Vulvodynia is a chronic pain disorder, usually characterized by pain localized to the vaginal entrance (localized provoked vulvodynia; Goldstein et al., 2016). Pain can be intense and may be associated with vaginismus, or spasm of pelvic floor muscles (Goldstein et al., 2016). However, vulvodynia is primarily a pain disorder and not secondary to factors such as

vaginismus, disordered arousal or lack of vaginal lubrication (Heim, 2001). Frequently there is no history of trauma or infection, though many women report prior candiasis (Leusink et al., 2018). Women and girls of all ages can be affected but most are in younger age groups and a high proportion under 25 years (Harlow et al., 2014). Many women with vulvodynia are unable to insert a tampon, engage in sexual activity involving vaginal penetration or undergo a gynecological examination. The impact on their self-esteem, relationships and fertility can be substantial.

The key pathological features of vulvodynia are vaginal hyperinnervation (Bohm-Starke et al., 1998; Tympanidis et al., 2003, 2004; Bornstein et al., 2004; Halperin et al., 2005; Goetsch et al., 2010; Leclair et al., 2011; Tommola et al., 2016; Liao et al., 2017) and nociceptor sensitization contributing to mechanical and thermal hyperalgesia (Bohm-Starke et al., 2001). Hyperinnervation includes multiple types of fibers including fibers containing calcitonin gene-related peptide (Bohm-Starke et al., 1999) and fibers expressing the receptor TRPV1 (Bohm-Starke et al., 1999; Tympanidis et al., 2004).

Despite evidence of structural and functional changes related to innervation, the recommended first-line treatments for vulvodynia are psychological interventions, pelvic floor physiotherapy and surgery to remove painful tissue (Goldstein et al., 2016). Whilst these interventions have shown benefit in clinical trials, vulvodynia remains a highly prevalent and recurrent pain disorder (Harlow et al., 2014). To date, clinical trials for treatment targeting the pathophysiology of vulvodynia have not demonstrated benefit (Goldstein et al., 2016). Vestibulectomy is an invasive procedure but an option if conservative treatments fail. Data from large clinical trials are lacking but a relatively recent study found 90% of women reported moderate or substantial improvement (Swanson et al., 2014). Beneficial effects of surgery for vulvodynia, and therefore removal of input from sensitized fibers, indicates peripheral mechanisms make a substantial contribution to the disorder, supporting the view that appropriate interventions targeting peripheral pathology will be beneficial (Keppel Hesselink et al., 2016).

IMMUNE CELLS AND VULVODYNIA PATHOPHYSIOLOGY

In addition to hyperinnervation, vestibular biopsies from women with vulvodynia contain increased abundance of immune cells (Lundqvist et al., 1997; Tommola et al., 2015; Liao et al., 2017) and vaginal swabs contain increased pro-inflammatory cytokines (Zanotta et al., 2018). Increased T cells, B cells and macrophages have been identified in samples from symptomatic areas compared to non-symptomatic areas or healthy controls (Liao et al., 2017). Symptomatic tissue also contained 70% increase in nerve fibers immunoreactive for the pan-neuronal marker PGP9.5, and over 100% increase in the density of TRPV4-immunoreactive, putative mechano-nociceptive fibers (Liao et al., 2017). Increased B lymphocytes, but not T cells or macrophages, have been identified in archival vestibulectomy tissue (Tommola et al., 2015). Conflicting findings are reported regarding the abundance of mast cells in vestibular biopsy samples (Bornstein et al., 2004; Liao et al., 2017). High numbers of immune cells immunoreactive for nerve growth factor (NGF) have been identified associated with intraepithelial nerve fibers in biopsy samples from women with vulvodynia, suggesting NGF may be a pathophysiological factor (Tommola et al., 2016). Fibroblast-mediated pro-inflammatory responses to Candida infection have also been implicated (Falsetta et al., 2015, 2017). Fibroblasts cultured from vestibular tissue of vulvodynia patients showed increased expression of receptors for bradykinin and increased Dectin-1 receptors that bind Candida albicans. These cells showed increased production of pro-inflammatory and proalgesic interleukin (IL)-6 and prostaglandin E2 (PGE2) in response to low-level exposure to Candida albicans or bradykinin stimulation (Falsetta et al., 2015, 2017). Interestingly, patients' pain sensitivity correlated with levels of cytokines produced by cultured fibroblasts exposed to Candida (Foster et al., 2015), consistent with a localized peripheral pathology making a substantial contribution to patients' pain.

Macrophages have an established role in many conditions associated with chronic pain (Pinho-Ribeiro et al., 2017) but few studies have investigated macrophage-neuron interactions that may contribute to hyperinnervation and nociceptor sensitization in vulvodynia. Macrophages are a heterogeneous population of cells with multiple functions in development, homeostasis and disease. In addition to phagocytosis of foreign pathogens and apoptotic cells, macrophages release hundreds of effector molecules and proteins including growth factors, cytokines and chemokines (Mantovani et al., 2005). They have high plasticity and depending on their phenotype or polarization state, make contributions to both the induction and resolution of inflammation. According to a simplified descriptive framework, M1, or classically activated macrophages promote inflammation and hyperalgesia. Their major release factors include reactive oxygen and nitrogen species, and the pro-inflammatory cytokines IL-1α, IL-1β, TNFα and IL-6 (Mantovani et al., 2005; Liu et al., 2019). M2 or alternatively activated macrophages have anti-inflammatory effects and promote hypoalgesia (Leung et al., 2016; Pannell et al., 2016; Huo et al., 2018). In addition to releasing IL-10, subtypes of M2 macrophages (M2a, M2b, M2c and M2d), contribute to functions that promote cell proliferation, cell maturation, resolution of inflammation and angiogenesis (Liu et al., 2019). The clear differentiation between M1 and M2 macrophages that can be seen *in vitro* does not fully represent the complex array of functional and phenotypic states found *in vivo*, including many transitional states of activation finely tuned to different microenvironments and also dependent on tissue specificity (Gordon and Taylor, 2005; Mosser and Edwards, 2008; Cassetta et al., 2011; Lawrence and Natoli, 2011; Murray and Stow, 2014). Distinguishing macrophage subsets based on the distinct expression of surface markers remains a challenge and overlap of antigenicity of subtypes is substantial, but a growing number of studies apply the M1/M2 framework to compare macrophage abundance and activation state in injury or disease conditions and in response to interventions.

In homeostatic conditions, a heterogeneous population of macrophages maintains a state of dynamic equilibrium within tissue, and those including embryonically derived tissue-resident macrophages derived from circulating monocytes of bone marrow origin (Jenkins et al., 2011; Epelman et al., 2014). In many tissues such as liver and skeletal muscle, influx of circulating monocytes and their differentiation into M1 macrophages is a critical part of the acute inflammatory response (Duffield et al., 2005; Arnold et al., 2007). Within tissue, both recruited and resident macrophages have the capacity for proliferation (Epelman et al., 2014). In response to injury, macrophages of different phenotypes are present simultaneously and work synergistically (Duffield et al., 2005). M1 macrophages transition to M2 phenotypes in a cytokine-driven process critical for repair and remodeling (Arnold et al., 2007; Dal-Secco et al., 2015). For example, in injured skeletal muscle, transition of M1 ($CX3CR1^{lo}$/Ly6C+) macrophages to M2 ($CX3CR1^{high}$/Ly6C-) phenotype has been shown following phagocytosis of muscle cell debris, and whereas M1 macrophages coculture promoted proliferation of muscles cells, coculture with M2 macrophages stimulated cell growth. The critical role of macrophages is highlighted by observations that macrophage depletion at the time of injury prevents muscle repair (Arnold et al., 2007).

MACROPHAGES AND REGULATION OF NOCICEPTIVE SIGNALING

Macrophages are implicated in the regulation of pain sensitivity in multiple conditions (Gong et al., 2016; Shepherd et al., 2018; Sakurai et al., 2019). Macrophage infiltration has been demonstrated in pain-associated synovial tissue from patients with advanced osteoarthritis and in pain-associated models of joint, muscle and paw inflammation (Gong et al., 2016; Shepherd et al., 2018; Sakurai et al., 2019). More importantly, macrophage depletion *via* clodronate liposomes reduces the elevated pro-inflammatory cytokines and NGF and reduces pain behaviors in a model of arthritis (Sakurai et al., 2019). Similarly, macrophage depletion prevents local hyperalgesia in response to plantar injection of angiotensin II (Shepherd et al., 2018), and widespread hyperalgesia in response to repeated intra-muscular injection of acidic saline and pro-inflammatory agents (Gong et al., 2016). Macrophage blockade using a toll-like receptor 4 antagonist also prevents hyperalgesia in this model (Gong et al., 2016). Increased abundance of ED-1+ monocytes/macrophages in injured rat sciatic nerves correlates with allodynia (Cui et al., 2000) whereas macrophage depletion alleviates thermal hyperalgesia following rat sciatic nerve ligation (Liu et al., 2000) and prevents mechanical allodynia associated with chemotherapy-induced peripheral neuropathy (Sekiguchi et al., 2018). Macrophage to neuron signaling, particularly nociceptor sensitization *via* the release of proalgesic cytokines, is well established.

Apart from animal models, there has been increased interest in identifying macrophage phenotypes in conditions associated with chronic pain in humans. Synovial fluid from patients with knee osteoarthritis was found to contain markedly higher ratios of M1 (CD11c+) to M2 (CD206+) macrophages compared to healthy controls, and this ratio correlated with measures of radiographic joint disease (Liu et al., 2018). Cadaveric intervertebral discs with degenerative changes contained increased M1 (CCR7+) macrophages and subtypes of M2 macrophages (M2c, CD163+), specifically localized in areas of nucleus, annulus and vertebral endplate showing structural defects (Nakazawa et al., 2018). These findings are supported by a mouse model of intervertebral disc injury that showed increased M1 macrophages at day 1 returning to normal levels at 28 days, and increased M2a (CD206+) and M2c macrophages (CD163) at days 7, 14 and 28 (Nakazawa et al., 2018).

The shift from M1 to M2 phenotypes appears critical for resolution of protective hyperalgesia associated with the acute inflammatory response. Spinal cord injury, a condition frequently associated with prolonged neuropathic pain, results in a sustained increased abundance of M1 phenotype cells in the spinal cord (Kigerl et al., 2009; Pruss et al., 2011). These cells produce pro-inflammatory and cytotoxic cytokines and they include M1 macrophages derived from circulating monocytes and activated microglia sharing the same antigenicity and morphology (David and Kroner, 2011). In rat models of spinal cord injury, a relatively brief increase in the total number of M2 (CD206+) macrophages/microglia is accompanied by a greater, sustained accumulation of M1 (arginase+) macrophages, with high ratios of M1 to M2 polarized macrophages at 28 days (Kigerl et al., 2009) and 70 days following injury (Pruss et al., 2011). This has implications for pain sensitivity as well as secondary injury such as demyelination. Bone cancer pain is another clinical challenge in which altered macrophage phenotype has been implicated. In a mouse model of bone cancer pain, increased M1 (iNOS+, CD16/32/Iba1+) spinal cord macrophages/microglia were identified, with increased production of IL-1β and reduced production of IL-10 (Huo et al., 2018). Administration of dehydrocorydaline, an alkaloidal component isolated from Rhizoma corydalis previously shown to reduce inflammatory pain (Yin et al., 2016), resulted in increased M2 (CD206/Iba1) spinal cord microglia/macrophages and reduced pain behavior (Huo et al., 2018).

Since vulvodynia is a condition affecting women, sex-related differences regarding nerve-immune cell interactions regulating nociceptive signaling are important to consider. Sex differences in clinical pain are well established, including higher prevalence of chronic pain among women compared to men, greater sensitivity of women to multiple measures of experimentally induced pain and different analgesic responses to opioid drugs (Bartley and Fillingim, 2013; Sorge and Totsch, 2017). Multi-disciplinary studies have implicated multiple biological, psychological and social factors. Interactions between sex hormones and the immune system, particularly involving microglia and T cells, are proposed to account for much of the biological component (Sorge and Totsch, 2017). Less is documented regarding sex-related differences in macrophage regulation of nociception, though ovarian hormone regulation of macrophage phenotype and number (Scotland et al., 2011) may show macrophages are particularly important for pain in females.

Microglial promotion of spinal cord neuron hyperexcitability in models of neuropathic and inflammatory pain appears more important in males than females. Intrathecal LPS to activate microglia produces allodynia only in male mice (Sorge et al., 2011) and analgesic responses to microglial inhibitors are testosterone dependent (Sorge et al., 2015). T cells may also contribute to sex-related differences in pain. T cells are more abundant in female compared to male mice and, partly due to diminished testosterone-related inhibition, produce more pro-inflammatory, proalgesic mediators (Sorge et al., 2015). Whereas female CD-1 mice require 2–3-fold more morphine for an equivalent analgesic response to males, the difference is abolished in T-cell deficient mice (Rosen et al., 2019). Female rodents have greater abundance of macrophages in peritoneal and pleural cavities, higher TLR expression by resident macrophages and greater production of pro-inflammatory cytokines on macrophage stimulation (Scotland et al., 2011; Ćuruvija et al., 2017). These findings support the view that further investigation into the role of macrophages in chronic pain conditions affecting women is warranted.

In summary, data from human studies and animal studies investigating chronic inflammatory, neuropathic and cancer pain, all support the view that macrophage phenotype may be an important peripheral factor influencing pain sensitivity. Additionally, there is evidence M2 macrophages promote analgesia. In a model of peripheral neuropathic pain, application of cultured M2 macrophages to the injured nerve reduced mechanical pain sensitivity (Pannell et al., 2016), possibly due M2 macrophage production of endogenous opioids (Pannell et al., 2016). Interestingly, regular exercise promotes M2 macrophage polarization in skeletal muscle (Leung et al., 2016) and protects against hyperalgesia in models of chronic muscle and paw pain, with no sex-related differences identified (Leung et al., 2016).

MACROPHAGE-NEURON SIGNALING AND HYPERINNERVATION

Macrophage to neuron signaling may promote axonal sprouting and hyperinnervation. Pronounced and persistent hyperinnervation has been described following inflammation in skin (Reynolds and Fitzgerald, 1995; Chakrabarty et al., 2013), synovium (Ghilardi et al., 2012), muscle (Ambalavanar et al., 2006) and deep fascia (Hoheisel et al., 2015), and in association with painful endometriotic lesions (Anaf et al., 2000; Morotti et al., 2014). This hyperinnervation involves sensory A- and C-fibers and is accompanied by mechanical and thermal hypersensitivity (Reynolds and Fitzgerald, 1995; Chakrabarty et al., 2013). All of these tissues contain abundant macrophages that release effector molecules and growth factors shown to promote hyperinnervation. Few studies have investigated the specific contributions of macrophages to hyperinnervation, though macrophages are shown to regulate the regeneration of injured peripheral nerves, by sensing hypoxia at the nerve bridge, recruiting endothelial cells and driving neovascularization critical for Schwann cell migration (Cattin et al., 2015). *In vitro* studies show distinct effects of M1 and M2 macrophages on neuronal growth and survival (Kigerl et al., 2009). Adult DRG neurons incubated in M1 macrophage conditioned media show shorter, more highly branched neurites whereas those incubated in M2 conditioned media showed a uni- or bi-polar phenotype with elongated axons. M1 conditioned media was toxic to cortical neurons whereas M2 conditioned media was not (Kigerl et al., 2009).

Cutaneous hyperinnervation induced by plantar injection of complete Freund's adjuvant is accompanied by abundant angiotensinogen and renin production in macrophages and T cells (Chakrabarty et al., 2013). Hyperinnervation and hyperalgesia were prevented by an angiotensin receptor II antagonist, indicating angiotensin II produced by macrophages and T cells modulates sensory fiber sprouting. Subsequent research by this team found vestibular biopsies from women with vulvodynia contain increased macrophages and T cells expressing renin and angiotensinogen (Liao et al., 2017), and that an angiotensin receptor II antagonist prevented vaginal hyperinnervation in rats in response to CFA (Chakrabarty et al., 2018).

The ability of macrophages to induce nerve sprouting is shown in sympathetic hyperinnervation following myocardial infarction in a mechanism involving their production of NGF (Hasan et al., 2006; Wernli et al., 2009). NGF also contributes to sensory hyperinnervation and hyperalgesia in response to inflammation (Woolf et al., 1994), and anti-NGF therapy has anti-nociceptive effects in the treatment of arthritis (Sakurai et al., 2019). Macrophages are an important source of NGF following injury (Lindholm et al., 1987). NGF not only acts on nerve fibers, but also acts on macrophages, potentially affecting polarization state. In cultured macrophages, NGF promotes cell survival and alters the release of 53 of 507 proteins secreted by macrophages, including growth factors, cytokines, and chemokines (Williams et al., 2015). Regarding proteins associated with classically activated or alternatively activated macrophages, NGF stimulation increased macrophage secretion of TGF-β and decreased secretion of IL-10, IL-1α and IL-1β (Williams et al., 2015).

Injury models indicate that actions of NGF mediated by macrophages may be sustained for prolonged periods. In the intervertebral disc injury model, injured discs contain increased abundance of macrophages, NGF mRNA and NGF protein 1 day following injury, and all three measures continue to be substantially increased 28 days following injury (Nakawaki et al., 2019).

SUMMARY AND CONCLUSIONS

For many years lack of suitable models of vulvodynia was a major barrier to the development of treatments that specifically target the pathophysiology of the disease. Recently developed models of vaginal hyperinnervation in rats and mice are an important advancement (Farmer et al., 2011; Barry et al., 2018; Chakrabarty et al., 2018; Sharma et al., 2018). Increased abundance of macrophages has been observed in these models accompanying

increased vaginal nerve fibers, consistent with signs in patient biopsies, but the extent to which macrophages contribute to hyperinnervation or nociceptor sensitivity in vulvodynia remains unclear. Indeed, macrophage polarization state has not yet been described in clinical vulvodynia or in models, and the impact of macrophage depletion has not been identified. Therefore, direct evidence for a specific role of macrophages in vulvodynia is lacking.

However, a significant body of research demonstrates macrophages can contribute to hyperinnervation and nociceptor sensitization in multiple pathological conditions. Therapeutic approaches that target angiotensin signaling, putatively involving macrophages, appears promising in addressing key pathological features of vulvodynia. As with other organs in the body, the composition of embryonically and adult-derived macrophage subpopulations in the vagina is not yet clear, nor the extent to which local proliferation and circulating monocytes replenish and expand populations within a tissue in homeostatic and disease states. This could have implications on the effectiveness of interventions targeting monocyte migration or proliferation of subtypes of macrophages, in addition to factors altering macrophage polarization state. Studies clearly show macrophages are highly dynamic and can transition between polarization states that have distinct effects on nociception, suggesting they are a potential target for interventions to modulate pain sensitivity. Modulation of the microenvironment by interventions including exercise, can alter macrophage phenotype and shift the balance of their functions and potentially protect against the development of chronic pain.

AUTHOR CONTRIBUTIONS

CB designed and drafted the manuscript. CB, DM and RH contributed to manuscript critical revision and read and approved the submitted version.

FUNDING

This research is supported by the Rebecca L Cooper Medical Research Foundation (PG2019395) and the Flinders Centre for Neuroscience.

REFERENCES

Ambalavanar, R., Moritani, M., Moutanni, A., Gangula, P., Yallampalli, C., and Dessem, D. (2006). Deep tissue inflammation upregulates neuropeptides and evokes nociceptive behaviors which are modulated by a neuropeptide antagonist. *Pain* 120, 53–68. doi: 10.1016/j.pain.2005.10.003

Anaf, V., Simon, P., El Nakadi, I., Fayt, I., Buxant, F., Simonart, T., et al. (2000). Relationship between endometriotic foci and nerves in rectovaginal endometriotic nodules. *Hum. Reprod.* 15, 1744–1750. doi: 10.1093/humrep/15.8.1744

Arnold, L., Henry, A., Poron, F., Baba-Amer, Y., Van Rooijen, N., Plonquet, A., et al. (2007). Inflammatory monocytes recruited after skeletal muscle injury switch into antiinflammatory macrophages to support myogenesis. *J. Exp. Med.* 204, 1057–1069. doi: 10.1084/jem.20070075

Barry, C. M., Huilgol, K. K., and Haberberger, R. V. (2018). New models to study vulvodynia: hyperinnervation and nociceptor sensitization in the female genital tract. *Neural Regen. Res.* 13, 2096–2097. doi: 10.4103/1673-5374.241455

Bartley, E. J., and Fillingim, R. B. (2013). Sex differences in pain: a brief review of clinical and experimental findings. *Br. J. Anaesth.* 111, 52–58. doi: 10.1093/bja/aet127

Bohm-Starke, N., Hilliges, M., Brodda-Jansen, G., Rylander, E., and Torebjörk, E. (2001). Psychophysical evidence of nociceptor sensitization in vulvar vestibulitis syndrome. *Pain* 94, 177–183. doi: 10.1016/s0304-3959(01)00352-9

Bohm-Starke, N., Hilliges, M., Falconer, C., and Rylander, E. (1998). Increased intraepithelial innervation in women with vulvar vestibulitis syndrome. *Gynecol. Obstet. Invest.* 46, 256–260. doi: 10.1159/000010045

Bohm-Starke, N., Hilliges, M., Falconer, C., and Rylander, E. (1999). Neurochemical characterization of the vestibular nerves in women with vulvar vestibulitis syndrome. *Gynecol. Obstet. Invest.* 48, 270–275. doi: 10.1159/000010198

Bornstein, J., Goldschmid, N., and Sabo, E. (2004). Hyperinnervation and mast cell activation may be used as histopathologic diagnostic criteria for vulvar vestibulitis. *Gynecol. Obstet. Invest.* 58, 171–178. doi: 10.1159/000079663

Cassetta, L., Cassol, E., and Poli, G. (2011). Macrophage polarization in health and disease. *ScientificWorldJournal* 11, 2391–2402. doi: 10.1100/2011/213962

Cattin, A. L., Burden, J. J., Van Emmenis, L., Mackenzie, F. E., Hoving, J. J., Garcia Calavia, N., et al. (2015). Macrophage-induced blood vessels guide schwann cell-mediated regeneration of peripheral nerves. *Cell* 162, 1127–1139. doi: 10.1016/j.cell.2015.07.021

Chakrabarty, A., Liao, Z., Mu, Y., and Smith, P. G. (2018). Inflammatory Renin-angiotensin system disruption attenuates sensory hyperinnervation and mechanical hypersensitivity in a rat model of provoked vestibulodynia. *J. Pain* 19, 264–277. doi: 10.1016/j.jpain.2017.10.006

Chakrabarty, A., Liao, Z., and Smith, P. G. (2013). Angiotensin II receptor type 2 activation is required for cutaneous sensory hyperinnervation and hypersensitivity in a rat hind paw model of inflammatory pain. *J. Pain* 14, 1053–1065. doi: 10.1016/j.jpain.2013.04.002

Cui, J. G., Holmin, S., Mathiesen, T., Meyerson, B. A., and Linderoth, B. (2000). Possible role of inflammatory mediators in tactile hypersensitivity in rat models of mononeuropathy. *Pain* 88, 239–248. doi: 10.1016/S0304-3959(00)00331-6

Ćuruvija, I., Stanojević, S., Arsenović-Ranin, N., Blagojević, V., Dimitrijević, M., Vidić-Danković, B., et al. (2017). Sex differences in macrophage functions in middle-aged rats: relevance of estradiol level and macrophage estrogen receptor expression. *Inflammation* 40, 1087–1101. doi: 10.1007/s10753-017-0551-3

Dal-Secco, D., Wang, J., Zeng, Z., Kolaczkowska, E., Wong, C. H., Petri, B., et al. (2015). A dynamic spectrum of monocytes arising from the *in situ* reprogramming of CCR2+ monocytes at a site of sterile injury. *J. Exp. Med.* 212, 447–456. doi: 10.1084/jem.20141539

David, S., and Kroner, A. (2011). Repertoire of microglial and macrophage responses after spinal cord injury. *Nat. Rev. Neurosci.* 12, 388–399. doi: 10.1038/nrn3053

Duffield, J. S., Forbes, S. J., Constandinou, C. M., Clay, S., Partolina, M., Vuthoori, S., et al. (2005). Selective depletion of macrophages reveals distinct, opposing roles during liver injury and repair. *J. Clin. Invest.* 115, 56–65. doi: 10.1172/JCI22675

Epelman, S., Lavine, K. J., and Randolph, G. J. (2014). Origin and functions of tissue macrophages. *Immunity* 41, 21–35. doi: 10.1016/j.immuni.2014.06.013

Falsetta, M. L., Foster, D. C., Bonham, A. D., and Phipps, R. P. (2017). A review of the available clinical therapies for vulvodynia management and new data implicating proinflammatory mediators in pain elicitation. *BJOG* 124, 210–218. doi: 10.1111/1471-0528.14157

Falsetta, M. L., Foster, D. C., Woeller, C. F., Pollock, S. J., Bonham, A. D., Haidaris, C. G., et al. (2015). Identification of novel mechanisms involved in generating localized vulvodynia pain. *Am. J. Obstet. Gynecol.* 213, 38.e1–38.e12. doi: 10.1016/j.ajog.2015.02.002

Farmer, M. A., Taylor, A. M., Bailey, A. L., Tuttle, A. H., Macintyre, L. C., Milagrosa, Z. E., et al. (2011). Repeated vulvovaginal fungal infections cause

persistent pain in a mouse model of vulvodynia. *Sci. Transl. Med.* 3:101ra191. doi: 10.1126/scitranslmed.3002613

Foster, D. C., Falsetta, M. L., Woeller, C. F., Pollock, S. J., Song, K., Bonham, A., et al. (2015). Site-specific mesenchymal control of inflammatory pain to yeast challenge in vulvodynia-afflicted and pain-free women. *Pain* 156, 386–396. doi: 10.1097/01.j.pain.0000460320.95267.5d

Ghilardi, J. R., Freeman, K. T., Jimenez-Andrade, J. M., Coughlin, K. A., Kaczmarska, M. J., Castaneda-Corral, G., et al. (2012). Neuroplasticity of sensory and sympathetic nerve fibers in a mouse model of a painful arthritic joint. *Arthritis Rheum.* 64, 2223–2232. doi: 10.1002/art.34385

Goetsch, M. F., Morgan, T. K., Korcheva, V. B., Li, H., Peters, D., and Leclair, C. M. (2010). Histologic and receptor analysis of primary and secondary vestibulodynia and controls: a prospective study. *Am. J. Obstet. Gynecol.* 202, 614.e61–614.e8. doi: 10.1016/j.ajog.2010.01.028

Goldstein, A. T., Pukall, C. F., Brown, C., Bergeron, S., Stein, A., and Kellogg-Spadt, S. (2016). Vulvodynia: assessment and treatment. *J. Sex. Med.* 13, 572–590. doi: 10.1016/j.jsxm.2016.01.020

Gong, W. Y., Abdelhamid, R. E., Carvalho, C. S., and Sluka, K. A. (2016). Resident macrophages in muscle contribute to development of hyperalgesia in a mouse model of noninflammatory muscle pain. *J. Pain* 17, 1081–1094. doi: 10.1016/j.jpain.2016.06.010

Gordon, S., and Taylor, P. R. (2005). Monocyte and macrophage heterogeneity. *Nat. Rev. Immunol.* 5, 953–964. doi: 10.1038/nri1733

Halperin, R., Zehavi, S., Vaknin, Z., Ben-Ami, I., Pansky, M., and Schneider, D. (2005). The major histopathologic characteristics in the vulvar vestibulitis syndrome. *Gynecol. Obstet. Invest.* 59, 75–79. doi: 10.1159/000082112

Harlow, B. L., Kunitz, C. G., Nguyen, R. H., Rydell, S. A., Turner, R. M., and Maclehose, R. F. (2014). Prevalence of symptoms consistent with a diagnosis of vulvodynia: population-based estimates from 2 geographic regions. *Am. J. Obstet. Gynecol.* 210, 40.e1–40.e8. doi: 10.1016/j.ajog.2013.09.033

Hasan, W., Jama, A., Donohue, T., Wernli, G., Onyszchuk, G., Al-Hafez, B., et al. (2006). Sympathetic hyperinnervation and inflammatory cell NGF synthesis following myocardial infarction in rats. *Brain Res.* 1124, 142–154. doi: 10.1016/j.brainres.2006.09.054

Heim, L. J. (2001). Evaluation and differential diagnosis of dyspareunia. *Am. Fam. Physician* 63, 1535–1544.

Hoheisel, U., Rosner, J., and Mense, S. (2015). Innervation changes induced by inflammation of the rat thoracolumbar fascia. *Neuroscience* 300, 351–359. doi: 10.1016/j.neuroscience.2015.05.034

Huo, W., Zhang, Y., Liu, Y., Lei, Y., Sun, R., Zhang, W., et al. (2018). Dehydrocorydaline attenuates bone cancer pain by shifting microglial M1/M2 polarization toward the M2 phenotype. *Mol. Pain* 14:1744806918781733. doi: 10.1177/1744806918781733

Jenkins, S. J., Ruckerl, D., Cook, P. C., Jones, L. H., Finkelman, F. D., van Rooijen, N., et al. (2011). Local macrophage proliferation, rather than recruitment from the blood, is a signature of TH2 inflammation. *Science* 332, 1284–1288. doi: 10.1126/science.1204351

Keppel Hesselink, J. M., Kopsky, D. J., and Sajben, N. (2016). New topical treatment of vulvodynia based on the pathogenetic role of cross talk between nociceptors, immunocompetent cells and epithelial cells. *J. Pain Res.* 9, 757–762. doi: 10.2147/JPR.S115407

Kigerl, K. A., Gensel, J. C., Ankeny, D. P., Alexander, J. K., Donnelly, D. J., and Popovich, P. G. (2009). Identification of two distinct macrophage subsets with divergent effects causing either neurotoxicity or regeneration in the injured mouse spinal cord. *J. Neurosci.* 29, 13435–13444. doi: 10.1523/JNEUROSCI.3257-09.2009

Lawrence, T., and Natoli, G. (2011). Transcriptional regulation of macrophage polarization: enabling diversity with identity. *Nat. Rev. Immunol.* 11, 750–761. doi: 10.1038/nri3088

Leclair, C. M., Goetsch, M. F., Korcheva, V. B., Anderson, R., Peters, D., and Morgan, T. K. (2011). Differences in primary compared with secondary vestibulodynia by immunohistochemistry. *Obstet. Gynecol.* 117, 1307–1313. doi: 10.1097/AOG.0b013e31821c33dc

Leung, A., Gregory, N. S., Allen, L. A., and Sluka, K. A. (2016). Regular physical activity prevents chronic pain by altering resident muscle macrophage phenotype and increasing interleukin-10 in mice. *Pain* 157, 70–79. doi: 10.1097/j.pain.0000000000000312

Leusink, P., van de Pasch, S., Teunissen, D., Laan, E. T., and Lagro-Janssen, A. L. (2018). The relationship between vulvovaginal candidiasis and provoked vulvodynia: a systematic review. *J. Sex. Med.* 15, 1310–1321. doi: 10.1016/j.jsxm.2018.07.011

Liao, Z., Chakrabarty, A., Mu, Y., Bhattacherjee, A., Goestch, M., Leclair, C. M., et al. (2017). A local inflammatory renin-angiotensin system drives sensory axon sprouting in provoked vestibulodynia. *J. Pain* 18, 511–525. doi: 10.1016/j.jpain.2016.12.008

Lindholm, D., Heumann, R., Meyer, M., and Thoenen, H. (1987). Interleukin-1 regulates synthesis of nerve growth factor in non-neuronal cells of rat sciatic nerve. *Nature* 330, 658–659. doi: 10.1038/330658a0

Liu, P., Peng, J., Han, G. H., Ding, X., Wei, S., Gao, G., et al. (2019). Role of macrophages in peripheral nerve injury and repair. *Neural Regen. Res.* 14, 1335–1342. doi: 10.4103/1673-5374.253510

Liu, T., van Rooijen, N., and Tracey, D. J. (2000). Depletion of macrophages reduces axonal degeneration and hyperalgesia following nerve injury. *Pain* 86, 25–32. doi: 10.1016/s0304-3959(99)00306-1

Liu, B., Zhang, M., Zhao, J., Zheng, M., and Yang, H. (2018). Imbalance of M1/M2 macrophages is linked to severity level of knee osteoarthritis. *Exp. Ther. Med.* 16, 5009–5014. doi: 10.3892/etm.2018.6852

Lundqvist, E. N., Hofer, P. A., Olofsson, J. I., and Sjöberg, I. (1997). Is vulvar vestibulitis an inflammatory condition? A comparison of histological findings in affected and healthy women. *Acta Derm. Venereol.* 77, 319–322.

Mantovani, A., Sica, A., and Locati, M. (2005). Macrophage polarization comes of age. *Immunity* 23, 344–346. doi: 10.1016/j.immuni.2005.10.001

Morotti, M., Vincent, K., Brawn, J., Zondervan, K. T., and Becker, C. M. (2014). Peripheral changes in endometriosis-associated pain. *Hum. Reprod. Update* 20, 717–736. doi: 10.1093/humupd/dmu021

Mosser, D. M., and Edwards, J. P. (2008). Exploring the full spectrum of macrophage activation. *Nat. Rev. Immunol.* 8, 958–969. doi: 10.1038/nri2448

Murray, R. Z., and Stow, J. L. (2014). Cytokine secretion in macrophages: SNAREs, rabs, and membrane trafficking. *Front. Immunol.* 5:538. doi: 10.3389/fimmu.2014.00538

Nakawaki, M., Uchida, K., Miyagi, M., Inoue, G., Kawakubo, A., Satoh, M., et al. (2019). Changes in nerve growth factor expression and macrophage phenotype following intervertebral disc injury in mice. *J. Orthop. Res.* doi: 10.1002/jor.24308 [Epub ahead of print].

Nakazawa, K. R., Walter, B. A., Laudier, D. M., Krishnamoorthy, D., Mosley, G. E., Spiller, K. L., et al. (2018). Accumulation and localization of macrophage phenotypes with human intervertebral disc degeneration. *Spine J.* 18, 343–356. doi: 10.1016/j.spinee.2017.09.018

Pannell, M., Labuz, D., Celik, M. Ö., Keye, J., Batra, A., Siegmund, B., et al. (2016). Adoptive transfer of M2 macrophages reduces neuropathic pain *via* opioid peptides. *J. Neuroinflammation* 13:262. doi: 10.1186/s12974-016-0735-z

Pinho-Ribeiro, F. A., Verri, W. A. Jr., and Chiu, I. M. (2017). Nociceptor sensory neuron-immune interactions in pain and inflammation. *Trends Immunol.* 38, 5–19. doi: 10.1016/j.it.2016.10.001

Pruss, H., Kopp, M. A., Brommer, B., Gatzemeier, N., Laginha, I., Dirnagl, U., et al. (2011). Non-resolving aspects of acute inflammation after spinal cord injury (SCI): indices and resolution plateau. *Brain Pathol.* 21, 652–660. doi: 10.1111/j.1750-3639.2011.00488.x

Reynolds, M. L., and Fitzgerald, M. (1995). Long-term sensory hyperinnervation following neonatal skin wounds. *J. Comp. Neurol.* 358, 487–498. doi: 10.1002/cne.903580403

Rosen, S. F., Ham, B., Haichin, M., Walters, I. C., Tohyama, S., Sotocinal, S. G., et al. (2019). Increased pain sensitivity and decreased opioid analgesia in T-cell-deficient mice and implications for sex differences. *Pain* 160, 358–366. doi: 10.1097/j.pain.0000000000001420

Sakurai, Y., Fujita, M., Kawasaki, S., Sanaki, T., Yoshioka, T., Higashino, K., et al. (2019). Contribution of synovial macrophages to rat advanced osteoarthritis pain resistant to cyclooxygenase inhibitors. *Pain* 160, 895–907. doi: 10.1097/j.pain.0000000000001466

Scotland, R. S., Stables, M. J., Madalli, S., Watson, P., and Gilroy, D. W. (2011). Sex differences in resident immune cell phenotype underlie more

efficient acute inflammatory responses in female mice. *Blood* 118, 5918–5927. doi: 10.1182/blood-2011-03-340281

Sekiguchi, F., Domoto, R., Nakashima, K., Yamasoba, D., Yamanishi, H., Tsubota, M., et al. (2018). Paclitaxel-induced HMGB1 release from macrophages and its implication for peripheral neuropathy in mice: Evidence for a neuroimmune crosstalk. *Neuropharmacology* 141, 201–213. doi: 10.1016/j.neuropharm.2018.08.040

Sharma, H., Ji, E., Yap, P., Vilimas, P., Kyloh, M., Spencer, N. J., et al. (2018). Innervation changes induced by inflammation in the murine vagina. *Neuroscience* 372, 16–26. doi: 10.1016/j.neuroscience.2017.12.026

Shepherd, A. J., Copits, B. A., Mickle, A. D., Karlsson, P., Kadunganattil, S., Haroutounian, S., et al. (2018). Angiotensin II triggers peripheral macrophage-to-sensory neuron redox crosstalk to elicit pain. *J. Neurosci.* 38, 7032–7057. doi: 10.1523/JNEUROSCI.3542-17.2018

Sorge, R. E., LaCroix-Fralish, M. L., Tuttle, A. H., Sotocinal, S. G., Austin, J. S., Ritchie, J., et al. (2011). Spinal cord Toll-like receptor 4 mediates inflammatory and neuropathic hypersensitivity in male but not female mice. *J. Neurosci.* 31, 15450–15454. doi: 10.1523/JNEUROSCI.3859-11.2011

Sorge, R. E., Mapplebeck, J. C., Rosen, S., Beggs, S., Taves, S., Alexander, J. K., et al. (2015). Different immune cells mediate mechanical pain hypersensitivity in male and female mice. *Nat. Neurosci.* 18, 1081–1083. doi: 10.1038/nn.4053

Sorge, R. E., and Totsch, S. K. (2017). Sex differences in pain. *J. Neurosci. Res.* 95, 1271–1281. doi: 10.1002/jnr.23841

Swanson, C. L., Rueter, J. A., Olson, J. E., Weaver, A. L., and Stanhope, C. R. (2014). Localized provoked vestibulodynia: outcomes after modified vestibulectomy. *J. Reprod. Med.* 59, 121–126.

Tommola, P., Butzow, R., Unkila-Kallio, L., Paavonen, J., and Meri, S. (2015). Activation of vestibule-associated lymphoid tissue in localized provoked vulvodynia. *Am. J. Obstet. Gynecol.* 212, 476.e1–478.e8. doi: 10.1016/j.ajog.2014.10.1098

Tommola, P., Unkila-Kallio, L., Paetau, A., Meri, S., Kalso, E., and Paavonen, J. (2016). Immune activation enhances epithelial nerve growth in provoked vestibulodynia. *Am. J. Obstet. Gynecol.* 215, 768.e1–768.e8. doi: 10.1016/j.ajog.2016.07.037

Tympanidis, P., Casula, M. A., Yiangou, Y., Terenghi, G., Dowd, P., and Anand, P. (2004). Increased vanilloid receptor VR1 innervation in vulvodynia. *Eur. J. Pain* 8, 129–133. doi: 10.1016/s1090-3801(03)00085-5

Tympanidis, P., Terenghi, G., and Dowd, P. (2003). Increased innervation of the vulval vestibule in patients with vulvodynia. *Br. J. Dermatol.* 148, 1021–1027. doi: 10.1046/j.1365-2133.2003.05308.x

Wernli, G., Hasan, W., Bhattacherjee, A., van Rooijen, N., and Smith, P. G. (2009). Macrophage depletion suppresses sympathetic hyperinnervation following myocardial infarction. *Basic Res. Cardiol.* 104, 681–693. doi: 10.1007/s00395-009-0033-3

Williams, K. S., Killebrew, D. A., Clary, G. P., Seawell, J. A., and Meeker, R. B. (2015). Differential regulation of macrophage phenotype by mature and pro-nerve growth factor. *J. Neuroimmunol.* 285, 76–93. doi: 10.1016/j.jneuroim.2015.05.016

Woolf, C. J., Safieh-Garabedian, B., Ma, Q. P., Crilly, P., and Winter, J. (1994). Nerve growth factor contributes to the generation of inflammatory sensory hypersensitivity. *Neuroscience* 62, 327–331. doi: 10.1016/0306-4522(94)90366-2

Yin, Z. Y., Li, L., Chu, S. S., Sun, Q., Ma, Z. L., and Gu, X. P. (2016). Antinociceptive effects of dehydrocorydaline in mouse models of inflammatory pain involve the opioid receptor and inflammatory cytokines. *Sci. Rep.* 6:27129. doi: 10.1038/srep27129

Zanotta, N., Campisciano, G., Scrimin, F., Blendi, U., Marcuzzi, A., Vincenti, E., et al. (2018). Cytokine profiles of women with vulvodynia: identification of a panel of pro-inflammatory molecular targets. *Eur. J. Obstet. Gynecol. Reprod. Biol.* 226, 66–70. doi: 10.1016/j.ejogrb.2018.05.035

Conflict of Interest Statement: The authors declare that the research was conducted in the absence of any commercial or financial relationships that could be construed as a potential conflict of interest.

Copyright © 2019 Barry, Matusica and Haberberger. This is an open-access article distributed under the terms of the Creative Commons Attribution License (CC BY). The use, distribution or reproduction in other forums is permitted, provided the original author(s) and the copyright owner(s) are credited and that the original publication in this journal is cited, in accordance with accepted academic practice. No use, distribution or reproduction is permitted which does not comply with these terms.

frontiers in Molecular Neuroscience

ORIGINAL RESEARCH
published: 14 August 2019
doi: 10.3389/fnmol.2019.00198

Secreted Amyloid Precursor Protein-Alpha Promotes Arc Protein Synthesis in Hippocampal Neurons

*Rhys W. Livingstone[1], Megan K. Elder[1], Maya C. Barrett[1], Courteney M. Westlake[1], Katie Peppercorn[2], Warren P. Tate[2], Wickliffe C. Abraham[3] and Joanna M. Williams[1]**

[1] Department of Anatomy, Brain Health Research Centre, Brain Research New Zealand, Rangahau Roro Aotearoa, University of Otago, Dunedin, New Zealand, [2] Department of Biochemistry, Brain Health Research Centre, Brain Research New Zealand, Rangahau Roro Aotearoa, University of Otago, Dunedin, New Zealand, [3] Department of Psychology, Brain Health Research Centre, Brain Research New Zealand, Rangahau Roro Aotearoa, University of Otago, Dunedin, New Zealand

Secreted amyloid precursor protein-α (sAPPα) is a neuroprotective and memory-enhancing molecule, however, the mechanisms through which sAPPα promotes these effects are not well understood. Recently, we have shown that sAPPα enhances cell-surface expression of glutamate receptors. Activity-related cytoskeletal-associated protein Arc (Arg3.1) is an immediate early gene capable of modulating long-term potentiation, long-term depression and homeostatic plasticity through regulation of α-amino-3-hydroxy-5-methyl-4-isoxazolepropionic acid receptor localization. Accordingly, we hypothesized that sAPPα may enhance synaptic plasticity, in part, by the *de novo* synthesis of Arc. Using primary cortical and hippocampal neuronal cultures we found that sAPPα (1 nM, 2 h) enhances levels of *Arc* mRNA and protein. Arc protein levels were increased in both the neuronal somata and dendrites in a Ca^{2+}/calmodulin-dependent protein kinase II-dependent manner. Additionally, dendritic Arc expression was dependent upon activation of mitogen-activated protein kinase and protein kinase G. The enhancement of dendritic Arc protein was significantly reduced by antagonism of *N*-methyl-D-aspartate (NMDA) and nicotinic acetylcholine (α7nACh) receptors, and fully eliminated by dual application of these antagonists. This effect was further corroborated in area CA1 of acute hippocampal slices. These data suggest sAPPα-regulated plasticity within hippocampal neurons is mediated by cooperation of NMDA and α7nACh receptors to engage a cascade of signal transduction molecules to enhance the transcription and translation of Arc.

Keywords: Arc/Arg3.1, sAPPα, plasticity, PKG, α7nACh, NMDA, Alzheimer's disease, FUNCAT-PLA

OPEN ACCESS

Edited by:
Jochen C. Meier, Technische Universität Braunschweig, Germany

Reviewed by:
Clive R. Bramham, University of Bergen, Norway
Andreas Vlachos, University of Freiburg, Germany
Michael R. Kreutz, Leibniz Institute for Neurobiology (LG), Germany

****Correspondence:***
Joanna M. Williams
joanna.williams@otago.ac.nz

Received: *16 May 2019*
Accepted: *30 July 2019*
Published: *14 August 2019*

Citation:
Livingstone RW, Elder MK, Barrett MC, Westlake CM, Peppercorn K, Tate WP, Abraham WC and Williams JM (2019) Secreted Amyloid Precursor Protein-Alpha Promotes Arc Protein Synthesis in Hippocampal Neurons. Front. Mol. Neurosci. 12:198. doi: 10.3389/fnmol.2019.00198

INTRODUCTION

Secreted amyloid precursor protein-alpha (sAPPα) is a neuroprotective and neurotrophic protein, derived from the same parent protein as neurotoxic amyloid-ß. The levels of endogenous sAPPα are reduced in neurological disorders, including Alzheimer's disease (AD; Lannfelt et al., 1995; Kim et al., 2009). By contrast, enhancement of sAPPα levels is protective against AD-associated memory impairments (Fol et al., 2016; Tan et al., 2018) and attenuates excitotoxic injury *in vivo*

and *in vitro* (Mucke et al., 1996; Ryan et al., 2013). Further, sAPPα is able to facilitate long-term potentiation (LTP; Taylor et al., 2008; Moreno et al., 2015), stimulate neurite outgrowth (Clarris et al., 1994), and regulate spine morphology (Hick et al., 2015). Recently, it has been shown that the molecular mechanisms underpinning these actions include enhancement of glutamate receptor trafficking, synaptodendritic protein synthesis and new gene transcription (Claasen et al., 2009; Chasseigneaux et al., 2011; Ryan et al., 2013; Mockett et al., 2019), yet these and other mechanisms have not been fully explored.

Numerous studies have identified the importance of the immediate early gene (IEG) activity-regulated cytoskeletal-associated protein Arc (also referred to as activity-regulated gene 3.1, Arg3.1) in mediating synaptic changes associated with LTP, long-term depression (LTD) and homeostatic plasticity, which together permit the formation and maintenance of long term memories (Lyford et al., 1995; Guzowski et al., 2000; Plath et al., 2006; Messaoudi et al., 2007; Nakayama et al., 2016). Arc transcription is a well-established marker of plasticity (Grinevich et al., 2009; Izumi et al., 2011) and can be driven by activation of ionotropic, metabotropic, and enzyme-linked receptors (Kristensen et al., 2007; Bloomer et al., 2008; Waung et al., 2008; Peng et al., 2010; Gangarossa et al., 2011; Kumar et al., 2011; Kuipers et al., 2016; Chen et al., 2017). Interestingly, *Arc* mRNA is translated in both somata and dendrites of activated neurons (Steward and Worley, 2001; Steward et al., 2014). In dendrites, newly translated Arc protein associates with the *F*-actin-binding protein debrin A (Nair et al., 2017), and components of the clathrin-mediated endocytic machinery, dynamin-2 and endophilin-3 (Chowdhury et al., 2006). Indeed, Arc has been shown to promote internalization of GluA1- and GluA2-containing α-amino-3-hydroxy-5-methyl-4-isoxazolepropionic acid (AMPA) receptors (Chowdhury et al., 2006; Rial Verde et al., 2006), as well as Ca^{2+}-permeable, homomeric GluA1-containing AMPARs; corroborated by a reduction in the rectification index of AMPA receptor-mediated miniature excitatory post-synaptic current amplitudes in Arc-overexpressing cortical neurons (DaSilva et al., 2016; Wall and Correa, 2018). Arc has also been shown to associate with CaMKIIβ, the so-called 'inverse tag' of inactive synapses, promoting AMPA receptor internalization (Okuno et al., 2012), as well as CaMKIIα (Husi et al., 2000) and stimulate neurite extension (Donai et al., 2003). While these data suggest a role for Arc in depotentiation or metaplasticity, new data indicate that Arc is released from neurons in virus-like caspids and thus may play a role in cell-to-cell communication (Pastuzyn et al., 2018).

Notably, while the receptor/s mediating the actions of sAPPα have not been conclusively identified, candidate receptors and downstream pathways overlap with those identified in relation to the regulation of Arc. Somatodendritic translation of *Arc* mRNA is dependent on Ca^{2+} signaling via ionotropic receptors, including the *N*-methyl-d-aspartate receptor (NMDA; Chen et al., 2017) and α7 nicotinic acetylcholine receptor (α7nAchR; Kristensen et al., 2007); these receptors are both candidates for mediating sAPPα's actions (Taylor et al., 2008; Richter et al., 2018; Mockett et al., 2019). Furthermore, downstream signaling molecules such as protein kinase G (PKG), mitogen activated protein kinase (MAPK) and CaMKII have not only been shown to enhance *Arc* mRNA or regulate Arc protein expression (Huang et al., 2007; Gakhar-Koppole et al., 2008; Ota et al., 2010; Chasseigneaux et al., 2011), but also mediates the neuroprotective, neurotrophic and plasticity-enhancing effects of sAPPα (Furukawa et al., 1996a; Claasen et al., 2009; Mockett et al., 2019).

Based on the commonality in pathways regulated by sAPPα and those which enchance Arc expression, we hypothesized that heightening sAPPα levels would upregulate Arc expression. Using primary neuronal cultures, we found that exogenously delivered recombinant sAPPα (1 nM, 2 h) enhanced both Arc mRNA and protein through activation of both NMDA and α7nACh receptors, and that this effect is dependent on the activity of CaMKII, MAPK and PKG.

RESULTS

In order to investigate the expression of the key plasticity protein Arc, we first sought to confirm that DIV24-27 primary neuronal cultures form mature synapses. Consistent with previous literature (Basarsky et al., 1994; Papa et al., 1995; Grabrucker et al., 2009), we found that our cultures coexpress the presynaptic marker synapsin-1 and the postsynaptic AMPA receptor subunit GluA1 on MAP2-positive neurons (**Figure 1A**). Co-expression was evident in both somatic and dendritic compartments, as previously observed (Richmond et al., 1996). Additionally, our cultures show populations of GFAP-positive astrocytes closely associated with GluA1-positive neurons (**Figure 1B**). This association has been shown to support the development of synapses *in vitro* (Jones et al., 2012). Further, ultrastructural analysis of our cultured neurons shows evidence of mature synapses (**Figure 1C**; Robert et al., 2012).

sAPPα Facilitates an Increase in Arc mRNA Expression

To test the hypothesis that sAPPα may regulate Arc expression we investigated the ability of recombinant sAPPα (1 nM) to promote transcription of *Arc* mRNA in rat cortical neurons (DIV 24-27). As a positive control we also assessed the levels of the known sAPPα-responsive IEG *Zif268* (Chasseigneaux et al., 2011; Penke et al., 2011; Ryan et al., 2013). As a negative control we assessed the levels of the constitutively expressed transcription factor SP2 (Suske, 1999). We found that treatment with sAPPα facilitated a slowly developing increase in the levels of *Arc* mRNA (**Figure 2**). There was no significant fold change in either *Arc* or *Zif268* mRNA after 15 or 30 min of sAPPα incubation (*Arc*: 15 min: 1.27 ± 1.00, $p = 0.35$; 30 min: 1.14 ± 0.28, $p = 0.49$; *Zif268*: 15 min: 0.96 ± 0.45, $p = 0.28$; 30 min: 1.30 ± 0.68, $p = 0.30$), but following 60 min exposure the levels of both *Arc* (2.29 ± 1.32, $p = 0.01$) and *Zif268* (1.78 ± 1.02, $p = 0.01$) mRNA increased significantly relative to no-drug controls. Interestingly, while both *Arc* (2.69 ± 1.53, $p < 0.0001$) and *zif268* mRNA remained significantly elevated at 120 min (1.38 ± 0.57, $p = 0.04$), and 240 min (*Arc*: 1.575 ± 1.15, $p = 0.03$; *Zif268*: 1.434 ± 0.86, $p = 0.03$), both Arc and Zif268 mRNA expression appeared

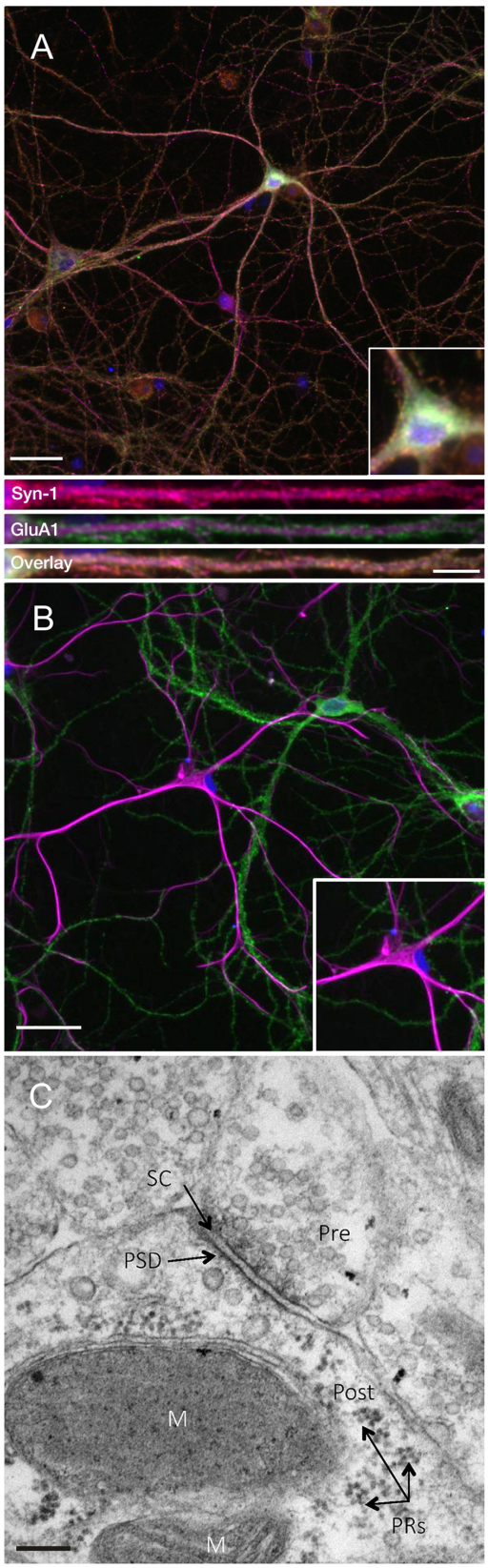

FIGURE 1 | Continued

FIGURE 1 | Primary cell cultures display normal expression of cellular and synaptic markers at DIV24-27. **(A)** Representative immunocytochemistry images of DIV 21-27 neurons show the colocalization of the presynaptic protein synapsin-1 (red) and the postsynaptic AMPA receptor subunit GluA1 (green) with MAP2-positive neurons (magenta) and nuclei (DAPI; blue) (scale bar = 50 μm). Lower panels show further magnified dendritic compartments (100 μm) from Synapsin-1 (top), GluA1 (middle) and the colocalization of both (bottom; scale bar = 10 μm). Primary cell cultures also show populations of **(B)** GFAP-positive astrocytes (magenta) closely associating with GluA1-positive neurons (green). Inset images show further magnified somatic compartments. **(C)** Representative electron micrograph showing the presence of synapses between neighboring primary hippocampal cells in culture. Pre- and postsynaptic regions were observed separated by a synaptic cleft. Pre, presynaptic terminal; Post, postsynaptic region; PRs, polyribosomes; PSD, postsynaptic density; SC, synaptic cleft; M, mitochondria. Scale bar = 100 nm.

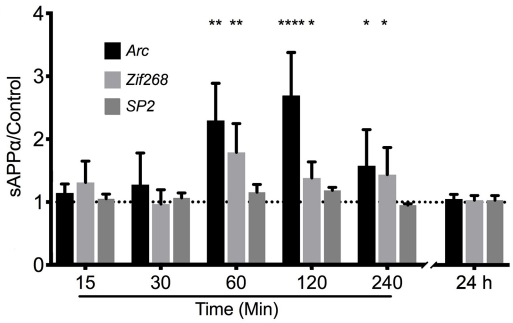

FIGURE 2 | sAPPα promotes the transcription of *Arc* and *Zif268* mRNA. RT-qPCR showed that sAPPα (1 nM) promotes an increase in the expression of *Arc* mRNA in primary cortical cells in culture at 60, 120 min ($n = 5$) and 240 min ($n = 4$) relative to no-drug controls ($n = 9$; mean ± SEM). No significant change was detected at 15 or 30 min, nor 24 h ($n = 4$), nor was there a significant change in the negative control gene SP2 ($n = 4$). One sample *t*-tests; $^{*}p \leq 0.05$, $^{**}p \leq 0.01$, $^{****}p \leq 0.0001$.

to decline at this timepoint and was not significantly different from controls 24 h later (Arc: 1.01 ± 0.14, $p = 0.42$; Zif268: 1.03 ± 0.14, $p = 0.15$). At no point was SP2 significantly different from controls (15 min: 1.04 ± 0.15, $p = 0.20$; 30 min: 1.14 ± 0.04, $p = 0.27$; 60 min: 1.15 ± 0.24, $p = 0.16$; 120 min: 1.18 ± 0.09, $p = 0.07$; 240 min: 0.94 ± 0.04, $p = 0.29$; 24 h: 1.03 ± 0.14, $p = 0.54$).

sAPPα Mediated New Synthesis of Arc Protein: Detected Using FUNCAT-PLA

Next, we directly visualized *de novo* Arc protein synthesis in response to sAPPα using fluorescence non-canonical amino acid tagging with proximity ligation assays (FUNCAT-PLA: **Figure 3**). Here, we found that sAPPα (1 nM, 2 h) induced a highly significant increase in newly synthesized Arc protein in both the dendrites (2.72 ± 0.41, $p \leq 0.0001$; **Figures 3C–E**) and somata (1.69 ± 0.32, $p = 0.03$) of cultured hippocampal neurons. Co-incubation with protein synthesis inhibitor anisomycin eliminated labeling (somata, 0.44 ± 0.06, $p \leq 0.0001$; dendrites, 0.004 ± 0.004, $p \leq 0.0001$; **Figures 3B,D,E**), confirming the punctate signal was specific for *de novo* synthesized protein.

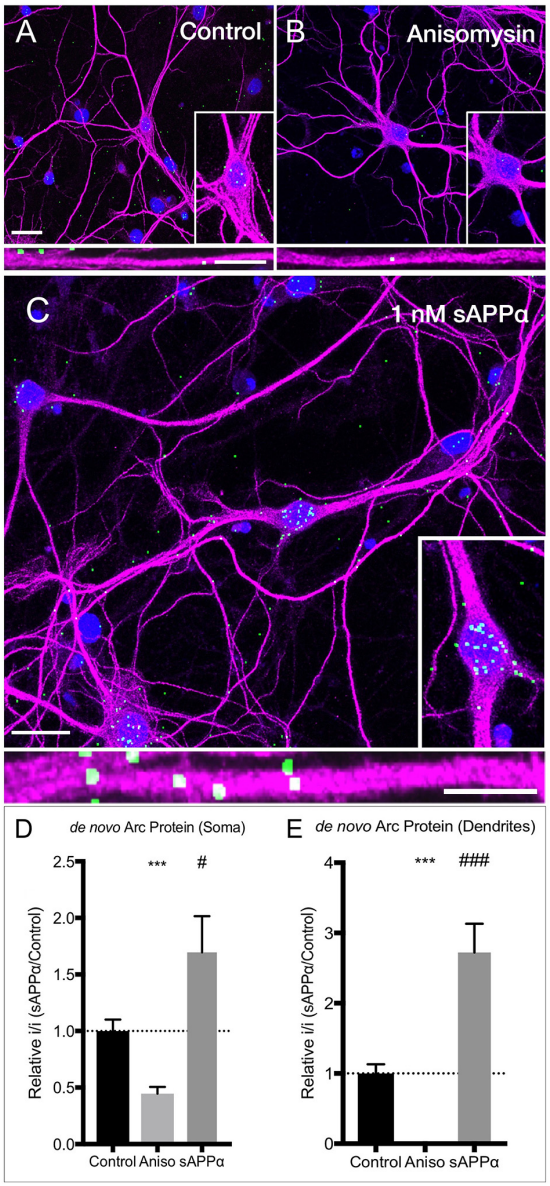

FIGURE 3 | sAPPα increases somatic and dendritic expression of *de novo* Arc protein. Representative images show neurons (MAP2 positive neurons; magenta) expressing FUNCAT-PLA signal (green puncta) representing newly synthesized Arc protein in **(A)** no-drug control cells, **(B)** anisomycin-treated, and **(C)** sAPPα-treated (1 nM, 2 h) primary hippocampal cultures. Nuclei are stained blue (DAPI). The relative integrated intensity of **(D)** somatic and **(E)** dendritic signal from treatment groups is expressed as drug/average of control and presented as mean ± SEM (n = 25–34 cells from three independent experiments). Co-incubation of AHA with anisomycin inhibited Arc protein synthesis. Incubation with sAPPα significantly increased the expression of *de novo* synthesized Arc protein in the somata and dendrites. Images show whole cell (scale bar = 50 μm), and magnified somatic (inset, bottom right) and dendritic (50 μm; lower panels; scale bar = 10 μm). Outliers were removed from each experiment prior to amalgamation using Grubb's tests, and normality was detected by D'Agostino and Pearson omnibus normality tests. Significance was calculated on data expressed relative to control by use of one sample t-tests; hashes (#) indicate significance between control and sAPPα-treated, asterisks (*) indicate significance between control and anisomycin treated, $^{\#}p = 0.038$, $^{***/\#\#\#}p \leq 0.0001$.

Interestingly, a few puncta were found located outside the MAP2 positive cells. These may reflect a low level of background stain or the synthesis of Arc within astorcytes (Rodriguez et al., 2008).

sAPPα Facilitates Arc Protein Expression in Primary Hippocampal Neurons

Using western blot analysis we showed that the anti-Arc primary antibody detected a signal band of the expected molecular weight (**Supplementary Figure 1**). Next, using this antibody in immunocytochemistry, we showed that application of sAPPα significantly increased Arc protein expression in a concentration dependent manner. Specifically, 0.1 nM sAPPα was sufficient to significantly increase dendritic Arc expression (1.35 ± 0.05, p = 0.0002), although it did not affect somatic Arc protein expression (1.15 ± 0.39, p = 0.24; **Figures 4A,B,F,G**). Conversely, 1 nM sAPPα significantly increased both somatic (1.35 ± 0.46, $p \leq 0.0001$) and dendritic (1.92 ± 0.81, p = 0.0003) Arc protein expression relative to controls (**Figures 4A,C,F,G**; see **Supplementary Figure 2** for Arc-only gray scale image). Further, using confocal microscopy we were able to show Arc expression to be punctate in dendrites, typical of synapse-associated proteins (**Supplementary Figure 3**).

sAPPβ differs from sAPPα by 16 C-terminal amino acids. sAPPα is derived following cleavage of amyloid precursor protein by a-secretase activity, whereas sAPPβ is liberated by β-secretase 1. sAPPβ has been described as 100-fold less effective in ameliorating excitotoxicity and attenuating glucose deprivation compared to sAPPα (Furukawa et al., 1996b; Turner et al., 2007), but appears to remain unaltered in AD (Sennvik et al., 2000). Accordingly, we next examined the effect of sAPPβ on Arc expression. We found that sAPPβ did not affect Arc protein in dendrites (0.1 nM: 0.97 ± 0.49; 1 nM: 0.92 ± 0.45, $p \geq 0.99$, respectively; **Figures 4D–G**). Interestingly, 0.1 nM sAPPβ did not affect Arc protein expression in the somata (0.91 ± 0.34, $p \geq 0.99$), while 1 nM sAPPβ resulted in a small but significant decrease in somatic Arc expression (0.82 ± 0.38, p = 0.03).

To extend our findings that sAPPα (1 nM, 2 h) increased dendritic Arc expression, we assessed fluorescence intensity levels and distribution of Arc protein throughout the dendrites according to the method of Gumy et al. (2017). Using this approach we found that dendritic Arc expression was significantly increased throughout primary dendrites in the initial 50 μm (control: 40.06 ± 14.93; 0.1 nM: 63.82 ± 20.1, $p \leq 0.0001$; 1 nM: 62.04 ± 22.6, $p \leq 0.0001$), middle 50 μm (control: 32.43 ± 15.69; 0.1 nM: 52.91 ± 25.57 p = 0.0005; 1 nM: 52.89 ± 22.29, $p \leq 0.0001$) and final 50 μm segment of primary dendrites (control: 27.09 ± 11.58; 0.1 nM; 43.72 ± 22.3, $p \leq 0.0001$; 1 nM 48.09 ± 24.17, p = 0.0311; **Figure 5A**). Increased Arc expression in secondary dendrites was observed in the initial 25 μm (control: 32.54 ± 13.55; 0.1 nM: 45.22 ± 19.61, p = 0.01; 1 nM: 43.73 ± 21.08, p = 0.01) and middle 25 μm dendritic segment (control: 27.03 ± 14.08; 0.1 nM: 37.64 ± 15.19, p = 0.002; 1 nM: 36.63 ± 17.49, p = 0.004; **Figure 5B**), however, Arc expression was not significantly

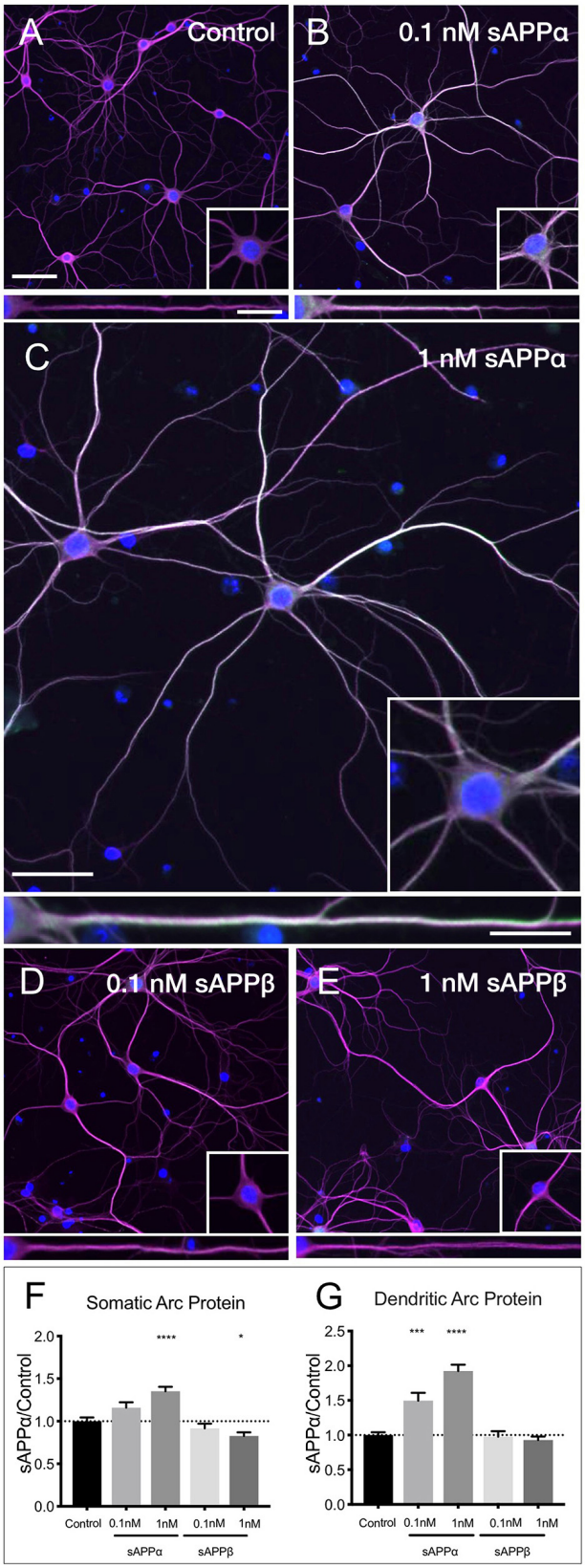

FIGURE 4 | Continued

FIGURE 4 | sAPPα promotes Arc protein expression in a concentration-dependent manner. Representative images showing Arc protein levels in **(A)** no drug control, **(B)** 0.1 nM sAPPα, **(C)** 1 nM sAPPα, **(D)** 0.1 nM sAPPβ and **(E)** 1 nM sAPPβ-treated primary hippocampal neurons. **(F)** Average data showing 1 nM sAPPα promotes an increase, and 1 nM sAPPβ a modest decrease in Arc protein expression in the somata. **(G)** Average data showing 0.1 and 1 nM sAPPα promotes an increase in dendritic Arc protein. Data are expressed as mean ± SEM from ≥4 experiments. 0.1 nM: $n = 40$ cells; 1 nM: $n = 80$ cells. Significance was calculated using a Kruskal–Wallis one-way ANOVA with Dunn's multiple comparisons test. $^{*}p = 0.0378$, $^{***}p = 0.0002$, $^{****}p \leq 0.0001$. Representative images show neuronal somata and dendritic projections (MAP2; magenta), Arc protein (green), nuclei (DAPI; blue), (scale bar = 50 μm), and magnified somatic (inset, bottom right) and dendritic (100 μm; lower panels; scale bar = 10 μm) compartments.

altered in the final 25 μm of secondary dendrites (control: 24.85 ± 12.25; 0.1 nM: 31.99 ± 13.06, $p = 0.26$; 1 nM: 30.06 ± 14.26, $p = 0.06$).

The sAPPα-induced increase in Arc protein expression in both somatic and dendritic compartments (**Figures 6A,B,E,F**) was blocked by co-application of the transcription inhibitor actinomycin-D (10 μM; somata: 0.81 ± 0.68; dendrites: 0.95 ± 0.61, respectively; $p < 0.0001$; **Figures 6C,E,F**). Additionally, co-application of the translation inhibitor anisomycin (40 μM) also eliminated the effect (somata: 0.62 ± 0.30; dendrites: 0.84 ± 0.41, $p < 0.0001$; **Figures 6D–F**). Together, these findings show that sAPPα promotes both Arc transcription and translation.

sAPPα-Induced Arc Protein Expression Is Dependent on CaMKII, MAPK, and PKG Signaling

Previous research has identified CaMKII, MAPK, and PKG as key downstream kinases regulating sAPPα-mediated protein synthesis in synaptoneurosomes (Claasen et al., 2009). Here we sought to determine whether the sAPPα-induced expression of Arc protein utilizes these same signaling kinases. We observed that the sAPPα-mediated increase in Arc protein in the somata (**Figures 7A,B,I,J**) was suppressed following inhibition of CaMKII by KN62 (10 μM; 0.90 ± 0.48, $p \leq 0.0001$; **Figures 7C,I,J**). Somatic Arc protein expression was also attenuated by the MAPK inhibitor PD98059 (50 μM; 1.15 ± 0.46, $p = 0.47$; **Figures 7D,I,J**), but not by the PKG inhibitor KT5823 (10 μM; 1.48 ± 0.82, $p \geq 0.99$; **Figures 7E,I,J**), the PKC inhibitor chelerythrine chloride (1 μM; 1.60 ± 0.83, $p \geq 0.99$; **Figures 7F,I,J**), the PKA inhibitor H-89 dihydrochloride (10 μM; 1.59 ± 0.80 $p \geq 0.99$; **Figures 7G,I,J**), or the mTOR inhibitor rapamycin (20 nM; 1.54 ± 0.71, $p \geq 0.99$; **Figures 7H,I,J**). Interestingly, by contrast dendritic Arc protein expression was significantly reduced via inhibition of CaMKII (0.72 ± 0.34, $p \leq 0.0001$; **Figures 7C,I,J**), MAPK (1.22 ± 0.80, $p = 0.04$; **Figures 7D,I,J**), and PKG (0.97 ± 0.45, $p \geq 0.0001$; **Figures 7E,I,J**), but it remained unaffected by inhibition of PKC (1.12 ± 0.51, $p = 0.08$; **Figure 7F**), PKA (1.57 ± 0.88, $p \geq 0.99$; **Figures 7G,I,J**), and mTOR (1.15 ± 0.58, $p = 0.051$; **Figures 7H,I,J**). These results suggest that activation of CaMKII, MAPK,

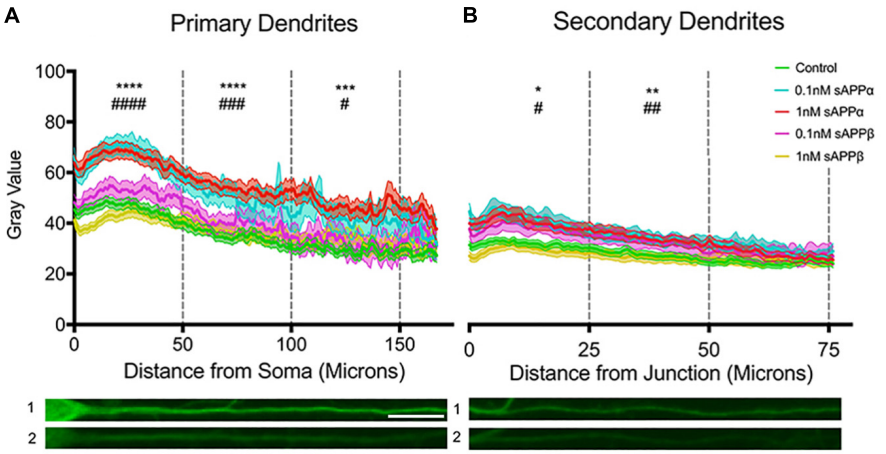

FIGURE 5 | Arc protein expression increases throughout primary and secondary dendrites. Average fluorescent intensity of Arc expression throughout **(A)** primary and **(B)** secondary dendrites (mean ± SEM, n = 40–141). Significance was determined by averaging dendritic gray value within each cell and is expressed per treatment group within **(A)** 50 and **(B)** 25 microns. Asterisks (*) and hashes (#) indicate significance found between 1 and 0.1 nM sAPPα, respectively, relative to controls. Representative fluorescence images illustrate Arc protein expression (green) within primary (A1,2) and secondary (B1,2) dendrites in the presence of 1 nM sAPPα (A1,B1) or no drug (A2,B2). Significance was determined by Kruskal–Wallis One-Way ANOVA and Dunn's multiple comparisons test. $^{*/\#}p = \leq 0.05$ $^{**/\#\#}p = \leq 0.005$, $^{***/\#\#\#}p = 0.0005$, $^{****/\#\#\#\#}p = \leq 0.0001$. Scale bar = 50 μm.

and PKG is necessary to facilitate sAPPα-induced Arc expression, but that different regulatory mechanisms may exist in somatic and dendritic compartments in primary hippocampal neurons.

sAPPα-Induced Dendritic Arc Protein Expression Is Dependent on Activation of NMDA- and α7nACh Receptors

Despite many studies, the cell surface receptor(s) which transduce the sAPPα signal are yet to be conclusively identified, though specific candidates have emerged (Rice et al., 2017, 2019; Richter et al., 2018; Mockett et al., 2019). Here, we pharmacologically inhibited likely candidates mediating sAPPα's plasticity-promoting effects and observed the effect on sAPPα-induced Arc protein levels (**Figure 8**). We found that application of antagonists targeting $GABA_B$ (CPG55845; 50 μM), TrkB (ANA-12; 100 μM), or mGluRI/II receptors (MCPG; 500 μM) had no significant effect on dendritic Arc protein expression (**Figures 8A,B,I**) following sAPPα treatment (1 nM, 2 h; CPG55845: 2.79 ± 1.08, $p \geq 0.99$, **Figures 8C,I**; ANA-12: 2.78 ± 1.29, $p \geq 0.99$, **Figures 8D,I**; MCPG: 2.29 ± 1.27, $p \geq 0.99$, **Figures 8E,I**). However, Arc protein expression was significantly reduced following antagonism of NMDA receptors by AP5 (50 μM; 1.67 ± 0.78, $p = 0.01$; **Figures 8F,I**) and α7nAch receptors with α-bungarotoxin (10 nM; 1.61 ± 1.18, $p = 0.0006$; **Figures 8G,I**). Combined antagonism of NMDA and α7nAch receptors completely abolished sAPPα-mediated Arc expression (0.78 ± 0.49, $p \leq 0.0001$; **Figures 8E,I**). These results suggest a novel mechanism whereby synergistic action between NMDA and α7nAch receptors governs an enhancement in sAPPα-mediated Arc protein expression.

sAPPα Increases CREB Phosphorylation and Arc Protein Levels in Area CA1 of Acute Hippocampal Slices

We next examined whether sAPPα could modulate transcription and Arc expression in acute hippocampal slices. Focusing on area CA1 (**Figure 9A**), we found that sAPPα (1 nM, 15 min) significantly increased phosphorylated cAMP element binding protein at serine 133 (pCREB) levels, a marker of transcriptional regulation as well as NMDAR signaling (Xia et al., 1996) (2.08 ± 0.60, $p = 0.01$; **Figures 9B,C,G**). We also showed that sAPPα (1 nM, 2 h) significantly increased Arc expression (1.55 ± 0.22, $p = 0.02$; **Figures 9D,E,H**) and that this effect was attenuated by co-incubation with NMDA and α7nAch antagonists APV and αBGT (1.08 ± 0.18, $p = 0.042$; **Figures 9F,H**).

MATERIALS AND METHODS

Animals

Sprague-Dawley rat pups (male or female, P0-P1) were sourced from a breeding colony maintained at the Hercus Taieri Resource Unit by the University of Otago (Dunedin, New Zealand), or at the Max Planck Institute for Brain Research (Frankfurt, Germany). All experimental protocols conducted in New Zealand were approved by the University of Otago Animals Ethics Committee and conducted in accordance with New Zealand Animal Welfare Legislation under the ethics approval ET18/15 and AUP-18-136 for cell culture work and DET19/16 for all acute slice work. All experiments conducted in Germany were compliant with German animal care guidelines, and Max Planck Society guidelines, and were approved by local authorities. The preparation of primary hippocampal cultures

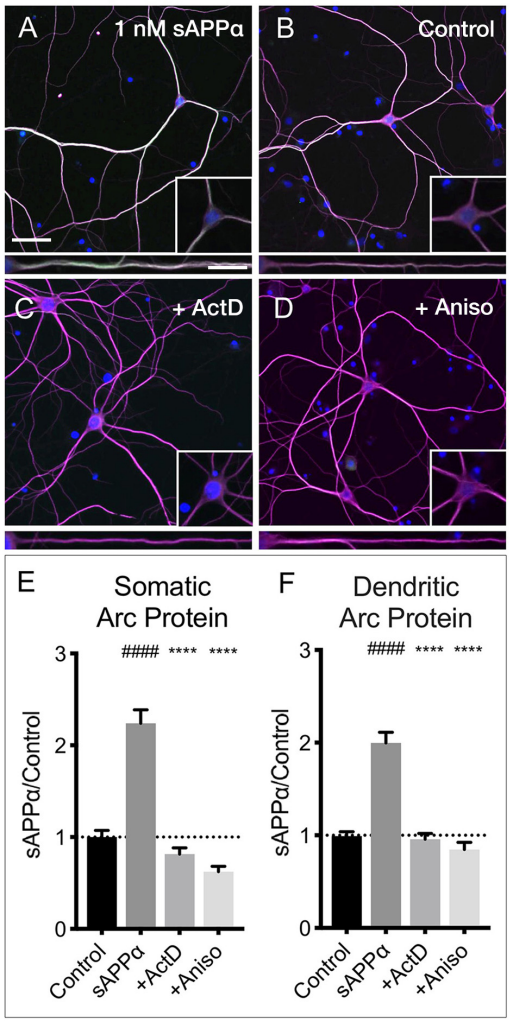

FIGURE 6 | Arc protein expression is prevented by inhibitors of transcription and translation. Representative images showing Arc protein levels in **(A)** sAPPα (1 nM, 2 h, $n = 157$) and **(B)** no drug control ($n = 115$ cells) conditions. sAPPα-mediated Arc increase is inhibited with co-application of **(C)** Actinomycin-D ($n = 104$) or **(D)** Anisomycin ($n = 30$) in the **(E)** somata and **(F)** dendrites. Significance was calculated using a Kruskal–Wallis one-way ANOVA with Dunn's multiple comparisons test. ****/#### $p \leq 0.0001$. Representative images show neurons (magenta), Arc protein (green), nuclei (DAPI; blue) (scale bar = 50 μm) and magnified somatic (inset, bottom right) and dendritic (100 μm; lower panels; scale bar = 10 μm).

followed a modified protocol based on Banker and Goslin (1998) and Kaech and Banker (2006). Cortex and hippocampi from Sprague-Dawley rat pups were dissociated using papain (Sigma) and plated at a low density on glass-bottomed culture dishes (40,000 cells/cm^2; Mattek) for immunolabelling, or at 300,000 cells/well of a 6-well plate for lysis and subsequent protein or RNA extraction and RT-qPCR. Cells were cultured in Neurobasal A medium (Life Technologies #10888-022), supplemented with B27 (Life Technologies, #17504-001) and Glutamax (Life Technologies, #35050-061) at 37°C/5% CO_2 for 24–27 days *in vitro* (DIV). Control samples were collected at the same time as treated cells in matched sets of culture dishes (immunocytochemistry, FUNCAT-PLA) or wells (RT-qPCR; western blot). All experiments conducted on acute tissue were prepared from young adult male Sprague-Dawley rats (42–56 days), as described previously (Mockett et al., 2019).

Drugs and Reagents

Inhibitors

KN62 (Tocris, #1277), PD98059 (Tocris, #1213), KT5823 (Tocris, #1289), Chelerythrine chloride (Tocris, #1330), H-89 dihydrochloride (Calbiochem, #371963), Rapamycin (Tocris, # 1292); Actinomycin-D (Tocris, #1229), Anisomycin (Sigma, #A9789) Sodium Fluoride (NaF; Sigma #S7920), Phenylmethylsulfonyl Fluoride (PMSF; Sigma, #P-7626) Okadaic Acid (Tocris, #1136).

Antagonists

CGP 55845 hydrochloride (Tocris, #1248), ±α-Methyl-4-carboxyphenylglycine (Sigma, #M-4796), ANA-12 (Tocris, #4781), D(−)-2-Amino-5-phosphonopentanoic acid (APV; Sigma, #A8054), α-Bungarotoxin (αBGT; Abcam, # ab120542).

sAPPα and sAPPβ production and purification was carried out according to the protocols developed by the Tate lab (Turner et al., 2007).

Immunocytochemistry

For experiments examining the effect of treatments, DIV24-27 primary hippocampal neurons were treated with sAPPα (0.1–1 nM, 2 h), sAPPβ (0.1–1 nM, 2 h) or culture media only. Following incubation, cells were fixed in 4% paraformaldehyde in PBS (pH 7.4; 20 min) supplemented with 1 mM $MgCl_2$ and 0.1 mM $CaCl_2$ (PBS-MC), and permeabilized with 0.5% Triton X-100 in PBS (pH 7.4; 15 min). Cells were then blocked in 4% normal goat serum in PBS (pH 7.4) for 1 h at room temperature (RT). Cells were incubated with primary antibodies of interest (2 h, RT), followed by 3 × 5 min washes (PBS, pH 7.4) and incubation in appropriate secondary antibody (30 min, RT), followed by 3 × 5 min washes (PBS, pH 7.4).

Primary and Secondary Antibodies

Primary Antibodies

Rabbit anti-Arc polyclonal (1:1000, synaptic systems, #156003), mouse anti-Biotin monoclonal (1:1000, Sigma, #B7653), guinea-pig anti-MAP2 polyclonal (1:1000, synaptic systems, #188004; monoclonal, 1:1000, Abcam, #AB11267), rabbit anti-pCREB (Ser133) monoclonal (1:500, cell signaling, #9198), mouse anti-Synapsin-1 monoclonal (1:1000, synaptic systems, #106011), rabbit anti-GluA1 polyclonal (1:1000, Abcam, #AB31232), mouse anti-GFAP monoclonal (1:1000, Abcam, #AB10062), mouse anti-αTubulin monoclonal (1:4000; Abcam, #AB7291).

Secondary Antibodies and Fluorescent Stains

Goat anti-Guinea Pig Alexa Fluor 488 (1:1000, Thermofisher, #A11073), Goat anti-rabbit Alexa Fluor 555 (1:1000, Invitrogen, #A21429), Goat anti-mouse Alexa Fluor 647 (1:1000, Invitrogen, #A21236), Donkey anti-mouse PLAminus probe (1:10, Sigma-Aldrich, #DUO92004), Donkey anti-rabbit

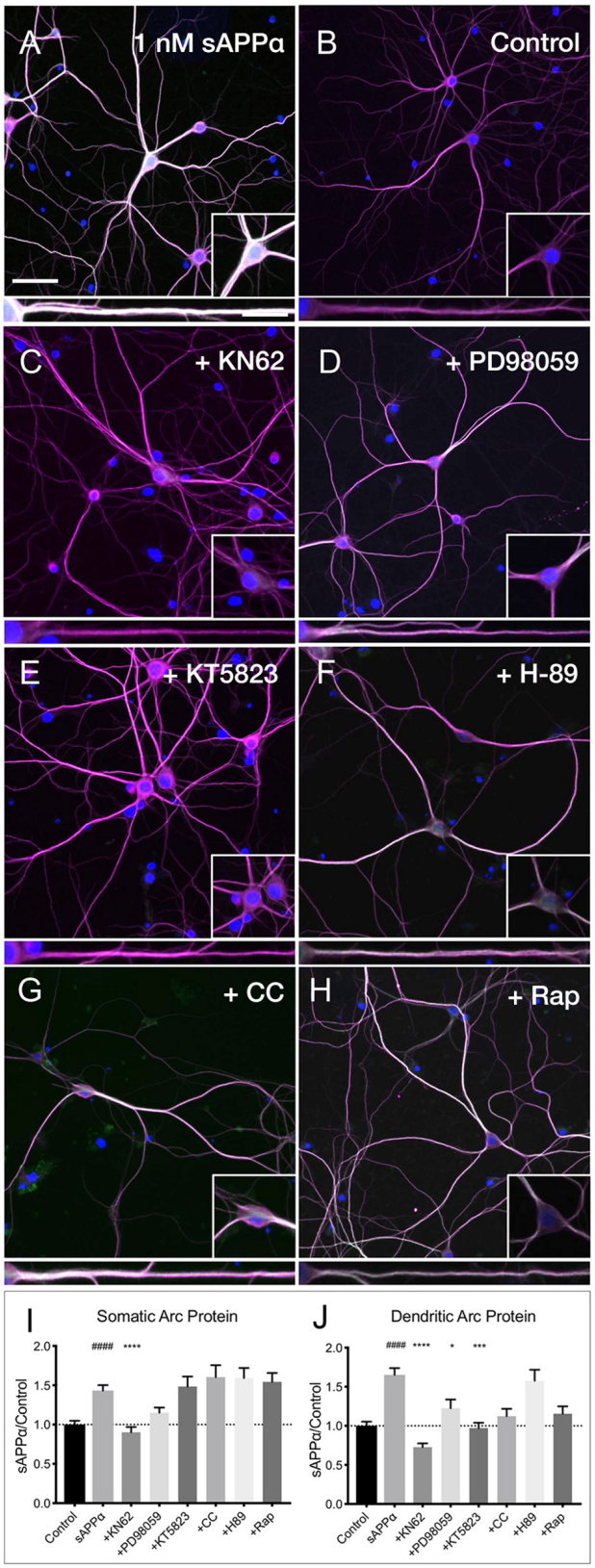

FIGURE 7 | Continued

FIGURE 7 | Arc protein expression in response to sAPPα is affected by kinase inhibitors. Representative images showing **(A)** sAPPα (1 nM, 2 h, $n = 125$) promotes an increase in the expression of Arc protein in cultured neurons relative to **(B)** no drug controls ($n = 134$). Cells were simultaneously treated with **(C)** KN62 ($n = 51$), **(D)** PD98059 ($n = 51$), and **(E)** KT5823 ($n = 42$), **(F)** H-89 dihydrochloride ($n = 40$), **(G)** Chelerythrine chloride ($n = 30$), or **(H)** Rapamycin ($n = 40$) and Arc levels in the **(I)** somata and **(J)** dendrites was measured. Data are expressed as mean ± SEM from ≥3 experiments. Significance was calculated using a Kruskal–Wallis one-way ANOVA with Dunn's multiple comparisons test. Hashes (#) indicate significance between control and sAPPα-treated; asterisks (*) indicate significance between sAPPα- and inhibitor-treated; $^{\#\#\#\#}p \leq 0.0001$, $^{*}p = 0.0428$, $^{***}p = 0.0001$, $^{****}p \leq 0.0001$. Representative images show neurons (magenta), Arc protein (green), DAPI (blue) (scale bar = 50 m), and magnified somatic (inset, bottom right) and dendritic (100 μm; lower panels; scale bar = 10 μm) compartments.

PLAplus probe (1:10, Sigma-Aldrich, #DUO92002), DAPI (1:1000, Thermofisher, #D1306), Duolink detection reagent Texas Red (1:5, Sigma-Aldrich, #DUO92008), DAPI (1:1000, Thermofisher, #D1306), goat anti-mouse IRDye 800CW (1:10,000, Licor, #926-32210), goat anti-rabbit IRDye 680RD (1:10,000, Licor, #926-68071).

RT-qPCR

Total RNA was extracted from cortical cell cultures prepared in 6-well plates at a density of 31,500 cells/cm2. Tissue was lysed by using 350 μl Buffer RL (Norgen Biotek Corp., #17200), RNA was bound to spin columns (Norgen Biotek Corp., #17200) by centrifugation, followed by an on-column DNA removal. Purified RNA was eluted and quantified by spectrometry (Nanodrop ND-1000 v3.8.1 and associated software (Thermofisher Scientific).

Primers:

Zif268: Fwd-GGGAGCCGAGGGAACAA, Rev-CGTTATTC AGAGCGATGTCAGAA; Arc: Fwd-AGCAGAATCAGAGATG GCCG, Rev-TGAATCACTGCTGGGGGC;

HPRT: Fwd-TGACACTGGTAAAACAATGCA, Rev-GGGA GCCGAGCGAACAA;

SP2: Fwd-CAGCCTGGGGAGAAACGGCG, Rev-GCCCTG CTCCCCAGACCTCTT. cDNA libraries were created from total RNA using SuperScript III RT (Invitrogen). RT-qPCR was performed using SYBR Green Master Mix (Thermo Fisher Scientific).

FUNCAT-PLA

FUNCAT-PLA labeling of newly synthesized proteins was conducted according to a previously published protocol (Dieterich et al., 2007; tom Dieck et al., 2015). Cells were incubated in 4 mM L-azidohomoalanine (AHA, courtesy of the Schuman laboratory, Max Planck Institute for Brain Research, Frankfurt) in the presence or absence of sAPPα or anisomycin. Following incubation, cells were washed with PBS-MC (pH 7.4), fixed in PFA in PBS-MC (pH 7.4), and permeabilized with 0.5% Triton X-100 in PBS (pH 7.4). Azide-labeled newly synthesized proteins were alkylated with biotin-linked alkyne via a copper-mediated click reaction. Click reaction mixture comprised of 200 μM triazole ligand [Tris ((1-benzyl-1H-1,2,3-triazol-4-yl)methyl) amine; TBTA, Aldrich], 500 μM TCEP (Tris(2-carboxyethyl)phosphine hydro-chloride, Thermo

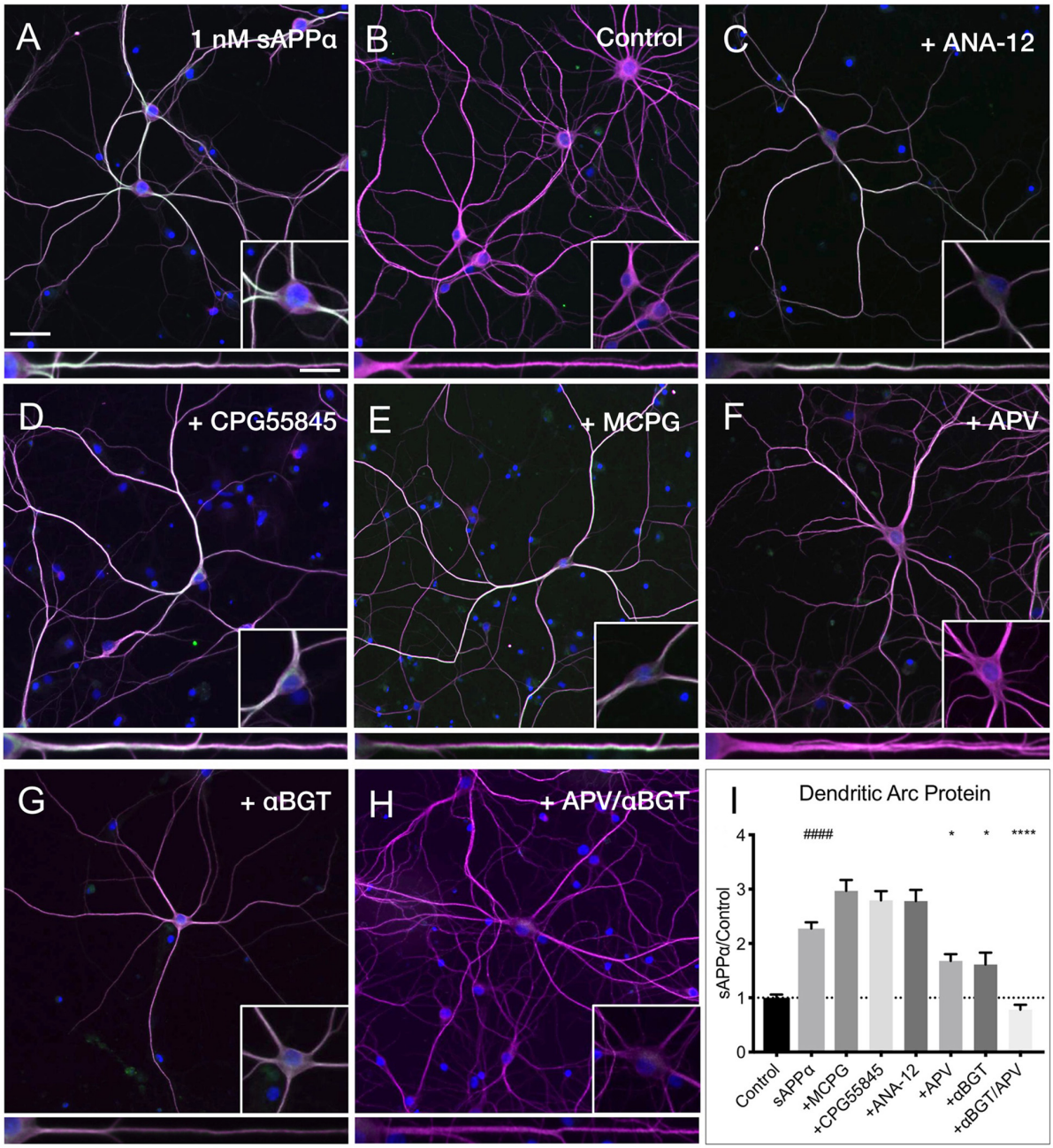

FIGURE 8 | Arc protein expression is dependent on NMDA and α7nAch receptors. Representative images showing **(A)** sAPPα (1 nM, 2 h, *n* = 80) promotes and increase in the expression of Arc protein in cultured hippocampal neurons relative to **(B)** no drug controls (*n* = 80). Co-incubation of sAPPα with **(C)** ANA-12 (*n* = 40), **(D)** CPG55845 (*n* = 40), and **(E)** MCPG (*n* = 40) had no effect on sAPPα-induced Arc expression. Co-incubation with **(F)** APV (*n* = 40), or **(G)** αBGT (*n* = 30) significantly reduced Arc protein expression, while co-incubation with both **(H)** APV and αBGT (*n* = 30) fully eliminated this effect in the **(I)** dendrites. Outliers were removed from each experiment prior to amalgamation using Grubb's tests, and normality was detected by D'Agostino and Pearson omnibus normality tests. Data are expressed as mean ± SEM from ≥3 experiments. Significance was calculated using a Kruskal–Wallis one-way ANOVA with Dunn's multiple comparisons test. Hashes (#) indicate significance between control and sAPPα-treated; asterisks (*) indicate significance between sAPPα- and antagonist-treated; $^{\#\#\#\#}p \leq 0.0001$, $^{*}p = 0.0163$, $^{****}p \leq 0.0001$. Representative images show neurons (magenta), Arc protein (green), DAPI (blue) (scale bar = 50 μm), and magnified somatic (inset, bottom right) and dendritic (100 μm; lower panels; scale bar = 10 μm) compartments.

Scientific), 25 μM Biotin-PEG4-alkyne (Biotin alkyne, Aldrich) and 200 μM CuSO4 in PBS pH 7.8 was incubated on cells overnight at RT. For detection of *de novo* Arc protein, cells were incubated with anti-biotin, anti-Arc antibodies diluted in 4% normal goat serum. Donkey anti-mouse PLA^{minus}, and donkey anti-rabbit PLA^{plus} probes were applied, followed by ligation

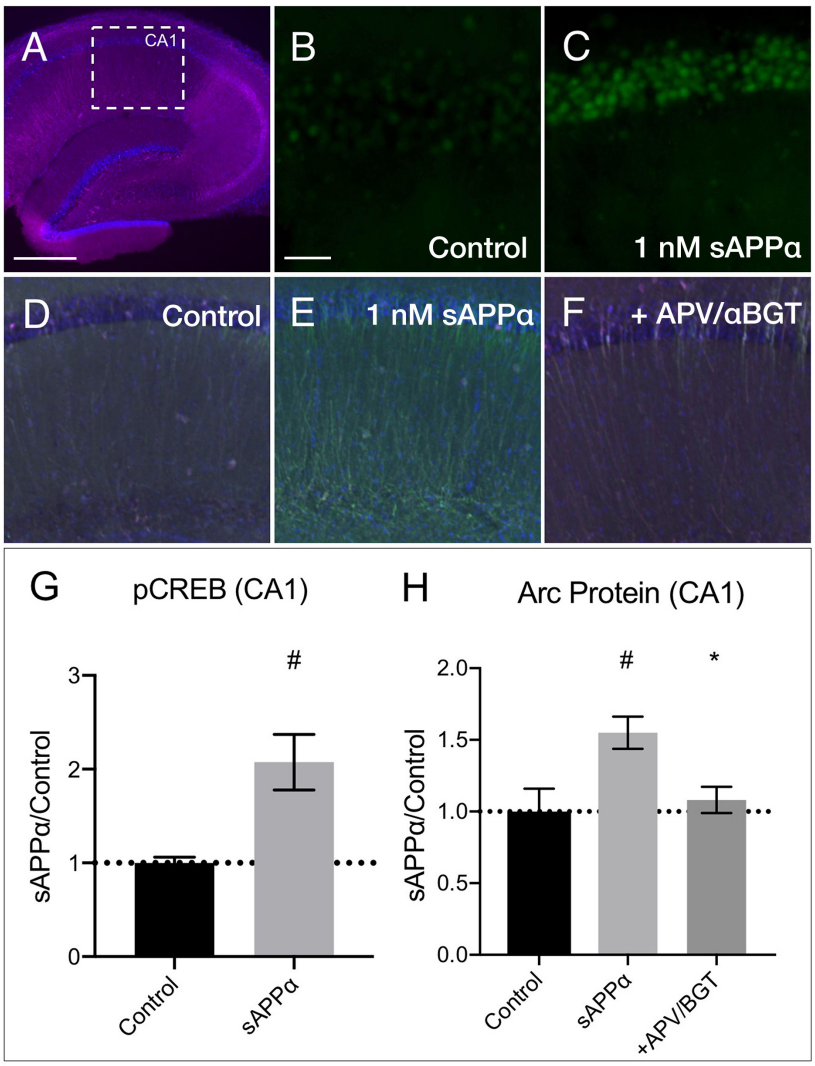

FIGURE 9 | sAPPα increases in CREB phosphorylation and Arc protein in acute hippocampal slices. **(A)** A representative transverse section of an acute hippocampal slice, with a subregion of area CA1, used for quantitative analysis, outlined by a white dotted box (neurons: MAP2/magenta; nuclei: DAPI/blue; imaged at 4x magnification; scale bar = (500 μm). Relative to **(B)** no drug controls, **(C)** incubation of slices with sAPPα (1 nM, 15 min, n = 2 rats, 4 slices) increased $pCREB_{ser133}$ (green; imaged at 20x magnification; scale bar = 100 μm) in the PCL of CA1. Relative to **(D)** no drug controls, **(E)** incubation of slices with sAPPα (1 nM, 2 h, n = 3 rats, 4 slices) significantly increased Arc protein expression (green; imaged at 4x magnification) in area CA1. Co-incubation of sAPPα with **(F)** APV and αBGT (n = 3 rats, 4 slices) attenuated this effect. Normality was detected by Shapiro–Wilk normality tests. Data are expressed as mean ± SEM. Significance of pCREB **(G)** and **(H)** Arc protein expression was calculated using a students t-test, and one-way ANOVA with Šidák's multiple comparisons test, respectively. Hashes (#) indicate significance between control and sAPPα-treated; asterisks (*) indicate significance between sAPPα- and antagonist-treated; $^{\#}p \leq 0.05$, $^{*}p = 0.04$. CA1, cornu ammonis 1; PCL, pyramidal cell layer.

and amplification with Duolink detection reagent Texas Red according to the manufacturer's instructions. Neuronal somata, dendrites and nuclei were visualized by addition of anti-Guinea Pig Alexa Fluor 488 and DAPI, respectively.

Sample Preparation for Transmission Electron Microscopy

Primary hippocampal neurons were grown on 3 mm carbon-coated sapphire disks until DIV 25, then fixed using 2% PFA with 2% glutaraldehyde in 0.1 M cacodylate buffer. Cells were postfixed with 1% osmium tetroxide, followed by 1% uranyl acetate. The samples were then dehydrated using an ethanol gradient, prior to infiltration with EmBed 812 epoxy resin (Electron Microscopy Sciences) using BDMA as an accelerator. Resin-filled BEEM capsules were attached to the cell surface to enable separation of the cell layer from the disk, and the resin was cured at 60°C for 36 h. Ultrathin sections (90 nm) were then cut by diamond knife using a Leica UC6 Ultramicrotome, and mounted on formvar-coated copper slot grids for viewing the ultrastructure.

Acute Hippocampal Slice Preparation

Rats were deeply anaesthetized with ketamine (100 mg/kg, i.p.), the brains removed and chilled in ice-cold and oxygenated modified aCSF for which sucrose was substituted for NaCl (composition in mM: sucrose 210, glucose 20, KCl 2.5, NaH2PO4 1.25, NaHCO3 26, CaCl2 0.5, MgCl2 3, pH 7.4 when gassed with 95% O2-5% CO2). Hippocampi were dissected and slices (400 μm) cut in a manner similar to that described previously (Mockett et al., 2011) using a vibroslicer (Leica, VT1000). Slices were bathed in standard aCSF (in mM: NaCl 124, KCl 3.2, NaH2PO4 1.25, NaHCO3 26, CaCl2 2.5, MgCl2 1.3, D-glucose 10, equilibrated with carbogen 95% O2-5% CO2; 1 ml/2 h/32°C) in 24-well tissue culture dishes (one well per treatment). sAPPα and other drug treatments were subsequently applied in warmed aCSF for 15 min or 2 h. When studying inhibitor effects on sAPPα treatment, slices were pre-incubated for 30 min with the inhibitors before subsequent co-incubation with sAPPα for 2 h. When studying the effects of sAPPα treatment on pCREB expression, slices were co-incubated with inhibitors of serine/threonine-protein phosphatases (NaF, 1 mM; PMSF, 100 μM; okadaic acid, 1 μM). Following treatment, slices were washed in PBS-MC (pH 7.4) and subsequently fixed in 4% PFA in PBS-MC (pH 7.4) overnight at 4°C. Following fixation, slices were washed in PBS (pH 7.4) and embedded in 3% agarose (Roche). Slices were resliced to 50 μm sections using a vibroslicer (Vibratome 1500, Warner instruments) and stored in PBS (pH 7.4) at 4°C until use.

Immunohistocemistry

For immunohistochemical analysis of protein in acute hippocampal slices, slices were permeabilized with 0.5% Triton X-100 in PBS (pH 7.4; 10 min). Slices were then blocked in 4% normal goat serum in PBS (pH 7.4) for 1 h at RT. Slices were incubated with primary antibodies of interest (overnight, 4°C), washed (3 × 10 min; PBS, pH 7.4) and incubated in appropriate secondary antibodies (1 h, RT), followed by 3 × 10 min washes (PBS, pH 7.4). All steps were performed with gentle agitation. Slices were mounted on coverslips (Histobond) in AquaPolymount mounting media (Polysciences) for imaging.

Microscopy

FUNCAT-PLA images were captured with a LSM780 confocal microscope (Zeiss), using a 40x/1.4-N.A oil objective (Plan Apochromat DIC M27), a pinhole setting of 90 μm and all lasers at 2% power. The images were acquired as 8-bit mode z stacks, with the 1,024 × 1,024 pixel xy resolution through the thickness of the cell. The optical slice thickness was set to two-times oversampling, and pixel dwell times were set to 0.39–0.80 μs. For experiments examining the expression of protein using immunofluorescence, images were acquired using an Olympus IX71 inverted light microscope using a 20x/0.45-N.A objective (LUCPFLN) or 4x/0.13-N.A objective (UPFLN). The images were captured using a Hamamatsu Orca-AG camera (C4742-80-12AG) in 1024 × 1024 pixel 8-bit mode. Images were saved as.*tif* files. Electron micrographs were captured using a Philips CM100 BioTWIN transmission electron microscope with a LaB6 emitter (Philips/FEI Corporation), and images were captured using a MegaView III digital camera (Olympus).

Image Analysis

To quantify the FUNCAT-PLA signal a custom-made ImageJ script created by Maximilian Heumüller (Max Planck Institute for Brain Research, Frankfurt) was used (tom Dieck et al., 2015), and punctate PLA signal was subsequently dilated using ImageJ for ease of viewing. To quantify immunofluorescence, neurons were outlined using ImageJ. An 'integrated intensity/neuronal area' value was generated for each cell and somatic compartment, including all dendrites up until intersection with neighboring dendrites. This value was corrected for average background fluorescence by subtracting average background fluorescence. Dendritic fluorescence was determined by subtracting corrected somatic values from whole cell values. Primary and secondary dendrites were analyzed by sampling gray values at 0.5 μm increments, and binning the average of each 50- and 25 μm segments, respectively. Statistical analysis was achieved by averaging each dendritic segment per cell, for a total cell average. For experiments examining pCREB expression in acute hippocampal slices, DAPI was used to define a 'mask' around the nuclear layer and pCREB was measured as 'integrated intensity/DAPI area.' For experiments examining Arc expression in acute hippocampal slices, area CA1 was defined by a square area adjacent to the hippocampal fissure (encompassing both the pyramidal cell layer and stratum radiatum) and an integrated intensity/area' value was generated for each slice.

Statistical Analysis

RT-qPCR

As the data exhibited a normal distribution (Shapiro–Wilk normality test), significance was assessed using Students *t*-tests where $P < 0.05$ was accepted as significantly different. Data were normalized to the control gene HPRT and expressed relative to no-drug control.

Imunocytochemistry

Statistics for all immunocytochemistry experiments were performed using Kruskal–Wallis one-way ANOVA with Dunn's multiple comparisons test. Data were not normally distributed (D'Agostino and Pearson omnibus normality test). Outliers within the raw data sets were detected using the Grubb's test.

FUNCAT-PLA

Prior to data amalgamation, outliers were removed from each experiment using Grubb's tests, and normality was assessed (D'Agostino and Pearson omnibus normality tests). Significance was calculated on data expressed relative to control by use of one sample *t*-tests.

Acute Hippocampal Slices

Data for all slice work exhibited a normal distribution (Shapiro–Wilk normality test). Experiments examining pCREB expression were analyzed by use of students *t*-tests, and experiments analyzing Arc protein expression were analyzed using one-way

ANOVA followed by Šidák's multiple comparisons test. Data are expressed as fold change relative to control values.

DISCUSSION

Here, we show that sAPPα promotes the expression of the key plasticity protein Arc in primary neuronal cultures. Notably, Arc expression was dependent on CaMKII, MAPK, and PKG activity, which is consistent with previous reports of these kinases being essential for sAPPα's facilitation of local protein synthesis in hippocampal synaptoneurosomes and glutamate receptor trafficking in acute hippocampal slices (Claasen et al., 2009; Mockett et al., 2019). Additionally, we have identified a critical interaction between NMDA and α7nAch receptors in triggering this effect.

Our research provides evidence of a coordinated set of signaling mechanisms through which sAPPα regulates the expression of Arc, and by association, synaptic plasticity. Similar to the well-studied neurotrophin brain-derived neurotrophic factor (BDNF), nanomolar amounts of sAPPα promotes a gradual increase in *Arc* and likewise an increase in *Zif268* mRNA. However, the relative change induced by sAPPα appears to be more modest than that of BDNF (El-Sayed et al., 2011), suggesting a neuromodulatory role for sAPPα. Further, we described a concentration-dependent effect in response to sAPPα, but not sAPPβ. While previous reports indicate that sAPPα is able to rescue morphological and plasticity-related deficits observed in APP and APP-like protein 2 (APPL2) knockout mice (Ring et al., 2007; Fol et al., 2016) and conditional APP/APPL2 NexCre knockdown mice (Li et al., 2010; Hick et al., 2015), sAPPβ is unable to ameliorate these deficits. This difference may underlie a divergence in signaling cascades between the two sAPP metabolites, further elucidating their distinct biological functions.

While previous work has described a multitude of signaling pathways mediating sAPPα-induced neuroprotection, and plasticity, of particular interest is sAPPα's ability to increase cGMP and MAPK activity (Furukawa et al., 1996a; Gakhar-Koppole et al., 2008). Strikingly, in previous studies using isolated synapses, we have shown that sAPPα enhances *de novo* protein synthesis in a manner partially dependent on CaMKII and MAPK, and fully depending on PKG (Claasen et al., 2009). Likewise, trafficking of GluA1-containing AMPA receptors following sAPPα-enhanced LTP requires CaMKII and PKG, as well as protein synthesis (Mockett et al., 2019). Interestingly, a recently published study (Martinsson et al., 2019) has shown that knockdown or knockout of endogenous APP leads to increased levels of GluA1. Given that Arc is known to internalize GluA1- and/or GluA2-containing AMPA receptors (Chowdhury et al., 2006; Rial Verde et al., 2006), this suggests that endogenous APP or sAPPα may contribute to regulation of Arc levels (and therefore surface expression of GluA1). Building on this, and as primary hippocampal neurons express GluA2-lacking AMPA receptors (Jaafari et al., 2012), we propose that the signaling mechanisms harnessed by sAPPα not only promote increased AMPA receptor cell surface expression, but also initiate a concomitant homeostatic response whereby Arc promotes delayed AMPA receptor internalization. Future experiments should aim to explore whether this occurs globally, or specifically at activated synapses.

In the present experiments, inhibition of CaMKII significantly impaired both somatic and dendritic Arc expression, while inhibition of MAPK and PKG significantly reduced Arc expression in the dendrites alone. Thus CaMKII, MAPK, and PKG may mediate distinct aspects of sAPPα-induced functions in each neuronal compartment. Indeed, evidence suggests that PKG may act to facilitate trafficking of Rab11-positive vesicles. Rab11 is a protein primarily associated with recycling endosomes, and can mediate anterograde trafficking from the *trans*-Golgi network and perinuclear endosome (Chen et al., 1998; Ang et al., 2004; Lock and Stow, 2005; Takahashi et al., 2012). This trafficking is achieved through close association with the Ca^{2+}-sensitive motor protein myosin Vb (Wang et al., 2008). Interestingly, PKG has been linked to the nitric oxide-dependent simulation of anterograde trafficking of Rab11A-positive recycling endosomes (Zhai et al., 2017) and has been shown to directly bind Rab11B (Reger et al., 2014). Importantly, Arc protein and mRNA colocalize with Rab11 (Wu et al., 2011) and inhibition of Rab11 activity impairs postsynaptic expression of Arc protein in *Drosophila* motor neurons (Ashley et al., 2018). Thus, PKG may play an important role in the activity-dependent transport of Arc-containing vesicles throughout the dendrites. Once present at the synapse, PKG, in concert with MAPK and CaMKII, may then regulate synthesis of Arc protein (Browning et al., 2000; Kleppisch et al., 2003; Atkins et al., 2004; Claasen et al., 2009; Michel et al., 2011; Mockett et al., 2011). CaMKII may also contribute to the localization of Arc protein within the somata and dendrites (Husi et al., 2000; Donai et al., 2003; Okuno et al., 2012), however, our studies do not distinguish between CaMKII isoforms. Further, it has been hypothesized that there may exist separate pools of translating and non-translating *Arc* mRNA (Steward et al., 2014) such that a pool of *Arc* mRNA may be translated within the somata, while a separate, translationally repressed pool is trafficked throughout the dendrites primed and waiting to be translated locally (Link et al., 1995). A third pool may govern rapid transcription-independent translation of *Arc* mRNA already associated with polyribosomes throughout the dendrites (Bagni et al., 2000; Na et al., 2016). Therefore, our data may reflect the presence of distinct pools of *Arc* mRNA, regulated differentially by CaMKII, MAPK, and PKG. Additionally, recent work has identified a novel role for Arc protein through shared properties with retroviral Gag proteins: Arc forms virus-like capsids capable of encapsulating and transporting functional RNA and protein between cells in endosomal-derived extracellular vesicles (Pastuzyn et al., 2018), therefore suggesting Arc can modulate synapse-, cell-, and network-wide plasticity.

A crucial, yet outstanding question in the literature is the identity of the 'sAPPα receptor.' Previous evidence has described a role of $GABA_B$ (Rice et al., 2017, 2019), Na/K ATP'ase (Dorard et al., 2018), α7nAch (Richter et al., 2018) and NMDA receptors (Gakhar-Koppole et al., 2008; Mockett et al., 2019) in

mediating sAPPα's plasticity enhancing effects. To understand the receptors contributing to the facilitated Arc expression, we investigated the possible contributions of these and other candidate receptors (mGluRI/II and TrkB) due to their similar neuromodulatory or plasticity-promoting properties (Raymond et al., 2000; Mockett et al., 2011). Our data suggest a synergistic effect between activation of NMDARs and α7nAChRs. Sole inhibition of either receptor alone led to a partial impairment in the sAPPα-mediated expression of Arc protein, whereas simultaneous inhibition of both receptors fully eliminated the enhancement of Arc protein expression in the dendrites. Further, we have extended our studies to the more complex biological system of acute hippocampal slices. Here, our findings closely reflected that of the primary hippocampal culture work, as sAPPα significantly enhanced Arc protein expression in area CA1 of the hippocampus in a manner dependent on activation of NMDA and α7nACh receptors. This finding was corroborated by an increase in pCREB, a downstream NMDAR signaling event (Xia et al., 1996), in area CA1. Importantly, many of the reports describing sAPPα's ability to enhance LTP has been shown in CA1, including the dependence on NMDAR (Mockett et al., 2019) and α7nACh receptors (Richter et al., 2018). The mechanism governing this effect may involve protein–protein interactions between α7nAChR-NMDAR complexes (Li et al., 2012, 2013), or direct binding of sAPPα to NMDA or α7nAChR (Cousins et al., 2009; Innocent et al., 2012; Forest et al., 2018). Likewise, trafficking of NMDA receptors has been observed in response to sAPPα (Mockett et al., 2019) and may occur through α7nAChR activation (Marchi et al., 2015). This therefore may be a mechanism which provides additive Ca^{2+} or activation of downstream signaling pathways (Aramakis and Metherate, 1998; Brunzell et al., 2003; Gould and Lewis, 2005). A similar synergistic effect has been found between the activation of NMDARs and Gs-coupled dopamine and β-adrenergic receptors in the PKA-dependent increase in Arc protein (Bloomer et al., 2008). PKG-dependent NMDAR activation has been shown to enhance the expression of IEG Arc, c-Fos and Zif268 in the lateral amygdala *in vivo* in response to both fear conditioning (Ota et al., 2010) and LTP-inducing stimulation (Ping and Schafe, 2010) and inhibition of neuronal nitric oxide (nNOS), soluble guanylyl cyclase (sGC), or PKG attenuated the bicuculline-induced expression of Arc, c-Fos and Zif268 in neuronal cultures (Gallo and Iadecola, 2011). Further, both NMDAR and α7nAch can facilitate CaMKII and MAPK activation (Cammarota et al., 2000; Thalhammer et al., 2006; Gubbins et al., 2010). Therefore, concerted activity between NMDARs and α7nAChRs may act to promote sAPPα-mediated Arc expression through synergistic activation of downstream cascades involving CaMKII, PKG and MAPK.

sAPPα shows hallmark neuroprotective and neurotrophic properties and is capable of stimulating neurite outgrowth, regulating spine morphology (Clarris et al., 1994; Hick et al., 2015), enhancing synaptodendritic protein synthesis, and facilitating protein synthesis-dependent LTP (Taylor et al., 2008; Claasen et al., 2009; Moreno et al., 2015; Mockett et al., 2019), as well as protecting against excitotoxic injury *in vitro* and *in vivo* (Mucke et al., 1996; Ryan et al., 2013). Likewise, the synthesis and function of Arc protein has been previously linked to many of these characteristics, such as stimulation of CaMKII-dependent neurite extension (Donai et al., 2003), the homeostatic intergration of synapse downscaling following seizure activity and chronic excitation (Lyford et al., 1995; Shepherd et al., 2006; Gao et al., 2010) with increased morphological plasticity and spine size (Messaoudi et al., 2007; Peebles et al., 2010), and its role in facilitating LTP (Guzowski et al., 2000; Plath et al., 2006; Messaoudi et al., 2007; Nakayama et al., 2016). Our studies provide insight into how sAPPα promotes the expression of these mechanisms through the utilization of Arc protein. It is important to note that we have titrated sAPPa concentrations and found that 1 nM is sufficient to initiate a variety of molecular events (Claasen et al., 2009; Ryan et al., 2013; Mockett et al., 2019). There is, however, only limited knowledge of the physiological levels of sAPPα and to what extent they are dynamically regulated *in vivo*.

CONCLUSION

This work extends the current understanding of possible mechanisms through which sAPPα enhances synaptic plasticity. Here we have described an enhancement of Arc protein synthesis driven by activation of NMDA and α7nAch receptors, and downstream activation of CaMKII, MAPK, and PKG. sAPPα levels are reduced in many disease states and neurological disorders, many of which involve impaired or altered plasticity (Lannfelt et al., 1995; Kim et al., 2009; Selnes et al., 2010; Jakobsson et al., 2013; Miyajima et al., 2013; Rolstad et al., 2015). Therefore, furthering our understanding of the underlying processes governing sAPPα's regulation of key plasticity proteins, including Arc, is a fundamental step in understanding dysfunction which arises in many cognitive diseases.

DATA AVAILABILITY

The raw data supporting the conclusions of this manuscript will be made available by the authors, without undue reservation, to any qualified researcher.

AUTHOR CONTRIBUTIONS

RL was the major contributor to the experimental aspects of the study, contributed to the design of the study, prepared the primary neuronal cultures, isolated RNA, carried out the RT-qPCR and immunochemistry experiments, analyzed and interpreted the corresponding data, and drafted the manuscript. ME carried out the FUNCAT-PLA study and the corresponding data analysis and critically revised the manuscript. MB and CW carried out immunochemistry experiments, analyzed and interpreted the corresponding data. KP produced recombinant sAPPα, analyzed and interpreted the corresponding data. WT designed the protocols for recombinant sAPPα production, analyzed and interpreted the corresponding data, critically

reviewed the manuscript. WA critically revised the manuscript. JW conceived and participated in the design and co-ordination of the study, undertook data analysis and interpretation, and critically assessed the manuscript.

FUNDING

Research reported in this article was supported by the Health Research Council of New Zealand, the University of Otago (Department of Anatomy, and postgraduate scholarships to RL and ME) and a German Academic Exchange Service scholarship to ME. We acknowledge the support and mentorship of Prof. E. Schuman (Max Planck Institute for Brain Research).

ACKNOWLEDGMENTS

The authors thank Dr. Laura Gumy for salient advice in analysis of dendritic Arc expression and Dr. Anurag Singh for assistance with preparing the acute hippocampal slices. The authors acknowledge the support of the Otago Micro and Nanoscale Imaging unit.

SUPPLEMENTARY MATERIAL

The Supplementary Material for this article can be found online at: https://www.frontiersin.org/articles/10.3389/fnmol.2019.00198/full#supplementary-material

REFERENCES

Ang, A. L., Taguchi, T., Francis, S., Folsch, H., Murrells, L. J., Pypaert, M., et al. (2004). Recycling endosomes can serve as intermediates during transport from the Golgi to the plasma membrane of MDCK cells. *J. Cell Biol.* 167, 531–543. doi: 10.1083/jcb.200408165

Aramakis, V. B., and Metherate, R. (1998). Nicotine selectively enhances NMDA receptor-mediated synaptic transmission during postnatal development in sensory neocortex. *J. Neurosci.* 18, 8485–8495. doi: 10.1523/JNEUROSCI.18-20-08485.1998

Ashley, J., Cordy, B., Lucia, D., Fradkin, L. G., Budnik, V., and Thomson, T. (2018). Retrovirus-like gag protein Arc1 binds RNA and traffics across synaptic boutons. *Cell* 172, 262–274.e11. doi: 10.1016/j.cell.2017.12.022

Atkins, C. M., Nozaki, N., Shigeri, Y., and Soderling, T. R. (2004). Cytoplasmic polyadenylation element binding protein-dependent protein synthesis is regulated by calcium/calmodulin-dependent protein kinase II. *J. Neurosci.* 24, 5193–5201. doi: 10.1523/jneurosci.0854-04.2004

Bagni, C., Mannucci, L., Dotti, C. G., and Amaldi, F. (2000). Chemical stimulation of synaptosomes modulates alpha -Ca2+/calmodulin-dependent protein kinase II mRNA association to polysomes. *J. Neurosci.* 20:Rc76.

Banker, G., and Goslin, K. (1998). *Culturing Nerve Cells*. Cambridge, MA: MIT Press.

Basarsky, T. A., Parpura, V., and Haydon, P. G. (1994). Hippocampal synaptogenesis in cell culture: developmental time course of synapse formation, calcium influx, and synaptic protein distribution. *J. Neurosci.* 14(11 Pt 1), 6402–6411.

Bloomer, W. A., VanDongen, H. M., and VanDongen, A. M. (2008). Arc/Arg3.1 translation is controlled by convergent N-methyl-D-aspartate and Gs-coupled receptor signaling pathways. *J. Biol. Chem.* 283, 582–592.

Browning, D. D., McShane, M. P., Marty, C., and Ye, R. D. (2000). Nitric oxide activation of p38 mitogen-activated protein kinase in 293T fibroblasts requires cGMP-dependent protein kinase. *J. Biol. Chem.* 275, 2811–2816.

Brunzell, D. H., Russell, D. S., and Picciotto, M. R. (2003). In vivo nicotine treatment regulates mesocorticolimbic CREB and ERK signaling in C57Bl/6J mice. *J. Neurochem.* 84, 1431–1441.

Cammarota, M., Bevilaqua, L. R., Ardenghi, P., Paratcha, G., Levi de Stein, M., Izquierdo, I., et al. (2000). Learning-associated activation of nuclear MAPK, CREB and Elk-1, along with Fos production, in the rat hippocampus after a one-trial avoidance learning: abolition by NMDA receptor blockade. *Brain Res. Mol. Brain Res.* 76, 36–46.

Chasseigneaux, S., Dinc, L., Rose, C., Chabret, C., Coulpier, F., Topilko, P., et al. (2011). Secreted amyloid precursor Protein β and secreted amyloid precursor protein α induce axon outgrowth *In Vitro* through Egr1 signaling pathway. *PLoS One* 6:e16301. doi: 10.1371/journal.pone.0016301

Chen, T., Zhu, J., Yang, L. K., Feng, Y., Lin, W., and Wang, Y. H. (2017). Glutamate-induced rapid induction of Arc/Arg3.1 requires NMDA receptor-mediated phosphorylation of ERK and CREB. *Neurosci. Lett.* 661, 23–28. doi: 10.1016/j.neulet.2017.09.024

Chen, W., Feng, Y., Chen, D., and Wandinger-Ness, A. (1998). Rab11 is required for trans-golgi network-to-plasma membrane transport and a preferential target for GDP dissociation inhibitor. *Mol. Biol. Cell* 9, 3241–3257.

Chowdhury, S., Shepherd, J. D., Okuno, H., Lyford, G., Petralia, R. S., Plath, N., et al. (2006). Arc/Arg3.1 interacts with the endocytic machinery to regulate AMPA receptor trafficking. *Neuron* 52, 445–459.

Claasen, A. M., Guevremont, D., Mason-Parker, S. E., Bourne, K., Tate, W. P., Abraham, W. C., et al. (2009). Secreted amyloid precursor protein-alpha upregulates synaptic protein synthesis by a protein kinase G-dependent mechanism. *Neurosci. Lett.* 460, 92–96. doi: 10.1016/j.neulet.2009.05.040

Clarris, H. J., Nurcombe, V., Small, D. H., Beyreuther, K., and Masters, C. L. (1994). Secretion of nerve growth factor from septum stimulates neurite outgrowth and release of the amyloid protein precursor of Alzheimer's disease from hippocampal explants. *J. Neurosci. Res.* 38, 248–258.

Cousins, S. L., Hoey, S. E., Anne Stephenson, F., and Perkinton, M. S. (2009). Amyloid precursor protein 695 associates with assembled NR2A- and NR2B-containing NMDA receptors to result in the enhancement of their cell surface delivery. *J. Neurochem.* 111, 1501–1513. doi: 10.1111/j.1471-4159.2009.06424.x

DaSilva, L. L., Wall, M. J., de Almeida, P. L., Wauters, S. C., Januário, Y. C., Müller, J., et al. (2016). Activity-Regulated cytoskeleton-associated protein controls AMPAR endocytosis through a direct interaction with clathrin-adaptor Protein 2. *eNeuro* 3:ENEURO.0144-15.2016 doi: 10.1523/eneuro.0144-15.2016

Dieterich, D. C., Lee, J. J., Link, A. J., Graumann, J., Tirrell, D. A., and Schuman, E. M. (2007). Labeling, detection and identification of newly synthesized proteomes with bioorthogonal non-canonical amino-acid tagging. *Nat. Protoc.* 2, 532–540. doi: 10.1038/nprot.2007.52

Donai, H., Sugiura, H., Ara, D., Yoshimura, Y., Yamagata, K., and Yamauchi, T. (2003). Interaction of Arc with CaM kinase II and stimulation of neurite extension by Arc in neuroblastoma cells expressing CaM kinase II. *Neurosci. Res.* 47, 399–408.

Dorard, E., Chasseigneaux, S., Gorisse-Hussonnois, L., Broussard, C., Pillot, T., and Allinquant, B. (2018). Soluble amyloid precursor protein alpha interacts with alpha3-Na, K-ATPAse to induce axonal outgrowth but not neuroprotection: evidence for distinct mechanisms underlying these properties. *Mol. Neurobiol.* 55, 5594–5610. doi: 10.1007/s12035-017-0783-780

El-Sayed, M., Hofman-Bang, J., and Mikkelsen, J. D. (2011). Effect of brain-derived neurotrophic factor on activity-regulated cytoskeleton-associated protein gene expression in primary frontal cortical neurons. Comparison with NMDA and AMPA. *Eur. J. Pharmacol.* 660, 351–357. doi: 10.1016/j.ejphar.2011.03.055

Fol, R., Braudeau, J., Ludewig, S., Abel, T., Weyer, S. W., Roederer, J. P., et al. (2016). Viral gene transfer of APPsalpha rescues synaptic failure in an Alzheimer's disease mouse model. *Acta Neuropathol.* 131, 247–266. doi: 10.1007/s00401-015-1498-1499

Forest, K. H., Alfulaij, N., Arora, K., Taketa, R., Sherrin, T., Todorovic, C., et al. (2018). Protection against β-amyloid neurotoxicity by a non-toxic endogenous

N-terminal β-amyloid fragment and its active hexapeptide core sequence. *J. Neurochem.* 144, 201–217. doi: 10.1111/jnc.14257

Furukawa, K., Barger, S. W., Blalock, E. M., and Mattson, M. P. (1996a). Activation of K+ channels and suppression of neuronal activity by secreted beta-amyloid-precursor protein. *Nature* 379, 74–78. doi: 10.1038/379074a0

Furukawa, K., Sopher, B. L., Rydel, R. E., Begley, J. G., Pham, D. G., Martin, G. M., et al. (1996b). Increased activity-regulating and neuroprotective efficacy of alpha-secretase-derived secreted amyloid precursor protein conferred by a C-terminal heparin-binding domain. *J. Neurochem.* 67, 1882–1896.

Gakhar-Koppole, N., Hundeshagen, P., Mandl, C., Weyer, S. W., Allinquant, B., Muller, U., et al. (2008). Activity requires soluble amyloid precursor protein alpha to promote neurite outgrowth in neural stem cell-derived neurons via activation of the MAPK pathway. *Eur. J. Neurosci.* 28, 871–882. doi: 10.1111/j.1460-9568.2008.06398.x

Gallo, E. F., and Iadecola, C. (2011). Neuronal nitric oxide contributes to neuroplasticity-associated protein expression through cGMP, protein kinase G, and extracellular signal-regulated kinase. *J. Neurosci.* 31, 6947–6955. doi: 10.1523/jneurosci.0374-11.2011

Gangarossa, G., Di Benedetto, M., O'Sullivan, G. J., Dunleavy, M., Alcacer, C., Bonito-Oliva, A., et al. (2011). Convulsant doses of a dopamine D1 receptor agonist result in Erk-Dependent increases in Zif268 and Arc/Arg3.1 expression in mouse dentate gyrus. *PLoS One* 6:e19415. doi: 10.1371/journal.pone.0019415

Gao, M., Sossa, K., Song, L., Errington, L., Cummings, L., Hwang, H., et al. (2010). A specific requirement of Arc/Arg3.1 for visual experience-induced homeostatic synaptic plasticity in mouse primary visual cortex. *J. Neurosci.* 30, 7168–7178. doi: 10.1523/JNEUROSCI.1067-10.2010

Gould, T. J., and Lewis, M. C. (2005). Coantagonism of glutamate receptors and nicotinic acetylcholinergic receptors disrupts fear conditioning and latent inhibition of fear conditioning. *Learn. Mem.* 12, 389–398.

Grabrucker, A., Vaida, B., Bockmann, J., and Boeckers, T. M. (2009). Synaptogenesis of hippocampal neurons in primary cell culture. *Cell Tissue Res.* 338, 333–341. doi: 10.1007/s00441-009-0881-z

Grinevich, V., Kolleker, A., Eliava, M., Takada, N., Takuma, H., Fukazawa, Y., et al. (2009). Fluorescent Arc/Arg3.1 indicator mice: a versatile tool to study brain activity changes in vitro and in vivo. *J. Neurosci. Methods* 184, 25–36. doi: 10.1016/j.jneumeth.2009.07.015

Gubbins, E. J., Gopalakrishnan, M., and Li, J. (2010). Alpha7 nAChR-mediated activation of MAP kinase pathways in PC12 cells. *Brain Res.* 1328, 1–11. doi: 10.1016/j.brainres.2010.02.083

Gumy, L. F., Katrukha, E. A., Grigoriev, I., Jaarsma, D., Kapitein, L. C., Akhmanova, A., et al. (2017). MAP2 defines a pre-axonal filtering zone to regulate KIF1- versus KIF5-dependent cargo transport in sensory neurons. *Neuron* 94, 347–362.e7. doi: 10.1016/j.neuron.2017.03.046

Guzowski, J. F., Lyford, G. L., Stevenson, G. D., Houston, F. P., McGaugh, J. L., Worley, P. F., et al. (2000). Inhibition of activity-dependent arc protein expression in the rat hippocampus impairs the maintenance of long-term potentiation and the consolidation of long-term memory. *J. Neurosci.* 20, 3993–4001.

Hick, M., Herrmann, U., Weyer, S. W., Mallm, J. P., Tschape, J. A., Borgers, M., et al. (2015). Acute function of secreted amyloid precursor protein fragment APPsalpha in synaptic plasticity. *Acta Neuropathol.* 129, 21–37. doi: 10.1007/s00401-014-1368-x

Huang, F., Chotiner, J. K., and Steward, O. (2007). Actin polymerization and ERK phosphorylation are required for Arc/Arg3.1 mRNA targeting to activated synaptic sites on dendrites. *J. Neurosci.* 27, 9054–9067. doi: 10.1523/jneurosci.2410-07.2007

Husi, H., Ward, M. A., Choudhary, J. S., Blackstock, W. P., and Grant, S. G. N. (2000). Proteomic analysis of NMDA receptor-adhesion protein signaling complexes. *Nat. Neurosci.* 3, 661–669.

Innocent, N., Cousins, S. L., and Stephenson, F. A. (2012). NMDA receptor/amyloid precursor protein interactions: a comparison between wild-type and amyloid precursor protein mutations associated with familial Alzheimer's disease. *Neurosci. Lett.* 515, 131–136. doi: 10.1016/j.neulet.2012.03.029

Izumi, H., Ishimoto, T., Yamamoto, H., Nishijo, H., and Mori, H. (2011). Bioluminescence imaging of Arc expression enables detection of activity-dependent and plastic changes in the visual cortex of adult mice. *Brain Struct. Funct.* 216, 91–104. doi: 10.1007/s00429-010-0297-292

Jaafari, N., Henley, J. M., and Hanley, J. G. (2012). PICK1 mediates transient synaptic expression of GluA2-lacking AMPA receptors during glycine-induced AMPA receptor trafficking. *J. Neurosci.* 32, 11618–11630. doi: 10.1523/JNEUROSCI.5068-11.2012

Jakobsson, J., Zetterberg, H., Blennow, K., Johan Ekman, C., Johansson, A. G., and Landen, M. (2013). Altered concentrations of amyloid precursor protein metabolites in the cerebrospinal fluid of patients with bipolar disorder. *Neuropsychopharmacology* 38, 664–672. doi: 10.1038/npp.2012.231

Jones, E. V., Cook, D., and Murai, K. K. (2012). A neuron-astrocyte co-culture system to investigate astrocyte-secreted factors in mouse neuronal development. *Methods Mol. Biol.* 814, 341–352. doi: 10.1007/978-1-61779-452-0_22

Kaech, S., and Banker, G. (2006). Culturing hippocampal neurons. *Nat. Protoc.* 1, 2406–2415.

Kim, M., Suh, J., Romano, D., Truong, M. H., Mullin, K., Hooli, B., et al. (2009). Potential late-onset Alzheimer's disease-associated mutations in the ADAM10 gene attenuate α-secretase activity. *Hum. Mol. Genet.* 18, 3987–3996. doi: 10.1093/hmg/ddp323

Kleppisch, T., Wolfsgruber, W., Feil, S., Allmann, R., Wotjak, C. T., Goebbels, S., et al. (2003). Hippocampal cGMP-dependent protein kinase I supports an age- and protein synthesis-dependent component of long-term potentiation but is not essential for spatial reference and contextual memory. *J. Neurosci.* 23, 6005–6012.

Kristensen, S. E., Thomsen, M. S., Hansen, H. H., Timmermann, D. B., Hay-Schmidt, A., and Mikkelsen, J. D. (2007). The alpha7 nicotinic receptor agonist SSR180711 increases activity regulated cytoskeleton protein (Arc) gene expression in the prefrontal cortex of the rat. *Neurosci. Lett.* 418, 154–158.

Kuipers, S. D., Trentani, A., Tiron, A., Mao, X., Kuhl, D., and Bramham, C. R. (2016). BDNF-induced LTP is associated with rapid Arc/Arg3.1-dependent enhancement in adult hippocampal neurogenesis. *Sci. Rep.* 6:21222. doi: 10.1038/srep21222

Kumar, V., Fahey, P. G., Jong, Y.-J. I., Ramanan, N., and O'Malley, K. L. (2011). Activation of the intracellular metabotropic glutamate receptor 5 in striatal neurons leads to upregulation of genes associated with sustained synaptic transmission including arc/arg3.1. *J. Biol. Chem.* 287, 5412–5425. doi: 10.1074/jbc.M111.301366

Lannfelt, L., Basun, H., Wahlund, L. O., Rowe, B. A., and Wagner, S. L. (1995). Decreased alpha-secretase-cleaved amyloid precursor protein as a diagnostic marker for Alzheimer's disease. *Nat. Med.* 1, 829–832.

Li, H., Wang, B., Wang, Z., Guo, Q., Tabuchi, K., Hammer, R. E., et al. (2010). Soluble amyloid precursor protein (APP) regulates transthyretin and Klotho gene expression without rescuing the essential function of APP. *Proc. Natl. Acad. Sci. U.S.A.* 107, 17362–17367. doi: 10.1073/pnas.1012568107

Li, S., Li, Z., Pei, L., Le, A. D., and Liu, F. (2012). The α7nACh–NMDA receptor complex is involved in cue-induced reinstatement of nicotine seeking. *J. Exp. Med.* 209, 2141–2147. doi: 10.1084/jem.20121270

Li, S., Nai, Q., Lipina, T. V., Roder, J. C., and Liu, F. (2013). alpha7nAchR/NMDAR coupling affects NMDAR function and object recognition. *Mol. Brain* 6:58. doi: 10.1186/1756-6606-6-58

Link, W., Konietzko, U., Kauselmann, G., Krug, M., Schwanke, B., Frey, U., et al. (1995). Somatodendritic expression of an immediate early gene is regulated by synaptic activity. *Proc. Natl. Acad. Sci. U.S.A.* 92, 5734–5738.

Lock, J. G., and Stow, J. L. (2005). Rab11 in recycling endosomes regulates the sorting and basolateral transport of E-cadherin. *Mol. Biol. Cell* 16, 1744–1755. doi: 10.1091/mbc.e04-10-0867

Lyford, G. L., Yamagata, K., Kaufmann, W. E., Barnes, C. A., Sanders, L. K., Copeland, N. G., et al. (1995). Arc, a growth factor and activity-regulated gene, encodes a novel cytoskeleton-associated protein that is enriched in neuronal dendrites. *Neuron* 14, 433–445.

Marchi, M., Grilli, M., and Pittaluga, A. M. (2015). Nicotinic modulation of glutamate receptor function at nerve terminal level: a fine-tuning of synaptic signals. *Front. Pharmacol.* 6:89. doi: 10.3389/fphar.2015.00089

Martinsson, I., Capetillo-Zarate, E., Faideau, M., Willén, K., Esteras, N., Frykman, S., et al. (2019). APP depletion alters selective pre- and post-synaptic proteins. *Mol. Cell. Neurosci.* 95, 86–95. doi: 10.1016/j.mcn.2019.02.003

Messaoudi, E., Kanhema, T., Soule, J., Tiron, A., Dagyte, G., da Silva, B., et al. (2007). Sustained Arc/Arg3.1 synthesis controls long-term potentiation consolidation through regulation of local actin polymerization in the dentate gyrus in vivo. *J. Neurosci.* 27, 10445–10455.

Michel, M., Green, C. L., Eskin, A., and Lyons, L. C. (2011). PKG-mediated MAPK signaling is necessary for long-term operant memory in Aplysia. *Learn. Mem.* 18, 108–117. doi: 10.1101/lm.2063611

Miyajima, M., Nakajima, M., Ogino, I., Miyata, H., Motoi, Y., and Arai, H. (2013). Soluble amyloid precursor protein alpha in the cerebrospinal fluid as a diagnostic and prognostic biomarker for idiopathic normal pressure hydrocephalus. *Eur. J. Neurol.* 20, 236–242. doi: 10.1111/j.1468-1331.2012.03781.x

Mockett, B. G., Guévremont, D., Elder, M. K., Parfitt, K. D., Peppercorn, K., Morrissey, J., et al. (2019). Glutamate receptor trafficking and protein synthesis mediate the facilitation of ltp by secreted amyloid precursor protein-alpha. *J. Neurosci.* 24, 3188–3203. doi: 10.1523/jneurosci.1826-18.2019

Mockett, B. G., Guévremont, D., Wutte, M., Hulme, S. R., Williams, J. M., and Abraham, W. C. (2011). Calcium/calmodulin-dependent protein kinase II mediates Group I Metabotropic glutamate receptor-dependent protein synthesis and long-term depression in rat hippocampus. *J. Neurosci.* 31, 7380–7391. doi: 10.1523/JNEUROSCI.6656-10.2011

Moreno, L., Rose, C., Mohanraj, A., Allinquant, B., Billard, J. M., and Dutar, P. (2015). sAbetaPPalpha improves hippocampal NMDA-Dependent functional alterations linked to healthy aging. *J. Alzheimers Dis.* 48, 927–935. doi: 10.3233/JAD-150297

Mucke, L., Abraham, C. R., and Masliah, E. (1996). Neurotrophic and neuroprotective effects of hAPP in transgenic mice. *Ann. N. Y. Acad. Sci.* 777, 82–88.

Nair, R. R., Patil, S., Tiron, A., Kanhema, T., Panja, D., Schiro, L., et al. (2017). Dynamic Arc SUMOylation and selective interaction with F-Actin-binding protein Drebrin A in LTP consolidation in vivo. *Front. Synaptic Neurosci.* 9:8. doi: 10.3389/fnsyn.2017.00008

Nakayama, D., Hashikawa-Yamasaki, Y., Ikegaya, Y., Matsuki, N., and Nomura, H. (2016). Late Arc/Arg3.1 expression in the basolateral amygdala is essential for persistence of newly-acquired and reactivated contextual fear memories. *Sci. Rep.* 6:21007. doi: 10.1038/srep21007

Na, Y., Park, S., Lee, C., Kim, D. K., Park, J., M., Sockanathan, S., et al. (2016). Real-time imaging reveals properties of glutamate-induced Arc/Arg 3.1 translation in neuronal dendrites. *Neuron* 9, 561–73. doi: 10.1016/j.neuron.2016.06.017

Okuno, H., Akashi, K., Ishii, Y., Yagishita-Kyo, N., Suzuki, K., Nonaka, M., et al. (2012). Inverse synaptic tagging of inactive synapses via dynamic interaction of Arc/Arg3.1 with CaMKIIβ. *Cell* 149, 886–898. doi: 10.1016/j.cell.2012.02.062

Ota, K. T., Monsey, M. S., Wu, M. S., Young, G. J., and Schafe, G. E. (2010). Synaptic plasticity and NO-cGMP-PKG signaling coordinately regulate ERK-driven gene expression in the lateral amygdala and in the auditory thalamus following Pavlovian fear conditioning. *Learn. Mem.* 17, 221–235. doi: 10.1101/lm.1592510

Papa, M., Bundman, M. C., Greenberger, V., and Segal, M. (1995). Morphological analysis of dendritic spine development in primary cultures of hippocampal neurons. *J. Neurosci.* 15(1 Pt 1), 1–11.

Pastuzyn, E. D., Day, C. E., Kearns, R. B., Kyrke-Smith, M., Taibi, A. V., McCormick, J., et al. (2018). The neuronal gene arc encodes a repurposed retrotransposon gag protein that mediates intercellular RNA transfer. *Cell* 172, 275–288.e18. doi: 10.1016/j.cell.2017.12.024

Peebles, C. L., Yoo, J., Thwin, M. T., Palop, J. J., Noebels, J. L., and Finkbeiner, S. (2010). Arc regulates spine morphology and maintains network stability in vivo. *Proc. Natl. Acad. Sci. U.S.A.* 107, 18173–18178. doi: 10.1073/pnas.1006546107

Peng, F., Yao, H., Bai, X., Zhu, X., Reiner, B. C., Beazely, M., et al. (2010). Platelet-derived growth factor-mediated induction of the synaptic plasticity gene Arc/Arg3.1. *J. Biol. Chem.* 285, 21615–21624. doi: 10.1074/jbc.M110.107003

Penke, Z., Chagneau, C., and Laroche, S. (2011). Contribution of Egr1/zif268 to Activity-Dependent Arc/Arg3.1 transcription in the dentate gyrus and Area CA1 of the Hippocampus. *Front. Behav. Neurosci.* 5:48. doi: 10.3389/fnbeh.2011.00048

Ping, J., and Schafe, G. E. (2010). The NO-cGMP-PKG signaling pathway coordinately regulates ERK and ERK-driven gene expression at pre- and postsynaptic sites following LTP-inducing stimulation of thalamo-amygdala synapses. *Neural Plast.* 2010:540940. doi: 10.1155/2010/540940

Plath, N., Ohana, O., Dammermann, B., Errington, M. L., Schmitz, D., Gross, C., et al. (2006). Arc/Arg3.1 is essential for the consolidation of synaptic plasticity and memories. *Neuron* 52, 437–444.

Raymond, C. R., Thompson, V. L., Tate, W. P., and Abraham, W. C. (2000). Metabotropic glutamate receptors trigger homosynaptic protein synthesis to prolong long-term potentiation. *J. Neurosci.* 20, 969–976.

Reger, A. S., Yang, M. P., Koide-Yoshida, S., Guo, E., Mehta, S., Yuasa, K., et al. (2014). Crystal structure of the cGMP-dependent protein kinase II leucine zipper and Rab11b protein complex reveals molecular details of G-kinase-specific interactions. *J. Biol. Chem.* 289, 25393–25403. doi: 10.1074/jbc.M114.575894

Rial Verde, E. M., Lee-Osbourne, J., Worley, P. F., Malinow, R., and Cline, H. T. (2006). Increased expression of the immediate-early Gene Arc/Arg3.1 reduces AMPA receptor-mediated synaptic transmission. *Neuron* 52, 461–474.

Rice, H. C., de Malmazet, D., Schreurs, A., Frere, S., Van Molle, I., Volkov, A. N., et al. (2019). Secreted amyloid-β precursor protein functions as a GABABR1a ligand to modulate synaptic transmission. *Science* 363:eaao4827. doi: 10.1126/science.aao4827

Rice, H. C., Wierda, K. D., Frere, S., Vertkin, I., Van Molle, I., Ranaivoson, F., et al. (2017). Soluble amyloid precursor protein is an isoform-specific gaba(b) receptor ligand that suppresses synaptic release probability. *Alzheimers Dement.* 13:206.

Richmond, S. A., Irving, A. J., Molnar, E., McIlhinney, R. A., Michelangeli, F., Henley, J. M., et al. (1996). Localization of the glutamate receptor subunit GluR1 on the surface of living and within cultured hippocampal neurons. *Neuroscience* 75, 69–82.

Richter, M. C., Ludewig, S., Winschel, A., Abel, T., Bold, C., Salzburger, L. R., et al. (2018). Distinct in vivo roles of secreted APP ectodomain variants APPsα and APPsβ in regulation of spine density, synaptic plasticity, and cognition. *EMBO J.* 37:e98335.

Ring, S., Weyer, S. W., Kilian, S. B., Waldron, E., Pietrzik, C. U., Filippov, M. A., et al. (2007). The secreted beta-amyloid precursor protein ectodomain APPs alpha is sufficient to rescue the anatomical, behavioral, and electrophysiological abnormalities of APP-deficient mice. *J. Neurosci.* 27, 7817–7826. doi: 10.1523/jneurosci.1026-07.2007

Robert, F., Cloix, J. F., and Hevor, T. (2012). Ultrastructural characterization of rat neurons in primary culture. *Neuroscience* 200, 248–260. doi: 10.1016/j.neuroscience.2011.10.002

Rodriguez, J. J., Davies, H. A., Errington, M. L., Verkhratsky, A., Bliss, T. V., and Stewart, M. G. (2008). ARG3.1/ARC expression in hippocampal dentate gyrus astrocytes: ultrastructural evidence and co-localization with glial fibrillary acidic protein. *J. Cell. Mol. Med.* 12, 671–678. doi: 10.1111/j.1582-4934.2007.00105.x

Rolstad, S., Jakobsson, J., Sellgren, C., Ekman, C. J., Blennow, K., Zetterberg, H., et al. (2015). Cognitive performance and cerebrospinal fluid biomarkers of neurodegeneration: a study of patients with bipolar disorder and healthy controls. *PLoS One* 10:e0127100. doi: 10.1371/journal.pone.0127100

Ryan, M. M., Morris, G. P., Mockett, B. G., Bourne, K., Abraham, W. C., Tate, W. P., et al. (2013). Time-dependent changes in gene expression induced by secreted amyloid precursor protein-alpha in the rat hippocampus. *BMC Genomics* 14:376. doi: 10.1186/1471-2164-14-376

Selnes, P., Blennow, K., Zetterberg, H., Grambaite, R., Rosengren, L., Johnsen, L., et al. (2010). Effects of cerebrovascular disease on amyloid precursor protein metabolites in cerebrospinal fluid. *Cerebrospinal Fluid Res.* 7:10. doi: 10.1186/1743-8454-7-10

Sennvik, K., Fastbom, J., Blomberg, M., Wahlund, L. O., Winblad, B., and Benedikz, E. (2000). Levels of alpha- and beta-secretase cleaved amyloid precursor protein in the cerebrospinal fluid of Alzheimer's disease patients. *Neurosci. Lett.* 278, 169–172.

Shepherd, J. D., Rumbaugh, G., Wu, J., Chowdhury, S., Plath, N., Kuhl, D., et al. (2006). Arc/Arg3.1 mediates homeostatic synaptic scaling of AMPA receptors. *Neuron* 52, 475–484. doi: 10.1016/j.neuron.2006.08.034

Steward, O., Farris, S., Pirbhoy, P. S., Darnell, J., and Driesche, S. J. (2014). Localization and local translation of Arc/Arg3.1 mRNA at synapses: some

observations and paradoxes. *Front. Mol. Neurosci.* 7:101. doi: 10.3389/fnmol.2014.00101

Steward, O., and Worley, P. F. (2001). A cellular mechanism for targeting newly synthesized mRNAs to synaptic sites on dendrites. *Proc. Natl. Acad. Sci. U.S.A.* 98, 7062–7068. doi: 10.1073/pnas.131146398

Suske, G. (1999). The Sp-family of transcription factors. *Gene* 238, 291–300. doi: 10.1016/S0378-1119(99)00357-351

Takahashi, S., Kubo, K., Waguri, S., Yabashi, A., Shin, H.-W., Katoh, Y., et al. (2012). Rab11 regulates exocytosis of recycling vesicles at the plasma membrane. *J. Cell Sci.* 125, 4049–4057. doi: 10.1242/jcs.102913

Tan, V. T. Y., Mockett, B. G., Ohline, S. M., Parfitt, K. D., Wicky, H. E., Peppercorn, K., et al. (2018). Lentivirus-mediated expression of human secreted amyloid precursor protein-alpha prevents development of memory and plasticity deficits in a mouse model of Alzheimer's disease. *Mol. Brain* 11:7. doi: 10.1186/s13041-018-0348-9

Taylor, C. J., Ireland, D. R., Ballagh, I., Bourne, K., Marechal, N. M., Turner, P. R., et al. (2008). Endogenous secreted amyloid precursor protein-alpha regulates hippocampal NMDA receptor function, long-term potentiation and spatial memory. *Neurobiol. Dis.* 31, 250–260. doi: 10.1016/j.nbd.2008.04.011

Thalhammer, A., Rudhard, Y., Tigaret, C. M., Volynski, K. E., Rusakov, D. A., and Schoepfer, R. (2006). CaMKII translocation requires local NMDA receptor-mediated Ca(2+) signaling. *EMBO J.* 25, 5873–5883. doi: 10.1038/sj.emboj.7601420

tom Dieck, S., Kochen, L., Hanus, C., Heumuller, M., Bartnik, I., Nassim-Assir, B., et al. (2015). Direct visualization of newly synthesized target proteins in situ. *Nat. Methods* 12, 411–414. doi: 10.1038/nmeth.3319

Turner, P. R., Bourne, K., Garama, D., Carne, A., Abraham, W. C., and Tate, W. P. (2007). Production, purification and functional validation of human secreted amyloid precursor proteins for use as neuropharmacological reagents. *J. Neurosci. Methods* 164, 68–74. doi: 10.1016/j.jneumeth.2007.04.001

Wall, M. J., and Correa, S. A. L. (2018). The mechanistic link between Arc/Arg3.1 expression and AMPA receptor endocytosis. *Semin. Cell Dev. Biol.* 77, 17–24. doi: 10.1016/j.semcdb.2017.09.005

Wang, Z., Edwards, J. G., Riley, N., Provance, D. W. Jr., Karcher, R., Li, X. D., et al. (2008). Myosin Vb mobilizes recycling endosomes and AMPA receptors for postsynaptic plasticity. *Cell* 135, 535–548. doi: 10.1016/j.cell.2008.09.057

Waung, M. W., Pfeiffer, B. E., Nosyreva, E. D., Ronesi, J. A., and Huber, K. M. (2008). Rapid translation of Arc/Arg3.1 selectively mediates mGluR-dependent LTD through persistent increases in AMPAR endocytosis rate. *Neuron* 59, 84–97. doi: 10.1016/j.neuron.2008.05.014

Wu, J., Petralia, R. S., Kurushima, H., Patel, H., Jung, M. Y., Volk, L., et al. (2011). Arc/Arg3.1 regulates an endosomal pathway essential for activity-dependent β-amyloid generation. *Cell* 147, 615–628. doi: 10.1016/j.cell.2011.09.036

Xia, Z., Dudek, H., Miranti, C. K., and Greenberg, M. E. (1996). Calcium influx via the NMDA receptor induces immediate early gene transcription by a MAP Kinase/ERK-dependent mechanism. *J. Neurosci.* 16, 5425–5436. doi: 10.1523/jneurosci.16-17-05425.1996

Zhai, X., Leo, M. D., and Jaggar, J. H. (2017). Endothelin-1 stimulates vasoconstriction through Rab11A Serine 177 phosphorylation. *Circ. Res.* 121, 650–661. doi: 10.1161/circresaha.117.311102

Conflict of Interest Statement: The authors declare that the research was conducted in the absence of any commercial or financial relationships that could be construed as a potential conflict of interest.

Copyright © 2019 Livingstone, Elder, Barrett, Westlake, Peppercorn, Tate, Abraham and Williams. This is an open-access article distributed under the terms of the Creative Commons Attribution License (CC BY). The use, distribution or reproduction in other forums is permitted, provided the original author(s) and the copyright owner(s) are credited and that the original publication in this journal is cited, in accordance with accepted academic practice. No use, distribution or reproduction is permitted which does not comply with these terms.

frontiers in Molecular Neuroscience

ORIGINAL RESEARCH
published: 27 August 2019
doi: 10.3389/fnmol.2019.00205

TrkB Agonist LM22A-4 Increases Oligodendroglial Populations During Myelin Repair in the Corpus Callosum

Huynh T. H. Nguyen[1], Rhiannon J. Wood[1], Alexa R. Prawdiuk[1], Sebastian G. B. Furness[2], Junhua Xiao[1], Simon S. Murray[1]† and Jessica L. Fletcher[1]*†*

[1]*Department of Anatomy and Neuroscience, School of Biomedical Sciences, Faculty of Medicine, Dentistry and Health Sciences, University of Melbourne, Parkville, VIC, Australia,* [2]*Drug Discovery Biology, Department of Pharmacology, Faculty of Pharmacy and Pharmaceutical Sciences, Monash Institute of Pharmaceutical Sciences, Monash University, Parkville, VIC, Australia*

The neurotrophin, brain-derived neurotrophic factor (BDNF) promotes central nervous system (CNS) myelination during development and after injury. This is achieved *via* activation of oligodendrocyte-expressed tropomyosin-related kinase (Trk) B receptors. However, while administration of BDNF has shown beneficial effects, BDNF itself has a poor pharmacokinetic profile. Here, we compare two TrkB-targeted BDNF-mimetics, the structural-mimetic, tricyclic dimeric peptide-6 (TDP6) and the non-peptide small molecule TrkB agonist LM22A-4 in a cuprizone model of central demyelination in female mice. Both mimetics promoted remyelination, increasing myelin sheath thickness and oligodendrocyte densities after 1-week recovery. Importantly, LM22A-4 exerts these effects in an oligodendroglial TrkB-dependent manner. However, analysis of TrkB signaling by LM22A-4 suggests rather than direct activation of TrkB, LM22A-4 exerts its effects *via* indirect transactivation of Trk receptors. Overall, these studies support the therapeutic strategy to selectively targeting TrkB activation to promote remyelination in the brain.

Keywords: myelin, neurotrophin, oligodendrocytes, remyelination, TrkB, BDNF

OPEN ACCESS

Edited by:
Jochen C. Meier, Technische Universitat Braunschweig, Germany

Reviewed by:
Albert I. Chen, Nanyang Technological University, Singapore
Elizabeth Hernández-Echeagaray, Universidad Nacional Autonóma de México, Mexico

***Correspondence:**
Simon S. Murray
ssmurray@unimelb.edu.au
Jessica L. Fletcher
jessica.fletcher@unimelb.edu.au

†These authors have contributed equally to this work

Received: *19 May 2019*
Accepted: *06 August 2019*
Published: *27 August 2019*

Citation:
Nguyen HTH, Wood RJ, Prawdiuk AR, Furness SGB, Xiao J, Murray SS and Fletcher JL (2019) TrkB Agonist LM22A-4 Increases Oligodendroglial Populations During Myelin Repair in the Corpus Callosum. Front. Mol. Neurosci. 12:205. doi: 10.3389/fnmol.2019.00205

INTRODUCTION

The neurotrophin, brain-derived neurotrophic factor (BDNF) is an attractive therapeutic for many neurodegenerative diseases due to its broad neuroprotective effects promoting neuronal survival, synaptic plasticity and central nervous system (CNS) myelination (Chao, 2003; Longo and Massa, 2013; Fletcher et al., 2018a). Its action *via* oligodendrocyte expressed tropomyosin-related kinase (Trk) B to potentiate and enhance myelination (Du et al., 2003; Xiao et al., 2011; Wong et al., 2013) makes it particularly promising for central demyelinating diseases such as multiple sclerosis (MS), where there is an unmet clinical need for remyelinating therapies to halt disease progression. However, BDNF itself has poor pharmacokinetic properties; it is non-selective, also acting through the pan-neurotrophic receptor $p75^{NTR}$, has a short-half life and has high molecular weight, limiting its ability to penetrate the blood-brain barrier (Poduslo and Curran, 1996; Longo and Massa, 2013). To overcome these limitations a range of small molecule BDNF-mimetics that selectively target the TrkB receptor have been developed (Longo and Massa, 2013). This includes tricyclic dimeric peptide-6 (TDP6; O'Leary and Hughes, 2003) and the partial TrkB agonist, LM22A-4 (Massa et al., 2010).

TDP6 is a structural peptide mimetic, designed to mimic the Loop 2 region of BDNF that is known to interact with TrkB (Chao, 2003; O'Leary and Hughes, 2003). We have previously shown that TDP6 mimics BDNF in promoting neuronal survival (O'Leary and Hughes, 2003) and enhancing myelination both *in vitro* (Wong et al., 2014) and during myelin repair following cuprizone demyelination *in vivo* (Fletcher et al., 2018b). Similarly, LM22A-4 was identified during an *in silico* screen to identify compounds with potential to mimic the Loop2 region of BDNF and is a non-peptide, partial TrkB agonist (Massa et al., 2010). It is 98% smaller than BDNF and has been shown to have therapeutic potential in preventing neurodegeneration in animal models of traumatic brain injury, stroke, Huntington's disease and Rhett syndrome (Massa et al., 2010; Han et al., 2012; Schmid et al., 2012; Simmons et al., 2013; Gu et al., 2018) but has not yet been tested in the context of central demyelinating disease.

Here, we compare the effect of intra-cerebroventricular (ICV) administration of these BDNF mimetics following cuprizone demyelination in mice. Both mimetics promoted myelin repair, increasing myelin sheath thickness, after 1-week recovery. Interestingly, LM22A-4 increased the density of oligodendroglia in the corpus callosum more than the structural BDNF mimetic, TDP6. Importantly, the effects of LM22A-4 were dependent on TrkB, as post-cuprizone treatment with LM22A-4 in mice with conditional deletion of TrkB from oligodendrocytes abrogated both remyelination and increased oligodendroglial density. While this indicates that LM22A-4 promotes myelin repair in a TrkB dependent manner, assessment of TrkB phosphorylation and signaling *in vitro* suggests that LM22A-4 may not activate TrkB directly, but rather result in delayed TrkB transactivation *via* a G-protein coupled receptor (GPCR) mediated mechanism. Collectively these data further verify that targeting TrkB activation is a cogent strategy to promote myelin repair in the brain and that alternate small molecule mimetic strategies are effective towards this end. Further studies aimed at elucidating the precise mechanism of action are warranted to optimize the therapeutic potential of this approach.

MATERIALS AND METHODS

Experimental Animals and Cuprizone Induced Demyelination

Female C57BL/6 mice aged 8 weeks were fed 0.2% cuprizone in normal chow (Teklad Custom Research Diets, New Brunswick, NJ, USA) for 6 weeks to induce demyelination. Female mice were used due to the increased incidence of MS in females (Wallin et al., 2019). Cuprizone feed was removed, and mice were sacrificed or received intracerebroventricular osmotic pumps for 7 days.

For experiments in conditional knockout mice, female, 8–10 week-old CNPaseCre$^{+/-}$ × TrkB$^{fl/fl}$ (Lappe-Siefke et al., 2003; Luikart et al., 2005; Fletcher et al., 2018b) on C57BL/6 background underwent the procedures described above.

All mice were housed in specific pathogen-free conditions at the Melbourne Brain Centre Animal Facility. All animal procedures were approved by the Florey Institute for Neuroscience and Mental Health Animal Ethics Committee and followed the Australian Code of Practice for the Care and Use of Animals for Scientific Purposes.

Intracerebroventricular Delivery of LM22A-4 and TDP6

Following cuprizone feeding, mice received either: 40 μM TDP6, 500 μM LM22A-4 or the artificial cerebrospinal fluid (aCSF) vehicle *via* ICV as described in Fletcher et al. (2018b). Briefly, cannulae of osmotic pumps (flow rate: 0.5 μL/h, Azlet) were stereotaxically inserted over the right lateral ventricle under isoflurane anesthesia. Infusion concentrations of TDP6 and LM22A-4 were determined based on previous *in vitro* studies characterizing their effective concentrations (Massa et al., 2010; Wong et al., 2014). TDP6 infused animals were the same animals from Fletcher et al. (2018b) and LM22A-4 infusion experiments were performed concurrently. Following stereotaxic surgery, all mice were placed in a recovery chamber maintained at 32°C and were monitored for adverse reactions immediately following surgery and then daily. After 7 days of ICV infusion, mice were taken for necropsy and brain removed for immunostaining and electron microscopy (EM).

Tissue Processing and Immunofluorescence

Mice were anesthetized and transcardially perfused with 0.1 M sterile mouse isotonic phosphate buffered saline (PBS) followed by 4% paraformaldehyde (PFA). Brains were collected and post-fixed overnight in 4% PFA. The first millimeter of the right hemisphere from the sagittal midline was selected for EM processing as previously described (Fletcher et al., 2018b). The remaining tissue and contralateral hemisphere were cryoprotected in 30% sucrose prior to embedding in OCT. Frozen sections were cut in the sagittal orientation at 10 μm thickness using a cryostat maintained between −20°C and −17°C and collected on SuperfrostPlus slides, air-dried and stored at −80°C until use. Approximately 70–100 μm separated adjacent sections on each slide. The sections beyond 2.64 μm Bregma laterally were excluded.

Immunofluorescent staining was performed as previously described (Fletcher et al., 2018b). Briefly, slides were washed in PBS before overnight incubation at room temperature with primary antibodies. Slides were then washed and incubated with the appropriate fluorophore-conjugated secondary antibody for 2 h at room temperature in the dark. Slides were washed, and counterstained with nuclear marker Hoescht33442 [omitted for myelin basic protein (MBP) and oligodendroglial stains] before mounting with aqueous mounting media (DAKO). All immunohistochemistry was performed in batches.

Antibodies used were: rat anti-MBP (1:200, MAB386, Millipore, MA, USA), rabbit anti-Olig2 (1:200, AB9610, Millipore, MA, USA), mouse anti-CC1 (1:200, APC, OP80, CalBioChem, CA, USA), goat anti-platelet derived growth factor

receptor-α (PDGFRα, 1:200, AF1062. R&D Systems, MN, USA), goat anti-Iba1 (1:200, ab5076, Abcam, UK), mouse anti-glial fibrially acidic protein (GFAP, 1:100, MA360, Millipore, MA, USA) and rabbit anti-phosphorylated TrkB^{S478} (1:200 R-1718-50, Biosensis).

Electron Microscopy and Analysis

Semi-thin (0.5–0.1 μm) sections of caudal corpus callosum in a sagittal plane were collected on glass slides and stained with 1% toluidine blue to select region of analysis. Ultrathin (0.1 μm) sections were subsequently collected on 3 × 3 mm copper grids and specimens examined using a JEOL 1001 transmission electron microscope. Images were captured with MegaView III CCD cooled camera operated with iTEM AnalySIS software (Olympus Soft Imaging Systems GmbH). A minimum of six distinct fields of view were imaged at 5,000 or 10,000× magnification for each animal. The proportion of myelinated axons, axon diameter and *g*-ratio were analyzed manually using FIJI/ImageJ (National Institutes of Health, Bethesda, MD, USA). For *g*-ratios at least 100 axons from three mice per group were measured. Resin embedding, sectioning and post-staining and EM imaging were performed at the Peter MacCallum Centre for Advanced Histology and Microscopy.

Fluorescence Imaging and Analysis

Imaging was performed blind to treatment group and restricted to the caudal corpus callosum approximately −1.1 to −3.0 mm from Bregma in the rostral-caudal direction. Tracts contributing to the dorsal hippocampal commissure were excluded from analysis. For each analysis, a minimum of three sections per animal was imaged.

To quantify the level of remyelination images of MBP stained sections were collected with an AxioVision Hr camera attached to a Zeiss Axioplan2 epi-fluorescence microscope under a 20× objective. Uniform exposure times were used. Remaining images were acquired with a Zeiss LSM780 or LSM880 confocal microscope with 405 nm, 488 nm, 561 nm and 633 nm laser lines. For each fluorescent stain uniform settings were used.

MBP staining was measured on single channel grayscale images using the default automated threshold function in FIJI/ImageJ and limited to a standard region of interest (ROI) of 625,000 μm^2 for each section. Data were expressed as a percentage area of positive staining in a single ROI.

Cell Counts

All cell counts were performed blind to sample identity, manually in FIJI/ImageJ using the Cell Counter plugin using a standard ROI size of 625,000 μm^2 applied over the caudal corpus callosum. Briefly, for oligodendroglia, Olig2 positive cells were counted first, and then CC1 and/or PDGRα channels were overlaid and double-positive cells were counted. Excess cells, that were Olig2$^+$ only were then visually inspected to confirm negative staining for CC1 and PDGFRα. For pTrkB staining, the Hoechst positive nuclei were counted first and then cells positive for pTrkB^{S478}. Data were expressed as the number of cell/mm^2 or proportion out of the total number of nuclei.

Generation of Isogenic TrkB Expressing Flp-In 293 Cells

The Flp-In 293 cell system (ThermoScientific) was used to generate isogenic TrkB expressing HEK293 cell lines where TrkB was integrated into the host cell genome. Flp-In cells express a hygromycin resistance gene, which enables the use of hygromycin (50 μg/μL) to exert selective pressure for cells carrying the Flp-In construct.

Briefly, to generate the TrkB expressing HEK293 cell line (**Supplementary Figure S1A**), Ntrk2 (NM_012731.2) was amplified by PCR from rat cDNA and recombined into pDONR201 entry vector by BP clonase II reaction (Invitrogen) according to the manufacturer's instructions. DH5α bacteria (ThermoScientific) were transformed with the entry vector by heat shock and positive colonies expressing the pDONR201 plasmid were selected using kanamycin resistance. pDONR201 plasmid containing Ntrk2 was purified using a mini-prep kit (Promega) and recombined into pEF5/FRT/V5-DEST destination vector by LR clonase II reaction (ThermoScientific). Following transformation with the destination vector, DH5α bacterial colonies were placed under ampicillin selective pressure and plasmid DNA extracted. At each step, successful recombination of Ntrk2 into the entry and destination vectors was confirmed by restriction ligase digest with ApaI (NEB) and Sanger sequencing (Australian Genome Research Facility).

Once the Ntrk2 destination vector was generated, the Flp-In HEK293 host cells were transfected with the Ntrk2 destination vector and the Flp-recombinase vector pOG44 with 50 μg/μL hygromycin according to the manufacturer's instructions. Flp-In HEK293 cells were maintained at 37°C with 5% CO_2 in Dulbecco's modified eagle medium (DMEM) with 10% fetal bovine serum, 1% L-glutamine, 1% penicillin and 1% streptomyocin. TrkB expression by the isogenic TrkB Flp-In HEK293 cells was verified by Western blot (**Supplementary Figures S1B–E**).

In vitro Testing of TrkB Phosphorylation by LM22A-4

To examine the capacity of LM22A-4 to mimic the BDNF-TrkB signaling cascade, isogenic TrkB FlP-In HEK293 cells were starved in serum-free media for 2 h before treatment with 4 nM BDNF or 500 nM LM22A-4 for 0, 5, 15, 30, 60 and 240 min. Concentrations were chosen based on previous work (Massa et al., 2010; Wong et al., 2014). Cells were lysed with TNE (Tris) buffer containing protease (Complete Mini) and phosphatase inhibitors (PhosStop Roche, 50 mM Sodium Fluoride). Protein concentrations were determined by Bradford assay and lysates stored at −80°C until use.

SDS-PAGE and Western Blot Analysis

Lysates were separated by SDS-PAGE (4%–12% Bis-Tris, Invitrogen, Carlsbad, CA, USA) and transferred to PVDF membrane and probed with antibodies against TrkB (1:1,000, sc-8316, SantaCruz Biotechnology, Santa Cruz, CA, USA) and pTrkB^{s478} (1:1,000, R-1718-50, Biosensis), p44/42 MAPK (ERK1/2, 1:1,000, #9102 Cell Signaling Technologies,

Danvers, MA, USA) and phosphorylated ERK1/2 (pERK1/2, 1:1,000, #9101 Cell Signaling Technologies, Danvers, MA, USA). All blots shown are representative of at least three independent experiments. Optical density value for each band was determined using FIJI/ImageJ and corrected to loading control and normalized against the relevant control condition.

Statistical Analyses

Data were analyzed by unpaired *t*-test, one-way analysis of variance (ANOVA) or mixed effect models for repeated measures (GraphPad Prism 8), to test the effect of TrkB agonist treatments with *post hoc* multiple comparisons as appropriate. Statistical significance was set as $p < 0.05$.

RESULTS

LM22A-4 and TDP6 Increase Myelin Sheath Thickness During Remyelination

We have previously shown treatment with TDP6, a structural mimetic of BDNF, enhances the number of axons remyelinated and increases myelin sheath thickness during recovery after 6-weeks cuprizone challenge in an oligodendroglial-TrkB dependent manner (Fletcher et al., 2018b). Here, we compared TDP6 with LM22A-4, a small molecule TrkB agonist reported to be a functional BDNF-mimetic (Massa et al., 2010). Demyelination by cuprizone feeding was confirmed by MBP immunostaining, with severely reduced levels of MBP expression observed in animals taken at 6 weeks of cuprizone feeding (minimum = 2/cohort; **Supplementary Figure S2**). Cuprizone feed was withdrawn and remaining animals received ICV minipumps containing artificial cerebrospinal fluid (aCSF), TDP6 (40 μM) or LM22A-4 (500 μM) for 7 days.

To examine the extent of remyelination, MBP-immunostaining in the caudal corpus callosum was assessed. This revealed both TDP6 and LM22A-4 treatment increased ($p < 0.0001$) the percentage area of MBP^+ staining compared to treatment with the aCSF vehicle (**Figure 1A**, quantified in **Figure 1B**). EM analysis indicated that mice treated with TDP6 exhibited a trend ($p = 0.09$) increase towards more remyelinated axons compared to those receiving aCSF, whereas for those receiving LM22A-4, no increase was observed ($p = 0.46$; **Figure 1C**). Both TDP6 and LM22A-4 treatment resulted in a significant ($p = 0.002$) reduction in mean g-ratio indicative of increased myelin thickness (**Figure 1D**). Linear regression analysis of g-ratio against axon diameter (**Figure 1E**) indicated that although both TDP6 and LM22A-4 treatments increase myelin sheath thickness during remyelination (**Figure 1D**), TDP6 exerted a more consistent effect with a significant decrease in y-intercept ($p = 0.0032$), but no change in slope ($p = 0.35$) indicating that g-ratio was reduced across all axonal diameters, whereas for LM22A-4 there was a significant increase in slope ($p = 0.006$), indicative of reduced g-ratio and thicker myelin on smaller diameter axons. Collectively, these data are consistent with our previous findings that BDNF-TrkB signaling increases myelin sheath thickness during remyelination *in vivo* (Fletcher et al., 2018b).

Treatment With LM22A-4 Profoundly Increases Oligodendroglial Densities During Myelin Repair

Next, we assessed oligodendroglial populations in the corpus callosum by co-immunostaining Olig2 with platelet-derived growth factor receptor-alpha (PDGFRα) and CC1 to identify $Olig2^+PDGFR\alpha^+$ oligodendrocyte progenitor cells (OPCs), $Olig2^+CC1^+$ post-mitotic oligodendrocytes (CC1 the clone for APC, a cytoplasmic marker highly expressed in post-mitotic oligodendrocytes) and an $Olig2^+PDGFR\alpha^-CC1^-$ intermediate oligodendroglial population (**Figure 2A**). Counts in the caudal corpus callosum revealed TDP6 and LM22A-4 increased the total population of $Olig2^+$ oligodendroglia compared to treatment with aCSF vehicle (**Figure 2B**, $p < 0.0001$). Interestingly, LM22A-4 treatment exerted a more profound effect, increasing the density of $Olig2^+$ oligodendroglia above TDP6 (**Figure 2B**, $p = 0.0001$). Both TDP6 and LM22A-4 treatments increased the density of $Olig2^+CC1^+$ post-mitotic oligodendrocytes compared to aCSF vehicle (**Figure 2D**, $p = 0.013$), consistent with the pro-differentiation effect of TrkB activation on oligodendroglia. However, assessment of $Olig2^+PDGFR\alpha^+$ OPCs indicated LM22A-4 also increased the density of OPCs compared to treatment with TDP6 or aCSF vehicle (**Figure 2C**, $p = 0.011$). Overall, these data suggest that selectively targeting TrkB during remyelination primarily enhances oligodendroglial differentiation.

To examine whether these effects of LM22A-4 and TDP6 were due to alterations in lineage progression during differentiation, the proportion of $Olig2^+PDGFR\alpha^+$, $Olig2^+CC1^+$ and $Olig2^+$ only cells out of the total $Olig2^+$ population were assessed (**Figure 2E**). The proportion of cells that were OPCs or post-mitotic oligodendrocytes were unchanged between groups. However, LM22A-4 treatment significantly increased the proportion of $Olig2^+$ only cells (26% ± 7%) compared to treatment with either TDP6 (6% ± 8%) or aCSF vehicle (10% ± 7%; **Figure 2E**, mean ± SD, $p < 0.0001$, χ^2 distribution test). These data suggest LM22A-4 treatment may exert a greater effect than TDP6 to increase the proliferation or survival of oligodendroglia during myelin repair.

TrkB Phosphorylation in the Corpus Callosum Is Elevated Following Treatment With TDP6 and LM22A-4 During Remyelination

To determine if TDP6 and LM22A-4 infusions stimulated TrkB phosphorylation on oligodendroglia we performed triple immunolabeling for $pTrkB^{S478}$ with PDGFRα and CC1 to identify OPCs and post-mitotic oligodendrocytes, respectively (**Figure 3A**). This revealed that TDP6 and LM22A-4 infusions were successful, with an increased proportion of $pTrkB^{S478+}$ cells in the corpus callosum during remyelination, compared to the aCSF vehicle (**Figure 3B**, $p = 0.0022$). Assessment of the proportion of $pTrkB^{S478+}$ cells positive for the OPC marker PDGFRα indicated treatment with TDP6 and LM22A-4 had no effect on TrkB activation on OPCs (**Figure 3C**, $p = 0.21$). However, the proportion of $TrkB^{S478+}CC1^+$

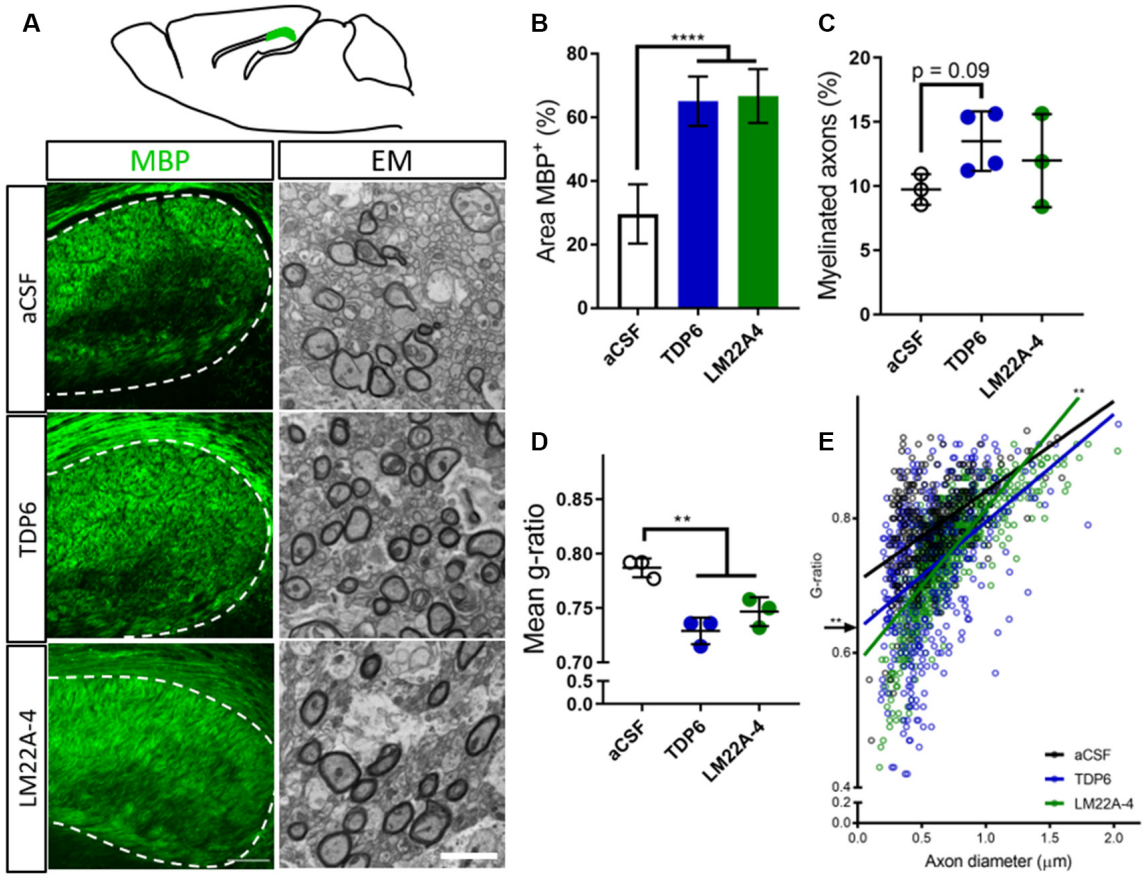

FIGURE 1 | Brain-derived neurotrophic factor (BDNF)-structural mimetic, tricyclic dimeric peptide-6 (TDP6) and tropomyosin-related kinase (Trk) B agonist, LM22A-4 increase myelin sheath thickness during remyelination in after cuprizone demyelination. **(A)** Schematic of a sagittal brain section 0.36 mm lateral from midline. Adapted from Paxinos and Franklin (2001); caudal region of the corpus callosum analysed shaded green (above). Representative myelin basic protein (MBP) immunostatining (sagittal plane, scale bar = 100 μm) and electron micrographs (scale bar = 2 μm) of the cadual corpus callosum of artificial cerebrospinal fluid (aCSF) vehicle, TDP6 and LM22A-4 treated cuprizone demyelinated mice (below). **(B)** Percentage of MBP staining increased ($p < 0.0001$) in TDP6 and LM22A-4 treated mice compared to those that received aCSF vehicle (n = 4–8/group). **(C)** The proportion of axons remyelinated trended towards increasing with TDP6 treatment ($p = 0.09$) compared to aCSF, but was unchanged between aCSF and LM22A-4 ($p = 0.48$) and LM22A-4 and TDP6 ($p = 0.31$, n = 3–4/group), however **(D)** the mean g-ratio was decreased ($p = 0.002$) in both TDP6 and LM22A-4 treated mice, indicative of thicker myelin sheaths compared to those receiving aCSF vehicle (n = 3/group). **(E)** Scatter plot of g-ratio against axonal diameter. Linear regression revealed that TDP6 treatment resulted in a decrease in y-intercept ($p = 0.0032$) but no change in slope ($p = 0.35$), while LM22A-4 treatment increased slope ($p = 0.0061$), both indicative of increased myelin sheath thickness compared to aCSF treatment (n = 3 mice/group, min. Hundred axons/animal). One-way analysis of variance (ANOVA) with Tukey's *post hoc* comparisons, $p < 0.05$ considered significant. Mean ± SD plotted. Six-weeks cuprizone feeding commenced at 8 weeks of age, tissue collected at 15 weeks of age. $^{**}p < 0.01$, $^{****}p < 0.0001$.

post-mitotic oligodendrocytes increased with TDP6 treatment compared to treatment with LM22A-4 (**Figure 3D**, $p = 0.046$). These data suggest that LM22A-4 can signal *via* TrkB during remyelination *in vivo* and is consistent with previous findings that TDP6 stimulates TrkB phosphorylation on $CC1^+$ oligodendrocytes.

LM22A-4 Mediated Increases in Myelin Sheath Thickness and Oligodendroglial Densities Require Oligodendrocyte TrkB Expression

To determine whether the effects of LM22A-4 on myelin sheath thickness and oligodendrocyte populations during myelin repair are dependent on oligodendroglial TrkB expression, we repeated the infusion experiment in $CNPaseCre^{+/-} \times TrkB^{fl/fl}$ mice in which TrkB is genetically deleted from maturing oligodendrocytes. These mice have a 3-fold reduction in $TrkB^+$ oligodendroglia but adult myelination and oligodendrocyte populations are unaffected (Fletcher et al., 2018b). Cuprizone was administered for 6 weeks, and LM22A-4 or aCSF vehicle was infused *via* ICV minipumps for 7 days. Immunostaining for MBP revealed that LM22A-4 treatment in the oligodendroglial TrkB knockout mice had no effect on the percentage area of MBP^+ immunostaining compared to the aCSF vehicle (**Figure 4A**, quantified in **Figure 4B**, $p = 0.21$). Similarly, EM analysis (**Figure 4D**) revealed there was no change in the proportion of axons myelinated with LM22A-4 treatment (**Figure 4C**,

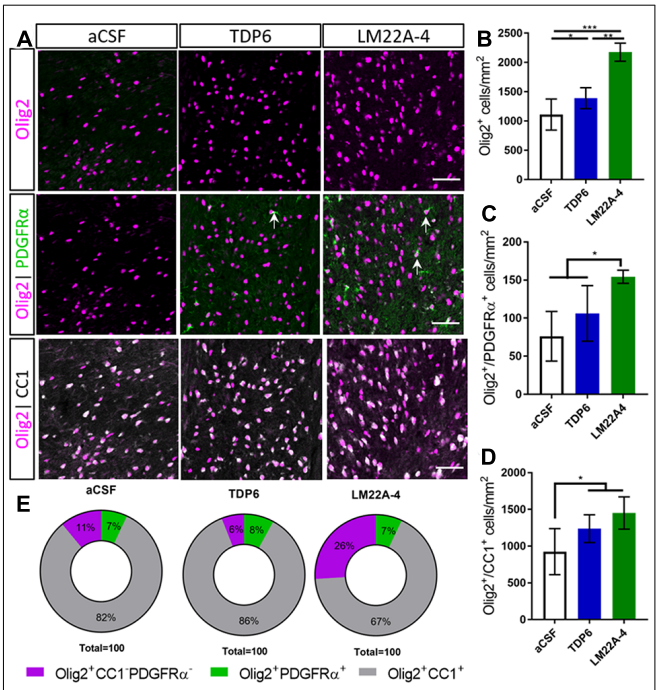

FIGURE 2 | TDP6 and LM22A-4 increase oligodendroglial densities in the corpus callosum during remyelination following cuprizone mediated demyelination. **(A)** Representative micrographs of Olig2-CC1-PDGFRα immunostaining in the caudal corpus callosum of aCSF vehicle, TDP6 and LM22A-4 treated C57BL/6 mice. Arrows: Olig2$^+$PDGFRα$^+$ oligodendrocyte progenitor cells (OPCs; sagittal plane, scale bar = 50 μm). **(B)** Olig2$^+$ densities increased with LM22A-4 treatment ($p < 0.0001$) compared to treatment with TDP6, which also increased Olig2$^+$ cell density ($p = 0.048$) compared to the aCSF vehicle ($n = 4$–8/group). **(C)** Olig2$^+$PDGFRα$^+$ OPC densities increased with LM22A-4 infusion ($p = 0.009$) compared to the aCSF vehicle, but not compared to TDP6 treatment ($p = 0.12$; $n = 4$–8/group). **(D)** Both TDP6 ($p = 0.023$) and LM22A-4 ($p = 0.007$) infusions increased Olig2$^+$CC1$^+$ post-mitotic oligodendrocyte densities compared to the aCSF vehicle ($n = 4$–8/group). **(E)** LM22A-4 treatment increased (26% ± 7%; $p < 0.0001$) the proportion of Olig2$^+$ only oligodendroglia compared to TDP6 (6% ± 8%) and aCSF treatment (10% ± 7%; χ^2 distribution test). For **(A–D)** one-way ANOVA with Tukey's *post hoc* comparisons, $p < 0.05$ considered significant. Mean ± SD plotted. Six-weeks cuprizone feeding commenced at 8 weeks of age, tissue collected at 15 weeks of age. *$p < 0.05$, **$p < 0.01$, ***$p < 0.001$.

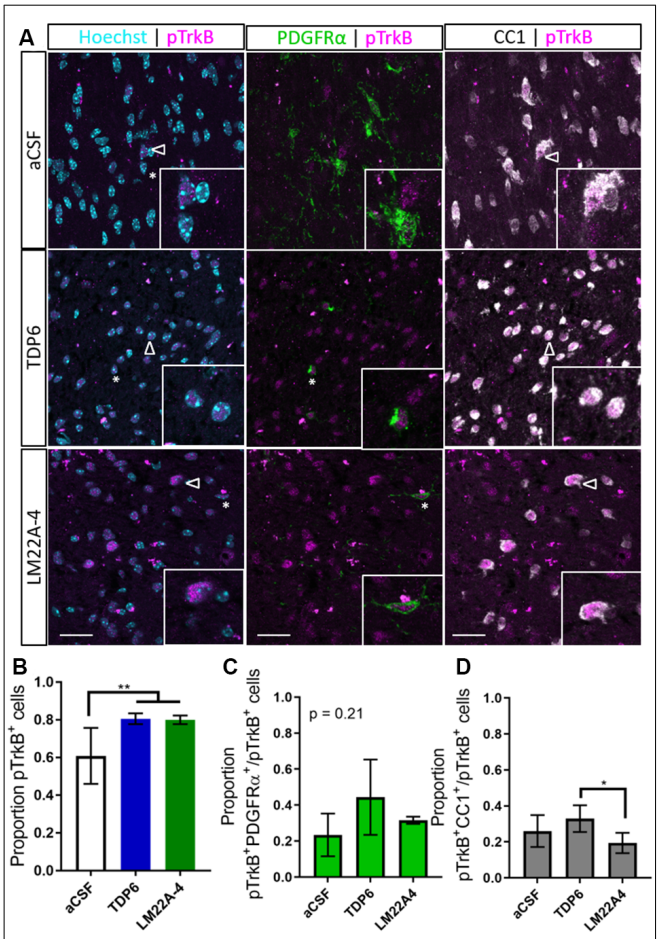

FIGURE 3 | Phosphorylation of TrkB in the corpus callosum during remyelination is elevated following treatment with TDP6 and LM22A-4. **(A)** Representative micrographs of pTrkB^{S478}-PDGFRα-CC1 immunostaining in the caudal corpus callosum of mice treated with aCSF vehicle, TDP6 or LM22A-4 (sagittal plane, scale bar = 20 μm). Asterisk: pTrkB^{s478+}PDGFRα$^+$ cell, open arrowhead: pTrkB^{s478+}CC1$^+$. Inset: enlarged image of marked cells. **(B)** Proportion of pTrkB^{s478+} cells increased ($p = 0.0022$) in the corpus callosum of mice treated with TDP6 and LM22A-4 compared to those that received aCSF vehicle ($n = 4$–8/group). **(C)** The proportion of pTrkB^{s478+} cells also PDGFRα$^+$ was unchanged across the three different treatments ($p = 0.21$, $n = 4$–8/group), while **(D)** the proportion of pTrkB^{s478+}CC1$^+$ cells increased ($p = 0.045$) in mice that received TDP6 infusion compared to those receiving LM22A-4 ($n = 4$–8/group). One-way ANOVA with Tukey's *post hoc* multiple comparisons, $p < 0.05$ considered significant. Mean ± SD plotted. Six-weeks cuprizone feeding commenced at 8 weeks of age, tissue collected at 15 weeks of age. *$p < 0.05$, **$p < 0.01$.

$p = 0.85$) or the mean g-ratio (aCSF: 0.77 ± 0.087; LM22A-4: 0.78 ± 0.088, $p = 0.90$, $n = 3$–4/group, unpaired *t*-test). These data are consistent with oligodendroglial TrkB expression being necessary for LM22A-4 to increase myelin sheath thickness during remyelination.

To determine if LM22A-4 treatment increased oligodendroglial populations during remyelination in oligodendroglial TrkB knockout mice, triple immunolabeling for Olig2-PDGFRα-CC1 was performed in the contralateral caudal corpus callosum (**Figure 5A**). Counts revealed that LM22A-4 treatment had exerted no change in the density of Olig2$^+$ oligodendroglia ($p = 0.91$; **Figure 5B**), Olig2$^+$PDGFRα$^+$ OPCs ($p = 0.38$; **Figure 5C**) or Olig2$^+$CC1$^+$ post-mitotic oligodendrocytes ($p = 0.94$; **Figure 5D**) compared to the aCSF vehicle. Similarly, there was no difference in the proportion of Olig2$^+$ only cells between aCSF vehicle and LM22A-4 treatment in the oligodendroglial TrkB knockout mice (**Figure 5E**, $p = 0.33$, χ^2 distribution test). Collectively, these data confirm that the action of LM22A-4 in increasing oligodendroglial populations is dependent on oligodendroglial expressed TrkB.

To examine the level of TrkB phosphorylation in LM22A-4 treated oligodendroglial TrkB knockout mice, immunohistochemistry for pTrkB^{S478} with oligodendrocyte markers PDGFRα and CC1 was performed (**Figure 6A**). Analysis of the caudal corpus callosum revealed that in the

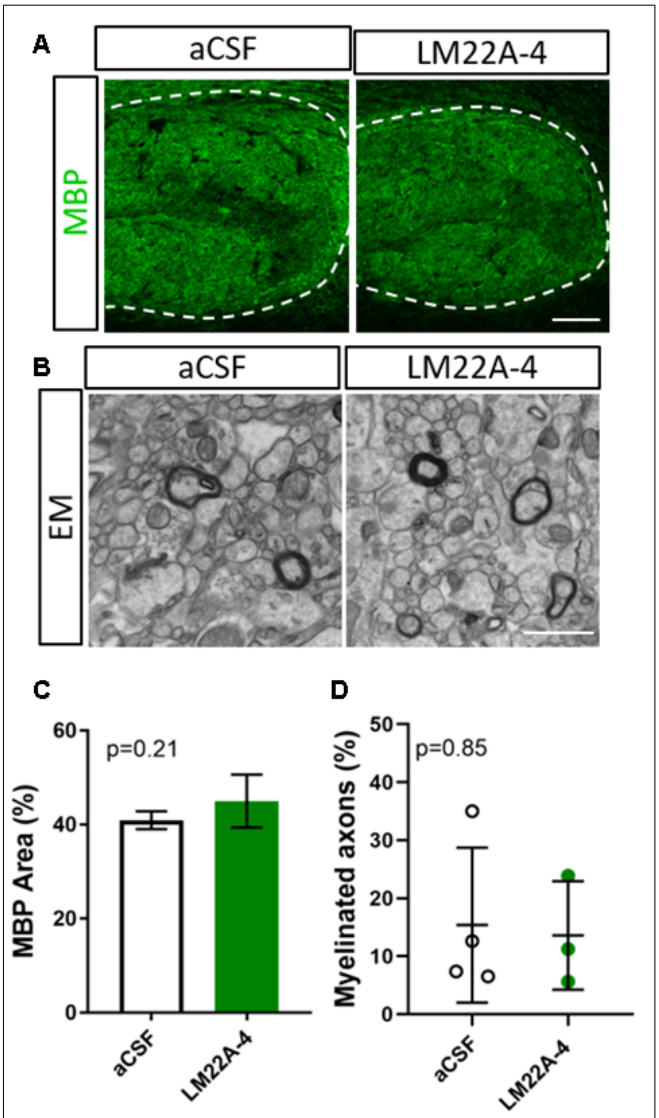

FIGURE 4 | The effects of LM22A-4 on myelin sheath thickness during myelin repair require oligodendrocyte TrkB. **(A)** Representative micrographs of MBP immunostaining in the caudal corpus callosum of CNPaseCre$^{+/-}$ × TrkB$^{fl/fl}$ mice treated with aCSF vehicle or LM22A-4 (sagittal plane, scale bar = 100 μm). **(B)** Representative electron micrographs of the caudal corpus callosum of conditional TrkB knockout mice receiving aCSF vehicle or LM22A-4 (scale bar = 2 μm). **(C)** There was no change ($p = 0.21$) in the percentage area of MBP^{+} immunostaining in the corpus callosi of oligodendroglial TrkB knockout mice treated with LM22A-4 compared to the aCSF vehicle. **(D)** The proportion of myelinated axons was unchanged between oligodendroglial TrkB knockout mice receiving aCSF vehicle and LM22A-4. For **(D)** unpaired *t*-test with equal variance, $p < 0.05$ considered significant, $n = 3$–4/group. Mean ± SD plotted. Six-weeks cuprizone feeding commenced at 8–10 weeks of age, tissue collected at 15–17 weeks of age.

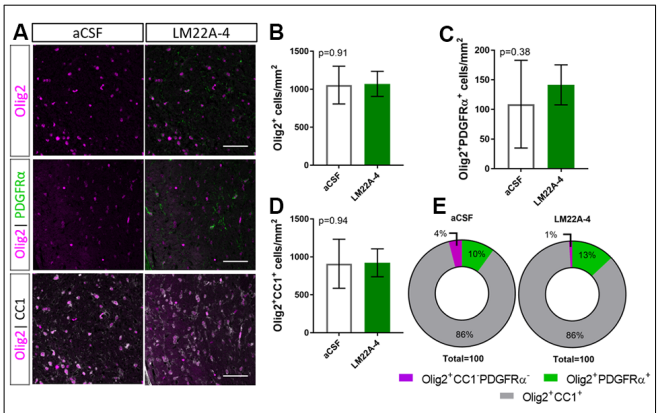

FIGURE 5 | Increased oligodendroglial density mediated by LM22A-4 during myelin repair requires oligodendroglial TrkB. **(A)** Representative micrographs of Olig2-CC1-PDGFRα immunostaining in the caudal corpus callosum of CNPaseCre$^{+/-}$ × TrkB$^{fl/fl}$ mice treated aCSF vehicle or LM22A44 (sagittal plane, scale bar = 20 μm). **(B)** Density of Olig2^{+} oligodendroglia was unchanged ($p = 0.91$) in TrkB conditional knockout mice treated with LM22A-4 compared to aCSF vehicle. **(C)** Olig2^{+}PDGFRα^{+} OPC densities were unchanged ($p = 0.38$) in oligodendroglial TrkB knockout mice treated with LM22A-4 compared to aCSF vehicle. **(D)** Density of Olig2^{+}CC1^{+} oligodendrocytes in TrkB conditional knockout mice was unchanged ($p = 0.94$) with LM22A-4 infusion compared to aCSF vehicle. **(E)** There was no change ($p = 0.34$) in the proportion of oligodendroglia that were Olig2^{+} only, Olig2^{+}PDGFRα^{+} or Olig2^{+}CC1^{+} with LM22A-4 or a CSF vehicle treatment (χ^2 distribution test). For **(A–D)** unpaired *t*-test with equal variance, $p < 0.05$ considered significant, $n = 3$–4/group. Mean ± SD plotted. Six-weeks cuprizone feeding commenced at 8–10 weeks of age, tissue collected at 15–17 weeks of age.

oligodendroglial TrkB knockout mice LM22A-4 treatment did not increase the proportion of pTrkB^{S478+} cells compared to the aCSF vehicle (**Figure 6B**, $p = 0.24$). This was also reflected with no change in the proportion of pTrkB^{S478+} cells positive for oligodendroglial markers PDGFRα ($p = 0.99$; **Figure 6C**) or CC1 ($p > 0.99$; **Figure 6D**). These data indicate that LM22A-4 mediated TrkB phosphorylation during remyelination requires oligodendroglial TrkB expression.

TrkB Signaling Dynamics Initiated by LM22A-4 Do Not Mimic BDNF

To determine if LM22A-4 elicits a signaling cascade mimicking typical BDNF-TrkB signaling, we generated an isogenic stable TrkB expressing HEK293 (293-TrkB) cell line using the Flp-In system (**Supplementary Figure S1A**). TrkB expression in the 293-TrkB cells was confirmed by Western blot and compared to TrkB expression generated by transiently transfecting Flp-In HEK293 cells with the Ntrk2 expression vector. This revealed that transiently transfected cells overexpress both mature glycosylated and unprocessed TrkB receptors, whereas the 293-TrkB cells express only the fully mature glycosylated form (**Supplementary Figure S1B**). To confirm that the 293-TrkB cells responded to BDNF, cells were treated with BDNF (0.04 nM to 40 nM) for 15 min (**Supplementary Figure S1C**) which resulted in increasing levels of TrkB and ERK1/2 phosphorylation (**Supplementary Figure S1D**).

As determined in the original report characterizing LM22A-4 as functional BDNF mimetic (Massa et al., 2010), we used 500 nM as the standard concentration for our *in vitro* studies. The 293-TrkB cells were treated with 4 nM BDNF or 500 nM LM22A-4 for a time course of 5, 15, 30, 60 and 240 min and assessed for TrkB and ERK1/2 phosphorylation by Western blot (**Figure 7A**). Densitometric analysis (**Figure 7B**) revealed

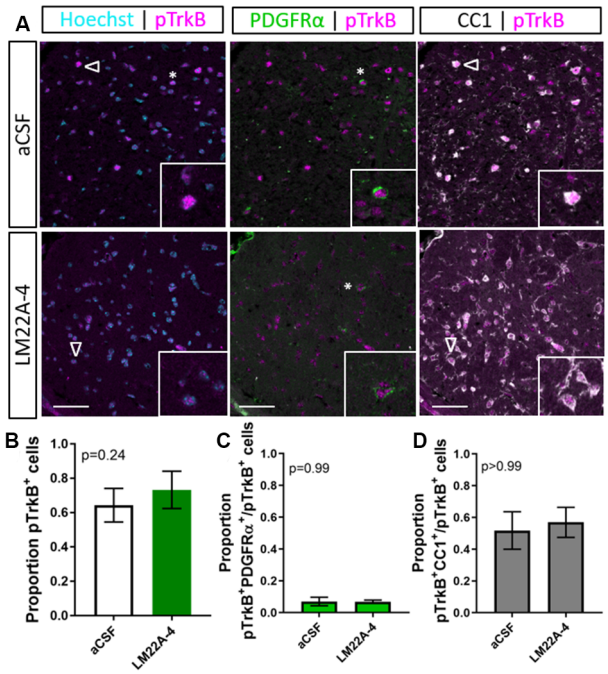

FIGURE 6 | TrkB phosphorylation with LM22A-4 treatment does not increase in the corpus callosi of mice with oligodendroglial TrkB deleted. **(A)** Representative micrographs of pTrkB^{S478}-PDGFRα-CC1 immunostaining in the corpus callosum of CNPaseCre$^{+/-}$ × TrkB$^{fl/fl}$ mice treated with LM22A-4 or aCSF vehicle (sagittal plane, scale bar = 20 μm). **(B)** Proportion of pTrkB^{s478+} cells was unchanged (p = 0.24) in oligodendroglial TrkB knockout mice treated with LM22A-4 compared to aCSF vehicle. Similarly, **(C)** the proportions of pTrkB^{s478+} PDGFRα^{+} and **(D)** pTrkB^{s478+}CC1^{+} cells were not changed (p = 0.99, p > 0.99 respectively) in conditional knockout mice treated LM22A-4 compared to those that received aCSF vehicle. Unpaired t-test with equal variance, p < 0.05 considered significant, n = 3–4/group. Mean ± SD plotted. Six-weeks cuprizone feeding commenced at 8–10 weeks of age, tissue collected at 15–17 weeks of age.

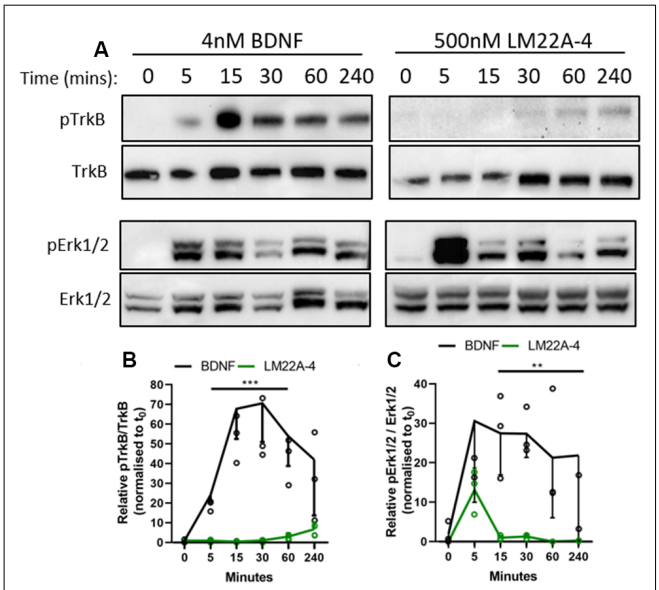

FIGURE 7 | Dynamics of TrkB signaling initiated by LM22A-4 do not mimic BDNF in a stably expressing TrkB isogenic HEK293 cell line. **(A)** Representative western blots of isogenic TrkB FlpIn HEK293 cell lysates treated with 4 nM BDNF or 500 nM LM22A-4 over a time course of 0, 5, 15, 30, 60 and 240 min. Densiometric analysis of western blots revealed that **(B)** BDNF elevated (p = 0.0003) levels of phosphorylated TrkB from 5 min until 240 min when it returned to similar levels elicited by LM22A-4 treatment, which did not increase over time (p = 0.10). **(C)** Levels of Erk1/2 phosphorylation increased (p = 0.002) after 5 min of BDNF treatment was sustained until 240 min, while phosphorylated Erk1/2 levels mediated by LM22A-4 treatment were similar to those evoked by BDNF at 5 min (p = 0.051), but elevated levels were not sustained. Mixed-effects model, fixed effects: treatment and time, random effects: plate, n = 3 independent cultures, p < 0.05 considered significant. Mean ± SD plotted. $^{**}p$ < 0.01, $^{***}p$ < 0.001.

that compared to BDNF treatment, which increased TrkB phosphorylation within 5 min (p = 0.012), LM22A-4 did not significantly increase levels of phosphorylated TrkB until 240 min of treatment (p = 0.02). The effects of LM22A-4 treatment on ERK1/2 phosphorylation where levels peaked at 5 min of treatment, and significantly declined compared to BDNF from 15 to 240 min (**Figure 7C**). Collectively, these data indicate that LM22A-4 does not elicit a signaling cascade that mimics typical BDNF-TrkB signaling, suggesting that pERK1/2 is upstream of TrkB phosphorylation in the pathway stimulated by LM22A-4.

DISCUSSION

There is an unmet clinical need for therapies that promote myelin repair to halt disease progression in MS. Here, we have shown that targeting oligodendroglial TrkB activation during remyelination increases post-mitotic oligodendrocyte density and myelin sheath thickness. By comparing TDP6, a structural peptide mimic of the Loop 2 region of BDNF, and LM22A-4, a small molecule TrkB agonist we have identified that while both promote myelin repair, they exert disparate effects upon OPCs and intermediate oligodendroglial populations. The effects of both TDP6 and LM22A-4 are dependent on the expression of oligodendroglial TrkB, indicating that while these two molecules putatively activate the same receptor, they may result in biased or differential signaling within oligodendroglia, as indicated by the differences in remyelination profile and progression of oligodendrocyte differentiation. This may reflect our *in vitro* analysis comparing the effect of LM22A-4 and BDNF upon TrkB and ERK1/2 phosphorylation which demonstrates that LM22A-4 activates BDNF-TrkB signaling pathways with substantially different kinetics and magnitude, compared to BDNF. Importantly, use of the oligodendroglial TrkB knockout mice to test its therapeutic efficacy provides the first *in vivo* genetic evidence that LM22A-4 action requires the presence of TrkB, although our data suggests that the mode of TrkB activation may differ to what was previously appreciated.

For decades the therapeutic promise of BDNF-TrkB signaling as a treatment for neurodegenerative and demyelinating conditions has been recognized (McTigue et al., 1998; Longo and Massa, 2013; Fletcher et al., 2018b). However, the poor

pharmacokinetic properties of BDNF have led to focused development of BDNF mimetics and small molecule TrkB agonists, including TDP6 and LM22A-4 among others (Longo and Massa, 2013; Boltaev et al., 2017). Previously, we showed that the structural BDNF-mimetic TDP6 enhances myelin repair, increasing the proportion of axons remyelinated, and density of post-mitotic oligodendrocytes compared to treatment with the vehicle and BDNF (Fletcher et al., 2018b). We found that LM22A-4 increased oligodendroglial density to a greater degree than TDP6, but instead of solely affecting maturing cells, LM22A-4 also increased OPC density. Both these effects were dependent on oligodendroglial TrkB expression. This raises the ongoing, unresolved question of whether oligodendroglial TrkB signaling exerts a direct influence on oligodendroglial proliferation and survival during remyelination, in addition to its well-established pro-differentiation effect (Xiao et al., 2011; Goebbels et al., 2017; Fletcher et al., 2018b). Previous studies in the BDNF heterozygous global knockout mice showed that oligodendroglial populations are sensitive to low BDNF levels during cuprizone demyelination, with reduced proliferating OPCs and subsequently differentiated oligodendrocytes (VonDran et al., 2011; Tsiperson et al., 2015). This appears to contrast our observations, where exogenous BDNF or TDP6 exerted no effect on the density or proliferative fraction of OPCs during remyelination after cuprizone (Fletcher et al., 2018b). The different observations between these two distinct experimental approaches may ultimately reflect context, wherein oligodendroglia subjected to a lifetime of BDNF haploinsufficiency simply behave differently. It is also unclear whether the increase in OPCs and intermediate oligodendroglia mediated by LM22A-4 provides a greater benefit towards myelin repair than the increase in post-mitotic oligodendroglia mediated by TDP6. To answer this, long-term follow up by labeling proliferating cells or inducing membrane-bound fluorescent reporter expression at the onset of treatment is required. Regardless, the survival and integration of immature oligodendroglia to the myelinating population over extended time-periods is a critical question in evaluating the efficacy of all potential remyelinating therapies.

The selective influence that LM22A-4 exerted upon OPCs remains to be explained. The doses used for TDP6 and LM22A-4 were determined from reported concentrations required for these compounds to mimic the neurotrophic activity of BDNF in *in vitro* myelinating co-culture or neuronal survival assays (O'Leary and Hughes, 2003; Massa et al., 2010; Wong et al., 2014). TDP6, like BDNF, demonstrates a strong signaling bias for MAPK/ERK in oligodendrocytes (Du et al., 2006; Xiao et al., 2011; Wong et al., 2014). In contrast, a recent report in a rat traumatic epileptogenesis model indicates LM22A-4 may demonstrate bias towards PI3K/Akt signaling (Gu et al., 2018). The PI3K/Akt and MAPK/ERK signaling pathways are known to act independently and cooperatively in oligodendrocytes to regulate distinct stages of oligodendrocyte myelination (Dai et al., 2014; Ishii et al., 2019) and PI3K/Akt signaling has been identified as necessary for OPC survival *in vitro* (Ebner et al., 2000; Ness et al., 2002). The potential signal bias towards PI3K/Akt over MAPK/ERK may explain why LM22A-4 elicited an increase in OPCs, as well as the anticipated increase in post-mitotic oligodendrocyte densities.

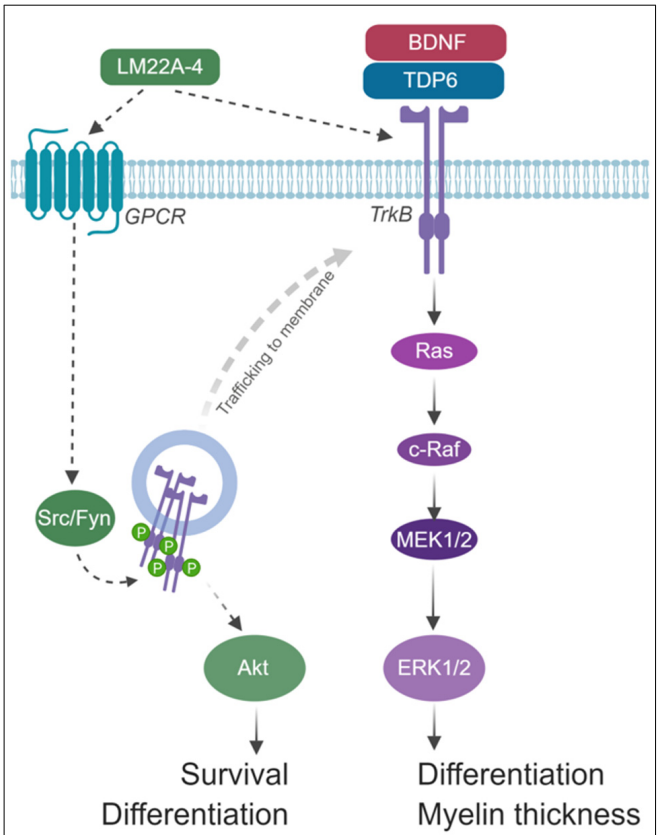

FIGURE 8 | Schematic of hypothesized mode of action for LM22A-4 in promoting remyelination. LM22A-4 acts as a ligand to directly activate an unidentified G-protein coupled receptor (GPCR), which initiates Src-family kinase, most likely Fyn, activation. Src-family members regulate the phosphorylation of Trk receptors on intracellular membranes, initiating Trk-specific signaling potentially biased towards PI3K/Akt, which regulates oligodendrocyte survival and differentiation. Activated Trk receptors may subsequently be trafficked to the cell membrane to initiate typical Trk signaling. Figure made in © BioRender—biorender.com).

Both TDP6 and LM22A-4 infusion increased myelin sheath thickness in a manner dependent on oligodendroglial TrkB expression, consistent with the demonstrated effects of TrkB signaling *via* MAPK/ERK in oligodendrocytes to promote myelin sheath growth (Ishii et al., 2012, 2016). It also confirms our previous findings where infusion of exogenous BDNF or TDP6 increased myelin sheath thickness during remyelination (Fletcher et al., 2018b). Intriguingly, LM22A-4 exerted its effect on myelin thickness almost selectively on smaller diameter axons, which was completely abrogated in the oligodendroglial TrkB knockout mice. This contrasts with TDP6, and our previous findings with BDNF (Fletcher et al., 2018b), where myelin sheath thickness increased across all axonal diameters. However, it echoes our findings that TDP6 treatment in oligodendroglial TrkB knockout mice resulted in increased

myelination of small diameter axons during myelin repair (Fletcher et al., 2018b). It is tempting to speculate that small diameter axons are exerting a selective effect in both instances, but it is critical to distinguish growth in myelin thickness as an oligodendrocyte-driven function (Ishii et al., 2012). To date, a direct axonal signal that instructs oligodendrocytes to increase myelin thickness has not been identified, although the number of myelin wraps is known to increase as circuit activity increases with the maturing brain (Sturrock, 1980). In contrast, initiation of myelination, particularly for small diameter axons is known to require axonally derived signals (Gautier et al., 2015; Bechler et al., 2018), suggestive that TrkB expression by neurons may potentially confer a pro-myelinating signal to oligodendrocytes.

Concerningly, a recent report indicates that LM22A-4 does not activate TrkB at all (Boltaev et al., 2017). The fact that LM22A-4 failed to promote remyelination and increase oligodendroglial density in the oligodendrocyte TrkB knockout mice clearly indicates TrkB is necessary for the action of LM22A-4 and this is the first *in vivo* genetic evidence that LM22A-4 requires TrkB for activity. Although LM22A-4 may exert its effect through direct activity on TrkB, our data and findings by Boltaev et al. (2017) raise the possibility that LM22A-4 is exerting an indirect effect, potentially by increasing BDNF or NT-4 expression in the demyelinated lesion. This is a possibility we certainly cannot discount. It is important to note, however, that Boltaev et al. (2017) used a model system of cortical cultures to assess TrkB activation. Our observations in the 293-TrkB cells identified that LM22A-4 produced a spike of ERK1/2 phosphorylation after 5 min independent of any evidence of TrkB phosphorylation, but then identified TrkB phosphorylation after 4 h of LM22A-4 exposure. This supports a model in which TrkB activation is an event downstream of LM22A-4 activity at another receptor, although this also contrasts with findings from the original report wherein TrkB phosphorylation was detected in cultured hippocampal neurons within 60 min (Massa et al., 2010). Notably, ERK1/2 phosphorylation was detected in these cultures within 10 min (Massa et al., 2010). Whilst 293-TrkB cells and the two types of neuronal cultures are contextually quite different cells, Boltaev et al. (2017) limited LM22A-4 treatment to 2 h, potentially missing this delayed response. Such a delay in Trk phosphorylation has been reported previously (Lee and Chao, 2001) and is a pattern consistent with Trk-receptor transactivation.

The extended 4-h timeframe required to detect TrkB phosphorylation following LM22A-4 treatment *in vitro* is consistent with Trk-receptor transactivation, where it can take up to 6 h to elicit detectable Trk receptor phosphorylation, and results in signal bias towards Akt (Lee and Chao, 2001). We propose that LM22A-4 mediates its increase in OPC density during remyelination by Trk-transactivation potentially *via* GPCRs (**Figure 8**). Multiple GPCRs are known to be critical for OPC proliferation and regulating OPC differentiation towards myelination (Chen et al., 2009; Giera et al., 2015; Yang et al., 2016). In our model, we hypothesize that LM22A-4 acts *via* unidentified GPCRs which engage Src-family kinases, most likely Fyn in oligodendrocytes; this results in intracellular phosphorylation of TrkB receptors confined in transport vesicles and not expressed at the cell surface (**Figure 8**). This could be tested *in vitro* with LM22A-4 treated TrkB-293 cells or primary oligodendrocytes co-treated with Src inhibitors. Full understanding of the mode of action for LM22A-4 is warranted in order to optimize its therapeutic potential. This is particularly important for assessing the potential for off-target effects. It also has implications for the use of LM22A-4 as a tool for probing neurotrophin biology as the conclusions drawn from the assumption it elicits a typical BDNF-TrkB signaling cascade may be misleading. Overall, our hypothesized mode of action for LM22A-4 is parsimonious with known roles of Src-family kinases/Fyn in Trk-transactivation (Rajagopal et al., 2004; Rajagopal and Chao, 2006) and oligodendroglial function (Sperber et al., 2001; Colognato et al., 2004; Peckham et al., 2016), as well as our current findings of delayed TrkB phosphorylation *in vitro* and TrkB-dependent remyelination outcomes *in vivo*.

We have demonstrated targeting TrkB activation on oligodendrocytes either *via* a peptide mimetic or small molecule partial agonist, enhances myelin repair after a central demyelinating insult by increasing the density of post-mitotic oligodendrocytes and increasing myelin sheath thickness. By directly comparing these two strategies we have also provided necessary insight on the recent controversies about the fidelity of small molecule TrkB agonists. Through *in vivo* genetic deletion of oligodendroglial TrkB, we have shown LM22A-4 is dependent on TrkB receptor expression for its effects on increasing oligodendroglial populations and myelin thickness, while our *in vitro* studies have shown that LM22A-4 acts in a delayed manner, potentially through GPCR-mediated TrkB transactivation. Overall, our results further verify that targeting TrkB with small molecule mimetics is a viable therapeutic strategy to promote myelin repair in central demyelinating diseases, such as MS.

DATA AVAILABILITY

The raw data supporting the conclusions of this manuscript will be made available by the authors, without undue reservation, to any qualified researcher.

ETHICS STATEMENT

Animal Subjects

The animal study was reviewed and approved by The Florey Animal Ethics Committee, Florey Institute of Neuroscience and Mental Health.

AUTHOR CONTRIBUTIONS

JF, JX and SM conceived and designed the study. JF, HN, RW, AP and SM performed the experiments. JF, HN and SF analyzed the data. SF provided reagents and analytic tools. JF wrote the first draft. JF, HN, SF, JX and SM reviewed and revised

the manuscript. All authors read, revised and approved the submitted version.

FUNDING

This work was supported by Australian National Health and Medical Research Council (NHMRC) Project Grants to JX (APP1058647) and SM (APP1105108). SF is an Australian Research Council Future Fellow. JF was supported by Multiple Sclerosis Research Australia (14-056) and Melbourne Neuroscience Institute (2018) Research Fellowships.

ACKNOWLEDGMENTS

We acknowledge the staff and facilities of the Biological Optical Microscope Platform, The University of Melbourne and the Centre for Advanced Microscopy and Histology, Peter MacCallum Centre.

SUPPLEMENTARY MATERIAL

The Supplementary Material for this article can be found online at: https://www.frontiersin.org/articles/10.3389/fnmol.2019.00205/full#supplementary-material

REFERENCES

Bechler, M. E., Swire, M., and Ffrench-Constant, C. (2018). Intrinsic and adaptive myelincation-a sequential mechanism for smart wiring in the brain. *Dev. Neurobiol.* 78, 68–79. doi: 10.1002/dneu.22518

Boltaev, U., Meyer, Y., Tolibzoda, F., Jacques, T., Gassaway, M., Xu, Q., et al. (2017). Multiplex quantitative assays indicate a need for re-evaluating reported small-molecule TrkB agonists. *Sci. Signal.* 10:eaal1670. doi: 10.1126/scisignal.aal1670

Chao, M. V. (2003). Neurotrophins and their receptors: a convergence point for many signalling pathways. *Nat. Rev. Neurosci.* 4, 299–309. doi: 10.1038/nrn1078

Chen, Y., Wu, H., Wang, S., Koito, H., Li, J., Ye, F., et al. (2009). The oligodendrocyte-specific G protein-coupled receptor GPR17 is a cell-intrinsic timer of myelination. *Nat. Neurosci.* 12, 1398–1406. doi: 10.1038/nn.2410

Colognato, H., Ramachandrappa, S., Olsen, I. M., and ffrench-Constant, C. (2004). Integrins direct Src family kinases to regulate distinct phases of oligodendrocyte development. *J. Cell Biol.* 167, 365–375. doi: 10.1083/jcb.200404076

Dai, J., Bercury, K. K., and Macklin, W. B. (2014). Interaction of mTOR and Erk1/2 signaling to regulate oligodendrocyte differentiation. *Glia* 62, 2096–2109. doi: 10.1002/glia.22729

Du, Y., Fischer, T. Z., Lee, L. N., Lercher, L. D., and Dreyfus, C. F. (2003). Regionally specific effects of BDNF on oligodendrocytes. *Dev. Neurosci.* 25, 2–4. Available online at: http://search.proquest.com.ezp.lib.unimelb.edu.au/docview/221154098?accountid=12372. Accessed April 3, 2017.

Du, Y., Lercher, L. D., Zhou, R., and Dreyfus, C. F. (2006). Mitogen-activated protein kinase pathway mediates effects of brain-derived neurotrophic factor on differentiation of basal forebrain oligodendrocytes. *J. Neurosci. Res.* 84, 1692–1702. doi: 10.1002/jnr.21080

Ebner, S., Dunbar, M., and McKinnon, R. D. (2000). Distinct roles for PI3K in proliferation and survival of oligodendrocyte progenitor cells. *J. Neurosci. Res.* 62, 336–345. doi: 10.1002/1097-4547(20001101)62:3<336::AID-JNR3>3.0.CO;2-H

Fletcher, J., Murray, S. S., and Xiao, J. (2018a). Brain-derived neurotrophic factor in central nervous system myelination: a new mechanism to promote myelin plasticity and repair. *Int. J. Mol. Sci.* 19:E4131. doi: 10.3390/ijms19124131

Fletcher, J. L., Wood, R. J., Nguyen, J., Norman, E. M. L., Jun, C. M. K., Prawdiuk, A. R., et al. (2018b). Targeting TrkB with a brain-derived neurotrophic factor mimetic promotes myelin repair in the brain. *J. Neurosci.* 38, 7088–7099. doi: 10.1523/JNEUROSCI.0487-18.2018

Gautier, H. O. B., Evans, K. A., Volbracht, K., James, R., Sitnikov, S., Lundgaard, I., et al. (2015). Neuronal activity regulates remyelination *via* glutamate signalling to oligodendrocyte progenitors. *Nat. Commun.* 6:8518. doi: 10.1038/ncomms9518

Giera, S., Deng, Y., Luo, R., Ackerman, S. D., Mogha, A., Monk, K. R., et al. (2015). The adhesion G protein-coupled receptor GPR56 is a cell-autonomous regulator of oligodendrocyte development. *Nat. Commun.* 6:6121. doi: 10.1038/ncomms7121

Goebbels, S., Wieser, G. L., Pieper, A., Spitzer, S., Weege, B., Yan, K., et al. (2017). A neuronal PI(3,4,5)P3-dependent program of oligodendrocyte precursor recruitment and myelination. *Nat. Neurosci.* 20, 10–15. doi: 10.1038/nn.4425

Gu, F., Parada, I., Yang, T., Longo, F. M., and Prince, D. A. (2018). Partial TrkB receptor activation suppresses cortical epileptogenesis through actions on parvalbumin interneurons. *Neurobiol. Dis.* 113, 45–58. doi: 10.1016/j.nbd.2018.01.018

Han, J., Pollak, J., Yang, T., Siddiqui, M. R., Doyle, K. P., Taravosh-Lahn, K., et al. (2012). Delayed administration of a small molecule tropomyosin-related kinase B ligand promotes recovery after hypoxic-ischemic stroke. *Stroke* 43, 1918–1924. doi: 10.1161/STROKEAHA.111.641878

Ishii, A., Furusho, M., Dupree, J. L., and Bansal, R. (2016). Strength of ERK1/2 MAPK activation determines its effect on myelin and axonal integrity in the adult CNS. *J. Neurosci.* 36, 6471–6487. doi: 10.1523/JNEUROSCI.0299-16.2016

Ishii, A., Furusho, M., Macklin, W., and Bansal, R. (2019). Independent and cooperative roles of the Mek/ERK1/2-MAPK and PI3K/Akt/mTOR pathways during developmental myelination and in adulthood. *Glia* 67, 1277–1295. doi: 10.1002/glia.23602

Ishii, A., Fyffe-Maricich, S. L., Furusho, M., Miller, R. H., and Bansal, R. (2012). ERK1/ERK2 MAPK signaling is required to increase myelin thickness independent of oligodendrocyte differentiation and initiation of myelination. *J. Neurosci.* 32, 8855–8864. doi: 10.1523/JNEUROSCI.0137-12.2012

Lappe-Siefke, C., Goebbels, S., Gravel, M., Nicksch, E., Lee, J., Braun, P., et al. (2003). Disruption of Cnp1 uncouples oligodendroglial functions in axonal support and myelination. *Nat. Genet.* 33, 366–374. doi: 10.1038/ng1095

Lee, F. S., and Chao, M. V. (2001). Activation of Trk neurotrophin receptors in the absence of neurotrophins. *Proc. Natl. Acad. Sci. U S A* 98, 3555–3560. doi: 10.1073/pnas.061020198

Longo, F. M., and Massa, S. M. (2013). Small-molecule modulation of neurotrophin receptors: a strategy for the treatment of neurological disease. *Nat. Rev. Drug Discov.* 12, 507–525. doi: 10.1038/nrd4024

Luikart, B. W., Nef, S., Virmani, T., Lush, M. E., Liu, Y., Kavalali, E. T., et al. (2005). TrkB has a cell-autonomous role in the establishment of hippocampal Schaffer collateral synapses. *J. Neurosci.* 25, 3774–3786. doi: 10.1523/JNEUROSCI.0041-05.2005

Massa, S. M., Yang, T., Xie, Y., Shi, J., Bilgen, M., Joyce, J. N., et al. (2010). Small molecule BDNF mimetics activate TrkB signaling and prevent neuronal degeneration in rodents. *J. Clin. Invest.* 120, 1774–1785. doi: 10.1172/JCI41356

McTigue, D. M., Horner, P. J., Stokes, B. T., and Gage, F. H. (1998). Neurotrophin-3 and brain-derived neurotrophic factor induce oligodendrocyte proliferation and myelination of regenerating axons in the contused adult rat spinal cord. *J. Neurosci.* 18, 5354–5365. doi: 10.1523/jneurosci.18-14-05354.1998

Ness, J. K., Mitchell, N. E., and Wood, T. L. (2002). IGF-I and NT-3 signaling pathways in developing oligodendrocytes: differential regulation and activation of receptors and the downstream effector Akt. *Dev. Neurosci.* 24, 437–445. doi: 10.1159/000069050

O'Leary, P. D., and Hughes, R. A. (2003). Design of potent peptide mimetics of brain-derived neurotrophic factor. *J. Biol. Chem.* 278, 25738–25744. doi: 10.1074/jbc.M303209200

Peckham, H., Giuffrida, L., Wood, R., Gonsalvez, D., Ferner, A., Kilpatrick, T. J., et al. (2016). Fyn is an intermediate kinase that BDNF utilizes to promote oligodendrocyte myelination. *Glia* 64, 255–269. doi: 10.1002/glia.22927

Poduslo, J. F., and Curran, G. L. (1996). Permeability at the blood-brain and blood-nerve barriers of the neurotrophic factors: NGF, CNTF, NT-3, BDNF. *Mol. Brain Res.* 36, 280–286. doi: 10.1016/0169-328x(95)00250-v

Rajagopal, R., and Chao, M. V. (2006). A role for Fyn in Trk receptor transactivation by G-protein-coupled receptor signaling. *Mol. Cell. Neurosci.* 33, 36–46. doi: 10.1016/j.mcn.2006.06.002

Rajagopal, R., Chen, Z.-Y., Lee, F. S., and Chao, M. V. (2004). Transactivation of Trk neurotrophin receptors by G-protein-coupled receptor ligands occurs on intracellular membranes. *J. Neurosci.* 24, 6650–6658. doi: 10.1523/JNEUROSCI.0010-04.2004

Schmid, D. A., Yang, T., Ogier, M., Adams, I., Mirakhur, Y., Wang, Q., et al. (2012). A TrkB small molecule partial agonist rescues TrkB phosphorylation deficits and improves respiratory function in a mouse model of Rett syndrome. *J. Neurosci.* 32, 1803–1810. doi: 10.1523/JNEUROSCI.0865-11.2012

Simmons, D. A., Belichenko, N. P., Yang, T., Condon, C., Monbureau, M., Shamloo, M., et al. (2013). A small molecule TrkB ligand reduces motor impairment and neuropathology in R6/2 and BACHD mouse models of Huntington's disease. *J. Neurosci.* 33, 18712–18727. doi: 10.1523/JNEUROSCI.1310-13.2013

Sperber, B. R., Boyle-Walsh, E. A., Engleka, M. J., Gadue, P., Peterson, A. C., Stein, P. L., et al. (2001). A unique role for Fyn in CNS myelination. *J. Neurosci.* 21, 2039–2047. doi: 10.1523/jneurosci.21-06-02039.2001

Sturrock, R. R. (1980). Myelination of the mouse corpus callosum. *Neuropathol. Appl. Neurobiol.* 6, 415–420. doi: 10.1111/j.1365-2990.1980.tb00219.x

Tsiperson, V., Huang, Y., Bagayogo, I., Song, Y., VonDran, M. W., DiCicco-Bloom, E., et al. (2015). Brain-derived neurotrophic factor deficiency restricts proliferation of oligodendrocyte progenitors following cuprizone-induced demyelination. *ASN Neuro* 7:1759091414566878. doi: 10.1177/1759091414566878

VonDran, M. W., Singh, H., Honeywell, J. Z., and Dreyfus, C. F. (2011). Levels of BDNF impact oligodendrocyte lineage cells following a cuprizone lesion. *J. Neurosci.* 31, 14182–14190. doi: 10.1523/JNEUROSCI.6595-10.2011

Wallin, M. T., Culpepper, W. J., Campbell, J. D., Nelson, L. M., Langer-Gould, A., Marrie, R. A., et al. (2019). The prevalence of MS in the United States. *Neurology* 92, e1029–e1040. doi: 10.1212/WNL.0000000000007044

Wong, A. W., Giuffrida, L., Wood, R., Peckham, H., Gonsalvez, D., Murray, S. S., et al. (2014). TDP6, a brain-derived neurotrophic factor-based TrkB peptide mimetic, promotes oligodendrocyte myelination. *Mol. Cell. Neurosci.* 63, 132–140. doi: 10.1016/j.mcn.2014.10.002

Wong, A. W., Xiao, J., Kemper, D., Kilpatrick, T. J., and Murray, S. S. (2013). Oligodendroglial expression of TrkB independently regulates myelination and progenitor cell proliferation. *J. Neurosci.* 33, 4947–4957. doi: 10.1523/JNEUROSCI.3990-12.2013

Xiao, J., Wong, A. W., Willingham, M. M., Van Den Buuse, M., Kilpatrick, T. J., and Murray, S. S. (2011). Brain-derived neurotrophic factor promotes central nervous system myelination *via* a direct effect upon oligodendrocytes. *Neurosignals* 18, 186–202. doi: 10.1159/000323170

Yang, H.-J., Vainshtein, A., Maik-Rachline, G., and Peles, E. (2016). G protein-coupled receptor 37 is a negative regulator of oligodendrocyte differentiation and myelination. *Nat. Commun.* 7:10884. doi: 10.1038/ncomms10884

Conflict of Interest Statement: The authors declare that the research was conducted in the absence of any commercial or financial relationships that could be construed as a potential conflict of interest.

Copyright © 2019 Nguyen, Wood, Prawdiuk, Furness, Xiao, Murray and Fletcher. This is an open-access article distributed under the terms of the Creative Commons Attribution License (CC BY). The use, distribution or reproduction in other forums is permitted, provided the original author(s) and the copyright owner(s) are credited and that the original publication in this journal is cited, in accordance with accepted academic practice. No use, distribution or reproduction is permitted which does not comply with these terms.

frontiers in Molecular Neuroscience

REVIEW
published: 27 August 2019
doi: 10.3389/fnmol.2019.00204

New Insights Into Cholinergic Neuron Diversity

*Noorya Yasmin Ahmed, Rhys Knowles and Nathalie Dehorter**

Eccles Institute of Neuroscience, John Curtin School of Medical Research, Australian National University, Canberra, ACT, Australia

Cholinergic neurons comprise a small population of cells in the striatum but have fundamental roles in fine tuning brain function, and in the etiology of neurological and psychiatric disorders such as Parkinson's disease (PD) or schizophrenia. The process of developmental cell specification underlying neuronal identity and function is an area of great current interest. There has been significant progress in identifying the developmental origins, commonalities in molecular markers, and physiological properties of the cholinergic neurons. Currently, we are aware of a number of key factors that promote cholinergic fate during development. However, the extent of cholinergic cell diversity is still largely underestimated. New insights into the biological basis of their specification indicate that cholinergic neurons may be far more diverse than previously thought. This review article, highlights the physiological features and the synaptic properties that segregate cholinergic cell subtypes. It provides an accurate picture of cholinergic cell diversity underlying their organization and function in neuronal networks. This review article, also discusses current challenges in deciphering the logic of the cholinergic cell heterogeneity that plays a fundamental role in the control of neural processes in health and disease.

Keywords: interneurons, acetylcholine, diversity, striatum, development

OPEN ACCESS

Edited by:
Christopher Alan Reid, Florey Institute of Neuroscience and Mental Health, Australia

Reviewed by:
Allan T. Gulledge, Dartmouth College, United States
Juan Mena-Segovia, Rutgers University, The State University of New Jersey, United States

****Correspondence:***
Nathalie Dehorter
nathalie.dehorter@anu.edu.au

Received: *19 May 2019*
Accepted: *05 August 2019*
Published: *27 August 2019*

Citation:
Ahmed NY, Knowles R and Dehorter N (2019) New Insights Into Cholinergic Neuron Diversity. Front. Mol. Neurosci. 12:204. doi: 10.3389/fnmol.2019.00204

INTRODUCTION

Cholinergic neurons are highly integral for fine tuning brain function (for review, see Bonsi et al., 2011) and maintaining the excitation-inhibition balance within neural circuits (Zhou et al., 2017). Although cholinergic neurons are distributed in various discrete regions, they can project to almost all parts of the brain (Dautan et al., 2016). These cells release acetylcholine (ACh), which plays a crucial role in the regulation of sensory function (Minces et al., 2017; for review, see Ballinger et al., 2016), and actions (Bradfield et al., 2013; Markowitz et al., 2018). ACh also attunes motivation (Marche et al., 2017), behavioral flexibility (Aoki et al., 2015, 2018; Okada et al., 2018), and associative learning (Atallah et al., 2014; for review, see Yamanaka et al., 2018). A major population is found in the striatum, which contains the highest levels of ACh in the brain (Macintosh, 1941; for review, see Lim et al., 2014). Cholinergic neurons are also found in the basal forebrain, which is classically segregated into four main regions: the Medial Septal Nucleus (MSN), the vertical and horizontal limbs of the Diagonal Band of Broca (DB), and the Nucleus Basalis (NB) of Meynert. Within the brainstem, cholinergic neurons are found in the

pedunculopontine nucleus (PPN) and the laterodorsal tegmentum (for review, see Mesulam et al., 1983). In addition to these groups, smaller cholinergic populations are located in the medial habenula (López et al., 2019), parabigeminal nucleus (Mufson et al., 1986), cerebral cortex (von Engelhardt et al., 2007), hypothalamus (Jeong et al., 2016), and olfactory bulb (Krosnowski et al., 2012).

It has been shown that changes in the activity of striatal cholinergic interneurons (CINs) play a critical role in motor control (Bordia et al., 2016), as well as behavioral flexibility (Okada et al., 2014), memory (Albert-Gascó et al., 2017), and social behavior (Martos et al., 2017). Alterations to the cholinergic system can lead to severe dysfunction of neuronal circuits (**Figure 1A**). For example, cholinergic neuron loss from the forebrain causes cognitive deficits associated with Parkinson's (PD; for review, see Pepeu and Grazia Giovannini, 2017) and Alzheimer's Disease (AD; for review, see Hampel et al., 2018). In the striatum, a decrease in cholinergic markers is a phenotypic consequence of Parkinson's (Maurice et al., 2015; Ztaou et al., 2016) and Huntington's diseases (HD; Smith et al., 2006). Cholinergic neuron populations are also linked to neuropsychiatric and neurodevelopmental pathologies. For instance, the activity of CINs through the expression and function of the hyperpolarization-activated cyclic nucleotide-gated channel 2 (HCN2) is decreased in the Nucleus Accumbens (NAc) in stress and depression (Cheng et al., 2019). There is also an established link between the cholinergic system and autism spectrum disorders, whereby autism is associated with decreased cholinergic tone and reduced neurite arborization (Nagy et al., 2017). Genetic alterations of the choline transporter cause attention deficit hyperactivity disorder (ADHD) and result in the promotion of ACh synthesis (English et al., 2009). Moreover, elevating ACh levels can relieve cognitive and social symptoms in a mouse model of autism (Karvat and Kimchi, 2014). Aberrant cholinergic signaling has also been reported in schizophrenia (for review, see Terry, 2008; Higley and Picciotto, 2014). However, there is still much debate over the mechanisms underlying cholinergic dysfunction in this disease (for review, see Hyde and Crook, 2001; Scarr et al., 2013). Considering that cholinergic dysfunction is associated with a diverse group of diseases, it is important to understand the functional intricacies of these cells.

Complex and dense cholinergic innervation is achieved in the brain from two categories of cholinergic neurons: the CINs—which synapse locally within a brain structure, and projecting cholinergic neurons—which send their axons to other structures (for review, see Allaway and Machold, 2017). CINs are present in a number of structures where they are important for local modulation. For example, cortical CINs, known for their expression of Vasoactive Intestinal Peptide (VIP), comprise approximately 12% of cortical inhibitory neurons (von Engelhardt et al., 2007; for review, see Rudy et al., 2011). They are primarily bi-tufted and found in layer 2/3 of the cortex (von Engelhardt et al., 2007). However, bipolar and multipolar CINs are also present and populate lower cortical layers (Li et al., 2018). On the contrary, striatal CINs are much larger, with extensive axonal fields (for review, see Lim et al., 2014)

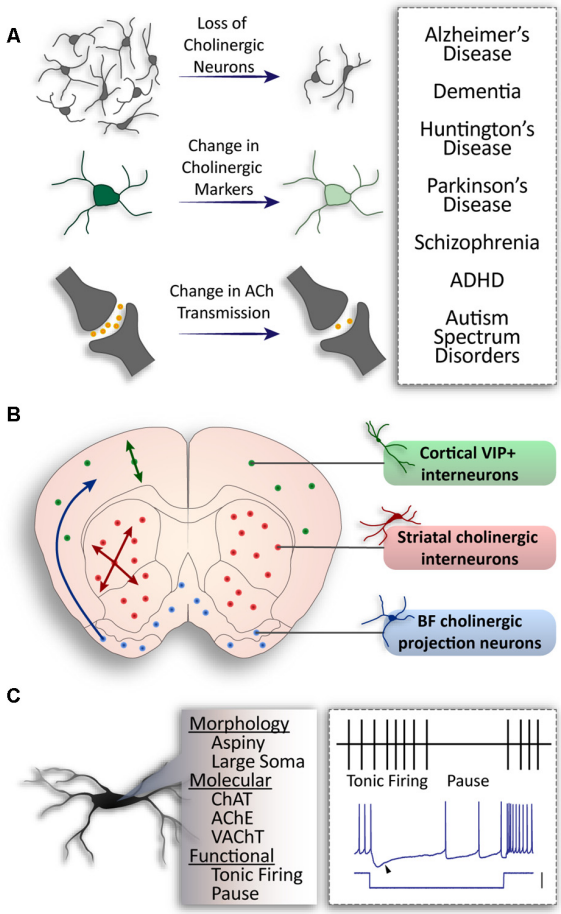

FIGURE 1 | General populations of cholinergic neurons and alterations in disease. **(A)** Pathologies associated with cholinergic alteration. **(B)** Three major populations of cholinergic neurons in the brain. Basal forebrain neurons project to higher structures (blue); striatal interneurons project locally throughout the striatum (red); cortical interneurons co-expressing Vasoactive Intestinal Peptide (VIP) and Choline Acetyltransferase (ChAT) project within cortical layers (green). **(C)** Common properties of cholinergic neurons: aspiny dendrites and a large soma; expression of ChAT, Acetylcholine Esterase (AChE), Vesicular Acetylcholine Transporter (VAChT) expression; tonic firing patterns with a distinct pause *in vivo*, and a sag in membrane voltage (arrow) in response to hyperpolarizing current (scale: 100 pA).

to control the output of the striatal projection neurons (SPNs). Projecting cholinergic neurons are found in the basal forebrain, hypothalamus and medial habenula (Li et al., 2018) and send long-range axonal projections to various cortical and subcortical regions (**Figure 1B**). Moreover, cholinergic neurons found in the PPN project to the basal ganglia, thalamus, and hypothalamus (for review, see Mena-Segovia and Bolam, 2017; French and Muthusamy, 2018).

In addition to their different projection patterns, cholinergic neurons can also be characterized by their firing properties. PPN cholinergic neurons display phasic and short-latency responses and provide a fast and transient response to sensory events (Petzold et al., 2015), whereas CINs of the striatum switch from

tonic firing to a transient pause (**Figure 1C**; Shimo and Hikosaka, 2001; Atallah et al., 2014). CINs precisely control striatal output (Goldberg and Reynolds, 2011; Faust et al., 2015; Zucca et al., 2018) by inhibiting the firing of SPNs *via* neuropeptide-Y expressing inhibitory interneurons (English et al., 2011). They also drive spontaneous activation of SPNs *via* muscarinic (Mamaligas and Ford, 2016) and glutamatergic transmission (Higley et al., 2011). The spontaneous firing patterns of striatal CINs are sculpted by the widely studied delayed rectifier (IKr) and hyperpolarized activated current (Ih; Oswald et al., 2009). Calcium-dependent potassium conductances also give rise to prominent afterhyperpolarizations, and striatal CIN firing includes two periodic patterns: single spiking and rhythmic bursting (Bennett et al., 2000; Goldberg and Wilson, 2005; **Figure 1C**).

In addition to physiological characteristics, cholinergic neurons share genetic commonalities. The expression of choline acetyl-transferase (ChAT) and acetylcholine esterase (AChE) are markers of all cholinergic neurons, as they are involved in the synthesis and degradation of ACh respectively (Taylor and Brown, 1999). During development, they express common transcription factors that are conserved across neuronal populations. For instance, the homeobox-encoding Nkx2.1 transcription factor is expressed in many sites of neurogenesis within the developing brain such as the Medial Ganglionic Eminence (MGE), preoptic area (POA), septal neuroepithelium (SE). It has been shown that most cholinergic neurons arise from Nkx2.1^{+} progenitors (for review, see Allaway and Machold, 2017), and that cells expressing Nkx2.1 that upregulate the LIM homeobox transcription factors Islet-1 (Isl1) and Lhx8 become cholinergic (Zhao et al., 2003; Cho et al., 2014). As these transcription factors are expressed early during development, their co-expression is likely to be one of the earliest traits of cholinergic fated neurons (Fragkouli et al., 2009). Moreover, a loss of Nkx2.1 expression during development halts the maturation and specification of cholinergic cells (Sussel et al., 1999; Du et al., 2008).

Developmental cell specification is an area of great current interest for uncovering how neurons are able to integrate information in a highly complex neural circuit (Tasic et al., 2018; for review, see Fishell and Heintz, 2013). The interplay between the expression of specific genetic factors and neuronal activity are essential contributors to the establishment of cell identity (Dehorter et al., 2015; Jabaudon, 2017) and function (for review, see Yap and Greenberg, 2018). Therefore, the concept of specification leads to diversity among neuronal populations and acts as an important foundation for circuit formation and overall brain function (for review, see Breunig et al., 2011; Dehorter et al., 2017; Wamsley and Fishell, 2017). The cholinergic cell population was believed to be relatively homogenous, despite spanning across various brain regions. However, recent studies have shed light on the diversity within these populations, and the importance of cholinergic subpopulations for brain function. This review article highlights developmental origins of cholinergic neurons and explores recent evidence for genetic, morphological, and electrophysiological diversity of the CINs of the striatum.

GENETIC DIVERSITY OF CHOLINERGIC INTERNEURONS

Cholinergic Cell Diversity Arises From Their Developmental Origin

It is reasonable to expect that cholinergic neurons in a single structure would originate and migrate from a single developmental zone. However, VIP-positive interneurons in the cortex are the only cholinergic population thought to originate from a single developmental proliferative zone, the caudal ganglionic eminence (CGE; Vogt et al., 2014). Cholinergic neurons within a single structure can arise from multiple developmental origins (Nóbrega-Pereira et al., 2010), and conversely, these proliferative areas can also give rise to cholinergic neurons fated to multiple structures in the brain (Marin et al., 2000; Pombero et al., 2011; Magno et al., 2017; **Figure 2A**). Most basal forebrain cholinergic neurons originate from the MGE, POA (for review, see Ballinger et al., 2016), and SE (Magno et al., 2017). Furthermore, subsets of neurons in the diagonal band and NB originate from the ventral area of the pallial telencephalon (pallium), which is located adjacent to the pallium/subpallium border (Pombero et al., 2011; Ceci et al., 2012; **Figure 2A**). Similarly, striatal CINs originate from the MGE and POA (Marin et al., 2000; Fragkouli et al., 2009), as well as the SE (Magno et al., 2017). Therefore, to fully appreciate the diversity within cholinergic populations, their developmental origins must be considered. However, as many progenitor regions have genetically defined sub-domains (Flames et al., 2007), neurons originating in the same region may display further genetic diversity.

Cholinergic Cell Diversity Is Controlled by Genetic Factors

Combinatorial gene expression during early developmental stages can translate to diversity within the mature striatum (Flames et al., 2007). For example, the Dbx1 transcription factor defines a sub-domain of the POA which gives rise to a subset of cholinergic striatal interneurons (Gelman et al., 2011). Similarly, fibroblast growth factor 8 (Fgf8) and fibroblast growth factor 17 (Fgf17) expressing progenitors in the ventral MGE and ventral SE give rise to individual subsets of CINs in the striatum (Hoch et al., 2015a).

A number of studies have also investigated the effect of gene expression on cholinergic cell specification and identity. The transcription factors Lhx8 and Isl1 drive cholinergic identity in MGE/POA-derived neurons that are fated to populate the basal forebrain and striatum (Zhao et al., 2003; Cho et al., 2014). The ablation of either of these genes results in a loss of most cholinergic neurons in the NB, diagonal band and septum (Zhao et al., 2003; Mori et al., 2004; Elshatory and Gan, 2008; Cho et al., 2014). Moreover, it has been shown that Isl1 is required for the specification of a subset of Nkx2.1+/Lhx8+ interneurons, as Isl1 ablation leads to a ∼40% of the Nkx2.1-expressing cells in the striatum (Cho et al., 2014). This partial loss of cholinergic cells suggests that the basal forebrain and striatal neuroepithelium contain Lhx8/Isl1-independent cholinergic fated cells. While the

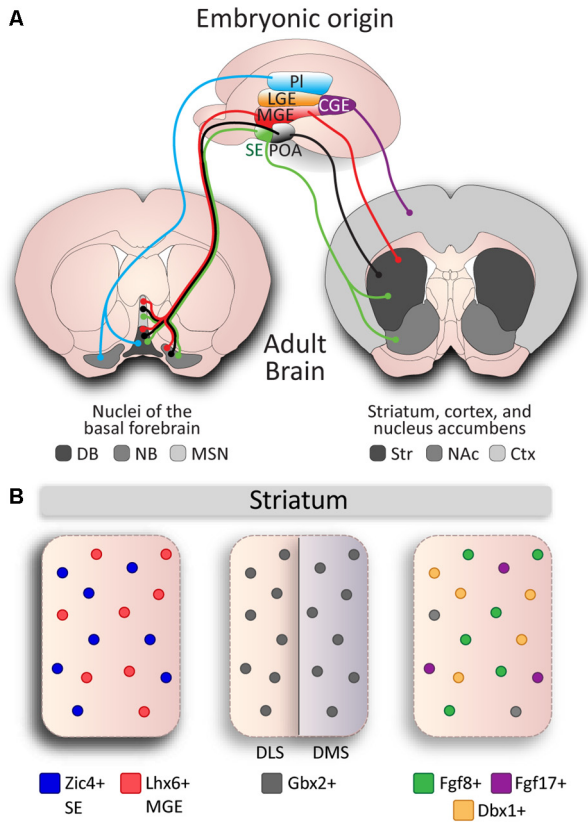

FIGURE 2 | Developmental diversity in cholinergic neurons. **(A)** Cholinergic neurons are derived from different embryonic structures. Proliferative zones of an E13.5 mouse brain embryo: Pallium (Pl), Medial Ganglionic Eminence (MGE), Lateral Ganglionic Eminence (LGE), Septal Epithelium (SE), Preoptic Area (POA), and Caudal Ganglionic Eminence (CGE) give rise to cholinergic neurons of different nuclei: Striatum (Str), Cerebral Cortex (Ctx), Nucleus Accumbens (NAc), and the Basal Forebrain: Nucleus Basalis (NB), Medial Septal Nucleus (MSN), Diagonal Band (DB). **(B)** Genetic diversity in cholinergic interneurons (CINs) in the striatum. Subsets of CINs express Zic4 (blue) and originate from the SE, and Lhx6 (red) and originate from the MGE. Gbx2 is expressed in almost all CINs and preferentially controls development of late-born CINs in the dorsomedial striatum (DMS), but not in early-born CINs in the dorsolateral striatum (DLS). MGE-derived Fgf8 (green) and Fgf17 (purple), and POA-derived Dbx1 (orange) mark three subgroups defined by genetic expression and reliant on developmental origin, but do not account for the entire CIN population (gray).

basal forebrain is divided into different nuclei, striatal CINs are spread throughout the striatum and were long considered as a single homogeneous population. However, studies into specific genetic factors have shown the diverse origins of CINs in the striatum. For instance, the expression of the transcription factor Zic4 in the SE defines septal cholinergic neurons but also 50% of the striatal CINs, which migrate from the SE (Magno et al., 2017). On the other hand, expression of the Otx2 transcription factor regulates the development of cholinergic neurons derived from the MGE and POA, and the specific ablation of the Otx2 gene from the Nkx2.1 domain results in a loss of some cholinergic neurons of the basal ganglia (Hoch et al., 2015b). It was previously thought that striatal cholinergic cell identity was exclusively defined by the upregulation of Lhx8 and coordinated downregulation of Lhx6 transcription factor (Fragkouli et al., 2009; Lopes et al., 2012), a developmental marker of MGE-derived striatal interneurons (Liodis et al., 2007). However, a subset of CINs was recently found to maintain Lhx6 expression alongside cholinergic markers, resulting in Lhx6 positive (53%) and negative (47%) populations in the striatum (Lozovaya et al., 2018). In addition, a proportion of striatal neurons express the Er81 transcription factor (Dehorter et al., 2015), and these are likely to also be derivatives of Er81-positive progenitor domains from the MGE/POA (Flames et al., 2007).

Another factor to consider to fully appreciate cholinergic cell specification is that during development, neurons acquire different identities according to their time of birth (Kao and Lee, 2010). CINs of the striatum are among the earliest cells born (between E12 and E15) along the caudal-rostral gradient respectively (Semba et al., 1988). Early- and late-born CINs migrate at different time points (Marin et al., 2000) and populate lateral and medial regions of the striatum, respectively (Chen et al., 2010). The Gbx2 transcription factor is implicated in the distinction between these early- and late-born cells and is expressed in almost all CINs. The absence of Gbx2 almost entirely ablates the late-born population (Chen et al., 2010; **Figure 2B**), and thus may also mark a cholinergic subpopulation in the striatum. These studies demonstrate the presence of diverse genetic patterning during development that is required for the control of cholinergic cell identity. The interactions and overlaying domains of these subgroups has yet to be determined; we are unaware whether they are discrete cholinergic populations or if they arise from combinatorial gene expression that leads to further diversity. In addition, our understanding of the developmental mechanisms behind the regulation of these crucial genetic factors is still limited.

Advances in Technology Point to Even More Genetic Diversity Within Populations Than First Imagined

An important advancement has been the introduction of single-cell sequencing of neuronal populations to identify patterns of genetic expression (Liu et al., 2018; Zeisel et al., 2018). Using this technique, a number of studies have found substantial genetic diversity among cholinergic neuron populations. For example, the neurochemical patterning of hypothalamic cholinergic neurons in the arcuate nucleus is heterogeneous. These cells show clustering of certain genes coding for POMC-derived peptides, enzymes responsible for the synthesis and release of GABA, glutamate and catecholamines. This heterogeneity has been proposed to be linked to the function of the arcuate nucleus in regulating feeding behavior. Indeed a subset of these cholinergic neurons was found to express leptin and insulin receptors alongside their downstream targets, indicating their specificity (Jeong et al., 2016). In addition, cortical VIP cholinergic neurons also appear genetically diverse when analyzed on a single-cell basis (Zeisel et al., 2015;

Tasic et al., 2016). Striatal CINs present diverse genetic patterning and this even extends to cholinergic markers. Individual CINs express different levels of ChAT and choline transporters, such as vesicular acetylcholine transporter (VAChT) and the high-affinity choline transporter (ChT; Muñoz-Manchado et al., 2018). Such genetic variation points to subsequent functional heterogeneity.

GENETIC DIVERSITY MAY LEAD TO FUNCTIONAL SUBGROUPS IN CHOLINERGIC NEURON POPULATIONS

Genetic diversity in cholinergic populations has consequential influences on their functional properties and integration within neuronal networks. For instance, there is documented diversity in cholinergic striatal activity, with higher levels of CIN baseline activity in the dorsomedial part compared to the ventrolateral part of the striatum (**Figure 3A**). The presence of a gradient of the phosphorylated ribosomal protein S6 (p-rpS6), a specific marker of cholinergic activity across the striatum (Matamales et al., 2016; Bertran-Gonzalez et al., 2012), suggests that the regulation of striatal output *via* cholinergic cell activity is heterogeneous within the structure. Several characteristics contribute to the functional features of cholinergic neurons.

Cholinergic Neurons Are Segregated Into Morphological Subgroups

A number of studies have found evidence for morphological diversity among cholinergic neurons in the brain. In addition to diversity between interneurons and projection neurons in different structures (**Figure 1C**), diversity within a single population or structure has also been found. For instance, olfactory bulb CINs in the mitral and plexiform cell layers can be segregated into three subsets: locally projecting, bipolar projecting, and non-bipolar projecting (Krosnowski et al., 2012). Similarly, VIP/ChAT-expressing cortical interneurons are also categorized into different morphological subtypes: bipolar, bi-tufted, and multipolar interneurons (Li et al., 2018). However, there is no established genetic or functional correlation for the diversity in these structures. In the striatum, some studies have described a relationship between molecular expression and morphological characteristics in CINs (**Figure 3A**). In particular, the absence of Gbx2 expression leads to abnormal neurite outgrowth and an increase in the complexity of the dendritic field of CINs (Chen et al., 2010). A correlation between the expression of the Lhx6 transcription factor and CINs morphology has also been recently reported (Lozovaya et al., 2018). The Lhx6-negative CINs present a more complex and vast dendritic arborization, compared to the Lhx6-expressing which are dual cholinergic/GABAergic interneurons (CGINs; **Figure 3A**). These examples of morphological diversity in cholinergic neurons indicate possible heterogeneity in their connectivity and the role they play within the local and distant circuitry.

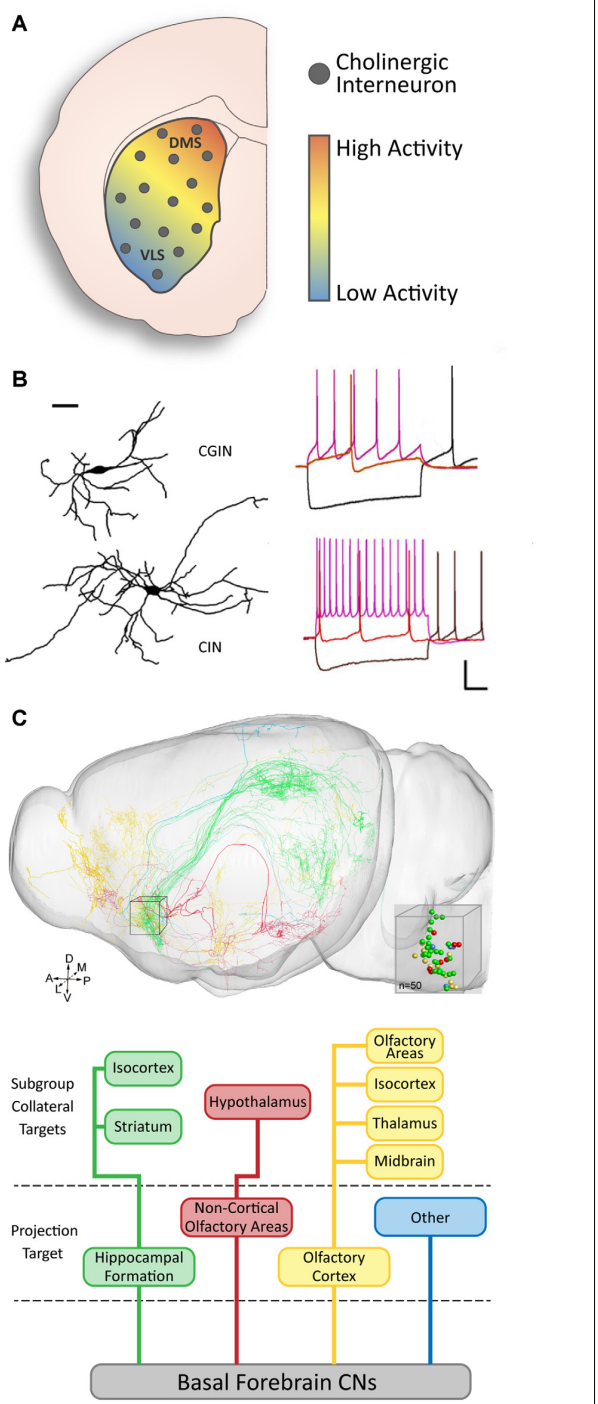

FIGURE 3 | Functional diversity of cholinergic neurons. **(A)** There is a gradient of baseline activity in striatal CINs along the DMS to ventrolateral (VLS) axis (modified from Matamales et al., 2016 with permission). **(B)** Two subsets of striatal CINs show morphological and electrophysiological differences. GABAergic CINs (GCIN) have smaller dendritic fields and slower firing rates than purely cholinergic CINs (adapted from Lozovaya et al., 2018 with permission). **(C)** Basal forebrain cholinergic neurons (CNs) have diverse projection targets and can be grouped into four major categories with subcategories based on collateral targets (adapted from Li et al., 2018 with permission).

Electrophysiological Properties Differentiate Cholinergic Cell Subtypes

Another critical aspect of circuit integration and formation during development is the electrophysiological properties of cholinergic neurons. In addition to their molecular and morphological characteristics, several cholinergic cell subtypes have been sorted in various brain structures based on their electrophysiological properties. For instance, basal forebrain cholinergic projection neurons are segregated into two subtypes, early firing and late firing (Unal et al., 2012). The early firing neurons (70%) are more excitable, as well as adaptive and susceptible to a depolarization block. The late firing neurons (30%), whilst less excitable, are able to maintain tonic firing at lower frequencies. As the basal forebrain is made up of four main regions, the functional diversity can be partly attributed to neuron location. For example, cholinergic neurons in the NB have properties consistent with early firing neurons (López-Hernández et al., 2017) whereas cholinergic neurons in the medial septal region have been found to display low frequency spiking properties (Simon et al., 2006).

Cholinergic neurons in the PPN are also functionally diverse and have been categorized into four groups. This is based on the neurons having low threshold spiking, a transient outward potassium current (known as A-current), both of these properties, or none. In addition, it has also been found that cells with A-current can be either early or late firing (Baksa et al., 2019). The diversity in functional properties of cholinergic neurons is important as they are tonically firing and thus different characteristics could lead to different ACh release patterns, altering circuit activity.

In local cholinergic circuitry, the cortical bipolar VIP+/ChAT+ interneurons have been characterized as mostly tonically firing with little to no adaptation, with a subset (approximately 12%) of stuttered firing neurons (von Engelhardt et al., 2007). Similarly, striatal CINs have also been found to show diversity in their functional properties (Lozovaya et al., 2018). CGINs have a higher sag amplitude following a hyperpolarizing current, a lower frequency of spontaneous tonic firing, and a more prominent pause response than the CINs. This functional cell diversity implies a fine control of information processing from cholinergic neuron subtypes.

Heterogeneity in Connectivity Underlies Cholinergic Neuron Diversity

Cholinergic neurons have the ability to modulate the activity of other neurons, therefore, facilitating higher-order processing in numerous nuclei (for review, see Teles-Grilo Ruivo and Mellor, 2013). Their specific and extensive pattern of connectivity is fundamental to their role, yet is different between different populations. The cholinergic projection neurons in the basal forebrain innervate various cortical and subcortical regions. Their organization into subgroups is defined by the cortical region that they target (Zaborszky et al., 2015); whereas the heterogeneity of their outputs is reciprocated in the inputs they received from different areas (Zheng et al., 2018; for review, see Záborszky et al., 2018). It was recently found that the connectivity pattern of cholinergic neurons can be even more complex. For example, within a single region of the basal forebrain, cholinergic neurons can be segregated by their main target region as well as the target locations of their collaterals (Li et al., 2018; **Figure 3C**). However, we still do not have a full understanding of the intricacies that underpin this system.

It is known that the cortical and thalamic innervation of the striatum follows an approximate topographical gradient, whereby the dorsomedial striatum (DMS) and dorsolateral striatum (DLS) receive inputs from different cortical, thalamic, and brainstem regions (McGeorge and Faull, 1989; Berendse et al., 1992; Bolam et al., 2000; Dautan et al., 2014; Assous et al., 2019). In addition, the dorsal striatum receives more excitatory innervation than the ventral striatum (Assous et al., 2019), indicating that neuronal activity in these regions may be modulated differently. These trends may also extend to influencing CINs, as they receive afferents from the cortex and thalamus (Doig et al., 2014; Klug et al., 2018). DMS CINs have higher levels of activity than those in the DLS (Matamales et al., 2016; **Figure 3A**).

In addition, a pathway from the PPN to the striatum has been reported, and interestingly consists of cholinergic and glutamatergic afferents that target striatal CINs (Dautan et al., 2014, 2016; Assous et al., 2019). Similarly, inputs from the parafascicular nucleus to the striatum form a topographic map and have also been shown to target CINs (Mandelbaum et al., 2019). Whilst extra-striatal sources of innervation onto CINs have been determined, whether they differently target and influence CIN subtypes is not known.

Striatal CINs are also heavily innervated by the local striatal network. They receive various inhibitory inputs from GABAergic neuron types (English et al., 2011; Straub et al., 2016), as well as the projecting SPNs (for review, see Abudukeyoumu et al., 2019). Moreover, CINs receive dense synaptic inputs from other CINs, forming microcircuitry that then modulates the overall striatal output *via* dense innervation of the spiny projection neurons (English et al., 2011; Straub et al., 2016; Abudukeyoumu et al., 2019). CINs virtually target all cells within the striatum (for review, see Lim et al., 2014). They primarily send connections to neuropeptide Y-expressing interneurons, projection neurons, weak inputs to parvalbumin-expressing interneurons (English et al., 2011; Straub et al., 2016) and likely target tyrosine hydroxylase-expressing interneurons (for review, see Tepper et al., 2018). The assortment of inputs and outputs of CINs may be reliant on their diverse identity. In conclusion, this aspect of striatal network connectivity is yet to be investigated and must be taken into account for future studies of the connectivity pattern of cholinergic cell subtypes.

Despite cholinergic neurons being primarily characterized by their release of Ach, there is a great deal of evidence supporting that some cell subtypes have the ability to co-release different neurotransmitters. For instance, cholinergic neurons from the basal forebrain (Takács et al., 2018) and the medial septum co-release gamma-Aminobutyric acid (GABA) and ACh (Desikan et al., 2018) and express synthesis enzymes for both neurotransmitters (Saunders et al., 2015; Granger et al., 2016).

GABAergic identity has also been reported in cortical CINs through their co-expression of glutamic acid decarboxylase (GAD) and cholinergic marker ChAT (von Engelhardt et al., 2007), as expected due to their initial characterization as inhibitory interneurons. Striatal CINs with GABAergic identity defined by Lhx6 expression co-release GABA alongside ACh (Lozovaya et al., 2018). On the other hand, the expression of a vesicular glutamate transporter VGluT3 has been shown in cholinergic axon terminals in the striatum (Gras et al., 2008; Higley et al., 2011; Nelson et al., 2014), implying the potential for co-release of Glutamate and ACh in all striatal CINs. If co-release mechanisms are shown to have a functional influence, they must be regulated to maintain normal circuit activity and may have a role in pathology.

DISCUSSION

Cholinergic Cell Diversity Is Established During Development

To understand the organizational logic of cholinergic neurons in circuitry, it is necessary to decipher the biological basis of their cellular diversity. As we have reviewed, the genetic, spatial, and temporal framework of cholinergic cell development provides a foundation for discovering and classifying subpopulations. There have been challenges to the exploration of cell specification due to technological limitations, however, the development of new techniques in the field of molecular genetics (single-cell RNA sequencing, patch-sequencing, optogenetics, and pharmacogenetics) has enabled the exposure of hidden neuronal diversity within cholinergic populations (Fuzik et al., 2016; Liu et al., 2018; Muñoz-Manchado et al., 2018).

It is well understood that the maturation of neuronal circuits requires tightly controlled gene expression cascades (Dehorter et al., 2012; Novak et al., 2013). The function and co-expression pattern of different markers that segregate cholinergic cell populations remain ambiguous. In particular, the role of Er81 (Dehorter et al., 2015) and Zic4 proteins (Magno et al., 2017) in striatal-fated CINs are currently unknown (**Figure 2B**). Cholinergic cell diversity is a consequence of different embryonic origins and exposure to transcriptional programs during maturation. As we have outlined, seemingly uniform populations of cholinergic neurons having common properties can be derived from multiple embryonic structures (**Figure 2A**), with unique chemical and morphological traits arising at distinct time points during development. It is likely that chemically, spatially and temporally-restricted domains give rise to unique neuronal populations. Since MGE-derived neurons are generated at different embryonic stages (Mi et al., 2018; Sandberg et al., 2018) and CINs proliferate along a caudal-rostral axis (Semba et al., 1988), future research may reveal which proliferation domains generate cholinergic cell subtypes. Subsequent to proliferation, cells use different migratory pathways that require the expression of specific receptors to detect chemoattractive and chemorepulsive cues (Wichterle et al., 2003; Gelman et al., 2012; Villar-Cerviño et al., 2015; Touzot et al., 2016). Therefore, development of cholinergic neurons that requires the accurate modulation of distinct transcriptional programs needs to be further investigated.

As the complex mechanisms behind neuronal development continue to be revealed, the vital role of activity-dependent processes is central to our understanding. These processes seem to be present throughout the developing brain, however, the transcriptional programs appear to be unique to specific neuronal cell-types (for review, see Dehorter et al., 2017; Yap and Greenberg, 2018). Similar mechanisms are also present in adulthood, modulating the output of neuronal circuitry (Dehorter et al., 2015). If we consider this in context of recently discovered striatal cholinergic subpopulations (Magno et al., 2017; Lozovaya et al., 2018), it is possible that different activity-induced processes tune cholinergic activity in specific ways (Krishnaswamy and Cooper, 2009), delineating further subtypes. However, research into the activity-dependent homeostatic specification of cholinergic neurons are, to the best of our knowledge, very limited (Borodinsky et al., 2004). As a result, studies into this field promise to highlight the fundamental mechanisms of cholinergic cell function.

Functional Complexity of Neuronal Networks Depends on Cholinergic Cell Diversity

Complex neuronal networks are necessary for higher-order processing and require various cell types and connections. We must consider that genetically-diverse CINs may fit into the striatal network in unique ways. For instance, Lhx6-positive and negative CINs in the striatum display functional differences (Lozovaya et al., 2018). Although they share several major common intrinsic membrane properties, Lhx6-positive CINs display higher sag amplitudes in response to hyperpolarizing pulses than Lhx6-negative CINs, lower spontaneous spiking frequency, and smaller dendritic arbors (**Figure 3B**). Therefore, there is the possibility that they form different connections, and integrate differently in the network.

The striatum has neurochemically diverse regions that are formed during development and may contribute to the formation of subnetworks. The striosome and matrix regions are three-dimensional, interlocked structures constituting neurochemically and morphologically distinct domains, which emerge during development and also have an important role in the mature striatum (Hagimoto et al., 2017; for review, see Brimblecombe and Cragg, 2017). Evidence has shown that early-born striatal cells migrate to striosomes and connect preferentially with limbic circuits, whereas late-born cells populate the matrix and receive dominant input from the neocortex (Crittenden et al., 2017; Hamasaki and Goto, 2019). In addition, CIN dendritic fields preferentially occupy the matrix compartments, alongside higher levels of cholinergic markers, suggesting that cholinergic neurons development is also dependent on the striosome-matrix structure (Crittenden et al., 2017). However, the correlation between CIN diversity and the compartmentalized structure of the striatum remains to be explored.

As we have described, cholinergic neurons can present different morphological and electrophysiological properties (**Figure 1B**). They are known to innervate other structures with different patterns of connectivity (Li et al., 2018; **Figure 3C**), and also receive inputs from various structures and cell types (for review, see Lim et al., 2014). It is thus crucial to determine whether cholinergic cell subtypes exhibit different morphological features (i.e., axonal and dendritic fields) or innervation patterns to ultimately fully characterize their involvement in various microcircuits.

Cholinergic transmission can mediate disparate actions *via* integration of postsynaptic signals (Calabresi et al., 2000). It is necessary to consider the function and distribution of postsynaptic receptors that are scattered across various cells and receptors with different signaling capacities that can be co-expressed in the same cell type. Increased understanding of the specific neuron types responsive to ACh and their functional connectivity is necessary to obtain a phenomenological understanding of neuromodulation and behavior both at the cellular and circuit levels. Interplay between ACh and other neurotransmitters are central for basal ganglia function (for review, see Bonsi et al., 2011), and ACh-dopamine (DA) coupling has been extensively studied, as their reciprocal interaction largely contributes to the control of the striatal output. For example, DA has a fundamental role in the striatum (Tritsch et al., 2012; for review, see Cools, 2011), as it controls the pause in CIN firing (Zhang et al., 2018), both in the medial and lateral areas. There are regional differences in the dopaminergic control of striatal CINs. It has been described that the pause of these cells in the DLS is shorter than in the DMS, *via* a mechanism of DA-glutamate co-transmission (Chuhma et al., 2018). Moreover, activation of glutamatergic receptors by cortical and thalamic inputs might lead to distinct integration strategies from CINs subtypes in the striatum (Kosillo et al., 2016).

CINs are fundamental to the integration of somatosensory information and motor-related signals (for review, see Robbe, 2018). There is a functional dissociation between the DMS, which is responsible for goal-directed actions, and the DLS, supporting procedural learning such as habit formation (Okada et al., 2018). There are also differences in the sensitivity of tonically active neurons to rewarding events between dorsal and ventral striatum (Marche et al., 2017). Determining whether responses of cholinergic cell types vary is an interesting topic for future studies utilizing *in vivo* optogenetics, calcium imaging or electrophysiological approaches.

Our understanding of the role of cholinergic subpopulations within pathological conditions is currently limited, however, a study reported unique roles of striatal CINs and GABA/ACh co-expressing striatal interneurons (CGINs; **Figure 3B**) in PD (Lozovaya et al., 2018). It shows that DA deprivation specifically strengthens CGIN-CGIN network and abolishes both GABAergic inhibition and pause response in CGINs. Future studies should focus on distinguishing between the different cholinergic subpopulations on the basis of their embryonic origin, molecular profile and connectivity, when analyzing cholinergic network dysfunction in disease conditions.

CONCLUSION

Despite significant research into cholinergic neurons, the recent discovery of diverse subpopulations has reinforced the notion that our understanding of these cells remains incomplete. In this review, we have combined the current literature surrounding cholinergic neurons in the brain with a specific focus on the newfound diversity within cholinergic population of the striatum. Whereas similarities between cholinergic populations predicated that neurons were relatively functionally homogenous, studies show genetic, morphological and electrophysiological properties in striatal cholinergic subpopulations. This diversity likely underpins their specific function in normal and pathological conditions. Future studies into cholinergic cell subpopulations aiming at understanding their development, morphology and activity are necessary to ultimately determine the implications of this new-found cell diversity in health and disease.

AUTHOR CONTRIBUTIONS

All authors contributed to the writing of the manuscript, and all have approved it for publication.

FUNDING

Some of the research in this review and its writing were supported by the Australian National University and the National Health and Medical Research Council (APP1144145).

ACKNOWLEDGMENTS

Images in **Figure 3B** comes from Lozovaya et al. (2018). Images included are encompassed under the Creative Commons license: http://creativecommons.org/licenses/by/4.0/. Images in **Figure 3C** comes from Li et al. (2018). Permission has been granted for the use of the material.

REFERENCES

Abudukeyoumu, N., Hernandez-Flores, T., Garcia-Munoz, M., and Arbuthnott, G. W. (2019). Cholinergic modulation of striatal microcircuits. *Eur. J. Neurosci.* 49, 604–622. doi: 10.1111/ejn.13949

Albert-Gascó, H., García-Avilés, A., Moustafa, S., Sánchez-Sarasua, S., Gundlach, A. L., Olucha-Bordonau, F. E., et al. (2017). Central relaxin-3 receptor (RXFP3) activation increases ERK phosphorylation in septal cholinergic neurons and impairs spatial working memory. *Brain Struct. Funct.* 222, 449–463. doi: 10.1007/s00429-016-1227-8

Allaway, K. C., and Machold, R. (2017). Developmental specification of forebrain cholinergic neurons. *Dev. Biol.* 421, 1–7. doi: 10.1016/j.ydbio.2016.11.007

Aoki, S., Liu, A. W., Akamine, Y., Zucca, A., Zucca, S., and Wickens, J. R. (2018). Cholinergic interneurons in the rat striatum modulate substitution of habits. *Eur. J. Neurosci.* 47, 1194–1205. doi: 10.1111/ejn.13820

Aoki, S., Liu, A. W., Zucca, A., Zucca, S., and Wickens, J. R. (2015). Role of striatal cholinergic interneurons in set-shifting in the rat. *J. Neurosci.* 35, 9424–9431. doi: 10.1523/JNEUROSCI.0490-15.2015

Assous, M., Dautan, D., Tepper, J. M., and Mena-Segovia, J. (2019). Pedunculopontine glutamatergic neurons provide a novel source of feedforward inhibition in the striatum by selectively targeting interneurons. *J. Neurosci.* 39, 4727–4737. doi: 10.1523/JNEUROSCI.2913-18.2019

Atallah, H. E., McCool, A. D., Howe, M. W., and Graybiel, A. M. (2014). Neurons in the ventral striatum exhibit cell-type-specific representations of outcome during learning. *Neuron* 82, 1145–1156. doi: 10.1016/j.neuron.2014.04.021

Baksa, B., Kovács, A., Bayasgalan, T., Szentesi, P., Koszeghy, Á., Szücs, P., et al. (2019). Characterization of functional subgroups among genetically identified cholinergic neurons in the pedunculopontine nucleus. *Cell. Mol. Life Sci.* 76, 2799–2815. doi: 10.1007/s00018-019-03025-4

Ballinger, E. C., Ananth, M., Talmage, D. A., and Role, L. W. (2016). Basal forebrain cholinergic circuits and signaling in cognition and cognitive decline. *Neuron* 91, 1199–1218. doi: 10.1016/j.neuron.2016.09.006

Bennett, B. D., Callaway, J. C., and Wilson, C. J. (2000). Intrinsic membrane properties underlying spontaneous tonic firing in neostriatal cholinergic interneurons. *J. Neurosci.* 20, 8493–8503. doi: 10.1523/JNEUROSCI.20-22-08493.2000

Berendse, H. W., Galis-de Graaf, Y., and Groenewegen, H. J. (1992). Topographical organization and relationship with ventral striatal compartments of prefrontal corticostriatal projections in the rat. *J. Comp. Neurol.* 316, 314–347. doi: 10.1002/cne.903160305

Bertran-Gonzalez, J., Chieng, B. C., Laurent, V., Valjent, E., and Balleine, B. W. (2012). Striatal cholinergic interneurons display activity-related phosphorylation of ribosomal protein S6. *PLoS One* 7:e53195. doi: 10.1371/journal.pone.0053195

Bolam, J. P., Hanley, J. J., Booth, P. A., and Bevan, M. D. (2000). Synaptic organisation of the basal ganglia. *J. Anat.* 196, 527–542. doi: 10.1046/j.1469-7580.2000.19640527.x

Bonsi, P., Cuomo, D., Martella, G., Madeo, G., Schirinzi, T., Puglisi, F., et al. (2011). Centrality of striatal cholinergic transmission in basal ganglia function. *Front. Neuroanat.* 5:6. doi: 10.3389/fnana.2011.00006

Bordia, T., Zhang, D., Perez, X. A., and Quik, M. (2016). Striatal cholinergic interneurons and D2 receptor-expressing GABAergic medium spiny neurons regulate tardive dyskinesia. *Exp. Neurol.* 286, 32–39. doi: 10.1016/j.expneurol.2016.09.009

Borodinsky, L. N., Root, C. M., Cronin, J. A., Sann, S. B., Gu, X., and Spitzer, N. C. (2004). Activity-dependent homeostatic specification of transmitter expression in embryonic neurons. *Nature* 429, 523–530. doi: 10.1038/nature02518

Bradfield, L. A., Bertran-Gonzalez, J., Chieng, B., and Balleine, B. W. (2013). The thalamostriatal pathway and cholinergic control of goal-directed action: interlacing new with existing learning in the striatum. *Neuron* 79, 153–166. doi: 10.1016/j.neuron.2013.04.039

Breunig, J. J., Haydar, T. F., and Rakic, P. (2011). Neural stem cells: historical perspective and future prospects. *Neuron* 70, 614–625. doi: 10.1016/j.neuron.2011.05.005

Brimblecombe, K. R., and Cragg, S. J. (2017). The striosome and matrix compartments of the striatum: a path through the labyrinth from neurochemistry toward function. *ACS Chem. Neurosci.* 8, 235–242. doi: 10.1021/acschemneuro.6b00333

Calabresi, P., Centonze, D., Gubellini, P., Pisani, A., and Bernardi, G. (2000). Acetylcholine-mediated modulation of striatal function. *Trends Neurosci.* 23, 120–126. doi: 10.1016/s0166-2236(99)01501-5

Ceci, M. L., Pedraza, M., and de Carlos, J. A. (2012). The embryonic septum and ventral pallium, new sources of olfactory cortex cells. *PLoS One* 7:e44716. doi: 10.1371/journal.pone.0044716

Chen, L., Chatterjee, M., and Li, J. Y. (2010). The mouse homeobox gene Gbx2 is required for the development of cholinergic interneurons in the striatum. *J. Neurosci.* 30, 14824–14834. doi: 10.1523/JNEUROSCI.3742-10.2010

Cheng, J., Umschweif, G., Leung, J., Sagi, Y., and Greengard, P. (2019). HCN2 channels in cholinergic interneurons of nucleus accumbens shell regulate depressive behaviors. *Neuron* 101, 662.e5–672.e5. doi: 10.1016/j.neuron.2018.12.018

Cho, H. H., Cargnin, F., Kim, Y., Lee, B., Kwon, R. J., Nam, H., et al. (2014). Isl1 directly controls a cholinergic neuronal identity in the developing forebrain and spinal cord by forming cell type-specific complexes. *PLoS Genet.* 10:e1004280. doi: 10.1371/journal.pgen.1004280

Chuhma, N., Mingote, S., Yetnikoff, L., Kalmbach, A., Ma, T., Ztaou, S., et al. (2018). Dopamine neuron glutamate cotransmission evokes a delayed excitation in lateral dorsal striatal cholinergic interneurons. *Elife* 7:e39786. doi: 10.7554/elife.39786

Cools, R. (2011). Dopaminergic control of the striatum for high-level cognition. *Curr. Opin. Neurobiol.* 21, 402–407. doi: 10.1016/j.conb.2011.04.002

Crittenden, J. R., Lacey, C. J., Weng, F. J., Garrison, C. E., Gibson, D. J., Lin, Y., et al. (2017). Striatal cholinergic interneurons modulate spike-timing in striosomes and matrix by an amphetamine-sensitive mechanism. *Front. Neuroanat.* 11:20. doi: 10.3389/fnana.2017.00020

Dautan, D., Hacioğlu Bay, H., Bolam, J. P., Gerdjikov, T. V., and Mena-Segovia, J. (2016). Extrinsic sources of cholinergic innervation of the striatal complex: a whole-brain mapping analysis. *Front. Neuroanat.* 10:1. doi: 10.3389/fnana.2016.00001

Dautan, D., Huerta-Ocampo, I., Witten, I. B., Deisseroth, K., Bolam, J. P., Gerdjikov, T., et al. (2014). A major external source of cholinergic innervation of the striatum and nucleus accumbens originates in the brainstem. *J. Neurosci.* 34, 4509–4518. doi: 10.1523/JNEUROSCI.5071-13.2014

Dehorter, N., Ciceri, G., Bartolini, G., Lim, L., del Pino, I., and Marín, O. (2015). Tuning of fast-spiking interneuron properties by an activity-dependent transcriptional switch. *Science* 349, 1216–1220. doi: 10.1126/science.aab3415

Dehorter, N., Marichal, N., Marín, O., and Berninger, B. (2017). Tuning neural circuits by turning the interneuron knob. *Curr. Opin. Neurobiol.* 42, 144–151. doi: 10.1016/j.conb.2016.12.009

Dehorter, N., Vinay, L., Hammond, C., and Ben-Ari, Y. (2012). Timing of developmental sequences in different brain structures: physiological and pathological implications. *Eur. J. Neurosci.* 35, 1846–1856. doi: 10.1111/j.1460-9568.2012.08152.x

Desikan, S., Koser, D. E., Neitz, A., and Monyer, H. (2018). Target selectivity of septal cholinergic neurons in the medial and lateral entorhinal cortex. *Proc. Natl. Acad. Sci. U S A* 115, E2644–E2652. doi: 10.1073/pnas.1716531115

Doig, N. M., Magill, P. J., Apicella, P., Bolam, J. P., and Sharott, A. (2014). Cortical and thalamic excitation mediate the multiphasic responses of striatal cholinergic interneurons to motivationally salient stimuli. *J. Neurosci.* 34, 3101–3117. doi: 10.1523/JNEUROSCI.4627-13.2014

Du, T., Xu, Q., Ocbina, P. J., and Anderson, S. A. (2008). NKX2.1 specifies cortical interneuron fate by activating Lhx6. *Development* 135, 1559–1567. doi: 10.1242/dev.015123

Elshatory, Y., and Gan, L. (2008). The LIM-homeobox gene Islet-1 is required for the development of restricted forebrain cholinergic neurons. *J. Neurosci.* 28, 3291–3297. doi: 10.1523/JNEUROSCI.5730-07.2008

English, B. A., Hahn, M. K., Gizer, I. R., Mazei-Robison, M., Steele, A., Kurnik, D. M., et al. (2009). Choline transporter gene variation is associated with attention-deficit hyperactivity disorder. *J. Neurodev. Disord.* 1, 252–263. doi: 10.1007/s11689-009-9033-8

English, D. F., Ibanez-Sandoval, O., Stark, E., Tecuapetla, F., Buzsáki, G., Deisseroth, K., et al. (2011). GABAergic circuits mediate the reinforcement-related signals of striatal cholinergic interneurons. *Nat. Neurosci.* 15, 123–130. doi: 10.1038/nn.2984

Faust, T. W., Assous, M., Shah, F., Tepper, J. M., and Koos, T. (2015). Novel fast adapting interneurons mediate cholinergic-induced fast $GABA_A$ inhibitory postsynaptic currents in striatal spiny neurons. *Eur. J. Neurosci.* 42, 1764–1774. doi: 10.1111/ejn.12915

Fishell, G., and Heintz, N. (2013). The neuron identity problem: form meets function. *Neuron* 80, 602–612. doi: 10.1016/j.neuron.2013.10.035

Flames, N., Pla, R., Gelman, D. M., Rubenstein, J. L., Puelles, L., and Marin, O. (2007). Delineation of multiple subpallial progenitor domains by the combinatorial expression of transcriptional codes. *J. Neurosci.* 27, 9682–9695. doi: 10.1523/jneurosci.2750-07.2007

Fragkouli, A., van Wijk, N. V., Lopes, R., Kessaris, N., and Pachnis, V. (2009). LIM homeodomain transcription factor-dependent specification of bipotential MGE progenitors into cholinergic and GABAergic striatal interneurons. *Development* 136, 3841–3851. doi: 10.1242/dev.038083

French, I. T., and Muthusamy, K. A. (2018). A review of the pedunculopontine nucleus in Parkinson's disease. *Front. Aging Neurosci.* 10:99. doi: 10.3389/fnagi.2018.00099

Fuzik, J., Zeisel, A., Mate, Z., Calvigioni, D., Yanagawa, Y., Szabo, G., et al. (2016). Integration of electrophysiological recordings with single-cell RNA-seq data identifies neuronal subtypes. *Nat. Biotechnol.* 34, 175–183. doi: 10.1038/nbt.3443

Gelman, D., Griveau, A., Dehorter, N., Teissier, A., Varela, C., Pla, R., et al. (2011). A wide diversity of cortical GABAergic interneurons derives from the embryonic preoptic area. *J. Neurosci.* 31, 16570–16580. doi: 10.1523/jneurosci.4068-11.2011

Gelman, D. M., Marin, O., and Rubenstein, J. L. R. (2012). "The generation of cortical interneurons," in *Jasper's Basic Mechanisms of the Epilepsies*, eds J. L. Noebels, M. Avoli, M. A. Rogawski, R. W. Olsen and A. V. Delgado-Escueta (Bethesda, MD: National Center for Biotechnology Information (US)), 1171–1186

Goldberg, J. A., and Reynolds, J. N. (2011). Spontaneous firing and evoked pauses in the tonically active cholinergic interneurons of the striatum. *Neuroscience* 198, 27–43. doi: 10.1016/j.neuroscience.2011.08.067

Goldberg, J. A., and Wilson, C. J. (2005). Control of spontaneous firing patterns by the selective coupling of calcium currents to calcium-activated potassium currents in striatal cholinergic interneurons. *J. Neurosci.* 25, 10230–10238. doi: 10.1523/jneurosci.2734-05.2005

Granger, A. J., Mulder, N., Saunders, A., and Sabatini, B. L. (2016). Cotransmission of acetylcholine and GABA. *Neuropharmacology* 100, 40–46. doi: 10.1016/j.neuropharm.2015.07.031

Gras, C., Amilhon, B., Lepicard, E. M., Poirel, O., Vinatier, J., Herbin, M., et al. (2008). The vesicular glutamate transporter VGLUT3 synergizes striatal acetylcholine tone. *Nat. Neurosci.* 11, 292–300. doi: 10.1038/nn2052

Hagimoto, K., Takami, S., Murakami, F., and Tanabe, Y. (2017). Distinct migratory behaviors of striosome and matrix cells underlying the mosaic formation in the developing striatum. *J. Comp. Neurol.* 525, 794–817. doi: 10.1002/cne.24096

Hamasaki, T., and Goto, S. (2019). Parallel emergence of a compartmentalized striatum with the phylogenetic development of the cerebral cortex. *Brain Sci.* 9:E90. doi: 10.3390/brainsci9040090

Hampel, H., Mesulam, M. M., Cuello, A. C., Farlow, M. R., Giacobini, E., Grossberg, G. T., et al. (2018). The cholinergic system in the pathophysiology and treatment of Alzheimer's disease. *Brain* 141, 1917–1933. doi: 10.1093/brain/awy132

Higley, M. J., Gittis, A. H., Oldenburg, I. A., Balthasar, N., Seal, R. P., Edwards, R. H., et al. (2011). Cholinergic interneurons mediate fast VGluT3-dependent glutamatergic transmission in the striatum. *PLoS One* 6:e19155. doi: 10.1371/journal.pone.0019155

Higley, M. J., and Picciotto, M. R. (2014). Neuromodulation by acetylcholine: examples from schizophrenia and depression. *Curr. Opin. Neurobiol.* 29, 88–95. doi: 10.1016/j.conb.2014.06.004

Hoch, R. V., Clarke, J. A., and Rubenstein, J. L. (2015a). Fgf signaling controls the telencephalic distribution of Fgf-expressing progenitors generated in the rostral patterning center. *Neural Dev.* 10:8. doi: 10.1186/s13064-015-0037-7

Hoch, R. V., Lindtner, S., Price, J. D., and Rubenstein, J. L. (2015b). OTX2 transcription factor controls regional patterning within the medial ganglionic eminence and regional identity of the septum. *Cell Rep.* 12, 482–494. doi: 10.1016/j.celrep.2015.06.043

Hyde, T. M., and Crook, J. M. (2001). Cholinergic systems and schizophrenia: primary pathology or epiphenomena? *J. Chem. Neuroanat.* 22, 53–63. doi: 10.1016/s0891-0618(01)00101-6

Jabaudon, D. (2017). Fate and freedom in developing neocortical circuits. *Nat. Commun.* 8:16042. doi: 10.1038/ncomms16042

Jeong, J. H., Woo, Y. J., Chua, S. Jr., and Jo, Y. H. (2016). Single-cell gene expression analysis of cholinergic neurons in the arcuate nucleus of the hypothalamus. *PLoS One* 11:e0162839. doi: 10.1371/journal.pone.0162839

Kao, C. F., and Lee, T. (2010). Birth time/order-dependent neuron type specification. *Curr. Opin. Neurobiol.* 20, 14–21. doi: 10.1016/j.conb.2009.10.017

Karvat, G., and Kimchi, T. (2014). Acetylcholine elevation relieves cognitive rigidity and social deficiency in a mouse model of autism. *Neuropsychopharmacology* 39, 831–840. doi: 10.1038/npp.2013.274

Klug, J. R., Engelhardt, M. D., Cadman, C. N., Li, H., Smith, J. B., Ayala, S., et al. (2018). Differential inputs to striatal cholinergic and parvalbumin interneurons imply functional distinctions. *Elife* 7:e35657. doi: 10.7554/elife.35657

Kosillo, P., Zhang, Y. F., Threlfell, S., and Cragg, S. J. (2016). Cortical control of striatal dopamine transmission *via* striatal cholinergic interneurons. *Cereb. Cortex* doi: 10.1093/cercor/bhw252 [Epub ahead of print].

Krishnaswamy, A., and Cooper, E. (2009). An activity-dependent retrograde signal induces the expression of the high-affinity choline transporter in cholinergic neurons. *Neuron* 61, 272–286. doi: 10.1016/j.neuron.2008.11.025

Krosnowski, K., Ashby, S., Sathyanesan, A., Luo, W., Ogura, T., and Lin, W. (2012). Diverse populations of intrinsic cholinergic interneurons in the mouse olfactory bulb. *Neuroscience* 213, 161–178. doi: 10.1016/j.neuroscience.2012.04.024

Li, X., Yu, B., Sun, Q., Zhang, Y., Ren, M., Zhang, X., et al. (2018). Generation of a whole-brain atlas for the cholinergic system and mesoscopic projectome analysis of basal forebrain cholinergic neurons. *Proc. Natl. Acad. Sci. U S A* 115, 415–420. doi: 10.1073/pnas.1703601115

Lim, S. A., Kang, U. J., and McGehee, D. S. (2014). Striatal cholinergic interneuron regulation and circuit effects. *Front. Synaptic Neurosci.* 6:22. doi: 10.3389/fnsyn.2014.00022

Liodis, P., Denaxa, M., Grigoriou, M., Akufo-Addo, C., Yanagawa, Y., and Pachnis, V. (2007). Lhx6 activity is required for the normal migration and specification of cortical interneuron subtypes. *J. Neurosci.* 27, 3078–3089. doi: 10.1523/jneurosci.3055-06.2007

Liu, Q., Herring, C. A., Sheng, Q., Ping, J., Simmons, A. J., Chen, B., et al. (2018). Quantitative assessment of cell population diversity in single-cell landscapes. *PLoS Biol.* 16:e2006687. doi: 10.1371/journal.pbio.2006687

Lopes, R., Verhey van Wijk, N., Neves, G., and Pachnis, V. (2012). Transcription factor LIM homeobox 7 (Lhx7) maintains subtype identity of cholinergic interneurons in the mammalian striatum. *Proc. Natl. Acad. Sci. U S A* 109, 3119–3124. doi: 10.1073/pnas.1109251109

López, A. J., Jia, Y., White, A. O., Kwapis, J. L., Espinoza, M., Hwang, P., et al. (2019). Medial habenula cholinergic signaling regulates cocaine-associated relapse-like behavior. *Addict. Biol.* 24, 403–413. doi: 10.1111/adb.12605

López-Hernández, G. Y., Ananth, M., Jiang, L., Ballinger, E. C., Talmage, D. A., and Role, L. W. (2017). Electrophysiological properties of basal forebrain cholinergic neurons identified by genetic and optogenetic tagging. *J. Neurochem.* 142, 103–110. doi: 10.1111/jnc.14073

Lozovaya, N., Eftekhari, S., Cloarec, R., Gouty-Colomer, L. A., Dufour, A., Riffault, B., et al. (2018). GABAergic inhibition in dual-transmission cholinergic and GABAergic striatal interneurons is abolished in Parkinson disease. *Nat. Commun.* 9:1422. doi: 10.1038/s41467-018-03802-y

Macintosh, F. C. (1941). The distribution of acetylcholine in the peripheral and the central nervous system. *J. Physiol.* 99, 436–442. doi: 10.1113/jphysiol.1941.sp003913

Magno, L., Barry, C., Schmidt-Hieber, C., Theodotou, P., Hausser, M., and Kessaris, N. (2017). NKX2–1 is required in the embryonic septum for cholinergic system development, learning, and memory. *Cell Rep.* 20, 1572–1584. doi: 10.1016/j.celrep.2017.07.053

Mamaligas, A. A., and Ford, C. P. (2016). Spontaneous synaptic activation of muscarinic receptors by striatal cholinergic neuron firing. *Neuron* 91, 574–586. doi: 10.1016/j.neuron.2016.06.021

Mandelbaum, G., Taranda, J., Haynes, T. M., Hochbaum, D. R., Huang, K. W., Hyun, M., et al. (2019). Distinct cortical-thalamic-striatal circuits through the parafascicular nucleus. *Neuron* 102, 636.e7–652.e7. doi: 10.1016/j.neuron.2019.02.035

Marche, K., Martel, A. C., and Apicella, P. (2017). Differences between dorsal and ventral striatum in the sensitivity of tonically active neurons to rewarding events. *Front. Syst. Neurosci.* 11:52. doi: 10.3389/fnsys.2017.00052

Marin, O., Anderson, S. A., and Rubenstein, J. L. (2000). Origin and molecular specification of striatal interneurons. *J. Neurosci.* 20, 6063–6076. doi: 10.1523/jneurosci.20-16-06063.2000

Markowitz, J. E., Gillis, W. F., Beron, C. C., Neufeld, S. Q., Robertson, K., Bhagat, N. D., et al. (2018). The striatum organizes 3D behavior *via* moment-to-moment action selection. *Cell* 174, 44.e17–58.e17. doi: 10.1016/j.cell.2018.04.019

Martos, Y. V., Braz, B. Y., Beccaria, J. P., Murer, M. G., and Belforte, J. E. (2017). Compulsive social behavior emerges after selective ablation of striatal cholinergic interneurons. *J. Neurosci.* 37, 2849–2858. doi: 10.1523/jneurosci.3460-16.2017

Matamales, M., Götz, J., and Bertran-Gonzalez, J. (2016). Quantitative imaging of cholinergic interneurons reveals a distinctive spatial organization and a functional gradient across the mouse striatum. *PLoS One* 11:e0157682. doi: 10.1371/journal.pone.0157682

Maurice, N., Liberge, M., Jaouen, F., Ztaou, S., Hanini, M., Camon, J., et al. (2015). Striatal cholinergic interneurons control motor behavior and basal ganglia function in experimental Parkinsonism. *Cell Rep.* 13, 657–666. doi: 10.1016/j.celrep.2015.09.034

McGeorge, A. J., and Faull, R. L. (1989). The organization of the projection from the cerebral cortex to the striatum in the rat. *Neuroscience* 29, 503–537. doi: 10.1016/0306-4522(89)90128-0

Mena-Segovia, J., and Bolam, J. P. (2017). Rethinking the pedunculopontine nucleus: from cellular organization to function. *Neuron* 94, 7–18. doi: 10.1016/j.neuron.2017.02.027

Mesulam, M. M., Mufson, E. J., Wainer, B. H., and Levey, A. I. (1983). Central cholinergic pathways in the rat: an overview based on an alternative nomenclature (Ch1-Ch6). *Neuroscience* 10, 1185–1201. doi: 10.1016/0306-4522(83)90108-2

Mi, D., Li, Z., Lim, L., Li, M., Moissidis, M., Yang, Y., et al. (2018). Early emergence of cortical interneuron diversity in the mouse embryo. *Science* 360, 81–85. doi: 10.1126/science.aar6821

Minces, V., Pinto, L., Dan, Y., and Chiba, A. A. (2017). Cholinergic shaping of neural correlations. *Proc. Natl. Acad. Sci. U S A* 114, 5725–5730. doi: 10.1073/pnas.1621493114

Mori, T., Yuxing, Z., Takaki, H., Takeuchi, M., Iseki, K., Hagino, S., et al. (2004). The LIM homeobox gene, L3/Lhx8, is necessary for proper development of basal forebrain cholinergic neurons. *Eur. J. Neurosci.* 19, 3129–3141. doi: 10.1111/j.0953-816x.2004.03415.x

Mufson, E. J., Martin, T. L., Mash, D. C., Wainer, B. H., and Mesulam, M. M. (1986). Cholinergic projections from the parabigeminal nucleus (Ch8) to the superior colliculus in the mouse: a combined analysis of horseradish peroxidase transport and choline acetyltransferase immunohistochemistry. *Brain Res.* 370, 144–148. doi: 10.1016/0006-8993(86)91114-5

Muñoz-Manchado, A. B., Bengtsson Gonzales, C., Zeisel, A., Munguba, H., Bekkouche, B., Skene, N. G., et al. (2018). Diversity of interneurons in the dorsal striatum revealed by single-cell RNA sequencing and PatchSeq. *Cell Rep.* 24, 2179.e7–2190.e7. doi: 10.1016/j.celrep.2018.07.053

Nagy, J., Kobolak, J., Berzsenyi, S., Abraham, Z., Avci, H. X., Bock, I., et al. (2017). Altered neurite morphology and cholinergic function of induced pluripotent stem cell-derived neurons from a patient with Kleefstra syndrome and autism. *Transl. Psychiatry* 7:e1179. doi: 10.1038/tp.2017.144

Nelson, A. B., Bussert, T. G., Kreitzer, A. C., and Seal, R. P. (2014). Striatal cholinergic neurotransmission requires VGLUT3. *J. Neurosci.* 34, 8772–8777. doi: 10.1523/jneurosci.0901-14.2014

Nóbrega-Pereira, S., Gelman, D., Bartolini, G., Pla, R., Pierani, A., and Marín, O. (2010). Origin and molecular specification of globus pallidus neurons. *J. Neurosci.* 30, 2824–2834. doi: 10.1523/jneurosci.4023-09.2010

Novak, G., Fan, T., O'Dowd, B. F., and George, S. R. (2013). Striatal development involves a switch in gene expression networks, followed by a myelination event: implications for neuropsychiatric disease. *Synapse* 67, 179–188. doi: 10.1002/syn.21628

Okada, K., Nishizawa, K., Fukabori, R., Kai, N., Shiota, A., Ueda, M., et al. (2014). Enhanced flexibility of place discrimination learning by targeting striatal cholinergic interneurons. *Nat. Commun.* 5:3778. doi: 10.1038/ncomms4778

Okada, K., Nishizawa, K., Setogawa, S., Hashimoto, K., and Kobayashi, K. (2018). Task-dependent function of striatal cholinergic interneurons in behavioural flexibility. *Eur. J. Neurosci.* 47, 1174–1183. doi: 10.1111/ejn.13768

Oswald, M. J., Oorschot, D. E., Schulz, J. M., Lipski, J., and Reynolds, J. N. (2009). IH current generates the afterhyperpolarisation following activation of subthreshold cortical synaptic inputs to striatal cholinergic interneurons. *J. Physiol.* 587, 5879–5897. doi: 10.1113/jphysiol.2009.177600

Pepeu, G., and Grazia Giovannini, M. (2017). The fate of the brain cholinergic neurons in neurodegenerative diseases. *Brain Res.* 1670, 173–184. doi: 10.1016/j.brainres.2017.06.023

Petzold, A., Valencia, M., Pal, B., and Mena-Segovia, J. (2015). Decoding brain state transitions in the pedunculopontine nucleus: cooperative phasic and tonic mechanisms. *Front. Neural Circuits* 9:68. doi: 10.3389/fncir.2015.00068

Pombero, A., Bueno, C., Saglietti, L., Rodenas, M., Guimera, J., Bulfone, A., et al. (2011). Pallial origin of basal forebrain cholinergic neurons in the nucleus basalis of Meynert and horizontal limb of the diagonal band nucleus. *Development* 138, 4315–4326. doi: 10.1242/dev.069534

Robbe, D. (2018). To move or to sense? Incorporating somatosensory representation into striatal functions. *Curr. Opin. Neurobiol.* 52, 123–130. doi: 10.1016/j.conb.2018.04.009

Rudy, B., Fishell, G., Lee, S., and Hjerling-Leffler, J. (2011). Three groups of interneurons account for nearly 100% of neocortical GABAergic neurons. *Dev. Neurobiol.* 71, 45–61. doi: 10.1002/dneu.20853

Sandberg, M., Taher, L., Hu, J., Black, B. L., Nord, A. S., and Rubenstein, J. L. R. (2018). Genomic analysis of transcriptional networks directing progression of cell states during MGE development. *Neural Dev.* 13:21. doi: 10.1186/s13064-018-0119-4

Saunders, A., Granger, A. J., and Sabatini, B. L. (2015). Corelease of acetylcholine and GABA from cholinergic forebrain neurons. *Elife* 4:e06412. doi: 10.7554/elife.06412

Scarr, E., Gibbons, A. S., Neo, J., Udawela, M., and Dean, B. (2013). Cholinergic connectivity: it's implications for psychiatric disorders. *Front. Cell. Neurosci.* 7:55. doi: 10.3389/fncel.2013.00055

Semba, K., Vincent, S. R., and Fibiger, H. C. (1988). Different times of origin of choline acetyltransferase- and somatostatin-immunoreactive neurons in the rat striatum. *J. Neurosci.* 8, 3937–3944. doi: 10.1523/jneurosci.08-10-03937.1988

Shimo, Y., and Hikosaka, O. (2001). Role of tonically active neurons in primate caudate in reward-oriented saccadic eye movement. *J. Neurosci.* 21, 7804–7814. doi: 10.1523/jneurosci.21-19-07804.2001

Simon, A. P., Poindessous-Jazat, F., Dutar, P., Epelbaum, J., and Bassant, M. H. (2006). Firing properties of anatomically identified neurons in the medial septum of anesthetized and unanesthetized restrained rats. *J. Neurosci.* 26, 9038–9046. doi: 10.1523/jneurosci.1401-06.2006

Smith, R., Chung, H., Rundquist, S., Maat-Schieman, M. L., Colgan, L., Englund, E., et al. (2006). Cholinergic neuronal defect without cell loss in Huntington's disease. *Hum. Mol. Genet.* 15, 3119–3131. doi: 10.1093/hmg/ddl252

Straub, C., Saulnier, J. L., Begue, A., Feng, D. D., Huang, K. W., and Sabatini, B. L. (2016). Principles of synaptic organization of GABAergic interneurons in the striatum. *Neuron* 92, 84–92. doi: 10.1016/j.neuron.2016.09.007

Sussel, L., Marin, O., Kimura, S., and Rubenstein, J. L. (1999). Loss of Nkx2.1 homeobox gene function results in a ventral to dorsal molecular respecification within the basal telencephalon: evidence for a transformation of the pallidum into the striatum. *Development* 126, 3359–3370.

Takács, V. T., Cserép, C., Schlingloff, D., Pósfai, B., Szonyi, A., Sos, K. E., et al. (2018). Co-transmission of acetylcholine and GABA regulates hippocampal states. *Nat. Commun.* 9:2848. doi: 10.1038/s41467-018-05136-1

Tasic, B., Menon, V., Nguyen, T. N., Kim, T. K., Jarsky, T., Yao, Z., et al. (2016). Adult mouse cortical cell taxonomy revealed by single cell transcriptomics. *Nat. Neurosci.* 19, 335–346. doi: 10.1038/nn.4216

Tasic, B., Yao, Z., Graybuck, L. T., Smith, K. A., Nguyen, T. N., Bertagnolli, D., et al. (2018). Shared and distinct transcriptomic cell types across neocortical areas. *Nature* 563, 72–78. doi: 10.1038/s41586-018-0654-5

Taylor, P., and Brown, J. H. (1999). "Synthesis, storage and release of acetylcholine," in *Basic Neurochemistry: Molecular, Cellular and Medical Aspects* 6th Edn., eds G. J. Siegel, B. W. Agranoff and R. W. Alberts (Philadelphia, PA: Lippincott-Raven), 213–242

Teles-Grilo Ruivo, L. M., and Mellor, J. R. (2013). Cholinergic modulation of hippocampal network function. *Front. Synaptic Neurosci.* 5:2. doi: 10.3389/fnsyn.2013.00002

Tepper, J. M., Koós, T., Ibanez-Sandoval, O., Tecuapetla, F., Faust, T. W., and Assous, M. (2018). Heterogeneity and diversity of striatal gabaergic interneurons: update 2018. *Front. Neuroanat.* 12:91. doi: 10.3389/fnana.2018.00091

Terry, A. V. Jr. (2008). Role of the central cholinergic system in the therapeutics of schizophrenia. *Curr. Neuropharmacol.* 6, 286–292. doi: 10.2174/157015908785777247

Touzot, A., Ruiz-Reig, N., Vitalis, T., and Studer, M. (2016). Molecular control of two novel migratory paths for CGE-derived interneurons in the developing mouse brain. *Development* 143, 1753–1765. doi: 10.1242/dev.131102

Tritsch, N. X., Ding, J. B., and Sabatini, B. L. (2012). Dopaminergic neurons inhibit striatal output through non-canonical release of GABA. *Nature* 490, 262–266. doi: 10.1038/nature11466

Unal, C. T., Golowasch, J. P., and Zaborszky, L. (2012). Adult mouse basal forebrain harbors two distinct cholinergic populations defined by their electrophysiology. *Front. Behav. Neurosci.* 6:21. doi: 10.3389/fnbeh.2012.00021

Villar-Cerviño, V., Kappeler, C., Nóbrega-Pereira, S., Henkemeyer, M., Rago, L., Nieto, M. A., et al. (2015). Molecular mechanisms controlling the migration of striatal interneurons. *J. Neurosci.* 35, 8718–8729. doi: 10.1523/JNEUROSCI.4317-14.2015

Vogt, D., Hunt, R. F., Mandal, S., Sandberg, M., Silberberg, S. N., Nagasawa, T., et al. (2014). Lhx6 directly regulates Arx and CXCR7 to determine cortical interneuron fate and laminar position. *Neuron* 82, 350–364. doi: 10.1016/j.neuron.2014.02.030

von Engelhardt, J., Eliava, M., Meyer, A. H., Rozov, A., and Monyer, H. (2007). Functional characterization of intrinsic cholinergic interneurons in the cortex. *J. Neurosci.* 27, 5633–5642. doi: 10.1523/JNEUROSCI.4647-06.2007

Wamsley, B., and Fishell, G. (2017). Genetic and activity-dependent mechanisms underlying interneuron diversity. *Nat. Rev. Neurosci.* 18, 299–309. doi: 10.1038/nrn.2017.30

Wichterle, H., Alvarez-Dolado, M., Erskine, L., and Alvarez-Buylla, A. (2003). Permissive corridor and diffusible gradients direct medial ganglionic eminence cell migration to the neocortex. *Proc. Natl. Acad. Sci. U S A* 100, 727–732. doi: 10.1073/pnas.242721899

Yamanaka, K., Hori, Y., Minamimoto, T., Yamada, H., Matsumoto, N., Enomoto, K., et al. (2018). Roles of centromedian parafascicular nuclei of thalamus and cholinergic interneurons in the dorsal striatum in associative learning of environmental events. *J. Neural Transm.* 125, 501–513. doi: 10.1007/s00702-017-1713-z

Yap, E. L., and Greenberg, M. E. (2018). Activity-regulated transcription: bridging the gap between neural activity and behavior. *Neuron* 100, 330–348. doi: 10.1016/j.neuron.2018.10.013

Zaborszky, L., Csordas, A., Mosca, K., Kim, J., Gielow, M. R., Vadasz, C., et al. (2015). Neurons in the basal forebrain project to the cortex in a complex topographic organization that reflects corticocortical connectivity patterns: an experimental study based on retrograde tracing and 3D reconstruction. *Cereb. Cortex* 25, 118–137. doi: 10.1093/cercor/bht210

Záborszky, L., Gombkoto, P., Varsanyi, P., Gielow, M. R., Poe, G., Role, L. W., et al. (2018). Specific basal forebrain-cortical cholinergic circuits coordinate cognitive operations. *J. Neurosci.* 38, 9446–9458. doi: 10.1523/JNEUROSCI.1676-18.2018

Zeisel, A., Hochgerner, H., Lönnerberg, P., Johnsson, A., Memic, F., van der Zwan, J., et al. (2018). Molecular architecture of the mouse nervous system. *Cell* 174, 999.e22–1014.e22. doi: 10.1016/j.cell.2018.06.021

Zeisel, A., Muñoz-Manchado, A. B., Codeluppi, S., Lonnerberg, P., La Manno, G., Jureus, A., et al. (2015). Brain structure. Cell types in the mouse cortex and hippocampus revealed by single-cell RNA-seq. *Science* 347, 1138–1142. doi: 10.1126/science.aaa1934

Zhang, Y. F., Reynolds, J. N. J., and Cragg, S. J. (2018). Pauses in cholinergic interneuron activity are driven by excitatory input and delayed rectification, with dopamine modulation. *Neuron* 98, 918.e3–925.e3. doi: 10.1016/j.neuron.2018.04.027

Zhao, Y., Marin, O., Hermesz, E., Powell, A., Flames, N., Palkovits, M., et al. (2003). The LIM-homeobox gene Lhx8 is required for the development of many cholinergic neurons in the mouse forebrain. *Proc. Natl. Acad. Sci. U S A* 100, 9005–9010. doi: 10.1073/pnas.1537759100

Zheng, Y., Feng, S., Zhu, X., Jiang, W., Wen, P., Ye, F., et al. (2018). Different subgroups of cholinergic neurons in the basal forebrain are distinctly innervated by the olfactory regions and activated differentially in olfactory memory retrieval. *Front. Neural Circuits* 12:99. doi: 10.3389/fncir.2018.00099

Zhou, K., Cherra, S. J. III., Goncharov, A., and Jin, Y. (2017). Asynchronous cholinergic drive correlates with excitation-inhibition imbalance *via* a neuronal Ca^{2+} sensor protein. *Cell Rep.* 19, 1117–1129. doi: 10.1016/j.celrep.2017.04.043

Ztaou, S., Maurice, N., Camon, J., Guiraudie-Capraz, G., Kerkerian-Le Goff, L., Beurrier, C., et al. (2016). Involvement of striatal cholinergic interneurons and M1 and M4 muscarinic receptors in motor symptoms of Parkinson's disease. *J. Neurosci.* 36, 9161–9172. doi: 10.1523/JNEUROSCI.0873-16.2016

Zucca, S., Zucca, A., Nakano, T., Aoki, S., and Wickens, J. (2018). Pauses in cholinergic interneuron firing exert an inhibitory control on striatal output *in vivo*. *Elife* 7:e32510. doi: 10.7554/eLife.32510

Conflict of Interest Statement: The authors declare that the research was conducted in the absence of any commercial or financial relationships that could be construed as a potential conflict of interest.

Copyright © 2019 Ahmed, Knowles and Dehorter. This is an open-access article distributed under the terms of the Creative Commons Attribution License (CC BY). The use, distribution or reproduction in other forums is permitted, provided the original author(s) and the copyright owner(s) are credited and that the original publication in this journal is cited, in accordance with accepted academic practice. No use, distribution or reproduction is permitted which does not comply with these terms.

frontiers in Molecular Neuroscience

ORIGINAL RESEARCH
published: 28 August 2019
doi: 10.3389/fnmol.2019.00211

Using a Multiplex Nucleic Acid *in situ* Hybridization Technique to Determine HCN4 mRNA Expression in the Adult Rodent Brain

*Julia Oyrer[1], Lauren E. Bleakley[1], Kay L. Richards[1], Snezana Maljevic[1], A. Marie Phillips[1,2], Steven Petrou[1], Cameron J. Nowell[3] and Christopher A. Reid[1]**

[1] Florey Institute of Neuroscience and Mental Health, The University of Melbourne, Melbourne, VIC, Australia, [2] School of Biosciences, The University of Melbourne, Parkville, VIC, Australia, [3] Drug Discovery Biology, Monash Institute of Pharmaceutical Sciences, Monash University, Parkville, VIC, Australia

Hyperpolarization-activated cyclic nucleotide-gated (HCN) channels carry a non-selective cationic conductance, I_h, which is important for modulating neuron excitability. Four genes (*HCN1-4*) encode HCN channels, with each gene having distinct expression and biophysical profiles. Here we use multiplex nucleic acid *in situ* hybridization to determine HCN4 mRNA expression within the adult mouse brain. We take advantage of this approach to detect HCN4 mRNA simultaneously with either HCN1 or HCN2 mRNA and markers of excitatory (VGlut-positive) and inhibitory (VGat-positive) neurons, which was not previously reported. We have developed a Fiji-based analysis code that enables quantification of mRNA expression within identified cell bodies. The highest HCN4 mRNA expression was found in the habenula (medial and lateral) and the thalamus. HCN4 mRNA was particularly high in the medial habenula with essentially no co-expression of HCN1 or HCN2 mRNA. An absence of I_h-mediated "sag" in neurons recorded from the medial habenula of knockout mice confirmed that HCN4 channels are the predominant subtype in this region. Analysis in the thalamus revealed HCN4 mRNA in VGlut2-positive excitatory neurons that was always co-expressed with HCN2 mRNA. In contrast, HCN4 mRNA was undetectable in the nucleus reticularis. HCN4 mRNA expression was high in a subset of VGat-positive cells in the globus pallidus external. The majority of these neurons co-expressed HCN2 mRNA while a smaller subset also co-expressed HCN1 mRNA. In the striatum, a small subset of large cells which are likely to be giant cholinergic interneurons co-expressed high levels of HCN4 and HCN2 mRNA. The amygdala, cortex and hippocampus expressed low levels of HCN4 mRNA. This study highlights the heterogeneity of HCN4 mRNA expression in the brain and provides a morphological framework on which to better investigate the functional roles of HCN4 channels.

Keywords: HCN4 channels, HCN1 channel, HCN2, multiplex nucleic acid *in situ* hybridization, Ih, quantifcation workflow

OPEN ACCESS

Edited by:
Mary Chebib,
University of Sydney, Australia

Reviewed by:
Ulf Strauss,
Charité – Berlin University of Medicine, Germany
Thomas Budde,
University of Münster, Germany

***Correspondence:**
Christopher A. Reid
careid@unimelb.edu.au

Received: *28 May 2019*
Accepted: *16 August 2019*
Published: *28 August 2019*

Citation:
Oyrer J, Bleakley LE, Richards KL, Maljevic S, Phillips AM, Petrou S, Nowell CJ and Reid CA (2019) Using a Multiplex Nucleic Acid in situ Hybridization Technique to Determine HCN4 mRNA Expression in the Adult Rodent Brain. Front. Mol. Neurosci. 12:211. doi: 10.3389/fnmol.2019.00211

INTRODUCTION

Four genes (*HCN1-4*) encode HCN channels that generate a non-selective cation conductance, I_h (Biel et al., 2009; He et al., 2014). I_h influences a number of fundamental functions including the determination of the resting membrane potential of a neuron, the integration of dendritic synaptic input, the control of synaptic transmission, and the modulation of neuronal firing properties (Biel et al., 2009; He et al., 2014). HCN channels have also been implicated in a variety of pathophysiological states including epilepsy and pain (Reid et al., 2012; DiFrancesco and DiFrancesco, 2015; Tsantoulas et al., 2016). HCN channels exist as both homo- and heterotetramers. The four HCN homomeric channel subtypes have distinct biophysical properties [as reviewed in Biel et al. (2009), Sartiani et al. (2017)]. For example, the activation voltage of HCN1 channels is more depolarized compared to that of HCN2 and HCN4 channels. Activation kinetics also differ, with the rate of channel activation being fastest for HCN1 and slowest for HCN4. Furthermore, HCN channel subtypes are modulated differently, with HCN2 and HCN4 channels being highly sensitive to cAMP concentrations, while HCN1 and HCN3 are less so. Heteromeric HCN channels tend to have hybrid properties extending the biophysical functional diversity of this channel class. These biophysical differences are tuned to specific functions in the brain (Lüthi and McCormick, 1999; Biel et al., 2009). Complementing this functional diversity is the distinct regional expression of the various HCN channel subunits throughout the brain (Santoro et al., 2000; Notomi and Shigemoto, 2004).

Despite the longstanding knowledge that HCN4 channels are expressed in the central nervous system, their role has been relatively understudied compared to HCN1 and HCN2 channels. Recent physiological studies in conditional HCN4 knockout mice reveal a role for these channels in controlling rhythmic intra-thalamic oscillations, presumably through driving intrinsic burst-firing in thalamocortical neurons (Zobeiri et al., 2019). From a pathophysiological perspective, there is some evidence that functional genetic variants are associated with epilepsy (Becker et al., 2017; Campostrini et al., 2018; DiFrancesco et al., 2019). HCN4 mRNA levels are also increased in the pilocarpine rodent model of temporal lobe epilepsy (Surges et al., 2012), while in a cortical stroke model in which seizures develop, there is a switch from HCN2 to HCN4 channel expression in thalamocortical neurons (Paz et al., 2013). A clear anatomical map of HCN4 channel expression is key to better understanding the physiological and pathophysiological roles of these channels. Previous studies have used traditional *in situ* hybridization and immunohistochemical methods to map HCN4 mRNA and HCN4 protein expression in the brain (Moosmang et al., 1999; Santoro et al., 2000; Hughes et al., 2013; Günther et al., 2019; Zobeiri et al., 2019). Here we take advantage of a multiplex *in situ* hybridization technique to map the expression of HCN4 mRNA in VGlut1, VGlut2, and VGat-positive neurons in different anatomical loci of the rodent brain. We also map the co-expression of HCN4 mRNA with both HCN1 and HCN2 mRNA.

MATERIALS AND METHODS

Animals

Experiments were carried out as approved by The Florey Institute of Neuroscience and Mental Health Animal Ethics Committee and in accordance with the guidelines of the NHMRC of Australia Code of Practice for the Care and Use of Animals for Experimental Purposes. Male C57BL/6J mice aged P40 – P42 were used for RNAscope®experiments (three mice for HCN4/HCN2 combination and three mice for HCN4/HCN1 combination). Tissue for Western blots was taken from one Nestin-Cre male and one Nestin-Cre x HCN4-floxed male, aged P31 and P37, respectively. For electrophysiological studies, four Nestin-HCN4 knockout mice (3 male and 1 female) aged P36 – P45 were used, together with four (3 male and 1 female) Nestin-Cre mice aged P29 - P35 for controls.

Western Blot

Mice were deeply anesthetized using isoflurane, decapitated, dissected to isolate thalamus-enriched tissue, and the tissues were stored at −80°C. The isolated tissues were lysed in RIPA buffer (10 mM Tris pH 8.0, 1% Triton X100, 0.1% sodium deoxycholate, 1% SDS 140 mM sodium chloride) and made to a final protein concentration of 5 μg/μl protein, 2 M Urea, and 1xSDS reducing loading buffer (Laemmli, 1970). Known protein concentrations (100 μg) of control and experimental samples were loaded on a gel (7% poly-acrylamide SDS PAGE), transferred to nitrocellulose, and satisfactory transfer of protein by Western blotting monitored by Ponceau S (Sigma-Aldrich; Cat No. P3504) staining. Filters were blocked in 0.5% skim milk 1xTBS 1.0% Igepal (Sigma-Aldrich; Cat No. I3021) for 1 h, incubated overnight at 4°C with primary antibodies [mouse anti-HCN4 (Neuromab; Cat No. 73-150) 1:500], washed, and incubated for 1 h at room temperature with secondary antibodies [goat anti-mouse poly HRP (Invitrogen, Cat No. 32230) 1:15,000]. The protein signal was visualized with Clarity Western ECL Substrate (BioRad; Cat No. 170-5061) and the signal captured by a BioRad ChemiDoc MP System and quantitated with ImageJ.

Electrophysiology

Mice were deeply anesthetized using isoflurane and decapitated. Brains were rapidly removed and mounted in a slice chamber containing chilled cutting solution (125 mM choline chloride, 20 mM D-Glucose, 0.4 mM $CaCl_2{\cdot}2H_2O$, 6 mM $MgCl_2{\cdot}6H_2O$, 2.5 mM KCl, 1.25 mM NaH_2PO_4 and 26 mM $NaHCO_3$). 300 μm thick coronal slices were cut using a vibratome (Leica VT1200 S). Slices were held in a holding chamber with artificial cerebrospinal fluid (125 mM NaCl, 10 mM D-Glucose, 2 mM $CaCl_2{\cdot}2H_2O$, 2 mM $MgCl_2{\cdot}6H_2O$, 2.5 mM KCl, 1.25 mM NaH_2PO_4, and 26 mM $NaHCO_3$) and bubbled continuously with carbogen gas at 32°C for at least 15 min and then room temperature for at least 30 min before recording. Whole-cell recordings from the medial habenula were made using borosilicate glass electrodes (3–6 MΩ) filled with an internal solution comprising 125 mM K-gluconate, 5 mM KCl, 2 mM $MgCl_2{\cdot}6H_2O$, 10 mM HEPES, 4 mM ATP-Mg, 0.3 mM GTP-Na, 10 mM phosphocreatine, 0.1 mM EGTA, and

0.2% biocytin; with a pH of 7.2 and osmolarity of 291 mOsm. Bridge balance and capacitance neutralization were applied. Neurons were maintained at a membrane potential of −50 mV with a 5 s −70 pA current injection used to elicit I_h-mediated "sag." The start-to-start interval was 6.5–7 s. A response over 5–10 sweeps was averaged. Sag was calculated as the difference between the most hyperpolarized point within the first second of the average trace and the final "steady state" of this trace.

Multiplex *in situ* Hybridization RNAscope®

Tissue Preparation

Mice were deeply anesthetized using isoflurane and decapitated. Brains were rapidly removed and snap frozen in a liquid nitrogen vapor phase. Tissue was stored at −80°C until sectioned.

The fresh-frozen brain was embedded in optimum cutting temperature (OCT) embedding gel (Tissue-Tek®, Sakura Finetek, United States). Coronal brain slices were cut at 15 μm thickness using a cryostat (CM 1800, Leica Microsystems) and mounted on positively charged microscope slides. Coronal sections were cut according to the Paxinos Mouse Brain Atlas (approximately bregma −1.70 mm) (Paxinos and Franklin, 2001). Cryosections were kept at −20°C during sectioning and stored for up to 3 weeks at −80°C until further processed for RNAscope® [advanced cell diagnostics (ACD), Newark, CA, United States].

RNAscope® Fluorescent Multiplex Assay

RNA *in situ* hybridization was performed using RNAscope® (ACD) (Wang et al., 2012). Standard mouse probes were used to examine the expression of HCN1 (ACD; Cat No. 423651-C2), HCN2 (ACD; Cat No. 427001-C2), and HCN4 (ACD; Cat No. 421271) mRNA. Probes to VGlut1 (Slc17a7-C2) (ACD; Cat No. 416631-C2), VGlut2 (Slc17a6-C3) (ACD; Cat No. 319171-C3), and VGat (Slc32a1-C3) (ACD; Cat No. 319191-C3). mRNA were used to mark excitatory and inhibitory neurons, respectively. DAPI (ACD; Cat No. 320850) was employed as a cell nucleus marker. Positive (mixture of three probes including Polr2a on C1, PPIB on C2, UBC on C3; ACD; Cat No. 320881) and negative (DapB; ACD; Cat No. 320871) control probes were used to test optimal permeabilization and probe RNA quality.

Tissue was processed according to the protocol set out in the user manual. Briefly, sections were fixed in 4% paraformaldehyde (PFA) for 15 min at 4°C and dehydrated for 5 min each at room temperature and with increasing concentrations of ethanol (50, 70, 100, and 100%) diluted in (RNase-free) diH_2O. Sections were air-dried for 5 min at room temperature and a hydrophobic barrier was drawn around each section using an ImmEdge Hydrophobic Barrier Pen (Vector Labs; Cat No. 310018). Sections were then incubated with protease pretreatment 4 (ACD; Cat No. 322340) for 30 min at room temperature and then washed twice in PBS (1x; RNase-free) before being incubated for 2 h at 40°C with three Mus musculus (Mm) multiplexed probe combinations: (a) Mm-HCN4 (channel 1), Mm-HCN1 (channel 2), and Mm-Slc32a1 (channel 3); (b) Mm-HCN4 (channel 1), Mm-HCN2 (channel 2), and Mm-Slc17a6 (channel 3); and (c) Mm-HCN4 (channel 1), Mm-Slc17a7 (channel 2), and Mm-Slc32a1 (channel 3). For each combination, sections from a minimum of three animals were processed in independent experiments. After hybridization, sections were washed twice in wash buffer (ACD; Cat No. 31009). Signals were amplified according to the protocol using four consecutive amplification steps with the fluorescent multiplex reagent kit (ACD; Cat No. 320850). For amplification step 4, the fluorescent label combination AltB was used. Sections were then washed twice using wash buffer, after which the sections were stained with DAPI for 30 s, covered with ProLong Diamond antifade reagent (Thermo Scientific Fisher; Cat No. P36962) and cover slipped. Company supplied positive and negative controls were both used to confirm specificity of staining.

Imaging

The sections were imaged on an 8 kHz resonant scanning confocal microscope using a pixel dwell time of 72 ns (Leica TCS SP8, Leica GmbH) with a U Plan Apo 40× oil immersion objective with a numerical aperture of 1.3. Complete coronal brain slices were captured using the tile scanning module and Z series were collected to compensate for focal drift. Images were acquired sequentially. Excitation (ex) and emission (em) spectra were set as follows: DAPI (ex 405 nm, em 411–490 nm) on Photomultiplier Tube (PMT); Alexa 488 (ex 488 nm, ex 500–540 nm) on Hybrid Detector (HyD); Atto 550 (ex 561 nm, em 565–620 nm) on HyD; and Alexa 647 (ex 633 nm, em 645–705 nm) on PMT. For quantification analysis, images were taken as single planes. To generate single images in **Figure 1**, maximum intensity projections of Z series were created. Brightness and contrast were adjusted just above saturation for illustration purposes.

RNAscope® Quantification

For each coronal slice, areas from a single opitcal plane were extracted according to "The Mouse Brain in stereotaxic coordinates" and "The Allen Mouse Brain Reference Atlas" (Paxinos and Franklin, 2001; Lein et al., 2007). The extracted areas were as follows: thalamus [without habenula and thalamic reticular nucleus (NRT)], habenula, NRT, striatum, globus pallidus external (GPe), hippocampus, somatosensory cortex, and retrosplenial cortex. Extracted areas were analyzed with a custom-built Fiji macro code (Schindelin et al., 2012). In brief, the macro code performed the following steps: nuclei were extracted using standard watershed segmentation. RNAscope channels were filtered for noise using a Gaussian (sigma = 1) filter. RNAscope positive foci were extracted using maximal point extraction with the user-defined tolerance values appropriate for each sample. Nuclei masks were dilated by three pixels to cover more of the "cell" area. The resulting nuclei areas were then used to count the number of RNAscope foci in each given cell. A cell was deemed positive if it contained three or more RNAscope foci. Our quantitative analysis method was not applied to brain regions where HCN4 mRNA expression was less than 4 dots per DAPI-defined cell or if cell bodies could not be separated due to their high density. The full macro code is available for download from https://doi.org/10.26180/5cde05da74ce0. For each extracted area a minimum of three coronal slices from three different animals was analyzed.

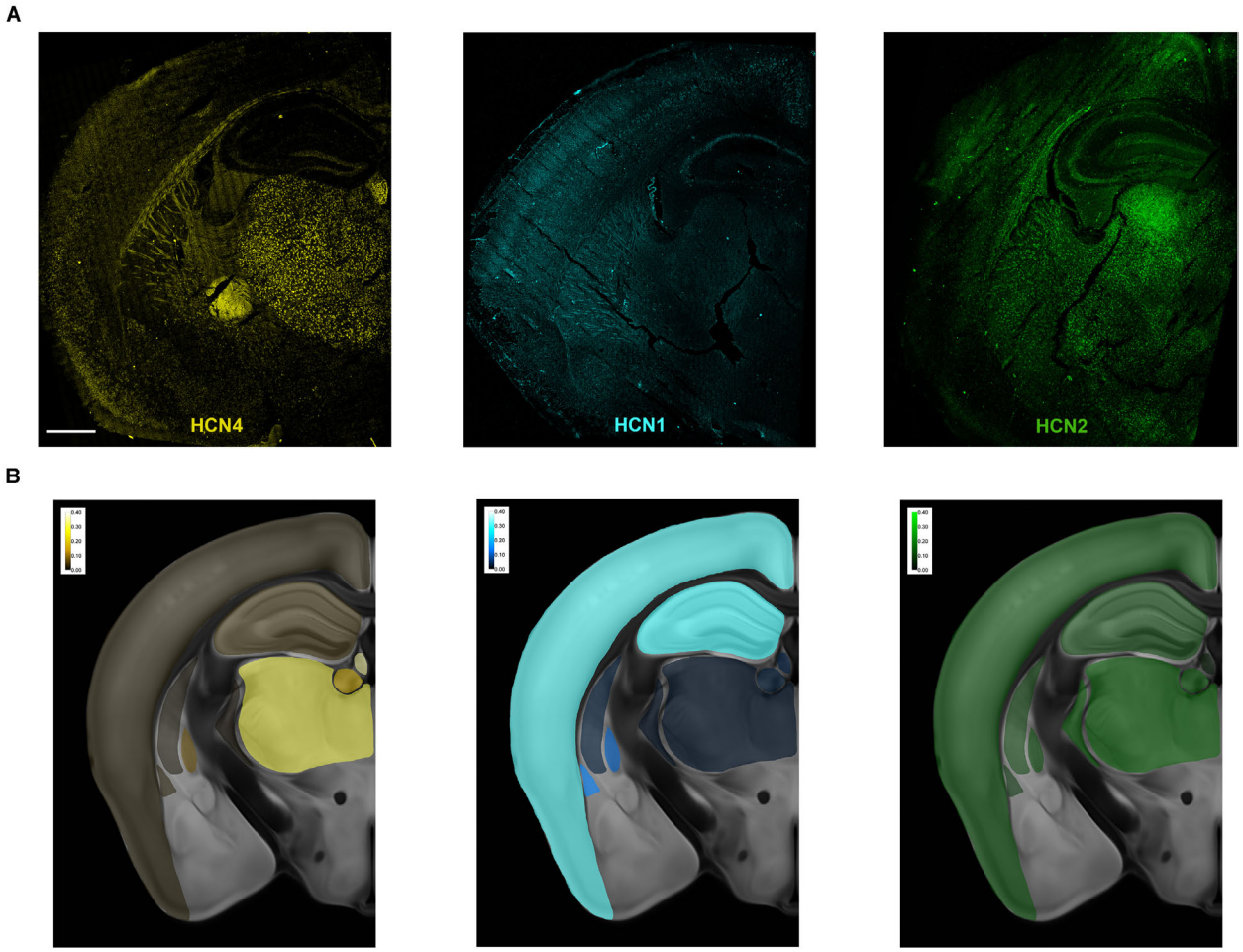

FIGURE 1 | Overview of HCN mRNA expression in the mouse brain. **(A)** Representative maximum intensity projection of a coronal brain slice showing HCN4, HCN2, and HCN1 mRNA expression. In these overview images, brightness, contrast, and γ (HCN4 0.6, HCN1 0.5, and HCN2 0.5) were adjusted purely for illustration purposes. The bright uniform staining below the thalamus in the HCN4 image is an optical aberration and was not analyzed. **(B)** Heatmaps of relative levels of mRNA for each HCN mRNA expressed as a% of total number of cells. Scale bar = 700 μm.

Statistics

All RNAscope data were directly extracted from the macro code and are presented as individual values and mean values. Error bars represent the standard error of the mean (SEM). For electrophysiological data, a Shapiro-Wilk test was initially applied to test for normality, and returned a value of >0.05 in all groups. Statistical significance was then determined using an unpaired two-tailed Student's *t* test (GraphPad Prism version 8.1, GraphPad Software).

RESULTS

Overview of HCN4 mRNA Expression in the Mouse Brain

Multiplex *in situ* hybridization was used to map the expression of HCN4, HCN1 and HCN2 mRNA in a single brain plane (approximately bregma −1.70 mm, **Figure 1A**). Maximum projection images of each subunit are presented in **Figure 1A**. The uniform staining seen below the thalamus in the HCN4 image is an optical aberration. Similarly, fluorescence observed in the fiber tracts in this image is uniform and due to auto-fluorescence. These areas were not quantified. Heatmaps showing the relative expression of each subunit across the brain slice are presented in **Figure 1B**. Expression of HCN4 mRNA was highest in thalamus and medial habenula but was also found in the globus pallidus external (GPe), striatum, hippocampus and cortex. We used a multiplex *in situ* hybridization technique to investigate the pattern of co-expression of HCN4 mRNA with HCN1 and HCN2 mRNA. VGlut1, VGlut2, and VGat were used to establish neuron type.

A Fiji-based code was developed to quantify mRNA expression[1]. The cell body was defined by the nuclear marker DAPI with cell volume estimated by expanding the boundaries by 3 pixels. We use this quantitative approach to describe HCN4

[1]https://doi.org/10.26180/5cde05da74ce0

mRNA expression in brain regions where we were able to separate individual DAPI marked cells and where mRNA clustered within the cell body. We structure the results by first focusing on brain regions that express the highest HCN4 mRNA levels and progressively describe brain regions with lower expression.

HCN4 mRNA Is Abundant in the Habenula

HCN4 mRNA is very highly expressed in the habenula (**Figure 2A**; Moosmang et al., 1999; Santoro et al., 2000). The habenula can be broadly divided into the lateral and medial habenula, with each playing a distinct physiological role (Mizumori and Baker, 2017; Lee et al., 2019). The medial habenula expressed high levels of HCN4 mRNA (**Figure 2A**). However, cells are too densely packed in this region to allow quantitative expression analysis. The HCN4 mRNA signal was also present in the lateral habenula in which quantitative analysis revealed HCN4 mRNA in 19 ± 2% (n = 7 slices) of DAPI-identified cells. In the same region, HCN2 mRNA was expressed in 59 ± 3% (n = 3 slices), while HCN1 expression was only seen in 0.9 ± 0.4% (n = 4 slices) of cells (**Figure 2B**). The vast majority of HCN4 mRNA positive-cells (89 ± 1%, n = 3 slices) co-expressed VGlut2 (**Figure 2C**), a marker of excitatory neurons. Furthermore 90 ± 2% (n = 3 slices) of HCN4 mRNA-positive cells also expressed HCN2 mRNA (**Figure 2C**). This indicates that HCN4 channels potentially co-express with HCN2 channels in excitatory neurons in the lateral habenula.

In contrast to HCN4, HCN1, and HCN2 mRNA expression was essentially undetectable in the medial habenula (**Figures 2A,B**). This implies that HCN4 channels are the major and potentially the sole carrier of I_h in this region. To test this hypothesis, whole-cell electrophysiological recordings were made from neurons identified in the medial habenula in Nestin-HCN4 knockout mice (**Figures 2D,E**). Recorded neurons had a small dendritic arbor (**Figure 2F**) with depolarizing current injections mostly generating tonic trains of action potential firing (**Figure 2G**). In all Nestin-Cre control neurons, hyperpolarizing current injections generated an I_h-mediated "sag" on the recorded voltage (**Figures 2H,I**). In brain-specific HCN4 knockout mice, I_h-mediated "sag" was absent, strongly supporting the role of HCN4 channels as the exclusive mediator of this current in the medial habenula (**Figures 2H,I**).

HCN4 mRNA Is Abundant in the Thalamus

As shown in previous studies, HCN4 mRNA was also highly expressed in the thalamus (**Figure 3**; Moosmang et al., 1999; Santoro et al., 2000). We completed analysis on thalamic sub-nuclei combined (excluding NRT and habenula) and measured HCN4 mRNA in 34 ± 3% (n = 8 slices) of cells. Using VGlut2 as a marker of excitatory thalamocortical neurons (Varoqui et al., 2002; Fremeau et al., 2004), 43 ± 5% (n = 4 slices) of cells were found positive for VGlut2 mRNA in the thalamus. HCN2 mRNA was seen in 67 ± 3% (n = 4 slices), with HCN1 mRNA essentially undetectable (0.6 ± 0.2%, n = 4 slices). The vast majority of VGlut2 positive cells expressed HCN4 and HCN2 mRNA (**Figures 3A,B**). HCN4 mRNA was only detected in VGlut2-positive neurons (90 ± 2%, n = 4 slices) and was always co-expressed with HCN2 mRNA (95 ± 1%, n = 4 slices) (**Figure 3C**). In contrast, only 58 ± 5% (n = 4 slices) of cells positive for HCN2 mRNA co-expressed VGlut2. This indicates that HCN2 is also expressed in cell types that are VGlut2- and HCN4-negative (see arrows **Figure 3A**).

HCN4 mRNA Is Very Low in the Thalamic Reticular Nucleus

The presence of VGat mRNA and absence of VGlut1 and VGlut2 mRNA is consistent with the predominance of GABAergic neurons in the NRT (**Figures 3D,E**; Houser et al., 1980; de Biasi et al., 1986; Huguenard and McCormick, 1992). Only 1 ± 0.3% (n = 7 slices) of cells were positive for HCN4 mRNA, suggesting very low expression in the NRT. Similarly, HCN1 expression was low, with only 0.5 ± 0.3% (n = 4 slices) cells being positive (**Figure 3D**). In contrast, 61 ± 7% of cells (n = 3 slices) were positive for HCN2 mRNA, indicating that this is the predominant HCN channel subtype expressed in the NRT (**Figure 3E**).

HCN4 mRNA Is Low in the Striatum but High in Putative Giant Cholinergic Interneurons

The striatum expressed HCN4 mRNA at very low levels (**Figure 4**). Only 2 ± 1% (n = 4 slices) of cells were positive for HCN4 mRNA, but in these cells, expression was very high (**Figure 4**). Further inspection revealed that HCN4 mRNA was only labeled in a small subset of very large cells (**Figure 4**). These cells did not express VGlut1, VGlut2 or VGat mRNA (**Figure 4**), suggesting that they were cholinergic interneurons, which comprise about 1–2% of striatal cells (Bolam et al., 1984; Contant et al., 1996; Lim et al., 2014). In the striatum, HCN2 mRNA was more widely expressed (40 ± 5% of cells, n = 4 slices), while HCN1 expression was very low (0.8 ± 0.4%, n = 3 slices). HCN4 mRNA-positive cells mostly co-expressed HCN2 mRNA (84 ± 10% of cells, n = 4 slices), while co-expression of HCN1 mRNA was essentially non-existent (2 ± 2% of cells, n = 3 slices).

HCN4 mRNA Is Low in the Globus Pallidus External (GPe) and Expressed Almost Exclusively in VGat-Positive Cells

HCN4 mRNA was expressed at low levels in the GPe (**Figure 5**) with 8 ± 2% (n = 7 slices) of cells positive. 78 ± 5% (n = 4 slices) of HCN4 mRNA-positive cells co-expressed VGat mRNA, indicating that these channels are predominantly expressed in GABAergic neurons in this region. However, 29 ± 3% (n = 4 slices) of VGat mRNA-positive cells co-expressed HCN4 mRNA, suggesting that HCN4 mRNA is only present in a subset of GABAergic neurons. In the GPe, HCN1 mRNA was also expressed at low levels (3 ± 0.8% of cells, n = 4 slices), while HCN2 mRNA was expressed more widely (49 ± 6% of cells, n = 3 slices). The majority of HCN4 mRNA-positive cells also expressed HCN2 mRNA, with a smaller subset co-expressing HCN1 mRNA (**Figure 5**).

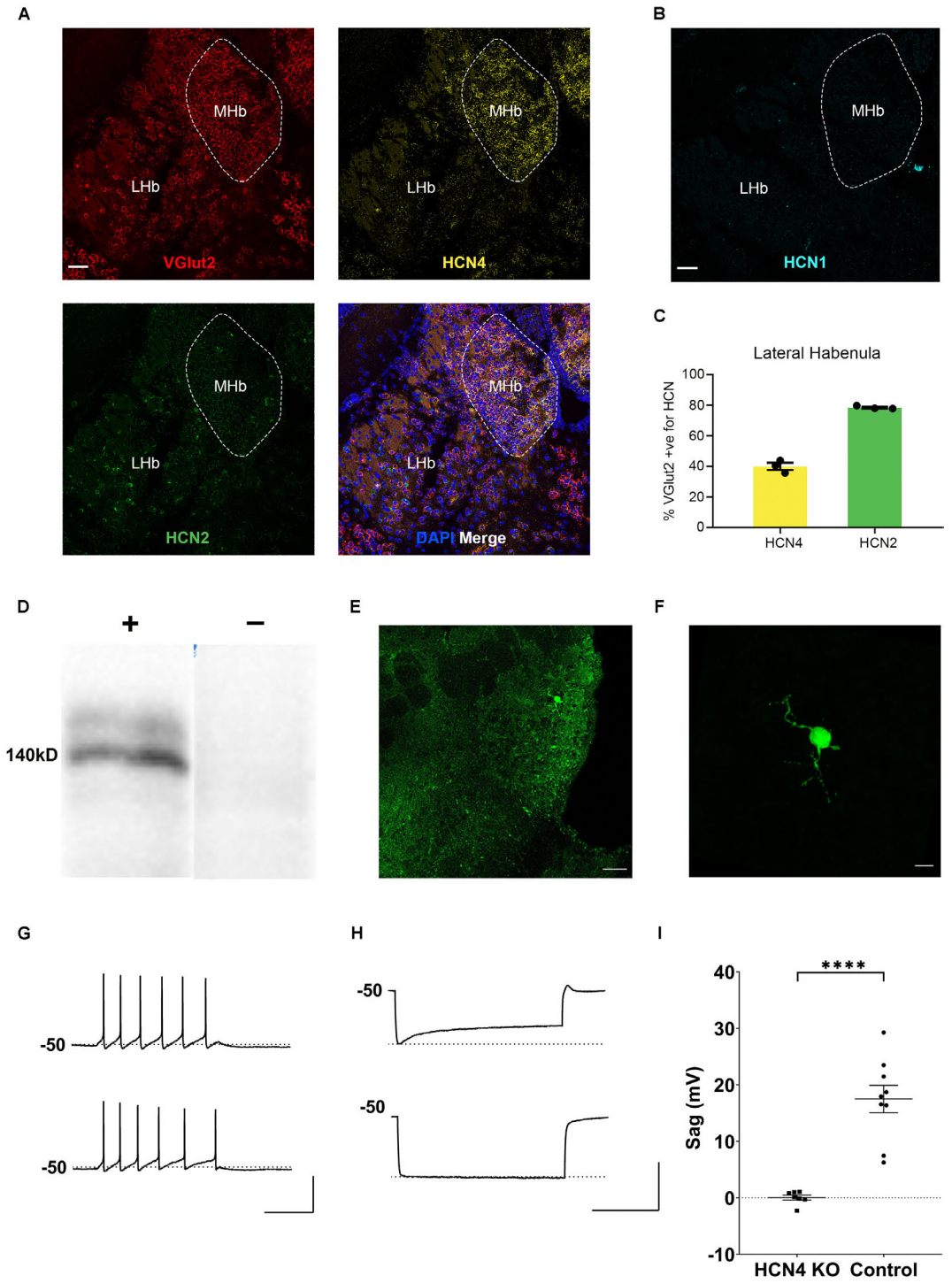

FIGURE 2 | HCN4 channels support I_h in the medial habenula. **(A)** Representative confocal images (single optical slice) of the lateral and medial habenula (LHb, MHb) showing VGlut2, HCN4, and HCN2 mRNA expression presented individually and as a composite with DAPI staining. Scale bar = 50 μm. **(B)** Representative confocal images (single optical slice) of LHb and MHb showing HCN1 mRNA expression from a different slice. Scale bar = 50 μm. **(C)** Percentage of VGlut2-positive neurons in the LHb expressing HCN4 or HCN2 mRNA. **(D)** Western blot analysis of a Nestin-HCN4 knockout mouse (–) and Nestin-Cre control (**+**). **(E)** Biocytin-filled neuron identifying a recorded neuron in the medial habenula. Scale bar = 50 μm. **(F)** Maximum intensity projection of the identified neuron. Scale bar = 10 μm. **(G)** Example traces showing action potential firing at rheobase in a medial habenula neuron from a Nestin-Cre control mouse (upper) and from a Nestin-HCN4 knockout mouse (lower). Scale bar = 200 ms (*x* axis), 50 mV (*y* axis). **(H)** Example traces of "sag" on the voltage recording (average of 5–10 sweeps) from a Nestin-Cre mouse (upper) and from a Nestin-HCN4 knockout mouse (lower). Scale bar = 2 s (x axis), 50 mV (y axis). **(I)** Scatter plot comparing "sag" in medial habenula neurons from Nestin-HCN4 knockout mice (7 cells) and Nestin-Cre mice (9 cells). ****$p < 0.0001$.

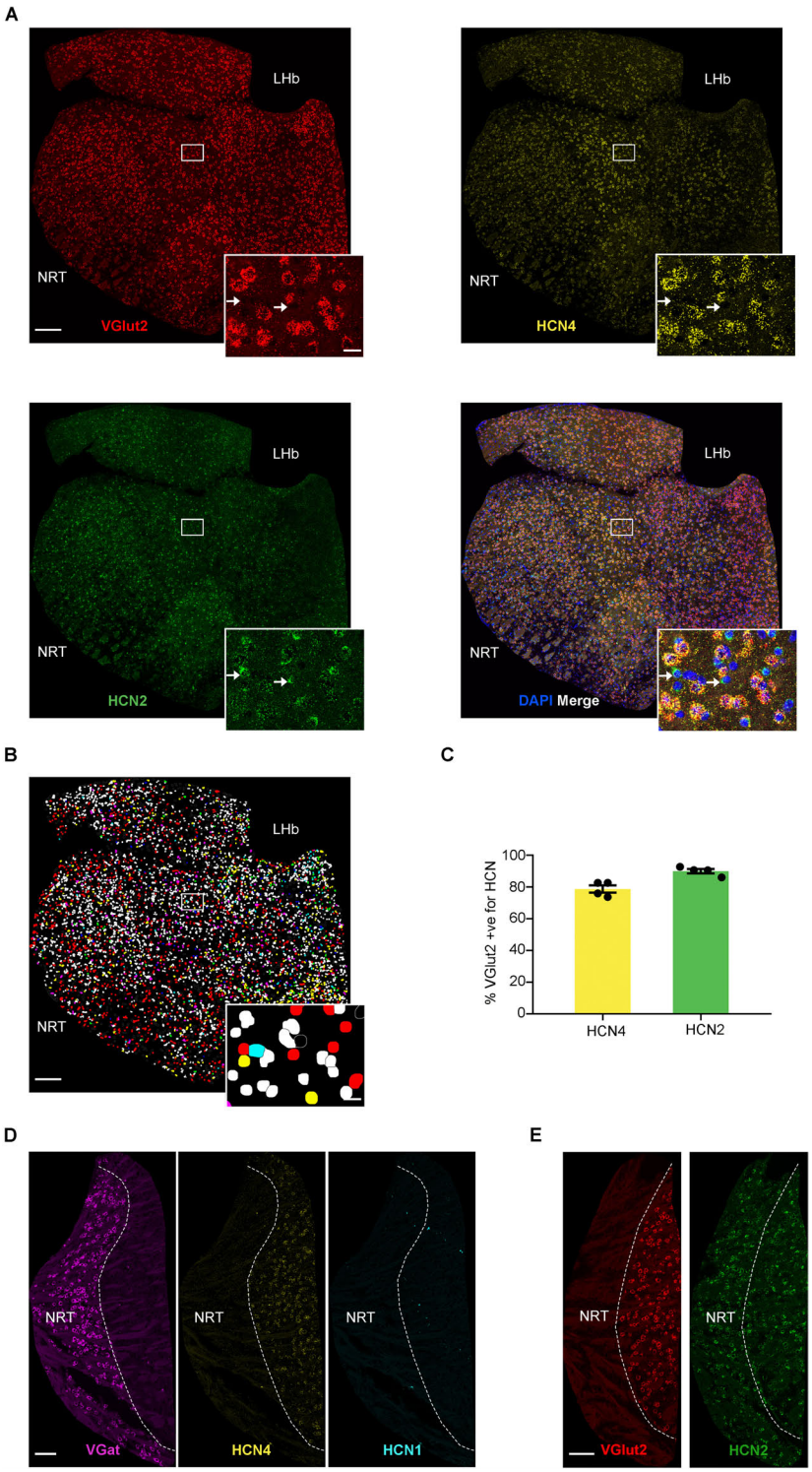

FIGURE 3 | High HCN4 mRNA expression in the thalamus. **(A)** Representative confocal images (single optical slice) of the thalamus showing VGlut2, HCN4, and HCN2 mRNA expression presented individually and as a composite with DAPI staining. For analysis, thalamus regions (excluding NRT and habenula) were cut out and areas other than the thalamus were masked as presented here. Scale bar = 200 μm. Inset scale bar = 20 μm. **(B)** Classification of thalamic cell types based on combination of mRNA expressed. Blue, HCN4; red, HCN2; green, VGlut2; yellow, co-expression of HCN2 and VGlut2; cyan, co-expression of VGlut2 and HCN4; magenta, co-expression of HCN2 and HCN4; white, triple expression. **(C)** Percentage of VGlut2-positive neurons that express HCN4 or HCN2 mRNA. **(D)** Representative confocal images (single optical slice) of the NRT showing VGat mRNA, HCN4 mRNA, and HCN1 mRNA. Scale bar = 100 μm. **(E)** Representative confocal images (single optical slice) of NRT showing VGlut2 and HCN2 mRNA. Scale bar = 100 μm.

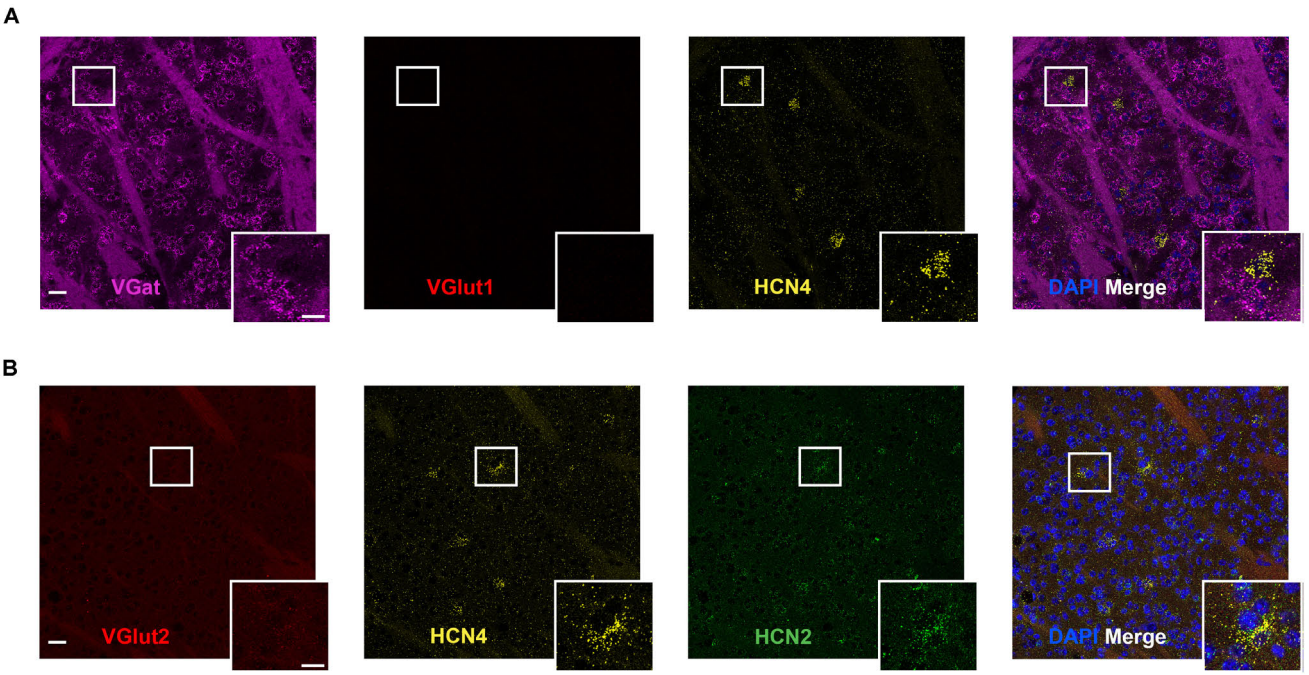

FIGURE 4 | High HCN4 mRNA expression in giant cholinergic neurons in the striatum. **(A)** Representative confocal images (single optical slice) in the striatum showing VGat, VGlut1, and HCN4 mRNA presented individually and as a composite with DAPI staining. Co-expression of magenta and yellow = white. Scale bar = 30 μm. Inset scale bar = 15 μm. **(B)** Representative confocal images (single optical slice) in the striatum showing VGlut2, HCN4, and HCN2 mRNA presented individually and as a composite with DAPI staining. Scale bar = 30 μm. Inset scale bar = 15 μm.

Low HCN4 mRNA Expression in the Hippocampus

In general, HCN4 mRNA expression was very low and diffuse (not clustered) in the hippocampus, making quantitative analysis unreliable. We specifically looked at co-expression using the GABAergic marker, VGat, given that HCN4 channel expression has been reported in parvalbumin-positive neurons (Hughes et al., 2013; Seo et al., 2015). Consistent with those findings, HCN4 mRNA clustered in a subset of VGat-positive neurons (**Figure 6**). Quantitative analysis revealed that 15 ± 8% of VGat positive cells (n = 3) slices expressed HCN4 mRNA, although it should be noted that this is only a rough estimate given the low expression.

HCN4 mRNA Expression in Other Brain Regions

HCN4 mRNA expression was above background in a number of other brain regions. However, in these regions the expression pattern was generally diffuse, making quantitative analysis unreliable. We have therefore only presented the HCN4 mRNA probe results in these regions without interpreting co-expression with other HCN channels or neuron markers. These regions include the somatosensory, auditory, piriform and retrosplenial cortices (**Figures 7A–D**), and the lateral amygdala (**Figure 7E**). Importantly, although quantification was not possible, our results show HCN4 mRNA expression above background and suggest that HCN4 channels have a functional role in these regions.

DISCUSSION

Multiplex nucleic acid *in situ* hybridization provides a powerful method to probe mRNA expression in tissue with improved specificity and sensitivity, as well as the ability to use multiple probes simultaneously (Wang et al., 2012). Here we investigated the expression of HCN4 mRNA in the adult rodent brain. HCN4 mRNA was found to be highest in the thalamus and habenula (medial and lateral). HCN4 mRNA expression was also high in giant cholinergic interneurons in the striatum and in a subset of VGat-positive interneurons in the GPe. The cortex, amygdala and hippocampus had lower, more diffuse expression patterns for HCN4 mRNA. These results generally recapitulate previous work using standard *in situ* techniques (Moosmang et al., 1999; Santoro et al., 2000). Importantly, we were able to extend these previous results by identifying the neuron types that expressed HCN4 mRNA using markers of excitatory and inhibitory neurons, and by establishing the co-expression pattern of HCN4 mRNA with other HCN channel subtypes in a subset of brain regions.

A workflow based on a Fiji macro enabled the quantification of mRNA expression within cell bodies identified by the nuclear marker, DAPI. This provides a powerful tool for understanding mRNA expression profiles. However, there are some important caveats to this approach. First, the method only works in regions of the brain in which cell bodies are separated sufficiently to identify single cells. In regions such as the medial habenula and piriform cortex, the high density of cell bodies precludes such analysis at the resolution imaged

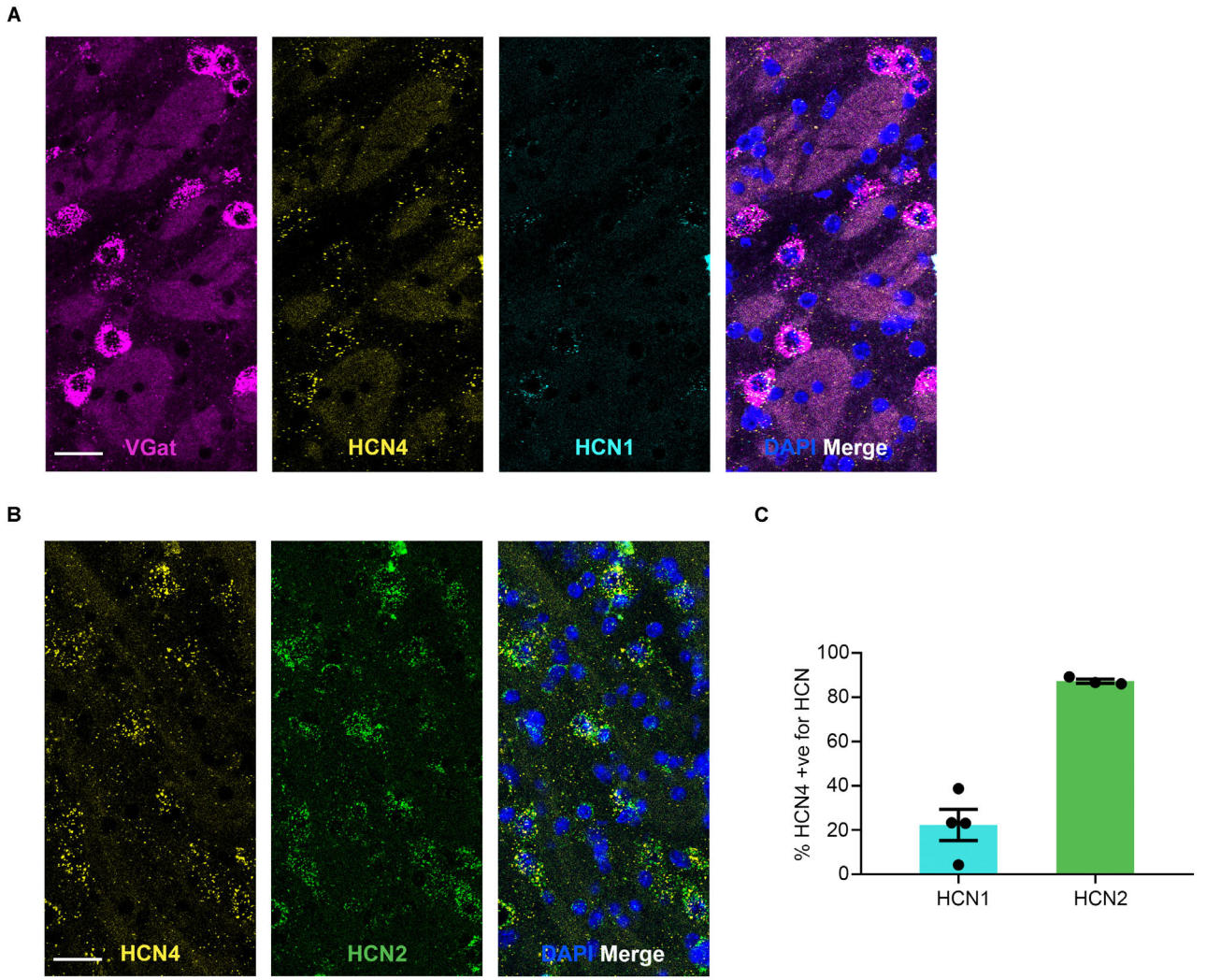

FIGURE 5 | HCN4 mRNA expression in GABAergic neurons in the globus pallidus external. **(A)** Representative confocal images (single optical slice) in the globus pallidus external showing VGat, HCN4, and HCN1 mRNA presented individually and as a composite with DAPI staining. Co-expression of magenta and yellow = white. Scale bar = 30 μm. **(B)** Representative confocal images (single optical slice) in the globus pallidus external showing HCN4 and HCN2 mRNA presented individually and as a composite with DAPI staining. Scale bar = 30 μm. **(C)** Percentage of HCN4 positive neurons that are expressing HCN1 or HCN2 mRNA.

here. Second, the method can only provide an estimate of mRNA expression in the defined cell body. This cannot take into account mRNA in other compartments such as dendrites and axons. Similarly, mRNA in dendrites and axons that cross the cell body may "contaminate" the signal. This analytical method therefore works best for situations where high mRNA expression is clustered at the cell body and should be avoided when mRNA expression is diffuse, as seen in the cortex and hippocampus for HCN4 mRNA. Furthermore, although the multiplex *in situ* hybridization technique allows high resolution mapping of HCN mRNA, the method cannot report on protein levels or post-translational aspects of function. This is especially important given that HCN channels are subject to a number of different post-translational mechanisms in both physiological and pathological settings, resulting in biophysical and trafficking changes (Lewis et al., 2010). This said, functional analysis at the cellular level in the different brain regions is largely consistent with HCN4 mRNA expression patterns observed in our study.

HCN4 mRNA expression is high across both the lateral and medial habenula. I_h is a critical modulator of neuronal excitability in the lateral habenula (Yang et al., 2018). HCN4 mRNA was expressed in VGlut2-positive cells and mostly co-expressed with HCN2 mRNA in the lateral habenula. I_h has a hyperpolarized activation voltage of ∼−110 mV in this region, which is consistent with a heteromeric channel containing both HCN4 and HCN2 isoforms (Good et al., 2013). In the medial habenula, HCN4 mRNA expression is strikingly high, with expression around background levels for HCN1 and HCN2 mRNA (Moosmang et al., 1999; Santoro et al., 2000). At a cellular level, I_h underlies spontaneous tonic

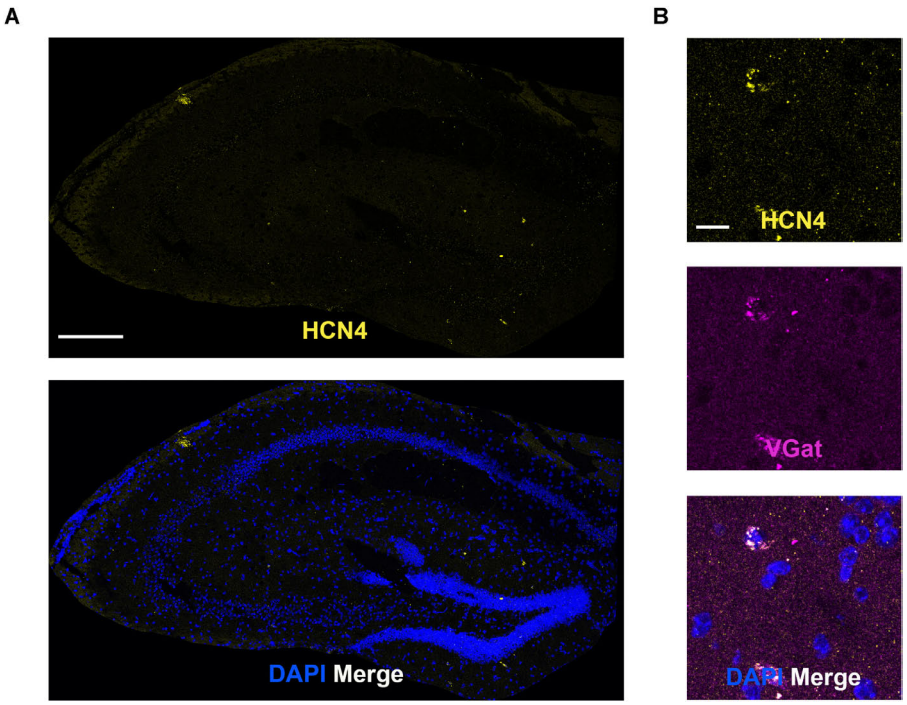

FIGURE 6 | Low HCN4 mRNA expression in the hippocampus. **(A)** Representative confocal images (single optical slice) in the hippocampus showing HCN4 mRNA presented individually and as a composite with DAPI staining. Scale bar = 250 μm. **(B)** Representative confocal images (single optical slice) in the dentate gyrus showing HCN4 and VGat mRNA expression presented individually and as a composite with DAPI staining. Co-expression of magenta and yellow = white. Scale bar = 20 μm.

firing in cholinergic neurons suggesting HCN channels play an important role in defining excitability at least in a subset of medial habenula neurons (Görlich et al., 2013). Using whole-cell electrophysiological recordings from knockout mice we confirmed that HCN4 channels are the predominant subtype underlying I_h in these neurons.

The medial habenula can be subdivided, with distinct gene expression patterns reported for neurons in the superior-inferior, ventral-central, and lateral regions (Lecourtier and Kelly, 2007; Aizawa et al., 2012). Despite this, our results suggest a relatively uniform expression of HCN4 mRNA across the medial habenula. Further studies investigating the co-expression of HCN4 mRNA with markers of substance P, interleukin-18 and choline acetyltransferase are warranted.

HCN4 mRNA was also highly expressed in the thalamus, the main integrator and relay of sensory information to the cortex. The thalamus can be subdivided into a large number of nuclei, but given that HCN4 mRNA expression was uniform across the thalamic sub-nuclei, we combined them for analysis. Most VGlut2-positive excitatory neurons were positive for HCN4 mRNA and co-expressed HCN2 mRNA. Consistent with this, I_h is significantly reduced in thalamocortical relay neurons of both HCN2 and HCN4 knockout mice (Ludwig et al., 2003; Zobeiri et al., 2019). This strongly suggests that HCN4 and HCN2 subunits form heteromeric channels and that they are found in the majority of thalamocortical neurons. One interesting finding from our analysis is that HCN2 mRNA expressed alone in a subset of cells that were not positive for VGlut2 or HCN4 mRNA. The identity of these cells remains unknown.

HCN4 mRNA expression is high in a very select subset of cells in the striatum (Santoro et al., 2000). These cells are large and do not express VGlut1, VGlut2 or VGat mRNA, strongly suggesting that they are giant cholinergic interneurons. This needs confirmation using other markers including choline acetyltransferase and VGlut3 (Fremeau et al., 2002; Gras et al., 2002). At the cellular level, I_h is important for autonomous pacemaker and spiking activity in these interneurons (Wilson, 2005). HCN4 and HCN2 mRNA was co-expressed in these neurons, while HCN1 mRNA was essentially absent. This is broadly consistent with results reported using single-cell PCR (Zhao et al., 2016) although our results suggest approximately equal expression of HCN4 and HCN2 mRNA.

HCN4 mRNA expression was low and diffuse in the hippocampus. HCN4 channel expression has been reported in parvalbumin-positive neurons in the adult rodent hippocampus (Hughes et al., 2013; Seo et al., 2015). The expression of HCN4 mRNA in a subset of VGat-positive neurons is consistent with this. In a number of regions, such as the cortex and amygdala, HCN4 mRNA levels were above background but expression was not clustered. In these regions it is very difficult to make statements about co-expression and we only present HCN4 mRNA data. This does not mean that expression of the HCN4 channel is unimportant, or that it does not play critical functional roles in these brain areas. For example, despite the low

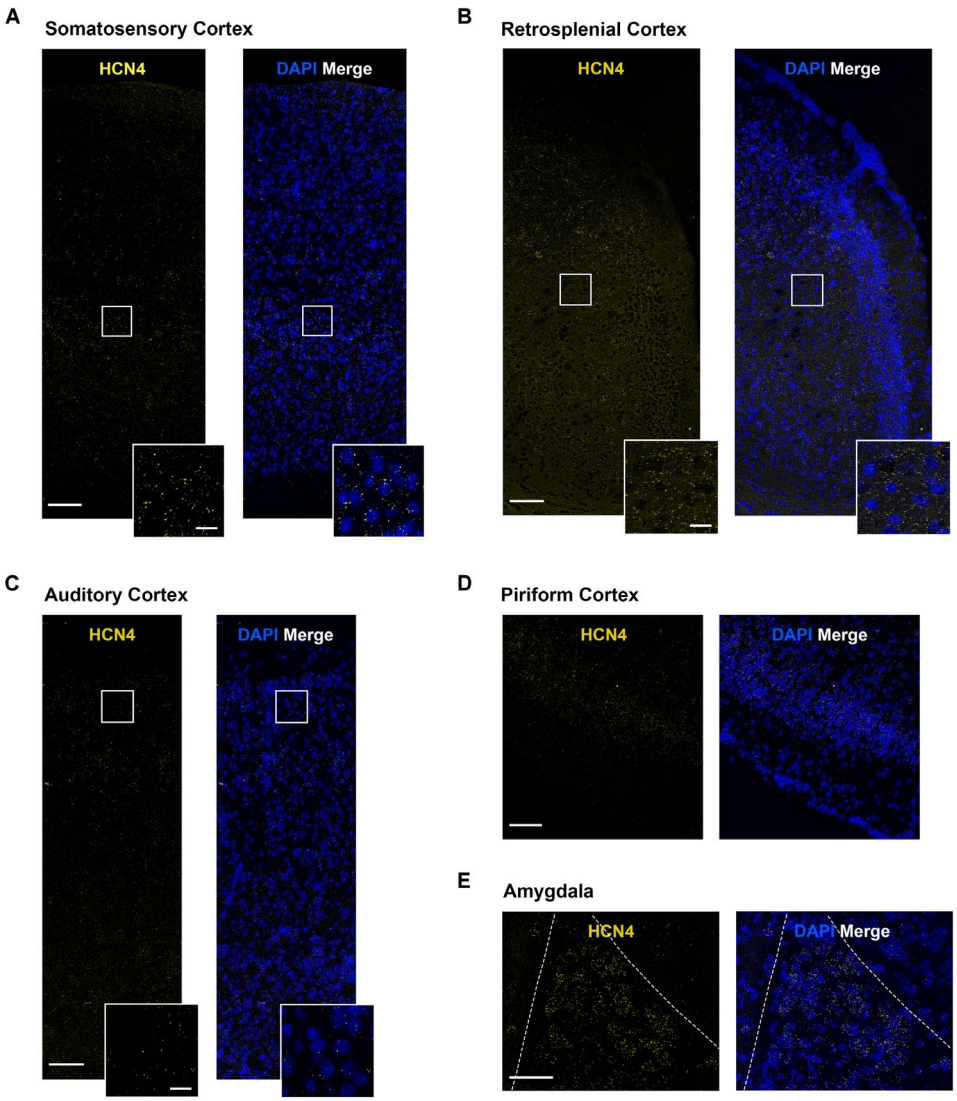

FIGURE 7 | HCN4 mRNA expression in the cortex and the amygdala is low and diffuse. **(A)** Representative confocal images (single optical slice) in the somatosensory cortex showing HCN4 mRNA presented individually and as a composite with DAPI staining. Scale bar = 100 μm. Inset scale bar = 20 μm. **(B)** Representative confocal images (single optical slice) in the retrosplenial cortex showing HCN4 mRNA presented individually and as a composite with DAPI staining. Scale bar = 100 μm. Inset scale bar = 20 μm. **(C)** Representative confocal images (single optical slice) in the auditory cortex showing HCN4 mRNA presented individually and as a composite with DAPI staining. Scale bar = 100 μm. Inset scale bar = 20 μm. **(D)** Representative confocal images (single optical slice) in the piriform cortex showing HCN4 mRNA presented individually and as a composite with DAPI staining. Scale bar = 100 μm. **(E)** Representative confocal images (single optical slice) in the amygdala showing HCN4 mRNA presented individually and as a composite with DAPI staining. Scale bar = 80 μm.

expression of HCN4 mRNA in the cortex, immunohistochemical analysis reveals that HCN4 channel protein is robustly expressed, although at lower levels than those seen in the thalamus (Zobeiri et al., 2019). The precise functional role of HCN4 channels in the cortex and amygdala remains to be determined.

This study focused on high-resolution imaging of a single brain slice plane that encompassed regions known to express HCN4 channels, and established a robust workflow to measure mRNA expression using the multiplex *in situ* hybridization technique. HCN4 channels are known to be expressed in other central nervous system regions not investigated here, including the olfactory bulb, the cerebellum, and the spinal cord (Fried et al., 2010; Hughes et al., 2013; Nakashima et al., 2013; Zúñiga et al., 2016; Peng et al., 2017). Future studies using the multiplex *in situ* hybridization technique in these regions are warranted. Furthermore, we focused our efforts on co-expression of HCN4 mRNA with only broad markers of excitatory and inhibitory neurons. Additional markers of cell types, for example cholinergic or more specific GABAergic neuron markers as well as glia markers would refine the knowledge of expression of this channel. We also have not explored the expression of HCN3 mRNA. The functional importance of this channel

is becoming evident (Kanyshkova et al., 2012; Stieglitz et al., 2017; Lainez et al., 2019) and the use of the multiplex *in situ* hybridization technique to map HCN3 mRNA expression is warranted. Finally, the multiplex *in situ* technique could be combined with immunohistochemical approaches to identify specific neuron compartments.

We have used the multiplex *in situ* hybridization technique to improve our knowledge about which neuron types express HCN4 mRNA. Furthermore, we have identified in several brain regions which other HCN channel subtypes co-express with HCN4 mRNA. These results provide a morphological framework on which to better investigate the functional roles of these important channels.

DATA AVAILABILITY

All datasets generated for this study are included in the manuscript and/or the supplementary files.

ETHICS STATEMENT

The animal study was reviewed and approved by The Florey Institute of Neuroscience and Mental Health Animal Ethics Committee and performed in accordance with the guidelines of the NHMRC of Australia Code of Practice for the Care and Use of Animals for Experimental Purposes.

AUTHOR CONTRIBUTIONS

JO, SP, and CR conceived the study. JO, LB, KR, and AP completed the experimental work. CN wrote the Fiji code for analysis of imaging data. JO and LB completed the analysis of data. All authors contributed to the writing of the manuscript.

FUNDING

This work was supported by the National Health and Medical Research Council (NHMRC) Program Grant (10915693) to SP and CR and an NHMRC Project Grant (1143101) to CR. LB acknowledges the support of an Australian Government Research Training Program Scholarship.

ACKNOWLEDGMENTS

We thank Paulo Pinares-Garcia and Timothy Sissons for reading the manuscript, Jan Terhag for the technical support, and Verena Wimmer for the imaging support. We acknowledge Dr. Ludwig for supplying the HCN4 floxed mouse.

REFERENCES

Aizawa, H., Kobayashi, M., Tanaka, S., Fukai, T., and Okamoto, H. (2012). Molecular characterization of the subnuclei in rat habenula. *J. Comp. Neurol.* 520, 4051–4066. doi: 10.1002/cne.23167

Becker, F., Reid, C. A., Hallmann, K., Tae, H.-S., Phillips, A. M., Teodorescu, G., et al. (2017). Functional variants inHCN4 andCACNA1H may contribute to genetic generalized epilepsy. *Epilepsia. Open* 2, 334–342. doi: 10.1002/epi4.12068

Biel, M., Wahl-Schott, C., Michalakis, S., and Zong, X. (2009). Hyperpolarization-activated cation channels: from genes to function. *Physiol. Rev.* 89, 847–885. doi: 10.1152/physrev.00029.2008

Bolam, J. P., Wainer, B. H., and Smith, A. D. (1984). Characterization of cholinergic neurons in the rat neostriatum. A combination of choline acetyltransferase immunocytochemistry, Golgi-impregnation and electron microscopy. *Neuroscience* 12, 711–718. doi: 10.1016/0306-4522(84)90165-90169

Campostrini, G., DiFrancesco, J. C., Castellotti, B., Milanesi, R., Gnecchi-Ruscone, T., Bonzanni, M., et al. (2018). A Loss-of-Function HCN4 Mutation associated with familial benign myoclonic epilepsy in infancy causes increased neuronal excitability. *Front. Mol. Neurosci.* 11:269. doi: 10.3389/fnmol.2018.00269

Contant, C., Umbriaco, D., Garcia, S., Watkins, K. C., and Descarries, L. (1996). Ultrastructural characterization of the acetylcholine innervation in adult rat neostriatum. *Neuroscience* 71, 937–947. doi: 10.1016/0306-4522(95)00507-502

de Biasi, S., Frassoni, C., and Spreafico, R. (1986). GABA immunoreactivity in the thalamic reticular nucleus of the rat. A light and electron microscopical study. *Brain Res.* 399, 143–147. doi: 10.1016/0006-8993(86)90608-6

DiFrancesco, J. C., Castellotti, B., Milanesi, R., Ragona, F., Freri, E., Canafoglia, L., et al. (2019). HCN ion channels and accessory proteins in epilepsy: genetic analysis of a large cohort of patients and review of the literature. *Epilepsy Res.* 153, 49–58. doi: 10.1016/j.eplepsyres.2019.04.004

DiFrancesco, J. C., and DiFrancesco, D. (2015). Dysfunctional HCN ion channels in neurological diseases. *Front. Cell Neurosci.* 6:174. doi: 10.3389/fncel.2015.00071

Fremeau, R. T., Burman, J., Qureshi, T., Tran, C. H., Proctor, J., Johnson, J., et al. (2002). The identification of vesicular glutamate transporter 3 suggests novel modes of signaling by glutamate. *Proc. Natl. Acad. Sci. U.S.A.* 99, 14488–14493. doi: 10.1073/pnas.222546799

Fremeau, R. T., Voglmaier, S., Seal, R. P., and Edwards, R. H. (2004). VGLUTs define subsets of excitatory neurons and suggest novel roles for glutamate. *Trends Neurosci.* 27, 98–103. doi: 10.1016/j.tins.2003.11.005

Fried, H.-U., Kaupp, U. B., and Müller, F. (2010). Hyperpolarization-activated and cyclic nucleotide-gated channels are differentially expressed in juxtaglomerular cells in the olfactory bulb of mice. *Cell Tissue Res.* 339, 463–479. doi: 10.1007/s00441-009-0904-909

Good, C. H., Wang, H., Chen, Y.-H., Mejias-Aponte, C. A., Hoffman, A. F., and Lupica, C. R. (2013). Dopamine D4 receptor excitation of lateral habenula neurons via multiple cellular mechanisms. *J. Neurosci.* 33, 16853–16864. doi: 10.1523/JNEUROSCI.1844-13.2013

Görlich, A., Antolin-Fontes, B., Ables, J. L., Frahm, S., Slimak, M. A., Dougherty, J. D., et al. (2013). Reexposure to nicotine during withdrawal increases the pacemaking activity of cholinergic habenular neurons. *Proc. Natl. Acad. Sci. U.S.A.* 110, 17077–17082. doi: 10.1073/pnas.1313103110

Gras, C., Herzog, E., Bellenchi, G. C., Bernard, V., Ravassard, P., Pohl, M., et al. (2002). A third vesicular glutamate transporter expressed by cholinergic and serotoninergic neurons. *J. Neurosci.* 22, 5442–5451. doi: 10.1523/jneurosci.22-13-05442.2002

Günther, A., Luczak, V., Gruteser, N., Abel, T., and Baumann, A. (2019). HCN4 knockdown in dorsal hippocampus promotes anxiety-like behavior in mice. *Genes Brain Behav.* 18, e12550. doi: 10.1111/gbb.12550

He, C., Chen, F., Li, B., and Hu, Z. (2014). Neurophysiology of HCN channels: from cellular functions to multiple regulations. *Prog. Neurobiol.* 112, 1–23. doi: 10.1016/j.pneurobio.2013.10.001

Houser, C. R., Vaughn, J. E., Barber, R. P., and Roberts, E. (1980). GABA neurons are the major cell type of the nucleus reticularis thalami. *Brain Res.* 200, 341–354. doi: 10.1016/0006-8993(80)90925-7

Hughes, D. I., Boyle, K. A., Kinnon, C. M., Bilsland, C., Quayle, J. A., Callister, R. J., et al. (2013). HCN4 subunit expression in fast-spiking interneurons of the rat spinal cord and hippocampus. *Neuroscience* 237, 7–18. doi: 10.1016/j.neuroscience.2013.01.028

Huguenard, J. R., and McCormick, D. A. (1992). Simulation of the currents involved in rhythmic oscillations in thalamic relay neurons. *J. Neurophysiol.* 68, 1373–1383. doi: 10.1152/jn.1992.68.4.1373

Kanyshkova, T., Meuth, P., Bista, P., Liu, Z., Ehling, P., Caputi, L., et al. (2012). Differential regulation of HCN channel isoform expression in thalamic neurons of epileptic and non-epileptic rat strains. *Neurobiol. Dis.* 45, 450–461. doi: 10.1016/j.nbd.2011.08.032

Laemmli, U. K. (1970). Cleavage of structural proteins during the assembly of the head of bacteriophage T4. *Nature* 227, 680–685. doi: 10.1038/227680a0

Lainez, S., Tsantoulas, C., Biel, M., and McNaughton, P. A. (2019). HCN3 ion channels: roles in sensory neuronal excitability and pain. *J. Physiol.* doi: 10.1113/JP278211 [Epub ahead of print].

Lecourtier, L., and Kelly, P. H. (2007). A conductor hidden in the orchestra? Role of the habenular complex in monoamine transmission and cognition. *Neurosci. Biobehav. Rev.* 31, 658–672. doi: 10.1016/j.neubiorev.2007.01.004

Lee, H. W., Yang, S. H., Kim, J. Y., and Kim, H. (2019). The role of the medial habenula cholinergic system in addiction and emotion-associated behaviors. *Front. Psychiatry* 10:100. doi: 10.3389/fpsyt.2019.00100

Lein, E. S., Hawrylycz, M. J., Ao, N., Ayres, M., Bensinger, A., Bernard, A., et al. (2007). Genome-wide atlas of gene expression in the adult mouse brain. *Nature* 445, 168–176. doi: 10.1038/nature05453

Lewis, A. S., Estep, C. M., and Chetkovich, D. M. (2010). The fast and slow ups and downs of HCN channel regulation. *Channels* 4, 215–231. doi: 10.4161/chan.4.3.11630

Lim, S. A. O., Kang, U. J., and McGehee, D. S. (2014). Striatal cholinergic interneuron regulation and circuit effects. *Front. Synaptic Neurosci.* 6:22. doi: 10.3389/fnsyn.2014.00022

Ludwig, A., Budde, T., Stieber, J., Moosmang, S., Wahl, C., Holthoff, K., et al. (2003). Absence epilepsy and sinus dysrhythmia in mice lacking the pacemaker channel HCN2. *EMBO J.* 22, 216–224. doi: 10.1093/emboj/cdg032

Lüthi, A., and McCormick, D. A. (1999). Modulation of a pacemaker current through Ca(2+)-induced stimulation of cAMP production. *Nat. Neurosci.* 2, 634–641. doi: 10.1038/10189

Mizumori, S. J. Y., and Baker, P. M. (2017). The lateral habenula and adaptive behaviors. *Trends Neurosci.* 40, 481–493. doi: 10.1016/j.tins.2017.06.001

Moosmang, S., Biel, M., Hofmann, F., and Ludwig, A. (1999). Differential distribution of four hyperpolarization-activated cation channels in mouse brain. *Biol. Chem.* 380, 975–980. doi: 10.1515/BC.1999.121

Nakashima, N., Ishii, T. M., Bessho, Y., Kageyama, R., and Ohmori, H. (2013). Hyperpolarisation-activated cyclic nucleotide-gated channels regulate the spontaneous firing rate of olfactory receptor neurons and affect glomerular formation in mice. *J. Physiol.* 591, 1749–1769. doi: 10.1113/jphysiol.2012.247361

Notomi, T., and Shigemoto, R. (2004). Immunohistochemical localization of Ih channel subunits, HCN1-4, in the rat brain. *J. Comp. Neurol.* 471, 241–276. doi: 10.1002/cne.11039

Paxinos, G., and Franklin, K. B. J. (2001). *The Mouse Brain in stereotaxic coordinates*, 2nd Edn. Cambridge, MA: Academic Press.

Paz, J. T., Davidson, T. J., Frechette, E. S., Delord, B., Parada, I., Peng, K., et al. (2013). Closed-loop optogenetic control of thalamus as a tool for interrupting seizures after cortical injury. *Nat. Neurosci.* 16, 64–70. doi: 10.1038/nn.3269

Peng, S.-C., Wu, J., Zhang, D.-Y., Jiang, C.-Y., Xie, C.-N., and Liu, T. (2017). Contribution of presynaptic HCN channels to excitatory inputs of spinal substantia gelatinosa neurons. *Neuroscience* 358, 146–157. doi: 10.1016/j.neuroscience.2017.06.046

Reid, C. A., Phillips, A. M., and Petrou, S. (2012). HCN channelopathies: pathophysiology in genetic epilepsy and therapeutic implications. *Br. J. Pharmacol.* 165, 49–56. doi: 10.1111/j.1476-5381.2011.01507.x

Santoro, B., Chen, S., Luthi, A., Pavlidis, P., Shumyatsky, G. P., Tibbs, G. R., et al. (2000). Molecular and functional heterogeneity of hyperpolarization-activated pacemaker channels in the mouse CNS. *J. Neurosci.* 20, 5264–5275. doi: 10.1523/jneurosci.20-14-05264.2000

Sartiani, L., Mannaioni, G., Masi, A., Novella Romanelli, M., and Cerbai, E. (2017). The Hyperpolarization-activated cyclic nucleotide-gated channels: from biophysics to pharmacology of a unique family of ion channels. *Pharmacol. Rev.* 69, 354–395. doi: 10.1124/pr.117.014035

Schindelin, J., Arganda-Carreras, I., Frise, E., Kaynig, V., Longair, M., Pietzsch, T., et al. (2012). Fiji: an open-source platform for biological-image analysis. *Nat. Methods* 9, 676–682. doi: 10.1038/nmeth.2019

Seo, H., Seol, M.-J., and Lee, K. (2015). Differential expression of hyperpolarization-activated cyclic nucleotide-gated channel subunits during hippocampal development in the mouse. *Mol. Brain* 8:13. doi: 10.1186/s13041-015-0103-104

Stieglitz, M. S., Fenske, S., Hammelmann, V., Becirovic, E., Schöttle, V., Delorme, J. E., et al. (2017). Disturbed processing of contextual information in HCN3 channel deficient mice. *Front. Mol. Neurosci.* 10:436. doi: 10.3389/fnmol.2017.00436

Surges, R., Kukley, M., Brewster, A., Rüschenschmidt, C., Schramm, J., Baram, T. Z., et al. (2012). Hyperpolarization-activated cation current Ih of dentate gyrus granule cells is upregulated in human and rat temporal lobe epilepsy. *Biochem. Biophys. Res. Commun.* 420, 156–160. doi: 10.1016/j.bbrc.2012.02.133

Tsantoulas, C., Mooney, E. R., and McNaughton, P. A. (2016). HCN2 ion channels: basic science opens up possibilities for therapeutic intervention in neuropathic pain. *Biochem. J.* 473, 2717–2736. doi: 10.1042/BCJ20160287

Varoqui, H., Schäfer, M. K. H., Zhu, H., Weihe, E., and Erickson, J. D. (2002). Identification of the differentiation-associated Na+/PI transporter as a novel vesicular glutamate transporter expressed in a distinct set of glutamatergic synapses. *J. Neurosci.* 22, 142–155. doi: 10.1523/jneurosci.22-01-00142.2002

Wang, F., Flanagan, J., Su, N., Wang, L.-C., Bui, S., Nielson, A., et al. (2012). RNAscope: a novel in situ RNA analysis platform for formalin-fixed, paraffin-embedded tissues. *J. Mol. Diagn.* 14, 22–29. doi: 10.1016/j.jmoldx.2011.08.002

Wilson, C. J. (2005). The mechanism of intrinsic amplification of hyperpolarizations and spontaneous bursting in striatal cholinergic interneurons. *Neuron* 45, 575–585. doi: 10.1016/j.neuron.2004.12.053

Yang, Y., Cui, Y., Sang, K., Dong, Y., Ni, Z., Ma, S., et al. (2018). Ketamine blocks bursting in the lateral habenula to rapidly relieve depression. *Nature* 554, 317–322. doi: 10.1038/nature25509

Zhao, Z., Zhang, K., Liu, X., Yan, H., Ma, X., Zhang, S., et al. (2016). Involvement of HCN channel in muscarinic inhibitory action on tonic firing of dorsolateral striatal cholinergic interneurons. *Front. Cell Neurosci.* 10:71. doi: 10.3389/fncel.2016.00071

Zobeiri, M., Chaudhary, R., Blaich, A., Rottmann, M., Herrmann, S., Meuth, P., et al. (2019). The hyperpolarization-activated HCN4 channel is important for proper maintenance of oscillatory activity in the thalamocortical system. *Cereb. Cortex* 29, 2291–2304. doi: 10.1093/cercor/bhz047

Zúñiga, R., González, D., Valenzuela, C., Brown, N., and Zúñiga, L. (2016). Expression and cellular localization of HCN channels in rat cerebellar granule neurons. *Biochem. Biophys. Res. Commun.* 478, 1429–1435. doi: 10.1016/j.bbrc.2016.08.141

Conflict of Interest Statement: The authors declare that the research was conducted in the absence of any commercial or financial relationships that could be construed as a potential conflict of interest.

Copyright © 2019 Oyrer, Bleakley, Richards, Maljevic, Phillips, Petrou, Nowell and Reid. This is an open-access article distributed under the terms of the Creative Commons Attribution License (CC BY). The use, distribution or reproduction in other forums is permitted, provided the original author(s) and the copyright owner(s) are credited and that the original publication in this journal is cited, in accordance with accepted academic practice. No use, distribution or reproduction is permitted which does not comply with these terms.

frontiers in Molecular Neuroscience

BRIEF RESEARCH REPORT
published: 06 September 2019
doi: 10.3389/fnmol.2019.00209

Dimethylethanolamine Decreases Epileptiform Activity in Acute Human Hippocampal Slices *in vitro*

*Larissa Kraus[1,2], Florian Hetsch[3], Ulf C. Schneider[4], Helena Radbruch[5], Martin Holtkamp[1,2], Jochen C. Meier[2,3] and Pawel Fidzinski[1]**

[1]Charité-Universitätsmedizin Berlin, corporate member of Freie Universität Berlin, Humboldt-Universität zu Berlin, and Berlin Institute of Health, Department of Neurology with Experimental Neurology, Berlin, Germany, [2]Berlin Institute of Health (BIH), Zoologisches Institut, Technische Universität Braunschweig, Braunschweig, Germany, [3]Zoologisches Institut, Technische Universität Braunschweig, Braunschweig, Germany, [4]Charité-Universitätsmedizin Berlin, corporate member of Freie Universität Berlin, Humboldt-Universität zu Berlin, and Berlin Institute of Health, Department of Neurosurgery, Berlin, Germany, [5]Charité-Universitätsmedizin Berlin, corporate member of Freie Universität Berlin, Humboldt-Universität zu Berlin, and Berlin Institute of Health, Department of Neuropathology, Berlin, Germany

Temporal lobe epilepsy (TLE) is the most common form of focal epilepsy with about 30% of patients developing pharmacoresistance. These patients continue to suffer from seizures despite polytherapy with antiepileptic drugs (AEDs) and have an increased risk for premature death, thus requiring further efforts for the development of new antiepileptic therapies. The molecule dimethylethanolamine (DMEA) has been tested as a potential treatment in various neurological diseases, albeit the functional mechanism of action was never fully understood. In this study, we investigated the effects of DMEA on neuronal activity in single-cell recordings of primary neuronal cultures. DMEA decreased the frequency of spontaneous synaptic events in a concentration-dependent manner with no apparent effect on resting membrane potential (RMP) or action potential (AP) threshold. We further tested whether DMEA can exert antiepileptic effects in human brain tissue *ex vivo*. We analyzed the effect of DMEA on epileptiform activity in the CA1 region of the resected hippocampus of TLE patients *in vitro* by recording extracellular field potentials in the pyramidal cell layer. Epileptiform burst activity in resected hippocampal tissue from TLE patients remained stable over several hours and was pharmacologically suppressed by lacosamide, demonstrating the applicability of our platform to test antiepileptic efficacy. Similar to lacosamide, DMEA also suppressed epileptiform activity in the majority of samples, albeit with variable interindividual effects. In conclusion, DMEA might present a new approach for treatment in pharmacoresistant TLE and further studies will be required to identify its exact mechanism of action and the involved molecular targets.

Keywords: epilepsy, drug development, human, hippocampus, *ex vivo*

OPEN ACCESS

Edited by:
Jaewon Ko,
Daegu Gyeongbuk Institute of Science and Technology (DGIST), South Korea

Reviewed by:
Aleksey V. Zaitsev,
Institute of Evolutionary Physiology and Biochemistry (RAS), Russia
Giuseppe Biagini,
University of Modena and Reggio Emilia, Italy

****Correspondence:***
Pawel Fidzinski
pawel.fidzinski@charite.de

Received: *19 May 2019*
Accepted: *09 August 2019*
Published: *06 September 2019*

Citation:
Kraus L, Hetsch F, Schneider UC, Radbruch H, Holtkamp M, Meier JC and Fidzinski P (2019) Dimethylethanolamine Decreases Epileptiform Activity in Acute Human Hippocampal Slices in vitro. Front. Mol. Neurosci. 12:209. doi: 10.3389/fnmol.2019.00209

INTRODUCTION

Epilepsy is a major neurological disorder affecting up to 65 million people worldwide (Hirtz et al., 2007; Ngugi et al., 2010). The need for adequate treatment is not only given by seizures itself along with associated risks of injury and premature death but also by comorbidities and social stigmatization. Specifically in focal epilepsy, 30%–40% of patients do not respond to

currently available antiepileptic drugs (AEDs), resulting in pharmacoresistance with ongoing seizures despite treatments with multiple AEDs at high dosages (Stephen et al., 2001). Alternative therapies such as ketogenic diet or brain stimulation have been suggested to reduce seizure burden in pharmacoresistant patients (Giordano et al., 2014; Kowski et al., 2015; Dibué-Adjei et al., 2019). However, ketogenic diet has been shown to be effective in children and with modification in adults but is still rarely considered as treatment in adults (Hallböök et al., 2015; Falco-Walter et al., 2019). Ongoing investigations show promising seizure reduction in pharmacoresistant patients by deep brain stimulation (Zangiabadi et al., 2019). However, this approach requires optimal selection of targeted brain regions and prospective trials are lacking. Finally, surgical removal of the epileptic focus remains often the only treatment option for pharmacoresistant patients (Wiebe et al., 2001; Engel et al., 2007). Yet, only in a minority of patients, epilepsy is amenable to surgery, and only 60%–70% of resected patients have a positive outcome with substantial reduction of the seizure burden (International League Against Epilepsy Outcome Scale 1–2; Mohan et al., 2018). Thus, identification of new antiepileptic treatment options in focal pharmacoresistant epilepsy is of paramount importance.

Dimethylethanolamine (DMEA) has previously been investigated as a stimulant and treatment for several neurological diseases, including tardive dyskinesia (TD), Alzheimer's disease (AD) and senile dementia (Ferris et al., 1977; Penovich et al., 1978; de Montigny et al., 1979; Fisman et al., 1981; George et al., 1981). First, application of DMEA to human healthy volunteers dates back to the 1960s when DMEA was reported to exert stimulating effects comparable to amphetamine (Murphree et al., 1960; Pfeiffer et al., 1963). Murphree et al. (1960) described improved concentration, increased muscle tone and changed sleeping habits in healthy males (21–26 years) with an intake of 10–20 mg DMEA (or Deanol) daily for 2–3 weeks compared to a placebo group. In later studies, DMEA was hypothesized as an acetylcholine (ACh) precursor and therefore tested in diseases that are considered to be linked to the cholinergic system. However, results of several studies were inconclusive and a systematic review could not confirm the positive effects of DMEA or other cholinergic compounds in patients with TD (Tammenmaa et al., 2004). In addition, *in vivo* experiments showed that DMEA is not methylated to choline and does not alter brain ACh levels (Millington et al., 1978; Jope and Jenden, 1979).

Interestingly, in both acute and chronic seizure models in rats, a conjugate of DMEA and valproate (DEVA) was shown to be more potent than valproate alone, potentially by facilitation of valproate transport *via* the blood brain barrier (Shekh-Ahmad et al., 2012). In this study, however, the effects of DMEA alone were not tested. To our knowledge, effects of DMEA on pathological neuronal network activity have never been investigated before.

In principle, resected human tissue of temporal lobe epilepsy (TLE) patients carries the potential to bridge the translational gap between preclinical and clinical drug development. Animal models have been instrumental in the discovery and preclinical development of novel AEDs (Löscher, 2011). However, animal models cannot represent all aspects of complex neurological disorders and sometimes produce misleading results as exemplified by the neuropeptide galanin. Galanin showed robust antiepileptic effects in a mouse model of epilepsy, however, the effect could not be reproduced in resected human tissue (Ledri et al., 2015).

Here, we decided to investigate the effects of DMEA on epileptiform activity directly in *ex vivo* human tissue resected from epilepsy patients.

MATERIALS AND METHODS

Primary Rat Hippocampal Neuronal Cell Culture

Hippocampal cultures from E18 Wistar rat embryos were prepared as previously described (Winkelmann et al., 2014) according to the approval by the Animal Care Committee of the Technical University Braunschweig (Zentrale Einrichtung für Tierhaltung der TU Braunschweig, §4 10.15.R TSB TU BS) and maintained in Neurobasal medium supplemented with B27 and 1% FCS (Brewer et al., 1993). Hippocampal neurons were subjected to whole cell patch clamp analysis at DIV13–16 to ensure that the cultures were mature enough to display synaptic activity.

Electrophysiological Recordings of Cultured Hippocampal Neurons

An EPC-7 amplifier (List-Medical, Darmstadt, Germany), ITC-18 interface and Patchmaster software (both HEKA, Lamprecht, Germany) were used for patch clamp recordings and data acquisition. Patch pipettes made from borosilicate glass (Science Products, Hofheim, Germany), had resistances of 4–7 MΩ when filled with the intracellular solution containing (in mM): KCl (130), NaCl (5), $CaCl_2$ (0.5), $MgCl_2$ (1), EGTA (5) and HEPES (30), pH 7.2 (KOH). Neurons were continuously perfused with carbogenated artificial cerebrospinal fluid (aCSF) containing (in mM): NaCl (125), KCl (2), $MgCl_2$ (1), $CaCl_2$ (2), $NaHCO_3$ (25), NaH_2PO_4 (1.25) and glucose (10), pH 7.4. Extracellular solution was supplied by gravity using a perfusion pencil (Automate Scientific Inc., Berkeley, CA, USA) for fast solution exchange. The extracellular solution was supplemented with 0.5, 2, 5 or 10 mM DMEA. Series resistances (Rs) were monitored by 5 mV voltage pulses (50 ms) applied every 5 s and varied between 10 MΩ and 30 MΩ. Data were acquired with a sampling rate of 20 kHz and filtered at 2.8 kHz. All experiments were carried out at room temperature (∼24°C).

The effect of DMEA on synaptic activity and excitability was tested in current-clamp mode with stepwise increase of DMEA concentration. DMEA was applied for 60 s, following 3–5 min wash-out with aCSF before applying the next drug concentration. No synaptic or intrinsic blockers were added. A steady current injected into the cell was used to hold the membrane potential around −50 mV never exceeded 150 pA. Action potential (AP) threshold was investigated by short current injections using 10 pA steps with or without the application of DMEA. AP threshold was determined as the mean between the minimum

membrane potential necessary for AP generation and membrane potential of the previous step current.

Human Tissue Transport and Preparation

Human hippocampal tissue from epilepsy surgery was collected from 12 TLE patients (10 males, two females), who all gave written consent prior to the procedure. Experiments were approved by the Ethics Committee of Charité-Universitätsmedizin Berlin on the 1st of November 2014 (EA2/111/14) and performed in agreement with the Declaration of Helsinki.

Hippocampal tissue was transferred to carbonated (95% O_2, 5% CO_2), ice-cold transport solution immediately after resection. Tissue was transported to the lab in <60 min and cut to 400 μm slices using a vibratome (Leica VT1200S, Wetzlar, Germany). N-methyl d-glucamine (NMDG)-aCSF was used for brain tissue transport and slice preparation from patients 1–7, while choline-aCSF was used to handle tissue of patient 8–12 in order to optimize transport. NMDG-aCSF contained (in mM): NMDG (93), KCl (2.5), NaH_2PO_4 (1.2), $NaHCO_3$ (30), $MgSO_4$ (10), $CaCl_2$ (0.5), HEPES (20), glucose (25), Na-L-ascorbate (5), thiourea (2), Na-pyruvate (3; Ting et al., 2014). Choline-aCSF contained (in mM): Choline chloride (110), KCl (2.5), NaH_2PO_4 (1.25), $NaHCO_3$ (26), $MgCl_2$ (7), $CaCl_2$ (0.5), glucose (10), Na-L-ascorbate (11.6), Na-pyruvate (3.1; Testa-Silva et al., 2010).

As part of the standard clinical routine, every third slice collected during the slicing procedure was fixed in 4% paraformaldehyde (PFA, pH 7.4, phosphate-buffered saline) and analyzed for pathological alterations. For electrophysiological recordings, slices were stored in an interface chamber for a recovery period of at least 5 h and continuously perfused with carbogenated aCSF containing (in mM): NaCl (129), NaH_2PO_4 (1.25), $CaCl_2$ (1.6), KCl (3.0), $MgSO_4$ (1.8), $NaHCO_3$ (21), Glucose (10; 1.6 ml/min, 35°C, pH 7.4). All slices were studied between 6 h and 20 h after resection.

Electrophysiological Recordings of Human Tissue

For electrophysiological recordings, slices were transferred to a custom modified version of the membrane chamber (Hill and Greenfield, 2011) and perfused with aCSF (10 ml/min, 32°C). The membrane chamber is a submerged-type recording chamber with a high flow rate but stable slice position, guaranteeing optimal oxygen supply and fast drug applications. Field potential recordings were performed with borosilicate pipettes (1.5 mm outer diameter, Science Products, Hofheim, Germany) pulled with a vertical puller (1–2 MΩ, PC-10, Narishige, Tokyo, Japan) and filled with NaCl (154 mM). Signals were recorded from CA1 pyramidal cell layer, sampled at 10 kHz, low-pass filtered at 2 kHz by a Digidata 1550 interface and processed by PClamp10 software (Molecular Devices, Sunnyvale, CA, USA).

Induction of epileptiform activity in rodent brain slices can be achieved by a stand-alone manipulation such as inhibition of potassium channels by 4-aminopyridine (4-AP; Perreault and Avoli, 1991; Avoli et al., 2002; Heuzeroth et al., 2019). On the contrary, induction of epileptiform activity in human brain tissue *ex vivo* is less straightforward and subject to controversy. In resected human brain tissue only application of 4-AP in combination with electrical stimulation or elevated extracellular potassium was able to show stable induction of epileptiform activity, not application of 10 or 12 mM potassium or 4-AP alone (Gabriel et al., 2004; Antonio et al., 2016). Here, we used bath application of high potassium (8 mM) and 4-AP (100 μM, Sigma, Munich, Germany) for the induction of epileptiform activity in human brain tissue. Increase of osmolarity by 8 mM KCl was balanced by lowering NaCl concentration from 129 mM to 124 mM.

Baseline epileptiform activity was recorded for ≥20 min. DMEA (10 mM, Sigma, Munich, Germany) or lacosamide (LAC, 100 μM, Biozol, Eching, Germany) were then applied for ≥20 min, followed by ≥20 min of wash-out. In initial experiments we tested 5 mM and 10 mM of DMEA in the same slice, starting with 5 mM DMEA (20 min), followed by 10 mM DMEA and wash-out as described above.

Addition of DMEA increases osmolarity of aCSF possibly affecting neuronal activity. Therefore, we performed control experiments with increasing the osmolarity of aCSF up to ∼310 mOsm by addition of 10 mM sucrose (patients 10, 11, and 12). This approach has been used to test hyperosmolar solutions before (Rosenmund and Stevens, 1996). Here, the recording sequence stated above was modified and consisted of the following steps: (1) baseline with stable epileptiform activity (≥10 min); (2) 10 mM sucrose (≥20 min); and (3) wash-out sucrose (≥10 min), 10 mM DMEA (≥20 min), wash-out DMEA (≥20 min).

Data Analysis and Statistics

Electrophysiological data recorded in single cells from primary neuronal cell cultures was quantified and measured using an IGOR Pro (Version 6.3.7.2, Wavemetrics Inc., Oregon, USA) procedure written by Dr. Marcus Semtner (MDC Berlin) and the extension PatchersPowerTools (written by Dr. Francisco Mendez and Frank Würriehausen).

Recordings in human hippocampal tissue were band pass filtered (1–1,000 Hz) and the 300 s long episodes (last 5 min of each application phase) were analyzed with Clampfit 10.7 (Molecular Devices, Sunnyvale, CA, USA) threshold analysis. All events visually identified as burst activity (defined by biphasic, positive and negative deflection and a duration ≥100 ms) were manually indicated for further analysis of event frequency (inter-event-interval, IEI), amplitude and total number of events during the analyzed time frame. Interictal spikes (defined by exclusive negative deflections and a duration <10 ms) were not analyzed. According to literature, interictal spikes, although pathologically relevant, are not significantly affected by AEDs (Spencer et al., 2008; D'Antuono et al., 2010).

All data were analyzed with GraphPad Prism 5 (GraphPad Software Inc., San Diego, CA, USA). Prior to analysis, data were subjected to D'Agostino and Pearson omnibus normality test and analyzed accordingly. In cases where sample size of tested groups was too small for evaluation of data distribution, data were analyzed using non-parametric tests.

Statistical analysis of normal distributed data was performed using repeated measurement analysis of variance (ANOVA)

and *post hoc* Tukey's comparison of all groups. Non-normal distributed data or data with small sample size was analyzed either using Friedman test and *post hoc* Dunnett's multiple comparison of individual groups or Wilcoxon signed-rank test. For all analysis, a p-value < 0.05 was considered statistically significant.

Data analyzed by parametric tests were presented as scatter plots with mean ± standard deviation (SD) while data analyzed by non-parametric tests were presented as scatterplots with median and interquartile range. Due to IEI variance during drug application (DMEA or LAC), frequency of events for all patients was summarized as number of events. IEI for individual recordings is presented as boxplots with median and Tukey whiskers (1.5× the interquartile distance) to show data distribution and inter-individual differences.

Human datasets analyzed in this study can be found in figshare repository (https://doi.org/10.6084/m9.figshare.8148572).

RESULTS

To investigate whether DMEA affects neuronal activity and to obtain information about potential molecular targets, we performed electrophysiological recordings in primary neuronal cultures. DMEA dose-dependently reduced spontaneous synaptic events and associated APs with an estimated EC50 of ∼0.5–1.0 mM. A full block of activity was observed in all recorded cells when using 5 mM or 10 mM DMEA (**Figures 1A,B,D,E**). Neither resting membrane potential (RMP) nor AP threshold changed upon DMEA application (**Figures 1C,F**, **Supplementary Figures S1A,B**), suggesting that intrinsic properties do not represent the main target of DMEA action.

We also investigated the effects of DMEA on epileptiform activity in hippocampal tissue resected from 12 patients undergoing epilepsy surgery. Histopathology of resected tissue revealed distinct pathologies: malformations of cortical development (MCD) were diagnosed in two patients [mild MCD changes in one and clear focal cortical dysplasia (FCD) in the other patient], unspecific astrogliosis in three patients and clear pathological changes indicating hippocampal sclerosis (HS) in seven patients (**Supplementary Table S1**). The changes in pyramidal layers of CA1, CA3 and CA4 included <10% neuronal cell loss in three patients (Wyler grade 1), up to 50% cell loss in three patients (Wyler grade 2) and more than 50% cell loss in one patient (Wyler grade 3).

From these 12 resected samples, a total of 30 hippocampal slices was used for electrophysiological recordings. After slice recovery, we tested our experimental approach by assessing whether: (1) epileptiform activity in human slices can be induced by elevated potassium and 4-AP; (2) whether this activity is stable for prolonged periods of time; and (3) sensitive to conventional AEDs. In 27 slices from 12 patients, both interictal spikes and ictal burst activity (**Figures 2A,B**) could be induced within a few minutes (**Figures 2C,F**). In three slices from three patients, burst events did not occur within 20 min, therefore these slices were excluded from the analysis.

In control recordings without drug application, the pathologically relevant burst activity was stable for at least 60 min (tested in three slices from three patients), suggesting good viability of human slices in our experimental setting. In more detail, both frequency and amplitude of burst activity did not change in most cases during the recording as indicated by stable IEI, amplitude and number of burst events (**Figures 2D,E**).

To test whether burst activity was sensitive to conventional AEDs, we investigated the effect of the sodium channel blocker LAC. During application of LAC, IEI increased in all recorded slices, which was reversible in three out of four patients (**Figure 2G**). Number of events of all recordings decreased during LAC application when compared to baseline activity, while amplitude of burst activity did not change (**Figure 2H**). In conclusion, we were able to induce stable epileptiform activity that can be inhibited by clinically approved AEDs.

Next, we investigated the effects of DMEA in 14 hippocampal slices from 10 TLE patients. In initial experiments, we tested the effects of 5 mM and 10 mM DMEA within one experiment (**Supplementary Figure S2**). As the inhibitory effect was more robust when using 10 mM DMEA (**Supplementary Figure S2B**, $p < 0.05$, $n = 6$; tested in patients 2–7), we decided to perform subsequent experiments with this effective concentration. In contrast to LAC, DMEA effects varied considerably between samples ranging from no effect (patient 8, **Figure 3A**) or only a moderate effect observed in slices of patient 7 (**Figure 3B**) to a full block of burst activity (**Figure 3C**) in four slices from patients 9, 10 and 11. Irrespective of the effect variability, DMEA displayed antiepileptic effects in 10 out of 11 patients (**Figure 4A**), as indicated by the increase of IEI and a significant decrease of number of events during application of DMEA (**Figure 4B**, $p < 0.01$, $n = 10$). In eight patients, these effects were clearly reversible upon wash-out of DMEA. Amplitude of epileptiform bursts was not affected (**Figure 4C**).

Addition of DMEA at 10 mM increases osmolarity of the extracellular environment (here, aCSF) which could possibly decrease epileptiform activity simply by osmotic effects (Traynelis and Dingledine, 1989; Dudek et al., 1990). To test whether DMEA effects are mediated by mechanisms beyond pure change in osmolarity, we investigated how sucrose and DMEA affect epileptiform activity in the same slice when applied sequentially. In six slices of three patients increase of osmolarity by sucrose (310 ± 5 mOsm) to match osmolarity of solutions containing 10 mM DMEA resulted in a weak increase of IEI and a weak decrease of number of events (**Supplementary Figure S3**). This decrease matched the observed decrease without intervention over time as shown in **Figure 2E** and was likely due to a slow decay in activity in the course of *in vitro* experiments. The mild effect of sucrose application stood in contrast to a full block of activity during subsequent application of DMEA in patients 10 and 11 and a strong decrease of activity in patient 12 (**Supplementary Figures S3A,B**).

In summary, in human brain slices DMEA exerted antiepileptic effects presented as an overall decrease in frequency

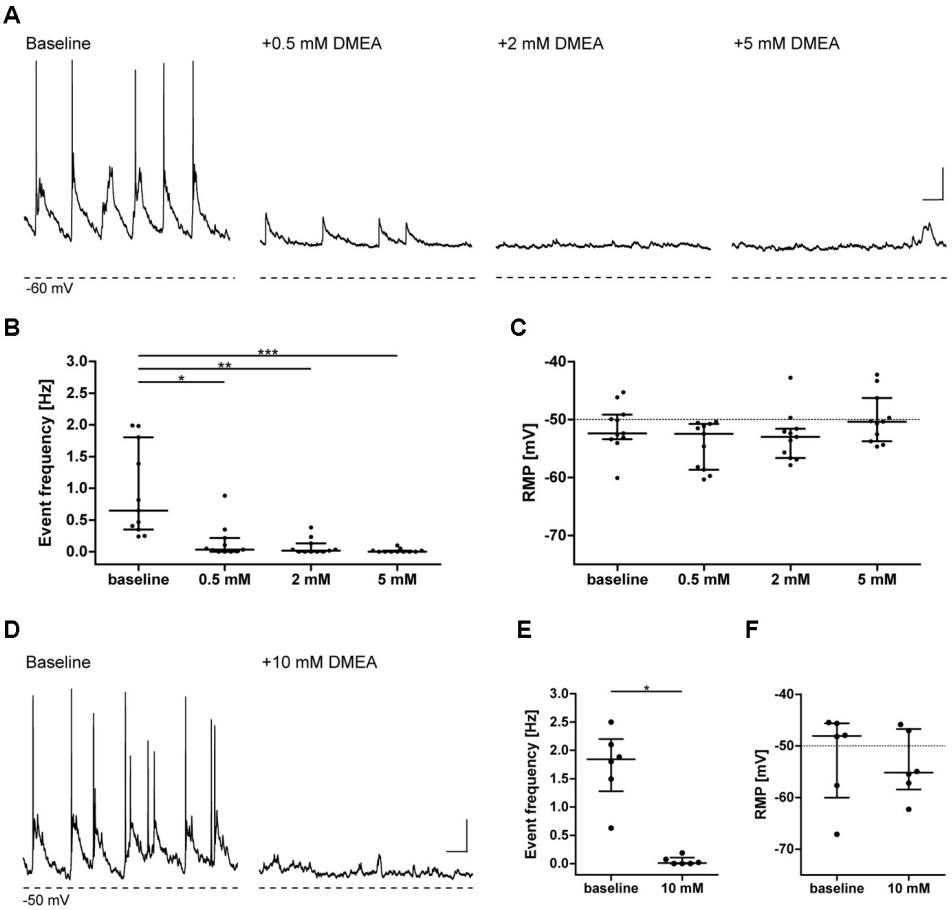

FIGURE 1 | Dimethylethanolamine (DMEA) decreases spontaneous neuronal activity in neuronal cultures in a concentration-dependent manner. Activity of cultured hippocampal neurons (DIV 13–16) was investigated in current-clamp mode in the absence or presence of DMEA. During baseline conditions, all neurons displayed excitatory synaptic events with associated action potentials (APs) at a frequency of ∼1 Hz. Both AP, as well as large amplitude synaptic event frequency, decreased with increasing DMEA concentration to reach a full block with 5 mM DMEA. **(A,D)** Exemplary recordings in neurons with application of 0.0, 0.5, 2.0 and 5.0 mM DMEA **(A)** or 10 mM DMEA **(D)**; note that due to experimental setup we could not perform repeated measurement in one cell including all concentrations and present the results here separately; Dashed lines below recordings indicate resting membrane potential (RMP, in mV) of cells. **(B,E)** DMEA significantly decreases event frequency in a concentration-dependent manner. **(C,F)** Application of DMEA does not affect RMP. All data are shown as scatter plots with median and interquartile range. Asterisks mark significant differences as assessed by Friedman test and *post hoc* by Dunnett's multiple comparison of groups **(B,C)** or by Wilcoxon signed-rank test (**E,F**; $*p < 0.05$, $**p < 0.01$, $***p < 0.001$). Scale bar: 10 mV, 0.5 s.

of burst events, which were not due to osmotic changes. A summary of all results is presented in **Supplementary Table S2**.

DISCUSSION

In the present study, we investigated the effect of DMEA on spontaneous activity in neuronal cultures and on epileptiform activity in human hippocampal tissue *ex vivo*. We were able to show a decrease of spontaneous activity in rodent neuronal cultures. In the majority of investigated human slices, DMEA displayed strong antiepileptic effects including full block of burst activity in slices of three patients. The effect of DMEA in human tissue varied considerably, implying interindividual differences in expression patterns of molecular DMEA targets.

The mechanism of DMEA action is not known. Our preliminary experiments in neuronal cultures showing dose-dependent inhibition of spontaneous neuronal activity without altering RMP or AP threshold suggest that DMEA likely affects synaptic but not intrinsic excitability. In previous clinical studies, DMEA was tested as a potential ACh precursor but did not improve disease symptoms in TD or AD. DMEA increased choline concentrations in plasma and brain though this did not affect brain ACh concentrations, questioning a beneficial effect of DMEA in diseases involving the cholinergic system (Millington et al., 1978; Jope and Jenden, 1979). Nevertheless, due to structural similarities of DMEA, ACh and choline, muscarinic ACh receptors (mAChRs) present possible targets of DMEA action. ACh and choline are both ligands of M2 and M3 mAChRs (Shi et al., 2004; Moreno-Galindo et al., 2016), which upon activation increase the open probability of G-protein coupled inwardly rectifying potassium (GIRK) channels, specifically GIRK1 and GIRK4 (Nemec et al., 1999). GIRK1 and

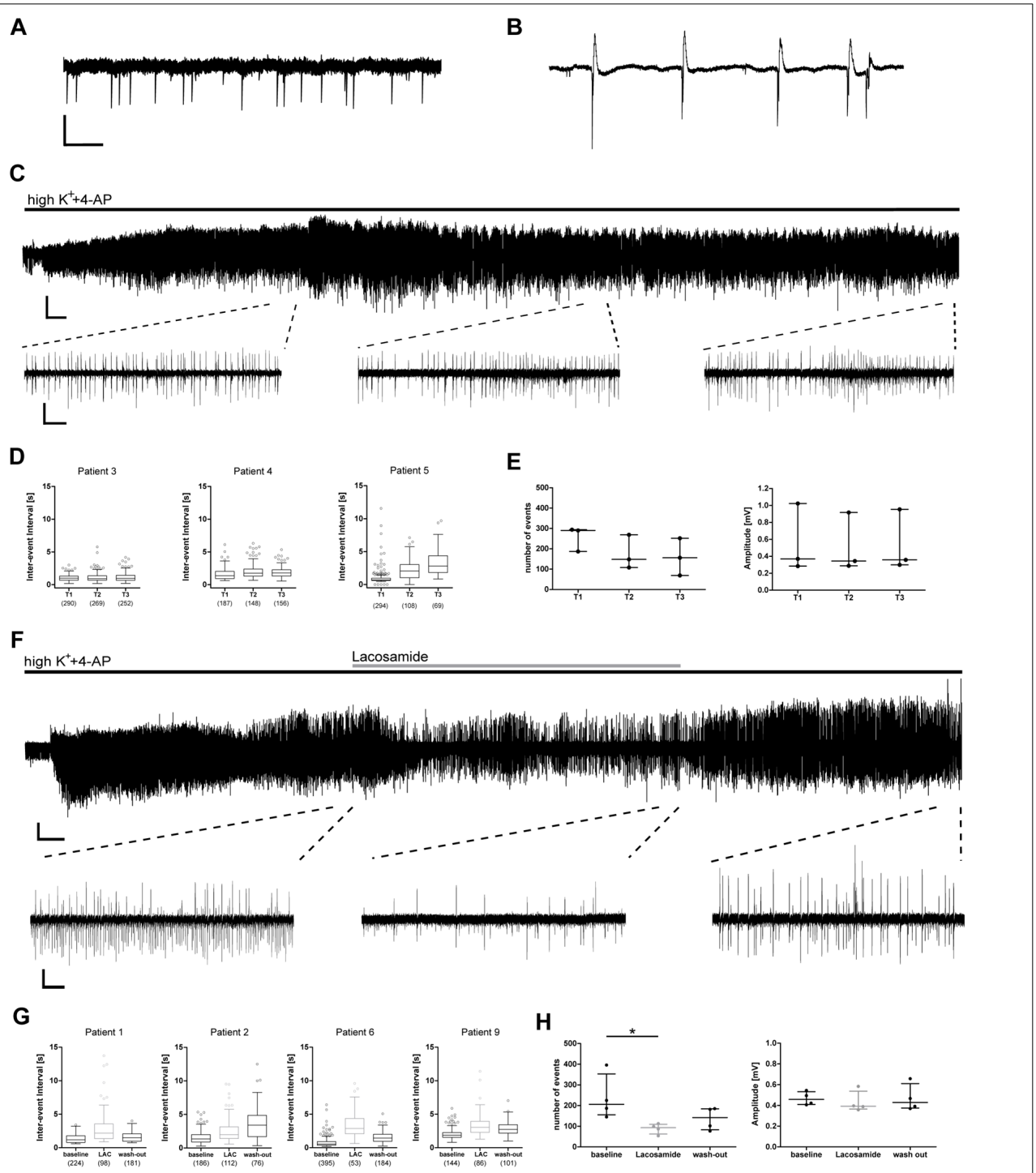

FIGURE 2 | Epileptic burst activity in human slices is stable over long time periods and decreases during application of lacosamide. Application of 8 mM K^+ and 100 μM 4-aminopyridine (4-AP) induces two patterns of network activity recorded by field potential electrodes in the CA1 area of human hippocampal slices: interictal spikes **(A)** and burst activity **(B)**. **(C–E)** Burst activity is induced a few minutes after application and stable for at least 60 min. **(F–H)** Induced burst activity decreases during application of lacosamide (LAC). **(C,F)** Exemplary recording with excerpts of regions used for analysis. **(D,G)** Inter-event intervals (IEI) of individual recordings shown as box plots with mean and 1.5× interquartile distance. Each dot represents data point outside the 1.5× interquartile distance. Total number of IEI during analyzed time frame are indicated in brackets. **(E,H)** Summarized results for all patients [number of events and amplitude as mean ± standard deviation (SD)]; each dot indicates one patient. Asterisks mark significant differences as assessed by Friedman test and *post hoc* with Dunnett's multiple comparison of groups ($p < 0.05$). T1, T2, T3 in **(D,E)** are periods analyzed for each patient, comparable to analyzed times in **(G,H)** and **Figure 3**. Scale bars: 0.2 mV, 500 ms **(A,B)**, 5 min (full recording, **C**), 2 min (full recording, **F**), 5 s (excerpts, **C,F**).

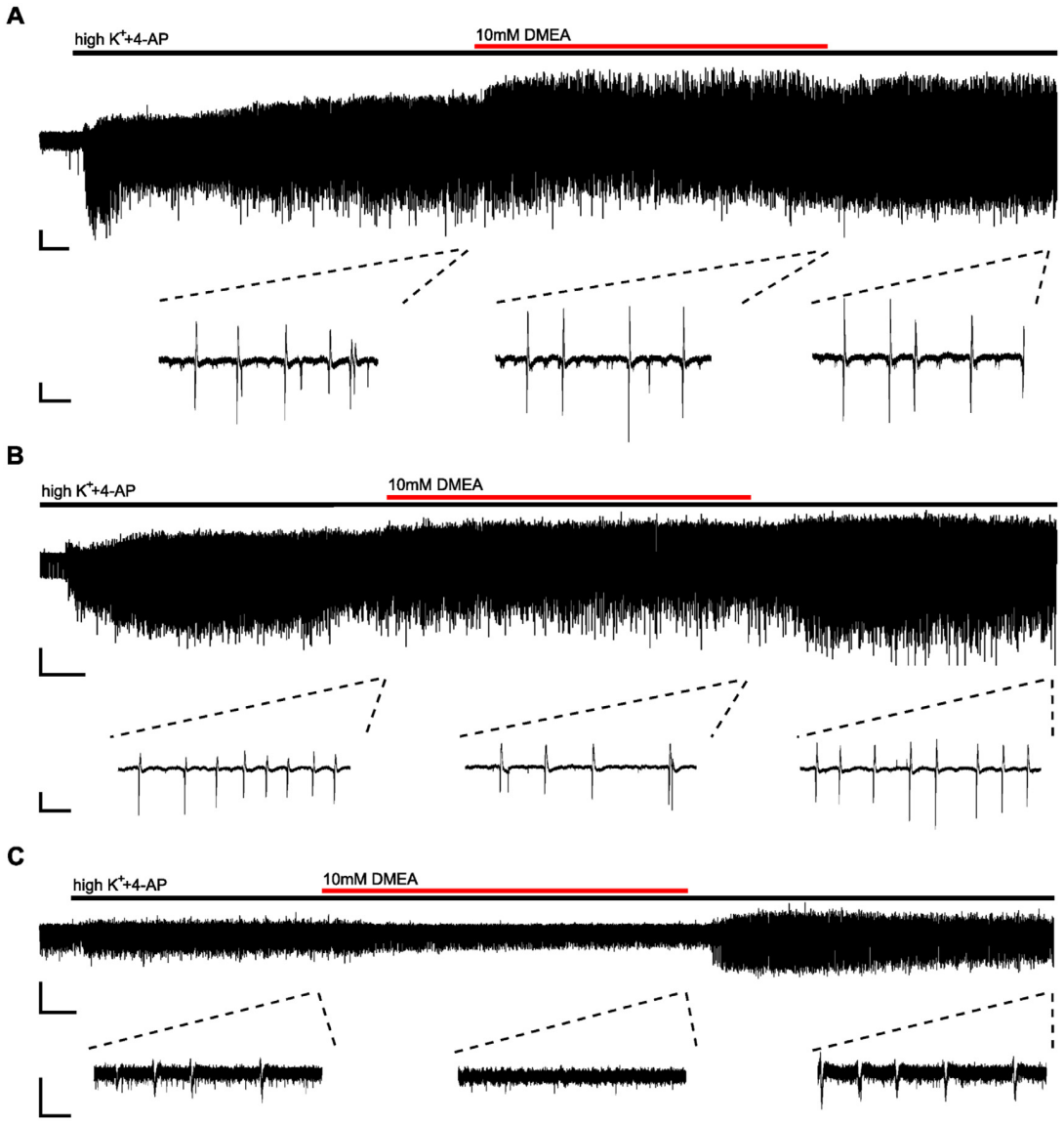

FIGURE 3 | Effects of DMEA on epileptiform activity in human brain tissue *ex vivo*. Example traces displaying variability of DMEA effects on burst activity; full recordings (top) and excerpts (bottom) from the end of each period (baseline, DMEA and wash-out) demonstrate different effects of DMEA including a lack of response (**A**, patient 8), a partial block (**B**, patient 7) and a full block (**C**, patient 11). Scale bars: 0.2 mV, 3 min (full recordings), 1 s (excerpts).

GIRK4 are expressed in the hippocampus (Miyashita and Kubo, 1997; Murer et al., 1997; Cea-del Rio et al., 2010) and pharmacological activation of GIRK results in antiepileptic effects *in vitro* and *in vivo* (Kaufmann et al., 2013). Thus, M2 or M3 mAChRs and GIRK channels present a possible mechanism for DMEA action.

Another possible candidate are glycine receptors (GlyR). In a separate project, our group analyzed the effects of DMEA on GlyR, which has been described as subject to increased RNA editing in TLE (Krestel et al., 2013; Winkelmann et al., 2014; Meier et al., 2016; Srivastava et al., 2017). Presynaptic RNA-edited GlyR facilitates neurotransmitter release resulting in increased neuronal gain and, depending on the neuronal subtype, network hyper- or hypoexcitability (Winkelmann et al., 2014; Caliskan et al., 2016). In an initial screen for antagonists against RNA-edited GlyR (data not shown), DMEA was considered as a candidate giving an additional incentive to test this substance in human brain slices. However, confirmatory experiments were not able to reproduce DMEA specificity against RNA-edited GlyR. Overall, the molecular targets of DMEA and its mechanism of action in brain tissue remain indeterminate.

The main goal of our study was to demonstrate a possibly clinically relevant effect of DMEA. DMEA has been tested in patients and healthy volunteers since 1960s (Murphree et al., 1960; Pfeiffer et al., 1963). In healthy males,

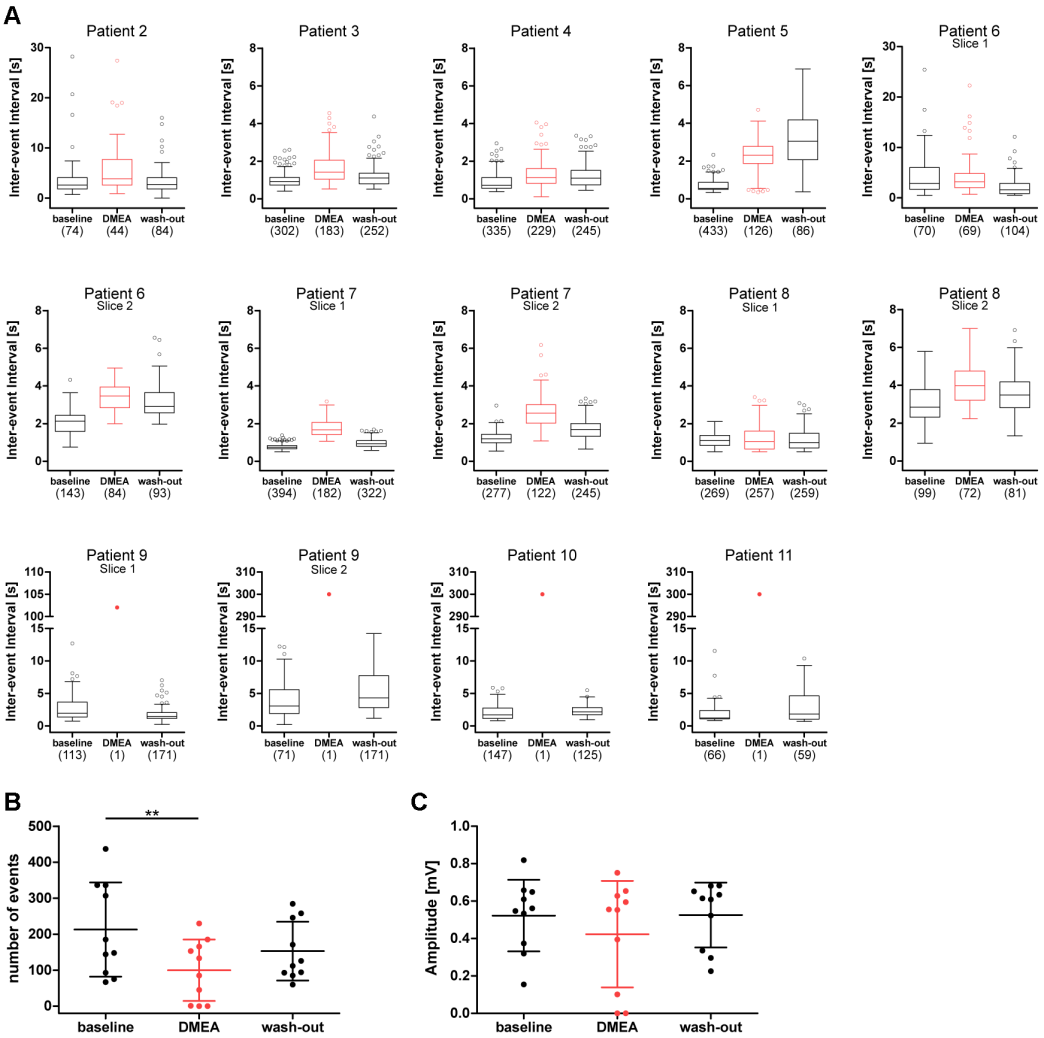

FIGURE 4 | DMEA reduces epileptiform activity in human hippocampal slices. Summary of DMEA effects on burst activity recorded in CA1 pyramidal cell layer of resected human hippocampus. **(A)** Box plots of IEIs with mean and 1.5× interquartile distance before, during and after DMEA application for each patient are shown for all recorded slices (n = 10 patients). Dots represent data points outside the 1.5× interquartile distance. Total number of IEI during analyzed time frame are indicated in brackets. **(B)** Summary of DMEA effects on number and **(C)** amplitude of burst events for all patients; each dot indicates one patient. Data is presented as scatter plots with mean ± SD, asterisks mark significant differences as assessed by repeated measurement analysis of variance (ANOVA) and *post hoc* with Tukey's comparison (**$p < 0.01$, n = 10).

Murphree et al. (1960) reported no change in heart rate, body weight, muscle power, hand steadiness or vital capacity with an intake of 10–20 mg DMEA (or Deanol) daily for 2–3 weeks. In two double-blinded, placebo-controlled studies of TD, DMEA led to side effects such as lethargy, drowsiness and a mild but significant increase in the schizophrenia score (de Montigny et al., 1979; George et al., 1981), although a systematic review was not able to confirm an increased risk for psychosis (Tammenmaa et al., 2004). Fisman et al. (1981) detected severe neurological and cardiovascular effects (apathy, motor retardation, increased confusion associated with rise in systolic and diastolic blood pressure) in two patients with AD when treated with 1,800 mg DMEA daily. In these studies, as compared to Murphree et al. (1960), DMEA was administered in a 100-fold higher daily dosage (10–20 mg vs. 1,000–2,000 mg). A dose of 2,000 mg DMEA corresponds to a molar amount of 22 mM and a final *in vivo* concentration of 0.44 mM assuming a distribution across all compartments and a body water content of approximately 50 l for an adult male. This concentration is lower by a factor of 20 when compared to 10 mM tested to be effective in human brain tissue *ex vivo* in our study, and this difference is rather underestimated when taking into account oral bioavailability. Of note, in neuronal cultures, the effective concentration to inhibit neuronal activity was lower by a factor of 10, implying that differences in microenvironment, neuronal connectivity and drug diffusion in different preparations and species might influence the effective concentration.

Addition of DMEA to our experimental solution increased the osmolarity by ∼10 mOsm. In previous studies, application of hyperosmolar solutions decreased neuronal excitability and epileptiform activity, but in most cases, an increase of 30 mOsm and more was necessary to induce these effects (Traynelis and Dingledine, 1989; Dudek et al., 1990; Rosen and Andrew, 1990). According to Rosen and Andrew (1990), an increase of extracellular osmolarity by 10 mOsm might result in a 10% decrease of EPSC amplitude in CA1 pyramidal neurons, but the effects of such EPSC alteration on network activity have not been investigated. Here, increase of aCSF osmolarity by application of 10 mM sucrose did not alter epileptiform activity, indicating that the antiepileptic effects of DMEA are not primarily mediated by changes in osmolarity.

Although our study clearly demonstrated an antiepileptic effect of DMEA, the large concentration difference between our work and previous clinical studies and the variability of underlying pathologies represent substantial limitations. The results suggest heterogeneous expression of DMEA targets, however, also differences in neuronal survival and the degree of HS could possibly contribute. An additional limitation is given by different transport solutions used in our study, namely either NMDG or choline aCSF (Testa-Silva et al., 2010; Eyal et al., 2018; Ting et al., 2018). Although we were unable to detect differences in tissue quality as seen by stable induction and properties of epileptiform activity, we cannot exclude differences in neuronal survival between these solutions.

The predictive value of brain activity for drug development in an *ex vivo* setting is still unclear. In our approach using a modified submerged chamber, we mostly observed burst activity (spike and burst activity) described before as interictal-like (Remy et al., 2003; Gabriel et al., 2004; Sandow et al., 2015; Reyes-Garcia et al., 2018) and standing in contrast to ictal discharges lasting >10 s. Brückner and Heinemann (2000) suggested that AEDs applied in brain slices (of non-epileptic animals) rather inhibit ictal but not interictal activity. Other animal studies *in vitro*, however, demonstrated a robust decrease in interictal activity in the hippocampus upon AED application (Fueta and Avoli, 1992; Holtkamp et al., 2017; Taing et al., 2017), which was comparable to our results with LAC and DMEA. We show that burst activity was sensitive to the approved antiepileptic LAC, indicating that our experimental setting is capable of validating and possibly predicting antiepileptic efficacy for drug development.

Taken together, our work identified the antiepileptic effect of DMEA in human hippocampal tissue from TLE patients. Interindividual effect variability, differences in the effective concentration range and previously reported side effects call for future, more detailed investigation of cell-type specific effects and molecular targets of DMEA.

DATA AVAILABILITY

All datasets generated for this study are included in the manuscript and/or the **Supplementary Files**. Human datasets analyzed in this study can be found in figshare repository (https://doi.org/10.6084/m9.figshare.8148572).

ETHICS STATEMENT

The studies involving human participants were reviewed and approved by Charité-Universitätsmedizin Berlin (EA2/111/14). The patients/participants provided their written informed consent to participate in this study. The animal study was reviewed and approved by Animal Care Committee of the Technical University Braunschweig (Zentrale Einrichtung für Tierhaltung der TU Braunschweig, §4 10.15.R TSB TU BS).

AUTHOR CONTRIBUTIONS

JM and PF designed the study. MH selected patients for operation. US operated patients. HR performed histopathological analysis. LK performed and analyzed recordings in human tissue. FH performed neuronal experiments. LK and FH analyzed neuronal experiments. LK and PF wrote the manuscript, which all authors edited and finalized.

FUNDING

JM thanks the Deutsche Forschungsgemeinschaft (DFG; Priority Programme SPP1784 ME2075/7-1).

ACKNOWLEDGMENTS

We thank Mandy Marbler-Pötter (Charite Unversitätsmedizin, Berlin) for excellent technical assistance and Tabea Tito for assistance with clinical data on patients.

SUPPLEMENTARY MATERIAL

The Supplementary Material for this article can be found online at: https://www.frontiersin.org/articles/10.3389/fnmol.2019.00209/full#supplementary-material

FIGURE S1 | DMEA does not change action potential threshold. Application of 10 mM DMEA does not change threshold for AP generation. **(A)** Exemplary recordings of patch-clamp recordings in current-clamp mode with step current without AP (first for each) and with AP generation (second); dashed lines below recordings show −60 mV value to indicate RMP of cells. **(B)** Quantified effect of DMEA on AP threshold in neurons. Data are shown as median with interquartile range and was subjected to Wilcoxon signed-rank test; $n = 6$.

FIGURE S2 | Dose-dependent effects of DMEA on epileptiform activity in human hippocampal slices. **(A)** Box plots of inter-event intervals (IEI) during baseline, 5 mM DMEA, 10 mM DMEA and wash-out for each patient given for all recorded slices ($n = 6$ patients). In all experiments, both concentrations were applied in the same brain slice. Box plots are shown with mean and Tukey whiskers (1.5× interquartile distance). Each dot represents a data point outside the 1.5× interquartile distance. Total number of IEI during analyzed time frame are indicated in brackets. **(B)** Summary of DMEA effects on the number and amplitude of burst

events for all tested patients; each dot indicates one patient. Data are presented as scatter plots with median ± interquartile range. Asterisks mark significant differences as assessed by Friedman test and *post hoc* with Dunnett's multiple comparison of groups (*$p < 0.05$).

FIGURE S3 | Increase of osmolarity by 10 mOsm does not affect epileptiform activity. For control purposes, sucrose was used to increase osmolarity and applied in the same slice before DMEA application. **(A)** Full time course and detailed excerpts of exemplary recording used for the analysis of potential hyperosmotic effects of DMEA on epileptiform activity. Note that sucrose application leading to the same osmotic change as DMEA does not significantly alter epileptiform activity, while DMEA application in the same slice clearly exerts an antiepileptic effect. **(B)** Inter-event intervals of individual recordings shown as box plots with a total number of IEI during analyzed time frames indicated in brackets. **(C)** Summarized number of events and amplitudes for all patients presented as scatterplots with median and interquartile range; each dot indicates one patient. Scale bars: 0.2 mV, 5 min (full recordings), 5 s (excerpts).

TABLE S1 | Clinical data of patients, who provided tissue for electrophysiological assessment of the effects of DMEA on epileptic activity.

TABLE S2 | Summarized results of burst activity in human tissue during application of DMEA, LAC, no intervention or sucrose as control for osmolarity effects.

REFERENCES

Antonio, L. L., Anderson, M. L., Angamo, E. A., Gabriel, S., Klaft, Z. J., Liotta, A., et al. (2016). *In vitro* seizure like events and changes in ionic concentration. *J. Neurosci. Methods* 260, 33–44. doi: 10.1016/j.jneumeth.2015.08.014

Avoli, M., D'Antuono, M., Louvel, J., Köhling, R., Biagini, G., Pumain, R., et al. (2002). Network and pharmacological mechanisms leading to epileptiform synchronization in the limbic system *in vitro*. *Prog. Neurobiol.* 68, 167–207. doi: 10.1016/s0301-0082(02)00077-1

Brewer, G. J., Torricelli, J. R., Evege, E. K., and Price, P. J. (1993). Optimized survival of hippocampal neurons in B27-supplemented Neurobasal, a new serum-free medium combination. *J. Neurosci.* 35, 567–576. doi: 10.1002/jnr.490350513

Brückner, C., and Heinemann, U. (2000). Effects of standard anticonvulsant drugs on different patterns of epileptiform discharges induced by 4-aminopyridine in combined entorhinal cortex-hippocampal slices. *Brain Res.* 859, 15–20. doi: 10.1016/s0006-8993(99)02348-3

Caliskan, G., Müller, I., Semtner, M., Winkelmann, A., Raza, A. S., Hollnagel, J. O., et al. (2016). Identification of parvalbumin interneurons as cellular substrate of fear memory persistence. *Cereb. Cortex* 26, 2325–2340. doi: 10.1093/cercor/bhw001

Cea-del Rio, C. A., Lawrence, J. J., Tricoire, L., Erdelyi, F., Szabo, G., and McBain, C. J. (2010). M3 muscarinic acetylcholine receptor expression confers differential cholinergic modulation to neurochemically distinct hippocampal basket cell subtypes. *J. Neurosci.* 30, 6011–6024. doi: 10.1523/JNEUROSCI.5040-09.2010

D'Antuono, M., Köhling, R., Ricalzone, S., Gotman, J., Biagini, G., and Avoli, M. (2010). Antiepileptic drugs abolish ictal but not interictal epileptiform discharges *in vitro*. *Epilepsia* 51, 423–431. doi: 10.1111/j.1528-1167.2009.02273.x

de Montigny, C., Chouinard, G., and Annable, L. (1979). Ineffectiveness of deanol in tardive dyskinesia: a placebo controlled study. *Psychopharmacology* 65, 219–223. doi: 10.1007/bf00492207

Dibué-Adjei, M., Brigo, F., Yamamoto, T., Vonck, K., and Trinka, E. (2019). Vagus nerve stimulation in refractory and super-refractory status epilepticus—a systematic review. *Brain Stimul.* doi: 10.1016/j.brs.2019.05.011 [Epub ahead of print].

Dudek, F. E., Obenaus, A., and Tasker, J. G. (1990). Osmolality-induced changes in extracellular volume alter epileptiform bursts independent of chemical synapses in the rat: importance of non-synaptic mechanisms in hippocampal epileptogenesis. *Neurosci. Lett.* 120, 267–270. doi: 10.1016/0304-3940(90)90056-f

Engel, J., Wiebe, S., French, J., Sperling, M., Williamson, P., Spencer, D., et al. (2007). Practice parameter: temporal lobe and localized neocortical resections for epilepsy. *Contin. Lifelong Learn. Neurol.* 13, 225–234. doi: 10.1212/01.CON.0000284531.20401.00

Eyal, G., Verhoog, M. B., Testa-Silva, G., Deitcher, Y., Benavides-Piccione, R., DeFelipe, J., et al. (2018). Human cortical pyramidal neurons: from spines to spikes *via* models. *Front. Cell. Neurosci.* 12:181. doi: 10.3389/fncel.2018.00181

Falco-Walter, J. J., Roehl, K., Ouyang, B., and Balabanov, A. (2019). Do certain subpopulations of adults with drug-resistant epilepsy respond better to modified ketogenic diet treatments? Evaluation based on prior resective surgery, type of epilepsy, imaging abnormalities, and vagal nerve stimulation. *Epilepsy Behav.* 93, 119–124. doi: 10.1016/j.yebeh.2019.01.010

Ferris, S. H., Sathananthan, G., Gershon, S., and Clark, C. (1977). Senile dementia: treatment with deanol†. *J. Am. Geriatr. Soc.* 25, 241–244. doi: 10.1111/j.1532-5415.1977.tb00407.x

Fisman, M., Mersky, H., and Helmes, E. (1981). Double-blind trial of 2-dimethylaminoethanol in Alzheimer's disease. *Am. J. Psychiatry* 138, 970–972. doi: 10.1176/ajp.138.7.970

Fueta, Y., and Avoli, M. (1992). Effects of antiepileptic drugs on 4-aminopyridine-induced epileptiform activity in young and adult rat hippocampus. *Epilepsy Res.* 12, 207–215.

Gabriel, S., Njunting, M., Pomper, J. K., Merschhemke, M., Sanabria, E. R. G., Eilers, A., et al. (2004). Stimulus and potassium-induced epileptiform activity in the human dentate gyrus from patients with and without hippocampal sclerosis. *J. Neurosci.* 24, 10416–10430. doi: 10.1523/jneurosci.2074-04.2004

George, J., Pridmore, S., and Aldous, D. (1981). Double blind controlled trial of deanol in tardive dyskinesia. *Aust. New Zeal. J. Psychiatry* 15, 68–71. doi: 10.3109/00048678109159413

Giordano, C., Marchiò, M., Timofeeva, E., and Biagini, G. (2014). Neuroactive peptides as putative mediators of antiepileptic ketogenic diets. *Front. Neurol.* 5:63. doi: 10.3389/fneur.2014.00063

Hallböök, T., Sjölander, A., Åmark, P., Miranda, M., Bjurulf, B., and Dahlin, M. (2015). Effectiveness of the ketogenic diet used to treat resistant childhood epilepsy in Scandinavia. *Eur. J. Paediatr. Neurol.* 19, 29–36. doi: 10.1016/j.ejpn.2014.09.005

Heuzeroth, H., Wawra, M., Fidzinski, P., Dag, R., and Holtkamp, M. (2019). The 4-aminopyridine model of acute seizures *in vitro* elucidates efficacy of new antiepileptic drugs. *Front. Neurosci.* 13:677. doi: 10.3389/fnins.2019.00677

Hill, M. R. H., and Greenfield, S. A. (2011). The membrane chamber: a new type of *in vitro* recording chamber. *J. Neurosci. Methods* 195, 15–23. doi: 10.1016/j.jneumeth.2010.10.024

Hirtz, D., Thurman, D. J., Gwinn-Hardy, K., Mohamed, M., Chaudhuri, A. R., and Zalutsky, R. (2007). How common are the "common" neurologic disorders? *Neurology* 68, 326–337. doi: 10.1212/01.wnl.0000252807.38124.a3

Holtkamp, D., Opitz, T., Niespodziany, I., Wolff, C., and Beck, H. (2017). Activity of the anticonvulsant lacosamide in experimental and human epilepsy *via* selective effects on slow Na^+ channel inactivation. *Epilepsia* 58, 27–41. doi: 10.1111/epi.13602

Jope, R. S., and Jenden, D. J. (1979). Dimethylaminoethanol (deanol) metabolism in rat brain and its effect on acetyicholine synthesis1. *J. Pharmacol. Exp. Ther.* 211, 472–479.

Kaufmann, K., Romaine, I., Days, E., Pascual, C., Malik, A., Yang, L., et al. (2013). ML297 (VU0456810), the first potent and selective activator of the GIRK potassium channel, displays antiepileptic properties in mice. *ACS Chem. Neurosci.* 4, 1278–1286. doi: 10.1021/cn400062a

Kowski, A. B., Voges, J., Heinze, H.-J., Oltmanns, F., Holtkamp, M., and Schmitt, F. C. (2015). Nucleus accumbens stimulation in partial epilepsy-A randomized controlled case series. *Epilepsia* 56, e78–e82. doi: 10.1111/epi.12999

Krestel, H., Raffel, S., von Lehe, M., Jagella, C., Moskau-Hartmann, S., Becker, A., et al. (2013). Differences between RNA and DNA due to RNA editing in temporal lobe epilepsy. *Neurobiol. Dis.* 56, 66–73. doi: 10.1016/j.nbd.2013.04.006

Ledri, M., Sørensen, A. T., Madsen, M. G., Christiansen, S. H., Ledri, L. N., Cifra, A., et al. (2015). Differential effect of neuropeptides on excitatory

synaptic transmission in human epileptic hippocampus. *J. Neurosci.* 35, 9622–9631. doi: 10.1523/JNEUROSCI.3973-14.2015

Löscher, W. (2011). Critical review of current animal models of seizures and epilepsy used in the discovery and development of new antiepileptic drugs. *Seizure* 20, 359–368. doi: 10.1016/j.seizure.2011.01.003

Meier, J. C., Kankowski, S., Krestel, H., and Hetsch, F. (2016). RNA editing-systemic relevance and clue to disease mechanisms? *Front Mol. Neurosci.* 9:124. doi: 10.3389/fnmol.2016.00124

Millington, W. R., McCall, A. L., and Wurtman, R. J. (1978). Deanol acetamidobenzoate inhibits the blood brain barrier transport of choline. *Ann. Neurol.* 4, 302–306. doi: 10.1002/ana.410040403

Miyashita, T., and Kubo, Y. (1997). Localization and developmental changes of the expression of two inward rectifying K^+-channel proteins in the rat brain. *Brain Res.* 750, 251–263. doi: 10.1016/s0006-8993(96)01365-0

Mohan, M., Keller, S., Nicolson, A., Biswas, S., Smith, D., Osman Farah, J., et al. (2018). The long-term outcomes of epilepsy surgery. *PLoS One* 13:e0196274. doi: 10.1371/journal.pone.0196274

Moreno-Galindo, E. G., Sanchez-Chapula, J. A., Tristani-Firouzi, M., and Navarro-Polanco, R. A. (2016). Pharmacological conversion of a cardiac inward rectifier into an outward rectifier potassium channel. *Mol. Pharmacol.* 90, 334–340. doi: 10.1124/mol.116.104950

Murer, G., Adelbrecht, C., Lauritzen, I., Lesage, F., Lazdunski, M., Agid, Y., et al. (1997). An immunocytochemical study on the distribution of two G-protein-gated inward rectifier potassium channels (GIRK2 and GIRK4) in the adult rat brain. *Neuroscience* 80, 345–357. doi: 10.1016/s0306-4522(97)00001-8

Murphree, H. B. Jr., Pfeiffer, C. C., and Backerman, I. A. (1960). The stimulant effect of 2-dimethylaminoethanol (deanol) in human volunteer subiects. *Clin. Pharmacol. Ther.* 1, 303–310. doi: 10.1002/cpt196013303

Nemec, J., Wickman, K., and Clapham, D. E. (1999). Gβγ binding increases the open time of IKACh: kinetic evidence for multiple Gβγ binding sites. *Biophys. J.* 76, 246–252. doi: 10.1016/s0006-3495(99)77193-6

Ngugi, A. K., Bottomley, C., Kleinschmidt, I., Sander, J. W., and Newton, C. R. (2010). Estimation of the burden of active and life-time epilepsy: a meta-analytic approach. *Epilepsia* 51, 883–890. doi: 10.1111/j.1528-1167.2009.02481.x

Penovich, P., Morgan, J. P., Kerzner, B., Karch, F., and Goldblatt, D. (1978). Double-blind evaluation of deanol in tardive dyskinesia. *JAMA J. Am. Med. Assoc.* 239, 1997–1998. doi: 10.1001/jama.1978.03280460065020

Perreault, P., and Avoli, M. (1991). Physiology and pharmacology of epileptiform activity induced by 4-aminopyridine in rat hippocampal slices. *J. Neurophysiol.* 65, 771–785. doi: 10.1152/jn.1991.65.4.771

Pfeiffer, C. C., Goldstein, L., Munoz, C., Murphree, H. B., and Jenney, E. H. (1963). Quantitative comparisons of the electroencephalographic stimulant effects of deanol, choline, and amphetamine. *Clin. Pharmacol. Ther.* 4, 461–466. doi: 10.1002/cpt196344461

Remy, S., Gabriel, S., Urban, B. W., Dietrich, D., Lehmann, T. N., Elger, C. E., et al. (2003). A novel mechanism underlying drug resistance in chronic epilepsy. *Ann. Neurol.* 53, 469–479. doi: 10.1002/ana.10473

Reyes-Garcia, S. Z., Scorza, C. A., Araújo, N. S., Ortiz-Villatoro, N. N., Jardim, A. P., Centeno, R., et al. (2018). Different patterns of epileptiform-like activity are generated in the sclerotic hippocampus from patients with drug-resistant temporal lobe epilepsy. *Sci. Rep.* 8:7116. doi: 10.1038/s41598-018-25378-9

Rosen, A. S., and Andrew, R. D. (1990). Osmotic effects upon excitability in rat neocortical slices. *Neuroscience* 38, 579–590. doi: 10.1016/0306-4522(90)90052-6

Rosenmund, C., and Stevens, C. F. (1996). Definition of the readily releasable pool of vesicles at hippocampal synapses. *Neuron* 16, 1197–1207. doi: 10.1016/s0896-6273(00)80146-4

Sandow, N., Kim, S., Raue, C., Päsler, D., Klaft, Z.-J., Antonio, L. L., et al. (2015). Drug resistance in cortical and hippocampal slices from resected tissue of epilepsy patients: no significant impact of p-glycoprotein and multidrug resistance-associated proteins. *Front. Neurol.* 6:30. doi: 10.3389/fneur.2015.00030

Shekh-Ahmad, T., Bialer, M., and Yavin, E. (2012). Synthesis and anticonvulsant evaluation of dimethylethanolamine analogues of valproic acid and its tetramethylcyclopropyl analogue. *Epilepsy Res.* 98, 238–246. doi: 10.1016/j.eplepsyres.2011.10.005

Shi, H., Wang, H., Yang, B., Xu, D., and Wang, Z. (2004). The M_3 receptor-mediated K^+ current (I_{KM3}), a G_q protein-coupled K^+ channel. *J. Biol. Chem.* 279, 21774–21778. doi: 10.1074/jbc.C400100200

Spencer, S. S., Goncharova, I. I., Duckrow, R. B., Novotny, E. J., and Zaveri, H. P. (2008). Interictal spikes on intracranial recording: behavior, physiology, and implications. *Epilepsia* 49, 1881–1892. doi: 10.1111/j.1528-1167.2008.01641.x

Srivastava, P. K., Bagnati, M., Delahaye-Duriez, A., Ko, J.-H., Rotival, M., Langley, S. R., et al. (2017). Genome-wide analysis of differential RNA editing in epilepsy. *Genome Res.* 27, 440–450. doi: 10.1101/gr.210740.116

Stephen, L. J., Kwan, P., and Brodie, M. J. (2001). Does the cause of localisation-related epilepsy influence the response to antiepileptic drug treatment? *Epilepsia* 42, 357–362. doi: 10.1046/j.1528-1157.2001.29000.x

Taing, K. D., O'Brien, T. J., Williams, D. A., and French, C. R. (2017). Anti-epileptic drug combination efficacy in an *in vitro* seizure model—phenytoin and valproate, lamotrigine and valproate. *PLoS One* 12:e0169974. doi: 10.1371/journal.pone.0169974

Tammenmaa, I. A., Sailas, E., McGrath, J. J., Soares-Weiser, K., and Wahlbeck, K. (2004). Systematic review of cholinergic drugs for neuroleptic-induced tardive dyskinesia: a meta-analysis of randomized controlled trials. *Prog. Neuropsychopharmacol. Biol. Psychiatry* 28, 1099–1107. doi: 10.1016/j.pnpbp.2004.05.045

Testa-Silva, G., Verhoog, M. B., Goriounova, N. B., Loebel, A., Hjorth, J., Baayen, J. C., et al. (2010). Human synapses show a wide temporal window for spike-timing-dependent plasticity. *Front. Synaptic Neurosci.* 2:12. doi: 10.3389/fnsyn.2010.00012

Ting, J. T., Daigle, T. L., Chen, Q., and Feng, G. (2014). Acute brain slice methods for adult and aging animals: application of targeted patch clamp analysis and optogenetics. *Methods Mol. Biol.* 1183, 221–242. doi: 10.1007/978-1-4939-1096-0_14

Ting, J. T., Kalmbach, B., Chong, P., de Frates, R., Keene, C. D., Gwinn, R. P., et al. (2018). A robust *ex vivo* experimental platform for molecular-genetic dissection of adult human neocortical cell types and circuits. *Sci. Rep.* 8:8407. doi: 10.1038/s41598-018-26803-9

Traynelis, S. F., and Dingledine, R. (1989). Role of extracellular space in hyperosmotic suppression of potassium-induced electrographic seizures. *J. Neurophysiol.* 61, 927–938. doi: 10.1152/jn.1989.61.5.927

Wiebe, S., Blume, W. T., Girvin, J. P., Eliasziw, M., and Effectiveness and Efficiency of Surgery for Temporal Lobe Epilepsy Study Group. (2001). A randomized, controlled trial of surgery for temporal-lobe epilepsy. *N. Engl. J. Med.* 345, 311–318. doi: 10.1056/nejm200108023450501

Winkelmann, A., Maggio, N., Eller, J., Caliskan, G., Semtner, M., Häussler, U., et al. (2014). Changes in neural network homeostasis trigger neuropsychiatric symptoms. *J. Clin. Invest.* 124, 696–711. doi: 10.1172/jci71472

Zangiabadi, N., Ladino, L. D., Sina, F., Orozco-Hernández, J. P., Carter, A., and Téllez-Zenteno, J. F. (2019). Deep brain stimulation and drug-resistant epilepsy: a review of the literature. *Front. Neurol.* 10:601. doi: 10.3389/fneur.2019.00601

Conflict of Interest Statement: The authors declare that the research was conducted in the absence of any commercial or financial relationships that could be construed as a potential conflict of interest.

Copyright © 2019 Kraus, Hetsch, Schneider, Radbruch, Holtkamp, Meier and Fidzinski. This is an open-access article distributed under the terms of the Creative Commons Attribution License (CC BY). The use, distribution or reproduction in other forums is permitted, provided the original author(s) and the copyright owner(s) are credited and that the original publication in this journal is cited, in accordance with accepted academic practice. No use, distribution or reproduction is permitted which does not comply with these terms.

frontiers in Molecular Neuroscience

REVIEW
published: 19 September 2019
doi: 10.3389/fnmol.2019.00221

Pavlovian Olfactory Fear Conditioning: Its Neural Circuity and Importance for Understanding Clinical Fear-Based Disorders

Marziah Hakim[1,2,3], *Andrew R. Battle*[1,2,3,4], *Arnauld Belmer*[2,3], *Selena E. Bartlett*[2,3,5], *Luke R. Johnson*[1,3,6,7] *and Fatemeh Chehrehasa*[1,2,3,8]*

[1]School of Biomedical Science, Queensland University of Technology, Brisbane, QLD, Australia, [2]Institute of Health and Biomedical Innovation, Queensland University of Technology, Kelvin Grove, QLD, Australia, [3]Mater Medical Research Institute and Queensland Health, Queensland University of Technology, The University of Queensland, Woolloongabba, QLD, Australia, [4]The University of Queensland Diamantina Institute, Translational Research Institute, Woolloongabba, QLD, Australia, [5]School of Clinical Sciences, Queensland University of Technology, Brisbane, QLD, Australia, [6]Division of Psychology, School of Medicine, University of Tasmania, Launceston, TAS, Australia, [7]Center for the Study of Traumatic Stress, School of Medicine, College of Health and Medicine, Uniformed Services University, Bethesda, MD, United States, [8]Clem Jones Centre for Neurobiology and Stem Cell Research, Griffith Institute for Drug Discovery, Griffith University, Nathan, QLD, Australia

Odors have proven to be the most resilient trigger for memories of high emotional saliency. Fear associated olfactory memories pose a detrimental threat of potentially transforming into severe mental illness such as fear and anxiety-related disorders. Many studies have deliberated on auditory, visual and general contextual fear memory (CFC) processes; however, fewer studies have investigated mechanisms of olfactory fear memory. Evidence strongly suggests that the neuroanatomical representation of olfactory fear memory differs from that of auditory and visual fear memory. The aim of this review article is to revisit the literature regarding the understanding of the neurobiological process of fear conditioning and to illustrate the circuitry of olfactory fear memory.

Keywords: memory, olfactory, fear conditioning, neurogenesis, amygdala, neuronal circuits, plasticity

OPEN ACCESS

Edited by:
Jochen C. Meier,
Technische Universitat Braunschweig, Germany

Reviewed by:
Oliver Stork,
Universitätsklinikum Magdeburg, Germany
Jennifer McGuire,
University of Cincinnati, United States

***Correspondence:**
Fatemeh Chehrehasa
fatemeh.chehrehasa@qut.edu.au

Received: *20 May 2019*
Accepted: *03 September 2019*
Published: *19 September 2019*

Citation:
Hakim M, Battle AR, Belmer A, Bartlett SE, Johnson LR and Chehrehasa F (2019) Pavlovian Olfactory Fear Conditioning: Its Neural Circuity and Importance for Understanding Clinical Fear-Based Disorders. Front. Mol. Neurosci. 12:221. doi: 10.3389/fnmol.2019.00221

INTRODUCTION

Odor-evoked memories possess the ability to take an individual back to a significant emotional event (Herz, 1998; Schettino and Otto, 2001; Wilson, 2003; Sevelinges et al., 2007; Nigri et al., 2013). They are an integral component of significant autobiographical memories that can allow us to revisit an experience or an event. This was demonstrated by Proust (1976), a French novelist who took a bite of madeleine biscuit that had been dipped in Linden tea and was flooded with memories of a long-forgotten moment from his childhood. This is now commonly known as the "Proust phenomenon" (Proust, 1976). This association between odor and memory seems to be more potent when the experience holds a higher emotional value (Herz and Cupchik, 1995; Herz, 1997b). Olfaction is known as the sense with the highest association with emotional context, and therefore holds a strong ability to trigger memories that carry high emotional saliency (Herz, 1998; Schettino and Otto, 2001; Wilson, 2003; Sevelinges et al., 2007; Nigri et al., 2013). This is a characteristic feature of odor evoked memories, in comparison to recollections triggered by other sensory stimuli such as visual, auditory and tactile (Abraham et al., 1993; Chu and Downes, 2000; Willander and Larsson, 2006; Miles and Berntsen, 2011).

Experimental evidence suggests that the olfactory components of autobiographical memories are more resilient than the visual and auditory components of the same experience

(Engen and Ross, 1973; Herz and Cupchik, 1995; Chu and Downes, 2000; Toffolo et al., 2012). Olfactory stimuli are able to persist despite the degradation of other sensory memory cues (Herz and Cupchik, 1995). Willander and Larsson (2006) found that autobiographical memories triggered by olfactory stimuli tend to be older than memories evoked by other sensory cues. This quality of endurance is what makes odors more effective as retrieval cues for emotional memories than other senses (Willander and Larsson, 2006).

Along with evoking highly emotional memories, it has been found that odors have an unusual effect on contextual memory cues. Many studies have found that odors are superior to other sensory stimuli in facilitating context-dependent memory (Cann and Ross, 1989; Schab, 1990; Smith et al., 1992; Herz, 1998) and the presence of odors at the time of the experience and at the time of recall can significantly enhance the retrieval of learned items (Herz, 1998; Otto et al., 2000). Additionally, there is increasing evidence suggesting that successful contextual conditioning is dependent on changes in the internal state of the subject occurring in the context, such as introducing a change in emotional state (Herz, 1997a; Otto and Giardino, 2001; Muñoz-Abellán et al., 2009). This explains the strength of olfactory contextual cues and its tight association with emotional neural substrates in fear conditioning (Herz, 1997b).

The ability of odors to increase a memory's evocative strength often poses a threat, as they include "fear" memories (Toffolo et al., 2012). There are a range of anxiety and trauma-related disorders which have an olfactory component (Cortese et al., 2015). Although olfaction has great influence on context associated fear and anxiety-related memory pathologies, the encoding and processing of aversive olfactory conditioning has been investigated limitedly (Otto et al., 2000; Schettino and Otto, 2001; Sevelinges et al., 2004; Valley et al., 2009; Ross and Fletcher, 2018).

Much of the research surrounding fear conditioning and its neuroanatomical changes has been predominantly with auditory and visual stimuli (LeDoux et al., 1986; Campeau and Davis, 1995; Valley et al., 2009; Johnson et al., 2012; Bergstrom et al., 2013; Bergstrom and Johnson, 2014; Daldrup et al., 2015), however odors are especially effective at triggering memories of high emotional saliency and intensity, much more so than other sensory cues (Herz, 1998). Furthermore, the olfactory fear memory pathway differs considerably from auditory and visual pathways (Campeau and Davis, 1995; Bergstrom and Johnson, 2014; Parma et al., 2015).

Therefore, studying the mechanisms of olfactory memory can not only provide insight into normal emotions but also mental disorders, in particular, those relating to fear. The focus of this review is to revisit the olfactory system, explore the literature on the neural circuitry of olfactory fear conditioning (OFC) and the effects of OFC on olfactory neurogenesis.

OLFACTORY SYSTEM

The olfactory sense is thought to be the most advanced sensory informant, and by virtue has evolved to a complex system (Eisthen, 1997; Pifferi et al., 2010). The organization of the olfactory system initiates in the olfactory epithelium, which houses primary olfactory receptor neurons (ORNs) and supporting cells. The primary ORNs are bipolar neurons that serve to transmit olfactory information to the olfactory bulb (OB). The unmyelinated axons of these neurons project to the lamina propria where they form large axon bundles which pass through the cribriform plate of the ethmoid bone to arborize and synapse with olfactory second-order neurons on glomeruli within the OB. These second-order neurons are known as mitral and tufted neurons which approximately 20–50 of these neurons emanate from each glomerulus. The axons of mitral and tufted neurons form the lateral olfactory tract which project and synapse at various areas of the olfactory cortex, including the olfactory tubercle (OT), piriform cortex (PC), amygdala, the anterior olfactory nucleus (AON) and entorhinal cortex (EC) which projects to the dentate gyrus (DG) of the hippocampus (**Figure 1**; Buck, 1996; Lledo et al., 2005; Mori et al., 2006; Illig and Wilson, 2009). The second-order neurons also have lateral dendrites that extend in the glomerular and granular layers of the OB and synapse with olfactory inhibitory interneurons known as periglomerular and granular neurons (Lledo et al., 2008; Bonzano et al., 2016).

The olfactory afferents all function to process, combine and store odor information. The role of the OT is manifold. Odor information reaches the OT predominantly *via* the tufted cells (Scott et al., 1980). The information is modulated by the PC, which receives input predominantly by the mitral cells (**Figure 1**) (Wesson and Wilson, 2011). This dual input then allows for distinct odor processing. The OT may also play a role in determining the source of an odor and odor discrimination (Wesson and Wilson, 2011). The AON further contributes to odor processing by detecting and storing correlations between olfactory features and creates representations of particular odors and combination of odors. The PC then detects and learns the representations and creates emotional associations (Haberly, 2001). This information is linked to memory *via* the EC. The EC has been found to be responsible for the relational organization of memory and provide differential inputs to the CA1 and CA3 regions of the hippocampus, where memory is consolidated (**Figure 1**; Eichenbaum et al., 2007; De La Rosa-Prieto et al., 2015; Chaaya et al., 2018). Furthermore, the EC sends olfactory information to the DG of the hippocampus. This connection is reciprocal in that information is carried back to the OB from the ventral subiculum and CA1 (**Figure 1**; de la Rosa-Prieto et al., 2009; Mohedano-Moriano et al., 2012). Based on these findings, each afferent connection of the OB plays a unique role in olfactory memory processing.

Many studies have explored the trajectory of the mitral and tufted cells from the OB to the PC (**Figure 1**; Stevens, 1969; Haberly, 1973; Devor, 1976; Schettino and Otto, 2001), which is the largest cortical recipient of direct OB and plays an important role in integrating cognition and experience into odor information stored in the AON (Woolsey and Van der Loos, 1970; Henkin et al., 1977; West and Doty, 1995; Stettler and Axel, 2009). This part of the olfactory cortex has two main subdivisions: anterior PC (APC), and posterior PC (PPC). The ventral part of APC may receive exclusive input from tufted

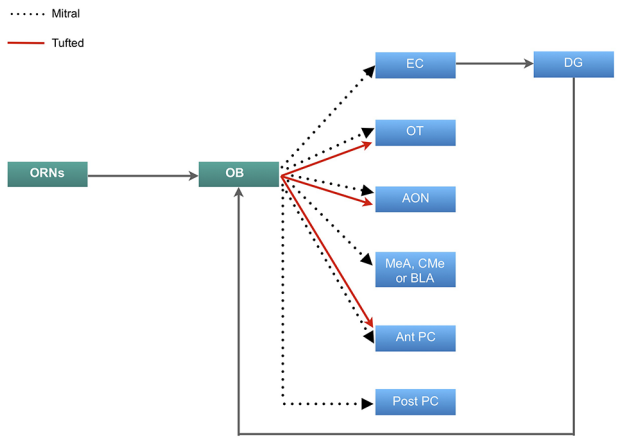

FIGURE 1 | Neural circuitry of olfactory information. Primary olfactory receptor neurons (ORNs) residing in the main olfactory epithelium of the nasal cavity carry information to the olfactory bulb (OB), which is then relayed by the mitral cells to the entorhinal cortex (EC) that sends inputs to the dentate gyrus (DG) and projects back to the OB. Mitral cells also project to the olfactory tubercle (OT), anterior olfactory nucleus (AON), either the medial (MeA), corticomedial (CMe) or basolateral amygdala (BLA) and both the anterior and posterior regions of the piriform cortex (PC). The tufted cells carry olfactory information to the OT, AON and exclusively to the posterior portion of the PC.

cells (Illig and Wilson, 2009) which discriminates and categorizes the information (**Figure 1**; Sharp et al., 1977; Stettler and Axel, 2009). Rennaker et al., 2007 showed that odor representations are transformed into ensemble patterns and distributed spatially and temporally in the APC (Rennaker et al., 2007). It was previously believed that the APC was exclusively involved in sensory processes and perceptual learning (Wilson, 1998, 2000, 2003; Rennaker et al., 2007), however more recently, it has been shown that the APC demonstrated post-fear conditional changes, which alludes to its involvement in odor memory recall, along with the PPC (Shepherd, 2010; Barnes et al., 2011; Chen et al., 2011). Furthermore, high resolution functional imaging has shown that the PPC is responsible for coding odor perceptions, a feature that is absent in the APC and amygdala (Howard et al., 2009).

The hippocampus has been studied extensively in regards to its role in spatial and contextual fear memory (CFC; Maren et al., 1998; Wiltgen et al., 2006; Maren, 2014; Zelikowsky et al., 2014; Hersman et al., 2017). Odors form a strong component of context-dependent memory (Herz, 1997a). Several studies have observed significant neuroplastic changes following CFC in the hippocampus (Fanselow, 2000; Han et al., 2016; Schmidt et al., 2017; Chaaya et al., 2018). Interestingly, there have been strong parallels observed between the function of the hippocampus in CFC and the PC in OFC. The hippocampus and PC have comparable circuit organizations in which neuron ensembles that are activated by learning, are necessary for olfactory and contextual memory retrieval (Haberly, 2001; Liu et al., 2012; Meissner-Bernard et al., 2019). Mandairon and colleagues demonstrated that following contextual conditioning, visual context alone was able to activate neural structures similar to that stimulated by odor alone; namely, the PC and OB (Mainland et al., 2014). These findings suggest that independent odor cues and odorants as part of context have similar neural representations. Nevertheless, further research is required to address whether odor-cued fear memories are relayed in the hippocampus directly or as part of contextual memory. This information can provide further insight into whether the circuitry in the PC and hippocampus associated with fear learning are distinct or both are simultaneously activated by olfactory cues.

ANIMAL MODELS OF FEAR MEMORY

Neuroanatomical studies in animal models and imaging of human brains have showed overlapping results regarding the neurobiology of emotional memories and conditioned fear memories (Delgado et al., 2006; Knapska et al., 2012; Vanelzakker et al., 2014). Therefore, most of the current literature utilizes animal models in order to replicate trauma-related emotional disorders (Wang et al., 2007; Chen et al., 2011; Moore et al., 2012; Russo and Parsons, 2017). One approach to induce fear memory is to introduce physical stressors such as forced swim paradigms, restraint stress, ether exposure and inescapable foot shocks (Vyas et al., 2002; McGuire et al., 2010; Moore et al., 2012; Bergstrom and Johnson, 2014).

Another approach involves psychosocial stressors such as housing instability, social defeat and social isolation. Housing instability is mimicked by changing home cages and cage mates daily, which has been shown to produce long-lasting anxiety-driven behaviors (Zoladz et al., 2012; Saavedra-Rodríguez and Feig, 2013). Social defeat is induced by placing an intruder animal in the territory of a larger resident animal, resulting in the resident attacking the intruder, which produces signs of anxiety in these animals (Huhman, 2006).

The prototypical form of fear learning is Pavlovian fear conditioning (Pavlov, 1927; Maren and Fanselow, 1996). It involves an aversive unconditioned stimulus (US) that evokes an innate negative response, irrespective of training, and a neutral conditioned stimulus (CS). Conditioning involves contingent associations of the CS with the US, such that the CS evokes an aversive conditioned response and predicts the occurrence of the US (Bolles and Collier, 1976). The most common protocol is that an animal receives mild foot shocks with a neutral sensory stimulus (odor, tone or light) concurrently (Johnson et al., 2012). The animal's learning is then tested by presenting the CS alone, which evokes a behavioral or physiological fear response including increased heart rate and blood pressure and more frequent defecation or urination (Davis, 1992; LeDoux, 1995; Goswami et al., 2013). Another method of measurement is the observation of a fear-potentiated startle response, a reflex that occurs in response to an abrupt acoustic stimulus and results in the rapid contraction of the facial and skeletal muscles (Davis, 1992; Russo and Parsons, 2017). Measuring the duration of freezing (complete immobility except for movements involved in respiration) has also been a common method used in behavioral studies (Bolles and Collier, 1976; Amorapanth et al., 1999; Lee et al., 2005; Daldrup et al., 2015). These are typical unconditioned

stress/anxiety responses for rodents, which have evolved into a cogent way to study the development and maintenance of fear and anxiety-related disorders, as they can often follow a similar neurobiological process to Pavlovian fear (Johnson et al., 2012).

OLFACTORY FEAR CONDITIONING AND AMYGDALA

In contrast to auditory and visual fear conditioning, fewer studies have investigated olfactory fear conditioning (OFC). Therefore, the neural circuitry of OFC is not fully understood. Some recent studies have begun to focus on the neuroanatomical changes occurring as a result of olfactory fear processing. A study using olfactory fear conditioning using M71 odorant receptor transgenic mice showed that there was an increase in the number of M71 odorant receptors in the nasal cavity and cross sectional of M71 glomeruli of the OB in response to olfactory fear. Furthermore, olfactory extinction training specific to the conditioned odor was shown to reverse the structural changes that occurred as a result of olfactory fear memory acquisition in the olfactory epithelium and the OB (Morrison et al., 2015).

Odorant receptors that are activated by specific odors can be structurally altered by both appetitive and aversive experiences (Ressler et al., 1994; Mori et al., 2006; Fletcher, 2012). Studies have shown that the number of olfactory sensory neurons expressing a specific odorant receptor doubled at 3 weeks post-conditioning and the odor-evoked synaptic outputs of the associated glomeruli were significantly enhanced following associative learning of fear (Kass et al., 2013; Morrison et al., 2015). These studies contribute to the premise that the primary olfactory sensory neurons play a significant role in the sensitivity and responsiveness to a learned cue or CS.

Investigations of the connections between the olfactory system and the amygdala began early in the 20th century (Herrick, 1921). The association of strong emotions with odors is found to be due to olfactory neurons projecting directly to the amygdala; the brain region where memories are given emotional context. Herrick (1921) was one of the first to discover that the amygdala has direct synapses with the OB. Unmyelinated axons of the dorsal olfactory tract are present in the lateral part of the amygdala (Herrick, 1921). Unlike auditory and visual fear conditioning, the olfactory conditioning pathway does not project directly and exclusively to the basolateral amygdala (BLA; Sevelinges et al., 2004; Keshavarzi et al., 2015; Luchkina and Bolshakov, 2018). Schettino and Otto (2001) also investigated the activation of amygdala subregions during the acquisition and expression of OFC. Their results demonstrated that the medial (MeA) and corticomedial (CMe) nuclei of the amygdala are activated by odor and shock, both individually and paired. Further refining its role (Walker et al., 2005) infused the NMDA receptor antagonist AP5 and the α-amino-3-hydroxy-5-methyl-4-isoxazolepropionic acid (AMPA)/kainate receptor antagonist 2,3-dihydroxy-6-nitro-7-sulfamoyl-benzoquinoxaline (NBQX) into the MeA, which ceased fear-potentiated responses to olfactory CS. This indicated the involvement of the MeA in eliciting fear expression behaviorally as opposed to being involved in fear memory consolidation. It is believed that fear conditioning induces structural changes in the lateral nuclei of the amygdala (LA), underlying acquisition and storage of CS and US or shock associations (LeDoux, 1995). Since the LA plays an integral role in the convergence of CS and US information, it is crucial for olfactory information to reach this region of the amygdala (Romanski et al., 1997; Johnson et al., 2012). Schettino and Otto (2001) proposed that the most likely pathway to the LA is through the periamygdaloid complex (PaC; **Figure 2**).

The role of the central amygdala (CeA) has been studied well in a review article by Keifer et al. (2015). This nucleus is subdivided into the centromedial (CEm) and centrolateral

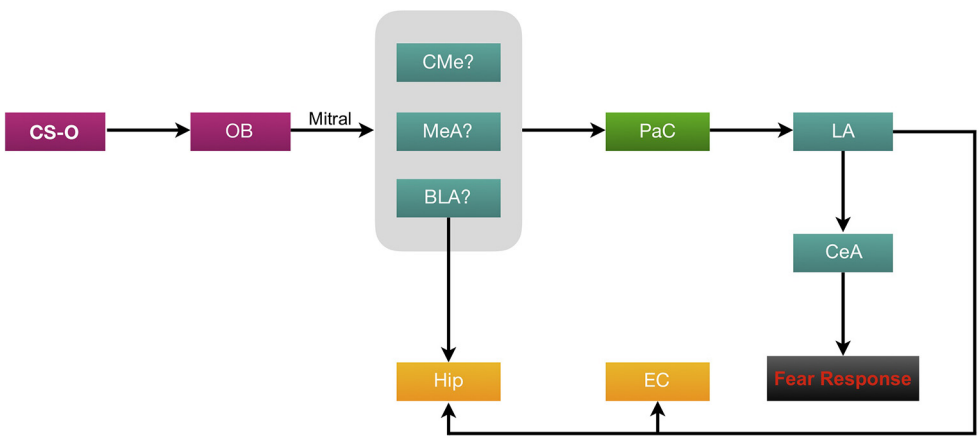

FIGURE 2 | Neural circuitry of olfactory fear conditioning (OFC). Olfactory conditioned stimuli (CS-O) travel through the ORNs to the OB then via the mitral cell axons (forming the olfactory tract), information is carried to the amygdala. Evidence suggests that the likely regions of termination in the amygdala are either the MeA, CMe or BLA. From here, the proposed pathway to the lateral amygdala (LA) is through the periamygdaloid complex (PaC). All CS information is then processed through the central (CeA) amygdala to elicit a fear response. The BLA and LA project heavily to the CA1 and CA3 regions of the hippocampus (Hip). The LA also sends afferents to the EC.

(CEl) nuclei. It has been suggested that the CEl plays a role in fear learning, whereas the CEm is more involved in fear output (Ciocchi et al., 2010). The CeA has inhibitory connections with the prefrontal cortex (PFC), a region which is activated in response to recall of an extinguished fear (Quirk et al., 2003; Milad et al., 2007). However, this has not yet been studied with OFC. While the exact role of the subnuclei of CeA in OFC is not fully understood, lesioning of CeA was shown to abolish OFC (Hitchcock et al., 1989; Sananes and Campbell, 1989). Additionally, a single study has shown that OFC also induces field potential signaling in the cortical amygdala (CoA; Sevelinges et al., 2004).

Furthermore, the BLA has also been responsive to OFC. *In vivo* intracellular recordings in the BLA have demonstrated that repeated odor-shock pairings resulted in enhanced post-synaptic potential responses to the odor (Rosenkranz and Grace, 2002). Similarly, Kilpatrick and Cahill (2003) found that inactivation of the BLA following olfactory conditioning resulted in a learning deficit, suggesting the involvement of the BLA in odor fear memory consolidation. These results were similar to (Cousens and Otto, 1998), who found that pre-training, excitotoxic lesions of the BLA abolished conditioned freezing to an odor. Overall, results from studies regarding the involvement of subregions of the amygdala in OFC have been highly multifarious in comparison to auditory and visual fear conditionings. Further study on OFC and investigation of the specific roles of the subregions of the amygdala could give significant insight on this field.

The amygdala has several connections to the EC and hippocampus, which further contributes to its connotation of memory consolidation. An investigation of its projections to the hippocampal formation revealed that the LA primarily projected to the ventral and dorsal intermediate entorhinal subfield (VIE and DIE, respectively; Pikkarainen et al., 1999). Part of the VIE and DIE also had light projections originating in the basal nucleus of the amygdala (BA). In addition, the BA and LA projected, respectively, to the CA1 and CA3 regions of the ventral hippocampus (Pikkarainen et al., 1999; Chaaya et al., 2018). These projections carry information of CFC to the EC and hippocampus where it undergoes consolidation (Maren and Fanselow, 1997; Chaaya et al., 2018). Further research investigating these projections from the amygdala to the hippocampal formation in relation to OFC would clarify its role further. Due to overlapping neuroanatomy thus found in OFC and CFC, it would be innocuous to the hypothesis that the connections of the amygdala would also overlap.

NEUROGENESIS IN RESPONSE TO OLFACTORY FEAR LEARNING

A striking aspect of the olfactory system is that it constantly receives supply of newborn interneurons from the (SVZ) directly to the OB (Sultan et al., 2010). Additionally, the ORNs lining the nasal cavity are capable of regenerating throughout life (Mackay-Sim and Kittel, 1991; Chehrehasa et al., 2005, 2010). Being under constant environmental detriment, ORNs have a short lifespan of 30–90 days (Mackay-Sim and Kittel, 1991). There are two cell populations in the basal layer of the olfactory epithelium, the horizontal basal cells and the globose basal cells. These cells are responsible for regeneration in the olfactory epithelium (Iwai et al., 2008). While regeneration of primary olfactory neurons is well understood, it is unclear how they respond to OFC and whether the regeneration of the primary olfactory neurons is affected by olfactory fear memory.

Introduction of thymidine analogs such as bromodeoxyuridine (BrdU), which labels newborn cells, contributed significantly to the field of adult neurogenesis (Biffo et al., 1992; Kempermann et al., 2003; Sadgrove et al., 2006; Kondziella et al., 2011). More recently, 5-ethynyl-2′-deoxyuridine (EdU), a new thymidine analog, was tested *in vivo*, which confirmed neurogenesis of the brain and of the olfactory system (Salic and Mitchison, 2008; Chehrehasa et al., 2009). Results of DNA labeling indicated that newborn neurons from the SVZ of the lateral ventricles continually migrated through the rostral migratory stream (RMS) to the OB (Gheusi and Lledo, 2014). As a result, the newborn interneurons continually integrate into the OB circuit (Sakamoto et al., 2014). In rodents, when neurogenesis of the OB was inhibited by various methods, such as a bulbectomy (removing the OB), SVZ ablation or suppression of neuroblast proliferation, olfactory memory retention was significantly impaired and learning of olfactory cues was delayed (Jaako-Movits and Zharkovsky, 2005; Valley et al., 2009). However, the significance of the olfactory inhibitory interneurons and postnatal neurogenesis on aversive olfactory learning and behavior remains inconclusive.

Interestingly, a study has shown that a bilateral bulbectomy decreased granule cell proliferation in the DG of the hippocampus, demonstrating the interconnectedness of the two structures (Jaako-Movits and Zharkovsky, 2005). Since the hippocampus is known to act as an input structure and processing house for visuospatial, auditory and olfactory information, it has been proposed that the OB affects the acquisition of context and formation of stable connections between olfactory components of contextual cues and US (Jaako-Movits and Zharkovsky, 2005).

Contrastingly, a study conducted by So et al. (2008) showed that OFC increased proliferation of neuroblasts in the SVZ, but not the DG. The study controlled for intrinsic contextual learning and therefore the results were only an effect of odor cued conditioning. Furthermore, there is a clear link between neurogenesis in the DG and contextual fear conditioning, however not OFC (Saxe et al., 2006). Despite the structural association between the OB and DG (**Figure 1**), olfactory and contextual learning tasks have shown to independently induce proliferation in either the SVZ or the DG, respectively. Together, these studies show that there is a distinction between the neurogenesis involved in contextual fear conditioning and in cued OFC. However, there is still a need for further research to gain strong evidence on the effect on neurogenesis in the DG following OFC.

Increasing adult hippocampal neurogenesis has been shown to improve pattern separation. Sahay et al. (2011) selectively

increased adult neurogenesis in the hippocampus and found that the mice were able to better distinguish between two similar contexts. Similarly, neurogenesis occurring in the OB functions to facilitate the distinction between odors. The survival and integration of newborn neurons enhance odor acuity following olfactory conditioning (Rochefort et al., 2002; Moreno et al., 2009). With this evidence, we can conclude that neurogenesis plays an adaptive role to optimally encode contextual and olfactory information.

The role of newborn olfactory granule cells in regard to learning and memory was further explored by analyzing neuronal activity of granule cells through electrophysiological recordings (Nissant et al., 2009). Nissant et al. (2009) investigated synaptic plasticity of newborn and mature granule cells in the OB following theta-burst stimulation which induced long term potentiation (LTP). This study showed that LTP-related plasticity could not be induced in mature granule cells in postnatal mice but was transiently induced in newborn granule cells in adults. This suggests that young adult-born neurons in the OB are particularly susceptible to synaptic plasticity related to LTP and proved that neurogenesis contributes to the retention of long-term memory.

Both perceptual and associative olfactory learnings cause selective recruitment of newborn neurons to the OB (Moreno et al., 2009; Sultan et al., 2010). At approximately 2–4 weeks following thymidine analog labeling, it was found that the newborn neurons underwent an elimination process and approximately half of the newly-generated cells encountered apoptosis (Rochefort et al., 2002; Dayer et al., 2003; Kempermann et al., 2003). The selection of the surviving neurons has been positively correlated with olfactory activity (So et al., 2008; Valley et al., 2009; Sultan et al., 2010). Reconstruction of spatial density maps of the granule cell layer of the OB demonstrate that recall of an associative task recruits young neurons in odor-specific areas of the OB and their survival is proportional to the strength of learning (Sultan et al., 2010). Although this study shows the importance of olfactory learning on survival of newborn neurons, it utilized a reward conditioning paradigm, which may not accurately represent fear memory and may not apply to anxiety-related pathologies.

Further experiments would be required to clarify the role of brain neurogenesis in olfactory fear learning and memory; such as the mechanisms underlying long term memory compared to that of short-term memory and the incorporation of adult-born neurons into the afferent connections of the OB.

CONCLUSION

The aim of this review article was to revisit the literature on OFC in order to understand the neuronal circuitry of olfactory fear memories. Recent studies showed that the amygdala, PC and OB are essential regions involved in olfactory fear memory processing. In addition, a small body of literature also suggests that the amygdala subnuclei, MeA, CMe, CeA and BLA, have a degree of involvement in the consolidation and expression of olfactory fear memory, however, this is not fully understood due to limited research in the area. Further experimental studies are required to determine which subnuclei of the amygdala and which subregions of the PC are involved in OFC and to understand their specific role in olfactory fear memory processing. In addition, it has been shown that olfactory fear conditioning results in an increase in neurogenesis in the SVZ. Moreover, newborn neurons are potential key players in the retention of long term memory, however, the specific role of the newborn neurons is yet to be investigated.

Overall, in order to provide efficient therapeutic strategies for patients with fear-related mental disorders, it is essential to understand the underlying neuronal circuits. Importantly, it has been shown that exposure therapy for fear-related disorders has not had long term efficacy due to the influence of context, which includes odor (Bouton, 2004). From this knowledge, a holistic and more targeted approach for treatment of fear memory-related disorders is needed, that includes all sensory inputs.

AUTHOR CONTRIBUTIONS

FC, ARB and LJ devised the study context. MH and FC conducted the literature review, selected the articles, and drafted the manuscript. FC, ARB, LJ, SB, and AB revised the manuscript. All authors revised the manuscript for intellectual content.

FUNDING

This work was supported by a grant from Queensland University of Technology to FC, ARB and LJ.

REFERENCES

Abraham, W. C., Mason, S. E., Demmer, J., Williams, J. M., Richardson, C. L., Tate, W. P., et al. (1993). Correlations between immediate early gene induction and the persistence of long-term potentiation. *Neuroscience* 56, 717–727. doi: 10.1016/0306-4522(93)90369-q

Amorapanth, P., Nader, K., and LeDoux, J. E. (1999). Lesions of periaqueductal gray dissociate-conditioned freezing from conditioned suppression behavior in rats. *Learn. Mem.* 6, 491–499. doi: 10.1101/lm.6.5.491

Barnes, D. C., Chapuis, J., Chaudhury, D., and Wilson, D. A. (2011). Odor fear conditioning modifies piriform cortex local field potentials both during conditioning and during post-conditioning sleep. *PLoS One* 6:e18130. doi: 10.1371/journal.pone.0018130

Bergstrom, H. C., and Johnson, L. R. (2014). An organization of visual and auditory fear conditioning in the lateral amygdala. *Neurobiol. Learn. Mem.* 116, 1–13. doi: 10.1016/j.nlm.2014.07.008

Bergstrom, H. C., Mcdonald, C. G., Dey, S., Fernandez, G. M., and Johnson, L. R. (2013). Neurons activated during fear memory consolidation and reconsolidation are mapped to a common and new topography in the lateral amygdala. *Brain Topogr.* 26, 468–478. doi: 10.1007/s10548-012-0266-6

Biffo, S., Verdun Di Cantogno, L., and Fasolo, A. (1992). Double labeling with non-isotopic in situ hybridization and BrdU immunohistochemistry: calmodulin (CaM) mRNA expression in post-mitotic neurons of the olfactory system. *J. Histochem. Cytochem.* 40, 535–540. doi: 10.1177/40.4.1552187

Bolles, R. C., and Collier, A. C. (1976). The effect of predictive cues on freezing in rats. *Anim. Learn. Behav.* 4, 6–8. doi: 10.3758/bf03211975

Bonzano, S., Bovetti, S., Gendusa, C., Peretto, P., and De Marchis, S. (2016). Adult born olfactory bulb dopaminergic interneurons: molecular determinants and experience-dependent plasticity. *Front. Neurosci.* 10:189. doi: 10.3389/fnins.2016.00189

Bouton, M. E. (2004). Context and behavioral processes in extinction. *Learn. Mem.* 11, 485–494. doi: 10.1101/lm.78804

Buck, L. B. (1996). Information coding in the mammalian olfactory system. *Cold Spring Harb. Symp. Quant. Biol.* 61, 147–155. doi: 10.1101/SQB.1996.061.01.017

Campeau, S., and Davis, M. (1995). Involvement of subcortical and cortical afferents to the lateral nucleus of the amygdala in fear conditioning measured with fear-potentiated startle in rats trained concurrently with auditory and visual conditioned stimuli. *J. Neurosci.* 15, 2312–2327. doi: 10.1523/jneurosci.15-03-02312.1995

Cann, A., and Ross, D. A. (1989). Olfactory stimuli as context cues in human memory. *Am. J. Psychol.* 102, 91–102. doi: 10.2307/1423118

Chaaya, N., Battle, A. R., and Johnson, L. R. (2018). An update on contextual fear memory mechanisms: transition between Amygdala and Hippocampus. *Neurosci. Biobehav. Rev.* 92, 43–54. doi: 10.1016/j.neubiorev.2018.05.013

Chehrehasa, F., Meedeniya, A. C., Dwyer, P., Abrahamsen, G., and Mackay-Sim, A. (2009). EdU, a new thymidine analogue for labelling proliferating cells in the nervous system. *J. Neurosci. Methods* 177, 122–130. doi: 10.1016/j.jneumeth.2008.10.006

Chehrehasa, F., St. John, J., and Key, B. (2005). The sorting behaviour of olfactory and vomeronasal axons during regeneration. *J. Mol. Histol.* 36, 427–436. doi: 10.1007/s10735-006-9015-z

Chehrehasa, F., Windus, L. C., Ekberg, J. A., Scott, S. E., Amaya, D., Mackay-Sim, A., et al. (2010). Olfactory glia enhance neonatal axon regeneration. *Mol. Cell. Neurosci.* 45, 277–288. doi: 10.1016/j.mcn.2010.07.002

Chen, C. F., Barnes, D. C., and Wilson, D. A. (2011). Generalized vs. stimulus-specific learned fear differentially modifies stimulus encoding in primary sensory cortex of awake rats. *J. Neurophysiol.* 106, 3136–3144. doi: 10.1152/jn.00721.2011

Chu, S., and Downes, J. J. (2000). Odour-evoked autobiographical memories: psychological investigations of proustian phenomena. *Chem. Senses* 25, 111–116. doi: 10.1093/chemse/25.1.111

Ciocchi, S., Herry, C., Grenier, F., Wolff, S. B., Letzkus, J. J., Vlachos, I., et al. (2010). Encoding of conditioned fear in central amygdala inhibitory circuits. *Nature* 468, 277–282. doi: 10.1038/nature09559

Cortese, B. M., Leslie, K., and Uhde, T. W. (2015). Differential odor sensitivity in PTSD: implications for treatment and future research. *J. Affect. Disord.* 179, 23–30. doi: 10.1016/j.jad.2015.03.026

Cousens, G., and Otto, T. (1998). Both pre- and posttraining excitotoxic lesions of the basolateral amygdala abolish the expression of olfactory and contextual fear conditioning. *Behav. Neurosci.* 112, 1092–1103. doi: 10.1037/0735-7044.112.5.1092

Daldrup, T., Remmes, J., Lesting, J., Gaburro, S., Fendt, M., Meuth, P., et al. (2015). Expression of freezing and fear-potentiated startle during sustained fear in mice. *Genes Brain Behav.* 14, 281–291. doi: 10.1111/gbb.12211

Davis, M. (1992). The role of the amygdala in fear-potentiated startle: implications for animal models of anxiety. *Trends Pharmacol. Sci.* 13, 35–41. doi: 10.1016/0165-6147(92)90014-w

Dayer, A. G., Ford, A. A., Cleaver, K. M., Yassaee, M., and Cameron, H. A. (2003). Short-term and long-term survival of new neurons in the rat dentate gyrus. *J. Comp. Neurol.* 460, 563–572. doi: 10.1002/cne.10675

De La Rosa-Prieto, C., De Moya-Pinilla, M., Saiz-Sanchez, D., Ubeda-Banon, I., Arzate, D. M., Flores-Cuadrado, A., et al. (2015). Olfactory and cortical projections to bulbar and hippocampal adult-born neurons. *Front. Neuroanat.* 9:4. doi: 10.3389/fnana.2015.00004

de la Rosa-Prieto, C., Ubeda-Banon, I., Mohedano-Moriano, A., Pro-Sistiaga, P., Saiz-Sanchez, D., Insausti, R., et al. (2009). Subicular and CA1 hippocampal projections to the accessory olfactory bulb. *Hippocampus* 19, 124–129. doi: 10.1002/hipo.20495

Delgado, M. R., Olsson, A., and Phelps, E. A. (2006). Extending animal models of fear conditioning to humans. *Biol. Psychol.* 73, 39–48. doi: 10.1016/j.biopsycho.2006.01.006

Devor, M. (1976). Fiber trajectories of olfactory bulb efferents in the hamster. *J. Comp. Neurol.* 166, 31–47. doi: 10.1002/cne.901660104

Eichenbaum, H., Yonelinas, A. P., and Ranganath, C. (2007). The medial temporal lobe and recognition memory. *Annu. Rev. Neurosci.* 30, 123–152. doi: 10.1146/annurev.neuro.30.051606.094328

Eisthen, H. L. (1997). Evolution of vertebrate olfactory systems. *Brain Behav. Evol.* 50, 222–233. doi: 10.1159/000113336

Engen, T., and Ross, B. M. (1973). Long-term memory of odors with and without verbal descriptions. *J. Exp. Psychol.* 100, 221–227. doi: 10.1037/h0035492

Fanselow, M. S. (2000). Contextual fear, gestalt memories, and the hippocampus. *Behav. Brain Res.* 110, 73–81. doi: 10.1016/s0166-4328(99)00186-2

Fletcher, M. L. (2012). Olfactory aversive conditioning alters olfactory bulb mitral/tufted cell glomerular odor responses. *Front. Syst. Neurosci.* 6:16. doi: 10.3389/fnsys.2012.00016

Gheusi, G., and Lledo, P. M. (2014). Adult neurogenesis in the olfactory system shapes odor memory and perception. *Prog. Brain Res.* 208, 157–175. doi: 10.1016/b978-0-444-63350-7.00006-1

Goswami, S., Rodriguez-Sierra, O., Cascardi, M., and Pare, D. (2013). Animal models of post-traumatic stress disorder: face validity. *Front. Neurosci.* 7:89. doi: 10.3389/fnins.2013.00089

Haberly, L. B. (1973). Summed potentials evoked in opossum prepyriform cortex. *J. Neurophysiol.* 36, 775–788. doi: 10.1152/jn.1973.36.4.775

Haberly, L. B. (2001). Parallel-distributed processing in olfactory cortex: new insights from morphological and physiological analysis of neuronal circuitry. *Chem. Senses* 26, 551–576. doi: 10.1093/chemse/26.5.551

Han, Y., Luo, Y., Sun, J., Ding, Z., Liu, J., Yan, W., et al. (2016). AMPK signaling in the dorsal hippocampus negatively regulates contextual fear memory formation. *Neuropsychopharmacology* 41, 1849–1864. doi: 10.1038/npp.2015.355

Henkin, R. I., Comiter, H., Fedio, P., and O'Doherty, D. (1977). Defects in taste and smell recognition following temporal lobectomy. *Trans. Am. Neurol. Assoc.* 102, 146–150.

Herrick, C. J. (1921). The connections of the vomeronasal nerve, accessory olfactory bulb and amygdala in amphibia. *J. Comp. Neurol.* 33, 213–280. doi: 10.1002/cne.900330303

Hersman, S., Cushman, J., Lemelson, N., Wassum, K., Lotfipour, S., and Fanselow, M. S. (2017). Optogenetic excitation of cholinergic inputs to hippocampus primes future contextual fear associations. *Sci. Rep.* 7:2333. doi: 10.1038/s41598-017-02542-1

Herz, R. S. (1997a). The effects of cue distinctiveness on odor-based context-dependent memory. *Mem. Cognit.* 25, 375–380. doi: 10.3758/bf03211293

Herz, R. S. (1997b). Emotion experienced during encoding enhances odor retrieval cue effectiveness. *Am. J. Psychol.* 110, 489–505. doi: 10.2307/1423407

Herz, R. S. (1998). Are odors the best cues to memory? A cross-modal comparison of associative memory stimuli. *Ann. N Y Acad. Sci.* 855, 670–674. doi: 10.1111/j.1749-6632.1998.tb10643.x

Herz, R. S., and Cupchik, G. C. (1995). The emotional distinctiveness of odor-evoked memories. *Chem. Senses* 20, 517–528. doi: 10.1093/chemse/20.5.517

Hitchcock, J. M., Sananes, C. B., and Davis, M. (1989). Sensitization of the startle reflex by footshock: blockade by lesions of the central nucleus of the amygdala or its efferent pathway to the brainstem. *Behav. Neurosci.* 103, 509–518. doi: 10.1037//0735-7044.103.3.509

Howard, J. D., Plailly, J., Grueschow, M., Haynes, J. D., and Gottfried, J. A. (2009). Odor quality coding and categorization in human posterior piriform cortex. *Nat. Neurosci.* 12, 932–938. doi: 10.1038/nn.2324

Huhman, K. L. (2006). Social conflict models: can they inform us about human psychopathology? *Horm. Behav.* 50, 640–646. doi: 10.1016/j.yhbeh.2006.06.022

Illig, K. R., and Wilson, D. A. (2009). "Olfactory cortex: comparative anatomy A2—squire, larry R," in *Encyclopedia of Neuroscience*, (Oxford: Academic Press), 101–106.

Iwai, N., Zhou, Z., Roop, D. R., and Behringer, R. R. (2008). Horizontal basal cells are multipotent progenitors in normal and injured adult olfactory epithelium. *Stem Cells* 26, 1298–1306. doi: 10.1634/stemcells.2007-0891

Jaako-Movits, K., and Zharkovsky, A. (2005). Impaired fear memory and decreased hippocampal neurogenesis following olfactory bulbectomy in rats. *Eur. J. Neurosci.* 22, 2871–2878. doi: 10.1111/j.1460-9568.2005.04481.x

Johnson, L. R., Mcguire, J., Lazarus, R., and Palmer, A. A. (2012). Pavlovian fear memory circuits and phenotype models of PTSD. *Neuropharmacology* 62, 638–646. doi: 10.1016/j.neuropharm.2011.07.004

Kass, M. D., Rosenthal, M. C., Pottackal, J., and Mcgann, J. P. (2013). Fear learning enhances neural responses to threat-predictive sensory stimuli. *Science* 342, 1389–1392. doi: 10.1126/science.1244916

Keifer, O. P. Jr., Hurt, R. C., Ressler, K. J., and Marvar, P. J. (2015). The physiology of fear: reconceptualizing the role of the central amygdala in fear learning. *Physiol.* 30, 389–401. doi: 10.1152/physiol.00058.2014

Kempermann, G., Gast, D., Kronenberg, G., Yamaguchi, M., and Gage, F. H. (2003). Early determination and long-term persistence of adult-generated new neurons in the hippocampus of mice. *Development* 130, 391–399. doi: 10.1242/dev.00203

Keshavarzi, S., Power, J. M., Albers, E. H., Sullivan, R. K., and Sah, P. (2015). Dendritic organization of olfactory inputs to medial amygdala neurons. *J. Neurosci.* 35, 13020–13028. doi: 10.1523/jneurosci.0627-15.2015

Kilpatrick, L., and Cahill, L. (2003). Modulation of memory consolidation for olfactory learning by reversible inactivation of the basolateral amygdala. *Behav. Neurosci.* 117, 184–188. doi: 10.1037/0735-7044.117.1.184

Knapska, E., Macias, M., Mikosz, M., Nowak, A., Owczarek, D., Wawrzyniak, M., et al. (2012). Functional anatomy of neural circuits regulating fear and extinction. *Proc. Natl. Acad. Sci. U S A* 109, 17093–17098. doi: 10.1073/pnas.1202087109

Kondziella, D., Strandberg, J., Lindquist, C., and Asztely, F. (2011). Lamotrigine increases the number of BrdU-labeled cells in the rat hippocampus. *Neuroreport* 22, 97–100. doi: 10.1097/wnr.0b013e328342d2fa

LeDoux, J. E. (1995). Emotion: clues from the brain. *Annu. Rev. Psychol.* 46, 209–235. doi: 10.1146/annurev.ps.46.020195.001233

LeDoux, J. E., Iwata, J., Pearl, D., and Reis, D. J. (1986). Disruption of auditory but not visual learning by destruction of intrinsic neurons in the rat medial geniculate-body. *Brain Res.* 371, 395–399. doi: 10.1016/0006-8993(86)90383-5

Lee, J. L., Dickinson, A., and Everitt, B. J. (2005). Conditioned suppression and freezing as measures of aversive Pavlovian conditioning: effects of discrete amygdala lesions and overtraining. *Behav. Brain Res.* 159, 221–233. doi: 10.1016/j.bbr.2004.11.003

Liu, X., Ramirez, S., Pang, P. T., Puryear, C. B., Govindarajan, A., Deisseroth, K., et al. (2012). Optogenetic stimulation of a hippocampal engram activates fear memory recall. *Nature* 484, 381–385. doi: 10.1038/nature11028

Lledo, P. M., Gheusi, G., and Vincent, J. D. (2005). Information processing in the mammalian olfactory system. *Physiol. Rev.* 85, 281–317. doi: 10.1152/physrev.00008.2004

Lledo, P. M., Merkle, F. T., and Alvarez-Buylla, A. (2008). Origin and function of olfactory bulb interneuron diversity. *Trends Neurosci.* 31, 392–400. doi: 10.1016/j.tins.2008.05.006

Luchkina, N. V., and Bolshakov, V. Y. (2018). Diminishing fear: optogenetic approach toward understanding neural circuits of fear control. *Pharmacol. Biochem. Behav.* 174, 64–79. doi: 10.1016/j.pbb.2017.05.005

Mackay-Sim, A., and Kittel, P. W. (1991). On the life span of olfactory receptor neurons. *Eur. J. Neurosci.* 3, 209–215. doi: 10.1111/j.1460-9568.1991.tb00081.x

Mainland, J. D., Keller, A., Li, Y. R., Zhou, T., Trimmer, C., Snyder, L. L., et al. (2014). The missense of smell: functional variability in the human odorant receptor repertoire. *Nat. Neurosci.* 17, 114–120. doi: 10.1038/nn.3598

Maren, S. (2014). Fear of the unexpected: hippocampus mediates novelty-induced return of extinguished fear in rats. *Neurobiol. Learn. Mem.* 108, 88–95. doi: 10.1016/j.nlm.2013.06.004

Maren, S., Anagnostaras, S. G., and Fanselow, M. S. (1998). The startled seahorse: is the hippocampus necessary for contextual fear conditioning? *Trends Cogn. Sci.* 2, 39–42. doi: 10.1016/s1364-6613(98)01123-1

Maren, S., and Fanselow, M. S. (1996). The amygdala and fear conditioning: has the nut been cracked? *Neuron* 16, 237–240. doi: 10.1016/s0896-6273(00)80041-0

Maren, S., and Fanselow, M. S. (1997). Electrolytic lesions of the fimbria/fornix, dorsal hippocampus, or entorhinal cortex produce anterograde deficits in contextual fear conditioning in rats. *Neurobiol. Learn. Mem.* 67, 142–149. doi: 10.1006/nlme.1996.3752

McGuire, J., Herman, J. P., Horn, P. S., Sallee, F. R., and Sah, R. (2010). Enhanced fear recall and emotional arousal in rats recovering from chronic variable stress. *Physiol. Behav.* 101, 474–482. doi: 10.1016/j.physbeh.2010.07.013

Meissner-Bernard, C., Dembitskaya, Y., Venance, L., and Fleischmann, A. (2019). Encoding of odor fear memories in the mouse olfactory cortex. *Curr. Biol.* 29, 367.e4–380.e4. doi: 10.1016/j.cub.2018.12.003

Milad, M. R., Wright, C. I., Orr, S. P., Pitman, R. K., Quirk, G. J., and Rauch, S. L. (2007). Recall of fear extinction in humans activates the ventromedial prefrontal cortex and hippocampus in concert. *Biol. Psychiatry* 62, 446–454. doi: 10.1016/j.biopsych.2006.10.011

Miles, A. N., and Berntsen, D. (2011). Odour-induced mental time travel into the past and future: do odour cues retain a unique link to our distant past? *Memory* 19, 930–940. doi: 10.1080/09658211.2011.613847

Mohedano-Moriano, A., De La Rosa-Prieto, C., Saiz-Sanchez, D., Ubeda-Banon, I., Pro-Sistiaga, P., De Moya-Pinilla, M., et al. (2012). Centrifugal telencephalic afferent connections to the main and accessory olfactory bulbs. *Front. Neuroanat.* 6:19. doi: 10.3389/fnana.2012.00019

Moore, N. L. T., Gauchan, S., and Genovese, R. F. (2012). Differential severity of anxiogenic effects resulting from a brief swim or underwater trauma in adolescent male rats. *Pharmacol. Biochem. Behav.* 102, 264–268. doi: 10.1016/j.pbb.2012.05.002

Moreno, M. M., Linster, C., Escanilla, O., Sacquet, J., Didier, A., and Mandairon, N. (2009). Olfactory perceptual learning requires adult neurogenesis. *Proc. Natl. Acad. Sci. U S A* 106, 17980–17985. doi: 10.1073/pnas.0907063106

Mori, K., Takahashi, Y. K., Igarashi, K. M., and Yamaguchi, M. (2006). Maps of odorant molecular features in the Mammalian olfactory bulb. *Physiol. Rev.* 86, 409–433. doi: 10.1152/physrev.00021.2005

Morrison, F. G., Dias, B. G., and Ressler, K. J. (2015). Extinction reverses olfactory fear-conditioned increases in neuron number and glomerular size. *Proc. Natl. Acad. Sci. U S A* 112, 12846–12851. doi: 10.1073/pnas.1505068112

Muñoz-Abellán, C., Daviu, N., Rabasa, C., Nadal, R., and Armario, A. (2009). Cat odor causes long-lasting contextual fear conditioning and increased pituitary-adrenal activation, without modifying anxiety. *Horm. Behav.* 56, 465–471. doi: 10.1016/j.yhbeh.2009.08.002

Nigri, A., Ferraro, S., D'Incerti, L., Critchley, H. D., Bruzzone, M. G., and Minati, L. (2013). Connectivity of the amygdala, piriform, and orbitofrontal cortex during olfactory stimulation: a functional MRI study. *Neuroreport* 24, 171–175. doi: 10.1097/wnr.0b013e32835d5d2b

Nissant, A., Bardy, C., Katagiri, H., Murray, K., and Lledo, P. M. (2009). Adult neurogenesis promotes synaptic plasticity in the olfactory bulb. *Nat. Neurosci.* 12, 728–730. doi: 10.1038/nn.2298

Otto, T., Cousens, G., and Herzog, C. (2000). Behavioral and neuropsychological foundations of olfactory fear conditioning. *Behav. Brain Res.* 110, 119–128. doi: 10.1016/s0166-4328(99)00190-4

Otto, T., and Giardino, N. D. (2001). Pavlovian conditioning of emotional responses to olfactory and contextual stimuli: a potential model for the development and expression of chemical intolerance. *Ann. N Y Acad. Sci.* 933, 291–309. doi: 10.1111/j.1749-6632.2001.tb05832.x

Parma, V., Ferraro, S., Miller, S. S., Ahs, F., and Lundström, J. N. (2015). Enhancement of odor sensitivity following repeated odor and visual fear conditioning. *Chem. Senses* 40, 497–506. doi: 10.1093/chemse/bjv033

Pavlov, I. P. (1927). *Conditioned Reflexes: An Investigation of the Physiological Activity of the Cerebral Cortex.* Oxford: Oxford University Press.

Pifferi, S., Menini, A., and Kurahashi, T. (2010). "Signal transduction in vertebrate olfactory cilia," in *The Neurobiology of Olfaction*, ed. A. Menini (Boca Raton, FL: CRC Press/Taylor and Francis), 203–224.

Pikkarainen, M., Rönkkö, S., Savander, V., Insausti, R., and Pitkänen, A. (1999). Projections from the lateral, basal, and accessory basal nuclei of the amygdala to the hippocampal formation in rat. *J. Comp. Neurol.* 403, 229–260. doi: 10.1002/(sici)1096-9861(19990111)403:2<229::aid-cne7>3.3.co;2-g

Proust, M. (1976). Letters of proust, marcel to baron lumbroso, albert and benda, julien. *Nouv. Rev. Fr.* 286, 57–62.

Quirk, G. J., Likhtik, E., Pelletier, J. G., and Paré, D. (2003). Stimulation of medial prefrontal cortex decreases the responsiveness of central amygdala

output neurons. *J. Neurosci.* 23, 8800–8807. doi: 10.1523/JNEUROSCI.23-25-08800.2003

Rennaker, R. L., Chen, C. F., Ruyle, A. M., Sloan, A. M., and Wilson, D. A. (2007). Spatial and temporal distribution of odorant-evoked activity in the piriform cortex. *J. Neurosci.* 27, 1534–1542. doi: 10.1523/JNEUROSCI.4072-06.2007

Ressler, K. J., Sullivan, S. L., and Buck, L. B. (1994). Information coding in the olfactory system: evidence for a stereotyped and highly organized epitope map in the olfactory bulb. *Cell* 79, 1245–1255. doi: 10.1016/0092-8674(94)90015-9

Rochefort, C., Gheusi, G., Vincent, J. D., and Lledo, P. M. (2002). Enriched odor exposure increases the number of newborn neurons in the adult olfactory bulb and improves odor memory. *J. Neurosci.* 22, 2679–2689. doi: 10.1523/JNEUROSCI.22-07-02679.2002

Romanski, L. M., Giguere, M., Bates, J. F., and Goldman-Rakic, P. S. (1997). Topographic organization of medial pulvinar connections with the prefrontal cortex in the rhesus monkey. *J. Comp. Neurol.* 379, 313–332. doi: 10.1002/(sici)1096-9861(19970317)379:3<313::aid-cne1>3.3.co;2-7

Rosenkranz, J. A., and Grace, A. A. (2002). Dopamine-mediated modulation of odour-evoked amygdala potentials during pavlovian conditioning. *Nature* 417, 282–287. doi: 10.1038/417282a

Ross, J. M., and Fletcher, M. L. (2018). Learning-dependent and -independent enhancement of mitral/tufted cell glomerular odor responses following olfactory fear conditioning in awake mice. *J. Neurosci.* 38, 4623–4640. doi: 10.1523/JNEUROSCI.3559-17.2018

Russo, A. S., and Parsons, R. G. (2017). Acoustic startle response in rats predicts inter-individual variation in fear extinction. *Neurobiol. Learn. Mem.* 139, 157–164. doi: 10.1016/j.nlm.2017.01.008

Saavedra-Rodríguez, L., and Feig, L. A. (2013). Chronic social instability induces anxiety and defective social interactions across generations. *Biol. Psychiatry* 73, 44–53. doi: 10.1016/j.biopsych.2012.06.035

Sadgrove, M. P., Laskowski, A., and Gray, W. P. (2006). Examination of granule layer cell count, cell density, and single-pulse BrdU incorporation in rat organotypic hippocampal slice cultures with respect to culture medium, septotemporal position, and time *in vitro*. *J. Comp. Neurol.* 497, 397–415. doi: 10.1002/cne.21000

Sahay, A., Wilson, D. A., and Hen, R. (2011). Pattern separation: a common function for new neurons in hippocampus and olfactory bulb. *Neuron* 70, 582–588. doi: 10.1016/j.neuron.2011.05.012

Sakamoto, M., Ieki, N., Miyoshi, G., Mochimaru, D., Miyachi, H., Imura, T., et al. (2014). Continuous postnatal neurogenesis contributes to formation of the olfactory bulb neural circuits and flexible olfactory associative learning. *J. Neurosci.* 34, 5788–5799. doi: 10.1523/JNEUROSCI.0674-14.2014

Salic, A., and Mitchison, T. J. (2008). A chemical method for fast and sensitive detection of DNA synthesis *in vivo*. *Proc. Natl. Acad. Sci. U S A* 105, 2415–2420. doi: 10.1073/pnas.0712168105

Sananes, C. B., and Campbell, B. A. (1989). Role of the central nucleus of the amygdala in olfactory heart rate conditioning. *Behav. Neurosci.* 103, 519–525. doi: 10.1037/0735-7044.103.3.519

Saxe, M. D., Battaglia, F., Wang, J. W., Malleret, G., David, D. J., Monckton, J. E., et al. (2006). Ablation of hippocampal neurogenesis impairs contextual fear conditioning and synaptic plasticity in the dentate gyrus. *Proc. Natl. Acad. Sci. U S A* 103, 17501–17506. doi: 10.1073/pnas.0607207103

Schab, F. R. (1990). Odors and the remembrance of things past. *J. Exp. Psychol. Learn. Mem. Cogn.* 16, 648–655. doi: 10.1037/0278-7393.16.4.648

Schettino, L. F., and Otto, T. (2001). Patterns of Fos expression in the amygdala and ventral perirhinal cortex induced by training in an olfactory fear conditioning paradigm. *Behav. Neurosci.* 115, 1257–1272. doi: 10.1037/0735-7044.115.6.1257

Schmidt, S. D., Furini, C. R. G., Zinn, C. G., Cavalcante, L. E., Ferreira, F. F., Behling, J. A. K., et al. (2017). Modulation of the consolidation and reconsolidation of fear memory by three different serotonin receptors in hippocampus. *Neurobiol. Learn. Mem.* 142, 48–54. doi: 10.1016/j.nlm.2016.12.017

Scott, J. W., McBride, R. L., and Schneider, S. P. (1980). The organization of projections from the olfactory bulb to the piriform cortex and olfactory tubercle in the rat. *J. Comp. Neurol.* 194, 519–534. doi: 10.1002/cne.901940304

Sevelinges, Y., Gervais, R., Messaoudi, B., Granjon, L., and Mouly, A. M. (2004). Olfactory fear conditioning induces field potential potentiation in rat olfactory cortex and amygdala. *Learn. Mem.* 11, 761–769. doi: 10.1101/lm.83604

Sevelinges, Y., Moriceau, S., Holman, P., Miner, C., Muzny, K., Gervais, R., et al. (2007). Enduring effects of infant memories: infant odor-shock conditioning attenuates amygdala activity and adult fear conditioning. *Biol. Psychiatry* 62, 1070–1079. doi: 10.1016/j.biopsych.2007.04.025

Sharp, F. R., Kauer, J. S., and Shepherd, G. M. (1977). Laminar analysis of 2-deoxyglucose uptake in olfactory bulb and olfactory cortex of rabbit and rat. *J. Neurophysiol.* 40, 800–813. doi: 10.1152/jn.1977.40.4.800

Shepherd, G. M. (2010). "New perspectives on olfactory processing and human smell," in *The Neurobiology of Olfaction*, ed. A. Menini (Boca Raton, FL: CRC Press), 395–403.

Smith, D. G., Standing, L., and de Man, A. (1992). Verbal memory elicited by ambient odor. *Percept. Mot. Skills* 74, 339–343. doi: 10.2466/pms.74.2.339-343

So, K., Moriya, T., Nishitani, S., Takahashi, H., and Shinohara, K. (2008). The olfactory conditioning in the early postnatal period stimulated neural stem/progenitor cells in the subventricular zone and increased neurogenesis in the olfactory bulb of rats. *Neuroscience* 151, 120–128. doi: 10.1016/j.neuroscience.2007.07.051

Stettler, D. D., and Axel, R. (2009). Representations of odor in the piriform cortex. *Neuron* 63, 854–864. doi: 10.1016/j.neuron.2009.09.005

Stevens, C. F. (1969). Structure of cat frontal olfactory cortex. *J. Neurophysiol.* 32, 184–192. doi: 10.1152/jn.1969.32.2.184

Sultan, S., Mandairon, N., Kermen, F., Garcia, S., Sacquet, J., and Didier, A. (2010). Learning-dependent neurogenesis in the olfactory bulb determines long-term olfactory memory. *FASEB J.* 24, 2355–2363. doi: 10.1096/fj.09-151456

Toffolo, M. B., Smeets, M. A., and van den Hout, M. A. (2012). Proust revisited: odours as triggers of aversive memories. *Cogn. Emot.* 26, 83–92. doi: 10.1080/02699931.2011.555475

Valley, M., Mullen, T., Schultz, L., Sagdullaev, B., and Firestein, S. (2009). Ablation of mouse adult neurogenesis alters olfactory bulb structure and olfactory fear conditioning. *Front. Neurosci.* 3:51. doi: 10.3389/neuro.22.003.2009

Vanelzakker, M. B., Dahlgren, M. K., Davis, F. C., Dubois, S., and Shin, L. M. (2014). From Pavlov to PTSD: the extinction of conditioned fear in rodents, humans, and anxiety disorders. *Neurobiol. Learn. Mem.* 113, 3–18. doi: 10.1016/j.nlm.2013.11.014

Vyas, A., Mitra, R., Rao, B. S. S., and Chattarji, S. (2002). Chronic stress induces contrasting patterns of dendritic remodeling in hippocampal and amygdaloid neurons. *J. Neurosci.* 22, 6810–6818. doi: 10.1523/JNEUROSCI.22-15-06810.2002

Walker, D. L., Paschall, G. Y., and Davis, M. (2005). Glutamate receptor antagonist infusions into the basolateral and medial amygdala reveal differential contributions to olfactory vs. context fear conditioning and expression. *Learn. Mem.* 12, 120–129. doi: 10.1101/lm.87105

Wang, D., Noda, Y., Tsunekawa, H., Zhou, Y., Miyazaki, M., Senzaki, K., et al. (2007). Behavioural and neurochemical features of olfactory bulbectomized rats resembling depression with comorbid anxiety. *Behav. Brain Res.* 178, 262–273. doi: 10.1016/j.bbr.2007.01.003

Wesson, D. W., and Wilson, D. A. (2011). Sniffing out the contributions of the olfactory tubercle to the sense of smell: hedonics, sensory integration, and more? *Neurosci. Biobehav. Rev.* 35, 655–668. doi: 10.1016/j.neubiorev.2010.08.004

West, S. E., and Doty, R. L. (1995). Influence of epilepsy and temporal lobe resection on olfactory function. *Epilepsia* 36, 531–542. doi: 10.1111/j.1528-1157.1995.tb02565.x

Willander, J., and Larsson, M. (2006). Smell your way back to childhood: autobiographical odor memory. *Psychon. Bull. Rev.* 13, 240–244. doi: 10.3758/bf03193837

Wilson, D. A. (1998). Synaptic correlates of odor habituation in the rat anterior piriform cortex. *J. Neurophysiol.* 80, 998–1001. doi: 10.1152/jn.1998.80.2.998

Wilson, D. A. (2000). Comparison of odor receptive field plasticity in the rat olfactory bulb and anterior piriform cortex. *J. Neurophysiol.* 84, 3036–3042. doi: 10.1152/jn.2000.84.6.3036

Wilson, D. A. (2003). Rapid, experience-induced enhancement in odorant discrimination by anterior piriform cortex neurons. *J. Neurophysiol.* 90, 65–72. doi: 10.1152/jn.00133.2003

Wiltgen, B. J., Sanders, M. J., Anagnostaras, S. G., Sage, J. R., and Fanselow, M. S. (2006). Context fear learning in the absence of the hippocampus. *J. Neurosci.* 26, 5484–5491. doi: 10.1523/JNEUROSCI.2685-05.2006

Woolsey, T. A., and Van der Loos, H. (1970). The structural organization of layer IV in the somatosensory region (SI) of mouse cerebral cortex. The description of a cortical field composed of discrete cytoarchitectonic units. *Brain Res.* 17, 205–242. doi: 10.1016/0006-8993(70)90079-x

Zelikowsky, M., Hersman, S., Chawla, M. K., Barnes, C. A., and Fanselow, M. S. (2014). Neuronal ensembles in amygdala, hippocampus, and prefrontal cortex track differential components of contextual fear. *J. Neurosci.* 34, 8462–8466. doi: 10.1523/JNEUROSCI.3624-13.2014

Zoladz, P. R., Fleshner, M., and Diamond, D. M. (2012). Psychosocial animal model of PTSD produces a long-lasting traumatic memory, an increase in general anxiety and PTSD-like glucocorticoid abnormalities. *Psychoneuroendocrinology* 37, 1531–1545. doi: 10.1016/j.psyneuen.2012.02.007

Conflict of Interest: The authors declare that the research was conducted in the absence of any commercial or financial relationships that could be construed as a potential conflict of interest.

Copyright © 2019 Hakim, Battle, Belmer, Bartlett, Johnson and Chehrehasa. This is an open-access article distributed under the terms of the Creative Commons Attribution License (CC BY). The use, distribution or reproduction in other forums is permitted, provided the original author(s) and the copyright owner(s) are credited and that the original publication in this journal is cited, in accordance with accepted academic practice. No use, distribution or reproduction is permitted which does not comply with these terms.

frontiers in Molecular Neuroscience

ORIGINAL RESEARCH
published: 27 September 2019
doi: 10.3389/fnmol.2019.00231

Developmental Expression of Mutant PFN1 in Motor Neurons Impacts Neuronal Growth and Motor Performance of Young and Adult Mice

Merryn Brettle[1,2], Holly Stefen[3], Aleksandra Djordjevic[1], Sandra Y. Y. Fok[1,2], Josephine W. Chan[1], Annika van Hummel[3], Julia van der Hoven[3], Magdalena Przybyla[3], Alexander Volkerling[1], Yazi D. Ke[3], Fabien Delerue[3], Lars M. Ittner[3†] and Thomas Fath[1,3†]*

[1]School of Medical Sciences, Faculty of Medicine, UNSW Sydney, Randwick, NSW, Australia, [2]Biomedical Imaging Facility, Mark Wainwright Analytical Centre, UNSW Sydney, Randwick, NSW, Australia, [3]Dementia Research Centre and Department of Biomedical Sciences, Faculty of Medicine and Health Sciences, Macquarie University, Sydney, NSW, Australia

OPEN ACCESS

Edited by:
Robert J. Harvey,
University of the Sunshine Coast, Australia

Reviewed by:
Bradley Turner,
Florey Institute of Neuroscience and Mental Health, Australia
Alexandre Henriques,
Neuro-Sys, France

***Correspondence:**
Thomas Fath
thomas.fath@mq.edu.edu

[†]These authors share senior authorship

Received: 17 June 2019
Accepted: 10 September 2019
Published: 27 September 2019

Citation:
Brettle M, Stefen H, Djordjevic A, Fok SYY, Chan JW, van Hummel A, van der Hoven J, Przybyla M, Volkerling A, Ke YD, Delerue F, Ittner LM and Fath T (2019) Developmental Expression of Mutant PFN1 in Motor Neurons Impacts Neuronal Growth and Motor Performance of Young and Adult Mice. Front. Mol. Neurosci. 12:231. doi: 10.3389/fnmol.2019.00231

Amyotrophic lateral sclerosis (ALS) is a devastating neurodegenerative disease with limited treatment and no cure. Mutations in *profilin 1* were identified as a cause of familial ALS (fALS) in 2012. We investigated the functional impact of mutant profilin 1 expression in spinal cords during mouse development. We developed a novel mouse model with the expression of profilin 1 C71G under the control of the *Hb9* promoter, targeting expression to α-motor neurons in the spinal cord during development. Embryos of transgenic mice showed evidence of a significant reduction of brachial nerve diameter and a loss of Mendelian inheritance. Despite the lack of transgene expression, adult mice presented with significant motor deficits. Transgenic mice had a significant reduction in the number of motor neurons in the spinal cord. Further analysis of these motor neurons in aged transgenic mice revealed reduced levels of TDP-43 and ChAT expression. Although profilin 1 C71G was only expressed during development, adult mice presented with some ALS-associated pathology and motor symptoms. This study highlights the effect of profilin 1 during neurodevelopment and the impact that this may have in later ALS.

Keywords: profilin 1, amyotrophic lateral sclerosis, actin, neurodegeneration, motor neurons

INTRODUCTION

Amyotrophic lateral sclerosis (ALS) is the most common form of motor neuron disease. The disease is characterized by progressive neurodegeneration, causing paralysis and death (Gordon, 2013). Approximately 10% of cases are familial with an average age of onset 10 years earlier than sporadic ALS (sALS; Chiò et al., 2009). Despite this difference in age of onset, familial ALS (fALS) and sALS present with clinically comparable features

(Neumann et al., 2006; Swarup et al., 2011; Renton et al., 2014). Mutations in the profilin 1-encoding *PFN1* gene were identified as a rare cause of ALS in 2012 (Wu et al., 2012). The study by Wu et al. (2012) identified four mutations in the *PFN1* gene; C71G, M114T, E117G and G118V. Subsequent studies have identified additional mutations in both sALS and fALS including A20T, T109M, Q139L and R136W (Chen et al., 2013; Ingre et al., 2013; Smith et al., 2015; Yang et al., 2016). PFN1 is historically known as an actin-binding protein (Witke et al., 1998). However, more recent studies have highlighted the importance of PFN1 as a potential regulator in the dynamics of both actin and microtubules (Nejedla et al., 2016; Henty-Ridilla et al., 2017).

The complexity of ALS is highlighted by the number of genes that have been directly implicated in cases of fALS. To date, mutations in 30 genes have been identified as a cause of fALS, including mutations in the *SOD1* and *TARDBP* genes, with some mutations more common than others (Rosen et al., 1993; Sreedharan et al., 2008; Leblond et al., 2014; Renton et al., 2014; Chia et al., 2018). Although mutations in *PFN1* are the etiological cause of less than 1% of fALS, understanding the role of PFN1 in disease has the potential to inform about the pathogenesis of sALS and assist in therapy development. It is currently unknown how mutations in a variety of functionally different genes can all converge to cause ALS.

PFN1 is an actin-binding protein with ubiquitous expression (Kwiatkowski and Bruns, 1988). PFN1 mediates the exchange between ADP-actin and ATP-actin, therefore enhancing actin filament extension (Mockrin and Korn, 1980; Wen et al., 2008). The regulation of PFN1 expression is important, as at high cellular concentrations, PFN1 can inhibit actin filament extension (Courtemanche and Pollard, 2013). PFN1 also controls filamentous actin by regulating the localization of actin monomers (Vitriol and Zheng, 2012; Lee et al., 2013). In addition to its traditional role in actin dynamics, PFN1 has been shown to impact on microtubule dynamics, hence forming a regulatory link between the complex interplay of the two major cytoskeletal systems (Nejedla et al., 2016; Henty-Ridilla et al., 2017; Dogterom and Koenderink, 2019). To date, two mouse models, expressing ALS-associated PFN1 mutations have been reported (Yang et al., 2016; Fil et al., 2017). Both studies detail mouse models that exhibit classical ALS phenotypes of progressive motor deficits, resulting in paralysis and a significant impact on survival. Yang et al. (2016) presented a triple transgenic *Thy1.2* PFN1$^{C71G/C71G}$/Prp PFN1^{C71G} mouse with an aggressive ALS phenotype. They utilized the *Thy1.2* promoter and prion promoter to drive pan-neuronal and ubiquitous expression of PFN1^{C71G} (Yang et al., 2016). The second mouse model used a prion promoter for the expression of PFN1^{G118V} (Fil et al., 2017). Both studies produced control mice overexpressing PFN1^{WT} and observed no significant changes between PFN1^{WT} and control mice (Yang et al., 2016; Fil et al., 2017). To this end, however, it remains unclear what effects of mutant PFN1 on α-motor neuron dysfunction can be attributed to its expression during development vs. those effects resulting from its disrupted function in mature neurons later in life.

Changes to α-motor neuron morphology and electrophysiology occur much earlier in ALS pathology than previously thought, as does α-motor neuron death (Avossa et al., 2006; Martin et al., 2013; Vinsant et al., 2013a,b). This indicates that morphological alterations during neurodevelopment may impact the electrophysiological properties of developing α-motor neurons and potentially prime them for an early neuronal death. Here, we have utilized an α-motor neuron-specific *Hb9* promoter to drive PFN1^{C71G} expression only during development (Arber et al., 1999). Driving the transgene expression with the *Hb9* promoter controls not only the spatial but also the temporal localization of the transgene. The temporally restricted expression of the mutant PFN1 in our mouse model allows us to interrogate whether there is a contribution of the early expression of mutant PFN1 to ALS disease pathology. We characterized PFN1 expression in the novel mouse model and studied the impact on neurodevelopment. We hypothesized that changes during development could lead to morphological changes in the spinal cord of adult mice, resulting in functional changes. To investigate this, we performed motor testing of both young and aged transgenic mice. Finally, we studied the molecular consequence of PFN1^{C71G} expression by looking for evidence of ALS pathology in the spinal cords of aged mice.

MATERIALS AND METHODS

Animals

All animal procedures were conducted in accordance with the Animal Care and Ethics Committee of UNSW Sydney. Mice were housed on a 12 h light/dark cycle. V5-hPFN1^{C71G} was cloned into the *Pme*I and *Spe*I sites of the p*Hb9*-MCS-IRES-EGFP plasmid (*mHb9* promoter) [TJ#103], which was a kind gift from Thomas Jessell (Addgene plasmid #16283; Wilson et al., 2005). A fragment, containing the *mHb9* promoter, the sequence for V5-hPFN1^{C71G}, and an IRES site followed by the sequence for EGFP was used for the generation of the *Hb9* V5-PFN1^{C71G} transgenic mouse line. The transgenic mice were generated on a C57Bl/6 background by pronuclear injection (Ittner and Gotz, 2007; Delerue and Ittner, 2017).

For the analysis of motor performance, C57Bl/6 Wild type (Wt) littermates were used as controls. Rotarod performance was analyzed as previously described (Ke et al., 2015). An acceleration mode was used with the speed increasing from 7 to 60 rpm over a 120 s period on a 5-wheel Rotarod treadmill (Ugo Basile). Latency to fall was measured and recorded. Each mouse was given four attempts and the best attempt was recorded. Forelimb grip strength was measured with a grip strength meter (Ametek). Each mouse was given five attempts and the highest peak force (N) exerted was recorded (Ittner et al., 2016). The hanging wire test was used as previously described (van Hummel et al., 2018). For this, mice completed two trials and the best performance was recorded.

Any deaths of *Hb9* V5-PFN1^{C71G} mice were recorded with the date and cause of death. If the condition of mice deteriorated, the

mice were euthanized, in accordance with ethics approval from the Animal Care and Ethics Committee at UNSW Sydney. Mice that were euthanized, or that were found dead in their cages, were included in the analysis of survival data.

Immunohistochemistry

For the collection of embryos, C57Bl/6 females were bred with *Hb9* V5-PFN1^{C71G} $^{Wt/Tg}$ males, using a timed mating protocol, where the time of plug check was considered to be E0.5. Pregnant females were euthanized by cervical dislocation at the appropriate timepoint. Embryos were harvested and immersion fixed in ice-cold 4% paraformaldehyde (PFA) for 90–120 min. Adult mice were anesthetized and transcardially perfused with ice-cold 1× phosphate-buffered saline (PBS). Brains were collected and fixed overnight in 4% PFA at 4°C.

The tissues were processed with an ethanol and xylene gradient in an Excelsior tissue processor (Thermo). Whole embryos were embedded in paraffin blocks. Spinal cords were cut into 2 mm segments and embedded into paraffin blocks with cervical to sacral sections arranged in a grid-like pattern. Samples were sectioned with a 5 μm thickness on a microtome (Leica). Sections were rehydrated and stained as previously described (Ittner et al., 2016). Antibodies used in this study were: anti-ChAT (Millipore), anti-profilin 1 (Abcam), anti-tau1 (Millipore), anti-TDP-43 (Proteintech) and anti-V5 (Invitrogen, Carlsbad, CA, USA).

Wholemount Staining and Lightsheet Microscopy

Embryos were collected as above and stained as previously described (Wurdak et al., 2005). Embryos were mounted in low melting temperature agarose (Sigma-Aldrich, St. Louis, MO, USA). Prior to imaging, embryos were cleared in CUBIC reagent 2 for 24 h with gentle agitation. The embryos were imaged on a Zeiss Lightsheet Z.1 microscope with a 5× clearing objective. The imaging chamber was filled with CUBIC reagent 2 to match the refractive index of the cleared specimen.

Image Collection and Analysis

Fluorescence imaging of sections was completed on either a BX51 (Olympus) or Axioskop 40 (Zeiss) epifluorescence microscope. Brightfield images were captured on a BX51 (Olympus) microscope with a white balance filter. All image analysis was performed with Fiji [(Fiji is just) ImageJ 2.0.0-rc-43/1.52d, National Institutes of Health; Schindelin et al., 2012]. Adobe Photoshop and Illustrator were used to prepare images and figures.

Analysis and Statistics

For behavioral tests, data were collected by staff, blinded to genotypes of experimental groups. Data were organized on Excel (Microsoft) and analyzed in GraphPad Prism software (version 6.0, Graphpad software). Normality of data was assessed using D'Agostino and Pearson omnibus normality test. Data with two groups that had Gaussian distribution was analyzed by student's *t*-tests and data with non-Gaussian distribution were analyzed by a Mann–Whitney test. Data with more than two groups and across multiple time points were analyzed with two-way analysis of variance (ANOVA). Mendelian inheritance was analyzed with Chi-squared analysis and the appropriate degree/s of freedom. Survival data were analyzed with a log-rank (Mantel-cox) test.

RESULTS

Hb9 V5-PFN1^{C71G} Transgenic Mice Express PFN1^{C71G} in the Spinal Cord Embryonic During Development

We generated a transgenic mouse line with a murine *Hb9* promoter to test whether early expression of mutant PFN1 in motor neurons has a detrimental effect on motor neuron development and function. *Hb9* is a homeobox gene that determines the fate of α-motor neurons, with expression switching on between embryonic day 9.5 (E9.5) and E10.5. Accordingly, the *Hb9* promoter restricts expression to α-motor neurons during specific developmental stages (Arber et al., 1999). We characterized the temporal expression of V5-PFN1^{C71G} in transgenic embryos. No staining was observed in Wt controls (**Figures 1A–C**) or in E9.5 transgenic embryos (data not shown). V5-positive staining is apparent in the basal plates of the spinal cords of E10.5, E12.5 and E14.5 transgenic embryos (**Figures 1D–F**). This is consistent with the published literature on the promoter activity (Arber et al., 1999). In P0 transgenic pups, expression of PFN1^{C71G} is lower than the expression in sections from transgenic embryos (**Supplementary Figure S1**). There is no expression of PFN1^{C71G} in the brain or spinal cords of adult *Hb9* V5-PFN1^{C71G} transgenic mice from 1 month to 18-month-old (**Supplementary Figure S1**).

We utilized Lightsheet imaging to characterize the spatial expression of EGFP (green) and V5 (red) in E10.5 transgenic embryos (**Figures 1G,H**). EGFP and V5-PFN1^{C71G} expression was observed throughout the length of the neural tube (arrows) and in the mid-hindbrain junction of the developing brain (arrowhead; **Figures 1G,H**). Expression of V5-PFN1^{C71G} appeared to extend further into the developing axons than EGFP (**Figures 1G,H**). This localization is consistent with the role of PFN1 in neurite extension.

To assess the level of PFN1^{C71G} expression, we analyzed PFN1 intensity in V5-positive tissue. Sections from E12.5 and E14.5 embryos were double immunolabeled for V5 (green) and PFN1 (red; **Figures 2A–L**). V5-positive regions of transgenic embryos showed a marked increase in PFN1 expression (**Figures 2A–L**). There was a significant increase in PFN1 intensity in V5-positive areas of neural tubes from transgenic mice when compared to PFN1 intensity in V5-negative areas of transgenic and Wt neural tubes (**Figures 2M,N**). The overexpression of PFN1^{C71G} resulted in a 2.11–2.25-fold increase in the total levels of PFN1 in the developing motor neurons of developing transgenic embryos.

Next, we confirmed that PFN1^{C71G} was being expressed in developing α-motor neurons. Sections from E12.5 and E14.5 embryos were double immunolabeled for V5 (green) and

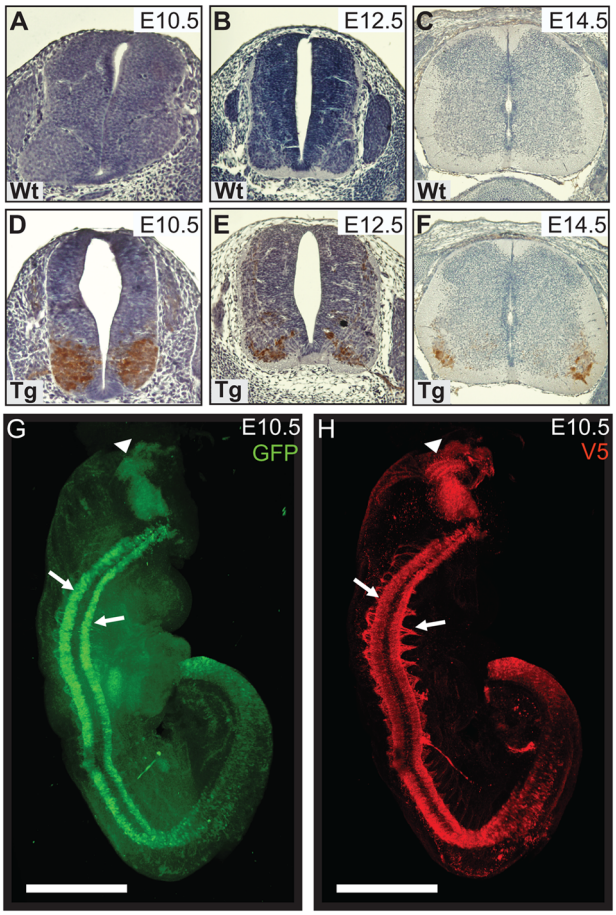

FIGURE 1 | Wild type control (Wt) and transgenic (Tg) tissues were stained for V5-DAB. Wt embryos have no expression of V5-PFN1^{C71G} **(A–C)**. V5-PFN1^{C71G} positive staining can be seen in the basal plate of the neural tube of Tg E10.5–14.5 embryos **(D–F)**. Whole E10.5 embryos were stained for GFP and V5-PFN1^{C71G} and imaged on a Zeiss Lightsheet Z.1 microscope. The rendered images show GFP (green) and V5 (red) expression in a Tg embryo **(G,H)**. V5-PFN1^{C71G} expression is present throughout the length of the neural tube in the lateral basal plates (arrows), in the axonal bundles extending from the neural tube, and in the mid-hindbrain junction of the developing brain (arrowhead). Scale bars = 500 μm.

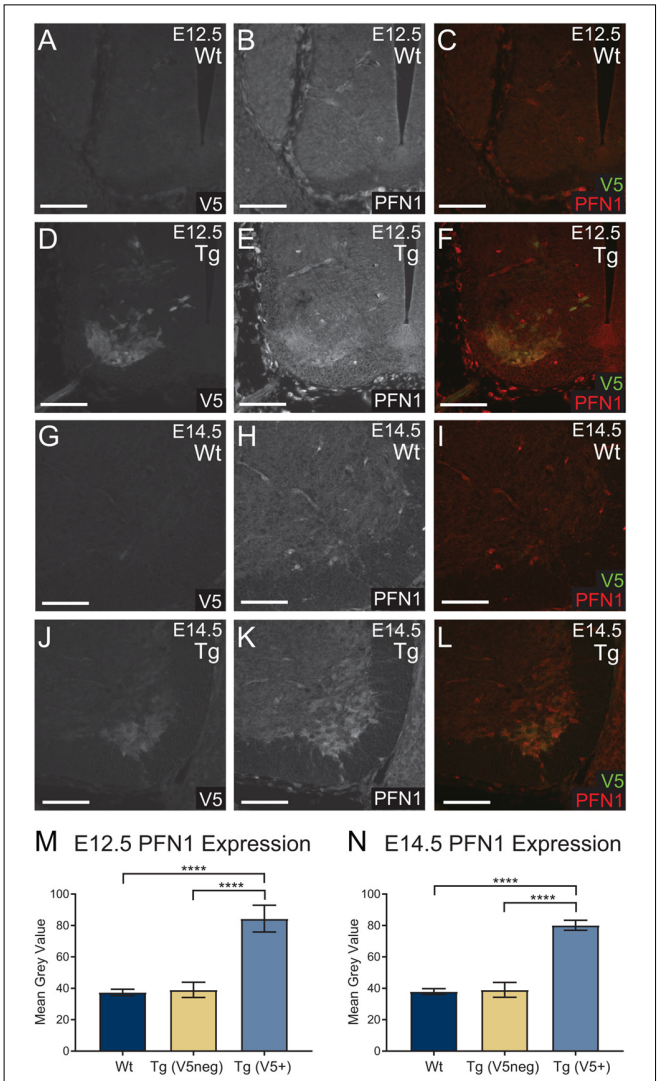

FIGURE 2 | Wild type control (Wt) and transgenic (Tg) sections were stained for V5 (green) and PFN1 (red). No V5 expression or PFN1 overexpression was detected in Wt embryos **(A–C,G–I)**. Sections from Tg E12.5 and E14.5 embryos had V5 expression and PFN1 overexpression in the anterior portion of the neural tube **(D–F,J–L)**. Analysis of Tg embryos was split into V5 negative and V5 positive areas. Tg E12.5 and E14.5 embryos had a significant increase of PFN1 in V5 positive areas when compared to V5 negative areas in Tg and Wt embryos **(M,N)**. Analyzed with one-way analysis of variance (ANOVA; **M,N**); $^{****}p \leq 0.0001$; graphed with SEM. Scale bars = 50 μm.

ChAT (red; **Figures 3A–L**). Staining showed that V5-positive neurons were also positive for ChAT in sections from transgenic embryos (**Figures 3A–L**). This confirmed that the expression of the transgene was in the correct neuronal subtype, developing motor neurons.

Developmental Expression of PFN1^{C71G} Reduces Brachial Nerve Diameter

Following the characterization of the transgene expression, we assessed the impact of PFN1^{C71G} expression on axonal outgrowth by analyzing brachial nerve diameter. Sections from E14.5 transgenic embryos were stained, using Tau1 antibody (axonal marker) to visualize developing axonal bundles. The shortest diameter was measured and analyzed. Transgenic animals had a significant reduction in brachial nerve diameter when compared to Wt controls (**Figures 4A–C**). Expression of PFN1^{C71G} in the developing α-motor neurons significantly impacted the formation of brachial nerves.

Developmental Expression of PFN1^{C71G} Impacts the Motor Performance, Transgene Penetrance and Survival of *Hb9* V5-PFN1^{C71G} Transgenic Mice

In order to understand the impact of PFN1^{C71G} during development, the *Hb9* V5-PFN1^{C71G} mouse line underwent

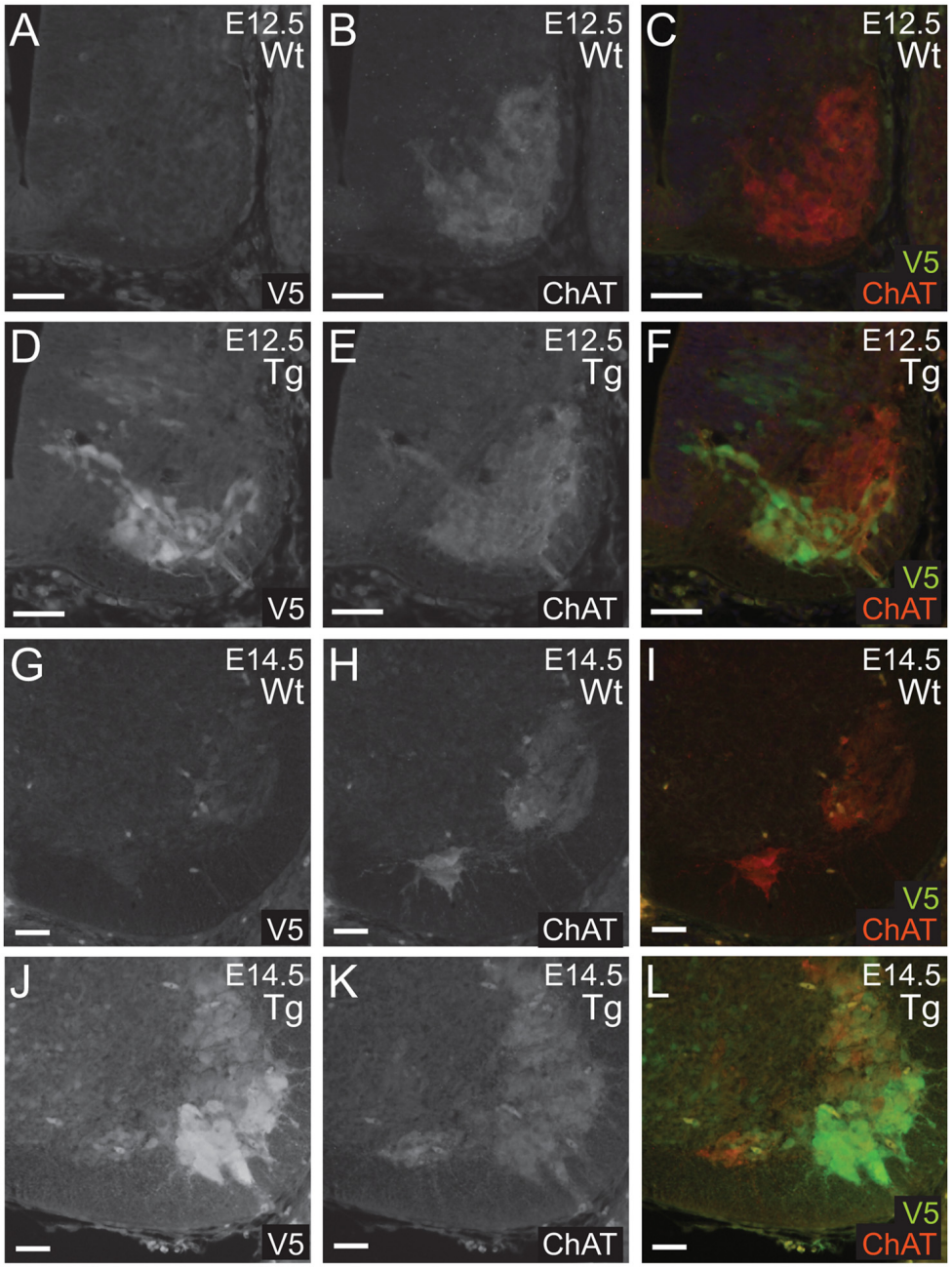

FIGURE 3 | Wild type control (Wt) and transgenic (Tg) sections were stained for V5 (green) and ChAT (red). ChAT expression was detected in Wt embryos **(A–C,G–I)**. Sections from E12.5 and E14.5 Tg embryos had V5 expression in ChAT positive areas of the anterior portion of the neural tube **(D–F,J–L)**. Scale bars = 50 μm.

postnatal motor testing. At 1 month and 3-month timepoints, both male and female transgenic mice weighed significantly less than the Wt controls (**Figures 5A–D**). When challenged on the accelerating Rotarod, 1-month and 3-month male transgenic mice fell from the treadmill significantly earlier than the Wt controls (**Figures 5E,F**). While 3-month-old female transgenic mice presented with a significant deficit on Rotarod when compared to Wt control, 1-month-old female transgenic mice had a fall latency that was comparable to Wt controls (**Figures 5G,H**). Expression of PFN1^{C71G} in developing α-motor neurons impacts the weight and motor performance of adult mice.

Over the course of the breeding program of *Hb9* V5-PFN1^{C71G} mice, we observed that the proportion of Wt controls and transgenic mice was not consistent with Mendelian inheritance. The breeding strategy should have yielded

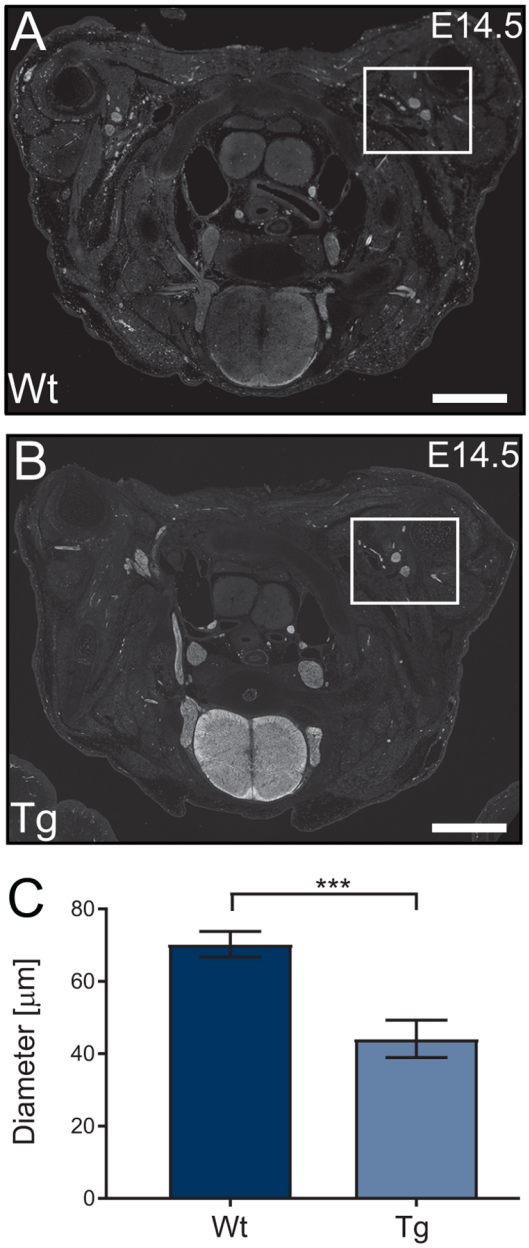

FIGURE 4 | Wild type control (Wt) and transgenic (Tg) sections from Wt and Tg embryos were stained with Tau1 **(A,B)** and the diameter of the brachial nerve bundles were analyzed. Analysis revealed that Tg animals had a reduction in the diameter of brachial nerves (**C**; $p = 0.0003$). $N = 4$ animals for each genotype. Analyzed with unpaired student *t*-test; $^{***}p \leq 0.001$; graphed with standard error of the mean (SEM). Scale bars = 500 μm.

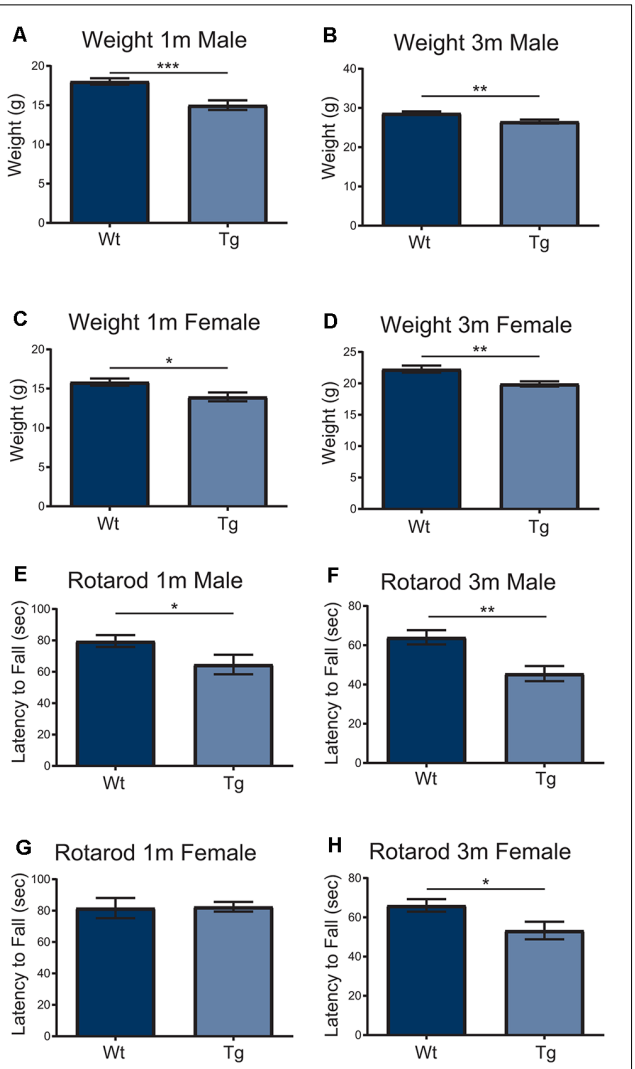

FIGURE 5 | Both male and female transgenic (Tg) mice aged 1–3-months weighed significantly less than Wild type (Wt) controls **(A–D)**. Mice were challenged with an accelerating RotaRod and male Tg animals had a significant decrease in latency to fall on RotaRod at 1-month and 3-months **(E,F)**. The performance of female Tg mice was comparable to Wt at 1-month-old **(G)** but presented with a significant decrease in latency to fall at 3-months-old **(H)**. Data were analyzed with unpaired student *t*-tests; $^{*}p \leq 0.05$; $^{**}p \leq 0.01$; $^{***}p \leq 0.001$; graphed with SEM. $N = 6$–26.

50% Wt controls and 50% transgenic mice. To assess this, we performed a chi-squared analysis on the proportion of mice with each genotype in both embryos and adult mice (**Figures 6A,B**). We found that the proportion of Wt controls and transgenic embryos fit within an expected Mendelian inheritance (**Figures 6A,B**). However, 65.9% of adult mice had a genotype of Wt control, with only 34.1% of adult mice with a transgenic genotype (**Figures 6A,B**). Therefore, expression of PFN1^{C71G} in developing α-motor neurons impacts Mendelian transgene inheritance of adult mice.

As mice were aged, additional weight and motor performance data were collected. Transgenic mice had a significantly decreased survival rate when compared with Wt controls (**Figure 7A**). From 6 m of age, an unusual split phenotype was revealed in both the weight and the motor performance of *Hb9* V5-PFN1^{C71G} transgenic mice. Transgenic mice older than 6 months separated into two significantly distinct weight groups; low weight and normal weight (**Figures 7B,C**). The low weight transgenic mice plateaued in weight from 6 months old, while the normal weight transgenic mice had weights

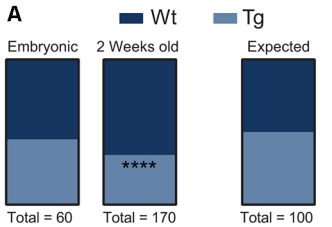

B

	Embryonic	2 Weeks old	Expected
Number of Wt	33	112	50
Number of Tg	27	58	50
Total	60	170	100
Chi-squared value	0.6	17.15	0
p value	0.439	<0.0001	1
Inheritance	Mendelian	Non-Mendelian	Mendelian

FIGURE 6 | *Hb9* V5-PFN1^{C71G} mouse embryos were genotyped at the time of harvest by polymerase chain reaction (PCR) and visualization of GFP in the neural tube. Postnatal mice were genotyped by PCR at 2 weeks old. Heterozygous *Hb9* V5-PFN1^{C71G} males were bred with C57Bl/6J females. The genotype of *Hb9* embryos fits the expected Mendelian inheritance pattern **(A)**. The mice in the mouse colony were genotyped at 2 weeks of age, and no longer fit with a Mendelian inheritance pattern **(B)**. ****$p < 0.0001$.

that were comparable to Wt controls (**Figures 7D–K**). When examining the Rotarod results of the two different phenotypes of transgenic mice another clear trend emerged. Surprisingly, only the normal weight transgenic mice showed significant motor deficits when compared to Wt controls and their low weight transgenic littermates (**Figures 7D–K**). Not all age groups showed significant differences, this is due to a reduction of power in the statistical tests due to the split phenotype. The split phenotype reduced the *n* number of transgenic mice for the analysis. Another confounding factor was the impact of transgene expression on the survival of *Hb9* V5-PFN1^{C71G} transgenic mice in both the low and normal weight group. Taken together these data show that expression of PFN1^{C71G} in developing α-motor neurons impacts the survival, weight and motor performance of aged mice.

Aged *Hb9* V5-PFN1^{C71G} Transgenic Mice Showed Evidence of Motor Neuron Loss and a Reduction of TDP-43 Expression in Motor Neurons

Hb9 V5-PFN1^{C71G} transgenic mice presented with significant motor deficits despite the lack of post-natal transgene expression. Next we analyzed the motor neurons in spinal cords to look for any molecular evidence of pathology. Spinal cords from 18-month-old mice were stained with ChAT (red; motor neuron marker) and TDP-43 (green), to assess motor neuron number and TDP-43 localization in motor neurons, respectively (**Figures 8A–F**). TDP-43 mis-localization is a key feature of ALS pathology (Tanaka et al., 2016; Fil et al., 2017). The number of ChAT positive motor neurons present in the cervical, thoracic and lumbar regions of spinal cords were analyzed in sections from 18-month-old mice. *Hb9* V5-PFN1^{C71G} transgenic mice had a significant reduction of motor neurons in all three regions when compared to Wt controls (**Figures 8G–I**). Analysis of the fluorescence intensity of ChAT in individual motor neurons revealed that 18-month-old old transgenic mice had a reduction in the levels of ChAT when compared to Wt controls (**Figures 8J,K**). The analysis of TDP-43 localization revealed that 18-month-old, normal weight male transgenic mice had a significant reduction in both cytoplasmic and nuclear levels of TDP-43 in motor neurons (**Figures 8K,L**). Aged *Hb9* V5-PFN1^{C71G} transgenic mice have some ALS-like features as they present with a reduced number of motor neurons and reduced ChAT staining intensity. They do not show evidence of a mis-localization of TDP-43 from the nucleus to the cytoplasm, instead, show a global reduction of TDP-43 in the nucleus and cytoplasm. Note that these changes in the spinal cord are present in 18-month-old transgenic mice, despite there being no transgene expression in adult mice.

DISCUSSION

The complex function of mutant PFN1 overexpression in neurons *in vitro* has previously been assessed, using cultured primary mouse hippocampal (Brettle et al., 2015) and motor neurons (Wu et al., 2012). Here, we specifically analyzed the impact of mutant PFN1 *in vivo* by α-motor neuron-specific expression of PFN1^{C71G}. We have shown that the expression of ALS-associated PFN1^{C71G} in developing α-motor neurons has a lasting impact on the health and motor performance of transgenic mice. These effects persist long after the transgene expression has ceased. We confirmed that the expression of PFN1^{C71G} was consistent with previous studies using the *Hb9* promoter (Arber et al., 1999; Detmer et al., 2008; McGovern et al., 2015). This expression was mostly restricted spatially to developing α-motor neurons, and temporally to embryonic and neonatal transgenic mice. Expression of PFN1^{C71G} was observed from E10.5 and had decreased by P0. By 1 m of age, no transgene expression was detected in the brain or spinal cord of transgenic mice. Although Hb9 has been found in a small subset of gamma-motor neurons and spinal motor neurons in adult mice (Vult von Steyern et al., 1999; Chang and Martin, 2011), we saw no evidence of this in our mouse line. Transgene expression was not present in all ChAT positive motor neurons in transgenic embryos. This is consistent with other transgenic mouse lines that have pan-neuronal expression (van Hummel et al., 2018). This confirms that the phenotypes present in the *Hb9* V5-PFN1^{C71G} transgenic mice are a direct result of the developmental and neonatal expression of the ALS-associated PFN1 mutant.

PFN1 knock-out mice are embryonically lethal, this is likely due to the important role that PFN1 plays in cell division and

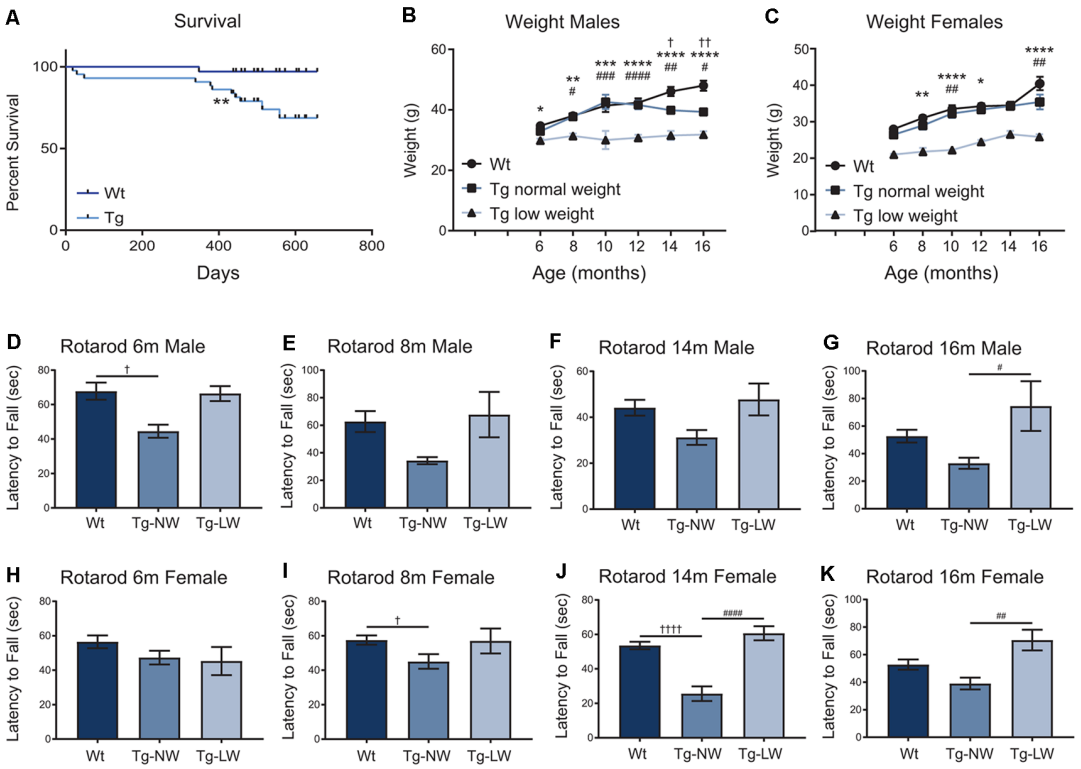

FIGURE 7 | The survival of transgenic (Tg) mice was significantly impacted when compared to Wt controls **(A)**. In animals older than 6 months, transgenic (Tg) mice separated into two groups; low weight (Tg-LW) and normal weight (Tg-NW; **B,C**). *Denotes a difference between Tg-LW and Wt, #denotes a difference between Tg-LW and Tg-NW, †denotes difference between Tg-NW and Wt. Weight data were analyzed with two-way ANOVA; Rotarod data were analyzed with one-way ANOVA **(D–K)**; Survival data were analyzed with a Log rank test; $^{*}p \leq 0.05$; $^{**}p \leq 0.01$; $^{***}p \leq 0.001$, $^{****}p \leq 0.0001$; $^{\#}p \leq 0.05$; $^{\#\#}p \leq 0.01$; $^{\#\#\#}p \leq 0.001$, $^{\#\#\#\#}p \leq 0.0001$; $^{\dagger}p \leq 0.05$; $^{\dagger\dagger}p \leq 0.01$; $^{\dagger\dagger\dagger\dagger}p \leq 0.0001$; graphed with SEM. *N* = 3–21.

migration (Witke et al., 2001; Kullmann et al., 2012, 2015). We showed that the expression of PFN1^{C71G} in developing motor neurons leads to the reduced diameter of brachial nerves in transgenic E14.5 embryos. This finding is consistent with *in vitro* reports that axonal outgrowth is reduced in cultured primary motor neurons, expressing PFN1^{C71G} (Wu et al., 2012). Axonal outgrowth is a dynamic process, for which PFN1 plays a key role. PFN1 localizes to the leading edge of growth cones, where it recruits actin monomers (Lee et al., 2013). Combined with the pivotal role that PFN1 plays in controlling the dynamics of actin and microtubules (Nejedla et al., 2016; Henty-Ridilla et al., 2017), we suggest that mutant PFN1^{C71G} has a loss of function in developing motor neurons. The synthetic PFN1^{H120E} mutant cannot bind to actin and reduces the recruitment of actin monomers to neuronal growth cones (Lee et al., 2013). If the PFN1^{C71G} also has a reduced capacity to recruit actin monomers to growth cones, this would be consistent with a loss of function hypothesis. The regulation of developmental nerves is an actin-dependent process. This is highlighted in a conditional knock-out of Rac1 in motor or sensory neurons. Rac1 knock-out in these neurons resulted in significantly thinner axonal bundles in fore and hind limbs (Hua et al., 2015). Rac1 and CDC42 are both Rho GTPases that are involved in actin dynamics and axonal outgrowth (Causeret et al., 2004; Schulz et al., 2016). An actin-deficient mutant of PFN1 suppressed CDC-42-dependent microspike formation and Rac1-dependent membrane ruffling (Suetsugu et al., 1998). We suggest that future studies focus on dissecting the impact that PFN1^{C71G} has at the growth cone with respect to the dynamics of actin and microtubules. Additionally, future studies should examine the impact of C71G mutation on the functional relationship between PFN1 and Rho GTPases.

Adult *Hb9* V5-PFN1^{C71G} transgenic mice presented with several distinct phenotypes. *Hb9* V5-PFN1^{C71G} mice have a Mendelian inheritance at embryonic stages, but not at the time of genotyping at 2 weeks old. We hypothesize that this is due to neonatal mortality, but further longitudinal studies would be needed to substantiate this. Weight and motor phenotypes were also identified. *Hb9* V5-PFN1^{C71G} transgenic mice weighed significantly less than the Wt controls at 1-month and 3-months. However, after 6 months of age, transgenic mice presented with a split weight phenotype consisting of a low weight and a normal weight group. The split weight phenotype could also be due to a metabolic change in the Hb9 V5-PFN1^{C71G} transgenic mice. Hb9 is expressed in the adult pancreas and knockout of Hb9 results in a reduction of the number of insulin-producing cells (Mu et al., 2016). This is particularly intriguing, given that diabetic gerbils have increased levels of PFN1 in liver tissue

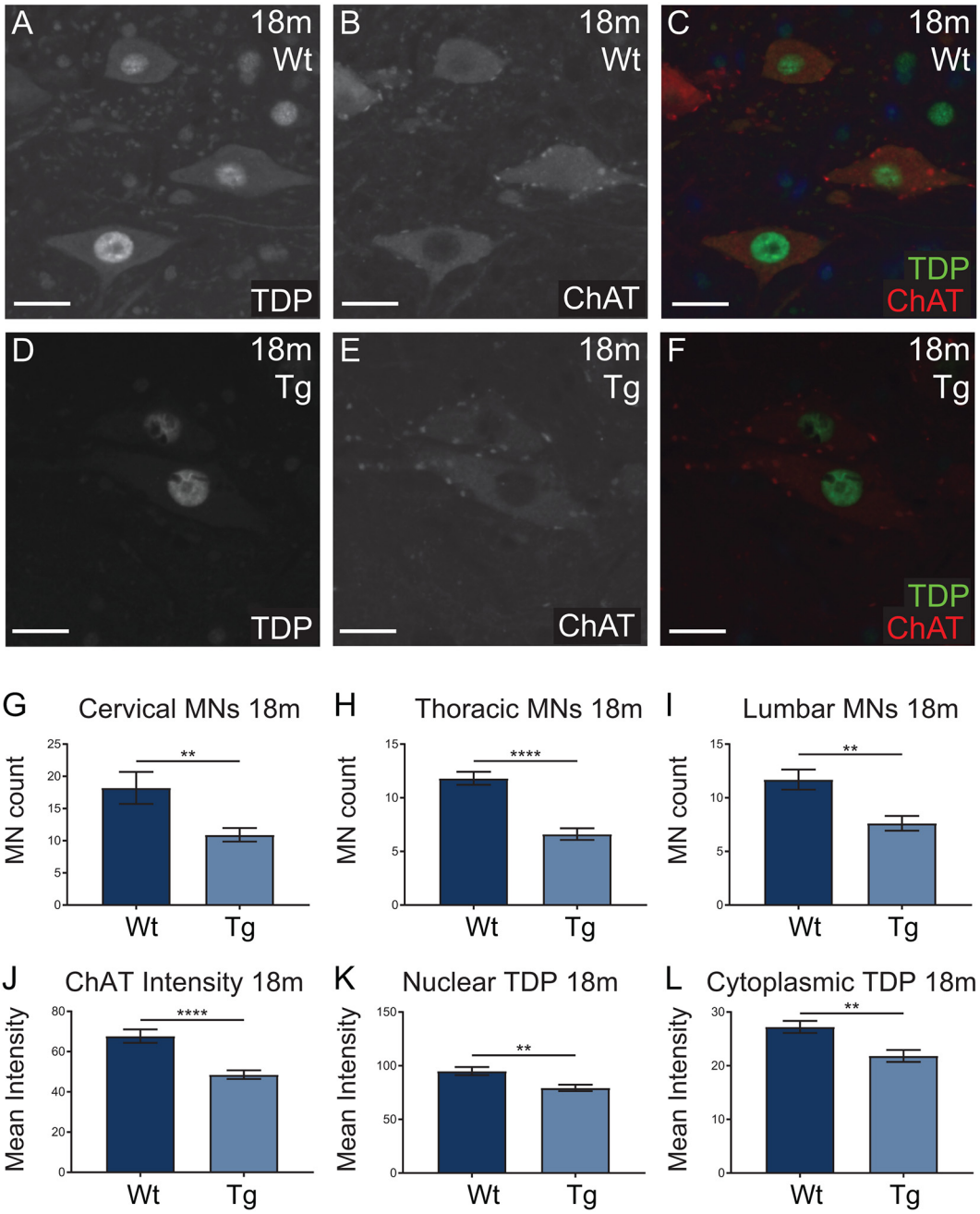

FIGURE 8 | Wild type (Wt) controls and transgenic (Tg) sections from 18-month-old *Hb9* V5-PFN1^{C71G} mice were stained for ChAT (red) and TDP-43 (green; **A–F**). Scale bars = 20 μm. At 18-month-old, Tg mice had significantly fewer motor neurons per ventral horn of the spinal cord when compared to Wt controls **(G–I)**. This was consistent across the cervical, thoracic and lumbar regions of the spinal cord **(G–I)**. The motor neurons of Tg mice had significantly lower levels of ChAT intensity when compared with Wt controls **(J)**. At 18 months, Tg mice had significantly lower levels of nuclear and cytoplasmic TDP-43 in motor neurons **(K,L)**. Data were analyzed with unpaired student *t*-test; $^{**}p \leq 0.01$, $^{****}p \leq 0.0001$; graphed with SEM. *N* = 3–5 mice, 11–41 sections or 81–97 cells.

(Gong et al., 2018). Future studies characterizing the metabolic phenotype of the Hb9 V5-PFN1^{C71G} mice may provide further information about the role of PFN1 in the pancreas.

The 1-month and 3-month-old male transgenic mice and 3-month-old female transgenic mice presented with significant motor deficits when challenged on an accelerating Rotarod. From 6 months of age, normal weight transgenic mice presented with significant deficits when compared to Wt controls, but this was not consistent. In contrast to the normal weight transgenic group, the low weight transgenic mice that were older than 6 months did not present with significant motor deficits. The low weight transgenic mice were comparable to

the Wt controls. A confounding factor is the reduction of the power of the statistical tests due to the split phenotype of the mice. Another factor was the reduction of mouse numbers over time, due to the reduced survival of *Hb9* V5-PFN1^{C71G} transgenic mice. Although young transgenic mice presented with motor deficits consistent with other ALS mouse models (Yang et al., 2016; van Hummel et al., 2018), the aged transgenic mice presented with a split motor phenotype which has not been previously reported. The split weight phenotype could be masking the motor phenotype in the low weight mice. Due to the relationship between motor performance and weight, lower weight mice would be predicted to perform better on Rotarod than heavier mice (Mao et al., 2015). The split weight phenotype could also indicate that the metabolic state of the transgenic mice is altered. A high body mass index has been implicated as a risk factor for ALS. Patient weight loss and hypermetabolism are associated with a decreased survival (Peter et al., 2017; Steyn et al., 2018). This, combined with the impact of animal weight on Rotarod performance, may contribute to the significant decrease in survival of low weight mice, despite the lack of an overt motor deficit. The expression of PFN1^{C71G} in developing motor neurons is sufficient to have a lasting impact on motor performance of *Hb9* V5-PFN1^{C71G} transgenic mice. However, this does not result in a full ALS phenotype.

The spinal cord analysis from aged 18-month-old transgenic mice revealed evidence of ALS-like pathology. There was a significant reduction in the number of ChAT-positive motor neurons throughout the spinal cords of 18-month-old transgenic mice. Furthermore, the levels of ChAT expression and global levels of TDP-43 expression were significantly reduced when compared to Wt controls. A reduction of ChAT expression is a hallmark of ALS and can be indicative of a loss of neuromuscular junctions (Casas et al., 2013; Fil et al., 2017). The reduction of ChAT expression in aged transgenic mice, combined with the reduced diameter of brachial nerve in transgenic embryos indicates that due to alterations in neuronal outgrowth, the circuitry of *Hb9* V5-PFN1^{C71G} transgenic mice may be irreparably altered. Although no cytoplasmic inclusions of TDP-43 were found in aged *Hb9* V5-PFN1^{C71G} transgenic mice, the reduction of TDP-43 expression levels in both the cytoplasm and nucleus of the motor neurons could impair the function of TDP-43. This reduction of TDP-43 could be due to several reasons, including increased clearance of TDP-43 or a downregulation of TDP-43 translation (Ke et al., 2015). The homozygous knock-out of TDP-43 is embryonically lethal and heterozygous knock-out mice with TDP-43 protein reduction have significant motor deficits (Kraemer et al., 2010). The downregulation of TDP-43 can induce neuronal death (Igaz et al., 2011). Taken together, the reduction of TDP-43 and ChAT levels is evidence of pathology in the aged *Hb9* V5-PFN1^{C71G} transgenic mice. This pathology is present despite no PFN1^{C71G} expression being present in adult *Hb9* V5-PFN1^{C71G} transgenic mice. Impaired neuronal health can lead to the reduction of neuromuscular junctions and eventually cell death. Aged transgenic mice presented with a significant reduction of motor neurons, supporting this possibility. Future studies should focus on the molecular cause of reduced TDP-43 in the aged *Hb9* V5-PFN1^{C71G} transgenic mice. This could be an important pathomechanism that links PFN1 mutations to other etiological causes of fALS.

The *Hb9* V5 PFN1^{C71G} transgenic mice differ in their phenotype from other *in vivo* models of ALS-associated PFN1 mutants (Yang et al., 2016; Fil et al., 2017). Although the motor deficits in young *Hb9* V5 PFN1^{C71G} transgenic mice emulated the motor deficits presented by Yang et al. (2016), our model did not progress to complete paralysis in aged mice. Furthermore, the model from Fil et al. (2017) showed cytoplasmic TDP-43 in α-motor neurons of transgenic mice, whereas aged *Hb9* V5 PFN1^{C71G} transgenic mice presented with an overall reduction of TDP-43. This finding further supports the link between PFN1 mutants and TDP-43 pathology, as our findings show that TDP-43 expression can be impacted in motor neurons long after transgene expression has ceased. This model of developmental expression of PFN1^{C71G} in motor neurons highlights the importance of PFN1 in development and in the pathogenesis of ALS.

The *Hb9* V5-PFN1^{C71G} transgenic mouse model shows a developmental phenotype that in part emulates existing *in vitro* and *in vivo* studies on PFN1^{C71G}. Although additional studies are necessary to dissect the precise molecular mechanisms responsible for this developmental phenotype, the lasting impact of this phenotype impacts adult transgenic mice. Studies elaborating on the points of divergence in this complex profile of the *Hb9* V5-PFN1^{C71G} transgenic mouse model would aid in the understanding of ALS pathogenesis.

DATA AVAILABILITY STATEMENT

All datasets generated for this study are included in the manuscript/**Supplementary Files**.

ETHICS STATEMENT

The animal study was reviewed and approved by University of New South Wales Animal Care and Ethics Committee.

AUTHOR CONTRIBUTIONS

TF, MB and LI designed the study. MB, HS, AD, SF, JC, AH, JH, MP and AV performed the experiments. MB analyzed all data. MB and TF wrote the manuscript. LI, YK and HS edited the manuscript. All coauthors read and confirmed the final manuscript. FD carried out the pronuclear injection for the generation of the mouse line. TF, YK and LI obtained funding. TF and LI supervised the project.

FUNDING

This work was supported by a Research Grant from the Motor Neuron Disease Research Institute Australia (LI and TF) and funding from the National Health and Medical Research Council

(NHMRC) to TF, YK and LI (#1083209, #1132524, #1143848). YK is a NHMRC Career Development Fellow (#1123564). LI is a NHMRC Principal Research Fellow (#1136241).

ACKNOWLEDGMENTS

We thank the staff at the Biological Resources Centre for the use of the facility. We wish to thank the National Imaging Facility for the use of the magnetic resonance imaging equipment. The imaging component of this study was carried out using instruments situated in, and maintained by, the Biomedical Imaging Facility (BMIF) at UNSW.

SUPPLEMENTARY MATERIAL

The Supplementary Material for this article can be found online at: https://www.frontiersin.org/articles/10.3389/fnmol.2019.00231/full#supplementary-material

REFERENCES

Arber, S., Han, B., Mendelsohn, M., Smith, M., Jessell, T. M., and Sockanathan, S. (1999). Requirement for the homeobox gene Hb9 in the consolidation of motor neuron identity. *Neuron* 23, 659–674. doi: 10.1016/s0896-6273(01)80026-x

Avossa, D., Grandolfo, M., Mazzarol, F., Zatta, M., and Ballerini, L. (2006). Early signs of motoneuron vulnerability in a disease model system: characterization of transverse slice cultures of spinal cord isolated from embryonic ALS mice. *Neuroscience* 138, 1179–1194. doi: 10.1016/j.neuroscience.2005.12.009

Brettle, M., Suchowerska, A. K., Chua, S. W., Ittner, L. M., and Fath, T. (2015). Amyotrophic lateral sclerosis-associated mutant profilin 1 increases dendritic arborisation and spine formation in primary hippocampal neurons. *Neurosci. Lett.* 609, 223–228. doi: 10.1016/j.neulet.2015.09.034

Casas, C., Herrando-Grabulosa, M., Manzano, R., Mancuso, R., Osta, R., and Navarro, X. (2013). Early presymptomatic cholinergic dysfunction in a murine model of amyotrophic lateral sclerosis. *Brain Behav.* 3, 145–158. doi: 10.1002/brb3.104

Causeret, F., Hidalgo-Sanchez, M., Fort, P., Backer, S., Popoff, M.-R., Gauthier-Rouvi, C., et al. (2004). Distinct roles of Rac1/Cdc42 and Rho/Rock for axon outgrowth and nucleokinesis of precerebellar neurons toward netrin 1. *Development* 131, 2841–2852. doi: 10.1242/dev.01162

Chang, Q., and Martin, L. J. (2011). Glycine receptor channels in spinal motoneurons are abnormal in a transgenic mouse model of amyotrophic lateral sclerosis. *J. Neurosci.* 31, 2815–2827. doi: 10.1523/jneurosci.2475-10.2011

Chen, Y., Zheng, Z. Z., Huang, R., Chen, K., Song, W., Zhao, B., et al. (2013). PFN1 mutations are rare in Han Chinese populations with amyotrophic lateral sclerosis. *Neurobiol. Aging* 34, 1922.e1–1922.e5. doi: 10.1016/j.neurobiolaging.2013.01.013

Chia, R., Chiò, A., and Traynor, B. J. (2018). Novel genes associated with amyotrophic lateral sclerosis: diagnostic and clinical implications. *Lancet Neurol.* 17, 94–102. doi: 10.1016/s1474-4422(17)30401-5

Chiò, A., Logroscino, G., Hardiman, O., Swingler, R., Mitchell, D., Beghi, E., et al. (2009). Prognostic factors in ALS: a critical review. *Amyotroph Lateral Scler.* 10, 310–323. doi: 10.3109/17482960802566824

Courtemanche, N., and Pollard, T. D. (2013). Interaction of profilin with the barbed end of actin filaments. *Biochemistry* 52, 6456–6466. doi: 10.1021/bi400682n

Delerue, F., and Ittner, L. M. (2017). Generation of genetically modified mice through the microinjection of oocytes. *J. Vis. Exp.* 124:e55765. doi: 10.3791/55765

Detmer, S. A., Velde, C. V., Cleveland, D. W., and Chan, D. C. (2008). Hindlimb gait defects due to motor axon loss and reduced distal muscles in a transgenic mouse model of Charcot-Marie-Tooth type 2A. *Hum. Mol. Genet.* 17, 367–375. doi: 10.1093/hmg/ddm314

Dogterom, M., and Koenderink, G. H. (2019). Actin-microtubule crosstalk in cell biology. *Nat. Rev. Mol. Cell Biol.* 20, 38–54. doi: 10.1038/s41580-018-0067-1

Fil, D., DeLoach, A., Yadav, S., Alkam, D., MacNicol, M., Singh, A., et al. (2017). Mutant Profilin1 transgenic mice recapitulate cardinal features of motor neuron disease. *Hum. Mol. Genet.* 26, 686–701. doi: 10.1093/hmg/ddw429

Gong, J., Du, X., Li, Z., Li, X., Guo, M., Lu, J., et al. (2018). Differential expression of genes identified by suppression subtractive hybridization in liver and adipose tissue of gerbils with diabetes. *PLoS One* 13:e0191212. doi: 10.1371/journal.pone.0191212

Gordon, P. H. (2013). Amyotrophic lateral sclerosis: an update for 2013 clinical features, pathophysiology, management and therapeutic trials. *Aging Dis.* 4, 295–310. doi: 10.14336/ad.2013.0400295

Henty-Ridilla, J. L., Juanes, M. A., and Goode, B. L. (2017). Profilin directly promotes microtubule growth through residues mutated in amyotrophic lateral sclerosis. *Curr. Biol.* 27, 3535.e4–3543.e4. doi: 10.1016/j.cub.2017.10.002

Hua, Z. L., Emiliani, F. E., and Nathans, J. (2015). Rac1 plays an essential role in axon growth and guidance and in neuronal survival in the central and peripheral nervous systems. *Neural Dev.* 10:21. doi: 10.1186/s13064-015-0049-3

Igaz, L. M., Kwong, L. K., Lee, E. B., Chen-Plotkin, A., Swanson, E., Unger, T., et al. (2011). Dysregulation of the ALS-associated gene TDP-43 leads to neuronal death and degeneration in mice. *J. Clin. Invest.* 121, 726–738. doi: 10.1172/JCI44867

Ingre, C., Landers, J. E., Rizik, N., Volk, A. E., Akimoto, C., Birve, A., et al. (2013). A novel phosphorylation site mutation in profilin 1 revealed in a large screen of US, Nordic, and German amyotrophic lateral sclerosis/frontotemporal dementia cohorts. *Neurobiol. Aging* 34, 1708.e1–1708.e6. doi: 10.1016/j.neurobiolaging.2012.10.009

Ittner, A., Chua, S. W., Bertz, J., Volkerling, A., van der Hoven, J., Gladbach, A., et al. (2016). Site-specific phosphorylation of tau inhibits amyloid-β toxicity in Alzheimer's mice. *Science* 354, 904–908. doi: 10.1126/science.aah6205

Ittner, L. M., and Gotz, J. (2007). Pronuclear injection for the production of transgenic mice. *Nat. Protoc.* 2, 1206–1215. doi: 10.1038/nprot.2007.145

Ke, Y. D., van Hummel, A., Stevens, C. H., Gladbach, A., Ippati, S., Bi, M., et al. (2015). Short-term suppression of A315T mutant human TDP-43 expression improves functional deficits in a novel inducible transgenic mouse model of FTLD-TDP and ALS. *Acta Neuropathol.* 130, 661–678. doi: 10.1007/s00401-015-1486-0

Kraemer, B. C., Schuck, T., Wheeler, J. M., Robinson, L. C., Trojanowski, J. Q., Lee, V. M., et al. (2010). Loss of murine TDP-43 disrupts motor function and plays an essential role in embryogenesis. *Acta Neuropathol.* 119, 409–419. doi: 10.1007/s00401-010-0659-0

Kullmann, J. A., Neumeyer, A., Wickertsheim, I., Bottcher, R. T., Costell, M., Deitmer, J. W., et al. (2012). Purkinje cell loss and motor coordination defects in profilin1 mutant mice. *Neuroscience* 223, 355–364. doi: 10.1016/j.neuroscience.2012.07.055

Kullmann, J. A., Wickertsheim, I., Minnerup, L., Costell, M., Friauf, E., and Rust, M. B. (2015). Profilin1 activity in cerebellar granule neurons is required for radial migration *in vivo*. *Cell Adh. Migr.* 9, 247–253. doi: 10.4161/19336918.2014.983804

Kwiatkowski, D. J., and Bruns, G. A. (1988). Human profilin. Molecular cloning, sequence comparison, and chromosomal analysis. *J. Biol. Chem.* 263, 5910–5915.

Leblond, C. S., Kaneb, H. M., Dion, P. A., and Rouleau, G. A. (2014). Dissection of genetic factors associated with amyotrophic lateral sclerosis. *Exp. Neurol.* 262, 91–101. doi: 10.1016/j.expneurol.2014.04.013

Lee, C. W., Vitriol, E. A., Shim, S., Wise, A. L., Velayutham, R. P., and Zheng, J. Q. (2013). Dynamic localization of G-actin during membrane protrusion in neuronal motility. *Curr. Biol.* 23, 1046–1056. doi: 10.1016/j.cub.2013.04.057

Mao, J.-H., Langley, S. A., Huang, Y., Hang, M., Bouchard, K. E., Celniker, S. E., et al. (2015). Identification of genetic factors that modify motor performance

and body weight using collaborative cross mice. *Sci. Rep.* 5:16247. doi: 10.1038/srep16247

Martin, E., Cazenave, W., Cattaert, D., and Branchereau, P. (2013). Embryonic alteration of motoneuronal morphology induces hyperexcitability in the mouse model of amyotrophic lateral sclerosis. *Neurobiol. Dis.* 54, 116–126. doi: 10.1016/j.nbd.2013.02.011

McGovern, V. L., Iyer, C. C., Arnold, W. D., Gombash, S. E., Zaworski, P. G., Blatnik, A. J., et al. (2015). SMN expression is required in motor neurons to rescue electrophysiological deficits in the SMNΔ7 mouse model of SMA. *Hum. Mol. Genet.* 24, 5524–5541. doi: 10.1093/hmg/ddv283

Mockrin, S. C., and Korn, E. D. (1980). Acanthamoeba profilin interacts with G-actin to increase the rate of exchange of actin-bound adenosine 5′-triphosphate. *Biochemistry* 19, 5359–5362. doi: 10.1021/bi00564a033

Mu, C., Wang, T., Wang, X., Tian, H., and Liu, Y. (2016). Identification of microRNAs regulating Hlxb9 gene expression during the induction of insulin-producing cells. *Cell Biol. Int.* 40, 515–523. doi: 10.1002/cbin.10586

Nejedla, M., Sadi, S., Sulimenko, V., de Almeida, F. N., Blom, H., Draber, P., et al. (2016). Profilin connects actin assembly with microtubule dynamics. *Mol. Biol. Cell* 27, 2381–2393. doi: 10.1091/mbc.e15-11-0799

Neumann, M., Sampathu, D. M., Kwong, L. K., Truax, A. C., Micsenyi, M. C., Chou, T. T., et al. (2006). Ubiquitinated TDP-43 in frontotemporal lobar degeneration and amyotrophic lateral sclerosis. *Science* 314, 130–133. doi: 10.1126/science.1134108

Peter, R. S., Rosenbohm, A., Dupuis, L., Brehme, T., Kassubek, J., Rothenbacher, D., et al. (2017). Life course body mass index and risk and prognosis of amyotrophic lateral sclerosis: results from the ALS registry Swabia. *Eur. J. Epidemiol.* 32, 901–908. doi: 10.1007/s10654-017-0318-z

Renton, A. E., Chio, A., and Traynor, B. J. (2014). State of play in amyotrophic lateral sclerosis genetics. *Nat. Neurosci.* 17, 17–23. doi: 10.1038/nn.3584

Rosen, D. R., Siddique, T., Patterson, D., Figlewicz, D. A., Sapp, P., Hentati, A., et al. (1993). Mutations in Cu/Zn superoxide dismutase gene are associated with familial amyotrophic lateral sclerosis. *Nature* 362, 59–62. doi: 10.1038/362059a0

Schindelin, J., Arganda-Carreras, I., Frise, E., Kaynig, V., Longair, M., Pietzsch, T., et al. (2012). Fiji: an open-source platform for biological-image analysis. *Nat. Methods* 9, 676–682. doi: 10.1038/nmeth.2019

Schulz, J., Franke, K., Frick, M., and Schumacher, S. (2016). Different roles of the small GTPases Rac1, Cdc42 and RhoG in CALEB/NGC-induced dendritic tree complexity. *J. Neurochem.* 139, 26–39. doi: 10.1111/jnc.13735

Smith, B. N. C., Vance, C., Scotter, E. L., Troakes, C., Wong, C. H., Topp, S., et al. (2015). Novel mutations support a role for Profilin 1 in the pathogenesis of ALS. *Neurobiol. Aging* 36, 1602.e17–1602.e27. doi: 10.1016/j.neurobiolaging.2014.10.032

Sreedharan, J., Blair, I. P., Tripathi, V. B., Hu, X., Vance, C., Rogelj, B., et al. (2008). TDP-43 mutations in familial and sporadic amyotrophic lateral sclerosis. *Science* 319, 1668–1672. doi: 10.1126/science.1154584

Steyn, F. J., Ioannides, Z. A., van Eijk, R. P. A., Heggie, S., Thorpe, K. A., Ceslis, A., et al. (2018). Hypermetabolism in ALS is associated with greater functional decline and shorter survival. *J. Neurol. Neurosurg. Psychiatry* 89, 1016–1023. doi: 10.1136/jnnp-2017-317887

Suetsugu, S., Miki, H., and Takenawa, T. (1998). The essential role of profilin in the assembly of actin for microspike formation. *EMBO J.* 17, 6516–6526. doi: 10.1093/emboj/17.22.6516

Swarup, V., Phaneuf, D., Dupre, N., Petri, S., Strong, M., Kriz, J., et al. (2011). Deregulation of TDP-43 in amyotrophic lateral sclerosis triggers nuclear factor κB-mediated pathogenic pathways. *J. Exp. Med.* 208, 2429–2447. doi: 10.1084/jem.20111313

Tanaka, Y., Nonaka, T., Suzuki, G., Kametani, F., and Hasegawa, M. (2016). Gain-of-function profilin 1 mutations linked to familial amyotrophic lateral sclerosis cause seed-dependent intracellular TDP-43 aggregation. *Hum. Mol. Genet.* 25, 1420–1433. doi: 10.1093/hmg/ddw024

van Hummel, A., Chan, G., van der Hoven, J., Morsch, M., Ippati, S., Suh, L., et al. (2018). Selective spatiotemporal vulnerability of central nervous system neurons to pathologic TAR DNA-binding protein 43 in aged transgenic mice. *Am. J. Pathol.* 188, 1447–1456. doi: 10.1016/j.ajpath.2018.03.002

Vinsant, S., Mansfield, C., Jimenez-Moreno, R., Del Gaizo Moore, V., Yoshikawa, M., Hampton, T. G., et al. (2013a). Characterization of early pathogenesis in the SOD1(G93A) mouse model of ALS: part I, background and methods. *Brain Behav.* 3, 335–350. doi: 10.1002/brb3.143

Vinsant, S., Mansfield, C., Jimenez-Moreno, R., Del Gaizo Moore, V., Yoshikawa, M., Hampton, T. G., et al. (2013b). Characterization of early pathogenesis in the SOD1(G93A) mouse model of ALS: part II, results and discussion. *Brain Behav.* 3, 431–457. doi: 10.1002/brb3.142

Vitriol, E. A., and Zheng, J. Q. (2012). Growth cone travel in space and time: the cellular ensemble of cytoskeleton, adhesion, and membrane. *Neuron* 73, 1068–1081. doi: 10.1016/j.neuron.2012.03.005

Vult von Steyern, F., Martinov, V., Rabben, I., Nja, A., de Lapeyriere, O., and Lomo, T. (1999). The homeodomain transcription factors Islet 1 and HB9 are expressed in adult alpha and gamma motoneurons identified by selective retrograde tracing. *Eur. J. Neurosci.* 11, 2093–2102. doi: 10.1046/j.1460-9568.1999.00631.x

Wen, K.-K., McKane, M., Houtman, J. C., and Rubenstein, P. A. (2008). Control of the ability of profilin to bind and facilitate nucleotide exchange from G-actin. *J. Biol. Chem.* 283, 9444–9453. doi: 10.1074/jbc.m709806200

Wilson, J. M., Hartley, R., Maxwell, D. J., Todd, A. J., Lieberam, I., Kaltschmidt, J. A., et al. (2005). Conditional rhythmicity of ventral spinal interneurons defined by expression of the Hb9 homeodomain protein. *J. Neurosci.* 25, 5710–5719. doi: 10.1523/jneurosci.0274-05.2005

Witke, W., Podtelejnikov, A. V., Di Nardo, A., Sutherland, J. D., Gurniak, C. B., Dotti, C., et al. (1998). In mouse brain profilin I and profilin II associate with regulators of the endocytic pathway and actin assembly. *EMBO J.* 17, 967–976. doi: 10.1093/emboj/17.4.967

Witke, W., Sutherland, J. D., Sharpe, A., Arai, M., and Kwiatkowski, D. J. (2001). Profilin I is essential for cell survival and cell division in early mouse development. *Proc. Natl. Acad. Sci. U S A* 98, 3832–3836. doi: 10.1073/pnas.051515498

Wu, C. H., Fallini, C., Ticozzi, N., Keagle, P. J., Sapp, P. C., Piotrowska, K., et al. (2012). Mutations in the profilin 1 gene cause familial amyotrophic lateral sclerosis. *Nature* 488, 499–503. doi: 10.1038/nature11280

Wurdak, H., Ittner, L. M., Lang, K. S., Leveen, P., Suter, U., Fischer, J. A., et al. (2005). Inactivation of TGFβ signaling in neural crest stem cells leads to multiple defects reminiscent of DiGeorge syndrome. *Genes Dev.* 19, 530–535. doi: 10.1101/gad.317405

Yang, C., Danielson, E. W., Qiao, T., Metterville, J., Brown, R. H. Jr., Landers, J. E., et al. (2016). Mutant PFN1 causes ALS phenotypes and progressive motor neuron degeneration in mice by a gain of toxicity. *Proc. Natl. Acad. Sci. U S A* 113, E6209–E6218. doi: 10.1073/pnas.1605964113

Conflict of Interest: The authors declare that the research was conducted in the absence of any commercial or financial relationships that could be construed as a potential conflict of interest.

Copyright © 2019 Brettle, Stefen, Djordjevic, Fok, Chan, van Hummel, van der Hoven, Przybyla, Volkerling, Ke, Delerue, Ittner and Fath. This is an open-access article distributed under the terms of the Creative Commons Attribution License (CC BY). The use, distribution or reproduction in other forums is permitted, provided the original author(s) and the copyright owner(s) are credited and that the original publication in this journal is cited, in accordance with accepted academic practice. No use, distribution or reproduction is permitted which does not comply with these terms.

frontiers in Cellular Neuroscience

ORIGINAL RESEARCH
published: 18 October 2019
doi: 10.3389/fncel.2019.00459

The Tripeptide RER Mimics Secreted Amyloid Precursor Protein-Alpha in Upregulating LTP

*Jodi A. Morrissey[1,2], Erin Bigus[3], Julie C. Necarsulmer[3], Vinay Srinivasan[3], Katie Peppercorn[2], Daniel J. O'Leary[3], Bruce G. Mockett[1], Warren P. Tate[2], Stephanie M. Hughes[2], Karen D. Parfitt[3] and Wickliffe C. Abraham[1]**

[1] Department of Psychology, Brain Health Research Centre, Brain Research New Zealand, University of Otago, Dunedin, New Zealand, [2] Department of Biochemistry, Brain Health Research Centre, Brain Research New Zealand, University of Otago, Dunedin, New Zealand, [3] Department of Neuroscience, Pomona College, Claremont, CA, United States

Secreted amyloid precursor protein-alpha (sAPPα), generated by enzymatic processing of the APP, possesses a range of neurotrophic and neuroprotective properties and plays a critical role in the molecular mechanisms of memory and learning. One of the key active regions of sAPPα is the central APP domain (E2) that contains within it the tripeptide sequence, RER. This sequence is exposed on the surface of a coiled coil substructure of E2. RER has by itself displayed memory-enhancing properties, and can protect newly formed engrams from interference in a manner similar to that displayed by sAPPα itself. In order to determine whether RER mimics other properties of sAPPα, we investigated the electrophysiological effects of the N-terminal protected acetylated RER (Ac-RER) and an isoform containing a chiral switch in the first amino acid from an l- to a d-orientation (Ac-rER), on synaptic plasticity. We found that, like sAPPα, exogenous perfusion with nanomolar concentrations of Ac-RER or Ac-rER enhanced the induction and stability of long-term potentiation (LTP) in area CA1 of rat and mouse hippocampal slices, in a protein synthesis- and trafficking-dependent manner. This effect did not occur with a control Ac-AAA or Ac-IFR tripeptide, nor with a full-length sAPPα protein where RER was substituted with AAA. Ac-rER also protected LTP against amyloid-beta ($A\beta_{25-35}$)-induced LTP impairment. Our findings provide further evidence that the RER-containing region of sAPPα is functionally significant and by itself can produce effects similar to those displayed by full length sAPPα, suggesting that this tripeptide, like sAPPα, may have therapeutic potential.

Keywords: Alzheimer's disease, amyloid precursor protein, amyloid-beta, long-term potentiation, field excitatory postsynaptic potential, hippocampus

OPEN ACCESS

Edited by:
Christopher Alan Reid, Florey Neuroscience Institute of Neuroscience and Mental Health, Australia

Reviewed by:
Thomas Behnisch, Fudan University, China
Julien Dine, Weizmann Institute of Science, Israel

***Correspondence:**
Wickliffe C. Abraham
cabraham@psy.otago.ac.nz

Specialty section:
This article was submitted to Cellular Neurophysiology, a section of the journal Frontiers in Cellular Neuroscience

Received: *02 July 2019*
Accepted: *26 September 2019*
Published: *18 October 2019*

Citation:
Morrissey JA, Bigus E, Necarsulmer JC, Srinivasan V, Peppercorn K, O'Leary DJ, Mockett BG, Tate WP, Hughes SM, Parfitt KD and Abraham WC (2019) The Tripeptide RER Mimics Secreted Amyloid Precursor Protein-Alpha in Upregulating LTP. Front. Cell. Neurosci. 13:459. doi: 10.3389/fncel.2019.00459

INTRODUCTION

There is a growing body of evidence supporting the potential therapeutic benefits of the secreted amyloid precursor protein-alpha (sAPPα) (Habib et al., 2017; Mockett et al., 2017). sAPPα is a product of non-amyloidogenic enzymatic cleavage of the amyloid precursor protein (APP), which is initiated by the α-secretase a-disintegrin-and-metalloprotease (ADAM10) and results

in the extracellular release of the N-terminal sAPPα fragment (Kuhn et al., 2010). Under basal conditions this pathway is dominant over the amyloidogenic APP processing pathway, which is initiated by β-secretase and results in the release of the smaller alternative ectodomain sAPPβ lacking 16 C-terminal residues. This latter pathway also results in production of the amyloid-β (Aβ) peptide after γ-secretase cleavage of the remaining C-terminal fragment of APP (Esch et al., 1990). In Alzheimer's disease (AD), there is a shift away from the non-amyloidogenic pathway toward amyloidogenic processing, which increases the availability of potentially pathological Aβ and simultaneously reduces availability of the neuroprotective sAPPα (Haass and Selkoe, 1993). This switch in sAPPα availability appears to directly contribute to the progression of AD pathology (Zhang et al., 2012).

To date attempts at therapeutic intervention in AD have largely focused on limiting Aβ production, an approach that has met with limited success, perhaps due in part to the key role of Aβ in regulating several vital neural functions (Drachman, 2014; Herrup, 2015; Burki, 2018). There is, however, a growing body of research regarding the potential of AD therapies focused on increasing the availability of sAPPα, since it has neurotrophic, neuroprotective, and neurogenic properties (Habib et al., 2017; Mockett et al., 2017). Moreover, virus-mediated overexpression of sAPPα in the hippocampus protects against impairments in synaptic morphology, plasticity, and behaviors in mouse models of AD pathology (Fol et al., 2015; Tan et al., 2018).

Among its many effects, exogenous recombinant sAPPα can enhance cognitive performance, as well as rescue memory performance under amnestic conditions (Meziane et al., 1998; Taylor et al., 2008; Hick et al., 2015). It is therefore interesting that the tripeptide RER from within the E2 domain ($sAPP\alpha_{328-330}$; **Figure 1**) mimics these effects in other models. For example, intracranial injection of *N*-acetylated RER (as well as longer sequences such as RERMS) in chicks enhances learning and protects against Aβ-induced memory loss (Mileusnic et al., 2004, 2007). While the mechanisms by which the tripeptide or its acetylated diastereomeric form Ac-rER protect or enhance memory are unclear, protein interaction assays indicate that Ac-rER interacts with collapsin response mediator protein 2 (CRMP2), a microtubule binding protein involved in the cytoskeleton (Mileusnic and Rose, 2011) that is known to be disrupted in AD and a possible therapeutic target for AD (Hensley and Kursula, 2016).

The memory-enhancing function of sAPPα may be mediated at least in part by its regulation of long-term potentiation (LTP). Treatment with function-blocking antibodies or an inhibitor of α-secretase reduces LTP and tetanus-evoked NMDA receptor-mediated currents, as well as performance on spatial memory tasks, all of which are rescued by treatment with exogenous sAPPα (Taylor et al., 2008). Perfusion of hippocampal slices with sAPPα also enhances *de novo* synthesis of glutamate receptor proteins, and facilitates their trafficking to the extrasynaptic cell surface, triggering the engagement of the cellular mechanisms which convert short-lasting potentiation to more permanent, late-phase LTP (L-LTP) (Mockett et al., 2019). Previous studies have identified that N-terminal acetylation of RER, or using a diastereomeric arginine for the first amino acid to enhance stability of the peptide, does not appear to alter its efficacy (Mileusnic et al., 2007). Here we sought to determine whether the memory-enhancing Ac-RER tripeptide is also able to enhance the induction and persistence of LTP in a protein synthesis-dependent fashion, and whether its presence in the full-length parent molecule, sAPPα, is necessary for sAPPα to exert its effects on LTP. We also tested whether the *N*-acetylated diastereomeric form (Ac-rER) is able to prevent the Aβ-mediated impairment of LTP, which would correlate with its ability to protect against Aβ-induced memory loss.

RESULTS

Ac-RER Is Sufficient to Enhance the Induction and Persistence of LTP in Acute Rat Hippocampal Slices

We have previously demonstrated that perfusion of hippocampal slices with a low (1 nM) concentration of recombinant human sAPPα significantly enhances both the induction and persistence of LTP in area CA1 following a brief TBS (theta burst stimulation) train of five bursts (Mockett et al., 2019). In order to determine whether Ac-RER could produce effects, we stimulated Schaffer collaterals and recorded evoked field excitatory postsynaptic potentials (fEPSPs) in stratum radiatum of area CA1 of acute rat hippocampal slices treated with either sAPPα (1 nM) or Ac-RER (1 nM) for 30 min prior to and continuing for 5 min following the delivery of the TBS. Using this protocol we observed an overall significant treatment effect on the initial induction of LTP ($F_{(2,21)} = 4.9$, $p = 0.02$), with both sAPPα and Ac-RER significantly increasing LTP induction over the first 5 min post-TBS (control: 51.1 ± 5.8%, $n = 9$; sAPPα: 85.9 ± 11.9%, $n = 8$, $p = 0.024$; RER: 86.1 ± 9.8%, $n = 7$, $p = 0.029$; **Figures 2A,B**). Moreover, when the persistence of LTP was measured 1 h post-TBS, there was again an overall significant effect ($F_{(2,21)} = 8.9$, $p = 0.0016$), with both sAPPα and RER enhancing LTP significantly above control levels and to a similar extent (control: 14.9 ± 2.9%, $n = 9$; sAPPα: 42.4 ± 4.6%, $n = 8$, $p = 0.002$; RER: 38.7 ± 7.9%, $n = 7$, $p = 0.004$; **Figures 2A,B**).

Secreted amyloid precursor protein-alpha displays a concentration-dependent effect on CA1 LTP using this mild TBS protocol, with an optimal concentration of 1 nM (Mockett et al., 2019). In the present experiments, we observed a similar concentration-dependent effect of Ac-RER on both the induction and persistence of LTP displayed. For LTP induction there was an overall treatment effect ($F_{(3,23)} = 5.3$, $p = 0.006$) with Ac-RER at 1 and 10 nM but not at 0.3 nM (control: 51.1 ± 5.9%, $n = 9$; 0.3 nM: 49.5 ± 8.5%, $n = 6$, $p = 0.99$; 1 nM: 86.4 ± 9.7%, $n = 7$, $p = 0.049$; 10 nM: 99.8 ± 21%, $n = 6$, $p = 0.01$). There were corresponding enhancements of LTP persistence 1 h post-TBS ($F_{(3,23)} = 6.4$, $p = 0.002$) for 1 and 10 nM Ac-RER (control: 14.9 ± 2.9%, $n = 9$; 0.3 nM: 16.4 ± 2.9%, $n = 6$, $a = 5$, $p = 0.99$; 1 nM: 38.7 ± 7.9%, $n = 7$, $p = 0.015$;

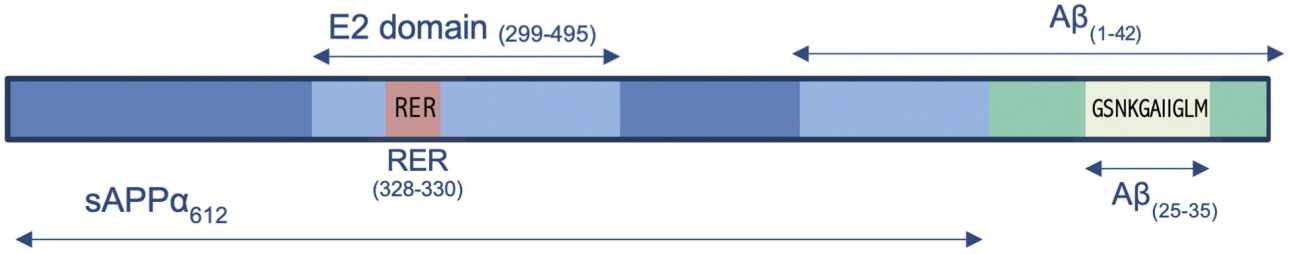

FIGURE 1 | Schematic representation of the location of RER within the E2 domain of the sAPPα, while also showing the relative locations of $A\beta_{(1-42)}$, $A\beta_{(25-35)}$, sAPPα, and sAPPβ.

10 nM: 45.3 ± 9.9%, n = 6, a = 5, p = 0.005; **Figures 2C,D**). Importantly, perfusion with Ac-RER (1 nM) did not alter baseline responses to stimulation in the absence of a TBS ($t_{(5)}$ = 0.1, p = 0.9; **Figure 2E**), nor did any of the other concentrations during peptide delivery (**Figures 2C,D**).

To determine whether altered presynaptic function contributed to the Ac-RER-mediated enhancement of LTP, we measured the effect of Ac-RER (1 nM) on paired-pulse facilitation (PPF) across a range of interpulse intervals under baseline conditions, as well as its effects on post-tetanic potentiation (PTP) following TBS in the presence of AP5 to prevent LTP induction. Neither of these measures of presynaptic activity were significantly altered by Ac-RER (two-way repeated measures ANOVA PPF: $F_{(1,5)}$ = 4.3, p = 0.09, **Figure 2F**; PTP: $F_{(1,5)}$ = 1.8, p = 0.24, **Figure 2G**), suggesting that the enhancement of LTP was not secondary to the enhancement of transmitter release probability during baseline or tetanic stimulation. Likewise, we observed that 10 nM Ac-rER had no effect on PPF or PTP in hippocampal slices from mice (data not shown). These data are consistent with the lack of effect on baseline responses shown in **Figure 2E**.

RER Within the E2 Domain Is Required for sAPPα's Enhancement of LTP

In order to determine whether the RER sequence within the E2 domain contributes to sAPPα's potency in enhancing LTP, a modified sAPPα was generated with the RER region (at position 228–230) substituted by site-directed mutagenesis of the cDNA to encode three alanine residues (sAPPα-AAA). Alanine residues were selected as substitutions for RER as they were considered to have a minimal influence on the structure of the coiled coil subdomain of E2 and thereby the properties of the larger molecule. sAPPα-AAA (1 nM) did not alter either the induction or persistence of LTP compared to untreated control slices from rats (induction: p = 0.97, persistence: p = 0.92; **Figures 3A,B**). An *N*-acetylated AAA (Ac-AAA, 1 nM) isolated tripeptide was also tested to confirm that the specific properties and character of the RER sequence is responsible for producing the observed effects, rather than simply any tripeptide. Ac-AAA had no effect on the induction or persistence of LTP (induction: p = 0.64, persistence, p = 0.84; **Figures 3A,B**), suggesting that it is the specific properties of the side chains of the charged amino acids in the RER sequence, either in isolation or within sAPPα, that are necessary for LTP enhancement.

LTP Enhancement by Ac-RER Is Protein Trafficking and Protein Synthesis-Dependent

Long-term potentiation enhancement by sAPPα is associated with the trafficking of glutamate receptors to the cell surface, with both effects blocked by the protein trafficking inhibitor Brefeldin A (BFA) (Mockett et al., 2019). To identify whether Ac-RER enhancement of LTP involves a similar mechanism, we used acute rat hippocampal slices where BFA (35 μM) was added to the perfusion solution 10 min prior to and during treatment with Ac-RER (1 nM) for the 30 min prior to delivery of the TBS, and then washed out 5 min after the TBS. As BFA was dissolved in 0.1% dimethyl sulfoxide (DMSO), all groups in this experiment [and the following one with cycloheximide (CHX)], were conducted with equal exposure to the solvent. Results were analyzed by ANOVA, which indicated an overall significant effect ($F_{(2,16)}$ = 18.9, p = 0.0002), which was followed by Dunnett's *post hoc* test to compare all results to the Ac-RER effect. The *post hoc* test showed that, as with sAPPα, BFA blocked LTP enhancement by Ac-RER (Ac-RER: 34.3 ± 2.8%, n = 8, a = 7; BFA + Ac-RER: 10.9 ± 5.0%, n = 6, p = 0.0001; control: 11.7 ± 1.7%, n = 5, p = 0.0003; **Figures 4A,B**). Interestingly, co-administration of BFA and Ac-RER also reduced the initial induction of LTP back to control levels ($F_{(2,16)}$ = 9.5, p = 0.0019; Dunnett's *post hoc* test: Ac-RER 86.7 ± 9.8%, n = 8, a = 7; BFA + Ac-RER: 48.6 ± 4.3%, n = 6, p = 0.003; control: 49.9 ± 6.5%, n = 5, p = 0.005; **Figure 4A**).

To confirm that perfusion with BFA alone during the same time-points (20–65 min) did not alter baseline responses in the absence of TBS, we compared the average baseline responses 5 min prior to introduction of the inhibitor to the last 5 min of recordings after BFA washout ($t_{(8)}$ = 0.12, p = 0.9; pre-BFA to post-BFA change of −1.6 ± 3.8%, n = 5; **Figures 4C,D**). LTP following perfusion with BFA prior to and during the TBS was comparable to the control level of LTP (control: 14.3 ± 3.6%, n = 5; BFA: $t_{(8)}$ = 1.1, 15.2 ± 2.7%, n = 5, p = 0.3, **Figures 4C,D**). These results indicate that BFA (and thus inhibition of protein

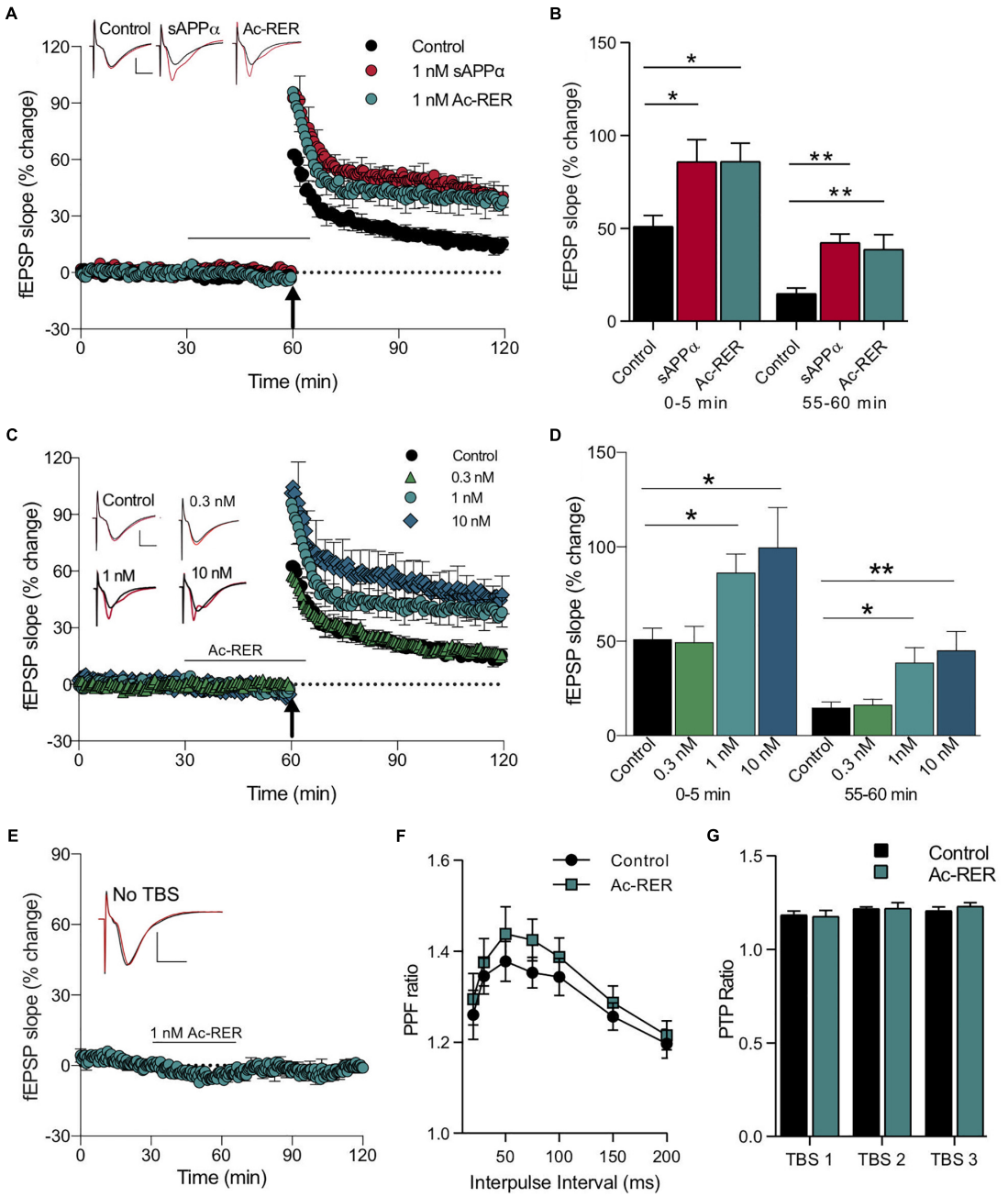

FIGURE 2 | Acute administration of Ac-RER enhances LTP. **(A)** A mild TBS delivered to acute rat hippocampal slices produced a rapidly decaying LTP. Adding 1 nM Ac-RER to the solution for 30 min prior to delivery of the TBS enhanced the induction and persistence of the LTP produced. This enhancement was similar to the LTP facilitation caused by sAPPα. The plot shows average LTP obtained from slices pre-treated for 30 min under control (n = 9), 1 nM sAPPα (n = 8), or 1 nM Ac-RER (n = 7) conditions. The black bar indicates the period of perfusion with 1 nM Ac-RER or 1 nM sAPPα. The arrow indicates the delivery of the mild TBS (five bursts of five pulses). Example waveforms are averages of 10 sweeps from a single slice for each group: black, baseline; red, final LTP; scale bars: 2 mV, 5 ms. **(B)** Summary bar graph displaying the degree of LTP for each group. *$p < 0.05$; **$p \leq 0.01$; Dunnett's *post hoc* t-test. **(C)** Plotted responses for Ac-RER at various concentrations demonstrating that increases in the induction and persistence of LTP were concentration dependent. The arrow indicates the delivery of the half TBS (five bursts of five pulses). Example waveforms are averages of 10 sweeps from a single slice for each group: black, baseline; red, final LTP; scale bars: 2 mV, 5 ms. **(D)** Bar graph comparing LTP following perfusion with various concentrations of Ac-RER. The lowest concentration (0.3 nM RER; n = 6 slices) did not alter induction or persistence of LTP from controls, whereas higher concentrations (1 nM; n = 7 and 10 nM; n = 6) did increase LTP. *$p < 0.05$; **$p \leq 0.01$. **(E)** Plot of responses following exposure to Ac-RER for 30–65 min of the protocol, but in the absence of TBS (n = 6). Basal responses to test pulses were not affected. Black bar indicates the period of perfusion with Ac-RER. Example waveforms are the average of 10 sweeps for pre- and post-Ac-RER treatment: black, pre-treatment; red, post-treatment; scale bars: 2 mV, 5 ms. **(F)** Paired-pulse facilitation, determined across a range of interpulse intervals, was not altered by superfusion with Ac-RER for 30 min prior to testing (1 nM, n = 9). **(G)** Presynaptic post-tetanic potentiation (PTP), measured 5 s after each of three TBS protocols delivered at 30 s intervals in the presence of D-AP5, was unchanged by administration of Ac-RER (1 nM, n = 9) for 30 min prior to the first TBS. All values in this and the following figures calculated as mean ± SEM.

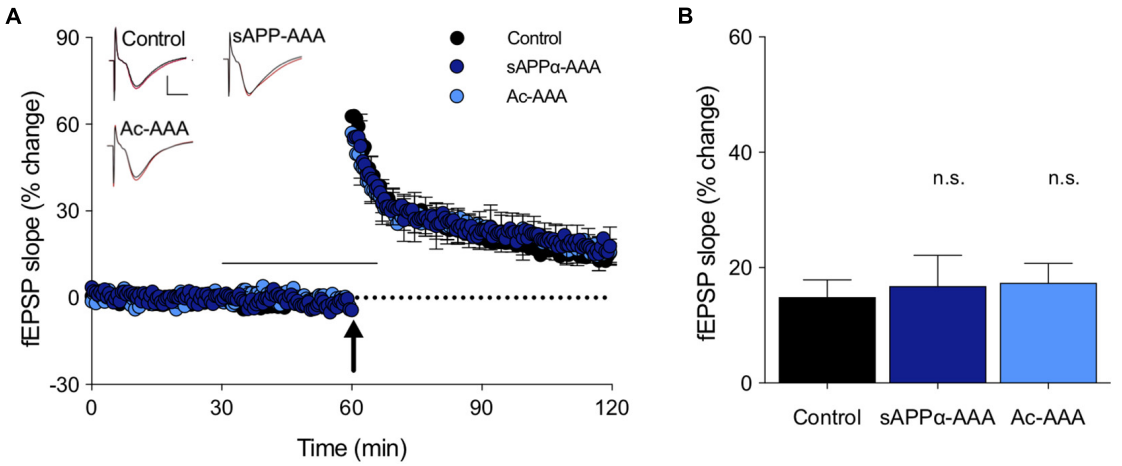

FIGURE 3 | Peptide sequence dependence of the LTP facilitation. **(A)** The full length sAPPα molecule, with the RER sequence replaced with AAA (sAPPα-AAA; $n = 5$) did not alter LTP in rat hippocampal slices. The control isolated tripeptide Ac-AAA ($n = 7$) also did not affect LTP. The black bar shows the period of perfusion, and the arrow the delivery of the TBS. Example waveforms are averages of 10 sweeps from a single slice for each group: black, baseline; red, final LTP; scale bars: 2 mV, 5 ms. **(B)** Summary bar graph shows that LTP obtained after exposure to these probe molecules was not altered from the control level. n.s., $p > 0.05$ compared to the control group.

trafficking) itself did not alter the early-phase LTP generated by the TBS.

Exposure to sAPPα is known to increase ***de novo*** protein synthesis, including the synthesis of glutamate receptor subunits, that contributes to its enhancement of LTP (Claasen et al., 2009; Mockett et al., 2019). To determine whether Ac-RER likewise enhances ***de novo*** protein synthesis, we used the surface sensing of translation (SUnSET) method (Schmidt et al., 2009), to directly measure the levels of newly synthesized proteins in hippocampal tissue isolated from area CA1. In this method newly synthesized proteins are isolated by immunoprecipitation and the relative total level of protein present in a lane following gel electrophoresis is compared across samples. Consistent with previous results (Claasen et al., 2009), incubation with 1 nM sAPPα for 30 min increased the levels of newly synthesized proteins as measured throughout the lanes ($p = 0.0033$, **Figures 4E,F** and **Supplementary Figure S1**). Likewise, administration of both 1 and 10 nM Ac-RER for 30 min also increased levels of newly synthesized proteins when compared to untreated controls ($F_{(6,30)} = 1.47$, $p = 0.0002$; 1 nM: $p = 0.006$, 10 nM: $p = 0.003$, **Figures 4E,F**). Incubation in either Ac-AAA or sAPP-AAA did not produce any change in the levels of newly synthesized proteins detected using this method (AAA: $p = 0.19$; sAPP-AAA: $p = 0.99$).

To determine whether Ac-RER enhancement of LTP is dependent on this *de novo* protein synthesis, the protein synthesis inhibitor CHX (60 μM) was given for 10 min prior to and during the perfusion with Ac-RER (1 nM). ANOVA revealed a significant overall effect ($F_{(2,17)} = 9.4$, $p = 0.002$). Dunnett's *post hoc* test to compare the effect of Ac-RER-treated slices to the other groups indicated that CHX blocked enhancement of LTP by Ac-RER (Ac-RER: 34.1 ± 2.0%, $n = 8$, $a = 7$; control: 11.7 ± 1.7%, $n = 5$, $p = 0.0006$; CHX + Ac-RER: 20.3 ± 4.2%, $n = 7$, $a = 6$, $p = 0.02$; **Figures 4G,H**), as well as the initial induction of LTP ($F_{(2,17)} = 5.5$, $p = 0.02$; control: 49.9 ± 6.5%, $n = 5$; CHX + Ac-RER: 56.5 ± 8.8%, $n = 7$, $p = 0.8$; Ac-RER: 86.7 ± 9.8%, $n = 8$, $a = 7$, $p = 0.03$; **Figure 4G**).

To confirm that perfusion with CHX alone did not alter baseline responses in the absence of a TBS, we applied CHX during the same time-points as other experiments (20–65 min) but did not deliver a TBS, and then compared the average baseline responses 5 min prior to introduction of the inhibitor to the last 5 min of recordings after washout and found no significant effect ($t_{(10)} = 0.91$, $p = 0.38$; change in pre- to post-CHX responses: −1.3 ± 1.4%, $n = 5$; **Figures 4I,J**). To confirm that the normal LTP observed with this mild TBS protocol was not affected by CHX, we perfused with CHX alone and observed LTP that was comparable to that seen in untreated slices ($t_{(8)} = 0.34$; control: 14.3 ± 3.6%, $n = 5$; CHX: 10.6 ± 2.8%, $n = 5$, $p = 0.7$; **Figures 4I,J**). These results indicate that CHX did not affect basal transmission or the early-phase LTP generated by the mild TBS.

LTP in Mice Is Enhanced by Ac-RER and Its Chiral Isoform Ac-rER

Previous experiments have explored changing the chirality of the first amino acid of the RER sequence from an l- to a d-orientation (rER) to stabilize the sequence and reduce its rate of degradation *in vivo* by peptidases. This modified peptide was effective in rescuing Aβ-induced memory deficits in chicks (Mileusnic et al., 2007). Here, we compared whether the Ac-rER was as effective at enhancing LTP as Ac-RER. We also extended our study by undertaking these experiments in young adult mice. Moreover, a different control tripeptide (IFR) of more hydrophobic character was synthesized due to the relative similarity in size and molecular weight of the amino acid side chains to RER.

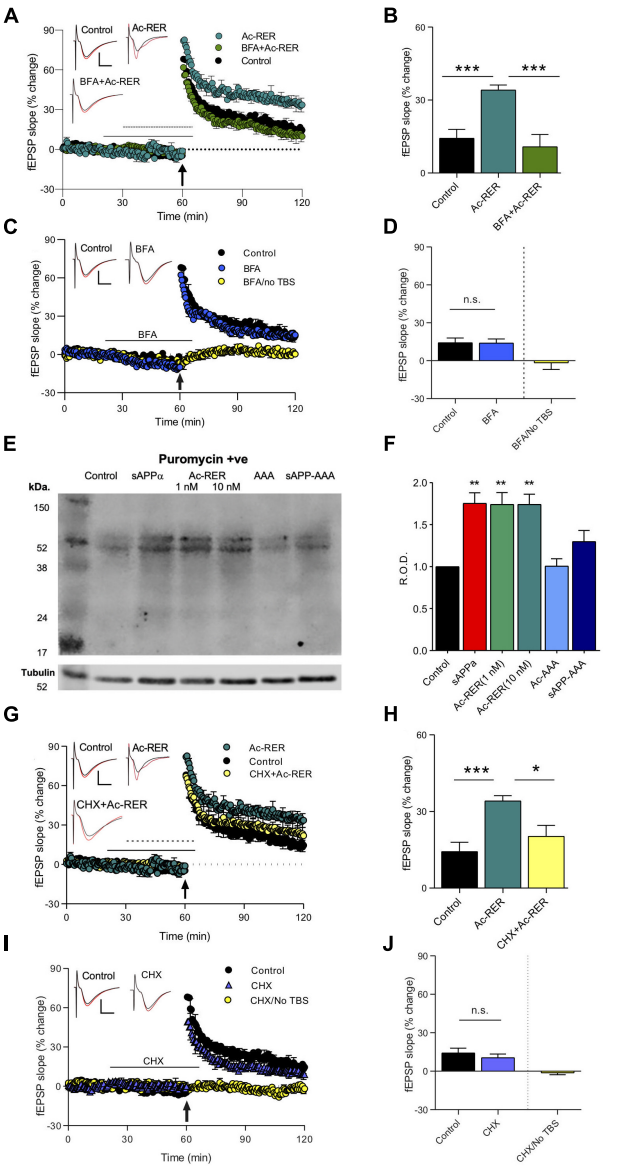

FIGURE 4 | Protein-synthesis and -trafficking inhibitors prevent Ac-RER enhancement of LTP in acute rat hippocampal slices. **(A)** BFA (35 μM) given 10 min prior to and during Ac-RER (1 nM) perfusion blocked the tripeptide enhancement of LTP induction and persistence. Solid line, BFA perfusion; perforated line, Ac-RER perfusion. Example waveforms are averages of 10 sweeps from a single slice for each group: black, baseline; red, final LTP; scale bars: 2 mV, 5 ms. **(B)** Bar graph comparing LTP in slices treated with BFA and Ac-RER ($n = 6$), to control ($n = 5$) and Ac-RER-treated slices ($n = 7$). The LTP enhancement was blocked by BFA. $^{***}p < 0.001$. **(C)** Plot of responses for control experiments ($n = 5$), BFA only perfusion ($n = 4$), and BFA with no TBS (far right bar, $n = 5$). Control LTP was not affected by BFA administration. In the absence of TBS, responses returned to basal levels following removal of BFA from the perfusion solution, indicating that the inhibitor did not persistently affect basal transmission. Example waveforms are averages of 10 sweeps from a single slice for each group: black, baseline; red, final LTP; scale bars: 2 mV, 5 ms. **(D)** Bar graph displaying the degree of response change for each group. n.s., $p > 0.05$ compared to the control group. **(E)** Sample blot showing the puromycin-containing proteins for each treatment condition. Tubulin was used as a loading control, as shown below. Incubation *(Continued)*

FIGURE 4 | Continued
of peptides was at 1 nM, except for Ac-RER, where both 1 and 10 nM concentrations were assessed. **(F)** Bar graph displaying the relative puromycin optical density throughout the lanes, normalized to tubulin and compared to controls. There was a significant increase in newly synthesized protein in tissue treated with both 1 and 10 nM ac-RER, and with 1 nM sAPPα. $^{**}p \leq 0.01$. **(G)** Inclusion of CHX for 10 min prior to and during Ac-RER (1 nM) perfusion reduced the effects of the tripeptide on LTP induction and persistence. Arrow indicates delivery of the TBS. Black line, CHX perfusion; perforated line, Ac-RER perfusion. Example waveforms are averages of 10 sweeps from a single slice for each group: black, baseline; red, final LTP; scale bars: 2 mV, 5 ms. **(H)** Bar graph comparing LTP between the different treatment groups in panel **(G)**. CXH + Ac-RER ($n = 7$), control ($n = 5$), Ac-RER-treated slices ($n = 7$). $^{*}p \leq 0.05$. **(I)** Plot of responses for controls ($n = 5$), CHX only ($n = 5$), and CHX with no TBS ($n = 6$). Responses returned to baseline levels following removal of CHX from the perfusion solution in the absence of a TBS. Control LTP was not affected by CHX perfusion. Example waveforms are averages of 10 sweeps from a single slice for each group: black = baseline; red = final LTP; scale bars: 2 mV, 5 ms. **(J)** Bar graph of the responses changes for the groups in panel **(I)**. CHX by itself did not alter either basal responses or LTP. n.s., $p > 0.05$ compared to the control group.

We found that, as in rats, Ac-RER (10 nM) enhanced TBS-induced LTP in mouse hippocampal CA1. Moreover, Ac-rER (10 nM) was also a potent enhancer of LTP in this preparation, with no difference between the two isoforms of the tripeptide ($F_{(3,29)} = 11.2$, $p = 0.0001$; control: 10.6 ± 5.7%, $n = 7$; Ac-RER: 41.7 ± 7.2%, $n = 8$; Ac-rER: 38.2 ± 4.8%, $n = 10$; Tukey's test adjusted p-values: control vs. Ac-RER: $p = 0.002$; control vs. Ac-rER: $p = 0.005$, Ac-RER vs. Ac-rER: $p = 0.96$; **Figures 5A,B**). There was no effect on LTP following superfusion during the same time period with the random tripeptide sequence IFR (10 nM) (IFR: 7.1 ± 2.7%, $n = 8$, control vs. IFR: $p = 0.97$; **Figures 5A,B**).

rER Rescues LTP in $A\beta_{(25-35)}$-Treated Mouse Slices

Amyloid-beta is known to impair LTP in area CA1 (Shankar et al., 2008), and the fragment $A\beta_{(25-35)}$ has specifically been shown to impair short-term forms of memory (Stepanichev et al., 2003). Since Ac-rER can protect against Aβ-induced memory loss (Mileusnic et al., 2004), we sought to determine whether Ac-rER could also protect against the $A\beta_{(25-35)}$-mediated impairment of LTP in slices from young adult mice. To induce stable LTP in control slices, a stronger TBS comprising 10 bursts of 5 pulses was used. This protocol induced LTP that was 58.5 ± 2.9% above baseline ($n = 7$). ANOVA ($F_{(3,17)} = 4.1$, $p = 0.02$; **Figures 6A,B**) followed by Tukey's *post hoc* test showed that Ac-rER (10 nM) did not enhance this stronger form of LTP (51.6 + 14.9%, $n = 5$, $p = 0.98$), presumably due to saturation of the LTP mechanisms. $A\beta_{(25-35)}$ (200 nM) delivered 28 min prior to the TBS and removed 2 min after (total 30 min) potently reduced the LTP (4.9 ± 5.3%, $n = 5$, $p = 0.03$; **Figures 6A,B**). Pretreatment of slices for 15 min with 10 nM Ac-rER prior to and then during delivery of $A\beta_{(25-35)}$ completely prevented the $A\beta_{(25-35)}$-induced impairment in LTP (Aβ + Ac-rER = 63.9 ± 22.9%, $n = 5$, Aβ + Ac-rER vs. Aβ: $p = 0.04$, **Figures 6A,B**), returning it to control levels (control vs. Aβ + Ac-rER: $p = 0.99$).

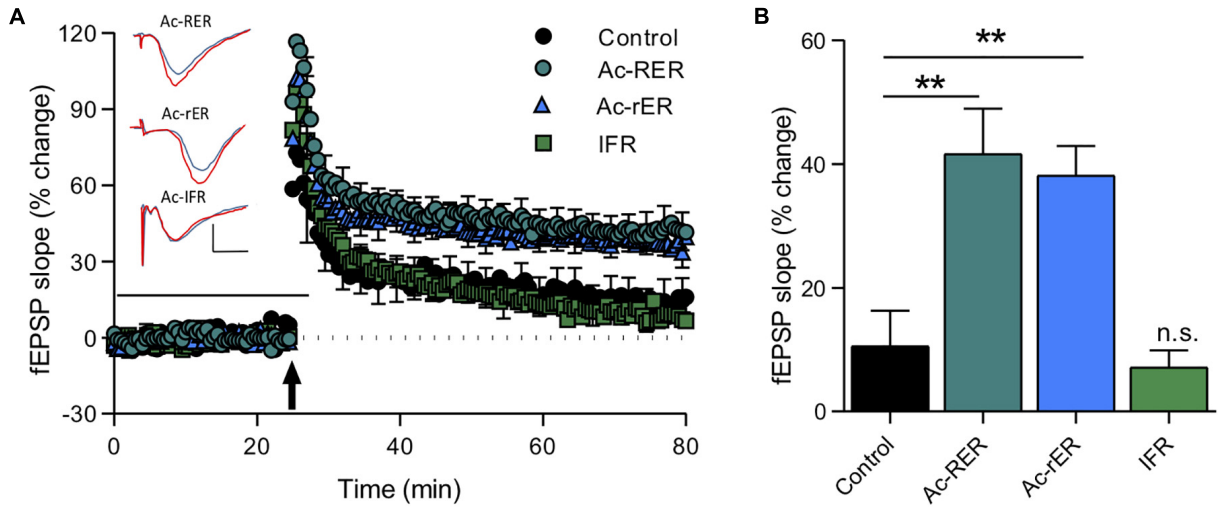

FIGURE 5 | Tripeptide effects in acute mouse slices. **(A)** The same Ac-RER tripeptide (n = 8) and a variant with the first arginine chirally switched to the d-oriented amino acid (Ac-rER; n = 10) were effective in enhancing LTP in adult C57/B6 mouse slices. An *N*-acetylated control tripeptide (Ac-IFR; n = 8) did not affect LTP. Example waveforms are averages of 10 sweeps from a single slice for each group: blue = sample EPSP 1 min before TBS; red = sample EPSP taken at 60 min post-TBS taken at 60 min post-TBS; scale bars: 1 mV, 10 ms. **(B)** Bar graph comparing the final level of LTP for the groups in panel **(A)**. $^{**}p \leq 0.01$; n.s., $p > 0.05$ compared to the control group.

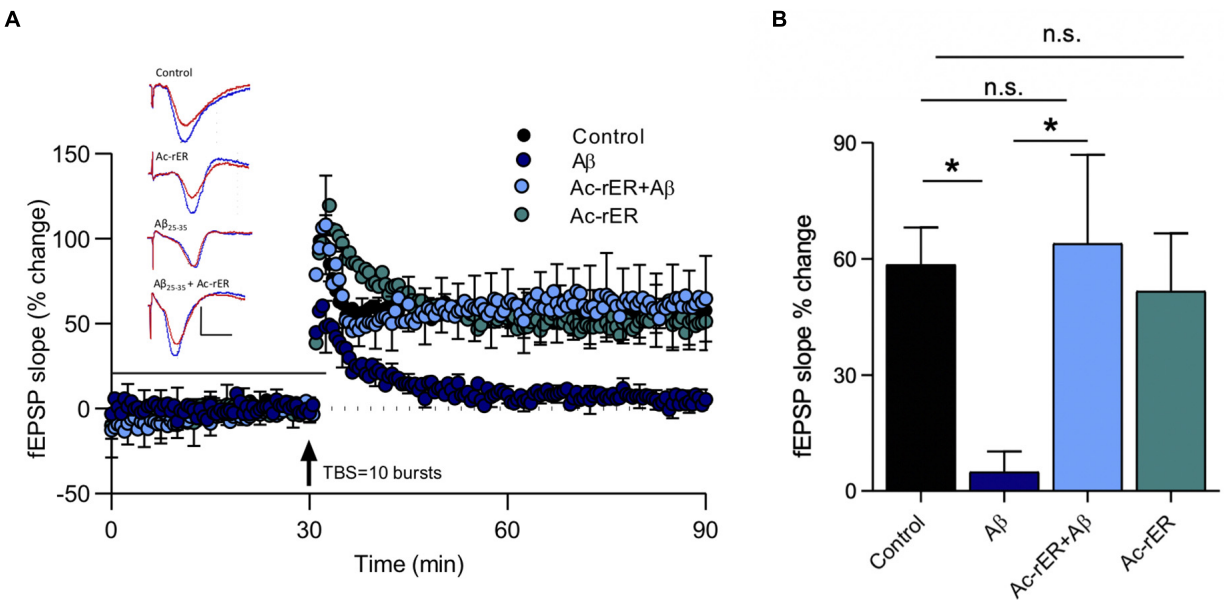

FIGURE 6 | Ac-rER prevents impairments in LTP following $A\beta_{(25-35)}$ exposure in mouse slices. **(A)** Perfusion of mouse slices in aCSF containing 200 nM $A\beta_{(25-35)}$ (Aβ; n = 5) for 28 min prior to and 2 min following the delivery of TBS (10 bursts) impaired LTP. Addition of 10 nM Ac-rER (n = 5) for 15 min prior to and during Aβ perfusion (n = 5) rescued the LTP. Solid line, treatment present. Arrow indicates delivery of TBS (10 bursts). Red = sample EPSP 1 min before TBS; blue = sample EPSP taken at 60 min post-TBS; scale bars: 1 mV, 10 ms. **(B)** Bar graph shows that perfusion with $A\beta_{(25-35)}$ induced impaired LTP, which was rescued by pre-treatment with Ac-rER. $^{*}p \leq 0.05$; n.s., $p > 0.05$ relative to the control group.

DISCUSSION

In this study, we confirmed many previous reports that either recombinant sAPPα or virus-mediated over-expression of sAPPα can facilitate LTP in area CA1 of the rodent hippocampus (Taylor et al., 2008; Fol et al., 2015; Tan et al., 2018). Remarkably, we found that a tripeptide fragment of sAPPα in its N-terminal E2 domain, RER, could replicate sAPPα's facilitation of LTP induction and persistence, transforming short-lasting E-LTP to a longer-lasting, protein synthesis-dependent L-LTP. Moreover, like sAPPα, neither Ac-RER nor Ac-rER affected basal synaptic transmission, while Ac-RER

also had no effect on presynaptic short-term plasticity (Taylor et al., 2008). Notably, other tripeptides (Ac-AAA, Ac-IFR) as well as sAPP-AAA, where the RER sequence had been substituted with the neutral and non-structurally disruptive amino acid alanine, failed to generate LTP enhancement at the same concentration. Thus, it is the specific sequence and properties of the amino acid side chains of RER (shared by rER) within the isolated peptide and when embedded within the normal structure of sAPPα, that are responsible for the tripeptide's effects.

As for sAPPα (Mockett et al., 2019), the facilitation of LTP by Ac-RER was blocked by BFA, an inhibitor of protein trafficking that acts by blocking export of proteins from Golgi (Misumi et al., 1986) and causing morphological changes in endosomes (Klausner et al., 1992). Previously we have shown that sAPPα causes the trafficking of both GluA1-containing AMPA receptors as well as NMDA receptors to the cell surface, effects that are blocked by BFA (Mockett et al., 2019). It remains to be determined whether RER can also elicit these specific effects, but this seems likely since the trafficking of GluA1-containing AMPA receptors in particular is associated with the priming of LTP (Oh et al., 2006). Moreover, the early expression of LTP is mediated by the trafficking to synapses of GluA1-only-containing AMPA receptors (Hayashi and Huganir, 2004; Plant et al., 2006; Williams et al., 2007). Such effects could explain the enhancement by RER of LTP even at its earliest stage of induction.

Secreted amyloid precursor protein-alpha also acts by stimulating protein synthesis, and both the trafficking of glutamate receptors and the facilitation of LTP were severely impaired by co-administration of protein synthesis inhibitors (Mockett et al., 2019). Here, we found using the SUnSET protein synthesis assay that there is an increase in the overall level of newly synthesized protein in tissue dissected from area CA1 of the hippocampus following incubation for 30 min in Ac-RER, observed at both 1 and 10 nM Ac-RER. There was no increase in protein synthesis observed following incubation (30 min) in Ac-AAA peptide or the modified protein sAPP-AAA. Consistent with this finding, CHX impaired the ability of Ac-RER to facilitate LTP when measured at either 5 or 60 min post-induction. Further studies will be needed to address identification and localization of newly synthesized or trafficked proteins in order to confirm whether RER mimics the enhanced *de novo* synthesis of glutamate receptors and trafficking to the cell membrane produced by sAPPα (Mockett et al., 2019).

In addition to the enhancement by Ac-RER and Ac-rER of LTP generated by a mild induction protocol in rats and wild-type mice, Ac-rER also prevented the impairment of LTP caused by acute administration of $A\beta_{25-35}$. The capacity of the tripeptides to support synaptic plasticity under conditions present in AD-like pathology is of particular interest for their potential therapeutic applications. This finding is consistent with previous observations that intracranial injection with Ac-rER protects against Aβ-induced memory loss in chicks performing a passive avoidance task (Mileusnic et al., 2007). Mileusnic and Rose (2011) have also observed that RER can bind to CRMP-2, heat shock cognate 71 (HSC71), and the syntaxin binding protein STXBP1. While the functional nature of these interactions is unclear, it is possible that the exposed RER in the monomeric form of sAPP or as an isolated peptide blocks the binding site of a signaling ligand to either prevent clearance of these proteins or to enhance their rate of interaction with their substrates. Abnormal hyperphosphorylation (Cole et al., 2007) and glycosylation (Kanninen et al., 2004) of both CRMP-2 and HSC-71 occur in AD and contribute to AD pathology, indicating that RER interaction with these proteins could be sites where the tripeptide may produce therapeutic benefits. On the other hand, both sAPPα and its isolated C-terminal 16 amino acids appear to bind to the α7 nicotinic receptor through a different binding interaction and can enhance nicotine-induced increases in intracellular calcium (Lawrence et al., 2014; Richter et al., 2018), while the enhancement of LTP is blocked by α-bungarotoxin (Richter et al., 2018; Morrissey et al., 2019). Whether RER can enhance normal or impaired LTP by this mechanism remains to be determined.

The observed failure of other tripeptides such as Ac-AAA and Ac-IFR to facilitate LTP suggest that the properties and hydrophilic charge characteristics of the RER sequence is necessary for enhancing synaptic plasticity. We have also demonstrated that the RER sequence is vital for the activity of sAPPα in enhancing LTP, as the sAPP-AAA also failed to increase protein synthesis and enhance LTP. These findings concerning the importance of the RER sequence within sAPPα are consistent with previous findings that deletion of RERMS amino acids from sAPPα removes its ability to protect against Aβ insult although this may have disrupted the structure of the coiled coil where the RER resides in the E2 domain (Li et al., 1997). This remarkable ability of a tripeptide sequence to replicate the effects of a 612 amino acid protein may provide insight into the structural importance of the 328–330 region of the full-length protein. RER with its palindromic sequence can facilitate interaction of two monomers oriented in opposite directions and this homodimer or a heterodimer with a molecule like the parent APP itself may have physiological significance. If the isolated peptide prevents such dimers forming it might be expected to have counter effects to sAPPα, however this has not been observed. sAPPα itself is too large to cross the cell membrane, leading to the conclusion that its effects are likely to be mediated by a cell surface receptor. While the identity of any sAPPα receptor has proven difficult to establish, our data suggest that the RER sequence plays some role in mediating the interaction of the molecules involved. Whether RER can replicate other aspects of sAPPα's functionality, such as neuroprotection, neurotrophism, and neurogenesis, remains to be studied.

In conclusion, our findings demonstrate that acetylated and chiral forms of RER are potent enhancers of hippocampal LTP, and can protect against Aβ-induced impairments of LTP, without affecting basal transmission. As such, RER may be a strong candidate for the development of a small peptide therapeutic to combat at least some aspects of AD pathology.

MATERIALS AND METHODS

Animals

Male Sprague-Dawley rats (6–8 weeks) were obtained from the University of Otago Breeding Station. Male C57BL/6N mice were obtained from Simonsen or Jackson Laboratories at 6–8 weeks of age. Animals were group housed in standard cages on a normal 12 h light cycle and fed *ad lib*. The use of rats at the University of Otago was compliant with the New Zealand Animal Welfare Act 1991, and performed under approval of the University of Otago Animal Ethics Committee. The work with mice at Pomona College was carried out in an AAALAC-certified facility and was approved by the Pomona College Institutional Animal Care and Use Committee.

Drugs and Reagents

All salts and sugars for electrophysiology were sourced from Merck Millipore (Billerica, MA, United States) or VWR Life Sciences (Visalia, CA, United States). For experiments at Otago, the tripeptides RER and rER were obtained from EZBiolab (Carmel, IN, United States), provided in lyophilized form and made into a stock at 1 mM in filtered 1× phosphate-buffered solution (PBS), stored at −80°C, then diluted to aliquots of 1 μM in 1× PBS stored at −20°C. For experiments at Pomona College, the tripeptides were obtained either from EZBiolab or synthesized in the laboratory of Daniel O'Leary and stored in lyophilized form at −80°C. They were dissolved in milliQ water at 1 μM, aliquoted, and stored at −20°C. These peptides were acetylated at the N-terminus to optimize longevity by reducing access of proteases to the peptides (Adessi and Soto, 2002). sAPPα and sAPPβ were produced recombinantly in HEK 294T cells as previously described (Turner et al., 2007). $A\beta_{25-35}$ was obtained from Bachem; stock solutions (2 mM) were prepared in milliQ H_2O and stored at −20°C. We and others have found that $A\beta_{(25-35)}$ disrupts both tetanus-induced LTP (as shown here) and chemically induced LTP (Shankar et al., 2008). All treatment molecules were added to artificial cerebrospinal fluid (aCSF) at the appropriate volume to obtain the required working concentration. BFA and CHX were supplied by Sigma–Aldrich (St. Louis, MO, United States), and dissolved in DMSO (Sigma–Aldrich) to aliquots of 60 (CHX), or 35 mM (BFA), which were stored at −20°C, then thawed as needed and added to aCSF at 1:1000 to achieve the working concentration of 65 μM CHX and 0.1% DMSO in aCSF.

Slice Preparation

Rats and mice were decapitated following intraperitoneal injection with ketamine (rats, 100 mg/kg, i.p.) or inhalation of isoflurane (mice), respectively. Slices were prepared as has been previously described (Mockett et al., 2004; Hegemann and Abraham, 2019), briefly, the brain was removed and transferred directly into ice-cold cutting solution (in mM: 210 sucrose, 26 $NaHCO_3$, 20 D-glucose, 2.5 KCl, 1.25 NaH_2PO_4, 0.5 $CaCl_2$, 3 $MgCl_2$) supersaturated with carbogen gas (95% oxygen, 5% carbon dioxide). For rats the hippocampus was isolated by dissection and CA3 removed, while for mice whole brain slices were used. Slices were attached to an agarose platform for cutting into transverse slices of 400 μm using a vibratome (Leica, VT1000). Slices were then held in interface in humidified incubation chambers containing aCSF pre-warmed to 32°C (rat slices) or not pre-warmed (mouse slices) and supersaturated with carbogen (aCSF in mM: 124 NaCl, 3.2 KCl, 1.25 NaH_2PO_4, 26 $NaHCO_3$, 2.5 $CaCl_2$, 1.3 $MgCl_2$, 10 D-glucose). After a recovery period of 30 min, the incubation chamber was maintained at room temperature for at least 90 min before slices were transferred to the electrophysiology recording chamber. In the recording chamber, slices were superfused in solution saturated with carbogen gas and held at 32.5 (rat slices) or 23°C (mouse slices), with a flow rate of 2 mL/min. Differences in slicing procedures, recovery and recording temperatures, and species did not appear to affect the short- or long-term synaptic plasticity or basal synaptic transmission.

Field-Potential Electrophysiology

Recording electrodes were pulled from filament capillary glass (OD = 1 mm, ID = 0.58 mm, AM Systems or World Precision Instruments) to form micropipettes using a P-97 Flaming/Brown micropipette puller (Sutter Instrument Co., CA, United States). Recording micropipettes (1.8–2.8 MΩ) were filled with aCSF. For rat electrophysiology experiments, stimulation was delivered via 50 μm Teflon-insulated tungsten monopolar electrodes coupled to constant current custom-made programmable stimulators at 0.033 Hz (diphasic pulse, 0.1 ms half-wave duration). For mouse electrophysiology experiments, stimulation was delivered via a concentric bipolar electrode (Fred Haer #30202) driven by an Axon Instruments stimulus isolation unit. Stimulating electrodes were placed midway between stratum pyramidale and stratum lacunosum moleculare in stratum radiatum. The stimulus intensity was set to elicit responses 40% of the slope of the response generated by a strong 200 μA test pulse. Slices were excluded from experiments if the amplitude of the response did not reach an amplitude of −2.5 mV with a 200 μA pulse. Recordings from rat slices were fed to Grass® P511A.C. amplifiers via high-impedance probes, and recordings were amplified at 1000× gain, with half-amplitude filter cut-off frequencies of 0.3 Hz and 3 kHz. Recordings from mouse slices were amplified at 1000× gain using a Dagan IX amplifier, and digitized at 1 kHz using an AD Instruments PowerLab and analyzed using AD Instruments Scope software.

Stable baseline responses (defined as changing <10% in slope) were recorded for 20–30 min before delivery of drugs or peptides. Twenty-five to 30 min after peptide delivery, TBS was delivered (five bursts of five pulses at 100 Hz, 200 ms inter-burst interval; termed 0.5 TBS) to induce LTP. Five minutes after the TBS, the bath solution was returned to standard aCSF for the remainder of the experiment, which continued for 1 h post-TBS. Control and treatment conditions were randomly interleaved throughout the study. For electrophysiology, the fEPSP slopes 5 min prior to TBS were averaged and all slope data were normalized to this baseline value. Induction of LTP (PTP) was calculated as the first 10 sweeps (5 min) after the delivery of the TBS. The final level

of LTP was calculated as the average slope of the last 10 sweeps (5 min) of the protocol expressed as a percentage change from the baseline value. All values used for LTP statistics or figures refer to this average 55–60 min post-TBS unless otherwise stated.

Paired-pulse facilitation and PTP were used to assess peptide effects on presynaptic function. PPF was tested immediately prior to and at the end of 30 min perfusion with Ac-RER, by delivering paired stimuli (three pairs, 10 s apart, for each interpulse interval) with interpulse intervals ranging from 20 to 200 ms in the presence of D-AP5 (50 μM, Tocris). PPF was expressed as a ratio calculated as EPSP2 slope/EPSP1 slope. PTP was assessed in the same slices by delivery of three bouts of TBS (five bursts) with 30 s intervals. Recordings recommenced 5 s after the TBS. PTP was expressed as a ratio calculated as the first post-TBS EPSP amplitude/the average of the three EPSP amplitudes immediately preceding the TBS.

In experiments examining the ability of Ac-rER to protect slices from Aβ-impaired synaptic plasticity, LTP was induced with a single train of TBS of 10 bursts (at 5 Hz, with five pulses at 100 Hz per burst) in the absence or presence of $A\beta_{25-35}$ (200 nM). Previous work by others has indicated that full-length Aβ oligomers may not be necessary for synaptic impairment, as proteases in the brain seem to convert full-length Aβ to shorter toxic fragments, such as Aβ25-35 (Kubo et al., 2002; Haass and Selkoe, 2007). Indeed, Aβ25-35 can induce the cognitive impairment (Stepanichev et al., 2003), CA1 hippocampal impairment (Peña et al., 2010), and dendritic spine reduction (Kim et al., 2014) characteristic of synaptic dysfunction in AD (Pozueta et al., 2013).

SUnSET Assay of *de novo* Protein Synthesis

Rat CA1 mini-slices used for SUnSET *de novo* protein synthesis detection were prepared as described previously (Mockett et al., 2007). Briefly, after anesthetizing rats with ketamine and preparing hippocampal slices as described for electrophysiology, mini-slices were prepared by manually dissecting CA1 from the rest of the slice on an ice-cold platform, before transfer to 35 mm culture dishes (four to five per dish) containing 1 mL of aCSF saturated with carbogen. Dishes were held at 32.5°C in a custom designed incubation chamber (Mockett et al., 2007), where they were allowed to recover for a further 2 h, prior to addition of puromycin (10 μg/ml (∼18 μM), Sigma–Aldrich) and the relevant concentration of Ac-RER or PBS (no drug control). Slices were incubated for a further 30 min, then snap frozen on dry ice, and stored at −80°C prior to analysis.

The SUnSET technique (Schmidt et al., 2009) utilizes the incorporation of a structural analogue of aminoacyl tRNAs, puromycin, into nascent polypeptide chains as an indicator of global protein synthesis for the period the puromycin is present. It is used at a concentration (up to 18 μM), where it does not affect the overall rate of protein synthesis and thereby enables monitoring and quantification of rates of global protein synthesis in individual mammalian cells and in heterogeneous cell populations. Puromycin incorporation prevents further polypeptide elongation, thus labeling only polypeptides already undergoing synthesis during the time of exposure to puromycin. Newly synthesized molecules tagged with puromycin are detected immunologically using western blotting, which is then used to determine the relative levels of *de novo* protein synthesis in each of the treatment conditions. Protein extraction for the assay was achieved by submersion in detergent-containing buffer [100 mM phosphate-buffered saline pH 7.4, 1 mM EDTA, 1 mM EGTA, 0.1 mM phenylmethylsulfonyl fluoride (PMSF), 1% (v/v) Triton-X, 0.1% (w/v) sodium dodecyl sulfate (SDS), and a protease inhibitor (cOmplete Ultra Mini Tablet, Roche)] used as per manufacturer's instructions. Slices were then homogenized by pestle 30× and proteins were solubilized by probe sonication (10 pulses at 1 s each; Qsonica, CT, United States) to produce a lysate mixture. A DC protein assay (Bio-Rad) was used to quantify protein concentrations using BSA (Sigma–Aldrich) as a standard.

Protein samples were separated on 12% (w/v) *bis*-acrylamide (Bio-Rad) gels before transferring to a nitrocellulose membrane (GE Healthcare). Blots were incubated in Odyssey blocking buffer (LI-COR) at room temperature for 1 h. The primary antibody mouse anti-puromycin (1:1000, Kerafast EQ0001) and rabbit anti-tubulin (1:6666, Abcam ab4074) was prepared in PBS-Tween, 0.1% (w/v) BSA, and 0.1% (v/v) normal goad serum. The blots were incubated with the primary antibodies overnight at 4°C with shaking. The secondary antibody solution was composed of IRDye goat anti-rabbit 680 (1:10,000, LI-COR) and IRDye goat anti-mouse 800 (1:15,000, LI-COR) in PBS/Tween. The blots were incubated in this solution for 1 h at room temperature. Blots were imaged on a LI-COR Odyssey imaging system, quantified using Image Studio Lite 5.2 (LI-COR) after normalizing to the loading control protein (tubulin). To quantify each lane, an identical length box was used to determine relative intensity of the puromycin labeling across the whole lane. A small box (3 mm) above and below each band was used to define the background, and the overall signal was determined as area-normalized background subtracted from the average density of the box.

Data Analysis

Analysis was undertaken in Microsoft Excel for Mac 15.3 or GraphPad Prism 8.0. Results are expressed as the mean for each treatment group ± SEM. Differences between treatment groups were statistically assessed using one-way ANOVA at $p < 0.05$. Where *post hoc* testing was appropriate, Dunnett's test for multiple comparisons was used when comparing treatment groups to a control group, and where all groups were compared to each other, *post hoc* testing was conducted using Tukey's test for multiple comparisons. For direct comparison between two samples, or for comparison between the same samples before and after exposure to a treatment, a two-tailed *t*-test was performed. For analysis of PPF and PTP, a two-way repeated measure ANOVA was used at $p < 0.05$. All reported *n*-values are for the number of slices, where the number of animals was different to the number of slices an $a = x$-value is also reported to indicate the total number of animals used to produce the slices used. For mice the number of slices is always equal to the number of animals.

DATA AVAILABILITY STATEMENT

The datasets generated for this study are available on request to the corresponding author.

ETHICS STATEMENT

The animal study was reviewed and approved by the University of Otago Animal Ethics Committee and the Pomona College Institutional Animal Care and Use Committee.

AUTHOR CONTRIBUTIONS

JM, WT, SH, KDP, and WA designed the experiments. JM, EB, JN, VS, and BM undertook the experiments. KP provided critical sAPPα constructs. DO'L designed and synthesized critical tripeptides. JM wrote the initial manuscript. JM, BM, WT, SH, KDP, and WA edited the manuscript.

FUNDING

This work was supported by the Brain Research New Zealand and the New Zealand Health Research Council to WA, SH, and WT; the University of Otago provided funding for Ph.D. and writing for JM. The work of EB, JN, VS, DO'L and KDP was supported by funding from Pomona College.

ACKNOWLEDGMENTS

We thank David Kweon for technical assistance in undertaking the SUnSET assays.

SUPPLEMENTARY MATERIAL

The Supplementary Material for this article can be found online at: https://www.frontiersin.org/articles/10.3389/fncel.2019.00459/full#supplementary-material

REFERENCES

Adessi, C., and Soto, C. (2002). Converting a peptide into a drug: strategies to improve stability and bioavailability. *Curr. Med. Chem.* 9, 963–978. doi: 10.2174/0929867024606731

Burki, T. (2018). Alzheimer's disease research: the future of BACE inhibitors. *Lancet* 391:2486. doi: 10.1016/s0140-6736(18)31425-9

Claasen, A. M., Guevremont, D., Mason-Parker, S. E., Bourne, K., Tate, W. P., Abraham, W. C., et al. (2009). Secreted amyloid precursor protein-alpha upregulates synaptic protein synthesis by a protein kinase G-dependent mechanism. *Neurosci. Lett.* 460, 92–96. doi: 10.1016/j.neulet.2009.05.040

Cole, A. R., Noble, W., Van Aalten, L., Plattner, F., Meimaridou, R., Hogan, D., et al. (2007). Collapsin response mediator protein-2 hyperphosphorylation is an early event in Alzheimer's disease progression. *J. Neurochem.* 103, 1132–1144. doi: 10.1111/j.1471-4159.2007.04829.x

Drachman, D. A. (2014). The amyloid hypothesis, time to move on: amyloid is the downstream result, not cause, of Alzheimer's disease. *Alzheimers Dement.* 10, 372–380. doi: 10.1016/j.jalz.2013.11.003

Esch, F. S., Keim, P. S., Beattie, E. C., Blacher, R. W., Culwell, A. R., Oltersdorf, T., et al. (1990). Cleavage of amyloid beta peptide during constitutive processing of its precursor. *Science* 248, 1122–1124. doi: 10.1126/science.2111583

Fol, R., Braudeau, J., Ludewig, S., Abel, T., Weyer, S. W., Roederer, J. P., et al. (2015). Viral gene transfer of APPsalpha rescues synaptic failure in an Alzheimer's disease mouse model. *Acta Neuropathol.* 131, 247–266. doi: 10.1007/s00401-015-1498-9

Haass, C., and Selkoe, D. J. (1993). Cellular processing of beta-amyloid precursor protein and the genesis of amyloid beta-peptide. *Cell* 75, 1039–1042. doi: 10.1016/0092-8674(93)90312-e

Haass, C., and Selkoe, D. J. (2007). Soluble protein oligomers in neurodegeneration: lesson from the Alzheimer's amyloid β-peptide. *Nat. Rev. Mol. Cell Biol.* 8, 101–112. doi: 10.1038/nrm2101

Habib, A., Sawmiller, D., and Tan, J. (2017). Restoring soluble amyloid precursor protein alpha functions as a potential treatment for Alzheimer's disease. *J. Neurosci. Res.* 95, 973–991. doi: 10.1002/jnr.23823

Hayashi, T., and Huganir, R. L. (2004). Tyrosine phosphorylation and regulation of the AMPA receptor by SRC family tyrosine kinases. *J. Neurosci.* 24, 6152–6160. doi: 10.1523/jneurosci.0799-04.2004

Hegemann, R. U., and Abraham, W. C. (2019). "Electrophysiological investigation of metabotropic glutamate receptor-dependent metaplasticity in the hippocampus," in *Glutamate Receptors. Methods in Molecular Biology*, Vol. 1941, eds C. Burger, and M. Velardo, (New York, NY: Humana Press), 79–91. doi: 10.1007/978-1-4939-9077-1_7

Hensley, K., and Kursula, P. (2016). Collapsin Response mediator protein-2 (CRMP2) is a plausible etiological factor and potential therapeutic target in Alzheimer's disease: comparison and contrast with microtubule-associated protein tau. *J. Alzheimers Dis.* 53, 1–14. doi: 10.3233/JAD-160076

Herrup, K. (2015). The case for rejecting the amyloid cascade hypothesis. *Nat. Neurosci.* 18, 794–799. doi: 10.1038/nn.4017

Hick, M., Herrmann, U., Weyer, S. W., Mallm, J. P., Tschape, J. A., Borgers, M., et al. (2015). Acute function of secreted amyloid precursor protein fragment APPsalpha in synaptic plasticity. *Acta Neuropathol.* 129, 21–37. doi: 10.1007/s00401-014-1368-x

Kanninen, K., Goldsteins, G., Auriola, S., Alafuzoff, I., and Koistinaho, J. (2004). Glycosylation changes in Alzheimer's disease as revealed by a proteomic approach. *Neurosci. Lett.* 367, 235–240. doi: 10.1016/j.neulet.2004.06.013

Kim, B. K., Shin, M. S., Kim, C. J., Baek, S. B., Ko, Y. C., and Kim, Y. P. (2014). Treadmill exercise improves short-term memory by enhancing neurogenesis in amyloid beta-induced Alzheimer disease rats. *J. Exerc. Rehabil.* 10, 2–8. doi: 10.12965/jer.140086

Klausner, R. D., Donaldson, J. G., and Lippincott-Schwartz, J. (1992). Brefeldin a: insights into the control of membrane traffic and organelle structure. *J. Cell Biol.* 116, 1071–1080. doi: 10.1083/jcb.116.5.1071

Kubo, T., Nishimura, S., Kumagae, Y., and Kaneko, I. (2002). In vivo conversion of racemized β- amyloid to truncated and toxic fragments and fragment presence in the brains of Alzheimer's patients. *J. Neurosci. Res.* 70, 474–483. doi: 10.1002/jnr.10391

Kuhn, P. H., Wang, H., Dislich, B., Colombo, A., Zeitschel, U., Ellwart, J. W., et al. (2010). ADAM10 is the physiologically relevant, constitutive alpha-secretase of the amyloid precursor protein in primary neurons. *EMBO J.* 29, 3020–3032. doi: 10.1038/emboj.2010.167

Lawrence, J. L., Tong, M., Alfulaij, N., Sherrin, T., Contarino, M., White, M. M., et al. (2014). Regulation of presynaptic Ca2+, synaptic plasticity and contextual fear conditioning by a N-terminal beta-amyloid fragment. *J. Neurosci.* 34, 14210–14218. doi: 10.1523/JNEUROSCI.0326-14.2014

Li, H. L., Roch, J. M., Sundsmo, M., Otero, D., Sisodia, S., Thomas, R., et al. (1997). Defective neurite extension is caused by a mutation in amyloid beta/A4 (A beta) protein precursor found in familial Alzheimer's disease. *J. Neurobiol.* 32, 469–480. doi: 10.1002/(sici)1097-4695(199705)32:5<469::aid-neu3>3.3.co;2-5

Meziane, H., Dodart, J. C., Mathis, C., Little, S., Clemens, J., Paul, S. M., et al. (1998). Memory-enhancing effects of secreted forms of the beta-amyloid precursor protein in normal and amnestic mice. *Proc. Natl. Acad. Sci. U.S.A.* 95, 12683–12688. doi: 10.1073/pnas.95.21.12683

Mileusnic, R., Lancashire, C., Clark, J., and Rose, S. P. (2007). Protection against abeta-induced memory loss by tripeptide D-Arg-L-Glu-L-Arg. *Behav. Pharmacol.* 18, 231–238. doi: 10.1097/fbp.0b013e32814fcde9

Mileusnic, R., Lancashire, C. L., and Rose, S. P. (2004). The peptide sequence Arg-Glu-Arg, present in the amyloid precursor protein, protects against memory loss caused by a beta and acts as a cognitive enhancer. *Eur. J. Neurosci.* 19, 1933–1938. doi: 10.1111/j.1460-9568.2004.03276.x

Mileusnic, R., and Rose, S. P. (2011). The memory enhancing effect of the APP-derived tripeptide Ac-rER is mediated through CRMP2. *J. Neurochem.* 118, 616–625. doi: 10.1111/j.1471-4159.2011.07193.x

Misumi, Y., Misumi, Y., Miki, K., Takatsuki, A., Tamura, G., and Ikehara, Y. (1986). Novel blockade by brefeldin a of intracellular transport of secretory proteins in cultured rat hepatocytes. *J. Biol. Chem.* 261, 11398–11403.

Mockett, B. G., Brooks, W. M., Tate, W. P., and Abraham, W. C. (2004). Dopamine D1/D5 receptor activation fails to initiate an activity-independent late-phase LTP in rat hippocampus. *Brain Res.* 1021, 92–100. doi: 10.1016/j.brainres.2004.06.039

Mockett, B. G., Guevremont, D., Elder, M. K., Parfitt, K. D., Peppercorn, K., Morrissey, J., et al. (2019). Glutamate receptor trafficking and protein synthesis mediate the facilitation of LTP by secreted amyloid precursor protein-alpha. *J. Neurosci.* 39, 3188–3203. doi: 10.1523/JNEUROSCI.1826-18.2019

Mockett, B. G., Guevremont, D., Williams, J. M., and Abraham, W. C. (2007). Dopamine D_1/D_5 receptor activation reverses NMDA receptor-dependent long-term depression in rat hippocampus. *J. Neurosci.* 27, 2918–2926. doi: 10.1523/JNEUROSCI.0838-06.2007

Mockett, B. G., Richter, M., Abraham, W. C., and Muller, U. C. (2017). Therapeutic potential of secreted amyloid precursor protein APPsalpha. *Front. Mol. Neurosci.* 10:30. doi: 10.3389/fnmol.2017.00030

Morrissey, J. A., Mockett, B. G., Singh, A., Kweon, D., Ohline, S. M., Tate, W. P., et al. (2019). A C-terminal peptide from secreted amyloid precursor protein-α enhances long-term potentiation in rats and a transgenic mouse model of Alzheimer's disease. *Neuropharmacology* 157:107670. doi: 10.1016/j.neuropharm.2019.107670

Oh, M. C., Derkach, V. A., Guire, E. S., and Soderling, T. R. (2006). Extrasynaptic membrane trafficking regulated by GluR1 serine 845 phosphorylation primes AMPA receptors for long-term potentiation. *J. Biol. Chem.* 281, 752–758. doi: 10.1074/jbc.m509677200

Peña, F., Ordaz, B., Balleza-Tapia, H., Bernal-Pedraza, R., Marquez-Ramos, A., Carmina-Aparicio, L., et al. (2010). Beta-amyloid protein (25-35) disrupts hippocampal network activity: role of fyn-kinase. *Hippocampus* 20, 78–96. doi: 10.1002/hipo.20592

Plant, K., Pelkey, K. A., Bortolotto, Z. A., Morita, D., Terashima, A., Mcbain, C. J., et al. (2006). Transient incorporation of native GluR2-lacking AMPA receptors during hippocampal long-term potentiation. *Nat. Neurosci.* 9, 602–604. doi: 10.1038/nn1678

Pozueta, J., Lefort, R., and Shelanski, M. L. (2013). Review: synaptic changes in Alzheimer's disease and its models. *Neuroscience* 251, 51–65. doi: 10.1016/j.neuroscience.2012.05.050

Richter, M. C., Ludewig, S., Winschel, A., Abel, T., Bold, C., Salzburger, L. R., et al. (2018). Distinct in vivo roles of secreted APP ectodomain variants APPsα and APPsβ in regulation of spine density, synaptic plasticity, and cognition. *EMBO J.* 37:e98335.

Schmidt, E. K., Clavarino, G., Ceppi, M., and Pierre, P. (2009). SUnSET, a nonradioactive method to monitor protein synthesis. *Nat. Methods* 6, 275–277. doi: 10.1038/nmeth.1314

Shankar, G. M., Li, S., Mehta, T. H., Garcia-Munoz, A., Shepardson, N. E., Smith, I., et al. (2008). Amyloid-beta protein dimers isolated directly from Alzheimer's brains impair synaptic plasticity and memory. *Nat. Med.* 14, 837–842. doi: 10.1038/nm1782

Stepanichev, M. Y., Moiseeva, Y. V., Lazareva, N. A., Onufriev, M. V., and Gulyaeva, N. V. (2003). Single intracerebroventricular administration of amyloid-beta (25-35) peptide induces impairment in short-term rather than long-term memory in rats. *Brain Res. Bull.* 61, 197–205. doi: 10.1016/s0361-9230(03)00118-7

Tan, V. T. Y., Mockett, B. G., Ohline, S. M., Parfitt, K. D., Wicky, H. E., Peppercorn, K., et al. (2018). Lentivirus-mediated expression of human secreted amyloid precursor protein-alpha prevents development of memory and plasticity deficits in a mouse model of Alzheimer's disease. *Mol. Brain* 11:7. doi: 10.1186/s13041-018-0348-9

Taylor, C. J., Ireland, D. R., Ballagh, I., Bourne, K., Marechal, N. M., Turner, P. R., et al. (2008). Endogenous secreted amyloid precursor protein-alpha regulates hippocampal NMDA receptor function, long-term potentiation and spatial memory. *Neurobiol Dis.* 31, 250–260. doi: 10.1016/j.nbd.2008.04.011

Turner, P. R., Bourne, K., Garama, D., Carne, A., Abraham, W. C., and Tate, W. P. (2007). Production, purification and functional validation of human secreted amyloid precursor proteins for use as neuropharmacological reagents. *J. Neurosci. Methods* 164, 68–74. doi: 10.1016/j.jneumeth.2007.04.001

Williams, J. M., Guevremont, D., Mason-Parker, S. E., Luxmanan, C., Tate, W. P., and Abraham, W. C. (2007). Differential trafficking of AMPA and NMDA receptors during long-term potentiation in awake adult animals. *J. Neurosci.* 27, 14171–14178. doi: 10.1523/jneurosci.2348-07.2007

Zhang, H., Ma, Q., Zhang, Y. W., and Xu, H. (2012). Proteolytic processing of Alzheimer's beta-amyloid precursor protein. *J. Neurochem.* 120(Suppl. 1), 9–21. doi: 10.1111/j.1471-4159.2011.07519.x

Conflict of Interest: The authors declare that the research was conducted in the absence of any commercial or financial relationships that could be construed as a potential conflict of interest.

Copyright © 2019 Morrissey, Bigus, Necarsulmer, Srinivasan, Peppercorn, O'Leary, Mockett, Tate, Hughes, Parfitt and Abraham. This is an open-access article distributed under the terms of the Creative Commons Attribution License (CC BY). The use, distribution or reproduction in other forums is permitted, provided the original author(s) and the copyright owner(s) are credited and that the original publication in this journal is cited, in accordance with accepted academic practice. No use, distribution or reproduction is permitted which does not comply with these terms.

frontiers in Molecular Neuroscience

REVIEW
published: 25 October 2019
doi: 10.3389/fnmol.2019.00258

The Role of Microglia and Astrocytes in Huntington's Disease

*Thulani H. Palpagama, Henry J. Waldvogel, Richard L. M. Faull and Andrea Kwakowsky**

Centre for Brain Research, Department of Anatomy and Medical Imaging, Faculty of Medical and Health Sciences, University of Auckland, Auckland, New Zealand

Huntington's disease (HD) is an autosomal dominant neurodegenerative disease. HD patients present with movement disorders, behavioral and psychiatric symptoms and cognitive decline. This review summarizes the contribution of microglia and astrocytes to HD pathophysiology. Neuroinflammation in the HD brain is characterized by a reactive morphology in these glial cells. Microglia and astrocytes are critical in regulating neuronal activity and maintaining an optimal milieu for neuronal function. Previous studies provide evidence that activated microglia and reactive astrocytes contribute to HD pathology through transcriptional activation of pro-inflammatory genes to perpetuate a chronic inflammatory state. Reactive astrocytes also display functional changes in glutamate and ion homeostasis and energy metabolism. Astrocytic and microglial changes may further contribute to the neuronal death observed with the progression of HD. Importantly, the degree to which these neuroinflammatory changes are detrimental to neurons and contribute to the progression of HD pathology is not well understood. Furthermore, recent observations provide compelling evidence that activated microglia and astrocytes exert a variety of beneficial functions that are essential for limiting tissue damage and preserving neuronal function in the HD brain. Therefore, a better understanding of the neuroinflammatory environment in the brain in HD may lead to the development of targeted and innovative therapeutic opportunities.

Keywords: neuroinflammation, huntington's disease, neurodegeneration, astrocytes, microglia

OPEN ACCESS

Edited by:
Robert J. Harvey, University of the Sunshine Coast, Australia

Reviewed by:
Jenny Sassone, Vita-Salute San Raffaele University, Italy
Christopher Alan Reid, Florey Neuroscience Institutes, Australia

****Correspondence:***
Andrea Kwakowsky
a.kwakowsky@auckland.ac.nz

Received: *18 May 2019*
Accepted: *10 October 2019*
Published: *25 October 2019*

Citation:
Palpagama TH, Waldvogel HJ, Faull RLM and Kwakowsky A (2019) The Role of Microglia and Astrocytes in Huntington's Disease. Front. Mol. Neurosci. 12:258. doi: 10.3389/fnmol.2019.00258

INTRODUCTION

Initially, neuroinflammation has been used to describe the infiltration of peripheral immune cells in the central nervous system (CNS), however, the term is currently also used in relation to neurodegenerative diseases. In these conditions such as Huntington's disease (HD), Alzheimer's disease (AD), Parkinson's disease (PD) and Amyotrophic lateral sclerosis (ALS) neuroinflammation is characterized by a reactive morphology of glial cells, including both astrocytes and microglia, along with the presence of inflammatory mediators in the brain parenchyma (Ransohoff, 2016a; Masgrau et al., 2017). Previous studies have identified changes in microglia, astrocytes, circulating cytokine levels, infiltration of macrophages along with changes in the transcription of genes

associated with the control of inflammation, in HD (Ben Haim et al., 2015a; Crotti and Glass, 2015; Ransohoff, 2016a).

Here, we will overview the astrocytic and microglial neuroinflammatory changes in HD presented in the literature. Whether this neuroinflammatory response is protective or damaging along with its role in controlling pathways leading to cell death is still not well understood (Ellrichmann et al., 2013; Crotti and Glass, 2015). However, considerable recent research is focused on understanding the role neuroinflammation plays in the progression of the disease.

HUNTINGTON'S DISEASE PATHOLOGY

HD is an autosomal dominant, genetic disease of the brain. Gene mapping studies carried out by Gusella et al. (1983) identified the genetic origin of HD as a mutation on the short arm of chromosome 4. This mutation, at locus 4p16.3, in the IT15 gene, was discovered to be an expansion of a CAG repeat in the huntingtin (HTT) gene resulting in an expanded polyglutamine tract (The Huntington's Disease Collaborative Research Group, 1993). A CAG repeat length of up to 35 repeats generally does not result in the onset of HD (Reiner et al., 2011; Dayalu and Albin, 2015). However, individuals with repeat numbers from 36 up should be viewed at as at risk of developing HD (Ha et al., 2012; Nance, 2017). CAG repeat lengths of greater than 40 are associated with a definite onset of HD within a normal lifespan (Reiner et al., 2011). Strikingly, an inverse correlation between the age of onset and CAG repeat length has been found through correlative studies (Andrew et al., 1993). This is thought to account for around 50–70% of the variation in the age of onset (Andrew et al., 1993; Myers, 2004; Ross and Tabrizi, 2011; Dayalu and Albin, 2015).

The diffuse degeneration of the striatum has become one of the hallmarks of HD progression (Vonsattel et al., 1985; Vonsattel, 2008). Degeneration in the striatum (caudate nucleus and putamen) has been found to move in the caudo-rostral, dorso-ventral and medio-lateral directions (Vonsattel et al., 1985). Brain weight is reduced in later stages of the disease and this is consistent with the reported heterogeneous cortical degeneration. Though initially described as degeneration of the striatum, widespread cortical atrophy has been reported in the HD brain. The degeneration of these brain regions has been linked to the presentation of clinical symptoms (Thu et al., 2010; Kim et al., 2014; Nana et al., 2014; Mehrabi et al., 2016; Singh-Bains et al., 2019).

Choreatic movements were first described in patients by George Huntington (Huntington, 2003). Since then a multitude of symptoms including movement-, cognitive-, mood- and psychiatric disorders have been identified in patients. As the disease progresses, the symptoms that patients present with change and vary between cases (Novak and Tabrizi, 2011). Some patients mainly exhibit motor dysfunction at clinical onset, and few if any mood symptoms. While others have severe mood and/or cognitive dysfunction at the clinical onset, but no or few movement changes. Others experience concomitant motor, mood and cognitive symptoms at onset. This clinical variability is demonstrated well in monozygotic twins with identical HD genes but marked differences in their behavioral symptoms (Georgiou et al., 1999).

The most common motor behavior symptom of HD is chorea, these unwanted rapid, short-lasting movements can be observed in all muscles of the trunk, face, and extremities. All patients also show mild or more severe parkinsonian symptoms, slowness in starting movement (akinesis), slowness in executing a movement (bradykinesia), showing fewer spontaneous automatic movements, and decrease in all motor activities (hypokinesia). The unwanted movements and increased muscle tone can result in dystonia, slowly twisting and turning movements. Tics, mainly occurring in the face and the arms are sometimes present but the patients are usually aware of these movements and some can learn to suppress them. Every patient has a specific pattern of motor behavior that is genetically and culturally determined (Shannon, 2011).

HD has been associated with pathological changes in multiple brain regions and the manifestation of cognitive symptoms effect a wide variety of skills. Declines in cognitive processing speed, executive function, working memory, visuomotor control and time production have been reported (Paulsen et al., 2017). Difficulties to maintain attention also lead to a reduction in memory function and in later stages of the disease a complete clinical picture of dementia develops (Nance, 2017). The most common psychiatric symptoms, with prevalence of 33%-76%, include depressed mood, anxiety, irritability, and apathy. Obsessive-compulsive symptoms and psychosis occur less often, with prevalence of 10%–52% and 3%–11%, respectively (van Duijn et al., 2007). Loss of body weight, sleep disturbances and autonomic disturbances that include hyperhidrosis, heat and cold intolerance, sialorrhoea, micturition and swallowing difficulties, and sexual dysfunction are secondary signs of HD (Aziz et al., 2010).

MICROGLIA

Making up 5%–10% of the cells in the brain, microglia have long been considered the resident immune cells of the brain (Frost and Schafer, 2016). When no inflammatory stimulus is present, microglia are in a surveilling state. Following an inflammatory stimulus, microglia become activated in order to respond to the stimulus and take part in an inflammatory response (**Figure 1**). Changes in morphology and transcriptional activation take place in the transition of microglia from surveilling to activated (Boche et al., 2013; Crotti and Glass, 2015). Surveilling microglia exhibit a ramified morphology. These microglia show more extensive branching and processes when in a surveilling state (Glenn et al., 1992). While in the surveilling state, microglial cells survey the area around their cell bodies, by dynamic reorganization of the microglial processes, to ensure the maintenance of homeostasis. This was demonstrated through an elegant set of experiments by Nimmerjahn et al. (2005) using *in vivo* two-photon imaging of the neocortex, they showed that microglial processes displayed remarkable motility and were able to cyclically form and

withdraw. Microglia further showed filopodia like protrusions along their processes. Microglia maintain a surveilling state due to the presence of contact receptor-ligand interactions, such as neuronal CD200 and microglial CD200 receptors, molecules released from neurons, such as CX3CL1 (also known as fractalkine) that act on microglial CX3CL1 receptors, and lipid mediators released from microglia, such as endocannabinoids (Hanisch and Kettenmann, 2007; Benarroch, 2013).

In the surveilling state, microglia have multiple roles in homeostasis. One such role is the maintenance of synapses and synaptic plasticity through facilitation of synaptic maturation, pruning and elimination (Tremblay and Majewska, 2011; Schafer and Stevens, 2015). This is achieved through the interactions between microglial processes, synaptic clefts, spines, termini and astrocytic processes which allow microglia to alter neural activity and structural environmental components. Microglia also facilitate the role of growth and development of surrounding neural networks by secreting neurotrophic factors, such as brain-derived neurotrophic factor (BDNF), nerve growth factor (NGF) and insulin-like growth factor (IGF-1; Nayak et al., 2014). There is significant evidence to suggest a role of microglia in promoting neurogenesis by phagocytosing apoptotic neural progenitor cells, facilitating the migration and differentiation of neural progenitor cells and secreting soluble factors which promote neurogenesis (Lira-Diaz and Gonzalez-Perez, 2016). Finally, upon detecting inflammatory stimuli, surveilling microglia can become activated and are a major part of the neuroinflammatory response (Crotti and Glass, 2015; Hickman et al., 2018). Following detection of inflammatory stimuli, such as damage associated molecular proteins (DAMPs) molecules and cytokines, microglia undergo morphological changes entering into an activated state (Boche et al., 2013). Activated microglia have a phagocytic role and are motile. Along with an active role in neuroinflammation, activated microglia also have been shown to have a role in synaptic plasticity and neuronal growth and survival (Lull and Block, 2010).

Activated microglia can adopt different states, commonly this polarization has been categorized as M1 and M2 states, and microglial cells can alternate between the two states. Recently the use of M1/M2 terminology to categorize microglial activation has been questioned (Ransohoff, 2016b) however, we will introduce the concept before discussing why this terminology is outdated in the light of recent research. M1 microglia are suggested to have a more "classic" role in the inflammatory response and are thought to be the major initiators of both innate and adaptive immunity in the brain (Nakagawa and Chiba, 2014). These cells have a phagocytic function and will release cytotoxic factors such as nitric oxide (NO), reactive oxygen species (ROS) and quinolinic acid to confer toxicity to invading pathogens (Lull and Block, 2010; Benarroch, 2013; Nakagawa and Chiba, 2014). Promotion of nuclear factor of kappa light polypeptide gene enhancer in B-cells (NF-κB) regulated transcription further results in the release of pro-inflammatory cytokines such as tumor necrosis factor alpha (TNF-α), interleukin 1 β (IL-1β) and interleukin 6 (IL-6; Lull and Block, 2010; Benarroch, 2013). These, pro-inflammatory cytokines enhance and stimulate the inflammatory response. Activated M1 microglia also show an upregulation in surface proteins which confer a role in an innate inflammatory response, such as MHC proteins which are critical in antigen presentation to T-cells (Lull and Block, 2010; Benarroch, 2013).

M2 microglia also carry out phagocytosis but contrary to the role of M1 microglia, M2 microglia exhibit an anti-inflammatory role (Nakagawa and Chiba, 2014). This is through the release of anti-inflammatory mediators such as interleukin 4 (IL-4), interleukin 13 (IL-13), IL-10 and transforming growth factor beta (TGF-β) to suppress inflammatory responses (Nakagawa and Chiba, 2014; Tang and Le, 2016). Anti-inflammatory cytokines inhibit initial phases of the immune response. Given the opposing roles of M1 and M2 microglia, it has been postulated that polarization of microglia to M1 or M2 states controls either promotion or resolution of inflammation in the brain (Nakagawa and Chiba, 2014). M2 microglia also have a role in tissue repair following the detection of anti-inflammatory cytokines, such as IL-13 and IL-4, from T helper cells and signals from apoptotic cells (Benarroch, 2013; Tang and Le, 2016).

However, *ex vivo* genome-wide expression profiling of microglia from different disease model mice failed to support the M1/M2 polarization theory (Chiu et al., 2013; Morganti et al., 2016; Wes et al., 2016). While polarization along the M1/M2 axis was not found, a consistent expression pattern profile has been observed specific for healthy and disease states in mice (Chiu et al., 2013; Bennett et al., 2016; Wes et al., 2016). Furthermore, microglia demonstrate a dynamic expression phenotype influenced by the local environment and stimuli but there is no evidence that this response promotes repair (Ransohoff, 2016b). The M1/M2 terminology in the light of findings from several recent studies has to be revised and based on transcriptomic and proteomic profiles of microglia obtained *ex vivo* from experimental subjects of healthy and different disease states, with trauma, infection, during development and aging (Bennett et al., 2016; Ransohoff, 2016b; Wes et al., 2016).

In the aged brain, microglia have also been observed to adopt an increased inflammatory profile (Norden and Godbout, 2013). This is a phenomenon referred to as microglial priming and refers to the upregulation of proteins such as major histocompatibility complex class II (MHCII) molecules, integrins and toll-like receptors which are activated in an inflammatory response (Norden and Godbout, 2013). This may contribute to the chronic inflammation seen in several neurodegenerative diseases including AD, PD and HD.

MICROGLIAL CONTRIBUTION TO HUNTINGTON'S DISEASE

Microglial Pathology

Microglia are primary mediators of neuroinflammation (Ransohoff and Perry, 2009; Ellrichmann et al., 2013; Crotti and Glass, 2015; Ransohoff, 2016a; Hickman et al., 2018). Changes in morphology and gene expression in microglia may underpin neuronal death in HD (**Figure 1**). When an insult to the brain occurs, surveilling microglia become activated and

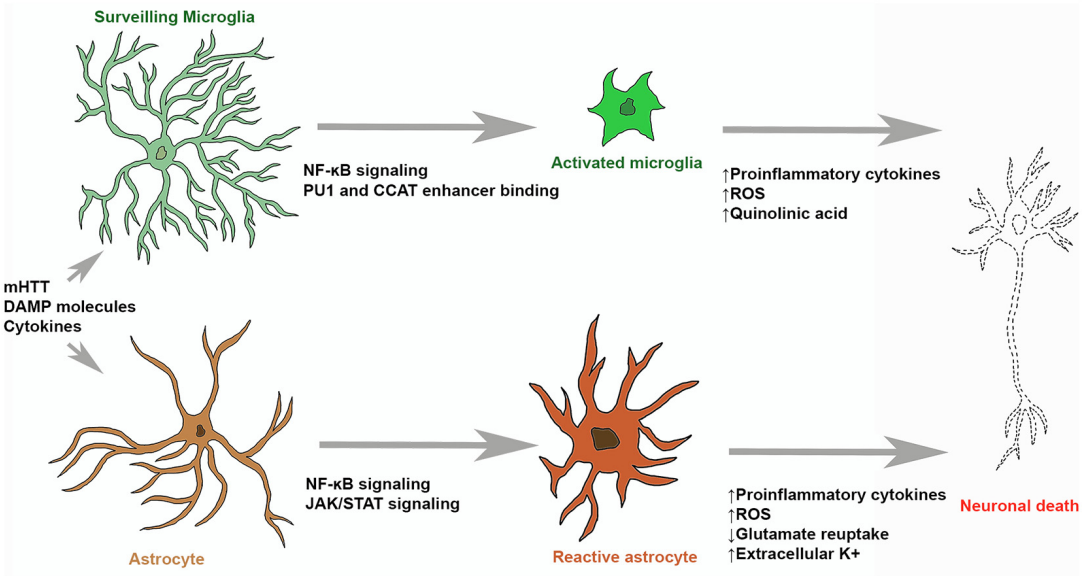

FIGURE 1 | Microglial and astrocytic contribution to neuronal death in Huntington's disease (HD). Surveilling microglia are activated by stimulating molecules through NF-κB signaling, upregulation of PU1 and CCAT binding. Activated microglia and reactive astrocytes produce reactive oxygen species (ROS) and neurotoxic molecules (such as quinolinic acid) which can induce molecular processes leading to neuronal death. Stimulatory molecules also induce reactive astrogliosis that leads to the upregulation of pro-inflammatory cytokine production, glutamate excitotoxicity and hyperexcitability of neurons.

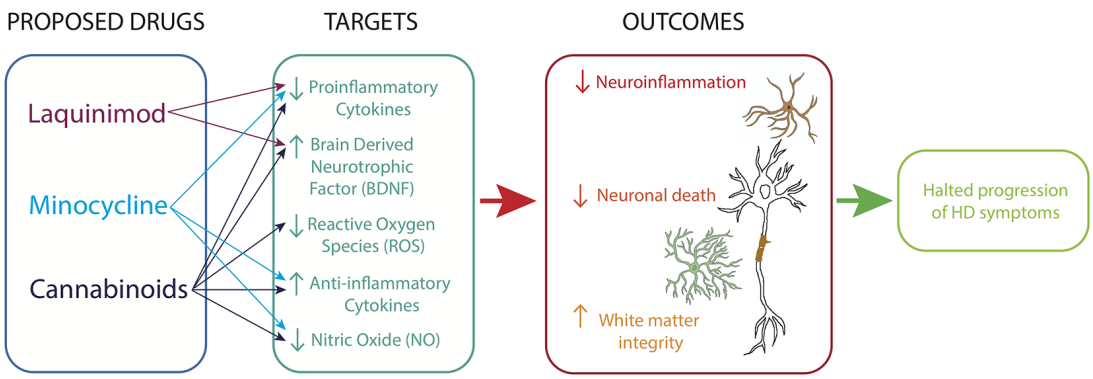

FIGURE 2 | Immunomodulatory therapy for HD. Drugs acting on microglia, astrocytes and neurons reduce neuroinflammatory processes, promote neurotrophic support and sustain white matter integrity.

initiate innate immunity in the CNS. With continued activation of microglia, prolonged production of inflammatory mediators by microglia results in chronic inflammation and implicated in further tissue damage (Ellrichmann et al., 2013). Atrophy of the striatum (caudate nucleus, putamen and globus pallidus) is the neuropathological hallmark of HD (Vonsattel et al., 1985). Immunohistochemical experiments in human HD brain tissue identified the presence of reactive microglia in the neostriatum, cortex and globus pallidus which were absent in control brain tissue (Sapp et al., 2001; Vonsattel et al., 1985, 2011). A study also noted that the number of activated microglia in the striatum and cortex showed a direct correlation with degree of neuronal loss and that microglia were closely associated with pyramidal neurons, suggesting that neuroinflammatory changes might be induced by the degenerating neurons (Sapp et al., 2001). In fact, infiltration of peripheral inflammatory cells is not an usual feature of HD (Sapp et al., 2001; Vonsattel et al., 1985). A study by Pavese et al. (2006) used Positron Emission Tomography (PET) imaging to identify markers of activated microglia and striatal GABAergic neurons in HD patients at varying stages of disease progression showed increased microglial activation with greater disease severity and striatal neuron loss. Interestingly, they also identified an increase in microglial activation in the anterior cingulate and prefrontal cortices (Pavese et al., 2006; Tai et al., 2007a,b). Microglia activation was also identified in PET studies undertaken in presymptomatic HD gene carriers.

These studies identified microglial activation as an early change in HD, prior to symptom onset (Tai et al., 2007b; Politis et al., 2015). Increased microglial activation was also detected in the striatum of presymptomatic R6/2 mice, a mouse model of HD expressing human mHTT exon 1 containing 150 CAG repeats (Simmons et al., 2007).

As mentioned above influx of peripheral immune cells such as lymphocytes and neutrophils has not been found in the HD brain and neuroinflammation is most likely sustained by the interactions of microglia, macroglia, neurons and inflammatory mediators released by these and other cells in the brain parenchyma or possibly infiltrated from periphery (Sapp et al., 2001; Silvestroni et al., 2009; Vonsattel et al., 1985). The literature suggests an upregulation of activated microglia in a number of human and animal HD studies and also reporting increases in cytokines secreted by microglia (Björkqvist et al., 2008; Yang et al., 2017). Peripheral inflammatory response has been well described in HD, key cytokines of the innate immune system are upregulated both centrally and peripherally. C-reactive protein and cytokine profile were altered in human plasma and mouse serum samples from three different mouse models (Stoy et al., 2005; Björkqvist et al., 2008; Sánchez-López et al., 2012). Elevations in IGF-β, IL-1β, IL-6, IL-8, IL-10, TNF-α, TGF-β, CCL2 and matrix metallopeptidase 9 (MMP-9) were measured in HD patient plasma, CSF and post-mortem brain tissue using ELISA and quantitative real time polymerase chain reaction (qRT-PCR; Björkqvist et al., 2008; Silvestroni et al., 2009; Chang et al., 2015; Politis et al., 2015). Some of these inflammatory mediators such as IL-1β and TNF-α showed increased levels only in the striatum but others, IL-6, IL-8 and MMP-9 were also upregulated in cortical regions and the cerebellum. These findings suggest that in contrast to other neurodegenerative diseases, such as AD and PD with a more generalized neuroinflammatory profile and a wide range of inflammatory mediators, the HD brain is characterized with a very different neuroinflammatory characteristics (Möller, 2010). In HD, cytokines such as IL-4 and IL-10 are increased at later stages of the disease, but normal Ig levels throughout the disease course suggest that there is no generalized activation of the adaptive immune response (Björkqvist et al., 2008). IL-6 and IL-8 production are triggered by NF-κB activation, while IL-4 and IL-10 act to downregulate NF-κB (Khoshnan et al., 2004; Björkqvist et al., 2008). This might suggest an adaptive response to chronic immune activation.

The correlation between plasma and CSF levels of cytokines such as IL-6 and IL-8 suggests that the central and peripheral immune activation in HD are linked. There is evidence that these cytokines do not cross the healthy blood-brain barrier and they are rapidly broken down after release but passage between the CNS and blood still remains a possibility (Steensberg et al., 2006; Pan and Kastin, 2007; Björkqvist et al., 2008). While microglia are considered as one of the main sources of cytokine production in the HD brain, their release could also be caused by monocytes, macrophages, astrocytes and other cell types such as endothelial cells and pericytes which are components of the neurovascular unit (Björkqvist et al., 2008; Govindpani et al., 2019). The role of upregulated mHTT in this process has been extensively investigated.

mHTT Accumulation and Microglial Activation

mHTT accumulation in neurons also has been linked to the activation of microglia. In primary neuronal cultures and cortico-striatal brain slices, from rat and mouse brain tissue, elevated numbers of microglia with an activated phenotype were observed in concurrence with the expression of mHTT in neurons and these microglia were positioned along irregular neurites (Kraft et al., 2012). The presence of mHTT inclusions in microglia have also been identified (Jansen et al., 2017). The cell autonomous expression of mHTT has also been implicated in the activation of microglia (Crotti et al., 2014; Yang et al., 2017). In genome wide studies, Crotti et al. (2014) found that an increase in the expression and transcriptional activity of PU.1 and CCAT/enhancer-binding protein in mHTT expressing microglia when compared to microglia not expressing the mHTT. The authors postulate that this leads to the enhanced transcription of basal pro-inflammatory gene expression and, in turn, increased levels of pro-inflammatory cytokines can perpetuate further inflammation and tissue damage. Furthermore, astrocytes isolated from R6/2 mice observed to react hyperactively to stimulation when compared to those isolated from wildtype mice, with the authors of this study postulating this was due to mHTT expression in microglia (Björkqvist et al., 2008). A recent study demonstrated that microglia expressing mHTT show significant elevations in NF-κB when stimulated with IL-6 but not when stimulated with LPS. This suggests that mHTT may alter immune responses in microglia in a stimuli dependent manner (Donley et al., 2019). However, the degree of the effect these microglial changes have on pathology of HD has come under scrutiny in a recent study. In this study depletion of mHTT in microglia of BACHD mice showed no significant rescue of behavioral performance, brain weight or striatal and cortical volume. Conversely depleting mHTT in all other cells except microglia resulted in rescue of behavioral performance and neuropathology (Petkau et al., 2019). However, while the presence of microglial changes due to the presence of mHTT may not be sufficient to induce the HD phenotype, it may contribute to pathology in conjunction with further changes in the brain. A future area of research could be to carry out similar studies on different animal models to corroborate these findings.

Major Signaling Pathways Implicated in Microglial Activation

A number of key signaling pathways have been implicated in the activation of microglia in HD. These include NF-κB signaling, the kyurenine pathway and the cannabinoid receptor pathway. As discussed above, the NF-κB signaling has been elucidated in the literature as a key pathway through which mHTT induces the activation of microglia in HD (Khoshnan et al., 2004; Khoshnan and Patterson, 2011). mHTT interacts with the IκB kinase (IKK) γ subunit of the IKK complex. This promotes the assembly and activation of the IKK complex

which contains the IKKα and IKKβ subunits. The IKKβ kinase phosphorylates IκBα, causing the liberation of NFκB to promote the gene expression of pro-inflammatory cytokines (Häcker and Karin, 2006; Khoshnan and Patterson, 2011). Khoshnan et al. (2004) demonstrated through immunohistochemistry, immunoprecipitation, western blotting and GST pulldown assays that mHTT interacts with IKKγ in a PC12 cell culture and that the IKK complex showed increased activity. This has also been observed in the striatum and cortex of R6/2 mice expressing mHTT (Khoshnan et al., 2004). Träger et al. (2014) corroborated that mHTT interacts with the IKK complex to allow signaling *via* the NF-κB pathway in peripheral blood mononuclear cells from HD patients. Lowering mHTT *via* the use of targeted siRNA alleviated excessive NF-κB signaling with a reduction in the levels of pro-inflammatory cytokines (Träger et al., 2014). Few recent studies have reported the interaction of mHTT and NF-κB in microglia in particular, but the presence of such interaction in myeloid cells and monocytes suggests that such a pathway may underlie the activation of microglia in HD.

A growing area of research in the role of microglia in HD focuses on the kynurenine pathway. This pathway for L-tryptophan metabolism produces several metabolites with neuroactive properties (Schwarcz et al., 2010). Tryptophan is metabolized to the neurotoxic quinolinic acid (QUIN) and 3-hydroxykynurenine (3HK) by the enzyme kyurenine 3-monooxygenase (KMO). QUIN is postulated to have a role in neurotoxicity as it is a selective agonist of N-Methyl-D-aspartic acid (NMDA) receptors while 3HK has a role in potentiating QUIN. Genome wide screening in yeast found the genes *BNA4* and *BNA1* coding for KMO and 3-hydroxyanthranilate 3, 4 dioxygenase respectively, regulated mHTT toxicity through its role in the production of QUIN and 3HK (Giorgini et al., 2005). In low-grade human HD tissue, elevations in 3HK and QUIN have been reported in the neostriatum and neocortex however these levels remained unchanged or declined with further progression of the disease. Therefore, it was postulated that the neurotoxic contribution kyurenine pathway metabolites may be involved in the early stages of HD pathophysiology (Guidetti et al., 2004). 3HK levels were elevated in the striatum and cortex of R6/2 mice and in primary microglial cultures from R6/2 mice and KMO activity was elevated in R6/2 mice as well (Giorgini et al., 2008). This increase of neurotoxic metabolites of the kynurenine pathway can be reduced in R6/2 mice by treatment with histone deacetylase inhibitors and these results might suggest the use of these agents as potential therapeutics to treat HD (Giorgini et al., 2008).

Altered activation of the cannabinoid pathway has also been observed in HD. Signaling through CB2 receptors have been shown to reduce immune activation in the brain. Real time PCR experiments revealed increased CB2 transcript levels in R6/2 mice, and mice with a genetic deletion of CB2 showed increased microglial activation and worse behavioral performance than standard R6/2 mice (Palazuelos et al., 2009). Western blotting experiments further showed an elevated expression of CB2 receptors in the caudate and putamen of HD patients when compared to control tissue (Palazuelos et al., 2009). Further immunohistochemistry experiments revealed expression of CB2 receptors on microglia striatum and the caudate-putamen of HD patients and R6/2 mice, but not on astrocytes. CB2 was also found expressed in microglia using immunohistochemistry in a malonate lesion rat model of HD (Sagredo et al., 2009). Dowie et al. (2014) however, reported that in human post mortem tissue there was an absence in CB2 receptors in microglia along with astrocytes using immunohistochemistry. This discrepancy may be due to the markers for microglia used. Dowie et al. (2014) used Iba1 while Palazuelos et al. (2009) used CD-68. Along with microglia, CD-68 is also present in monocytes which might have been stained in this study as well. A further study determined that CB2 ablation in BACHD mice resulted in poorer performance in the balance beam behavioral task (Bouchard et al., 2012). However, this study concluded that suppression of neuroinflammation is likely through CB2 signaling in peripheral immune cells rather than resident microglia in the brain. These findings highlight a weakness in current mouse models at recapitulating HD, wherein mouse models, it appears that microglia are responsible for inflammatory suppression through CB2 signaling pathways while this does not appear to be the case in the humans.

ASTROCYTES

Astrocytes are one of the most prevalent glial cell types in the mammalian brain (von Bartheld et al., 2016). They are characteristic star-shaped cells with many processes that envelop synapses made by neurons. Astrocytes have specialized processes called astrocyte end-feet that extend from the astrocyte cell body and attach to the basement membrane that surrounds the endothelial cells and pericytes on the brain vasculature. Over the last few decades increasing evidence suggests that besides their housekeeping function astrocytes carry out a number of roles in maintenance and control of healthy brain function (Verkhratsky and Nedergaard, 2018). They are involved in synaptic function by regulating synapse formation and maturation, neurotransmitter homeostasis and release of gliotransmitters; they regulate pH, water and ion homeostasis; they form an integral part of the blood-brain barrier and are involved in regulation of neurovascular coupling, vascular tone and blood flow (Simard and Nedergaard, 2004; Benarroch, 2005; Blackburn et al., 2009; Sofroniew and Vinters, 2010; MacVicar and Newman, 2015; Verkhratsky and Nedergaard, 2018; Govindpani et al., 2019). Astrocytes form broad cellular networks connected through gap junctions, which allow intercellular diffusion of ions, second messengers and small molecules. Astrocytic intercellular diffusion has been reported for cyclic AMP, inositol-1,4,5-trisphosphate (InsP3), Ca^{2+}, glutamate, adenosine triphosphate (ATP) and energy metabolites (glucose, glucose-6-phosphate and lactate; Nagy et al., 1999; Tabernero et al., 2006). Neurovascular coupling, the local perfusion that occurs in response to changes in neuronal activity, is primarily mediated at the level of the neurovascular unit (Muoio et al., 2014). Astrocytes as integral parts of the neurovascular unit are key regulators of neurovascular coupling and help to meet dynamic energy requirements in the brain. As mentioned above astrocytes and other components of the NVU are functionally linked *via* gap

junctions, adhesion molecules and the local release of vasoactive agents and neuromodulators. The release of these molecules in particular by interneurons and astrocytes is critical for the rapid and precise modulation of blood flow as well as vascular cell function and homeostasis in response to local metabolic demand (Muoio et al., 2014; Nuriya and Hirase, 2016; Mishra, 2017).

Astrocytic processes lie in close contact with neuronal somata, bundles of axonal internodes and synapses. Astrocytes mediate synaptic function through controlling the levels of various neurotransmitters at the synapse (Blackburn et al., 2009; Chung et al., 2015; Sofroniew and Vinters, 2010). By controlling the levels of γ-aminobutyric acid (GABA) production through provision of glutamine to neurons, and GABA clearance, affecting the time that GABA is left at the synaptic cleft, astrocytes regulate the inhibition of post-synaptic neurons (Blackburn et al., 2009; Schousboe et al., 2013; Sofroniew and Vinters, 2010). Glutamine is also a precursor to the synthesis of glutamate and glutamatergic neurons are supplied glutamine by astrocytes after astrocytic uptake of synaptic glutamate and its metabolism (Bélanger and Magistretti, 2009). Cycling of glutamine to neurons ensures that depletion of glutamate at synapses does not occur and neurotransmission can resume (Bélanger and Magistretti, 2009). The uptake of glutamate from the synapse by astrocytes is particularly important as prolonged exposure to excess glutamate can result in glutamate-mediated excitotoxicity (Bélanger and Magistretti, 2009).

Astrocytes have a role in ion homeostasis at the synapse. K^+, Na^+, HCO^{3-}, Cl^- and H^+ ion levels are all regulated by astrocytes to ensure neuronal cell survival and continued efficient neurotransmission (Simard and Nedergaard, 2004). Along with mediating homeostasis within the synapse, astrocytes also exhibit an active role in neuronal signaling (Simard and Nedergaard, 2004; Blackburn et al., 2009; Sofroniew and Vinters, 2010). The pre-synaptic neuron, post-synaptic neuron and astroglial cell make up the tripartite synapse. The release of glial transmitters such as glutamate, GABA, ATP and D-serine impact excitation and inhibition of the CNS. Water homeostasis is achieved through the presence of aquaporins on astrocytes, such as AQP4, in the plasma membrane. These are especially prevalent in astrocytic processes surrounding blood vessels and play a critical role in fluid homeostasis (Benarroch, 2005).

Astrocytic end-feet come into close contact with the endothelial cells of the vasculature and form part of the blood-brain barrier (Abbott et al., 2006). Further evidence also suggests that astrocytes are able to secrete angiogenic factors to propagate the formation of capillaries in the brain (Blackburn et al., 2009; Sofroniew and Vinters, 2010). Takano et al. (2006) identified that astrocytes have a role in blood vessel diameter regulation with vasodilation noted in blood vessels ensheathed by astrocytic end-feet.

Following an insult to the brain, astrocytes undergo a process known as "reactive astrogliosis" (**Figure 1**; Zamanian et al., 2012). Here, astrocytes undergo significant morphological changes along with significant gene expression alterations (Wilhelmsson et al., 2006; Sofroniew, 2009), they become hypertrophic and show enhanced GFAP expression (Ben Haim et al., 2015a). This process has been found to be both protective and harmful. Of particular note in the context of inflammation is that reactive astrocytes have been shown to produce chemokines such as chemokine C-C motif ligand 2 (CCL2) and C-X-C motif ligand 1 (CXCL1), pro-inflammatory cytokines such as interleukin 12 (IL-12) and TNF-α, and anti-inflammatory cytokines such as interleukin 10 (IL-10) and TGF-β (Cekanaviciute and Buckwalter, 2016). Reactive astrogliosis is a gradual continuum of changes that occur in context-dependent manners regulated by specific signaling events. Astrocytes, like microglia, are actively maintained in a resting state. The exact molecular triggers of astrocyte and microglia reactivity during initial stages of neurodegenerative disorders, before significant neuronal loss are unknown but it was suggested that they might detect altered neurotransmission, release of stress signals and abnormally folded proteins (Ben Haim et al., 2015a). Furthermore, cytokines, growth factors and purines can activate these cells and intracellular signalling cascades that will lead to their transition into reactive states (Buffo et al., 2010; Ben Haim et al., 2015a).

Recent findings also suggest that reactive astrocytosis in certain context being an adaptive beneficial response. Astrocytosis could lead to increased neuroprotection and trophic support of insult-stressed neurons; isolation of the damaged area from the rest of the CNS tissue, reconstruction of the blood brain barrier and the facilitation of remodeling of brain circuits following an insult (Buffo et al., 2010; Pekny et al., 2016). Reactive astrocytes can acquire properties of stem cells and support the remodeling of neuronal circuits, and removal of these cells can increase tissue damage and neuronal death (Robel et al., 2011; Sofroniew and Vinters, 2010). Astrocytes also produce high levels of antioxidants for neurons, including ascorbic acid, glutathione and its precursors (Allaman et al., 2011). However, reactive astrocytes can produce decreased levels of antioxidants and they also release more ROS and NOS in neurodegenerative disorders such as AD and HD (Ben Haim et al., 2015a). Reactive astrocytes also phagocytose debris and have a role in the repair of damaged tissue (Sofroniew and Vinters, 2010). Recent research suggests the existence of two subtypes of reactive astrocytes. These are the proinflammatory, neurotoxic A1 type and the anti-inflammatory, neuroprotective A2 type cells (Liddelow and Barres, 2017; Sofroniew, 2009). Though further subtypes have not been identified in the literature, it is hypothesized that astrocyte populations might exist in a continuum between A1 and A2 polarized states or may even exist in a number of separate activation states (Liddelow and Barres, 2017). The fate of astrocytes to either of these subtypes is dependent on the insult to the brain that occurs and cell signaling pathways that are triggered in these insults (Liddelow and Barres, 2017; Sofroniew, 2009). The "detrimental" activated astrocytes are speculated to be resultant of inflammatory stimulus and show upregulation of genes which are linked to synapse destruction leading to neuronal loss (Zamanian et al., 2012). These astrocytes are postulated to be induced through NF-κB signaling and are reported present in a number of neurodegenerative diseases including AD, PD, ALS, Multiple Sclerosis (MS) and HD (Li et al., 2019; Liddelow and Barres, 2017; Liddelow

et al., 2017). The "helpful" reactive astrocytes induced by an ischemic event show the upregulation of neurotrophic factors, cytokines and thrombospondins and are postulated to stimulate synapse development and neuronal survival (Zamanian et al., 2012). In summary, reactive astrogliosis is a finely regulated continuum of molecular, cellular, and functional changes and these changes can exert both beneficial and detrimental effects in a context-dependent manner determined by specific molecular signaling cascades.

ASTROCYTIC CONTRIBUTION TO HUNTINGTON'S DISEASE

Astrocyte Pathology

Previous literature suggests the contribution of astrocytes to neuron death and other hallmarks of HD pathology (**Figure 1**). In postmortem HD brains an increased number of astrocytes has been observed. While microglial density and activation were detected prior to symptom onset and neuropathological changes, no reactive astrocytes were found in grade 0 HD brains, reactive astrocytosis is observed only after neurodegeneration (Vonsattel et al., 1985, 2011). Importantly the levels of both microglial activation and reactive astrocytosis are correlated with disease severity. In the HD striatum, the increased number of GFAP positive reactive astrocytes is correlated with the gradient of striatal neurodegeneration (Vonsattel et al., 1985). However, this is not the case in the cortex, no astrocytosis is seen in the HD cortex in regions of neuronal loss and microglia activation (Zalneraitis et al., 1981; Sotrel et al., 1991). A prominent astrocytosis has also been detected in HD animal models (Lin et al., 2001; Gu et al., 2005, 2007; Faideau et al., 2010). Besides neuronal death reactive astrocytosis in HD might also contribute to pericyte death along the cerebral blood vessels and further accelerate progression of the disease (Hsiao et al., 2015).

There is growing evidence for the heterogeneity among reactive astrocytes across different brain regions, but also locally within the same region as regards astrocyte proliferation, morphology and gene expression. Single-cell level analysis shows that reactive astrocytes can exhibit different expression levels of chemokines or cytokines, signaling molecules and transcription factors (Herrmann et al., 2008; Garcia et al., 2010; Hamby et al., 2012). Despite this heterogeneity large-scale gene expression studies show that inflammatory mediators can drive astrocyte transcriptome profiles towards pro-inflammatory phenotypes (Hamby et al., 2012; Zamanian et al., 2012) that may be beneficial in microbial infection but can be detrimental in neurodegenerative disease (Sofroniew, 2014).

mHTT Accumulation and Astrocyte Activation

Recent literature also suggests mHTT is expressed and aggregates in astrocytes, and contributes to neuronal excitotoxicity *via* downregulation of glutamate transporters EAAT2/GLT1, resulting in impaired glutamate uptake (Arzberger et al., 1997; Liévens et al., 2001; Shin et al., 2005; Faideau et al., 2010; Estrada-Sánchez and Rebec, 2012; Ellrichmann et al., 2013; Khakh et al., 2017). This loss of GLT1 expression has been noted as one of the earliest signs of astrocytic dysfunction in HD (Khakh et al., 2017). In a further study, R6/2 mice were injected with ceftriaxone, an antibiotic known to raise the expression of GLT1. This study found that ceftriaxone injected R6/2 mice showed enhanced performance in behavioral tests in comparison with vehicle-injected controls (Miller et al., 2008). This study confirmed that mice injected with ceftriaxone showed greater expression of GLT1, demonstrated through western blotting and immunohistochemistry. Furthermore, microdialysis data showed a decrease in extracellular glutamate levels in the striatum of ceftriaxone injected mice when compared with vehicle control mice. It is interesting to note that a reduction in glutamate uptake in HD models can occur independently of changes in GLT-1 protein levels suggesting that the functionality of these transporters is also reduced (Estrada-Sánchez and Rebec, 2012).

Using a mouse genetic approach by breading the conditional mHTT-expressing BACHD mouse model with GFAP-CreERT2-tam mice produced offspring with significantly reduced expression of mHTT protein in the striatum and cortex. The BACHD/GFAP-CreERT2-tam mice showed better performance in the rotarod and open field tests when compared to standard BACHD mice (Wood et al., 2019). These mice also showed increased expression of postsynaptic density protein 95 (PSD-95), α actinin2 and aB-crystallin expression compared to standard BACHD mice, along with improvements in the electrophysiological phenotype (Wood et al., 2019).

Astrocytes with nuclear mHTT inclusions showed decreased expression of Kir4.1 channel, leading to impaired K^+ homeostasis in HD (Tong et al., 2014). Kir4.1 channels allow the influx of K^+, thereby maintaining membrane conductance in astrocytes. Recent literature suggests that, in HD, there is a loss in the expression of these K^+ channels, in turn resulting in decreased membrane conductance in astrocytes. Kir4.1 channels were found to be reduced in striatal tissue of R6/2 and Q175 mice and significant proportion of striatal astrocytes that presented nuclear mHTT inclusions showed reduced Kir4.1 channel expression (Tong et al., 2014). It is postulated that a reduction in Kir4.1 channels results in an increase in extracellular K^+ levels which in turn results in medium spiny neurons being 3–13 mV more depolarized in HD mouse models than in wild-type mice (Tong et al., 2014). This increased depolarization may further underlie the hyperexcitability of the striatal medium spiny neurons in HD.

mHtt expression in astrocytes, and not in neurons, is sufficient to trigger oxidative stress in neurons by diffusible factors (Boussicault et al., 2014). The release of ascorbic acid by astrocytes is altered in HD (Rebec, 2013). In the R6/2 mouse model, extracellular ascorbic acid levels are lower than in age-matched WT mice but only during behavioral activity (Rebec et al., 2002). Therefore, reactive astrocytes may not only produce fewer antioxidant molecules in the HD brain, but they might also release more pro-oxidant factors (Ben Haim et al., 2015a).

Furthermore, mHTT has been shown to reduce astrocytic release of BDNF (Wang et al., 2012; Hong et al., 2016). Interestingly, phosphorylation of mutant huntingtin at the S421 residue promotes neuroprotection in HD, by restoring huntingtin function in the transport of BDNF (Zala et al., 2004).

A recent study demonstrated the modeling of HD in *in vitro* derived monkey astrocytes and the therapeutic efficacy of astrocyte targeted RNAi, expression of small-hairpin RNA against *HTT* (shHD) ameliorated and reversed HD phenotypes in astrocytes (Cho et al., 2019). The therapeutic potential of this targeted approach has to be tested in human astrocytes.

Major Signaling Pathways Implicated in Astrocytic Activation

In HD, the degenerating neurons, activated microglia, pericytes, endothelial cell and astrocytes release molecules that activate astrocytic intracellular signaling pathways such as the janus kinase/signal transducer and activator of transcription (JAK/STAT), NF-κB mitogen-activated protein kinase (MAPK) and calcineurin (CN). Activation of the JAK/STAT3 pathway is a universal feature of astrocyte reactivity in models of different neurodegenerative disorders (Ben Haim et al., 2015a). STAT3 accumulates in the nucleus of reactive astrocytes in the striatum of mouse and primate HD models (Ben Haim et al., 2015b). Lentiviral overexpression of suppressor of cytokine signaling 3 (SOCS3), the endogenous inhibitor of the JAK/STAT3 pathway in astrocytes *in vivo*, inhibited this pathway and prevented astrocyte reactivity but also increased the number of mHTT and did not influence neuronal death (Ben Haim et al., 2015b). N171-82Q and Hdh140 mice display behavioral abnormalities and striatal atrophy with no substantial astrocyte reactivity in endstage N171-82Q mice or before 17 months of age in Hdh140 mice. The JAK/STAT3 pathway was activated in the few reactive astrocytes of the old Hdh140 mice (Tong et al., 2014). In contrast, a significant astrocytosis is found in the brains of HD patients (Faideau et al., 2010) but this discrepancy might be related to the absence of massive neuronal death in HD transgenic models. Therefore, the JAK/STAT3 pathway seems ultimately responsible for triggering astrocyte reactivity. However, due to the crosstalk between the NF-κB and the JAK/STAT3 pathways, there is possibility that the NF-κB pathway secondarily activates the JAK/STAT3 pathway or STAT3 inhibits the NF-κB pathway and other signaling pathways are also involved in astrocyte activation (Fan et al., 2013; Ben Haim et al., 2015b). Activation of the JAK/STAT3 pathway is involved in cell proliferation, survival, and differentiation. In astrocytes the activation of the pathway increases the expression of cytoskeletal proteins, such as GFAP and vimentin, but many other genes are induced that are involved in the release of cytokines and chemokines (Burda and Sofroniew, 2014).

The NF-κB pathway have been associated with astrocyte reactivity and neuroinflammation (Kang and Hebert, 2011). Studies carried out on primary R6/2 mouse astrocyte cultures showed increased activation of NF-κB resulting in an efflux of pro-inflammatory cytokines (Hsiao et al., 2013). This study postulated that this was achieved through the enhanced activation of IkB kinase leading to prolongation of NF-κB activation, thus upregulating pro-inflammatory factors. Enhanced activation of nuclear factor NF-κB-p65 (p65) was also observed in astrocytes of patients and mice with HD (Hsiao et al., 2013). Another study that examined the abundance of IκBα, the master inhibitor of the NF-κB pathway which is degraded during pathway activation, did not show decrease in the lentivirus Htt82Q-injected mouse striatum (Ben Haim et al., 2015b). The NF-κB pathway is involved in a range of cellular processes including immune response, inflammation, cell division and apoptosis (Mattson and Meffert, 2006). Hsiao et al. (2013) showed that aberrant activation of NF-kB occurred only in HD astrocytes, and not in HD microglia or HD neurons, under basal conditions and suggest that enhanced NF-kB-mediated inflammatory response in HD astrocytes might play a crucial role in regulating the initial response of HD brains to inflammatory stimuli. Furthermore, they showed that mHTT enhanced IKK activity leading to prolonged NF-kB activation in astrocytes during inflammation. Upregulation of iNOS and increased production of inflammatory mediators (e.g., NO, TNF-α and IL-1β) by LPS and cytokines (TNF-α + IL-1β) were also observed *in vitro* in R6/2 primary astrocytes when compared with WT astrocytes. As discussed above, several studies suggest that this pathway plays a key role in microglia activation but might not be critical to initiate astrocyte reactivity, hence further studies are needed to understand the role of NF-kB in astrocytes in HD.

The MAPK pathway is activated in many cell types in patients with neurodegenerative conditions and mouse models, but there is no evidence showing that it is directly involved in the initiation of astrocyte reactivity and activation of microglia (Bachstetter et al., 2011; Ben Haim et al., 2015a). Further experiments are needed to delineate which ligands and receptors activate which components of this signaling in HD astrocytes and microglia, and determine the functionally relevant downstream genes that are regulated by the MAPK pathway.

The effects of CN on astrocyte reactivity are complex and context-dependent, CN can both trigger and prevent reactivity, particularly in AD. CN modulates transcription factors such as nuclear factor of activated T-cells (NFATs) and NF-κB (Buffo et al., 2010; Ben Haim et al., 2015a). Increase in calcineurin activity in the brain of *Hdh*Q111/Q111 HD knock-in mice can lead to the selective loss of huntingtin phosphorylation and contributing to neuronal cell death in HD. Inhibition of calcineurin by FK506 led to sustained phosphorylation of mutant huntingtin at S421 and restored BDNF transport in rat primary neuronal cultures expressing mHTT and mouse cortical neurons from *Hdh*Q111/Q111 mice (Pineda et al., 2009). Based on previous AD studies CN seems to modulate rather than induce astrocyte reactivity but more research is required to determine the role of CN in HD astrocytes (Ben Haim et al., 2015a).

Reactive Astrocytes Confer a Neurotoxic Role in HD?

The role of reactive astrocytes in HD progression is not well understood. Some studies suggest that in HD there is an imbalance in the neuroprotective and neurotoxic roles of reactive astrocytes favoring neurotoxicity (Sofroniew, 2009). A loss of neuroprotective function is likely due to the genetic mutation causing HD which results in abnormal, dysfunctional astrocytes expressing the mHTT protein and the promotion of neuroinflammation as discussed above. Furthermore, dysfunctional astrocytes lose their ability to provide support for neurons and this might lead to the

neuronal death reported in HD. Although based on these studies reactive astrocytes are generally considered detrimental for neuronal function, this is mainly due to the lack of studies focusing on their beneficial effects (Khakh et al., 2017; Liddelow and Barres, 2017). Another important point is, while a few studies suggest that reactive astrocytes might have beneficial effects and promote neuronal survival in neurodegenerative and other CNS disorders, there is a lack of HD focused research (Escartin and Bonvento, 2008; Hamby and Sofroniew, 2010). Importantly, recent studies are just the start of beginning to understand the contribution of astrocyte to HD in mouse models but their contribution to disease pathology in the human brain remains to be determined. Therefore, the analysis of human HD specimens is critical and urgently needed.

NEUROINFLAMMATION TARGETED HD THERAPEUTICS

Currently there are no therapeutic treatments available for the cure of HD. Though the presence of chronic inflammation has been established in HD, few targeted therapies have been proposed (**Figure 2**). Minocycline is a second-generation tetracycline with anti-inflammatory and antiapoptotic properties (Rocha et al., 2016). A metanalysis study looking at the efficacy of minocycline in rodents found that a low dose (5 mg/kg/day) of minocycline brought about a large treatment benefit and better behavioral performance of mice (Li et al., 2013). A 2 years clinical trial of minocycline administered at a dose of 100 mg/day showed promising results with a stabilization of general neuropsychological and general motor symptoms and, a significant amelioration in psychiatric symptoms (Bonelli et al., 2004). However, it is important to note that this study had a low sample size of 11 patients and therefore these results needed to be corroborated in studies with more patients treated. A further clinical trial on 30 patients over a 6 months period found a trend toward improvement on the Unified Huntington's Disease Rating Scale (URHDS; Thomas et al., 2004). The authors noted that lack of statistical significance may be due to the relatively short treatment period. A larger study of 87 HD patients over 18 months assessed the potential benefits of this drug treatment in a phase 3 clinical trial (clinicaltrials.gov ID: NCT00277355) and found that patient improvement did not reach a futility threshold, based on these findings further trials of minocycline 200 mg/day were not warranted (Cudkowicz, 2010).

Cannabinoids have also been seen as potential therapeutic agents due to their anti-inflammatory properties (Stella, 2009; Möller, 2010; Rocha et al., 2016). A clinical trial of cannabidiol on 15 HD patients showed no improvements in motor function over a 6 weeks period (Consroe et al., 1991). Again, this study had a low sample size, therefore caution must be taken when concluding the efficacy of cannabidiol. Similarly, a double-blind, randomized, placebo-controlled, cross-over pilot clinical trial with Sativex®, a botanical extract with an equimolecular combination of delta-9-tetrahydrocannabinol and cannabidiol conducted over 12 weeks on 24 HD patients reported no significant symptomatic effects (clinicaltrials.gov ID: NCT01502046; Moreno et al., 2016).

Liquinimod is an immunomodulator which acts to reduce the production of pro-inflammatory cytokines. Liquinimod treatment of YAC128 mice resulted in improved motor function and motor learning as well as a reduction in depressive-like behaviors (Garcia-Miralles et al., 2019). A clinical trial of liquinimod HD patients has been completed (LEGATO-HD, clinicaltrials.gov ID: NCT02215616). While the results are yet to be published, it has been reported that the drug failed to meet the primary endpoint of the trial (Carroll, 2018).

The failure of these clinicals trials might suggest that the effects of anti-inflammatory treatments (e.g., nonsteroidal anti-inflammatory drugs) and global immunosuppression (e.g., corticosteroids) are probably too broad, current approaches do not consider the high heterogeneity in microglia and astrocyte phenotypes (Ransohoff, 2016b; Masgrau et al., 2017; Matias et al., 2019). A better understanding of the characteristics and function of these cells in healthy and different disease states, trauma, infection, during development and aging is absolutely critical. These cells may gain gain toxic function and produce factors that are harmful to neurons and other cell types in the CNS but there is no convincing evidence of astrocyte or microglia-dependent toxicity in human patients in most neurodegenerative condition, including HD, AD and PD (Masgrau et al., 2017). This highlights the need for more studies on human materials such as primary cell lines, neural progenitor cells generated from induced pluripotent stem cells and differentiated to glial cells and biopsy-derived microglia and astrocytes. These active processes are difficult to study in the human brain but detailed anatomical studies investigating the relationship of the various types of glial cells in relation to neuronal dysfunction in the various regions of the post-mortem human brain could reveal more on the glial-neuronal interactions in HD. As there is a large heterogeneity in cell loss throughout the brain which is linked to symptomatology (Nana et al., 2014), regions of high cell loss can be compared with regions which are spared or are less affected by the disease process. These combined research studies could lead to the development of successful or improved HD therapies.

CONCLUDING REMARKS

The current understanding of neuroinflammation in HD exposes a crucial role of astrocytes and microglia to the progression of HD. The role of these cells in the perpetuation of chronic inflammation and neuronal death highlights these cells as a promising therapeutic target for HD. There are no currently available disease-modifying treatments for HD. In recent years, RNA interference has emerged as the most promising area of therapeutic development for the disease. Currently, the development of antisense oligonucleotides to mHTT are providing a promising future therapy for HD. As discussed in this review, mHTT interacts with astrocytes and microglia to perpetuate neuroinflammation and subsequent cell death. Therefore, the clearance of mHTT using antisense oligonucleotides could possibly lead

to the reduction of neuroinflammation. Furthermore, using these RNA interference therapeutics in conjunction with anti-inflammatory therapies might lead to more effective treatment of HD.

AUTHOR CONTRIBUTIONS

TP and AK prepared the figure. TP, HW, RF and AK wrote the article.

FUNDING

This work was supported by Alzheimers New Zealand (AK; 3718869), Freemasons New Zealand (AK; 3719321), Alzheimers New Zealand Charitable Trust, Aotearoa Foundation, Centre for Brain Research and University of Auckland (AK; 3705579), Neurological Foundation of New Zealand (AK and TP; 848010), Brain Research New Zealand, Health Research Council of New Zealand (RF and HW; 3627373).

REFERENCES

Abbott, N. J., Rönnbäck, L., and Hansson, E. (2006). Astrocyte-endothelial interactions at the blood-brain barrier. *Nat. Rev. Neurosci.* 7, 41–53. doi: 10.1038/nrn1824

Allaman, I., Bélanger, M., and Magistretti, P. J. (2011). Astrocyte-neuron metabolic relationships: for better and for worse. *Trends Neurosci.* 34, 76–87. doi: 10.1016/j.tins.2010.12.001

Andrew, S. E., Goldberg, Y. P., Kremer, B., Telenius, H., Theilmann, J., Adam, S., et al. (1993). The relationship between trinucleotide (CAG) repeat length and clinical features of Huntington's disease. *Nat. Genet.* 4, 398–403. doi: 10.1038/ng0893-398

Arzberger, T., Krampfl, K., Leimgruber, S., and Weindl, A. (1997). Changes of NMDA receptor subunit (NR1, NR2B) and glutamate transporter (GLT1) mRNA expression in Huntington's disease—an *in situ* hybridization study. *J. Neuropathol. Exp. Neurol.* 56, 440–454. doi: 10.1097/00005072-199704000-00013

Aziz, N. A., Anguelova, G. V., Marinus, J., van Dijk, J. G., and Roos, R. A. C. (2010). Autonomic symptoms in patients and pre-manifest mutation carriers of Huntington's disease. *Eur. J. Neurol.* 17, 1068–1074. doi: 10.1111/j.1468-1331.2010.02973.x

Bachstetter, A. D., Xing, B., de Almeida, L., Dimayuga, E. R., Watterson, D. M., and Van Eldik, L. J. (2011). Microglial p38α MAPK is a key regulator of proinflammatory cytokine up-regulation induced by toll-like receptor (TLR) ligands or β-amyloid (Aβ). *J. Neuroinflammation* 8:79. doi: 10.1186/1742-2094-8-79

Bélanger, M., and Magistretti, P. J. (2009). The role of astroglia in neuroprotection. *Dialogues Clin. Neurosci.* 11, 281–295.

Ben Haim, L., Carrillo-de Sauvage, M. A., Ceyzériat, K., and Escartin, C. (2015a). Elusive roles for reactive astrocytes in neurodegenerative diseases. *Front. Cell. Neurosci.* 9:278. doi: 10.3389/fncel.2015.00278

Ben Haim, L., Ceyzeriat, K., Carrillo-de Sauvage, M. A., Aubry, F., Auregan, G., Guillermier, M., et al. (2015b). The JAK/STAT3 pathway is a common inducer of astrocyte reactivity in Alzheimer's and Huntington's diseases. *J. Neurosci.* 35, 2817–2829. doi: 10.1523/JNEUROSCI.3516-14.2015

Benarroch, E. E. (2005). Neuron-astrocyte interactions: partnership for normal function and disease in the central nervous system. *Mayo Clin. Proc.* 80, 1326–1338. doi: 10.4065/80.10.1326

Benarroch, E. E. (2013). Microglia: multiple roles in surveillance, circuit shaping, and response to injury. *Neurology* 81, 1079–1088. doi: 10.1212/WNL.0b013e3182a4a577

Bennett, M. L., Bennett, F. C., Liddelow, S. A., Ajami, B., Zamanian, J. L., Fernhoff, N. B., et al. (2016). New tools for studying microglia in the mouse and human CNS. *Proc. Natl. Acad. Sci. U S A* 113, E1738–E1746. doi: 10.1073/pnas.1525528113

Björkqvist, M., Wild, E. J., Thiele, J., Silvestroni, A., Andre, R., Lahiri, N., et al. (2008). A novel pathogenic pathway of immune activation detectable before clinical onset in Huntington's disease. *J. Exp. Med.* 205, 1869–1877. doi: 10.1084/jem.20080178

Blackburn, D., Sargsyan, S., Monk, P. N., and Shaw, P. J. (2009). Astrocyte function and role in motor neuron disease: a future therapeutic target? *Glia* 57, 1251–1264. doi: 10.1002/glia.20848

Boche, D., Perry, V. H., and Nicoll, J. A. R. (2013). Review: activation patterns of microglia and their identification in the human brain. *Neuropathol. Appl. Neurobiol.* 39, 3–18. doi: 10.1111/nan.12011

Bonelli, R. M., Hödl, A. K., Hofmann, P., and Kapfhammer, H.-P. (2004). Neuroprotection in Huntington's disease: a 2-year study on minocycline. *Int. Clin. Psychopharmacol.* 19, 337–342. doi: 10.1097/00004850-200411000-00004

Bouchard, J., Truong, J., Bouchard, K., Dunkelberger, D., Desrayaud, S., Moussaoui, S., et al. (2012). Cannabinoid receptor 2 signaling in peripheral immune cells modulates disease onset and severity in mouse models of Huntington's disease. *J. Neurosci.* 32, 18259–18268. doi: 10.1523/JNEUROSCI.4008-12.2012

Boussicault, L., Herard, A. S., Calingasan, N., Petit, F., Malgorn, C., Merienne, N., et al. (2014). Impaired brain energy metabolism in the BACHD mouse model of Huntington's disease: critical role of astrocyte-neuron interactions. *J. Cereb. Blood Flow Metab.* 34, 1500–1510. doi: 10.1038/jcbfm.2014.110

Buffo, A., Rolando, C., and Ceruti, S. (2010). Astrocytes in the damaged brain: molecular and cellular insights into their reactive response and healing potential. *Biochem. Pharmacol.* 79, 77–89. doi: 10.1016/j.bcp.2009.09.014

Burda, J. E., and Sofroniew, M. V. (2014). Reactive gliosis and the multicellular response to CNS damage and disease. *Neuron* 81, 229–248. doi: 10.1016/j.neuron.2013.12.034

Carroll, J. (2018). Disappointing news from LEGATO-HD trial of laquinimod in Huntington's disease. Available online at: https://en.hdbuzz.net/262.

Cekanaviciute, E., and Buckwalter, M. S. (2016). Astrocytes: integrative regulators of neuroinflammation in stroke and other neurological diseases. *Neurotherapeutics* 13, 685–701. doi: 10.1007/s13311-016-0477-8

Chang, K.-H., Wu, Y.-R., Chen, Y.-C., and Chen, C.-M. (2015). Plasma inflammatory biomarkers for Huntington's disease patients and mouse model. *Brain Behav. Immun.* 44, 121–127. doi: 10.1016/j.bbi.2014.09.011

Chiu, I. M., Morimoto, E. T., Goodarzi, H., Liao, J. T., O'Keeffe, S., Phatnani, H. P., et al. (2013). A neurodegeneration-specific gene-expression signature of acutely isolated microglia from an amyotrophic lateral sclerosis mouse model. *Cell Rep.* 4, 385–401. doi: 10.1016/j.celrep.2013.06.018

Cho, I. K., Yang, B., Forest, C., Qian, L., and Chan, A. W. S. (2019). Amelioration of Huntington's disease phenotype in astrocytes derived from iPSC-derived neural progenitor cells of Huntington's disease monkeys. *PLoS One* 14:e0214156. doi: 10.1371/journal.pone.0214156

Chung, W.-S., Allen, N. J., and Eroglu, C. (2015). Astrocytes control synapse formation, function, and elimination. *Cold Spring Harb. Perspect. Biol.* 7:a020370. doi: 10.1101/cshperspect.a020370

Consroe, P., Laguna, J., Allender, J., Snider, S., Stern, L., Sandyk, R., et al. (1991). Controlled clinical trial of cannabidiol in Huntington's disease. *Pharmacol. Biochem. Behav.* 40, 701–708. doi: 10.1016/0091-3057(91)90386-g

Crotti, A., Benner, C., Kerman, B. E., Gosselin, D., Lagier-Tourenne, C., Zuccato, C., et al. (2014). Mutant Huntingtin promotes autonomous microglia activation *via* myeloid lineage-determining factors. *Nat. Neurosci.* 17, 513–521. doi: 10.1038/nn.3668

Crotti, A., and Glass, C. K. (2015). The choreography of neuroinflammation in Huntington's disease. *Trends Immunol.* 36, 364–373. doi: 10.1016/j.it.2015.04.007

Cudkowicz, M. (2010). A futility study of minocycline in Huntington's disease. *Mov. Disord.* 25, 2219–2224. doi: 10.1002/mds.23236

Dayalu, P., and Albin, R. L. (2015). Huntington disease: pathogenesis and treatment: pathogenesis and treatment. *Neurol. Clin.* 33, 101–114. doi: 10.1016/j.ncl.2014.09.003

Donley, D., Nelson, R., Gigley, J., and Fox, J. (2019). Mutant huntingtin protein alters the response of microglial cells to inflammatory stimuli. *bioRxiv* [Preprint].

Dowie, M. J., Grimsey, N. L., Hoffman, T., Faull, R. L. M., and Glass, M. (2014). Cannabinoid receptor CB2 is expressed on vascular cells, but not astroglial cells in the post-mortem human Huntington's disease brain. *J. Chem. Neuroanat.* 59–60, 62–71. doi: 10.1016/j.jchemneu.2014.06.004

Ellrichmann, G., Reick, C., Saft, C., and Linker, R. (2013). The role of the immune system in Huntington's disease. *Clin. Dev. Immunol.* 2013:541259. doi: 10.1155/2013/541259

Escartin, C., and Bonvento, G. (2008). Targeted activation of astrocytes: a potential neuroprotective strategy. *Mol. Neurobiol.* 38, 231–241. doi: 10.1007/s12035-008-8043-y

Estrada-Sánchez, A. M., and Rebec, G. V. (2012). Corticostriatal dysfunction and glutamate transporter 1 (GLT1) in Huntington's disease: interactions between neurons and astrocytes. *Basal Ganglia* 2, 57–66. doi: 10.1016/j.baga.2012.04.029

Faideau, M., Kim, J., Cormier, K., Gilmore, R., Welch, M., Auregan, G., et al. (2010). *In vivo* expression of polyglutamine-expanded huntingtin by mouse striatal astrocytes impairs glutamate transport: a correlation with Huntington's disease subjects. *Hum. Mol. Genet.* 19, 3053–3067. doi: 10.1093/hmg/ddq212

Fan, Y., Mao, R., and Yang, J. (2013). NF-kappaB and STAT3 signaling pathways collaboratively link inflammation to cancer. *Protein Cell* 4, 176–185. doi: 10.1007/s13238-013-2084-3

Frost, J. L., and Schafer, D. P. (2016). Microglia: architects of the developing nervous system. *Trends Cell Biol.* 26, 587–597. doi: 10.1016/j.tcb.2016.02.006

Garcia, A. D., Petrova, R., Eng, L., and Joyner, A. L. (2010). Sonic hedgehog regulates discrete populations of astrocytes in the adult mouse forebrain. *J. Neurosci.* 30, 13597–13608. doi: 10.1523/JNEUROSCI.0830-10.2010

Garcia-Miralles, M., Tan, J., Radulescu, C., Sidik, H., Belinson, H., Zach, N., et al. (2019). Laquinimod treatment improves myelination deficits at the transcriptional and ultrastructural levels in the YAC128 mouse model of Huntington disease. *Mol. Neurobiol.* 56, 4464–4478. doi: 10.1007/s12035-018-1393-1

Georgiou, N., Bradshaw, J. L., Chiu, E., Tudor, A., O'Gorman, L., and Phillips, J. G. (1999). Differential clinical and motor control function in a pair of monozygotic twins with Huntington's disease. *Mov. Disord.* 14, 320–325. doi: 10.1002/1531-8257(199903)14:2<320::aid-mds1018>3.0.co;2-z

Giorgini, F., Guidetti, P., Nguyen, Q., Bennett, S. C., and Muchowski, P. J. (2005). A genomic screen in yeast implicates kynurenine 3-monooxygenase as a therapeutic target for Huntington disease. *Nat. Genet.* 37, 526–531. doi: 10.1038/ng1542

Giorgini, F., Möller, T., Kwan, W., Zwilling, D., Wacker, J. L., Hong, S., et al. (2008). Histone deacetylase inhibition modulates kynurenine pathway activation in yeast, microglia and mice expressing a mutant huntingtin fragment. *J. Biol. Chem.* 283, 7390–7400. doi: 10.1074/jbc.m708192200

Glenn, J. A., Ward, S. A., Stone, C. R., Booth, P. L., and Thomas, W. E. (1992). Characterisation of ramified microglial cells: detailed morphology, morphological plasticity and proliferative capability. *J. Anat.* 180, 109–118.

Govindpani, K., McNamara, L. G., Smith, N. R., Vinnakota, C., Waldvogel, H. J., Faull, R. L., et al. (2019). Vascular dysfunction in Alzheimer's disease: a prelude to the pathological process or a consequence of it? *J. Clin. Med.* 8:E651. doi: 10.3390/jcm8050651

Gu, X., André, V. M., Cepeda, C., Li, S. H., Li, X. J., Levine, M. S., et al. (2007). Pathological cell-cell interactions are necessary for striatal pathogenesis in a conditional mouse model of Huntington's disease. *Mol. Neurodegener.* 2:8. doi: 10.1186/1750-1326-2-8

Gu, X., Li, C., Wei, W., Lo, V., Gong, S., Li, S. H., et al. (2005). Pathological cell-cell interactions elicited by a neuropathogenic form of mutant Huntingtin contribute to cortical pathogenesis in HD mice. *Neuron* 46, 433–444. doi: 10.1016/j.neuron.2005.03.025

Guidetti, P., Luthi-Carter, R. E., Augood, S. J., and Schwarcz, R. (2004). Neostriatal and cortical quinolinate levels are increased in early grade Huntington's disease. *Neurobiol. Dis.* 17, 455–461. doi: 10.1016/j.nbd.2004.07.006

Gusella, J. F., Wexler, N. S., Conneally, P. M., Naylor, S. L., Anderson, M. A., Tanzi, R. E., et al. (1983). A polymorphic DNA marker genetically linked to Huntington's disease. *Nature* 306, 234–238. doi: 10.1038/306234a0

Ha, A. D., Beck, C. A., and Jankovic, J. (2012). Intermediate CAG repeats in Huntington's disease: analysis of COHORT. *Tremor Other Hyperkinet. Mov.* 2:tre-02-64-287-4. doi: 10.7916/D8FF3R2P

Häcker, H., and Karin, M. (2006). Regulation and function of IKK and IKK-related kinases. *Sci. STKE* 2006:re13. doi: 10.1126/stke.3572006re13

Hamby, M. E., Coppola, G., Ao, Y., Geschwind, D. H., Khakh, B. S., and Sofroniew, M. V. (2012). Inflammatory mediators alter the astrocyte transcriptome and calcium signaling elicited by multiple G-protein-coupled receptors. *J. Neurosci.* 32, 14489–14510. doi: 10.1523/JNEUROSCI.1256-12.2012

Hamby, M. E., and Sofroniew, M. V. (2010). Reactive astrocytes as therapeutic targets for CNS disorders. *Neurotherapeutics* 7, 494–506. doi: 10.1016/j.nurt.2010.07.003

Hanisch, U.-K., and Kettenmann, H. (2007). Microglia: active sensor and versatile effector cells in the normal and pathologic brain. *Nat. Neurosci.* 10, 1387–1394. doi: 10.1038/nn1997

Herrmann, J. E., Imura, T., Song, B., Qi, J., Ao, Y., Nguyen, T. K., et al. (2008). STAT3 is a critical regulator of astrogliosis and scar formation after spinal cord injury. *J. Neurosci.* 28, 7231–7243. doi: 10.1523/JNEUROSCI.1709-08.2008

Hickman, S., Izzy, S., Sen, P., Morsett, L., and El Khoury, J. (2018). Microglia in neurodegeneration. *Nat. Neurosci.* 21, 1359–1369. doi: 10.1038/s41593-018-0242-x

Hong, Y., Zhao, T., Li, X.-J., and Li, S. (2016). Mutant huntingtin impairs BDNF release from astrocytes by disrupting conversion of Rab3a-GTP into Rab3a-GDP. *J. Neurosci.* 36, 8790–8801. doi: 10.1523/JNEUROSCI.0168-16.2016

Hsiao, H. Y., Chen, Y. C., Huang, C. H., Chen, C. C., Hsu, Y. H., Chen, H. M., et al. (2015). Aberrant astrocytes impair vascular reactivity in Huntington disease. *Ann. Neurol.* 78, 178–192. doi: 10.1002/ana.24428

Hsiao, H.-Y., Chen, Y.-C., Chen, H.-M., Tu, P.-H., and Chern, Y. (2013). A critical role of astrocyte-mediated nuclear factor-κB-dependent inflammation in Huntington's disease. *Hum. Mol. Genet.* 22, 1826–1842. doi: 10.1093/hmg/ddt036

Huntington, G. (2003). On chorea. *J. Neuropsychiatry Clin. Neurosci.* 15, 109–112. doi: 10.1176/jnp.15.1.109

Jansen, A. H. P., van Hal, M., Op den Kelder, I. C., Meier, R. T., de Ruiter, A.-A., Schut, M. H., et al. (2017). Frequency of nuclear mutant huntingtin inclusion formation in neurons and glia is cell-type-specific. *Glia* 65, 50–61. doi: 10.1002/glia.23050

Kang, W., and Hebert, J. M. (2011). Signaling pathways in reactive astrocytes, a genetic perspective. *Mol. Neurobiol.* 43, 147–154. doi: 10.1007/s12035-011-8163-7

Khakh, B. S., Beaumont, V., Cachope, R., Munoz-Sanjuan, I., Goldman, S. A., and Grantyn, R. (2017). Unravelling and exploiting astrocyte dysfunction in Huntington's disease. *Trends Neurosci.* 40, 422–437. doi: 10.1016/j.tins.2017.05.002

Khoshnan, A., Ko, J., Watkin, E. E., Paige, L. A., Reinhart, P. H., and Patterson, P. H. (2004). Activation of the IkappaB kinase complex and nuclear factor-kappaB contributes to mutant huntingtin neurotoxicity. *J. Neurosci.* 24, 7999–8008. doi: 10.1523/JNEUROSCI.2675-04.2004

Khoshnan, A., and Patterson, P. H. (2011). The role of IκB kinase complex in the neurobiology of Huntington's disease. *Neurobiol. Dis.* 43, 305–311. doi: 10.1016/j.nbd.2011.04.015

Kim, E. H., Thu, D. C. V., Tippett, L. J., Oorschot, D. E., Hogg, V. M., Roxburgh, R., et al. (2014). Cortical interneuron loss and symptom heterogeneity in Huntington disease. *Ann. Neurol.* 75, 717–727. doi: 10.1002/ana.24162

Kraft, A. D., Kaltenbach, L. S., Lo, D. C., and Harry, G. J. (2012). Activated microglia proliferate at neurites of mutant huntingtin-expressing neurons. *Neurobiol. Aging* 33, 621.e17–621.e33. doi: 10.1016/j.neurobiolaging.2011.02.015

Li, K., Li, J., Zheng, J., and Qin, S. (2019). Reactive astrocytes in neurodegenerative diseases. *Aging Dis.* 10, 664–675. doi: 10.14336/AD.2018.0720

Li, C., Yuan, K., and Schluesener, H. (2013). Impact of minocycline on neurodegenerative diseases in rodents: a meta-analysis. *Rev. Neurosci.* 24, 553–562. doi: 10.1515/revneuro-2013-0040

Liddelow, S. A., and Barres, B. A. (2017). Reactive astrocytes: production, function, and therapeutic potential. *Immunity* 46, 957–967. doi: 10.1016/j.immuni.2017.06.006

Liddelow, S. A., Guttenplan, K. A., Clarke, L. E., Bennett, F. C., Bohlen, C. J., Schirmer, L., et al. (2017). Neurotoxic reactive astrocytes are induced by activated microglia. *Nature* 541, 481–487. doi: 10.1038/nature21029

Liévens, J. C., Woodman, B., Mahal, A., Spasic-Boscovic, O., Samuel, D., Kerkerian-Le Goff, L., et al. (2001). Impaired glutamate uptake in the R6 Huntington's disease transgenic mice. *Neurobiol. Dis.* 8, 807–821. doi: 10.1006/nbdi.2001.0430

Lin, C. H., Tallaksen-Greene, S., Chien, W. M., Cearley, J. A., Jackson, W. S., Crouse, A. B., et al. (2001). Neurological abnormalities in a knock-in mouse model of Huntington's disease. *Hum. Mol. Genet.* 10, 137–144. doi: 10.1093/hmg/10.2.137

Lira-Diaz, E., and Gonzalez-Perez, O. (2016). Emerging roles of microglia cells in the regulation of adult neural stem cells. *Neuroimmunol. Neuroinflamm.* 3, 204–206. doi: 10.20517/2347-8659.2016.32

Lull, M., and Block, M. (2010). Microglial activation and chronic neurodegeneration. *Neurotherapeutics* 7, 354–365. doi: 10.1016/j.nurt.2010.05.014

MacVicar, B. A., and Newman, E. A. (2015). Astrocyte regulation of blood flow in the brain. *Cold Spring Harb. Perspect. Biol.* 7:a020388. doi: 10.1101/cshperspect.a020388

Masgrau, R., Guaza, C., Ransohoff, R. M., and Galea, E. (2017). Should we stop saying "glia" and "neuroinflammation"? *Trends Mol. Med.* 23, 486–500. doi: 10.1016/j.molmed.2017.04.005

Matias, I., Morgado, J., and Gomes, F. C. A. (2019). Astrocyte heterogeneity: impact to brain aging and disease. *Front. Aging Neurosci.* 11:59. doi: 10.3389/fnagi.2019.00059

Mattson, M. P., and Meffert, M. K. (2006). Roles for NF-kappaB in nerve cell survival, plasticity, and disease. *Cell Death Differ.* 13, 852–860. doi: 10.1038/sj.cdd.4401837

Mehrabi, N. F., Waldvogel, H. J., Tippett, L. J., Hogg, V. M., Synek, B. J., and Faull, R. L. M. (2016). Symptom heterogeneity in Huntington's disease correlates with neuronal degeneration in the cerebral cortex. *Neurobiol. Dis.* 96, 67–74. doi: 10.1016/j.nbd.2016.08.015

Miller, B. R., Dorner, J. L., Shou, M., Sari, Y., Barton, S. J., Sengelaub, D. R., et al. (2008). Up-regulation of GLT1 expression increases glutamate uptake and attenuates the Huntington's disease phenotype in the R6/2 mouse. *Neuroscience* 153, 329–337. doi: 10.1016/j.neuroscience.2008.02.004

Mishra, A. (2017). Binaural blood flow control by astrocytes: listening to synapses and the vasculature. *J. Physiol.* 595, 1885–1902. doi: 10.1113/jp270979

Möller, T. (2010). Neuroinflammation in Huntington's disease. *J. Neural Transm.* 117, 1001–1008. doi: 10.1007/s00702-010-0430-7

Moreno, J. L. L. S., Caldentey, J. G., Cubillo, P. T., Romero, C. R., Ribas, G. G., Arias, M. A. A. A., et al. (2016). A double-blind, randomized, cross-over, placebo-controlled, pilot trial with Sativex in Huntington's disease. *J. Neurol.* 263, 1390–1400. doi: 10.1007/s00415-016-8145-9

Morganti, J. M., Riparip, L. K., and Rosi, S. (2016). Call Off the Dog(ma): M1/M2 polarization is concurrent following traumatic brain injury. *PLoS One* 11:e0148001. doi: 10.1371/journal.pone.0148001

Muoio, V., Persson, P. B., and Sendeski, M. M. (2014). The neurovascular unit—concept review. *Acta Physiol.* 210, 790–798. doi: 10.1111/apha.12250

Myers, R. (2004). Huntington's disease genetics. *NeuroRx* 1, 255–262. doi: 10.1602/neurorx.1.2.255

Nagy, J. I., Patel, D., Ochalski, P. A., and Stelmack, G. L. (1999). Connexin30 in rodent, cat and human brain: selective expression in gray matter astrocytes, co-localization with connexin43 at gap junctions and late developmental appearance. *Neuroscience* 88, 447–468. doi: 10.1016/s0306-4522(98)00191-2

Nakagawa, Y., and Chiba, K. (2014). Role of microglial m1/m2 polarization in relapse and remission of psychiatric disorders and diseases. *Pharmaceuticals* 7, 1028–1048. doi: 10.3390/ph7121028

Nana, A. L., Kim, E. H., Thu, D. C. V., Oorschot, D. E., Tippett, L. J., Hogg, V. M., et al. (2014). Widespread heterogeneous neuronal loss across the cerebral cortex in Huntington's disease. *J. Huntingtons Dis.* 3, 45–64. doi: 10.3233/JHD-140092

Nance, M. A. (2017). Genetics of Huntington disease. *Handb. Clin. Neurol.* 144, 3–14. doi: 10.1016/b978-0-12-801893-4.00001-8

Nayak, D., Roth, T. L., and McGavern, D. B. (2014). Microglia development and function. *Annu. Rev. Immunol.* 32, 367–402. doi: 10.1146/annurev-immunol-032713-120240

Nimmerjahn, A., Kirchhoff, F., and Helmchen, F. (2005). Resting microglial cells are highly dynamic surveillants of brain parenchyma *in vivo*. *Science* 308, 1314–1318. doi: 10.1126/science.1110647

Norden, D. M., and Godbout, J. P. (2013). Review: microglia of the aged brain: primed to be activated and resistant to regulation. *Neuropathol. Appl. Neurobiol.* 39, 19–34. doi: 10.1111/j.1365-2990.2012.01306.x

Novak, M. J. U., and Tabrizi, S. J. (2011). "Huntington's disease: clinical presentation and treatment" in *International Review of Neurobiology*, (Vol. 98) eds J. Brotchie, E. Bezard and P. Jenner (London, UK: Academic Press), 297–323.

Nuriya, M., and Hirase, H. (2016). Involvement of astrocytes in neurovascular communication. *Prog. Brain Res.* 225, 41–62. doi: 10.1016/bs.pbr.2016.02.001

Palazuelos, J., Aguado, T., Pazos, M. R., Julien, B., Carrasco, C., Resel, E., et al. (2009). Microglial CB 2 cannabinoid receptors are neuroprotective in Huntington's disease excitotoxicity. *Brain* 132, 3152–3164. doi: 10.1093/brain/awp239

Pan, W., and Kastin, A. J. (2007). Adipokines and the blood-brain barrier. *Peptides* 28, 1317–1330. doi: 10.1016/j.peptides.2007.04.023

Paulsen, J. S., Miller, A. C., Hayes, T., and Shaw, E. (2017). Cognitive and behavioral changes in Huntington disease before diagnosis. *Handb. Clin. Neurol.* 144, 69–91. doi: 10.1016/b978-0-12-801893-4.00006-7

Pavese, F. N., Gerhard, K. A., Tai, A. Y., Ho, J. A., Turkheimer, J. F., Barker, J. R., et al. (2006). Microglial activation correlates with severity in Huntington disease: a clinical and PET study. *Neurology* 66, 1638–1643. doi: 10.1212/01.wnl.0000222734.56412.17

Pekny, M., Pekna, M., Messing, A., Steinhauser, C., Lee, J. M., Parpura, V., et al. (2016). Astrocytes: a central element in neurological diseases. *Acta Neuropathol.* 131, 323–345. doi: 10.1007/s00401-015-1513-1

Petkau, T. L., Hill, A., Connolly, C., Lu, G., Wagner, P., Kosior, N., et al. (2019). Mutant huntingtin expression in microglia is neither required nor sufficient to cause the Huntington's disease-like phenotype in BACHD mice. *Hum. Mol. Genet.* 28, 1661–1670. doi: 10.1093/hmg/ddz009

Pineda, J. R., Pardo, R., Zala, D., Yu, H., Humbert, S., and Saudou, F. (2009). Genetic and pharmacological inhibition of calcineurin corrects the BDNF transport defect in Huntington's disease. *Mol. Brain* 2:33. doi: 10.1186/1756-6606-2-33

Politis, M., Lahiri, N., Niccolini, F., Su, P., Wu, K., Giannetti, P., et al. (2015). Increased central microglial activation associated with peripheral cytokine levels in premanifest Huntington's disease gene carriers. *Neurobiol. Dis.* 83, 115–121. doi: 10.1016/j.nbd.2015.08.011

Ransohoff, R. M. (2016a). How neuroinflammation contributes to neurodegeneration. *Science* 353, 777–783. doi: 10.1126/science.aag2590

Ransohoff, R. M. (2016b). A polarizing question: do M1 and M2 microglia exist? *Nat. Neurosci.* 19, 987–991. doi: 10.1038/nn.4338

Ransohoff, R. M., and Perry, V. H. (2009). Microglial physiology: unique stimuli, specialized responses. *Annu. Rev. Immunol.* 27, 119–145. doi: 10.1146/annurev.immunol.021908.132528

Rebec, G. V. (2013). Dysregulation of corticostriatal ascorbate release and glutamate uptake in transgenic models of Huntington's disease. *Antioxid. Redox Signal.* 19, 2115–2128. doi: 10.1089/ars.2013.5387

Rebec, G. V., Barton, S. J., and Ennis, M. D. (2002). Dysregulation of ascorbate release in the striatum of behaving mice expressing the Huntington's disease gene. *J. Neurosci.* 22:RC202. doi: 10.1523/JNEUROSCI.22-02-j0006.2002

Reiner, A., Dragatsis, I., and Dietrich, P. (2011). "Genetics and neuropathology of Huntington's disease," in *International Review of Neurobiology*, (Vol. 98) eds J. Brotchie, E. Bezard and P. Jenner (Tennesee, USA: Academic Press), 325–372.

Robel, S., Berninger, B., and Gotz, M. (2011). The stem cell potential of glia: lessons from reactive gliosis. *Nat. Rev. Neurosci.* 12, 88–104. doi: 10.1038/nrn2978

Rocha, N. P., Ribeiro, F. M., Furr-Stimming, E., and Teixeira, A. L. (2016). Neuroimmunology of Huntington's disease: revisiting evidence from human studies. *Mediators Inflamm.* 2016:8653132. doi: 10.1155/2016/8653132

Ross, C. A., and Tabrizi, S. J. (2011). Huntington's disease: from molecular pathogenesis to clinical treatment. *Lancet Neurol.* 10, 83–98. doi: 10.1016/s1474-4422(10)70245-3

Sagredo, O., González, S., Aroyo, I., Pazos, M. R., Benito, C., Lastres-Becker, I., et al. (2009). Cannabinoid CB 2 receptor agonists protect the striatum against malonate toxicity: relevance for Huntington's disease. *Glia* 57, 1154–1167. doi: 10.1002/glia.20838

Sánchez-López, F., Tasset, I., Agüera, E., Feijóo, M., Fernández-Bolaños, R., Sánchez, F. M., et al. (2012). Oxidative stress and inflammation biomarkers in the blood of patients with Huntington's disease. *Neurol. Res.* 34, 721–724. doi: 10.1179/1743132812Y.0000000073

Sapp, B. E., Kegel, G. K., Aronin, P. N., Hashikawa, P. T., Uchiyama, P. Y., Tohyama, P. K., et al. (2001). Early and progressive accumulation of reactive microglia in the Huntington disease brain. *J. Neuropathol. Exp. Neurol.* 60, 161–172. doi: 10.1093/jnen/60.2.161

Schafer, D. P., and Stevens, B. (2015). Microglia function in central nervous system development and plasticity. *Cold Spring Harb. Perspect. Biol.* 7:a020545. doi: 10.1101/cshperspect.a020545

Schousboe, A., Bak, L. K., and Waagepetersen, H. S. (2013). Astrocytic control of biosynthesis and turnover of the neurotransmitters glutamate and GABA. *Front. Endocrinol. Lausanne.* 4, 102–102. doi: 10.3389/fendo.2013.00102

Schwarcz, R., Guidetti, P., Sathyasaikumar, K. V., and Muchowski, P. J. (2010). Of mice, rats and men: revisiting the quinolinic acid hypothesis of Huntington's disease. *Prog. Neurobiol.* 90, 230–245. doi: 10.1016/j.pneurobio.2009.04.005

Shannon, K. M. (2011). Huntington's disease—clinical signs, symptoms, presymptomatic diagnosis, and diagnosis. *Handb. Clin. Neurol.* 100, 3–13. doi: 10.1016/b978-0-444-52014-2.00001-x

Shin, J.-Y., Fang, Z.-H., Yu, Z.-X., Wang, C.-E., Li, S.-H., and Li, X.-J. (2005). Expression of mutant huntingtin in glial cells contributes to neuronal excitotoxicity. *J. Cell Biol.* 171, 1001–1012. doi: 10.1083/jcb.200508072

Silvestroni, L. M. A., Faull, D. R., Strand, D. A., and Möller, D. T. (2009). Distinct neuroinflammatory profile in post-mortem human Huntington's disease. *Neuroreport* 20, 1098–1103. doi: 10.1097/wnr.0b013e32832e34ee

Simard, M., and Nedergaard, M. (2004). The neurobiology of glia in the context of water and ion homeostasis. *Neuroscience* 129, 877–896. doi: 10.1016/j.neuroscience.2004.09.053

Simmons, D. A., Casale, M., Alcon, B., Pham, N., Narayan, N., and Lynch, G. (2007). Ferritin accumulation in dystrophic microglia is an early event in the development of Huntington's disease. *Glia* 55, 1074–1084. doi: 10.1002/glia.20526

Singh-Bains, M. K., Mehrabi, N. F., Sehji, T., Austria, M. D. R., Tan, A. Y. S., Tippett, L. J., et al. (2019). Cerebellar degeneration correlates with motor symptoms in Huntington disease. *Ann. Neurol.* 85, 396–405. doi: 10.1002/ana.25413

Sofroniew, M. V. (2009). Molecular dissection of reactive astrogliosis and glial scar formation. *Trends Neurosci.* 32, 638–647. doi: 10.1016/j.tins.2009.08.002

Sofroniew, M. V. (2014). Multiple roles for astrocytes as effectors of cytokines and inflammatory mediators. *Neuroscientist* 20, 160–172. doi: 10.1177/1073858413504466

Sofroniew, M., and Vinters, H. (2010). Astrocytes: biology and pathology. *Acta Neuropathol.* 119, 7–35. doi: 10.1007/s00401-009-0619-8

Sotrel, A., Paskevich, P. A., Kiely, D. K., Bird, E. D., Williams, R. S., and Myers, R. H. (1991). Morphometric analysis of the prefrontal cortex in Huntington's disease. *Neurology* 41, 1117–1123. doi: 10.1212/wnl.41.7.1117

Steensberg, A., Dalsgaard, M. K., Secher, N. H., and Pedersen, B. K. (2006). Cerebrospinal fluid IL-6, HSP72, and TNF-α in exercising humans. *Brain Behav. Immun.* 20, 585–589. doi: 10.1016/j.bbi.2006.03.002

Stella, N. (2009). Endocannabinoid signaling in microglial cells. *Neuropharmacology* 56, 244–253. doi: 10.1016/j.neuropharm.2008.07.037

Stoy, N., Mackay, G. M., Forrest, C. M., Christofides, J., Egerton, M., Stone, T. W., et al. (2005). Tryptophan metabolism and oxidative stress in patients with Huntington's disease. *J. Neurochem.* 93, 611–623. doi: 10.1111/j.1471-4159.2005.03070.x

Tabernero, A., Medina, J. M., and Giaume, C. (2006). Glucose metabolism and proliferation in glia: role of astrocytic gap junctions. *J. Neurochem.* 99, 1049–1061. doi: 10.1111/j.1471-4159.2006.04088.x

Takano, T., Tian, G.-F., Peng, W., Lou, N., Libionka, W., Han, X., et al. (2006). Astrocyte-mediated control of cerebral blood flow. *Nat. Neurosci.* 9, 260–267. doi: 10.1038/nn1623

Tai, Y. F., Pavese, N., Gerhard, A., Tabrizi, S. J., Barker, R. A., Brooks, D. J., et al. (2007a). Imaging microglial activation in Huntington's disease. *Brain Res. Bull.* 72, 148–151. doi: 10.1016/j.brainresbull.2006.10.029

Tai, Y. F., Pavese, N., Gerhard, A., Tabrizi, S. J., Barker, R. A., Brooks, D. J., et al. (2007b). Microglial activation in presymptomatic Huntington's disease gene carriers. *Brain* 130, 1759–1766. doi: 10.1093/brain/awm044

Tang, Y., and Le, W. (2016). Differential roles of M1 and M2 microglia in neurodegenerative diseases. *Mol. Neurobiol.* 53, 1181–1194. doi: 10.1007/s12035-014-9070-5

The Huntington's Disease Collaborative Research Group (1993). A novel gene containing a trinucleotide repeat that is expanded and unstable on Huntington's disease chromosomes. *Cell* 72, 971–983. doi: 10.1016/0092-8674(93)90585-E

Thomas, M., Ashizawa, T., and Jankovic, J. (2004). Minocycline in Huntington's disease: a pilot study. *Mov. Disord.* 19, 692–695. doi: 10.1002/mds.20018

Thu, D. C. V., Oorschot, D. E., Tippett, L. J., Nana, A. L., Hogg, V. M., Synek, B. J., et al. (2010). Cell loss in the motor and cingulate cortex correlates with symptomatology in Huntingtonandrsquo s disease. *Brain* 133, 1094–1110. doi: 10.1093/brain/awq047

Tong, X., Ao, Y., Faas, G. C., Nwaobi, S. E., Xu, J., Haustein, M. D., et al. (2014). Astrocyte Kir4.1 ion channel deficits contribute to neuronal dysfunction in Huntington's disease model mice. *Nat. Neurosci.* 17, 694–703. doi: 10.1038/nn.3691

Träger, U., Andre, R., Lahiri, N., Magnusson-Lind, A., Weiss, A., Grueninger, S., et al. (2014). HTT-lowering reverses Huntington's disease immune dysfunction caused by NFκB pathway dysregulation. *Brain* 137, 819–833. doi: 10.1093/brain/awt355

Tremblay, M.-È., and Majewska, A. K. (2011). A role for microglia in synaptic plasticity? *Commun. Integr. Biol.* 4, 220–222. doi: 10.4161/cib.4.2.14506

van Duijn, E., Kingma, E. M., and van der Mast, R. C. (2007). Psychopathology in verified Huntington's disease gene carriers. *J. Neuropsychiatry Clin. Neurosci.* 19, 441–448. doi: 10.1176/appi.neuropsych.19.4.441

Verkhratsky, A., and Nedergaard, M. (2018). Physiology of astroglia. *Physiol. Rev.* 98, 239–389. doi: 10.1152/physrev.00042.2016

von Bartheld, C. S., Bahney, J., and Herculano-Houzel, S. (2016). The search for true numbers of neurons and glial cells in the human brain: a review of 150 years of cell counting. *J. Comp. Neurol.* 524, 3865–3895. doi: 10.1002/cne.24040

Vonsattel, J. P. G. (2008). Huntington disease models and human neuropathology: similarities and differences. *Acta Neuropathol.* 115, 55–69. doi: 10.1007/s00401-007-0306-6

Vonsattel, J. P., Keller, C., and Cortes Ramirez, E. P. (2011). Huntington's disease—neuropathology. *Handb. Clin. Neurol.* 100, 83–100. doi: 10.1016/B978-0-444-52014-2.00004-5

Vonsattel, H. J.-P., Myers, J. R., Stevens, J. T., Ferrante, D. R., Bird, P. E., and Richardson, P. E. (1985). Neuropathological classification of Huntington's disease. *J. Neuropathol. Exp. Neurol.* 44, 559–577. doi: 10.1097/00005072-198511000-00003

Wang, L., Lin, F., Wang, J., Wu, J., Han, R., Zhu, L., et al. (2012). Truncated N-terminal huntingtin fragment with expanded-polyglutamine (htt552–100Q) suppresses brain-derived neurotrophic factor transcription in astrocytes. *Acta Biochim. Biophys. Sin.* 44, 249–258. doi: 10.1093/abbs/gmr125

Wes, P. D., Holtman, I. R., Boddeke, E. W., Moller, T., and Eggen, B. J. (2016). Next generation transcriptomics and genomics elucidate biological complexity of microglia in health and disease. *Glia* 64, 197–213. doi: 10.1002/glia.22866

Wilhelmsson, U., Bushong, E. A., Price, D. L., Smarr, B. L., Phung, V., Terada, M., et al. (2006). Redefining the concept of reactive astrocytes as cells that remain within their unique domains upon reaction to injury. *Proc. Natl. Acad. Sci. U S A* 103, 17513–17518. doi: 10.1073/pnas.0602841103

Wood, T. E., Barry, J., Yang, Z., Cepeda, C., Levine, M. S., and Gray, M. (2019). Mutant huntingtin reduction in astrocytes slows disease progression in the BACHD conditional Huntington's disease mouse model. *Hum. Mol. Genet.* 28, 487–500. doi: 10.1093/hmg/ddy363

Yang, H.-M., Yang, S., Huang, S.-S., Tang, B.-S., and Guo, J.-F. (2017). Microglial activation in the pathogenesis of Huntington's disease. *Front. Aging Neurosci.* 9:193. doi: 10.3389/fnagi.2017.00193

Zala, D., Bensadoun, J. C., Pereira de Almeida, L., Leavitt, B. R., Gutekunst, C. A., Aebischer, P., et al. (2004). Long-term lentiviral-mediated expression of ciliary neurotrophic factor in the striatum of Huntington's disease transgenic mice. *Exp. Neurol.* 185, 26–35. doi: 10.1016/j.expneurol.2003.09.002

Zalneraitis, E. L., Landis, D. M. D., Richardson, E. P., and Selkoe, D. J. (1981). A comparison of astrocytic structure in cerebral-cortex and striatum in Huntington disease. *Neurology* 31, 151–151.

Zamanian, J. L., Xu, L., Foo, L. C., Nouri, N., Zhou, L., Giffard, R. G., et al. (2012). Genomic analysis of reactive astrogliosis. *J. Neurosci.* 32, 6391–6410. doi: 10.1523/JNEUROSCI.6221-11.2012

Conflict of Interest: The authors declare that the research was conducted in the absence of any commercial or financial relationships that could be construed as a potential conflict of interest.

The reviewer CR declared his involvement as co-editor in the Research Topic, and confirms the absence of any other collaboration.

Copyright © 2019 Palpagama, Waldvogel, Faull and Kwakowsky. This is an open-access article distributed under the terms of the Creative Commons Attribution License (CC BY). The use, distribution or reproduction in other forums is permitted, provided the original author(s) and the copyright owner(s) are credited and that the original publication in this journal is cited, in accordance with accepted academic practice. No use, distribution or reproduction is permitted which does not comply with these terms.

frontiers in Molecular Neuroscience

ORIGINAL RESEARCH
published: 19 November 2019
doi: 10.3389/fnmol.2019.00275

Imaging and Quantification of Myelin Integrity After Injury With Spectral Confocal Reflectance Microscopy

*David G. Gonsalvez†, SangWon Yoo†, Jessica L. Fletcher, Rhiannon J. Wood, Georgina A. Craig, Simon S. Murray and Junhua Xiao**

Neurotrophin and Myelin Laboratory, Department of Anatomy and Neuroscience, School of Biomedical Sciences, Faculty of Medicine, Dentistry and Health Sciences, The University of Melbourne, Parkville, VIC, Australia

Developing a high-throughput approach to quantify the extent of myelin integrity in preclinical models of demyelinating diseases will enhance our capacity to identify novel therapies for myelin repair. In light of the technical limitations of electron microscopy and immunohistochemical analyses of myelination, we have utilized a novel imaging technique, spectral confocal reflectance (SCoRe) microscopy. SCoRe takes advantage of the optically reflective properties of compact myelin, allowing the integrity of compact myelin to be quantified over the course of the cuprizone-induced model of central demyelination. We applied SCoRe imaging on fixed frozen brain sections. SCoRe analysis of control mice identified an increase in corpus callosum myelination during the period of cuprizone administration and recovery, suggesting that the normal developmental processes of myelination are ongoing at this time. Importantly, analysis of mice subjected to cuprizone identified a significant reduction in compact myelin in both rostral and caudal corpus callosum compared to age-matched control mice. SCoRe microscopy also allowed the visualization and quantification of the amount of myelin debris in demyelinating lesions. Combining SCoRe imaging with immunohistochemistry, we quantified the amount of myelin debris within IBA-1+ microglia and found that 11% of myelin debris colocalized in microglia irrespective of the callosal regions, with the vast majority of debris outside of microglia. In summary, we have demonstrated that SCoRe microscopy is an effective and powerful tool to perform both quantitative and qualitative analyses of compact myelin integrity in health or after injury *in vivo*, demonstrating its future application in high-throughput assessments and screening of the therapeutic efficacy of myelin repair therapies in preclinical animal models of demyelinating diseases.

Keywords: imaging, myelination, demyelination and remyelination, myelin debris, cuprizone model

OPEN ACCESS

Edited by:
Robert J. Harvey, University of the Sunshine Coast, Australia

Reviewed by:
Shin Hyeok Kang, Temple University, United States
Anna Maria Pugliese, University of Florence, Italy

****Correspondence:***
Junhua Xiao
xiaoj@unimelb.edu.au

† These authors have contributed equally to this work

Received: *15 June 2019*
Accepted: *29 October 2019*
Published: *19 November 2019*

Citation:
Gonsalvez DG, Yoo S, Fletcher JL, Wood RJ, Craig GA, Murray SS and Xiao J (2019) Imaging and Quantification of Myelin Integrity After Injury With Spectral Confocal Reflectance Microscopy. Front. Mol. Neurosci. 12:275. doi: 10.3389/fnmol.2019.00275

INTRODUCTION

Myelin is a specialized protein–lipid bilayer sheath that extends from myelin-producing glia, the oligodendrocytes in the central nervous system (CNS), and Schwann cells in the peripheral nervous system. Myelin sheaths surround axons, forming a compact multilamellar structure, which not only facilitates rapid conduction of electrical signals along axons but also provides metabolic and trophic support to neurons (Kramer-Albers et al., 2007; Nave, 2010). Adequate generation and maintenance of compact myelin are critical for the normal

function of the nervous system, and any disruptions in the process of myelination or damage to myelin can result in demyelination and subsequent neuronal degeneration or loss. Most notably, this occurs in multiple sclerosis (MS), where there is a direct autoimmune attack against the myelin sheath. During myelin damage, the fragmented myelin sheaths aggregate and form large, irregular clusters of myelin debris (Prineas et al., 1984). Efficient removal of myelin debris by microglia is known to be a prerequisite for facilitating myelin repair (Kotter et al., 2005; Lampron et al., 2015). Therefore, techniques that enable quantitative and high-throughput analyses of changes to compact myelin, including the visualization of myelin debris in diseases such as MS or its preclinical animal models, are highly desirable for the development of new myelin repair therapies. However, current imaging techniques of studying compact myelin integrity *in vivo* have clear limitations.

Conventionally, transmission electron microscopy (TEM) has been the only method able to produce a satisfactory resolution of myelin ultrastructure and debris. Despite the unparalleled resolution in EM, the technique has major downsides in terms of the extensive tissue preparation process and sampling capacity (Skripuletz et al., 2011). Immunohistochemical staining against myelin protein is a common approach used as a surrogate measure for the extent of myelination. However, in immunostaining, in order to expose the proteins "hidden" within the tightly compacted myelin sheaths, antigen retrieval procedures and detergents are employed to disrupt the structure of the lipid-rich myelin membranes, inevitably altering the level of myelin proteins exposed for antibody detection. This represents a confounding factor for immunostaining-based analysis of myelination. Recently, a novel label-free reflectance imaging technique that allows direct visualization of myelin was developed (Schain et al., 2014). The technique, known as spectral confocal reflectance (SCoRe) microscopy, exploits a unique feature of compact myelin, which optically reflects incident laser lights (Schain et al., 2014). Being label-free and utilizing conventional confocal systems, SCoRe microscopy involves minimal tissue preparation and allows sampling of a substantially greater area of the CNS (Schain et al., 2014; Hill et al., 2018; Hughes et al., 2018). However, it is unclear if SCoRe microscopy enables quantitative analysis of the extent of myelin damage and repair in animal models of CNS demyelination.

In this study, we used SCoRe microscopy to quantify changes to compact myelin and myelin debris in the cuprizone-induced murine model of CNS demyelination. Here, we show that SCoRe imaging is able to detect a significant difference in the extent of compact myelin between cuprizone-challenged mice and age-matched healthy control groups, in rostral and caudal corpus callosum. In the cuprizone-challenged animals, we detected and quantified the presence of atypical reflection of myelin (myelin debris), most of which persists outside macrophages even after 1 week of remyelination. Together, results of this study demonstrates that SCoRe is a highly reproducible and powerful technique that allows quantification of compact myelin integrity including myelin debris *in vivo*.

MATERIALS AND METHODS

Animals and Cuprizone Administration

C56BL/6 female mice were used in all experiments. Mice were housed in specific pathogen-free conditions at the Melbourne Brain Centre Animal Facility. All animal procedures were approved by The Florey Institute of Neuroscience and Mental Health Animal Ethics Committee and followed the Australian Code of Practice for the Care and Use of Animals for Scientific Purposes. Mice were housed three animals per cage. A minimum of 1 week of acclimation time to the new environment was allowed prior to the start of cuprizone administration. Demyelination was induced by administration of manufactured rodent chow pellet containing 0.2% cuprizone [bis(cyclohexanone)oxaldihydrazone; Envigo RMS Division, Indianapolis, IN, United States] to 6- to 8-week-old C57BL/6 mice for 6 weeks (**Figure 1**). Age-matched control mice were kept on normal chow formulated to have the same nutrient levels as the cuprizone pellets. Food pellets and cages were changed twice a week. Water was provided *ad libitum*.

Tissue Collection

All mice were anesthetized using isoflurane and were intraperitoneally injected with sodium pentobarbital (80 mg/kg). Mice were then fixed via transcardial perfusion using 0.1 M of sterile phosphate-buffered saline (PBS) followed by 4.0% paraformaldehyde (PFA) in 0.1 M of PBS at a rate of 4 ml/min using an NE-1000 programmable single syringe pump. Brains were dissected out and post-fixed overnight at 4°C in 4% PFA. Tissue was then washed in PBS and placed in 30% sucrose overnight at 4°C; the brains were next embedded in optimal cutting temperature (OCT) and frozen in isopentane cooled with dry ice. Serial sections in a coronal orientation were captured on a cryostat microtome at 25-μm thickness (**Figure 2A**).

Immunohistochemistry

For immunostaining without membrane permeabilization, 25-μm-thick brain sections were incubated with primary antibodies (see **Table 1**) prepared in a diluent containing PBS with 10% normal donkey serum (NDS) for at least 3 days at room temperature. Sections were then incubated with secondary antibodies prepared in PBS for 2 h at room temperature in the dark. Hoechst 33342 (Sigma, 23491-52-3) was added to secondary antibodies as a nuclear marker. For some myelin basic protein (MBP) immunostaining with membrane permeabilization steps, slides with 25-μm-thick brain sections were dipped in cold methanol (80%) for 10 min followed by washes in PBS for three times. Sections were then incubated with primary antibodies prepared in a diluent containing PBS with 10% NDS and 0.3% Triton X-100 for at least 3 days, followed by the incubation with appropriate secondary antibodies for a minimum of 2 h.

Spectral Confocal Reflectance Microscopy and Image Analysis

All images were captured on a Zeiss LSM 880 (Airyscan) or Zeiss LSM780 confocal microscope using a water immersion

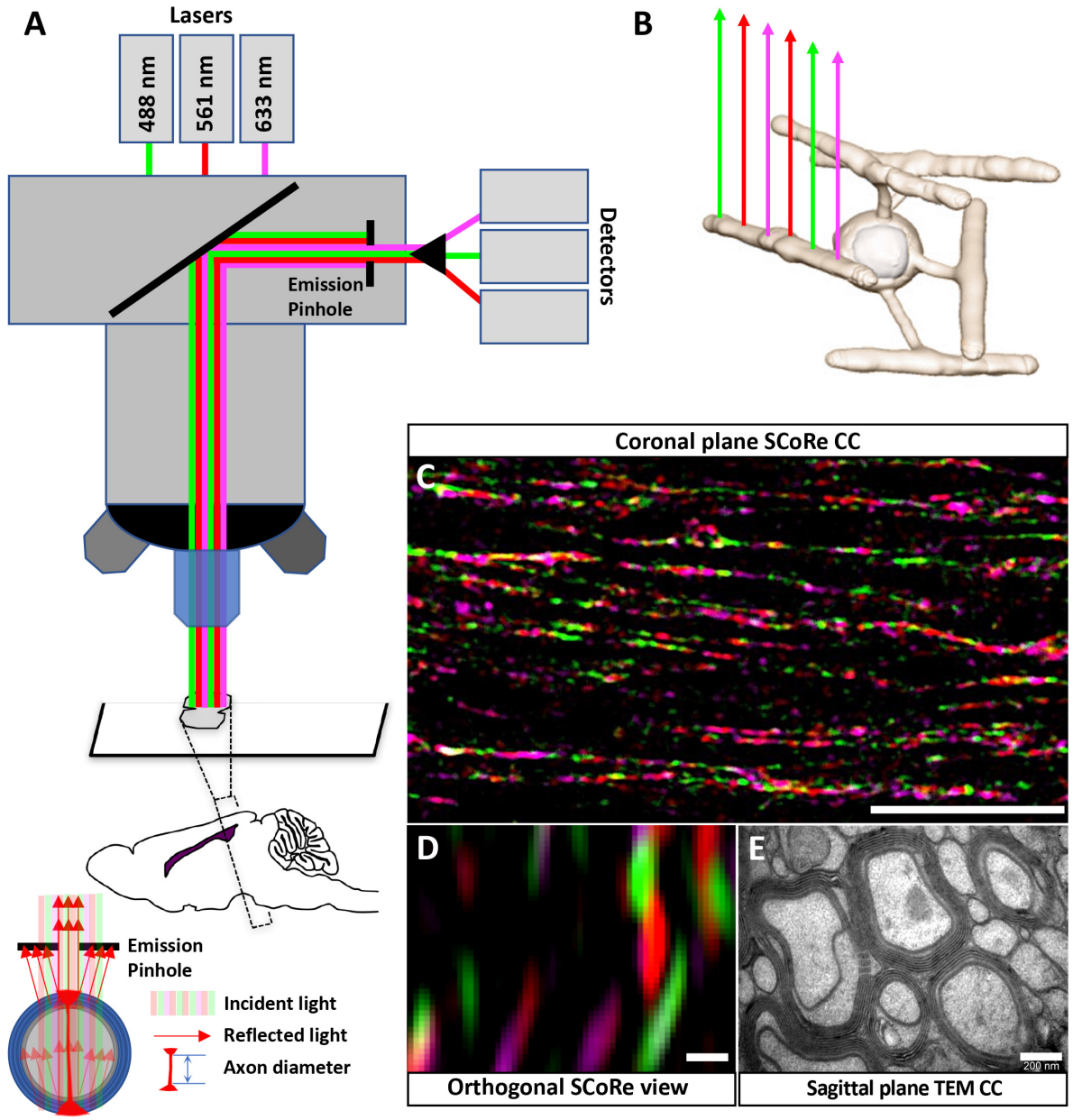

FIGURE 1 | Using SCoRe to visualize compact myelin in fixed frozen brain sections. **(A)** Schematic representation of microscope configuration and the reflected signal captured in SCoRe. The picture of the reflection pattern indicates how SCoRe imaging can be utilized to estimate axon diameter. **(B)** Different wavelengths of light are preferentially reflected back along the length of an internode, which has been attributed to changes in thin film interference along the length of an internode (Schain et al., 2014). **(C)** Single optical slice of a coronal section through the corpus callosum demonstrating how different wavelengths of light are reflected along the myelin internode (scale bar, 10 μm). **(D)** Orthogonal slice from a *Z*-stack SCoRe image of callosal axons (scale bar, 200 nm). **(E)** TEM section taken through the corpus callosum indicating individual myelin lamellae compacted around axons (scale bar, 200 nm). Panels **(D,E)** are taken from the same animal, where half of the brain went to TEM processing and the other half went to SCoRe imaging. The SCoRe reflection signal is stereotypical for healthy myelin. SCoRe, spectral confocal reflectance; TEM, transmission electron microscopy.

objective (Zeiss W Plan-Apochromat 40/1.0 NA DIC or Zeiss W Plan-Apochromat 20/1.0 NA DIC) using 458-, 561-, and 633-nm laser wavelengths passed through the acousto-optical tunable filters (AOTF) 488–640 filter/splitter and a 20/80 partially reflective mirror. The reflected light was collected using three photodetectors set to collect light through narrow bands defined by prism and mirror sliders, centered around the laser wavelengths of 488, 561, and 633 nm (**Figure 1A**). To perform quantitative analysis, the channels from each photodetector were overlaid as one composite image. Compact myelin was assessed by positive pixel identification using a minimum threshold cutoff in FIJI (v1.52k National Institutes of Health, United States).

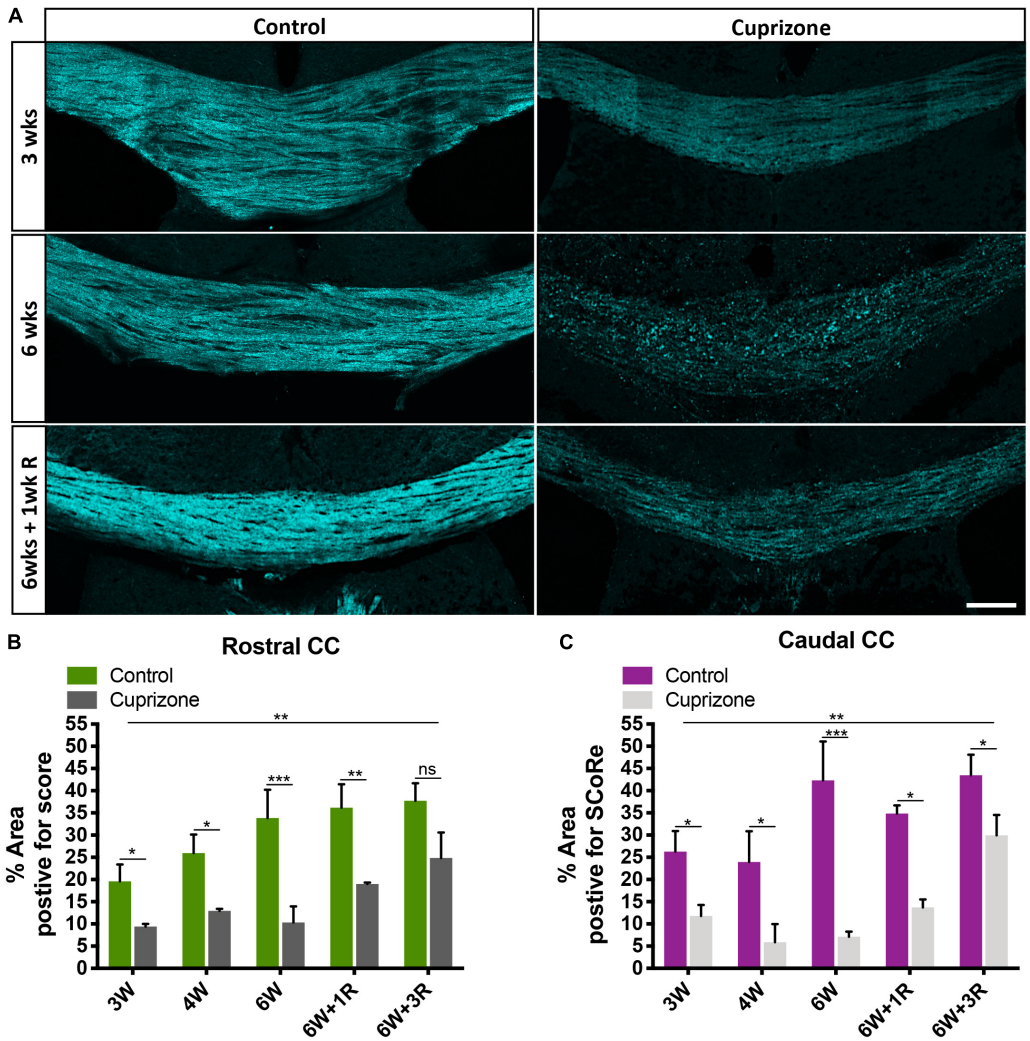

FIGURE 2 | SCoRe imaging can be used to quantify changes to compact myelin after *in vivo* myelin injury. **(A)** Representative SCoRe images of myelin signals in midline corpus callosum demonstrating changes to compact myelin in cuprizone-challenged mice compared with the age-matched healthy control (scale bar, 150 μm). **(B,C)** Quantification of the myelinated area positive for SCoRe signal (pixels) as a percentage of total area measured. The SCoRe signal is significantly reduced in both rostral **(B)** and caudal **(C)** corpus callosum of all cuprizone-challenged mice compared with age-matched healthy control, indicative of demyelination. For each data, point $n = 3$ mice per group, statistics stars indicate a significant interaction (large line) between time and cuprizone exposure determined by two-way ANOVA, multiple comparisons, and Tukey's *post hoc* testing (short lines to indicate pairwise comparisons) (*$P < 0.05$, **$P < 0.01$, ***$P < 0.001$; data = mean ± SD). SCoRe, spectral confocal reflectance.

To generate a percentage, the area positive for SCoRe signal was divided by the total area of the region of interest (ROI). In all cases, the ROI was a trace made to include the total cross-sectional area of the corpus callosum in each section analyzed (Govier-Cole et al., 2019).

Normal-appearing compact myelin reflects light in a very stereotypical pattern (Schain et al., 2014; Hill et al., 2018). Only reflected light that passes through a pinhole can be identified by the detector, and internodes have a stereotypical appearance of long thin lines. Compacted myelin debris is present as round and large aggregates, which are strikingly distinct from the linear appearance of normal compact myelin. This compacted debris/demyelination can be identified using semiautomated process: The threshold function in FIJI was used to create a binary mask of the combined SCoRe signal and the "Analyze Particles" tool was then applied to identify any SCoRe signal that had high (0.75–1.0) circularity with a diameter of 0.6 μm or larger. These parameters were chosen as reflected signal from undamaged myelin has a very stereotypical oblong appearance, and although cortical axons can exceed 0.6 μm in diameter, the reflected width of an internodal segment is rarely greater than 0.5 μm. All selections were inspected by an observer blind to sample identity to ensure no erroneous detection of healthy compact myelin occurred. To identify debris colocalized within IBA-1-positive macrophages, first, a binary mask on the IBA-1 immunosignal was created, and then an analysis of particle

TABLE 1 | List of primary and secondary antisera.

	Source	Concentration
Primary antisera		
Rat anti-myelin basic protein	Millipore, MAB386	1:200
Rabbit anti-IBA-1	WAKO 019-19741	1:1000
Goat anti-IBA-1	Abcam (ab5067)	1:200
Secondary antisera and reagents		
Alexa 647 donkey anti-mouse	Abcam A31571	1:200
Alexa 594 donkey anti-rat	Abcam A21209	1:200
Alexa 488 donkey anti-rabbit	Abcam A21206	1:200
Alexa 488 donkey anti-goat	Abcam A15077	1:200
Hoechst 33342 (bisbenzimide)	Sigma 23491-52-3	1 μg/ml

criteria was applied to exclude normal myelin and positively quantify area of pixels positive for atypically reflected myelin within microglia. All volumetric reconstructions of IBA-1 cells or SCoRe were carried out in IMARIS software. All analyses were performed blinded to sample identity.

Transmission Election Microscopy

To prepare sections for TEM, the whole brain fixed in 4% PFA overnight was cut through the sagittal midline, with the first millimeter of both hemispheres transferred to Karnovsky's buffer overnight and washed in 0.1 M of sodium cacodylate, before being embedded in epoxy resin at the Peter MacCallum Centre for Advanced Histology and Microscopy. Semi-thin sections (0.5–1.0 μm) of the corpus callosum were collected on glass slides and stained with 1% toluidine blue for region selection. Ultra-thin (0.1 μm) sections were subsequently collected on 3 × 3-mm copper grids. Specimens were examined using a JEOL1011 TEM, and images were collected with MegaView II CCD cooled camera operated with iTEM AnalysSIS software (Olympus Soft Imaging Systems).

Statistical Analysis

In assessing MBP with or without permeabilization, there were three variables: (1) treatment with cuprizone, (2) permeabilization condition, and (3) collection time (cuprizone or recovery). To adequately preform statistics with three variables, we employed a three-way ANOVA mixed-model analysis and Tukey's multiple comparisons *post hoc* testing to compare means. In all other cases, two-way ANOVA analysis was performed with Tukey's multiple comparison *post hoc* testing to compare means. All statistical analyses were performed using GraphPad Prism version 8.1.1 for MacOS, GraphPad Software, San Diego, CA, United States. In all cases, the statistical tests and error are reported in the figure legends.

RESULTS

Using SCoRe Imaging to Quantify Cortical Myelin in Fixed Frozen Sections

Spectral confocal reflectance imaging is a powerful, label-free tool to visualize compact myelin *in vivo* (Schain et al., 2014). It has been demonstrated that SCoRe imaging is compatible with fixation (Schain et al., 2014), and it has recently been adopted to assay compact myelin following administration of putative therapeutic agents in animal models of peripheral and central demyelination (Gonsalvez et al., 2017; Govier-Cole et al., 2019). In fixed frozen sections, SCoRe imaging can only be applied when the tissue is sectioned with the myelin internodes and axons parallel to the cut surface of the section (i.e., coronal sections for the corpus callosum; **Figure 1**). The composition of compact myelin, overlapping layers of lipid-rich sheaths, leads to constructive and destructive interference of wavelengths; such wavelengths are preferentially reflected whereas others are suppressed (Schain et al., 2014). This means single laser lines are preferentially reflected from different components along the length of an internode (Schain et al., 2014; **Figures 1B,C**). We find that this pattern of reflection is maintained in coronal sections of the corpus callosum (**Figure 1C**). It is theoretically possible to estimate axon diameter by evaluating the orthogonal SCoRe reflection pattern generated by *z*-stack confocal images. In the corpus callosum, the outer diameter (myelin + axon) corresponds to TEM images taken from the same individuals. However, the reflections from the upper and lower surfaces of myelinated callosal axons are unable to be resolved (**Figure 1D**), indicating these axons are too small to be measured by this technique. For comparison, a TEM image taken from the same individual animal is shown (**Figure 1E**).

Using SCoRe Imaging to Quantify Cortical Myelin Changes Following Demyelination

To test the sensitivity of SCoRe imaging as a quantitative approach to measure changes to compact myelin in the context of demyelination, we employed the cuprizone model. Cuprizone is a copper chelator that leads to oligodendrocyte death and subsequent demyelination. Commencing at 6–8 weeks of age, mice were fed 0.2% cuprizone for 3 weeks (n = 3), 4 weeks (n = 3), 6 weeks (n = 3), 6 weeks with 1-week recovery following cuprizone withdrawal (n = 3), and 6 weeks with 3-week recovery following cuprizone withdrawal (n = 3). To compare with normal myelination, at each time point, age-matched control animals on normal chow were also collected (n = 3/group). SCoRe imaging was highly sensitive to the changes in compact myelin in the corpus callosum that occur because of normal aging, as well those that occur in response to ongoing cuprizone exposure (**Figure 2A**). Quantifying the SCoRe signal by assessing the percentage of the total cross-sectional area of the corpus callosum in each section positive for SCoRe signal (pixels) revealed that cuprizone resulted in a significant ($p < 0.01$) decrease in SCoRe signal in both rostral (**Figure 2B**) and caudal (**Figure 2C**) corpus callosum from 3 weeks of cuprizone administration, indicative of demyelination and disruption to compact myelin integrity. Moreover, SCoRe was able to detect significant differences in the level of myelination between cuprizone and healthy control groups during 1 and 3 weeks of recovery (**Figures 2B,C**), suggesting that SCoRe is a valid method to measure the extent of myelin integrity during recover. Notably, quantification of

SCoRe signal was also sensitive enough to detect a significant increase of compact myelin in both rostral and caudal corpus callosum in the age-matched healthy control mice from ∼10 to ∼14 weeks of age (**Figures 2B,C**), consistent with published data showing that the murine corpus callosum acquires about 15% of its total myelin over this period (Sturrock, 1980). This finding suggests that SCoRe imaging is sensitive to identify the normal developmental processes of myelination that are ongoing over this period, consistent with previous studies undertaken in the cerebral cortex (Hill et al., 2018; Hughes et al., 2018). Together, our data demonstrate that SCoRe is a sensitive imaging modality that can be used to measure the extent of not only myelin damage/repair in animal models of diseases but also ongoing myelination during normal development.

Combined Use of SCoRe Imaging With Immunohistochemistry to Identify Areas of Structural Damage

Typical approaches to quantify the level of myelin protein expression by immunohistochemistry (or immunofluorescence) require aggressive membrane permeabilization steps to expose myelin proteins and increase their antigenicity. Using routine membrane permeabilization techniques, we were able to detect changes in the immunofluorescence of MBP over the course of the cuprizone model (**Figures 3A,B**). However, recent evidence suggests that cuprizone leads to early structural modifications in myelin. Importantly, these structural changes may be required for immune interactions that are likely significant during the course of demyelination (Liu et al., 2010; Caprariello et al., 2018). We hypothesized that the damaged to or loss of compact myelin structure will increase antigenicity and the ability to detect myelin specific proteins in the presence of membrane permeabilization agents/steps. To determine if damaged myelin has a higher level of antigenicity, we performed immunohistochemistry against MBP without processing the tissues with traditional permeabilization steps. We found that after omitting standard tissue permeabilization steps (methanol and Triton X-100), MBP immunofluorescence was almost absent from control mice. This was unsurprising as compact layers of lipid membrane shield myelin proteins, leading to low antigenicity. Surprisingly, we observed a significant increase in MBP immunofluorescence in cuprizone-treated mice compared with controls when membrane permeabilization steps were omitted from the tissue processes. Furthermore, imaging with SCoRe revealed that the immunofluorescence for MBP (in the absence of permeabilization steps) corresponded to the areas of decreased and patchy SCoRe signal, indicative of a loss/damage of compact myelin. No MBP positive staining was detectable in areas where compact myelin is intact, as assessed by SCoRe imaging (**Figure 3C**). In addition to this, the detection of IBA-1 clearly demonstrates the profound and highly localized infiltration of macrophages to these demyelinated regions, with IBA-1+ cells sparse in regions of intact compact myelin detected by SCoRe (**Figure 3C**). Overall, our results provide strong evidence that structural breakdown of compact myelin such as that occurring in the cuprizone model results in increased detection of myelin proteins using antibody-based assays when permeabilization steps are not carried out. Furthermore, this approach may present a means to positively identify areas within tissues where myelin structure has been damaged even early on in the cuprizone model.

SCoRe Imaging Can Be Used to Quantify Atypical Appearing Myelin and Myelin Debris

It is well established that experimentally generated myelin debris, injected back into remyelinating tissues, exerts an inhibitory effect on oligodendrocyte precursor cell (OPC) differentiation and has the capacity to increase macrophage activity (Kotter et al., 2006). At present, the only means to visualize myelin debris is via TEM. Our TEM analysis of callosal tissue following 6 weeks of cuprizone reveals the presence of myelin debris, both within and outside of macrophages (**Figure 4A**). Importantly, the imaging demonstrates that debris artifacts are densely compacted yet structurally distinct from those of normal white matter (**Figure 4A**). Unfortunately, TEM is extremely time-consuming and only samples a tiny fraction of tissue, such that quantification of myelin and debris in this way is likely not completely representative and unreliable. Previous studies have indicated that myelin debris can be identified using SCoRe on the basis of its differential reflection pattern (Hill et al., 2018). To determine the extent of myelin debris and whether it has been engulfed by macrophages after 6 weeks of cuprizone exposure (typically considered peak demyelination) and whether it changed after 1 and 3 weeks of remyelination, combined IBA-1 immunofluorescence and SCoRe images were analyzed (**Figures 4B,C**). This revealed that there was no change in the percentage area positive for myelin debris in either the rostral (**Figure 4D**) or caudal (**Figure 4E**) corpus callosum of mice fed cuprizone for 6 weeks than of those allowed to also remyelinate for 1 week. Intriguingly, there was also no change in the percent of myelin debris localized within IBA-1+ macrophages between peak demyelination and 1-week remyelination (**Figures 4D,E**). At 3 weeks of remyelination, there was a profound decrease in profiles that resembled myelin debris by SCoRe imaging (**Figure 4E**). However, during the remyelinating process, approximately 10% of all detected myelin debris was found within macrophages (**Figure 4E**), indicating that, at any instant, ∼90% of myelin debris detectable by SCoRe imaging is observed outside of macrophages and during remyelination following cuprizone. Furthermore, to investigate if SCoRe signal captures compact myelin or not a unique myelin composition of lipid, we performed SCoRe imaging together with lipofuscin as well as IBA-1. Lipofuscin is a lipid containing residue and is also autofluorescent. We found that at 3 weeks of remyelination, autofluorescent lipofuscin aggregates were observed within IBA-1+ macrophages (**Figure 5**). Although these aggregations are lipid, they are not compact and hence not colocalized with the SCoRe signal (**Figure 5**), further demonstrating that the laser light can only be reflected of unique compacted myelin, rather than the membrane composition of lipid. Together, we show that combining SCoRe imaging with

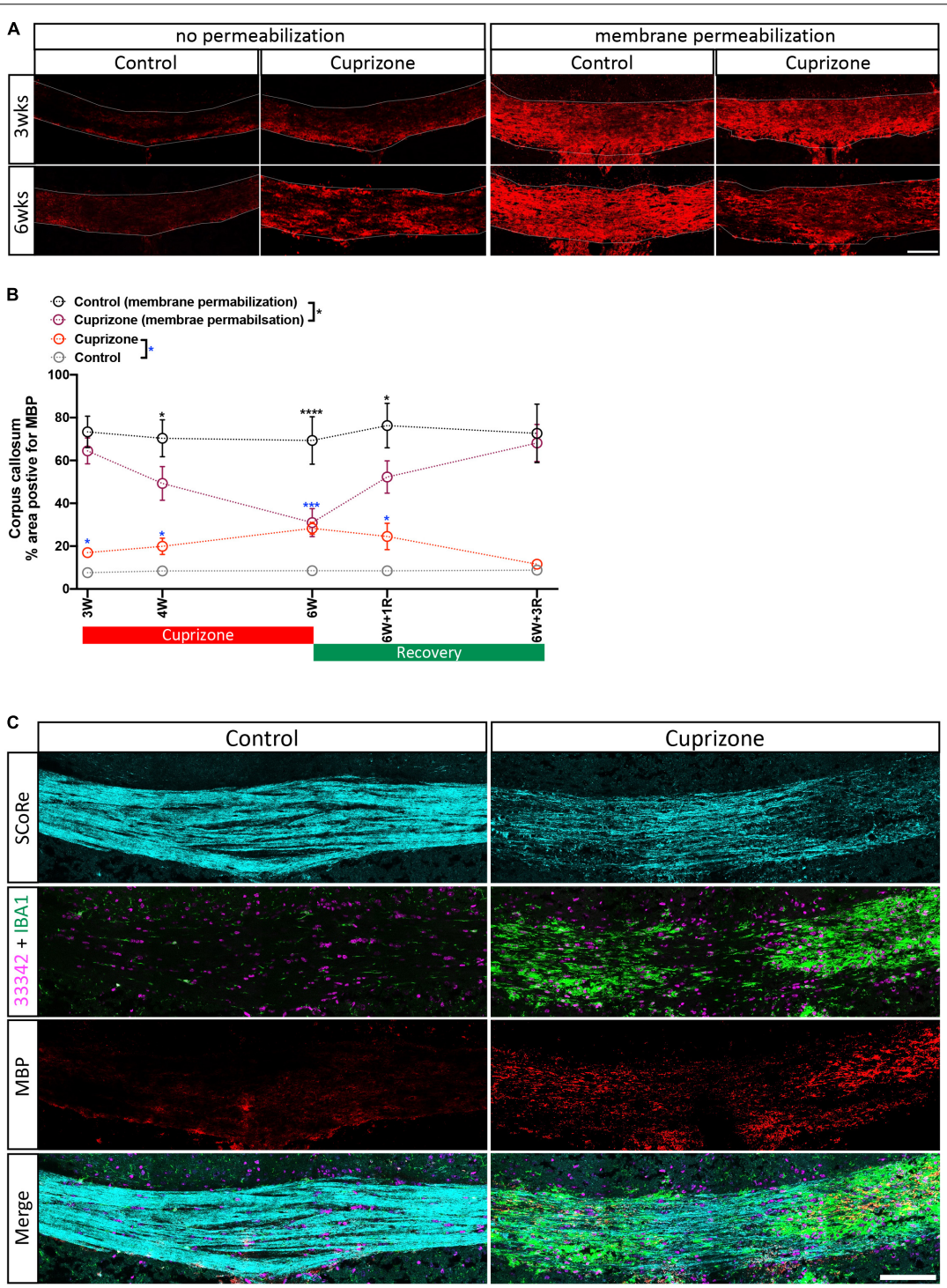

FIGURE 3 | Antigenicity of myelin proteins is increased following myelin damage. **(A)** Representative micrographs of myelin protein MBP immunostaining in the corpus callosum of healthy control and cuprizone-challenged mice without or with membrane permeability steps being employed in the histological processing (scale bar, 100 μm). **(B)** Quantification of the percentage area positive for myelin protein MBP immunoreactivity. Irrespective of treatments, the area of pixels positive for MBP immunofluorescence is greater in staining with membrane permeabilization steps than in those without. When membrane permeabilization is omitted from the tissue processing, the area of pixels positive of MBP immunofluorescence is elevated in cuprizone-fed mice compared with healthy controls ($n = 3$ mice per group, statistics stars indicate a significance between cuprizone and control groups by three-way ANOVA testing using multiple comparisons, $^{*}P < 0.05$, $^{**}P < 0.01$, $^{***}P < 0.001$, $^{****}P < 0.0001$, data = mean ± SD). **(C)** SCoRe imaging combined with immunofluorescence imaging against MBP and IBA-1 in the corpus callosum of healthy control and cuprizone-challenged mice. Areas with reduced SCoRe signal indicate demyelination, which overlaps with elevated microglia infiltration (IBA-1-positive cells) and enhanced intensity of MBP immunoreactivity (scale bar, 100 μm). MBP, myelin basic protein.

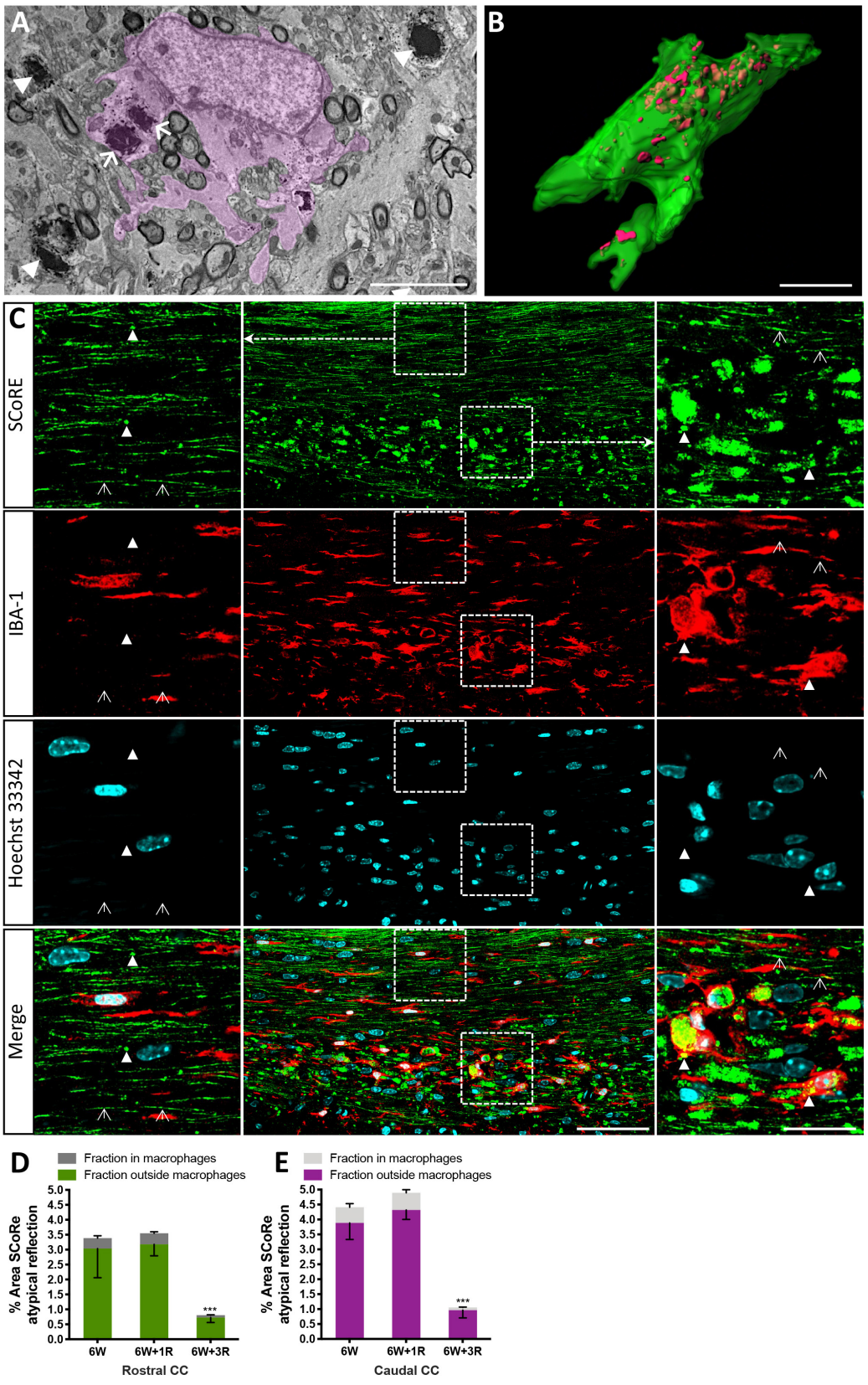

FIGURE 4 | Continued

FIGURE 4 | Pathological myelin and myelin debris can be quantified using SCoRe imaging. **(A)** Transmission electron microscopy micrograph through the corpus callosum at the peak of demyelination (after 6 weeks of feeding of 0.2% cuprizone in normal chow). A CNS macrophage (pink shading) containing electron dense myelin debris (arrows). Compact myelin surrounding axons in a **(B)** *Z*-projection and 3D reconstruction of an IBA-1-positive macrophage (green) with myelin debris identified by SCoRe (red) (scale bar, 5 μm). **(C)** Coronal single *Z* plane image through the corpus callosum of a mouse administrated with cuprizone for 6 weeks followed by 1-week recovery. The SCoRe reflectance from normal-appearing compact myelin is identified by open arrowheads. Compact myelin debris is indicated with solid arrowheads and can be observed within IBA-1-positive macrophages (scale bar, 10 μm). **(D,E)** The percentage area of myelin debris in the rostral **(D)** and caudal **(E)** corpus callosum at the peak of demyelination and during recovery. At all points, ∼10% of the debris was identifiable in IBA-1 positive macrophages (statistics: $n = 3$ mice per group for each data point, ANOVA with multiple comparisons, and Tukey's *post hoc*, $^{***}P < 0.01$, data = mean ± SD). SCoRe, spectral confocal reflectance; CNS, central nervous system.

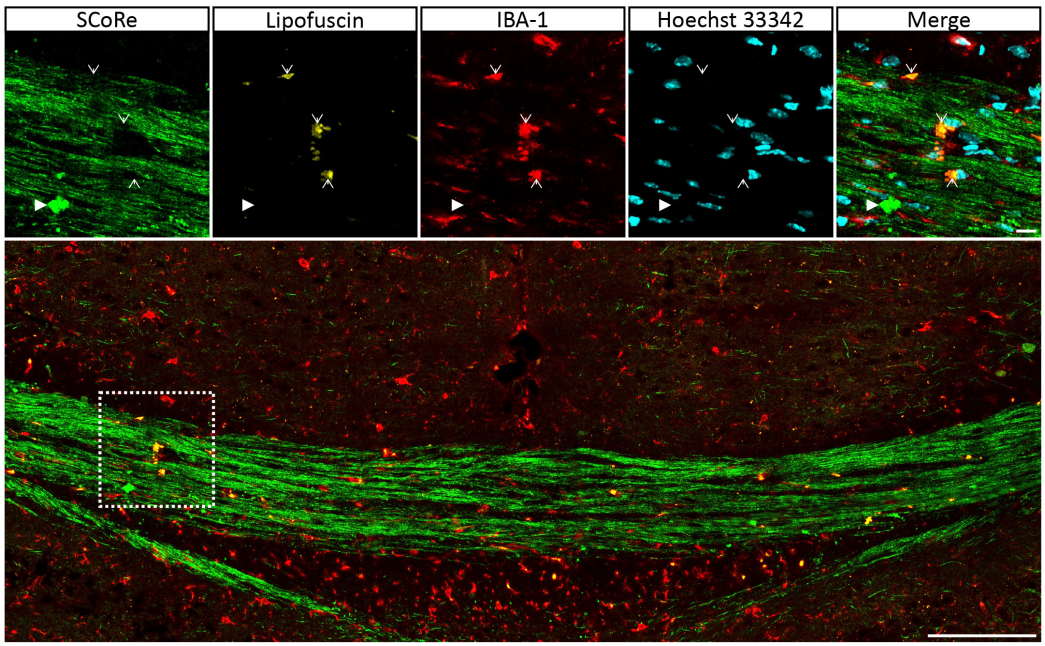

FIGURE 5 | Autofluorescent lipofuscin aggregations in IBA-1 macrophages do not generate a SCoRe signal. Coronal single *Z* plane image through the corpus callosum of a mouse administrated with cuprizone for 6 weeks followed by 3 weeks of recovery. The autofluorescent lipofuscin is localized within IBA-1+ macrophages (open arrowheads) but not colocalized with compact debris (closed arrowhead). Scale bar of 10 μm for the small images and 100 μm for the large images. SCoRe, spectral confocal reflectance.

immunofluorescence is an exciting way to detect and quantify myelin debris *ex vivo*.

DISCUSSION

Quantification of the extent of myelin damage and repair is highly dependent upon techniques being used. This study is the first to quantitatively analyze myelin integrity after a demyelinating insult *in vivo* has used SCoRe microscopy, a novel label-free structural-based myelin imaging technique. We have demonstrated that this technique enables high-throughput quantitative analysis of myelin integrity of the whole corpus callosum in a murine model of CNS demyelination, avoiding the confounding changes to myelin protein antigenicity that occur as a result of myelin injury and limited sampling capacity of TEM. Through combining SCoRe imaging with immunohistochemistry, we have quantified the amount of myelin debris and found the majority of myelin debris is localized outside of macrophages even during remyelination. In summary, we demonstrated that SCoRe is an effective and high-throughput tool to quantify changes in compact myelin structure owing to demyelination *in vivo*, implicating its broad applications in other model systems where changes in myelination are of interest.

SCoRe Enables High-Throughput Quantitative Analysis of Myelination After Injury *in vivo*

Currently, relatively few approaches have been used for *in vivo* imaging of myelinated axons and myelin-forming glial cells. For example, confocal and two-photon microscopy has been used with genetically labeled fluorescent markers to image oligodendrocytes and myelin sheaths within zebrafish (Kirby et al., 2006; Czopka et al., 2013; Simons and Lyons, 2013; Hines et al., 2015; Baraban et al., 2018). However, imaging myelinated axons or compact myelin sheath using fluorescent reporters requires complex imaging systems, and labeling myelin sheaths with fluorescent dyes is often inconsistent, creating challenges for quantitative analysis of myelin dynamics

over time in rodent disease models *in vivo*. SCoRe uses a conventional confocal microscope, making it easy to implement. Other label-free imaging modalities could also be applied to image myelin and myelin debris. Coherent anti-Stokes Raman scattering (CARS) microscopy utilizes intrinsic molecular vibration of lipid structures to enable imaging of myelinated fibers (Wang et al., 2005) and *in vivo* mouse brain (Fu et al., 2008). However, these imaging techniques require complex setups, and the equipment required for this complex imaging is rarely available, making them difficult to implement and hence not widely used (Farrar et al., 2011), whereas SCoRe imaging requires confocal microscopy, which is commonly available, easy to implement, and readily accessible. Importantly, those imaging techniques that enable label-free quantification of myelin that is second or third harmonic generation (S/THG) depends on the molecular composition of the myelin for the generation of its signal and requires the use of multiphoton-specialized equipment that may not be readily available. The key point of difference between the signals collected using CARS and S/THG compared with SCoRe is that the SCoRe signal relies on the structural organization of the lipid rather than the molecular structure of the lipid *per se*. Thus, SCoRe allows the imaging of the unique compact myelin than do other label-free imaging techniques. This is highly important, as the SCoRE signal is binary only to compact myelin that reflects the incident light and the compacted lipid layers that are unique to myelin (Schain et al., 2014; Hill et al., 2018). In this study, we applied SCoRe imaging directly onto frozen brain sections of adult mice and have demonstrated its capacity to be combined with immunohistochemistry. Consistent with the previous study (Schain et al., 2014), we found that SCoRe is highly sensitive to myelin changes during normal aging and demyelination and allows repeated imaging over a large anatomical ROI with high resolution. Importantly, the acquisition of SCoRe signals enables both qualitative and quantitative analyses of changes to compact myelin during cuprizone-induced CNS demyelination.

Several studies have reported that cuprizone induces CNS demyelination in anatomically diverse regions, including the cerebral cortex (Gudi et al., 2009; Skripuletz et al., 2011), cerebellum (Groebe et al., 2009), hippocampus (Norkute et al., 2009), and the key white matter tract corpus callosum (Gudi et al., 2009; Skripuletz et al., 2011), with the corpus callosum recognized as the most prominent and reproducible demyelinating region (Skripuletz et al., 2011). TEM analysis of myelin ultrastructure suggests that, in the murine cuprizone model, there exists a rostral–caudal pattern of myelin damage in the corpus callosum (Stidworthy et al., 2003; Steelman et al., 2012), with the caudal part exhibiting a greater and more reproducible demyelination (Steelman et al., 2012), whereas the extent of demyelination and remyelination is more variable in the rostral portion (Stidworthy et al., 2003). Indeed, a limited number of studies conclude that the rostral corpus callosum displays subtle demyelination in the cuprizone model (Stidworthy et al., 2003; Steelman et al., 2012) and that analysis using traditional histology or TEM fails to reveal a significant difference between cuprizone-challenged mice and unchallenged controls (Stidworthy et al., 2003; Steelman et al., 2012). Our study demonstrates that SCoRe has the sensitivity required to quantify the extent of myelin damage in both rostral and caudal corpus callosum during cuprizone-induced demyelination, identifying significant differences between cuprizone-challenged mice and age-matched control mice. Collectively, the literature together with our data suggests that although the EM technique is an excellent approach to quantify myelin, it does not have the sampling power to account for the innate myelin variability in the rostral corpus callosum. In this study, SCoRe microscopy markedly facilitates sampling of large areas of tissues, allowing high-throughput and sensitive detection of myelin damage/loss *in vivo*. In addition, corpus callosum undergoes ongoing myelination over the life span in mice (Sturrock, 1980). Our study also identifies the temporal change of myelination in the corpus callosum of mice during late development and early adulthood, which is consistent with the age-dependent increase previously reported using traditional TEM analysis (Sturrock, 1980). Together, our findings highlight the advantage of adopting SCoRe to quantitatively assess myelin integrity over a large anatomical ROI *in vivo*.

ScoRe Is Independent of Myelin Protein Antigenicity After Myelin Injury *in vivo*

Analysis of myelin damage and repair after an injury is more complex than normal development owing to the presence of damaged myelin sheaths in lesions. In addition to TEM, immunohistochemical analysis of myelin protein expression is a commonly used conventional approach to assess myelination after injury *in vivo*. Indeed, many publications that have assessed demyelination and remyelination via this technique utilize some forms of antigen retrieval to improve the antigenicity of proteins located between the lamellae of compact myelin (Lindner et al., 2008; Gudi et al., 2009; Xu et al., 2009). In the context of myelin injury such as the cuprizone model, damage to myelin sheaths increases the exposure of internal myelin proteins, resulting in greater antibody recognition and is consequently not a true selective representation of myelinated axons. In this study, we found that immunohistochemical staining against the myelin protein MBP in cuprizone-demyelinated brain without using detergent or antigen retrieval revealed counterintuitive results with a significantly higher level of myelin protein expression in the corpus callosum after cuprizone-induced demyelination. Importantly, comparison with the SCoRe signal was highly informative, as the high level of MBP immunofluorescence corresponded to decreased SCoRe signal. This indicates immunostaining for myelin proteins without membrane permeabilization may be a good surrogate for quantifying the extent of myelin damage, rather than the level of intact myelin.

Use of immunostaining for myelin proteins as a surrogate marker for myelin damage is the inverse of how myelin protein immunofluorescence is traditionally used. It also highlights the variable nature of myelin immunostaining, which depends on the extent of physical disruption by either damage or membrane permeabilization methods. Although this problem

of structural disruption and antigenicity may be overcome with antigen retrieval steps to a certain extent, this is not always the case. Xu et al. (2009) reported that the use of detergent during immunostaining of myelin proteins resulted in high fluorescent intensity of the myelin protein MBP in the corpus callosum at the peak of demyelination of cuprizone-fed mice compared with unchallenged control mice. Hence, the amount of myelin protein assessed via immunohistochemistry failed to accurately identify level of intact myelin after injury. This represents a significant limitation for the use of fluorescent intensity to quantify myelin. SCoRe microscopy exploits the reflective property of compact myelin (Schain et al., 2014; Hill et al., 2018; Hughes et al., 2018), enabling direct visualization of the structure of compact myelin and objective quantitative analysis of myelin integrity through postimage acquisition. It allows an antibody-free imaging modality, which is not compatible with membrane permeabilization methods during immunohistochemical staining. Moreover, immunostaining against myelin proteins does not discriminate intact compact myelin from disorganized atypical myelin such as myelin debris, ultimately leading to an overestimation of myelination, confounding the analysis of myelin integrity (Skripuletz et al., 2011). In a study by Lampron et al. (2015), higher levels of MBP fluorescent intensity, initially thought to indicate greater myelination, were, in fact, abnormal patterns of myelin. Concordant with this finding, in our study, we have demonstrated that myelin protein expression detected by immunohistochemistry is found in areas where there is a low level of compact myelin signal via SCoRe, accompanied via a high density of macrophages. Therefore, our study together with others suggests that immunohistochemical analysis of myelin protein expression is not an accurate measurement of compact myelin after injury and that ScoRe has a unique capacity to measure intact myelin *in vivo*.

SCoRe Imaging Enables Quantitative Analysis of Myelin Debris After Injury *in vivo*

Pathology from postmortem MS brains indicates that myelin debris exists in MS lesions as clustered aggregations of compact myelin fragments (Prineas et al., 1984). Myelin debris is present within resident and infiltrating peripheral macrophages, indicative of debris clearance by both microglia and macrophages (Prineas et al., 1984). Currently, beyond *in vivo* imaging with appropriate fluorescent reporters, TEM is the most accessible method to detect myelin debris. However, the chance of encountering a debris event in a TEM image is low owing to the extremely small size of sample regions, limiting its utility for accurately quantitating the amount of myelin debris. Using the SCoRe imaging, Hill et al. (2018) identified not only the ongoing cortical myelination but also occasional debris fragments colocalized in IBA-1-positive microglia in mice beyond 24 months of age *in vivo*. Consistent with the published work, we show that SCoRe microscopy enables visualization of myelin debris with a distinct appearance from healthy intact compact myelin on *ex vivo* slides. Importantly, we, for the first time, demonstrate that SCoRe microscopy allows quantification of intracellular and extracellular myelin debris. Our data have shown that cuprizone-challenged animals display a substantially higher amount of myelin debris in the corpus callosum than have age-matched healthy control mice. Interestingly, we found only approximately 10% of myelin debris resides within microglia irrespective of callosal regions, whereas the vast majority (90%) is located outside of cells without being in intact axons. There has been continuous interest in the association between the presence and clearance of myelin debris and remyelinating efficiency. Several studies have revealed that efficient removal of myelin debris by microglia is a prerequisite for facilitating remyelination (Kotter et al., 2005; Lampron et al., 2015). Furthermore, a delay in myelin debris clearance has been shown to obstruct the differentiation of OPCs into mature myelin-forming cells (Kotter et al., 2005), hindering myelin repair (Lampron et al., 2015). Our study indicates that SCoRe imaging enables quantitative analysis of intracellular and extracellular myelin debris after injury *in vivo*, indicating that this is a new and powerful approach in evaluating the therapeutic efficacy of new myelin repair strategies that may incorporate efficient myelin debris clearance.

This study demonstrates an application of SCoRe imaging for assessing myelin integrity, overcoming the confounding myelin protein antigenicity after injury and limited sampling capacity of TEM. Despite these advantages, current SCoRe imaging also has limitations. It is important to note that the compact myelin has to be in a specific orientation to the incident light in order generate the SCoRe signal (Schain et al., 2014). In combination with immunohistochemistry, SCoRe imaging is able to capture mature myelinating oligodendrocytes and the longitudinal growth of myelin sheaths, allowing the measurement of the number and length of myelin internodes per oligodendrocyte (Hughes et al., 2018). However, the light reflective nature of this imaging method for assessing myelin does not equip it to determine the radial growth of myelin sheaths such as myelin membrane thickness, an important indicator of myelin development and regeneration. Given this orientation limitation, the quantification of compact myelin debris assessed via SCoRe imaging would be underestimated.

CONCLUSION

In summary, we have demonstrated that SCoRe microscopy is a high-throughput imaging modality that can sensitively detect and quantify changes in myelin integrity including compact myelin and myelin debris. It supplements TEM for more defined analysis of myelin integrity. Being able to detect myelin debris, this label-free and easy-to-implement technique can replace the conventional approach of immunohistochemistry against myelin proteins and supplement TEM regarding sampling size. Application of SCoRe imaging in future preclinical analysis of putative MS therapies will allow efficient and accurate assessment of drug efficacy in promoting myelin repair.

DATA AVAILABILITY STATEMENT

All datasets generated for this study are included in the article/supplementary material.

ETHICS STATEMENT

The animal study was reviewed and approved by The Florey Institute for Neuroscience and Mental Health Animal Ethics Committee of the University of Melbourne (Australia).

AUTHOR CONTRIBUTIONS

DG and JX conceived the study. DG, SY, RW, and GC performed the experiments. DG and SY analyzed the data. DG, SY, and JX wrote the manuscript. DG, JF, and JX reviewed and revised the manuscript. All authors read, revised, and approved the submitted version of the manuscript.

FUNDING

We would like to thank all grant sponsors: Australian Research Council Discovery Project Grant (#DP180102397) and the Australian National Health and Medical Research Council (NHMRC) Project Grant (#APP1058647) to JX; NHMRC ECF Fellowship (#APP1111041) to DG; Multiple Sclerosis Research Australia Postdoctoral Fellowship (#14-056) to JF; and the Sir John Eccles Vacation Scholarship and the Melbourne Research scholarship to SY and GC. Confocal imaging was performed at the Biological Optical Microscope Platform, The University of Melbourne.

REFERENCES

Baraban, M., Koudelka, S., and Lyons, D. A. (2018). Ca (2+) activity signatures of myelin sheath formation and growth *in vivo*. *Nat. Neurosci.* 21, 19–23. doi: 10.1038/s41593-017-0040-x

Caprariello, A. V., Rogers, J. A., Morgan, M. L., Hoghooghi, V., Plemel, J. R., Koebel, A., et al. (2018). Biochemically altered myelin triggers autoimmune demyelination. *Proc. Natl. Acad. Sci. U.S.A.* 115, 5528–5533. doi: 10.1073/pnas.1721115115

Czopka, T., Ffrench-Constant, C., and Lyons, D. A. (2013). Individual oligodendrocytes have only a few hours in which to generate new myelin sheaths *in vivo*. *Dev. Cell* 25, 599–609. doi: 10.1016/j.devcel.2013.05.013

Farrar, M. J., Wise, F. W., Fetcho, J. R., and Schaffer, C. B. (2011). In vivo imaging of myelin in the vertebrate central nervous system using third harmonic generation microscopy. *Biophys. J.* 100, 1362–1371. doi: 10.1016/j.bpj.2011.01.031

Fu, Y., Huff, T. B., Wang, H. W., Wang, H., and Cheng, J. X. (2008). *Ex vivo* and *in vivo* imaging of myelin fibers in mouse brain by coherent anti-Stokes Raman scattering microscopy. *Opt. Express* 16, 19396–19409.

Gonsalvez, D. G., Tran, G., Fletcher, J. L., Hughes, R. A., Hodgkinson, S., Wood, R. J., et al. (2017). A brain-derived neurotrophic factor-based p75(NTR) peptide mimetic ameliorates experimental autoimmune neuritis induced axonal pathology and demyelination. *eNeuro* 4:ENEURO.0142-17.2017. doi: 10.1523/ENEURO.0142-17.2017

Govier-Cole, A. E., Wood, R. J., Fletcher, J. L., Gonsalvez, D. G., Merlo, D., Cate, H. S., et al. (2019). Inhibiting bone morphogenetic protein 4 type I receptor signaling promotes remyelination by potentiating oligodendrocyte differentiation. *eNeuro* 6:ENEURO.0399-18.2019. doi: 10.1523/ENEURO.0399-18.2019

Groebe, A., Clarner, T., Baumgartner, W., Dang, J., Beyer, C., and Kipp, M. (2009). Cuprizone treatment induces distinct demyelination, astrocytosis, and microglia cell invasion or proliferation in the mouse cerebellum. *Cerebellum* 8, 163–174. doi: 10.1007/s12311-009-0099-3

Gudi, V., Moharregh-Khiabani, D., Skripuletz, T., Koutsoudaki, P. N., Kotsiari, A., Skuljec, J., et al. (2009). Regional differences between grey and white matter in cuprizone induced demyelination. *Brain Res.* 1283, 127–138. doi: 10.1016/j.brainres.2009.06.005

Hill, R. A., Li, A. M., and Grutzendler, J. (2018). Lifelong cortical myelin plasticity and age-related degeneration in the live mammalian brain. *Nat. Neurosci.* 21, 683–695. doi: 10.1038/s41593-018-0120-6

Hines, J. H., Ravanelli, A. M., Schwindt, R., Scott, E. K., and Appel, B. (2015). Neuronal activity biases axon selection for myelination *in vivo*. *Nat. Neurosci.* 18, 683–689. doi: 10.1038/nn.3992

Hughes, E. G., Orthmann-Murphy, J. L., Langseth, A. J., and Bergles, D. E. (2018). Myelin remodeling through experience-dependent oligodendrogenesis in the adult somatosensory cortex. *Nat. Neurosci.* 21, 696–706. doi: 10.1038/s41593-018-0121-5

Kirby, B. B., Takada, N., Latimer, A. J., Shin, J., Carney, T. J., Kelsh, R. N., et al. (2006). In vivo time-lapse imaging shows dynamic oligodendrocyte progenitor behavior during zebrafish development. *Nat. Neurosci.* 9, 1506–1511. doi: 10.1038/nn1803

Kotter, M. R., Li, W. W., Zhao, C., and Franklin, R. J. (2006). Myelin impairs CNS remyelination by inhibiting oligodendrocyte precursor cell differentiation. *J. Neurosci.* 26, 328–332. doi: 10.1523/jneurosci.2615-05.2006

Kotter, M. R., Zhao, C., van Rooijen, N., and Franklin, R. J. (2005). Macrophage-depletion induced impairment of experimental CNS remyelination is associated with a reduced oligodendrocyte progenitor cell response and altered growth factor expression. *Neurobiol. Dis.* 18, 166–175. doi: 10.1016/j.nbd.2004.09.019

Kramer-Albers, E. M., Bretz, N., Tenzer, S., Winterstein, C., Möbius, W., Berger, H., et al. (2007). Oligodendrocytes secrete exosomes containing major myelin and stress-protective proteins: trophic support for axons? *Proteomics Clin. Appl.* 1, 1446–1461. doi: 10.1002/prca.200700522

Lampron, A., Larochelle, A., Laflamme, N., Préfontaine, P., Plante, M. M., Sánchez, M. G., et al. (2015). Inefficient clearance of myelin debris by microglia impairs remyelinating processes. *J. Exp. Med.* 212, 481–495. doi: 10.1084/jem.20141656

Lindner, M., Heine, S., Haastert, K., Garde, N., Fokuhl, J., Linsmeier, F., et al. (2008). Sequential myelin protein expression during remyelination reveals fast and efficient repair after central nervous system demyelination. *Neuropathol. Appl. Neurobiol.* 34, 105–114.

Liu, L., Belkadi, A., Darnall, L., Hu, T., Drescher, C., Cotleur, A. C., et al. (2010). CXCR2-positive neutrophils are essential for cuprizone-induced demyelination: relevance to multiple sclerosis. *Nat. Neurosci.* 13, 319–326. doi: 10.1038/nn.2491

Nave, K. A. (2010). Myelination and support of axonal integrity by glia. *Nature* 468, 244–252. doi: 10.1038/nature09614

Norkute, A., Hieble, A., Braun, A., Johann, S., Clarner, T., Baumgartner, W., et al. (2009). Cuprizone treatment induces demyelination and astrocytosis in the mouse hippocampus. *J. Neurosci. Res.* 87, 1343–1355. doi: 10.1002/jnr.21946

Prineas, J. W., Kwon, E. E., Cho, E. S., and Sharer, L. R. (1984). Continual breakdown and regeneration of myelin in progressive multiple sclerosis plaques. *Ann. N Y Acad. Sci.* 436, 11–32. doi: 10.1111/j.1749-6632.1984.tb14773.x

Schain, A. J., Hill, R. A., and Grutzendler, J. (2014). Label-free in vivo imaging of myelinated axons in health and disease with spectral confocal reflectance microscopy. *Nat. Med.* 20, 443–449. doi: 10.1038/nm.3495

Simons, M., and Lyons, D. A. (2013). Axonal selection and myelin sheath generation in the central nervous system. *Curr. Opin. Cell Biol.* 25, 512–519. doi: 10.1016/j.ceb.2013.04.007

Skripuletz, T., Gudi, V., Hackstette, D., and Stangel, M. (2011). De- and remyelination in the CNS white and grey matter induced by cuprizone: the old,

the new, and the unexpected. *Histol. Histopathol.* 26, 1585–1597. doi: 10.14670/HH-26.1585

Steelman, A. J., Thompson, J. P., and Li, J. (2012). Demyelination and remyelination in anatomically distinct regions of the corpus callosum following cuprizone intoxication. *Neurosci. Res.* 72, 32–42. doi: 10.1016/j.neures.2011.10.002

Stidworthy, M. F., Genoud, S., Suter, U., Mantei, N., and Franklin, R. J. (2003). Quantifying the early stages of remyelination following cuprizone-induced demyelination. *Brain Pathol.* 13, 329–339. doi: 10.1111/j.1750-3639.2003.tb00032.x

Sturrock, R. R. (1980). Myelination of the mouse corpus callosum. *Neuropathol. Appl. Neurobiol.* 6, 415–420. doi: 10.1111/j.1365-2990.1980.tb00219.x

Wang, H., Fu, Y., Zickmund, P., Shi, R., and Cheng, J. X. (2005). Coherent anti-stokes Raman scattering imaging of axonal myelin in live spinal tissues. *Biophys. J.* 89, 581–591. doi: 10.1529/biophysj.105.061911

Xu, H., Yang, H. J., Zhang, Y., Clough, R., Browning, R., and Li, X. M. (2009). Behavioral and neurobiological changes in C57BL/6 mice exposed to cuprizone. *Behav. Neurosci.* 123, 418–429. doi: 10.1037/a0014477

Conflict of Interest: The authors declare that the research was conducted in the absence of any commercial or financial relationships that could be construed as a potential conflict of interest.

Copyright © 2019 Gonsalvez, Yoo, Fletcher, Wood, Craig, Murray and Xiao. This is an open-access article distributed under the terms of the Creative Commons Attribution License (CC BY). The use, distribution or reproduction in other forums is permitted, provided the original author(s) and the copyright owner(s) are credited and that the original publication in this journal is cited, in accordance with accepted academic practice. No use, distribution or reproduction is permitted which does not comply with these terms.

frontiers in Molecular Neuroscience

REVIEW
published: 05 December 2019
doi: 10.3389/fnmol.2019.00297

Application of Urine-Derived Stem Cells to Cellular Modeling in Neuromuscular and Neurodegenerative Diseases

*Mitsuto Sato[1,2], Hotake Takizawa[1], Akinori Nakamura[3], Bradley J. Turner[4], Fazel Shabanpoor[4] and Yoshitsugu Aoki[1]**

[1]*Department of Molecular Therapy, National Institute of Neuroscience, National Center of Neurology and Psychiatry, Kodaira, Japan,* [2]*Department of Medicine (Neurology and Rheumatology), Shinshu University School of Medicine, Matsumoto, Japan,* [3]*Department of Clinical Research, National Hospital Organization Matsumoto Medical Center, Matsumoto, Japan,* [4]*The Florey Institute of Neuroscience and Mental Health, University of Melbourne, Parkville, VIC, Australia*

Neuromuscular and neurodegenerative diseases are mostly modeled using genetically modified animals such as mice. However, animal models do not recapitulate all the phenotypes that are specific to human disease. This is mainly due to the genetic, anatomical and physiological difference in the neuromuscular systems of animals and humans. The emergence of direct and indirect human somatic cell reprogramming technologies may overcome this limitation because they enable the use of disease and patient-specific cellular models as enhanced platforms for drug discovery and autologous cell-based therapy. Induced pluripotent stem cells (iPSCs) and urine-derived stem cells (USCs) are increasingly employed to recapitulate the pathophysiology of various human diseases. Recent cell-based modeling approaches utilize highly complex differentiation systems that faithfully mimic human tissue- and organ-level dysfunctions. In this review, we discuss promising cellular models, such as USC- and iPSC-based approaches, that are currently being used to model human neuromuscular and neurodegenerative diseases.

Keywords: urine-derived stem cells (USCs), induced pluripotent stem cells (iPSCs), disease modeling, direct-reprogramming, precision medicine

OPEN ACCESS

Edited by:
Robert J. Harvey, University of the Sunshine Coast, Australia

Reviewed by:
Ludo M. Van Den Bosch, KU Leuven, Belgium
Peter Claus, Hannover Medical School, Germany

****Correspondence:***
Yoshitsugu Aoki
tsugu56@ncnp.go.jp

Received: *19 July 2019*
Accepted: *20 November 2019*
Published: *05 December 2019*

Citation:
Sato M, Takizawa H, Nakamura A, Turner BJ, Shabanpoor F and Aoki Y (2019) Application of Urine-Derived Stem Cells to Cellular Modeling in Neuromuscular and Neurodegenerative Diseases. Front. Mol. Neurosci. 12:297. doi: 10.3389/fnmol.2019.00297

INTRODUCTION

Understanding the mechanisms underlying the pathology of human disease is essential for drug development. Studies on fundamental principles of human disease and testing of therapeutic modalities are commonly conducted in mouse models (Partridge, 2013). The use of animal models to mimic human diseases presents challenges arising from genetic and physiological differences between humans and animals, in pathologic mechanisms and therapeutic effect. However, due to

the lack of biologically-relevant human disease models, animal models represent the only available approach, which could recapitulate, a physiological and anatomical condition *in vivo*. In contrast, cellular models of human disease, which recapitulate the pathophysiology of various neuromuscular and neurodegenerative diseases, bring us closer to achieving personalized therapy for the individual patient.

It is still being debated as to which cells can be used for cell-based studies. For example, primary myoblasts are usually employed for the study of Duchenne muscular dystrophy (DMD). DMD is a devastating muscle disorder caused by frameshift mutations in the DMD gene. The responsible gene (DMD) encodes the subsarcolemmal protein, dystrophin. In DMD, various frameshift mutations in DMD prevent the full translation of dystrophin. Primary myoblasts express enough levels of dystrophin mRNA but do not express dystrophin protein. This renders them a suitable surrogate for DMD, but collecting myoblasts requires invasive muscle biopsy. Dystrophin mRNA has also been detected in lymphocytes and fibroblasts, as shown by nested real-time polymerase chain reaction (RT-PCR). However, dystrophin protein is not detected in these cells because of illegitimate dystrophin transcripts present at a very low level. Fibroblasts can be converted to myotubes by virally-mediated MyoD1 transduction. Although the transduced cells express dystrophin mRNA and protein, achieving enough expression at the protein level remains challenging. In our previous study, we overcame this issue by designing an *in vitro* assay based on MyoD1-converted fibroblasts isolated using fluorescence-activated cell sorting (FACS) to determine patient eligibility before clinical trials (Saito et al., 2010).

In the neuromuscular diseases, it is challenging to generate a disease model that faithfully represent the patient's pathology, and there are situations in which enough efficacy and safety cannot be confirmed in clinical trials. This is in contradiction to the results in animal models. Human-induced pluripotent stem cells (iPSCs) are an attractive platform for overcoming these limitations. Therefore, patient-specific iPSCs can provide unlimited disease-relevant cells in a personalized manner. This serves as an essential resource for cell types previously considered rare or inaccessible, including skeletal and cardiac myocytes, neurons, and glia. However, there are some limitations about genome instability and epigenetic memory associated with the reprogramming of iPSC, integrity of iPSC derivatives, inherent biological and technical variability between iPSC lines and differentiated cells, and modeling of diseases that are epigenetically influenced by environmental factors or largely sporadic in etiology. Disease modeling using somatic stem cells have also been conducted as a way to solve epigenetic and environmental factors.

In this review, we discuss the current status of cellular modeling of neuromuscular and neurodegenerative diseases, and how such models can contribute towards developing precision therapies for patients with these diseases. In addition, we review a new approach to disease modeling based on urine-derived stem cells (USCs) that is used as a model for neuromuscular disease.

STEM CELLS USED FOR MODELING DISEASE

Stem cells are a valuable research tool for basic, pre-clinical, and clinical studies. Stem cells are defined by two essential characteristics; one is the ability to divide indefinitely and self-replicate, and the other is the ability to differentiate into mature cells under appropriate conditions and specific signals (Malaver-Ortega et al., 2012). According to differentiation potential, stem cells are classified as follows; totipotent, pluripotent, multipotent, oligopotent, and unipotent (Malaver-Ortega et al., 2012). Totipotent and pluripotent cells, which can differentiate into three embryonic lineages and change to any cell type, correspond to embryonic stem cells. Pluripotent stem cells can be obtained from adult somatic cells by incorporating pluripotent transcription factors into the cell's genome. These cells are called iPSCs that have been fully reprogrammed to achieve an induced pluripotent state. Somatic stem cells, multipotent cells that can differentiate into a limited number of mature cell types, can be found among the tissues such as the brain, skeletal muscle, skin, bone marrow, blood, adipose tissue, and liver. These cells have the role of repairing damaged tissue and obtaining tissue homeostasis when tissue damage occurs. One type of somatic stem cell is a mesenchymal stem cell (MSC) that can differentiate into various mesodermal cells such as osteoblasts, chondrocytes, muscle cells, and adipocytes (Nombela-Arrieta et al., 2011). MSCs are an example of multipotent stem cells that are characterized by adherence to plastic surfaces with a wide range of proliferative potentials *in vitro* and *in vivo*. Lymphoid and myeloid cells are called oligopotent stem cells, and skeletal muscle satellite cells are examples of unipotent cells involved in muscle regeneration. These stem cells are used in cellular modeling of neuromuscular diseases, especially iPSCs are extensively applied. The generation of disease model cells with somatic cells has technical difficulties, and the number of reports on this approach is limited (Grath and Dai, 2019).

MODELING OF MUSCLE AND NEURONAL DISEASES USING iPSCs

Human iPSCs are an attractive platform for overcoming the limitations of animal models in disease modeling and drug discovery. In 2006, a study from Japan showed that murine adult fibroblasts could be successfully reprogrammed by the introduction of four transcription genes including Oct3/4, Sox2, Klf4, and c-Myc *via* retroviral vectors (Takahashi and Yamanaka, 2006). In 2007, differentiated human somatic cells were reprogrammed to enter a pluripotent state allowing for the creation of patient and disease-specific stem cells (Takahashi et al., 2007). iPSCs have the capacity for self-renewal and differentiation and can also be directly generated from skin fibroblasts and blood cells of the patients as well as from other somatic cell sources. However, recently developed approaches employ lymphocytes, squamous cells, and urine-derived cells, which can be obtained in a less invasive

manner. iPSCs can differentiate into almost any cell type including skeletal and cardiac myocytes, neurons, and glias. Because these cell lines are patient-specific, they are expected to recapitulate disease-specific phenotypes and elucidate the molecular mechanisms that drive neuromuscular and neurodegenerative diseases.

Obtaining tissues from patients with muscle and neuronal diseases is difficult because muscle biopsy is invasive, and brain biopsy is almost impractical, and involve risks such as pain, bleeding, infection, anesthesia-related complications, and seizures. Therefore, numerous studies are developing methods to derive myogenic and neuronal cells from iPSCs.

There are two different approaches that are commonly used to differentiate iPSCs into myogenic precursor cells (Kodaka et al., 2017). One approach involves overexpressing myogenic transcription factors, MyoD1 and Pax7, in iPSCs using integrated vectors such as lentiviruses (Maffioletti et al., 2015). This approach is highly efficient, but vector integration can lead to genotoxicity. Another method involves mimicking key signaling events such as dual modulation of the Wnt and bone morphogenetic protein signaling pathways to induce myogenesis in iPSCs (Chal et al., 2016). This direct reprogramming approach requires a month to generate robust myogenesis but avoids the need for genetic modification or cell sorting, thereby enabling abundant production of myogenic promoters for therapeutic applications.

Although optimized methods of iPSC differentiation induction have been developed (Revilla et al., 2016), the protocol for neuronal differentiation induction varies greatly depending on the desired cell type. Neuronal differentiation, development, and maturation are modeled on the progression of chemical signaling that occurs *in vivo*. The appropriate composition, concentration, and timing of the growth factor signals induce the differentiation of the target neuron. Furthermore, in order to convert to fully differentiated cells with sufficient differentiation efficiency, it is necessary to consider the environment suitable for the development and maturation of the target neuron (Engel et al., 2016). Evaluation using a disease-specific marker has been reported to have a differentiation efficiency of around 90% in cholinergic neurons (Crompton et al., 2013) and astrocytes (Krencik et al., 2011; Serio et al., 2013).

Using current protocols, iPSCs can be differentiated into cells with phenotypes resembling those of dopaminergic, glutamatergic, GABAergic, and motor neurons, those of medium spiny neurons of the striatum, and those of glial progenitors (Ross and Akimov, 2014). iPSCs are used to study various neuromuscular and neurodegenerative diseases such as spinal muscular atrophy (SMA; Sareen et al., 2012), amyotrophic lateral sclerosis (ALS; Egawa et al., 2012), Huntington's (Kaye and Finkbeiner, 2013), Parkinson's disease (PD; Devine et al., 2011), and Alzheimer's disease (AD; Ooi et al., 2013).

In the study of the effects of a single genetic abnormality, it is necessary to consider the genetic background and disease-related mutations that are thoroughly permeated in the iPSCs used. Since disease-specific iPSCs exhibit a disease phenotype, their genetic background might be considered to be permissible in the phenotype. But in the genome-edited wild-type iPSCs, if a genetic background is not taken into account, the disease state is not accurately reflected (Musunuru et al., 2018). Genomic editing techniques such as CRISPR/Cas9 are currently used to minimize these variations due to genetic background. That is, use genome editing techniques to correct genetic abnormalities in patient-derived cells or introduce putative genetic abnormalities into cells derived from healthy individuals. By creating two patterns of isogenic cell pairs and comparing their phenotypes, it is thought that the underlying pathological mechanisms can be understood in more detail (Bassett, 2017).

Although iPSCs are excellent for cellular modeling in neuromuscular and neurodegenerative diseases, some limitations still remain and hinder the use of iPSC-based assays. First, collecting somatic cells for iPSC preparation may require invasive procedures. For example, the harvesting of patient-derived fibroblasts requires a skin biopsy, which is not ideal for young patients. Inducing iPSC differentiation into specific cells can be time-consuming, and may require special techniques and equipments. Differentiation efficiency of iPSCs derived from a single patient can vary among clones. Additionally, these iPSCs are heterogeneous which complicates reproducibility of directed differentiation and analyses such as high-throughput screening. Future studies will increase iPSC homogeneity which will improve differentiation efficiency. Methods used to differentiate iPSC into neuronal cells often require long-term culture during which the cells develop mature functional properties. iPSCs may require 1–2 months to differentiate into dopamine neurons, often achieving only 10–20% on the tyrosine hydroxylase index, which is used as an indicator of dopaminergic neurons (Playne and Connor, 2017). Cerebellar Purkinje cells are challenging to culture *in vitro* because of their large size, complex morphology, unique firing properties, and extended period of maturation (over 150 days; Watson et al., 2015). Patient-derived iPSCs used to model neurologic diseases need to be developed with greater efficiency than one provided by currently available methods. Additionally, several studies have shown that iPSC-derived neurons recapitulate only early-, but not late-onset, phenotypes of neurologic diseases (Nguyen et al., 2011; Patterson et al., 2012). This is primarily due to the fetal nature and immature phenotype of iPSC-derived neurons (Ho et al., 2016). The process of iPSC reprogramming, which involves an embryo-like pluripotent state, results in the loss of specific age-related characteristics (Lapasset et al., 2011). Environmental and aging-related factors also present a significant risk in late-onset neuromuscular and neurodegenerative diseases. Therefore, it is essential to establish cellular models corresponding to the fundamental features of these diseases.

DIRECT CONVERSION OF SOMATIC CELLS INTO NEURONS AND MUSCLE CELLS

Previous studies have examined whether one differentiated cell type can be directly converted into another desired cell

type by genetic manipulation without passing through an intermediate or pluripotent state. Such direct differentiation of mature somatic cells into other cell types was first reported by Lassar and co-workers who showed that introducing the MyoD1 transcription factor can convert fibroblasts into skeletal muscle cells (Davis et al., 1987; Tapscott et al., 1988). Thereafter, Xie et al. (2004) differentiated mature B lymphocytes into macrophages, Zhou et al. (2008) transdifferentiated exocrine cells into pancreatic endocrine cells, Ieda et al. (2010) converted fibroblasts into functional cardiomyocytes. Currently, direct cell conversion is not limited to cell types originating from the same germ layer. Human fibroblasts and hepatocytes can also be converted into functional neurons using transcription factors and/or microRNAs. Such direct cell conversion generates targeted cell types more rapidly than do iPSC-based techniques. However, methods to verify cellular identity, uniform phenotype, functionality, and safety throughout the process of transformation have not yet been established.

Several studies have shown that brain neurons and cardiomyocytes converted directly from somatic cells preserve the cellular ageing markers and possibly even the state of maturation (Qian et al., 2012; Mertens et al., 2015; Huh et al., 2016). Specifically, Tang et al. (2017) have shown that motor neurons, generated by direct reprogramming from fibroblasts can maintain the characteristics of aging donors including extensive DNA damage, loss of heterochromatin and nuclear tissue, and increased SA-β-Gal activity. Preservation of these characteristics has not been observed in iPSC-based models. Furthermore, Liu et al. (2016) demonstrated that direct reprogramming of motor neurons from fibroblasts maintain the biological age of ALS patients, showing degenerative morphology, hypoactivity, and reduced survival. These studies indicate that somatic cells converted directly into neurons without undergoing the intermediate pluripotent state may retain the age-related biochemical phenotype of the donor. As mentioned above, in neurodegenerative diseases, ageing and environmental factors influence the onset and progression of the disease state. Therefore, maintenance of the age-related phenotype is essential in the modeling of these diseases. Overall, these findings suggest that neurons obtained directly from converted somatic cells may be more appropriate than iPSCs for modeling of neurological diseases.

USING URINE-DERIVED STEM CELLS TO MODEL NEUROMUSCULAR AND NEURODEGENERATIVE DISEASES

Cells used in *in vitro* disease research should be obtained from patients of all ages, genders, and genetic origin by procedures that are non-invasive, low-cost, and straightforward to implement (Zhang et al., 2008). Obtaining cells from urine presents a non-invasive approach, and urine is a readily available and nearly unlimited source of biological samples. In recent years, cells with stem-like characteristics have been identified in urine samples and have been recognized as useful materials in disease modeling (Falzarano and Ferlini, 2019).

CHARACTERIZATION OF URINE-DERIVED STEM CELLS

USCs are progenitor cells that can self-renew and differentiate (Zhang et al., 2008). USCs can be induced to differentiate into several cell types, including endothelial cells, uroepithelial cells, smooth muscle cells, neural stem cells, and beta cells (Bharadwaj et al., 2011). USCs are thought to originate specifically from kidney glomerular parietal epithelial cells (PECs). USCs isolated from the upper urinary tract and voided USCs are similar in morphology, cell growth pattern, and differentiation potential (Zhang et al., 2014). Furthermore, USCs from a woman who received a kidney transplanted from a male donor contained a Y chromosome and exhibited normal kidney cell markers (PAX2 and PAX8; Bharadwaj et al., 2013). These findings indicate that USCs originate from the kidney and/or the upper urinary tract. USCs express specific genes, protein markers (synaptopodin and podocin) and a high percentage of $CD146^{+}/CD31^{-}$ that expressed in glomerular wall cells and podocytes (Bharadwaj et al., 2013). These markers are not detected in other cells of the urinary system, such as urinary tract epithelium and smooth muscle cells of the bladder and ureter (Bharadwaj et al., 2013). PECs have been reported to self-renew and regenerate podocytes and proximal tubule cells (Sagrinati et al., 2006; Poulsom and Little, 2009; Miesen et al., 2017). These facts strongly support that USCs are derived from PECs. USCs show high expandability that is comparable to that of other widely used stem cells such as bone marrow stem cells, blood progenitor cells, keratinocyte progenitor cells, umbilical cord stem cells, and adipose-derived stem cells (Terstegge et al., 2007; Zhang et al., 2014; Abdelalim and Emara, 2015; Guan et al., 2015). USCs express high levels of mesenchymal stem-cell markers, such as CD44, CD73, CD29, CD105, CD166, CD90, and CD13 (He et al., 2016), and pluripotent stem cell markers including POU5F1 or Oct 3/4, c-Myc, SSEA-1/4, and Klf-4 (Bharadwaj et al., 2011). USCs are multipotent and can differentiate into cells of mesodermal, endodermal and ectodermal lineage (Bharadwaj et al., 2013). USCs also show a high proliferative ability that is comparable to that of other commonly used stem cells such as bone marrow stem cells (Zhang et al., 2014), umbilical cord stem cells (Liu et al., 2018), and adipose-derived stem cells (Kang et al., 2015).

Isolation of USCs is straightforward and reproducible. The method for USC isolation has been described previously (Zhou et al., 2012). In our previous study, we used an existing protocol with some modifications (Takizawa et al., 2019); briefly, our methods are described in **Figure 1**. Urine collection is a straightforward, repeatable procedure that is non-invasive to the patient. Additionally, reducing the costs associated with cell culture presents considerable advantages. The isolation of USCs requires simple centrifugation and standard culture plates without particular substrates, which decreases isolating cost to less than US$70 per sample (Pavathuparambil Abdul Manaph et al., 2018). Conversely, iPSC reprogramming requires expertise

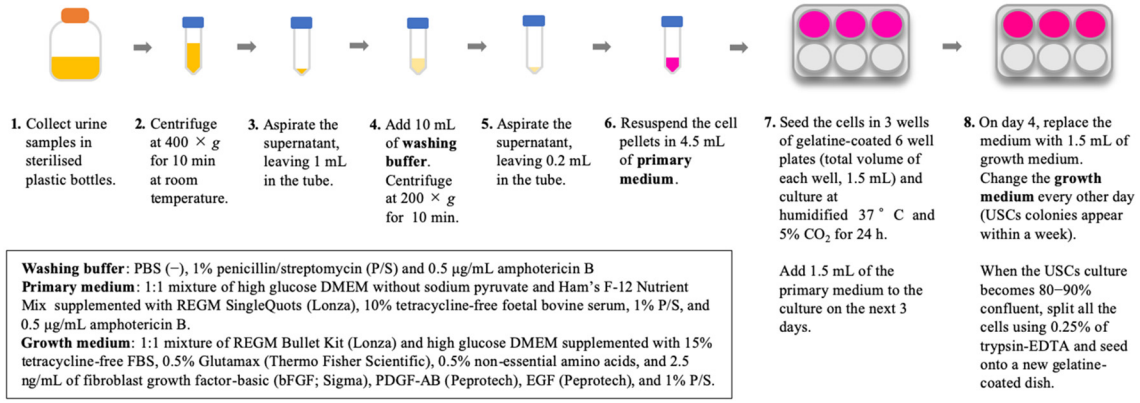

FIGURE 1 | Method for isolation of urine-derived stem cells (USCs).

and various types of equipment, raising the cost to more than US$120–200 per sample (Beers et al., 2015).

APPLICATION OF URINE-DERIVED STEM CELLS IN NEUROMUSCULAR DISEASE

Few studies have evaluated the usefulness of USCs in disease modeling and drug screening. The following summarizes the reports on the generation of cellular models for muscle and neurological diseases using USCs. One is to induce USCc into iPSC and create a cellular model (urine-derived induced pluripotent stem cells, UiPSCs), and another is to induce USC into the target cell by direct reprogramming **Supplementary Table S1**.

URINE-DERIVED INDUCED PLURIPOTENT STEM CELLS

Presently, human iPSCs can be generated from various donor sources. Urine may represent an ideal source of cells for generating iPSCs. After Zhou et al. (2012) generated iPSCs from USCs, numerous studies revealed that iPSCs generated from USCs might have several advantages over iPSCs generated from other somatic cells. Induction of UiPSCs requires less time than do iPSCs derived from fibroblasts, lymphocytes, and keratinocytes (Zhou et al., 2012). Moreover, UiPSCs show a high reprogramming efficiency of 0.1%–4% (Benda et al., 2013) and generating efficiency of approximately 1.5% which is a hundredfold higher than that of fibroblasts (0.01%; Ousterout et al., 2015). It has been demonstrated that mesenchymal-to-epithelial transition (MET) is an essential early step in reprogramming fibroblasts to iPSCs, and a critical rate-limiting step during conversion (Li et al., 2010; Samavarchi-Tehrani et al., 2010). The USCs, which mainly originated from epithelial cells, do not require MET. This fact may affect their differentiation potential. Furthermore, iPSCs derived from fibroblasts may possess epigenetic memory, which is easily differentiated into a lineage related to the donor cell type, the mesoderm lineage (Kim et al., 2010, 2011). However, this tendency has not been observed in UiPSC (Shi et al., 2016).

UiPSCs have already been used in numerous studies on disease modeling (Ji et al., 2017) such as those on Type 2 long QT syndrome (Jouni et al., 2015), dilated cardiomyopathy (Lin et al., 2016), multiple endocrine neoplasia type 1 syndrome (Guo et al., 2017), hemophilia A (Jia et al., 2014), systemic lupus erythematosus (Chen et al., 2013), Down syndrome (Lee et al., 2017), SMA (Zhou et al., 2018), spinal cord injury (Liu et al., 2017), and muscular dystrophy (Afzal and Strande, 2015).

DIRECT REPROGRAMMING OF URINE-DERIVED STEM CELLS INTO MYOGENIC LINEAGE

Several studies on skeletal muscle diseases indicate that USC can be induced into myogenic lineage by direct reprogramming *via* muscle transcription factor MyoD1. Falzarano et al. (2016) demonstrated that USC derived from patients with DMD retain the patient-specific DMD mutation and that USCs converted *via* MyoD1 show no dystrophin expression. Falzarano et al. (2016) additionally showed that truncated dystrophin is restored by in-framing with antisense oligonucleotides against exon 44 of *DMD*. Kim et al. (2016) demonstrated that myogenic reprogramming of urine cells derived from patients with DMD and limb-girdle muscular dystrophy (LGMD) type 2 could recapitulate the disease phenotype. They additionally showed that USC genomes could be edited using CRISPR/Cas9.

Recently, we developed a novel MyoD1-converted, urine-derived cell to *in vitro* model of the pathological processes of muscle cells affected by DMD (Takizawa et al., 2019). In that study, we showed that 3-deazaneplanocin A hydrochloride (DZNep) promotes the differentiation of USCs into myotubes. DZNep-treated USCs, differentiated *via* MyoD1, are excellent *in vitro* models of muscle cells affected by DMD. Moreover, this system, which is based on urine-derived cells obtained from patients with DMD, can be successfully used to evaluate exon skipping therapy using antisense oligonucleotide for DMD. This

newly-established *in vitro* assay will be used in a wide range of studies regardless of age, sex, and muscular disease type of patients. Direct reprogramming of USCs could potentially be used to study the pathophysiology of various diseases, and to diagnose and develop novel therapies for patients with these conditions.

DIRECT REPROGRAMMING OF URINE-DERIVED STEM CELLS INTO NEURONAL LINEAGE

Urine-derived cells can be differentiated into neural-lineage cells by culture in neural induction medium supplemented with basic fibroblast growth factor (Bharadwaj et al., 2013; Guan et al., 2014; Zhang et al., 2016). However, few studies have examined the direct differentiation of neuronal cells from urine-derived cells. Wang et al. (2013) developed integration-free and expandable human neural progenitor cells which can self-renew and differentiate into multi-functional neuronal subtypes and glial cells *in vitro*. Several groups reported that approximately 40% of the induced cells express several neural markers and show neurogenic extensions and processes (Bharadwaj et al., 2013; Guan et al., 2014). USCs treated with growth factors and cultured on laminin-treated plates readily convert into immature neuronal cells (Guan et al., 2014; Kim et al., 2018). Human urinary cells can be converted into neural stem cells by a non-integration-free method using small molecules, and it takes less time than through iPSCs (Cheng et al., 2014). The induced neural progenitor cells can then be converted into astrocytes, oligodendrocytes, and neurons, and may play an essential role in identifying and developing safe and effective therapies for patients with neurodegenerative conditions.

FUTURE ASPECTS OF USING URINE-DERIVED STEM CELLS AS CELLULAR MODELS OF HUMAN DISEASE

As discussed previously, USCs also present an advantageous *in vitro* model to study disease mechanisms, identify new biomarkers, evaluate therapeutic approaches, and screen drugs (**Figure 2**). USCs can be obtained reliably and non-invasively in a short period of time and cultured at low cost. This newly-established *in vitro* assay can, therefore, be adapted for various studies and platforms. Direct reprogramming is an efficient and economical approach because it can be used to generate patient-specific cell lineages without the presence of iPSC intermediates. USCs could show superior differentiation, and can, therefore, be used to delineate the mechanisms of common and rare genetic diseases and to screen drugs for the treatment of these conditions. However, the directed differentiation efficiency of USCs used to produce the mature target-cell types, needs to be optimized. Models recapitulating neurological diseases *in vitro* need to possess not only the gene and protein expression of neuron-surface markers but also characteristics of functional maturation such as synapses and cellular homeostasis. Neurons obtained directly from reprogrammed USCs must be evaluated *via* genetic, biological, and electrophysiological assessment. Future differentiation of neural cells from USCs will be inspired by the previous studies on iPSC reprogramming and other somatic cells direct reprogramming. USCs may play a complementary role in developing methods for rapid and efficient creation of iPSCs, and can be used to directly generate relevant cells for *in vitro* disease models.

There is some essential and critical issue about USCs that there is limited understanding about the biological characteristics and the ability to differentiate into other cell lines of USC as

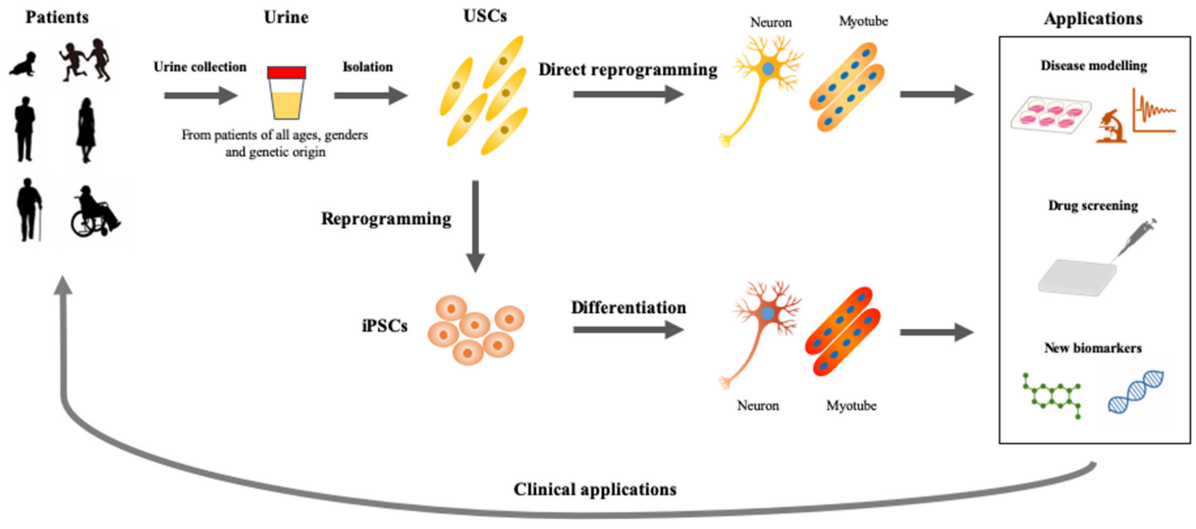

FIGURE 2 | Applications of USCs as cellular models of human diseases. Urine represents an ideal material, which could be obtained from patients of all ages and genders by non-invasive and straightforward procedures. USCs- and induced pluripotent stem cells (iPSCs)-based disease modelings would be useful for basic and applied research, which accelerate the development of personalized medicine.

mentioned above. The neurons differentiated from USCs are not enough to determine neuronal model cells by functional evaluation, and cannot clarify the pathological mechanism. However, as mentioned above, there is a lot of potentials for USC to become a new platform, making it possible to supplement the issues of iPSC technology and to approach pathophysiology from a new aspect.

The USCs platform is still in the infancy stage and expected that this technology will be further developed and adapted by a wider research community. We believe that USCs will play an essential role in the study of diseases and drug screening. Future studies should develop more advanced USC-based differentiation systems, which will faithfully recapitulate human tissue-level and organ-level dysfunction (Rowe and Daley, 2019).

CONCLUSIONS

The difficulties present in obtaining brain and muscular tissue, and lack of adequate preclinical models with high predictive and translational power, pose limitations in the study of neuromuscular diseases and also in developing effective drugs for patients with these disorders. Currently, advances in human iPSC-based technologies are clearly helping to overcome the limitations. Additionally, USC-based modeling will provide valuable information for establishing a diagnosis and providing effective treatment options, although USCs have not been extensively investigated in disease modeling. It should be a critical question of whether the iPSCs and USCs will be able to mimic the complexity of the human neuromuscular system or not.

Application of iPSCs and USCs will be useful for predicting drug response and assessing environmental disease triggers in neuromuscular and neurodegenerative diseases. The development of USCs- and iPSCs-based technology provides a new platform in the field of disease modeling and works in complementary ways, it is expected to benefit research and clinical applications in personalized medicine.

AUTHOR CONTRIBUTIONS

MS and YA wrote the initial draft of the manuscript. HT assisted in the preparation and wrote the manuscript. BT, FS, and AN have contributed critically and reviewed the manuscript.

FUNDING

This work was supported by a Japan Society for the Promotion of Science Grant-in-Aid for Scientific Research (C) (Grant No. 18K07544 to YA), Grants-in-Aid for Research on Nervous and Mental Disorders (Grant No. 28-6 to YA), and the Japan Agency for Medical Research and Development (Grant No. 18ek0109239h0002, 18lm0203066h0001, and 18lm0203069h0001 to YA) and an Australian NHMRC-ARC Dementia Research Leadership Fellowship (APP1137024 to BT).

SUPPLEMENTARY MATERIAL

The Supplementary Material for this article can be found online at: https://www.frontiersin.org/articles/10.3389/fnmol.2019.00297/full#supplementary-material.

REFERENCES

Abdelalim, E. M., and Emara, M. M. (2015). Advances and challenges in the differentiation of pluripotent stem cells into pancreatic β cells. *World J. Stem Cells* 7, 174–181. doi: 10.4252/wjsc.v7.i1.174

Afzal, M. Z., and Strande, J. L. (2015). Generation of induced pluripotent stem cells from muscular dystrophy patients: efficient integration-free reprogramming of urine derived cells. *J. Vis. Exp.* 95:52032. doi: 10.3791/52032

Bassett, A. R. (2017). Editing the genome of hiPSC with CRISPR/Cas9: disease models. *Mamm. Genome* 28, 348–364. doi: 10.1007/s00335-017-9684-9

Beers, J., Linask, K. L., Chen, J. A., Siniscalchi, L. I., Lin, Y., Zheng, W., et al. (2015). A cost-effective and efficient reprogramming platform for large-scale production of integration-free human induced pluripotent stem cells in chemically defined culture. *Sci. Rep.* 5:11319. doi: 10.1038/srep11319

Benda, C., Zhou, T., Wang, X., Tian, W., Grillari, J., Tse, H. F., et al. (2013). Urine as a source of stem cells. *Adv. Biochem. Eng. Biotechnol.* 129, 19–32. doi: 10.1007/10_2012_157

Bharadwaj, S., Liu, G., Shi, Y., Markert, C., Andersson, K.-E., Atala, A., et al. (2011). Characterization of urine-derived stem cells obtained from upper urinary tract for use in cell-based urological tissue engineering. *Tissue Eng. Part A* 17, 2123–2132. doi: 10.1089/ten.TEA.2010.0637

Bharadwaj, S., Liu, G., Shi, Y., Wu, R., Yang, B., He, T., et al. (2013). Multipotential differentiation of human urine-derived stem cells: potential for therapeutic applications in urology. *Stem Cells* 31, 1840–1856. doi: 10.1002/stem.1424

Chal, J., Al Tanoury, Z., Hestin, M., Gobert, B., Aivio, S., Hick, A., et al. (2016). Generation of human muscle fibers and satellite-like cells from human pluripotent stem cells *in vitro*. *Nat. Protoc.* 10, 1833–1850. doi: 10.1038/nprot.2016.110

Chen, Y., Luo, R., Xu, Y., Cai, X., Li, W., Tan, K., et al. (2013). Generation of systemic lupus erythematosus-specific induced pluripotent stem cells from urine. *Rheumatol. Int.* 33, 2127–2134. doi: 10.1007/s00296-013-2704-5

Chen, W., Xie, M., Yang, B., Bharadwaj, S., Song, L., Liu, G., et al. (2017). Skeletal myogenic differentiation of human urine-derived cells as a potential source for skeletal muscle regeneration. *J. Tissue Eng. Regen. Med.* 11, 334–341. doi: 10.1002/term.1914

Cheng, L., Hu, W., Qiu, B., Zhao, J., Yu, Y., Guan, W., et al. (2014). Generation of neural progenitor cells by chemical cocktails and hypoxia. *Cell Res.* 24, 665–679. doi: 10.1038/cr.2014.32

Crompton, L. A., Byrne, M. L., Taylor, H., Kerrigan, T. L., Bru-Mercier, G., Badger, J. L., et al. (2013). Stepwise, non-adherent differentiation of human pluripotent stem cells to generate basal forebrain cholinergic neurons via hedgehog signaling. *Stem Cell Res.* 11, 1206–1221. doi: 10.1016/j.scr.2013.08.002

Davis, R. L., Weintraub, H., and Lassar, A. B. (1987). Expression of a single transfected cDNA converts fibroblasts to myoblasts. *Cell* 51, 987–1000. doi: 10.1016/0092-8674(87)90585-x

Devine, M. J., Ryten, M., Vodicka, P., Thomson, A. J., Burdon, T., Houlden, H., et al. (2011). Parkinson's disease induced pluripotent stem cells with triplication of the α-synuclein locus. *Nat. Commun.* 2:440. doi: 10.1038/ncomms1453

Egawa, N., Kitaoka, S., Tsukita, K., Naitoh, M., Takahashi, K., Yamamoto, T., et al. (2012). Drug screening for ALS using patient-specific induced pluripotent

stem cells. *Sci. Transl. Med.* 4:145ra104. doi: 10.1126/scitranslmed.3004052

Engel, M., Do-Ha, D., Muñoz, S. S., and Ooi, L. (2016). Common pitfalls of stem cell differentiation: a guide to improving protocols for neurodegenerative disease models and research. *Cell. Mol. Life Sci.* 73, 3693–36709. doi: 10.1007/s00018-016-2265-3

Falzarano, M. S., D'Amario, D., Siracusano, A., Massetti, M., Amodeo, A., La Neve, F., et al. (2016). Duchenne muscular dystrophy myogenic cells from urine-derived stem cells recapitulate the dystrophin genotype and phenotype. *Hum. Gene Ther.* 27, 772–783. doi: 10.1089/hum.2016.079

Falzarano, M. S., and Ferlini, A. (2019). Urinary stem cells as tools to study genetic disease: overview of the literature. *J. Clin. Med.* 8:627. doi: 10.3390/jcm8050627

Gaignerie, A., Lefort, N., Rousselle, M., Forest-Choquet, V., Flippe, L., Francois-Campion, V., et al. (2018). Urine-derived cells provide a readily accessible cell type for feeder-free mRNA reprogramming. *Sci. Rep.* 8:14363. doi: 10.1038/s41598-018-32645-2

Grath, A., and Dai, G. (2019). Direct cell reprogramming for tissue engineering and regenerative medicine. *J. Biol. Eng.* 13:14. doi: 10.1186/s13036-019-0144-9

Guan, J.-J., Niu, X., Gong, F.-X., Hu, B., Guo, S.-C., Lou, Y.-L., et al. (2014). Biological characteristics of human-urine-derived stem cells: potential for cell-based therapy in neurology. *Tissue Eng. Part A* 20, 1794–1806. doi: 10.1089/ten.TEA.2013.0584

Guan, J., Zhang, J., Li, H., Zhu, Z., Guo, S., Niu, X., et al. (2015). Human urine derived stem cells in combination with β-TCP can be applied for bone regeneration. *PLoS One* 10:e0125253. doi: 10.1371/journal.pone.0125253

Guo, D., Wu, F., Liu, H., Gao, G., Kou, S., Yang, F., et al. (2017). Generation of non-integrated induced pluripotent stem cells from a 59-year-old female with multiple endocrine neoplasia type 1 syndrome. *Stem Cell Res.* 18, 64–66. doi: 10.1016/j.scr.2016.12.009

He, W., Zhu, W., Cao, Q., Shen, Y., Zhou, Q., Yu, P., et al. (2016). Generation of mesenchymal-like stem cells from urine in pediatric patients. *Transplant. Proc.* 48, 2181–2185. doi: 10.1016/j.transproceed.2016.02.078

Ho, R., Sances, S., Gowing, G., Amoroso, M. W., O'Rourke, J. G., Sahabian, A., et al. (2016). ALS disrupts spinal motor neuron maturation and aging pathways within gene co-expression networks. *Nat. Neurosci.* 19, 1256–1267. doi: 10.1038/nn.4345

Huh, C. J., Zhang, B., Victor, M. B., Dahiya, S., Batista, L. F., Horvath, S., et al. (2016). Maintenance of age in human neurons generated by microRNA-based neuronal conversion of fibroblasts. *Elife* 20:e18648. doi: 10.7554/eLife.18648

Ieda, M., Fu, J. D., Delgado-Olguin, P., Vedantham, V., Hayashi, Y., Bruneau, B. G., et al. (2010). Direct reprogramming of fibroblasts into functional cardiomyocytes by defined factors. *Cell* 142, 375–386. doi: 10.1016/j.cell.2010.07.002

Ji, X., Wang, M., Chen, F., and Zhou, J. (2017). Urine-derived stem cells: the present and the future. *Stem Cells Int.* 2017:4378947. doi: 10.1155/2017/4378947

Jia, B., Chen, S., Zhao, Z., Liu, P., Cai, J., Qin, D., et al. (2014). Modeling of hemophilia A using patient-specific induced pluripotent stem cells derived from urine cells. *Life Sci.* 108, 22–29. doi: 10.1016/j.lfs.2014.05.004

Jouni, M., Si-Tayeb, K., Es-Salah-Lamoureux, Z., Latypova, X., Champon, B., Caillaud, A., et al. (2015). Toward personalized medicine: using cardiomyocytes differentiated from urine-derived pluripotent stem cells to recapitulate electrophysiological characteristics of type 2 long QT syndrome. *J. Am. Heart Assoc.* 4:e002159. doi: 10.1161/JAHA.115.002159

Kang, H. S., Choi, S. H., Kim, B. S., Choi, J. Y., Park, G. B., Kwon, T. G., et al. (2015). Advanced properties of urine derived stem cells compared to adipose tissue derived stem cells in terms of cell proliferation, immune modulation and multi differentiation. *J. Korean Med. Sci.* 30, 1764–1776. doi: 10.3346/jkms.2015.30.12.1764

Kaye, J. A., and Finkbeiner, S. (2013). Modeling Huntington's disease with induced pluripotent stem cells. *Mol. Cell. Neurosci.* 56, 50–64. doi: 10.1016/j.mcn.2013.02.005

Kim, E. Y., Barefield, D. Y., Vo, A. H., Gacita, A. M., Schuster, E. J., Wyatt, E. J., et al. (2019). Distinct pathological signatures in human cellular models of myotonic dystrophy subtypes. *JCI Insight* 4:122686. doi: 10.1172/jci.insight.122686

Kim, J. Y., Chun, S. Y., Park, J. S., Chung, J. W., Ha, Y. S., Lee, J. N., et al. (2018). Laminin and platelet-derived growth factor-BB promote neuronal differentiation of human urine-derived stem cells. *Tissue Eng. Regen. Med.* 15, 195–209. doi: 10.1007/s13770-017-0102-x

Kim, K., Doi, A., Wen, B., Ng, K., Zhao, R., Cahan, P., et al. (2010). Epigenetic memory in induced pluripotent stem cells. *Nature* 467, 285–290. doi: 10.21236/ada544181

Kim, E. Y., Page, P., Dellefave-Castillo, L. M., McNally, E. M., and Wyatt, E. J. (2016). Direct reprogramming of urine-derived cells with inducible MyoD for modeling human muscle disease. *Skelet. Muscle* 6:32. doi: 10.1186/s13395-016-0103-9

Kim, K., Zhao, R., Doi, A., Ng, K., Unternaehrer, J., Cahan, P., et al. (2011). Donor cell type can influence the epigenome and differentiation potential of human induced pluripotent stem cells. *Nat. Biotechnol.* 29, 1117–1119. doi: 10.1038/nbt.2052

Kodaka, Y., Rabu, G., and Asakura, A. (2017). Skeletal muscle cell induction from pluripotent stem cells. *Stem Cells Int.* 2017:1376151. doi: 10.1155/2017/1376151

Krencik, R., Weick, J. P., Liu, Y., Zhang, Z. J., and Zhang, S. C. (2011). Specification of transplantable astroglial subtypes from human pluripotent stem cells. *Nat. Biotechnol.* 29, 528–534. doi: 10.1038/nbt.1877

Lapasset, L., Milhavet, O., Prieur, A., Besnard, E., Babled, A., Ät-Hamou, N., et al. (2011). Rejuvenating senescent and centenarian human cells by reprogramming through the pluripotent state. *Genes Dev.* 25, 2248–2253. doi: 10.1101/gad.173922.111

Lee, Y. M., Zampieri, B. L., Scott-McKean, J. J., Johnson, M. W., and Costa, A. C. S. (2017). Generation of integration-free induced pluripotent stem cells from urine-derived cells isolated from individuals with down syndrome. *Stem Cells Transl. Med.* 6, 1465–1476. doi: 10.1002/sctm.16-0128

Li, R., Liang, J., Ni, S., Zhou, T., Qing, X., Li, H., et al. (2010). A mesenchymal-to-epithelial transition initiates and is required for the nuclear reprogramming of mouse fibroblasts. *Cell Stem Cell* 7, 51–63. doi: 10.1016/j.stem.2010.04.014

Lin, Y. H., Chen, X. M., Zhang, J. W., He, X. Q., Dai, W. J., and Chen, M. S. (2016). Preclinical study on induction of pluripotent stem cells from urine of dilated cardiomyopathy patients. *Eur. Rev. Med. Pharmacol. Sci.* 20, 1450–1457.

Liu, G., Pareta, R. A., Wu, R., Shi, Y., Zhou, X., Liu, H., et al. (2013). Skeletal myogenic differentiation of urine-derived stem cells and angiogenesis using microbeads loaded with growth factors. *Biomaterials* 34, 1311–1326. doi: 10.1016/j.biomaterials.2012.10.038

Liu, G., Wu, R., Yang, B., Deng, C., Lu, X., Walker, S. J., et al. (2018). Human urine-derived stem cell differentiation to endothelial cells with barrier function and nitric oxide production. *Stem Cells Transl. Med.* 7, 686–698. doi: 10.1002/sctm.18-0040

Liu, M.-L., Zang, T., and Zhang, C.-L. (2016). Direct lineage reprogramming reveals disease-specific phenotypes of motor neurons from human ALS patients. *Cell Rep.* 14, 115–128. doi: 10.1016/j.celrep.2015.12.018

Liu, Y., Zheng, Y., Li, S., Xue, H., Schmitt, K., Hergenroeder, G. W., et al. (2017). Human neural progenitors derived from integration-free iPSCs for SCI therapy. *Stem Cell Res.* 19, 55–64. doi: 10.1016/j.scr.2017.01.004

Maffioletti, S. M., Gerli, M. F. M., Ragazzi, M., Dastidar, S., Benedetti, S., Loperfido, M., et al. (2015). Efficient derivation and inducible differentiation of expandable skeletal myogenic cells from human ES and patient-specific iPS cells. *Nat. Protoc.* 10, 941–958. doi: 10.1038/nprot.2015.057

Malaver-Ortega, L. F., Sumer, H., Liu, J., and Verma, P. J. (2012). The state of the art for pluripotent stem cells derivation in domestic ungulates. *Theriogenology* 78, 1749–1762. doi: 10.1016/j.theriogenology.2012.03.031

Mertens, J., Paquola, A. C. M., Ku, M., Hatch, E., Böhnke, L., Ladjevardi, S., et al. (2015). Directly reprogrammed human neurons retain aging-associated transcriptomic signatures and reveal age-related nucleocytoplasmic defects. *Cell Stem Cell* 17, 705–718. doi: 10.1016/j.stem.2015.09.001

Miesen, L., Steenbergen, E., and Smeets, B. (2017). Parietal cells—new perspectives in glomerular disease. *Cell Tissue Res.* 369, 237–244. doi: 10.1007/s00441-017-2600-5

Musunuru, K., Sheikh, F., Gupta, R. M., Houser, S. R., Maher, K. O., Milan, D. J., et al. (2018). Induced pluripotent stem cells for cardiovascular disease modeling and precision medicine: a scientific statement from the American

Heart Association. *Circ. Genomic Precis. Med.* 11:e000043. doi: 10.1161/hcg.0000000000000043

Nguyen, H. N., Byers, B., Cord, B., Shcheglovitov, A., Byrne, J., Gujar, P., et al. (2011). LRRK2 mutant iPSC-derived da neurons demonstrate increased susceptibility to oxidative stress. *Cell Stem Cell* 8, 267–280. doi: 10.1016/j.stem.2011.01.013

Nombela-Arrieta, C., Ritz, J., and Silberstein, L. E. (2011). The elusive nature and function of mesenchymal stem cells. *Nat. Rev. Mol. Cell Biol.* 12, 126–131. doi: 10.1038/nrm3049

Ooi, L., Sidhu, K., Poljak, A., Sutherland, G., O'Connor, M. D., Sachdev, P., et al. (2013). Induced pluripotent stem cells as tools for disease modelling and drug discovery in Alzheimer's disease. *J. Neural Transm.* 120, 103–111. doi: 10.1007/s00702-012-0839-2

Ousterout, D. G., Kabadi, A. M., Thakore, P. I., Majoros, W. H., Reddy, E., and Gersbach, C. A. (2015). Multiplex CRISPR/Cas9-based genome editing for correction of dystrophin mutations that cause Duchenne muscular dystrophy. *Nat. Commun.* 6:6244. doi: 10.1038/ncomms7244

Partridge, T. A. (2013). The mdx mouse model as a surrogate for Duchenne muscular dystrophy. *FEBS J.* 280, 4177–4186. doi: 10.1111/febs.12267

Patterson, M., Chan, D. N., Ha, I., Case, D., Cui, Y., Van Handel, B., et al. (2012). Defining the nature of human pluripotent stem cell progeny. *Cell Res.* 22, 178–193. doi: 10.1038/cr.2011.133

Pavathuparambil Abdul Manaph, N., Al-Hawaas, M., Bobrovskaya, L., Coates, P. T., and Zhou, X. F. (2018). Urine-derived cells for human cell therapy. *Stem Cell Res. Ther.* 9:189. doi: 10.1186/s13287-018-0932-z

Playne, R., and Connor, B. (2017). Understanding Parkinson's disease through the use of cell reprogramming. *Stem Cell Rev. Rep.* 13, 151–169. doi: 10.1007/s12015-017-9717-5

Poulsom, R., and Little, M. H. (2009). Parietal epithelial cells regenerate podocytes. *J. Am. Soc. Nephrol.* 20, 231–233. doi: 10.1681/asn.2008121279

Qian, L., Huang, Y., Spencer, C. I., Foley, A., Vedantham, V., Liu, L., et al. (2012). *in vivo* reprogramming of murine cardiac fibroblasts into induced cardiomyocytes. *Nature* 485, 593–598. doi: 10.1038/nature11044

Revilla, A., González, C., Iriondo, A., Fernández, B., Prieto, C., Marín, C., et al. (2016). Current advances in the generation of human iPS cells: implications in cell-based regenerative medicine. *J. Tissue Eng. Regen. Med.* 10, 893–907. doi: 10.1002/term.2021

Ross, C. A., and Akimov, S. S. (2014). Human-induced pluripotent stem cells: potential for neurodegenerative diseases. *Hum. Mol. Genet.* 23, R17–R26. doi: 10.1093/hmg/ddu204

Rowe, R. G., and Daley, G. Q. (2019). Induced pluripotent stem cells in disease modelling and drug discovery. *Nat. Rev. Genet.* 20, 377–388. doi: 10.1038/s41576-019-0100-z

Sagrinati, C., Netti, G. S., Mazzinghi, B., Lazzeri, E., Liotta, F., Frosali, F., et al. (2006). Isolation and characterization of multipotent progenitor cells from the Bowman's capsule of adult human kidneys. *J. Am. Soc. Nephrol.* 17, 2443–2456. doi: 10.1681/ASN.2006010089

Saito, T., Nakamura, A., Aoki, Y., Yokota, T., and Okada, T. (2010). Antisense PMO found in dystrophic dog model was effective in cells from exon 7-deleted DMD patient. *PLoS One* 5:e12239. doi: 10.1371/journal.pone.0012239

Samavarchi-Tehrani, P., Golipour, A., David, L., Sung, H. K., Beyer, T. A., Datti, A., et al. (2010). Functional genomics reveals a BMP-Driven mesenchymal-to-epithelial transition in the initiation of somatic cell reprogramming. *Cell Stem Cell* 7, 64–77. doi: 10.1016/j.stem.2010.04.015

Sareen, D., Ebert, A. D., Heins, B. M., McGivern, J. V., Ornelas, L., and Svendsen, C. N. (2012). Inhibition of apoptosis blocks human motor neuron cell death in a stem cell model of spinal muscular atrophy. *PLoS One* 7:e39113. doi: 10.1371/journal.pone.0039113

Serio, A., Bilican, B., Barmada, S. J., Ando, D. M., Zhao, C., Siller, R., et al. (2013). Astrocyte pathology and the absence of non-cell autonomy in an induced pluripotent stem cell model of TDP-43 proteinopathy. *Proc. Natl. Acad. Sci. U S A* 110, 4697–4702. doi: 10.1073/pnas.1300398110

Shi, L., Cui, Y., Luan, J., Zhou, X., and Han, J. (2016). Urine-derived induced pluripotent stem cells as a modeling tool to study rare human diseases. *Intractable Rare Dis. Res.* 5, 192–201. doi: 10.5582/irdr.2016.01062

Takahashi, K., Tanabe, K., Ohnuki, M., Narita, M., Ichisaka, T., Tomoda, K., et al. (2007). Induction of pluripotent stem cells from adult human fibroblasts by defined factors. *Cell* 131, 861–872. doi: 10.1016/j.cell.2007.11.019

Takahashi, K., and Yamanaka, S. (2006). Induction of pluripotent stem cells from mouse embryonic and adult fibroblast cultures by defined factors. *Cell* 126, 663–676. doi: 10.1016/j.cell.2006.07.024

Takizawa, H., Hara, Y., Mizobe, Y., Ohno, T., Suzuki, S., Inoue, K., et al. (2019). Modelling duchenne muscular dystrophy in MYOD1-converted urine-derived cells treated with 3-deazaneplanocin A hydrochloride. *Sci. Rep.* 9:3807. doi: 10.1038/s41598-019-40421-z

Tang, Y., Liu, M.-L., Zang, T., and Zhang, C.-L. (2017). Direct reprogramming rather than iPSC-based reprogramming maintains aging hallmarks in human motor neurons. *Front. Mol. Neurosci.* 10:359. doi: 10.3389/fnmol.2017.00359

Tapscott, S. J., Davis, R. L., Thayer, M. J., Cheng, P. F., Weintraub, H., and Lassar, A. B. (1988). MyoD1: a nuclear phosphoprotein requiring a Myc homology region to convert fibroblasts to myoblasts. *Science* 242, 405–411. doi: 10.1126/science.3175662

Terstegge, S., Laufenberg, I., Pochert, J., Schenk, S., Itskovitz-Eldor, J., Endl, E., et al. (2007). Automated maintenance of embryonic stem cell cultures. *Biotechnol. Bioeng.* 96, 195–201. doi: 10.1002/bit.21061

Wang, L., Wang, L., Huang, W., Su, H., Xue, Y., Su, Z., et al. (2013). Generation of integration-free neural progenitor cells from cells in human urine. *Nat. Methods* 10, 84–89. doi: 10.1038/nmeth.2283

Watson, L. M., Wong, M. M. K., and Becker, E. B. E. (2015). Induced pluripotent stem cell technology for modelling and therapy of cerebellar ataxia. *Open Biol.* 5:150056. doi: 10.1098/rsob.150056

Xie, H., Ye, M., Feng, R., and Graf, T. (2004). Stepwise reprogramming of B cells into macrophages. *Cell* 117, 663–676. doi: 10.1016/s0092-8674(04)00419-2

Yi, H., Xie, B., Liu, B., Wang, X., Xu, L., Liu, J., et al. (2018). Derivation and identification of motor neurons from human urine-derived induced pluripotent stem cells. *Stem Cells Int.* 2018:3628578. doi: 10.1155/2018/3628578

Zhang, S. Z., Ma, L. X., Qian, W. J., Li, H. F., Wang, Z. F., Wang, H. X., et al. (2016). Modeling neurological disease by rapid conversion of human urine cells into functional neurons. *Stem Cells Int.* 2016:2452985. doi: 10.1155/2016/2452985

Zhang, Y., McNeill, E., Tian, H., Soker, S., Andersson, K. E., Yoo, J. J., et al. (2008). Urine derived cells are a potential source for urological tissue reconstruction. *J. Urol.* 180, 2226–2233. doi: 10.1016/j.juro.2008.07.023

Zhang, D., Wei, G., Li, P., Zhou, X., and Zhang, Y. (2014). Urine-derived stem cells: a novel and versatile progenitor source for cell-based therapy and regenerative medicine. *Genes Dis.* 1, 8–17. doi: 10.1016/j.gendis.2014.07.001

Zhou, T., Benda, C., Dunzinger, S., Huang, Y., Ho, J. C., Yang, J., et al. (2012). Generation of human induced pluripotent stem cells from urine samples. *Nat. Protoc.* 7, 2080–2089. doi: 10.1038/nprot.2012.115

Zhou, Q., Brown, J., Kanarek, A., Rajagopal, J., and Melton, D. A. (2008). *in vivo* reprogramming of adult pancreatic exocrine cells to β-cells. *Nature* 455, 627–632. doi: 10.1038/nature07314

Zhou, M., Hu, Z., Qiu, L., Zhou, T., Feng, M., Hu, Q., et al. (2018). Seamless genetic conversion of SMN2 to SMN1 *via* CRISPR/Cpf1 and single-stranded oligodeoxynucleotides in spinal muscular atrophy patient-specific induced pluripotent stem cells. *Hum. Gene Ther.* 29, 1252–1263. doi: 10.1089/hum.2017.255

Conflict of Interest: The authors declare that the research was conducted in the absence of any commercial or financial relationships that could be construed as a potential conflict of interest.

Copyright © 2019 Sato, Takizawa, Nakamura, Turner, Shabanpoor and Aoki. This is an open-access article distributed under the terms of the Creative Commons Attribution License (CC BY). The use, distribution or reproduction in other forums is permitted, provided the original author(s) and the copyright owner(s) are credited and that the original publication in this journal is cited, in accordance with accepted academic practice. No use, distribution or reproduction is permitted which does not comply with these terms.

frontiers in Behavioral Neuroscience

BRIEF RESEARCH REPORT
published: 09 January 2020
doi: 10.3389/fnbeh.2019.00270

Separating Probability and Reversal Learning in a Novel Probabilistic Reversal Learning Task for Mice

*Jeremy A. Metha[1,2,3], Maddison L. Brian[1,2], Sara Oberrauch[1,2], Samuel A. Barnes[4], Travis J. Featherby[5], Peter Bossaerts[3], Carsten Murawski[3], Daniel Hoyer[1,2,6] and Laura H. Jacobson[1,2]**

[1] Sleep and Cognition, The Florey Institute of Neuroscience and Mental Health, Parkville, VIC, Australia, [2] Translational Neuroscience, Department of Pharmacology and Therapeutics, School of Biomedical Sciences, Faculty of Medicine, Dentistry and Health Sciences, The University of Melbourne, Parkville, VIC, Australia, [3] Brain, Mind and Markets Laboratory, Department of Finance, Faculty of Business and Economics, The University of Melbourne, Parkville, VIC, Australia, [4] Department of Psychiatry, School of Medicine, University of California, San Diego, La Jolla, CA, United States, [5] Behavioral Core, The Florey Institute of Neuroscience and Mental Health, Parkville, VIC, Australia, [6] Department of Molecular Medicine, The Scripps Research Institute, La Jolla, CA, United States

The exploration/exploitation tradeoff – pursuing a known reward vs. sampling from lesser known options in the hope of finding a better payoff – is a fundamental aspect of learning and decision making. In humans, this has been studied using multi-armed bandit tasks. The same processes have also been studied using simplified probabilistic reversal learning (PRL) tasks with binary choices. Our investigations suggest that protocols previously used to explore PRL in mice may prove beyond their cognitive capacities, with animals performing at a no-better-than-chance level. We sought a novel probabilistic learning task to improve behavioral responding in mice, whilst allowing the investigation of the exploration/exploitation tradeoff in decision making. To achieve this, we developed a two-lever operant chamber task with levers corresponding to different probabilities (high/low) of receiving a saccharin reward, reversing the reward contingencies associated with levers once animals reached a threshold of 80% responding at the high rewarding lever. We found that, unlike in existing PRL tasks, mice are able to learn and behave near optimally with 80% high/20% low reward probabilities. Altering the reward contingencies towards equality showed that some mice displayed preference for the high rewarding lever with probabilities as close as 60% high/40% low. Additionally, we show that animal choice behavior can be effectively modelled using reinforcement learning (RL) models incorporating learning rates for positive and negative prediction error, a perseveration parameter, and a noise parameter. This new decision task, coupled with RL analyses, advances access to investigate the neuroscience of the exploration/exploitation tradeoff in decision making.

Keywords: reinforcement, probabilistic, discrimination, reversal, learning, mouse, cognition, operant

OPEN ACCESS

Edited by:
Robert J. Harvey, University of the Sunshine Coast, Australia

Reviewed by:
Marco Venniro, National Institute on Drug Abuse (NIDA), United States
Paul M. Nealen, Indiana University of Pennsylvania, United States

***Correspondence:**
Laura H. Jacobson
laura.jacobson@florey.edu.au

Specialty section:
This article was submitted to Motivation and Reward, a section of the journal Frontiers in Behavioral Neuroscience

Received: *31 July 2019*
Accepted: *27 November 2019*
Published: *09 January 2020*

Citation:
Metha JA, Brian ML, Oberrauch S, Barnes SA, Featherby TJ, Bossaerts P, Murawski C, Hoyer D and Jacobson LH (2020) Separating Probability and Reversal Learning in a Novel Probabilistic Reversal Learning Task for Mice. Front. Behav. Neurosci. 13:270. doi: 10.3389/fnbeh.2019.00270

INTRODUCTION

To survive and thrive in an ever-changing world, both human and non-human animals must make a multitude of rapid decisions about how they interact with, and adapt to, the environment around them in order to optimize gains and minimize losses associated with their behaviors. One large component influencing these decisions is the explore–exploit trade off

(Addicott et al., 2017)– to pursue the current best option (exploit), or to test alternative options in the hopes of finding something better (explore). Importantly, exploitative and exploratory behavior must be appropriately balanced to maximize optimal long-term behavior (Addicott et al., 2017).

Probabilistic Reversal Learning (PRL) is a powerful behavioral task which has been used to assess this trade off, as well as cognitive flexibility, impulsivity, and compulsivity. PRL allows the evaluation of how positive or negative feedback differently affect learning in a range of neurological and psychological conditions including Autism Spectrum Disorder, Schizophrenia and Huntington's Disease in both patient populations (Lawrence et al., 1999) and animal models of disease (Amitai et al., 2014; Amodeo et al., 2014). Additionally, PRL tasks have been used more generally to understand the neurobiological systems and neurotransmitters governing these behaviors (Cohen, 2008; Bari et al., 2010; Costa et al., 2015).

A PRL task involves subjects making a series of choices between binary options, one with high and low probabilities, respectively (e.g., in both rodent and human PRL task, 80% and 20% reward contingencies are commonly used (Mehta et al., 2001; Bari et al., 2010; Dalton et al., 2014)). Subjects are free to choose between the two options and are expected to quickly acquire a preference for the high rewarding option. Once this preference has been established (typically, in the rodent version, as evidenced by eight consecutive choices of the high value option) reward contingencies are reversed; the high value option becomes low value and vice versa. These reversals take place with no additional cues, and in order to successfully engage in the task, subjects are required to do three things. Firstly, subjects must learn to discriminate between the high and low rewarding lever option and learn to favor the high reward lever. Secondly, following a reversal, subjects must realize that the value of the previously high rewarding option has shifted, and lastly, disengage from responding at this previous high value choice and shift toward preferring the other, now high value, option.

Experiments in rats have shown an average peak of three reversals per session in sessions of 200 trials (Bari et al., 2010; Dalton et al., 2014, 2016), and an average peak of six reversals per session in sessions of 600 trials (Amitai et al., 2014), whereas in mice, an average peak between one and two reversals per session in sessions of 400 trials has been reported (Milienne-Petiot et al., 2017).

To put this in perspective, simulations suggest that the expected number of reversals made by an animal responding randomly in these PRL tasks increases linearly with the number of trials presented in a session (**Figure 1A**). More precisely, random responding would result in at least three reversals in sessions of 200 trials in 0.55% of cases (**Figure 1B**), and at least six reversals in sessions of 600 trials in 0.076% of cases (**Figure 1D**). Conversely, random responding in sessions of 400 trials would result in at least one reversal in 55% of cases, and at least two reversals in 18% of cases (**Figure 1C**). Together these data indicate that mice perform this task substantially worse than rats, and in a manner much closer to random responding.

To account for this comparatively poor performance, other groups have developed simplified mouse probabilistic learning tasks (Ineichen et al., 2012) in which the high value choice maintains an 80% probability of reward, but choosing the low value option will never provide reward. After sufficient training this presentation of the PRL task is one which mice can easily achieve, with animals making between four and five out of seven possible reversals in a 60 trial session, which is much greater than the 1–2 reversals in 400 trials of mice in the PRL task optimized for rats. However, this simplification changes the task in two major ways. Firstly, it makes it easier to inhibit responding at the previously high rewarding option, as perseverating at this option provides no value at all, compared to the required detection of reduction in value in the full PRL task. And, secondly, it requires only a single rewarded response at the high value option to establish without a doubt that it is indeed the high value option. In both cases, the result is a reduction of uncertainty. Combined, these changes result in a task that is much closer to deterministic reversal learning, in which there is no uncertainty of reward, than to probabilistic learning.

In the present study, we established a task with a different simplification. Rather than altering the probabilistic nature of the task, we focused on allowing mice to acquire a clear preference for the high value option first in an initial block of probabilistic learning sessions, then subsequently reversed the reward contingencies and allowed multiple sessions for animals to inhibit this preference and to learn the new reversed reward contingencies. We found that most animals trained to respond in an operant task were able to successfully acquire an initial preference and subsequently reverse that preference with 80%/20% high/low reward probabilities. As such, we propose that this modified PRL task with 80%/20% reward probabilities would be suitable in subsequent studies to investigate the neurobiology of reinforcement and reversal learning in mice. Additionally, we presented animals with increasingly noisy reward probabilities (70%/30% and 60%/40% on high/low rewarding levers, respectively) and found that some mice were also able to discriminate and reverse in these more complex, uncertain environments, illustrating access to a cognitive gradient within the task.

MATERIALS AND METHODS

Animals

A total of sixteen 10-week old male C57BL/6J Arc mice were used. Mice were kept in a 12-h reversed light dark cycle with free access to water and food-restricted to maintain 90% of their free feeding body weight. Behavioral testing occurred daily between the 3rd and 6th hours of the dark phase. Animal experimentation was conducted in accordance with the Prevention of Cruelty to Animals Act and National Health and Medical Research Code of Practice for the Use of Animals and approved by The Florey Animal Ethics Committee (Application 17-035).

Apparatus

All behavioral testing was conducted in 8 operant chambers (Med Associates, St. Albans, VT, United States) enclosed in light and sound attenuating boxes. Each chamber contained two

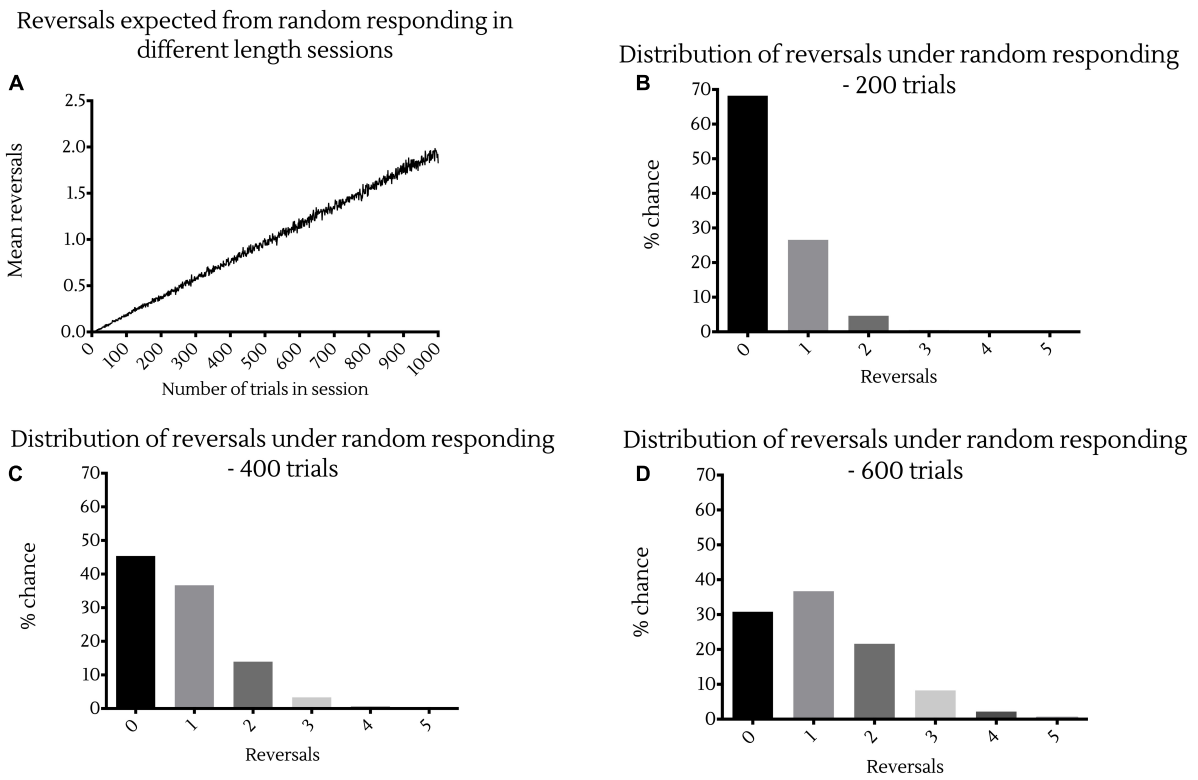

FIGURE 1 | Probability of reversal under random responding with different session lengths. **(A)** Expected reversals averaged across 10,000 simulations of session lengths from 1 to 1,000 trials. Probability distributions showing the likelihood of a certain number of reversal occurring in a session under random responding from 1,000,000 bootstrapped random samples of sessions of **(B)** 200 trials, **(C)** 400 trials or **(D)** 600 trials in length.

retractable levers, located on either side of a central reward port calibrated to deliver ∼10 μL of sodium-saccharin solution (0.1% w/v, in water) on a rewarding trial, coupled with a 1000 Hz, 75 dB tone. The enclosing boxes were equipped with fans to provide ventilation and to mask extraneous noise, as well as infrared cameras for observing animals during their sessions (**Figure 2A**).

Behavioral Tasks

Mice were presented with a single operant session every day throughout the course of the experiment.

Habituation

Initially, mice were given a single 30-min session to freely explore the chamber, with no levers presented and ∼50 μL saccharin solution provided in the central reward port.

Training

Prior to entering the PRL task, animals underwent several stages of habituation, single lever training on both levers, dual lever training, then dual lever FR-2 training as described below and in **Figure 2B**.

Throughout training and testing, trials were initiated by the extension of one or both levers in the operant chambers. During each trial, animals had 10 s to make a response at a lever. After responding, or at the end of the 10 s trial if no response was made, the lever was retracted and a 10 s inter-trial interval (ITI) elapsed before the lever extended again and the subsequent trial began.

Single lever training

Following habituation, mice were exposed to daily sessions of 100 trials with the lever at the back of the chamber in operation and the lever at the front of the box retracted. If an animal pressed the lever within this window, a reinforcing tone sounded, and a 10 μL saccharin reward was delivered to the central reward port 0.5 s after a successful lever press.

Mice remained in this phase of training with the *back* lever extended until they completed two sessions with greater than 60 rewarded trials and were trained subsequently on the *front* lever until the same criteria were reached.

Dual lever training

Next, mice were given sessions with both levers active, with one lever extended at a time, pseudo-randomized to provide five front/back lever extensions per 10-trial block in the 100-trial session. Again, animals remained in this phase of training until two sessions with at least 60 responses were achieved.

Dual lever FR-2 training

In previous operant chamber experiments, we observed that mice sometimes made "accidental" lever presses by inadvertent contact with the levers, rather than actively pressing them. To minimize these unintentional responses, we trained animals to

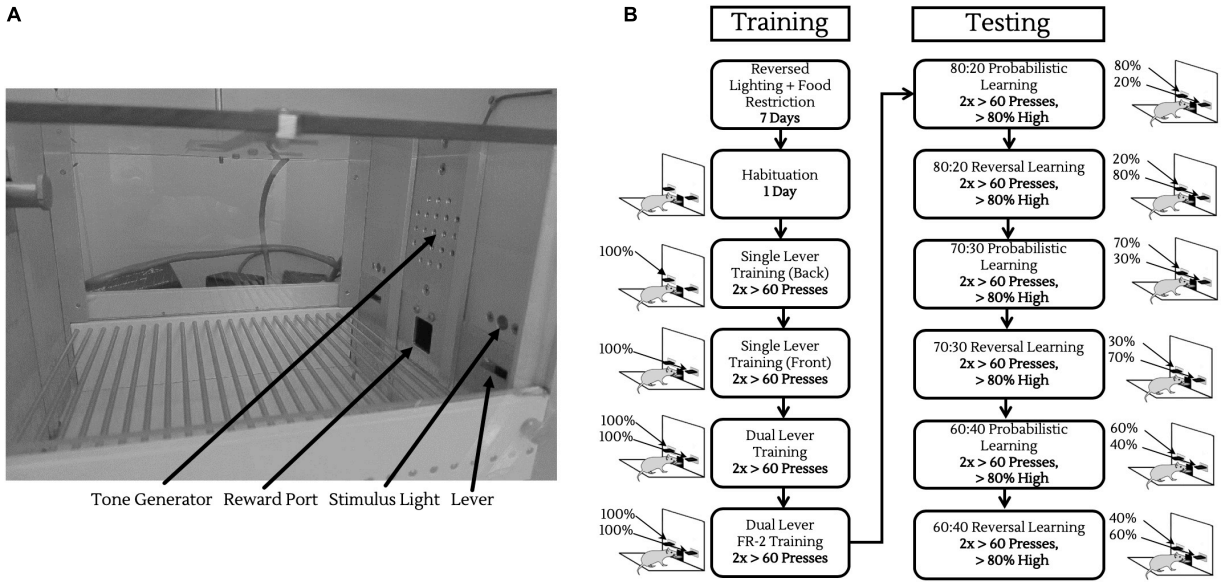

FIGURE 2 | Operant chamber and training/testing protocols. **(A)** Operant chamber fitted with tone generator for reinforcing rewarded trials, liquid reward port for saccharin delivery, two retractable levers, and two stimulus lights located above to indicate when a lever was active. **(B)** Schematic of operant training/testing. Before testing, animals were trained to push levers on both sides of the chamber, and then to push levers twice consecutively for reward (left column). Following this, animals were introduced to probabilistic rewards and reversals, progressively moving to noisier reward contingencies.

press the same lever twice consecutively for reward, using the same randomized lever extensions as in the dual lever training. After achieving two sessions with at least 60 responses, mice progressed into probabilistic learning.

Testing

Probabilistic learning

In these sessions, both levers were extended simultaneously, with two consecutive presses on the front/back levers providing an 80%/20% chance of reward, respectively. On rewarded trials, levers were retracted, the conditioning tone sounded, and the saccharin reward simultaneously delivered, whereas on unrewarded trials levers were retracted, but with no tone or reward delivery. Mice remained in probabilistic learning until they achieved two sessions with at least 60 responses, and greater than 80% of lever presses made on the high rewarding lever.

Reversal learning

Upon achieving criterion in the probabilistic learning task, reward contingencies were reversed; the previously high, 80% reward lever now rewarding on only 20% of trials and vice versa. This task required mice to make a substantial change in their behavior, suppressing their previously learned reward/lever associations and adapting to the new contingencies. As in the probabilistic learning phase, animals remained in reversal learning until they achieved two sessions with at least 60 responses, and greater than 80% of lever presses made on the high-rewarding lever.

Further reversal learning

After mice reached criterion in the reversal learning phase, the high and low rewarding levers were again reversed, but now with a 70%/30% probability of reward, rather than 80%/20%. Once mice reached the same levels of performance as above, the levers were again reversed, keeping the 70%/30% reward contingencies. Following completion of reversal learning with the 70%/30% reward contingencies, animals were lastly presented with 60%/40% reward contingencies and reversal.

Data and Analyses

At each trial, we recorded (a) whether a mouse made a response or not, and whether the chosen lever was associated with high or low reward (high/low/omit), (b) whether a trial was rewarded or not (rewarded/unrewarded), and (c) the time from lever extension to response in milliseconds.

Data were processed in R version 3.6.1 (R Core Team, 2019) with RStudio (Allaire, 2012) using the *tidyverse* package (Wickham, 2016). Choice data were analyzed using reinforcement learning (RL) models (Rutledge et al., 2009; Sutton and Barto, 2018), the parameters of which were estimated on a subject-by-subject basis, and fit by maximizing the likelihood of the observed choices compounded across all trials. These optimizations were carried out using the *optimx* package (Nash and Varadhan, 2011) in RStudio.

Analysis of Task Progression

Time taken to reach criterion in different reversal learning stages was compared in a mixed-effects model fitted using restricted maximum likelihood (REML) with days to criterion as main effect and random intercepts for individual animals in order to account for repeated measures.

Analysis of Choice Data

We fitted choice and reward data from individual animals to a range of RL algorithms (Sutton and Barto, 2018). These models use the sequence of choices and rewards to estimate and update the expected reward value of each lever on a trial by trial basis (Rutledge et al., 2009; Sutton and Barto, 2018). The expected values were initialized to one as animals were initially trained to push levers for a sure reward at every trial. Model comparisons were made using the relative Akaike Information Criterion (AIC) (Akaike, 1998; Anderson and Burnham, 2002).

Parameters for learning from positive or negative outcomes were compared within animals using a Wilcoxon matched pairs signed-ranks test in Prism 8.0 (GraphPad Software, San Diego, CA, United States).

Single learning rate RL model

The simplest model consisted of two parameters; a learning rate α, through which the value of an option is updated following a trial, and the softmax parameter β governing how much the expected values of options affect choices being made. Given expected values $V_f(t)$ for the front lever, and $V_b(t)$ for the back lever, the probability of choosing the front lever $P_f(t)$ was calculated using the softmax rule:

$$P_f(t) = \frac{1}{1 + e^{-\beta(V_f(t) - V_b(t))}}$$

and following each trial, the expected value of the chosen lever (V_f, for example) was updated according to the following rule:

$$V_f(t+1) = V_f(t) + \alpha[R(t) - V_f(t)]$$

where $R(t) - V_f(t)$ is the reward prediction error – the difference between the reward received on a given trial $R(t)$, and the expected value of the lever $V_f\ (t)$.

Dual learning rates RL model

This model separated out the α learning rate parameter into two different parameters for positive (α_{pos}) and negative (α_{neg}) reward prediction errors reflecting the idea that learning rates may be different for positive versus negative experiences (Daw et al., 2002; Frank et al., 2007; Rutledge et al., 2009). In this model, $P_f(t)$ was calculated in the same manner as in the standard RL model, but following each trial, values were updated according to the rule:

$$V_f\ (t+1) = V_f\ (t) + \begin{cases} \alpha_{pos}[R\ (t) - V_f(t)] | R\ (t) \geq V_f\ (t) \\ \alpha_{neg}[R\ (t) - V_f(t)] | R\ (t) < V_f\ (t) \end{cases}$$

Perseverative RL model

This model introduced an additional perseveration parameter δ, which enters into the softmax rule for determining probability of choosing a lever as:

$$P_f(t) = \frac{1}{1 + e^{-\beta(V_f(t) - V_b(t)) + \delta(C_f(t-1) - C_b(t-1))}}$$

In this model, C_f and C_b are indicator variables, taking the value of 1 if the relevant lever is chosen, and 0 otherwise. A positive δ indicates that an animal is more likely to respond on the same side as the previous trial (perseveration), while a negative δ indicates that animals are more likely to switch from side to side on consecutive trials (alternation).

Perseverative dual learning rates RL model

We also fitted a combination of the perseverative and dual learning rates RL models, incorporating α_{pos}, α_{neg}, β, and δ with $P_f(t)$ determined by:

$$P_f(t) = \frac{1}{1 + e^{-\beta(V_f(t) - V_b(t)) + \delta(C_f(t-1) - C_b(t-1))}}$$

and expected reward values updated by:

$$V_f\ (t+1) = V_f\ (t) + \begin{cases} \alpha_{pos}[R\ (t) - V_f(t)] | R\ (t) \geq V_f\ (t) \\ \alpha_{neg}[R\ (t) - V_f(t)] | R\ (t) < V_f\ (t) \end{cases}$$

RESULTS

Performance Across Different Stages of Task Progression

From our initial 16 animals, 12 progressed through operant lever training and into the probabilistic learning tasks, all of which were able to reach criterion in the initial 80:20 probabilistic learning phase. Of these 12 animals, 10 were then able to complete the first reversal learning phase. As difficulty increased, fewer animals were able to complete each task, with 7, 4, 3, and 2 animals able to complete the 70:30 Learning, 70:30 Reversal, 60:40 Learning and 60:40 Reversal tasks, respectively (**Figure 3A**). Despite the increasing complexity of the task, there was no significant difference in the number of days it took animals to reach criterion under different reward contingencies, as analyzed using a mixed-effects model fitted using REML with random intercepts for individual animals (**Figure 3B**).

Choice Data Analysis

We fitted data from the 12 animals that progressed into the operant tasks. Of these 12 datasets, the MLE estimation procedure successfully converged to parameter point estimates for the 10 animals able to complete both the 80%/20% Probabilistic Learning and Reversal Learning tasks, with models failing to converge for the two animals unable to complete the 80:20 Reversal Learning task.

In 8 of these 10 mice, the perseverative dual learning rates RL model gave the lowest AIC, and hence the best fit, followed by the perseverative RL model. In the remaining two subjects, this order was reversed, with the perseverative RL model providing the best fit, followed by the perseverative dual learning rates RL model.

Investigating the distributions of these parameters across animals resulted in the following population level values (**Figure 4A**):

- Learning from positive outcomes parameter $\alpha_{pos} = 0.00923$ (95% CI : 0.00694, 0.0115).
- Learning from negative outcomes parameter $\alpha_{neg} = 0.0282$ (95% CI : 0.0107, 0.0457).

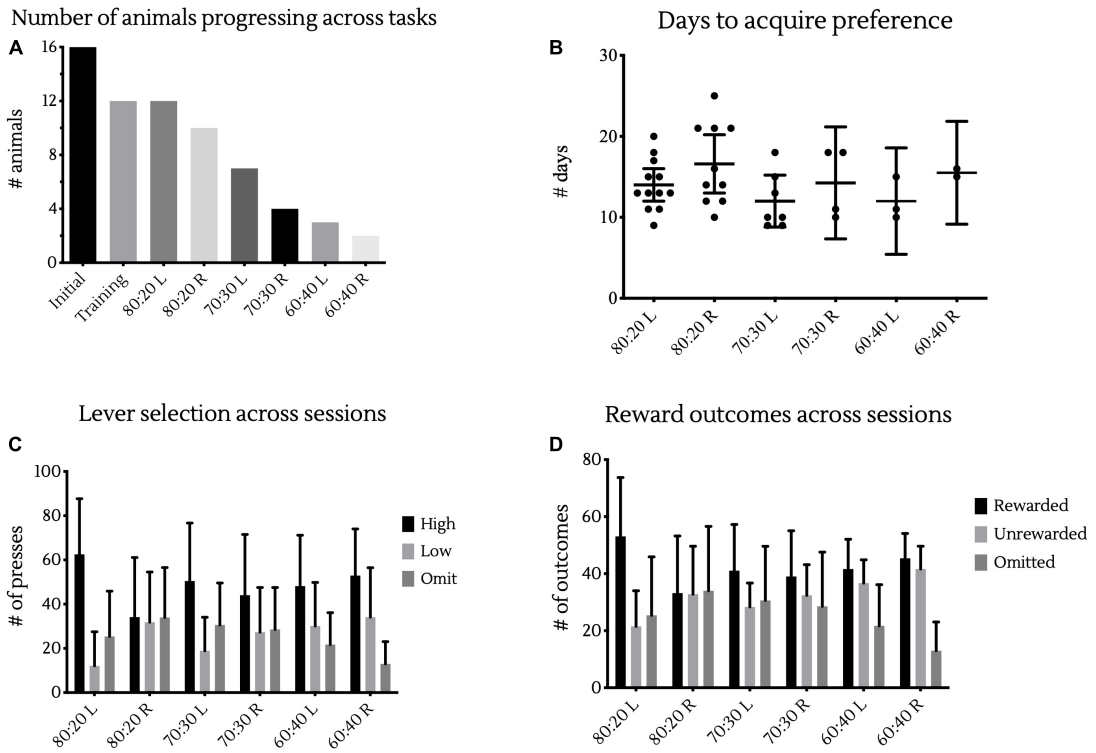

FIGURE 3 | Differences across reward contingencies. **(A)** Bars represent the number of animals able to complete training and each different reward contingency in testing. **(B)** Days to reach criterion in each reward contingency. Points represent the number of sessions individual animals took to achieve >80% of responses at the high rewarding lever in two sessions. Bars represent cohort mean ±95% CI. **(C)** Bars represent the mean ± SD presses in a session made at the high or low levers, as well as the number of response omissions made. **(D)** Bars represent the mean ± SD presses in a resulting in rewards or a lack thereof, as well as the number of omissions made.

- Softmax parameter
  $\beta = 3.275$ (95% CI : 2.5, 4.05).
- Perseveration parameter
  $\delta = 0.744$ (95% CI : 0.529, 0.959).

A Wilcoxon matched pairs signed-ranks test showed that α_{pos} was significantly smaller than α_{neg} ($p < 0.05$) and suggests that animals were learning significantly more from negative outcomes than positive ones (**Figure 4B**). However, this was not observed in all animals, with some exhibiting a higher α_{pos} than α_{neg}. Such differences may be expected to occur between individuals and may be suggestive of different underlying neurobiological substrates in learning from positive versus negative outcomes (Daw et al., 2002; Cazé and Van Der Meer, 2013). Additionally, whether an animal showed a higher learning rate to positive or negative outcomes did not impact on its ability to develop preferences for the high value option in the reversal learning tasks. For example, one of the two animals able to perform the most complex 60:40 Reversal Learning task, showed a higher α_{pos} (**Figure 4C**) whereas the other displayed a higher α_{neg} (**Figure 4D**).

Although the perseverative dual learning rates model provided the best fit to animal choice data, the *Q*-values generated by this model and used as estimates for the softmax decision rule did not accurately estimate the true probabilities of reward associated with each lever. *Q*-value estimates from models with a greater α_{pos} than α_{neg} were systemically greater than the true reward probabilities (**Figure 4E**), while *Q*-value estimates from models with a greater α_{neg} than α_{pos} were systemically lower than the true reward probabilities (**Figure 4F**). Despite this, *Q*-values were accurate on an ordinal level in both situations, with the high rewarding option associated with higher *Q*-values than the low rewarding option.

Interestingly, the perseverative RL model with a single learning rate was better able to accurately track the true probability of reward, with *Q*-values falling much closer to the true probability of reward for each option (**Figures 4E,F**, blue lines).

DISCUSSION

We assessed the ability of mice to perform a probabilistic learning task in a two lever operant chamber and determined that: (1) of those animals able to reliably push both levers in the chambers, all were able to "solve" the 80:20 probabilistic learning task, and more than 80% of these animals were also able to reverse under these contingencies; (2) some mice were able to discern and show preference for the high rewarding lever with 70:30 reward contingencies, and a few were even able to solve the highly

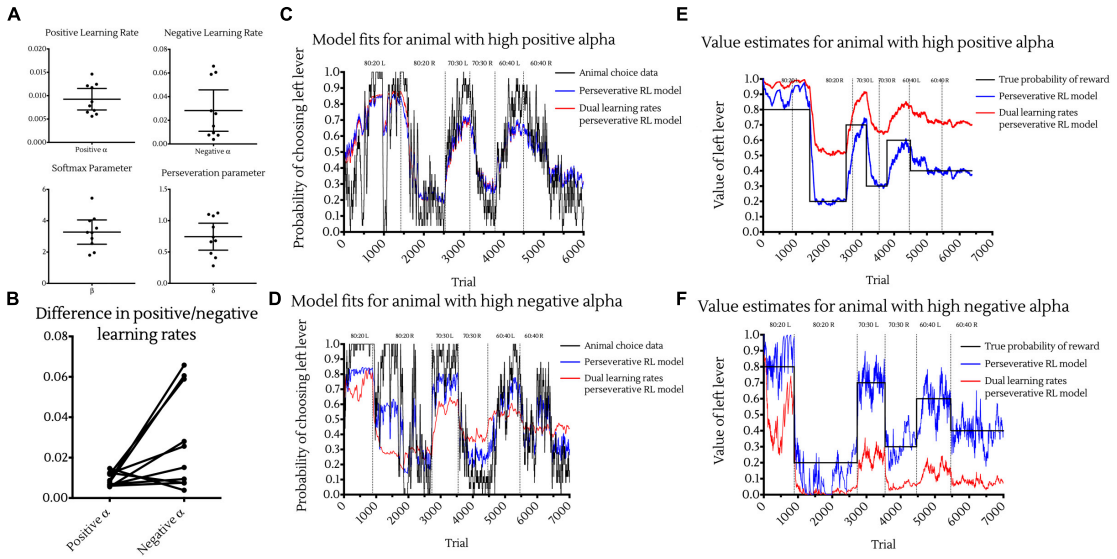

FIGURE 4 | Choice data and reinforcement learning model fits. **(A)** Maximum likelihood estimated parameter values of the Perseverative Dual Learning Rate model. Points represent individual animal estimates. Bars represent cohort mean ±95% CI. **(B)** Individual differences between positive and negative reward prediction error learning rates. Points represent individual animal parameter estimates. Joining lines indicate parameters coming from the same subject. While on average animals had higher α_{neg} than α_{pos} learning rates, this was not apparent in all animals, with much greater variance in negative than positive learning rates. **(C,D)** Observed and model predicted choices for example animals with high positive alpha **(C)** and high negative alpha **(D)** and best fitting models. Choice data were fit with the perseverative reinforcement learning model (blue) and perseverative dual learning rate reinforcement learning model (red) and model predictions plot against the true animal choices using 25-point moving average smoothing (black). Vertical lines indicate changes to reward contingencies. **(E,F)** Value estimates of reinforcement learning models for example animal with high positive alpha **(E)** and high negative alpha **(F)**. Value estimates of one lever from both the perseverative (blue) and dual learning rate perseverative (red) models were plotted against the true probability of reward of that lever (black) over time. Vertical lines indicate changes to reward contingencies.

complex 60:40 learning and reversal tasks; (3) a four parameter RL model, incorporating learning from positive and negative outcomes parameters α_{pos} and α_{neg}, softmax parameter β and perseveration parameter δ, was best able to capture animal choice behavior, while a simpler three parameter model with a single α learning rate was able to estimate the true expected values of options across different reward contingencies.

Of those animals capable of reliably pushing both levers in the chambers, all were able to "solve" the 80:20 probabilistic learning task, showing a robust preference for the high rewarding lever after a mean of 14 daily sessions. Additionally, more than 80% of these animals were able to suppress this learned behavior in the 80:20 reversal learning task, showing an equally strong preference for the new high rewarding lever after a mean of 16.6 days. This suggests that mice are able to discriminate reward values and perform PRL when rewards on both the high and low value options are stochastic, although at a much slower rate than rats and/or other species expected to have greater cognitive capabilities. This in turn provides some explanation as to why the performance of mice (Milienne-Petiot et al., 2017) at traditional within-session PRL tasks is so much lower than that of rats (Bari et al., 2010). In within-session PRL tasks, subjects are required to develop and switch preference on the order of 10s of trials, within a single day session consisting of several hundred trials, while our data suggests that mice require >1,000 individual trials to develop these strong preferences and reversals, spread over many separate 100 trial days.

Moving beyond the 80:20 reward contingencies, some mice were able to discern and develop preference for the high rewarding lever in the noisier 70:30 and even 60:40 reward contingency environments (**Figures 3C,D**). This ability to successfully develop preferences and reverse behavior under the 60:40 reward contingencies is particularly impressive for a number of reasons.

Firstly, it is substantially harder to discern which is the high rewarding side between a 60% and 40% chance of reward than 70%/30% or 80%/20%. Secondly, there is little drive to inhibit the developed preference and explore the alternative option when perseverating at the previously high option will still net almost as many rewards as adapting behavior to the new contingencies. To put this in context, previous progressive ratio studies using saccharin have shown that mice will press a lever upward of 20 times for a single saccharin reward (Beeler et al., 2012), a much lower rate of rewarding than the 40% of the low lever in these situations. It is also interesting to note that there was no significant difference in the time taken to acquire a preference for the high rewarding lever under the different reward contingencies. Were our animals truly behaving according to a RL strategy, we would expect to see acquisition of preference in noisier environments like those in the 60:40 tasks to take longer than in simpler environments like the 80:20 tasks.

One possible explanation of this, is that animals are meta-learning to reverse (that is, increasing task complexity being offset by increasing subject experience/competence), as suggested by Costa et al. (2015) in a monkey reversal learning task. However, given that all our animals received the same reward contingencies and in the same order in this experiment, further work would be required to test these hypotheses.

Lastly, a four-parameter perseverative dual learning rates RL model provided a good fit for choice data from individual animals. Estimated parameters of this model suggest that mice learn more rapidly following negative outcomes than positive outcomes. The positive δ also provides some insight into animal behavior, implying that mice are more likely to perseverate on the same side for multiple trials than to swap from side to side regularly. This δ is quite substantial, accounting for a $\sim$ 30% increase in the probability of choosing the same option as the trial before, if there was no difference in the expected value of both choices. This drive to perseverate gives further reason as to why mice struggle so much with traditional PRL tasks.

Another point of interest is to compare how these parameter estimates differ from human subjects. A study examining the effects of dopaminergic drugs in Parkinson's patients and healthy controls (Rutledge et al., 2009) fitted the same perseverative dual learning rates RL model to data from humans performing a dynamic foraging task and found that for healthy young adults the best fitting parameters were $\alpha_{pos} \approx \alpha_{neg} \approx 0.6$, $\beta = 1.73$ and $\delta = 0.39$. While the human parameters show somewhat smaller β and δ compared to mice, thus implying less noisy behavior and less perseveration, the biggest difference is in the α 's, with the human parameter orders of magnitude greater than that of a mouse, reflecting a much faster learning rate in humans than mice, as expected.

In addition to providing a good fit to our data, the RL model consisted of only a few, simple, yet highly informative parameters. For example, an intervention which causes an increase in α_{pos} could be interpreted as increasing the salience of reward signals, either by increasing the value of reward, or the rate at which positively reinforced learning occurs, where an intervention causing a decrease in δ might be interpreted as decreasing compulsive, perseverative behaviors. Lastly, this model can serve as an easily adaptable base on which to build other, more complex models with additional parameters; for example an additional updating step could, at the end of a session, help to explain between-session memory consolidation, or a temporal shrinking parameter within-session which might be useful in assessing appetitive satiation/reward devaluation over the course of a session (Isles et al., 2003; Rudebeck et al., 2013).

CONCLUSION

This study describes a novel, simplified variant of the PRL task for mice. Rather than removing or simplifying the probabilistic element of the task, we separate the initial discrimination from the reversal learning component. We found that, unlike in the traditional probabilistic learning tasks, mice were able to both acquire an initial preference for a high rewarding probabilistic option, as well as inhibit that acquired preference and subsequently adapt to an altered reward state with very close contingencies. Additionally, we show that RL models provide an appropriate tool for examining choice behavior, offering a framework for evaluating the effects of pharmacological and other interventions on different aspects of probability and reversal learning. However, it is likely that RL is not the complete process governing animal behavior in these tasks as higher order meta-learning or model-based learning processes may be in action. Further experimentation utilizing repeated reversals with the same reward contingencies, or alterations of the order of reward contingencies given, would be required to investigate this aspect further.

DATA AVAILABILITY STATEMENT

The raw data supporting the conclusions of this article will be made available by the authors, without undue reservation, to any qualified researcher.

ETHICS STATEMENT

The animal study was reviewed and approved by The Florey Animal Ethics Committee.

AUTHOR CONTRIBUTIONS

JM, SB, PB, CM, DH, and LJ contributed to the conception and design of the study. JM, MB, SO, and TF collected the data. JM and CM performed the statistical analyses. JM, SB, CM, DH, and LJ wrote the manuscript. All authors contributed to the manuscript revision, read, and approved the submitted version.

FUNDING

LJ and DH are supported by the Alzheimer's Association (2016-NIRG-396905) and the National Health and Medical Research Council (APP1105284). The Florey Institute of Neuroscience and Mental Health acknowledge the support of the Victorian Government and in particular the funding from the Operational Infrastructure Support Grant. SB was supported by a National Institute of Mental Health grant (R01MH108653) and a NARSAD YIG. PB received funding from The University of Melbourne through the R@MAP program.

ACKNOWLEDGMENTS

We thank H. Daykin and L. Cornthwaite-Duncan for assistance in running some operant sessions and their aid in providing husbandry for animals used in these experiments. We also thank Dr. R. Rutledge for providing insights and advice on reinforcement learning model fitting.

REFERENCES

Addicott, M. A., Pearson, J. M., Sweitzer, M. M., Barack, D. L., and Platt, M. L. (2017). A primer on foraging and the explore/exploit trade-off for psychiatry research. *Neuropsychopharmacology* 42, 1931–1939. doi: 10.1038/npp.2017.108

Akaike, H. (1998). "A new look at the statistical model identification," in *Selected Papers of Hirotugu Akaike*, eds E. Parzen, K. Tanabe, and G. Kitagawa, (New York, NY: Springer), 215–222. doi: 10.1007/978-1-4612-1694-0_16

Allaire, J. (2012). *RStudio: Integrated Development Environment for R*. Boston, MA: RStudio, Inc., 770.

Amitai, N., Young, J. W., Higa, K., Sharp, R. F., Geyer, M. A., and Powell, S. B. (2014). Isolation rearing effects on probabilistic learning and cognitive flexibility in rats. *Cogn. Affect. Behav. Neurosci.* 14, 388–406. doi: 10.3758/s13415-013-0204-4

Amodeo, D. A., Jones, J. H., Sweeney, J. A., and Ragozzino, M. E. (2014). Risperidone and the 5-HT 2A receptor antagonist M100907 improve probabilistic reversal learning in BTBR T + tf / J Mice. *Autism Res.* 2014, 555–567. doi: 10.1002/aur.1395

Anderson, D. R., and Burnham, K. P. (2002). Avoiding pitfalls when using information-theoretic methods. *J. Wildl. Manag.* 66, 912–918.

Bari, A., Theobald, D. E., Caprioli, D., Mar, A. C., Aidoo-Micah, A., Dalley, J. W., et al. (2010). Serotonin modulates sensitivity to reward and negative feedback in a probabilistic reversal learning task in rats. *Neuropsychopharmacology* 35, 1290–1301. doi: 10.1038/npp.2009.233

Beeler, J. A., Mccutcheon, J. E., Cao, Z. F. H., Murakami, M., Alexander, E., Roitman, M. F., et al. (2012). Taste uncoupled from nutrition fails to sustain the reinforcing properties of food. *Eur. J. Neurosci.* 36, 2533–2546. doi: 10.1111/j.1460-9568.2012.08167.x

Cazé, R. D., and Van Der Meer, M. A. A. (2013). Adaptive properties of differential learning rates for positive and negative outcomes. *Biol. Cybern.* 107, 711–719. doi: 10.1007/s00422-013-0571-5

Cohen, M. X. (2008). Neurocomputational mechanisms of reinforcement-guided learning in humans: a review. *Cogn. Affect. Behav. Neurosci.* 8, 113–125. doi: 10.3758/cabn.8.2.113

Costa, V. D., Tran, V. L., Turchi, J., and Averbeck, B. B. (2015). Reversal learning and dopamine: a bayesian perspective. *J. Neurosci.* 35, 2407–2416. doi: 10.1523/JNEUROSCI.1989-14.2015

Dalton, G. L., Phillips, A. G., and Floresco, S. B. (2014). Preferential involvement by nucleus accumbens shell in mediating probabilistic learning and reversal shifts. *J. Neurosci.* 34, 4618–4626. doi: 10.1523/JNEUROSCI.5058-13.2014

Dalton, G. L., Wang, N. Y., Phillips, A. G., and Floresco, S. B. (2016). Multifaceted contributions by different regions of the orbitofrontal and medial prefrontal cortex to probabilistic reversal learning. *J. Neurosci.* 36, 1996–2006. doi: 10.1523/JNEUROSCI.3366-15.2016

Daw, N. D., Kakade, S., and Dayan, P. (2002). Opponent interactions between serotonin and dopamine. *Neural Netw.* 15, 603–616. doi: 10.1016/s0893-6080(02)00052-7

Frank, M. J., Moustafa, A. A., Haughey, H. M., Curran, T., and Hutchison, K. E. (2007). Genetic triple dissociation reveals multiple roles for dopamine in reinforcement learning. *Proc. Natl. Acad. Sci. U.S.A.* 104, 16311–16316. doi: 10.1073/pnas.0706111104

Ineichen, C., Sigrist, H., Spinelli, S., Lesch, K. P., Sautter, E., Seifritz, E., et al. (2012). Neuropharmacology establishing a probabilistic reversal learning test in mice : evidence for the processes mediating reward-stay and punishment-shift behaviour and for their modulation by serotonin. *Neuropharmacology* 63, 1012–1021. doi: 10.1016/j.neuropharm.2012.07.025

Isles, A. R., Humby, T., and Wilkinson, L. S. (2003). Measuring impulsivity in mice using a novel operant delayed reinforcement task: effects of behavioural manipulations and d-amphetamine. *Psychopharmacology* 170, 376–382. doi: 10.1007/s00213-003-1551-6

Lawrence, A. D., Sahakian, B. J., Rogers, R. D., Hodges, J. R., and Robbins, T. W. (1999). Discrimination, reversal, and shift learning in Huntington's disease: mechanisms of impaired response selection. *Neuropsychologia* 37, 1359–1374. doi: 10.1016/s0028-3932(99)00035-4

Mehta, M. A., Swainson, R., Ogilvie, A. D., Sahakian, B., and Robbins, T. W. (2001). Improved short-term spatial memory but impaired reversal learning following the dopamine D2 agonist bromocriptine in human volunteers. *Psychopharmacology* 159, 10–20. doi: 10.1007/s002130100851

Milienne-Petiot, M., Kesby, J. P., Graves, M., van Enkhuizen, J., Semenova, S., Minassian, A., et al. (2017). The effects of reduced dopamine transporter function and chronic lithium on motivation, probabilistic learning, and neurochemistry in mice: modeling bipolar mania. *Neuropharmacology* 113, 260–270. doi: 10.1016/j.neuropharm.2016.07.030

Nash, J. C., and Varadhan, R. (2011). Unifying optimization algorithms to aid software system users: optimx for R. *J. Stat. Softw.* 43, 1–14.

R Core Team, (2019). *R: A Language and Environment for Statistical Computing*. Vienna: R Core Team.

Rudebeck, P. H., Saunders, R. C., Prescott, A. T., Chau, L. S., and Murray, E. A. (2013). Prefrontal mechanisms of behavioral flexibility, emotion regulation and value updating. *Nat. Neurosci.* 16, 1140–1145. doi: 10.1038/nn.3440

Rutledge, R. B., Lazzaro, S. C., Lau, B., Myers, C. E., Gluck, M. A., and Glimcher, P. W. (2009). Dopaminergic drugs modulate learning rates and perseveration in Parkinson's patients in a dynamic foraging task. *J. Neurosci.* 29, 15104–15114. doi: 10.1523/jneurosci.3524-09.2009

Sutton, R. S., and Barto, A. G. (2018). *Reinforcment Learning*. Cambridge, MA: The MIT Press.

Wickham, H. (2016). *The Tidyverse*. Available at: https://CRAN.R-project.org/package=tidyverse

Conflict of Interest: The authors declare that the research was conducted in the absence of any commercial or financial relationships that could be construed as a potential conflict of interest.

Copyright © 2020 Metha, Brian, Oberrauch, Barnes, Featherby, Bossaerts, Murawski, Hoyer and Jacobson. This is an open-access article distributed under the terms of the Creative Commons Attribution License (CC BY). The use, distribution or reproduction in other forums is permitted, provided the original author(s) and the copyright owner(s) are credited and that the original publication in this journal is cited, in accordance with accepted academic practice. No use, distribution or reproduction is permitted which does not comply with these terms.

frontiers in Molecular Neuroscience

MINI REVIEW
published: 21 January 2020
doi: 10.3389/fnmol.2019.00334

Dopamine and Noradrenaline in the Brain; Overlapping or Dissociate Functions?

Yadollah Ranjbar-Slamloo[1] and Zeinab Fazlali[2]**

[1] Eccles Institute of Neuroscience, The John Curtin School of Medical Research, The Australian National University, Canberra, ACT, Australia, [2] Department of Biomedical Engineering, Columbia University, New York, NY, United States

Dopamine and noradrenaline are crucial neuromodulators controlling brain states, vigilance, action, reward, learning, and memory processes. Ventral tegmental area (VTA) and Locus Coeruleus (LC) are canonically described as the main sources of dopamine (DA) and noradrenaline (NA) with dissociate functions. A comparison of diverse studies shows that these neuromodulators largely overlap in multiple domains such as shared biosynthetic pathway and co-release from the LC terminals, convergent innervations, non-specificity of receptors and transporters, and shared intracellular signaling pathways. DA–NA interactions are mainly studied in prefrontal cortex and hippocampus, yet it can be extended to the whole brain given the diversity of catecholamine innervations. LC can simultaneously broadcast both dopamine and noradrenaline across the brain. Here, we briefly review the molecular, cellular, and physiological overlaps between DA and NA systems and point to their functional implications. We suggest that DA and NA may function in parallel to facilitate learning and maintain the states required for normal cognitive processes. Various signaling modules of NA and DA have been targeted for developing of therapeutics. Understanding overlaps of the two systems is crucial for more effective interventions in a range of neuropsychiatric conditions.

Keywords: dopamine, noradrenaline, ventral tegmental area, Locus Coeruleus, co-transmission, neuromodulator, signaling

OPEN ACCESS

Edited by:
Christopher Alan Reid, The Florey Institute of Neuroscience and Mental Health, Australia

Reviewed by:
Elisabet Jerlhag, University of Gothenburg, Sweden
Heinrich J. G. Matthies, The University of Alabama at Birmingham, United States

****Correspondence:***
Yadollah Ranjbar-Slamloo
yadollah.ranjbar@anu.edu.au
Zeinab Fazlali
zeinab.fazlali@columbia.edu

Received: *15 October 2019*
Accepted: *27 December 2019*
Published: *21 January 2020*

Citation:
Ranjbar-Slamloo Y and Fazlali Z (2020) Dopamine and Noradrenaline in the Brain; Overlapping or Dissociate Functions? Front. Mol. Neurosci. 12:334. doi: 10.3389/fnmol.2019.00334

INTRODUCTION

Central nervous system produces diverse neurochemicals which bind to specific receptors coupled to the intricate intracellular signaling pathways. Synthesis and release of a primary neurotransmitter with a simplified action (e.g., excitatory or inhibitory) has been a ground for classification of neurons and synapses in the CNS. As knowledge of neurotransmission rapidly grew in the past few decades, it became soon clear that the actions of neurotransmitters are complex and some neurons produce and release two or more chemicals as fast neurotransmitters, neuromodulators, or neuropeptides (Vaaga et al., 2014). This often confounded the integration of connectivity knowledge with neurophysiology. Moreover, a single neurochemical can bind to different receptors and the receptor expression at the level of individual neurons are highly variable. For example, numerous metabotropic receptors have been identified for glutamate alone, with diverse distribution and function (Reiner and Levitz, 2018). Unlike glutamate and GABA

which are known for their binding to the fast-acting ionotropic receptors, others predominantly activate metabotropic receptors, hence they are commonly called neuromodulators. These include monoamines such as noradrenaline (NA, also called norepinephrine), adrenaline (also called epinephrine), dopamine (DA), serotonin, and histamine. Monoamines are produced by small populations of neurons located in specific brain nuclei. These neurons project to widespread brain regions with numerous ramifications to broadcast specific signals about external stimuli and internal states.

The effect of neuromodulators on the target neurons is often mediated by G-protein coupled receptors. Multiple receptors may share a specific signaling pathway. Specificity of a neuromodulator then should depend on the source of release, concentration, efficacy, and the rate of depletion or reuptake from the extracellular space. Although the main neuromodulators, such as acetylcholine, dopamine, noradrenaline, and serotonin have a key role in controlling the brain states (Brown et al., 2012) and computations (Dayan, 2012), their interactions are yet mysterious. Dopamine and noradrenaline in particular, appear to significantly cross-talk in cortex and hippocampus (Devoto et al., 2006). Dopamine producing neurons are located in the midbrain nuclei; mainly ventral tegmental area (VTA) and substantia nigra pars compacta (Poulin et al., 2018). Noradrenergic nuclei are located in pons and medulla. Among these nuclei, LC contains the major proportion of the noradrenergic cells and targets multiple regions of the brain (Robertson et al., 2013). Although DA and NA have been studied as two separate systems, they overlap in multiple domains such as; shared biosynthetic pathway, co-release from noradrenergic terminals, innervation of similar area, non-specific receptor, transporter affinity, and shared intracellular signaling pathways (**Figure 1**). What are the functional consequences of these overlaps? In the following paragraphs, we expand the major domains of overlap and their neurophysiological and behavioral implications of such overlaps.

VOLUME TRANSMISSION, RECEPTOR SIGNALLING, AND TRANSPORTER FUNCTIONS

Neuromodulators such as DA, NA, and acetylcholine can diffuse far from the release site and activate receptors in a considerable distance from the terminal (Agnati et al., 1995; Fuxe et al., 2010). This process, which is known as volume transmission, can activate receptors as far as 8 μm from the release site, in case of striatal dopamine (Sulzer et al., 2016). A long-range diffusion is also possible due to the circulation of the cerebrospinal fluid (CSF) along the peri-vascular space (Taber and Hurley, 2014). Peri-vascular CSF currents may supply neuromodulators far from their site of release, to activate receptors in area lacking direct projections.

Noradrenaline acts on three main G-protein coupled receptors, known as β-, α-1, and α-2 adrenoceptors (**Figure 1C**). These receptors have complex effects on neuronal excitability and synaptic transmission, depending on their site of action and concentration of NA (Berridge and Waterhouse, 2003; Arnsten et al., 2012; Waterhouse and Navarra, 2019). β-adrenoceptors are coupled to G_s which enhances cAMP signaling while α_2-adrenoceptors are coupled with G_i which suppresses adenylyl cyclase and reduces cAMP. Activation of presynaptic α_2-adrenoceptors suppresses the synaptic release of neurotransmitters in various brain regions (Yavich et al., 1997; Nasse and Travers, 2014). α_1-adrenoceptors activate phospholipase C signaling pathway through G_q. Dopamine acts on five types of G-protein coupled receptors, D_1–D_5, which are categorized in two main functional classes of D_1 and D_2 (Beaulieu and Gainetdinov, 2011). D_1-class of receptors comprises D_1 and D_5 which are coupled to G_s and enhance cAMP production (D_1 and D_5) and phospholipase C activity (D_5 or D_1:D_2 heterodimers, **Figure 1C**). D_2-class of dopamine receptors comprises D_2, D_3, and D_4. These receptors are coupled to G_i and hence reduce the production of cAMP (Beaulieu and Gainetdinov, 2011). D_1-class is expressed in the target cells, while D_2-class is expressed in the presynaptic dopamine terminals as well as in the target cells (Beaulieu and Gainetdinov, 2011). D_1-class of dopamine receptors share the same stimulating pathways which are used by the β-adrenoceptors (cAMP production) and α_1-adrenoceptors (G_q and PLC, **Figure 1C**). D_2-class share the pathways used by α_2-adrenoceptors which involve inhibitory G-proteins (Beaulieu and Gainetdinov, 2011; Schmidt and Weinshenker, 2014). Dopamine can directly activate α_2-adrenoceptors in LC and hippocampus (Guiard et al., 2008; El Mansari et al., 2010). Therefore, dissociation of DA and NA functions is particularly hard in areas with high concentrations of both, such as prefrontal cortex and hippocampus.

Dissociation of the physiological effects of DA and NA on target cells may be implemented by mechanisms controlling transmitter overflow and pooling. For example, DA transporter restricts the time course of dopaminergic currents in VTA while decay of noradrenergic currents in LC scales with amplitude due to lower transporter efficacy (Courtney and Ford, 2014). Such temporal variations might be a ground for functional dissociations. However, DA is not always cleared by its specific transporter; In frontal cortex and hippocampus for example, DA is primarily cleared by NA transporters (Morón et al., 2002; Guiard et al., 2008). Notably, both DA and NA can also be cleared by low affinity transporters (Duan and Wang, 2010) which can further shape their actions. Therefore, DA reuptake through shared transporters may cause a similar time course of catecholamine signaling. This can be clarified by comparing the synaptic effects of DA and NA in cortex or hippocampus and identifying transporters involved in these regions.

DA AND NA INNERVATIONS AND RECEPTOR EXPRESSIONS VARY ACROSS BRAIN AREA

The pattern of catecholamine receptor expression varies across the brain. For example, noradrenergic projections are sparse in dorsal striatum. Similarly, in the core subregion of nucleus accumbens (NAc), noradrenergic inputs are sparse while considerably dense noradrenergic fibers were found in the shell

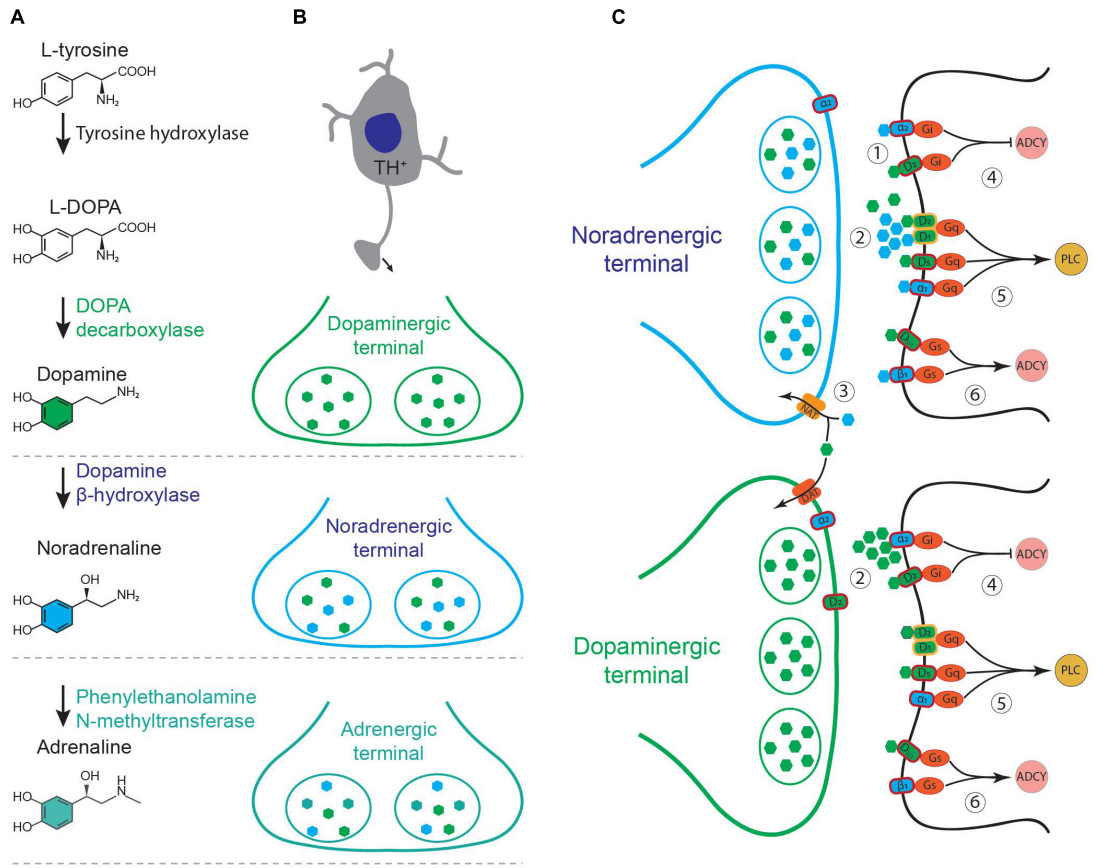

FIGURE 1 | (A) Biosynthesis of catecholamines from L-tyrosine. **(B)** Schematic of a tyrosine hydroxylase positive (TH^+) neuron and its axonal terminals containing different combination of catecholamines, depending on the type of the neuron. **(C)** Noradrenergic and dopaminergic terminals. (1) Co-release of dopamine (green) and noradrenaline (blue) and their binding to specific receptors on target neurons. (2) Non-specific binding at high concentrations. (3) Non-specific transporter function. NAT, noradrenaline transporter; DAT, dopamine transporter. (4–6) Intracellular pathways shared between noradrenergic and dopaminergic receptors. ADCY, adenylyl cyclase; PLC, phospholipase C.

subregion (Berridge et al., 1997; Nomura et al., 2014). It should be mentioned, however, that the noradrenergic fibers in NAc shell originate mainly from α_2 group of noradrenergic cells (Delfs et al., 1998). Consistent with the projection patterns, earlier studies showed a low NA concentration in the dorsal regions of striatum, while ventral striatum had a relatively high concentration of NA (Brownstein et al., 1974; Versteeg et al., 1976). The concentration of NA may rise due to a phasic release following novel stimuli, or tonic increase due to the changes in the brain state. Both β_1 and α_{2c} type of adrenoceptors are highly expressed in the striatal projection neurons, dopaminergic terminals (Paschalis et al., 2009; Hara et al., 2010) and cholinergic interneurons (Pisani et al., 2003). Such dense receptor expression can make the striatal circuits sensitive to NA signaling despite overall low noradrenergic inputs. We should also consider that DA effects can also be partially mediated by α_2 adrenoceptors (Cornil et al., 2008; Guiard et al., 2008). Consistently, both DA and NA can modulate the cAMP signaling pathway in the striatum (Nomura et al., 2014). Unlike basal ganglia, corticothalamic regions receive much denser input from LC (Nomura et al., 2014). Cortical regions and layers receive a relatively dense and homogeneous LC projections, while VTA projections are layer and region specific (Nomura et al., 2014). Overall, large overlaps in receptor expression and signaling pathway suggest that DA and NA may mediate similar physiological functions (**Table 1**). Specificity of their actions might depend on their local concentration, the timing of their release and reuptake and activity of the synaptic terminals.

SIGNIFICANCE OF DA AND NA SIGNALING AND THEIR FUNCTIONAL SIMILARITIES

Locus Coeruleus-noradrenaline system is known as the major regulator of wakefulness, vigilance, arousal, and memory formation (Aston-Jones et al., 1999; Berridge and Waterhouse, 2003; Aston-Jones and Cohen, 2005; Sara, 2009; Brown et al., 2012). LC-NA also mediates drug associated memory and reinstatement of the drug seeking behavior in addiction (Weinshenker and Schroeder, 2007;

TABLE 1 | Similarities in physiological roles of dopamine and noradrenaline.

Physiological role	Dopamine	Noradrenaline
Wakefulness/ arousal/brain state	Eban-Rothschild et al., 2016	Aston-Jones and Cohen, 2005; Carter et al., 2010; Fazlali et al., 2016
Attention	Noudoost and Moore, 2011	Berridge and Waterhouse, 2003; Eldar et al., 2013
Memory formation	Vijayraghavan et al., 2007; Shohamy and Adcock, 2010	Berridge and Waterhouse, 2003; Sara, 2009
Memory consolidation	Vijayraghavan et al., 2007; Yamasaki and Takeuchi, 2017	Berridge and Waterhouse, 2003; Sara, 2009
Novelty induced memory encoding	Kempadoo et al., 2016; Takeuchi et al., 2016	Kempadoo et al., 2016; Takeuchi et al., 2016
Reward/ addiction	Schultz, 2001, 2007; Berke, 2018; Cox and Witten, 2019	Weinshenker and Schroeder, 2007; Aston-Jones and Kalivas, 2008; Sara and Bouret, 2012; Bouret and Richmond, 2015

Aston-Jones and Kalivas, 2008). Although VTA-DA system is mainly involved in action and reward processing (Schultz, 2001, 2007; Berke, 2018; Cox and Witten, 2019). It also mediates selective attention, working memory and memory consolidation in cortex and hippocampus (Vijayraghavan et al., 2007; Noudoost and Moore, 2011; Yamasaki and Takeuchi, 2017). These effects may be mediated by parallel catecholamine signaling in multiple target regions.

Convergence of the DA and NA signaling pathways suggest that they might have parallel neurophysiological effects. Indeed, from the very early intracellular studies, complex effects of both NA and DA on neuronal excitability were observed (Madison and Nicoll, 1986; Foote and Morrison, 1987; McCormick and Prince, 1988; McCormick, 1989; Zhou and Hablitz, 1999; Kröner et al., 2005). Depending on the neuronal targets and their specific receptors, DA and NA can modulate various intrinsic currents and hence excitability of the neurons (McCormick, 1989; Cathala and Paupardin-Tritsch, 1999; Seamans and Yang, 2004; Rosenkranz and Johnston, 2006; Arencibia-Albite et al., 2007). The most prominent effect of the NA is the modulation of synaptic transmission and various forms of plasticity (Harley, 1987; Mouradian et al., 1991; Sara, 2009), which are analogous to those of DA (Seamans and Yang, 2004; Tritsch and Sabatini, 2012; Froemke, 2015). In various sensory systems, both dopaminergic and noradrenergic systems were effective in remodeling the tuning properties of the cortical neurons (Bao et al., 2001; Manunta and Edeline, 2004; Edeline et al., 2011; Martins and Froemke, 2015; McBurney-Lin et al., 2019; Waterhouse and Navarra, 2019). Notably, both systems also contribute to the maintenance and transitions of global brain states, wakefulness, arousal, attention, and memory consolidation (Berridge, 2008; Carter et al., 2010; Lee and Dan, 2012; Eban-Rothschild et al., 2016; Fazlali et al., 2016; Sara, 2017; Schicknick et al., 2019). Reward or punishment related stimuli appear to activate catecholamine producing neurons in both LC and VTA (Bouret and Sara, 2004; Sara, 2009; Sara and Bouret, 2012; Bouret and Richmond, 2015). Furthermore, adrenergic and noradrenergic projections to VTA (Mejías-Aponte et al., 2009) may serve to rapidly broadcast behaviorally relevant signals.

In multiple brain regions the activation of adrenergic receptors enhances long term potentiation, working memory, memory consolidation and retrieval (Sara, 2009). These functions are similar to dopaminergic effects on memory processes (Shohamy and Adcock, 2010). It is assumed that the reward related memory consolidation and learning is mediated through VTA-DA system (Schultz, 2001; Berke, 2018). However, LC neuronal activity is also correlated with reward expectation (Bouret and Richmond, 2015). In parallel with VTA-DA system, dopamine release from dense LC terminals in prefrontal cortex and hippocampus may also serve as a strong reward associated signal to facilitate learning and novelty induced memory encoding (Kempadoo et al., 2016; Takeuchi et al., 2016). Overall DA and NA appear to have parallel effects on learning, brain state and reward processing.

DA AND NA CO-RELEASE FROM THE LOCUS COERULEUS

Locus Coeruleus has long been identified as a noradrenergic center, where majority of the cells produce noradrenaline from dopamine by expressing dopamine-beta-hydroxylase (**Figure 1A**). A long-standing challenge, however, was to establish whether these cells store and release DA as a co-transmitter together with NA (**Figures 1B,C**). The first evidence for DA–NA co-release came from measurements of the DA and NA concentrations in the cortical area following psychoactive drugs or LC pharmacological stimulation (Kawahara et al., 2001; Devoto et al., 2005a, 2006). These studies showed that noradrenergic stimulation/suppression causes a parallel change in concentration of both DA and NA in cortical regions. This was often interpreted as a direct or indirect interaction between VTA and LC projections in the cortical area (Kawahara et al., 2001; Chandler et al., 2014; Xing et al., 2016). Such interactions can be due to the direct projections from noradrenergic nuclei to VTA (Mejías-Aponte et al., 2009), control of DA release from dopaminergic terminals via adrenoceptors (Yavich et al., 1997; Ihalainen and Tanila, 2002) and/or competition of NA and DA for the same transporter (Morón et al., 2002; Yamamoto and Novotney, 2002; Borgkvist et al., 2011). Alternatively, it was also hypothesized that DA can be released from LC terminals as a co-transmitter (Devoto et al., 2006).

Earlier pharmacological studies provided strong evidence for DA–NA co-transmission hypothesis; (1) It was shown that the DA levels in parietal, occipital, and cerebellar cortices – which are poorly innervated by DA fibers – were as high as densely

innervated medial prefrontal cortex (Devoto et al., 2001). (2) Dopamine receptor antagonists which were known to enhance DA concentration in striatum, were not as effective as adrenergic agonists and antagonists in modifying DA levels in cortex (Kuroki et al., 1999; Devoto et al., 2001, 2003b, 2004). (3) Chemical and electrical alterations of the LC activity significantly modulated the NA and DA concentrations in cortical regions (Kawahara et al., 2001; Devoto et al., 2003a, 2005a,b; Masana et al., 2011). (4) Electrical stimulation of the LC did not change DA concentration in striatum but significantly increased NA level in this region (Devoto et al., 2005a,b). (5) Selective lesion studies and specific disruption of catecholamine production in VTA and LC confirmed that noradrenergic terminals are the main source of dopamine in cortical regions (Pozzi et al., 1994; Devoto et al., 2008, 2015, 2019; Smith and Greene, 2012). Moreover, several medications for neuropsychiatric conditions increase both DA and NA in the brain (Devoto et al., 2006).

Novel genetic and optogenetic techniques make it possible to study the function of neuromodulator nuclei with greater specificity (Carter et al., 2010; Eban-Rothschild et al., 2016). Using these methods, recent studies dissected VTA and LC projections in hippocampus and found that dopamine release from dense LC projections is the primary cause of learning and memory in certain tasks (Kempadoo et al., 2016; Takeuchi et al., 2016; McNamara and Dupret, 2017). Optogenetic stimulation of LC terminals in hippocampus enhanced DA together with NA and specific LC lesion reduced both neurochemicals (Kempadoo et al., 2016). More importantly, these studies for the first time revealed a strong causal link between dopamine release from LC projections and performance in certain learning and memory tasks. Kandle and colleagues showed that photo-stimulation of LC projections in dorsal hippocampus improved mice performance in spatial learning and memory tasks (Kempadoo et al., 2016). At the same time, Morris and colleagues found that LC dopaminergic activity in the hippocampus is necessary for novelty associated memory formation (Takeuchi et al., 2016). Surprisingly, noradrenergic blockade in hippocampus had no effect on either spatial memory or novelty associated memory enhancement (Kempadoo et al., 2016; Takeuchi et al., 2016), despite earlier studies showing beta-adrenergic dependent memory-encoding and plasticity (Straube et al., 2003; Lemon et al., 2009). Overall these studies confirmed the DA–NA co-transmission and the significant role of LC-DA in spatial memory encoding and novelty induced memory consolidation. Whether DA–NA release from LC contributes to distinct memory processes from VTA-DA remains elusive (Yamasaki and Takeuchi, 2017; Duszkiewicz et al., 2019).

CONCLUDING REMARKS AND FUTURE DIRECTIONS

An overview of the studies on dopamine and noradrenaline signaling and function in the CNS suggests that these systems may act in parallel and overlapping manner. Here we provided an integrative approach to support this view. Highly overlapping functions of catecholamines raise important questions; Does LC release DA throughout the brain? What are the functional interactions of LC and VTA? How does the distribution of receptors and transporters of catecholamines determine their specific function? Is ratio of DA/NA important and how can it change? Recent developments of the synthetic and genetically encoded catecholamine sensors (Patriarchi et al., 2018; Sun et al., 2018; Beyene et al., 2019; Feng et al., 2019) together with well-established optogenetic and two-photon imaging techniques make it possible to dissect the role of these neuromodulators in brain computations. Superior spatiotemporal resolution of these sensors makes it possible to examine local/global signaling, volume transmission, co-release and interactions of catecholamines. DA and NA are involved in major brain computations such as sensory processing, motor planning, plasticity, and memory encoding. They are also crucial in mood maintenance, motivation, and concentration.

Future studies should attempt to decode behaviorally relevant signals in LC and VTA and compare the modulatory effects of LC-DA, LC-NA, and VTA-DA in cortex, hippocampus, and ventral striatum. Adrenergic and noradrenergic nuclei other than LC also require a fresh attention in this regard. A better understanding of these systems would facilitate the advent of more effective therapeutics for a range of psychiatric conditions, such as depression (Nutt et al., 2007; Hare et al., 2019), schizophrenia (Winograd-Gurvich et al., 2006; Howes et al., 2017; Matthews et al., 2018), ADHD (Levy, 2009; Tripp and Wickens, 2009), PTSD (Hendrickson and Raskind, 2016), and addiction (Weinshenker and Schroeder, 2007). It is not clear how different neuromodulatory systems are disrupted in these disorders. Research on the overlapping functions of the neuromodulators can provide a new insight into the mechanisms of neuropsychiatric disorders.

AUTHOR CONTRIBUTIONS

YR-S and ZF equally contributed to the conception and writing of the manuscript.

REFERENCES

Agnati, L. F., Zoli, M., Strömberg, I., and Fuxe, K. (1995). Intercellular communication in the brain: wiring versus volume transmission. *Neuroscience* 69, 711–726. doi: 10.1016/0306-4522(95)00308-6

Arencibia-Albite, F., Paladini, C., Williams, J. T., and Jiménez-Rivera, C. A. (2007). Noradrenergic modulation of the hyperpolarization-activated cation current (Ih) in dopamine neurons of the ventral tegmental area. *Neuroscience* 149, 303–314. doi: 10.1016/j.neuroscience.2007.08.009

Arnsten, A. F., Wang, M. J., and Paspalas, C. D. (2012). Neuromodulation of thought: flexibilities and vulnerabilities in prefrontal cortical network synapses. *Neuron* 76, 223–239. doi: 10.1016/j.neuron.2012.08.038

Aston-Jones, G., and Cohen, J. D. (2005). An integrative theory of locus coeruleus-norepinephrine function: adaptive gain and optimal performance. *Annu. Rev. Neurosci.* 28, 403–450. doi: 10.1146/annurev.neuro.28.061604.135709

Aston-Jones, G., and Kalivas, P. W. (2008). Brain norepinephrine rediscovered in addiction research. *Biol. Psychiatry* 63, 1005–1006. doi: 10.1016/j.biopsych.2008.03.016

Aston-Jones, G., Rajkowski, J., and Cohen, J. (1999). Role of locus coeruleus in attention and behavioral flexibility. *Biol. Psychiatry* 46, 1309–1320. doi: 10.1016/s0006-3223(99)00140-7

Bao, S., Chan, V. T., and Merzenich, M. M. (2001). Cortical remodelling induced by activity of ventral tegmental dopamine neurons. *Nature* 412, 79–83. doi: 10.1038/35083586

Beaulieu, J.-M., and Gainetdinov, R. R. (2011). The physiology, signaling, and pharmacology of dopamine receptors. *Pharmacol. Rev.* 63, 182–217. doi: 10.1124/pr.110.002642

Berke, J. D. (2018). What does dopamine mean? *Nat. Neurosci.* 21, 787–793. doi: 10.1038/s41593-018-0152-y

Berridge, C. W. (2008). Noradrenergic modulation of arousal. *Brain Res. Rev.* 58, 1–17. doi: 10.1016/j.brainresrev.2007.10.013

Berridge, C. W., Stratford, T. L., Foote, S. L., and Kelley, A. E. (1997). Distribution of dopamine beta-hydroxylase-like immunoreactive fibers within the shell subregion of the nucleus accumbens. *Synapse* 27, 230–241. doi: 10.1002/(sici)1098-2396(199711)27:3<230::aid-syn8>3.0.co;2-e

Berridge, C. W., and Waterhouse, B. D. (2003). The locus coeruleus–noradrenergic system: modulation of behavioral state and state-dependent cognitive processes. *Brain Res. Brain Res. Rev.* 42, 33–84. doi: 10.1016/S0165-0173(03)00143-7

Beyene, A. G., Delevich, K., Del Bonis-O'Donnell, J. T., Piekarski, D. J., Lin, W. C., Thomas, A. W., et al. (2019). Imaging striatal dopamine release using a nongenetically encoded near infrared fluorescent catecholamine nanosensor. *Sci. Adv.* 5:eaaw3108. doi: 10.1126/sciadv.aaw3108

Borgkvist, A., Malmlöf, T., Feltmann, K., Lindskog, M., and Schilström, B. (2011). Dopamine in the hippocampus is cleared by the norepinephrine transporter. *Int. J. Neuropsychopharmacol.* 15, 1–10. doi: 10.1017/S1461145711000812

Bouret, S., and Richmond, B. J. (2015). Sensitivity of locus ceruleus neurons to reward value for goal-directed actions. *J. Neurosci.* 35, 4005–4014. doi: 10.1523/JNEUROSCI.4553-14.2015

Bouret, S., and Sara, S. J. (2004). Reward expectation, orientation of attention and locus coeruleus-medial frontal cortex interplay during learning. *Eur. J. Neurosci.* 20, 791–802. doi: 10.1111/j.1460-9568.2004.03526.x

Brown, R. E., Basheer, R., McKenna, J. T., Strecker, R. E., and McCarley, R. W. (2012). Control of sleep and wakefulness. *Physiol. Rev.* 92, 1087–1187. doi: 10.1152/physrev.00032.2011

Brownstein, M., Saavedra, J. M., and Palkovits, M. (1974). Norepinephrine and dopamine in the limbic system of the rat. *Brain Res.* 79, 431–436. doi: 10.1016/0006-8993(74)90440-5

Carter, M. E., Yizhar, O., Chikahisa, S., Nguyen, H., Adamantidis, A., Nishino, S., et al. (2010). Tuning arousal with optogenetic modulation of locus coeruleus neurons. *Nat. Neurosci.* 13, 1526–1533. doi: 10.1038/nn.2682

Cathala, L., and Paupardin-Tritsch, D. (1999). Effect of catecholamines on the hyperpolarization-activated cationic I h and the inwardly rectifying potassium I Kir currents in the rat substantia nigra pars compacta. *Eur. J. Neurosci.* 11, 398–406. doi: 10.1046/j.1460-9568.1999.00452.x

Chandler, D. J., Waterhouse, B. D., and Gao, W.-J. (2014). New perspectives on catecholaminergic regulation of executive circuits: evidence for independent modulation of prefrontal functions by midbrain dopaminergic and noradrenergic neurons. *Front. Neural Circuits* 8:53. doi: 10.3389/fncir.2014.00053

Cornil, C. A., Castelino, C. B., and Ball, G. F. (2008). Dopamine binds to α2-adrenergic receptors in the song control system of zebra finches (*Taeniopygia guttata*). *J. Chem. Neuroanat.* 35, 202–215. doi: 10.1016/J.JCHEMNEU.2007.10.004

Courtney, N. A., and Ford, C. P. (2014). The timing of dopamine- and noradrenaline-mediated transmission reflects underlying differences in the extent of spillover and pooling. *J. Neurosci.* 34, 7645–7656. doi: 10.1523/JNEUROSCI.0166-14.2014

Cox, J., and Witten, I. B. (2019). Striatal circuits for reward learning and decision-making. *Nat. Rev. Neurosci.* 20, 482–494. doi: 10.1038/s41583-019-0189-2

Dayan, P. (2012). Twenty-five lessons from computational neuromodulation. *Neuron* 76, 240–256. doi: 10.1016/j.neuron.2012.09.027

Delfs, J. M., Zhu, Y., Druhan, J. P., and Aston-Jones, G. S. (1998). Origin of noradrenergic afferents to the shell subregion of the nucleus accumbens: anterograde and retrograde tract-tracing studies in the rat. *Brain Res.* 806, 127–140. doi: 10.1016/s0006-8993(98)00672-6

Devoto, P., Flore, G., and Brodie, B. B. (2006). On the origin of cortical dopamine: is it a co-transmitter in noradrenergic neurons? *Curr. Neuropharmacol.* 4, 115–125. doi: 10.2174/157015906776359559

Devoto, P., Flore, G., Longu, G., Pira, L., and Gessa, G. L. (2003a). Origin of extracellular dopamine from dopamine and noradrenaline neurons in the medial prefrontal and occipital cortex. *Synapse* 50, 200–205. doi: 10.1002/syn.10264

Devoto, P., Flore, G., Vacca, G., Pira, L., Arca, A., Casu, M. A., et al. (2003b). Co-release of noradrenaline and dopamine from noradrenergic neurons in the cerebral cortex induced by clozapine, the prototype atypical antipsychotic. *Psychopharmacology* 167, 79–84. doi: 10.1007/s00213-002-1381-y

Devoto, P., Flore, G., Pani, L., and Gessa, G. L. (2001). Evidence for co-release of noradrenaline and dopamine from noradrenergic neurons in the cerebral cortex. *Mol. Psychiatry* 6, 657–664. doi: 10.1038/sj.mp.4000904

Devoto, P., Flore, G., Pira, L., Longu, G., and Gessa, G. L. (2004). Alpha2-adrenoceptor mediated co-release of dopamine and noradrenaline from noradrenergic neurons in the cerebral cortex. *J. Neurochem.* 88, 1003–1009. doi: 10.1046/j.1471-4159.2003.02239.x

Devoto, P., Flore, G., Saba, P., Castelli, M. P., Piras, A. P., Luesu, W., et al. (2008). 6-Hydroxydopamine lesion in the ventral tegmental area fails to reduce extracellular dopamine in the cerebral cortex. *J. Neurosci. Res.* 86, 1647–1658. doi: 10.1002/jnr.21611

Devoto, P., Flore, G., Saba, P., Fà, M., and Gessa, G. L. (2005a). Co-release of noradrenaline and dopamine in the cerebral cortex elicited by single train and repeated train stimulation of the locus coeruleus. *BMC Neurosci.* 6:31. doi: 10.1186/1471-2202-6-31

Devoto, P., Flore, G., Saba, P., Fà, M., and Gessa, G. L. (2005b). Stimulation of the locus coeruleus elicits noradrenaline and dopamine release in the medial prefrontal and parietal cortex. *J. Neurochem.* 92, 368–374. doi: 10.1111/j.1471-4159.2004.02866.x

Devoto, P., Flore, G., Saba, P., Frau, R., and Gessa, G. L. (2015). Selective inhibition of dopamine-beta-hydroxylase enhances dopamine release from noradrenergic terminals in the medial prefrontal cortex. *Brain Behav.* 5:e00393. doi: 10.1002/brb3.393

Devoto, P., Flore, G., Saba, P., Scheggi, S., Mulas, G., Gambarana, C., et al. (2019). Noradrenergic terminals are the primary source of α2-adrenoceptor mediated dopamine release in the medial prefrontal cortex. *Prog. Neuro Psychopharmacol. Biol. Psychiatry* 90, 97–103. doi: 10.1016/J.PNPBP.2018.11.015

Duan, H., and Wang, J. (2010). Selective transport of monoamine neurotransmitters by human plasma membrane monoamine transporter and organic cation transporter 3. *J. Pharmacol. Exp. Ther.* 335, 743–753. doi: 10.1124/jpet.110.170142

Duszkiewicz, A. J., McNamara, C. G., Takeuchi, T., and Genzel, L. (2019). Novelty and dopaminergic modulation of memory persistence: a tale of two systems. *Trends Neurosci.* 42, 102–114. doi: 10.1016/j.tins.2018.10.002

Eban-Rothschild, A., Rothschild, G., Giardino, W. J., Jones, J. R., and de Lecea, L. (2016). VTA dopaminergic neurons regulate ethologically relevant sleep–wake behaviors. *Nat. Neurosci.* 19, 1356–1366. doi: 10.1038/nn.4377

Edeline, J.-M., Manunta, Y., and Hennevin, E. (2011). Induction of selective plasticity in the frequency tuning of auditory cortex and auditory thalamus neurons by locus coeruleus stimulation. *Hear. Res.* 274, 75–84. doi: 10.1016/j.heares.2010.08.005

Eldar, E., Cohen, J. D., and Niv, Y. (2013). The effects of neural gain on attention and learning. *Nat. Neurosci.* 16, 1146–1153. doi: 10.1038/nn.3428

El Mansari, M., Guiard, B. P., Chernoloz, O., Ghanbari, R., Katz, N., and Blier, P. (2010). Relevance of norepinephrine-dopamine interactions in the treatment of major depressive disorder. *CNS Neurosci. Ther.* 16, e1–e17. doi: 10.1111/j.1755-5949.2010.00146.x

Fazlali, Z., Ranjbar-Slamloo, Y., Adibi, M., and Arabzadeh, E. (2016). Correlation between locus coeruleus activity and cortical state : implications for sensory coding in rat barrel cortex. *Front. Neural Circuits* 10:e14. doi: 10.3389/fncir.2016.00014

Feng, J., Zhang, C., Lischinsky, J. E., Jing, M., Zhou, J., Wang, H., et al. (2019). A genetically encoded fluorescent sensor for rapid and specific *in vivo* detection of norepinephrine. *Neuron* 102, 745.e8–761.e8. doi: 10.1016/j.neuron.2019.02.037

Foote, S. L., and Morrison, J. H. (1987). Extrathalamic modulation of cortical function. *Annu. Rev. Neurosci.* 10, 67–95. doi: 10.1146/annurev.ne.10.030187.000435

Froemke, R. C. (2015). Plasticity of cortical excitatory-inhibitory balance. *Annu. Rev. Neurosci.* 38, 195–219. doi: 10.1146/annurev-neuro-071714-034002

Fuxe, K., Dahlström, A. B., Jonsson, G., Marcellino, D., Guescini, M., Dam, M., et al. (2010). The discovery of central monoamine neurons gave volume transmission to the wired brain. *Prog. Neurobiol.* 90, 82–100. doi: 10.1016/J.PNEUROBIO.2009.10.012

Guiard, B. P., El Mansari, M., and Blier, P. (2008). Cross-Talk between dopaminergic and noradrenergic systems in the rat ventral tegmental area. locus ceruleus, and dorsal Hippocampus. *Mol. Pharmacol.* 74, 1463–1475. doi: 10.1124/mol.108.048033

Hara, M., Fukui, R., Hieda, E., Kuroiwa, M., Bateup, H. S., Kano, T., et al. (2010). Role of adrenoceptors in the regulation of dopamine/DARPP-32 signaling in neostriatal neurons. *J. Neurochem.* 113, 1046–1059. doi: 10.1111/j.1471-4159.2010.06668.x

Hare, B. D., Shinohara, R., Liu, R. J., Pothula, S., DiLeone, R. J., and Duman, R. S. (2019). Optogenetic stimulation of medial prefrontal cortex Drd1 neurons produces rapid and long-lasting antidepressant effects. *Nat. Commun.* 10:223. doi: 10.1038/s41467-018-08168-9

Harley, C. W. (1987). A role for norepinephrine in arousal, emotion and learning : limbic modulation by norepinephrine and the kety hypothesis. *Prog. Neuro Psychopharmacol. Biol. Psychiatry* 11, 419–458. doi: 10.1016/0278-5846(87)90015-7

Hendrickson, R. C., and Raskind, M. A. (2016). Noradrenergic dysregulation in the pathophysiology of PTSD. *Exp. Neurol.* 284, 181–195. doi: 10.1016/J.EXPNEUROL.2016.05.014

Howes, O. D., McCutcheon, R., Owen, M. J., and Murray, R. M. (2017). The role of genes, stress, and dopamine in the development of schizophrenia. *Biol. Psychiatry* 81, 9–20. doi: 10.1016/J.BIOPSYCH.2016.07.014

Ihalainen, J. A., and Tanila, H. (2002). In vivo regulation of dopamine and noradrenaline release by α2A-adrenoceptors in the mouse prefrontal cortex. *Eur. J. Neurosci.* 15, 1789–1794. doi: 10.1046/j.1460-9568.2002.02014.x

Kawahara, H., Kawahara, Y., and Westerink, B. H. C. (2001). The noradrenaline-dopamine interaction in the rat medial prefrontal cortex studied by multi-probe microdialysis. *Eur. J. Pharmacol.* 418, 177–186. doi: 10.1016/S0014-2999(01)00863-9

Kempadoo, K. A., Mosharov, E. V., Choi, S. J., Sulzer, D., and Kandel, E. R. (2016). Dopamine release from the locus coeruleus to the dorsal hippocampus promotes spatial learning and memory. *Proc. Natl. Acad. Sci.U.S.A.* 113, 14835–14840. doi: 10.1073/pnas.1616515114

Kröner, S., Rosenkranz, J. A., Grace, A. A., and Barrionuevo, G. (2005). Dopamine modulates excitability of basolateral amygdala neurons *in vitro*. *J. Neurophysiol.* 93, 1598–1610. doi: 10.1152/jn.00843.2004

Kuroki, T., Meltzer, H. Y., and Ichikawa, J. (1999). Effects of antipsychotic drugs on extracellular dopamine levels in rat medial prefrontal cortex and nucleus accumbens. *J. Pharmacol. Exp. Ther.* 266, 1374–1384.

Lee, S.-H., and Dan, Y. (2012). Neuromodulation of brain states. *Neuron* 76, 209–222. doi: 10.1016/j.neuron.2012.09.012

Lemon, N., Aydin-Abidin, S., Funke, K., and Manahan-Vaughan, D. (2009). Locus coeruleus activation facilitates memory encoding and induces hippocampal ltd that depends on -adrenergic receptor activation. *Cereb. Cortex* 19, 2827–2837. doi: 10.1093/cercor/bhp065

Levy, F. (2009). Dopamine vs noradrenaline: inverted-U effects and ADHD theories. *Aust. N. Z. J. Psychiatry* 43, 101–108. doi: 10.1080/00048670802607238

Madison, D. V., and Nicoll, R. A. (1986). Actions of noradrenaline recorded intracellularly in rat hippocampal CA1 pyramidal neurones, *in vitro*. *J. Physiol.* 372, 221–244. doi: 10.1113/jphysiol.1986.sp016006

Manunta, Y., and Edeline, J.-M. (2004). Noradrenergic induction of selective plasticity in the frequency tuning of auditory cortex neurons. *J. Neurophysiol.* 92, 1445–1463. doi: 10.1152/jn.00079.2004

Martins, A. R. O., and Froemke, R. C. (2015). Coordinated forms of noradrenergic plasticity in the locus coeruleus and primary auditory cortex. *Nat. Neurosci.* 18, 1483–1492. doi: 10.1038/nn.4090

Masana, M., Bortolozzi, A., and Artigas, F. (2011). Selective enhacement of mesocortical dopaminergic transmission by noradrenergic drugs: therapeutic opportunities in schizophrenia. *Int. J. Neuropsychopharmacol.* 14, 53–68. doi: 10.1017/S1461145710000908

Matthews, P. R. L., Horder, J., and Pearce, M. (2018). Selective noradrenaline reuptake inhibitors for schizophrenia. *Cochrane Database Syst. Rev.* 2018:CD010219. doi: 10.1002/14651858.CD010219.pub2

McBurney-Lin, J., Lu, J., Zuo, Y., and Yang, H. (2019). Locus coeruleus-norepinephrine modulation of sensory processing and perception: a focused review. *Neurosci. Biobehav. Rev.* 105, 190–199. doi: 10.1016/J.NEUBIOREV.2019.06.009

McCormick, D. A. (1989). Cholinergic and noradrenergic modulation of thalamocortical processing. *Trends Neurosci.* 12, 215–221. doi: 10.1016/0166-2236(89)90125-2

McCormick, D. A., and Prince, D. A. (1988). Noradrenergic modulation of firing pattern in guinea pig and cat thalamic neurons, *in vitro*. *J. Neurophysiol.* 59, 978–996. doi: 10.1152/jn.1988.59.3.978

McNamara, C. G., and Dupret, D. (2017). Two sources of dopamine for the hippocampus. *Trends Neurosci.* 40, 383–384. doi: 10.1016/j.tins.2017.05.005

Mejías-Aponte, C. A., Drouin, C., and Aston-Jones, G. (2009). Adrenergic and noradrenergic innervation of the midbrain ventral tegmental area and retrorubral field: prominent inputs from medullary homeostatic centers. *J. Neurosci.* 29, 3613–3626. doi: 10.1523/JNEUROSCI.4632-08.2009

Morón, J. A., Brockington, A., Wise, R. A., Rocha, B. A., and Hope, B. T. (2002). Dopamine uptake through the norepinephrine transporter in brain regions with low levels of the dopamine transporter: evidence from knock-out mouse lines. *J. Neurosci.* 22, 389–395. doi: 10.1523/JNEUROSCI.22-02-00389.2002

Mouradian, R. D., Sessler, F. M., and Waterhouse, B. D. (1991). Noradrenergic potentiation of excitatory transmitter action in cerebrocortical slices: evidence for mediation by an α1 receptor-linked second messenger pathway. *Brain Res.* 546, 83–95. doi: 10.1016/0006-8993(91)91162-T

Nasse, J. S., and Travers, J. B. (2014). Adrenoreceptor modulation of oromotor pathways in the rat medulla. *J. Neurophysiol.* 112, 580–593. doi: 10.1152/jn.00091.2014

Nomura, S., Bouhadana, M., Morel, C., Faure, P., Cauli, B., Lambolez, B., et al. (2014). Noradrenalin and dopamine receptors both control cAMP-PKA signaling throughout the cerebral cortex. *Front. Cell. Neurosci.* 8:247. doi: 10.3389/fncel.2014.00247

Noudoost, B., and Moore, T. (2011). The role of neuromodulators in selective attention. *Trends Cogn. Sci.* 15, 585–591. doi: 10.1016/J.TICS.2011.10.006

Nutt, D., Demyttenaere Gasthuisberg, K. U., Psychiatry, G., Zoltan Janka, B., Aarre, T., Bourin, M., et al. (2007). The other face of depression, reduced positive affect: the role of catecholamines in causation and cure. *J. Psychopharmacol.* 21, 461–471. doi: 10.1177/0269881106069938

Paschalis, A., Churchill, L., Marina, N., Kasymov, V., Gourine, A., and Ackland, G. (2009). β1-Adrenoceptor distribution in the rat brain: an immunohistochemical study. *Neurosci. Lett.* 458, 84–88. doi: 10.1016/j.neulet.2009.04.023

Patriarchi, T., Cho, J. R., Merten, K., Howe, M. W., Marley, A., Xiong, W. H., et al. (2018). Ultrafast neuronal imaging of dopamine dynamics with designed genetically encoded sensors. *Science* 360:eaat4422. doi: 10.1126/science.aat4422

Pisani, A., Bonsi, P., Centonze, D., Martorana, A., Fusco, F., Sancesario, G., et al. (2003). Activation of beta1-adrenoceptors excites striatal cholinergic interneurons through a cAMP-dependent, protein kinase-independent pathway. *J. Neurosci.* 23, 5272–5282. doi: 10.1523/JNEUROSCI.23-12-05272.2003

Poulin, J.-F., Caronia, G., Hofer, C., Cui, Q., Helm, B., Ramakrishnan, C., et al. (2018). Mapping projections of molecularly defined dopamine neuron subtypes using intersectional genetic approaches. *Nat. Neurosci.* 21, 1260–1271. doi: 10.1038/s41593-018-0203-4

Pozzi, L., Invernizzi, R., Cervo, L., Vallebuona, F., and Samanin, R. (1994). Evidence that extracellular concentrations of dopamine are regulated by noradrenergic neurons in the frontal cortex of rats. *J. Neurochem.* 63, 195–200. doi: 10.1046/j.1471-4159.1994.63010195.x

Reiner, A., and Levitz, J. (2018). Glutamatergic signaling in the central nervous system: ionotropic and metabotropic receptors in concert. *Neuron* 98, 1080–1098. doi: 10.1016/j.neuron.2018.05.018

Robertson, S. D., Plummer, N. W., de Marchena, J., and Jensen, P. (2013). Developmental origins of central norepinephrine neuron diversity. *Nat. Neurosci.* 16, 1016–1023. doi: 10.1038/nn.3458

Rosenkranz, J. A., and Johnston, D. (2006). Dopaminergic regulation of neuronal excitability through modulation of IH in layer V entorhinal cortex. *J. Neurosci.* 23, 2686–2695. doi: 10.1523/jneurosci.4333-05.2006

Sara, S. J. (2009). The locus coeruleus and noradrenergic modulation of cognition. *Nat. Rev. Neurosci.* 10, 211–223. doi: 10.1038/nrn2573

Sara, S. J. (2017). Sleep to remember. *J. Neurosci.* 37, 457–463. doi: 10.1523/JNEUROSCI.0297-16.2017

Sara, S. J., and Bouret, S. (2012). Orienting and reorienting: the locus coeruleus mediates cognition through arousal. *Neuron* 76, 130–141. doi: 10.1016/j.neuron.2012.09.011

Schicknick, H., Henschke, J. U., Budinger, E., Ohl, F. W., Gundelfinger, E. D., and Tischmeyer, W. (2019). β-adrenergic modulation of discrimination learning and memory in the auditory cortex. *Eur. J. Neurosci.* 50, 3141–3163. doi: 10.1111/ejn.14480

Schmidt, K. T., and Weinshenker, D. (2014). Adrenaline rush: the role of adrenergic receptors in stimulant-induced behaviors. *Mol. Pharmacol.* 85, 640–650. doi: 10.1124/mol.113.090118

Schultz, W. (2001). Reward signaling by dopamine neurons. *Neuroscientist* 7, 293–302. doi: 10.1177/107385840100700406

Schultz, W. (2007). Multiple dopamine functions at different time courses. *Annu. Rev. Neurosci.* 30, 259–288. doi: 10.1146/annurev.neuro.28.061604.135722

Seamans, J. K., and Yang, C. R. (2004). The principal features and mechanisms of dopamine modulation in the prefrontal cortex. *Prog. Neurobiol.* 74, 1–58. doi: 10.1016/J.PNEUROBIO.2004.05.006

Shohamy, D., and Adcock, R. A. (2010). Dopamine and adaptive memory. *Trends Cogn. Sci.* 14, 464–472. doi: 10.1016/J.TICS.2010.08.002

Smith, C. C., and Greene, R. W. (2012). CNS dopamine transmission mediated by noradrenergic innervation. *J. Neurosci.* 32, 6072–6080. doi: 10.1523/JNEUROSCI.6486-11.2012

Straube, T., Korz, V., Balschun, D., and Uta Frey, J. (2003). Requirement of β-adrenergic receptor activation and protein synthesis for LTP-reinforcement by novelty in rat dentate gyrus. *J. Physiol.* 552, 953–960. doi: 10.1113/jphysiol.2003.049452

Sulzer, D., Cragg, S. J., and Rice, M. E. (2016). Striatal dopamine neurotransmission: regulation of release and uptake. *Basal Ganglia* 6, 123–148. doi: 10.1016/J.BAGA.2016.02.001

Sun, F., Zeng, J., Jing, M., Zhou, J., Feng, J., Owen, S. F., et al. (2018). A Genetically Encoded Fluorescent Sensor Enables Rapid and Specific Detection of Dopamine in Flies, Fish, and Mice. *Cell* 174, 481.e19–496.e19. doi: 10.1016/J.CELL.2018.06.042

Taber, K. H., and Hurley, R. A. (2014). Volume transmission in the brain: beyond the synapse. *J. Neuropsychiatry Clin. Neurosci.* 26, 1–4. doi: 10.1176/appi.neuropsych.13110351

Takeuchi, T., Duszkiewicz, A. J., Sonneborn, A., Spooner, P. A., Yamasaki, M., Watanabe, M., et al. (2016). Locus coeruleus and dopaminergic consolidation of everyday memory. *Nature* 537, 357–362. doi: 10.1038/nature19325

Tripp, G., and Wickens, J. R. (2009). Neurobiology of ADHD. *Neuropharmacology* 57, 579–589. doi: 10.1016/J.NEUROPHARM.2009.07.026

Tritsch, N. X., and Sabatini, B. L. (2012). Dopaminergic modulation of synaptic transmission in cortex and striatum. *Neuron* 76, 33–50. doi: 10.1016/J.NEURON.2012.09.023

Vaaga, C. E., Borisovska, M., and Westbrook, G. L. (2014). Dual-transmitter neurons: functional implications of co-release and co-transmission. *Curr. Opin. Neurobiol.* 29, 25–32. doi: 10.1016/j.conb.2014.04.010

Versteeg, D. H. G., Van der Gugten, J., De Jong, W., and Palkovits, M. (1976). Regional concentrations of noradrenaline and dopamine in rat brain. *Brain Res.* 113, 563–574. doi: 10.1016/0006-8993(76)90057-3

Vijayraghavan, S., Wang, M., Birnbaum, S. G., Williams, G. V., and Arnsten, A. F. T. (2007). Inverted-U dopamine D1 receptor actions on prefrontal neurons engaged in working memory. *Nat. Neurosci.* 10, 376–384. doi: 10.1038/nn1846

Waterhouse, B. D., and Navarra, R. L. (2019). The locus coeruleus-norepinephrine system and sensory signal processing: a historical review and current perspectives. *Brain Res.* 1709, 1–15. doi: 10.1016/J.BRAINRES.2018.08.032

Weinshenker, D., and Schroeder, J. P. (2007). There and back again: a tale of norepinephrine and drug addiction. *Neuropsychopharmacology* 32, 1433–1451. doi: 10.1038/sj.npp.1301263

Winograd-Gurvich, C., Fitzgerald, P. B., Georgiou-Karistianis, N., Bradshaw, J. L., and White, O. B. (2006). Negative symptoms: a review of schizophrenia, melancholic depression and Parkinson's disease. *Brain Res. Bull.* 70, 312–321. doi: 10.1016/J.BRAINRESBULL.2006.06.007

Xing, B., Li, Y.-C., and Gao, W.-J. (2016). Norepinephrine versus dopamine and their interaction in modulating synaptic function in the prefrontal cortex. *Brain Res.* 1641, 217–233. doi: 10.1016/J.BRAINRES.2016.01.005

Yamamoto, B. K., and Novotney, S. (2002). Regulation of extracellular dopamine by the norepinephrine transporter. *J. Neurochem.* 71, 274–280. doi: 10.1046/j.1471-4159.1998.71010274.x

Yamasaki, M., and Takeuchi, T. (2017). Locus coeruleus and dopamine-dependent memory consolidation. *Neural Plast.* 2017, 1–15. doi: 10.1155/2017/8602690

Yavich, L., Lappalainen, R., Sirviö, J., Haapalinna, A., and MacDonald, E. (1997). α2-Adrenergic control of dopamine overflow and metabolism in mouse striatum. *Eur. J. Pharmacol.* 339, 113–119. doi: 10.1016/S0014-2999(97)01375-7

Zhou, F.-M., and Hablitz, J. J. (1999). Dopamine modulation of membrane and synaptic properties of interneurons in rat cerebral cortex. *J. Neurophysiol.* 81, 967–976. doi: 10.1152/jn.1999.81.3.967

Conflict of Interest: The authors declare that the research was conducted in the absence of any commercial or financial relationships that could be construed as a potential conflict of interest.

Copyright © 2020 Ranjbar-Slamloo and Fazlali. This is an open-access article distributed under the terms of the Creative Commons Attribution License (CC BY). The use, distribution or reproduction in other forums is permitted, provided the original author(s) and the copyright owner(s) are credited and that the original publication in this journal is cited, in accordance with accepted academic practice. No use, distribution or reproduction is permitted which does not comply with these terms.

frontiers in Molecular Neuroscience

ORIGINAL RESEARCH
published: 06 February 2020
doi: 10.3389/fnmol.2020.00014

Analyzing Event-Related Transients: Confidence Intervals, Permutation Tests, and Consecutive Thresholds

*Philip Jean-Richard-dit-Bressel *, Colin W. G. Clifford and Gavan P. McNally*

School of Psychology, University of New South Wales, Sydney, NSW, Australia

Fiber photometry has enabled neuroscientists to easily measure targeted brain activity patterns in awake, freely behaving animal. A focus of this technique is to identify functionally-relevant changes in activity around particular environmental and/or behavioral events, i.e., event-related activity transients (ERT). A simple and popular approach to identifying ERT is to summarize peri-event signal [e.g., area under the curve (AUC), peak activity, etc.,] and perform standard analyses on this summary statistic. We highlight the various issues with this approach and overview straightforward alternatives: waveform confidence intervals (CIs) and permutation tests. We introduce the rationale behind these approaches, describe the results of Monte Carlo simulations evaluating their effectiveness at controlling Type I and Type II error rates, and offer some recommendations for selecting appropriate analysis strategies for fiber photometry experiments.

Keywords: analysis, event-related transients, fiber photometry, family-wise error rate, bootstrap, permutation test

OPEN ACCESS

Edited by:
Christopher Alan Reid, Florey Neuroscience Institutes, Australia

Reviewed by:
John J. Woodward, Medical University of South Carolina, United States
Andy Wai Kan Yeung, The University of Hong Kong, Hong Kong

****Correspondence:***
Philip Jean-Richard-dit-Bressel p.jean-richardditbressel@unsw.edu.au

Received: *22 November 2019*
Accepted: *17 January 2020*
Published: *06 February 2020*

Citation:
Jean-Richard-dit-Bressel P, Clifford CWG and McNally GP (2020) Analyzing Event-Related Transients: Confidence Intervals, Permutation Tests, and Consecutive Thresholds. Front. Mol. Neurosci. 13:14. doi: 10.3389/fnmol.2020.00014

INTRODUCTION

A broad objective for neuroscience involves identifying brain activity patterns and determining their function. The development of highly sensitive, novel fluorescent biosensors (e.g., calcium indicator GCaMP) and measurement techniques (e.g., fiber photometry) for use in the awake, freely moving animal have given behavioral neuroscientists powerful tools to chronically record neural dynamics of genetically- and circuit-defined populations *in vivo* (Gunaydin et al., 2014). Typically, the focus of this research is to determine whether there are phasic increases or decreases in activity around particular environmental and/or behavioral events, i.e., event-related activity transients (ERT). The presence of ERT implicates the targeted dynamic in a function related to that event, perhaps encoding signals that enable task-relevant perception, learning and/or behavior. Equally revealing is the types of events and situations that do not evoke ERT (**Figure 1**).

A widespread issue faced by researchers when using fiber photometry is how to best analyze the rich datasets they produce. A biosensor readout is a proxy for some underlying biological process (receptor binding, action potential, etc.,), so units of measurement are generally arbitrary. The recording time series is typically normalized into a delta F (dF) to represent relative activity change. Like all analysis strategies, the experimenter is confronted with a variety of choices such as whether to select these strategies before (*a priori*) or after (*post hoc*) data collection, how to avoid Type 1 (false positive) errors whilst achieving appropriate power to avoid Type II errors (false negative).

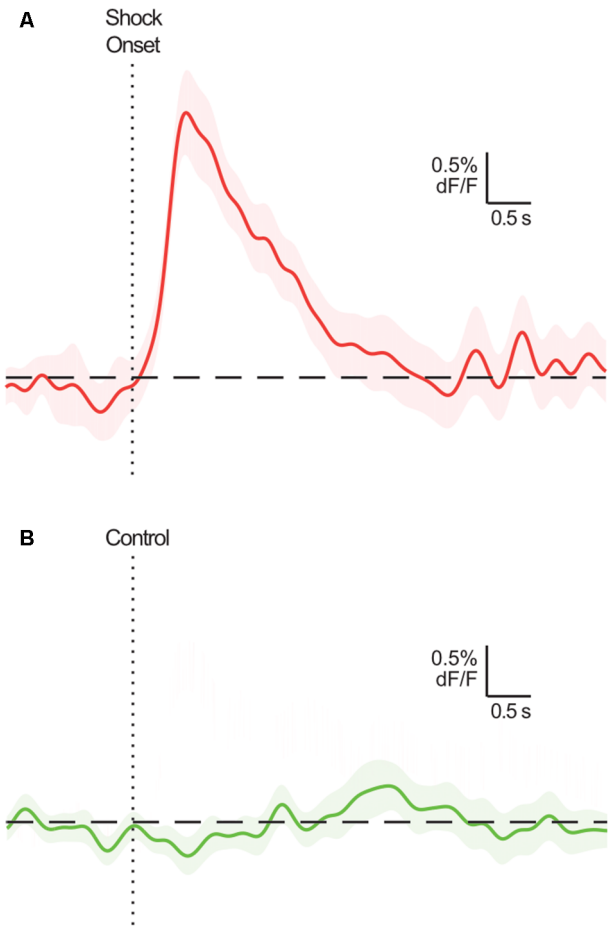

FIGURE 1 | Example event-related calcium transients in BLA principal neurons (mean ± SEM; adapted from Sengupta et al., 2018; Figure 1C). These neurons exhibit a characteristic excitatory transient following shock delivery **(A)**, but not during a comparable period where the shock is not delivered **(B)**. Assuming the true response of these neurons is, in fact, excitatory for **(A)** and null for **(B)**, it would be optimal for statistical analyses to identify a significant excitatory transient at relevant time points in **(A)**, and no significant transients across the time points in **(B)**.

To determine the presence of ERT, the dF around defined events can be collated and analyzed. The most common method involves obtaining a single number statistic quantifying a specific feature of the peri-event dF, such as the Area Under the Curve (AUC) or peak dF. This statistic is then used as input for null hypothesis tests, the results of which form the basis of interpretation (Gunaydin et al., 2014; Lerner et al., 2015; Sengupta et al., 2018).

Although simple and popular, the use of summary statistics such as AUC or peak dF raises concerns. This approach adds a cumbersome and problematic step to analysis: researchers choose the specific time window relative to events to summarize and analyze. If the window is too small, activity of interest is potentially missed; if the window is too large, the statistic loses meaningfulness (the temporal relationship between activity and event is undetermined). Even when a suitable window is chosen, results only reveal whether overall activity within the window is significantly different to the null, not where in this window activity is significant or whether activity beyond this window is significantly different from null. Therefore, using a summary of a time window discards potentially pertinent temporal information. Additionally, to minimize the probability of "missing" ERT, the analysis window is often chosen *post hoc*, after the experimenter has examined mean dF around an event. This is generally inconvenient, relatively arbitrary, and can introduce unwanted *post hoc* biases into the analyses, running the risk of significantly inflating the Type I error rate.

An alternative is to dispense with this kind of summary analysis to determine the presence of ERTs, and instead automatically analyze the entire peri-event period to determine whether, and when, a significant ERT occurs. This can overcome the limitations of AUC or peak dF approaches, but also raises its own concerns. For example, what kind of analysis is appropriate and how to effectively control the Type I error (false positive) rate whilst still achieving sufficient statistical power? Here we consider two straightforward alternatives to the use of summary statistics when analyzing fiber photometry data: (1) confidence intervals (CIs) around the peri-event dF waveform (e.g., Choi et al., 2019); and (2) permutation tests across the peri-event window (e.g., Pascoli et al., 2018).

Confidence Intervals and Permutation Tests

A CI is a ranged estimate of a population parameter. In the case of mean peri-event activity, this would be a CI estimating the true population peri-event activity. Periods where the CI does not contain the null (e.g., $dF = 0$) can be flagged as significant, i.e., indicative of an ERT. In general applications, the parametric t interval (tCI) is most commonly used and is computationally simple to obtain: tCI = mean ± (SEM * t_{crit}). However, a key assumption is that the underlying population distribution is normal, an assumption that may not be met by the recording data.

A non-parametric method to obtain CI is bootstrapping. Bootstrapping involves randomly resampling (with replacement) from the dataset and obtaining a bootstrap estimate from this sample. This is done repeatedly for all possible combinations of the dataset or a sufficiently high number of times (1,000 times or more). CIs can then be derived from the relevant percentiles of the resultant bootstrap distribution [percentile bootstrapped confidence interval (bCI); Efron and Tibshirani, 1993]. Importantly, this method makes no relevant assumptions about the underlying distribution and is more precise and accurate than tCI when using larger sample sizes. However, percentile bCIs have a narrowness bias for small sample sizes by an average factor of $\sqrt{(n-1)/n}$ (Hesterberg, 2015). This occurs because bootstrapping as an algorithm does not make any stipulations or adjustments related to n, leaving it open to issues related to small sample distributions. There are numerous ways to improve on these small sample properties (see Scholz, 2007; Hersterberg, 2014). A simple way is to expand the percentile bCI by a factor that accounts for n, as is done for tCI *via* SEM and t_{crit}.

Permutation tests, like bootstrapping, are a non-parametric resampling-based method. They evaluate whether the distributions of the two groups of data are exchangeable. This is achieved by randomly regrouping the data to evaluate how unlikely the observed difference between groups was. The proportion of permutations that have a larger difference than the actual difference translates to the permutation *p*-value. If datasets are exchangeable, a large proportion of the permutations would produce a larger difference than that observed and the *p*-value would be large (i.e., insignificant). If the distributions are not exchangeable, it is unlikely for a random permutation to produce a larger difference, and the *p*-value may be critically small, leading to rejection of the null that datasets are exchangeable.

Permutation tests effectively produce an exact *p*-value, and can thus control Type I error at α, which is not true of percentile bCI. However, permutation tests do have some caveats. Permutation tests specifically concern distributions, not parameters. Permutation tests must compare two distributions (e.g., a peri-event sample vs. a baseline sample). Interpretation of significance must take into account that an effect may be driven by either distribution and may be caused by differences in the distributions beyond the parameter of interest (e.g., may be driven by differences in underlying population variances, not the population mean). They cannot be used to derive CI for a parameter such as mean dF (Hersterberg, 2014) and cannot test hypotheses regarding single-sample means (e.g., $dF = 0$). Finally, the level of significance detectable by permutation tests is constrained by the number of possible permutations and thus requires a minimum sample size for a given α (e.g., $n = 4$ has a minimum *p*-value of 0.014). That said, permutation tests are straightforward, have appealing statistical properties, and have been used to analyze peri-event neural activity (Maris and Oostenveld, 2007; Pascoli et al., 2018).

Consecutive Thresholds

A key advantage of both CI and permutation tests is that they can be used to analyze peri-event activity by constructing a CI or performing a permutation test for each time point within the peri-event window. This dispenses with the need to choose a restricted window from which to obtain a summary statistic, as the entire peri-event dF can be analyzed for the presence of ERT. An additional benefit is that multiple ERT features, excitatory and/or inhibitory, can be identified using a single analysis without substantial input from the researcher.

However, testing each point of the peri-event window raises the problem of multiple comparisons. Given that a null signal is not static—it is composed of random fluctuations (i.e., noise)—the risk of producing a Type I error somewhere within the peri-event window will increase as the window size increases, inflating the family-wise Type I error rate (FWER) above the nominal rate, α. This could be dealt with by adopting a more conservative per comparison α to reduce the FWER (e.g., Bonferroni correction). However, a well-known issue with this approach is that it can be prohibitively conservative (Sedgwick, 2014), increasing the Type II error rate (failure to detect real differences). This can be particularly disadvantageous for fiber photometry, as sample sizes can be small (particularly when using subject-based analysis, as might be desirable in fiber photometry; (Recommendations… 2018) and the number of tests done across a peri-event window may render correction prohibitively conservative.

Consecutive thresholds offer a simple, yet powerful, way to reduce Type I errors when detecting ERT, without commensurately increasing Type II errors. Consecutive thresholds demand a minimum period of continuous significance before accepting a transient as significant. The rationale here is that random fluctuations will generally produce Type I errors at the α rate, but are unlikely to do so for an extended period. This is intuitive when visualizing the interplay of random fluctuations and variance across the analysis window. The points of lowest variance will occur at time points when sample traces cross over (i.e., are equal). These cross-overs are inevitable and common for signals fluctuating around baseline, regardless of how signals are collated and averaged. Due to the low variance at these time points, they have low standard error and narrow CI that may not encompass the null. These cross-overs are generally a product of sample traces moving in opposite directions (e.g., one going up, the other going down) and thus represent a point, not an extended period, of low standard error (see **Figure 2C**). For an extended Type I error, the fluctuation must be aligned (i.e., be in phase), which is exponentially less likely, particularly as sample size increases. In contrast, ERTs by definition temporally coincide and are thus much more likely to yield a continuous period of significance. Adopting a moderate consecutive threshold, where the analysis demands a minimum period of continuous significance before accepting a transient as significant, can therefore greatly reduce Type I (and FWER) without necessarily affecting detection of true transients.

To evaluate the effectiveness of CIs, permutation tests and consecutive thresholds at controlling Type I and Type II error rates when detecting ERT, we assessed these methods in Monte Carlo simulations of artificially generated time-series datasets.

MATERIALS AND METHODS

Artificial datasets were generated and Monte Carlo simulations of analyses were conducted using custom MATLAB scripts (available at https://github.com/philjrdb/ERTsimulation).

Lines were generated for a null condition and ERT condition (n = 10,000 for each population type). Each line vector began as 100 zeros, representing a 10 speri-event baseline sampled at 10 Hz, to which Gaussian noise (10 dB) was added and low-pass filtered (2 Hz) to emulate randomly fluctuating noisy signal. A transient was operationalized as a one sparabolic curve (magnitude randomized using positive tail of z distribution). Each line in the ERT condition had a transient inserted at the halfway point of the window. Lines in the null condition had a 50% chance of a transient being inserted somewhere within the window, to emulate unrelated transients, or did not have any transient inserted. To

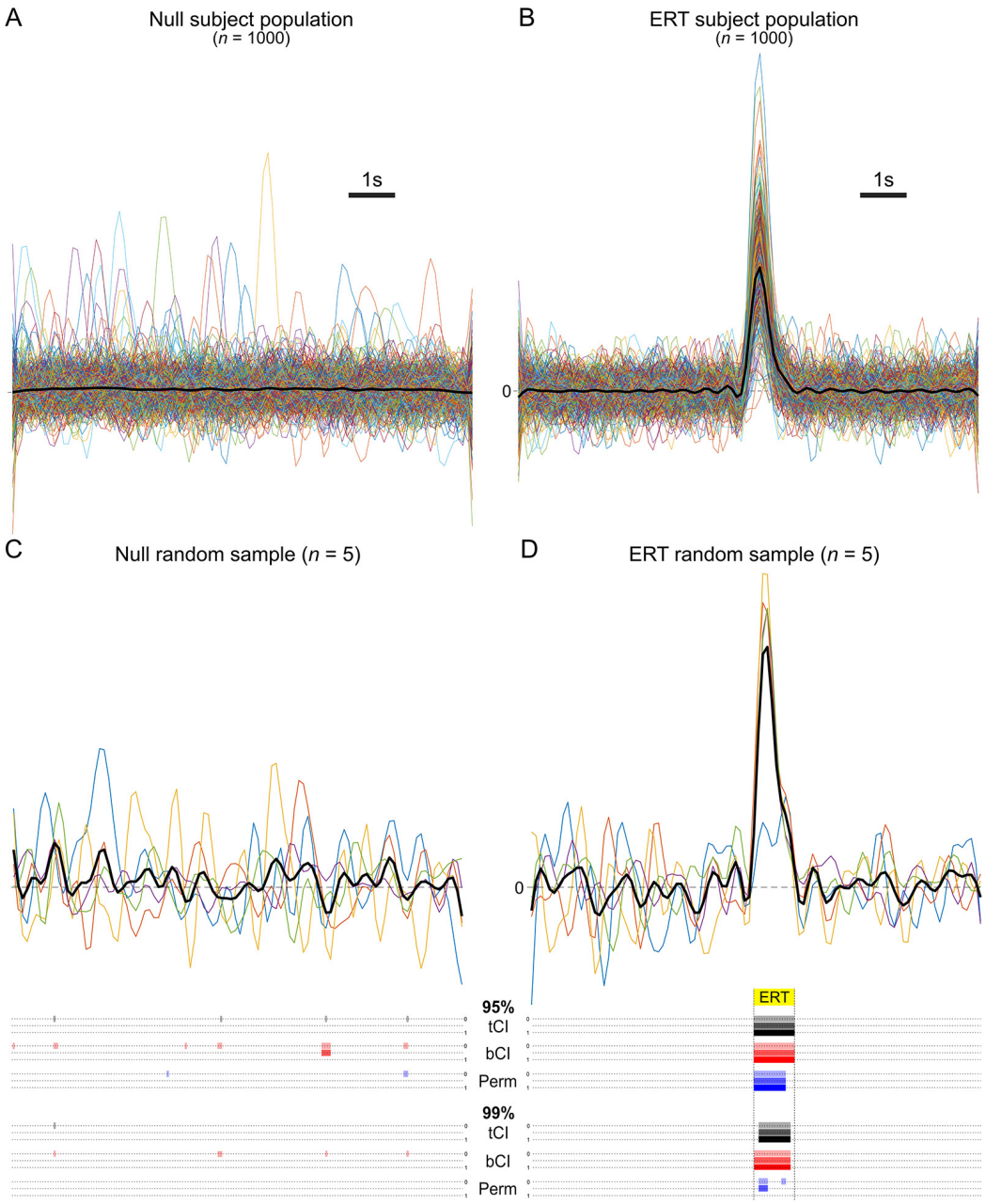

FIGURE 2 | (A,B) Population of mean subject waveforms. **(C,D)** Example run [sample $n = 5$ (colored lines; mean = black line)] from Monte Carlo simulation and results of various analyses [parametric t interval (tCI), bootstrapped confidence interval (bCI), permutation test (Perm)] at 95% and 99% significance levels. **(C)** Example run when sampling from the null population. Colored bars beneath sample traces indicate where significant differences from null were incorrectly detected (Type I error), per analysis method. Without a consecutive threshold (top dotted line/colored bars per method), all analysis methods detected significant deviations from null at the 95% level; each produced Type I errors. A consecutive threshold (low-pass frequency window) prevented this error (bottom dotted line/colored bars per method). **(D)** Example run when sampling from event-related activity transients (ERT) population. Colored bars beneath sample traces indicate where in the ERT period (yellow highlighted period) significant differences from null were correctly detected, per analysis method. At the 95% level, tCI and bCI correctly rejected the null for the full extent of the ERT period, while the permutation test correctly rejected 80%. Consecutive thresholds did not impact this finding. At the 99% level, a smaller proportion of the ERT was identified. Importantly, the permutation test failed to meet the full low-pass consecutive threshold, and thus failed to identify a significant transient (Type II error).

emulate subject-based analysis, a subject population for each condition ($n = 1{,}000$; **Figures 2A,B**) was generated by randomly sampling and averaging 1–31 lines from their respective activity populations. These parameters correspond approximately to data generated by fiber photometry recordings (Sengupta et al., 2018; Choi et al., 2019).

The two key questions were: (1) How effective are tCI, bCI, and permutation tests in detecting the ERT when sampling from the ERT population, while retaining the null (not detecting a "transient") when sampling from the null population? (2) What is the effect of applying a consecutive threshold to these results? We considered the effect of three different thresholds: no threshold (0), half the size of the low-pass frequency window (0.5), and the size of the low-pass frequency window (1). Half of the low-pass frequency window corresponds to the unidirectional component of noise at this threshold and therefore represents a cut-off for the most common source of Type I errors: unaligned high-frequency noise. However, this threshold is relatively lenient; phase-aligned noise and noise from slightly lower frequencies may still trigger Type I errors. An alternative threshold is the full length of the low-pass filter window. This window would more effectively remove Type I errors caused by high-frequency noise, like aligned random fluctuations, but could come at the expense of statistical power. A 2 Hz low-pass filter window is 0.5 s (1 s/Hz). Given that our simulation used a 10 Hz sampling rate, the $\frac{1}{2}$ consecutive threshold is three consecutive data points (rounded up) and the full consecutive threshold is five consecutive data points.

In total, we conducted 1,000 Monte Carlo simulations per sample size (n = 5–100). We randomly sampled n subjects from each subject population and analyzed them at 95% and 99% confidence levels, with and without consecutive thresholds (see **Figures 2C,D**). A tCI was calculated for each time point across the event window. For bCI, a bootstrap matrix of 1,000 bootstrapped means was acquired from n randomly resampled lines (with replacement). CI for each timepoint were percentiles at that timepoint of the bootstrap matrix (95%: 2.5, 97.5 percentiles; 99%: 0.5, 99.5% percentiles), which were then expanded by a factor of $\sqrt{n/(n-1)}$ to counter small sample narrowness bias. For either CI, a significant difference was flagged whenever the CI did not contain the null of 0 (Bird, 2004; Bland and Altman, 2015). Permutation tests require a comparison distribution, so ERT and null condition samples were tested against another random sample from the null population to represent a baseline comparison (new baseline comparison per simulation). All possible permutation or 1,000 random permutations, whichever was fewer, was used. The p-value for a time point was the proportion of permutations whose mean difference values were more extreme than that observed between the actual samples. A time point was flagged as significant if $p < \alpha$.

The critical measures were FWER under the null condition and the correct reject rate for the ERT condition. FWER was determined as the proportion of null sample simulations that produced a significant effect (Type I error) within the peri-event window. Each simulation either had or did not have a Type I error. The correct reject rate was the proportion of the 1 sERT identified as significant per simulation; each simulation rejected 0–100% of the ERT.

Lastly, we use tCI, bCI and permutation tests to analyze the exemplar ERT and null data in **Figure 1** (from Sengupta et al., 2018). The exemplar ERT data is of CS+ offset (coincident with shock delivery) trials on day 1 of fear conditioning (n = 23), whereas exemplar null data is of CS− offset (no shock comparison) trials on day 3 of fear conditioning (n = 24)[1]. tCI and bCI were used to determine the presence of ERT within each peri-event period (null: dF/F = 0). To demonstrate a relevant extension of these analyses, these peri-event waveforms were also compared against each other using the two-sample t-test and bootstrap (bootstrap difference distribution of randomly resampled means; Hersterberg, 2014). As permutation tests can only compare two samples, permutation tests were used to compare CS+ and CS−. A consecutive threshold equalling the low-pass frequency (3 Hz) window (1/3 s was applied to control FWER.

RESULTS

The summary of results from the 1,000 simulations per selected sample sizes are shown in **Figure 3**. Without a consecutive threshold, all analysis methods were likely to detect a significant "transient" somewhere within the peri-event window, despite drawing from the null population (**Figure 3A**). In other words, the actual FWER was extremely high without a consecutive threshold, regardless of n or confidence level. The use of a consecutive threshold substantially reduced the FWER. A $\frac{1}{2}$ threshold substantially reduced FWER, although not to nominal rate, α. A full low-pass threshold reduced FWER to at or below nominal rate, α.

Regarding detection of the ERT (**Figure 3B**), each analysis method generally detected large proportions of the transient across simulations (on average >50%), with detection rate improving as sample size increased. Importantly, the use of consecutive thresholds had little impact on this. The bCI appeared to have the highest correct reject rate, while permutation tests had the lowest. This sensitivity was reflected in the likelihood for these methods to detect the ERT at all (i.e., whether a significant difference was detected within the ERT period or not). The bCI almost always correctly rejected the null—it only failed to detect the ERT <1% of simulations for n = 5, 99% confidence level, full consecutive threshold (no failure to reject for any other parameters). In contrast, permutation tests were most likely to miss rejecting the null, doing so under various conditions when $n < 15$ (for n = 5, 99% confidence level, full consecutive threshold, almost 10% of simulations failed to detect the ERT). It is worth noting here that previous applications of permutation tests to detecting ERTs (Pascoli et al., 2018) analyzed trials, not subject means. The choice of trials, rather than subjects, as the basis for the analysis of fiber photometry data, provides substantially larger n for analyses but raises independent, non-trivial concerns about correlations among the data (see Recommendations… 2018).

To illustrate the effectiveness of these methods on real data, we applied them to the exemplar data depicted in **Figure 1** (from Sengupta et al., 2018). Both tCI and bCI readily identified

[1] Different days were used because waveforms from other days were less exemplary, making them less suitable for the current purpose of demonstration. For instance, activity for Day 1 CS− trended negatively (apparent in AUC; Sengupta et al., 2018).

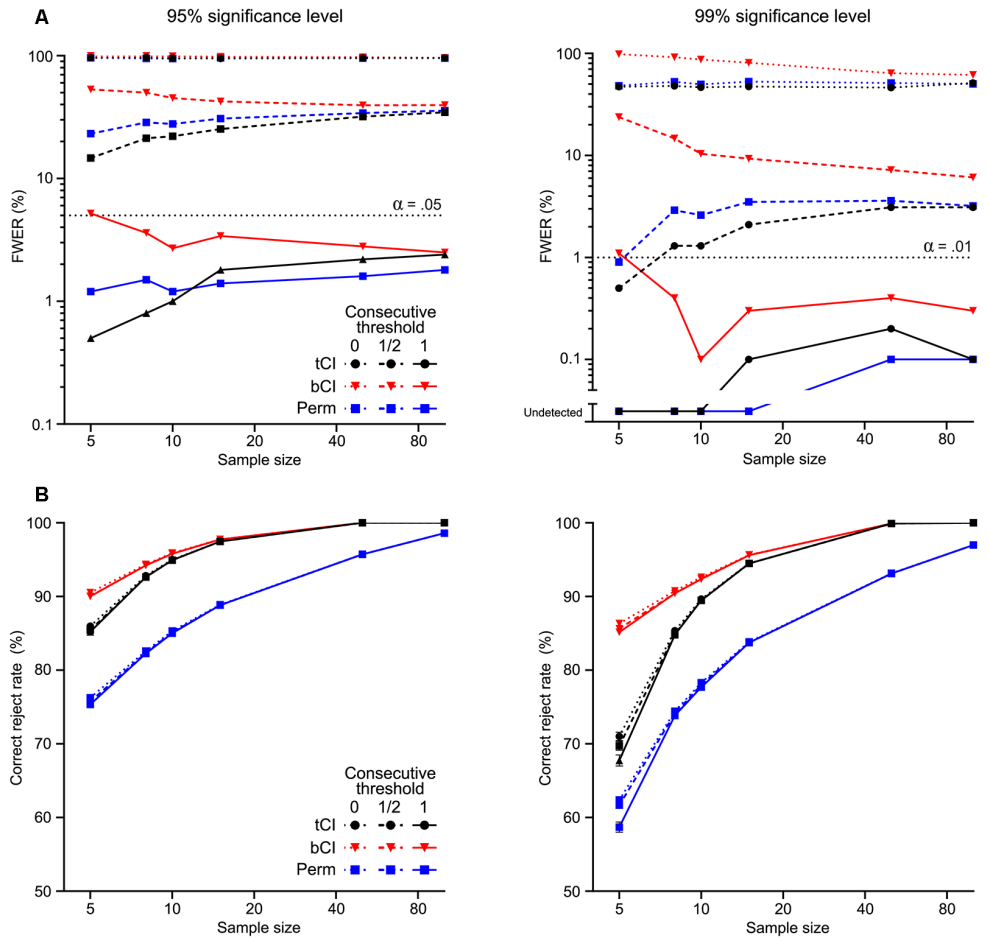

FIGURE 3 | Performance of parametric *t* interval [tCI (black)], bootstrapped CI [bCI (red)] and permutation test [Perm (blue)] across 1,000 Monte Carlo simulations at various sample sizes (n = 5–100). Each simulation was tested at two significance levels [95% (left), 99% (right)]. **(A)** Family-wise Type I error rate (FWER) was determined as any false rejection of the null across the time window (i.e., detection of a "significant transient" from signals drawn from the null population). Each method had extremely high false-positive rates without a consecutive significance threshold (=0), regardless of the significance level. Use of a consecutive threshold substantially reduced FWER; a threshold set at the low-pass frequency (=1) reduced FWER to at or below nominal rates (α). **(B)** Correct rejection rate was determined as proportion of the artificial transient that was identified as non-zero. Bootstrapped CI was the most powerful, while permutation tests were the least powerful at detecting the extent (and presence) of the transient. Consecutive thresholds did not substantially reduce power to detect this transient.

a significant excitatory ERT (relative to null of dF/F = 0) following shock delivery (**Figure 4**). The same analysis of CS− (no shock delivery) did not identify any event-related changes in the activity. Direct comparison of CS+ and CS− activity *via* two-sample tCI, bCI and permutation tests revealed that these traces significantly differed from each other for the duration of the identified shock ERT.

DISCUSSION

Identifying event-related transients (ERT) is a common focus of neural recording studies. A common approach to detecting ERT involves obtaining a summary statistic from a *post hoc*-specified period relative to an event (e.g., AUC). This introduces a problematic step within analysis. The current study considered alternative strategies that instead analyze the entire peri-event period for ERT: CIs and permutation tests. The effectiveness of these analyses, in combination with consecutive thresholds, at controlling Type I and Type II error rates was assessed in Monte Carlo simulations of artificial datasets that approximate fiber photometry data.

We found that CI or permutation tests can be effectively used in combination with consecutive thresholds to analyze peri-event periods for significant ERT. Both approaches afford good control over the Type I error rate; rates of inappropriate ERT detection (null condition) were acceptably low across n when using a consecutive threshold equalling the low-pass frequency window. Both also provided reasonable statistical power. In both cases, correct rejection of the null in the ERT condition was high, increasing with n, and was largely unaffected by the consecutive thresholds. Of the methods considered here, the bCI appears to be the most sensitive. The bCI had the highest likelihood of rejecting the null, especially at smaller sample sizes ($n < 20$), whereas permutation tests were the least

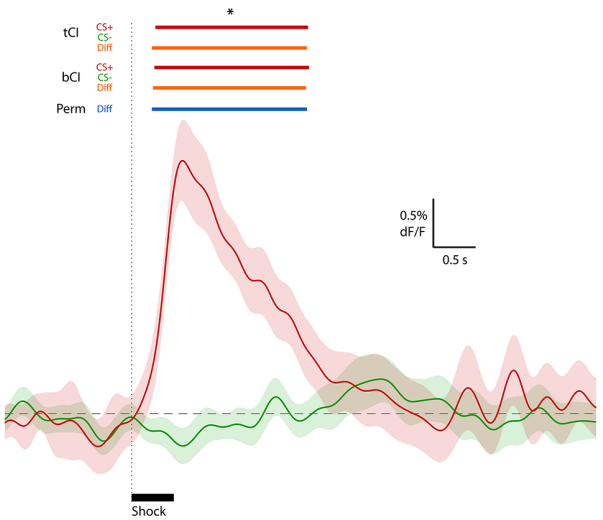

FIGURE 4 | Waveform analysis of real peri-shock (CS+; red waveform) and control (CS−; green waveform) data depicted in **Figure 1** (from Sengupta et al., 2018; Figure 1C). An excitatory ERT following shock onset for CS+ (red bars above graph), but no ERT for the CS− comparison, was identified using *t* interval (tCI) and bCI. A significant difference between CS+ and CS− (two-sample comparison) was also determined using these CI methods (orange bars above graph) and permutation tests (blue bar above graph). *Significant at 95% confidence level (full low-pass consecutive threshold).

sensitive. These differences between bCI and permutation tests narrowed as n increased, with little difference between bCI and permutation tests at $n > 40$. Compared to permutation tests, tCI had good properties, with similar FWER rates and fewer Type II errors.

When applied to real data, CI methods readily identified the extent of excitatory transients in amygdala to footshock, while showing a comparison shock-free period was not associated with changes in amygdala activity. We also compared these peri-shock and peri-control signals using two-sample CI methods and permutation tests to show the extent those signals diverged. These results demonstrate that these methods can effectively assess and convey the significance of peri-event activity change, and are amenable to making pertinent comparisons between signals (e.g., those around different events). Permutation tests are limited to two-sample comparisons, but CI methods could theoretically be applied within more complex analyses (e.g., polynomial contrasts) to assess diversity of questions regarding neural activity. However, there remain several issues that should be considered when analyzing photometry data, which we discuss below.

Considerations for Analysis

Choosing the Analysis Procedure

There are a variety of options for analyzing fiber photometry data that each have merits and drawbacks (**Table 1**). Although the ideal analysis will depend on a researcher's needs, we argue here that detection and comparisons of ERT is achieved more efficiently and effectively using waveform analysis methods. Waveform analyses automatically detect the extent of significant transients, whereas summary analyses typically require inconvenient and problematic *post hoc* input while discarding temporal information. However, a summary statistic may still be preferable when using peri-event activity in analyses that are overly complicated by the waveform vector. For instance, it is simpler to assess and convey the correlation between behavior and AUCs (Choi et al., 2019) than behavior and waveforms.

A major conclusion of the current study is that consecutive thresholds effectively reduce the Type I error rate in waveform analyses without commensurately impacting ERT detection. This duration requirement is a simple but blunt way to filter out the most common source of Type I error—brief blips of significance due to chance alignments in high-frequency noise. ERT by definition align for extended periods of time and are thus less affected. However, consecutive thresholds can increase the Type II error rate, particularly if the threshold is overly conservative or the ERT very brief. It is therefore important to choose a threshold that will efficiently reduce FWER without undermining detection of ERT. The right threshold will depend on the temporal dynamics of neural activity and biosensor, as well as the properties of the signal being analyzed. We discuss these considerations in turn and explain why a consecutive threshold based on the low-pass filter window is a decent rule-of-thumb.

Of the most commonly used biosensors, GCaMP6f has the fastest dynamics and is thus more vulnerable to Type II errors from consecutive thresholds. Like most biosensors, GCaMP6f acts like a leaky integrator, such that its output over time is a decaying compound of inputs (Chen et al., 2013). This means the duration of a transient, not just the magnitude, is proportional to activity change. For instance, GCaMP6f dF/F is elevated (20%-peak) for ∼0.4 s following a single action potential, but this duration is multiplied by the number of action potentials that occur within that window; a sub-second burst of population activity can produce a prolonged multi-second transient (Chen et al., 2013). This means ERT detection is resilient to consecutive thresholds in proportion to the effect size of activity change.

Regarding Type I errors, the effectiveness of a consecutive threshold in reducing FWER depends on the degree of high and low-frequency noise in the signal. As stated previously, high-frequency noise is responsible for frequent but brief instances of Type I errors, which consecutive thresholds effectively counteract. Type I errors due to chance alignments in low-frequency noise is less likely, but have a higher chance of lasting for extended periods, and are thus more resilient to consecutive thresholds. In fiber photometry, high-frequency components (>10 Hz) are typically attributed to electrical noise and are thus low-pass filtered out. The low-pass filter frequency is usually chosen based on the cut-off between signals of interest (e.g., temporal dynamics of the biosensor) and noise present in the signal, and therefore represent a natural cut-off for ERT vs. noise. Additionally, low-pass filters reduce the power of high-frequency components of a signal, allowing low-frequency components to dominate, which increases the autocorrelation of noise and the likelihood of extended Type I errors. Setting the consecutive threshold to the low-pass filter period is a way to

TABLE 1 | Overview of transient analysis methods.

	Temporally-defined transient	Non-parametric	Single mean comparison?	Exact *p* value*	Range estimate	Pros	Considerations
Summary analyses							
AUC	×	Possible	✓	✓	Possible	• Simple	• Undefined extent/location of transient • Jittered transient still detected • Issues with defining analysis window
Features (peak dF, peak frequency)	×	Possible	×	✓	Possible	• Intuitive • Analysis of various features	• Requires a comparison period • Issues with defining analysis window
Waveform analyses							
t interval	✓	×	✓	✓*	✓	• Simple	• Parametric assumption
Bootstrap interval	✓	✓	✓	×*	✓	• Powerful • Few assumptions	• Computationally demanding compared to tCI • Percentile interval does not inherently control per comparison Type I error rate at α
Permutation tests	✓	✓	×	✓*	×	• Conservative	• Lowest power of methods considered • Computationally demanding compared to tCI • Requires a comparison distribution • Distribution difference only—cannot directly indicate parameter range/direction

**Per comparison p value—diverges from alpha when using consecutive thresholds. Note. AUC, area under the curve; tCI, t interval.*

peg the threshold to a factor that increases the need for a more conservative threshold.

It is also worth noting consecutive thresholds reduce FWER independently of per-comparison α. It, therefore, diverges from standard conceptions of α and *p*-values. If future studies ascertained the precise relationship between FWER, α and consecutive thresholds, the relevant equation could be used to calculate exact *p*-values, or be used to fine-tune the consecutive threshold for a given α and FWER. Such an equation would capture the likelihood of consecutive Type I errors—errors become exponentially less likely as the consecutive threshold increases ($\alpha^{threshold}$) unless there is a high degree of autocorrelation across that period. Autocorrelation of noise tends to decrease across time, so increasing the consecutive threshold also reduces this effect of autocorrelation. Given a fixed peri-event window, the threshold also decreases the number of consequential data points (i.e., degrees of freedom). Increasing the peri-event window (i.e., increasing the number of comparisons) increases FWER, although in a less substantial way than consecutive thresholds.

Finally, it is important to state that comparisons between event signals, as was done on the data in **Figure 4**, can be valid but should be done thoughtfully. Fiber photometry depends on a population-level biosensor readout. This readout depends on biosensor expression and fiber placement, which inevitably differ between subjects, making between-subject comparisons controversial. Furthermore, biosensor expression is dynamic, generally increasing over days and weeks, while recording causes bleaching of biosensor fluorophores within-session, making within-subject comparisons across time similarly contentious. Appropriate normalization of signal (see below) combats these influences but cautious interpretation remains warranted.

Interpreting Significance

Waveform analyses provide temporally-defined significance. Interpretation should factor in the relationship between the biological process of interest and biosensor readings. For instance, calcium-indicator (e.g., GCaMP) readout is a common proxy for neural firing rates. Signals from GCaMP are slightly lagged relative to spiking activity and have non-trivial decay times (Chen et al., 2013). The resultant leaky-integrator readout has two repercussions for interpretation: (1) an identified ERT is likely due to more confined, slightly earlier changes in underlying neural activity; and (2) the temporal extent of an ERT can be affected by both the magnitude or duration of activity change. This limits highly specific inferences about neural activity and the duration of ERT, although more general inferences about the anticipatory or deliberative activity when an ERT precedes event onset remain valid.

Both summary and waveform CI methods allow for single-mean comparisons. That is, the presence or absence of ERT can be inferred by testing against a specified null (e.g., dF/F = 0). This raises the important issue of having a valid null when using this method. Typical calculations for dF/F (e.g., subtraction of fitted isosbestic from the calcium-dependent signal; Lerner et al., 2015) normalizes the signal, giving it a mean of zero across the period that was used to calculate dF/F. However, trends may still exist in the data (e.g., a general decrease in a signal across the session) that impact peri-event signals and analysis. A common means to combat these trends are to detrend dF/F and/or zero peri-event signals to a pre-event baseline (Lerner et al., 2015; Pascoli et al., 2018; Sengupta et al., 2018; Choi et al., 2019). Although putatively effective, it remains important to consider the potential unintended effects of normalization and interpret accordingly (e.g., effects are relative to a particular baseline). Choosing an appropriate null will depend on the dataset and procedures applied, but it stands to reason that appropriate normalization and detrending render null of dF/F = 0 valid.

CONCLUSIONS AND RECOMMENDATIONS

There are a variety of options for analyzing fiber photometry data. Each of the methods described here has merits (**Table 1**). The waveform analyses we have considered here offer key advantages over summary analyses and the key recommendation from our findings is to use a sufficient consecutive threshold to reduce FWER when using these waveform analyses. The ideal threshold would consider the temporal dynamics of the specific biosensor being used (i.e., duration of transients), noise present in the recording signal, and the size of the peri-event window. A reasonable, effective rule-of-thumb is to apply a threshold equalling the low-pass frequency period, which itself should reflect the temporal cut-off between actual transients (i.e., at minimum, the temporal dynamics of the biosensor) and noise.

DATA AVAILABILITY STATEMENT

The datasets generated for this study are available on request to the corresponding author.

AUTHOR CONTRIBUTIONS

PJ and CC contributed to programming and statistical analysis. PJ and GM wrote the first draft of the manuscript. All authors contributed to manuscript revision.

FUNDING

This work was supported by grants from the Australian Research Council (DP190100482).

REFERENCES

Bird, K. D. (2004). *Analysis of Variance via Confidence Intervals*. London: SAGE.

Bland, J. M., and Altman, D. G. (2015). Statistics notes: bootstrap resampling methods. *BMJ* 350:h2622. doi: 10.1136/bmj.h2622

Chen, T. W., Wardill, T. J., Sun, Y., Pulver, S. R., Renninger, S. L., Baohan, A., et al. (2013). Ultrasensitive fluorescent proteins for imaging neuronal activity. *Nature* 499, 295–300. doi: 10.1038/nature12354

Choi, E. A., Jean-Richard-Dit-Bressel, P., Clifford, C. W. G., and McNally, G. P. (2019). Paraventricular thalamus controls behavior during motivational

conflict. *J. Neurosci.* 39, 4945–4958. doi: 10.1523/JNEUROSCI.2480-18.2019

Efron, B., and Tibshirani, R. J. (1993). *An Introduction to the Bootstrap*. Boca Raton, FL: CRC Press.

Gunaydin, L. A., Grosenick, L., Finkelstein, J. C., Kauvar, I. V., Fenno, L. E., Adhikari, A., et al. (2014). Natural neural projection dynamics underlying social behavior. *Cell* 157, 1535–1551. doi: 10.1016/j.cell.2014.05.017

Hersterberg, T. C. (2014). What teachers should know about the bootstrap: resampling in the undergraduate statistics. Available online at: https://arxiv.org/abs/1411.5279. Accessed December 22, 2019.

Hesterberg, T. C. (2015). What Teachers should know about the bootstrap: resampling in the undergraduate statistics curriculum. *Am. Stat.* 69, 371–386. doi: 10.1080/00031305.2015.1089789

Lerner, T. N., Shilyansky, C., Davidson, T. J., Evans, K. E., Beier, K. T., Zalocusky, K. A., et al. (2015). Intact-brain analyses reveal distinct information carried by SNc dopamine subcircuits. *Cell* 162, 635–647. doi: 10.1016/j.cell.2015.07.014

Maris, E., and Oostenveld, R. (2007). Nonparametric statistical testing of EEG- and MEG-data. *J. Neurosci. Methods* 164, 177–190. doi: 10.1016/j.jneumeth.2007.03.024

Pascoli, V., Hiver, A., Van Zessen, R., Loureiro, M., Achargui, R., Harada, M., et al. (2018). Stochastic synaptic plasticity underlying compulsion in a model of addiction. *Nature* 564, 366–371. doi: 10.1038/s41586-018-0789-4

Recommendations for the Design and Analysis of *in vivo* Electrophysiology Studies. (2018). *J. Neurosci.* 38, 5837–5839. doi: 10.1523/jneurosci.1480-18.2018

Scholz, F. W. (2007). The bootstrap small sample properties. 1–90, University of Washington, Seattle, WA. Available online at: http://faculty.washington.edu/fscholz/Reports/bootstrap-report.pdf.

Sedgwick, P. (2014). Multiple hypothesis testing and Bonferroni's correction. *BMJ* 349:g6284. doi: 10.1136/bmj.g6284

Sengupta, A., Yau, J. O. Y., Jean-Richard-Dit-Bressel, P., Liu, Y., Millan, E. Z., Power, J. M., et al. (2018). Basolateral amygdala neurons maintain aversive emotional salience. *J. Neurosci.* 38, 3001–3012. doi: 10.1523/jneurosci.2460-17.2017

Conflict of Interest: The authors declare that the research was conducted in the absence of any commercial or financial relationships that could be construed as a potential conflict of interest.

Copyright © 2020 Jean-Richard-dit-Bressel, Clifford and McNally. This is an open-access article distributed under the terms of the Creative Commons Attribution License (CC BY). The use, distribution or reproduction in other forums is permitted, provided the original author(s) and the copyright owner(s) are credited and that the original publication in this journal is cited, in accordance with accepted academic practice. No use, distribution or reproduction is permitted which does not comply with these terms.

frontiers in Molecular Neuroscience

ORIGINAL RESEARCH
published: 11 February 2020
doi: 10.3389/fnmol.2020.00012

Expanding Clinical Presentations Due to Variations in THOC2 mRNA Nuclear Export Factor

*Raman Kumar[1†], Elizabeth Palmer[2,3†], Alison E. Gardner[1], Renee Carroll[1], Siddharth Banka[4,5], Ola Abdelhadi[5], Dian Donnai[4,5], Ype Elgersma[6,7], Cynthia J. Curry[8], Alice Gardham[9], Mohnish Suri[10], Rishikesh Malla[11], Lauren Ilana Brady[12], Mark Tarnopolsky[12], Dimitar N. Azmanov[13,14], Vanessa Atkinson[13,14], Michael Black[13,14], Gareth Baynam[15], Lauren Dreyer[16,17], Robin Z. Hayeems[18], Christian R. Marshall[19], Gregory Costain[20], Marja W. Wessels[21], Julia Baptista[22], James Drummond[23], Melanie Leffler[2], Michael Field[2] and Jozef Gecz[1,24]**

[1]Adelaide Medical School and the Robinson Research Institute, The University of Adelaide, Adelaide, SA, Australia, [2]Genetics of Learning Disability Service, Hunter Genetics, Waratah, NSW, Australia, [3]School of Women's and Children's Health, University of New South Wales, Randwick, NSW, Australia, [4]Faculty of Biology, Medicine and Health, Division of Evolution and Genomic Sciences, School of Biological Sciences, University of Manchester, Manchester, United Kingdom, [5]Manchester Centre for Genomic Medicine, St. Mary's Hospital, Manchester University NHS Foundation Trust, Health Innovation Manchester, Manchester, United Kingdom, [6]Department of Neuroscience, Erasmus MC University Medical Center, Rotterdam, Netherlands, [7]ENCORE Expertise Centre for Neurodevelopmental Disorders, Erasmus MC University Medical Center, Rotterdam, Netherlands, [8]Genetic Medicine, Department of Pediatrics, University of California, San Francisco, San Francisco, CA, United States, [9]North West Thames Regional Genetics Service, Northwick Park Hospital, Harrow, United Kingdom, [10]Nottingham Clinical Genetics Service, Nottingham University Hospitals NHS Trust, and the 100,000 Genomes Project and the Genomics England Research Consortium, Nottingham, United Kingdom, [11]Division of Pediatric Neurology, Medical University of South Carolina, Charleston, SC, United States, [12]Department of Pediatrics, McMaster University Medical Centre, Hamilton, ON, Canada, [13]Department of Diagnostic Genomics, PathWest, Nedlands, WA, Australia, [14]Division of Pathology and Laboratory Medicine, Medical School, University of Western Australia, Crawley, WA, Australia, [15]Faculty of Health and Medical Sciences, University of Western Australia Medical School, Perth, WA, Australia, [16]Genetic Services of Western Australia, Undiagnosed Diseases Program, Department of Health, Government of Western Australia, Perth, WA, Australia, [17]Linear Clinical Research, Perth, WA, Australia, [18]Child Health Evaluative Sciences, Research Institute, The Hospital for Sick Children, and Institute of Health Policy Management and Evaluation, University of Toronto, Toronto, ON, Canada, [19]Genome Diagnostics, Department of Paediatric Laboratory Medicine, The Hospital for Sick Children, and Laboratory Medicine and Pathobiology, University of Toronto, Toronto, ON, Canada, [20]Department of Paediatrics, Division of Clinical and Metabolic Genetics, The Hospital for Sick Children, Toronto, ON, Canada, [21]Department of Clinical Genetics, Erasmus MC University Medical Center, Rotterdam, Netherlands, [22]Royal Devon and Exeter NHS Foundation Trust, Exeter, United Kingdom, [23]Neuroradiology, Royal North Shore Hospital, Sydney, NSW, Australia, [24]Childhood Disability Prevention, South Australian Health and Medical Research Institute, Adelaide, SA, Australia

OPEN ACCESS

Edited by:
Robert J. Harvey,
University of the Sunshine Coast,
Australia

Reviewed by:
Jia Nee Foo,
Nanyang Technological University,
Singapore
Ferdinando Di Cunto,
University of Turin, Italy

***Correspondence:**
Jozef Gecz
jozef.gecz@adelaide.edu.au

[†]These authors have contributed equally to this work

Received: 18 October 2019
Accepted: 15 January 2020
Published: 11 February 2020

Citation:
Kumar R, Palmer E, Gardner AE, Carroll R, Banka S, Abdelhadi O, Donnai D, Elgersma Y, Curry CJ, Gardham A, Suri M, Malla R, Brady LI, Tarnopolsky M, Azmanov DN, Atkinson V, Black M, Baynam G, Dreyer L, Hayeems RZ, Marshall CR, Costain G, Wessels MW, Baptista J, Drummond J, Leffler M, Field M and Gecz J (2020) Expanding Clinical Presentations Due to Variations in THOC2 mRNA Nuclear Export Factor. Front. Mol. Neurosci. 13:12. doi: 10.3389/fnmol.2020.00012

Multiple TREX mRNA export complex subunits (e.g., THOC1, THOC2, THOC5, THOC6, THOC7) have now been implicated in neurodevelopmental disorders (NDDs), neurodegeneration and cancer. We previously implicated missense and splicing-defective *THOC2* variants in NDDs and a broad range of other clinical features. Here we report 10 individuals from nine families with rare missense *THOC2* variants including the first case of a recurrent variant (p.Arg77Cys), and an additional individual with an intragenic *THOC2* microdeletion (Del-Ex37-38). *Ex vivo* missense variant testing and patient-derived cell line data from current and published studies show 9 of the 14 missense THOC2 variants result in reduced protein stability. The splicing-defective

and deletion variants result in a loss of small regions of the C-terminal THOC2 RNA binding domain (RBD). Interestingly, reduced stability of THOC2 variant proteins has a flow-on effect on the stability of the multi-protein TREX complex; specifically on the other NDD-associated THOC subunits. Our current, expanded cohort refines the core phenotype of THOC2 NDDs to language disorder and/or ID, with a variable severity, and disorders of growth. A subset of affected individuals' has severe-profound ID, persistent hypotonia and respiratory abnormalities. Further investigations to elucidate the pathophysiological basis for this severe phenotype are warranted.

Keywords: mRNA export, THOC2, intellectual disability, neurodevelopmental disorders, microdeletion

INTRODUCTION

Neurodevelopmental disorders (NDDs) caused by genetic, epigenetic and environmental factors are clinically heterogeneous conditions affecting the central nervous system in children and include intellectual disability (ID), epilepsy, autism and cerebral palsy. NDDs affect more than 3% of children worldwide. Genetic causes are attributed to variants at over 1,000 loci and include single nucleotide changes (single nucleotide variants, SNV; coding and non-coding variants) and larger losses, gains or rearrangements (structural variants; Tarlungeanu and Novarino, 2018).

Many molecular causes of NDDs disrupt diverse cellular pathways, particularly affecting neuronal development, proliferation and/or migration of cells to cause learning and behavioral disabilities (Srivastava and Schwartz, 2014). One such pathway—that has been the focus of our ongoing investigations—is of the highly conserved TREX (TRanscription-EXport) mRNA export pathway. Multiple TREX complex subunits (e.g., THOC1, THOC2, THOC5, THOC6, and THOC7) have been implicated in NDDs and human disease (Kumar et al., 2015, 2018; Heath et al., 2016; Amos et al., 2017; Mattioli et al., 2019). TREX-mediated mRNA export from the nucleus to the cytoplasm is a complex and highly conserved pathway in all eukaryotes. The TREX complex is composed of a THO sub-complex of a set of six stoichiometric and stable subunits (THOC1-3, 5–7) and accessory proteins (UAP56, UIF, Aly, CIP29, PDIP3, ZC11A, SRRT, Chtop; Heath et al., 2016). THOC subunits are ubiquitously expressed, including in the human brain (Uhlén et al., 2015). The TREX complex has critical roles in developmental processes such as pluripotency maintenance and hematopoiesis as well as in gene regulation, 3′ mRNA processing, stress responses, mitotic progression and genome stability in mammalian cells (Mancini et al., 2010; Yamazaki et al., 2010). We have previously reported genetic and molecular evidence implicating a large number of missense and splicing-defective variants in *THOC2*–which codes for the largest subunit of the TREX mRNA export complex—in NDDs (Mental retardation, X-linked 12/35 MIM 300957; Kumar et al., 2015, 2018). Here we present genetic and molecular evidence on a set of novel *THOC2* variants, and using aggregate data, refine the core clinical phenotype of *THOC2* NDDs.

MATERIALS AND METHODS

Clinical Studies

Through direct contact with clinicians, facilitated by the genotype-phenotype database DECIPHER and the Human Disease Gene Web series, where we moderate a THOC2-related disorder site[1], 10 individuals from 9 families were identified with rare (absent from gnomAD 2.1) missense variants or an intragenic microdeletion. Eight of these variants were novel and one recurrent (p.Arg77Cys) that was a maternally inherited in individual 8 as previously reported by us (detailed in **Supplementary Data**; Kumar et al., 2018). In our previous report, we designated p.Arg77Cys as a variant of uncertain clinical significance in the absence of functional studies at the time (Kumar et al., 2018). All families consented to publication of de-identified clinical information, neuroimaging and, for seven families, clinical photographs, in line with local ethics board regulations. The variants have been submitted to ClinVar[2]; accession numbers SCV001132790-SCV001132797.

Molecular Studies

RNA extraction and RT-qPCR (primers listed in **Supplementary Tables S1, S2**) were performed as reported previously (Kumar et al., 2015). We used THOC2 Del-Ex37-38 (lymphoblastoid cell lines, LCLs and skin fibroblasts) and p.Asn666Asp (skin fibroblasts) cells from the affected individuals and their carrier heterozygous mothers. However, we used THOC2 p.Arg77Cys and p.Tyr881Cys variant LCLs of only probands. THOC2 Del-Ex37-38 (LCLs and skin fibroblasts) cDNAs (generated by reverse transcribing the total RNAs with Superscript IV reverse transcriptase; Life Technologies, VIC, Australia) were amplified using KAPA HiFi PCR Kit with GC buffer (Kapa Biosystems, IN, USA) and hTHOC2-4326F/P276 and hTHOC3-3′UTR-R2/P392 primers (**Supplementary Table S1**) at 95°C for 3 min, 35 cycles of 98°C-10 s, 59°C-10 s, 72°C-80 s, incubation at 72°C for 10 min, gel purified (Qiagen MinElute Gel Extraction kit; Qiagen, Victoria, Australia) and Sanger sequenced using the same primers. Genomic deleted region in THOC2 Del-Ex-37-38 carrier mother and

[1]https://humandiseasegenes.nl/thoc2/

[2]https://www.ncbi.nlm.nih.gov/clinvar/?term="GOLD%20service%2C%20Hunter%20New%20England%20Health"[submitter]+AND+"THOC2"[gene]

affected son was identified by PCR amplification of the target regions from their blood gDNAs using LongAmp Hot Start Taq 2× Master Mix (Promega, Alexandria, NSW, Australia) and hTHOC2-4460-F/P390 and hTHOC2-gDNA-R1/P415 primers (**Supplementary Table S1**) at 94°C for 30 s, 35 cycles of 94°C-15 s, 64°C-15 s, 65°C-8 min 30 s, incubation at 65°C for 10 min. Appropriate PCR products were gel-purified (Qiagen MinElute Gel Extraction Kit) and Sanger sequenced using hTHOC2-gDNA-F7/P421 and hTHOC2-gDNA-R7/P422 primers (**Supplementary Table S1**).

Cellular Studies

We performed THOC2 immunofluorescence staining in Del-Ex37-38 and p.Asn666Asp skin fibroblasts using two anti-THOC2 antibodies; anti-THOC2-I to region between amino acids 1,400–1,450 (Bethyl Laboratories A303-629A, Montgomery, TX, USA) and anti-THOC2-II to a region between amino acids 1543–1593 (Bethyl Laboratories A303-630A) of the THOC2 protein. Both the antibodies were used for detecting the THOC2 protein in Del-Ex37-38 affected individuals and his carrier heterozygous mother fibroblasts but only anti-THOC2-I for detecting the THOC2 p.Asn666Asp in the affected individuals and his carrier heterozygous mother fibroblasts.

Western Blotting

The Epstein–Barr virus (EBV)-immortalized B-cell lines (LCLs) established from peripheral blood lymphocytes of affected individuals and controls were maintained in RPMI1640 supplemented with 10% fetal bovine serum, 2 mM L-glutamine and 1% Penicillin-Streptomycin at 37°C with 5% CO_2. Affected individual-derived fibroblasts were cultured in Dulbecco's modified Eagle's medium (Sigma) containing 10% fetal bovine serum (Life Technologies), 2 mM L-glutamine, and 1% Penicillin-Streptomycin at 37°C with 5% CO_2. Total fibroblast proteins were extracted in 50 mM Tris-HCl pH 7.5, 150 mM NaCl, 0.1% Triton-X-100, 1 mM EDTA, 50 mM NaF, 1× Protease inhibitor/no EDTA cocktail and 0.1 mM Na_3VO_4 and LCLs in 50 mM Tris-HCl pH 7.5, 5 mM EDTA, 50 mM KCl, 0.1% NP-40 and 1× Protease inhibitor/no EDTA cocktail (Roche protease inhibitor cocktail; Sigma–Aldrich, Castle Hill, NSW, Australia) by low frequency sonication for 12 s and centrifugation at 13,000× *g*. Proteins were assayed using Pierce BCA Protein Assay Kit (Thermo Scientific) according to manufacturer's protocol. Eight to Ten microgram of protein was resolved on NuPAGE 3–8% Tris-Acetate gel (THOC2) or 8% SDA-PAGE (Laemmli, 1970), transferred to nitrocellulose membranes and western blotted with the following antibodies: anti-THOC1 (Bethyl Laboratories A302-839A), anti-THOC2 (Bethyl Laboratories A303-630A and A303-629A), anti-THOC3 (HPA044009; Sigma–Aldrich, Castle Hill, NSW, Australia), anti-THOC5 (Bethyl Laboratories A302-120A), anti-β-Tubulin (Ab6046; Abcam, Melbourne, VIC, Australia) and polyclonal goat anti-rabbit IgG/HRP (Dako; P0448) as secondary antibody. Signal was detected by Clarity Western ECL Substrate (BIO-RAD 170-5061) and captured using Gel documentation System (BIO-RAD, Gladesville, NSW, Australia).

In silico Pathogenicity Prediction

We used CADD v1.3 (Kircher et al., 2014), SIFT (Sim et al., 2012), Provean (Choi and Chan, 2015), GERP++ (Davydov et al., 2010), PhyloP (Pollard et al., 2010), gnomAD frequency (v2.1.1; Karczewski et al., 2019), Polyphen2 (Adzhubei et al., 2010), MutPred2 (Pejaver et al., 2017), VEST3 (Carter et al., 2013), and Mutation Assessor Score and Pred (Reva et al., 2011) tools for *in silico* prediction of the pathogenicity of different variants (**Table 1**).

RESULTS

Identification of *THOC2* Variants

We previously implicated missense and splicing-defective *THOC2* variants in NDDs with a broad range of clinical features (Kumar et al., 2015, 2018). Here we report 10 previously unreported affected individuals with *THOC2* variants, including the first case of a recurrent *THOC2* variant (c.229C>T; p.Arg77Cys). We also identify a novel intragenic *THOC2* microdeletion (Del-Ex37-Ex38) [NM_001081550.2 c.4678–572_4782 + 1215; p.(1559fs16)] (**Tables 1**, **2**, **Figures 1**, **2**). These variants were identified from either whole exome (WES) or whole-genome sequencing (WGS) of the affected individuals and confirmed by Sanger sequencing of the PCR amplified variant-carrying region from gDNAs of the parents and the affected individuals (detailed in **Supplementary Data**). The missense *THOC2* variants affect amino acids that are highly conserved (**Supplementary Figure S1**), are absent in the gnomAD database and are predicted to be pathogenic based on a number of *in silico* analyses tools (**Table 1**). We have also performed cellular and molecular investigations on variants p.Arg77Cys, p.Tyr881Cys, p.Asn666Asp and Del-Ex37-38, for which we had access to affected individual-derived cells (**Table 1**; also see below).

Clinical Presentations

The clinical phenotype of affected individuals with *THOC2* variants in this cohort is presented in **Table 2** and summarized in **Figures 2A,B**. The available photographs are shown in **Figure 2C**. Additional information relating the clinical features is included in case reports in the **Supplementary Data** and **Supplementary Table S2**, using an HPO (Human Phenotype Ontology) term framework (Köhler et al., 2019). The main phenotypic features were compared to the individuals reported previously by our group (**Table 2**, Kumar et al., 2015, 2018). This allowed us to make some general observations about the clinical phenotype of the $n = 38$ individuals with *THOC2* variants (this cohort; Kumar et al., 2015, 2018). First, there is no clear genotypic-phenotypic correlation between the severity or spectrum of phenotypic differences and either the type of genetic variant (missense, splicing-defective or microdeletion) or the part of the protein affected by the variant (**Table 2**). Second, compared to the first published cohort, which consisted of hemizygous affected males in multi-generational families, the second and this cohort also include many males with *de novo* *THOC2* variants or *THOC2* variants in siblings which, on further segregation, were shown to be *de novo* in the heterozygous

TABLE 1 | Pathogenicity predictions and descriptions for the *THOC2* variants.

Variant (NM_001081550.2)	Individual 1 c.229C>T:p. Arg77Cys	Individual 2 c.1996A>G: Asn666Asp	Individual 3 c.2170A>G: p.Lys724Glu	Individual 4 c.2642A>G: p.Tyr881Cys	Individual 5a c.2942G>A: p.Cys981Tyr	Individual 5b c.2942G>A: p.Cys981Tyr	Individual 6 c.3223C>T: p.Arg1075Trp	Individual 7 c.3300G>T: p.Trp1100Cys	Individual 8 c.4646A>G: p.Lys1549Arg	Individual 9 Nullizygosity for the last two coding exons (Ex37-38)
Gender	Male	Male	Male	Male	Male	Male	Male	Male	Male	Male
Mode of inheritance	*De novo*	Mat	*De novo*	*De novo*	Mat	Mat	*De novo*	Mat	*De novo*	Mat
CADD	25.8	26	26.6	26.6	28.3	28.3	27.2	31	22.1	NA
SIFT	Tolerated	Deleterious	Deleterious	Deleterious	Deleterious	Deleterious	Deleterious	Deleterious	Tolerated	NA
Provean score	−3.1	−4.56	−3.6	−5.7	−10.4	−10.4	−7.2	−12.27	−0.52	NA
Provean prediction	Deleterious	Deleterious	Deleterious	Deleterious	Deleterious	Deleterious	Deleterious	Deleterious	Neutral	NA
GERP++	5.09	5.11	5.73	5.73	5.83	5.83	3.02	5.87	4.64	NA
Phylop	2.219	1.69	1.927	2.034	2.458	2.458	0.2	2.479	1.956	NA
gnomAD frequency (v2.1.1)	Absent	Absent	Absent	Absent	Absent	Absent	Absent	Absent	Absent	NA
Polyphen2	P	D	P	D	D	D	D	D	B	NA
MutPred2	0.65	0.843	0.668	0.871	0.95	0.95	0.714	0.955	0.086	NA
VEST3	0.869	0.357	0.864	0.964	0.979	0.979	0.91	0.976	0.168	NA
Mutation Assessor Score	2.39	2.325	2.63	2.855	3.17	3.17	2.67	2.875	0.55	NA
Mutation Assessor Pred	M	M	M	M	M	M	M	M	N	NA
Cell Line available	LCL	Fibroblast	N/A	LCL	N/A	N/A	N/A	N/A	N/A	LCLs and Fibroblasts
Effect of variant on protein	Reduced	Moderately reduced	N/A	Reduced	N/A	N/A	N/A	N/A	N/A	Truncated and increased

Mat, maternally inherited; D, probably damaging; P, possibly damaging; B, benign; M, Medium; N, Neutral; N/A, not applicable.

mother. The initial cohort described males with typically mild to moderate ID. Of 20 individuals, 30% (6/20) had borderline-mild ID, 55% (11/20) moderate ID and only 15% (3/20) severe ID (Kumar et al., 2015). In contrast, our last (Kumar et al., 2018) and current cohort includes a higher proportion [75% this cohort; 62.5% (Kumar et al., 2018)] of males with severe to profound ID. In striking contrast to our overall findings is individual 4 with the p.Tyr881Cys variant. This male, in whom pathogenicity of p.Tyr881Cys variant is supported by evidence from functional studies (**Figures 5B,C**: detailed results below), is unique in our cohort as having no evidence of general cognitive dysfunction. On psychometric testing, he had a performance IQ of 104, within the normal range. He did have significant language disorder, with a formal diagnosis of speech apraxia. At the age of 5, he could effectively communicate by sign language. He has a history of mild gross motor delay. Therefore, this publication clarifies that the range of cognitive disability in THOC2-related disorder is very broad—ranging from a normal IQ to a profound ID (**Figure 2A**).

Third, data in **Figure 2B** and **Table 2** suggest that THOC2-related disorder should be considered a multi-systemic disorder in a significant proportion of individuals. The most common extra-neurological feature is disorders of growth. Growth disorders are common across the whole expanded cohort (**Figure 2B**); a half (52%) have persistent short stature, a third (34%) are microcephalic and 29% have intrauterine growth restriction (IUGR). There was no relationship between IUGR in the offspring and carrier status in the mother. 26% of the expanded cohort have increased body weight, with obesity in older males particularly noted. Congenital anomalies of the cardiorespiratory, genitorenal and skeletal systems, severe feeding difficulties and gastroesophageal reflux, and visual and hearing impairments are present in a significant proportion (10–30%). Therefore, comprehensive evaluation including detailed systems review by a pediatrician, cardiac echocardiogram, hearing screening and ophthalmological review in all newly diagnosed patients is highly recommended. Photographs where available are shown in **Figure 2C**. As was the case in our previous publications, an easily recognizable facial gestalt is not apparent, although children with a more severe phenotype (Individuals 1, 6, 8 and 9) have downturned corners of their mouth and deep-set almond-shaped eyes: a facial appearance, which may reflect reduced tone.

Fourth, a more complex neuromuscular phenotype is emerging in a proportion of the cohort: that of severe to profound ID, persistent muscular hypotonia, recurrent aspiration and respiratory tract infections, excessive salivation and an increased risk of congenital anomalies, including laryngo/tracheomalacia, cardiac and palatal anomalies. This phenotype was present in the individual with p.Arg77Cys variant for which initial functional studies using exogenous THOC2 variant expression in HEK293T cells were not conclusive (Kumar et al., 2018). We classified this as a variant of uncertain significance, also in view of this patient's phenotype, which was quite different from the majority of the cohort. We are now more confident that this variant is pathogenic. The variant is recurrent and *de novo* in individual 1 in this cohort and molecular studies from

TABLE 2 | Summary of clinical data of *THOC2* variants.

	This Cohort											
Individual Variant details	**Individual 1 c.229C>T:p. Arg77Cys**	**Individual 2 c.1996A>G: Asn666Asp**	**Individual 3 c.2170A>G: p.Lys724Glu**	**Individual 4 c.2642A>G: p.Tyr881Cys**	**Individual 5a c.2942G>A: p.Cys981Tyr**	**Individual 5b c.2942G>A: p.Cys981Tyr**	**Individual 6 c.3223C>T: p.Arg1075Trp**	**Individual 7 c.3300G>T: p.Trp1100Cys**	**Individual 8 c.4646A>G: p.Lys1549Arg**	**Individual 9 Nullizygosity for the last two coding exons**	**Percentage this cohort (*n* = 10)**	**Percentage total cohort (*n* = 38)**
Gender	Male	Male	Male	Male	Male	Male	Male	Male	Male	Male	100% (10/10)	97% (37/38)
Age (years)	6	5	20	5	15	10	2.5	4.5	2	11	2–20 years	2–61 years
Perinatal features												
Prematurity	No	No	Yes	No	No	No	No	No	No	No	10% (1/10)	18% (6/34)
Low birth weight (<2.5kg)	Yes	No	Yes	No	No	No	No	No	Yes	No	30% (3/10)	29% (10/34)
Neurologic features												
Intellectual disability	Yes—Profound	Yes—Profound	Yes—Severe	No	Yes—Severe	Yes—Severe	Yes—Mod+	Yes—Severe	Yes—Severe	Yes—Mod+	9/10 (90%) [22% mod; 78% severe to profound]	97% (37/38) [16% borderline-mild; 27% moderate; 39% severe-profound]
Speech delay	Yes	Yes	Yes	Yes	Yes	Yes	Yes	Yes	Yes	Yes	100% (10/10)	82% (31/38)
Hypotonia	Yes	No	Yes	No	Yes	Yes	Yes	Yes	Yes	Yes	80% (8/10)	61% (22/36)
Spasticity	No	No	Yes	No	Yes	No	No	No	No	Yes	30% (3/10)	13% (5/38)
Hyperkinesia	Yes	No	No	No	No	No	No	No	No	No	10% (1/10)	21% (8/38)
Tremor	No	No	No	No	No	No	No	No	No	No	0% (0/10)	26% (10/38)
Epilepsy	Yes—IS and tonic/myoclonic	No	No	No	No	No	Yes—IS	No	Suspected	Suspected	20% (2/10) confirmed, 20% (2/10) suspected	21% (8/38) confirmed, 8% (3/38) suspected
Gait disturbances	Non ambulatory, hyperkinetic	No	Yes—dystonia, spasticity	No	Yes—poor balance and coordination, weakness, spasticity	Yes—poor balance and coordination, weakness, spasticity	Non ambulatory	Non ambulatory	Non ambulatory	Appendicular spasticity	80% (8/10)	48% (18/38)
Behavior problems	No	No	No	No	No	Yes	No	No	No	No	10% (1/10)	39% (15/38)
Anxiety	No	No	No	No	No	No	No	No	No	No	0% (0/10)	5% (2/38)
Depression	No	No	No	No	No	No	No	No	No	No	0% (0/10)	5% (2/38)
Brain MRI/CT	Delayed myelination, ventriculomegaly, small midbrain	Abnormal CNS myelination	Ventriculomegaly	Normal	ND	Cerebellar atrophy & periventricular changes	Gray matter heterotopia	Delayed myelination, right perisylvian polymicrogyria, short corpus callosum	Ventriculo megaly, small midbrain, abnormal cerebellar vermis	Abnormal myelination	89% (8/9)	47% (15/32): 43% ventriculomegaly or cerebral atrophy; 48% white matter

(Continued)

TABLE 2 | Continued

	This Cohort											
Individual Variant details	**Individual 1 c.229C>T:p.Arg77Cys**	**Individual 2 c.1996A>G:Asn666Asp**	**Individual 3 c.2170A>G:p.Lys724Glu**	**Individual 4 c.2642A>G:p.Tyr881Cys**	**Individual 5a c.2942G>A:p.Cys981Tyr**	**Individual 5b c.2942G>A:p.Cys981Tyr**	**Individual 6 c.3223C>T:p.Arg1075Trp**	**Individual 7 c.3300G>T:p.Trp1100Cys**	**Individual 8 c.4646A>G:p.Lys1549Arg**	**Individual 9 Nullizygosity for the last two coding exons**	**Percentage this cohort (*n* = 10)**	**Percentage total cohort (*n* = 38)**
												abnormality; 19% cerebellar abnormality; 19% abnormality of neuronal migration
Growth parameters												
Microcephaly (≤3%)	Yes	Yes	Yes	No	No	No	Yes	No	No	Yes	50% (5/10)	34% 13/38
Short stature (≤3%)	Yes	No	Yes	No	Yes	Yes	No	No	Yes	No	50% (5/10)	52% 20/38
Overweight (BMI≥25)	No	No	No	No	No	No	No	No	No	No	0% (0/10)	26% (10/38)
Other features												
Visual abnormality	Yes—high myopia	No	Yes—visual impairment	No	No	No	Yes—visual impairment, unilateral coloboma	No	Yes—bilateral exotropia	Yes—blepharophimosis, exotropia	50% (5/10)	9/38 (24%) [11% strabismus; 5% nystagmus]
Hearing abnormality	Yes—bilateral OME	Yes—SNHL	No	No	No	No	Yes—mixed	No	No	Yes—mixed	40% (4/10)	6/38 (16%)[8% OME; 8% SNHL]
Genitorenal abnormality	Yes—recurrent UTI		Yes—cryptorchidism	No	No	No	No	No	No	Yes—cryptorchidism	30% (3/10)	10/38 (26%) [19% cryptorchidism]
Gastrointestinal abnormality	Yes—severe feeding difficulties, drooling, GORD : g-tube fed	No	Yes—severe feeding difficulties, GORD	No	Yes—drooling	No	Yes—severe feeding difficulties, GORD	Yes—severe feeding difficulties, chronic constipation	Yes—severe feeding difficulties, oropharangeal dysplasia, drooling, GORD: g-tube fed	Yes—feeding difficulties	70% (7/10)	7/38 (18%) [18% feeding difficulties; 5% dysphagia, 11% GORD, 11% drooling]
Respiratory abnormality	Yes— CLD + oxygen dependency	No	Yes—CLD	No	No	No	Yes—tracheomalacia	Yes—recurrent LRTI	Yes— recurrent apnea and bradycardia,	Yes—recurrent LRTI	60% (6/10)	10/38 (26%) [11% laryngo or tracheomalacia; 5% apnoea; 11% abnormal lung morphology]
Skeletal abnormality	Yes—aquired coxa valga	No	Yes—kyphosis	No	No	No	No	Yes— scoliosis; DDH	No	Yes—scoliosis	40% (4/10)	6/38 (16%)[5% subluxation of the hips and joint laxity]

(Continued)

TABLE 2 | Continued

Individual Variant details	This Cohort										Percentage this cohort (n = 10)	Percentage total cohort (n = 38)
	Individual 1 c.229C>T;p.Arg77Cys	**Individual 2 c.1996A>G:p.Asn666Asp**	**Individual 3 c.2170A>G:p.Lys724Glu**	**Individual 4 c.2642A>G:p.Tyr881Cys**	**Individual 5a c.2942G>A:p.Cys981Tyr**	**Individual 5b c.2942G>A:p.Cys981Tyr**	**Individual 6 c.3223C>T:p.Arg1075Trp**	**Individual 7 c.3300G>T:p.Trp1100Cys**	**Individual 8 c.4646A>G:p.Lys1549Arg**	**Individual 9 Nullizygosity for the last two coding exons**		
Cardiovascular abnormality	No	No	Yes— abnormal pulmonary artery morphology	No	No	No	Yes— ASD; VSD	Yes— VSD	No	No	30% (3/30)	7/38 (18%)
Other features				Severe speech apraxia with normal IQ.	Dry skin		Cleft palate,		Severe eczema			

Abbreviations: %, centile; ASD, atral septal defect; VSD, ventricular septal defect; g-tube, gastrostomy tube; mod+, at least moderate severity; GORD, gastroesophageal reflux; DDH, developmental dysplasia of the hip; CLD, chronic lung disease due to recurrent infections; SNHL, sensorineural hearing loss; OME, otitis media with effusions/; UTI, urinary tract infection; NR, not reported; ND, not done; MRI, magnetic resonance imaging; IS, infantile spasms.

patient-derived cell lines available from this second family are consistent with reduced protein levels. Both individuals with the p.Arg77Cys variant has strikingly overlapping phenotypes (see **Supplemental Data** for detailed case reports). Individuals 6, 8 and 9 from the current cohort also have similarities to this phenotype. This more severe phenotype is also frequently associated with neuroradiological abnormalities and an increased chance of a seizure disorder. Seizure disorder, although not very common over the whole cohort (**Figure 2B**: 21%), can be problematic – with a severe developmental and epileptic encephalopathy picture, commonly including infantile spasms. Therefore, the clinicians should have a low threshold for investigating neurological symptoms or signs with an EEG and MRI brain.

Fifth, although for many individuals the phenotype is static, a more complex neurological phenotype also emerges with age in several males; in the expanded cohort 13% develop hypertonia and spasticity or contractures, and 53% have some abnormality of motor coordination, stereotypic or involuntary movements. In the current cohort, three individuals had received an additional diagnosis of cerebral palsy. Of the nine affected individuals included in this cohort, cases 1, 4, 5, 6, 7 have had multi-timepoint MRI neuro-imaging reviewed by a single Neuroradiology Attending Consultant with dedicated pediatric expertise (*data not shown*). Although no unifying neuroradiological abnormalities were delineated from this small cohort, one affected individual demonstrated interval cerebellar hemispheric volume loss after a 6-year period, and another demonstrated volume loss of the corpus callosum and mild reduction in myelination at an early post-natal 4-month scan. A further patient had reported features of nodular heterotopia although this imaging was not available for review. No other definitive migrational anomaly, midline defect or development abnormality was identified. The potential implications on white matter development and degeneration in this cohort require long term follow-up imaging.

Lastly, all heterozygous female carriers in this cohort had normal intelligence, as was the case for the entire cohort, with the exception of the one female reported to date with a *de novo THOC2* variant with a developmental and epileptic encephalopathy (Kumar et al., 2018). When tested, asymptomatic female carriers are highly skewed for X inactivation (Kumar et al., 2015, 2018).

In summary, this expanded cohort has clarified that the core phenotype of THOC2 related disorder in hemizygous males is that of language disorder and ID, with a wide variability in severity, and that disorders of growth are common, and multi-systemic involvement is present in a significant proportion. A subpopulation of patients has a very severe phenotype with severe-profound ID, persistent hypotonia, respiratory abnormalities and a higher chance of other congenital anomalies. Some affected males show the progression of neurological symptoms and progressive neuroradiological features. Further research to explore the underlying pathophysiological basis for these more severe phenotypes is warranted, but likely reflect the involvement of THOC2 in multi-organ development and function.

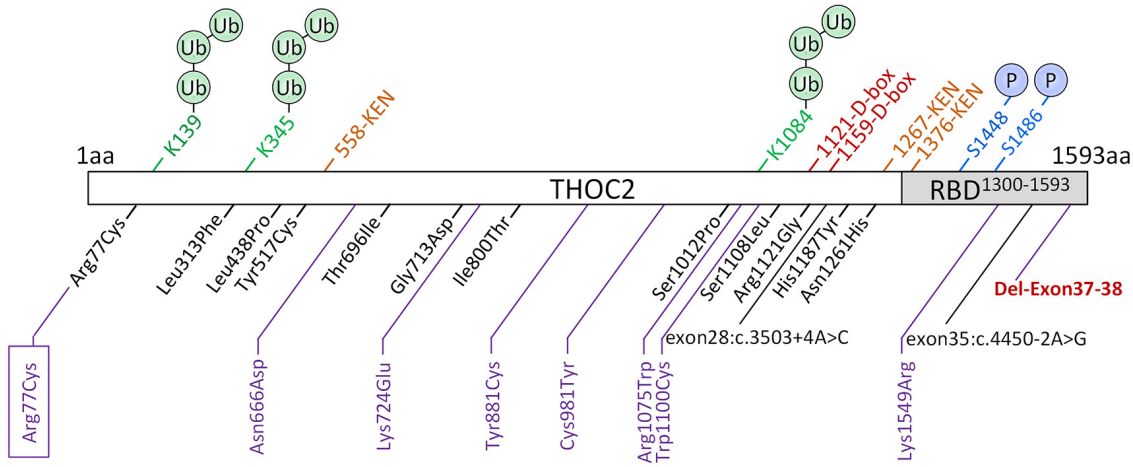

FIGURE 1 | New *THOC2* variants (purple). These include the first Arg77Cys recurrent (boxed) and Del-Exon-37-38 variants (red bold). Previously published *THOC2* variants (black) and structural features are also shown (Kumar et al., 2015, 2018).

Molecular Studies

We used primary skin fibroblasts and/or immortalized B-lymphocytes (LCLs) derived from affected individuals and where available, also their heterozygous carrier mothers.

Del-Ex37-38 THOC2 Variant

We found an affected male with deletion of *THOC2* Ex37-38 (NM_001081550.2) as identified by massively parallel sequencing (see **Figure 3**). We have subsequently validated this as a 2.4 kb X-chromosome gDNA microdeletion (encompassing Ex37-38 sequence) which was also present in his carrier mother (**Figure 4**). In addition, we PCR amplified the Ex35-Ex39 coding region from cDNAs prepared by reverse transcribing the LCL and fibroblast mRNAs from the affected individual and his normal carrier mother (**Figure 3C**). Sanger sequencing of the amplified products showed deletion of Ex37-38, but not Ex39 coding sequences, in the affected individual (**Figures 3B,C**). The carrier mother's cells showed mRNAs with Ex37-38 sequences consistent with her X-inactivation skewing (10:90; **Figures 3A–C**). We detected a slightly smaller THOC2 protein (due to Ex37-38-encoded C-terminal 34 amino acid deletion) in affected son's LCLs and fibroblasts but normal full-length THOC2 protein in the unaffected carrier mother on western blots probed with anti-THOC2-I antibody that binds to a region between amino acids 1,400–1,450 coded by Ex32-33 mRNA sequences (compare lanes 1 and 2, upper panel, **Figure 5A** and lanes 3 and 4, **Figure 5B**). Notably, C-terminal THOC2 truncated protein levels were higher in both the affected LCLs and fibroblasts (**Figures 5A,B**). As expected, the anti-THOC2-II antibody that binds to a region between amino acids 1543–1593 coded by Ex37-38 mRNA sequences (lower panel) did not detect the THOC2 protein in affected son's LCLs and fibroblasts that express a C-terminally-deleted THOC2 protein. This antibody however detected THOC2 protein in the carrier mother-derived cells as she expressed normal full-length THOC2 protein (compare lanes 1 and 2, lower panel, **Figure 5A** and lanes 3 and 4, **Figure 5B**). THOC1 and THOC5 levels were similar in fibroblasts of the affected son and carrier mother (**Figure 5A**). Likewise, anti-THOC2-I antibody detected nuclear THOC2 protein in both the affected son and carrier mother's fibroblasts by immunofluorescence but anti-THOC2-II antibody, as expected, detected the THOC2 protein in the mother's but not son's fibroblasts (**Figures 6A–C**). Normal nuclear THOC2 localization was detected in fibroblasts of the affected son and carrier mother (**Figure 6F**). We observed no significant difference in *THOC2* mRNA level in LCLs and fibroblasts of the affected son and carrier mother (**Figure 7A**).

THOC2 Missense Variants

LCLs were available from affected individuals' hemizygous for the p.Arg77Cys and p.Tyr881Cys variants and fibroblasts from the affected individual and his carrier mother with the Trp.Asn666Asp variant (**Figure 5**). p.Arg77Cys and p.Tyr881Cys THOC2 variants resulted in reduced protein levels compared to control LCLs (**Figures 5B,C**). THOC1 and THOC5 levels were also moderately reduced in these LCLs (**Figures 5B,C**). Interestingly, a reduction in p.Arg77Cys and p.Tyr881Cys THOC2 variant protein levels were similar to unstable p.Leu438Pro variant THOC2 protein reported previously (**Figure 5C**; Kumar et al., 2015). Note that RT-qPCR assays in p.Arg77Cys and p.Tyr881Cys THOC2 variant LCLs also showed reduced mRNA expression compared to unrelated normal controls (**Figure 7B**). Western blotting on p.Asn666Asp fibroblasts also showed a small but reproducible reduction in THOC2 protein and related THO complex subunits THOC1, THOC3 and THOC5 compared to his unaffected carrier mother and unrelated normal controls (**Figure 5D**). p.Asn666Asp THOC2 reduction was much less

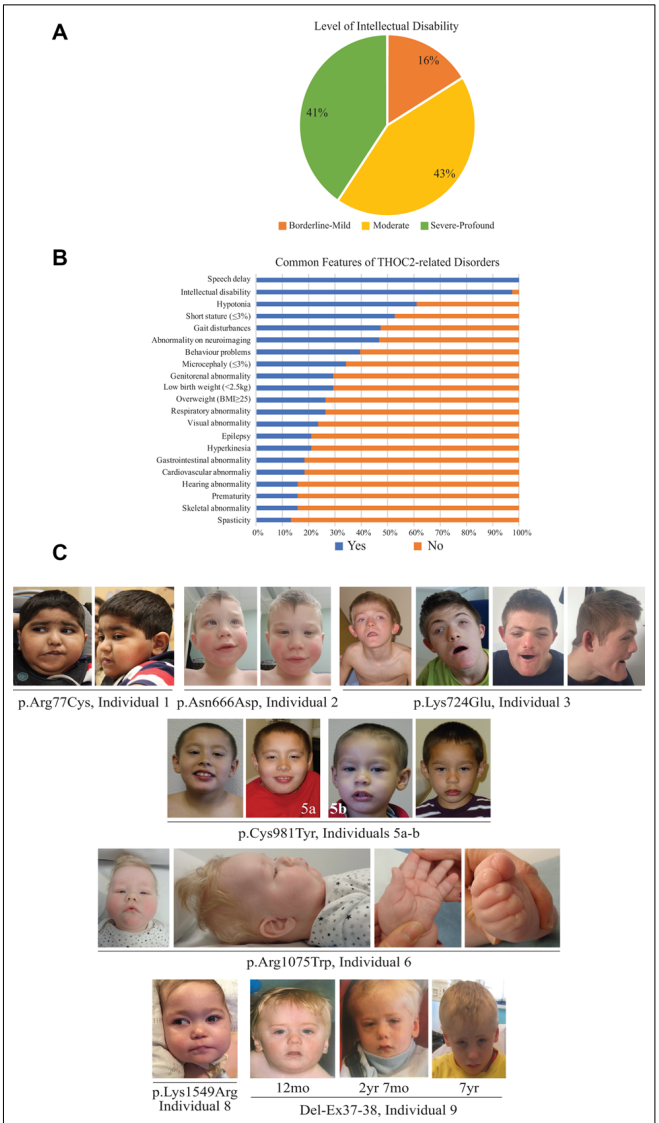

FIGURE 2 | Clinical presentations of the affected individuals identified so far. **(A)** Percentage of individuals with different levels of ID. **(B)** Percentage of individuals with common features. **(C)** Photographs of the affected individuals in the current cohort.

pronounced than that of highly unstable p.Leu438Pro THOC2 as well as THOC1 and THOC5 proteins in affected fibroblasts (**Figure 5D**). p.Asn666Asp THOC2 localization was not affected (**Figures 6D,E**). Levels of mRNA expression in p.Asn666Asp affected LCLs were similar to that of the patient's carrier mother and unrelated controls (**Figure 7A**).

DISCUSSION

TREX-mediated mRNA export is a fundamental process that is essential for the export of mRNA from the cytoplasm to the nucleus to allow translation of the normal level of protein required for efficient growth and development. We and others have presented evidence showing that perturbed mRNA export leads to altered cellular function, thus causing a range of diseases (Di Gregorio et al., 2013; Kumar et al., 2015, 2018; Heath et al., 2016; Mattioli et al., 2019). During the last few years, we have focussed on the association of variation in the *THOC2* gene and NDDs. *THOC2* is intolerant to complete loss of function [probability of loss of function or pLI = 1; o/e = 0.02 (0.01–0.08): gnomAD v.2.1.1]. We first reported four *THOC2* missense inherited variants in the affected individuals with variable degrees of ID and commonly observed features such as speech delay, elevated BMI, short stature, seizure disorders, gait disturbance, and tremors (Kumar et al., 2015). In 2018, we reported an additional six affected individuals from five unrelated families with two *de novo* and three maternally inherited pathogenic or likely pathogenic missense and splicing-defective *THOC2* variants. The study also included a *de novo* variant in a female with epileptic encephalopathy. We observed a core ID phenotype and common behavioral features, infantile hypotonia, gait disturbance and growth impairment (Kumar et al., 2018). In the current cohort, we present molecular and clinical findings on ten additional *THOC2* variant individuals, confirming a more severe THOC2-related phenotype associated with severe hypotonia, respiratory and other congenital anomalies, and summarize the phenotypic impact of all *THOC2* variants to date in 38 individuals. This publication, therefore, may serve as the most up to date reference of this X-linked NDD condition.

Variants in TREX subunit proteins can alter their stability (Kumar et al., 2015, 2018; e.g., THOC2 ID variants), interaction (e.g., THOC6 syndromic ID variants; Mattioli et al., 2019) and/or localization (e.g., THOC6 syndromic ID variants; Mattioli et al., 2019). We observed reduced levels of p.Arg77Cys THOC2 (although the stability of this variant exogenously expressed in HEK293T cells was uninformative, see Figure 3 in Kumar et al., 2018) and p.Tyr881Cys THOC2 in the affected LCLs and p.Asn666Asp THOC2 affected fibroblasts (without THOC2 mislocalization). Variant THOC2 protein reduction also impacted the THOC1, THOC3 and THOC5 stability in the variant cells, which is consistent with a number of reports showing that instability of THO subunits—either by missense changes or siRNA-mediated knockdown—results in reduced levels of other THO subunits (Chi et al., 2013; Kumar et al., 2015, 2018). As the *THOC2* mRNA levels in the affected LCLs or fibroblasts were comparable to the controls, the reduced THOC2 variant protein levels are most likely due to enhanced proteasome-mediated degradation of ubiquitinated THOC2 (Lopitz-Otsoa et al., 2012). Reduced or depleted THO subunit proteins have been shown to cause severe to mild nuclear mRNA retention (Chi et al., 2013) and hence can cause variable molecular and cellular consequences both in mammalian cells and lower organisms. For example, THOC2 depletion impacts chromosome alignment, mitotic progression, and genomic stability in human HeLa cells (Yamazaki et al., 2010). Thoc2 knockdown in *Drosophila* S2 cells inhibits cell proliferation and heat-shock mRNA export (Rehwinkel et al., 2004). Thoc2 depletion results in a significant increase in the length of neurites in cultured rat primary hippocampal neurons and *C. elegans thoc2* knockout worms are

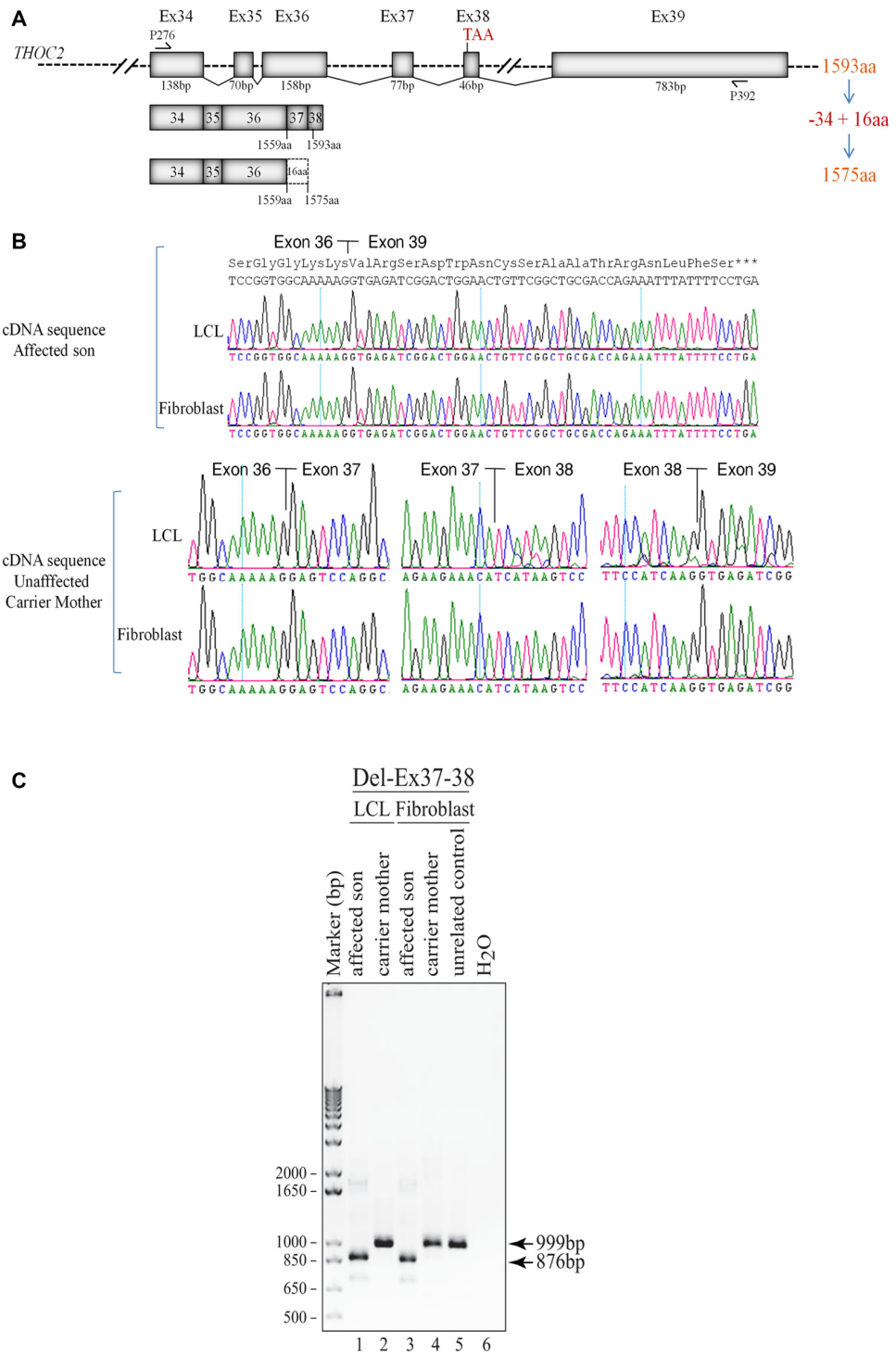

FIGURE 3 | Del-Ex37-38 results in the loss of 34 C-terminal amino acids in the affected individual. **(A)** Part of the *THOC2* gene showing Ex34 to Ex39 and positions of primers. Ex37-38 deleted mRNA translates a 1575 amino acid protein, lacking 34 C-terminal amino acids but adding 16 amino acids encoded from the 3′ UTR region of the deleted mRNAs. **(B)** Sanger sequencing chromatograms of DNA amplified from LCL and fibroblast cDNAs of the affected individual and his heterozygous unaffected carrier mother using primers P276/P392 located within Ex34 and Ex39. Wild type (1593 amino acid) and C-terminal deleted THOC2 protein (1575 amino acids) translated from Del-Ex37-38 mRNA is also shown. **(C)** Ex37-38 coding sequence is deleted in both fibroblast and LCL THOC2 mRNAs of the affected son but not in the unaffected carrier mother. Total fibroblast and LCL RNAs were reverse transcribed and PCR amplified using primers P276/P392. PCR products (999 bp from the carrier mother and 876 bp from the affected son) were gel purified and Sanger sequenced using P276 and P392 primers.

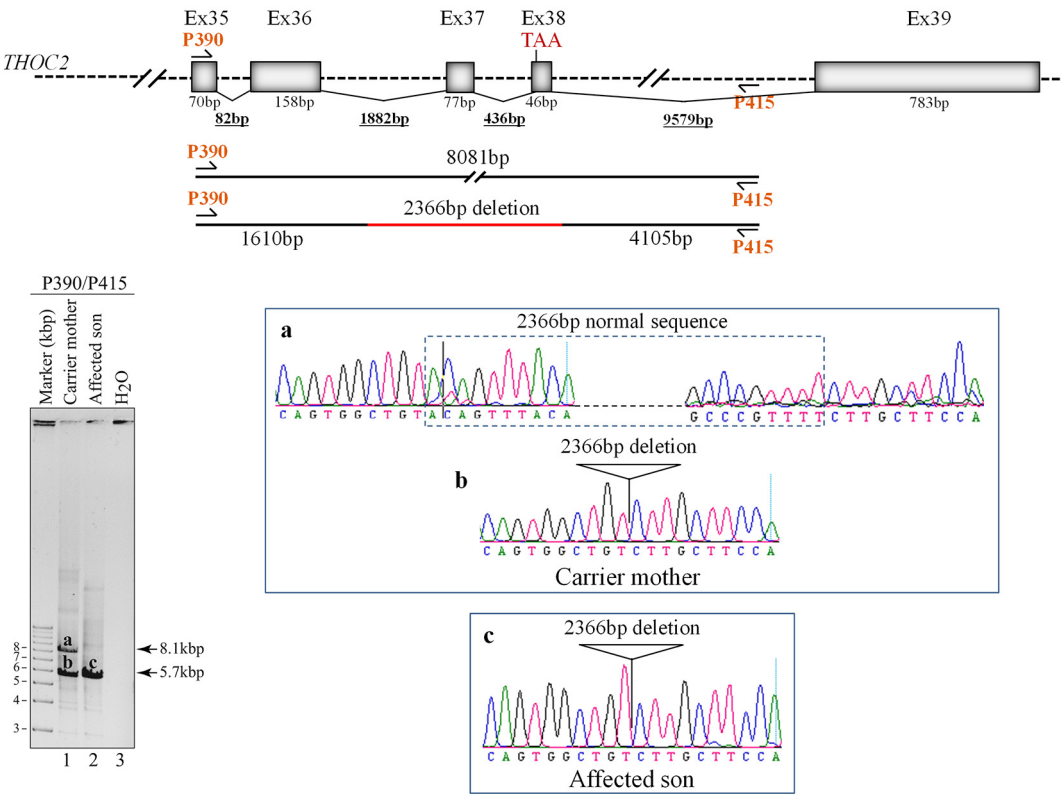

FIGURE 4 | Del-Ex37-38 results from the deletion of approximately 2.4 kb genomic DNA (chrX:122743574-122745939) flanking the Ex37-38. Sequences around the deleted target region were amplified from the affected son and carrier mother's blood gDNA using P390/P415 primers using LongAmp Hot Start Taq 2× Master Mix, resolved on agarose gel and bands a-c were eluted and Sanger sequenced. Positions of the P390/P415 primers and sequencing chromatograms (a–c) around the deleted gDNA regions are shown.

slow-growing, sterile, have functional defects in specific sensory neurons and die prematurely (Di Gregorio et al., 2013). *Danio rerio Thoc2* is essential for embryonic development (Amsterdam et al., 2004). Interestingly, a *de novo* translocation creating a *PTK2-THOC2* fusion that reduced the expression of the two genes in a female patient was implicated in cognitive impairment and cerebellar hypoplasia (also reported in 4/19 of our cases; Di Gregorio et al., 2013). THOC2 or THOC5 depletion leads to dedifferentiation of vascular smooth muscle cells, characterized by increased migration and proliferation (Yuan et al., 2018). Thoc2 and Thoc5 depletion was shown to cause retention of self-renewal (Oct4) and pluripotent gene transcripts (*Nanog*, *Sox2*, *Esrrb*, and *Klf4*) as well as increased differentiation gene expression (*Cdx2*, *Gata3* and *Gata4*) in mouse embryonic stem cells, resulting in a decrease in cell pluripotency and proliferation (Wang et al., 2013).

We observed accumulation of 34 C-terminal amino acid THOC2 truncated protein in Del-Ex37-38 LCLs and fibroblasts that is similar to the accumulation of 110 C-terminal amino acid deleted THOC2 protein in fibroblasts of the affected individual carrying the exon35:c.4450–2A>G splice-variant and potential loss of the 1,300–1,593 amino acid putative RNA binding domain (RBD) in a proportion of blood cells with the exon28:c.3503 + 4A>C defective splice-variant (Kumar et al., 2018). The truncated proteins in these individuals had normal nuclear localization. Together, the affected individuals (at least in Del-Ex37-38 and exon35:c.4450–2A>G splice-variant) not only have truncated THOC2 protein (where a part of the RBD is lost) but actually more of it, which may indicate presence of a degradation signal within this region and/or stabilization due to structural changes to the THOC2 protein that may or may not be impacting interactions with other TREX subunits. That C-terminally truncated THOC2 protein potentially has perturbed function is consistent with yeast Tho2 studies showing that Tho2Δ1408–1597 (small C-terminal RBD deletion) grows slower than the wild-type strain and ThoΔ1271–1597 (complete RBD deletion) strain barely grows at restrictive temperature (Peña et al., 2012).

THOC2 depletion leads to almost complete retention of mRNAs in the cell nucleus, suggesting that it is an essential mRNA export factor whose complete knockout can be potentially toxic to the cell (Chi et al., 2013). We, therefore, suggest that all the identified *THOC2* variants result in partial loss-of-function that alters normal mRNA export in neuronal and likely other cells, thereby causing a broad range of clinical presentations in the affected individuals carrying the *THOC2*

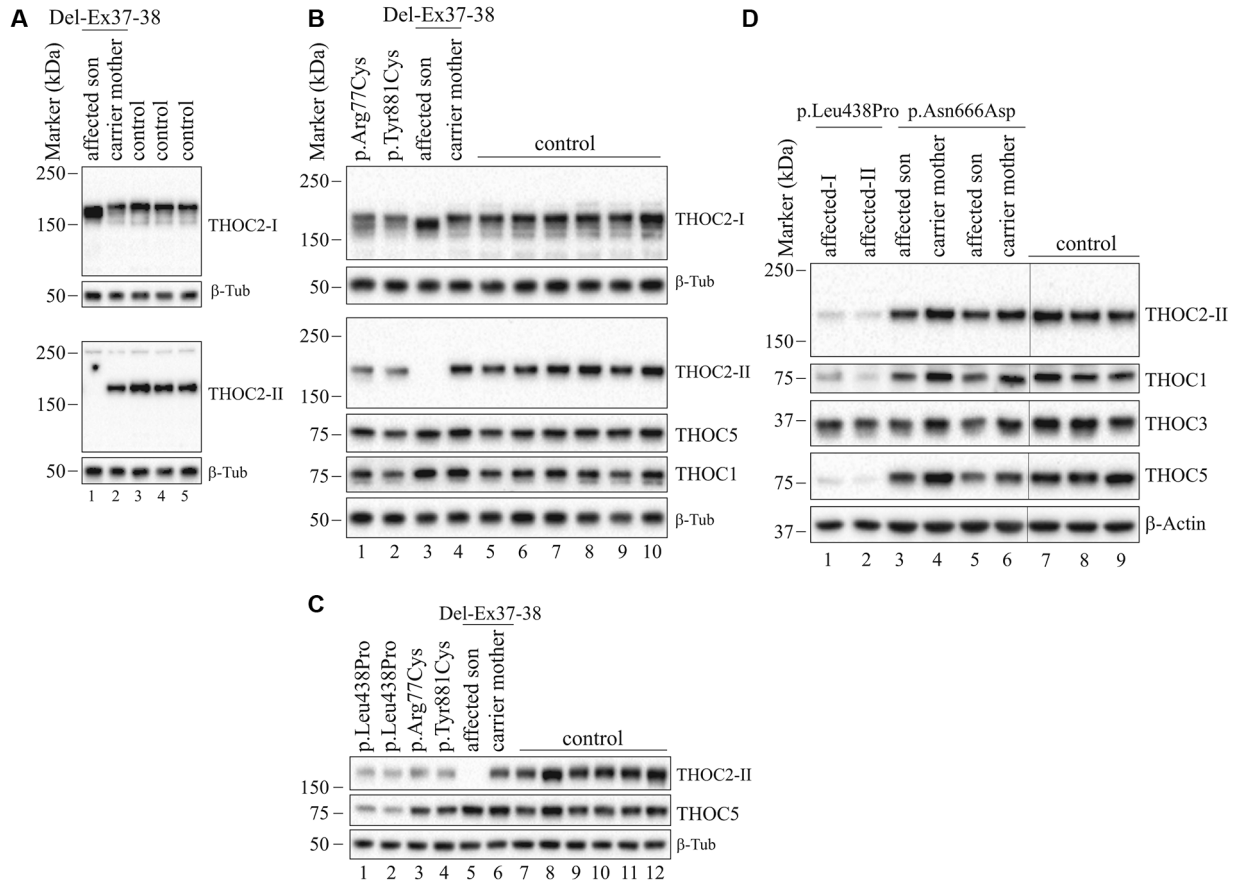

FIGURE 5 | THOC2 variant protein analysis in patient-derived cell lines. **(A)** THOC2 protein in affected son with Del-Ex37-38, unaffected carrier mother and control fibroblasts. Total protein lysates were western blotted with an anti-THOC2-I antibody that binds to a region between amino acids 1,400–1,450 coded by Ex32-34 mRNA (upper panel) and anti-THOC2-II antibody that binds to a region between amino acids 1543–1593 coded by Ex37-38 mRNA (lower panel). Samples were probed for β-Tubulin as a loading control. **(B)** THOC2 protein in p.Arg77Cys, p.Tyr881Cys, affected son with Del-Ex37-38, unaffected carrier mother and control LCLs. Total protein lysates were western blotted with anti-THOC2-I, anti-THOC2-II, anti-THOC1, anti-THOC5 and anti-β-Tubulin (loading control) antibodies. Del-Ex37-38 affected fibroblasts (Lane 1 in panel **A**) and LCLs (Lane 3 in panel **B**) showing presence of a C-terminally deleted smaller but higher levels of the THOC2 protein when western blotted with anti-THOC2-I antibody (upper panels) that is absent in the affected fibroblast lysates probed with anti-THOC2-II antibody (lower panels). However, normal full-length THOC2 protein is present in the carrier mother and controls western blotted with both the anti-THOC2-I and anti-THOC2-II antibodies (Lane 2 in upper and lower panels in **A** and Lane 4 in upper and lower panels in **B**). The p.Arg77Cys and p.Tyr881Cys THOC2 levels are reduced. **(C)** THOC2 protein levels in p.Leu438Pro (reported to have reduced protein stability; Kumar et al., 2015), p.Arg77Cys, p.Tyr881Cys, Del-Ex37-38 affected son, his unaffected carrier mother and control LCLs. Total protein lysates were western blotted with anti-THOC2-II, anti-THOC5 and anti-β-Tubulin (loading control) antibodies. **(D)** The p.Asn666Asp levels are moderately reduced in the affected fibroblasts. p.Asn666Asp affected son, his unaffected carrier mother and control fibroblast total lysates were western blotted with the antibodies as shown. p.Leu438Pro fibroblasts previously reported having reduced THOC2 protein stability were included as controls (Kumar et al., 2015). Vertical lines on western blot images indicate the site of deleted sample lanes.

variants. However, although THOC2 depletion causes bulk mRNA nuclear retention in HeLa cells (Chi et al., 2013), whether *THOC2* variants affect—bulk or specific—mRNA export in neuronal cells has not been elucidated. TREX complex was originally thought to be a bulk mRNA export pathway but a number of reports have shown its role in specific mRNA export. For example, the Thoc1/2 and Thoc5 or Thoc6 are responsible for nuclear export of only a subset of mRNAs (e.g., heat shock mRNAs) in Drosophila and mammalian cells, respectively (Rehwinkel et al., 2004; Katahira et al., 2009; Guria et al., 2011). Thoc2 and Thoc5 selectively bind and regulate the export of mRNAs involved in the maintenance of pluripotency (e.g., *Nanog*, *Sox2*, *Esrrb*, and *Klf4* mRNAs (Wang et al., 2013) and Thoc5 in hematopoiesis (Mancini et al., 2010).

The published data in conjunction with our molecular and cellular data, and broader clinical presentations in our cohort indicate that THOC2 reduction (and consequently other THO subunits) or potential alterations in TREX subunit interactions due to intragenic deletion of C-terminal RBD and/or structural interactions as a result of THOC2 missense changes result in perturbed mRNA export, causing cellular dysfunction and NDDs. This view is supported by the published evidence showing that slight perturbations in mRNA export can

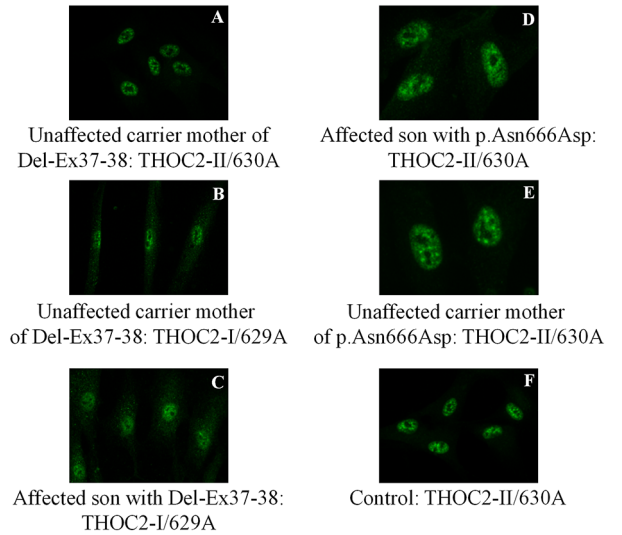

FIGURE 6 | THOC2 localization is unaltered in variant fibroblasts. THOC2-II antibody detects THOC2 protein in fibroblasts of the Del-Ex37-38 unaffected carrier mother **(A)** but not affected son (not shown, as we detected no fluorescence signal). However, the THOC2-I antibody detects THOC2 protein in fibroblasts of unaffected carrier mother **(B)** and the affected son with Del-Ex37-38 **(C)**. Localization p.Asn666Asp THOC2 protein in fibroblasts of an affected son **(D)**, his unaffected carrier mother **(E)** and control **(F)**.

lead to NDDs (Beaulieu et al., 2013; Kumar et al., 2015, 2018; Mattioli et al., 2019), neurodegenerative disease (Woerner et al., 2016) and cancer (Domínguez-Sánchez et al., 2011). There are also examples showing how variants in the human mRNA export mediator GLE1 result in a severe fetal motor neuron disease (Nousiainen et al., 2008) and amyotrophic lateral sclerosis (ALS; Kaneb et al., 2015), and toxic CUG expansion in the 3′ untranslated region of the DM protein kinase mRNA can cause myotonic dystrophy type I by impairing RNA transport out of the nucleus (Brook et al., 1992).

Based on clinical and, where available, molecular data on 38 individuals, we have come to a realization that the THOC2-linked NDDs can present with highly variable phenotypes. Intriguingly, we also identify a case of severe expressive dysphasia without obvious intellectual impairment. This particular case and observation still awaits replication and as such further validation. In hindsight, it is perhaps not surprising that even subtle perturbation to a crucial cellular mechanism like TREX mRNA export can yield complex and often variable clinical presentations which can not only be driven by the *THOC2* gene variation itself, but can also be modified by genome-wide polygenic risk (Niemi et al., 2018) or other yet to be identified factors.

DATA AVAILABILITY STATEMENT

The datasets have been uploaded to ClinVar and are available here: https://www.ncbi.nlm.nih.gov/clinvar/SCV001132790[clv_acc] under accession numbers SCV001132790, SCV001132791, SCV001132792, SCV001132793, SCV001132794, SCV001132795, SCV001132796 and SCV001132797.

ETHICS STATEMENT

The studies involving human participants were reviewed and approved by WCHN Human Research Ethics Committee and University of Adelaide, Adelaide. Written informed consent to participate in this study was provided by the participants' legal guardian/next of kin. Written informed consent was obtained

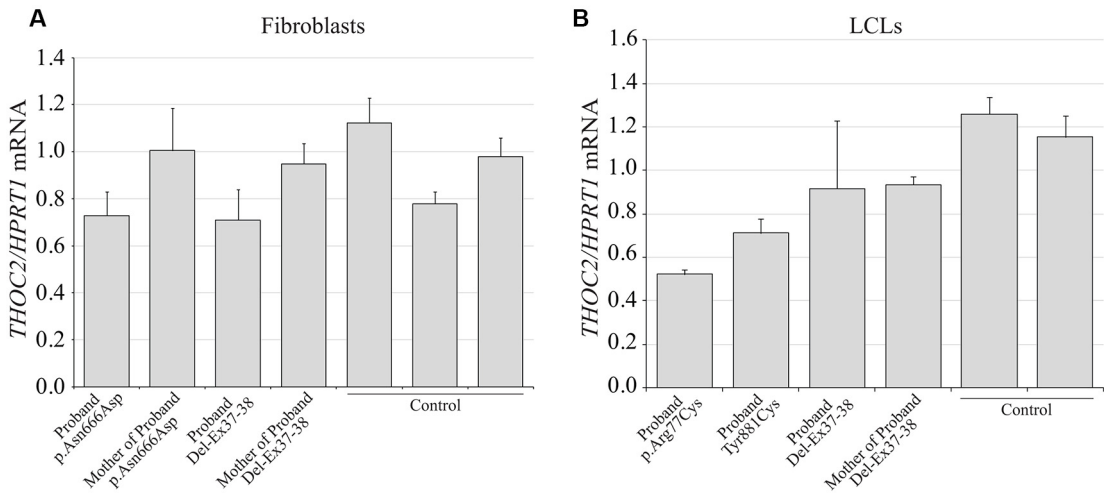

FIGURE 7 | THOC2 mRNA expression in the variant cell lines. cDNA was generated by reverse transcribing the total RNA extracted from variant fibroblasts **(A)**, LCLs **(B)** and appropriate controls using SuperScript IV reverse transcriptase and assayed for *THOC2* expression (relative to *HPRT1* housekeeping gene) with SYBR green master mix and primer pairs listed in **Supplementary Table S1**. Assays were performed two times independently and error bars show SDs.

from the minor(s)' legal guardian/next of kin for the publication of any potentially identifiable images or data included in this article.

AUTHOR CONTRIBUTIONS

RK, EP, MF, and JG designed the experiments and wrote the article. RK performed the molecular studies. AEG helped with pathogenicity predictions. RC with tissue culture. SB, OA, DD, YE, CC, AG, MS, RM, LB, MT, DA, VA, MB, GB, LD, RH, CM, GC, MW, and JB contributed THOC2 variants, photos, clinical data, and in some cases, the patient-derived cells for molecular investigations. JD reviewed MRI neuro-images. EP and ML collated the clinical data. All authors read and made suggestions on the manuscript.

FUNDING

This work was supported by National Health and Medical Research Council (NHMRC) Program Grant APP1091593 (JG), NHMRC Project Grant APP1163240 (JG, RK), Australian Research Council Discovery Project 170103090 (JG, RK) and Senior Research Fellowship APP1041920 (JG). The Toronto group (RH, CM, GC) acknowledges funding support from the Norm Saunders Complex Care Initiative, SickKids Centre for Genetic Medicine, and the University of Toronto McLaughlin Centre. We thank the individuals and families for their contribution to this study. The c.3300G>T p.(Trp1100Cys) THOC2 variant was identified as part of the 100,000 Genomes Project that is managed by Genomics England Limited (a wholly-owned company of the Department of Health and Social Care) and funded by the National Institute for Health Research and NHS England. The Wellcome Trust, Cancer Research UK and the Medical Research Council have also funded research infrastructure. The 100,000 Genomes Project uses data provided by patients and collected by the National Health Service as part of their care and support.

SUPPLEMENTARY MATERIAL

The Supplementary Material for this article can be found online at: https://www.frontiersin.org/articles/10.3389/fnmol.2020.00012/full#supplementary-material.

REFERENCES

Adzhubei, I. A., Schmidt, S., Peshkin, L., Ramensky, V. E., Gerasimova, A., Bork, P., et al. (2010). A method and server for predicting damaging missense mutations. *Nat. Methods* 7, 248–249. doi: 10.1038/nmeth0410-248

Amos, J. S., Huang, L., Thevenon, J., Kariminedjad, A., Beaulieu, C. L., Masurel-Paulet, A., et al. (2017). Autosomal recessive mutations in THOC6 cause intellectual disability: syndrome delineation requiring forward and reverse phenotyping. *Clin. Genet.* 91, 92–99. doi: 10.1111/cge.12793

Amsterdam, A., Nissen, R. M., Sun, Z., Swindell, E. C., Farrington, S., and Hopkins, N. (2004). Identification of 315 genes essential for early zebrafish development. *Proc. Natl. Acad. Sci. U S A* 101, 12792–12797. doi: 10.1073/pnas.0403929101

Beaulieu, C. L., Huang, L., Innes, A. M., Akimenko, M. A., Puffenberger, E. G., Schwartz, C., et al. (2013). Intellectual disability associated with a homozygous missense mutation in THOC6. *Orphanet J. Rare Dis.* 8:62. doi: 10.1186/1750-1172-8-62

Brook, J. D., Mccurrach, M. E., Harley, H. G., Buckler, A. J., Church, D., Aburatani, H., et al. (1992). Molecular basis of myotonic dystrophy: expansion of a trinucleotide (CTG) repeat at the 3′ end of a transcript encoding a protein kinase family member. *Cell* 69:385. doi: 10.1016/0092-8674(92)90418-c

Carter, H., Douville, C., Stenson, P. D., Cooper, D. N., and Karchin, R. (2013). Identifying Mendelian disease genes with the variant effect scoring tool. *BMC Genomics* 14:S3. doi: 10.1186/1471-2164-14-s3-s3

Chi, B., Wang, Q., Wu, G., Tan, M., Wang, L., Shi, M., et al. (2013). Aly and THO are required for assembly of the human TREX complex and association of TREX components with the spliced mRNA. *Nucleic Acids Res.* 41, 1294–1306. doi: 10.1093/nar/gks1188

Choi, Y., and Chan, A. P. (2015). PROVEAN web server: a tool to predict the functional effect of amino acid substitutions and indels. *Bioinformatics* 31, 2745–2747. doi: 10.1093/bioinformatics/btv195

Davydov, E. V., Goode, D. L., Sirota, M., Cooper, G. M., Sidow, A., and Batzoglou, S. (2010). Identifying a high fraction of the human genome to be under selective constraint using GERP++. *PLoS Comput. Biol.* 6:e1001025. doi: 10.1371/journal.pcbi.1001025

Di Gregorio, E., Bianchi, F. T., Schiavi, A., Chiotto, A. M., Rolando, M., Verdun Di Cantogno, L., et al. (2013). A *de novo* X;8 translocation creates a PTK2-THOC2 gene fusion with THOC2 expression knockdown in a patient with psychomotor retardation and congenital cerebellar hypoplasia. *J. Med. Genet.* 50, 543–551. doi: 10.1136/jmedgenet-2013-101542

Domínguez-Sánchez, M. S., Saez, C., Japon, M. A., Aguilera, A., and Luna, R. (2011). Differential expression of THOC1 and ALY mRNP biogenesis/export factors in human cancers. *BMC Cancer* 11:77. doi: 10.1186/1471-2407-11-77

Guria, A., Tran, D. D., Ramachandran, S., Koch, A., El Bounkari, O., Dutta, P., et al. (2011). Identification of mRNAs that are spliced but not exported to the cytoplasm in the absence of THOC5 in mouse embryo fibroblasts. *RNA* 17, 1048–1056. doi: 10.1261/rna.2607011

Heath, C. G., Viphakone, N., and Wilson, S. A. (2016). The role of TREX in gene expression and disease. *Biochem. J.* 473, 2911–2935. doi: 10.1042/bcj20160010

Kaneb, H. M., Folkmann, A. W., Belzil, V. V., Jao, L. E., Leblond, C. S., Girard, S. L., et al. (2015). Deleterious mutations in the essential mRNA metabolism factor, hGle1, in amyotrophic lateral sclerosis. *Hum. Mol. Genet.* 24, 1363–1373. doi: 10.1093/hmg/ddu545

Karczewski, K. J., Francioli, L. C., Tiao, G., Cummings, B. B., Alföldi, J., Wang, Q., et al. (2019). Variation across 141,456 human exomes and genomes reveals the spectrum of loss-of-function intolerance across human protein-coding genes. *bioRxiv* [Preprint]. doi: 10.1101/531210

Katahira, J., Inoue, H., Hurt, E., and Yoneda, Y. (2009). Adaptor Aly and co-adaptor Thoc5 function in the Tap-p15-mediated nuclear export of HSP70 mRNA. *EMBO J.* 28, 556–567. doi: 10.1038/emboj.2009.5

Kircher, M., Witten, D. M., Jain, P., O'Roak, B. J., Cooper, G. M., and Shendure, J. (2014). A general framework for estimating the relative pathogenicity of human genetic variants. *Nat. Genet.* 46, 310–315. doi: 10.1038/ng.2892

Köhler, S., Carmody, L., Vasilevsky, N., Jacobsen, J. O. B., Danis, D., Gourdine, J. P., et al. (2019). Expansion of the human phenotype ontology (HPO) knowledge base and resources. *Nucleic Acids Res.* 47, D1018–D1027. doi: 10.1093/nar/gky1105

Kumar, R., Corbett, M. A., Van Bon, B. W., Woenig, J. A., Weir, L., Douglas, E., et al. (2015). THOC2 mutations implicate mRNA-export pathway in X-linked intellectual disability. *Am. J. Hum. Genet.* 97, 302–310. doi: 10.1016/j.ajhg.2015.05.021

Kumar, R., Gardner, A., Homan, C. C., Douglas, E., Mefford, H., Wieczorek, D., et al. (2018). Severe neurocognitive and growth disorders due to variation in THOC2, an essential component of nuclear mRNA export machinery. *Hum. Mutat.* 39, 1126–1138. doi: 10.1002/humu.23557

Laemmli, U. K. (1970). Cleavage of structural proteins during the assembly of the head of bacteriophage T4. *Nature* 227, 680–685. doi: 10.1038/227680a0

Lopitz-Otsoa, F., Rodriguez-Suarez, E., Aillet, F., Casado-Vela, J., Lang, V., Matthiesen, R., et al. (2012). Integrative analysis of the ubiquitin proteome isolated using tandem ubiquitin binding entities (TUBEs). *J. Proteomics* 75, 2998–3014. doi: 10.1016/j.jprot.2011.12.001

Mancini, A., Niemann-Seyde, S. C., Pankow, R., El Bounkari, O., Klebba-Farber, S., Koch, A., et al. (2010). THOC5/FMIP, an mRNA export TREX complex protein, is essential for hematopoietic primitive cell survival *in vivo*. *BMC Biol.* 8:1. doi: 10.1186/1741-7007-8-1

Mattioli, F., Isidor, B., Abdul-Rahman, O., Gunter, A., Huang, L., Kumar, R., et al. (2019). Clinical and functional characterization of recurrent missense variants implicated in THOC6-related intellectual disability. *Hum. Mol. Genet.* 28, 952–960. doi: 10.1093/hmg/ddy391

Niemi, M. E. K., Martin, H. C., Rice, D. L., Gallone, G., Gordon, S., Kelemen, M., et al. (2018). Common genetic variants contribute to risk of rare severe neurodevelopmental disorders. *Nature* 562, 268–271. doi: 10.1038/s41586-018-0566-4

Nousiainen, H. O., Kestilä, M., Pakkasjärvi, N., Honkala, H., Kuure, S., Tallila, J., et al. (2008). Mutations in mRNA export mediator GLE1 result in a fetal motoneuron disease. *Nat. Genet.* 40, 155–157. doi: 10.1038/ng.2007.65

Pejaver, V., Urresti, J., Lugo-Martinez, J., Pagel, K. A., Lin, G. N., Nam, H.-J., et al. (2017). MutPred2: inferring the molecular and phenotypic impact of amino acid variants. *bioRxiv* [Preprint]. doi: 10.1101/134981

Peña, A., Gewartowski, K., Mroczek, S., Cuellar, J., Szykowska, A., Prokop, A., et al. (2012). Architecture and nucleic acids recognition mechanism of the THO complex, an mRNP assembly factor. *EMBO J.* 31, 1605–1616. doi: 10.1038/emboj.2012.10

Pollard, K. S., Hubisz, M. J., Rosenbloom, K. R., and Siepel, A. (2010). Detection of nonneutral substitution rates on mammalian phylogenies. *Genome Res.* 20, 110–121. doi: 10.1101/gr.097857.109

Rehwinkel, J., Herold, A., Gari, K., Kocher, T., Rode, M., Ciccarelli, F. L., et al. (2004). Genome-wide analysis of mRNAs regulated by the THO complex in *Drosophila melanogaster*. *Nat. Struct. Mol. Biol.* 11, 558–566. doi: 10.1038/nsmb759

Reva, B., Antipin, Y., and Sander, C. (2011). Predicting the functional impact of protein mutations: application to cancer genomics. *Nucleic Acids Res.* 39:e118. doi: 10.1093/nar/gkr407

Sim, N. L., Kumar, P., Hu, J., Henikoff, S., Schneider, G., and Ng, P. C. (2012). SIFT web server: predicting effects of amino acid substitutions on proteins. *Nucleic Acids Res.* 40, W452–W457. doi: 10.1093/nar/gks539

Srivastava, A. K., and Schwartz, C. E. (2014). Intellectual disability and autism spectrum disorders: causal genes and molecular mechanisms. *Neurosci. Biobehav. Rev.* 46, 161–174. doi: 10.1016/j.neubiorev.2014.02.015

Tarlungeanu, D. C., and Novarino, G. (2018). Genomics in neurodevelopmental disorders: an avenue to personalized medicine. *Exp. Mol. Med.* 50:100. doi: 10.1038/s12276-018-0129-7

Uhlén, M., Fagerberg, L., Hallström, B. M., Lindskog, C., Oksvold, P., Mardinoglu, A., et al. (2015). Proteomics. Tissue-based map of the human proteome. *Science* 347:1260419. doi: 10.1126/science.1260419

Wang, L., Miao, Y.-L., Zheng, X., Lackford, B., Zhou, B., Han, L., et al. (2013). The THO complex regulates pluripotency gene mRNA export and controls embryonic stem cell self-renewal and somatic cell reprogramming. *Cell Stem Cell* 13, 676–690. doi: 10.1016/j.stem.2013.10.008

Woerner, A. C., Frottin, F., Hornburg, D., Feng, L. R., Meissner, F., Patra, M., et al. (2016). Cytoplasmic protein aggregates interfere with nucleocytoplasmic transport of protein and RNA. *Science* 351, 173–176. doi: 10.1126/science.aad2033

Yamazaki, T., Fujiwara, N., Yukinaga, H., Ebisuya, M., Shiki, T., Kurihara, T., et al. (2010). The closely related RNA helicases, UAP56 and URH49, preferentially form distinct mRNA export machineries and coordinately regulate mitotic progression. *Mol. Biol. Cell* 21, 2953–2965. doi: 10.1091/mbc.e09-10-0913

Yuan, X., Zhang, T., Yao, F., Liao, Y., Liu, F., Ren, Z., et al. (2018). THO complex-dependent posttranscriptional control contributes to vascular smooth muscle cell fate decision. *Circ. Res.* 123, 538–549. doi: 10.1161/circresaha.118.313527

Conflict of Interest: The authors declare that the research was conducted in the absence of any commercial or financial relationships that could be construed as a potential conflict of interest.

Copyright © 2020 Kumar, Palmer, Gardner, Carroll, Banka, Abdelhadi, Donnai, Elgersma, Curry, Gardham, Suri, Malla, Brady, Tarnopolsky, Azmanov, Atkinson, Black, Baynam, Dreyer, Hayeems, Marshall, Costain, Wessels, Baptista, Drummond, Leffler, Field and Gecz. This is an open-access article distributed under the terms of the Creative Commons Attribution License (CC BY). The use, distribution or reproduction in other forums is permitted, provided the original author(s) and the copyright owner(s) are credited and that the original publication in this journal is cited, in accordance with accepted academic practice. No use, distribution or reproduction is permitted which does not comply with these terms.

frontiers in Molecular Neuroscience

OPINION
published: 18 February 2020
doi: 10.3389/fnmol.2020.00022

Building a Human Brain for Research

Maina Bitar[1] *and Guy Barry*[1,2]*

[1] QIMR Berghofer Medical Research Institute, Herston, QLD, Australia, [2] The School of Biomedical Sciences, The University of Queensland, Brisbane, QLD, Australia

Keywords: human brain, iPSC, organoid, assembloid, microfluidics, ethics

It is vital for our understanding of human-specific development, behavior, cognition, and disease that we possess a reliable, manipulatable, and accurate experimental model of the human brain. Historically, the ability to view and manipulate a human brain model system on a molecular scale in real-time was not achievable. However, recent advances in stem cell technologies make it possible to reproduce, at least partly, human brain development in a laboratory. We are now able to replicate human neural cell types, distinct brain regions and produce organoids from embryonic and induced pluripotent stem cells. Here, we address the main developments in producing multiple neural cell types and organoids and discuss how these technologies are allowing an effective way forward to gain functional insight into human brain development and disorders. We conclude with a brief discussion on potential upcoming ethical implications of this rapidly progressing field.

2D *IN VITRO* MODELS OF HUMAN BRAIN CELLS AND NETWORKS

The human brain, similar to all other species that have a brain structure, has specific gene expression patterns, pathways, and cell types that make it unique. Although there are many similarities across species, it is the differences that are needed to be considered when investigating species-specific development and disease. Until recently, research on the human brain could only be conducted using post-mortem tissue or imaging or by establishing parallels to observations made using animal models. Although useful, these techniques cannot yield vital molecular information of dynamic neural processes particular to humans. In 2006, a breakthrough in the field was achieved by Takahashi and Yamanaka, who first performed the conversion of mouse fibroblasts into induced pluripotent stem cells (iPSCs) (Takahashi and Yamanaka, 2006), a process which was soon after replicated using human fibroblasts in 2007 (Takahashi et al., 2007; Yu et al., 2007). Among many other applications, this exciting discovery opened the door for building a system to investigate the development and function of human brain cells with potential to be reliable, manipulatable, and dynamic. The differentiation of human iPSCs to somatic lineages, including neural cell types, soon followed, and the field moved rapidly to determine the factors and conditions necessary for the specific conversion of iPSCs into neural cell types such as forebrain cortical neurons (Chambers et al., 2009; Shi et al., 2012), midbrain dopaminergic neurons (Cooper et al., 2010), spinal motor neurons (Jiang et al., 2012), GABA interneurons (Liu et al., 2013), astrocytes (Emdad et al., 2012), oligodendrocytes (Wang et al., 2013), and microglia (Abud et al., 2017; Pocock and Piers, 2018). Two dimensional (2D) integrated networks are now produced in a tailored process, adjusted to reflect the cell types required to answer specific questions (**Figure 1**) that investigate, for example, human brain-specific development (Weick et al., 2011; Ardhanareeswaran et al., 2017) and neuropsychiatric diseases such as Rett Syndrome (Marchetto et al., 2010), schizophrenia (Brennand et al., 2011; Barry et al., 2014; Roussos et al., 2016), and autism (Russo et al., 2019).

Neurodegenerative models, e.g., for Alzheimer's disease and Parkinson's disease (Shi et al., 2017), can now be studied in a species appropriate experimental model, although the issue of a suitable aging and maturation system remains a work in progress. Techniques are being developed to

OPEN ACCESS

Edited by:
Robert J. Harvey, University of the Sunshine Coast, Australia

Reviewed by:
Snezana Maljevic, University of Melbourne, Australia

***Correspondence:**
Guy Barry
guy.barry@qimrberghofer.edu.au

Received: *10 October 2019*
Accepted: *31 January 2020*
Published: *18 February 2020*

Citation:
Bitar M and Barry G (2020) Building a Human Brain for Research. Front. Mol. Neurosci. 13:22. doi: 10.3389/fnmol.2020.00022

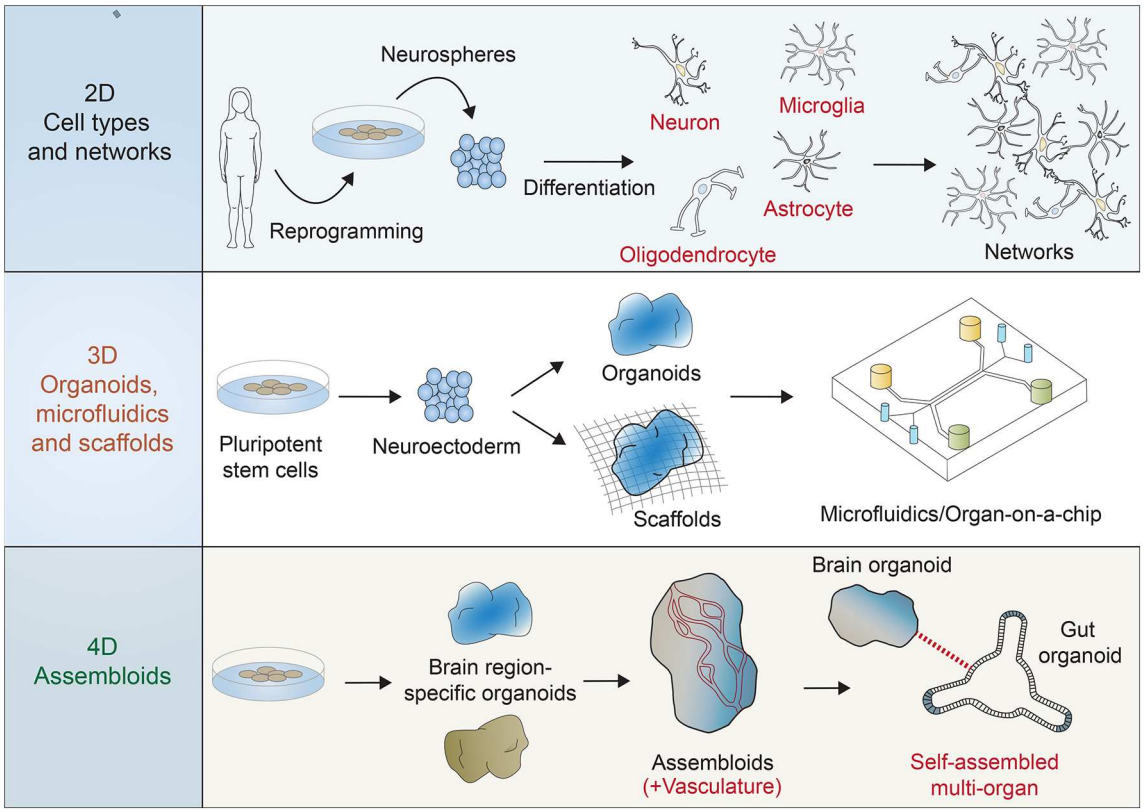

FIGURE 1 | Multiple systems are possible for the use of reprogrammed human stem cells in the investigation of human brain development, function, and disease. Two dimensional (2D) functional, activatable, and manipulatable networks can incorporate many neuronal subtypes (e.g., motor neurons, cortical neurons, and interneurons) and other neural cell types (e.g., astrocytes, oligodendrocytes, and microglia). Three dimensional (3D) networks can be formed using scaffolds and microfluidic devices to include the features of 3D regionalization, whereas some organoid models can also be scaffold-free and free-floating. Four dimensional (4D) "assembloids" can expand 3D models by integrating vasculature, for example, and combining other body region organoid models, such as the gut in order to mimic the brain/gut axis.

overcome these limitations so as to produce more relevant aging changes at a molecular level. For example, iPSC-derived aging models have been undertaken using direct conversion methods, such as those resulting in induced neurons (iNs) (Vierbuchen et al., 2010) that avoid a return to the pluripotent stem cell stage and in doing so retain, at least partly, age-related epigenetic marks in a variety of iN subtypes (Mertens et al., 2018).

3D MODELS USING BRAIN ORGANOIDS AND SCAFFOLDS

One of the major limitations with 2D models is that they cannot recapitulate regional specificity and connectivity as they mature in the normal developing human brain. Although much progress has being made through *in vivo* studies using model animals, human development is unique in many aspects and the brain is perhaps where these particular differences are more noticeable. Studying the human brain in its uniqueness is not only important for gaining insight into organ development, but also crucial for understanding disease and performing preliminary pharmacological tests for new drugs. To begin to overcome the issues caused by such limitations in researching the human brain, scientists have coupled the recent advances in cell reprogramming and previous knowledge of the brain structure to achieve significant progress in the field. Key advances were made by producing three dimensional (3D) networks using non-adherent conditions to generate a 3D cerebral cortex-like structure (Pasca et al., 2015), 3D human multi-cell type culture models using 3D microfluidic platforms (Park et al., 2018), organs-on-a-chip used for high throughput drug screening (Ronaldson-Bouchard and Vunjak-Novakovic, 2018), and a variety of conventional scaffold substrates for 3D cultures (Willerth and Sakiyama-Elbert, 2008). These frameworks improved on 2D networks to include space, time, and inputs to allow the prospects of interrogating new paradigms.

Through the exploration of self-organizing capabilities of the brain, Lancaster et al. in 2013 established an iPSC-derived, 3D culture system that opened up new opportunities for modeling and exploring human brain development. Through self-organization, these cerebral organoids formed specific human cortical brain regions and cell types (Lancaster et al.,

2013). For example, the human cortex possesses an expanded outer subventricular zone (OSVZ) that provides the capacity for increased proliferation to augment cortical size and complexity (Hansen et al., 2010), and this is recapitulated in cerebral organoids (Lancaster et al., 2013). In parallel, further progress was achieved by injecting selective molecular signals into the system to induce the formation of specific brain regions (Jo et al., 2016; Qian et al., 2016). Qian et al. used mini bioreactors to produce forebrain organoids with a well-defined OSVZ and demonstrated the presence of outer radial glial cells with selected molecular markers.

Once a basic structure has emerged that resembles a rudimentary human brain and mimics its cellular properties, either by self-organization or via supplementary stimuli, further experiments can be conducted. Molecular characterization can then inform human-specific transcriptomic and epigenomic changes that occur during human brain development (Amiri et al., 2018). Combined with engineering innovations (Brassard and Lutolf, 2019), organoids represent a rich source of possibilities for investigating human brain function and disease, responses to multiple stimuli, and assessing drug treatments.

Although much has been achieved using organoids, a major shortcoming being currently addressed is reproducibility. Even when more sophisticated 3D models of the brains are developed that can accurately recapitulate the complexity and structural features of this human organ, if the models are not reproducible, it can significantly limit their applications. As we are now beginning to understand the processes guiding organoid formation and improving the techniques to measure molecular diversity, future research will focus on minimizing variability. Indeed, advances have been made and results are promising, although studies still suggest there is more to be done to ensure reproducibility across laboratories (Krefft et al., 2018; Velasco et al., 2019).

4D MODELS CONNECTING 3D MODELS TO VASCULATURE AND OTHER BODY REGIONS SUCH AS THE GUT (BRAIN/GUT AXIS) TO MIMIC DYNAMIC INTERPLAY

Although the field is still in its infancy and many advances should occur in the next few years regarding the development of 3D models, researchers have already started to assess its further applications. The next step is to physically connect region-specific organoids to build a more comprehensive functional system. Studies have demonstrated fusion of distinct brain region-derived organoids, such as the medial ganglionic eminence and cortical areas for the analysis of interneuron migration (Xiang et al., 2017), CA1 and CA3 regions in the hippocampus modeling functional connectivity (Sarkar et al., 2018), and dorsal and ventral forebrain (Birey et al., 2017). As these multiple domain structures self-organize in close proximity and form connections, the dynamic interplay can be analyzed as the human brain develops. To further enhance these four dimensional (4D) models, and allow improved growth and maturation, the issues of improving oxygen and nutrient diffusion (McMurtrey, 2016), and incorporating a functional vasculature, have significantly improved recently (Wimmer et al., 2019). Overall, these studies show the rapid advancement and potential in developing a more relevant human brain model that recapitulates functional *in vivo* features.

It may also be possible in the near future to connect brain organoids to other body organ-specific organoids. The brain controls many functions peripherally via the central and peripheral nervous systems and connecting these organs through appropriate neural connectivity could yield valuable inter-organ information. For example, the gut organoids were the first organoids to be developed (Sato et al., 2009) and the brain and gut are connected via enteroendocrine cells that synapse with vagal neurons (Kaelberer et al., 2018). Combining these two organoid systems in the future could allow investigation into the communication between the organs and a better understanding of the underlying principles of food and nutrient sensing and the control of eating and related disorders. The future of organoids could lead to the ability to create almost any system of brain connections, both within the brain as "assembloids" (Pasca, 2019), but also within the whole body wherever the brain is connected via the central and peripheral nervous systems.

WHEN DOES HUMAN BRAIN ORGANOID BECOME CONSCIOUS?

As research on brain organoids rapidly progresses, both ethical and philosophical questions arise. As we have illustrated in this review, during the past decade, efforts have culminated in the development of robust and complex neural systems that successfully recapitulate some of the fundamental structures of the brain microscopic and macroscopic environment, self-organize and show spontaneous activity. Remarkably, researchers have recently demonstrated that human cortical-type organoids display electrical patterns that resemble those seen in developing preterm human babies (Trujillo et al., 2019). These organoids showed regular oscillatory activity and synchronous network events during their development that were comparable to those of preterm babies. Spontaneous brain activity in a dish certainly does stir up the consciousness debate and leading organoid researchers have raised concerns and advise caution in order to appropriately utilize this technology (Reardon, 2018). The development of "assembloids" that connect brain regions and peripheral organs, certainly demonstrates the limitless boundaries of this technology through combining engineering, organoid biology and scientific creativity. Furthermore, recent studies demonstrated successful transplantation of cerebral organoids derived from human neural stem cells into mouse brains that showed enhanced integration into the surrounding tissue, and robust differentiation and maturation (Daviaud et al., 2018; Mansour et al., 2018). An unexpected development, however, was the observation of graft-to-host synaptic connectivity,

with the growth of human axonal projections extending into the mice brain. The debate is whether these mice are "humanized" and at what point "human" thoughts and behaviors may arise.

The scientific community may need to more clearly define the boundary between biological materials and conscious systems. A general theoretical definition is that the conscious experience is both informative and integrative and, from these axioms, quantitative methods for measuring consciousness can be derived. One objective measure consists of an index resulting from assessing the complexity of the electrical response generated in the remaining of brain in response to local perturbations to the cortex (by magnetic stimulation). This index would only reach higher levels when the response is widespread (which indicates it is integrative) and diversified (which indicates it is informative). If cerebral organoids, or assembloids, begin to shows signs of consciousness, using current clinical standards, the need for forward-thinking recommendations and guidelines will be required.

PERSPECTIVE

Human brain development at a molecular level, and the subsequent resulting thought and behavior, have historically been areas of study impossible to be investigated until now. While the technology of stem cell-derived networks and organoids is still somewhat new, the speed of innovation and progress has resulted in the opportunity to learn about the human brain as never before. We are now building human brains for research and can ask questions, for example, regarding what the molecular foundations of behavior and consciousness may be. Or, what are the underpinnings of neurodegenerative and psychiatric disease, how do the brain and peripheral organs communicate, and can we heal and regenerate the brain? These answers may seem distant but, with a relevant human brain model in hand, they are now much closer than ever before.

AUTHOR CONTRIBUTIONS

MB and GB conceptualized and wrote the manuscript.

REFERENCES

Abud, E. M., Ramirez, R. N., Martinez, E. S., Healy, L. M., Nguyen, C. H. H., Newman, S. A., et al. (2017). iPSC-derived human microglia-like cells to study neurological diseases. *Neuron* 94, 278–293.e9. doi: 10.1016/j.neuron.2017.03.042

Amiri, A., Coppola, G., Scuderi, S., Wu, F., Roychowdhury, T., Liu, F., et al. (2018). Transcriptome and epigenome landscape of human cortical development modeled in organoids. *Science* 362:6420. doi: 10.1126/science.aat6720

Ardhanareeswaran, K., Mariani, J., Coppola, G., Abyzov, A., and Vaccarino, F. M. (2017). Human induced pluripotent stem cells for modelling neurodevelopmental disorders. *Nat. Rev. Neurol.* 13, 265–278. doi: 10.1038/nrneurol.2017.45

Barry, G., Briggs, J. A., Vanichkina, D. P., Poth, E. M., Beveridge, N. J., Ratnu, V. S., et al. (2014). The long non-coding RNA Gomafu is acutely regulated in response to neuronal activation and involved in schizophrenia-associated alternative splicing. *Mol. Psychiatr.* 19, 486–494. doi: 10.1038/mp.2013.45

Birey, F., Andersen, J., Makinson, C. D., Islam, S., Wei, W., Huber, N., et al. (2017). Assembly of functionally integrated human forebrain spheroids. *Nature* 545, 54–59. doi: 10.1038/nature22330

Brassard, J. A., and Lutolf, M. P. (2019). Engineering stem cell self-organization to build better organoids. *Cell Stem Cell* 24, 860–876. doi: 10.1016/j.stem.2019.05.005

Brennand, K. J., Simone, A., Jou, J., Gelboin-Burkhart, C., Tran, N., Sangar, S., et al. (2011). Modelling schizophrenia using human induced pluripotent stem cells. *Nature* 473, 221–225. doi: 10.1038/nature09915

Chambers, S. M., Fasano, C. A., Papapetrou, E. P., Tomishima, M., Sadelain, M., and Studer, L. (2009). Highly efficient neural conversion of human ES and iPS cells by dual inhibition of SMAD signaling. *Nat. Biotechnol.* 27, 275–280. doi: 10.1038/nbt.1529

Cooper, O., Hargus, G., Deleidi, M., Blak, A., Osborn, T., Marlow, E., et al. (2010). Differentiation of human ES and Parkinson's disease iPS cells into ventral midbrain dopaminergic neurons requires a high activity form of SHH, FGF8a and specific regionalization by retinoic acid. *Mol. Cell Neurosci.* 45, 258–266. doi: 10.1016/j.mcn.2010.06.017

Daviaud, N., Friedel, R. H., and Zou, H. (2018). Vascularization and engraftment of transplanted human cerebral organoids in mouse cortex. *eNeuro* 5:ENEURO.0219-18.2018. doi: 10.1523/ENEURO.0219-18.2018

Emdad, L., D'Souza, S. L., Kothari, H. P., Qadeer, Z. A., and Germano, I. M. (2012). Efficient differentiation of human embryonic and induced pluripotent stem cells into functional astrocytes. *Stem Cells Dev.* 21, 404–410. doi: 10.1089/scd.2010.0560

Hansen, D. V., Lui, J. H., Parker, P. R., and Kriegstein, A. R. (2010). Neurogenic radial glia in the outer subventricular zone of human neocortex. *Nature* 464, 554–561. doi: 10.1038/nature08845

Jiang, Y., Zhang, M. J., and Hu, B. Y. (2012). Specification of functional neurons and glia from human pluripotent stem cells. *Protein Cell* 3, 818–825. doi: 10.1007/s13238-012-2086-6

Jo, J., Xiao, Y., Sun, A. X., Cukuroglu, E., Tran, H. D., Goke, J., et al. (2016). Midbrain-like organoids from human pluripotent stem cells contain functional dopaminergic and neuromelanin-producing neurons. *Cell Stem Cell* 19, 248–257. doi: 10.1016/j.stem.2016.07.005

Kaelberer, M. M., Buchanan, K. L., Klein, M. E., Barth, B. B., Montoya, M. M., Shen, X., et al. (2018). A gut-brain neural circuit for nutrient sensory transduction. *Science* 361:eaat5236. doi: 10.1126/science.aat5236

Krefft, O., Jabali, A., Iefremova, V., Koch, P., and Ladewig, J. (2018). Generation of standardized and reproducible forebrain-type cerebral organoids from human induced pluripotent stem cells. *J. Vis. Exp.* 131:e56768. doi: 10.3791/56768

Lancaster, M. A., Renner, M., Martin, C. A., Wenzel, D., Bicknell, L. S., Hurles, M. E., et al. (2013). Cerebral organoids model human brain development and microcephaly. *Nature* 501, 373–379. doi: 10.1038/nature12517

Liu, Y., Liu, H., Sauvey, C., Yao, L., Zarnowska, E. D., and Zhang, S. C. (2013). Directed differentiation of forebrain GABA interneurons from human pluripotent stem cells. *Nat. Protoc.* 8, 1670–1679. doi: 10.1038/nprot.2013.106

Mansour, A. A., Goncalves, J. T., Bloyd, C. W., Li, H., Fernandes, S., Quang, D., et al. (2018). An *in vivo* model of functional and vascularized human brain organoids. *Nat. Biotechnol.* 36, 432–441. doi: 10.1038/nbt.4127

Marchetto, M. C., Carromeu, C., Acab, A., Yu, D., Yeo, G. W., Mu, Y., et al. (2010). A model for neural development and treatment of Rett syndrome using human induced pluripotent stem cells. *Cell* 143, 527–539. doi: 10.1016/j.cell.2010.10.016

McMurtrey, R. J. (2016). Analytic models of oxygen and nutrient diffusion, metabolism dynamics, and architecture optimization in three-dimensional tissue constructs with applications and insights in cerebral organoids. *Tissue Eng. Part C Methods* 22, 221–249. doi: 10.1089/ten.tec.2015.0375

Mertens, J., Reid, D., Lau, S., Kim, Y., and Gage, F. H. (2018). Aging in a dish: iPSC-derived and directly induced neurons for studying brain aging and age-related neurodegenerative diseases. *Annu. Rev. Genet.* 52, 271–293. doi: 10.1146/annurev-genet-120417-031534

Park, J., Wetzel, I., Marriott, I., Dreau, D., D'Avanzo, C., Kim, D. Y., et al. (2018). A 3D human triculture system modeling neurodegeneration

and neuroinflammation in Alzheimer's disease. *Nat. Neurosci.* 21, 941–951. doi: 10.1038/s41593-018-0175-4

Pasca, A. M., Sloan, S. A., Clarke, L. E., Tian, Y., Makinson, C. D., Huber, N., et al. (2015). Functional cortical neurons and astrocytes from human pluripotent stem cells in 3D culture. *Nat. Methods* 12, 671–678. doi: 10.1038/nmeth.3415

Pasca, S. P. (2019). Assembling human brain organoids. *Science* 363, 126–127. doi: 10.1126/science.aau5729

Pocock, J. M., and Piers, T. M. (2018). Modelling microglial function with induced pluripotent stem cells: an update. *Nat. Rev. Neurosci.* 19, 445–452. doi: 10.1038/s41583-018-0030-3

Qian, X., Nguyen, H. N., Song, M. M., Hadiono, C., Ogden, S. C., Hammack, C., et al. (2016). Brain-region-specific organoids using mini-bioreactors for modeling ZIKV exposure. *Cell* 165, 1238–1254. doi: 10.1016/j.cell.2016.04.032

Reardon, S. (2018). Lab-grown 'mini brains' produce electrical patterns that resemble those of premature babies. *Nature* 563:453. doi: 10.1038/d41586-018-07402-0

Ronaldson-Bouchard, K., and Vunjak-Novakovic, G. (2018). Organs-on-a-chip: a fast track for engineered human tissues in drug development. *Cell Stem Cell* 22, 310–324. doi: 10.1016/j.stem.2018.02.011

Roussos, P., Guennewig, B., Kaczorowski, D. C., Barry, G., and Brennand, K. J. (2016). Activity-dependent changes in gene expression in schizophrenia human-induced pluripotent stem cell neurons. *JAMA Psychiatr.* 73, 1180–1188. doi: 10.1001/jamapsychiatry.2016.2575

Russo, F. B., Brito, A., de Freitas, A. M., Castanha, A., de Freitas, B. C., and Beltrao-Braga, P. C. B. (2019). The use of iPSC technology for modeling autism spectrum disorders. *Neurobiol. Dis.* 130:104483. doi: 10.1016/j.nbd.2019.104483

Sarkar, A., Mei, A., Paquola, A. C. M., Stern, S., Bardy, C., Klug, J. R., et al. (2018). Efficient generation of CA3 neurons from human pluripotent stem cells enables modeling of hippocampal connectivity *in vitro*. *Cell Stem Cell* 22, 684–697.e9. doi: 10.1016/j.stem.2018.04.009

Sato, T., Vries, R. G., Snippert, H. J., van de Wetering, M., Barker, N., Stange, D. E., et al. (2009). Single Lgr5 stem cells build crypt-villus structures *in vitro* without a mesenchymal niche. *Nature* 459, 262–265. doi: 10.1038/nature07935

Shi, Y., Inoue, H., Wu, J. C., and Yamanaka, S. (2017). Induced pluripotent stem cell technology: a decade of progress. *Nat. Rev. Drug. Discov.* 16, 115–130. doi: 10.1038/nrd.2016.245

Shi, Y., Kirwan, P., and Livesey, F. J. (2012). Directed differentiation of human pluripotent stem cells to cerebral cortex neurons and neural networks. *Nat. Protoc.* 7, 1836–1846. doi: 10.1038/nprot.2012.116

Takahashi, K., Tanabe, K., Ohnuki, M., Narita, M., Ichisaka, T., Tomoda, K., et al. (2007). Induction of pluripotent stem cells from adult human fibroblasts by defined factors. *Cell.* 131, 861–872. doi: 10.1016/j.cell.2007.11.019

Takahashi, K., and Yamanaka, S. (2006). Induction of pluripotent stem cells from mouse embryonic and adult fibroblast cultures by defined factors. *Cell* 126, 663–676. doi: 10.1016/j.cell.2006.07.024

Trujillo, C. A., Gao, R., Negraes, P. D., Gu, J., Buchanan, J., Preissl, S., et al. (2019). Complex oscillatory waves emerging from cortical organoids model early human brain network development. *Cell Stem Cell* 25, 558–69.e7. doi: 10.1016/j.stem.2019.08.002

Velasco, S., Kedaigle, A. J., Simmons, S. K., Nash, A., Rocha, M., Quadrato, G., et al. (2019). Individual brain organoids reproducibly form cell diversity of the human cerebral cortex. *Nature* 570, 523–527. doi: 10.1038/s41586-019-1289-x

Vierbuchen, T., Ostermeier, A., Pang, Z. P., Kokubu, Y., Sudhof, T. C., and Wernig, M. (2010). Direct conversion of fibroblasts to functional neurons by defined factors. *Nature* 463, 1035–1041. doi: 10.1038/nature08797

Wang, S., Bates, J., Li, X., Schanz, S., Chandler-Militello, D., Levine, C., et al. (2013). Human iPSC-derived oligodendrocyte progenitor cells can myelinate and rescue a mouse model of congenital hypomyelination. *Cell Stem Cell* 12, 252–264. doi: 10.1016/j.stem.2012.12.002

Weick, J. P., Liu, Y., and Zhang, S. C. (2011). Human embryonic stem cell-derived neurons adopt and regulate the activity of an established neural network. *Proc. Natl. Acad. Sci. U.S.A.* 108, 20189–20194. doi: 10.1073/pnas.1108487108

Willerth, S. M., and Sakiyama-Elbert, S. E. (2008). *Combining Stem Cells and Biomaterial Scaffolds for Constructing Tissues and Cell Delivery.* Cambridge, MA: StemBook.

Wimmer, R. A., Leopoldi, A., Aichinger, M., Wick, N., Hantusch, B., Novatchkova, M., et al. (2019). Human blood vessel organoids as a model of diabetic vasculopathy. *Nature* 565, 505–510. doi: 10.1038/s41586-018-0858-8

Xiang, Y., Tanaka, Y., Patterson, B., Kang, Y. J., Govindaiah, G., Roselaar, N., et al. (2017). Fusion of regionally specified hPSC-derived organoids models human brain development and interneuron migration. *Cell Stem Cell* 21, 383–98.e7. doi: 10.1016/j.stem.2017.07.007

Yu, J., Vodyanik, M. A., Smuga-Otto, K., Antosiewicz-Bourget, J., Frane, J. L., Tian, S., et al. (2007). Induced pluripotent stem cell lines derived from human somatic cells. *Science* 318, 1917–1920. doi: 10.1126/science.1151526

Conflict of Interest: The authors declare that the research was conducted in the absence of any commercial or financial relationships that could be construed as a potential conflict of interest.

Copyright © 2020 Bitar and Barry. This is an open-access article distributed under the terms of the Creative Commons Attribution License (CC BY). The use, distribution or reproduction in other forums is permitted, provided the original author(s) and the copyright owner(s) are credited and that the original publication in this journal is cited, in accordance with accepted academic practice. No use, distribution or reproduction is permitted which does not comply with these terms.

frontiers in Molecular Neuroscience

REVIEW
published: 28 February 2020
doi: 10.3389/fnmol.2020.00030

Probing Cortical Activity During Head-Fixed Behavior

*Ann-Sofie Bjerre and Lucy M. Palmer**

Florey Institute of Neuroscience and Mental Health, University of Melbourne, Parkville, VIC, Australia

The cortex is crucial for many behaviors, ranging from sensory-based behaviors to working memory and social behaviors. To gain an in-depth understanding of the contribution to these behaviors, cellular and sub-cellular recordings from both individual and populations of cortical neurons are vital. However, techniques allowing such recordings, such as two-photon imaging and whole-cell electrophysiology, require absolute stability of the head, a requirement not often fulfilled in freely moving animals. Here, we review and compare behavioral paradigms that have been developed and adapted for the head-fixed preparation, which together offer the needed stability for live recordings of neural activity in behaving animals. We also review how the head-fixed preparation has been used to explore the function of primary sensory cortices, posterior parietal cortex (PPC) and anterior lateral motor (ALM) cortex in sensory-based behavioral tasks, while also discussing the considerations of performing such recordings. Overall, this review highlights the head-fixed preparation as allowing in-depth investigation into the neural activity underlying behaviors by providing highly controllable settings for precise stimuli presentation which can be combined with behavioral paradigms ranging from simple sensory detection tasks to complex, cross-modal, memory-guided decision-making tasks.

Keywords: cortex, head-fixed, sensory-based behavior, primary sensory cortices, posterior parietal cortex, anterior lateral motor cortex, Go/NoGo, 2AFC

OPEN ACCESS

Edited by:
Robert J. Harvey, University of the Sunshine Coast, Australia

Reviewed by:
Christina Cerkevich, University of Pittsburgh, United States
Thomas Bessaïh, Université Pierre et Marie Curie, France

***Correspondence:**
Lucy M. Palmer
lucy.palmer@florey.edu.au

Received: *18 October 2019*
Accepted: *10 February 2020*
Published: *28 February 2020*

Citation:
Bjerre A-S and Palmer LM (2020) Probing Cortical Activity During Head-Fixed Behavior. Front. Mol. Neurosci. 13:30. doi: 10.3389/fnmol.2020.00030

INTRODUCTION

Our behavior, the way one acts or conducts oneself, is key to survival. Animals must behave in an appropriate manner to successfully navigate and interact with their surroundings. This involves billions of neurons working together to formulate a cohesive motor output. Therefore, due simply to the sheer numbers involved, understanding the neural basis of behavior is complicated. It is further confounded by the diversity of behaviors, ranging from perception to social interactions to navigation, which involve different classes of neurons, neural interactions as well as brain regions. The activity of individual neurons within the cortex are often highlighted as being crucial for many behaviors, such as sensory-based (Xu et al., 2012; Takahashi et al., 2016) and social behaviors (Rao et al., 2014; Lenschow and Brecht, 2015), as well as anticipation (Erlich et al., 2011; Guo et al., 2014b) and decision making (Harvey et al., 2012). However, it is difficult to clearly state the overall role of the cortex, or a class of cortical neurons, during behavior as the underlying neural activity is dependent on many factors, such as changes in feedforward and feedback information, as well as overall brain state (Poulet and Petersen, 2008).

To understand the contribution of individual neurons during behavior, recordings must be performed from an individual or population of identified neurons, during an active behavioral task. Recording action potential firing in a population of neurons in freely-behaving rodents can be achieved using extracellular probes with a high density of recording sites (Buzsáki, 2004). However, extracellular recordings are fraught with analysis considerations (Buzsáki et al., 2012; Higley, 2012) and cannot typically measure sub-threshold and sub-cellular activity (although see Suzuki and Larkum, 2017). The mere act of behaving makes recording the activity of individual neurons challenging, as most techniques used to measure the activity of individual neurons, such as calcium imaging and patch-clamp electrophysiology, requires absolute stability of the recording preparation. Although miniaturized equipment can record sub-cellular calcium (Helmchen et al., 2001; Ghosh et al., 2011; Cai et al., 2016) and voltage (Burgalossi et al., 2011; Tang et al., 2014) activity from single neurons in animals as they physically move through an environment, these are highly specialized and difficult to implement. Therefore, most studies delving into the sub-cellular neural activity associated with behavior are performed in the head-fixed condition. Unlike the freely moving animal models, the head-fixed preparation allows for highly controllable settings, such as stimulus presentation and motor output. Whether it requires precise stimuli for studying perception, discrimination, decision making or other cognitive tasks, the head-fixed preparation provides the opportunity to precisely control the stimulus delivered to the animal. Head-fixed behavioral models also typically provide high repeatability and employment of standardized techniques (Guo et al., 2014a). This review article brings together studies investigating the neural activity during various behaviors developed for head-fixed preparation. Here, we focus primarily on the role of the cortex in sensory-based behaviors. Historically, research into the role of the cortex during sensory perception and decision making was typically performed in primates (for review see Parker and Newsome, 1998), however, due to recent advances in molecular and optical techniques, rodents are now a crucial animal model and will be the focus of this review.

BEHAVIORAL PARADIGMS

Since there is no one-fits-all behavioral model or task that will highlight the role of all brain regions, it is crucial to consider which model or task will be the most appropriate to engage a particular brain region and how to pair this with an appropriate recording technique. In the head-fixed preparation, the stimulus typically needs to be brought to the animal, as opposed to the animal moving to the stimulus in the freely moving scenario. Therefore, various behavioral tasks have been specifically developed for the head-fixed preparation. These tasks range in complexity, from presenting specific sensory stimuli to the animals to reconstructing an entire sensory environment.

Go/NoGo

Perhaps the easiest way to explore perception and decision making is by presenting one stimulus associated with a single response. This is the basis of the Go/NoGo task (**Figure 1A**), where an animal is presented with a stimulus and trained to report the perception of the stimulus, by either responding or withholding an action. This creates a Hit/Miss scenario for Go trials and a Correct Rejection/False Alarm scenario for NoGo trials. The Go/NoGo task can be used to address simple questions such as sensory perception and modulation (Petreanu et al., 2012; Xu et al., 2012; Takahashi et al., 2016; Micallef et al., 2017). In general, this paradigm takes only a few days to implement (1–3 days; Guo et al., 2014a; Micallef et al., 2017), however, a common weakness of the task, is a potential deviation in motivation leading to erroneous reporting. To overcome the decreased motivation towards obtaining a reward, the Go/NoGo task can be further advanced by applying the signal detection theory, as reviewed by Carandini and Churchland (2013). By introducing a stimulus-based NoGo signal that is of same stimulus type but of different character (rather than the absence of a stimulus as a NoGo signal, commonly referred to as "Catch trials"), the animal has to discriminate between two stimuli, reporting only one of them, instead of simply reporting whenever the stimulus is detected. Tasks using this paradigm are often referred to as discrimination tasks (**Figure 1B**; Gilad et al., 2018; Helmchen et al., 2018) and in general take longer to learn than the simple Go/NoGo task (1–3 weeks; Guo et al., 2014a; Gilad et al., 2018; Helmchen et al., 2018). When water-deprived, animals are typically highly motivated to perform the task (Guo et al., 2014a). Since the instinctive reaction is to lick as soon as the stimuli has been detected, a short delay can be incorporated between stimulus and response period to temporally separate the different epochs (Guo et al., 2014a), however implementing a delay requires further training (Helmchen et al., 2018).

Two Alternative Forced Choice

Similar to the Go/NoGo task, the two-alternative forced-choice (2AFC) task (**Figure 1C**) can be used to explore perceptual decision making. Here, an animal is presented with two stimuli however, instead of withholding a response to one of the stimuli (as in the Go/NoGo task), the animal now must report in both cases. This can be accomplished by either having the animal lick left or right (O'Connor et al., 2010a,b; Guo et al., 2014b; Peron et al., 2015; Zhong et al., 2019), turn a steering wheel (Burgess et al., 2017) or push a joystick (Estebanez et al., 2017; Morandell and Huber, 2017). The 2AFC task adds another level of clarity to behavioral outcomes, as the task design eliminates uncertainty behind NoGo responses, which may not be due to an inability to perform the task, but instead due to lack of motivation/engagement. The 2AFC task is however not completely immune to behavioral response misinterpretations, as animals can be biased toward one side of reporting (Guo et al., 2014a). As with all behaviors, the time it takes an animal to learn the 2AFC task depends on several factors such as sensory modality, type of stimulus, training methods and number of trials per session. However, due to its increased complexity compared to the simple discrimination tasks, learning the 2AFC task, in general, takes longer, ranging between 1 and 6 weeks (Mayrhofer et al., 2013; Guo et al.,

2014a,b). Although it potentially can be considered a more robust behavior than the Go/NoGo tasks, the increased learning time can be a consideration for various chronic recording techniques. The 2AFC task is adaptable and can be changed according to particular experiments/questions, such as the two alternative unforced choices (2AUC) task which combines the 2AFC task with a "NoGo" signal, rewarding the animal for not responding (Burgess et al., 2017). The adaptability of the 2AFC task has led to many sensory systems being probed using this two-response behavior, including the vibrissal (Mayrhofer et al., 2013; Li et al., 2015; Peron et al., 2015), olfactory (Zariwala et al., 2013), visual (Busse et al., 2011; Burgess et al., 2017) and auditory (Znamenskiy and Zador, 2013; Wei et al., 2019) to name a few.

Working Memory Models

To probe the neural basis of higher cognitive functions such as working memory in the head-fixed preparation, behaviors have been developed that are based on the simpler behavioral tasks, such as the Go/NoGo and 2AFC. Working memory has been addressed using a delay-task in both monkeys (Quintana et al., 1988; Yajeya et al., 1988; Fuster, 2001) and rodents (Gilad et al., 2018; Inagaki et al., 2019). Here, animals are presented with a stimulus followed by a delay during which the animal needs to retain their decision until they are able to report their decision, often indicated by a response cue (**Figure 1D**). Of greater complexity are the comparison-based working memory tasks such as (but not limited to) Delayed Nonmatch to Sample (**Figure 1E**; Dudchenko, 2004), which engages working memory by having two sensory stimuli separated by an inter-stimulus delay, forcing the animal to retain a memory trace of the first stimulus to compare to the second stimulus. For the Nonmatch to Sample working memory task the animal has to compare the stimuli and report if the second stimulus is different (mismatch) to the sample or withhold its response if the two are identical (match). This working memory task builds on the principles of the Go/NoGo task and has for example been used for odor samples (Liu et al., 2014). The comparison-based working memory tasks can also build upon the principles of the 2AFC paradigm, as is the case for the pioneering Flutter Discrimination task developed for primates (Mountcastle et al., 1990; Hernández et al., 1997). This task has been successfully adapted to freely moving rats (Fassihi et al., 2014), but to our knowledge, it has not yet been successfully adapted to head-fixed rodents. For a review on other working memory tasks in rodents, see Dudchenko (2004).

Locomotion and Exploration

Many, if not all, behaviors require the integration of feedforward and feedback information from multiple senses. Take for example spatial exploration. Here, the visual system relies on the coordination of visual input with motor output to successfully explore and navigate through an environment (Randel et al., 2014; Heindorf et al., 2018). Probing sub-cellular neural activity during locomotion requires a behavioral platform that enables movement and associated stimuli in a head-fixed preparation. This can be achieved with a spherical (Dombeck et al., 2007; Harvey et al., 2012; Schmidt-Hieber and Häusser, 2013; Heindorf et al., 2018), circular (Hawrylycz et al., 2016; Schneider et al., 2018) or linear (Domnisoru et al., 2013; Lovett-Barron et al., 2014; Cichon and Gan, 2015; Bittner et al., 2017) track which allows precise location to be measured during locomotion in small laboratory animals. These platforms can be paired with a virtual reality-based environment. Combined with various sensory stimuli, platforms that enable locomotion during head-fixation are used to address various questions, including the neural activity underlying spatial navigation (Harvey et al., 2009; Dombeck et al., 2010; Domnisoru et al., 2013; Sheffield et al., 2017; Thurley and Ayaz, 2017), sensory processing (Niell and Stryker, 2010; Saleem et al., 2013; Makino and Komiyama, 2015; Sofroniew et al., 2015; Radvansky and Dombeck, 2018), arousal (Niell and Stryker, 2010; Polack et al., 2013; McGinley et al., 2015; Vinck et al., 2015; Shimaoka et al., 2018) and learning and memory (Lovett-Barron et al., 2014; Cichon and Gan, 2015). Behavioral platforms have also been developed that enable head-fixed mice to navigate through a physical environment (Kislin et al., 2014; Nashaat et al., 2016), as opposed to a virtual reality-based environment. Termed the air-track system (Nashaat et al., 2016), this is a lightweight maze floating on air, much like the spherical ball used in virtual reality set-ups, where the animal is head-fixed and uses its paws to navigate the maze. The air-track system offers both the stability required for most single-cell recording techniques as well as activation of different sensory modalities coupled to motor output in a "real-world" fashion.

EXPLORING CORTICAL FUNCTIONS USING HEAD-FIXED BEHAVIORAL MODELS

The neocortex is enigmatic. It is a diverse structure with various regions dedicated to specific aspects of behaviors such as encoding sensory information and integrating this information with other sensory inputs. With the classical view of the role of the cortex during simple sensory-based behavior and encoding recently being challenged (Hong et al., 2018; Beltramo and Scanziani, 2019), deeper insight into the neural networks contributing to sensory perception and cognition is required. Below are summaries of the neural encoding of behavior in selected cortical regions that aim to disentangle their role in sensory-based behaviors (**Figure 2**).

Primary Sensory Cortices

The role of the primary sensory cortex is to encode sensory information. To investigate the neural basis of sensory encoding at the cellular or sub-cellular level, various head-fixed behavioral paradigms have been developed. Combining the clearly defined cortical-microstructure with the prominent and easily assessable location of whiskers, the barrel cortex provides an ideal primary sense to probe during sensory-based behavior in the head-fixed preparation. Therefore, numerous studies have probed the neural activity contributing to vibrissae–based behavior. For example, the neural activity underlying perception of whisker deflection, induced by magnetic stimulation of identified whiskers coated

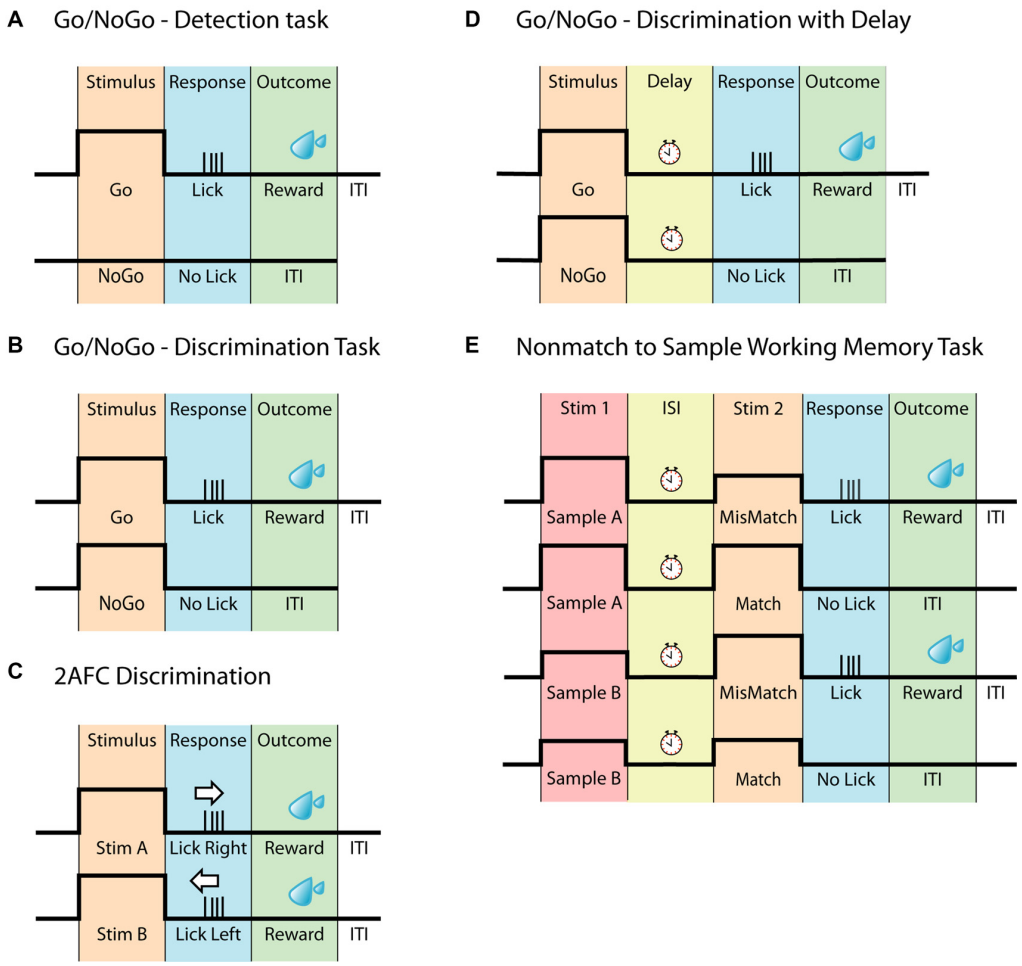

FIGURE 1 | Head-fixed behavioral paradigms. **(A)** Schematic of the Go/NoGo task often referred to as a detection task. The animal should only respond upon detecting the stimulus. **(B)** Schematic of the Go/NoGo task involving discrimination of two stimuli. The animal should only respond to the Go-stimulus. This task is often referred to as a discrimination task. **(C)** Schematic of the two-alternative forced-choice (2AFC) task. Similar to **(B)**, this task requires the discrimination between two different stimuli however, to eliminate pseudo responses, the animal must respond to both stimuli, for example by either licking left or licking right. **(D)** Schematic of the Go/NoGo discrimination task with delay. This task differs from **(B)** by having a delay separating the stimulus and the response. **(E)** Schematic of the Nonmatch to Sample Working memory task, based on the Go/NoGo discrimination paradigm. In this task, the animal is presented with two consecutive stimuli, separated by a delay. The animal must compare the two stimuli and respond accordingly.

with metallic particles has been probed using two-photon calcium imaging (Takahashi et al., 2016) and whole-cell patch-clamp (Sachidhanandam et al., 2013). Using a simple Go/NoGo behavioral task, these studies reveal that the perception of highly controlled whisker deflection requires calcium spikes in apical dendrites of layer 5 pyramidal neurons (Takahashi et al., 2016) and generates a reliable excitatory response in the somatic membrane potential which depends on cortical state (Sachidhanandam et al., 2013). Similarly, several studies have contributed to the understanding of whisker-mediated object localization, using variations of the Go/NoGo paradigm. For instance, active touch, which is the combination of whisking and touch, generates a strong activation of the apical tuft dendrites of layer 5 pyramidal neurons in the barrel cortex, driven by projections from the primary motor cortex (Xu et al., 2012). Axonal projections from the primary motor cortex to S1 were found to relay signals related to many task-related features, which, combined with ongoing sensory input, allows S1 neurons to combine and compute object localization (Petreanu et al., 2012). Moreover, S1 projections are recruited differently depending on task conditions. Chen et al. (2013) reported higher activity in neurons projecting to the primary motor cortex during the object localization task, while more neurons which project to secondary somatosensory cortex were active during texture discrimination. Despite these differences, both primary motor cortex-projecting and secondary somatosensory cortex-projecting S1 neurons could discriminate between Go and NoGo trials. Neural encoding of trial type during whisker-based object localization has also been shown to be both cell-type (Yu et al., 2019) and layer-specific, with a greater proportion of discriminating neurons located within layer 4 and 5 of the barrel cortex (O'Connor et al., 2010b). Taken

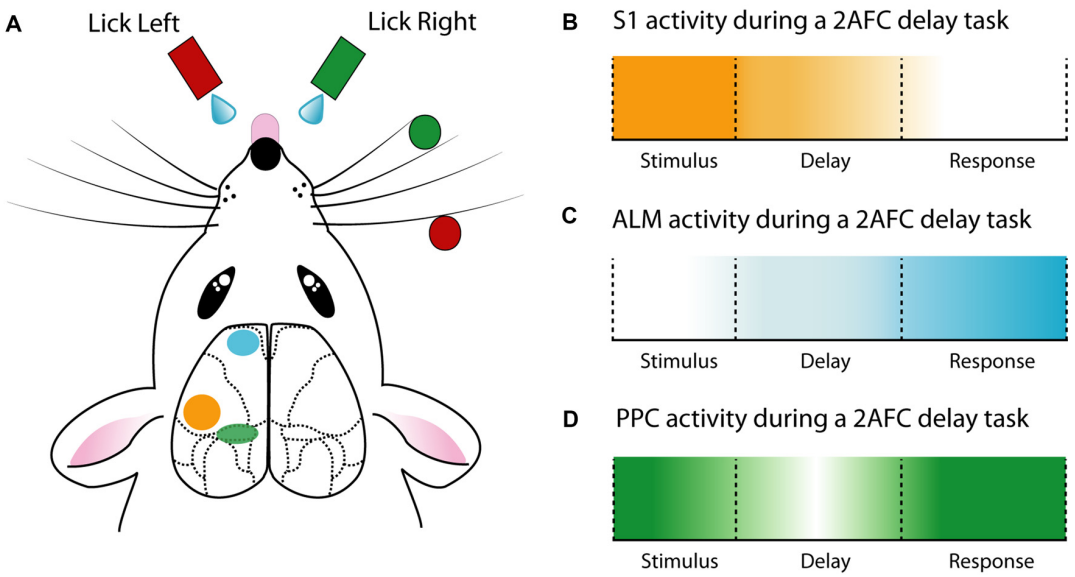

FIGURE 2 | Cortical activity during a delay 2AFC task. **(A)** Schematic of a whisker-mediated object localization 2AFC task. Modified from O'Connor et al. (2010a,b), Guo et al. (2014b) and Chen et al. (2017). **(B)** The primary somatosensory cortex (S1) has maximal influence during stimulus presentation (Guo et al., 2014b). **(C)** Anterior lateral motor cortex (ALM) ramps activity during the delay epoch and reaches a maximum during the response epoch (Guo et al., 2014b; Li et al., 2015; Inagaki et al., 2018). **(D)** The posterior parietal cortex (PPC) is active throughout the 2AFC task, especially the stimulus and response epochs (Harvey et al., 2012; Goard et al., 2016).

together, the simple Go/NoGo behavioral task adopted in various laboratories has helped unravel the complex microcircuitry underlying touch perception and object localization.

Another sensory cortical region that has been the focus of much research is the primary visual cortex (V1). Here, the head-fixed preparation is advantageous as the animal can be oriented towards the visual stimulus (although this does not ensure stereotyped pupil location, see Wallace et al., 2013). By combining the head-fixed preparation with a spherical treadmill (Niell and Stryker, 2010) illustrated that the V1 response is strongly modulated by behavioral state, i.e., moving, stationary, sleeping, etc. Surprisingly, even in the absence of visual input, V1 neurons typically respond to a combination of running speed and visual speed (Polack et al., 2013; Saleem et al., 2013). Other studies have focused on the involvement of V1 in perceptual decision-making tasks. Here, V1 neurons were found to respond mainly during stimulus presentation, and inhibition of V1 impaired performance of the task (Goard et al., 2016). The head-fixed preparation also enables precise control over the direction and intensity of sound delivery for investigating sensory encoding and functional connectivity in the primary auditory cortex (A1; Francis et al., 2018). Using a sound-guided detection task (Kato et al., 2015) found that task engagement results in an increase in the fraction of responsive excitatory neurons, whereas responsive somatostatin expressing interneurons were reduced. Similar results were obtained in another study using two behavioral tasks of different complexity. Here, A1 can be bypassed when discriminating between simple sounds but is necessary when the discrimination involves more complex sounds with frequency overlap (Ceballo et al., 2019).

Posterior Parietal Cortex

The posterior parietal cortex (PPC) is a classical association cortical area which is involved in various behaviors, such as decision making (Raposo et al., 2014; Goard et al., 2016; Runyan et al., 2017), evidence accumulation (Morcos and Harvey, 2016), navigation (Krumin et al., 2018) and sensory representation (Song et al., 2017; Akrami et al., 2018; Mohan et al., 2018). Often described as an integrative hub for multiple senses (Song et al., 2017; Mohan et al., 2018; Lyamzin and Benucci, 2019), the PPC receives input from various sensory cortices (Wilber et al., 2015; Zhuang et al., 2017), the thalamus (Reep et al., 1994) as well as neuromodulatory input from the basal forebrain (Broussard, 2012).

Using a memory-guided navigation task in a virtual reality setup (Harvey et al., 2012) explored the neural dynamics of L2/3 pyramidal neurons within PPC using two-photon calcium imaging. Here, neurons exhibited choice-specific sequences that could be categorized according to their activity pattern during different task epochs (epoch-specific activity). This encoding of memory-guided decisions was mostly stable on single days but was reorganized over weeks (Driscoll et al., 2017). Although overall PPC activity reaches a set point to perform the memory-guided navigation task, individual neurons shift their activity over days, some being more inconsistent than others. Learned task features may have less consistency over time, as the neurons with the least consistent relationship between activity and behavior received greater information about task features, such as trial type and maze position (Driscoll et al., 2017). Since the PPC encodes posture (Mimica et al., 2018), it is important to note that similar involvement of the PPC during

memory-guided decisions was also recorded in head-fixed visual discrimination tasks that did not involve navigation (Goard et al., 2016).

Anterior Lateral Motor Cortex

Due to the known involvement in motor planning and movement, the role of the anterior lateral motor cortex (ALM) has been extensively investigated during behavior. Building on previous work (Guo et al., 2014b) demonstrated the importance of the ALM in a 2AFC whisker-mediated delay task. Here, the ALM showed choice-specific preparatory activity as well as movement-related activity, with unilateral inhibition of the ALM during the delay epoch biasing the choice to the ipsilateral direction. Confirming and expanding on these findings (Li et al., 2015) demonstrated that ALM neurons have lateralized preference for contralateral movements. This lateralization was found to be driven by pyramidal tract neurons and not intratelencephallic neurons, although both were activated during preparatory activity. Within the ALM, the preparatory activity in intratelencephallic neurons was converted to motor output in pyramidal tract neurons, affecting the upcoming motor output. Interestingly, despite encoding sensory information (Chen et al., 2017), the ALM is required for motor planning independent of sensory modality (Inagaki et al., 2018). Here, tactile- or auditory-based tasks both displayed diverse but consistent ALM activity during a delay epoch, with behavioral performance decreasing during ALM photoinhibition. Combined with recordings during free-behavior (Erlich et al., 2011), these studies highlight the important role of the ALM in the planning and execution of motor output.

IMPORTANT CONSIDERATIONS WHEN EXPLORING CORTICAL ACTIVITY USING HEAD-FIXED PARADIGMS

While head-fixation is crucial for exploring the cellular and sub-cellular basis of many behaviors, the head-fixed state can alter overall behavior. For example, head-restrained rats have far fewer whisking movements compared with freely moving behavior (Sellien et al., 2005). Likewise (Whishaw et al., 2017) illustrated that rats used alternative strategies during exploration and reach-and-grasp movement when in the head-fixed state locating objects using "touch-release-grasp" rather than sniffing. However, when directly compared, there was no difference in performance during odor discrimination in head-fixed and freely moving mice (Abraham et al., 2012). Although sensory perception may not be dramatically altered, the head-fixed preparation limits natural aspects of behavior and the ability to naturally explore and maneuver the body during a sensory-based task. Therefore, although the head-fixed preparation is advantageous in the delivery of precise and reproducible stimuli, it has the disadvantage of a non-physiological restraint of the animal. Since recordings in both the head-fixed and freely-moving preparations illustrate that the head-fixed preparation influences brain state and neural activity (Lovett-Barron et al., 2014; Chung et al., 2017; Whishaw et al., 2017), simply freeing the animal's body to move during recordings would not mitigate the non-physiological aspect of the head-fixed preparation. However, it must be noted that when reviewing neural activity underlying sensory-based cognitive tasks, limiting feedback from other systems such as the motor (Vinck et al., 2015; Dadarlat and Stryker, 2017; Ayaz et al., 2019) and head direction (Peyrache et al., 2015) systems can be advantageous.

It is important to consider the caveats of behavioral paradigms when exploring the cortical function and it must be noted that not all behaviors can be investigated using the head-fixed preparation, such as complex social behavior that requires physical interactions. Avoiding the need for head-fixation, miniaturized head-mounted microscopes and probes (Flusberg et al., 2008; Ghosh et al., 2011; Cai et al., 2016) allow the investigation of neural activity during natural behaviors (Helmchen et al., 2001; Sawinski et al., 2009; Miyamoto and Murayama, 2016; Chung et al., 2017; Zong et al., 2017; Meyer et al., 2018; Valero and English, 2019). Further advances using wireless head-mounted microscopes (Fan et al., 2011; Pinnell et al., 2015) remove the mechanical disturbances caused by cables attached to the animal. The use of miniaturized recording techniques allows freedom of movement, which is advantageous from an overall behavioral aspect, however freely moving animals do not allow the same highly controllable settings the head-fixed preparation allows. Furthermore, not all recording techniques have been developed for the freely moving preparation, and some head-mounted probes are not suitable for mice (due to weight and size requirements). Therefore, the head-fixed preparation is still typically deemed necessary for the in-depth investigation of cortical and sub-cortical activity during many behaviors.

CONCLUSION

The cortex and its role in behavior is enigmatic. To understand the underlying cortical circuits required for the execution of behaviors, it is crucial to examine neural activity while an animal is behaving. This can be achieved using the head-fixed preparation which provides highly controllable settings, and thereby precise stimuli presentation while allowing simultaneous cellular and sub-cellular recordings. The head-fixed preparation can be combined with behavioral paradigms ranging from simple sensory detection tasks, to complex, cross-modal, memory-guided decision-making tasks, allowing in-depth investigation into the neural activity underlying behaviors. Experiments using this preparation have provided insight into neural activity in various brain regions during sensory processing and higher-order cognitive functions. Although the head-fixed preparation limits natural behavior due to the head restraint, it provides valuable information about cognitive behaviors and the cortices involved. We are only beginning to understand and unravel the complexity of the neural activity underlying behavior, and while there is a rapid improvement in tethered and wireless recording techniques, the head-fixed preparation seems unlikely to be replaced as improvements to the head-fixed preparation steadily provides new platforms and setups, as well as new

behavioral tasks to explore cortical functions during simple and complex behaviors. As recording techniques continue to push the boundaries of possibilities, such as functional imaging of deep brain structures with three-photon imaging (Wang et al., 2018) and simultaneous extracellular voltage recordings from hundreds of channels over 10 mm using the neuropixel probes (Jun et al., 2017), the head-fixed preparation will also continue to advance. For example, self-initiated head-fixation in the home cage will allow for the neural activity underlying more physiological behaviors to be investigated (Murphy et al., 2016). While there is no one-fits-all behavioral model, the flexibility of the head-fixed behavioral paradigms, combined with functional cellular and subcellular recordings and manipulations, provides insight into the neural dynamics underlying behaviors. Not only does this offer valuable information about single-cell dynamics, but it also expands our understanding of the individual cortices, both their individual and combined contributions to the overall behavioral output.

AUTHOR CONTRIBUTIONS

A-SB and LP conceptualized and wrote the manuscript.

FUNDING

This work was supported by the NHMRC (APP1086082, APP1063533), ARC (DP160103047) and the Sylvia and Charles Viertel Charitable Foundation.

REFERENCES

Abraham, N. M., Guerin, D., Bhaukaurally, K., and Carleton, A. (2012). Similar odor discrimination behavior in head-restrained and freely moving mice. *PLoS One* 7:e51789. doi: 10.1371/journal.pone.0051789

Akrami, A., Kopec, C. D., Diamond, M. E., and Brody, C. D. (2018). Posterior parietal cortex represents sensory history and mediates its effects on behaviour. *Nature* 554, 368–372. doi: 10.1038/nature25510

Ayaz, A., Stauble, A., Hamada, M., Wulf, M. A., Saleem, A. B., and Helmchen, F. (2019). Layer-specific integration of locomotion and sensory information in mouse barrel cortex. *Nat. Commun.* 10:2585. doi: 10.1038/s41467-019-10564-8

Beltramo, R., and Scanziani, M. (2019). A collicular visual cortex: neocortical space for an ancient midbrain visual structure. *Science* 363, 64–69. doi: 10.1126/science.aau7052

Bittner, K. C., Milstein, A. D., Grienberger, C., Romani, S., and Magee, J. C. (2017). Behavioral time scale synaptic plasticity underlies CA1 place fields. *Science* 357, 1033–1036. doi: 10.1126/science.aan3846

Broussard, J. I. (2012). Posterior parietal cortex dynamically ranks topographic signals *via* cholinergic influence. *Front. Integr. Neurosci.* 6:32. doi: 10.3389/fnint.2012.00032

Burgalossi, A., Herfst, L., Von Heimendahl, M., Forste, H., Haskic, K., Schmidt, M., et al. (2011). Microcircuits of functionally identified neurons in the rat medial entorhinal cortex. *Neuron* 70, 773–786. doi: 10.1016/j.neuron.2011.04.003

Burgess, C. P., Lak, A., Steinmetz, N. A., Zatka-Haas, P., Bai Reddy, C., Jacobs, E. A. K., et al. (2017). High-yield methods for accurate two-alternative visual psychophysics in head-fixed mice. *Cell Rep.* 20, 2513–2524. doi: 10.1016/j.celrep.2017.08.047

Busse, L., Ayaz, A., Dhruv, N. T., Katzner, S., Saleem, A. B., Scholvinck, M. L., et al. (2011). The detection of visual contrast in the behaving mouse. *J. Neurosci.* 31, 11351–11361. doi: 10.1523/JNEUROSCI.6689-10.2011

Buzsáki, G. (2004). Large-scale recording of neuronal ensembles. *Nat. Neurosci.* 7, 446–451. doi: 10.1038/nn1233

Buzsáki, G., Anastassiou, C. A., and Koch, C. (2012). The origin of extracellular fields and currents—EEG, ECoG, LFP and spikes. *Nat. Rev. Neurosci.* 13, 407–420. doi: 10.1038/nrn3241

Cai, D. J., Aharoni, D., Shuman, T., Shobe, J., Biane, J., Song, W., et al. (2016). A shared neural ensemble links distinct contextual memories encoded close in time. *Nature* 534, 115–118. doi: 10.1038/nature17955

Carandini, M., and Churchland, A. K. (2013). Probing perceptual decisions in rodents. *Nat. Neurosci.* 16, 824–831. doi: 10.1038/nn.3410

Ceballo, S., Piwkowska, Z., Bourg, J., Daret, A., and Bathellier, B. (2019). Targeted cortical manipulation of auditory perception. *Neuron* 104, 1168.e5–1179.e5. doi: 10.1016/j.neuron.2019.09.043

Chen, J. L., Carta, S., Soldado-Magraner, J., Schneider, B. L., and Helmchen, F. (2013). Behaviour-dependent recruitment of long-range projection neurons in somatosensory cortex. *Nature* 499, 336–340. doi: 10.1038/nature12236

Chen, T. W., Li, N., Daie, K., and Svoboda, K. (2017). A map of anticipatory activity in mouse motor cortex. *Neuron* 94, 866.e4–879.e4. doi: 10.1016/j.neuron.2017.05.005

Chung, J., Sharif, F., Jung, D., Kim, S., and Royer, S. (2017). Micro-drive and headgear for chronic implant and recovery of optoelectronic probes. *Sci. Rep.* 7:2773. doi: 10.1038/s41598-017-03340-5

Cichon, J., and Gan, W. B. (2015). Branch-specific dendritic Ca^{2+} spikes cause persistent synaptic plasticity. *Nature* 520, 180–185. doi: 10.1038/nature14251

Dadarlat, M. C., and Stryker, M. P. (2017). Locomotion enhances neural encoding of visual stimuli in mouse V1. *J. Neurosci.* 37, 3764–3775. doi: 10.1523/jneurosci.2728-16.2017

Dombeck, D. A., Harvey, C. D., Tian, L., Looger, L. L., and Tank, D. W. (2010). Functional imaging of hippocampal place cells at cellular resolution during virtual navigation. *Nat. Neurosci.* 13, 1433–1440. doi: 10.1038/nn.2648

Dombeck, D. A., Khabbaz, A. N., Collman, F., Adelman, T. L., and Tank, D. W. (2007). Imaging large-scale neural activity with cellular resolution in awake, mobile mice. *Neuron* 56, 43–57. doi: 10.1016/j.neuron.2007.08.003

Domnisoru, C., Kinkhabwala, A. A., and Tank, D. W. (2013). Membrane potential dynamics of grid cells. *Nature* 495, 199–204. doi: 10.1038/nature11973

Driscoll, L. N., Pettit, N. L., Minderer, M., Chettih, S. N., and Harvey, C. D. (2017). Dynamic reorganization of neuronal activity patterns in parietal cortex. *Cell* 170, 986.e16–999.e16. doi: 10.1016/j.cell.2017.07.021

Dudchenko, P. A. (2004). An overview of the tasks used to test working memory in rodents. *Neurosci. Biobehav. Rev.* 28, 699–709. doi: 10.1016/j.neubiorev.2004.09.002

Erlich, J. C., Bialek, M., and Brody, C. D. (2011). A cortical substrate for memory-guided orienting in the rat. *Neuron* 72, 330–343. doi: 10.1016/j.neuron.2011.07.010

Estebanez, L., Hoffmann, D., Voigt, B. C., and Poulet, J. F. A. (2017). Parvalbumin-expressing GABAergic neurons in primary motor cortex signal reaching. *Cell Rep.* 20, 308–318. doi: 10.1016/j.celrep.2017.06.044

Fan, D., Rich, D., Holtzman, T., Ruther, P., Dalley, J. W., Lopez, A., et al. (2011). A wireless multi-channel recording system for freely behaving mice and rats. *PLoS One* 6:e22033. doi: 10.1371/journal.pone.0022033

Fassihi, A., Akrami, A., Esmaeili, V., and Diamond, M. E. (2014). Tactile perception and working memory in rats and humans. *Proc. Natl. Acad. Sci. U S A* 111, 2331–2336. doi: 10.1073/pnas.1315171111

Flusberg, B. A., Nimmerjahn, A., Cocker, E. D., Mukamel, E. A., Barretto, R. P., Ko, T. H., et al. (2008). High-speed, miniaturized fluorescence microscopy in freely moving mice. *Nat. Methods* 5, 935–938. doi: 10.1038/nmeth.1256

Francis, N. A., Winkowski, D. E., Sheikhattar, A., Armengol, K., Babadi, B., and Kanold, P. O. (2018). Small networks encode decision-making in primary auditory cortex. *Neuron* 97, 885.e6–897.e6. doi: 10.1016/j.neuron.2018.01.019

Fuster, J. M. (2001). The prefrontal cortex—an update: time is of the essence. *Neuron* 30, 319–333. doi: 10.1016/s0896-6273(01)00285-9

Ghosh, K. K., Burns, L. D., Cocker, E. D., Nimmerjahn, A., Ziv, Y., Gamal, A. E., et al. (2011). Miniaturized integration of a fluorescence microscope. *Nat. Methods* 8, 871–878. doi: 10.1038/nmeth.1694

Gilad, A., Gallero-Salas, Y., Groos, D., and Helmchen, F. (2018). Behavioral strategy determines frontal or posterior location of short-term memory in neocortex. *Neuron* 99, 814.e7–828.e7. doi: 10.1016/j.neuron.2018.07.029

Goard, M. J., Pho, G. N., Woodson, J., and Sur, M. (2016). Distinct roles of visual, parietal and frontal motor cortices in memory-guided sensorimotor decisions. *Elife* 5:e13764. doi: 10.7554/elife.13764

Guo, Z. V., Hires, S. A., Li, N., O'Connor, D. H., Komiyama, T., Ophir, E., et al. (2014a). Procedures for behavioral experiments in head-fixed mice. *PLoS One* 9:e88678. doi: 10.1371/journal.pone.0088678

Guo, Z. V., Li, N., Huber, D., Ophir, E., Gutnisky, D., Ting, J. T., et al. (2014b). Flow of cortical activity underlying a tactile decision in mice. *Neuron* 81, 179–194. doi: 10.1016/j.neuron.2013.10.020

Harvey, C. D., Coen, P., and Tank, D. W. (2012). Choice-specific sequences in parietal cortex during a virtual-navigation decision task. *Nature* 484, 62–68. doi: 10.1038/nature10918

Harvey, C. D., Collman, F., Dombeck, D. A., and Tank, D. W. (2009). Intracellular dynamics of hippocampal place cells during virtual navigation. *Nature* 461, 941–946. doi: 10.1038/nature08499

Hawrylycz, M., Anastassiou, C., Arkhipov, A., Berg, J., Buice, M., Cain, N., et al. (2016). Inferring cortical function in the mouse visual system through large-scale systems neuroscience. *Proc. Natl. Acad. Sci. U S A* 113, 7337–7344. doi: 10.1073/pnas.1512901113

Heindorf, M., Arber, S., and Keller, G. B. (2018). Mouse motor cortex coordinates the behavioral response to unpredicted sensory feedback. *Neuron* 99, 1040.e5–1054.e5. doi: 10.1016/j.neuron.2018.07.046

Helmchen, F., Fee, M. S., Tank, D. W., and Denk, W. (2001). A miniature head-mounted two-photon microscope. high-resolution brain imaging in freely moving animals. *Neuron* 31, 903–912. doi: 10.1016/s0896-6273(01)00421-4

Helmchen, F., Gilad, A., and Chen, J. L. (2018). Neocortical dynamics during whisker-based sensory discrimination in head-restrained mice. *Neuroscience* 368, 57–69. doi: 10.1016/j.neuroscience.2017.09.003

Hernández, A., Salinas, E., Garcia, R., and Romo, R. (1997). Discrimination in the sense of flutter: new psychophysical measurements in monkeys. *J. Neurosci.* 17, 6391–6400. doi: 10.1523/jneurosci.17-16-06391.1997

Higley, M. J. (2012). "Determination of cortical circuit function using current source-density analysis *in vivo*," in *Neuronal Network Analysis*, eds T. Fellin and M. Halassa (Totowa, NJ: Humana Press), 205–218.

Hong, Y. K., Lacefield, C. O., Rodgers, C. C., and Bruno, R. M. (2018). Sensation, movement and learning in the absence of barrel cortex. *Nature* 561, 542–546. doi: 10.1038/s41586-018-0527-y

Inagaki, H. K., Fontolan, L., Romani, S., and Svoboda, K. (2019). Discrete attractor dynamics underlies persistent activity in the frontal cortex. *Nature* 566, 212–217. doi: 10.1038/s41586-019-0919-7

Inagaki, H. K., Inagaki, M., Romani, S., and Svoboda, K. (2018). Low-dimensional and monotonic preparatory activity in mouse anterior lateral motor cortex. *J. Neurosci.* 38, 4163–4185. doi: 10.1523/jneurosci.3152-17.2018

Jun, J. J., Steinmetz, N. A., Siegle, J. H., Denman, D. J., Bauza, M., Barbarits, B., et al. (2017). Fully integrated silicon probes for high-density recording of neural activity. *Nature* 551, 232–236. doi: 10.1038/nature24636

Kato, H. K., Gillet, S. N., and Isaacson, J. S. (2015). Flexible sensory representations in auditory cortex driven by behavioral relevance. *Neuron* 88, 1027–1039. doi: 10.1016/j.neuron.2015.10.024

Kislin, M., Mugantseva, E., Molotkov, D., Kulesskaya, N., Khirug, S., Kirilkin, I., et al. (2014). Flat-floored air-lifted platform: a new method for combining behavior with microscopy or electrophysiology on awake freely moving rodents. *J. Vis. Exp.* 88:e51869. doi: 10.3791/51869

Krumin, M., Lee, J. J., Harris, K. D., and Carandini, M. (2018). Decision and navigation in mouse parietal cortex. *Elife* 7:e42583. doi: 10.7554/elife.42583

Lenschow, C., and Brecht, M. (2015). Barrel cortex membrane potential dynamics in social touch. *Neuron* 85, 718–725. doi: 10.1016/j.neuron.2014.12.059

Li, N., Chen, T. W., Guo, Z. V., Gerfen, C. R., and Svoboda, K. (2015). A motor cortex circuit for motor planning and movement. *Nature* 519, 51–56. doi: 10.1038/nature14178

Liu, D., Gu, X., Zhu, J., Zhang, X., Han, Z., Yan, W., et al. (2014). Medial prefrontal activity during delay period contributes to learning of a working memory task. *Science* 346, 458–463. doi: 10.1126/science.1256573

Lovett-Barron, M., Kaifosh, P., Kheirbek, M. A., Danielson, N., Zaremba, J. D., Reardon, T. R., et al. (2014). Dendritic inhibition in the hippocampus supports fear learning. *Science* 343, 857–863. doi: 10.1126/science.1247485

Lyamzin, D., and Benucci, A. (2019). The mouse posterior parietal cortex: anatomy and functions. *Neurosci. Res.* 140, 14–22. doi: 10.1016/j.neures.2018.10.008

Makino, H., and Komiyama, T. (2015). Learning enhances the relative impact of top-down processing in the visual cortex. *Nat. Neurosci.* 18, 1116–1122. doi: 10.1038/nn.4061

Mayrhofer, J. M., Skreb, V., Von Der Behrens, W., Musall, S., Weber, B., and Haiss, F. (2013). Novel two-alternative forced choice paradigm for bilateral vibrotactile whisker frequency discrimination in head-fixed mice and rats. *J. Neurophysiol.* 109, 273–284. doi: 10.1152/jn.00488.2012

McGinley, M. J., David, S. V., and Mccormick, D. A. (2015). Cortical membrane potential signature of optimal states for sensory signal detection. *Neuron* 87, 179–192. doi: 10.1016/j.neuron.2015.05.038

Meyer, A. F., Poort, J., O'Keefe, J., Sahani, M., and Linden, J. F. (2018). A head-mounted camera system integrates detailed behavioral monitoring with multichannel electrophysiology in freely moving mice. *Neuron* 100, 46.e7–60.e7. doi: 10.1016/j.neuron.2018.09.020

Micallef, A. H., Takahashi, N., Larkum, M. E., and Palmer, L. M. (2017). A reward-based behavioral platform to measure neural activity during head-fixed behavior. *Front. Cell. Neurosci.* 11:156. doi: 10.3389/fncel.2017.00156

Mimica, B., Dunn, B. A., Tombaz, T., Bojja, V., and Whitlock, J. R. (2018). Efficient cortical coding of 3D posture in freely behaving rats. *Science* 362, 584–589. doi: 10.1126/science.aau2013

Miyamoto, D., and Murayama, M. (2016). The fiber-optic imaging and manipulation of neural activity during animal behavior. *Neurosci. Res.* 103, 1–9. doi: 10.1016/j.neures.2015.09.004

Mohan, H., De Haan, R., Mansvelder, H. D., and De Kock, C. P. J. (2018). The posterior parietal cortex as integrative hub for whisker sensorimotor information. *Neuroscience* 368, 240–245. doi: 10.1016/j.neuroscience.2017.06.020

Morandell, K., and Huber, D. (2017). The role of forelimb motor cortex areas in goal directed action in mice. *Sci. Rep.* 7:15759. doi: 10.1038/s41598-017-15835-2

Morcos, A. S., and Harvey, C. D. (2016). History-dependent variability in population dynamics during evidence accumulation in cortex. *Nat. Neurosci.* 19, 1672–1681. doi: 10.1038/nn.4403

Mountcastle, V. B., Steinmetz, M. A., and Romo, R. (1990). Frequency discrimination in the sense of flutter: psychophysical measurements correlated with postcentral events in behaving monkeys. *J. Neurosci.* 10, 3032–3044. doi: 10.1523/jneurosci.10-09-03032.1990

Murphy, T. H., Boyd, J. D., Bolanos, F., Vanni, M. P., Silasi, G., Haupt, D., et al. (2016). High-throughput automated home-cage mesoscopic functional imaging of mouse cortex. *Nat. Commun.* 7:11611. doi: 10.1038/ncomms11611

Nashaat, M. A., Oraby, H., Sachdev, R. N., Winter, Y., and Larkum, M. E. (2016). Air-track: a real-world floating environment for active sensing in head-fixed mice. *J. Neurophysiol.* 116, 1542–1553. doi: 10.1152/jn.00088.2016

Niell, C. M., and Stryker, M. P. (2010). Modulation of visual responses by behavioral state in mouse visual cortex. *Neuron* 65, 472–479. doi: 10.1016/j.neuron.2010.01.033

O'Connor, D. H., Clack, N. G., Huber, D., Komiyama, T., Myers, E. W., and Svoboda, K. (2010a). Vibrissa-based object localization in head-fixed mice. *J. Neurosci.* 30, 1947–1967. doi: 10.1523/jneurosci.3762-09.2010

O'Connor, D. H., Peron, S. P., Huber, D., and Svoboda, K. (2010b). Neural activity in barrel cortex underlying vibrissa-based object localization in mice. *Neuron* 67, 1048–1061. doi: 10.1016/j.neuron.2010.08.026

Parker, A. J., and Newsome, W. T. (1998). Sense and the single neuron: probing the physiology of perception. *Annu. Rev. Neurosci.* 21, 227–277. doi: 10.1146/annurev.neuro.21.1.227

Peron, S. P., Freeman, J., Iyer, V., Guo, C., and Svoboda, K. (2015). A cellular resolution map of barrel cortex activity during tactile behavior. *Neuron* 86, 783–799. doi: 10.1016/j.neuron.2015.03.027

Petreanu, L., Gutnisky, D. A., Huber, D., Xu, N. L., O'Connor, D. H., Tian, L., et al. (2012). Activity in motor-sensory projections reveals distributed coding in somatosensation. *Nature* 489, 299–303. doi: 10.1038/nature11321

Peyrache, A., Lacroix, M. M., Petersen, P. C., and Buzsáki, G. (2015). Internally organized mechanisms of the head direction sense. *Nat. Neurosci.* 18, 569–575. doi: 10.1038/nn.3968

Pinnell, R. C., Dempster, J., and Pratt, J. (2015). Miniature wireless recording and stimulation system for rodent behavioural testing. *J. Neural Eng.* 12:066015. doi: 10.1088/1741-2560/12/6/066015

Polack, P. O., Friedman, J., and Golshani, P. (2013). Cellular mechanisms of brain state-dependent gain modulation in visual cortex. *Nat. Neurosci.* 16, 1331–1339. doi: 10.1038/nn.3464

Poulet, J. F., and Petersen, C. C. (2008). Internal brain state regulates membrane potential synchrony in barrel cortex of behaving mice. *Nature* 454, 881–885. doi: 10.1038/nature07150

Quintana, J., Yajeya, J., and Fuster, J. M. (1988). Prefrontal representation of stimulus attributes during delay tasks. I. Unit activity in cross-temporal integration of sensory and sensory-motor information. *Brain Res.* 474, 211–221. doi: 10.1016/0006-8993(88)90436-2

Radvansky, B. A., and Dombeck, D. A. (2018). An olfactory virtual reality system for mice. *Nat. Commun.* 9:839. doi: 10.1038/s41467-018-03262-4

Randel, N., Asadulina, A., Bezares-Calderon, L. A., Veraszto, C., Williams, E. A., Conzelmann, M., et al. (2014). Neuronal connectome of a sensory-motor circuit for visual navigation. *Elife* 3:e02730. doi: 10.7554/eLife.02730

Rao, R. P., Mielke, F., Bobrov, E., and Brecht, M. (2014). Vocalization-whisking coordination and multisensory integration of social signals in rat auditory cortex. *Elife* 3:e03185. doi: 10.7554/eLife.03185

Raposo, D., Kaufman, M. T., and Churchland, A. K. (2014). A category-free neural population supports evolving demands during decision-making. *Nat. Neurosci.* 17, 1784–1792. doi: 10.1038/nn.3865

Reep, R. L., Chandler, H. C., King, V., and Corwin, J. V. (1994). Rat posterior parietal cortex: topography of corticocortical and thalamic connections. *Exp. Brain Res.* 100, 67–84. doi: 10.1007/bf00227280

Runyan, C. A., Piasini, E., Panzeri, S., and Harvey, C. D. (2017). Distinct timescales of population coding across cortex. *Nature* 548, 92–96. doi: 10.1038/nature23020

Sachidhanandam, S., Sreenivasan, V., Kyriakatos, A., Kremer, Y., and Petersen, C. C. (2013). Membrane potential correlates of sensory perception in mouse barrel cortex. *Nat. Neurosci.* 16, 1671–1677. doi: 10.1038/nn.3532

Saleem, A. B., Ayaz, A., Jeffery, K. J., Harris, K. D., and Carandini, M. (2013). Integration of visual motion and locomotion in mouse visual cortex. *Nat. Neurosci.* 16, 1864–1869. doi: 10.1038/nn.3567

Sawinski, J., Wallace, D. J., Greenberg, D. S., Grossmann, S., Denk, W., and Kerr, J. N. (2009). Visually evoked activity in cortical cells imaged in freely moving animals. *Proc. Natl. Acad. Sci. U S A* 106, 19557–19562. doi: 10.1073/pnas.0903680106

Schmidt-Hieber, C., and Häusser, M. (2013). Cellular mechanisms of spatial navigation in the medial entorhinal cortex. *Nat. Neurosci.* 16, 325–331. doi: 10.1038/nn.3340

Schneider, D. M., Sundararajan, J., and Mooney, R. (2018). A cortical filter that learns to suppress the acoustic consequences of movement. *Nature* 561, 391–395. doi: 10.1038/s41586-018-0520-5

Sellien, H., Eshenroder, D. S., and Ebner, F. F. (2005). Comparison of bilateral whisker movement in freely exploring and head-fixed adult rats. *Somatosens. Mot. Res.* 22, 97–114. doi: 10.1080/08990220400015375

Sheffield, M. E. J., Adoff, M. D., and Dombeck, D. A. (2017). Increased prevalence of calcium transients across the dendritic arbor during place field formation. *Neuron* 96, 490.e5–504.e5. doi: 10.1016/j.neuron.2017.09.029

Shimaoka, D., Harris, K. D., and Carandini, M. (2018). Effects of arousal on mouse sensory cortex depend on modality. *Cell Rep.* 25:3230. doi: 10.1016/j.celrep.2018.11.105

Sofroniew, N. J., Vlasov, Y. A., Hires, S. A., Freeman, J., and Svoboda, K. (2015). Neural coding in barrel cortex during whisker-guided locomotion. *Elife* 4:e12559. doi: 10.7554/eLife.12559

Song, Y. H., Kim, J. H., Jeong, H. W., Choi, I., Jeong, D., Kim, K., et al. (2017). A neural circuit for auditory dominance over visual perception. *Neuron* 93, 1236–1237. doi: 10.1016/j.neuron.2017.02.026

Suzuki, M., and Larkum, M. E. (2017). Dendritic calcium spikes are clearly detectable at the cortical surface. *Nat. Commun.* 8:276. doi: 10.1038/s41467-017-00282-4

Takahashi, N., Oertner, T. G., Hegemann, P., and Larkum, M. E. (2016). Active cortical dendrites modulate perception. *Science* 354, 1587–1590. doi: 10.1126/science.aah6066

Tang, Q., Brecht, M., and Burgalossi, A. (2014). Juxtacellular recording and morphological identification of single neurons in freely moving rats. *Nat. Protoc.* 9, 2369–2381. doi: 10.1038/nprot.2014.161

Thurley, K., and Ayaz, A. (2017). Virtual reality systems for rodents. *Curr. Zool.* 63, 109–119. doi: 10.1093/cz/zow070

Valero, M., and English, D. F. (2019). Head-mounted approaches for targeting single-cells in freely moving animals. *J. Neurosci. Methods* 326:108397. doi: 10.1016/j.jneumeth.2019.108397

Vinck, M., Batista-Brito, R., Knoblich, U., and Cardin, J. A. (2015). Arousal and locomotion make distinct contributions to cortical activity patterns and visual encoding. *Neuron* 86, 740–754. doi: 10.1016/j.neuron.2015.03.028

Wallace, D. J., Greenberg, D. S., Sawinski, J., Rulla, S., Notaro, G., and Kerr, J. N. (2013). Rats maintain an overhead binocular field at the expense of constant fusion. *Nature* 498, 65–69. doi: 10.1038/nature12153

Wang, T., Ouzounov, D. G., Wu, C., Horton, N. G., Zhang, B., Wu, C. H., et al. (2018). Three-photon imaging of mouse brain structure and function through the intact skull. *Nat. Methods* 15, 789–792. doi: 10.1038/s41592-018-0115-y

Wei, Z., Inagaki, H., Li, N., Svoboda, K., and Druckmann, S. (2019). An orderly single-trial organization of population dynamics in premotor cortex predicts behavioral variability. *Nat. Commun.* 10:216. doi: 10.1038/s41467-018-08141-6

Whishaw, I. Q., Faraji, J., Kuntz, J., Mirza Agha, B., Patel, M., Metz, G. A. S., et al. (2017). Organization of the reach and grasp in head-fixed vs. freely-moving mice provides support for multiple motor channel theory of neocortical organization. *Exp. Brain Res.* 235, 1919–1932. doi: 10.1007/s00221-017-4925-4

Wilber, A. A., Clark, B. J., Demecha, A. J., Mesina, L., Vos, J. M., and Mcnaughton, B. L. (2015). Cortical connectivity maps reveal anatomically distinct areas in the parietal cortex of the rat. *Front. Neural Circuits* 8:146. doi: 10.3389/fncir.2014.00146

Xu, N. L., Harnett, M. T., Williams, S. R., Huber, D., O'Connor, D. H., Svoboda, K., et al. (2012). Nonlinear dendritic integration of sensory and motor input during an active sensing task. *Nature* 492, 247–251. doi: 10.1038/nature11601

Yajeya, J., Quintana, J., and Fuster, J. M. (1988). Prefrontal representation of stimulus attributes during delay tasks: II. The role of behavioral significance. *Brain Res.* 474, 222–230. doi: 10.1016/0006-8993(88)90437-4

Yu, J., Hu, H., Agmon, A., and Svoboda, K. (2019). Recruitment of GABAergic interneurons in the barrel cortex during active tactile behavior. *Neuron* 104, 412.e4–427.e4. doi: 10.1016/j.neuron.2019.07.027

Zariwala, H. A., Kepecs, A., Uchida, N., Hirokawa, J., and Mainen, Z. F. (2013). The limits of deliberation in a perceptual decision task. *Neuron* 78, 339–351. doi: 10.1016/j.neuron.2013.02.010

Zhong, L., Zhang, Y., Duan, C. A., Deng, J., Pan, J., and Xu, N. L. (2019). Causal contributions of parietal cortex to perceptual decision-making during stimulus categorization. *Nat. Neurosci.* 22, 963–973. doi: 10.1038/s41593-019-0383-6

Zhuang, J., Ng, L., Williams, D., Valley, M., Li, Y., Garrett, M., et al. (2017). An extended retinotopic map of mouse cortex. *Elife* 6:e18372. doi: 10.7554/eLife.18372

Znamenskiy, P., and Zador, A. M. (2013). Corticostriatal neurons in auditory cortex drive decisions during auditory discrimination. *Nature* 497, 482–485. doi: 10.1038/nature12077

Zong, W., Wu, R., Li, M., Hu, Y., Li, Y., Li, J., et al. (2017). Fast high-resolution miniature two-photon microscopy for brain imaging in freely behaving mice. *Nat. Methods* 14, 713–719. doi: 10.1038/nmeth.4305

Conflict of Interest: The authors declare that the research was conducted in the absence of any commercial or financial relationships that could be construed as a potential conflict of interest.

Copyright © 2020 Bjerre and Palmer. This is an open-access article distributed under the terms of the Creative Commons Attribution License (CC BY). The use, distribution or reproduction in other forums is permitted, provided the original author(s) and the copyright owner(s) are credited and that the original publication in this journal is cited, in accordance with accepted academic practice. No use, distribution or reproduction is permitted which does not comply with these terms.

frontiers in Aging Neuroscience

BRIEF RESEARCH REPORT
published: 28 February 2020
doi: 10.3389/fnagi.2020.00019

Impaired Fluid Intake, but Not Sodium Appetite, in Aged Rats Is Mediated by the Cyclooxygenase-Prostaglandin E_2 Pathway

Denovan P. Begg[1]*, *Andrew J. Sinclair*[2] *and Richard S. Weisinger*[3]

[1]School of Psychology, UNSW Sydney, Sydney, NSW, Australia, [2]Faculty of Health, Deakin University, Burwood, VIC, Australia, [3]School of Psychology, La Trobe University, Bundoora, VIC, Australia

Aging results in decreased fluid intake following dehydration and other dipsogenic stimuli; similar reductions in sodium intake have also been observed with aging. Given that cyclooxygenase (COX)-derived prostanoids are elevated in aged rats in the midbrain and proinflammatory prostanoids are known to decrease fluid intake in dehydrated rats, the aim of this study was to determine if the reductions of fluid intake and sodium intake in aging are mediated by proinflammatory eicosanoid signaling. Therefore, we examined the effect of acute COX inhibition in adult (4 months-old) and aged (30 months-old) rats prior to ingestive behavior challenges. COX inhibition, using acetylsalicylic acid (ASA), increased fluid intake in aged, but not adult, rats in response to 24-h dehydration. ASA had no effect on salt intake following sodium depletion and ASA did not change basal fluid or sodium consumption in either age group. Hypothalamic COX-1 and -2, prostaglandin E synthase (PGES) and inducible nitric oxide synthase (iNOS) mRNA expression were all elevated in aged animals, leading to elevated PGE_2 levels. COX expression in the hypothalamus was reduced by ASA treatment in rats of both ages resulting in reduced PGE_2 levels in aged ASA treated animals. These data indicate that the reduced fluid intake that occurs in aging is due to increased COX-PGE_2-mediated inflammation. However, the reduced sodium intake in these animals appears to occur *via* an alternate mechanism.

Keywords: thirst and drinking, water intake, aging, salt appetite, sodium

OPEN ACCESS

Edited by:
Robert J. Harvey, University of the Sunshine Coast, Australia

Reviewed by:
Talitha Best, Central Queensland University, Australia
José Antunes Rodrigu, University of São Paulo, Brazil

***Correspondence:**
Denovan P. Begg
d.begg@unsw.edu.au

Received: *31 July 2019*
Accepted: *20 January 2020*
Published: *28 February 2020*

Citation:
Begg DP, Sinclair AJ and Weisinger RS (2020) Impaired Fluid Intake, but Not Sodium Appetite, in Aged Rats Is Mediated by the Cyclooxygenase-Prostaglandin E_2 Pathway. Front. Aging Neurosci. 12:19. doi: 10.3389/fnagi.2020.00019

INTRODUCTION

Aging significantly impairs fluid and sodium balance in mammals (Phillips et al., 1984; Thunhorst and Johnson, 2003); these impairments result from alterations to both behaviorally-mediated intake (Thunhorst et al., 2009) and reduced renal function and renin-angiotensin system (RAS) activity (Ledingham et al., 1987; Antunes-Rodrigues et al., 2004). Aged animals have reduced fluid intake following dehydration (Thunhorst and Johnson, 2003; McKinley et al., 2006) and also have reduced sodium intake following peripheral angiotensin converting-enzyme (ACE) inhibition (Rowland et al., 1996; Thunhorst and Johnson, 2003) and sodium depletion (Begg et al., 2012a,b).

Prostaglandins (PG) are produced when cyclooxygenase (COX) enzymes metabolize polyunsaturated long-chain fatty acids to prostaglandin (PG) H; PG synthases then metabolize PGH into active PGs. Suppression of fluid intake in response to dehydration occurs following administration of E series prostaglandins (Goldstein et al., 1979; Pérez Guaita and Chiaraviglio, 1980). Aged rats have increased PGE synthase (Tang and Vanhoutte, 2008) and PGE_2 in the midbrain (Meydani et al., 1985); these effects are suppressed and drinking behavior restored when animals are fed omega-3 fatty acids (Begg et al., 2012a,b). There are additional changes related to inflammatory signals with aging including an up-regulation of inducible (i) nitric oxide synthase (NOS; Wu et al., 1997; Adachi et al., 2010), a COX activator (Salvemini et al., 1993). Together, these observations may indicate involvement of prostanoids in the reduced fluid intake that occurs with aging.

Non-steroidal anti-inflammatory drugs are commonly used to reduce inflammation caused by PGE_2 through inhibition of COX enzymes. Therefore, the aim of the current study was to determine whether the reduced fluid and sodium intakes that occur in aging are the result of increased eicosanoid levels, and whether inhibition of COX restores this deficit. Furthermore, given that there are established interactions between inducible nitric oxide synthase (iNOS) and the COX/PGE pathway, mRNA expression of these genes in hypothalamic tissue levels were examined.

MATERIALS AND METHODS

Animals, Drugs and Measurements

Forty-six male Brown Norway rats were bred in the central animal house, La Trobe University. Animals were tested at either 4 months-of-age (adult animals; $n = 22$) or 30 months-of-age (aged animals; $n = 24$). Standard laboratory rat chow and water were available *ad libitum* except during challenges, as noted. Animals were single housed for the duration of the experiment and were maintained on a 12-h light/dark cycle. Acetylsalicylic acid (ASA; Sigma-Aldrich, Saint Louis, MO, USA) was dissolved in 20% dimethyl sulfoxide (DMSO) and water. Injections of ASA were given IP at 50 mg/kg, vehicle injections were 20% DMSO and 80% water. Water and sodium intakes were measured using an automated drinking system as previously described (Begg and Weisinger, 2008). There were 2 weeks between the drinking challenges described and a further 2 weeks prior to animal sacrifice. For experimental timeline, please refer to **Figure 1.** La Trobe University Animal Ethics Committee approved all animal procedures.

24-Hour Dehydration

Baseline 2-h water intakes were established 1 week before testing. Baseline measurement was performed 1 h after ASA or vehicle injection. For dehydration measurements, rats had water removed the morning prior to testing. Twenty-three hour later, animals were injected with ASA or vehicle. Then, 1 h later, drinking water was returned. Cumulative water intake was measured for 2 h, and then food was returned.

Sodium Depletion

As previously described (Weisinger et al., 2010) rats were provided access to 0.5 M NaCl solution, water and food for 2 weeks prior to sodium depletion. One week prior to sodium depletion, baseline 2-h sodium intakes were measured 1 h after ASA or vehicle injection. On the day of sodium depletion, 0.5 M NaCl solution and food were removed, while access to water remained and animals were administered furosemide (20 mg/kg I.P.; Apex Laboratories, Australia). Twenty-three hour after furosemide administration animals were injected with ASA or vehicle, 1 h later, 0.5 M NaCl solution was returned and intake was measured for a 2-h period. After 2-h, food was also returned.

Hypothalamic mRNA Expression

Animals were injected with ASA or vehicle and 1 h later injected with pentobarbital sodium (325 mg/kg). Brains were removed, the hypothalamic block dissected and stored at −80°C. RNA was extracted from ∼50 mg of hypothalamic tissue ($n = 7$/group) using a standard Tri-reagent technique (Trizol; Ambion, TX, USA), RNA quality was determined using a Nanodrop 2000 spectrophotomer (Nanodrop, DE) and converted to cDNA (SuperArray, MD, USA). Real-Time quantitative PCR was performed as previously described (Begg et al., 2012a,b) using primers for $cPLA_2$, COX-1, COX-2, PGES, EP_1, EP_2, EP_3, EP_4, neuronal (n) NOS, endothelial (e) NOS and iNOS (SuperArray, MD, USA). Relative expression ratios were normalized to β-actin and are expressed relative to adult animals using the $2\text{-}\Delta\Delta C_t$ method.

Hypothalamic PGE_2 Concentration

Hypothalamic concentrations of PGE_2 were determined from the hypothalamic block. The supernatant of homogenized tissue was filtered through C18 columns based on previous descriptions and analyzed using ELISA ($n = 4$–5/group; Assay Designs).

Statistical Analysis

Three-way (age × drug × time) ANOVAs were used to compare the effects of age and COX inhibition on behavioral measures. Two-way (age × drug) ANOVAs were used to analyze gene expression and PGE_2, *post hoc* comparisons were performed using Fisher's protected Least Significant Difference tests, significance was accepted at $p < 0.05$, data are reported as mean ± SEM.

RESULTS

24-Hour Dehydration

There were no differences in baseline 2-h water intakes between the groups (**Figure 2A**). Following 24-h dehydration all groups had increased 2-h drinking responses ($p < 0.05$; **Figure 2B**). Thirty-months-old rats drank less fluid in the 2 h following fluid return compared with young adult animals ($p < 0.05$). Pre-treatment with ASA significantly increased water intake in 30-months-old but not young adult rats ($p < 0.05$; **Figure 2B**).

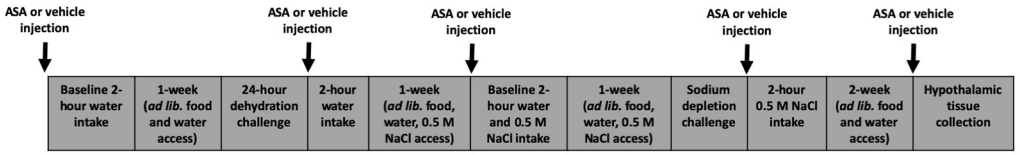

FIGURE 1 | A timeline of the experimental procedures.

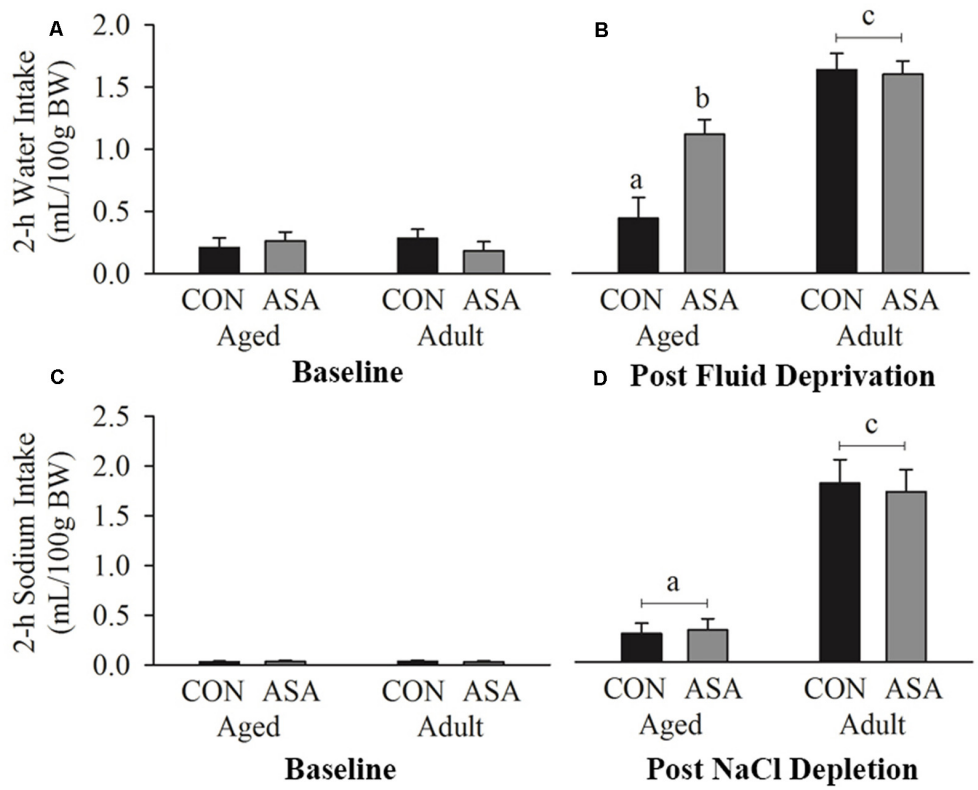

FIGURE 2 | Water intake **(A)** did not differ between groups at baseline, however **(B)** following 24-h fluid deprivation, aged rats (n = 24) drank significantly less water relative to young adult rats (n = 22). Rats treated with acetylsalicylic acid (ASA) consumed significantly more water than vehicle treated (CON) rats in the aged but not the young adult population. **(C)** 0.5 M NaCl intake did not differ between groups at baseline, however **(D)** following sodium depletion aged rats (n = 24) consumed significantly less NaCl than young adult rats (n = 22). There was no effect of ASA treatment within the groups. Differences between groups are denoted by different superscript letters.

Sodium Depletion

Baseline intakes of sodium were not different between the groups (**Figure 2C**). All groups had greater sodium intake following depletion than at baseline ($p < 0.05$), however, 2-h 0.5 M NaCl solution intake was lower in aged rats than in adult rats ($p < 0.05$; see **Figure 2D**). ASA administration did not alter sodium intake in either young adult or aged rats ($p < 0.05$).

Hypothalamic mRNA Expression

There was significant up-regulation of mRNA expression of $cPLA_2$ ($p < 0.05$), COX-1 ($p < 0.05$), and COX-2 ($p < 0.05$) in aged control animals relative to young adult animals. COX-1 ($p < 0.05$), but not COX-2 or $cPLA_2$, was significantly lower by ASA administration in aged animals. There were no differences in EP receptor or PGES mRNA expression related to age or ASA administration (see **Figure 3A**). mRNA expression of iNOS was significantly increased in aged animals ($p < 0.05$), this was unaffected by ASA treatment. nNOS and eNOS mRNA expression were not affected by age or ASA (see **Figure 3B**).

Hypothalamic PGE_2 Concentration

There was significant increase of hypothalamic PGE_2 in aged control animals relative to young adult animals ($p < 0.05$).

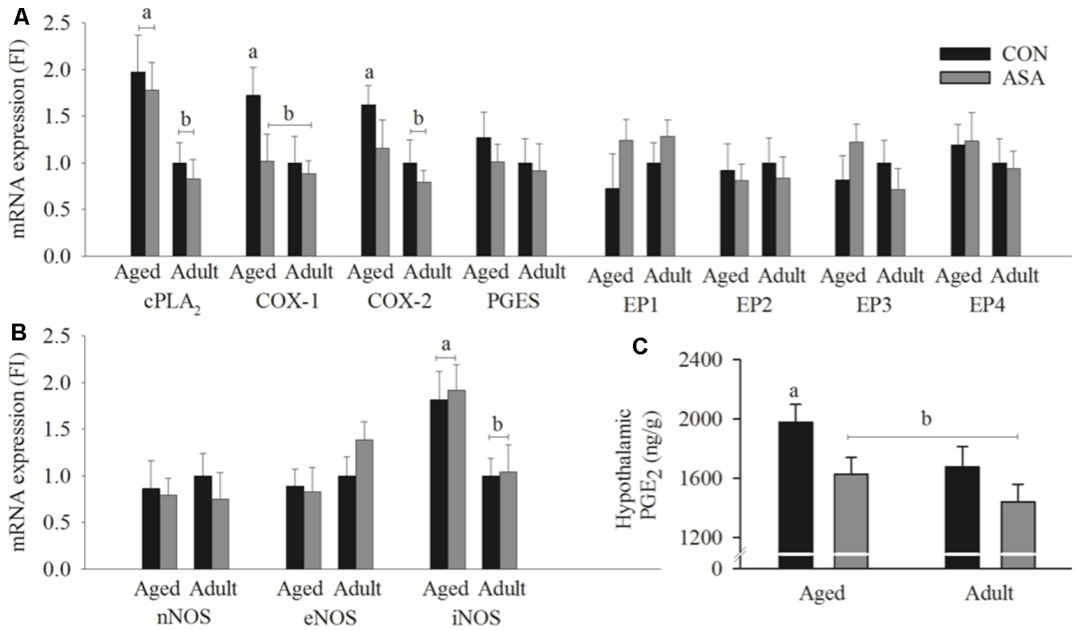

FIGURE 3 | Hypothalamic mRNA expression of **(A)** cPLA2, COX-1 and COX-2 was significantly increased in hypothalamic tissue of aged control rats relative to young adult rats. COX-1 expression was significantly reduced in the ASA treatment group of aged animals. No significant differences were seen between groups in the expression of PGES and EP1–4 (n = 7/group). **(B)** There were no significant differences between groups in the hypothalamic expression of nNOS and eNOS, however inducible nitric oxide synthesis (iNOS) mRNA expression in hypothalamic tissue was significantly increased in aged rats relative to young adult rats (n = 7/group). **(C)** Hypothalamic PGE2 concentrations in the hypothalamic tissue of aged control rats was significantly increased relative to young adult rats. PGE2 was significantly reduced in the ASA treated group of aged animals. Young adult and aged control rats; n = 4–5/group; black. ASA treated rats; n = 5/group; gray. Differences between groups are denoted by different superscript letters, the absence of a letter indicates no significant differences.

Hypothalamic PGE_2 was significantly lowered by ASA administration in aged animals ($p < 0.05$; see **Figure 3C**).

DISCUSSION

Aging leads to a significant decline in fluid intake in response to dipsogenic stimuli (Silver et al., 1991; Whyte et al., 2004; McKinley et al., 2006) and sodium intake in response sodium depletion and ACE inhibition or sodium depletion (Rowland et al., 1996; Thunhorst and Johnson, 2003). The current study assessed whether the mechanism of this effect was mediated *via* COX-PGE_2 induced inflammation in the hypothalamus. Following 24-h fluid deprivation ASA treatment increased water intake in aged animals; the effect was not attributable to a generalized effect on water intake, as ASA did not increase drinking in hydrated aged rats. These data are consistent with previous work demonstrating no changes in drinking following COX inhibition in adult rats (Foca et al., 1985).

This study also aimed to establish if the increased prostanoid levels observed in aging also caused the reduced intake of sodium, following sodium depletion. Unlike the observations of water intake, ASA did not increase sodium intake following furosemide injection in aged or young adult rats. These data indicate that the reduced intakes of water following dehydration, and sodium, following depletion, are most likely controlled by separate mechanisms. This study found higher levels of $cPLA_2$ in aged animals $cPLA_2$ indicating an increased in release of arachidonic acid from cell membrane phospholipids in the hypothalamus which allows for increased metabolism to series 2 prostanoids (Touqui et al., 1986).

Aging resulted in increased mRNA levels of both COX-1 and COX-2 in the hypothalamus. Conversion of arachidonic acid to PGH_2 occurs *via* the COX-1 or COX-2 enzymes and it has previously been demonstrated that COX-1 mRNA expression is elevated in aging (Aïd and Bosetti, 2007). ASA significantly suppressed mRNA expression of COX in aged rats; similar observations have previously been reported with ASA treatment in models of high COX expression (Trujillo-Murillo et al., 2008). mRNA expression of genes downstream of COX, including PGES, the final enzyme in the conversion of PGE_2 and the target receptors for PGE_2 (EP_{1-4}) were unaffected by age or ASA administration. This finding demonstrates that the increases observed in hypothalamic PGE_2 in aging (Begg et al., 2012a,b) are not a function of PGES expression. The lack of differences observed on EP_{1-4} receptor expression may indicate that the changes observed in PGE_2 levels are not great enough to produce changes in receptor regulation.

The data also indicate that iNOS may be involved in the reduced fluid intake in aging. Indeed, iNOS mRNA expression, but not nNOS or eNOS, was significantly upregulated in aged

animals. This is expected given that NO modulates PGE_2 during the inflammatory response. However, ASA treatment did not reduce iNOS expression. This is of note given that suppression of PGE_2 generally results in concurrent NO suppression. Given that there is possible involvement of NOS in both fluid intake (Calapai et al., 1992) and sodium intake (Abrão Saad et al., 2004), the effect of central NOS inhibition in the aging rat may be of interest and may help determine the observed differences in ingestive behaviors in the current study. For example, reduced fluid intake in aging may be eicosanoid mediated in regions such as the median preoptic nucleus of the anterior hypothalamus, while increased NOS may reduce sodium intake acting in regions such as the lamina terminalis (Begg, 2017).

The results of this study indicate that the reduction of fluid intake following dehydration in aging is mediated by an increase in central eicosanoid production and that drinking can be restored by COX inhibition. They also demonstrate that the reduced sodium intake is independent of this pathway, with the NO system being a possible target for future research in this model.

DATA AVAILABILITY STATEMENT

The datasets generated for this study are available on request to the corresponding author.

ETHICS STATEMENT

The animal study was reviewed and approved by La Trobe University Animal Ethics Committee.

AUTHOR CONTRIBUTIONS

DB, AS and RW designed the experiments. DB and RW collected and analyzed the data. DB wrote the manuscript. All authors reviewed and edited the manuscript.

FUNDING

This work was supported by the Australian Research Council (DE160100088 and DP170100063) and a Ramaciotti Foundation Establishment Grant.

REFERENCES

Abrão Saad, W., Guarda, I. F., Camargo, L. A., Garcia, G., Gutierrez, L. I., Abrão Simoes, W., et al. (2004). Lateral hypothalamus lesions influences water and salt intake and sodium and urine excretion, and arterial blood pressure induced by L-NAME and FK 409 injections into median preoptic nucleus in conscious rats. *Life Sci* 75, 685–697. doi: 10.1016/j.lfs.2004.01.018

Adachi, M., Abe, M., Sasaki, T., Kato, H., Kasahara, J., and Araki, T. (2010). Role of inducible or neuronal nitric oxide synthase in neurogenesis of the dentate gyrus in aged mice. *Metab. Brain Dis.* 25, 419–424. doi: 10.1007/s11011-010-9224-8

Aïd, S., and Bosetti, F. (2007). Gene expression of cyclooxygenase-1 and Ca^{2+}-independent phospholipase A_2 is altered in rat hippocampus during normal aging. *Brain Res. Bull.* 73, 108–113. doi: 10.1016/j.brainresbull.2007.02.015

Antunes-Rodrigues, J., de Castro, M., Elias, L. L., Valença, M. M., and McCann, S. M. (2004). Neuroendocrine control of body fluid metabolism. *Physiol. Rev.* 84, 169–208. doi: 10.1152/physrev.00017.2003

Begg, D. P., Sinclair, A. J., and Weisinger, R. S. (2012a). Reductions in water and sodium intake by aged male and female rats. *Nutr. Res.* 32, 865–872. doi: 10.1016/j.nutres.2012.09.014

Begg, D. P., Sinclair, A. J., and Weisinger, R. S. (2012b). Thirst deficits in aged rats are reversed by dietary omega-3 fatty acid supplementation. *Neurobiol. Aging* 33, 2422–2430. doi: 10.1016/j.neurobiolaging.2011.12.001

Begg, D. P., and Weisinger, R. S. (2008). The role of adrenal or testicular hormones in voluntary ethanol and NaCl intake of crowded and individually housed rats. *Physiol. Behav.* 93, 408–413. doi: 10.1016/j.physbeh.2007.09.007

Begg, D. P. (2017). Disturbances of thirst and fluid balance associated with aging. *Physiol. Behav.* 178, 28–34. doi: 10.1016/j.physbeh.2017.03.003

Calapai, G., Squadrito, F., Altavilla, D., Zingarelli, B., Campo, G. M., Cilia, M., et al. (1992). Evidence that nitric oxide modulates drinking behaviour. *Neuropharmacology* 31, 761–764. doi: 10.1016/0028-3908(92)90038-q

Foca, A., Matera, G., Mastroeni, P., and Caputi, A. P. (1985). Evidence that prostaglandins within preoptic area (POA) may mediate the antidipsogenic effect of Escherichia coli endotoxin in the rat. *Circ. Shock* 17, 137–145.

Goldstein, D. J., Marante Perez, D. J., Gunst, J. P., and Halperin, J. A. (1979). Prostaglandin E1 inhibits acute cell dehydration thirst. *Pharmacol. Biochem. Behav.* 10, 895–898. doi: 10.1016/0091-3057(79)90064-9

Ledingham, J. G., Crowe, M. J., Forsling, M. L., Phillips, P. A., and Rolls, B. J. (1987). Effects of aging on vasopressin secretion, water excretion and thirst in man. *Kidney Int. Suppl.* 21, S90–S92.

McKinley, M. J., Denton, D. A., Thomas, C. J., Woods, R. L., and Mathai, M. L. (2006). Differential effects of aging on fluid intake in response to hypovolemia, hypertonicity, and hormonal stimuli in Munich Wistar rats. *Proc. Natl. Acad. Sci. U S A* 103, 3450–3455. doi: 10.1073/pnas.0511099103

Meydani, M., Meydani, S. N., Macauley, J. B., and Blumberg, J. R. (1985). Influence of dietary vitamin E and selenium on the *ex vivo* synthesis of prostaglandin E2 in brain regions of young and old rats. *Prostaglandins Leukot. Med.* 18, 337–346. doi: 10.1016/0262-1746(85)90066-6

Pérez Guaita, M. F., and Chiaraviglio, E. (1980). Effect of prostaglandin E1 and its biosynthesis inhibitor indomethacin on drinking in the rat. *Pharmacol. Biochem. Behav.* 13, 787–792. doi: 10.1016/0091-3057(80)90208-7

Phillips, P. A., Rolls, B. J., Ledingham, J. G., Forsling, M. L., Morton, J. J., Crowe, M. J., et al. (1984). Reduced thirst after water deprivation in healthy elderly men. *N. Engl. J. Med.* 311, 753–759. doi: 10.1056/nejm198409203111202

Rowland, N. E., Del Bianco, A., and Fregly, M. J. (1996). Age-related decline in thirst and sodium appetite in rats related to kininase II inhibition. *Regul. Pept.* 66, 163–167. doi: 10.1016/s0167-0115(96)00095-x

Salvemini, D., Misko, T. P., Masferrer, J. L., Seibert, K., Currie, M. G., and Needleman, P. (1993). Nitric oxide activates cyclooxygenase enzymes. *Proc. Natl. Acad. Sci. U S A* 90, 7240–7244. doi: 10.1073/pnas.90.15.7240

Silver, A. J., Flood, J. F., and Morley, J. E. (1991). Effect of aging on fluid ingestion in mice. *J. Gerontol.* 46, B117–B121. doi: 10.1093/geronj/46.3.b117

Tang, E. H., and Vanhoutte, P. M. (2008). Gene expression changes of prostanoid synthases in endothelial cells and prostanoid receptors in vascular smooth muscle cells caused by aging and hypertension. *Physiol. Genomics* 32, 409–418. doi: 10.1152/physiolgenomics.00136.2007

Thunhorst, R. L., Beltz, T. G., and Johnson, A. K. (2009). Hypotension- and osmotically induced thirst in old Brown Norway rats. *Am. J. Physiol. Regul. Integr. Comp. Physiol.* 297, R149–R157. doi: 10.1152/ajpregu.00118.2009

Thunhorst, R. L., and Johnson, A. K. (2003). Thirst and salt appetite responses in young and old Brown Norway rats. *Am. J. Physiol. Regul. Integr. Comp. Physiol.* 284, R317–R327. doi: 10.1152/ajpregu.00368.2002

Touqui, L., Rothhut, B., Shaw, A. M., Fradin, A., Vargaftig, B. B., and Russo-Marie, F. (1986). Platelet activation—a role for a 40K anti-phospholipase A2 protein indistinguishable from lipocortin. *Nature* 321, 177–180. doi: 10.1038/321177a0

Trujillo-Murillo, K., Rincón-Sánchez, A. R., Martínez-Rodríguez, H., Bosques-Padilla, F., Ramos-Jiménez, J., Barrera-Saldaña, H. A., et al. (2008). Acetylsalicylic acid inhibits hepatitis C virus RNA and protein expression through cyclooxygenase 2 signaling pathways. *Hepatology* 47, 1462–1472. doi: 10.1002/hep.22215

Weisinger, R. S., Armitage, J. A., Chen, N., Begg, D. P., Mathai, M. L., Jayasooriya, A. P., et al. (2010). Sodium appetite in adult rats following ω-3 polyunsaturated fatty acid deficiency in early development. *Appetite* 55, 393–397. doi: 10.1016/j.appet.2010.07.006

Whyte, D. G., Thunhorst, R. L., and Johnson, A. K. (2004). Reduced thirst in old, thermally dehydrated rats. *Physiol. Behav.* 81, 569–576. doi: 10.1016/j.physbeh.2004.02.030

Wu, M. D., Kimura, M., Inafuku, S., and Ishigami, H. (1997). Effect of aging on the expression of iNOS and cell death in the mouse cochlear spiral ganglion. *Okajimas Folia Anat. Jpn.* 74, 155–165. doi: 10.2535/ofaj1936.74.5_155

Conflict of Interest: The authors declare that the research was conducted in the absence of any commercial or financial relationships that could be construed as a potential conflict of interest.

Copyright © 2020 Begg, Sinclair and Weisinger. This is an open-access article distributed under the terms of the Creative Commons Attribution License (CC BY). The use, distribution or reproduction in other forums is permitted, provided the original author(s) and the copyright owner(s) are credited and that the original publication in this journal is cited, in accordance with accepted academic practice. No use, distribution or reproduction is permitted which does not comply with these terms.

frontiers in Molecular Neuroscience

ORIGINAL RESEARCH
published: 17 April 2020
doi: 10.3389/fnmol.2020.00032

Transgenic Cross-Referencing of Inhibitory and Excitatory Interneuron Populations to Dissect Neuronal Heterogeneity in the Dorsal Horn

Tyler J. Browne[1,2†], *Mark A. Gradwell*[1,2†], *Jacqueline A. Iredale*[1,2], *Jessica F. Maden*[1], *Robert J. Callister*[1,2], *David I. Hughes*[3*†], *Christopher V. Dayas*[1,2†] *and Brett A. Graham*[1,2*†]

[1]School of Biomedical Sciences & Pharmacy, Faculty of Health, University of Newcastle, New Lambton Heights, NSW, Australia, [2]Hunter Medical Research Institute (HMRI), Callaghan, NSW, Australia, [3]Institute of Neuroscience Psychology, College of Medical, Veterinary & Life Sciences, University of Glasgow, Glasgow, United Kingdom

The superficial dorsal horn (SDH, LI-II) of the spinal cord receives and processes multimodal sensory information from skin, muscle, joints, and viscera then relay it to the brain. Neurons within the SDH fall into two broad categories, projection neurons and interneurons. The later can be further subdivided into excitatory and inhibitory types. Traditionally, interneurons within the SDH have been divided into overlapping groups according to their neurochemical, morphological and electrophysiological properties. Recent clustering analyses, based on molecular transcript profiles of cells and nuclei, have predicted many more functional groups of interneurons than expected using traditional approaches. In this study, we used electrophysiological and morphological data obtained from genetically-identified excitatory (vGLUT2) and inhibitory (vGAT) interneurons in transgenic mice to cluster cells into groups sharing common characteristics and subsequently determined how many clusters can be assigned by combinations of these properties. Consistent with previous reports, we show differences exist between excitatory and inhibitory interneurons in terms of their excitability, nature of the ongoing excitatory drive, action potential (AP) properties, sub-threshold current kinetics, and morphology. The resulting clusters based on statistical and unbiased assortment of these data fell well short of the numbers of molecularly predicted clusters. There was no clear characteristic that in isolation defined a population, rather multiple variables were needed to predict cluster membership. Importantly though, our analysis highlighted the appropriateness of using transgenic lines as tools to functionally subdivide both excitatory and inhibitory interneuron populations.

Keywords: pain, spinal cord, neuron classification, patch clamp, excitability, neuron morphology

OPEN ACCESS

Edited by:
Robert J. Harvey, University of the Sunshine Coast, Australia

Reviewed by:
Ying Zhang, Dalhousie University, Canada
Ludovic Tricoire, Université Pierre et Marie Curie, France

***Correspondence:**
Brett A. Graham
brett.graham@newcastle.edu.au
David I. Hughes
David.I.Hughes@glasgow.ac.uk

†These authors have contributed equally to this work

Received: *18 October 2019*
Accepted: *11 February 2020*
Published: *17 April 2020*

Citation:
Browne TJ, Gradwell MA, Iredale JA, Maden, JF, Callister RJ, Hughes DI, Dayas CV and Graham BA (2020) Transgenic Cross-Referencing of Inhibitory and Excitatory Interneuron Populations to Dissect Neuronal Heterogeneity in the Dorsal Horn. Front. Mol. Neurosci. 13:32. doi: 10.3389/fnmol.2020.00032

INTRODUCTION

The superficial dorsal horn (SDH) of the spinal cord receives and processes primary afferent input conveying noxious, thermal, tactile, and pruritic sensory signals from the body destined for the brain. A key feature of the SDH, which includes laminae I and II, is the considerable heterogeneity within the local interneurons that make up >95% of the neurons in this region (Todd, 2010; Braz et al., 2014; Ross et al., 2014). In contrast, projection neurons, which are responsible for relaying

sensory signals out of the SDH to the brain are scarce, accounting for <5% of neurons in this region (Polgár et al., 2010; Cameron et al., 2015). With this skew in the proportions of output to modulatory neurons, it is widely accepted that LI-II interneurons play a crucial role in processing sensory information before it is transmitted to the brain (Todd, 2010; Peirs and Seal, 2016).

Recent models of spinal sensory processing have provided a framework for understanding how interneurons contribute to spinal processing mechanisms. Specifically, they have highlighted the important interplay between inhibitory gating mechanisms (Bourane et al., 2015; Foster et al., 2015; Petitjean et al., 2015; François et al., 2017; Sun et al., 2017; Boyle et al., 2019) and polysynaptic excitatory pathways (Torsney and MacDermott, 2006; Takazawa and MacDermott, 2010; Peirs et al., 2015; Takazawa et al., 2017) for normal sensory experience. As these models have developed, so too has the need to differentiate subpopulations of interneurons with unique features and connections that can fulfill specific roles in spinal sensory circuits. For example, intersectional transgenic ablation and optogenetic activation studies have implicated somatostatin-expressing dorsal horn neurons in mechanical pain (Duan et al., 2014; François et al., 2017), whereas dynorphin (Dyn)-expressing neurons suppress this action (Duan et al., 2014). Chemogenetic manipulation of transiently expressing VGLUT3 neurons has shown these cells receive touch-related sensory inputs from myelinated afferents and relay them through a circuit implicated in generating mechanical allodynia (Peirs et al., 2015). Genetic ablation and chemogenetic activation of parvalbumin (PV) expressing inhibitory interneurons have also implicated the PV population in mechanical allodynia (Petitjean et al., 2015). Similar observations have also been reported using tetanus toxin-based silencing of the PV interneurons with detailed optogenetic circuit mapping confirming these cells are a source of presynaptic inhibition on myelinated afferents, as well as mediating postsynaptic inhibition to excitatory interneurons that relay touch-related signals into lamina I (Boyle et al., 2019).

Alternatively, experiments ablating interneurons expressing the gastrin-releasing peptide (GRP) receptor have shown this population to be integral for spinal itch transmission (Sun et al., 2017). Subsequent optogenetic activation studies of GRP-expressing neurons in the same region highlighted the action of GRP in volume transmission and its ability to also produce itch responses in transgenic mice (Pagani et al., 2019). Finally, using a combination of chemogenetics and targeted ablation approaches, somatostatin-mediated activation of Dyn expressing interneurons has also been implicated in spinal itch signaling (Huang et al., 2018).

While far from exhaustive, the above snapshot of recent work on the involvement of interneuron types in pain and itch signaling highlights the value of these new approaches for understanding spinal sensory processing circuits. However, it also demonstrates the piecemeal and often overlapping nature of these studies. An improved understanding of spinal sensory processing will require these discrete microcircuits and connections to be examined in a way that better accounts for the well-known neuron heterogeneity that exists in the SDH.

Advances in single-cell and single nucleus sequencing techniques have provided a new approach for differentiating distinct neuron subpopulations (Zeisel et al., 2015). These approaches have the advantage of simultaneously comparing and then subdividing the entire dorsal horn population. This provides a complete taxonomy/classification for nonoverlapping neuronal subpopulations based on their molecular profile. Using the single-cell approach, 30 different dorsal-horn neuron types have been identified, 15 excitatory and 15 inhibitory (Haring et al., 2018). A similar exercise using single nucleus expression data identified 16 excitatory and nine inhibitory neuron classes (Sathyamurthy et al., 2018). These results far exceed the number of cell types predicted by the existing literature, which subdivides the dorsal horn population using morphological, electrophysiological or neurochemical properties (Grudt and Perl, 2002; Yasaka et al., 2010; Gutierrez-Mecinas et al., 2016, 2019; Boyle et al., 2017).

One result of these two broad approaches for classifying neuron types is that as more and more neurochemically defined interneurons are identified and classified, they will often span several molecularly defined classes. For example, somatostatin expression occurs in 10 of the 15 excitatory molecular subclasses, while PV and Dyn are expressed in 3 of the 15 inhibitory molecular subclasses. A simple interpretation of this relationship is that either smaller subpopulations exist within the neuron types that have been studied functionally. Alternatively, multiple distinct molecular cell classes of neurons show phenotypic convergence and assume the same role in spinal sensory processing circuits (Zeisel et al., 2015; Harris et al., 2018). The possibility remains that phenotypic divergence also exists, where cells in a single molecular class can assume distinct roles within sensory circuits. Thus, reconciling the relationship between molecular taxonomies and functional approaches to neuronal characterization will be important for our future understanding of heterogeneity in the SDH.

To address this challenge, we have adopted a population-level approach to functional characterization. We generated mice where the fluorescent reporter protein, TdTomato, is expressed in neurons containing the vesicular γ-aminobutyric acid transporter (vGAT) or the vesicular glutamate transporter-2 (vGLUT2). This enabled us to study inhibitory and excitatory dorsal horn neurons, respectively. Several studies have also used reporter proteins (eg GFP/TdTomato) expressed in specific cell types to study excitatory and inhibitory populations (Hantman et al., 2004; Heinke et al., 2004; Zeilhofer et al., 2005; Hughes et al., 2012; Duan et al., 2014; Punnakkal et al., 2014; Smith et al., 2015; Dickie et al., 2019). Electrophysiological and morphological data from the labeled populations in our experiments, as well as adjoining unlabeled cells, were compared to resolve features unique or shared within each cell type and group. Our results reinforce and highlight a number of features that differ between cell classes, including action potential (AP) spiking, subthreshold current activation and excitatory synaptic drive. Likewise, some key morphological features also segregate cell classes, however, no electrophysiological

or morphological property was uniquely expressed in one population, cautioning against using these features to predict cell type. Finally, in an attempt to account for the large numbers of interneuron populations identified using molecular profiles we used both electrophysiological and morphological data to form hierarchical clusters. Similar exercises in other CNS regions including the cortex (Cauli et al., 2000; Gouwens et al., 2019) and hippocampus (Graves et al., 2012) have successfully resolved functionally discrete subpopulations. In the dorsal horn, we show that electrophysiological properties better differentiate cell classes than morphological characteristics. This analysis lends support to the existence of functionally distinct subpopulations of excitatory and inhibitory dorsal horn interneurons, though far less than proposed using molecular expression data.

MATERIALS AND METHODS

Mice for experiments were generated by crossing either a VGAT−Cre line [B6J.129S6(FVB)-Slc32a1$^{tm2(cre)Lowl}$/MwarJ, Jackson Laboratories, Bar Harbor, ME, USA, #028862] or, a VGLUT2−Cre line [B6J.129S6(FVB)-Slc32a1$^{tm2(cre)Lowl}$/MwarJ, Jackson Laboratories, Bar Harbor, ME, USA, #028863] with a mouse reporter line to express a Cre-dependent∼Td tomato [B6.Cg-Gt(ROSA)26Sortm14(CAG-TdTomato)Hze/J, Jackson Laboratories, Bar Harbor, ME, USA, #007914]. This generated mice where TdTomato is expressed in either vGAT (inhibitory) or vGLUT2 (excitatory) positive neurons. Both Cre-lines have previously been used to manipulate these populations in the dorsal horn using chemogenetics (Koga et al., 2017; Wang et al., 2018), validating their utility in the dorsal horn and highlighting the need for a detailed electrophysiological and morphological characterization. All experimental procedures were performed in accordance with the University of Newcastle's animal care and ethics committee. Animals of both sexes (aged 4–7 months) were used for electrophysiology and subsequent morphological analyses. This age range ensured data was collected from mature animals at a stage where electrophysiological properties are thought to be stable. This is on the basis of work from our group showing significant alterations in the electrophysiological properties of DH neurons that occur very early in postnatal development—either side of a critical developmental period from P6 to P10 (Walsh et al., 2009). In other work, we have shown there are subtle but significant changes in excitability, excitatory drive, and GABA signaling between young adulthood (3–4 months) and advanced age (28–32 months; Mayhew et al., 2019). Taken together, this supports the view our comparisons are unlikely to be influenced by animal age.

Tissue Preparation for Immunocytochemistry

To assess the validity of TdTom expression in vGAT expressing neurons as a marker for inhibitory interneurons in the dorsal horn, we assessed co-expression of an accepted developmental marker for all inhibitory interneurons, Pax2, in this tissue (Foster et al., 2015; Boyle et al., 2017; Larsson, 2017). Pax2 expression was also assessed in vGLUT2 animals to validate our capacity to identify excitatory interneurons—the expectation being no overlap between TdTom and Pax2 expression in the vGLUT2 tissue. Briefly, animals (n = 3, vGAT:TdTom and vGLUT2:TdTom) were overdosed with sodium pentobarbitone (30 mg/kg i.p) and perfused transcardially with 0.9% sodium chloride solution followed by 4% fresh depolymerized formaldehyde in 0.1 M phosphate buffer (pH 7.4). Spinal cords were dissected out and post-fixed in the same fixative for 2 h. Transverse sections (30 μm thick) were cut from the lumbar enlargement (L3–L5) on a cryostat (CM1900 Leica, Wetzlar, Germany) at −20°C. Sections were then incubated in primary antibody, anti-Pax2 (Invitrogen—Thermo Fisher, Waltham, MA, USA, #71-6000), reacted with a secondary antibody conjugated to Cy5 (Jackson Immunoresearch Laboratories, West Grove, PA, USA), before mounting on slides in glycerol. Image stacks (>10 optical sections) were captured using laser-scanning confocal microscopy on a Leica TCS SP8 microscope (equipped with 405 nm diode, argon multiline, solid-state, and HeNe lasers) using a 10×/0.4 apochromat air interface objective (field of view: 1,117 × 1,117 μm, z = 2 μm, pinhole 1 AU), or 40×/1.3 apochromat oil immersion objectives (field of view: 281 × 281 μm, z = 1 μm, pinhole: 1 AU) to capture "whole of dorsal horn" and higher resolution images, respectively.

Analysis of Confocal Image Stacks

Images were analyzed offline using the open-source image processing software Fiji (including the cell counting plugin; Schindelin et al., 2012). Three separate areas (100 μm × 100 μm square superimposed) were sampled across the dorsal horn including a medial area, bordering on the dorsal columns; lateral area, bordering on the lateral spinal nucleus and a middle position (between medial and lateral). Cells were counted in image stacks and only marked in the analysis only if they could be visualized in four or more adjacent optical sections. Each channel representing a neurochemical marker (vGAT/vGLUT2∼Tdtomato, or Pax2∼Cy5) was visualized separately. All positive profiles on each channel were marked without observing the other channel, before merging the fields and assessing the overlap between Tdtomato and Pax2, or lack thereof. Maximum intensity Z-projections of images were generated to summarize these distributions.

Spinal Cord Slice Preparation

Spinal cord slices for patch-clamp electrophysiology were prepared using previously reported methods (Smith et al., 2015). In brief, animals were anesthetized with ketamine (100 mg/kg i.p) and decapitated. The ventral surface of the vertebral column was exposed, and the spinal cord rapidly dissected out (within 8–10 min) in ice-cold sucrose substituted cerebrospinal fluid (ACSF) containing (in mM): 250 sucrose, 25 $NaHCO_3$, 10 glucose, 2.5 KCl, 1 NaH_2PO_4, 1 $MgCl_2$ and 2.5 $CaCl_2$. All recordings were undertaken in parasagittal slices (L1-L5, 200 μm thick), prepared using a vibrating microtome (Campden Instruments 7000 smz, Loughborough, UK). Slices were transferred to an air interface incubation chamber containing oxygenated ACSF (118 mM NaCl substituted for

sucrose) and allowed to equilibrate at room temperature (∼23°) for at least 1 h prior to recording.

Patch-Clamp Electrophysiology

Following incubation, slices were transferred to a recording chamber and continuously superfused with Carbanox-bubbled ACSF (95% O_2, 5% CO_2) to achieve a final pH of 7.3–7.4. All recordings were made at room temperature. Neurons were visualized using a 40× objective and near-IR differential interference contrast optics. To identify vGAT and vGLUT2 positive neurons that expressed red fluorescent protein (RFP; TdTomato), slices were viewed under fluorescence using a TRITC filter set. vGAT and vGLUT2 neurons within substantia gelatinosa (LI-II) were targeted for recordings and were easily identified by their clear somatic fluorescence (**Figure 1**). In addition, some recordings also selectively targeted unlabeled (TdTom negative) neurons in tissue from vGAT/vGLUT2:TdTomato animals. All recordings used patch pipettes (4–8 MΩ) filled with a potassium gluconate based internal containing (in mM): 135 $C_6H_{11}KO_7$, 6 NaCl, 2 $MgCl_2$, 10 HEPES, 0.1 EGTA, 2 MgATP, 0.3 NaGTP, pH 7.3 (with KOH), to record excitatory synaptic input and AP discharge (series resistance <40 MΩ). Neurobiotin (0.2%) was included in the internal solution for studying *post hoc* cell morphology. All data were acquired using a Multiclamp 700B amplifier (Molecular Devices, Sunnyvale, CA, USA), digitized online (sampled at 10 kHz, filtered at 5 kHz) using an ITC-18 computer interface (Instrutech, Long Island, NY, USA) and stored on the computer. This data capture and subsequent analysis used Axograph X software (Molecular Devices, Sunnyvale, CA, USA).

AP discharge patterns were assessed in the current clamp from a membrane potential of −60 mV by delivering a series of depolarizing current steps (1 s duration, 20 pA increments), with rheobase defined as the first current step that induced AP discharge. AP discharge patterns were classified using previously described criteria (Graham et al., 2004, 2007, 2008). Briefly, delayed firing (DF) neurons exhibited a clear, ramped interval between current injection and the onset of the first AP; tonic firing (TF) neurons exhibited continuous repetitive AP discharge for the duration of current injection; initial bursting (IB) neurons were characterized by a burst of AP discharge at the onset of current injection, and single spiking (SS) neurons only fired a single AP at the beginning of the current step. In addition, we observed one rarely described discharge profile that we termed a rapid burst (RB) response. In these recordings, a rapid burst of AP discharge occurred during a pronounced depolarizing current hump at the rheobase step, which is consistent with the activation of low threshold T-type calcium channels. While the resulting spiking in this population could be classified as IB, their unique underlying features clearly differentiated these responses and warranted classification as a distinct group.

The subthreshold currents underlying AP discharge were identified in a voltage-clamp protocol. This protocol consisted of an initial hyperpolarization from a holding potential of −70 mV to −100 mV (1 s duration) followed by a depolarizing step to −40 mV (200 ms duration) and applied P/N leak subtraction for analysis (within Axograph software). Four major ionic currents previously described in dorsal horn neurons could be identified in responses, including the outward potassium currents (I_A) and the inward currents; T-type calcium and the non-specific cationic current, I_h. Input resistance and series resistance were monitored throughout all recordings and data were excluded if either value changed by more than 10%. No correction was made for liquid junction potentials.

Patch-Clamp Data Analysis

All electrophysiology data were analyzed offline using Axograph X software. Input resistance was calculated from the averaged current response (30 trials) generated in each cell during a 5 mV hyperpolarizing step. Spontaneous excitatory postsynaptic currents (sEPSCs) were detected using a sliding template method (a semi-automated procedure in the Axograph package). sEPSCs frequency was determined from at least 30 s of continuous recording at a membrane potential of −70 mV. Peak amplitude, rise time (10–90% of peak), and decay time constant (fitted over 10–90% of the decay phase) were measured from the averaged sEPSC obtained for each neuron. The excitatory drive was calculated as the area under the curve of the averaged sEPSC multiplied by sEPSC frequency. Resting membrane potential (RMP) was taken as the average of 30 s of current clamp recording immediately after entering the whole-cell mode (input current = 0 pA). Individual AP properties for each neuron were assessed from the first spike generated at rheobase current. APs were captured using a derivative threshold method with AP threshold defined as the inflection point during spike initiation (dV/dt ≥15 V/s). The difference between the AP threshold and its maximum positive peak was defined as the AP peak. AP half-width was measured at 50% of AP peak, and AP afterhyperpolarization (AHP) amplitude was taken as the difference between the AP threshold and the maximum negative peak following the AP. AP discharge pattern properties were all assessed in the response to multiple steps with the response exhibited at two-step injections above rheobase (Rh40) used to measure key characteristics. AP delay was the time between step onset and the first AP discharged during the response. The first interspike interval (1st AP ISI) was the time between the onset of the first and second APs in the response. AP duration was the time between the first and last AP in the step response. AP number (AP n) was the number of spikes discharged in the entire response, and spiking AP adaptation was the ratio of the first interspike interval divided by the last interspike interval. For subthreshold currents, I_A was identified by an outward positive peak in the depolarizing step of the subthreshold current protocol (−100 mV to −40 mV) whereas I_{Ca} was identified as an inward current during this step. Peak current was measured (positive or negative) and used to designate cells as exhibiting dominant I_A or I_{Ca} (or no current) responses. This approach cannot exclude the possibility that some cells expressed both I_A and I_{Ca} currents, though even if occurring in combination our protocol yields the current likely to have the greatest functional relevance for spiking by predominating. I_h was characterized by a sag in the hyperpolarizing step (−70 mV to −100 mV). Peak I_h current was quantified as the difference between the immediate current

response to this step subtracted from the maximum steady-state current at the end of this step.

Anatomical Characterization of vGAT and vGLUT2∼TdTomato Neurons

As noted above, Neurobiotin (0.2%) was included in the recording pipette for morphological analysis of recorded neurons. Slices containing filled cells were incubated in Streptavidin-Alexafluor 488 secondary antibody (1:50, 2 h, Thermofisher Scientific, #S11223). They were mounted on slides with glycerol and imaged on a Leica TCS SP8 scanning confocal microscope using a 25 × 0.95 fluotar-water immersion objective (working distance 2.4 mm, z = 1 μm, the field of view 445 μm × 445 μm). The dendritic architecture was analyzed for all cell recoveries deemed adequate to assess the rostrocaudal and dorsoventral extent occupied by processes. Specifically, as all recordings were undertaken in sagittal slices, the dorsoventral and rostrocaudal axes of each image were first oriented. Only cells with a clearly differentiated filled soma and processes, not overlapping with other filled cells in the same slice were analyzed. Three measurements were taken for each cell of these images: (1) the rostrocaudal extent, which was the distance between the most rostral and caudal labeled processes in the rostrocaudal plane; (2) the dorsal extent, which was the distance between the center of the cells soma and the dorsal-most labeled process in the dorsoventral plane; and (3) the ventral extent, which was the distance between the center of the cells soma and the ventral-most labeled process in the dorsoventral plane. A series of measures were also derived from this data, with dorsal and ventral measures added to yield dorsoventral extent, rostrocaudal extent was divided by the dorsoventral extent to provide a rostrocaudal/dorsoventral (RC:DV) ratio, and dorsal extent was subtracted from the ventral extent to yield a measure of dorsoventral bias. These measures have previously been shown to efficiently distinguish neuronal morphology in the dorsal horn (Alba-Delgado et al., 2015). Processes with axonal characteristics (small, non-tapering diameter) were also occasionally observed within dendritic profiles and beyond, however, when present their distribution was not assessed in this study.

Clustering Analysis: Electrophysiological and Morphological Parameters

Clustering analyses were completed using Orange (v3.2) data analysis software (Demšar et al., 2013). Electrophysiological, morphological and combined (i.e., electrophysiology and morphology) datasets were imported into the Orange data mining toolbox. Euclidean distance was calculated for these values and hierarchical cluster analyses were completed using Ward's minimum variance method. Given the potential for variables with larger scales to overly influence clustering, Euclidean distance calculations and clustering was also repeated with scale of all variables normalized (0–1). Clustering was identical between raw and normalized data and thus outputs from the least processed (raw) data are presented. Dendrograms were generated for cluster analysis outputs and heat maps were obtained for each property included in these analyses—with the color range scaled to maximum (brown-red) and minimum (white-beige) values. A parsimonious cluster number was determined for each analysis using the K-means elbow method with the sum of squared errors (SSE) calculated for n = 2 to 15 clusters. Under this approach, the number of clusters was assigned for each hierarchical analysis (electrophysiology, morphology, electrophysiology and morphology) by determining where additional clusters no longer yielded an appreciable improvement to the SSE.

Statistical Analysis

All data are presented as mean ± standard deviation (SD) unless otherwise stated. One-way ANOVAs were performed with a student Newman–Keuls *post hoc* test to compare electrophysiological and morphological properties between neuron classes (identified inhibitory, identified excitatory, putative inhibitory, and putative excitatory). Chi-squared tests compared the distribution of AP discharge patterns and subthreshold current expression between neuron classes.

RESULTS

The following results include data from 198 dorsal horn neurons recorded in the SDH (laminae I-II) of spinal cord slices prepared from VGAT:TdTomato (vGAT:Td, n = 6) and VGLUT2:TdTomato mice (vGLUT2:Td, n = 3). In each transgenic mouse line, recordings were targeted to labeled TdTomato positive neurons (vGAT+, vGLUT2+) and unlabeled TdTomato negative neurons (VGAT−, VGLUT2−). Thus, four-cell groups are differentiated and reported on: (1) targeted inhibitory interneurons (VGAT+, n = 76); (2) putative excitatory interneurons (VGAT−, n = 57); (3) targeted excitatory interneurons (VGLUT2+, n = 40); and (4) putative inhibitory interneurons (VGLUT2−, n = 25). It follows that VGAT+ and VGLUT2− samples should come from the same overall (inhibitory) population, and likewise, the VGLUT2+ and VGAT− (excitatory) samples should overlap substantially.

TdTomato Labeling in VGAT:Td and VGLUT2:Td Mice

To assess our capacity to reliably identify inhibitory and excitatory interneurons in VGAT:Td and VGLUT2:Td mice, we first undertook immunolabeling experiments. TdTomato-expression (TdTom) in the lumbar spinal cord sections from each genotype was compared to Pax2 immunolabeling (five sections per animal from three mice per genotype), which provides a reliable marker of inhibitory neuron phenotype in the dorsal horn (**Figure 1**). Cell counts were undertaken in standardized "regions of interest" (100 μm × 100 μm) superimposed on the medial, middle, and lateral SDH to assess the likelihood that TdTom+ cell distribution was concentrated in a particular region. There was no difference in the number of TdTom+ cells across the mediolateral axis in VGAT:Td sections (mean ± SD cells per section = 17.9 ± 4.6 vs. 21.3 ± 4.9 vs. 20.3 ± 4.5, p = 0.144; lateral vs. middle vs. medial, respectively). In contrast, TdTom+ cell counts were lower in the medial dorsal horn compared to the middle region counts in VGLUT2:Td

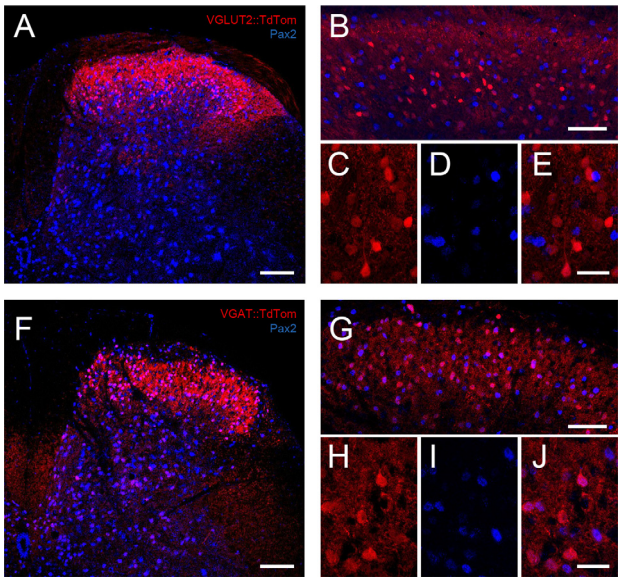

FIGURE 1 | TdTomato expression in VGLUT2:Td and VGAT:Td dorsal horn neurons. **(A)** Low magnification image is a maximum intensity z-projection showing the distribution of TdTom expression (red) in the dorsal horn of a spinal cord section (medial to left) from a VGLUT2:Td mouse merged with Pax2 immunolabeling (blue), which identifies inhibitory neurons. **(B)** A higher magnification image is a maximum intensity z-projection also showing the distribution of VGLUT2:Td and Pax2 expression within the superficial dorsal horn (SDH). Note, the lack of overlap of red and blue cell profiles. **(C–E)** Expanded images (from **B**) show VGLUT2:Td, Pax2, and both merged, highlighting the lack of overlap and confirming VGLUT2:Td expression is limited to excitatory (Pax2−) profiles. **(F)** Low magnification image is a maximum intensity z-projection showing the distribution of TdTom expression (red) across the dorsal horn of a spinal cord section from a VGAT:Td mouse merged with Pax2 immunolabeling (blue) to identify inhibitory neurons. **(G)** Higher magnification image is a maximum intensity z-projection also showing the distribution of VGAT:Td and Pax2 expression within the SDH. Note, the substantial overlap. **(H–J)** Expanded images (from **G**) show VGAT:Td, Pax2, and both merged. The overlap of fluorescent profiles confirms VGAT:Td expression is commonly found in inhibitory (Pax2+) profiles (pink; Scale bars: **A,B,F,G**: 100 μm; **C–E,H–J**: 25 μm).

sections (20.5 ± 7.7 vs. 23.7 ± 3.4 vs. 18.1 ± 6.1 cells per section, $p = 0.047$; lateral vs. middle vs. medial, respectively). Despite this minor regional difference for the VGLUT2:Td tissue, the number of TdTom+ cells per section was similar between VGAT:Td and VGLUT2:Td animals (59.5 ± 10.2 vs. 62.3 ± 10.8 cells per section, $p = 0.471$). Likewise, the number of Pax2+ cells was similar between VGAT:Td and VGLUT:Td animals (64.2 ± 11.3 vs. 60.3 ± 8.5 cells per section, $p = 0.297$). This analysis rules out inconsistent labeling as a cause for any subsequent difference in electrophysiological or morphological comparisons. In contrast, differences in the number of TdTom+ cells that exhibited overlapping Pax2+ immunolabeling in VGAT:Td vs. VGLUT2:Td animals were dramatic. For the VGAT:Td animal: 93.9% of TdTom+ cells were Pax2+, 87.3% of Pax2+ profiles were TdTom+, and 6.1% of TdTom+ did not express Pax2. This shows cells labeled in the vGAT:Td line are mostly inhibitory, some inhibitory interneurons are undetected, and importantly the chance of falsely identifying inhibitory interneurons is low.

As an excitatory cell marker was not readily available for this study a similar analysis to that above was not possible for the VGLUT2:Td animals. We could, however, use an exclusion approach to assess the capacity of TdTom+ expression to reliably identify excitatory interneurons by showing 91.6% of TdTom+ cells were Pax2−, and only 8.3% of TdTom+ cells were Pax2+. These data indicate that almost all vGLUT2 profiles were not inhibitory and thus the chance of falsely identifying an excitatory interneuron was low. The fraction of excitatory interneurons captured by the VGLUT2:Td animal could not be assessed without an excitatory cell marker. This value can, however, be estimated by comparison with the VGAT:Td animal using the well-established ratio of excitatory to inhibitory interneurons in the dorsal horn (∼75%:25%; Polgár et al., 2013; Gutierrez-Mecinas et al., 2019). As the VGAT:Td animals captured most inhibitory interneurons, but similar cell numbers are labeled in VGAT:Td and VGLUT2:Td animals, we estimate the VGLUT2:Td animal captures ∼30% of the excitatory interneurons in the region. Thus, a population of excitatory interneurons appears to remain unidentifiable (TdTom−) in this tissue.

Distinct Electrophysiological Properties in VGAT:Td and VGLUT2:Td Populations

A comparison of the electrical properties across excitatory and inhibitory interneurons revealed some differences between these populations (**Table 1**). First, the input resistance of the inhibitory VGAT+ group was lower than the excitatory VGLUT2+ group ($p < 0.001$). This difference was also conserved between inhibitory VGAT+ cells and putative excitatory VGAT− cells ($p < 0.001$). Likewise, input resistance was lower in putative inhibitory (VGLUT2−) cells vs. excitatory VGLUT2+ cells ($p = 0.05$), but not in the putative excitatory VGAT− population. Differences in RMP were less prominent, with only targeted inhibitory VGAT+ cells exhibiting more depolarized membrane potentials than excitatory VGLUT2+ cells ($p = 0.04$). Finally, the rheobase current required to initiate AP discharge did not differ across the four neuron groups.

TABLE 1 | Passive membrane properties.

Cell type	Input resistance (MΩ)	RMP (mV)	Rheobase (pA)
VGAT+ (*targeted inhibitory*, $n = 76$)	170 ± 99* (VGAT−, VGLUT2+)	−55.5 ± 10.1* (VGLUT2+)	51.9 ± 22.4
VGAT− (*putative excitatory*, $n = 57$)	270 ± 133* (VGAT+)	−59.4 ± 12.8	48.1 ± 26.3
VGLUT2+ (*targeted excitatory*, $n = 40$)	303 ± 178* (VGAT+, VGLUT2−)	−61.5 ± 12.8	48.2 ± 26.6
VGLUT2− (*putative inhibitory*, $n = 25$)	214 ± 128* (VGLUT2+)	−59.3 ± 11.7	47.0 ± 23.8

*Mean ± SD. Significant differences between groups denoted by *(bracketed below, $p < 0.05$).*

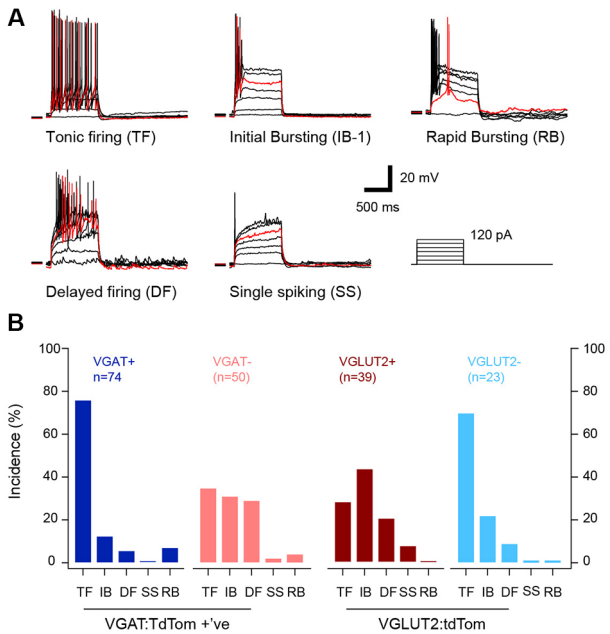

FIGURE 2 | Distinct action potential (AP) discharge patterns in excitatory and inhibitory populations. **(A)** Overlaid traces show representative examples of the characteristic patterns of AP discharge observed during increasing levels of current step injection (20 pA steps, 1 s duration). The red trace shows an exemplary response for each AP discharge pattern. Tonic firing (TF) responses included repetitive AP discharge throughout the depolarizing current step injection; initial bursting (IB) responses exhibited AP discharge that was restricted to the depolarization onset; Rapid Bursting responses were similar to IB, but spike onset coincided with a depolarizing hump that was clearly visible in the rheobase current response; Delayed firing (DF) responses exhibited AP discharge only after a delay from the depolarizing step onset; and Single Spiking responses only discharged a single AP at depolarization onset, regardless of depolarizing step amplitude. **(B)** Bar plots compare the incidence of each AP discharge patterns between cell types. Most (>70%) inhibitory interneurons (VGAT+ and VGLUT2−, blue and light blue bars) exhibited TF and the incidence of IB, DF and rapid bursting was low (<20%). In contrast, excitatory populations (VGLUT2+ and VGAT−, brown and red bars) exhibited a wider range of AP discharge properties with IB, DF and TF each accounting for >20% of the distribution.

Despite a similar overall rheobase current, the properties of rheobase APs did differ (**Table 2**). Specifically, the AP threshold was more hyperpolarized in the targeted and putative inhibitory populations (VGAT+ and VGLUT2−) compared to the targeted and putative excitatory populations (VGLUT2+ and VGAT−; $p < 0.001$, Student Newman–Keuls *post hoc* test). The amplitude of APs was larger for the inhibitory cell groups compared to the excitatory populations (VGAT+ and VGLUT2− vs. VGLUT2+ and VGAT−, $p < 0.001$), and the time course (rise time and half-width) was faster in the inhibitory vs. excitatory subsets (VGAT+ and VGLUT2− vs. VGLUT2+ and VGAT−, $p < 0.001$). Finally, AHP amplitude was larger in VGLUT2− vs. VGLUT2+ neurons ($p = 0.02$). Thus, inhibitory dorsal horn populations exhibited AP spikes that had larger amplitudes and faster time courses than their excitatory counterparts.

We next assessed the features of AP discharge initiated by depolarizing current step injection (1 s), because the literature

TABLE 2 | Action potential properties.

Cell type	AP threshold (mV)	AP peak (mV)	AP rise time (ms)	AP half-width (ms)	AHP peak (mV)
VGAT+ (*targeted inhibitory, n = 74*)	−33.2 ± 3.7* (VGAT−, VGLUT2+)	63.7 ± 11.7* (VGAT−, VGLUT2+)	0.86 ± 0.23 (VGAT−, VGLUT2+)	3.18 ± 0.78 (VGAT−, VGLUT2+)	−20.5 ± 7.3
VGAT− (*putative excitatory, n = 51*)	−27.2 ± 6.0* (VGAT+, VGLUT2−)	52.8 ± 11.3 (VGAT+, VGLUT2−)	1.11 ± 0.40 (VGAT+, VGLUT2−)	3.90 ± 1.30 (VGAT+, VGLUT2−)	−20.9 ± 6.5
VGLUT2+ (*targeted excitatory, n = 39*)	−27.8 ± 6.0* (VGAT+, VGLUT2−)	49.9 ± 11.4 (VGAT+, VGLUT2−)	1.22 ± 0.48 (VGAT+, VGLUT2−)	3.99 ± 1.09 (VGAT+, VGLUT2−)	−18.1 ± 6.5 (VGLUT2−)
VGLUT2− (*putative inhibitory, n = 23*)	−30.2 ± 5.6* (VGAT−, VGLUT2+)	58.7 ± 9.7 (VGAT−, VGLUT2+)	0.80 ± 0.20 (VGAT−, VGLUT2+)	3.06 ± 0.87 (VGAT−, VGLUT2+)	−23.9 ± 5.8 (VGLUT2+)

*Mean ± SD. Significant differences between groups denoted by * (bracketed below, $p < 0.05$).*

TABLE 3 | Action potential discharge pattern characteristics.

	TF	IB	DF	SS	RB
Rheobase (pA)	43.57 ± 17.61 *DF, SS, RB	47.06 ± 25.05 *DF, SS	71.30 ± 25.46 *TF, IB	110.00 ± 14.14 *TF, IB	74.29 ± 29.92 *TF
AP spiking delay (ms)	40.51 ± 18.89 *DF	32.60 ± 14.61 *DF	193.73 ± 128.25 *TF, IB, SS, RB	8.65 ± 2.76 *DF	20.01 ± 13.13 *DF
1st AP ISI (ms)	54.72 ± 25.68	69.56 ± 160.43	88.46 ± 143.75	-	95.45 ± 202.67
APs (*n*)	12.98 ± 6.97 *IB, SS, RB	6.38 ± 3.63 *TF	9.30 ± 5.52	1.00 ± 0.00 *TF	5.14 ± 2.48 *TF
AP spiking duration (ms)	861.42 ± 128.04 *IB, DF, RB	365.24 ± 262.93 *TF, DF	605.11 ± 277.12 *TF, IB	-	372.56 ± 348.35 *TF
AP spiking adaptation	0.49 ± 0.20 *RB	0.55 ± 0.29 *RB	0.85 ± 0.41 *RB	-	2.60 ± 5.71 *TF, IB, DF

*$p < 0.05$.

suggests certain discharge responses are features of inhibitory and excitatory interneurons (**Figure 2A**). Consistent with our previous work, discharge patterns could be distinguished by distinct characteristics of repetitive AP discharge (**Table 3**). For example, TF was characterized by low rheobase, a high number of APs, and long discharge durations. In contrast, AP discharge commenced significantly later following step onset in DF, responses were limited to one AP in Sigle Spiking, and Rapid bursting exhibited significant spike adaptation. A comparison of the relative distribution of discharge responses across the inhibitory and excitatory populations (**Figure 2B**) highlighted important differences ($p < 0.001$). The TF was the dominant response among inhibitory interneurons (∼70% vs. 30%; VGAT+/VGLUT2− vs. VGLUT2+/VGAT−). In contrast, IB and DF responses were more frequent in excitatory interneurons (IB ∼35% vs. 15%, DF ∼25% vs. 7%; VGLUT2+/VGAT− vs. VGAT+/VGLUT2−). Finally, although rare, rapid burst discharge (**Figure 2A**) was observed in VGAT+ and VGAT− neurons (7% and 4%, respectively).

Consistent with the above distribution of AP discharge patterns, the subthreshold voltage-activated currents that shape AP discharge was also differentially expressed across the cell groupings (**Figure 3**). Specifically, voltage steps from −90 mV to −40 mV unmasked two opposing rapidly activating transient voltage-activated currents in LI-II neurons, either an outward A-type potassium current or an inward T-type calcium current (**Figure 3A**). Recordings from excitatory interneurons showed a strong bias towards outward A-type current responses (∼69% for the excitatory VGLUT2+ and VGAT− neurons vs. 30% for the inhibitory VGAT+ and VGLUT2− populations, $p < 0.001$). Conversely, inhibitory interneurons were more likely to express T-type currents than excitatory populations (∼38% vs. 14%, $p < 0.001$). In addition, voltage steps to −90 mV often evoked slowly activating hyperpolarization-activated cation currents in the inhibitory populations, reflecting I_h that was less common in excitatory populations (∼78% vs. 35%, $p < 0.001$). Measurement of peak currents during steps to −40 mV (regardless of direction) and −90 mV provides an indication of the relative magnitude of these currents in each population. This comparison for the −40 mV response confirmed A-type currents dominate in excitatory populations (170 ± 203 and 169 ± 205 pA vs. −1.2 ± 96.8 and −1.7 ± 111.5 pA, for VGLUT2+ and VGAT− vs. VGAT+ and VGLUT2− cells, $p < 0.001$). This is consistent with the greater incidence of A-type potassium currents and DF AP discharge in these cells. In contrast, the lower peak current values for the inhibitory populations (VGAT+ and VGLUT2−) reflected a subset of these cells expressing pronounced inward T-type current responses (−100 to −250 pA), which is consistent with rapid burst and initial burst responses. Consistent with reports of a high incidence of TF in inhibitory populations, peak current responses during the −90 mV step (i.e., I_h) were also larger in these cells (−26.6 ± 44.2 and −13.7 ± 25.4 pA vs. −5.8 ± 4.9 and −6.8 ± 7.3 pA, for VGAT+/VGLUT2− vs. VGLUT2+/VGAT− cells, $p < 0.001$). Thus, inhibitory dorsal horn populations tend to express voltage-gated currents that support repetitive AP discharge and TF responses dominate.

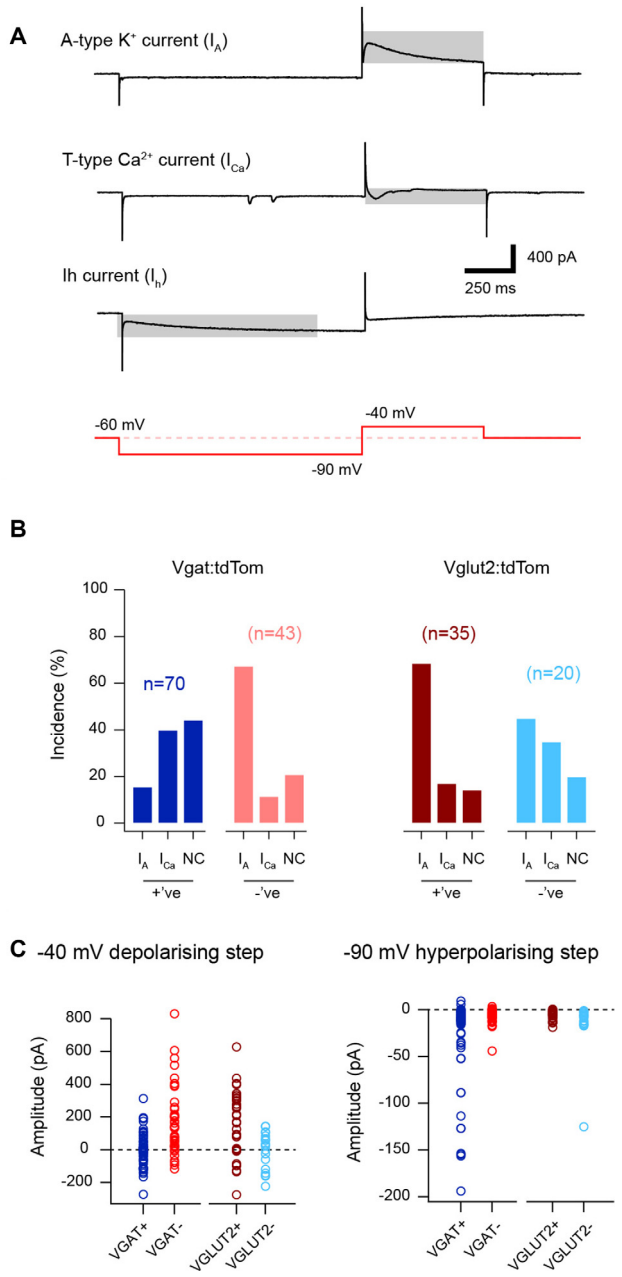

FIGURE 3 | Subthreshold voltage-activated current expression in excitatory and inhibitory populations. **(A)** Traces show representative responses to a voltage step protocol (red lower trace). Three subthreshold voltage-activated currents are identified (highlighted by gray rectangle). These include outward A-type potassium currents (upper trace), inward low threshold T-type calcium currents (middle), and inward hyperpolarization-activated cation currents (I_h, lower). **(B)** Plots show the relative incidence of voltage-activated currents taken from the response to a current step from −90 mV to −40 mV. A-type currents were frequently observed in recordings from excitatory populations (vGLUT2+ and VGAT−, brown and red bars) whereas T-type Ca-currents were more commonly expressed by inhibitory neurons (VGAT+ and VGLUT2−, blue and light blue bars). Note, between 15–40% of recordings in each population did not exhibit a subthreshold current response to this step and they are termed no current (NC) on the bar plots. **(C)** Plots showing the peak amplitude of the subthreshold current responses for the depolarizing

(*Continued*)

FIGURE 3 | Continued
−90 mV to −40 mV (left), and the hyperpolarizing −70 mV to −90 mV steps (right). The left plot shows the dominance of outward current values (i.e., above the dotted line showing zero pA) in the excitatory population, because of the dominance of A-type potassium currents in these cells. In contrast, the inhibitory populations (VGAT+ and VGLUT2−) exhibit smaller currents (i.e., near or below the dotted line), consistent with greater expression of inward T-type calcium currents. The right plot shows the amplitude of I_h in the four neuron types. Note, the large peak amplitude of I_h, among the inhibitory populations (VGAT+ and VGLUT2−).

In contrast, excitatory populations are more likely to express voltage-gated currents that can suppress AP discharge, with DF being more prominent in these cells.

The excitatory synaptic drive that recruits inhibitory and excitatory dorsal horn cell populations was also assessed (**Figure 4**, **Table 4**) by recording spontaneous excitatory postsynaptic currents (sEPSCs). This analysis showed that the sEPSC frequency was four times higher in the excitatory populations (VGLUT2+/VGAT− vs. VGAT+/VGLUT2− cells, $p < 0.001$), whereas the sEPSC decay time constant was slower in inhibitory interneurons (VGAT+ vs. VGLUT2+/VGAT− cells, $p < 0.001$). In contrast, sEPSC amplitude and rise time were similar across all groups ($p = 0.99$ and $p = 0.12$, respectively). Together, this is consistent with excitatory populations in LI-II receiving greater ongoing excitatory drive than inhibitory populations and, based on faster sEPSC decay times, this drive may occur at synapses located closer to their soma.

Morphological Characteristics of VGAT:Td and VGLUT2:Td Populations

Neurobiotin was included in recording pipettes for *post hoc* recovery and characterization of cell morphology. Interestingly, recovery was more successful in inhibitory rather than excitatory interneuron populations with yields of 55% (42/76) and 44% (11/25) for VGAT+ and VGLUT− cells, respectively (**Figure 5A**). In contrast, recovery yields were 35% (14/40) and 26% (15/57) for VGLUT2+ and VGAT− cells (**Figure 5B**). The extent of the somatodendritic tree in the rostrocaudal and dorsoventral planes was assessed for each recovered neuron (**Figure 5C**). Inhibitory interneurons exhibited significantly longer rostrocaudal dimensions than excitatory neurons (322 ± 124 and 304 ± 145 μm vs. 199 ± 73 and 189 ± 65 μm, VGAT+ and VGLUT2− vs. VGLUT2+ and VGAT−, $p < 0001$). In contrast, dorsoventral dimensions were similar across the four neuron types (76 ± 33 vs. 85 ± 36 vs. 76 ± 25 vs. 84 ± 38 μm, VGAT+, VGLUT2− vs. VGLUT2+, and VGAT−; $p = 0.77$).

A ratio of the rostrocaudal to dorsoventral cell dimensions (RC/DV in **Figure 5C**) was also calculated. This ratio was larger for the identified (VGAT+) inhibitory cells ($p < 0.01$), compared to identified and putative excitatory populations (VGLUT2+ and VGAT−). Finally, the relative bias for processes in the dorsoventral plane was assessed by calculating the difference between a cell's ventral and dorsal extent (D-V, **Figure 5C**, far-right plot, both measured from the soma); a value of 0 meant cells had equivalent dorsal and ventral expansions, positive values indicated processes were more likely to extend dorsally in LI-II,

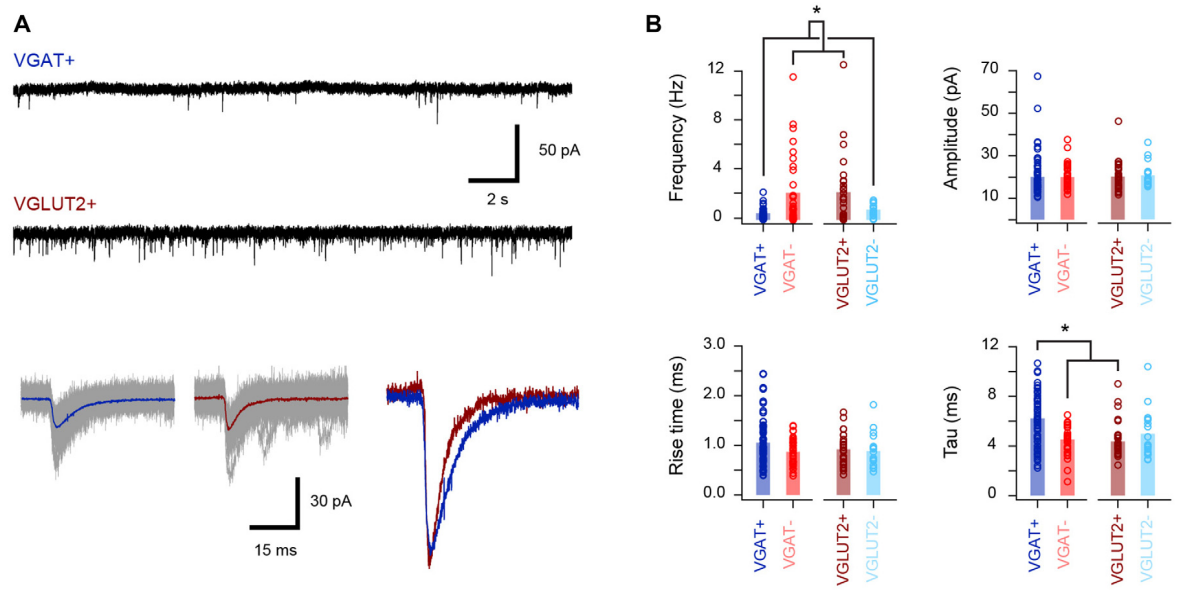

FIGURE 4 | Properties of the excitatory synaptic drive to excitatory and inhibitory populations. **(A)** Upper traces show representative voltage-clamp recordings from inhibitory (vGAT+) and excitatory (vGLUT2+) neurons (holding potential −70 mV). Note the higher frequency of spontaneous excitatory postsynaptic currents (sEPSCs) in the excitatory neuron recording. Lower traces show overlaid sEPSCs captured from the above recordings with averaged currents shown as colored traces. Right traces are averages from a VGAT+ (blue) and VGLUT2+ (red) neuron scaled to the same amplitude. Note the faster sEPSCs decay kinetics in the excitatory neuron. **(B)** Group data plots comparing sEPSC properties for inhibitory and excitatory neurons. Consistent with representative traces in **(A)**, sEPSC frequency was significantly higher in excitatory neurons (VGLUT2+ and VGAT−), while sEPSC decay kinetics were slower in recordings from inhibitory cells (VGAT+ and VGLUT2−). In contrast, sEPSC amplitudes and rise times were similar across the four neuron groups. *$p < 0.05$.

TABLE 4 | Excitatory synaptic input characteristics.

Cell type	sEPSC frequency (Hz)	sEPSC peak (pA)	sEPSC rise (ms)	sEPSC Tau (ms)
VGAT+ (*targeted inhibitory*, *n* = 67)	0.41 ± 0.40* (VGAT−, VGLUT2+)	−20.33 ± 9.32	1.06 ± 0.47	6.22 ± 2.10* (VGAT−, VGLUT2+)
VGAT− (*putative excitatory*, *n* = 37)	2.06 ± 2.74* (VGAT+, VGLUT2−)	−20.09 ± 5.55	0.90 ± 0.27	4.51 ± 1.51* (VGAT+)
VGLUT2+ (*targeted excitatory*, *n* = 29)	2.11 ± 2.76* (VGAT+, VGLUT2−)	−20.44 ± 6.78	0.93 ± 0.31	4.38 ± 1.58* (VGAT+)
VGLUT2− (*putative inhibitory*, *n* = 18)	0.68 ± 0.50* (VGAT−, VGLUT2+)	−20.89 ± 5.59	0.89 ± 0.34	4.99 ± 1.95

*Mean ± SD. Significant differences between groups denoted by *(bracketed below, $p < 0.05$).*

whereas negative values showed processes extended ventrally (LII_i-III). No difference was detected in dorsoventral bias across cell groups ($p = 0.22$). However, the identified excitatory interneuron group exhibited a distribution of dorsoventral measures that was heavily skewed in the ventral plane (**Figure 5C**, far right). Because it is likely that our putative inhibitory (VGLUT−) sample contained some excitatory interneurons, we also compared dorsoventral bias between VGAT+ and VGLUT+ cells. This showed the identified (TdTom+) excitatory population had a ventral bias compared to identified inhibitory cells ($p = 0.04$). Together, these results support the view that inhibitory dorsal horn cells exhibit extensive rostrocaudal territories, whereas excitatory interneuron processes are often biased to extend in the ventral plane.

Heterogeneity Within VGAT:Td and VGLUT2:Td Populations

To further analyze cellular heterogeneity a series of hierarchical cluster analyses were performed using electrophysiological, morphological, and both sets of properties. This analysis was restricted to neurons in which we obtained both electrophysiological and morphological data ($n = 72$). Hierarchical clustering based on electrophysiological data alone yielded six distinct clusters (**Figure 6**). Three clusters contained many neurons (>5) whereas three were small (<5 neurons). The efficiency by which clustering segregated inhibitory and excitatory neurons was calculated by first assigning a cluster identity to the cell type that was in majority, and then determining the proportion of all neurons in this cluster that shared the same phenotype (inhibitory or excitatory). Despite some variability from cluster to cluster (78–100% cell-type purity), there was a high degree of accurate segregation, with 92% of neurons successfully clustered into their correct phenotype. Heatmaps of the properties used in this analysis showed RMP, AP threshold (AP threshold) and rise time (AP rise), voltage-activated current expression (peak at −40 peak and at −90 mV steps), and certain sEPSC properties (rise and decay time constant) were important in forming the clusters.

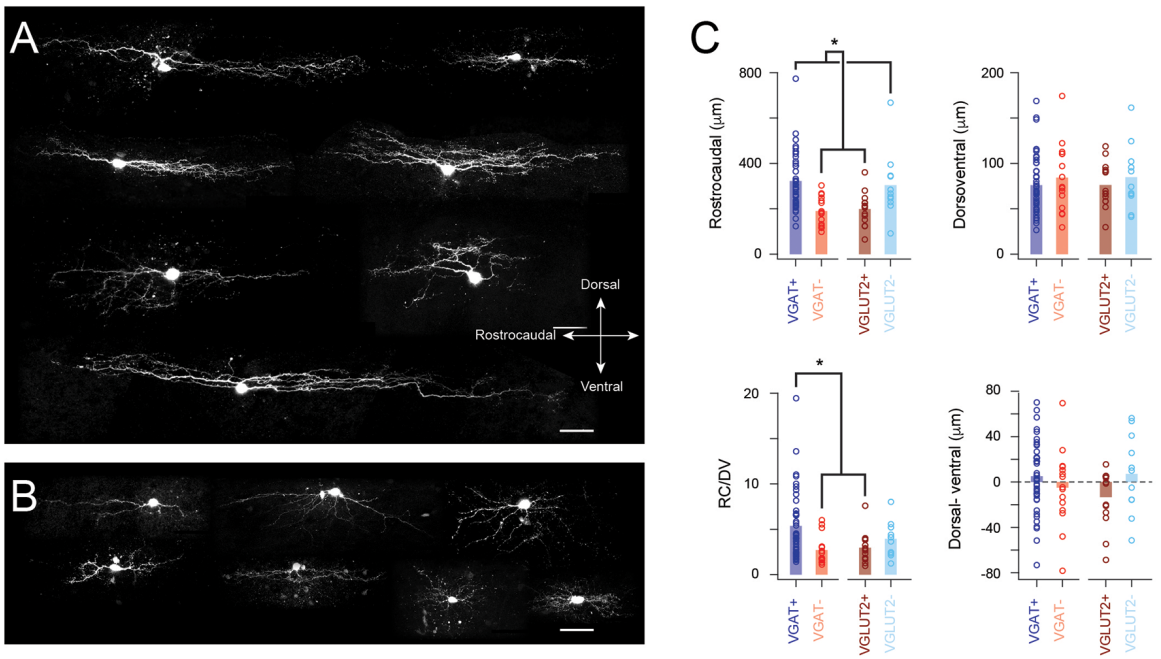

FIGURE 5 | Distinct morphological features in excitatory and inhibitory populations. **(A)** Images show example morphologies from inhibitory SDH neurons. Note, these neurons exhibit extensive rostrocaudally oriented dendritic arbors. **(B)** Images show example morphologies from excitatory SDH neurons. Morphology is more diverse in this neuron population and rostrocaudal dendritic expansion is limited. **(C)** Group-data plots comparing measures of dendritic extent and orientation for inhibitory and excitatory neurons. Consistent with examples above, inhibitory neurons (VGAT+ and VGLUT2−) exhibit larger dendritic fields in the rostrocaudal plane, whereas the dorsoventral field is similar in both populations. These measurements were used to calculate a dorsoventral dendritic field ratio (RV/DV). Note, this was the largest for VGAT+ neurons compared to the excitatory population. Finally, any preference for dorsal or ventral dendritic orientation was quantified by subtracting ventral expansion from dorsal expansion. There was no difference between inhibitory and excitatory populations. Despite this, a bias in the distribution of these data was observable in the excitatory (VGLUT2+ and VGAT−) but not inhibitory (VGAT+ and VGLUT2−) datasets. This difference became significant when comparisons were limited to the VGAT+ and VGLUT2+ data (Scale bar: 50 μm). *$p < 0.05$.

Hierarchical clustering of the same 72 neurons according to morphological features segregated four distinct clusters with similar proportions of cells (**Figure 7**). One cluster contained purely inhibitory neurons, while the remaining three clusters contained a mix of inhibitory and excitatory neurons. Thus, morphology-based clustering did not segregate neurons as well as our electrophysiological analysis (**Figure 6**), with only 66% of neurons segregating with the same phenotype. This suggests electrophysiological properties better discriminate between the excitatory and inhibitory cell phenotypes, however, fewer properties were used in the morphology vs. electrophysiology analysis (4 vs. 19). Regardless, the heatmaps of the four dendritic dimension measurements (rostrocaudal length, dorsoventral length, rostrocaudal/dorsoventral ratio, and dorsoventral bias) suggest each parameter contributed to segregation.

Hierarchical clustering combining electrophysiological and morphological features yielded five distinct clusters (**Figure 8**, **Table 5**), two excitatory groups (Ex1 and Ex2) and three inhibitory groups (In1, In2, and In3). Only two of the inhibitory clusters contained any excitatory cells. The addition of morphological features did not appreciably improve clustering accuracy (93% of neurons segregating with the same phenotype, vs. 92% in electrophysiology only clustering). Heatmaps also showed the same properties that influenced independent electrophysiological or morphological clustering also did so in the combined clustering analysis. **Table 5** highlights a range of properties that differed across clusters, not surprising given the nature of the hierarchical clustering approach. Also predictable, given the differences between excitatory and inhibitory interneurons (**Tables 1**, **2**, **4**; and **Figures 2**–**5**), many properties differed between excitatory vs. inhibitory clusters. Most interesting, however, were properties that distinguished within the excitatory or inhibitory clusters. AP properties including peak amplitude, rise and half-width, as well as the duration of spiking and number of spikes discharged all differed between excitatory clusters (Ex1 vs. Ex2). In addition, peak A-current (VC −40 mV peak) and sEPSC frequency also differed between the excitatory clusters. For inhibitory clusters, Rheobase current, AP and AHP peak, Ih current peak (VC -90 mV peak), the first AP interspike interval (1st AP ISI), AP adaptation, sEPSC time course (rise time and Tau), and morphological features (rostrocaudal extent, dorsoventral extent, and the RC:DV ratio) distinguished clusters (In1 vs. In2 vs. In3).

Finally, we compared how cluster membership for individual neurons changed between analyses based on electrophysiological, morphological or combined morphological

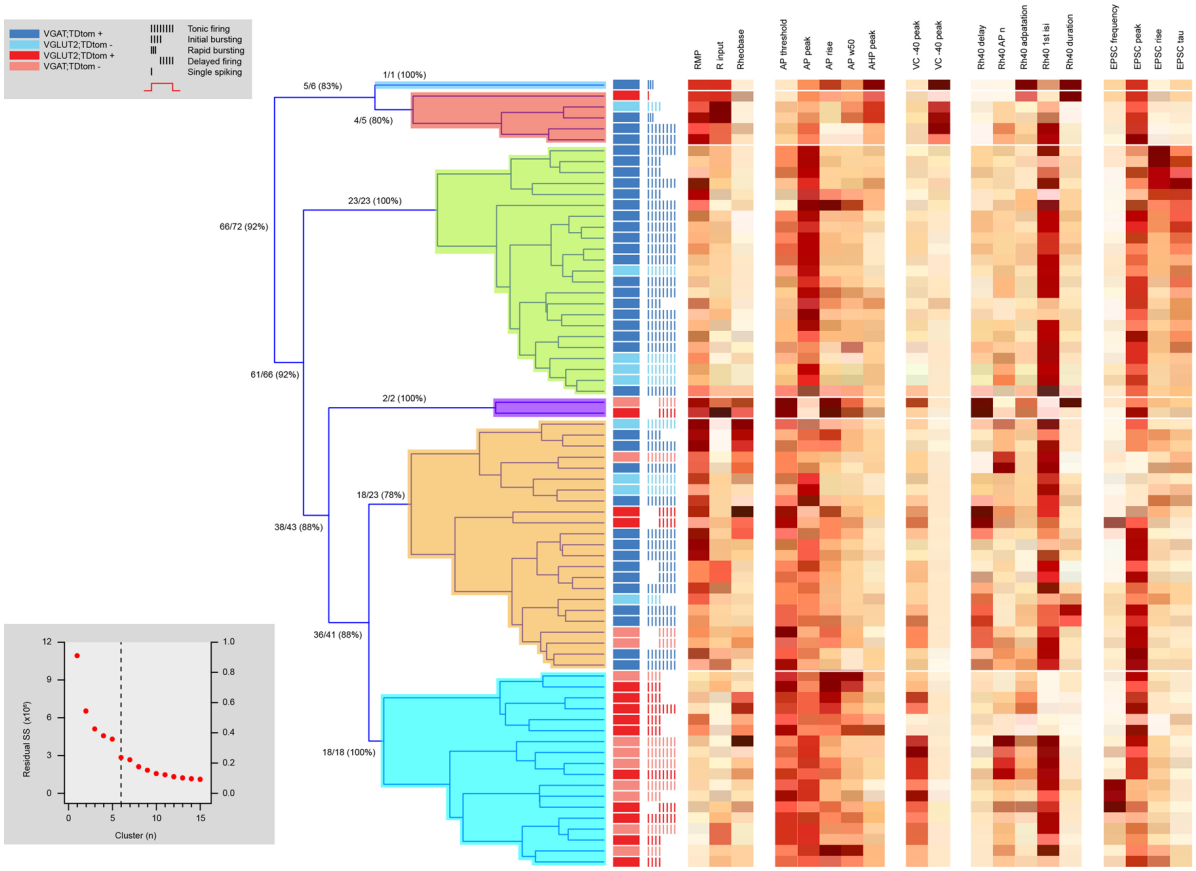

FIGURE 6 | Hierarchical cluster analysis of excitatory and inhibitory dorsal horn neurons on electrophysiological attributes. Dendrogram and heatmaps plotting the assignment of dorsal horn neurons into clusters based on their electrophysiological properties. The distribution of excitatory and inhibitory neurons and their AP discharge responses are annotated using the key summarized in the upper left gray box, denoting neuron type and discharge pattern (inset). Dendrograms show the clusters (six for this analysis) determined using a K-Means elbow method, which plots the sum of squares error (SSE) for increasing cluster number to determine the point where adding another cluster does not appreciably improve the SSE (lower gray box inset). Clusters included one large inhibitory population (green cluster in dendrogram), one large excitatory population (blue), and one large mixed population of cells (orange), as well as three smaller clusters (deep blue, red, and purple). Heat maps highlight the relationship of 19 electrophysiological characteristics to each cell cluster assignment.

and electrophysiological datasets (**Figure 9**). For the electrophysiological approach (**Figure 9A**), most cells from each of the original six clusters remained grouped together when morphology data were added (100%, 100%, 78%, 100%, 83%, 67%). For excitatory neurons, one large cluster split into two distinct clusters and a smaller population merged with one of these groups. Inhibitory neurons, which originally segregated into two large and two small clusters, remained grouped together with some cells switching or merging to form three distinct clusters. For the morphological approach, inhibitory neurons from one original cluster stayed tightly grouped (81%), while two other mixed cell clusters (excitatory and inhibitory neuron membership) split, contributing to each of the five clusters that were resolved when electrophysiological data was added. Not surprisingly, given the initial cluster analysis results, the variety of electrophysiological attributes resolved relatively pure clusters in terms of correct assignment of excitatory and inhibitory phenotypes. While the addition of morphological features did not change cluster purity, it did further distinguish these groups providing an enhanced view of this heterogeneous population.

DISCUSSION

Resolving functionally discrete populations of neurons that serve specific roles in neuronal circuits remains a major challenge in neuroscience (Zeng and Sanes, 2017). This is certainly true of the dorsal horn where neuronal heterogeneity is substantial, and knowledge of how cell populations are assembled into circuits is essential to understand the normal sensory experience. Historically, a variety of approaches have been used to dissect these heterogeneous populations including electrophysiological properties, morphology, and neurochemical content (Grudt and Perl, 2002; Graham et al., 2004, 2008; Yasaka et al., 2010; Gutierrez-Mecinas et al., 2016; Boyle et al., 2017). Recent single-cell molecular techniques, however, have provided an alternative approach to neuron classification and, in the dorsal horn, suggested many more discrete subpopulations exist

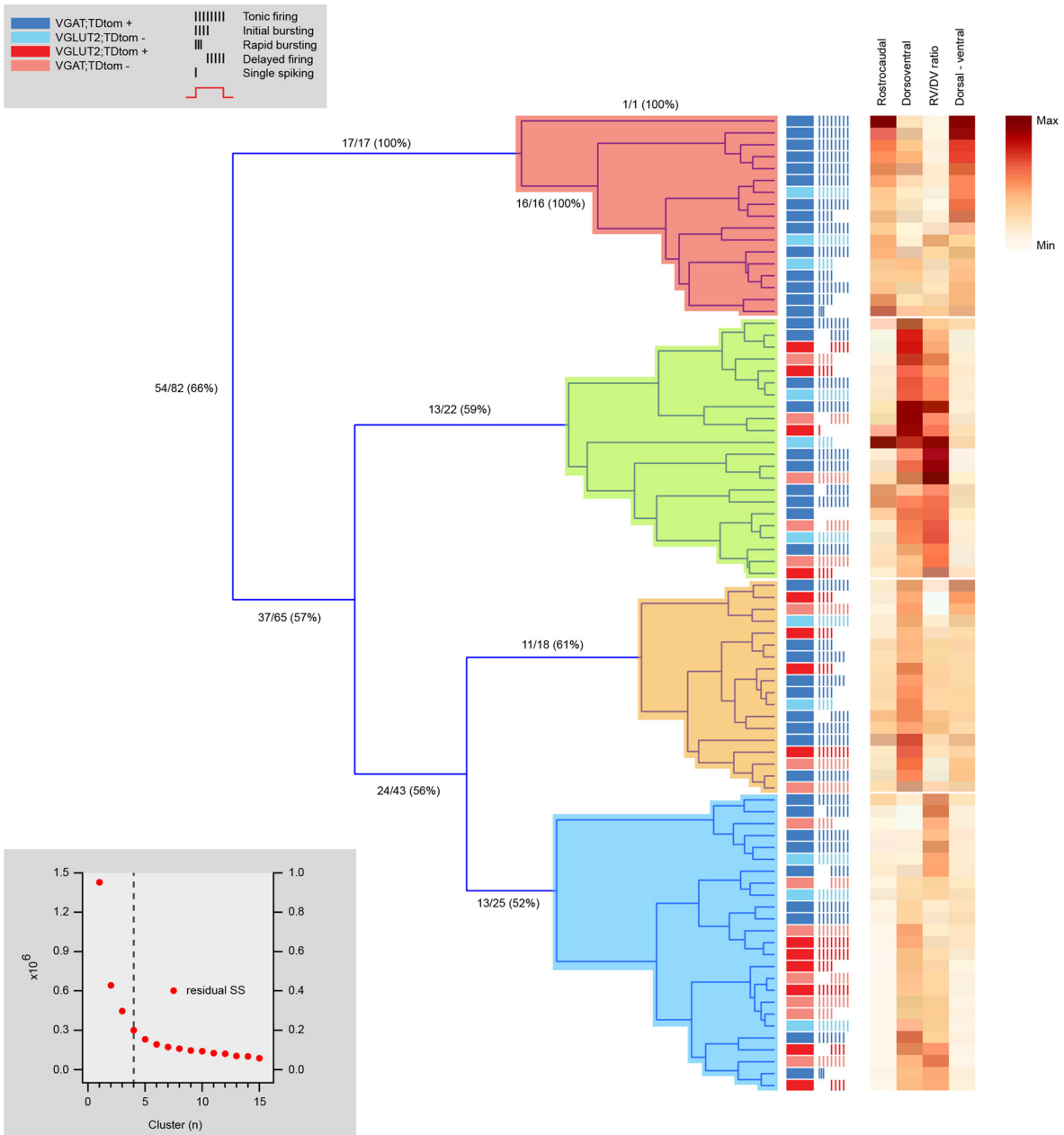

FIGURE 7 | Hierarchical cluster analysis of excitatory and inhibitory dorsal horn neurons on morphological attributes. Dendrogram and heatmap showing assignment of dorsal horn neurons into clusters based on morphological properties. The distribution of excitatory and inhibitory neurons, as well as each neuron's AP discharge response pattern, are annotated using the key summarized in the upper left gray box, denoting neuron type and discharge pattern (inset). The number of clusters (four for this analysis) was assigned using a K-Means elbow method. This method plots the sum of squares error (SSE) for increasing cluster numbers to determine when adding additional clusters does not appreciably improve the SSE (lower gray box inset). One cluster contains a population of purely inhibitory interneurons with larger rostrocaudal dendritic dimensions (red). All remaining clusters include a mix of inhibitory and excitatory neurons (green, orange, and blue). Heat maps to the right highlight the relationship of four morphological characteristics to each cell cluster assignment.

than predicted by the historical literature. This prompted the current study.

Our results highlight a number of electrophysiological properties that distinguish excitatory or inhibitory dorsal horn neurons, though these properties do not segregate entirely to either population. When a suite of electrophysiological parameters are used to perform a hierarchical cluster analysis, excitatory and inhibitory interneurons reliably segregate into relatively pure cluster groups (with 92% purity, **Figure 5**). In contrast, the same analysis on morphological features yielded poorer clustering (66% purity, **Figure 6**), though one cluster did contain only inhibitory cells and most likely

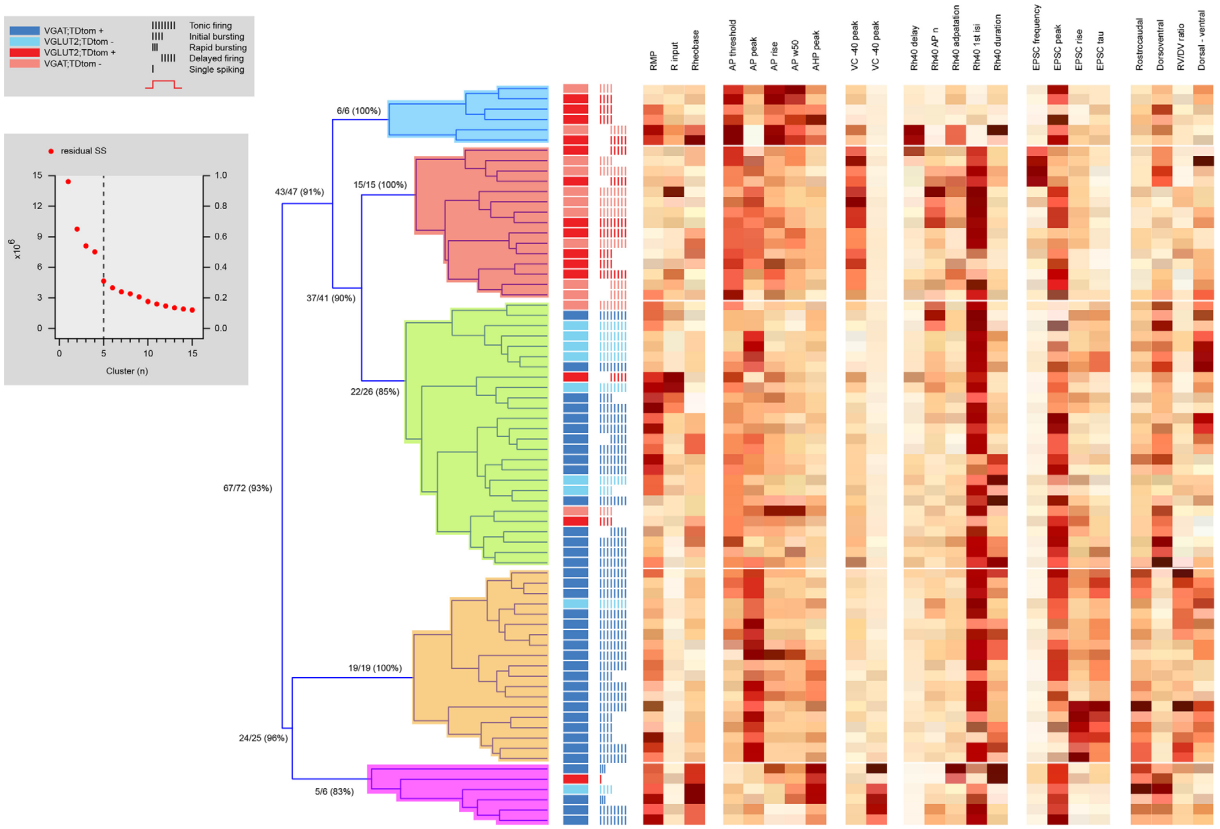

FIGURE 8 | Hierarchical cluster analysis of excitatory and inhibitory dorsal horn neurons on combined electrophysiological and morphological attributes. Dendrogram and heatmap plotting the assignment of dorsal horn neurons into clusters based on their electrophysiological and morphological properties. The distribution of excitatory and inhibitory neurons, as well as the AP discharge response pattern for each neuron, are annotated using the key summarized in the lower-left gray box, denoting neuron type and discharge pattern (inset). The number of clusters (four for this analysis) was assigned using a K-Means elbow method that plots the sum of squares error (SSE) for increasing cluster number to determine the point where additional clusters do not appreciably improve the SSE (upper gray box inset). Clustering using both electrophysiological and morphological attributes differentiates two purely excitatory clusters (blue and red), one purely inhibitory cluster (orange), and two clusters also dominated by inhibitory cells (green and pink). Heat maps highlight the relationship of 19 electrophysiological, and four morphological characteristics to each cell cluster assignment.

represents the well-established islet-inhibitory phenotype. When electrophysiological and morphological features were combined, clustering was similar to using electrophysiological properties alone, discriminating five distinct groups; two excitatory and three inhibitory. Our findings have a number of implications for our views of dorsal horn neuron heterogeneity and they also raise a number of questions and caveats for future studies.

LIMITATIONS

Although the use of transgenic animals to prospectively identify excitatory and inhibitory populations has obvious advantages, it also has limitations. First, our immunolabeling indicated that transgenically labeled populations (*via* Tdtomato expression) reliably marked excitatory and inhibitory cells (>90% of excitatory and inhibitory cells correctly labeled). Thus, we can be confident that most targeted recordings and subsequent morphological analysis assessed the intended excitatory or inhibitory cell types. We also collect data from unlabeled cells in each transgenic line under the premise that these cells should represent the opposing population (e.g., presumptive inhibitory cells in the VGLUT2:Td mouse). This assumption appears to largely hold with the VGAT:Td line as TdTom labeled 87% of inhibitory cells (assessed by co-labeling for Pax2) leaving a fraction of the VGAT−Td negative cells (∼13%) were also inhibitory. Thus, recordings from VGAT− cells, assumed to be excitatory neurons, may include some inhibitory cells.

Contrasting the relatively high capture of inhibitory interneurons in VGAT:Td mice, we estimate that the TdTom labeled approximately a third of the excitatory interneurons in VGLUT2:Td mice. This data did not allow us to determine if the TdTom−labeled population represented a cross-section of excitatory dorsal horn neurons or a discrete subset. The similarity in the values and distribution of electrophysiological and morphological data between the VGLUT+ and VGAT− samples favors the likelihood that the VGLUT2+ sample captures a cross-section of these cells. Future work screening a panel of neurochemical (Gutierrez-Mecinas et al., 2016) or

molecular (Haring et al., 2018) markers known to be restricted to excitatory populations will be necessary to further clarify this point.

Another implication of the lower labeling yield in VGLUT2:Td mice is the potential TdTom−negative recordings included both inhibitory and excitatory interneurons. Despite this caveat, many of the comparisons between VGAT+ and VGLUT2− cells are strikingly similar. For example, the similar distributions of AP discharge patterns and spontaneous EPSC frequency in VGAT+/VGLUT2− compared to the VGLUT2+/VGAT− data (**Figures 2**, **4**). A number of factors may have contributed to this result, including a difference in identification and sampling of TdTom−labeling in fixed tissue vs. endogenous TdTom−expression in fresh spinal slices. Specifically, immunolabeling enhanced the fluorescence signal in fine dendrites and axons in fixed tissue. This effectively increased background labeling in the dense VGLUT2+ plexus of the dorsal horn, making it challenging to resolve weakly labeled somatic profiles. Alternatively, fluorescent TdTom−signals in fresh tissue could only be resolved in cell somas, and exposure was varied to verify the presence or absence of even weak signals. Thus, the populations described in fixed tissue samples may not be identical to those recorded in fresh slices. In addition, an inherent unintended bias when selecting cells to record in slice (always present in patch-clamp recordings) may have influenced our sampling across mouse lines (Smith et al., 2015). Regardless, some data still points to contamination of the VGLUT2-negative sample by excitatory cells, such as an elevated incidence of A-type potassium currents (∼45%), which is widely regarded as a property restricted to excitatory populations. Altogether, these caveats informed our use of the terms "identified" excitatory/inhibitory neurons for VGAT+/VGLUT2-samples and "putative" excitatory/inhibitory neurons for VGAT−/VGLUT2− data. These considerations will be important for future studies employing the VGAT-cre and VGLUT2-cre animals to study populations in the dorsal horn.

Our targeted recording approach allowed us to obtain similar sample sizes for excitatory and inhibitory neurons. While this was a statistically appropriate approach, it is at odds with the established ratio of approximately 3:1 for excitatory and inhibitory populations (Harris et al., 2018; Sathyamurthy et al., 2018), and thus introduces a sampling bias that may have influenced our clustering results. Similarly, our cluster analysis was restricted to cells that yielded both electrophysiological and morphology data. This limited our overall sample size for cluster analyses. These factors likely affected our capacity to confidently resolve smaller subpopulations of excitatory and inhibitory neurons. Future work that expands these samples may resolve a greater degree of functional and morphological heterogeneity. Also regarding clustering, we used the K-means elbow method to determine the number of clusters within our data, which is a conservative method. Thus, our data may contain additional electrophysiologically and morphologically distinct populations obscured by this approach. This is supported by the heatmap data for the hierarchical clustering (**Figures 6**–**8**), which contains a number of AP, sEPSC, and morphological parameters that are distinctly distributed with clear boundaries, even within clusters. Larger sample sizes could address this issue, as well as the inclusion of comparable data from other genetically identified populations. For example, incorporating electrophysiological and morphological data from somatostatin, dynorphin, PV, transient VGLUT3, and calretinin expressing populations would test whether these well-characterized populations cluster discretely, or if they overlap with the identified excitatory and inhibitory populations in the current study.

Distinguishing Excitatory and Inhibitory Interneuron Characteristics

A recent study relates closely to the excitatory vs. inhibitory dataset in our experiments (Punnakkal et al., 2014). Using a Bac-transgenic mouse, which labeled VGLUT2-positive neurons with a green fluorescent protein (VGLUT2:GFP), a variety of electrophysiological and morphological properties were compared with two other commonly used transgenic lines that label GABAergic (GAD67:GFP) and glycinergic (GlyT2:GFP) interneurons, respectively. A number of electrophysiological properties were identified that differentiated the VGLUT2:GFP population from GAD67:GFP and GlyT2:GFP recordings. For example, DF AP discharge was more prevalent in VGLUT2:GFP recordings, whereas TF dominated in the GAD67:GFP and GlyT2:GFP samples. This work also highlighted a larger mean rheobase current, a more depolarized AP threshold, and broader APs for the VGLUT2:GFP neurons. The anatomy of VGLUT2:GFP neurons showed that these cells had central, radial and vertical, but never islet cell morphologies. Our data broadly agree with this study, though we did identify differences in properties such as input resistance, RMP, AP peak, and AP rise time not reported in the previous study. Likewise, we did not detect differences in rheobase current. While some of these disparities may be due to technical differences, both studies highlight that each transgenic line did not identify all VGLUT2+ neurons with TdTomato (∼30%) or GFP (20–40%), respectively. Thus, datasets may overlap, without necessarily sampling the same population. Regardless, the similarity of our results and this work provide confidence that the VGLUT2:Td mouse line provides an opportunity to better understand heterogeneity within dorsal horn populations.

Another study has sought to clarify the inhibitory nature of labeled VGAT-positive cells, before going on to manipulate these cells and monitor behavioral outcomes (Koga et al., 2017). This work compared VGAT-RFP expression with total Pax2 and showed that the labeled vGAT+ cells were almost all inhibitory (∼98% of vGAT+ were Pax2+). The proportion of all inhibitory cells captured was, however, much smaller (∼25% Pax2 overlapped with the vGAT+) and most likely reflects sparse viral labeling of the VGAT-Cre population in contrast to our transgenic breeding approach. Some targeted recordings ($n = 5$) were made in this study and showed that all recorded cells exhibited the TF discharge pattern that is typical of inhibitory interneurons. While the majority of vGAT+ cells (∼75%) in our study exhibited TF, there was more diversity including; initial/rapid bursting (∼18%), delayed (5%) and single spiking (1%) patterns. This suggests we captured a more heterogeneous population, which can only be uncovered in a larger sample

TABLE 5 | Cluster specific properties.

	Cluster 1 (Ex1)	Cluster 2 (Ex2)	Cluster 3 (In1)	Cluster 4 (In2)	Cluster 5 (In3)
RMP (mV)	−60.22 ± 11.58	−71.28 ± 5.20 *In1, In2, In3	−57.64 ± −10.20 *Ex2	−61.60 ± 8.55 *Ex2	−50.69 ± 3.950 *Ex2
Rinput (MΩ)	268.04 ± 94.98	257.49 ± 136.12 *In2	243.68 ± 159.52 *In2	116.83 ± 28.80 *Ex2, In1	144.86 ± 99.012
Rheobase (pA)	60.00 ± 35.78 *In3	45.33 ± 20.66 *In3	45.38 ± 19.23 *In3	46.32 ± 13.42 *In3	100.00 ± 17.89 *Ex1, Ex2, In1, In2
AP threshold (mV)	−21.26 ± 5.75 *In1, In2, In3	−26.43 ± 3.25 *In1, In2, In3	−30.77 ± 3.23 *Ex1, Ex2, In3	−33.58 ± 4.15 *Ex1, Ex2	−37.74 ± 3.18 *Ex1, Ex2, In1
AP peak (mV)	42.30 ± 18.05 *Ex2, In1, In2	58.78 ± 9.68 *Ex1, In2	57.30 ± 9.54 *Ex1, In2	72.00 ± 7.00 *Ex1, Ex2, In1, In3	47.94 ± 6.83 *In2
AP rise (ms)	1.40 ± 0.29 *Ex2, In1, In2, In3	0.99 ± 0.145 *Ex1	0.87 ± 0.19 *Ex1	0.87 ± 0.18 *Ex1	0.77 ± 0.27 *Ex1
AP w50 (ms)	5.17 ± 1.17 *Ex2, In1, In2, In3	3.61 ± 0.43 *Ex1	3.10 ± 0.73 *Ex1	3.41 ± 0.53 *Ex1	3.33 ± 1.01 *Ex1
AHP peak (mV)	−15.34 ± 6.85 *In1	−23.42 ± 4.51 *In3	−23.96 ± 3.39 *Ex1, In3	−20.76 ± 5.19 *In3	−6.11 ± 11.13 *Ex2, In1, In2
VC −40 mV peak (mV)	50.03 ± 184.73 *Ex2	356.82 ± 162.81 *Ex1, In1, In2, In3	34.99 ± 110.61 *Ex2	−26.61 ± 61.69 *Ex2	9.99 ± 44.36 *Ex2
VC −90 mV peak (mV)	−3.43 ± 1.47 *In3	−6.15 ± 3.63 *In3	−6.72 ± 5.50 *In3	−16.15 ± 13.79 *In3	−119.92 ± 67.64 *Ex1, Ex2, In1, In2
AP delay (ms)	106.30 ± 114.65 *In3	53.09 ± 49.44	52.10 ± 34.06	43.51 ± 11.77	13.37 ± 3.88 *Ex1
1st AP ISI (ms)	148.87 ± 287.51	40.57 ± 9.87 *In3	60.29 ± 37.33 *In3	63.01 ± 16.70 *In3	279.93 ± 407.22 *Ex2, In1, In2
AP duration (ms)	132.38 ± 116.80 *Ex2, In1, In2, In3	786.07 ± 233.29 *Ex1	816.68 ± 157.41 *Ex1	784.15 ± 208.03 *Ex1	633.77 ± 349.83 *Ex1
APs (*n*)	3.17 ± 1.33 *Ex2	15.33 ± 7.86 *Ex1, In2	11.15 ± 6.04	8.95 ± 3.24 *Ex2	8.00 ± 6.20
AP spiking adaptation	0.60 ± 0.38	0.63 ± 0.34	0.45 ± 0.18 *In3	0.45 ± 0.12 *In3	3.02 ± 6.14 *In1, In2
sEPSC frequency (Hz)	0.51 ± 0.41 *Ex2	2.65 ± 2.59 *Ex1, In1, In2	0.585 ± 0.44 *Ex2	0.43 ± 0.45 *Ex2	1.01 ± 0.57
sEPSC peak (pA)	−17.53 ± 6.10	−18.52 ± 4.21	−19.32 ± 6.56	−19.61 ± 5.32	−15.31 ± 2.64
sEPSC rise (ms)	0.77 ± 0.27 *In2	0.91 ± 0.19 *In2	1.00 ± 0.29 *In2	1.43 ± 0.54 *Ex1, Ex2, In1, In3	0.61 ± 0.30 *In2
sEPSC tau (ms)	4.85 ± 1.01 *In2	3.71 ± 0.73 *In1, In2	5.27 ± 1.55 *Ex2, In2	7.97 ± 1.86 *Ex1, Ex2, In1, In3	3.97 ± 0.65 *In2
Rostrocaudal (μm)	217.71 ± 68.86 *In2, In3	169.30 ± 55.87 *In2, In3	245.76 ± 75.50 *In2, In3	381.71 ± 130.52 *Ex1, Ex2, In1	413.18 ± 172.95 *Ex1, Ex2, In1
Dorsoventral (μm)	79.50 ± 23.97	64.58 ± 23.97 *In1, In3	90.72 ± 26.81 *Ex2, In2	48.58 ± 11.67 *In1, In3	101.62 ± 33.07 *Ex2, In2
RC:DV	2.87 ± 1.02 *In2	3.19 ± 2.02 *In2	2.92 ± 1.19 *In2	8.36 ± 3.76 *Ex1, Ex2, In1, In3	4.167 ± 1.65 *In2
Dorsal—ventral (μm)	−11.76 ± 34.76	−1.52 ± 28.38	3.73 ± 37.21	10.99 ± 21.17	−13.22 ± 37.98

*$p < 0.05$.

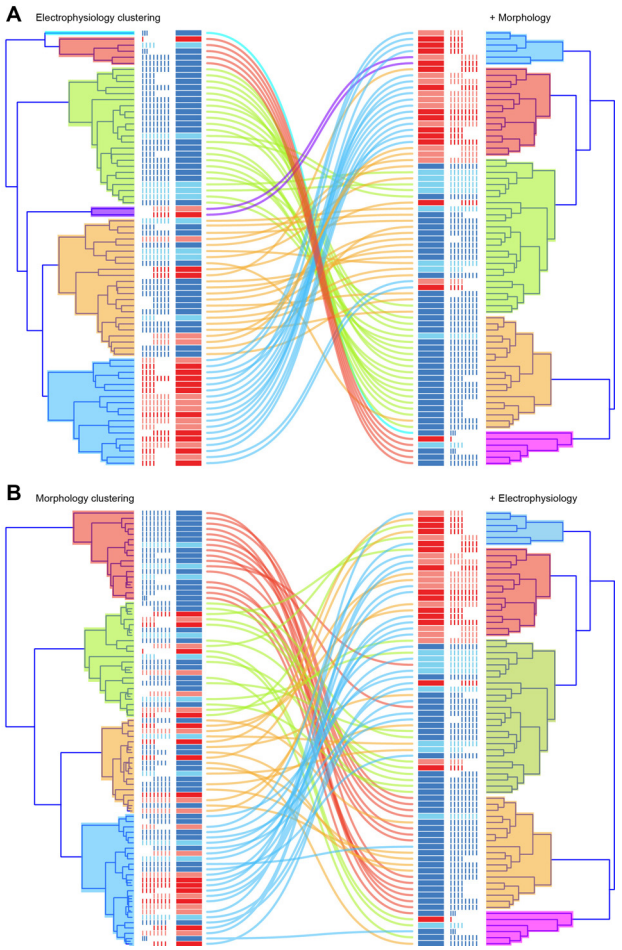

FIGURE 9 | Correlation of cluster membership across clustering approaches. The figure compares individual cell cluster membership when clustering is based on electrophysiological (**A**, upper left) or morphological data (**B**, lower left), and when both datasets are combined (right for both **A,B**). Corresponding dendrograms are presented side-by-side, with lines denoting cell location in clustering (left vs. right). When the path of a colored line remains close to others from its original cluster the clusters are shared: electrophysiological vs. electrophysiological plus morphological clustering **(A)**; or morphological vs. morphological plus electrophysiological clustering **(B)**. Note cluster membership remains similar in **(A)** but diversifies more dramatically in (**B**; i.e., there is more mixing of the colored lines).

size (n = 5 vs. n = 74, respectively). Nevertheless, these data show a VGAT−Tdtom mouse is a useful tool for teasing apart, from and inhibitory standpoint, the complex circuitry of the dorsal horn.

Other studies have also undertaken electrophysiological and morphological characterizations of identified dorsal horn neurons (Hantman et al., 2004; Heinke et al., 2004; Zeilhofer et al., 2005; Hughes et al., 2012; Duan et al., 2014; Punnakkal et al., 2014; Smith et al., 2015; Dickie et al., 2019). Together with the above work, they provide a number of insights into the features that distinguish different subpopulations. For example, TF AP discharge is associated with inhibitory populations (Hantman et al., 2004; Heinke et al., 2004; Zeilhofer et al., 2005; Smith et al., 2015), whereas DF is usually associated with excitatory cell types (Punnakkal et al., 2014; Smith et al., 2015; Dickie et al., 2019). Consistent with these observations, the hyperpolarization-activated cation current (Ih), which supports repetitive AP discharge, is common among inhibitory populations. The A-type potassium current, on the other hand, delays AP discharge and is typically expressed in excitatory dorsal horn neurons (Punnakkal et al., 2014; Smith et al., 2015; Dickie et al., 2019). We, and others, have also noted that inhibitory dorsal horn neurons receive low frequency spontaneous excitatory input, whereas excitatory interneurons often receive much higher frequency input. The data presented here agree with these observations but also cautions against using these properties to distinguish inhibitory and excitatory populations. For example, the TF was also observed among subsets of excitatory neurons, A-type currents were observed in some inhibitory interneurons, and not all excitatory cells received high frequency spontaneous excitatory input.

In addition to the above differences, a number of other properties differed in recordings from inhibitory and excitatory dorsal horn neurons. Specifically, inhibitory neurons had lower input resistances, more depolarized membrane potentials, hyperpolarized AP threshold, larger AP peak amplitude, faster AP kinetics (rise and half-width), and slower sEPSC decay kinetics than the excitatory population. Many of these properties are consistent with the more excitable electrophysiological phenotype of TF inhibitory interneurons. In addition, some of these differences likely relate to the distinct morphological features of inhibitory and excitatory neurons in the dorsal horn. Specifically, our inhibitory sample showed much longer rostrocaudal dendritic profiles, whereas dorsoventral arborizations were similar to the excitatory sample. The larger dendritic trees are consistent with the lower input resistance of our inhibitory neurons (Barrett and Crill, 1974) and that distal excitatory synaptic inputs in this population have slower decay time courses (Rall et al., 1967).

Our morphological observations are also consistent with the well-established morphological categories for classifying dorsal horn neurons in lamina II (Grudt and Perl, 2002; Maxwell et al., 2007; Yasaka et al., 2010), where many of our recordings were made. Lamina II cells that exhibit expansive dendritic arbors in the rostrocaudal plane are classified as having islet morphology, and this appearance is reliably associated with inhibitory cell phenotypes. By contrast, cells with compact dendritic fields extending in all planes (i.e., radial cell morphology) are associated with an excitatory phenotype. Likewise, cells with a distinct bias towards ventrally projecting dendrites, often emanating from a common dendrite, are termed vertical cells and are typically excitatory, though these characteristics have also been described in some inhibitory cells. Finally, dorsal horn neurons with rostrocaudally oriented dendritic arbors like the islet category, but smaller in overall size, are classified as central cells and are observed in both excitatory and inhibitory populations. Our results on morphology, with longer rostrocaudal spread and larger rostrocaudal to dorsoventral ratios for dendrites in inhibitory interneurons, as well as the ventral bias of dendrites in excitatory interneurons, agree with this literature.

Despite the above associations, we did not classify the morphology of recorded cells in this study for two reasons. First, the morphological classification described above was developed specifically for neurons in lamina II, however, our recordings sampled a region that would include lamina I cells and potentially some in lamina III. Precisely locating cells to laminae require additional immunolabeling to confidently identify laminae borders. The second reason relates to cells that do not fit the criteria for this classification. In most studies that classify dorsal horn neurons in this way, an additional group of unclassified neurons is typically reported (Grudt and Perl, 2002; Heinke et al., 2004; Maxwell et al., 2007; Yasaka et al., 2010). Hence, to avoid omission of cells we simply reported and compared pertinent morphological characteristics and tested the ability of these properties to provide insight on neuronal heterogeneity. Interestingly, although differences were detected between the two populations (excitatory and inhibitory) in group comparisons, the hierarchical cluster analysis showed that morphological parameters did not efficiently separate excitatory and inhibitory populations into discrete clusters (**Figure 7**, 66% cluster purity). This is not surprising, as widely-accepted anatomical schema correlating morphologies (other than islet) to an excitatory or inhibitory phenotype is still elusive (Grudt and Perl, 2002; Heinke et al., 2004). This lack of cluster discrimination, however, may also reflect the limited dataset used for this analysis, which only used four morphological properties. This contrasts with clustering on the basis of electrophysiological properties (**Figure 6**), where 19 properties were used and yielded a cluster purity of 92%. Finally, as noted above a relatively small sample size will have constrained the capacity of this approach to distinguish clusters. This was influenced by the difficulty in obtaining sufficient morphological recoveries from small interneuron populations in the dorsal horn, reducing the data included for cluster analysis. Morphological recovery data also reinforced a developing view that excitatory dorsal horn neurons are more difficult to fill and recover during patch-clamp experiments than inhibitory cell types. The current dataset, which recorded (and attempted to recover morphology) from both excitatory and inhibitory populations using identical conditions provides quantitative data to support this view, with a recovery rate of 53% for inhibitory cells but only 30% for excitatory cells. This identifies a technical bias that potentially influences sampling in previous studies that rely on neurobiotin recovery to characterize dorsal horn populations. Furthermore, it suggests that transgenic sparse labeling approaches (Jefferis and Livet, 2012), or the use of rainbow labeling techniques (Cai et al., 2013) will be required to properly survey the morphological properties of these populations.

CONCLUSIONS

The two transgenic lines utilized throughout this study, vGAT:Td and vGLUT2:TdTom, positively identify inhibitory and excitatory cells and are thus useful for studying these broad cell populations. Furthermore, in cross-referencing the electrophysiological and morphological properties of these excitatory and inhibitory neurons in the SDH, our experiments support the conclusions of several previous studies characterizing various dorsal horn subpopulations. Inhibitory interneurons in this region are generally more excitable and easily recruited with TF discharge responses dominating, while the ongoing excitatory synaptic drive to this population is weak. This population also exhibits extensive rostrocaudal dendritic arborizations and features synaptic inputs on their distal dendrites that undergo substantial filtering. In contrast, excitatory interneurons are generally less excitable with a greater degree of DF and IB discharge profiles, and excitatory synaptic drive to this population is strong. This population exhibits a general bias in their dendritic arbors in the ventral plane, consistent with dorsal horn models that assign excitatory interneurons a role in transmitting signals from ventral to dorsal aspects of this region (Torsney and MacDermott, 2006). An important caveat to these findings is that although the above overall associations were clear, most of the properties highlighted also occurred (on occasion) in the opposing population. This cautions against using electrophysiological characteristics or morphology to differentiate excitatory and inhibitory cells and suggests the collection of multiple electrophysiological characteristics is a more accurate approach. The other key finding from these comparisons is that while as many as 30 different molecular classes of dorsal horn neurons have been differentiated (Haring et al., 2018), only five relatively distinct groups can be differentiated on electrophysiological and morphological grounds. A number of considerations may help to reconcile these differences. First, there may be some level of phenotypic convergence in the properties we assessed among the molecular classes (Konstantinides et al., 2018). Assessing additional properties such as inhibitory input (Smith et al., 2016) and connectivity (Kosugi et al., 2013; Hachisuka et al., 2018) may help to further differentiate the functional classes we identified. Further, increasing the sample size for our data, incorporating recordings from other transgenic mouse lines to identify additional distinct subpopulations (Hantman et al., 2004; Heinke et al., 2004; Zeilhofer et al., 2005; Hughes et al., 2012; Duan et al., 2014; Peirs et al., 2015; Smith et al., 2015; Hachisuka et al., 2018; Dickie et al., 2019), and balancing the relative ratio of excitatory to inhibitory recordings may help clustering methods to differentiate functionally distinct dorsal horn neurons classes. Ultimately, however, a unifying view of the subpopulations of dorsal horn neurons that play unique roles in function is likely to require integration of molecular, functional and connectomic approaches to heterogeneity. The data presented here represents one step towards this process.

DATA AVAILABILITY STATEMENT

All datasets generated for this study are included in the article.

ETHICS STATEMENT

The animal study was reviewed and approved by The University of Newcastle Animal Care and Ethics Committee under Section 25 of the NSW Animal Research Act, 1985.

AUTHOR CONTRIBUTIONS

TB, CD, RC, DH, and BG conceived and designed the research study. TB, MG, and JI conducted experiments and acquired data. TB, MG, JI, JM, DH, and BG analyzed data. BG, TB, and RC wrote the manuscript. All authors edited the final version of the manuscript.

FUNDING

This work was funded by the National Health and Medical Research Council (NHMRC) of Australia (Grants 631000, 1043933, 1144638, and 1184974 to BG and RC), the Biotechnology and Biological Sciences Research Council (BB/J000620/1, BB/P007996/1 to DH) and the Hunter Medical Research Institute (Glenn Moss grant to BG).

REFERENCES

Alba-Delgado, C., El Khoueiry, C., Peirs, C., Dallel, R., Artola, A., and Antri, M. (2015). Subpopulations of PKCγ interneurons within the medullary dorsal horn revealed by electrophysiologic and morphologic approach. *Pain* 156, 1714–1728. doi: 10.1097/j.pain.0000000000000221

Barrett, J. N., and Crill, W. E. (1974). Specific membrane properties of cat motoneurones. *J. Physiol.* 239, 301–324. doi: 10.1113/jphysiol.1974.sp010570

Bourane, S., Duan, B., Koch, S. C., Dalet, A., Britz, O., Garcia-Campmany, L., et al. (2015). Gate control of mechanical itch by a subpopulation of spinal cord interneurons. *Science* 350, 550–554. doi: 10.1126/science.aac8653

Boyle, K. A., Gradwell, M. A., Yasaka, T., Dickie, A. C., Polgar, E., Ganley, R. P., et al. (2019). Defining a spinal microcircuit that gates myelinated afferent input: implications for tactile allodynia. *Cell Rep.* 28, 526.e6–540.e6. doi: 10.1016/j.celrep.2019.06.040

Boyle, K. A., Gutierrez-Mecinas, M., Polgár, E., Mooney, N., O'Connor, E., Furuta, T., et al. (2017). A quantitative study of neurochemically defined populations of inhibitory interneurons in the superficial dorsal horn of the mouse spinal cord. *Neuroscience* 363, 120–133. doi: 10.1016/j.neuroscience.2017.08.044

Braz, J., Solorzano, C., Wang, X., and Basbaum, A. I. (2014). Transmitting pain and itch messages: a contemporary view of the spinal cord circuits that generate gate control. *Neuron* 82, 522–536. doi: 10.1016/j.neuron.2014.01.018

Cai, D., Cohen, K. B., Luo, T., Lichtman, J. W., and Sanes, J. R. (2013). Improved tools for the Brainbow toolbox. *Nat. Methods* 10, 540–547. doi: 10.1038/nmeth.2450

Cameron, D., Polgár, E., Gutierrez-Mecinas, M., Gomez-Lima, M., Watanabe, M., and Todd, A. J. (2015). The organisation of spinoparabrachial neurons in the mouse. *Pain* 156, 2061–2071. doi: 10.1097/j.pain.0000000000000270

Cauli, B., Porter, J. T., Tsuzuki, K., Lambolez, B., Rossier, J., Quenet, B., et al. (2000). Classification of fusiform neocortical interneurons based on unsupervised clustering. *Proc. Natl. Acad. Sci. U S A* 97, 6144–6149. doi: 10.1073/pnas.97.11.6144

Demšar, J., Curk, T., Erjavec, A., Gorup, C., Hocevar, T., Milutinovic, M., et al. (2013). Orange: data mining toolbox in python. *J. Machine Learn. Res.* 14, 2349–2353.

Dickie, A. C., Bell, A. M., Iwagaki, N., Polgár, E., Gutierrez-Mecinas, M., Kelly, R., et al. (2019). Morphological and functional properties distinguish the substance P and gastrin-releasing peptide subsets of excitatory interneuron in the spinal cord dorsal horn. *Pain* 160, 442–462. doi: 10.1097/j.pain.0000000000001406

Duan, B., Cheng, L., Bourane, S., Britz, O., Padilla, C., Garcia-Campmany, L., et al. (2014). Identification of spinal circuits transmitting and gating mechanical pain. *Cell* 159, 1417–1432. doi: 10.1016/j.cell.2014.11.003

Foster, E., Wildner, H., Tudeau, L., Haueter, S., Ralvenius, W. T., Jegen, M., et al. (2015). Targeted ablation, silencing, and activation establish glycinergic dorsal horn neurons as key components of a spinal gate for pain and itch. *Neuron* 85, 1289–1304. doi: 10.1016/j.neuron.2015.02.028

François, A., Low, S. A., Sypek, E. I., Christensen, A. J., Sotoudeh, C., Beier, K. T., et al. (2017). A brainstem-spinal cord inhibitory circuit for mechanical pain modulation by GABA and enkephalins. *Neuron* 93, 822.e6–839.e6. doi: 10.1016/j.neuron.2017.01.008

Gouwens, N. W., Sorensen, S. A., Berg, J., Lee, C., Jarsky, T., Ting, J., et al. (2019). Classification of electrophysiological and morphological neuron types in the mouse visual cortex. *Nat. Neurosci.* 22, 1182–1195. doi: 10.1038/s41593-019-0417-0

Graham, B. A., Brichta, A. M., and Callister, R. J. (2004). *In vivo* responses of mouse superficial dorsal horn neurones to both current injection and peripheral cutaneous stimulation. *J. Physiol.* 561, 749–763. doi: 10.1113/jphysiol.2004.072645

Graham, B. A., Brichta, A. M., and Callister, R. J. (2008). Recording temperature affects the excitability of mouse superficial dorsal horn neurons, *in vitro*. *J. Neurophysiol.* 99, 2048–2059. doi: 10.1152/jn.01176.2007

Graham, B. A., Brichta, A. M., Schofield, P. R., and Callister, R. J. (2007). Altered potassium channel function in the superficial dorsal horn of the spastic mouse. *J. Physiol.* 584, 121–136. doi: 10.1113/jphysiol.2007.138198

Graves, A. R., Moore, S. J., Bloss, E. B., Mensh, B. D., Kath, W. L., and Spruston, N. (2012). Hippocampal pyramidal neurons comprise two distinct cell types that are countermodulated by metabotropic receptors. *Neuron* 76, 776–789. doi: 10.1016/j.neuron.2012.09.036

Grudt, T. J., and Perl, E. R. (2002). Correlations between neuronal morphology and electrophysiological features in the rodent superficial dorsal horn. *J. Physiol.* 540, 189–207. doi: 10.1113/jphysiol.2001.012890

Gutierrez-Mecinas, M., Davis, O., Polgár, E., Shahzad, M., Navarro-Batista, K., Furuta, T., et al. (2019). Expression of calretinin among different neurochemical classes of interneuron in the superficial dorsal horn of the mouse spinal cord. *Neuroscience* 398, 171–181. doi: 10.1016/j.neuroscience.2018.12.009

Gutierrez-Mecinas, M., Furuta, T., Watanabe, M., and Todd, A. J. (2016). A quantitative study of neurochemically defined excitatory interneuron populations in laminae I-III of the mouse spinal cord. *Mol. Pain* 12:1744806916629065. doi: 10.1177/1744806916629065

Hachisuka, J., Omori, Y., Chiang, M. C., Gold, M. S., Koerber, H. R., and Ross, S. E. (2018). Wind-up in lamina I spinoparabrachial neurons: a role for reverberatory circuits. *Pain* 159, 1484–1493. doi: 10.1097/j.pain.0000000000001229

Hantman, A. W., van den Pol, A. N., and Perl, E. R. (2004). Morphological and physiological features of a set of spinal substantia gelatinosa neurons defined by green fluorescent protein expression. *J. Neurosci.* 24, 836–842. doi: 10.1523/JNEUROSCI.4221-03.2004

Haring, M., Zeisel, A., Hochgerner, H., Rinwa, P., Jakobsson, J. E. T., Lonnerberg, P., et al. (2018). Neuronal atlas of the dorsal horn defines its architecture and links sensory input to transcriptional cell types. *Nat. Neurosci.* 21, 869–880. doi: 10.1038/s41593-018-0141-1

Harris, K. D., Hochgerner, H., Skene, N. G., Magno, L., Katona, L., Bengtsson Gonzales, C., et al. (2018). Classes and continua of hippocampal CA1 inhibitory neurons revealed by single-cell transcriptomics. *PLoS Biol.* 16:e2006387. doi: 10.1371/journal.pbio.2006387

Heinke, B., Ruscheweyh, R., Forsthuber, L., Wunderbaldinger, G., and Sandkuhler, J. (2004). Physiological, neurochemical and morphological properties of a subgroup of GABAergic spinal lamina II neurones identified by expression of green fluorescent protein in mice. *J. Physiol.* 560, 249–266. doi: 10.1113/jphysiol.2004.070540

Huang, J., Polgar, E., Solinski, H. J., Mishra, S. K., Tseng, P. Y., Iwagaki, N., et al. (2018). Circuit dissection of the role of somatostatin in itch and pain. *Nat. Neurosci.* 21, 707–716. doi: 10.1038/s41593-018-0119-z

Hughes, D. I., Sikander, S., Kinnon, C. M., Boyle, K. A., Watanabe, M., Callister, R. J., et al. (2012). Morphological, neurochemical and electrophysiological features of parvalbumin-expressing cells: a likely source of axo-axonic inputs in the mouse spinal dorsal horn. *J. Physiol.* 590, 3927–3951. doi: 10.1113/jphysiol.2012.235655

Jefferis, G. S., and Livet, J. (2012). Sparse and combinatorial neuron labelling. *Curr. Opin. Neurobiol.* 22, 101–110. doi: 10.1016/j.conb.2011.09.010

Koga, K., Kanehisa, K., Kohro, Y., Shiratori-Hayashi, M., Tozaki-Saitoh, H., Inoue, K., et al. (2017). Chemogenetic silencing of GABAergic dorsal horn interneurons induces morphineresistant spontaneous nocifensive behaviours. *Sci. Rep.* 7:4739. doi: 10.1038/s41598-017-04972-3

Konstantinides, N., Kapuralin, K., Fadil, C., Barboza, L., Satija, R., and Desplan, C. (2018). Phenotypic convergence: distinct transcription factors regulate common terminal features. *Cell* 174, 622.e13–635.e13. doi: 10.1016/j.cell.2018.05.021

Kosugi, M., Kato, G., Lukashov, S., Pendse, G., Puskar, Z., Kozsurek, M., et al. (2013). Subpopulation-specific patterns of intrinsic connectivity in mouse superficial dorsal horn as revealed by laser scanning photostimulation. *J. Physiol.* 591, 1935–1949. doi: 10.1113/jphysiol.2012.244210

Larsson, M. (2017). Pax2 is persistently expressed by GABAergic neurons throughout the adult rat dorsal horn. *Neurosci. Lett.* 638, 96–101. doi: 10.1016/j.neulet.2016.12.015

Maxwell, D. J., Belle, M. D., Cheunsuang, O., Stewart, A., and Morris, R. (2007). Morphology of inhibitory and excitatory interneurons in superficial laminae of the rat dorsal horn. *J. Physiol.* 584, 521–533. doi: 10.1113/jphysiol.2007.140996

Mayhew, J. A., Callister, R. J., Walker, F. R., Smith, W. D., and Graham, B. A. (2019). Aging alters signaling properties in the mouse spinal dorsal horn. *Mol. Pain* 15:1744806919839860. doi: 10.1177/1744806919839860

Pagani, M., Albisetti, G. W., Sivakumar, N., Wildner, H., Santello, M., Johannssen, H. C., et al. (2019). How gastrin-releasing peptide opens the spinal gate for itch. *Neuron* 103, 102.e5–117.e5. doi: 10.1016/j.neuron.2019.04.022

Peirs, C., and Seal, R. P. (2016). Neural circuits for pain: recent advances and current views. *Science* 354, 578–584. doi: 10.1126/science.aaf8933

Peirs, C., Williams, S. P., Zhao, X., Walsh, C. E., Gedeon, J. Y., Cagle, N. E., et al. (2015). Dorsal horn circuits for persistent mechanical pain. *Neuron* 87, 797–812. doi: 10.1016/j.neuron.2015.07.029

Petitjean, H., Pawlowski, S. A., Fraine, S. L., Sharif, B., Hamad, D., Fatima, T., et al. (2015). Dorsal horn parvalbumin neurons are gate-keepers of touch-evoked pain after nerve injury. *Cell Rep.* 13, 1246–1257. doi: 10.1016/j.celrep.2015.09.080

Polgár, E., Durrieux, C., Hughes, D. I., and Todd, A. J. (2013). A quantitative study of inhibitory interneurons in laminae I-III of the mouse spinal dorsal horn. *PLoS One* 8:e78309. doi: 10.1371/journal.pone.0078309

Polgár, E., Wright, L. L., and Todd, A. J. (2010). A quantitative study of brainstem projections from lamina I neurons in the cervical and lumbar enlargement of the rat. *Brain Res.* 1308, 58–67. doi: 10.1016/j.brainres.2009.10.041

Punnakkal, P., von Schoultz, C., Haenraets, K., Wildner, H., and Zeilhofer, H. U. (2014). Morphological, biophysical and synaptic properties of glutamatergic neurons of the mouse spinal dorsal horn. *J. Physiol.* 592, 759–776. doi: 10.1113/jphysiol.2013.264937

Rall, W., Burke, R. E., Smith, T. G., Nelson, P. G., and Frank, K. (1967). Dendritic location of synapses and possible mechanisms for the monosynaptic EPSP in motoneurons. *J. Neurophysiol.* 30, 1169–1193. doi: 10.1152/jn.1967.30.5.1169

Ross, S. E., Hachisuka, J., and Todd, A. J. (2014). "Spinal microcircuits and the regulation of itch," in *Itch: Mechanisms and Treatment*, eds E. Carstens and T. Akiyama (Boca Raton, FL: CRC Press/Taylor and Francis).

Sathyamurthy, A., Johnson, K. R., Matson, K. J. E., Dobrott, C. I., Li, L., Ryba, A. R., et al. (2018). Massively parallel single nucleus transcriptional profiling defines spinal cord neurons and their activity during behavior. *Cell Rep.* 22, 2216–2225. doi: 10.1016/j.celrep.2018.02.003

Schindelin, J., Arganda-Carreras, I., Frise, E., Kaynig, V., Longair, M., Pietzsch, T., et al. (2012). Fiji: an open-source platform for biological-image analysis. *Nat. Methods* 9, 676–682. doi: 10.1038/nmeth.2019

Smith, K. M., Boyle, K. A., Madden, J. F., Dickinson, S. A., Jobling, P., Callister, R. J., et al. (2015). Functional heterogeneity of calretinin-expressing neurons in the mouse superficial dorsal horn: implications for spinal pain processing. *J. Physiol.* 593, 4319–4339. doi: 10.1113/jp270855

Smith, K. M., Boyle, K. A., Mustapa, M., Jobling, P., Callister, R. J., Hughes, D. I., et al. (2016). Distinct forms of synaptic inhibition and neuromodulation regulate calretinin-positive neuron excitability in the spinal cord dorsal horn. *Neuroscience* 326, 10–21. doi: 10.1016/j.neuroscience.2016.03.058

Sun, S., Xu, Q., Guo, C., Guan, Y., Liu, Q., and Dong, X. (2017). Leaky gate model: intensity-dependent coding of pain and itch in the spinal cord. *Neuron* 93, 840.e5–853.e5. doi: 10.1016/j.neuron.2017.01.012

Takazawa, T., Choudhury, P., Tong, C. K., Conway, C. M., Scherrer, G., Flood, P. D., et al. (2017). Inhibition mediated by glycinergic and GABAergic receptors on excitatory neurons in mouse superficial dorsal horn is location-specific but modified by inflammation. *J. Neurosci.* 37, 2336–2348. doi: 10.1523/JNEUROSCI.2354-16.2017

Takazawa, T., and MacDermott, A. B. (2010). Synaptic pathways and inhibitory gates in the spinal cord dorsal horn. *Ann. N Y Acad. Sci.* 1198, 153–158. doi: 10.1111/j.1749-6632.2010.05501.x

Todd, A. J. (2010). Neuronal circuitry for pain processing in the dorsal horn. *Nat. Rev. Neurosci.* 11, 823–836. doi: 10.1038/nrn2947

Torsney, C., and MacDermott, A. B. (2006). Disinhibition opens the gate to pathological pain signaling in superficial neurokinin 1 receptor-expressing neurons in rat spinal cord. *J. Neurosci.* 26, 1833–1843. doi: 10.1523/JNEUROSCI.4584-05.2006

Walsh, M. A., Graham, B. A., Brichta, A. M., and Callister, R. J. (2009). Evidence for a critical period in the development of excitability and potassium currents in mouse lumbar superficial dorsal horn neurons. *J. Neurophysiol.* 101, 1800–1812. doi: 10.1152/jn.90755.2008

Wang, L., Chen, S. R., Ma, H., Chen, H., Hittelman, W. N., and Pan, H. L. (2018). Regulating nociceptive transmission by VGluT2-expressing spinal dorsal horn neurons. *J. Neurochem.* 147, 526–540. doi: 10.1111/jnc.14588

Yasaka, T., Tiong, S. Y., Hughes, D. I., Riddell, J. S., and Todd, A. J. (2010). Populations of inhibitory and excitatory interneurons in lamina II of the adult rat spinal dorsal horn revealed by a combined electrophysiological and anatomical approach. *Pain* 151, 475–488. doi: 10.1016/j.pain.2010.08.008

Zeilhofer, H. U., Studler, B., Arabadzisz, D., Schweizer, C., Ahmadi, S., Layh, B., et al. (2005). Glycinergic neurons expressing enhanced green fluorescent protein in bacterial artificial chromosome transgenic mice. *J. Comp. Neurol.* 482, 123–141. doi: 10.1002/cne.20349

Zeisel, A., Muñoz-Manchado, A. B., Codeluppi, S., Lönnerberg, P., La Manno, G., Juréus, A., et al. (2015). Brain structure. Cell types in the mouse cortex and hippocampus revealed by single-cell RNA-seq. *Science* 347, 1138–1142. doi: 10.1126/science.aaa1934

Zeng, H., and Sanes, J. R. (2017). Neuronal cell-type classification: challenges, opportunities and the path forward. *Nat. Rev. Neurosci.* 18, 530–546. doi: 10.1038/nrn.2017.85

Conflict of Interest: The authors declare that the research was conducted in the absence of any commercial or financial relationships that could be construed as a potential conflict of interest.

Copyright © 2020 Browne, Gradwell, Iredale, Maden, Callister, Hughes, Dayas and Graham. This is an open-access article distributed under the terms of the Creative Commons Attribution License (CC BY). The use, distribution or reproduction in other forums is permitted, provided the original author(s) and the copyright owner(s) are credited and that the original publication in this journal is cited, in accordance with accepted academic practice. No use, distribution or reproduction is permitted which does not comply with these terms.

frontiers in Molecular Neuroscience

ORIGINAL RESEARCH
published: 05 May 2020
doi: 10.3389/fnmol.2020.00036

Functional and Molecular Analysis of Proprioceptive Sensory Neuron Excitability in Mice

Jessica F. Madden[1,2], Olivia C. Davis[3], Kieran A. Boyle[3], Jacqueline A. Iredale[1,2], Tyler J. Browne[1,2], Robert J. Callister[1,2], Douglas W. Smith[1,2], Phillip Jobling[1,2], David I. Hughes[3] and Brett A. Graham[1,2]**

[1]School of Biomedical Sciences and Pharmacy, Faculty of Health and Medicine, University of Newcastle, Callaghan, NSW, Australia, [2]Hunter Medical Research Institute (HMRI), New Lambton Heights, NSW, Australia, [3]Institute of Neuroscience Psychology, College of Medical, Veterinary and Life Sciences, University of Glasgow, Glasgow, United Kingdom

Neurons located in dorsal root ganglia (DRG) are crucial for transmitting peripheral sensations such as proprioception, touch, temperature, and nociception to the spinal cord before propagating these signals to higher brain structures. To date, difficulty in identifying modality-specific DRG neurons has limited our ability to study specific populations in detail. As the calcium-binding protein parvalbumin (PV) is a neurochemical marker for proprioceptive DRG cells we used a transgenic mouse line expressing green fluorescent protein (GFP) in PV positive DRGs, to study the functional and molecular properties of putative proprioceptive neurons. Immunolabeled DRGs showed a 100% overlap between GFP positive (GFP+) and PV positive cells, confirming the PVeGFP mouse accurately labeled PV neurons. Targeted patch-clamp recording from isolated GFP+ and GFP negative (GFP−) neurons showed the passive membrane properties of the two groups were similar, however, their active properties differed markedly. All GFP+ neurons fired a single spike in response to sustained current injection and their action potentials (APs) had faster rise times, lower thresholds and shorter half widths. A hyperpolarization-activated current (I_h) was observed in all GFP+ neurons but was infrequently noted in the GFP− population (100% vs. 11%). For GFP+ neurons, I_h activation rates varied markedly, suggesting differences in the underlying hyperpolarization-activated cyclic nucleotide-gated channel (HCN) subunit expression responsible for the current kinetics. Furthermore, quantitative polymerase chain reaction (qPCR) showed the HCN subunits 2, 1, and 4 mRNA (in that order) was more abundant in GFP+ neurons, while HCN 3 was more highly expressed in GFP− neurons. Likewise, immunolabeling confirmed HCN 1, 2, and 4 protein expression in GFP+ neurons. In summary, certain functional properties of GFP+ and GFP− cells differ markedly, providing evidence for modality-specific signaling between the two groups. However,

OPEN ACCESS

Edited by:
Jochen C. Meier, Technische Universitat Braunschweig, Germany

Reviewed by:
Judith Ann Strong, University of Cincinnati, United States
Wenrui Xie, University of Cincinnati, United States

***Correspondence:**
David I. Hughes
david.i.hughes@glasgow.ac.uk
Brett A. Graham
brett.graham@newcastle.edu.au

Received: *18 October 2019*
Accepted: *20 February 2020*
Published: *05 May 2020*

Citation:
Madden JF, Davies OC, Boyle KA, Iredale JA, Browne TJ, Callister RJ, Smith DW, Jobling P, Hughes DI and Graham BA (2020) Functional and Molecular Analysis of Proprioceptive Sensory Neuron Excitability in Mice. Front. Mol. Neurosci. 13:36. doi: 10.3389/fnmol.2020.00036

Abbreviations: AP, Action Potential; Ct, Cycle Threshold; DH, Dorsal Horn; dNTP, Deoxynucleotide triphosphates; DRG, Dorsal Root Ganglia; DTT, Dithiothreitol; EGTA, ethylene glycol-bis(β-aminoethyl ether)-N,N,N′,N′-tetraacetic acid; GFP+, Green Fluorescent Protein Positive; GFP−, Green Fluorescent Protein Negative; HCN channel, hyperpolarization-activated cyclic nucleotide-gated channel; I_h, Hyperpolarization-Activated Current; PBS, Phosphate Buffer Solution; PEG, Poly-Ethylene Glycol; PV, Parvalbumin; qPCR, Quantitative Polymerase Chain Reaction; RT, Reverse Transcription; RT+, Reverse transcription with reverse transcriptase; RT−, Reverse transcription without reverse transcriptase; sACSF, Substituted Artificial Cerebrospinal Fluid; SEM, Standard Error of the Mean; TrkC, Tyrosine Receptor Kinase C; ZD7288, 4-(N-Ethyl-N-phenylamino)-1,2 dimethyl-6-(methylamino) pyrimidinium chloride.

the GFP+ DRG population demonstrates considerable internal heterogeneity when hyperpolarization-activated cyclic nucleotide-gated channel (HCN channel) properties and subunit expression are considered. We propose this heterogeneity reflects the existence of different peripheral receptors such as tendon organs, muscle spindles or mechanoreceptors in the putative proprioceptive neuron population.

Keywords: parvalbumin, proprioception, dorsal root ganglia, sensory neuron, action potential, I_h, HCN channel

INTRODUCTION

Our experience of somatosensory stimuli such as proprioception, pain, and touch, results from the detection of stimuli in the periphery by specialized receptors before the propagation of these signals along primary afferents. Primary afferents are the peripheral axons of pseudo-unipolar sensory neurons, whose cell bodies are clustered in dorsal root ganglia (DRG). These neurons are responsible for the transmission of sensory information into the dorsal horn (DH) of the spinal cord and on to higher brain structures (Krames, 2014). Importantly, the anatomical positioning of the DRG outside the blood-nerve barriers of the central nervous system (CNS; Hu and McLachlan, 2002), has made sensory neurons a prime target for altering incoming sensory signals, especially those associated with nociception or pain. In particular, pharmacological (anti-inflammatory steroids; Manchikanti, 2000; Vad et al., 2002), neuromodulation *via* electrical stimulation (Deer et al., 2013) and physical interventions such as ganglionectomy (Acar et al., 2008), radio-frequency ablation (Nash, 1986; de Louw et al., 2001) and pulsed-radio frequency activation (Van Zundert et al., 2007) have targeted sensory neurons to treat aberrant sensory signaling.

These above intervention strategies, however, do not account for the fact that sensory neurons are a heterogeneous population and carry different types of information. Most studies on DRG signaling have focused on nociception where nociceptive sensory neurons are distinguished by their small soma diameters, unmyelinated or lightly myelinated axons, and nociceptor-specific molecular markers such as transient receptor potential channels, TRPV1 and TRPA1 (Berta et al., 2017). The same approach has rarely been applied to the other modalities transmitted *via* sensory neurons such as proprioception, which relays information about movement and body position, from peripheral receptors located in muscle, tendon, and joints (Delhaye et al., 2018). Broadly, proprioceptive sensory neurons have been identified by their typically large neuron diameter, axon myelination and fast conduction velocities vs. the smaller sensory neurons that transmit light touch, temperature, and nociception (Lawson, 2005).

The calcium-binding protein parvalbumin (PV) has been used to mark proprioceptive sensory neurons in rodents because it is expressed in large diameter DRG cells (Celio, 1990; Ichikawa et al., 1994, 2004; Honda, 1995; Arber et al., 2000; de Nooij et al., 2013). PV is co-localized with Tyrosine receptor kinase C (Trk C) and Neurotrophin-3 proteins, which are linked to the development of proprioceptive receptors and their primary afferent neurons (Ernfors et al., 1994). Additionally, PV is selectively expressed in muscle spindle afferents in the periphery (Ichikawa et al., 2004). Together, these findings suggest PV is a reliable neurochemical marker for proprioceptive DRG neurons.

The rationale for characterizing the properties of DRG neuron subtypes is to characterize unique properties (e.g., ion channel subtypes) that might be targeted by therapeutic agents to alter sensory function. Similar to whole DRG targeting, this approach has been primarily applied in the pain field. For example, sodium channel blockers, which target specific channel types, are now in clinical trials (Haberberger et al., 2019). Recently, hyperpolarization-activated cyclic nucleotide-gated (HCN) channels and the hyperpolarization-activated current (I_h) they mediate have been implicated in chronic pain states (Young et al., 2014; Tsantoulas et al., 2017; Lainez et al., 2019). This inward current is activated at hyperpolarized potentials and plays a role in adjusting resting membrane potential and generating rhythmic action potentials (APs; Hughes et al., 2013).

Interestingly, several studies have shown that I_h is present in both large (presumably proprioceptive) and small (nociceptive) diameter neuronal populations. Their specific electrophysiological properties, however, are known to differ (Doan and Kunze, 1999; Gao et al., 2012). This suggests sensory neurons of different modalities express a unique pattern of hyperpolarization activated cyclic nucleotide gated (HCN) channels that form tetramers and can be comprised of four distinct subunits, HCN1-4. Until recently, specific blocking agents for HCN subunits have not been described and their varied expression in a variety of tissues has limited our ability to target these channels. More recent studies, however, have reported subunit-specific blockers for HCN 1 and 2 over HCN 4, and these are currently being explored as a pain therapy (Dini et al., 2018). This work underscores the importance of understanding the expression pattern of HCN subunits across modality-specific sensory neuron populations. Importantly, the role of I_h in proprioceptive sensory neurons, identified by characteristics other than size, has not yet been investigated.

To address this gap in our knowledge, we used a transgenic mouse line expressing green fluorescent protein (GFP) under a PV promoter gene (PV-eGFP) to study the functional and molecular properties of putative proprioceptive sensory neurons. Targeted-patch clamp recording was undertaken on isolated green fluorescent protein positive (GFP+) and green fluorescent protein negative (GFP−) sensory neurons to study their electrophysiological properties with a focus on I_h currents in each population. We also undertook quantitative polymerase chain reaction (qPCR) and immunolabeling analysis to compare the expression of HCN subunits 1–4.

EXPERIMENTAL PROCEDURES

Dissection and Preparation of Dissociated Cells

All experiments carried out at the University of Newcastle were in accordance with the Animal Research Act 1985 (NSW), under the guidelines of the National Health and Medical Research Council Code for the Care and Use of Animals for Scientific Purposes in Australia (2013). All experiments carried out in Glasgow were in accordance with the European Community directive 86/609/EEC and UK Animals (Scientific Procedures) Act 1986. We used a BAC transgenic BALB/c mouse (PVeGFP) generated to express an enhanced fluorescent protein (EGFP) under the control of the PV gene promoter (Meyer et al., 2002). The initial description of this mouse showed eGFP was selectively expressed in PV neurons throughout the nervous system. We have also used this mouse previously to characterize PV-positive cells in the DH of the spinal cord (Hughes et al., 2012; Gradwell et al., 2017). Some experiments also used tissue from C57Bl/6 mice for additional immunolabeling analysis.

Adult PVeGFP mice (eight male, nine female, average body weight = 24.4 g) were deeply anesthetized with Ketamine (100 mg/kg i.p, Troy Laboratories, NSW, Australia) and sacrificed *via* rapid decapitation. Lumbar DRGs (L2-L6) from both sides were quickly removed with the aid of a dissecting microscope and placed in substituted artificial cerebrospinal fluid (sACSF) containing in mM: 236 Sucrose, 25 $NaHCO_3$, 11 glucose, 1 NaH_2PO_4, 2.5 KCl, 2.5 $CaCl_2$, and 1 MgCl. For both electrophysiology and molecular experiments, DRGs were further dissociated into a single cell suspension. Briefly, DRGs were transferred to a HEPES based collagenase solution (10 mg/ml, Worthington Pty Ltd) for 40–60 min at 37°C. Three flame polished glass Pasteur pipettes of decreasing diameter were then used to mechanically triturate the tissue and form a dissociated cell suspension (10× for each pipette diameter). The suspension was washed, and the supernatant replaced with a fresh HEPES solution. In patch-clamp recording experiments the cell suspension (100 μl) was pipetted into a 22 mm plastic Petri dish. Recording commenced after cells had settled and adhered to the bottom of the Petri dish (∼15 min), which also acted as the recording bath. For all gene expression analysis, the dissection and dissociation process remained the same, except all solutions, were prepared using diethylpyrocarbonate (DEPC) treated water (0.1%, Sigma Aldrich Pty Ltd), and underwent 24 h of agitation followed by autoclaving (120°C for 30 min) to inactivate RNase enzymes.

Immunolabeling

The immunolabeling analysis was undertaken to examine the co-localization of native/endogenous PV and transgenic eGFP expression in DRGs from PVeGFP mice. The DRGs were removed as above (without dissociation) and emersion-fixed in 4% depolymerized paraformaldehyde (in phosphate buffer solution—PBS, pH 7.3) for 2–3 h. This tissue was subsequently treated with Dimethyl Sulfoxide (DMSO, Thermo Fisher Scientific) to permeabilize cellular membranes (3 × 15 mins) and then dehydrated in 100% ethanol (3 × 15 mins, Thermo Fisher Scientific). The tissue was submerged in poly-ethylene glycol (PEG-1000 molecular weight, Acros Organics) for 2 h, before setting in PEG 1450 and subsequent sectioning (20 μm) on a microtome. The sections were incubated in primary antibodies (polyclonal chicken anti-GFP 1:500, polyclonal rabbit anti-PV 1:400, Sapphire Bioscience Pty Ltd) diluted in a hypertonic PBS containing 10% donkey serum at room temperature for 15–18 h. After washing (3 × 15 mins in PBS), sections were incubated in species-specific secondary antibodies conjugated to Cy3 and FITC fluorophores (1:50, Jackson ImmunoResearch Pty Ltd) at room temperature for 2 h. The secondary antibody was removed by washing (3 × 15 min in PBS) and slices were mounted on glass slides using buffered glycerol (33% 0.5M Na_2CO_3 pH 8.6 in glycerol).

In addition to the above PV vs. GFP comparison, DRGs from wildtype (C57Bl/6) mice were processed to immunolabel and compare PV-expression with HCN 1, HCN 2, and HCN 4 expression. HCN 3 was not included in this analysis as antibodies to this subunit were found to only yield non-specific labeling. A total of three adult male C57Bl6 mice (20–22 g) were deeply anesthetized with pentobarbitone and perfused transcardially with 4% depolymerized formaldehyde. Lumbar DRG were removed and post-fixed in the same solution for an additional 2 h. Free-floating sections of ganglia (60 μm thick) were cut on a vibratome and subsequently incubated in 50% ethanol for 30 min to enhance antibody penetration. The sections were then incubated in a cocktail of primary antibodies containing guinea pig anti-PV (1:500; Frontier Institute Cat# PV-GP-Af1000, RRID:AB_2336938) with either rabbit anti HCN1 (1:250; Alomone Labs Cat# APC-056, RRID:AB_2039900), rabbit anti-HCN2 (1:500; Alomone Labs Cat# APC-030, RRID:AB_2313726) or mouse anti-HCN4 (diluted 1:500; UC Davis/NIH NeuroMab Facility Cat# 73–150, RRID:AB_10673158). Immunolabeling for PV was visualized using a goat anti-guinea pig secondary antibody conjugated to Alexa488, and the HCN subunits were visualized using the tyramide signal amplification approach described previously (Hughes et al., 2012). All primary and secondary antibody cocktails were made up of 0.3 M phosphate-buffered saline with 0.3% Triton X-100. Sections were incubated in primary antibodies for 72 h and in secondary antibodies for 12–18 h at 4°C.

Sections were cover-slipped and examined on an epifluorescence microscope (Olympus BX51) or confocal microscope (Zeiss LSM710, Hemel Hempstead, United Kingdom). Single images were captured using either a 10× or 20× objective in epifluorescence analysis. In confocal analysis, representative sections from each animal were scanned with image stacks collected using a 20× objective (0.9 digital zoom, 1 μm z-separation). Resulting images were analyzed off-line using Neurolucida for Confocal software (MicroBrightField, Colchester, VT, USA) to determine the expression of GFP, HCN1, 2 or 4 immunolabeling in PV-expressing cells.

Electrophysiology Experiments

Recording micropipettes were made from borosilicate glass (1.5 mm OD, Harvard Apparatus, Kent, UK) and filled with

a HEPES based internal solution containing in mM: 124 K-gluconate, 10 phosphocreatine di tris salt, 10 HEPES, 0.2 EGTA, 4 Mg2ATP, and 0.3 Na2GTP (pH 7.3, adjusted with KOH; Wang et al., 1994; Xu et al., 1997; Hayar et al., 2008). Series resistance (R_S), membrane capacitance, and input resistance (R_{IN}) were assessed based on the response to a hyperpolarizing 5 mV voltage step. These values were monitored throughout each experiment and when R_{IN} and/or R_S changed by more than 20% or >25 MΩ, respectively, cells were excluded from the analysis. Recordings were made at room temperature (22–24°C) and membrane potentials were not corrected for liquid junction potential.

To study APs, a depolarizing step protocol (100 pA increments, 800 ms duration) was applied to cells in the current clamp recording mode. Rheobase current was calculated as the smallest current step that evoked an AP. The AP generated for each cell at rheobase was used to measure AP threshold, rise time, amplitude, and width. AP threshold was determined on an expanded time scale by identifying the inflection point where membrane potential change exceeded 15 V/s. AP rise time was measured as 10–90% of the duration between AP threshold and the maximum positive peak, AP amplitude was the voltage difference between AP threshold and the maximum positive peak, and AP width was the duration of the positive spike at AP threshold. A derivative method was also used to differentiate between monophasic and biphasic repolarization phases on differentiated Rheobase APs. Previous work has shown biphasic repolarization reflects a depolarizing hump that is characteristic of nociceptive DRGs and can be used to identify this class. To test for the presence of I_h, a current clamp protocol delivered several hyperpolarizing steps of increasing amplitude (−100 pA increments, 800 ms duration, −50 mV holding potential). If I_h was observed, a voltage clamp protocol was applied (10 mV steps, 800 ms duration, −50 mV holding potential) to the maximum amplitude of −110 mV. Current amplitude and activation kinetics were assessed using Axograph X analysis software.

Pharmacology

The identity of the hyperpolarization-evoked currents as I_h current was confirmed by the addition of 4-(N-Ethyl-N-phenylamino)-1,2 dimethyl-6-(methylamino) pyrimidinium chloride (ZD7288, Sigma-Aldrich), to the bath at a final concentration of 100 μM. In these experiments, a single −300 pA step (800 ms every 8.5 s) was applied to the cell in the current-clamp. This step was sufficient to monitor the I_h block during the ZD7288 application. Although some work indicates ZD7288 also affects Na channels (Wu et al., 2012), this off-target effect did not influence the large hyperpolarizing current step responses we assess.

Molecular Experiments

Cell Collection

Using DEPC treated solutions, DRGs were removed and dissociated as described above. From the resulting suspension, 200–300 μl was plated on a plastic coverslip. Cells were allowed to settle for 15–20 min before the excess fluid was replaced with fresh HEPES buffer. GFP+ cells were visualized under fluorescent microscopy and collected, *via* gentle suction, into a glass micropipette (filled with DEPC HEPES) mounted on a micromanipulator. Once 50 cells were collected, they were expelled *via* positive pressure into a 2 ml Eppendorf tube. This process was repeated to collect 50 GFP− cells.

RNA Extraction and DNase Digestion

RNA extraction and purification from the 50-cell samples were completed as per the protocol "Cells" included in the RNeasy Micro Handbook (2nd Edition, Qiagen, 2007), using the solutions included in an RNeasy Micro kit (Qiagen Cat No 74004). RNA concentrations were then determined using a Nanodrop-1000 spectrophotometer (ThermoFisher Scientific Inc, Waltham, MA USA). This process provided approximately 10 μl of RNA sample to be used for reverse transcription (RT). To eliminate residual genomic DNA contamination, a DNA digestion step was performed at room temperature for 15 min after RNA extraction. In PCR grade microtubes (Scientific Specialties Incorporated, Lodi, CA, USA), 5 μl of the RNA samples were incubated with 1 μl DNase and 1 μl DNase 10× Buffer (both included in Invitrogen™ DNase I, Kit I) and 3 μl Nuclease free water (Qiagen). This process was halted by adding 1 μl of EDTA (25 mM, Invitrogen™ DNase I Kit I) and heating the samples in a thermocycler (Eppendorf, South Pacific) at 65°C for 10 min.

Reverse Transcription (RT)

For RT, a 5 μl aliquot from each of the DNA-free RNA samples (GFP+/−) was obtained for cDNA reactions. Oligo dT primers and Deoxynucleotide triphosphates (dNTPs, both from Bioline Pty Ltd.) as well as random hexamers (GeneWorks Pty Ltd, Adelaide, SA Australia) were added to the RT reaction and processed in a thermocycler for 5 min at 65°C before being cooled to 4°C and placed on ice for 1 min. Following this, 4 μl of 5× First Strand buffer, 1 μl RNase inhibitor, 1 μl Dithiothreitol (DTT, all from Bioline Pty Ltd.), as well as 1 μl reverse transcriptase (Superscript III, Invitrogen), was added before running in a thermocycler at 50°C for 60 mins, then 75 °C for 15 mins. For quality control, each RT sample was paired with a reverse transcriptase absent sample (called RT+ and RT−, respectively), where the 3 μl volume was replaced with Nuclease free water (Qiagen).

Qualitative Polymerase Chain Reaction (qPCR)

Based on RNA spectrophotometer readings, the cDNA samples were diluted in nuclease-free water to a final concentration of 0.2 ng/μl. Forward and reverse 5 prime (5′) primers for the four HCN subunits (Horwitz et al., 2011), GFP (Klein et al., 2000) and ß-actin were included (see **Table 1**). Separate qPCR master mixes were made for each gene to be investigated (GFP, ß-actin and HCN 1–4). Each master mix contained forward and reverse primers for the target gene at a final concentration of 20 μM. The SYBR green-based master mix from Bioline was used for all qPCRs. Each qPCR reaction comprised 7 μl of the master mix, primers, and water, plus 5 μl of cDNA sample for

TABLE 1 | Primer sequence details.

Primer	Sequence	Supplier
HCN1	Forward—ACATGCTGTGCATT GGTTATGGCG Reverse—AACAAACATTGCGT AGCAGGTGGC	GeneWorks Pty Ltd
HCN2	Forward—ACTTCCGCACCG GCATTGTTATTG Reverse—TCGATTCCCTTCTT CACTATGAGG	GeneWorks Pty Ltd
HCN3	Forward—CCTCATCCGCTACA TACACCAGT Reverse—GACACAGAGCAA CATCATTCC	GeneWorks Pty Ltd
HCN4	Forward—GCATGATGCTTCTG CTGTGTCACT Reverse—TTCACCATGCCATT GATGGACACC	GeneWorks Pty Ltd
Beta Actin	Forward—ATGGAGGGGAAT ACAGCCC Reverse—TTCTTTGCAGCTCC TTCGTT	GeneWorks Pty Ltd
eGFP	Forward—ATCATGGCCGAC AAGCAGAAGAAC Reverse—GTACAGCTCGTC CATGCCGAGAGT	GeneWorks Pty Ltd

a total reaction volume of 12 μl. All reactions were run on an ABI 7500 Real-Time Thermal Cycler (ThermoFisher Scientific, Australia). After an initial polymerase activation step at 95°C for 10 min, there were 40 amplification cycles comprising a 95°C, 15 s denaturation step, followed by a 60°C 1 min annealing and extension step. All samples from a single animal (GFP+ and GFP−) were run in triplicate on the same qPCR plate. In addition to the RT+ and RT− samples, water controls were included on all plates, where nuclease-free water was substituted for cDNA.

Analysis

For the electrophysiological data, statistical analysis was carried out using SPSS v10 (SPSS Inc., Chicago, IL, USA). Following normality checks (Shapiro–Wilks), independent *t*-tests and non-parametric Mann-Whitney tests were applied as appropriate across each measurement. The qPCR analysis was undertaken on paired samples of GFP+ and GFP− cells (n = 50). Each sample was tested in triplicate using forward and reverse primers for GFP and HCN 1–4 and the internal control gene β actin. Mean cycle threshold (Ct) values were determined for each triplicate (from each animal) and were used to determine ΔCt by subtracting the mean Ct of the internal control (β actin) from the mean Ct of the target primer (i.e., GFP and HCN 1–4). The resulting ΔCt values were analyzed for normality using a Shapiro–Wilks test. Normality was satisfied in all comparison groups except HCN 3. Thus, a two-tailed paired sample *T*-test was applied to the HCN 1, 2 and 4, while a nonparametric Wilcoxon test was applied to HCN 3 to compare GFP+ and GFP− groups. ΔCt values were converted to fold-change values between groups for each primer. Statistical significance was set at $p < 0.05$. All values are presented in the text as means ± SEM.

RESULTS

Co-localization of Green Fluorescent Protein and Endogenous Parvalbumin

To first confirm reliable and selective GFP expression, DRGs were extracted and immunolabeled for PV and GFP. Co-localization between PV immunoreactive neurons and GFP expression occurred in 100% of the 645 cells analyzed from PVGFP mice (n = 3, two DRGs per mouse). Additionally, we found that there were no instances of cells expressing GFP or PV in isolation (see **Figure 1**). These data show the PVeGFP transgenic mouse line reliably marks sensory neurons expressing PV.

Electrophysiological Properties

Whole cell patch clamp recordings were made from isolated cells taken from 21 adult PV-eGFP mice (average yield = 3.1 recordings per animal). The data (presented herein as GFP+ vs. GFP−) for passive membrane properties are summarized in **Figure 2**. Input resistance was lower in GFP+ cells when compared with GFP− cells (152.18 ± 18.34 vs. 388.63 ± 68.79 MΩ, p = 0.01, n = 35 and 32, respectively). Series resistance was similar in GFP+ and GFP− cells (12.0 ± 0.5 vs. 12.4 ± 0.6 MΩ, p = 0.64, n = 35 and 32, respectively, data not shown). Membrane capacitance (32.16 ± 2.02 vs. 34.47 ± 2.34 pF, p = 0.46, n = 35 and 32, respectively) and resting membrane potential (−42.99 ± 1.43 and −41.14 ± 2.26 mV, p = 0.88, n = 35 and 32, respectively) were similar in GFP+ and GFP− cells. Cell diameter (29.72 ± 0.94 vs. 28.08 ± 0.67 μm, p = 0.21, n = 25 and 26, respectively), as measured *via* a calibrated scale bar, was also similar in both populations.

AP discharge was assessed in response to multiple depolarizing step injections in the recorded cell as shown in **Figure 3**. The resulting AP discharge was classified as either single (SS) or multiple spiking (MS). All GFP+ cells exhibited the SS discharge profile (25/25 cells), whereas only 70% (17/24 cells) of the GFP− population exhibited the SS spiking profile. The remaining GFP− cells fired multiple spikes that were a mix of phasic bursting and tonic firing phenotypes. The properties of the first AP generated in response to current injection (rheobase) were also compared between groups. No differences in rheobase current (325 ± 25.52 vs. 388.89 ± 52.79 pA, p = 0.80, n = 28 and 27, respectively) or AP peak amplitude (57.55 ± 2.76 vs. 47.64 ± 4.53 mV, p = 0.06, n = 28 and 27, respectively) were identified between GFP+ and GFP− cells. In contrast, AP threshold occurred at more hyperpolarized potentials (−16.44 ± 1.15 vs. −1.40 ± 2.23 mV p = 0.01, n = 28 and 27, respectively); rise time was faster (0.77 ± 0.06 vs. 1.83 ± 0.19 ms, p = 0.00, n = 28 and 27, respectively); and AP half-width was significantly shorter (1.15 ± 0.07 vs. 2.55 ± 0.28 ms, p = 0.00, n = 28 and 27, respectively) in GFP+ recordings compared with the GFP− population. Rheobase AP traces were also differentiated to assess the presence of biphasic repolarization, which has been shown to reflect a depolarizing hump featured in APs from nociceptive afferents (**Figure 3C**). This assessment showed

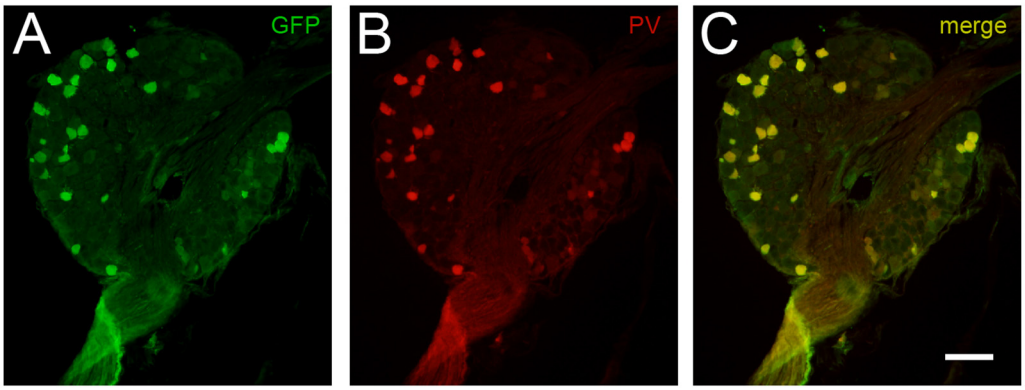

FIGURE 1 | Comparison of GFP-expression and parvalbumin (PV) immunolabeling in dorsal root ganglia (DRG) cells. The fidelity of GFP expression in PV-expressing DRG neurons was tested to confirm the utility of tissue from the PVeGFP transgenic mouse line. Panels **(A,B)** show a representative DRG section immunolabeled for GFP (green) and PV (red), respectively. Overlaid image **(C)** shows co-localization (yellow) of GFP and endogenous PV in DRG cells. This analysis showed complete overlap (100%) in 645 DRG cells examined (n = 3 animals). Scale **(A–C)** = 100 μm.

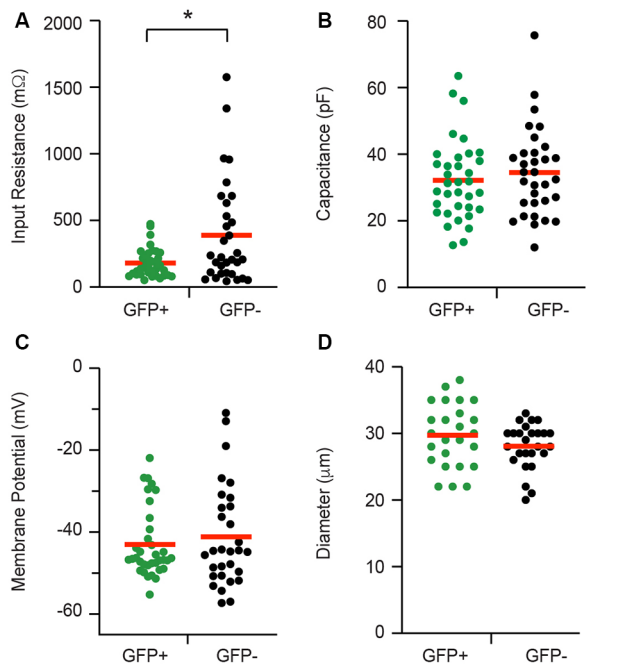

FIGURE 2 | Passive electrical properties of proprioceptive DRG cells. Baseline properties of green fluorescent protein positive (GFP+) proprioceptive neurons and unidentified green fluorescent protein negative (GFP−) neurons were assessed during patch-clamp recordings. Scatter plots compare passive properties, including input resistance **(A)**, membrane capacitance **(B)**, resting membrane potential **(C)**, and cell diameter **(D)**. Values for GFP+ cells are shown in green while GFP− data appear black. Red horizontal bars indicate the mean for each group. Input resistance was the only property that differed between the two groups and was significantly lower in GFP+ recordings (p = 0.008). *$p \leq 0.05$.

that all GFP+ cells exhibited a monophasic repolarization, whereas 15/24 GFP− cells exhibited biphasic responses (**Figure 3D**).

During current-clamp recordings hyperpolarizing current step injection responses often featured a "sag" in membrane potential, which then returned towards RMP, consistent with an I_h current (**Figures 4A,B**). All recordings that assessed this feature confirmed GFP+ cells exhibited I_h-like currents (18/18 recordings), whereas these currents were only detected in 11% (2/17) of the GFP− cells. The identity of this current was verified in a subset of recordings by testing ZD7288 (100 μM) sensitivity, a commonly used blocker of I_h (**Figure 4C**, n = 3). I_h currents were also studying in voltage-clamp using a protocol that stepped membrane potential from −50 mV to more hyperpolarized potentials in 10 mV increments (**Figure 4D**). The average I_h amplitude for each voltage step was calculated as the difference between values immediately after the onset and conclusion of seven hyperpolarizing steps (−50 to −110 mV). The box-whisker plots (**Figure 4E**) show average I_h amplitude did not differ for the first two voltage steps (to −50 and −60 mV) in GFP+ and GFP− cells (p = 0.70 and 0.16, respectively). However, I_h currents were much larger in GFP+ cells for the steps between −70 and −110 mV. This is indicative of the presence of substantial I_h in GFP+ cells (−70 mV p = 0.001, −80 mV p = 0.002, −90 mV p = 0.004, −100 mV p = 0.003 and −110 mV p = 0.003).

The activation rate of I_h was also assessed by fitting an exponential over 10%–90% of the maximum current amplitude (i.e., the −110 mV step) for GFP+ and GFP− cells (**Figure 4D**). The resulting I_h activation time constant values varied markedly for GFP+ cells (0.08–0.83 s). Values for the two GFP− cells that expressed I_h had similar activation rates (0.27 and 0.24 s) and fell within the range expressed by the GFP+ cells.

Gene Expression: qPCR Ct Analysis for HCN Channel Subunits

We next examined the mRNA expression levels of HCN 1–4 subunits to gain insight into the molecular determinants of the I_h currents and activation rates reported above (**Figure 4F**).

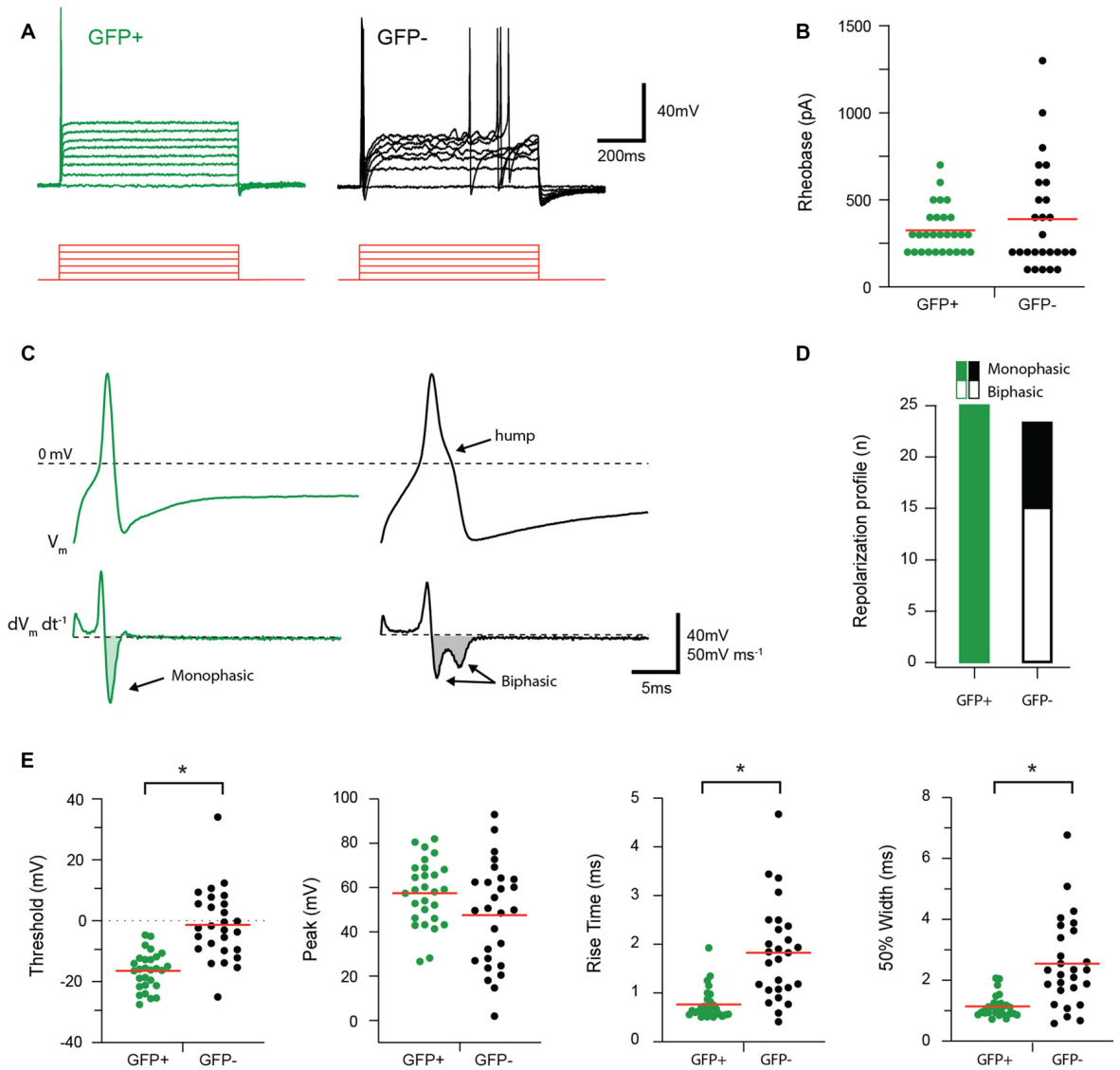

FIGURE 3 | Discharge and action potential (AP) properties of proprioceptive DRG cells. Two types of AP discharge were observed in DRG neurons during step current injections (100 pA increments, 800 ms duration, red traces). **(A)** Overlaid traces show a typical response from GFP+ and GFP− cells, contrasting a single spike response at the onset of current injection in GFP+ cells with multi-spiking responses observed in some GFP− recordings (7/24). **(B)** Scatter plot shows group data comparing Rheobase in GFP+ (green circles) and GFP− (black circles) cells. While group means (red lines) are similar for both groups, the spread, and range of data in GFP− cells is greater. **(C)** Upper traces show rheobase APs from a GFP+ (green trace) and GFP− cell (black trace) on an expanded time scale. Note while APs exhibit a similar amplitude, the time courses are distinct, with GFP+ cells exhibiting faster APs and a distinct hump appearing on the repolarization phase in the GFP− trace. Lower traces are differentiated AP data (from above) clearly identifying the distinct repolarization phases of GFP+ and GFP− cells as monophasic and biphasic waveforms, respectively. **(D)** Bar graph summarizes relative incidence of cells exhibiting monophasic (filled bar) and biphasic (open bar) differentiated waveforms. All GFP+ cells exhibited monophasic waveforms, whereas more than half the GFP− cells exhibited biphasic responses (15/24). **(E)** Scatter plots show group data comparing AP properties in GFP+ (green circles) and GFP− (black circles) cells. AP height was similar in GFP+ and GFP− cells, but AP threshold, rise time, and half-width differed in the two cell types, with faster kinetics and more hyperpolarized thresholds in the GFP+ sample ($p < 0.05$). *$p \leq 0.05$.

A qPCR analysis was first undertaken on paired samples of pooled GFP+ vs. GFP− cells for specific GFP primers to confirm our isolation procedures faithfully captured populations of GFP+ and GFP− cells (**Figure 5A**). Mean Ct values show there was a large difference in ΔCt values for the GFP+ and GFP− sample (−0.11 ± 0.25 vs. 6.19 ± 0.15, $p > 0.01$). When expressed as a fold difference, there was >90 times more GFP expression in our GFP+ vs. GFP− sample. This confirmed our procedures provided a highly enriched sample of PV positive (GFP-expressing putative proprioceptive) cells for subsequent analysis of HCN subunit expression.

Regarding HCN subunit mRNA expression, significantly higher levels of HCN 1, 2 and 4 were detected in the GFP+ vs. GFP− sample, reflected in lower ΔCt values (**Figure 5B**)

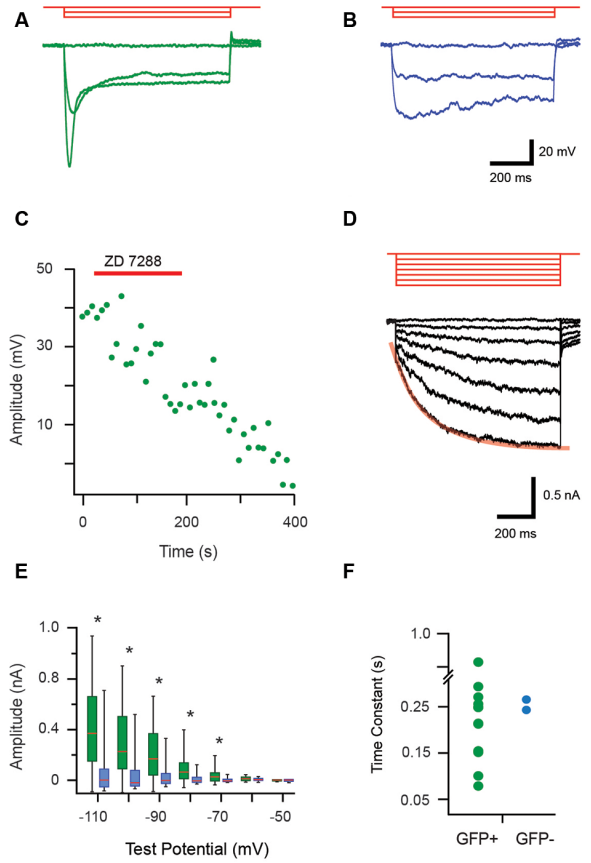

FIGURE 4 | Properties of hyperpolarization-activated currents (I_h) in proprioceptive DRG cells. **(A,B)** Overlaid traces showing current-clamp recordings from isolated GFP+ and GFP− DRG neurons during hyperpolarizing current injection (3 steps, 100 pA increments, 1 s duration, red traces). All GFP+ cells exhibited a prominent sag characterized by a rapid return towards resting membrane potential that became more prominent as hyperpolarized step injection amplitude increased **(A)**. This profile is associated with a hyperpolarization activated current, termed I_h. In contrast, few GFP− cells exhibited evidence of the I_h current and when present it was minimal (**B**, sag less prominent). **(C)** Bath application of an antagonist (ZD7288, 100 μM) was used to confirm the identity of I_h in current-clamp mode. Peak I_h voltage amplitude, measured every 8.5 s in response to a 300 pA hyperpolarizing current step was sensitive to the addition of ZD7288 (100 μM), which abolished I_h responses. **(D)** Overlaid traces show I_h currents recorded from a GFP+ cell during a voltage clamp protocol (−10 mV steps, holding potential −50 mV, red traces). These responses feature a prominent voltage-activated current that becomes more pronounced as hyperpolarization is increased. Note red line shows an exponential fit to the I_h activation profile during the largest hyperpolarizing step. **(E)** Box and whisker plot shows group data comparing I_h amplitude in GFP+ (green) and GFP− (blue) cells from the hyperpolarizing step responses (shown in **D**). I_h amplitude is minimal until steps reach −70 mV before hyperpolarization I_h amplitude begins to increase substantially in GFP+ neurons ($p < 0.005$). **(F)** An exponential was fit to the largest I_h current trace (i.e., −110 mV step, overlaid red line) providing a time constant (or, activation rate) for I_h in GFP+ (green) and the two GFP− cells (blue). Activation rates varied markedly for GFP+ cells while the two GFP− cells had similar values that fell within the range of GFP+ activation rates. *$p \leq 0.05$.

and equating to 1,5-, 3-, and 3.5-fold differences, respectively. In contrast, HCN 3 was the only subunit to show lower expression in the GFP+ vs. GFP− sample (ΔCt = 8.7 ± 0.3 vs. 7.7 ± 0.1, $p = 0.03$; **Figure 5B**), representing a 0.5-fold difference. Within each group, HCN 2 was the most highly expressed subunit in GFP+ and GFP− samples. For GFP+ cells, HCN 2 expression was highest, followed by HCN 1 then HCN 4 (ΔCt = 2.96 ± 0.16 vs. 5.49 ± 0.150 vs. 7.35 ± 0.15).

HCN Channel Subunit Expression in PV DRG Neurons

To assess the impact of the above findings at a protein level, DRGs from wildtype tissue were immunolabeled for PV and HCN subunit expression. PV positive DRG cells were identified by immunolabeling in the cytoplasm of subpopulations of DRG neurons, whereas that for HCN1 and HCN2 was confined to membranes of cell bodies and axons in restricted subsets of cells (**Figures 6A,B**). In contrast, immunolabeling for HCN4 was expressed in the cytoplasm, and therefore deemed nonspecific. In earlier pilot experiments using tissue from PVeGFP mice, HCN2 and HCN4 immunolabeling were confined to membranes and axons of GFP labeled DRG neurons, but not analyzed (**Figures 6C,D**). Nevertheless, this observation confirms some PV positive DRG neurons also express HCN4 in their membranes, albeit without formal quantification. Regarding HCN1 and HCN2 subunit labeling that could be analyzed, less than half of PV-IR neurons expressed immunolabeling for HCN1 (mean 43.8% ± 8.8; 15/34 PV cells; $n = 2$ animals), whereas HCN2 was expressed in half than half the PV-IR sample (mean 65.3% ± 11.0; 48/75 PV cells; $n = 3$). These observations confirm that the HCN subunit mRNA identified in qPCR experiments does translate to functional protein in PV DRG cells, and the relative incidence of HCN1 and HCN2 subunit expression among PV cells also mirrors the mRNA levels detected in this population.

DISCUSSION

This study used targeted patch-clamp electrophysiology and molecular analysis of HCN channel subtypes to compare the properties of putative proprioceptive neurons (GFP+) with a group of non-proprioceptive "other" sensory populations (GFP−). Our main electrophysiology findings are that GFP+ and GFP− neurons differed in their active and I_h properties. Molecular analysis, supported by immunolabeling, showed expression of HCN 1, 2 and 4 subunits were higher in GFP+ neurons. In contrast, HCN 3 subunits, though expressed at low levels, were more highly expressed in GFP− cells. Below, we discuss the caveats associated with our experiments and our main findings in terms of their relevance to proprioceptive signaling.

During depolarizing current step injection, GFP+ neurons always exhibited a single spike phenotype whereas GFP− neurons showed a mix of single and MS (**Figure 3**). The phasic firing and strong adaptation in GFP+ neurons are consistent with the *in vivo* responses of sensory neurons that innervate Pacinian corpuscles and muscle spindles (Lawson, 2005). Both receptor types are classed as low threshold mechanoreceptors, have fast conduction velocities, and are best suited to signaling rapid changes in pressure and muscle length, respectively. Such

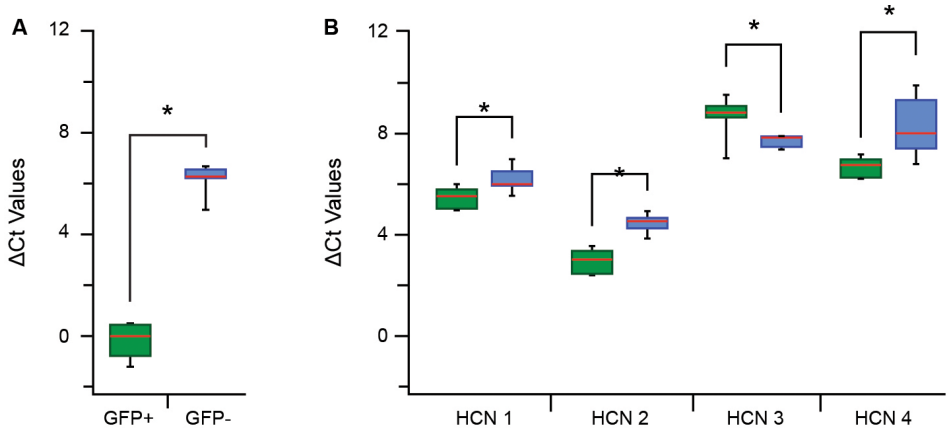

FIGURE 5 | Quantitative polymerase chain reaction (qPCR) ΔCt analysis for hyperpolarization-activated cyclic nucleotide-gated channel (HCN channel) subunits in proprioceptive DRG cells. **(A)** Box and whisker plot show group data comparing ΔCt for GFP expression in GFP+ (green) and GFP− (blue) samples (normalized to β actin expression). The low GFP ΔCt in GFP+, but not GFP−, confirm high expression in this sample and the reliability of this sampling approach. **(B)** Box whisker plots plot shows group data comparing ΔCt values for HCN1–4 in GFP+ (green) and GFP− (blue) samples. The expression of all HCN subunits was significantly different between GFP+ and GFP− groups (where $*p < 0.05$). HCN 2 had the greatest overall expression in both samples whilst HCN 3 and 4 were both expressed at much lower levels. Expression levels were highest for HCN 2, then HCN 1 and HCN 4 in the GFP+ sample and these values all exceeded corresponding values in the GFP− samples. In contrast, HCN 3 expression was lower in the GFP+ sample vs. GFP− cells.

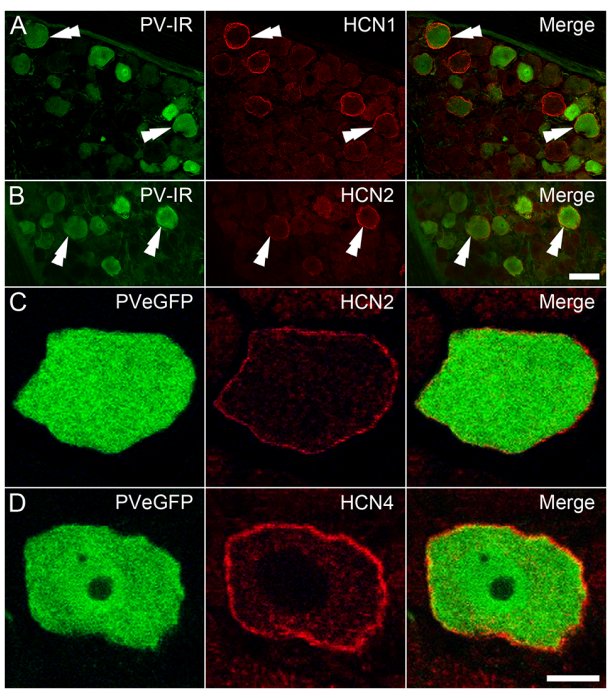

FIGURE 6 | Immunohistochemical localization of HCN subunits in PV-expressing DRG neurons. **(A,B)** PV-IR DRG neurons (green) in wild-type mice were shown to express both HCN1 (**A**; red) and HCN2 (**B**; red), with examples denoted by double arrowheads. **(C,D)** In DRGs from PVeGFP mice, GFP-expressing cells (green) showed immunolabeling for both HCN2 (**C**; red) and HCN4 (**D**; red). Immunolabeling for each of the HCN subunits was restricted to the cell membrane. Scale Bars (μm): **(A,B)** = 50; **(C,D)** = 10.

signaling would require AP discharge at the onset or offset of a stimulus. Their phasic discharge (**Figure 3A**), however, is at odds with the known ability of muscle spindle afferents to support high-frequency firing, especially at the onset and cessation of muscle lengthening.

This above discrepancy presumably relates to a number of factors. First, the use of a long square step stimulus does not reflect the way neurons are excited *in vivo* with different stimulus profiles shown to produce different responses depending on other neuronal populations (Graham et al., 2004). Second, our recordings were made from the soma of isolated sensory neurons vs. an intact preparation. *In vivo*, AP generation occurs in peripheral terminals and is conducted in a centrally-projecting axon that is linked to the soma of sensory neurons. The excitability of the terminal and axon of proprioceptive fibers, missing in our preparation, maybe more important for determining the firing pattern. Nevertheless, reduced somatic DRG preparations continue to be a useful approach to assay the proteins and channels expressed by different afferent types. Finally, there is evidence that neurons can undergo changes in reduced or isolated preparations that potentially alter the suite of ion channels that support AP generation and/or repetitive discharge (Turrigiano et al., 1994; Hayar et al., 2008; Werner et al., 2012). Future experiments that deliver short depolarizing steps at high frequency, ramps, and stimuli with other profiles would allow exploration of the capacity of GFP+ neurons to support firing modes and frequencies observed *in vivo*. In the future, it may also be possible to record directly from the peripheral terminals of GFP− labeled proprioceptors. These would be heroic experiments, however, such recordings have been made from the terminals of peripheral sensory nerves in the cornea (Carr et al., 2009).

In addition to the above differences in patterns of discharge, there were also marked differences in individual AP characteristics between the two groups of neurons in our study. APs in GFP+ neurons had faster kinetics, based on AP rise time and half-width (**Figure 3C**). This finding is consistent with

data from numerous studies showing large-diameter neurons (like the proprioceptive population) generate narrow APs and respond to much lower stimulation intensities than other DRG cell types (Fang et al., 2005). These properties are also consistent with a role in proprioceptive signaling, where fast and repetitive AP generation is required in response to changes in muscle length (muscle spindles) and/or force (Golgi tendon organs). Similarly, the broader APs in GFP− neurons match the function of high threshold receptors, such as nociceptors, recorded from intact DRG neurons *in vivo* (Djouhri et al., 1998).

Our assessment of I_h showed this current to be present in all GFP+ neurons vs. only ∼10% of GFP− neurons. This is consistent with early work which showed significant I_h in most large sensory neurons (putative proprioceptors; Scroggs et al., 1994). It also fits with the role hyperpolarization-activated cationic currents play in high-frequency AP discharge, as occurs in the spindle and GTO afferents (Moosmang et al., 2001; Stevens et al., 2001; Notomi and Shigemoto, 2004; Baruscotti et al., 2005). As multiple HCN channel subunits exist and shape the properties of I_h currents, we investigated both amplitude and activation rates of this current (based on fitting exponentials to current onset; **Figure 4D**). GFP+ neurons exhibited a range of I_h amplitudes (**Figure 4E**) and activation rates (**Figure 4F**), consistent with the expression of different HCN channels/subunits (Acosta et al., 2012; Hughes et al., 2013). Molecular analysis showed all four HCN subunits could be detected in isolated sensory neurons (both GFP+ and GFP− neurons; **Figure 5**). However, expression profiles were distinct between the GFP+ and GFP− samples. Specifically, HCN 2, 1, and 4 expressions (listed in descending levels based on ΔCt values; **Figure 5B**) were higher in GFP+ vs. GFP− neurons. Alternatively, HCN 3 expression was higher in the GFP− population. Recent data on HCN 3 subunits (Lainez et al., 2019) suggest the expression of HCN 3 in the GFP− population is not important for (small) c-fiber afferents, rather it plays a role in setting excitability in medium-sized neurons that conduct in the δ and Aβ range (i.e., not muscle spindle and GTO afferents; Lawson, 2002). This finding marries well with the similar cell diameters of GFP and GFP− neurons in our sample. It also suggests or recordings in GFP− neurons may have been biased towards the larger δ and Aβ DRG cell types, as opposed to the much smaller c-fiber cell population. In contrast, HCN 2 and 1 were highly expressed in GFP+ neurons These observations were also validated at the protein level, with immunolabeling for HCN1, 2, and 4 resolved in PV positive DRG cells. Furthermore, the proportion of PV DRG cells expressing HCN 1 and 2 mirrored mRNA levels and suggested a degree of heterogeneity in subunit expression among proprioceptive afferents identified by PV expression.

Expression patterns favoring HCN1 and 2 subunits also agree with functional data indicating these subunits exhibit the fastest activation rates of the four HCN isoforms (Jiang et al., 2008), correlating with the fast I_h activation times we recorded in many GFP+ neurons (**Figure 4F**). This also fits with the high *in vivo* discharge rates recorded in proprioceptors because fast HCN channel activation rates elevate resting potential and AP firing frequency (Pape and McCormick, 1989; Pape, 1996; Ludwig et al., 2003; Nolan et al., 2003; Chan et al., 2004; Momin et al., 2008). The higher levels of HCN 4 in GFP+ neurons (vs. GFP− neurons) also match a proposed association between these subunits with high discharge rates (Hughes et al., 2013).

Of course, our examination of the contribution of I_h and HCN subunits to GFP+ and GFP− neuron function comes with several caveats. First, we could not determine if the peripheral axon of GFP+ neurons was in fact connected to a proprioceptor (muscle spindle or GTO) due to the dissociated nature of the preparation employed here. This limitation could be addressed in future experiments by making recordings from an *ex vivo* preparation consisting of a DRG—peripheral nerve—peripheral organ. Such preparations were originally developed to study sensory neurons connected to tactile and nociceptive afferents in the skin (Woodbury et al., 2001). More recently an attached *ex vivo* muscle preparation was used to study nociceptors in the muscle (Jankowski et al., 2013). The use of an *ex vivo* muscle preparation in combination with stimuli that selectively activate muscle spindles or GTOs (e.g., ramped muscle stretch) and targeted recording from neurons in DRGs from the PVGFP mouse could address this issue. Achieving visualized high-resolution patch-clamp recordings from GFP+ neurons would also necessitate gentle treatment of DRGs with enzymes that loosen connective tissue and allow for patch pipette access as successfully employed in other ganglia (Yawo, 1989).

A second limitation relates to the population contrasted against the GFP+ proprioceptive neurons, which was a mixed population selected at random, presumably including recordings from a range of afferent types. This would have limited our ability to resolve distinct proprioceptive properties from a mixed control sample. Testing the responsiveness of control (GFP−) recordings to modality-specific agonists such as capsaicin, icilin, menthol, chloroquine, or temperature changes could be used to further dissect this population. Despite this, our analysis of the falling phase of APs did detect biphasic repolarization in many GFP− cells, confirming a depolarization hump associated with nociceptive afferents. Given the similarity of soma size between samples, these are more likely to represent δ than c-fiber nociceptors. Finally, our examination of the HCN subunit expression was undertaken on populations of pooled cells. Thus, the higher expression could reflect elevated expression across one sample or very high expression in a subset of cells. Our immunolabeling data goes some way to addressing this issue, showing that only subsets of PV cells express HCN1 and 2 (∼45% vs. 65%, respectively), supporting heterogeneity within the PV population. This could be further explored by characterizing I_h properties in *single* dissociated neurons (GFP+ and GFP−) and subsequent single-cell qPCR analysis for HCN expression. These data would also speak to our conclusion that a range of I_h amplitudes and activation rates (**Figure 4**) implies distinct proprioceptive types can be differentiated within GFP+ neurons, based on their HCN channel profiles.

In summary, this study was motivated by the notion that distinct properties in a sensory neuron population are likely to impart modality-specific function and as such, may represent targets to alter function in that neuron population. This strategy's value has been highlighted in the successful targeting of sensory neurons involved in nociception and pain (Haberberger et al., 2019). We asked what properties might distinguish proprioceptive neurons from other afferents because a better understanding of these features will be relevant to the well-known age-related decline in proprioceptive function and the increased incidence of falls (Greaves et al., 1991; Kim et al., 2007; Rosant et al., 2007; Wingert et al., 2014). Our analysis of proprioceptive neurons, identified by PV expression, show they indeed have a range of different properties to putative non-proprioceptive neurons. However, the proprioceptive neuron population was not homogeneous, at least based on the expression of HCN channel subtypes. Notwithstanding these limitations, our study provides a foundation for future studies on the excitability of proprioceptive afferents and how they change with age and/or under sensorimotor pathologies.

DATA AVAILABILITY STATEMENT

All datasets generated for this study are included in the article.

ETHICS STATEMENT

All experimental procedures performed at the University of Newcastle were approved by The University of Newcastle Animal Care and Ethics Committee under Section 25 of the NSW Animal Research Act, 1985. All experimental procedures performed at the University of Glasgow were conducted in accordance with the European Community directive 86/609/EEC and UK Animals (Scientific Procedures) Act 1986.

AUTHOR CONTRIBUTIONS

JM, RC, PJ, DH, DS, and BG conceived and designed the research study. JM, OD, and KB conducted experiments and acquired data. JM, TB, JI, RC, OD, KB, and BG analyzed data. JM, TB, RC, DH, and BG wrote the manuscript. All authors edited the final version of the manuscript.

FUNDING

This work was funded by the National Health and Medical Research Council (NHMRC) of Australia (Grants 631000, 1043933, 1144638, and 1184974 to BG and RC), the Biotechnology and Biological Sciences Research Council (BB/J000620/1, BB/P007996/1 to DH) and the Hunter Medical Research Institute (Glenn Moss grant to BG).

REFERENCES

Acar, F., Miller, J., Golshani, K. J., Israel, Z. H., McCartney, S., and Burchiel, K. J. (2008). Pain relief after cervical ganglionectomy (C2 and C3) for the treatment of medically intractable occipital neuralgia. *Stereotact. Funct. Neurosurg.* 86, 106–112. doi: 10.1159/000113872

Acosta, C., McMullan, S., Djouhri, L., Gao, L., Watkins, R., Berry, C., et al. (2012). HCN1 and HCN2 in Rat DRG neurons: levels in nociceptors and non-nociceptors, NT3-dependence and influence of CFA-induced skin inflammation on HCN2 and NT3 expression. *PLoS One* 7:e50442. doi: 10.1371/journal.pone.0050442

Arber, S., Ladle, D. R., Lin, J. H., Frank, E., and Jessell, T. M. (2000). ETS gene Er81 controls the formation of functional connections between group Ia sensory afferents and motor neurons. *Cell* 101, 485–498. doi: 10.1016/s0092-8674(00)80859-4

Baruscotti, M., Bucchi, A., and Difrancesco, D. (2005). Physiology and pharmacology of the cardiac pacemaker ("funny") current. *Pharmacol. Ther.* 107, 59–79. doi: 10.1016/j.pharmthera.2005.01.005

Berta, T., Qadri, Y., Tan, P. H., and Ji, R. R. (2017). Targeting dorsal root ganglia and primary sensory neurons for the treatment of chronic pain. *Expert Opin. Ther. Targets* 21, 695–703. doi: 10.1080/14728222.2017.1328057

Carr, R. W., Pianova, S., McKemy, D. D., and Brock, J. A. (2009). Action potential initiation in the peripheral terminals of cold-sensitive neurones innervating the guinea-pig cornea. *J. Physiol.* 587, 1249–1264. doi: 10.1113/jphysiol.2008.167023

Celio, M. R. (1990). Calbindin D-28k and parvalbumin in the rat nervous system. *Neuroscience* 35, 375–475. doi: 10.1016/0306-4522(90)90091-h

Chan, C. S., Shigemoto, R., Mercer, J. N., and Surmeier, D. J. (2004). HCN2 and HCN1 channels govern the regularity of autonomous pacemaking and synaptic resetting in globus pallidus neurons. *J. Neurosci.* 24, 9921–9932. doi: 10.1523/JNEUROSCI.2162-04.2004

Deer, T. R., Grigsby, E., Weiner, R. L., Wilcosky, B., and Kramer, J. M. (2013). A prospective study of dorsal root ganglion stimulation for the relief of chronic pain. *Neuromodulation* 16, 67–71; discussion 71–62. doi: 10.1111/ner.12013

de Louw, A. J., Vles, H. S., Freling, G., Herpers, M. J., Arends, J. W., and Kleef, M. (2001). The morphological effects of a radio frequency lesion adjacent to the dorsal root ganglion (RF-DRG)—an experimental study in the goat. *Eur. J. Pain* 5, 169–174. doi: 10.1053/eujp.2001.0228

Delhaye, B. P., Long, K. H., and Bensmaia, S. J. (2018). Neural basis of touch and proprioception in primate cortex. *Compr. Physiol.* 8, 1575–1602. doi: 10.1002/cphy.c170033

de Nooij, J. C., Doobar, S., and Jessell, T. M. (2013). Etv1 inactivation reveals proprioceptor subclasses that reflect the level of NT3 expression in muscle targets. *Neuron* 77, 1055–1068. doi: 10.1016/j.neuron.2013.01.015

Dini, L., Del Lungo, M., Resta, F., Melchiorre, M., Spinelli, V., Di Cesare Mannelli, L., et al. (2018). Selective blockade of HCN1/HCN2 channels as a potential pharmacological strategy against pain. *Front. Pharmacol.* 9:1252. doi: 10.3389/fphar.2018.01252

Djouhri, L., Bleazard, L., and Lawson, S. N. (1998). Association of somatic action potential shape with sensory receptive properties in guinea-pig dorsal root ganglion neurones. *J. Physiol.* 513, 857–872. doi: 10.1111/j.1469-7793.1998.857ba.x

Doan, T. N., and Kunze, D. L. (1999). Contribution of the hyperpolarization-activated current to the resting membrane potential of rat nodose sensory neurons. *J. Physiol.* 514, 125–138. doi: 10.1111/j.1469-7793.1999.125af.x

Ernfors, P., Lee, K. F., Kucera, J., and Jaenisch, R. (1994). Lack of neurotrophin-3 leads to deficiencies in the peripheral nervous system and loss of limb proprioceptive afferents. *Cell* 77, 503–512. doi: 10.1016/0092-8674(94)90213-5

Fang, X., McMullan, S., Lawson, S. N., and Djouhri, L. (2005). Electrophysiological differences between nociceptive and non-nociceptive dorsal root ganglion neurones in the rat *in vivo*. *J. Physiol.* 565, 927–943. doi: 10.1113/jphysiol.2005.086199

Gao, L. L., McMullan, S., Djouhri, L., Acosta, C., Harper, A. A., and Lawson, S. N. (2012). Expression and properties of hyperpolarization-activated current in rat

dorsal root ganglion neurons with known sensory function. *J. Physiol.* 590, 4691–4705. doi: 10.1113/jphysiol.2012.238485

Gradwell, M. A., Boyle, K. A., Callister, R. J., Hughes, D. I., and Graham, B. A. (2017). Heteromeric α/β glycine receptors regulate excitability in parvalbumin-expressing dorsal horn neurons through phasic and tonic glycinergic inhibition. *J. Physiol.* 595, 7185–7202. doi: 10.1113/jp274926

Graham, B. A., Brichta, A. M., and Callister, R. J. (2004). *in vivo* responses of mouse superficial dorsal horn neurones to both current injection and peripheral cutaneous stimulation. *J. Physiol.* 561, 749–763. doi: 10.1113/jphysiol.2004.072645

Greaves, D. S., Dufresne, M. J., Fackrell, H. B., and Warner, A. H. (1991). Age-related changes and tissue distribution of parvalbumin in normal and dystrophic mice of strain 129 ReJ. *Muscle Nerve* 14, 543–552. doi: 10.1002/mus.880140609

Haberberger, R. V., Barry, C., Dominguez, N., and Matusica, D. (2019). Human dorsal root ganglia. *Front. Cell. Neurosci.* 13:271. doi: 10.3389/fncel.2019.00271

Hayar, A., Gu, C., and Al-Chaer, E. D. (2008). An improved method for patch clamp recording and calcium imaging of neurons in the intact dorsal root ganglion in rats. *J. Neurosci. Methods* 173, 74–82. doi: 10.1016/j.jneumeth.2008.05.023

Honda, C. N. (1995). Differential distribution of calbindin-D28k and parvalbumin in somatic and visceral sensory neurons. *Neuroscience* 68, 883–892. doi: 10.1016/0306-4522(95)00180-q

Horwitz, G. C., Risner-Janiczek, J. R., Jones, S. M., and Holt, J. R. (2011). HCN channels expressed in the inner ear are necessary for normal balance function. *J. Neurosci.* 31, 16814–16825. doi: 10.1523/JNEUROSCI.3064-11.2011

Hu, P., and McLachlan, E. M. (2002). Macrophage and lymphocyte invasion of dorsal root ganglia after peripheral nerve lesions in the rat. *Neuroscience* 112, 23–38. doi: 10.1016/s0306-4522(02)00065-9

Hughes, D. I., Boyle, K. A., Kinnon, C. M., Bilsland, C., Quayle, J. A., Callister, R. J., et al. (2013). HCN4 subunit expression in fast-spiking interneurons of the rat spinal cord and hippocampus. *Neuroscience* 237, 7–18. doi: 10.1016/j.neuroscience.2013.01.028

Hughes, D. I., Sikander, S., Kinnon, C. M., Boyle, K. A., Watanabe, M., Callister, R. J., et al. (2012). Morphological, neurochemical and electrophysiological features of parvalbumin-expressing cells: a likely source of axo-axonic inputs in the mouse spinal dorsal horn. *J. Physiol.* 590, 3927–3951. doi: 10.1113/jphysiol.2012.235655

Ichikawa, H., Deguchi, T., Nakago, T., Jacobowitz, D. M., and Sugimoto, T. (1994). Parvalbumin, calretinin and carbonic anhydrase in the trigeminal and spinal primary neurons of the rat. *Brain Res.* 655, 241–245. doi: 10.1016/0006-8993(94)91620-9

Ichikawa, H., Mo, Z., Xiang, M., and Sugimoto, T. (2004). Effect of Brn-3a deficiency on parvalbumin-immunoreactive primary sensory neurons in the dorsal root ganglion. *Dev. Brain Res.* 150, 41–45. doi: 10.1016/j.devbrainres.2004.02.004

Jankowski, M. P., Rau, K. K., Ekmann, K. M., Anderson, C. E., and Koerber, H. R. (2013). Comprehensive phenotyping of group III and IV muscle afferents in mouse. *J. Neurophysiol.* 109, 2374–2381. doi: 10.1152/jn.01067.2012

Jiang, Y. Q., Sun, Q., Tu, H. Y., and Wan, Y. (2008). Characteristics of HCN channels and their participation in neuropathic pain. *Neurochem. Res.* 33, 1979–1989. doi: 10.1007/s11064-008-9717-6

Kim, G. H., Suzuki, S., and Kanda, K. (2007). Age-related physiological and morphological changes of muscle spindles in rats. *J. Physiol.* 582, 525–538. doi: 10.1113/jphysiol.2007.130120

Klein, D., Bugl, B., Gunzburg, W. H., and Salmons, B. (2000). Accurate estimation of transduction efficiency necessitates a multiplex real-time PCR. *Gene Ther.* 7, 458–463. doi: 10.1038/sj.gt.3301112

Krames, E. S. (2014). The role of the dorsal root ganglion in the development of neuropathic pain. *Pain Med.* 15, 1669–1685. doi: 10.1111/pme.12413

Lainez, S., Tsantoulas, C., Biel, M., and McNaughton, P. A. (2019). HCN3 ion channels: roles in sensory neuronal excitability and pain. *J. Physiol.* 597, 4661–4675. doi: 10.1113/jp278211

Lawson, S. N. (2002). Phenotype and function of somatic primary afferent nociceptive neurones with C-, Aδ- or Aα/β-fibres. *Exp. physiol.* 87, 239–244. doi: 10.1113/eph8702350

Lawson, S. N. (2005). "The peripheral sensory nervous system: dorsal root ganglion neurons," in *Peripheral Neuropathy (Fourth Edition)*, eds P. J. Dyck and P. K. Thomas (Philadelphia, WB: Saunders), 163–202.

Ludwig, A., Budde, T., Stieber, J., Moosmang, S., Wahl, C., Holthoff, K., et al. (2003). Absence epilepsy and sinus dysrhythmia in mice lacking the pacemaker channel HCN2. *EMBO J.* 22, 216–224. doi: 10.1093/emboj/cdg032

Manchikanti, L. (2000). Transforaminal lumbar epidural steroid injections. *Pain Physician* 3, 374–398.

Meyer, A. H., Katona, I., Blatow, M., Rozov, A., and Monyer, H. (2002). *in vivo* labeling of parvalbumin-positive interneurons and analysis of electrical coupling in identified neurons. *J. Neurosci.* 22, 7055–7064. doi: 10.1523/JNEUROSCI.22-16-07055.2002

Momin, A., Cadiou, H., Mason, A., and McNaughton, P. A. (2008). Role of the hyperpolarization-activated current Ih in somatosensory neurons. *J. Physiol.* 586, 5911–5929. doi: 10.1113/jphysiol.2008.163154

Moosmang, S., Stieber, J., Zong, X., Biel, M., Hofmann, F., and Ludwig, A. (2001). Cellular expression and functional characterization of four hyperpolarization-activated pacemaker channels in cardiac and neuronal tissues. *Eur. J. Biochem.* 268, 1646–1652. doi: 10.1046/j.1432-1327.2001.02036.x

Nash, T. P. (1986). Percutaneous radiofrequency lesioning of dorsal root ganglia for intractable pain. *Pain* 24, 67–73. doi: 10.1016/0304-3959(86)90027-8

Nolan, M. F., Malleret, G., Lee, K. H., Gibbs, E., Dudman, J. T., Santoro, B., et al. (2003). The hyperpolarization-activated HCN1 channel is important for motor learning and neuronal integration by cerebellar Purkinje cells. *Cell* 115, 551–564. doi: 10.1016/s0092-8674(03)00884-5

Notomi, T., and Shigemoto, R. (2004). Immunohistochemical localization of Ih channel subunits, HCN1–4, in the rat brain. *J. Comp. Neurol.* 471, 241–276. doi: 10.1002/cne.11039

Pape, H. C. (1996). Queer current and pacemaker: the hyperpolarization-activated cation current in neurons. *Annu. Rev. Physiol.* 58, 299–327. doi: 10.1146/annurev.ph.58.030196.001503

Pape, H. C., and McCormick, D. A. (1989). Noradrenaline and serotonin selectively modulate thalamic burst firing by enhancing a hyperpolarization-activated cation current. *Nature* 340, 715–718. doi: 10.1038/340715a0

Rosant, C., Nagel, M. D., and Pérot, C. (2007). Aging affects passive stiffness and spindle function of the rat soleus muscle. *Exp. Gerontol.* 42, 301–308. doi: 10.1016/j.exger.2006.10.007

Scroggs, R. S., Todorovic, S. M., Anderson, E. G., and Fox, A. P. (1994). Variation in IH, IIR, and ILEAK between acutely isolated adult rat dorsal root ganglion neurons of different size. *J. Neurophysiol.* 71, 271–279. doi: 10.1152/jn.1994.71.1.271

Stevens, D. R., Seifert, R., Bufe, B., Müller, F., Kremmer, E., Gauss, R., et al. (2001). Hyperpolarization-activated channels HCN1 and HCN4 mediate responses to sour stimuli. *Nature* 413, 631–635. doi: 10.1038/35098087

Tsantoulas, C., Laínez, S., Wong, S., Mehta, I., Vilar, B., and McNaughton, P. A. (2017). Hyperpolarization-activated cyclic nucleotide-gated 2 (HCN2) ion channels drive pain in mouse models of diabetic neuropathy. *Sci. Transl. Med.* 9:eaam6072. doi: 10.1126/scitranslmed.aam6072

Turrigiano, G., Abbott, L. F., and Marder, E. (1994). Activity-dependent changes in the intrinsic properties of cultured neurons. *Science* 264, 974–977. doi: 10.1126/science.8178157

Vad, V. B., Bhat, A. L., Lutz, G. E., and Cammisa, F. (2002). Transforaminal epidural steroid injections in lumbosacral radiculopathy: a prospective randomized study. *Spine* 27, 11–16. doi: 10.1097/00007632-200201010-00005

Van Zundert, J., Patijn, J., Kessels, A., Lamé, I., van Suijlekom, H., and van Kleef, M. (2007). Pulsed radiofrequency adjacent to the cervical dorsal root ganglion in chronic cervical radicular pain: a double blind sham controlled randomized clinical trial. *Pain* 127, 173–182. doi: 10.1016/j.pain.2006.09.002

Wang, Z., Van den Berg, R. J., and Ypey, D. L. (1994). Resting membrane potentials and excitability at different regions of rat dorsal root ganglion

neurons in culture. *Neuroscience* 60, 245–254. doi: 10.1016/0306-4522(94)90218-6

Werner, M., Van De Water, T. R., Andersson, T., Arnoldsson, G., and Berggren, D. (2012). Morphological and morphometric characteristics of vestibular hair cells and support cells in long term cultures of rat utricle explants. *Hear. Res.* 283, 107–116. doi: 10.1016/j.heares.2011.11.003

Wingert, J. R., Welder, C., and Foo, P. (2014). Age-related hip proprioception declines: effects on postural sway and dynamic balance. *Arch. Phys. Med. Rehabil.* 95, 253–261. doi: 10.1016/j.apmr.2013.08.012

Woodbury, C. J., Ritter, A. M., and Koerber, H. R. (2001). Central anatomy of individual rapidly adapting low-threshold mechanoreceptors innervating the "hairy" skin of newborn mice: early maturation of hair follicle afferents. *J. Comp. Neurol.* 436, 304–323. doi: 10.1002/cne.1069

Wu, X., Liao, L., Liu, X., Luo, F., Yang, T., and Li, C. (2012). Is ZD7288 a selective blocker of hyperpolarization-activated cyclic nucleotide-gated channel currents? *Channels* 6, 438–442. doi: 10.4161/chan.22209

Xu, Z. Q., Zhang, X., Grillner, S., and Hökfelt, T. (1997). Electrophysiological studies on rat dorsal root ganglion neurons after peripheral axotomy: changes in responses to neuropeptides. *Proc. Natl. Acad. Sci. U S A* 94, 13262–13266. doi: 10.1073/pnas.94.24.13262

Yawo, H. (1989). Rectification of synaptic and acetylcholine currents in the mouse submandibular ganglion cells. *J. Physiol.* 417, 307–322. doi: 10.1113/jphysiol.1989.sp017803

Young, G. T., Emery, E. C., Mooney, E. R., Tsantoulas, C., and McNaughton, P. A. (2014). Inflammatory and neuropathic pain are rapidly suppressed by peripheral block of hyperpolarisation-activated cyclic nucleotide-gated ion channels. *Pain* 155, 1708–1719. doi: 10.1016/j.pain.2014.05.021

Conflict of Interest: The authors declare that the research was conducted in the absence of any commercial or financial relationships that could be construed as a potential conflict of interest.

Copyright © 2020 Madden, Davies, Boyle, Iredale, Browne, Callister, Smith, Jobling, Hughes and Graham. This is an open-access article distributed under the terms of the Creative Commons Attribution License (CC BY). The use, distribution or reproduction in other forums is permitted, provided the original author(s) and the copyright owner(s) are credited and that the original publication in this journal is cited, in accordance with accepted academic practice. No use, distribution or reproduction is permitted which does not comply with these terms.

Advantages of publishing in Frontiers

OPEN ACCESS
Articles are free to read for greatest visibility and readership

FAST PUBLICATION
Around 90 days from submission to decision

HIGH QUALITY PEER-REVIEW
Rigorous, collaborative, and constructive peer-review

TRANSPARENT PEER-REVIEW
Editors and reviewers acknowledged by name on published articles

Frontiers
Avenue du Tribunal-Fédéral 34
1005 Lausanne | Switzerland

Visit us: www.frontiersin.org
Contact us: frontiersin.org/about/contact

REPRODUCIBILITY OF RESEARCH
Support open data and methods to enhance research reproducibility

DIGITAL PUBLISHING
Articles designed for optimal readership across devices

FOLLOW US
@frontiersin

IMPACT METRICS
Advanced article metrics track visibility across digital media

EXTENSIVE PROMOTION
Marketing and promotion of impactful research

LOOP RESEARCH NETWORK
Our network increases your article's readership